

Chemistry and Physics of Energetic Materials

NATO ASI Series

Advanced Science Institutes Series

A Series presenting the results of activities sponsored by the NATO Science Committee, which aims at the dissemination of advanced scientific and technological knowledge, with a view to strengthening links between scientific communities.

The Series is published by an international board of publishers in conjunction with the NATO Scientific Affairs Division

A Life Sciences

Plenum Publishing Corporation

B Physics

London and New York

**C Mathematical
and Physical Sciences**

Kluwer Academic Publishers
Dordrecht, Boston and London

D Behavioural and Social Sciences

E Applied Sciences

F Computer and Systems Sciences

Springer-Verlag

G Ecological Sciences

Berlin, Heidelberg, New York, London,

H Cell Biology

Paris and Tokyo



Chemistry and Physics of Energetic Materials

edited by

Surya N. Bulusu

Energetic and Warheads Division,
Armaments Engineering Directorate,
U.S. Army Armament Research,
Development and Engineering Center (ARDEC),
Picatinny Arsenal, NJ, U.S.A.



Kluwer Academic Publishers

Dordrecht / Boston / London

Published in cooperation with NATO Scientific Affairs Division

Proceedings of the NATO Advanced Study Institute on
Chemistry and Physics of the Molecular Processes in Energetic Materials
Altavilla Milicia, Sicily, Italy
September 3–15, 1989

Library of Congress Cataloging in Publication Data

NATO Advanced Study Institute on Chemistry and Physics of the
Molecular Processes in Energetic Materials (1989 : Altavilla
Milicia, Italy)
Chemistry and physics of energetic materials : proceedings of the
NATO Advanced Study Institute on Chemistry and Physics of the
Molecular Processes in Energetic Materials, Altavilla Milicia,
Sicily, Italy, September 3–15, 1989 / edited by Surya N. Bulusu.
p. cm. -- (NATO ASI series. Series C, Mathematical and
physical sciences ; v. 309)
"Published in cooperation with NATO Scientific Affairs Divisions."
1. Combustion--Congresses. 2. Thermodynamics--Congresses.
3. Explosives--Congresses. 4. Propellants--Congresses. I. Bulusu,
Surya N., 1927- . II. North Atlantic Treaty Organization.
Scientific Affairs Division. III. Title. IV. Series: NATO advanced
study institutes series. Series C, Mathematical and physical
sciences ; v. 309.
QD516.N318 1989
541.3'61--dc20 90-4356

ISBN-13: 978-94-010-7413-1 e-ISBN-13: 978-94-009-2035-4

DOI: 10.1007/978-94-009-2035-4

Published by Kluwer Academic Publishers,
P.O. Box 17, 3300 AA Dordrecht, The Netherlands.

Kluwer Academic Publishers incorporates the publishing programmes of
D. Reidel, Martinus Nijhoff, Dr W. Junk and MTP Press.

Sold and distributed in the U.S.A. and Canada
by Kluwer Academic Publishers,
101 Philip Drive, Norwell, MA 02061, U.S.A.

In all other countries, sold and distributed
by Kluwer Academic Publishers Group,
P.O. Box 322, 3300 AH Dordrecht, The Netherlands.

Printed on acid-free paper

All Rights Reserved
© 1990 by Kluwer Academic Publishers
Softcover reprint of the hardcover 1st edition 1990

No part of the material protected by this copyright notice may be reproduced or
utilized in any form or by any means, electronic or mechanical, including photo-
copying, recording or by any information storage and retrieval system, without written
permission from the copyright owner.

CONTENTS

Preface	ix
Organizing Committee & Cosponsors	xi
1. Fundamental Principles of Thermal Explosions and Recent Applications Peter Gray	1
2. Modelling Isothermal Waves of Chemical Reaction Peter Gray	13
3. Thermochemical Modeling: I. Application to Decomposition of Energetic Materials Carl F. Melius	21
4. Thermochemical Modeling: II. Application to Ignition and Combustion of Energetic Materials Carl F. Melius	51
5. Fundamental Physics and Chemistry Behind Molecular Crystal Detonations at a Microscopic Level Simone Odier	79
6. On the $X\alpha$ Local Spin Density Approximation in the Study of Organic Molecules S. Fliszar	131
7. On the Dissociation of Chemical Bonds S. Fliszar	143
8. Structure-Sensitivity Relationships in Energetic Compounds J.S. Murray and P. Politzer	157
9. Computational Studies of Energetic Nitramines J.S. Murray and P. Politzer	175
10. Molecular Dynamics Approach to Detonation Studies and Related Problems in the Condensed Phase D.H. Tsai	195
11. Molecular Dynamical Studies of Energy Transport and Energy Sharing in Molecular Dissociation D.H. Tsai	229

12. Fast Thermolysis-Fourier Transform Infrared Spectroscopy Methods to Study Energetic Materials Thomas B. Brill	255
13. Structure-Thermolysis Relationships for Energetic Materials Thomas B. Brill	277
14. The Application of Simultaneous Thermogravimetric Modulated Beam Mass Spectrometry and Time-of-flight Velocity Spectra Measurements to the Study of the Pyrolysis of Energetic Materials Richard Behrens	327
15. Thermal Decomposition of HMX and RDX: Decomposition Processes and Mechanisms Based on STMBMS and TOF Velocity-Spectra Measurements Richard Behrens	347
16. The Diamond Anvil Cell for Physical and Chemical Investigations of Energetic Materials at High Pressures Gasper J. Piermarini, Stanley Block, and Philip J. Miller	369
17. Effects of Pressure on the Thermal Decomposition Rates, Chemical Reactivity, and Phase Behavior of HMX, RDX and Nitromethane Gasper J. Piermarini, Stanley Block, and Philip J. Miller	391
18. Mechanistic Investigations of Condensed Phase Energetic Material Decomposition Processes using the Kinetic Deuterium Isotope Effect Scott A. Shackelford	413
19. Mechanistic Relationships of the Decomposition Process to Combustion and Explosion Events from Kinetic Deuterium Isotope Effect Investigations Scott A. Shackelford	433
20. KIVA Reactive Hydrodynamics Code Applied to Detonations in High Vacuum N. Roy Greiner	457
21. Detonation Chemistry Studies of Energetic Materials using Laboratory Scale Samples N.C. Blais, N.R. Greiner, and W.J. Fernandez	477
22. Analysis of Reaction Products of Propellants and High Explosives F. Volk	511

23. Chemical Sensitisation in Nitro, Nitramine, and Nitrate Explosives J. Connor	525
24. The Response of Energetic Materials to Projectile Impact J. Connor	545
25. Fundamentals of X-Ray Photoelectron Spectroscopy (XPS) and its Applications to Explosives and Propellants J. Sharma and B.C. Beard	569
26. XPS Study of Hot Spots and Sensitization Centers in Energetic Materials J. Sharma and B.C. Beard	587
27. Sensitivity Relationships in Energetic Materials C.B. Storm, J.R. Stine, and J.F. Kramer	605
28. Molecular Architecture Versus Chemistry and Physics of Energetic Materials Jack Alster, Sury Iyer, and Oscar Sandus	641
29. Emission Spectroscopy as a Tool to Detect Decomposition Products of Laser Irradiated Explosives B.J. van der Meer	653
30. Tandem Mass Spectrometry (MS/MS) and Collision Induced Dissociation (CID) - An Introduction J. Yinon	685
31. MS/MS of Energetic Compounds: Collision Induced Dissociation (CID) Studies of Fragmentation Processes in Energetic Molecules J. Yinon	695
32. NQR/NMR Studies of Solid Phase Energetic Materials Robert A. Marino	715
List of Participants	739
Subject Index	747

PREFACE

This book represents a collection of lectures presented at the NATO Advanced Study Institute(ASI) on "Chemistry & Physics of the Molecular Processes in Energetic Materials", held at Hotel Torre Normanna, Altavilla Milicia, Sicily, Italy, September 3 to 15, 1989. The institute was attended by seventy participants including twenty lecturers, drawn from thirteen countries.

The purpose of the institute was to review the major advances made in recent years in the theoretical and experimental aspects of explosives and propellants. In accordance with the format of the NATO ASI, it was arranged to have a relatively small number of speakers to present in depth, review type lectures emphasizing the basic research aspects of the subject, over a two week period. Most of the speakers gave two lectures, each in excess of one hour with additional time for discussions. The scope of the meeting was limited to molecular and spectroscopic studies since the hydrodynamic aspects of detonation and various performance criteria of energetic materials are often covered adequately in other international meetings. An attempt was made to have a coherent presentation of various theoretical, computational and spectroscopic approaches to help a better understanding of energetic materials from a molecular point of view. The progress already made in these areas is such that structure-property (e.g., sensitivity) relationships are now predictable to enable tailoring of energetic materials at the molecular level to meet specific criteria of safety and performance. It is hoped that the science of detonation phenomena, the discussions of which were once relegated to classified meetings of defense establishments, has much to gain from being interwoven into open forums on fundamental chemistry and physics. The sponsorship of this meeting by the NATO Scientific Affairs Division presented just such an opportunity and it is gratefully acknowledged.

I am most thankful to Dr. Norman Slagg, Chief, Explosives and Warheads Branch at the ARDEC, for his encouragement and support in organizing this NATO institute. An international meeting such as this takes a considerable effort in planning and organizing. It is a pleasure for me to acknowledge the help and advice I received from a number of individuals in this effort. First, I am very much indebted to Dr. Theodore Axenrod of the City University of New York, for giving me the benefit of his experience in organizing other ASIs in the past. His advice and suggestions in developing the program and planning the logistics of the meeting were invaluable.

able. Equally crucial was the generous help I received from Dr. Guilio Ceccarelli of the University of Pisa in making the arrangements for the conference in Italy. His admirable attention to details was responsible for the smoothness with which the meeting went from the start to finish. The meeting was highly successful and enjoyable due to their diligent efforts and most of all to the valuable contributions made by the authors in this volume and the lively discussions that ensued.

Surya N. Bulusu

**PROCEEDINGS OF THE NATO ADVANCED STUDY INSTITUTE ON CHEMISTRY
AND PHYSICS OF THE MOLECULAR PROCESSES IN ENERGETIC MATERIALS**

Held at : Altavilla Milicia, Sicily, Italy
September 3-15, 1989.

ORGANIZING COMMITTEE :

Surya N. Bulusu (Director) (U.S.A.)
Theodore Axenrod (U.S.A.)
Guilio Ceccarelli (Italy)
Jehuda Yinon (Israel)
Fred Volk (FRG)

COSPONSORS OF THE INSTITUTE :

U.S. Army Armaments Research, Development and Engineering
Center (ARDEC)

U.S. Office of Naval Research (ONR)

Sandia National Laboratory, Livermore

Los Alamos National Laboratory (LANL)

Royal Armament Research and Development Establishment (RARDE)

Naval Surface Warfare Center (NSWC)

U.S. Army Research Office, Europe (ERO)

National Science Foundation (NSF)

FUNDAMENTAL PRINCIPLES OF THERMAL EXPLOSIONS AND RECENT APPLICATIONS

PETER GRAY

University Chemical Laboratory, Lensfield Road,
Cambridge CB2 1EW, U.K.

ABSTRACT. This paper may serve as a useful opening to the Advanced Study Institute because it deals with the most basic of thermal instabilities - the sudden explosion of a uniformly heated mass of material: thermal explosion. Its application to energetic materials is wide, spreading from the autoignition of chemically unstable materials, through combustion processes to the safety of explosives exposed to fire, and to the sustaining of detonation waves. We set out some of the fundamentals, look at some old problems in a new way, and study some new applications, including programmed ambient temperatures.

1. INTRODUCTION

Spontaneous ignition means the sudden inflammation of a uniformly heated mass. It is an autoignition. Just how sudden and how uniformly heated require further consideration but this definition serves to exclude certain problems from an initial survey of the ground. Amongst the exclusions are ignitions by impact, friction, electric sparks, other flames and localized shocks: at the margin stand ignitions by heated surfaces or by hot wires. We are, temporarily at least, excluding systems with sharp temperature-discontinuities.

Spontaneous ignition is widespread. It is best characterized under controlled laboratory conditions, but examples from a host of fields are known [1-4]. We shall be mainly concerned with stationary bodies (no flow, or only low-velocity flow) and with homogeneous systems. The classic studies concerned gaseous systems where a critical reactant pressure had to be exceeded for reaction to change its character from quiescent to explosive. One of the best modern examples is the spontaneous ignition of di-tert-butyl peroxide in decomposition, studied by J. F. Griffiths [5, 6]. It is a system that looks complex to non-chemists but the molecule falls apart in well-understood elementary steps. Bond fissions actually absorb energy. Only the re-assembly of the free-radical fragments involves heat:





Steps (1) and (2) are endothermic; step (3) involves energy equal to the carbon-carbon bond dissociation energy in ethane. There is no bright flash of light: the 'dark ignition' proceeds in a subterranean way. Matters are different when oxygen is present. The same steps again occur but methyl radicals are now oxidized, albeit in a roundabout manner. Amongst the additional steps the following are prominent:



Reactions (4), (5) and (6) immediately compete with reaction (3) - and others as well - so that more energy is released per mole of peroxide reacted, yet the rate of overall reaction is still controlled by the initial O-O bond fission in step (1).

2. CHARACTERISTIC FEATURES

Whether spontaneous ignition is encountered on the large scale or small, certain striking features are frequently displayed [1-3]. Two of these are:

- (a) Induction periods normally precede ignition. During them there is little or no observable change. They can vary from microseconds after a shockwave or detonation, through milliseconds in the hot, gaseous mixture in an automobile engine, to weeks or months in a large bale of wool in a warehouse.
- (b) Special conditions - 'critical' conditions of size or temperature exist which are not intrinsic properties of the hazardous material. Thus long, thin crystals of cadmium azide may be safe when more compact ones of equal mass may explode; a thousand-ton cargo of ammonium nitrate may be dangerous at temperatures where a single 50 kg sack is safe.

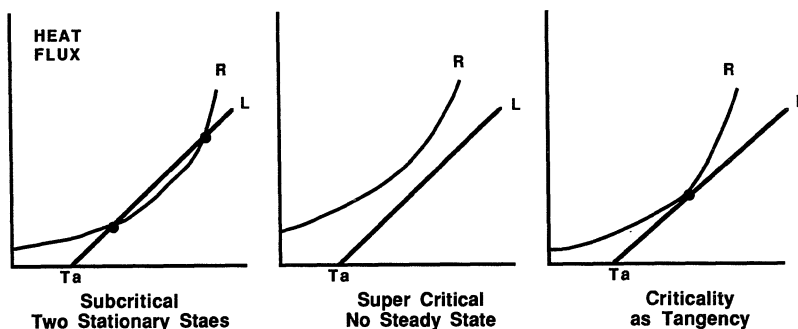
Of all the commonly met factors - shape, size, concentration, intimacy of mixing - it is the temperature to which affairs are nearly always most sensitive. Commonly a system will ignite if it is too hot, or if its surroundings exceed a critical temperature. But it is usually a crude simplification and frequently meaningless to ascribe a critical ignition temperature to any particular substance: its mass, arrangement and its surroundings are all involved. This has been known and emphasized [7] for more than sixty years.

The systems just described are taken as adopting the temperature of their surroundings before evolving much heat. Another frequent circum-

stance sees systems suddenly taken to temperatures above their surroundings. A diesel engine, for example, compresses a combustible gaseous mixture to a temperature above that of the cylinder walls: the manufacture of chipboard ends with piling the hot product in stacks. Similar circumstances attend the laundering of sheets. These generate problems that we shall class together as "hot assembly" [8].

3. THERMAL THEORY OF SPONTANEOUS IGNITION IN CLOSED SYSTEMS

Thermal explosion theory effectively begins with Semenov in 1928. He presented his arguments [7] in terms of a "thermal diagram". Such a picture had been employed earlier in France but not interpreted mathematically.



Semenov's assumptions were: (1) Newtonian heat-losses $L = \chi S(T - T_a)$ and Arrhenius temperature-dependence of heat-release rate by reaction; (2) other features independent of temperature; (3) no reactant consumption. For criticality, $R = L$ and $dR/dT = dL/dT$ simultaneously. So long as $R \propto \exp(-E/RT)$ and $L \propto (T - T_a)$, this leads to the famous expression for the critical self-heating:

$$\Delta T_{cr} = RT_{cr}^2/E \approx RT_a^2/E.$$

This value is small, around 10-20 K. If no heat were lost, less than 1% reactant consumption could suffice to bring a system to criticality.

Numerous developments have been made since these foundations were laid. Nevertheless the central results remain:

- (a) almost any exothermic reaction is potentially explosive - thermal runaway is a hazard that must never be ignored.
- (b) for thermal runaway to be impossible in principle, reaction must either be scarcely exothermic at all ($Q < 5RT_a$, say), or only sluggishly responsive to temperature ($E < 4RT_a$). In practice, systems with $(E/RT_a) < 10$ and $(Q/RT_a < 10)$ are unlikely to do anything startling.

- (c) very little self-heating is required to surpass the bounds of safety:
 $\Delta T_{cr} \approx RT_a^2/E \approx 10 \text{ K}$, say.
- (d) The conditions linking size, concentrations, temperatures, etc. at criticality may be encapsulated in a single dimensionless group, the Semenov number:

$$\frac{EQVC_o \text{ exo } (-E/RT_a)}{LS(RT_a^2/E)} = \psi = \frac{1}{e}$$

- (e) the group (RT_a^2/E) was subsequently adopted as a useful measure of temperature to define dimensionless temperature-excess, Θ :

$$\Theta = (T - T_a)/(RT_a^2/E).$$

In these terms the condition for stationary states is $\Theta e^{-\Theta} = \psi$. Clearly $\psi_{crit} = e^{-1}$, for above this value of ψ stationary states are impossible. In what follows we shall illustrate some recent developments in thermal explosion theory by working in terms of Θ and ψ . One more dimensionless group is particularly important. This is the Zeldovich number, B , that measures the intensity of thermal feedback. If we define Θ in terms of any particular reference temperature T_{rf} , then the group $B = (Qc_o/\sigma c_v)(E/RT_{rf}^2)$, where σ denotes density and c_v^{rf} specific heat capacity, expresses adiabatic temperature rise $(T - T_a)$ in units of (RT_{rf}^2/E) . For ignition we choose $T_{rf} = T_a$; for extinctions, $T_{rf} = T_{ad}$. The group $B' = \Delta T_{ad}/(RT_{ad}^2/E)$ is now called the Zeldovich number. It measures the intensity of thermal feedback.

4. REFINEMENTS AND EXTENSIONS: BODIES OF SIMPLE SHAPE

In 1939 Frank-Kamenetskii considered circumstances where Newtonian cooling was only an empirical approximation, and where the escape of heat was impeded internally by the thermal properties of the medium. (This will always be the case for a large enough system.) An internal temperature-distribution with a maximum at the middle results. For stability, this central temperature may not exceed a critical value. For a sphere with its surface at T_a the relationship is:

$$\Delta T_{cr}^{centre} = 1.61 RT_a^2/E.$$

Criticality for a spherical mass is now expressed by the relationship:

$$\frac{e EQ r_o^2 c_o^n A \exp(-E/RT_a)}{\kappa RT_a^2} \equiv \delta_{cr}^{sph} = 3.322.$$

The important points to notice are (a) that relationships are quantitatively similar in scale and size to Semenov's, (b) there are no "unknowns" or adjustable parameters in the expression above, (c) this work was able to treat only the sphere, the infinite cylinder and the

infinite slab - the three "class A geometries" in which position is defined by a single co-ordinate.

5. AWKWARD SHAPES

Real systems often have awkward shapes. We meet cones, prisms, bricks, barrels or even doughnuts. The best practical means of treating them is first to decide what body of simple geometry is the best model for them. For a compact body this is usually the sphere; for an extended one, either the infinite slab or infinite cylinder may be appropriate.

The correct size for the equivalent sphere etc. is then got by working out an appropriate mean radius or half-width of the real body. Semenov's route would lead us to consider simply the quotient (volume/surface area). A more reliable route is to work out the square root of the harmonic mean-square radius. That is, narrow dimensions are to be emphasized. A compromise, probably entirely adequate for work involving factors of safety, is often the sphere of equal volume. This will inevitably be more explosive than, and inferior in stability to, the non-spherical system. The presumed superior stability of the inscribed sphere sets the other bound.

This aspect is currently pursued by several groups. A (rather austere mathematical) commentary on them all is given by Boddington and Gray [9]. Useful numerical results were reported by Anderson and Zienkiewicz [10]. Some representative values for δ_{crit} are:

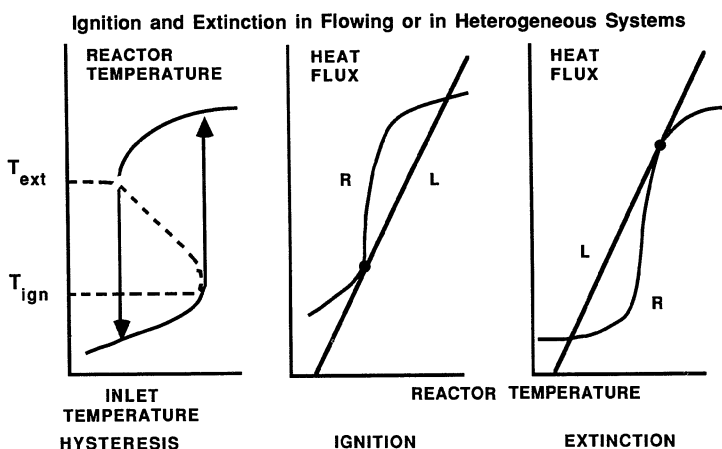
	δ_{crit}
∞ slab, width $2r_o$	0.878
∞ cylinder, diameter $2r_o$	2
∞ square rod, side $2r_o$	1.70
sphere, radius r_o	3.322
equicylinder, radius r_o	2.76
cube, side $2r_o$	2.45
tetrahedron, side $2r_o$	3.85

6. HETEROGENEOUS SYSTEMS: IGNITION AND EXTINCTION

These constitute a richly varied and complex field, but the interaction between reaction rate and heat release has enough in common with the homogeneous cases for the mathematical models exploited there to give clear insights into the 'old' phenomenon of ignition and to predict or explain a 'new' phenomenon viz. extinction.

The simplest kinds of system are exemplified by a (heated) plane surface of a reactive material - like graphite in contact with a (heated) gas like air or oxygen. Products move out and reactants move in, and the surface recedes as 'solid combustion' occurs. Chemically different but physically similar is the situation where the (heated) plane surface is not consumed, as when a solid catalyst accelerates an exothermic gas reaction. A Semenov-like treatment is quite appropriate with (i) Newtonian cooling representing heat flow and (ii) a parallel equation representing the flow of matter across a concentration step between surface layers and the bulk fluid. Ignition almost exactly

parallels the ignition of a homogeneous exothermic reactant and it normally happens close to $\Delta T_{cr} = RT_b^2/E$: but this estimate is now a lower limit. The state reached on ignition is that of reaction so rapid that it proceeds as fast as diffusion will let it - it is no longer chemically controlled. The reacting gas is at a high temperature T_b governed by the balance between exothermicity, efficiency of heat loss and of reactant transport. Extinction enters the scene. If conditions are made less favourable to reaction (e.g. by diluting the gas), the surface temperature declines slowly at first and then at T_{ext} falls suddenly to a value even beneath the old ignition temperature. A rough guide for first-order kinetics is: $T_{ext} = T_b - RT_b^2/E$.



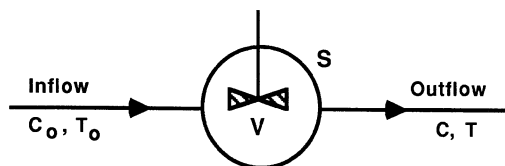
In practice heterogeneous systems of interest are far more complex than these one-dimensional idealisations. However, there are many saving features. First, a sufficiently large assembly of systems heterogeneous on the microscopic scale may be quite adequately treatable as if it were homogeneous so long as the overall reaction rates, etc. are correctly represented in terms of overall concentrations and so forth. Secondly, a heterogeneous catalyst bed may be usefully examined at the level of individual particles. These questions lie outside the scope of today's discussions. But thermal theory can very adequately describe the major features of fires in oil-soaked lagging of hot pipes, ignition of wool bales, sawdust or haystacks and even illuminate the oscillatory flickering of catalyst gauzes; and this is worth stating.

7. OPEN SYSTEMS

Chemical changes carried out in tubular reactors or catalyst beds or stirred tanks are studied more by chemical engineers than by any other group, often in connection with problems of control. Where reaction is exothermic and temperature-sensitive, then spontaneous ignition is again

possible. Quantitative realisation of the factors involved goes back to Liljenroth in 1918 but his pioneering thermal diagrams seem to have been forgotten as soon as published, and his work has had to be rediscovered not only by combustion scientists such as Semenov and his successors (especially Zeldovich) in the period 1926-1941 but also by the chemical engineers from 1953 onwards (van Heerden). The magic group of terms (RT_a^2/E) as indicative of dangerously critical self-heating seems to have been first put forward for a flowing system by a British chemical engineer in 1946, but again not much noticed. Since Amundson's contributions in 1955, however, our understanding has been transformed and the chemical engineering literature is rich in sources. Perlmutter's book [11] stands out for its clarity and chemical relevance. Like heterogeneous systems, stirred reactors show ignition and extinction and ranges of multi-stability.

In open systems a continuous flow of reactant allows truly stationary states to be attained. We may illustrate the simplest of open systems, the well-stirred reactor (cstr), as:



Outflow Rate u ; Residence Time = V/u

7.1 Adiabatic operation

We now have conservation equations for heat-balance and mass-balance that can be combined to give

$$\frac{t_{\text{res}}}{t_{\text{ch}}} = \frac{\Theta e^{-\Theta}}{B - \Theta},$$

as the condition for stationary states under adiabatic operation. The term $t_{\text{res}} = V/u$ is the mean residence-time. If we multiply throughout by B , the l.h.s. becomes $\zeta = (B t_{\text{res}} / t_{\text{ch}})$, ζ resembling the Semenov group, ψ . For stationary states to be possible

$$\zeta = \Theta \left(1 - \frac{\Theta}{B}\right)^{-1} e^{-\Theta},$$

an equation that can have one or three solutions. We have now explained extinctions as well as ignitions, and conditions for either phenomenon are again economically expressed in terms of Θ and ζ . When $B > 1$, $\zeta_{\text{ign}} \approx e^{-1}$, whilst $\Theta_{\text{ext}} \approx B-1$ and $\zeta_{\text{ext}} \approx e^{-B}$.

7.2 Non-adiabatic operation

In normal circumstances, where operation is not strictly adiabatic, heat-losses may often be represented adequately by the value of the Newtonian cooling time, $t_N = (\sigma C V / h S)$. (For adiabatic operation, $h \rightarrow 0$ and $t_N \rightarrow \infty$). However, the same type of equation as before governs stationary states, save that B is replaced by B_N where

$$\frac{B_N}{B} = \frac{1}{1 + (t_{res} / t_N)}.$$

It is easy to control values of B not only by choice of reaction but also by dilution, etc. Ignitions and extinctions cease to exist if B is too small. For zero heat-loss we require $B > 4$; for non-adiabatic conditions, with cooling time t_N and residence time t_{res} , we require $B_N > 4$ or $B > 4[1 + (t_{res} / t_N)]$. This condition places an upper limit on the residence time. There are no jumps of ignition or extinction if the flow is too slow:

$$t_{res} < t_N / (\frac{1}{4}B - 1).$$

8. INDUCTION PERIODS WHEN REACTANT CONSUMPTION IS SMALL

The time that elapses between bringing an exothermic reactant into surroundings that put it at risk and the moment of ignition depends strongly upon the temperature. If heat-losses are small, then regarding the system as an adiabatic one overestimates the risk and gives a safer lower limit. For a first-order reaction in the terms we have introduced,

$$t_{ad} = \frac{(RT_a^2 / E)}{(Qc_o / \sigma c_v)} \frac{1}{k(T_a)} = \frac{1}{Bk(T_a)},$$

so that

$$\ln t_{ad} \approx \text{const} + (E / RT_a).$$

This is the basis for using the temperature-dependence of induction periods to derive activation energies: such estimates should be accounted molehills of knowledge.

When heat-losses are important, induction periods lengthen considerably as the point of criticality is approached. In marginally super-critical systems:

$$\frac{t}{t_{ad}} = \frac{2\pi^2 / e)^{\frac{1}{2}}}{(\psi / \psi_{cr} - 1)^{\frac{1}{2}}}$$

Formulae like this are exact for open systems but they ignore the consumption of reactant and may not guide us well enough for real circumstances in enclosed systems which are considered next.

9. THERMAL RUNAWAY IN CLOSED SYSTEMS AT CONSTANT AMBIENT TEMPERATURE

In closed systems reactant consumption blurs the distinction between thermal runaway and quiescent behaviour. In all cases temperatures at first increase in time but there is no longer a set of curves reaching infinite values. All temperature histories pass through a single maximum value (T^* or Θ^*) and subsequently fall back to ambient. Our problem becomes one of understanding sensitivity, not locating a discontinuity. Nevertheless, the quantities introduced above (ψ , Θ , B) form the appropriate framework for investigation. We consider how Θ^* depends upon the value of ψ , and we identify and define maximum sensitivity of events to initial conditions as those for which $d\Theta^*/d\psi$ has its maximum value. There, $(d^2\Theta^*/d\psi^2) = 0$. These attitudes allow us to assign an operational value for a 'critical' value of ψ though we are now overworking the word critical. For exothermic reactions with B large, this presents no difficulty. For $B = 20$, for example, $d\Theta^*/d\psi$ is greatest for $\psi_{cr} = 0.545$. As the exothermicity is diminished, high sensitivity is lost, and when $B = 4$ or below nothing much remains.

We may generalize the treatment to any deceleratory reaction of order m , and when the exothermicity is large it is the quotient (B/m) that is important in describing the increase in ψ_{cr} from its 'zero-order' value e^{-1} . Rather roughly,

$$\Delta\psi_{cr} \approx 1.1 (m/B)^{2/3}.$$

Our general sensitivity treatment and this asymptotic expression join without discontinuity.

10. THE EFFECTS OF A LINEARLY INCREASING (RAMPED) AMBIENT TEMPERATURE ON EXOTHERMIC REACTIONS

Temperature-programmed thermal analyses (TA, TGA, DSC) in general and differential scanning calorimetry (DSC) in particular offer rapid, automated and computerized techniques for characterizing reactive materials. If reaction is not complex, values for exothermicities, velocity coefficients and Arrhenius parameters may also be extracted from the dynamic measurements. The basis of most interpretations is not deep and quite commonly rests only upon analyses of static situations in which responses to different (but constant) ambient temperatures have been considered. It is possible, however, to extend the ideas already presented to cover these interesting situations better. The form of the rate-law is supposed to obey $d\lambda/dt = k f(\lambda)$, where λ is the fractional concentration and k is a rate-coefficient satisfying the Arrhenius equation with $k \propto \exp(-E/RT)$. Procedures can be illustrated for deceleratory first-order kinetics for which $f(\lambda) = \lambda^m$ and $m = 1$. (Other cases involve only a different intermediate numerical calculation.) The details have been set out by Boddington et al. [12]. Two temperature-excesses need to be handled: that of the reactant, Θ , and that of the programmed ambient temperature, φ . Reactant consumption is very important. The new treatment highlights the efficiency of thermal contact between the reactive sample and the pan, and exploits the familiar parameter ψ of thermal ex-

plosion theory. New dimensionless variables, $u = \Theta - \varphi = (T_{\text{sample}} - T_{\text{pan}})/(RT_{\text{rf}}^2/E)$ and $s = e^\varphi$, enable the essential equations to be set out as:

$$\frac{du}{ds} = \frac{u(1-se^u)}{s(1-u)} \text{ with } \frac{u}{s} \rightarrow \psi \text{ as } s \rightarrow 0.$$

In a (u, s) phase-plane there are two singular points. One is a nodal point at the origin $(0, 0)$ and the other is a saddle point at $(1, e^{-1})$. The (unique) trajectory connecting these points separates "supercritical" evolutions from quiescent ones. The value of ψ belonging to it must be found by numerical calculation. For a first-order reaction it is $\psi \approx 1.7987$; for other orders it takes other values. Three significant figures are enough: effectively $\psi_{\text{cr}} = 1.80$.

The same approach leads directly to Kissinger's equation [13] relating maxima in signal temperatures T_m to heating-rates W and activation energies E :

$$\ln \frac{W}{T_m^2} = \text{const.} - \frac{E}{RT_m}.$$

This relationship remains valid even when significant differences develop between reactive sample and inert reference temperatures so long as T_m relates to sample temperature, not the programmed temperature.

11. CONCLUSIONS

The last ten years have seen thermal explosion theory developed in many ways and the present paper has illustrated its usefulness in a variety of circumstances. Amongst other systematic developments are the correction of Arrhenius parameters for self-heating effects and the behaviour of consecutive and competitive exothermic reactions. Another big area is the study of systems with distributed temperatures, including single and multiple hot-spots. Numerical computation must take over in many individual treatments but to make this efficient the kind of map offered by theory is absolutely essential.

ACKNOWLEDGEMENTS

I am grateful to many colleagues from the University of Leeds for collaboration and discussion, to NATO for travel support, and to Gonville and Caius College, Cambridge.

REFERENCES

1. Bowes, P. C. (1984) Self-heating: evaluating and controlling the hazards, H.M.S.O., London.
2. Frank-Kamenetskii, D. A. (1969) Diffusion and heat exchange in chemical kinetics, 2nd edn., Plenum Press, New York.
3. Gray, P. and Lee, P. R. (1967) Oxidation and Combustion Reviews, vol. 2, pp. 1-184.
4. Gray, P. and Sherrington, M. E. (1977) 'Self-heating, chemical kine-

- tics and spontaneously unstable systems', Spec. Periodical Reports, vol. 2, ch. 8, Chemical Society, London.
5. Griffiths, J. F. and Singh, H. J. (1982) J. Chem. Soc. Faraday Trans. I 78 747-760.
 6. Griffiths, J. F. and Mullins, J. (1984) Comb. and Flame 56 135-148.
 7. Semenov, N. N. (1928) Zeit. Phys. 48, 571.
 8. Gray, B. F. and Scott, S. K. (1985) Comb. and Flame, 61, 227-236.
 9. Boddington, T. and Gray, P. (1970) Phil. Trans. Royal Soc. Lond. A270 467-506.
 10. Anderson, J. and Zienkiewicz, O. (1974) Int. J. Heat. Transfer (1974) J. Heat Transfer 96, 398.
 11. Perlmutter, D. D. (1972) Stability of chemical reactors, Prentice Hall, New Jersey.
 12. Boddington, T., Gray, P. and Kay, S. R. (1989) Proc. Royal Soc. Lond., A425 269-283.
 13. Kissinger, H. E. (1956) J. Res. Nat. Bur. Stand., 57 217-221.

MODELLING ISOTHERMAL WAVES OF CHEMICAL REACTION

PETER GRAY
Chemical Laboratory
Lensfield Road
Cambridge CB2 1EW
England

ABSTRACT. Autocatalysis forms the basis for propagating waves of isothermal chemical reaction. When autocatalysis is represented by the "mass action" cubic and quadratic forms ($A + 2B \rightarrow 3B$ and $A + B \rightarrow 2B$ respectively), extremely simple prototypes are generated. They apply very well to more complex schemes. The fact that in the cubic case simple analytical solutions are possible is of great value in recognizing trends and making predictions.

1. INTRODUCTION, BACKGROUND AND AIMS

The clear demonstration that autocatalysis can be the driving force behind the propagation of isothermal waves of chemical reactions goes back at least to 1906 when R. Luther of Leipzig demonstrated several such systems [1] at a meeting of the Bunsen Society. His work seems to have been largely forgotten: it has recently been re-published in an English translation [2]. In any case, although he suggested a formula relating the speed of the chemical wave to the rate-coefficient of the chemical reaction, the concentration of the chemical species and its diffusivity, it is not clear that he employed more than dimensional analysis. The earliest mathematical studies happened simultaneously in England and in the Soviet Union when Fisher [3] and Kolmogorov et al. [4] studied similar equations in different contexts. That was in 1937; in 1939 Voronkov and Semenov [5] made the first chemical applications to the virtually isothermal, autocatalytic oxidation of carbon disulphide. This oxidation can support a feebly luminescent, cold flame - I call it cold not cool to emphasize its difference from cool-flame propagation in hydrocarbons where self-heating is very important. This paper also seems to have been virtually unknown until attention was drawn to it in the 1980s by Zel'dovich et al. [6].

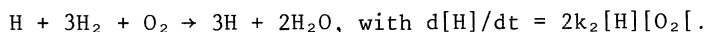
Autocatalysis and chain-branching are different names for the same thing. Both terms crop up when the interpretation of explosive behaviour is undertaken and both phenomena have been rather casually invoked during the first week of this meeting. Accordingly, we may begin with a brief survey of autocatalysis and some of its consequences, and continue by presenting systematic means of modelling it. We shall see how, because virtually all known autocatalytic behaviour lies between two extremes - quadratic and cubic - very simple model schemes offer a great deal of information and understanding. These schemes are:

Quadratic autocatalysis (linear branching) $A + B \rightarrow 2B$;
 Cubic autocatalysis (quadratic branching) $A + 2B \rightarrow 3B$.

It might seem natural to begin with the quadratic case, but this does not give the simplest of solutions. Instead we follow the pioneering contributions of Voronkov [5] and Showalter [7] and begin with the cubic case. This presentation draws heavily on Showalter's work [7] and on sustained collaboration with Drs Merkin, Needham and Scott, to all of whom clear understanding in a modern chemical contest is largely due.

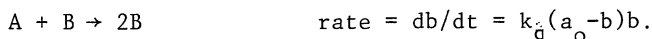
2. MODELLING CHEMICAL AUTOCATALYSIS

Autocatalytic reactions in closed, homogeneous systems characteristically start slowly or at imperceptible speeds, accelerate to a maximum rate and then subside until all the material has been transformed. The most deeply studied example is the explosively rapid reaction between oxygen and hydrogen for which the observed rate is the consequence of a network of elementary steps with linear chain-branching. The acceleratory phase is dominated by the sequence: $HO + H_2 \rightarrow H_2O + H$; $H + O_2 \rightarrow HO + O$; $O + H_2 \rightarrow HO + H$. The second of these three steps is the slowest, and at low temperatures it controls the rate. The overall stoichiometry corresponds to:



This, of course, produces exponential growth at first but even if no other factors are present, reactant consumption sets limits to such growth in the usual way.

An elementary representation of the kinetics that does not neglect reactant consumption is thus:



It is natural to measure time from the time of maximum rate: k_q is the velocity constant for quadratic autocatalysis. If we make time and concentrations dimensionless by setting $\tau = k_q a_0 t = \phi t$, and $\beta = b/a_0$ we have:

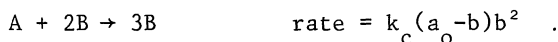
$$\frac{d\beta}{d\tau} = \beta(1-\beta) \qquad \text{and} \qquad \beta = \frac{e^\tau}{1+e^\tau} = \frac{e^{\phi t}}{1+e^{\phi t}}.$$

In these circumstances, there is a problem about reaction beginning. When the only pathway is autocatalytic and no catalyst is added artificially, pure reactant A will never react at all: induction periods preceding maximum rates are infinite. If there is either a slow, uncatalyzed path or if some catalyst is present initially, then reaction takes only a finite time to reach its maximum velocity:

$$IP \approx \frac{1}{\phi} - \ln \frac{1}{\beta_0}.$$

Control of φ rather than of size of β_0 offers the means of controlling autocatalytic reactions. This underlies the practical use of inhibitors and antioxidants.

The other extreme of autocatalyses has not only zero speed but also zero acceleration at the point of zero conversion. Its simplest kinetic representation is:



Dimensionless concentrations and times turn this into:

$$\frac{d\beta}{d\tau} = \beta^2(1-\beta) \quad \text{or} \quad \frac{d\beta}{d\tau} = \varphi\beta^2(1-\beta).$$

In the foregoing, k_c denotes the velocity constant for cubic autocatalysis, and a_0 the initial concentration of reactant. Dimensionless time $\tau = k_c a_0^2 t = \varphi \tau$. One integrated form of this rate-expression is:

$$\tau = \ln \left(\frac{\beta}{1-\beta} \right) - \frac{1}{\beta}$$

wherein we have measured times from the point ($\beta \approx 0.782$) where the r.h.s. is zero.

It is interesting to evaluate the average rate of these autocatalytic reactions - average meaning with respect to concentration. For the quadratic case:

$$\bar{r}_q = \int_0^1 k_q a_0^2 \beta(1-\beta) d\beta = \frac{1}{6} k_q a_0^2.$$

and for the cubic case:

$$\bar{r}_c = \int_0^1 k_c a_0^3 \beta^2(1-\beta) d\beta = \frac{1}{12} k_c a_0^3.$$

For $\bar{r}_q = \bar{r}_c$, we require $k_q = \frac{1}{2} k_c a_0$.

Cubic autocatalysis is less common than quadratic. It was first invoked to interpret hydrocarbon oxidation and carbon disulphide oxidation [5]. Both these are gas-phase examples. In aqueous solution, it has been used very successfully to interpret the iodate-arsenous acid oxidation [8, 9].

3. TRAVELLING ISOTHERMAL WAVES MAINTAINED BY CUBIC AUTOCATALYSIS: ONE-DIMENSIONAL CASE

3.1 Conservation equations

We shall consider the single, cubic, autocatalytic step $A + 2B \rightarrow 3B$ with rate equal to $k_c ab^2$. The rates of change of concentration of A and B at any point satisfy the conservation equations:

$$\begin{array}{rclcl}
 \partial a / \partial t & = & D_A \partial^2 a / \partial x^2 & - & k_c a b^2 \\
 \partial b / \partial t & = & D_B \partial^2 b / \partial x^2 & + & k_c a b^2 \\
 \text{accumulation} & & \text{dispersion} & & \text{autocatalysis}
 \end{array}$$

To begin with the simplest of circumstances, let us assume that the species A and B have equal diffusivities, setting $D_A = D_B = D$. The boundary conditions to be satisfied are:

$$a = a_0, b = 0 \text{ at } x = +\infty; a = 0, b = a_0 \text{ at } x = -\infty.$$

These restrictions imply that

$$\partial(a+b)/\partial t = D \partial^2(a+b)/\partial x^2$$

and that $a+b = a_0$ in a steady state. This link between a and b leads to a simple conservation equation for a wave of constant properties (the expected long-time solution):

$$\partial b / \partial t = D \partial^2 b / \partial x^2 + f(b),$$

where $f(b)$ denotes $k_c(a-b)b^2$ in the present case and more generally represents the kinetic terms. Very important subsidiary cases include circumstances where b decays (e.g. by first-order or second-order paths) or where reaction is reversible, or where cubic catalysis is accompanied by a concurrent quadratic contribution, $k_q(a_0-b)b$.

3.2 Dimensionless equations

Although not too difficult to handle as they stand, these equations are better expressed in dimensionless form for solution and manipulation. What are the natural references to choose for time and length and concentration? To reduce times to dimensionless form we use the characteristic chemical time $t_{ch} = 1/k_c a_0^2$ and write $\tau = k_c a_0^2 t = t/t_{ch}$. Since the product $D t_{ch}$ has dimensions of (length)², we adopt a dimensionless length $\rho = x(2k_c a_0^2/D)^{1/2}$. The factors $\frac{1}{2}$ and 2 have been incorporated into our definition in anticipation of the dimensionless wave-speed v that we shall find later: in these terms it turns out that $v = 1$. By these substitutions, our conservation equation becomes:

$$\begin{array}{rclcl}
 \frac{\partial B}{\partial \tau} & = & 2 \frac{\partial^2 B}{\partial \rho^2} & + & \varphi(B) \\
 \text{accumulation} & & \text{dispersion} & & \text{generation}
 \end{array}$$

with $\beta = 0$ at $\rho = +\infty$ and $\beta = 1$ at $\rho = -\infty$.

Again, as a start, we consider only a wave of constant form and constant speed $v = d\rho/dt$. This constant spatial velocity may also be expressed in terms of the appropriate partial derivatives as:

$$v = -(\partial\beta/\partial\tau)_\rho / (\partial\beta/\partial\rho)_\tau.$$

We also now define a new "moving coordinate" system

$$\xi = \rho - v\tau \quad .$$

At a fixed point ($\rho = \text{const}$), ξ describes a wave moving past at speed v : at a fixed instant, ξ describes the spatial dependence. Any constant-velocity solution can be written in terms of ξ alone or of ρ and τ . Because $\partial\beta/\partial\tau = -v d\beta/d\xi$ and $\partial^2\beta/\partial\rho^2 = \partial^2\beta/d\xi^2$, our wave-equation may be expressed as

$$2 \frac{d^2\beta}{d\xi^2} + v \frac{d\beta}{d\xi} + \varphi(\beta) = 0 \quad .$$

This is the equation for which we seek an analytical solution, and we shall use results already discovered by Showalter and others [6, 7]. The simplest attack [7] anticipates the fact that cubic autocatalysis generates a steady wave-front of quadratic form:

$$d\beta/d\xi = (\text{const.}) \beta(1-\beta).$$

The value of the constant coefficient is obtained by evaluating $d^2\beta/d\xi^2$, substituting back into the wave-equation and matching coefficients. For a system in which β decreases as ξ increases, the constant coefficient is $-1/2$ and $v = 1$. This equation may be integrated to yield $\beta(\xi)$. In terms of time and distance:

$$\beta(\rho, \tau) = \frac{1}{1 + \exp[\frac{1}{2}(\rho - \tau)]} \quad .$$

3.3 Some properties of the wave

The speed of the wave in conventional form is:

$$V = (k_c a_o^2) \left(\frac{1}{2} D / k_c a_o^2 \right)^{\frac{1}{2}} = \left(\frac{1}{2} D k_c a_o^2 \right)^{\frac{1}{2}}.$$

If D is measured in $\text{m}^2 \text{s}^{-1}$, a_o in mole m^{-3} and k_c in $\text{m}^6 \text{mol}^{-2} \text{s}^{-1}$, the limits of V are metres per second.

The steepness of the wave is the maximum gradient: in dimensionless terms $(d\beta/d\xi)_{\text{max}} = 1/8$. In terms of concentration and distance the maximum gradient is given by $(db/dx)_{\text{max}} = (1/8) a (2k_c a_o^2/D)^{\frac{1}{2}}$. The thickness of the wave is an arbitrary concept. Practically, it may be defined as

$$\Delta x = \frac{b_\infty - b_o}{(db/dx)_{\text{max}}} = \sqrt{32} \left(\frac{D}{k_c a_o^2} \right)^{\frac{1}{2}} \quad .$$

3.4 Stability of the wave

A very important question has not been asked in the development sketched above. We have accepted a very special solution as if no others need be considered. In fact, the stability of the special solution shows up in numerical computations - what we have found is correct. However, we need to be sure in principle that no other members of the possible spectrum of wave speeds, of which the dimensionless value $v=1$ is the slowest wave, are acceptable. Two comments may be made. First, slower waves require physically unrealisable features (like negative concentrations) and can immediately be ruled out here in the same way as they are also ruled out for quadratic autocatalysis. Secondly, it is possible to study the effect of perturbations on other solutions and this slowest wave is indeed the one to which others tend. Its own stability has recently been investigated [10] systematically and the long-time decay of perturbations found to possess the form $t^{-3/2}e^{-t/8}$.

4. COMPLEX CASES INVOLVING CUBIC AUTOCATALYSIS

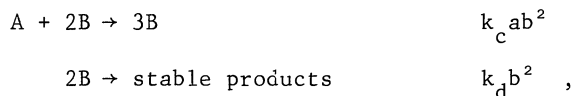
Three further sets of circumstances are particularly illuminating: one where the autocatalytic reaction is reversible ($A+2B \rightleftharpoons 3B$); one where the catalyst B itself decays according to a first-order or second-order law; and finally, one where cubic and quadratic autocatalysis occur simultaneously. The last case is discussed in section 5.

4.1 Reversible autocatalysis

These circumstances have been investigated especially by S. K. Scott (see [9, 12]). It suffices here to recognize that if the equilibrium constant E for the reverse reaction ($3B \rightleftharpoons 2B+A$) is not zero (irreversible change) but small, very simple results are still obtainable. The kinetic term $f(b)$ in the mass conservation equations is changed from $k_1(a-b)b^2$ to $[k_1(a-b)b^2 - k_{-1}b^3]$ or $k_1b^2[a_0 - (1+E)b]$, and one of the boundary conditions is altered from complete to partial conversion. We now find a somewhat slower wave with $v = (1+E)^{-1/2}$ instead of $v=1$, with $v \approx 1 - \frac{1}{2}E$ for $E \ll 1$.

4.2 Cubic autocatalysis with quadratic decay

The scheme is now:



and has recently been studied by Merkin & Needham [10, 11]. Here we find that a stable wave develops only if $k_c a_0 > k_d$. In circumstances where the quotient $\kappa = k_d / k_c a_0$ is small the front of the wave is not much affected but the tail is. The speed is somewhat changed: when $\kappa \ll 1$, the fractional reduction is $O(\kappa)$.

5. SIMULTANEOUS CUBIC AND QUADRATIC AUTOCATALYSIS [12]

The kinetic scheme is now written:



Two channels are open simultaneously for converting the reactant A into the (autocatalytic) product B, and we may expect to find reaction rates and wave speeds faster than when either channel is closed. The relative contributions of the two channels may be expressed in terms of a dimensionless quotient, $\mu = k_{q,ab}/k_{c,ab}$.

The obvious path to be taken towards solution of this composite case seems to be that exploited by Hanna, Saul and Showalter [7]. We might expect to begin with an equation:

$$\frac{\partial \beta}{\partial \tau} = \frac{\partial^2 \beta}{\partial \xi^2} + \beta^2(1-\beta) + \mu\beta(1-\beta)$$

and try by the same process as before (assuming constant speed and constant wave profile, with gradient g proportional to $\beta(1-\beta)$) to seek a self-consistent solution. This is indeed possible and a speed that matches previous findings for the cubic extreme ($\mu=0$) and suggests a linear dependence of v on μ nearby (for $\mu>0$) is found. There is a seeming paradox in that this result seems to apply as well for large μ as for small, and thus to provide a solution at the quadratic extreme where we know, however, that such a result does not apply.

The paradox is resolved by a deeper study [11] of wave stability. Up to $\mu=\frac{1}{2}$, our new solution is correct: $v = (1+2\mu)$. Beyond $\mu=\frac{1}{2}$, the form is $v = \sqrt{2\mu}$. These two forms have the same ordinate and slope at $\mu=\frac{1}{2}$ and here their behaviour switches smoothly from one form to the other. We may note that since the average rates of these autocatalytic reactions are $(1/12)k_{c,ab}^3$ and $(1/6)k_{q,ab}^2$ respectively, the value $\mu=\frac{1}{2}$ is one implying equal flow through the two channels.

6. ACKNOWLEDGEMENTS

I thank Gonville and Caius College, Cambridge for their generous support and many colleagues and collaborators for discussions, recalling especially Drs Scott, Showalter, Needham and Merkin.

7. REFERENCES

1. Luther, R. (1906) Z. Elek. 12, 596.
2. Luther, R., Arnold, R., Showalter, K. and Tyson, J. J. (1987) J. Chem. Educ. 64, 740, 742.
3. Fisher, R. A. (1937) Ann. Eugen. 7, 355.
4. Kolmogorov, A., Petrovsky, I. & Piscounov, N. (1937) Moscow Univ. Bull. Math. 11, 1.
5. Voronkov, V. G. & Semenov, N. N. (1939) Zh..Fiz. Khim, 13, 1695.

6. Zel'dovich, Y. B. (1980) *Mathematical Theory of Combustion and Flames*, Nauka, Moscow.
7. Hanna, A., Saul, A. & Showalter, K. (1982) *J. Am. Chem. Soc.* 104, 3838; Showalter, K., Noyes, R. M. & Turner, H. (1979) *J. Am. Chem. Soc.* 101, 7463.
8. Showalter, K. (1987) in G. R. Freeman (ed.), *Kinetics of Nonhomogeneous Processes*, John Wiley.
9. Gray, P., Showalter, K. & Scott, S. K. (1987) *J. Chimie Physique* 84,
10. Gray, P., Merkin, J. H., Needham, D. J., & Scott, S. K. (in press) *Proc. Roy. Soc. A*.
11. Merkin, J. & Needham, D. J. (1989) *Proc. Roy. Soc. A* 424, 187.
12. Gray, P. & Scott, S. K. (1990) *Chemical Oscillations and Instabilities*, Clarendon Press, Oxford.

Thermochemical Modeling: I. Application to Decomposition of Energetic Materials*

Carl F. Melius
*Combustion Research Facility
Sandia National Laboratories
Livermore, CA 94551-0969*

*Lecture presented at NATO Advanced Study Institute on
Chemistry and Physics of the Molecular Processes in Energetic Materials,
Altavilla Milicia, Sicily, September 3-15, 1989*

Abstract. The reaction mechanisms by which energetic materials decompose depend strongly on the thermochemical properties (e.g., heats of formation, entropies, free energies) of the energetic molecule of interest as well as on the thermochemistry of the intermediate species formed during the decomposition process. In this paper, we discuss the quantum chemical BAC-MP4 method for calculating thermochemical properties of molecular species involved in the decomposition of energetic materials. The resulting BAC-MP4 thermochemistry is used to determine bond dissociation energies for various classes of energetic molecules. This data is then used to determine decomposition pathways. Simple bond fissioning, multicentered elimination, as well as auto-catalytic decomposition mechanisms are presented and discussed. As a particular example, the decomposition mechanisms of nitramine compounds are presented in detail.

1. Introduction

The decomposition mechanisms of energetic materials, such as nitramines, are very dependent upon the chemical environment and heating rates of the energetic material¹⁻¹⁰. The ability to model energetic materials requires a knowledge of the thermochemical properties of the initial energetic compound as well as those of the intermediates formed during the decomposition process¹¹⁻¹⁴. Important thermochemical properties of a molecule include its heat of formation, heat capacity, entropy, and free energy. From these molecular properties one can determine the bond dissociation energies of a molecular species. However, the thermochemical properties for many of the intermediate species in the decomposition process are not known experimentally, since the species are highly reactive and short lived. Also,

*Work supported by a Memorandum of Understanding between the Department of Army and the Department of Energy.

the environment in which they are produced can involve high temperatures and pressures that make experimental diagnostic techniques difficult to apply. It has therefore been necessary to develop theoretical quantum chemical techniques that can provide accurate thermochemical data. In addition, in order to determine how fast a given decomposition process occurs, one must have thermochemical information regarding the reaction pathways and the activation energies involved in going from reactants to products. The thermochemistry of reaction rates can also be obtained theoretically using the same quantum chemical techniques. The results of the theoretically derived thermochemistry can then be used to determine the order in which the bonds will break in an energetic molecule and whether or not more complicated reaction pathways will occur¹²⁻¹⁶.

In this paper, we present a quantum chemical procedure called BAC-MP4,¹⁷⁻²¹ which has proven reliable in calculating the thermochemical properties of the molecular species involved in the energetic materials. We then apply this procedure to investigate the bond dissociation energies of various energetic molecules. Using these results, we then develop decomposition pathways for the breaking apart of energetic materials, with particular emphasis on nitramines. Next, we investigate more complicated decomposition mechanisms involving multiple bond breaking and formation, using the thermochemical data to evaluate rate constants for these complex decomposition mechanisms. Finally, we briefly address the effects of autocatalysis on the decomposition, indicating how additional molecular species can change the decomposition mechanism, providing lower activation energy pathways. Many of the details discussed in this paper have been taken from previous papers^{13,14,17}.

2. The BAC-MP4 Method for Thermochemical Properties

Since the thermochemical stabilities of the transient species involved in the decomposition of energetic materials may not be known, it is important to have an accurate theoretical method for determining their heats of formation. The BAC-MP4 method provides a means of obtaining thermochemical energies of molecular species accurate to approximately 3 kcal-mol⁻¹. This method can also be used to obtain estimates of activation barriers along reaction pathways, although the error uncertainty is somewhat larger. In this section, we present the theoretical procedure for the BAC-MP4 (Bond-Additivity-Corrected Møller-Plesset 4th order perturbation theory) method.

In order to determine the thermochemical properties for a given molecular species (e.g., its heat of formation, entropy, heat capacity, and free energy), we need to determine its structure, vibrational frequencies, and bond energies. Over the past several years¹⁷⁻²¹, we have developed a systematic procedure, denoted the BAC-MP4 method, which allows one to treat a large number of molecular species composed of elements of the first and second row of the periodic table, with particular emphasis on species involving carbon, hydrogen, nitrogen, and oxygen that are involved in energetic materials.

Given the size of current computers, one is limited in the size of molecular species whose energy can be calculated with great precision²²⁻²⁴. For larger molecules, approximations must be made in the size of the electronic structure calculation performed (i.e., restrictions in the number of basis functions and in the number of

configurations used in determining the electronic correlation energy). This introduces subsequent errors in the resulting geometry, vibrational frequencies, and bond energies.

We have therefore developed a systematic procedure which has the following properties. First, the BAC-MP4 method can treat molecular species containing up to eight or nine heavy atoms (e.g., C, N, O, F, etc.) with varying numbers of hydrogen atoms attached. By the use of symmetry, we have been able to calculate nitrobenzene, $\text{C}_6\text{H}_5\text{NO}_2$, which has nine heavy atoms. This size has been sufficient to address various chemically important subgroups involved in energetic materials. Second, the BAC-MP4 procedure is able to treat unstable or radical species as well as closed-shell stable molecules. While the group-additivity techniques developed by Benson *et al.*¹¹ have been very successful in addressing species of importance in combustion, this approach has somewhat limited applicability for radical species. Also, the thermochemistries of certain chemical subgroups of importance in energetic materials are not known experimentally or may be inaccurate. This is particularly true of many species involving nitrogen. Third, the BAC-MP4 procedure can provide thermochemical heats of formation accurate to several kcal-mol⁻¹. This accuracy is sufficient for most of the molecular intermediates needed in modeling the thermal decomposition, ignition, and combustion processes in energetic materials. Fourth, the procedure represents a reasonable compromise between computational time consumed in the geometry optimization, vibrational frequency, and bond energy calculations, on the one hand, and the desired thermochemical accuracy, on the other hand.

Since the most difficult part of the theoretical procedure is obtaining accurate bond energies, a major part of the computational time must be spent in calculating the electronic energy of the molecule. We have found that the errors in the bond energies obtained from *ab initio* methods involving highly correlated electronic wave functions are systematic and can be separated, to a large extent, into errors due to individual bonds. This observation has led us to the development of the BAC-MP4 method, in which the electronic energy is augmented by energy corrections which are bond-wise additive. This BAC procedure has been combined with statistical mechanics calculations to provide thermochemical properties of molecules. The overall BAC-MP4 procedure is shown in Fig. 1. In the following sections we present details of the BAC-MP4 procedure, with particular emphasis on the bond additivity corrections and on the statistical mechanical calculations.

2.1. Electronic Structure Calculations for Structure, Vibrational Frequencies, and Electronic Energy

The BAC-MP4 method first involves *ab initio* electronic structure calculations to determine the structure, vibrational frequencies, and electronic energy. These calculations are carried out using the Gaussian 8x series of codes²⁵ (e.g., G82, G86, G88) developed by Pople *et al.* The equilibrium geometry of the molecule is determined using the Hartree-Fock method (restricted Hartree-Fock²⁶, RHF, for closed shell molecules and unrestricted Hartree-Fock²⁷, UHF, for open shell molecules). The basis set used to describe the electronic wave function is split-valence with polarization functions on the heavy atoms (denoted 6-31G*²⁸). For a

BAC-MP4 Quantum Chemical Calculations of Thermochemical Data and Reaction Mechanisms

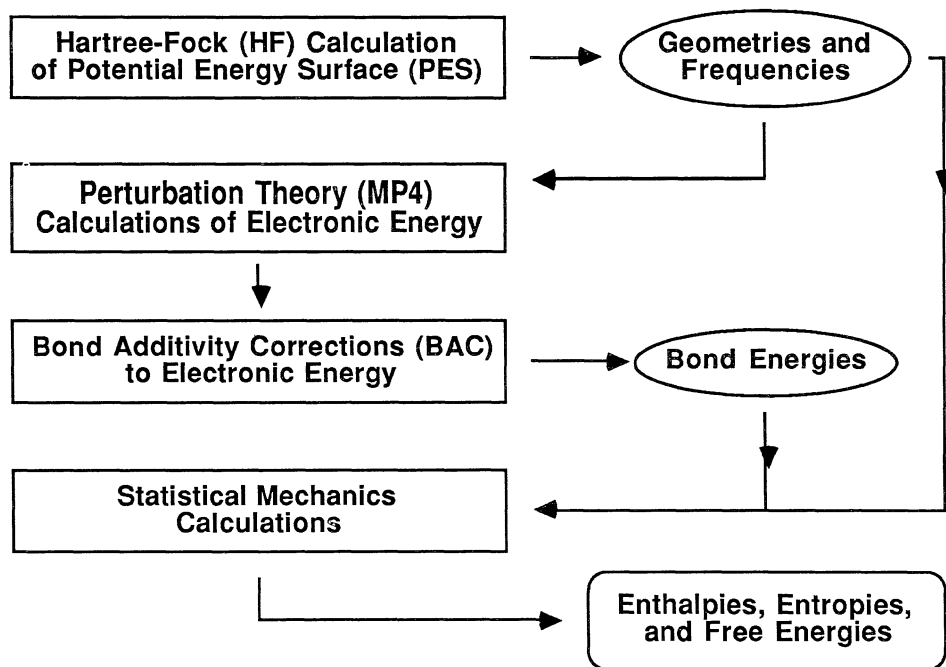


Figure 1. Hierarchical diagram of the BAC-MP4 method for determining thermochemical properties of molecules. First, a Hartree-Fock calculation provides the molecular geometries and frequencies. Fourth-order Møller-Plesset perturbation theory (MP4) provides the ab initio electronic energy to which bond-additivity corrections (BAC) are then added to obtain chemical bond energies. Finally, statistical mechanics calculations are used to determine the enthalpy, entropy, and free energy of the molecule.

stable structure, one optimizes the molecular geometry to a minimum on the HF (RHF or UHF) potential energy surface (PES), i.e., a point on the PES which has zero gradients and zero imaginary vibrational frequencies). For a transition state structure, one searches for a stationary point on the PES which has one imaginary vibrational frequency. Since the true geometry is a stationary point on the PES, the optimized HF geometry, in general, should be close to the true geometry²⁹. This assumption can break down for transition state structures, either for those cases where multireference wave functions are needed or where the potential energy barriers are greatly reduced due to higher order electron correlation or to bond-

additivity corrections. Such a concern is less severe for stable structures, except where very weak bonds exist.

Having determined the optimized molecular geometry, harmonic vibrational frequencies are calculated³⁰ at the same level of theory (RHF or UHF) with the same basis set (6-31G*). Actually, the first and second derivatives of the potential energy surface at the stationary point are calculated. Thus, the harmonic vibrational frequencies along with their corresponding normal modes can be determined for any isotopic form of the molecule. This provides the ability to determine the thermochemistry of isotopically labeled molecules as well as isotopic effects of rate constants using transition state theory (TST). At this level of theory, the vibrational frequencies tend to be too large compared to experimental values. We therefore scale the HF harmonic frequencies downward by 12 per cent, as suggested by Pople³¹. The resulting vibrational frequencies are used subsequently in determining the zero-point energy of the molecule and other statistical mechanical properties of the molecule.

Having determined the structure and vibrational frequencies of the molecule, the next step is to determine the electronic energy. To obtain useful electronic energies, higher levels of electronic structure theory must be used which incorporate electronic correlation. We have found that Møller-Plesset perturbation theory through fourth order, MP4³², provides a practical way to obtain consistently accurate electron energies for a wide range of chemical bonds. The MP4 method includes electron correlation involving single, double, triple, and quadruple excitations (the method is also denoted MP4SDTQ). Using a split-valence basis set with polarization functions on all atoms (6-31G**)²⁸, the method is denoted MP4/6-31G**. Since the geometry is optimized at the HF/6-31G* level of theory, the overall theoretical method is denoted MP4/6-31G** // HF/6-31G*. Using a larger basis set would increase the accuracy of the electronic energy²⁴. However, since the computational time increases rapidly with the number of basis functions, larger basis sets soon become prohibitively expensive. The choice of MP4 level of theory with the 6-31G** basis set allows us to address molecules with as many as eight or nine heavy atoms using current computer technology.

2.2. Bond Additivity Corrections

While the MP4 method is a very sophisticated ab initio electronic structure method, the energy provided by the 6-31G** basis set does not provide the level of accuracy required for useful heats of formation. However, we find that at this level of theory and basis set, the resulting errors in the electronic energy are quite systematic. In particular, we find that the errors in electronic energy can be treated to a large degree as bond-wise additive. Furthermore, these energy corrections depend only on the bond type and the bond distance with small corrections for neighboring bonds.

For the chemical bond between atoms A_i and A_j in the molecule $A_k-A_i-A_j-A_l$, the empirically derived functional form of the bond-additivity energy correction has the form

$$E_{\text{BAC}}(A_i-A_j) = f_{ij} g_{kij} g_{ijl} \quad (1)$$

where

$$f_{ij} = A_{ij} \exp(-a_{ij} R_{ij}) \quad (2)$$

$$g_{kij} = (1 - h_{ik} h_{ij}) \quad (3)$$

and

$$h_{ik} = B_k \exp\{-a_{ik}(R_{ik} - 1.4 \text{ \AA})\} \quad (4)$$

In the above equations, A_{ij} and a_{ij} are empirical parameters which depend on the bond type A_i-A_j (e.g., a carbon-carbon bond or a carbon-oxygen bond) and R_{ij} is the bond distance determined from the HF geometry optimization of the molecule. Since E_{BAC} (Eqn. 1) is a positive value, the bond-additivity correction increases the bond energy of the molecule relative to that obtained from the ab initio calculation. The primary cause of this underestimation of the bond energy in the ab initio calculation is due to the finite basis set used and the correspondingly finite number of configurations used to treat the electron correlation. The factor f_{ij} (Eqn. 2) is the dominant term in the correction factor, depending on the bond type and bond distance. As the bond distance shortens (e.g., becomes multiply bonded), the energy correction increases exponentially. The factor g_{kij} (Eqn. 3) is an empirically determined correction term due to a neighboring bond A_k-A_i . This factor (which is < 1), reduces the size of the bond-additivity correction. An additional term g exists in Eqn.1 for each additional bond adjacent to bond A_i-A_j in the molecule. The parameters A_{ij} , a_{ij} , and B_k are empirically determined by fitting the heats of formation of selected molecules to match experimental values.

In the BAC-MP4 method, an additional error in determining heats of formation occurs for open-shell molecules. This error arises from the use of the unrestricted Hartree-Fock (UHF) wavefunction in calculating the Møller-Plesset perturbation theory energy. We include a BAC spin correction energy term, $E_{BAC}(\text{Spin})$, given by

$$E_{BAC}(\text{Spin } s^2) = E(\text{UMP3}) - E(\text{PUMP3}) \quad (5)$$

where MP3 indicates Møller-Plesset third order perturbation theory, the U in PUMP3 and UMP3 indicates that the unrestricted Hartree-Fock wavefunction is used and $E(\text{PUMP3})$ is an approximation to the spin-projected MP3 energy defined by Schlegel³³.

Since the MP4 method is based on a single reference Hartree-Fock configuration, MP4 energies can yield poor results for those molecular systems which possess significant multiple reference character, such as nitro groups. An additional correction term, given by

$$E_{BAC}(\text{Spin UHF-I}) = K_{\text{UHF-I}} S(S+1), \quad (6)$$

mitigates some of the deficiency in the single-reference-configuration-based MP4 method. The $S(S+1)$ term is the S^2 spin contamination in the UHF wavefunction if the RHF wavefunction is UHF unstable, while $K_{\text{UHF-I}}$ has the value of $10.0 \text{ kcal}\cdot\text{mol}^{-1}$.

As will be seen later, there still appears to be a large systematic error for transition state structures involving closed shell molecular species, causing the BAC-MP4 activation energies to be too high.

The resulting BAC energy correction is given by

$$E_{\text{BAC}} (\text{Total}) = \sum_{ij} E_{\text{BAC}} (A_i - A_j) + E_{\text{BAC}} (\text{Spin } s_2) + E_{\text{BAC}} (\text{Spin UHF-I}) \quad (7)$$

where ij is summed over chemical bonds in the molecule. The BAC energy correction (which is > 0) is subtracted from the ab initio MP4 energy, providing a BAC-MP4 energy.

We have also developed an error estimate¹⁷ (or confidence level) for the BAC-MP4 energy. The approach is based on the convergence of the molecular energy at lower levels of perturbation theory, i.e., BAC-MP2, BAC-MP3, and BAC-MP4SDQ. In addition, the BAC correction due to spin contamination, $E_{\text{BAC}} (\text{Spin } s_2)$, or UHF instability, $E_{\text{BAC}} (\text{Spin UHF-I})$, also has error uncertainties. We define a BAC-MP4 error estimate as

$$\begin{aligned} \text{Error (BAC-MP4)} = & \text{Sqrt} \{ 1.0 \text{ kcal-mol}^{-1} + (\Delta H_{\text{BAC-MP4}} - \Delta H_{\text{BAC-MP3}})^2 \\ & + (\Delta H_{\text{BAC-MP4}} - \Delta H_{\text{BAC-MP4SDQ}})^2 \\ & + 0.25 (E_{\text{BAC}} (\text{Spin } s_2) \text{ or } E_{\text{BAC}} (\text{Spin UHF-I}))^2 \} \quad (8) \end{aligned}$$

For many molecular species, the dominating term in the uncertainty is due to the spin correction. Transition state structures tend to have larger BAC-MP4 energy uncertainties than stable structures.

2.3. Heats of Formation, Entropies, and Free Energies

Having obtained the structure, vibrational energies, ab initio electronic energy, and the BAC energy corrections, we can then calculate the enthalpies, entropies, and free energies of a molecule using statistical mechanics (see Fig. 1). The statistical mechanics equations used in these calculations are an extension of the subroutines in the Gaussian codes²⁵. These subroutines use standard statistical mechanical expressions for an ideal gas in the canonical ensemble to compute the entropy, heat capacity, and internal energy.

The heat of formation at 0 K (ΔH_{f0}^0) is determined by adding the E_{MP4} energy to the zero-point energy (using unscaled frequencies) and then subtracting the resulting energy from the E_{MP4} energies of the atoms. This gives an MP4 heat of atomization. Referencing this energy against the experimental ΔH_{f0}^0 of the atoms in the gas phase yields the MP4 ΔH_{f0}^0 . Adding the BAC corrections to this energy finally yields ΔH_{f0}^0 at 0 K. The statistical mechanical calculations then provide the thermochemical

properties of the molecule, e.g., partition functions, enthalpy, heat capacity, and entropy for given temperatures. The values of these thermochemical properties as a function of temperature are then fit to an analytic polynomial (such as in Chemkin³⁴) for the modeling of ignition, combustion, and detonation processes in energetic materials.

2.4. Comparison of BAC-MP4 and Experimental Heats of Formation

The accuracy of the BAC-MP4 method has been determined by comparison of BAC-MP4 heats of formation with experimental values for approximately ninety stable molecular species¹⁷. The average difference between theory and experiment was 1.3 kcal-mol⁻¹. In Table I we present comparisons for selected molecular species of importance in energetic materials^{12-14,18,19}. One can see that in general the agreement is very good, not only for the stable species but for the radicals as well. This is particularly important for nitrogen-containing species for which the experimental data of radical species is lacking or of questionable accuracy. As the chemical environment of the nitrogen atom in the molecule becomes more electropositive (i.e., increasing hypervalent bonding, as in NO₂ and NO₃ groups), the BAC-MP4 results become more uncertain, as indicated by the error estimates given in Table I. Overall, the BAC-MP4 method appears to give reliable results which can be used in investigating the thermochemistry of energetic materials. Further details of the BAC-MP4 method, with applications to hydrocarbon combustion, can be found in ref. 17.

3. Bond Dissociation Energies and Energetics of Decomposition

3.1. Simple Bond Fission

The bond dissociation energy (BDE) required to break a molecule represents the difference in the heats of formation of the initial molecule and the resulting molecular fragments

$$\text{BDE} = \Delta H_{f298}^0 (\text{A}) + \Delta H_{f298}^0 (\text{B}) - \Delta H_{f298}^0 (\text{A-B}). \quad (9)$$

Having calculated the various heats of formation of both the stable and radical species, we can develop tables of BDE's of energetic species for comparison^{13,14}. The resulting bond dissociation energies of various nitro, nitroso, nitrite, nitrate, and azido compounds are given in Table II. Such a table provides various pieces of information. For instance, one can compare relative bond strengths within a given class of compounds. Thus, we see that CH₃ and C₂H₅ have similar BDE's for the various classes. When we replace the saturated C₂H₅ group by the unsaturated C₂H₃ group, we find that the bond strengths become significantly stronger. On the other hand, when we replace the saturated CH₃NH group by the unsaturated CH₂N group, we find that the bond strengths become weaker. We can also compare bond strengths between the various NO_x groups. For instance, we find that the BDE's for C-NO₂ compounds are stronger than the corresponding C-NO BDE's, while N-NO₂ BDE's

Table I. BAC-MP4 heats of formation at 298 K (ΔH_{f298}^0) along with calculated error estimates for selected molecular species of interest to energetic materials. Also given are the differences in energy between theory and experiment. Experimental values are taken from commonly referenced thermochemical data compilations. Energies are given in kcal-mol⁻¹.

Molecule	ΔH_{f298}^0	Theor. - Exp.	Molecule	ΔH_{f298}^0	Theor. - Exp.
CH ₃ NO ₂	-16.8±2.1	1.0 ^c	NO	21.6±1.2	0.0 ^b
CH ₃ ONO	-15.3±1.3	0.3 ^c	NO ₂	7.1±4.2	-0.8 ^b
CH ₃ ONO ₂	-26.1±3.6	2.5 ^d	NO ₃	22.7±9.5	5.7 ^b
C ₂ H ₅ NO ₂	-24.8±1.8	-0.4 ^c	OH	9.5±1.1	0.1 ^a
C ₆ H ₅ NO ₂	14.2±2.6	-1.5 ⁱ	HO ₂	3.6±1.8	1.1 ^a
C ₂ H ₅ ONO	-23.3±1.4	0.9 ⁱ	HCO	9.3±1.7	0.4 ^a
(CH ₃) ₂ N ₂ H ₂	21.1±2.1	1.0 ^c	CH ₃	34.9±1.2	0.1 ^a
HONO	-19.1±1.1	-0.8 ^h	C ₂ H ₅	28.8±1.3	0.5 ^a
HONO ₂	-30.2±3.9	2.1 ^b	NH ₂	46.1±1.1	0.6 ^g
N ₂ O	18.6±1.2	-1.0 ^b	NH	87.0±1.1	1.9 ^g
HN ₃	69.5±1.0	-0.9 ^f	CN	108.2±6.4	4.2 ^b
CH ₃ NHNH ₂	21.5±1.1	-1.1 ^c	CH ₂ NH ₂	35.7±1.3	0.0 ^e
HNO	23.3±2.1	-0.5 ^b	CH ₃ NH	44.8±1.1	2.4 ^e

^aW. Tsang and R. F. Hampson, J. Phys. Chem. Ref. Data 15, 1087 (1986); W. Tsang, J. Phys. Chem. Ref. Data 16, 471 (1987).

^bD. L. Baulch, R. A. Cox, R. F. Hampson, J. A. Kerr, J. Troe, and R. T. Watson, J. Phys. Chem. Ref. Data 13, 1259 (1984).

^cJ. D. Cox and G. Pilcher, Thermochemistry of Organic and Organometallic Compounds, Academic, London (1970).

^dD. R. Stull, E. F. Westrum, and G. C. Sinke, The Chemical Thermodynamics of Organic Compounds, John Wiley and Sons, New York (1969).

^eD. F. McMillen and D. M. Golden, Ann. Rev. Phys. Chem., p. 413, B. S. Rabinovitch, Ed., (1982).

^fS. Benson, Thermochemical Kinetics, John Wiley and Sons, New York (1976).

^gR. J. Kee, F. M. Rupley, and J. A. Miller, The Chemkin Thermodynamic Data Base, SAND87-8215, April (1987).

^hD. R. Stull and H. Prophet, JANAF Thermochemical Tables, NSRDS-NBS 37 (1971).

ⁱL. Batt and G. N. Robinson, in Supplement F: The Chemistry of Amino, Nitroso, and Nitro Compounds and Their Derivatives, Pt. 2, p. 1035, S. Patai, ed, John Wiley and Sons (1982).

Table II. Calculated bond dissociation energies for various nitro, nitroso, nitrite, nitrate, and azido molecular species. BDE's are determined from BAC-MP4 heats of formation at 298 K. (Energies in kcal-mol⁻¹.)

Nitroso Compounds		Nitro Compounds	
H--NO	50.3	H--NO ₂	73.4
CH ₃ --NO	37.6	CH ₃ --NO ₂	58.9
NH ₂ --NO	49.4	NH ₂ --NO ₂	51.4
HO--NO	50.2	HO--NO ₂	46.8
CH ₃ O--NO	43.5	CH ₃ O--NO ₂	39.9
CH ₂ N--NO	22.1	CH ₂ N--NO ₂	37.1
CH ₃ NH--NO	48.7	CH ₃ NH--NO ₂	50.6
CH ₂ CH--NO	51.0	CH ₂ CH--NO ₂	70.2
C ₂ H ₅ --NO	38.5	C ₂ H ₅ --NO ₂	60.8
NH ₂ CHCH--NO	60.6	NH ₂ CHCH--NO ₂	78.2
CHO--NO	29.2	CHO--NO ₂	49.8
NH ₂ O--NO	17.1	(CH ₃) ₂ N--NO ₂	45.9
HOO--NO	25.5	NH ₂ CHCH--NO ₂	78.2
CH ₃ NHO--NO	12.1		
CH ₂ CHO--NO	15.5		
Nitrite Compounds		Nitrate Compounds	
H--ONO	78.3	H--ONO ₂	105.0
CH ₃ --ONO	57.3	CH ₃ --ONO ₂	83.7
NH ₂ --ONO	32.9		
HO--ONO	17.1	Azido Compounds	
CH ₃ NH--ONO	29.3	H--NNN	90.1
(CH ₃) ₂ N--ONO	28.1	CH ₃ --NNN	70.5
CH ₂ N--ONO	22.1	C ₂ H ₅ --NNN	71.7
CH ₂ CH--ONO	68.5	NH ₂ CH ₂ --NNN	69.1
C ₂ H ₅ --ONO	59.3	CH ₂ CH--NNN	85.3
CHO--ONO	60.0		

are similar in strength to N-NO BDE's. However, C-NO₂ bond strengths are similar to C-ONO bond strengths while N-NO₂ bond strengths are stronger than N-ONO bond strengths. We find that all the azido bond strengths are significantly stronger than the corresponding nitro bond strengths. One can also use the table to determine which bond in a molecule is weakest. For instance, one finds that CH₃ONO and CH₃ONO₂ will decompose by breaking the O-N bond rather than the C-O bond.


Further information can be obtained by studying the BDE's of nitro compounds in greater detail. In Table III, we present the bond dissociation energies of the nitro compounds separated by classes (e.g., C-NO₂, N-NO₂, and O-NO₂). In comparing the various classes, we find that the R₂N-NO₂ compounds have larger bond strengths than the RO-NO₂ compounds but are weaker than the R₃C-NO₂ compounds which are weaker than the R₂C=CR-NO₂ compounds. This is consistent with the general trend that sensitivity of energetic materials correlates to some extent with the NO₂ bond strength.

Additional information can be obtained from looking at a given class of compounds, such as the nitramines (N-NO₂). One can see, for instance, that nitramine (NH₂NO₂), methyl nitramine (CH₃NHNO₂), and dimethylnitramine ((CH₃)₂NNO₂) have similar N-NO₂ bond dissociation energies (~ 47-51 kcal-mol⁻¹). This indicates that group-additivity concepts can be applied to estimating heats of formation of larger energetic materials that cannot be calculated using the BAC-MP4 method. Furthermore, we find that the BDE's of the nitramines do not change significantly when strain energy is introduced, such as in N-nitro azetidine.

Looking at the C-nitro class, we can see the effects of neighboring groups on the bond dissociation energy. For instance, replacing a hydrogen atom of nitromethane by a methyl or amino group has little effect on the BDE. One sees that replacing two hydrogen atoms of nitromethane by a C=C double bond increases the BDE significantly, replacing the hydrogens by a C=N double bond has little effect on the BDE, and replacing them by a C=O double bond decreases the BDE significantly. Note that the BDE of nitrobenzene, C₆H₅NO₂, is similar to that of nitroethylene, both containing an unsaturated C=C double bond. Furthermore, replacing the β-hydrogen of nitroethylene, C₂H₃NO₂, by a methyl group has little effect on the BDE while replacing the β-hydrogen by a amino or hydroxyl group increases the BDE significantly. The large C-NO₂ BDE for the NH₂CH=CHNO₂ molecular species, which possesses an amino group on the β-carbon connected to the nitro group through the unsaturated C=C double bond, is representative of triamino-trinitro-benzene, TATB, which is a highly insensitive explosive.

As a final observation of Table III, one finds that the nitro group BDE for geminal dinitro compounds, i.e., CH₂(NO₂)₂ and NH(NO₂)₂ are only slightly weaker than the corresponding mononitro compounds.

Table III. Calculated bond dissociation energies for various classes of nitro compounds. BDE's are determined from BAC-MP4 heats of formation at 298 K. (Energies in kcal-mol⁻¹.)

<u>C-Nitro Compounds</u>		<u>H-Nitro Compounds</u>	
CH ₃ --NO ₂	58.9	H--NO ₂	73.4
C ₂ H ₅ --NO ₂	60.8		
NH ₂ CH ₂ --NO ₂	59.2	<u>N-Nitro Compounds</u>	
HN=CH--NO ₂	59.8		
HOCH ₂ CH ₂ --NO ₂	61.8	NH ₂ --NO ₂	51.4
O ₂ N-CH ₂ CH ₂ --NO ₂	61.1	CH ₃ NH--NO ₂	50.6
CH ₂ =CH--NO ₂	70.2	(CH ₃) ₂ N--NO ₂	47.2
CH ₃ CH=CH--NO ₂	69.5	 --NO ₂	50.6
HOCH=CH--NO ₂ (no h.b.)	70.0	O ₂ NNH--NO ₂	47.8
HOCH=CH--NO ₂ (h.b.)	77.0	CH ₂ =N--NO ₂	37.1
cis-NH ₂ CH=CH--NO ₂	78.2		
trans-NH ₂ CH=CH--NO ₂	76.5	<u>O-Nitro Compounds</u>	
C ₆ H ₅ --NO ₂	72.4		
O ₂ N-CH ₂ --NO ₂	55.5	HO--NO ₂	46.8
HC(O)--NO ₂	49.8	CH ₃ O--NO ₂	39.9

3.2. Bond Fission of Radicals

The energy required to break a bond in a radical species can differ from the bond dissociation energy¹²⁻¹⁴. In general, for radical species, one must also consider a barrier to dissociation in addition to the bond dissociation energy. These energies are indicated in Table's IV and V, where we present the bond dissociation energies and activation energies for the reverse process of the radical attack, leading to insertion into the π bond of the stable molecule to form the radical adduct. Note that the BDE for removing the radical species from the radical adduct is much smaller than the corresponding BDE for a stable molecule. This is due to the energy gained back by formation of a π bond. In fact, for some adducts, the BDE is negative because the π bond is stronger than the σ bond that is formed, particularly when the σ bond is between two electronegative atoms.

Table IV. Bond dissociation energies for selected radicals bonded to various π -bond-containing molecules. This corresponds to the heat of reaction for $AR \rightarrow A + R$. The arrow indicates the atomic site to which the radical is bonded. Heats of formation at 298 K are given in parentheses. Energies are in $\text{kcal}\cdot\text{mol}^{-1}$.

Molecule \ Radical	H (52.1)	CH ₃ (34.9)	NH ₂ (46.1)	OH (9.5)	O (59.4)
\downarrow HCCH (54.2)	35.3	24.4	25.3	33.4	50.8
\downarrow H ₂ CCH ₂ (12.3)	35.6	22.4	16.9	26.4	22.1
\downarrow HCN (31.8)	25.0	16.5	21.0	27.7	31.0
\downarrow HCN (31.8)	18.0	-2.2	18.6	-20.4	-17.0
\downarrow CH ₂ O (-25.9)	19.5	9.5	8.2	22.8	6.8
\downarrow CH ₂ O (-25.9)	31.1	7.6	-18.0	-33.2	-25.0

Table V. Activation energies for selected radicals attaching to various π -bond-containing molecules. This corresponds to the barrier height for the reaction $A + R \rightarrow AR$. The arrow indicates the atomic site to which the radical will bond. The energy required to break the bond is equal to the bond dissociation energy (see Table IV) plus this activation energy. Energies are in $\text{kcal}\cdot\text{mol}^{-1}$.

Molecule \ Radical	H	CH ₃	NH ₂	OH	O
\downarrow HCCH	3.5	8.2	8.4	<0.0	5.0
\downarrow H ₂ CCH ₂	2.9	7.6	2.1	<0.0	<0.0
\downarrow HCN	5.6	8.5		<0.0	9.0
\downarrow HCN	9.0	23.9		<20.4	25.0
\downarrow CH ₂ O	5.9	7.8	1.8	<0.0	10.3
\downarrow CH ₂ O	9.4	14.7	25.9		27.2

4. Complex Fission

4.1. Five-centered HONO Elimination

So far we have discussed simple bond fission in which only one bond is broken. In this section we discuss decomposition pathways in which multiple bonds are broken and formed simultaneously¹³⁻¹⁴. In particular, we present results for five-centered HONO elimination from nitro compounds containing a β -hydrogen as well as results for concerted decomposition of six-membered ring compounds.

For simple bond fission, the activation energy generally corresponds to the bond energy. However, for multiple bond breaking, as in a multi-centered elimination process, the barrier height may be less than the individual bond energies. The dominating reaction process will depend not only on the barrier height but also on the entropy terms entering the pre-exponential factor¹¹. By taking differences between the free energy of a molecular species at the transition state theory (TST) structure, ΔG^\ddagger , and the free energies of the reactant(s), $\Delta G_{\text{reactants}}$, one can use TST to obtain rate constants $k(T)$ at any given temperature, e.g.,

$$k(T) = (kT/h) (RT)^{-\Delta\nu} \exp(-(\Delta G^\ddagger - \sum \Delta G_{\text{reactants}})/RT). \quad (10)$$

For more complicated reactions, RRKM theory can be applied, using the statistical mechanical partition functions calculated within the BAC-MP4 method³⁵⁻³⁸.

Thus one needs to know the free energies as well as the heats of formation of the reactants, transition state structures, and possible intermediate complexes. The results for methylnitramine decomposition are given in Table VI and compared with nitroethane. Using Eqn. 10 above and the free energies given in Table VI to determine the five-centered elimination rate constant, the resulting theoretical rate constant for nitroethane is presented in Fig. 2 and compared with experimental values. The activation energy was shifted downward by 3.4 kcal-mol⁻¹, corresponding to an earlier estimate of the activation energy (see Ref. 13 or 14). Notice in Table VI the large uncertainty in the BAC-MP4 estimate of the transition state structure's heat of formation. Based on the comparison in Fig. 2, it would appear that the BAC-MP4 method overestimates the activation energy by 3-6 kcal-mol⁻¹, while the resulting pre-exponential A factor is in excellent agreement. At the highest temperatures, there is a departure from the five-centered-elimination curve due to the introduction of the direct NO₂ bond fissioning process. The experimental slope of 60 kcal-mol⁻¹ is in good agreement with the calculated bond dissociation energy of 60.8 kcal-mol⁻¹ given in Table III.

In Fig. 3, we compare the energetics for NO₂ bond fission and HONO elimination for various classes of nitro compounds, represented by CH₃ONO₂, CH₃NHNO₂, CH₃CH₂NO₂, and CH₂=CHNO₂. We see that the nitramine and nitrate ester have weaker NO₂ BDE's than does the C-nitro compound, nitroethane, though methylnitramine and nitroethane have similar energy barriers for HONO elimination. Thus, NO₂ formation is more likely to occur than direct HONO elimination under the fast heating rates for the O-nitro and N-nitro compounds. From Fig. 3, we see that

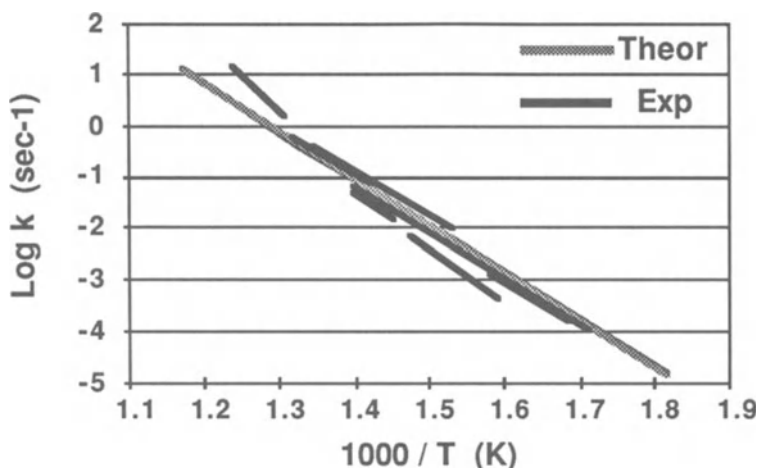


Fig. 2. Comparison of experimental and theoretical decomposition rate constants for nitroethane, $\text{CH}_3\text{CH}_2\text{NO}_2$. Theoretical curve represents the five-centered elimination, calculated using the BAC-MP4 method, using an activation energy of 41 $\text{kcal}\cdot\text{mol}^{-1}$ taken from ref. 13. Experimental data is taken from G. M. Nazin, G. B. Manelis, and F. L. Dubovitskii, *Russ. Chem. Rev.* **37**, p. 603 (1968).

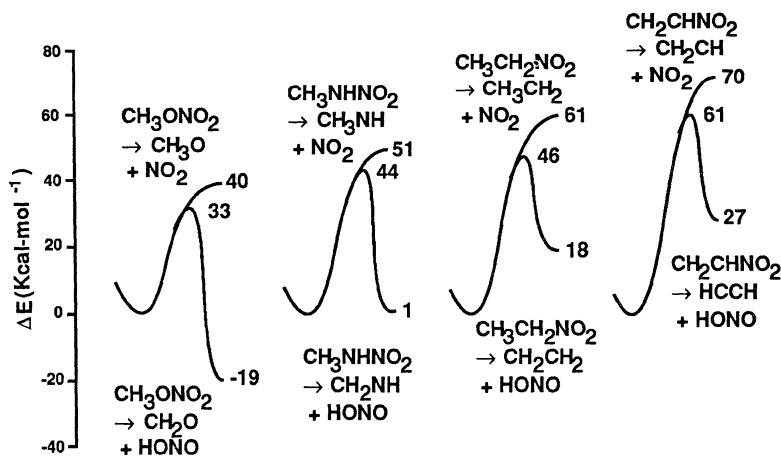


Fig. 3. Comparison of decomposition energetics of NO_2 bond breaking and HONO elimination for CH_3ONO_2 , CH_3NHNO_2 , $\text{CH}_3\text{CH}_2\text{NO}_2$, and $\text{CH}_2=\text{CHNO}_2$, calculated using the BAC-MP4 heats of formation at 298 K. For each molecule, the top energy value represents the bond dissociation energy for NO_2 bond fission, the middle energy value represents the barrier height for the five-centered elimination to form HONO, while the bottom energy value represents the heat of dissociation for the formation of HONO. (Energies are in $\text{kcal}\cdot\text{mol}^{-1}$.)

Table VI. BAC-MP4 calculated $\Delta H_f^\circ(T)$'s and $\Delta G_f^\circ(T)$'s for species involved in the decomposition of methylnitramine and nitroethane. Error estimates are given for 0 K; uncertainties in entropies will increase the error estimates for the free energies. (Energy is in kcal-mol⁻¹, temperature in K.)

Molecular species /Temperature	$\Delta H_f^\circ(T)$		$\Delta G_f^\circ(T)$			
	0	300	300	600	1000	1500
CH ₃ NHNO ₂	6.1±5.4	1.4	26.1	51.7	86.8	130.2
CH ₃ CH ₂ NO ₂	-19.8±1.8	-24.8	-3.1	19.4	50.5	89.4
NO ₂	7.8±4.2	7.1	11.5	16.0	22.1	29.6
CH ₃ NH	47.7±1.1	44.8	52.5	61.1	73.6	89.8
CH ₃ CH ₂	31.5±1.3	28.8	34.1	40.3	49.9	62.6
HONO	-17.5±1.1	-19.1	-10.9	-2.5	8.9	23.1
CH ₂ NH	23.5±1.1	21.6	26.4	31.6	39.6	50.0
CH ₂ CH ₂	14.5±1.0	12.3	15.9	20.0	26.7	35.9
CH ₃ NHNO ₂ → CH ₂ NH + HONO	50.2±14.3	45.4	71.5	98.4	135.2	180.8
CH ₃ CH ₂ NO ₂ → C ₂ H ₄ + HONO	25.5±9.3	20.7	44.5	69.2	103.2	145.7

there is a strong correlation between the heat of reaction for HONO elimination and heat of reaction for NO₂ bond fissioning across the classes of nitro compounds (corresponding to similar bond strengths of the β -hydrogen). We believe that the trend in sensitivities for the various classes of nitro compounds (decreasing from left to right in Fig. 3), which inversely correlates with the NO₂ BDE's, is actually correlated with the heats of reaction to form the HONO. HONO formation (which equilibrates with NO, NO₂, and H₂O) represents the end of the first stage in the decomposition of energetic materials, whereby the NO₂ formed in the initial steps of decomposition reacts rapidly with the weakly bond hydrogen atoms from the energetic material in order regain energy lost in the initial bond breaking steps in the decomposition.

4.2 Concerted Decomposition

An alternative decomposition reaction pathway to the those discussed above is a concerted process, in which the activation energy can be considerably lower than any of the individual bonds to be broken. In Table VII, we present the heats of reaction and activation energies for the concerted decomposition of six-membered rings into three molecular species. Also given are the calculated rate constants. For trioxane, the experimental and theoretical rate constants are in very good agreement, the BAC-MP4 value being too high by approximately 2 kcal-mol⁻¹. While the BAC-MP4 method cannot treat a molecule the size of RDX, the results of the hydrogen analog, hexahydro-*s*-triazine, indicates that the rate constant should have a large pre-exponential A factor similar to that of NO₂ bond fissioning, with an activation energy somewhat larger than the NO₂ BDE.

Table VII. Energetics of the concerted decomposition of six-membered ring compounds. Tabulated rate constant parameters, i.e., the pre-exponential A factors and activation energies, ΔE 's, represent the tangential value of the calculated BAC-MP4 rate constants at 600 K. ΔH_{Rxn} and ΔE_{Rxn} are evaluated at 298 K. Energies are in kcal-mol⁻¹.

	ΔH_{Rxn}	ΔE_{Rxn}	Rate Constant A(sec ⁻¹)	ΔE
Trioxane				
(-CH ₂ O-) ₃ → 3 CH ₂ O	32.9	49.3	10 ^{16.0}	52.3
Experimental	35.3		10 ^{15.0}	47.4
Hexahydro- <i>s</i> -Triazine				
(-CH ₂ NH-) ₃ → 3 CH ₂ NH	30.1	61.7	10 ^{16.5}	65.2
Cyclohexane				
(-CH ₂ CH ₂ -) ₃ → 3 CH ₂ CH ₂	66.3	122.1	10 ^{17.1}	125.7
<i>s</i> -Triazine				
(-CHN-) ₃ → 3 HCN	33.4	81.5	10 ^{16.9}	80.6
RDX				
RDX → 3 CH ₂ NNO ₂	41.1			

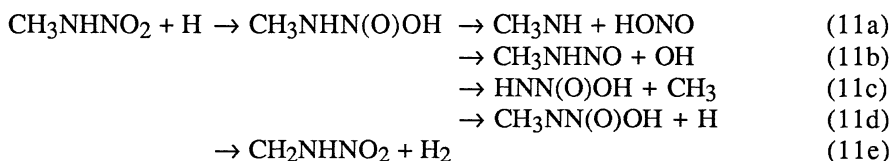
5. Autocatalytic Decomposition

As an alternative reaction pathway to unimolecular decomposition in which the molecule rearranges or fissions by itself, one must also consider mechanisms in which the decomposition process is assisted by other molecular species formed during the decomposition. Such alternative reaction pathways can greatly reduce the effective activation energy of decomposition. In this section, we consider two possible decomposition pathways, radical assisted and water assisted.

5.1. Radical Attack on Energetic Materials

Radical species such as H atoms and OH molecules can react with energetic molecules in either of two ways. On the one hand, the radical species can abstract a hydrogen atom from the energetic molecule to form a radical species containing one fewer atoms. On the other hand, the attacking radical can form a radical adduct that can either be stabilized by collisions with its surroundings or can directly undergo further bond fissioning. As an example of such a reaction, the detailed reaction pathways for $\text{HCN} + \text{OH}$ can be found in ref. 37, where RRKM theory has been applied to determine the branching ratios and rate constants for the reaction.

In Fig. 4 we present the reaction pathways for hydrogen atom attacking methylnitramine:



One can see from Fig. 4 that the net energy required to break the N-N bond (reaction 11a) is less than $10 \text{ kcal}\cdot\text{mol}^{-1}$. This energy, corresponding to the activation barrier for addition of the H atom to the oxygen atom of the NO_2 group, is considerably less than the $51 \text{ kcal}\cdot\text{mol}^{-1}$ energy required to unimolecularly break the N-N bond (see Table III). Also, the overall N-N bond breaking process is exothermic. Meanwhile, as one can see from Fig. 4, other reaction pathways (reactions 11b-11d) exist which can produce other radicals, e.g., CH_3 and OH . Competing with the reaction pathways which proceed through the $\text{CH}_3\text{NHN}(\text{O})\text{OH}$ adduct is the direct abstraction reaction 11e.

The reaction of radicals with unsaturated molecules, such as nitro and nitroso groups, to form radical adducts is the reverse process of bond fissioning of radicals discussed in section 3.2 above. The rate constants for the bimolecular reaction of radicals with energetic molecules should be on the order of $10^{11}\text{-}10^{12} \text{ mol}\cdot\text{cm}^{-3}\cdot\text{sec}^{-1}$. The rates are also proportional to the concentration of radicals¹¹. In general, the formation of a significant concentration of radicals requires fairly high temperatures. In this case, however, direct unimolecular decomposition can occur, due to the large pre-exponential factor for simple bond fissioning¹¹. Furthermore, NO_2 and NO ,

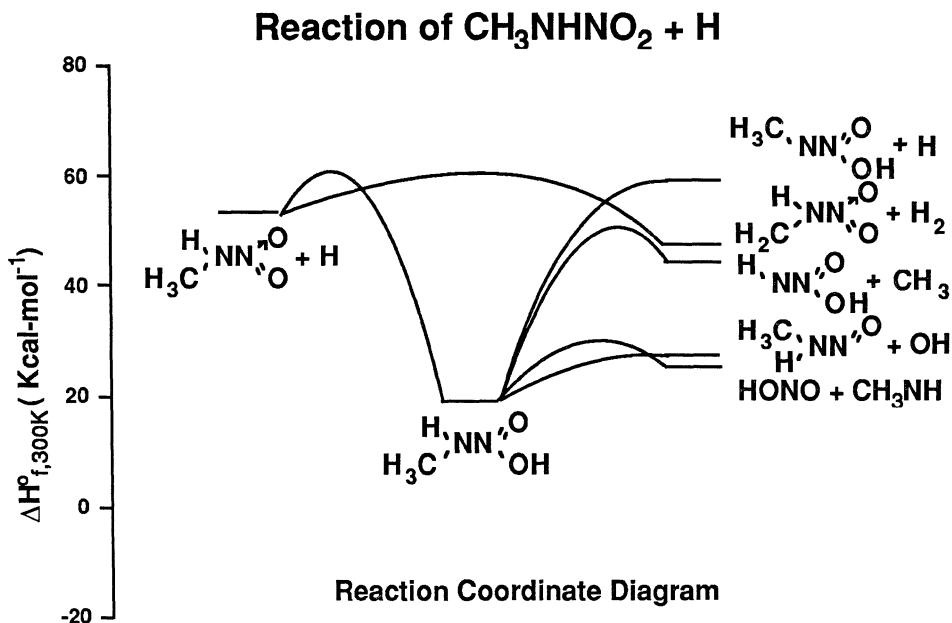
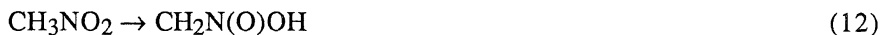


Figure 4. Calculated reaction pathways for the reaction of $\text{CH}_3\text{NHNO}_2 + \text{H} \rightarrow$ products, based on BAC-MP4 heats of formation at 298 K for stable species and transition state structures. Energies are in kcal-mol⁻¹.

themselves weakly reacting radicals, are intermediates of decomposition which scavenge the H and other radicals, decreasing the importance of these radicals in assisting the initial reaction step for decomposition. On the other hand, the NO_2 and NO radicals, along with OH , react readily with the large radical species formed from the unimolecular decomposition by abstracting hydrogen atoms to form stable intermediates along with HONO , HNO , and H_2O , respectively. In modeling of the chemical reactions occurring in the ignition and combustion of energetic materials¹⁵⁻¹⁶, we find that radicals play a more important role in the subsequent gas phase reactions involving the intermediates formed in the decomposition processes.

5.2. Water-assisted Reactions

The internal rearrangement of molecules, such as the 1,3-hydrogen shift of a nitro compound to form its *aci* form, e.g.,



or



typically requires a large activation energy^{12,14}. In aqueous media, this process can occur through an acid-base reaction process in which, for instance, the nitro compound can first be protonated on the oxygen and then deprotonated at the β site. We have found that rearrangements such as reactions (12) and (13) can be catalyzed by a single water molecule through a concerted reaction. In fact, we find that the *aci* form of nitramine can be further catalytically converted to N_2O and H_2O by an additional water molecule. The two-step concerted reaction mechanism is shown in Fig. 5. The resulting energetics of the reaction are shown in Fig. 6. The higher curve in Fig. 6 represents the barrier heights if the reaction proceeded as a unimolecular process with no additional water molecule present, i.e., uncatalyzed. The lower curve in Fig. 6 represents the barrier heights for the catalyzed, bimolecular reaction process as indicated in Fig. 5. We thus see that the presence of water molecules can have an enormous effect on assisting the decomposition process.

Another way in which water can catalyze the decomposition process is through hydration and hydrolysis. For example, the reaction of methylene-nitramine, CH_2NNO_2 , with a water molecule assists in the conversion of CH_2NNO_2 to CH_2O and N_2O . The water-catalyzed reaction pathway is indicated in Fig. 7. The first step, hydration, has the higher activation energy. Using transition state theory with the BAC-MP4 free energies, the resulting bimolecular reaction rate is found to be $10^{8.92} e^{-24.1/RT} \text{ mol}\cdot\text{cm}^{-3}\cdot\text{sec}^{-1}$. Replacing the hydrogen atoms by deuterium atoms, we find an interesting result for the deuterium kinetic isotope effect, DKIE, defined by $k_{\text{H}} / k_{\text{D}}$. The same reaction step has a DKIE value of 1.29 at 600 K while it has a value of 0.97 at 300 K.

As a final reaction mechanism catalyzed by water, we consider the hydration/hydrolysis reaction of an imine, CH_2NH . The reaction energetics are shown in Fig. 8. As a simple bimolecular reaction, the four-centered addition transition state structures leading to hydration and hydrolysis have high activation barriers. The presence of an additional water molecule, providing six-centered transition state structures, lowers the barrier heights significantly. It should be noted that the hydrated form of the imine is the more stable form of the imine in aqueous solutions, as indicated in Fig. 8. This is also true of formaldehyde, for which the hydrated form, $\text{CH}_2(\text{OH})_2$, is the more stable.

We therefore see that when water is present, decomposition mechanisms can be altered by the catalytic effect of water. Additional water molecules will lead to further lowering of the activation energies. However, the participation of the additional water molecules in the transition state structure imposes a constraint in the entropy, leading to smaller pre-exponential A factors. Thus, the catalytic effects of water and other species such as formaldehyde will be most important at lower temperatures and higher densities, as in the condensed phase.

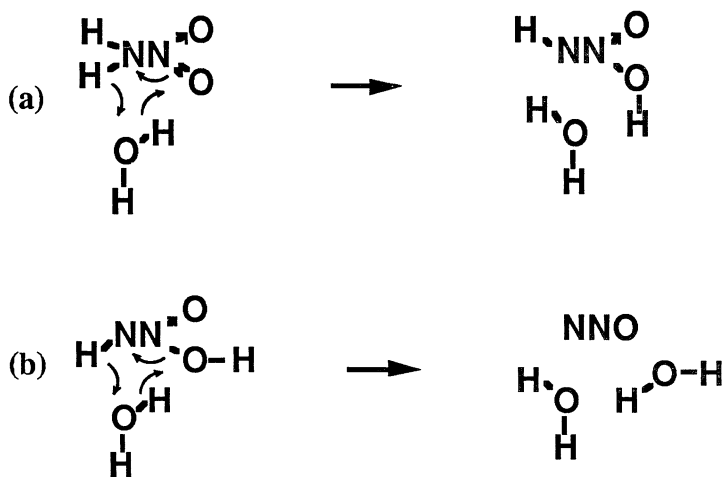


Figure 5. Reaction diagrams for the water-catalyzed concerted reaction for the conversion of nitramine, NH_2NO_2 , to $\text{N}_2\text{O} + \text{H}_2\text{O}$ through the intermediate *aci* form, $\text{HNN}(\text{O})\text{OH}$. In the first concerted mechanism (a), the hydrogen from the nitramine shifts to the water molecule while the hydrogen on the water molecule shifts to the oxygen of the nitramine, thereby forming the *aci* molecule. In the second step (b), the *aci* molecule is converted to N_2O and H_2O by again having the hydrogen bonded to the nitrogen shifting to the water molecule while the hydrogen on the water molecule is shifted to the hydroxyl group of the *aci* molecule.

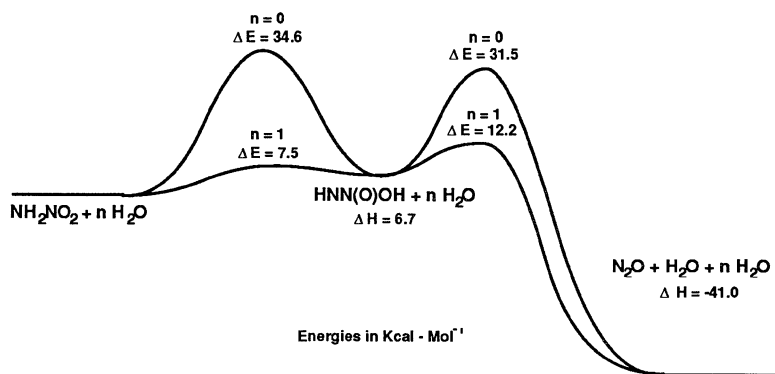


Figure 6. Energetics of the reaction pathways for the conversion of nitramine, NH_2NO_2 , to N_2O and H_2O . As a unimolecular four-centered process with no water molecule present ($n = 0$), the activation energies are high. On the other hand, as a six-centered bimolecular process involving another water molecule ($n = 1$), the activation energies are greatly lowered. Energies are in kcal·mol⁻¹.

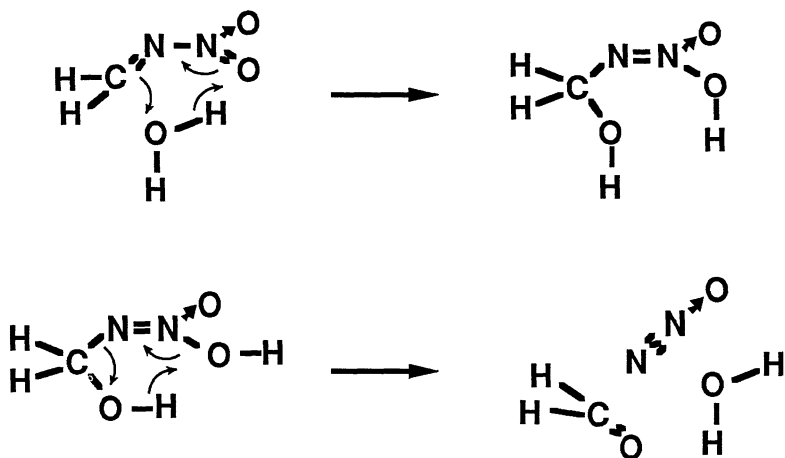


Figure 7. Reaction diagrams for the water-catalyzed concerted reaction for the conversion of methylene-nitramine, CH_2NNO_2 , to $\text{CH}_2\text{O} + \text{N}_2\text{O}$ through the hydrated intermediate $\text{CH}_2\text{OHNN}(\text{O})\text{OH}$. In the first concerted mechanism, the CH_2NNO_2 molecule is hydrated. In the second step, the hydrated molecule is unimolecularly converted to CH_2O and N_2O . Note that the oxygen atom in the CH_2O molecule arises from the water molecule rather than the NO_2 group.

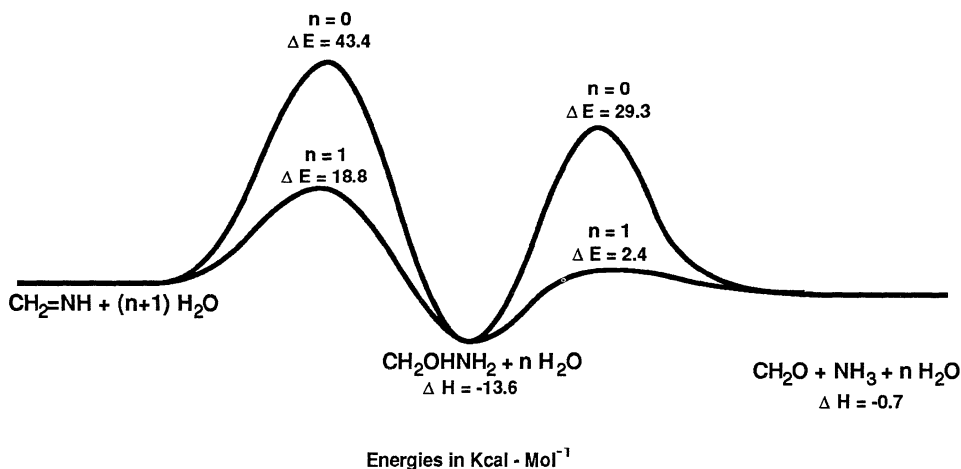


Figure 8. Energetics of the reaction pathways for the hydrolysis of $\text{CH}_2=\text{NH}$ to $\text{CH}_2\text{O} + \text{NH}_3$ through the hydrated intermediate CH_2OHNH_2 . As a bimolecular four-centered process with no additional water molecule present ($n = 0$), the activation energies are high. On the other hand, as a six-centered trimolecular process involving a second water molecule ($n = 1$), the activation energies are greatly lowered. Energies are in $\text{kcal} \cdot \text{mol}^{-1}$.

6. Decomposition Pathways for Nitramine Compounds

Given the bond dissociation energies for various prototype molecular species including radicals, we can estimate the BDE's for larger molecular species of importance to energetic materials¹²⁻¹⁴. We can then formulate the order in which the chemical bonds will break, i.e., how the molecule will decompose. This is illustrated in Fig. 9 for HMX where the bond breaking energies (including any additional activation barrier energies) have been estimated from smaller prototype molecular species¹². In the HMX molecule, the weakest bond is N-NO₂, which is ~48 kcal-mol⁻¹. The C-N and C-H bonds are significantly stronger. However, after the NO₂ group has left, the resulting second-nearest-neighbor bond breaking energies become very weak (e.g., the C-N bond breaking energy is ~18 kcal-mol⁻¹). Similarly, if an H atom has been removed, the second-nearest-neighbor bond energies also become very weak (e.g., the N-NO₂ bond energy is negative with only a 2 kcal-mol⁻¹ barrier for leaving). Similar results apply for the RDX molecule.

Combining this information, we can develop a pathway for unimolecular decomposition of HMX or RDX. The decomposition steps for RDX are shown in Fig. 10. The order of bond breaking and the bond breaking energies are indicated in the figure. The net products are HCN, NO₂, and H atoms. The decomposition pathway shown in Fig. 10 is appropriate for rapid thermal heating rates, where catalytic effects are not important, since the unimolecular rate constants will be sufficiently fast. Typically, the pre-exponential A factor of the rate constant, used in the Arrhenius form, $k = A T^n \exp(-\Delta E/RT)$, for bond fissioning of the nitro group will be on the order of 10¹⁶ sec⁻¹ (see ref. 11). The A factors for bond fissioning of the radical species will be somewhat smaller due to the tighter transition state structures, particularly if there is a significant barrier (see Table V). However, the significantly weaker bond dissociation energies of the radical will make up for the smaller A factors, allowing the molecule to unravel by simple bond fissioning.

In the condensed phase, alternative decomposition mechanisms can occur. For instance, the NO₂ group which breaks off the energetic material can be trapped in the vicinity of the corresponding energetic molecular radical. This process has been called the cage effect¹⁰. The NO₂ molecule can then recombine as a nitrite, which can decompose by breaking the O-N bond to form NO. As can be seen from Table II, the conversion of the NO₂ group to the NO group is thermodynamically favored. On the other hand, the NO₂ molecule can abstract weakly bond hydrogen atoms from the resulting radical (see Fig. 9 and Table IV), forming HONO. The HONO rapidly equilibrates by the reaction



to form water. As was discussed in section 5.2, water can catalyze the decomposition of nitramines. In Fig. 11, we present a reaction diagram for the unraveling of HMX or RDX (which contain the repeating substructure -CH₂N(NO₂)-) to form CH₂O and N₂O. The first step is the hydrolysis of the C-N bond in species (1) to form a primary

Initially

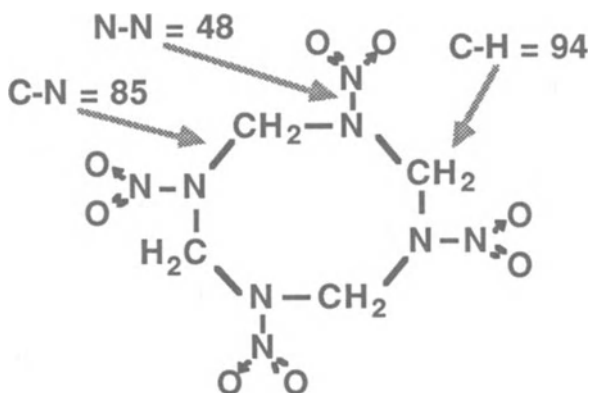
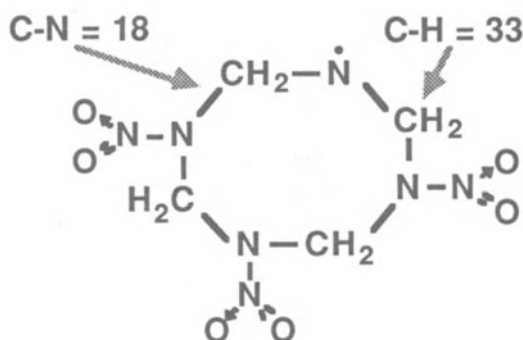
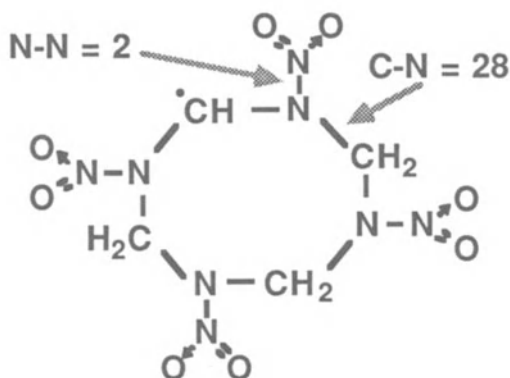
After NO₂
RemovalAfter H
Removal

Figure 9. Bond breaking energies (bond dissociation energies plus any additional activation energies) for (a) HMX, (b) HMX radical after a nitro group has been removed, and (c) the HMX radical after a hydrogen atom has been removed. Note that when a radical center exists (denoted by a dot), it is the second-nearest-neighbor bonds which become significantly weaker. Energies are in kcal-mol⁻¹.

nitramine species (2) and a hydroxymethyl species (3). In a process analogous to Figs. 5 and 6, the primary nitramine (2) is then converted with the assistance of water to the *aci* form and then to the hydroxymethyl species (3) with the formation of N_2O . In a process analogous the the second step in Fig. 8, the hydroxymethyl species (3) is converted to a primary nitramine (2) with the formation of CH_2O . These unzipping processes are repeated, until the nitramine is converted to CH_2O and N_2O . We see that these products are very different from those obtained from the high heating rate, simple bond fissioning decomposition mechanism presented in Fig. 10. The initial hydrolysis step (breaking the C-N bond) is likely to be the rate determining step within Fig. 11, since the subsequent reactions should be rapid.

Decomposition of RDX

At Fast Heating Rates

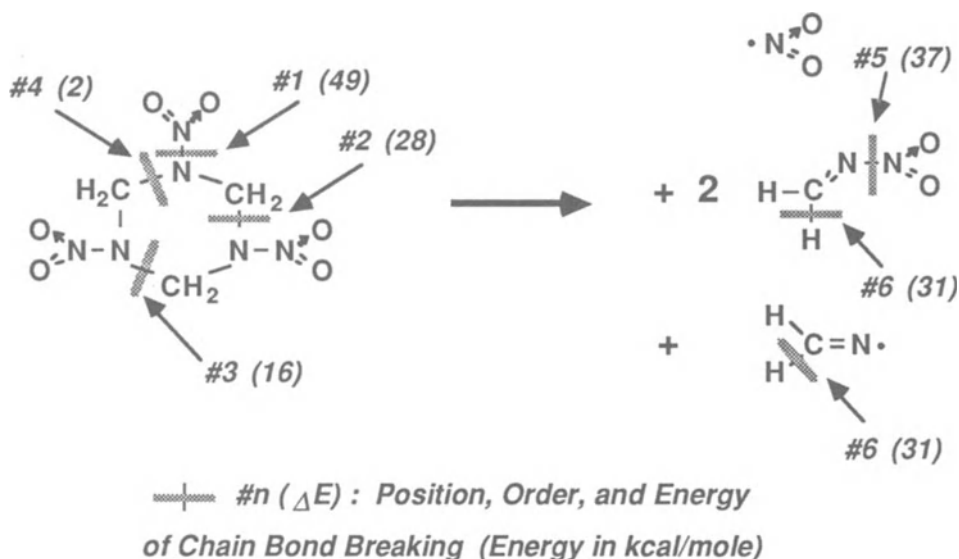


Figure 10. Decomposition mechanism for RDX under rapid heating rates. The number indicates the order in which the bonds are broken. The bond breaking energies (in $\text{kcal}\cdot\text{mol}^{-1}$) are given in parentheses. The final products are HCN , NO_2 , and H . A similar decomposition pathway exists for HMX.

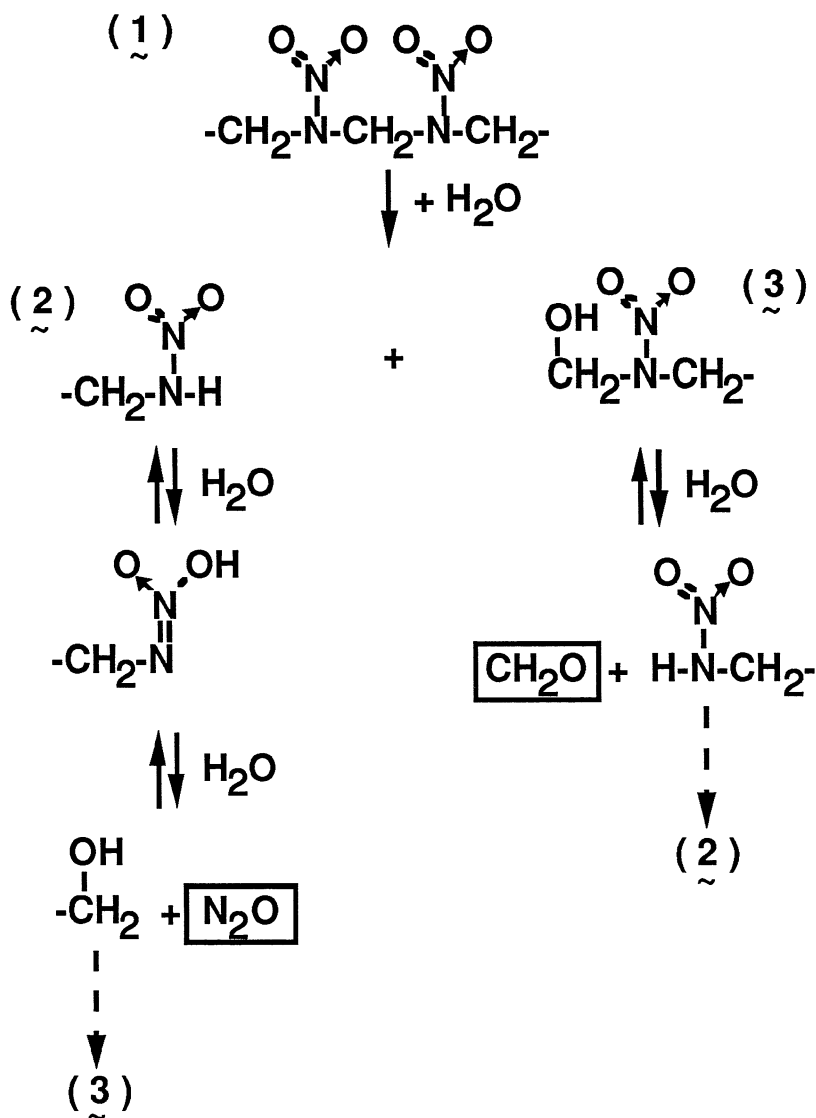


Figure 11. The water-catalyzed decomposition pathway for nitramines containing the $(-\text{CH}_2\text{N}(\text{NO}_2)-)$ subgroup. The initial step is the hydrolysis of the C-N bond in (1) to form the primary nitramine (2) and the hydroxymethyl species (3). The primary nitramine undergoes further decomposition to form N_2O and the hydroxymethyl species (3), which undergoes further decomposition to form CH_2O and the primary nitramine (2)

In an analogous manner to the development of decomposition pathways for nitramines, estimates can be made for the decomposition pathways of other classes of energetic materials. For instance, nitrate esters will first break off an NO_2 group. From Tables IV and V, one concludes that the resulting alkoxy radical will readily decompose to form an aldehyde, with the subsequent radical eliminating a nitro group, forming another aldehyde.

7. Conclusions

The decomposition of energetic materials has been presented from a theoretical viewpoint based on the thermochemical properties of energetic molecules and their intermediates. The BAC-MP4 method was presented as a means of calculating accurate heats of formation, entropies, and free energies of these molecular species. These thermochemical data, providing bond energies and activation energies, were used to determine initial bond breaking in energetic molecules. Both simple bond fissioning as well as concerted decomposition mechanisms were considered. Catalytic decomposition mechanisms, due to radical species attack and water-assisted concerted pathways, were presented. The thermochemistry of these reaction mechanisms was then applied to develop unimolecular as well as autocatalyzed decomposition mechanisms for the nitramines. The theoretical concepts presented in this paper can be applied to other classes of energetic materials. In the second paper by this author in this NATO ASI proceedings, these results are used to develop detailed chemical kinetics models for the ignition and combustion of energetic materials.

References

- ¹R. A. Fifer, in Fundamentals of Solid Propellant Combustion, M. Summerfield and K. Kuo, Eds., 1984, Chapter 4, p 177.
- ²T. L. Boggs, in Fundamentals of Solid Propellant Combustion, M. Summerfield and K. Kuo, Eds., 1984, Chapter 3, p 121.
- ³D. A. Flanagan, "Nitramine Combustion", AFRPL TR-84-004, January 1984.
- ⁴M. A. Schroeder, BRL Technical Report BRL-TR-2659, June 1985, and references therein.
- ⁵M. A. Schroeder, BRL Technical Report BRL-TR-2673, September 1985, and references therein.
- ⁶F. I. Dubovitskii and B. L. Korsunskii, Russian Chemical Reviews 50, p. 958 (1981).
- ⁷R. Shaw and F. E. Walker, J. Phys. Chem., 81, p. 2572, 1977.
- ⁸D. F. McMillen, J. R. Barker, K. E. Lewis, P. L. Trevor, and D. M. Golden, Final Report on SRI Project PYU 5787, June 1979 (AD-A039 019).
- ⁹T. B. Brill and Y. Oyumi, J. Phys. Chem. 90, 6848 (1986) and references therein.
- ¹⁰R. A. Fifer, Proceedings of the 19th JANNAF Combustion Meeting, Vol. I, p. 311, October 1982, CPIA Publication 366.
- ¹¹S. Benson, Thermochemical Kinetics, 2nd ed., John Wiley and Sons, New York (1976).
- ¹²C. F. Melius and J. S. Binkley, Twenty-first Symp. (Internat.) on Comb., p. 1953, The Comb. Inst. (1986).

- ¹³C. F. Melius, Proceedings of the 23rd JANNAF Combustion Meeting, Vol. I, p.157, October 1986.
- ¹⁴C. F. Melius, J. de Physique Colloque C4, Vol. 48, p. 341 (1987).
- ¹⁵C. F. Melius, Proceedings of the 24th JANNAF Combustion Meeting, October 1987.
- ¹⁶C. F. Melius, Proceedings of the 25th JANNAF Combustion Meeting, October 1988.
- ¹⁷C. F. Melius, "Thermochemistry of Hydrocarbon Intermediates in Combustion: Application of the BAC-MP4 Method", in DFVLR Lecture Series, T. Just, ed., Springer Verlag, in press.
- ¹⁸C. F. Melius and J. S. Binkley, Twentieth Symp. (Internat.) on Comb., p. 575, The Comb. Inst. (1984).
- ¹⁹C. F. Melius and J. S. Binkley, ACS Combustion Symposium, 249, p. 103 (1984).
- ²⁰P. Ho, M. E. Coltrin, J. S. Binkley, and C. F. Melius, J. Phys. Chem. 89, 4647 (1985); J. Phys. Chem. 90, 3399 (1986).
- ²¹C. F. Melius and J. S. Binkley, Western States Section/Combustion Institute 83-61, Oct. 1983.
- ²²C. W. Bauschlicher, Jr. and S. R. Langhoff, Chem. Phys. Lett. 135, 67 (1987).
- ²³C. W. Bauschlicher, Jr., S. R. Langhoff, and P. R. Taylor, Astrophys. J. 332, 531 (1988).
- ²⁴J. A. Pople, B. T. Luke, M. J. Frisch, and J. S. Binkley, J. Phys. Chem. 89, 2198 (1985).
- ²⁵See, for example, "Gaussian 86", M. J. Frisch, J. S. Binkley, H. B. Schlegel, K. Raghavachari, C. F. Melius, R. L. Martin, J. J. P. Stewart, F. W. Bobrowicz, C. M. Rohlfing, L. R. Kahn, D. J. DeFrees, R. Seeger, R. A. Whiteside, D. J. Fox, E. M. Fluder, S. Topiol, and J. A. Pople, Carnegie-Mellon Quantum Chemistry Publishing Unit, Carnegie-Mellon University, Pittsburgh PA 15213.
- ²⁶C. C. J. Roothaan, Rev. Mod. Phys. 23, 69 (1951).
- ²⁷J. A. Pople and R. K. Nesbet, J. Chem. Phys. 22, 571 (1954).
- ²⁸P. C. Hariharan and J. A. Pople, Theor. Chim. Acta 28, 213 (1973); M. M. Francl, W. J. Pietro, W. J. Hehre, J. S. Binkley, M. S. Gordon, D. J. DeFrees, and J. A. Pople, J. Chem. Phys. 77, 3654 (1982).
- ²⁹D. J. DeFrees, B. A. Levi, S. K. Pollack, W. J. Hehre, J. S. Binkley, and J. A. Pople, J. Amer. Chem. Soc. 101, 4085 (1979); 102, 2513 (1980); D. J. DeFrees, K. Raghavachari, H. B. Schlegel, and J. A. Pople, J. Amer. Chem. Soc. 104, 5576 (1982).
- ³⁰J. A. Pople, R. Krishnan, H. B. Schlegel, and J. S. Binkley, Int. J. Quant. Chem. S13, 225 (1979).
- ³¹J. A. Pople, H. B. Schlegel, R. Krishnan, D. J. DeFrees, J. S. Binkley, M. J. Frisch, and R. A. Whiteside, Int. J. Quant. Chem. S15, 269 (1981).
- ³²R. Krishnan and J. A. Pople, Int. J. Quant. Chem. 14, 91 (1978); R. Krishnan, M. J. Frisch and J. A. Pople, J. Chem. Phys. 72, 4244 (1980).
- ³³H. B. Schlegel, J. Chem. Phys. 84, 4530 (1986).
- ³⁴R. J. Kee, F. M. Rupley, and J. A. Miller, The Chemkin Thermodynamic Data Base, SAND87-8215, April (1987).
- ³⁵R. A. Perry and C. F. Melius, 20th Symp. (Int.) on Comb., p. 639, The Combustion Institute 1984.
- ³⁶J. A. Miller, C. Parrish, and N. J. Brown, J. Phys. Chem. 90, 3339 (1986).

³⁷J. A. Miller and C. F. Melius, 21st Symp. (Int.) on Comb., p. 919, The Combustion Institute 1986.

³⁸J. A. Miller and C. F. Melius 22nd Symp. (Int.) on Comb., The Combustion Institute 1986, in press.

Thermochemical Modeling: II. Application to Ignition and Combustion of Energetic Materials*

Carl F. Melius
Combustion Research Facility
Sandia National Laboratories
Livermore, CA 94551-0969

*Lecture presented at NATO Advanced Study Institute on
Chemistry and Physics of the Molecular Processes in Energetic Materials,
Altavilla Milicia, Sicily, September 3-15, 1989*

Abstract. The ignition and combustion of energetic materials is modeled using detailed chemical kinetics combined with mass and energy transport in the chemically reacting fluid. The chemically reacting flow models, including the conservation equations for energy and mass, are discussed. The development of the set of elementary chemical reactions used in modeling of the decomposition and combustion chemistry is presented. These models are used to study the ignition and combustion of nitramines. The resulting chemistry, involving decomposition and two combustion stages, are discussed. In addition, we discuss the resulting chemistry for the detonation of nitromethane.

1. Introduction

The chemical reactions involved in the ignition and combustion of energetic materials are not well understood, due to the hostile environment in which these processes occur. In particular, high temperatures and pressures exist, making experimental diagnostics of the chemical mechanisms difficult. Even under steady state combustion conditions, the high pressures of interest cause the length scales to be microns, experimentally too small for diagnostics. Furthermore, the highly reactive nature of energetic materials makes the chemical intermediates of ignition and combustion short lived.

Unlike hydrocarbon combustion, the chemical reaction mechanisms occurring in energetic materials are complex,¹ involving decomposition and multiple gas phase flame stages, including conversion of NO₂ to NO, and finally conversion of NO to N₂. There have been many experimental and theoretical studies of the combustion and

*Work supported by a Memorandum of Understanding between the Department of Army and the Department of Energy.

decomposition of nitramines.²⁻¹⁷ However, very little is known about the detailed nitramine chemistry involved.^{3,5,18-21} For other energetic materials, efforts have been made to identify the chemical species for nitromethane²²⁻²⁴ and methyl nitrate.²⁵ Hatch has carried out a detailed chemical model of the gas phase of a nitrate ester.²⁶

In the past few years, we have used quantum chemical calculations to develop a gas phase decomposition mechanism for the ringed nitramines HMX and RDX.²⁷⁻²⁹ The thermochemistry of these decomposition processes has been reviewed in the preceding paper in this NATO ASI series.³⁰ This thermochemistry has been used to develop chemical mechanisms for ignition and combustion of nitramines.^{31,32} In this paper, we review the theoretical models used for treating chemically reacting flows, such as combustion. We also present the detailed elementary reactions used in the chemistry modeling. These detailed chemical kinetics models are then used to investigate the chemical reaction steps involved in the ignition and combustion of nitramines. Finally, as an example of treating the chemistry of detonation, we present results for nitromethane.

2. Theoretical Approach

The ability to model the detailed chemistry of ignition and combustion of energetic materials requires the simultaneous treatment of the chemical kinetics behavior of large chemical reaction systems combined with convective and diffusive transport of mass, momentum, and energy. Such models require the evaluation of equations of state, thermodynamic properties, chemical rate expressions, and transport properties. The computer software used to evaluate these quantities is referred to as the Chemkin package.³³⁻³⁵ It includes an interpreter for the chemical reactions, a thermochemical data base, a linking file, and gas-phase subroutine libraries. The interpreter reads in the list of elementary chemical reactions. The forward reaction rates are given in the form of the Arrhenius rate expression

$$k_f = A T^\beta \exp (E_0 / RT). \quad (1)$$

The reverse reaction rates are determined through the use of the thermodynamic equilibrium constant. The thermochemical data base³⁶ is a modification of that used by Gordon and McBride³⁷ in the NASA Chemical Equilibrium program. The thermochemical data is stored as polynomial fits for the specific heat c_p , enthalpy H^0 , and entropy S^0 , given by

$$c_p / R = a_1 + a_2 T + a_3 T^2 + a_4 T^3 + a_5 T^4 \quad (2)$$

$$H^0 / RT = a_1 + \frac{a_2}{2} T + \frac{a_3}{3} T^2 + \frac{a_4}{4} T^3 + \frac{a_5}{5} T^4 + \frac{a_6}{T} \quad (3)$$

and

$$S^0 / R = a_1 \ln T + a_2 T + \frac{a_3}{2} T^2 + \frac{a_4}{3} T^3 + \frac{a_5}{4} T^4 + a_7. \quad (4)$$

The Chemkin gas-phase subroutine library provides the evaluation of information about species, reactions, gas constants and units, equations of state, mole-mass conversion, thermodynamic properties, chemical production rates, equilibrium constants, rate of progress variables, and sensitivity parameters, along with the appropriate derivatives of the above quantities.

Coupled with the Chemkin software package is a transport package which treats the effects of fluid transport. This transport package,³⁵ including a preprocessor, transport data base, linking file, and transport subroutines, can treat diffusive fluxes of mass, momentum, and energy by evaluating transport coefficients such as viscosity, thermal conductivity, species diffusion coefficients, and thermal diffusion coefficients. The transport data base contains information such as Lennard-Jones parameters, dipole moments, and polarizabilities for each species. Kinetic theory provides polynomial fits for pure-species viscosities, conductivities, and binary diffusion coefficients. The transport library subroutines can then provide pure-species, mixed-averaged, or multicomponent gas mixture transport properties.

Given a set of elementary chemical reaction mechanisms and rate constants along with the corresponding thermochemical and transport properties, one can solve for the detailed chemistry of a chemically reacting flow.³³ One solves the continuity and conservation equations along with the equation of state. Such models incorporating the Chemkin package have been developed for well-stirred reactors,³⁸ reacting boundary layers,³⁹ premixed flames,⁴⁰⁻⁴² counter-flow diffusion flames,⁴³ and shock tubes.⁴⁴

As an example, in this paper we treat the combustion of a nitramine propellant, using extensions of a steady laminar one-dimensional premixed flame code.⁴⁰ The flame chemistry is treated as a detailed set of single-step elementary reactions. The governing equations for conservation of mass, momentum, and energy for the combustion of a solid propellant can be found in the general literature.⁴⁵

In the gas phase, we have the following equations governing the chemically reacting flow. The continuity equation for constant pressure is given by

$$\rho_g V_g A_g = \dot{M} = \text{constant.} \quad (5)$$

The equation of state is given by the ideal gas relationship

$$\rho_g = \frac{\bar{p}\bar{W}}{RT}. \quad (6)$$

The energy conservation equation is given by

$$\begin{aligned} \dot{M} \frac{dT}{dx} = & \frac{1}{c_p} \frac{d}{dx} (\lambda_g A \frac{dT}{dx}) \\ & - \frac{A}{c_p} \sum_{k=1}^{K_{\text{gas}}} \rho_g Y_k V_k c_{pk} \frac{dT}{dx} - \frac{A}{c_p} \sum_{k=1}^{K_{\text{gas}}} \dot{\omega}_k h_k W_k, \end{aligned} \quad (7)$$

while the mass conservation equation for each of the species is given by

$$\dot{M} \frac{dY_k}{dx} = - \frac{d}{dx} (\rho_g A Y_k V_k) + A \dot{\omega}_k W_k \quad (k = 1, \dots, K_{\text{gas}}). \quad (8)$$

In the above equations, x is the spatial coordinate, T is the temperature, Y_k the mass fraction of the k^{th} species, v_g is the velocity of the fluid mixture in the gas phase, ρ_g is the mass density of the gas, W_k is the molecular weight of the k^{th} species, \bar{W} is the mean molecular weight of the mixture, R is the universal gas constant, λ is the thermal conductivity of the gas mixture, c_p is the constant pressure heat capacity of the mixture, c_{pk} is the constant pressure heat capacity of the k^{th} species, $\dot{\omega}_k$ is the molar rate of production of the k^{th} species, V_k is the diffusion velocity of the k^{th} species, h_k is the specific enthalpy of the k^{th} species, and A is the cross-sectional area of the stream tube encompassing the flame. The thermochemical dynamic properties and chemical production rates are evaluated using the Chemkin package.³⁴

The above equations are appropriate for a single-phase combustion process. For solid or liquid propellant combustion, there is a similar set of continuity and conservation equations for the condensed phase. The continuity equation for constant pressure is given by

$$\rho_s V_s A_s = \dot{M} = \text{constant}. \quad (9)$$

The remaining equations for the solid have been simplified, since the Chemkin package does not yet handle condensed phase chemistry and transport. The equation of state for the solid is taken to be

$$\rho_s = \text{constant}, \quad (10)$$

equal to the initial density of the condensed phase propellant. The energy and mass conservation equations, given by

$$\begin{aligned} \dot{M} \frac{dT}{dx} = & \frac{1}{c_p} \frac{d}{dx} (\lambda_s A \frac{dT}{dx}) \\ & - \frac{A}{c_p} \sum_{k=1}^{K_{\text{solid}}} \rho_s Y_k V_k c_{pk} \frac{dT}{dx} - \frac{A}{c_p} \sum_{k=1}^{K_{\text{solid}}} \dot{\omega}_k h_k W_k \end{aligned} \quad (11)$$

and

$$\dot{M} \frac{dY_k}{dx} = - \frac{d}{dx} (\rho_s A Y_k V_k) + A \dot{\omega}_k W_k \quad (k = 1, \dots, K_{\text{solid}}), \quad (12)$$

have been reduced to

$$\dot{M} \frac{dT}{dx} = \frac{1}{c_p} \frac{d}{dx} (\lambda_s A \frac{dT}{dx}) - \frac{A}{c_p} \sum_{k=1}^{K_{\text{solid}}} \dot{\omega}_k h_k W_k \quad (13)$$

and

$$\dot{M} \frac{dY_k}{dx} = A \dot{\omega}_k W_k \quad (k = 1, \dots, K_{\text{solid}}). \quad (14)$$

That is, we ignore the species diffusion in the solid (i.e., $V_k = 0$). This approximation is reasonable for nitramine flames, since diffusion in condensed phases is much slower than in the gas phase, and the reaction zone of the condensed is thin relative to the surface regression rate of the propellant.

The presence of a two-phase system requires boundary conditions at the interface. The flux balances for energy, mass, and momentum at the gas-solid interface are given by

$$\begin{aligned} \lambda_g \frac{dT^+}{dx} &= \lambda_s \frac{dT^-}{dx} + \sum_{k=1}^{K_{\text{gas}}} \rho_g Y_k^{\text{gas}} V_k h_k \\ &+ \rho_g V_g \sum_{k=1}^{K_{\text{gas}}} Y_k^{\text{gas}} h_k^{\text{gas}} - \rho_s V_s \sum_{k=1}^{K_{\text{solid}}} Y_k^{\text{solid}} h_k^{\text{solid}} \end{aligned} \quad (15)$$

$$\rho_s V_s Y_k^{\text{solid}} - \rho_g V_g Y_k^{\text{gas}} = \rho_g Y_k^{\text{gas}} V_k \quad (k = 1, \dots, K) \quad (16)$$

and

$$\rho_s V_s = \dot{\omega}_{\text{evap}} - \dot{\omega}_{\text{cond}}. \quad (17)$$

The g subscript refers to the gas phase while the s subscript refers to the solid phase. In these equations, we have taken $V_k = 0$ for species in the condensed phase,

consistent with equations (13) and (14) above. Mass flux balance requires that \dot{M} is a constant for the whole system. Taking $A_s = A_g = \text{constant}$, we have $\rho_s V_s = \rho_g V_g$.

The above equations are for a steady-state flame at constant pressure. For time-dependent problems, such as pressure oscillations or ignition, the above equations must be modified to include the time dependent derivatives of the energy, species, and momentum (see, e.g., Ref. 45 for a detailed description). Examples of the equations governing other chemically reacting systems, such as for a plug flow reactor or detonation, are given elsewhere.³³

Currently, Chemkin only treats chemical reactions for an ideal gas. Efforts are currently underway to extend the Chemkin chemistry to handle the non-idealities of higher pressures. Also, Chemkin does not currently treat the condensed phase. Therefore, for the solid propellant combustion model treated in this paper, a single-step condensed phase reaction mechanism was hard-wired into the computer code.

The computational procedure used to solve the chemically reacting flow problem depends on the form of the equations and boundary conditions defining the problem. In all cases, the system of differential equations that model the elementary chemical kinetics processes are typically quite stiff. For those systems which do not incorporate diffusive process, we use an implicit linear multistep algorithm involving a backward differentiation formula (BDF). Specifically, we use a software package called DASAC,^{46,47} (Differential Algebraic Sensitivity Analysis Code) which includes sensitivity analysis within the ODE solver (or, more generally, the differential-algebraic equation (DAE) solver DASSL⁴⁸).

For chemically reacting flows which include diffusive processes such as the steady one-dimensional flame, the governing equations become elliptic. Eqn. 17 above represents the boundary value or eigenvalue for the flame speed. For these boundary value problems, we use a hybrid Newton/time-integration procedure.⁴² The time stepping algorithm, the Jacobian updating, and adaptive gridding in this integration procedure have been modified for the propellant flame in order to improve the convergence. These codes also include sensitivity analysis for post processing of the results.

3. Chemical Kinetics Model

The chemical kinetics model was derived using an extension of a generalized hydrocarbon/air flame model of Miller and coworkers.⁴⁹⁻⁵¹ The chemical mechanisms include the oxidation of HCN, the conversion of NH_i species to NO and N_2 , as well as the flame chemistry of $\text{C}_2\text{N}_2/\text{NO}_2$.⁵² This set was augmented by various reactions obtained from a $\text{N}_2\text{H}_4/\text{NO}_2$ flame study by Hepler and Smith.⁵³ Additional reactions were included to treat the decomposition of the RDX and reactions of the subsequent intermediates. The thermochemistry of chemical species that were not in the CHEMKIN thermochemical data base³⁶ were calculated using the BAC-MP4 quantum chemical method.²⁷⁻³⁰ A total of 62 species and 310 reactions were used to study the time-dependent ignition chemistry of RDX. Chemical species which were not important in the ignition chemistry were then eliminated from the reaction list, generating an earlier RDX flame reaction mechanism set involving a total of 31 chemical species and 131 elementary reactions. Later, this reaction mechanism set was extended to 38 chemical species and 158 elementary reactions, given in Tables I and II.

For RDX, the initial decomposition mechanism was taken to occur by two pathways: 1) bond scissioning of a NO_2 group and 2) the formation of CH_2O and N_2O . The reactions for the decomposition of RDX (i.e., reactions 117-119 in table II) were developed as a result of quantum chemical BAC-MP4 studies on the decomposition mechanisms of nitramines.²⁷⁻³⁰ The species RDXR denotes the

Table I. List of chemical species used in the detailed chemical kinetic modeling of the RDX propellant flame. Also given are the heats of formation at 298 K ($\Delta H_{f,298}^0$), where energies are given in kcal-mol⁻¹. The species RDXR represents the radical formed from RDX by removal of a nitro group. The species RDXRO represents the ring-opening species resulting from RDXR. Species indicated by * were not included in the earlier reaction set (Ref. 32).

*1	H2CNO	39.30	2	RDX	45.79
3	RDXR	83.79	*4	RDXRO	103.80
5	H2CNNO2	33.64	*6	H2CNNO	60.51
*7	H2CNH	21.85	8	H	52.09
9	H2	0.00	10	O	59.56
11	O2	0.00	12	OH	9.32
13	H2O	-57.80	14	HO2	2.50
15	NO	21.58	16	NO2	7.91
17	HNO	23.80	18	HONO	-18.34
19	N2O	19.61	20	N	112.95
21	N2	0.00	22	NH	85.20
23	NH2	45.50	*24	NH3	-10.97
25	NNH	58.57	26	CN	104.01
27	HCN	32.30	28	H2CN	59.11
29	C2N2	73.88	30	NCO	38.10
31	HNCO	-24.90	32	HOCN	-2.28
*33	HCNO	38.43	*34	CNO	94.43
35	CO	-26.42	36	CO2	-94.06
37	HCO	10.40	38	CH2O	-27.70

Table II. Elementary chemical reaction mechanism rate coefficients in the form $k_i = A T^\beta \exp(-E_0/RT)$ used in modeling the RDX solid propellant flame. Units are moles, cubic centimeters, seconds, Kelvins and calories-mole⁻¹. Reactions indicated by * were not included in the earlier reaction set (Ref. 32).

	Reaction	A	β	E_0
1.	CO+O+M=CO2+M	0.617e+15	0.	3000.
2.	CO+OH=CO2+H	0.151e+08	1.3	-758.
3.	CO+O2=CO2+O	0.160e+14	0.	41000.
4.	HO2+CO=CO2+OH	0.580e+14	0.	22934.
5.	H2+O2=2OH	0.170e+14	0.	47780.
6.	OH+H2=H2O+H	0.117e+10	1.3	3626.
7.	O+OH=O2+H	0.361e+15	-0.5	0.
8.	O+H2=OH+H	0.506e+05	2.67	6290.
9.	H+O2+M=HO2+M	0.361e+18	-0.72	0.

	H2O	enhanced by	18.6			
	CO2	enhanced by	4.2			
	H2	enhanced by	2.86			
	CO	enhanced by	2.11			
	N2	enhanced by	1.26			
10.	OH+HO2=H2O+O2			0.750e+13	0.	0.
11.	H+HO2=2OH			0.140e+15	0.	1073.
12.	O+HO2=O2+OH			0.140e+14	0.	1073.
13.	2OH=O+H2O			0.600e+09	1.3	0.
14.	H+H+M=H2+M			0.100e+19	-1.	0.
15.	H+H+H2=H2+H2			0.920e+17	-0.6	0.
16.	H+H+H2O=H2+H2O			0.600e+20	-1.25	0.
17.	H+H+CO2=H2+CO2			0.549e+21	-2.	0.
18.	H+OH+M=H2O+M			0.160e+23	-2.	0.
	H2O	enhanced by	5.0			
19.	H+O+M=OH+M			0.620e+17	-0.6	0.
	H2O	enhanced by	5.0			
20.	O+O+M=O2+M			0.189e+14	0.	-1788.
21.	H+HO2=H2+O2			0.125e+14	0.	0.
*22.	HCNO+H=HCN+OH			0.500e+14	0.	12000.
23.	CO2+N=NO+CO			0.190e+12	0.	3400.
24.	HCN+OH=CN+H2O			0.145e+14	0.	10929.
25.	HCN+OH=HOCN+H			0.919e+13	0.	15000.
26.	HCN+OH=HNCO+H			0.477e+12	0.	11000.
27.	HOCN+H=HNCO+H			0.100e+14	0.	0.
28.	HCN+O=NCO+H			0.138e+05	2.64	4980.
29.	HCN+O=NH+CO			0.345e+04	2.64	4980.
30.	HCN+O=CN+OH			0.270e+10	1.58	26600.
31.	CN+H2=HCN+H			0.295e+06	2.45	2237.
32.	CN+O=CO+N			0.180e+14	0.	0.
33.	CN+O2=NCO+O			0.560e+13	0.	0.
34.	CN+OH=NCO+H			0.600e+14	0.	0.
35.	CN+HCN=C2N2+H			0.200e+14	0.	0.
36.	CN+NO2=NCO+NO			0.300e+14	0.	0.
37.	CN+N2O=NCO+N2			0.100e+14	0.	0.
38.	C2N2+O=NCO+CN			0.457e+13	0.	8880.
39.	C2N2+OH=HOCN+CN			0.186e+12	0.	2900.
40.	HO2+NO=NO2+OH			0.211e+13	0.	-479.
41.	NO2+H=NO+OH			0.350e+15	0.	1500.
42.	NO2+O=NO+O2			0.100e+14	0.	600.
43.	NCO+H=NH+CO			0.500e+14	0.	0.
44.	NCO+O=NO+CO			0.200e+14	0.	0.
45.	NCO+N=N2+CO			0.200e+14	0.	0.
46.	NCO+OH=NO+CO+H			0.100e+14	0.	0.
47.	NCO+M=N+CO+M			0.310e+17	-0.5	48000.
48.	NCO+NO=N2O+CO			0.100e+14	0.	-390.
49.	NCO+H2=HNCO+H			0.858e+13	0.	9000.

50.	$\text{HNCO} + \text{H} = \text{NH}_2 + \text{CO}$	0.200e+14	0.	3000.
51.	$\text{NH} + \text{O}_2 = \text{HNO} + \text{O}$	0.100e+14	0.	12000.
52.	$\text{NH} + \text{O}_2 = \text{NO} + \text{OH}$	0.140e+12	0.	2000.
53.	$\text{NH} + \text{NO} = \text{N}_2\text{O} + \text{H}$	0.433e+15	-0.5	0.
54.	$\text{N}_2\text{O} + \text{H} = \text{N}_2 + \text{OH}$	0.760e+14	0.	15200.
55.	$\text{NH} + \text{OH} = \text{HNO} + \text{H}$	0.200e+14	0.	0.
56.	$\text{NH} + \text{OH} = \text{N} + \text{H}_2\text{O}$	0.500e+12	0.5	2000.
57.	$\text{NH} + \text{N} = \text{N}_2 + \text{H}$	0.300e+14	0.	0.
58.	$\text{NH} + \text{H} = \text{N} + \text{H}_2$	0.300e+14	0.	0.
59.	$\text{NH}_2 + \text{O} = \text{HNO} + \text{H}$	0.663e+15	-0.5	0.
60.	$\text{NH}_2 + \text{O} = \text{NH} + \text{OH}$	0.675e+13	0.	0.
61.	$\text{NH}_2 + \text{OH} = \text{NH} + \text{H}_2\text{O}$	0.450e+13	0.	2200.
62.	$\text{NH}_2 + \text{H} = \text{NH} + \text{H}_2$	0.692e+14	0.	3650.
63.	$\text{NH}_2 + \text{NO} = \text{NNH} + \text{OH}$	0.882e+16	-1.25	0.
64.	$\text{NH}_2 + \text{NO} = \text{N}_2 + \text{H}_2\text{O}$	0.378e+16	-1.25	0.
*65.	$\text{NH}_3 + \text{OH} = \text{NH}_2 + \text{H}_2\text{O}$	0.204e+07	2.04	566.
*66.	$\text{NH}_3 + \text{H} = \text{NH}_2 + \text{H}_2$	0.699e+07	2.39	10171.
*67.	$\text{NH}_3 + \text{O} = \text{NH}_2 + \text{OH}$	0.210e+14	0.	9000.
68.	$\text{NNH} + \text{M} = \text{N}_2 + \text{H} + \text{M}$	0.200e+15	0.	2000.
69.	$\text{NNH} + \text{NO} = \text{N}_2 + \text{HNO}$	0.500e+14	0.	0.
70.	$\text{NNH} + \text{H} = \text{N}_2 + \text{H}_2$	0.370e+14	0.	3000.
71.	$\text{HNO} + \text{M} = \text{H} + \text{NO} + \text{M}$	0.150e+17	0.	48680.
72.	$\text{HNO} + \text{OH} = \text{NO} + \text{H}_2\text{O}$	0.360e+14	0.	0.
73.	$\text{HNO} + \text{H} = \text{H}_2 + \text{NO}$	0.500e+13	0.	0.
74.	$\text{N} + \text{NO} = \text{N}_2 + \text{O}$	0.327e+13	0.3	0.
75.	$\text{N} + \text{O}_2 = \text{NO} + \text{O}$	0.640e+10	1.	6280.
76.	$\text{N} + \text{OH} = \text{NO} + \text{H}$	0.380e+14	0.	0.
77.	$\text{CH}_2\text{O} + \text{OH} = \text{HCO} + \text{H}_2\text{O}$	0.343e+10	1.18	-447.
78.	$\text{CH}_2\text{O} + \text{H} = \text{HCO} + \text{H}_2$	0.219e+09	1.77	3000.
79.	$\text{CH}_2\text{O} + \text{M} = \text{HCO} + \text{H} + \text{M}$	0.331e+17	0.	81000.
80.	$\text{CH}_2\text{O} + \text{O} = \text{HCO} + \text{OH}$	0.180e+14	0.	3080.
81.	$\text{HCO} + \text{OH} = \text{H}_2\text{O} + \text{CO}$	0.100e+15	0.	0.
82.	$\text{HCO} + \text{M} = \text{H} + \text{CO} + \text{M}$	0.250e+15	0.	16802.
	CO enhanced by	1.87		
	H2 enhanced by	1.87		
	CO2 enhanced by	3.0		
	H2O enhanced by	5.0		
83.	$\text{HCO} + \text{H} = \text{CO} + \text{H}_2$	0.168e+14	0.25	0.
84.	$\text{HCO} + \text{O} = \text{CO} + \text{OH}$	0.300e+14	0.	0.
85.	$\text{HCO} + \text{O} = \text{CO}_2 + \text{H}$	0.300e+14	0.	0.
86.	$\text{HCO} + \text{O}_2 = \text{HO}_2 + \text{CO}$	0.330e+14	-0.4	0.
87.	$\text{NH}_2 + \text{NO}_2 = \text{N}_2\text{O} + \text{H}_2\text{O}$	0.200e+21	-3.	0.
88.	$\text{NH}_2 + \text{NO} = \text{N}_2\text{O} + \text{H}_2$	0.500e+14	0.	24640.
89.	$\text{NH}_2 + \text{NO} = \text{HNO} + \text{NH}$	0.100e+14	0.	40000.
90.	$\text{NH} + \text{NO}_2 = \text{NO} + \text{HNO}$	0.100e+12	0.5	4000.
91.	$\text{N} + \text{N}_2\text{O} = \text{N}_2 + \text{NO}$	0.100e+14	0.	19870.
92.	$\text{N} + \text{NO}_2 = \text{NO} + \text{NO}$	0.400e+13	0.	0.

93.	$N+NO_2=N_2O+O$	0.500e+13	0.	0.
94.	$N+NO_2=N_2+O_2$	0.100e+13	0.	0.
95.	$N+HNO=NH+NO$	0.100e+14	0.	2000.
96.	$N+HNO=N_2O+H$	0.500e+11	0.5	3000.
97.	$N+HO_2=NH+O_2$	0.100e+14	0.	2000.
98.	$N+HO_2=NO+OH$	0.100e+14	0.	2000.
99.	$N_2O+M=N_2+O+M$	0.130e+12	0.	59610.
	Fall-off Parameters	1.884e-13	2.5	-5385.
100.	$N_2O+NO=N_2+NO_2$	0.100e+15	0.	49675.
101.	$N_2O+OH=N_2+HO_2$	0.630e+12	0.	10000.
102.	$N_2O+O=N_2+O_2$	0.100e+15	0.	28020.
103.	$N_2O+O=NO+NO$	0.692e+14	0.	26630.
104.	$NO_2+M=NO+O+M$	0.110e+17	0.	65570.
105.	$NO_2+NO_2=2NO+O_2$	0.200e+13	0.	26820.
106.	$NO_2+NO=N_2O+O_2$	0.100e+13	0.	60000.
107.	$NO+M=N+O+M$	0.400e+21	-1.5	150000.
108.	$NO+NO=N_2+O_2$	0.130e+15	0.	75630.
109.	$NO+HNO=N_2O+OH$	0.200e+13	0.	26000.
110.	$NO+HO_2=HNO+O_2$	0.200e+12	0.	2000.
111.	$OH+NO+M=HONO+M$	0.160e+15	-0.5	0.
	Fall-off Parameters	2.300e-10	2.1	0.
112.	$HONO+OH=NO_2+H_2O$	0.100e+14	0.	0.
113.	$HNO+O=NO+OH$	0.500e+12	0.5	2000.
114.	$HNO+O=NO_2+H$	0.500e+11	0.5	2000.
115.	$HNO+HNO=N_2O+H_2O$	0.100e+10	0.	3300.
116.	$HONO+HNO=H_2O+NO+NO$	0.100e+13	0.	40000.
117.	$RDX+M=RD XR+NO_2+M$	0.200e+17	0.	45000.
	Fall-off Parameters	1.300e-01	0.	17000.
*118.b	$RD XR+M=RD XRO+M$	0.100e+17	0.	23000.
	Fall-off Parameters	1.300e-01	0.	5000.
*119.b	$RD XRO+M=2H_2CNNO_2+H_2CN+M$	0.100e+17	0.	23000.
	Fall-off Parameters	1.300e-01	0.	5000.
120.	$RD X+H=RD XR+HONO$	0.100e+14	0.	5000.
121.	$RD X+OH=2H_2CNNO_2+HCN+NO_2+H_2O$	0.100e+14	0.	5000.
122.c	$H_2CNNO_2+M=H_2CN+NO_2+M$	0.100e+17	0.	31000.
	Fall-off Parameters	1.300e-01	0.	5000.
*123.	$H_2CNNO+M=H_2CN+NO+M$	0.100e+17	0.	20000.
	Fall-off Parameters	1.300e-01	0.	5000.
124.	$H_2CNNO_2+H=H_2CN+HONO$	0.100e+13	0.	5000.
125.d	$H_2CNNO_2+OH=HCN+NO_2+H_2O$	0.100e+14	0.	3000.
*126.	$H_2CNNO_2+OH=CH_2O+N_2O+OH$	0.100e+14	0.	0.
127.	$H_2CN+M=HCN+H+M$	0.100e+17	0.	30000.
128.	$H_2CN+NO_2=HCN+HONO$	0.100e+13	0.	1000.
*129.	$H_2CN+NO_2=H_2CNO+NO$	0.100e+13	0.	3000.
130.	$H_2CN+NO=HCN+HNO$	0.100e+13	0.	3000.
131.	$CH_2O+O_2=HO_2+HCO$	0.200e+14	0.	38950.
132.	$HCO+HNO=CH_2O+NO$	0.200e+13	0.	5000.

*133.	HCO+HNO=HNCO+OH	0.100e+13	0.	2000.
134. ^e	HCO+HONO=CH ₂ O+NO ₂	0.200e+13	0.	12000.
135.	HCO+NO=CO+HNO	0.720e+14	-0.4	0.
136. ^f	HCO+NO ₂ =CO+HONO	0.120e+14	0.	-430.
137. ^g	HCO+NO ₂ =CO ₂ +H+NO	0.400e+13	0.	-430.
138.	CO+NO ₂ =CO ₂ +NO	0.126e+15	0.	27600.
139.	HONO+H=H ₂ +NO ₂	0.100e+13	0.	1000.
*140.	H ₂ CNO+M=HCNO+H	0.100e+17	0.	50000.
*141.	H ₂ CNO+OH=HCNO+H ₂ O	0.100e+14	0.	0.
*142.	H ₂ CNO+NO ₂ =HCNO+HONO	0.100e+13	0.	2000.
*143.	H ₂ CNO+NO ₂ =CH ₂ O+NO+NO	0.100e+13	0.	0.
*144.	H ₂ CNO+NO=HCNO+HNO	0.100e+13	0.	25000.
*145.	H ₂ CNO+HNO=H ₂ CN+HONO	0.100e+13	0.	2000.
*146.	HCNO+OH=HCO+HNO	0.100e+14	0.	5000.
*147.	HCNO+OH=CNO+H ₂ O	0.100e+13	0.	2000.
*148.	HCNO+O=HCO+NO	0.100e+13	0.	9000.
*149.	HCNO+CN=HCN+CNO	0.100e+13	0.	2000.
*150.	CNO+N ₂ O=N ₂ +CO+NO	0.100e+13	0.	15000.
*151.	CNO+NO ₂ =CO+2NO	0.100e+14	0.	0.
*152.	CNO+O=CO+NO	0.100e+14	0.	0.
*153.	H ₂ CN+HNO=H ₂ CNH+NO	0.100e+13	0.	4000.
*154.	H ₂ CNH+OH=H ₂ CN+H ₂ O	0.100e+14	0.	0.
*155.	H ₂ CNH+CN=H ₂ CN+HCN	0.100e+14	0.	0.
*156.	H ₂ CN+HONO=H ₂ CNH+NO ₂	0.100e+13	0.	12000.
*157.	H ₂ CN+CH ₂ O=H ₂ CNH+HCO	0.100e+13	0.	14000.
*158.	H ₂ CNNO ₂ +H ₂ O=CH ₂ O+N ₂ O+H ₂ O	0.100e+12	0.	2000.

^aIn the earlier mechanism, the global reaction $\text{RDX}+\text{M}=3\text{CH}_2\text{O}+3\text{N}_2\text{O}+\text{M}$ with $A = 0.100\text{e}+14$, $n = 0.$, and $E_0 = 36000.$ was included as a gas phase reaction.

^bIn the earlier mechanism, reactions 118 and 119 were replaced by a single reaction step $\text{RDXR}+\text{M}=2\text{H}_2\text{CNNO}_2+\text{H}_2\text{CN}+\text{M}$ with $E_0 = 18000.$

^cIn the earlier mechanism, $E_0 = 28000.$ and $A = 0.1\text{e}+17.$

^dIn the earlier mechanism, $E_0 = 1000.$

^eIn the earlier mechanism, $E_0 = 8000.$

^fIn the earlier mechanism, $A = 0.15\text{e}+14.$

^gIn the earlier mechanism, $A = 0.15\text{e}+12.$

radical formed by removing a nitro group from RDX, i.e., $\text{C}_3\text{H}_6\text{N}_5\text{O}_4$. The species RDXRO represents the ring-opened structure of RDXR. The second decomposition pathway, represented by the global reaction



was included as a condensed phase global chemical reaction with a rate constant of $A = 4.66 \times 10^{18} \text{ sec}^{-1}$ and $E_0 = 47.8 \text{ kcal}\cdot\text{mol}^{-1}$ taken from Ref. 20. In the study of RDX

ignition and in the initial study of the RDX flame at 17 atm,³² this reaction was included as one of the gas phase reactions, with the rate constant given in the footnote to Table II.

4. Nitromethane Ignition Studies

The study of ignition in a uniformly heated system, such as in a shock tube, allows us to study the combustion chemistry of energetic materials in a environment that is simpler than that occurring in a flame. The energetic material can be treated as a homogeneous gas mixture in a closed system, in which we follow the time-dependent evolution of the chemical species. For instance, we can treat an adiabatic system with constant pressure or volume, or we can follow the chemistry under shock detonation conditions.⁵⁴ We use the SENKIN program,⁴⁶ which includes sensitivity analysis, for the integration of the energy and mass conservation equations. These codes have also been used to follow the chemistry of chemical subsystems of energetic materials, such as CH₂O/NO₂, under shock tubes conditions.⁵⁵

In this section, we apply this theoretical approach to study the chemistry of nitromethane ignition and detonation. This problem is considered zero-dimensional since it does not involve any spatial dimensions for mass and energy diffusion. We begin our example by studying the ignition of nitromethane under constant volume. The governing equations are⁴⁶

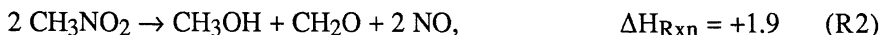
$$\frac{dY_k}{dt} = v \dot{\omega}_k W_k \quad (k = 1, \dots, K). \quad (18)$$

and

$$c_v \frac{dT}{dt} = -v \sum_{k=1}^K e_k \dot{\omega}_k W_k, \quad (19)$$

where t is time, $v = V/m$ is the specific volume, e_k is the internal energy of the k^{th} species, and the other variables have been defined above. The chemical reaction mechanism included 35 species and 150 elementary reactions.

In Fig. 1, we present the temperature, pressure, and species profiles as a function of time for the ignition of 100 per cent CH₃NO₂ at 6.85 atmospheres and 1202 K, representative of the experimental conditions in Ref. 24. We see from the figure that the overall reaction chemistry of the first stage ignition is primarily



with the later conversion of formaldehyde to carbon monoxide



In these reactions, we give the heats of reaction (in kcal-mol⁻¹). Note that these

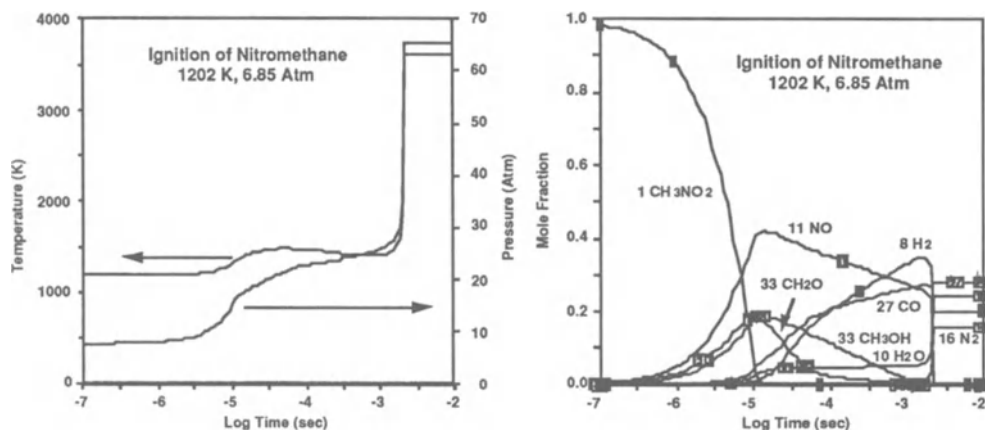


Fig. 1. Temperature and major species concentration (mole fraction) profiles as a function of time for the ignition of nitromethane in a shock tube. Starting conditions were 1202 K and 6.85 atm.

reactions are essentially thermoneutral, yielding very little temperature rise (see Fig. 1). The increase in pressure arises from the conversion of nitromethane into two molecules. The overall reaction, which reduces the free energy, is driven by the increase in entropy of phase space resulting from the increase in the number of molecules formed. The majority of heat release in nitromethane occurs in the second stage ignition which converts NO to N_2 . It was necessary to include reactions involving CH_3OH to the mechanism of Hsu and Lin²³ in order to reproduce the observed rate of formation of CO in their experiments as well as to obtain the observed ignition delay times for the first stage ignition of Guirguis *et al.*²⁴

Included in the information obtained from the calculations is the time-dependent rate of production or removal of each molecular species due to the elementary reactions. Using this production/removal rate data, we can develop a reaction flow diagram for the first stage ignition, given in Fig. 2. Information about reaction pathways provides an important understanding of the role of NO_2 and NO chemistry in ignition and combustion. Further information can be obtained from sensitivity analysis. Yetter and Rabitz have used this approach to determine the rate sensitive reactions leading to the production of CO and NO as well as the ignition delay time for nitromethane.⁵⁶

In nitromethane, the conversion of CH_3O to CH_3OH and CH_2O provides the source of heat for the short (microsecond) first ignition stage, after which CH_3OH is converted back to CH_2O and then to CO during the first stage ignition. We find the same role of CH_3OH occurring in methyl nitrate ignition.

In Fig. 3 we present the temperature, pressure, and species concentration profiles as a function of time for nitromethane following shock detonation.⁵⁴ The time is plotted on a logarithmic scale in order to see both the first and second stages of

Decomposition Reaction Mechanism for the First Stage Ignition of CH_3NO_2

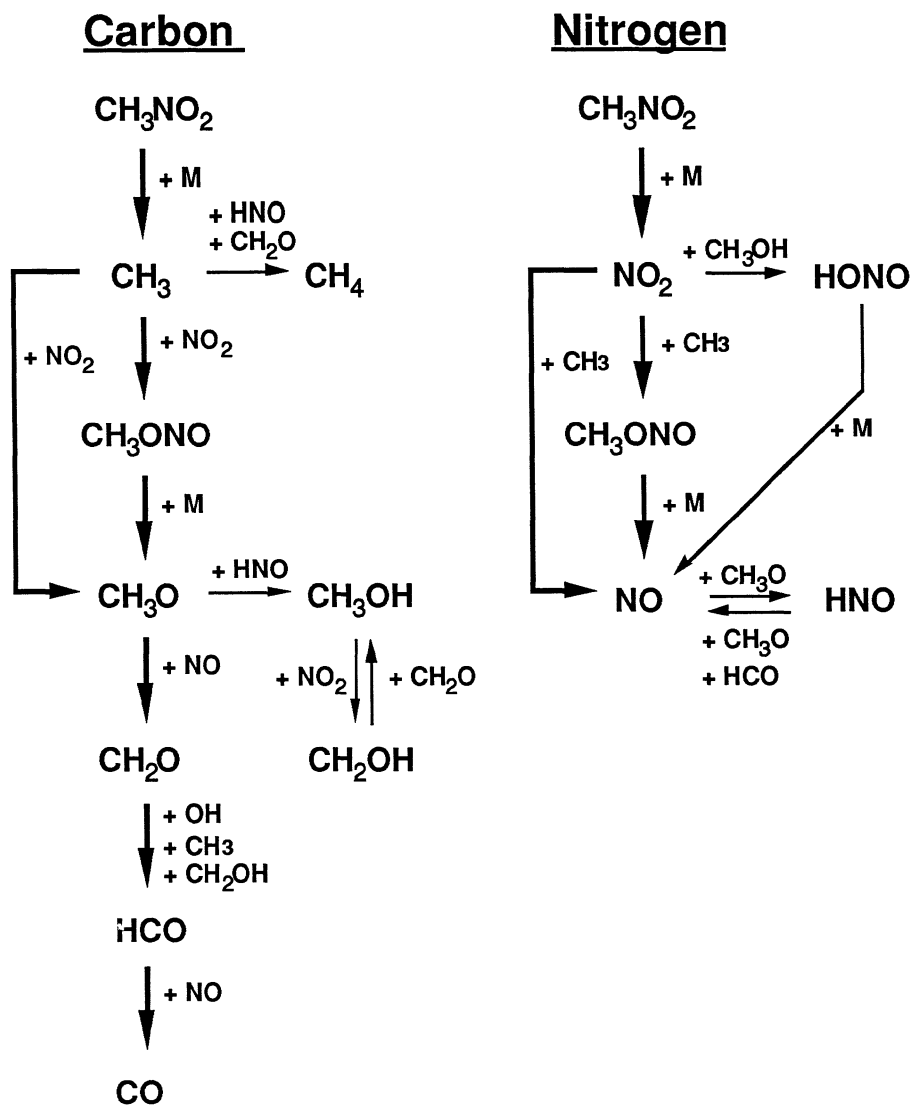


Fig. 2. Reaction mechanism diagrams for the carbon-containing and nitrogen-containing species during the ignition of nitromethane. Starting conditions are 1202 K and 6.85 atm. Unimolecular decomposition is indicated by the third-body notation +M. Thick arrows indicate major reaction pathways.

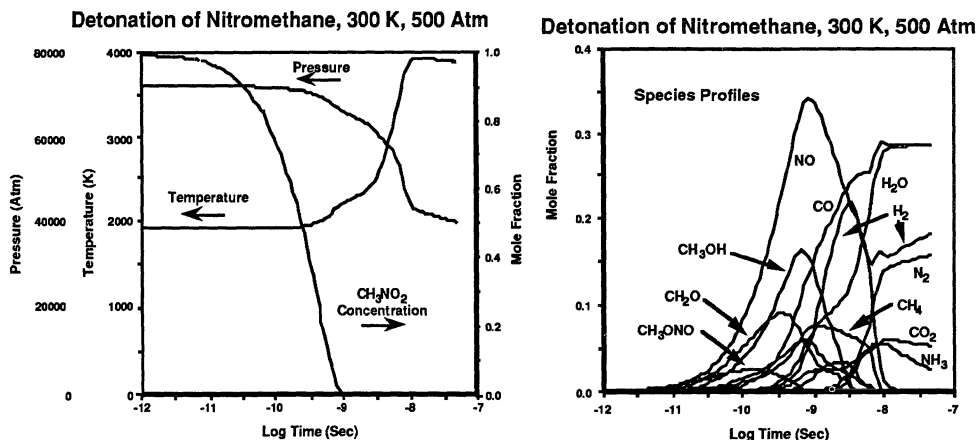


Fig. 3. Temperature and major species concentration (mole fraction) profiles as a function of time for the detonation of nitromethane. Starting conditions were 300 K and 500 atm.

ignition. The main difference in the chemistry from that in the low pressure, constant volume ignition is that more of the CH_2O is converted to CO and H_2 (reaction R3) under detonation conditions. This may seem surprising since the extremely high pressures involved in detonation might suggest that larger molecules would be formed. However, the higher temperatures increase the importance of entropy, which drives the system to produce a greater number of molecules. It should be noted that the current thermochemical model assumes an ideal gas, so that the actual effect will be shifted from these calculated results.

5. Nitramine Ignition and Flame Studies

In this section, we consider the chemical and physical processes occurring under ignition and steady-state flame conditions. We first present the global chemistry and temperature characteristics and then the detailed chemical reaction mechanisms involved. We use RDX as the example nitramine. As we shall find, the RDX chemistry is simpler than HMX, since it more readily vaporizes before decomposing, resulting in the gas-phase chemistry controlling the combustion process.

5.1 RDX Ignition

RDX ignition was modeled³¹ by following the time evolution of the molecular species formed from gas-phase decomposition of RDX and subsequent chemical reactions. For the ignition studies, we took the thermodynamic conditions to be an adiabatic system at constant pressure. The resulting time-dependent, nonlinear coupled equations were solved using a total of 49 chemical species and 236

elementary reactions. The initial conditions started with gaseous RDX at a prescribed temperature T_0 and pressure P_0 .

We first consider the time dependence of the temperature profile. The ignition of RDX was solved for various starting temperatures, T_0 , ranging from 500 K to 1400 K. The resulting temperature and species concentration profiles as a function of time for T_0 equal 573 K and 1 atm are shown in Fig. 4. The results indicate a two stage ignition, which also occurs for the other starting conditions of temperature and pressure. However, the corresponding temperature profile at higher T_0 is more complex, i.e., the temperature does not necessarily rise monotonically with time. As an example, the temperature-time profile for T_0 equal 850 K is shown in Fig. 5. The temperature initially drops (due to decomposition) and goes through a minimum (denoted initial minimum in Fig. 5) before it starts rising. As T_0 is increased, the rise time for the first stage ignition becomes comparable to the first stage ignition delay time τ_1 . The plateau temperature (during the time between the first and second stages of ignition) goes through a slight minimum (denoted plateau minimum in Fig. 5). The initial temperature minimum, the first stage maximum temperature (the temperature achieved at the end of the first stage ignition), and the subsequent plateau minimum temperature are shown in Fig. 6 as a function of starting temperature T_0 . Note that the maximum temperature achieved at the first stage of ignition decreases with increasing T_0 until 800 K is reached. A plateau temperature minimum occurs for T_0 between 600 K and 1100 K.

The resulting times to first stage ignition τ_1 and second stage ignition τ_2 are shown in Fig. 7 as an inverse function of the starting temperature T_0 . For starting temperatures T_0 between 700 K and 950 K, the temperature-time curves exhibit a knee in the temperature rise (as indicated in Fig. 6 for T_0 equal 850 K), corresponding to temporally separated chemical reaction stages.

The ignition delay time for the first stage, τ_1 , follows predicted behavior, decreasing monotonically with increasing temperature. The effective activation energy for first stage ignition, estimated from $\tau_1 \approx \exp(-\Delta E/RT)$, is 28 to 34 kcal-mol⁻¹ at low starting temperatures ($T_0 < 700$ K), but becomes smaller at higher T_0 , due in part to significant temperature drops during the initial stage of decomposition at the higher initial T_0 (see Fig. 6). The second stage ignition time, τ_2 , on the other hand, yields very unusual results. From Fig. 7 one can see that τ_2 decreases as T_0 goes from 500 K to 600 K, then τ_2 increases from 600 K to 850 K, and finally τ_2 decreases monotonically with T_0 above 850 K. The strange behavior of τ_2 is a result of the temperature achieved after first stage ignition (see Fig. 7) going through a minimum as T_0 increases. We find, at low temperatures, that pressure has little effect on the first stage ignition time but significantly decreases the time between the first and second stages of ignition. At higher initial temperatures, increases in pressure significantly decreased both ignition times.

5.2. RDX Flame

Ermolin *et al.*¹⁰ have theoretically investigated the detailed chemistry of the secondary luminous stage of an RDX flame which they have successfully compared

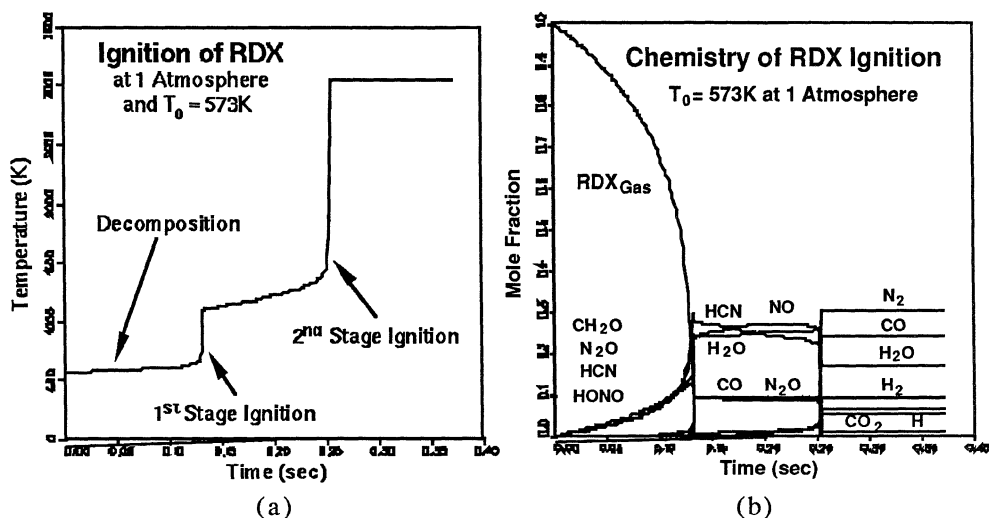


Fig. 4. Temperature (a) and major species concentration (mole fraction) (b) profiles as a function of time for the ignition of gaseous RDX at a constant pressure. Starting conditions were T_0 equal 573K and 1 atm.

Temperature-Time Profile of RDX Ignition

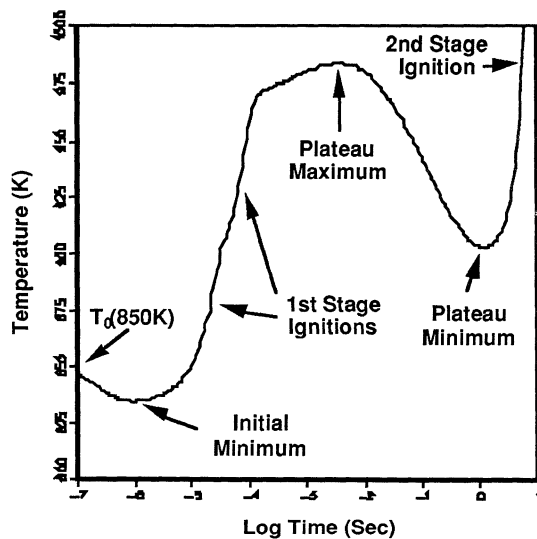


Fig. 5. Temperature profile as a function of time for the ignition of gaseous RDX at T_0 equal 850 K and 1 atm. The time has been plotted on a log scale as opposed to Fig. 4.

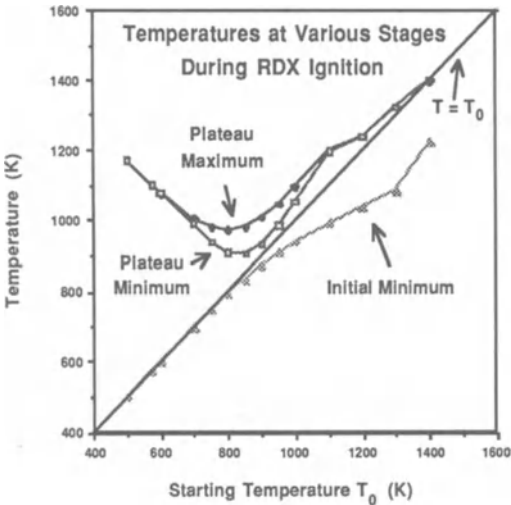


Fig. 6. Temperatures for various stages during the ignition of gaseous RDX as a function of initial starting temperature T_0 . Initial minimum corresponds to the lowest temperature achieved during the initial decomposition stage. First stage maximum corresponds to the temperature achieved following the first stage of ignition. The plateau minimum corresponds to the resulting temperature minimum achieved following the first stage ignition. The pressure was held fixed at 1 atm.

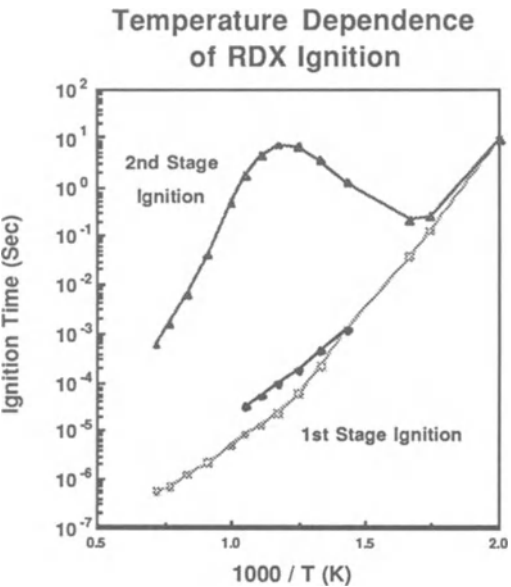


Fig. 7. Dependence of gaseous RDX ignition times on the initial starting temperature T_0 . The pressure was held fixed at 1 atm.

with corresponding experimental composition profiles. Their theoretical approach is computationally equivalent to our ignition code calculations. That is, they do not include mass or energy diffusion, thereby reducing the problem to one dimension. In our ignition calculations, time is the variable, while in the flame case of Ermolin *et al.*, the spatial distance is the variable. However, for constant pressure, these are related by the density of the gas, which decreases with increasing temperature as one moves downstream in the flame.

In our case, we solve³² the one-dimensional flame problem, including mass and species diffusion, given by Eqns. 5-17. Hatch²⁶ has also used detailed chemistry to study the gas phase chemistry of a nitrate-ester flame and has recently applied this approach to study the gas phase chemistry of an HMX flame¹³.

The resulting temperature and species profiles as a function of distance above the gas/solid surface of the steady-state RDX flame at 1 atm are given in Fig. 8. The results of the temperature profile indicate that the RDX flame burns as a single flame, i.e., the secondary (or luminous) stage flame does not stand off the surface, as in a nitramine composite or double base propellant. Thus, we see that energy and mass diffusion have changed the two-staged temperature characteristics of the ignition studies. However, as we shall see later, profiles of species production and removal rates still indicate multiple stages of chemistry. Before discussing the chemistry we present the physical characteristics of the gas-solid interface.

The gas/solid interface boundary conditions were given in Eqns. 15-17. The results of these flame boundary conditions are given in Table III for 1.0 and 20.0 atm RDX flames. The results indicate that less than eight percent of the RDX has decomposed in the condensed phase. Also note that the rates of RDX molecules leaving and returning to the surface (evaporation and condensation) are large compared to the net regression rate of the surface (burn rate). Also, the temperature gradients (dT/dx) at the surface are large, indicative of the secondary (luminous) flame standing very near the surface.

Table III. Calculated gas-solid boundary mass end energy conditions for an RDX flame at 1 atm and 20 atm.

Flame Pressure (atm)	1.0	20.0
Surface Temperature (K)	549 K	634 K
Mass Transport ($\text{gm}\cdot\text{cm}^{-2}\cdot\text{sec}^{-1}$)		
Rate of Evaporation	7.582	120.06
Rate of Condensation	7.550	119.55
Burn Rate	0.032	0.51
Fraction of Solid Decomposed in Condensed Phase	0.047	0.073
Heat Transport ($10^8 \text{ erg}\cdot\text{cm}^{-2}\cdot\text{sec}^{-1}$)		
Gas Phase Heat Conduction ($\lambda_g (dT/dx)^+$)	2.58	45.2
Condensed Phase Heat Conduction ($\lambda_g (dT/dx)^-$)	1.42	30.0
Enthalpy of Vaporization ($\rho v \Delta H_{\text{evap}}$)	0.19	-2.4
Gas Phase Mass Diffusion ($\sum \rho_i v_i h_i$)	0.96	17.6

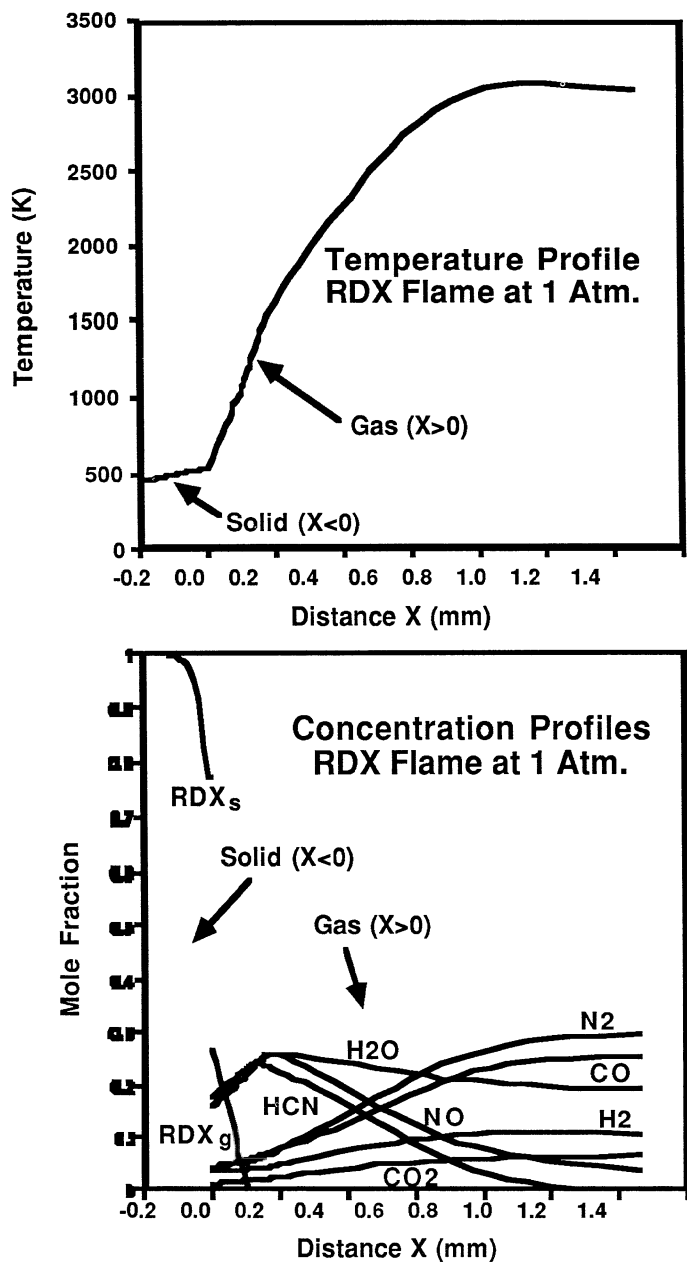


Fig. 8. Temperature and species concentration (mole fraction) profiles as a function of distance (mm) for the RDX flame at 1 atm. Origin corresponds to the gas-solid interface.

5.3. Chemical Reactions Involved in the Gas Phase RDX Ignition and Flame Chemistry

In the following section we discuss the net chemical reactions occurring during the various stages of ignition (Fig. 4) and flame combustion (Fig. 8). The species profiles for both the ignition and the steady-state flame indicate that similar chemistry is occurring, though the separate chemistry stages of ignition in Fig. 4 do not appear in the flame profile in Fig. 8. To investigate this further, in Fig. 9 we present the formation and destruction rates for HCN and CO for a 17 atm flame. The oscillatory behaviors in the HCN formation and removal rates indicate that several reaction zones (or stages) are, in fact, occurring in the flame. The results indicate that a multiple-stage flame exists, similar to the multiple stage observed in ignition. In the primary flame zone, there is a decomposition or pyrolysis region (corresponding to the formation of HCN), and a combustion region (corresponding to the conversion of HCN to C_2N_2). In the secondary (or luminous) flame zone (corresponding to the final removal of HCN), there are two interdispersed combustion regions, which differ primarily in their reaction pathways. The results show that, while the primary and secondary flames touch, they have not interpenetrated. The production and destruction rates for each chemical species (as shown for HCN and CO in Fig. 9) indicate that they are still separated.

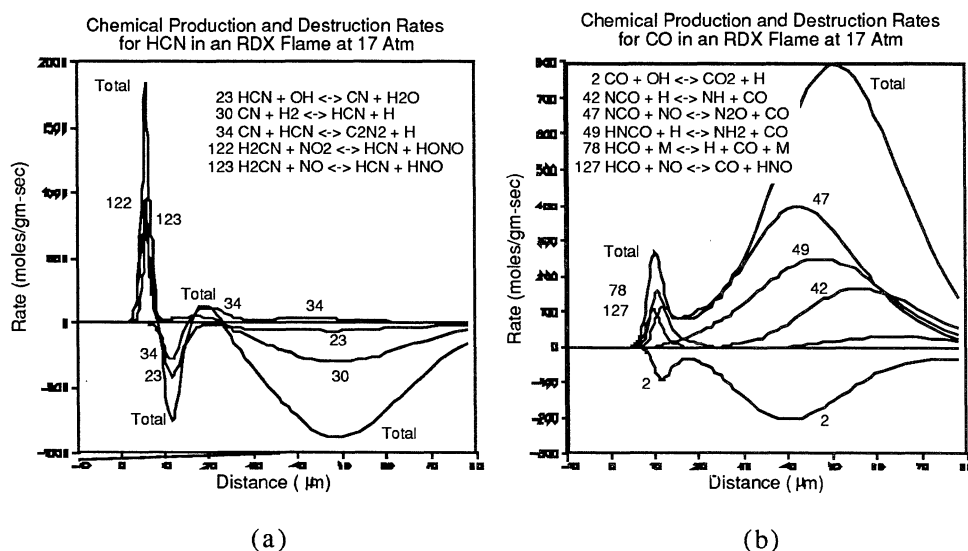


Fig. 9. Chemical production and removal rates as a function of distance (μm) for (a) HCN and (b) CO in the RDX flame at 17 atm, indicating the various reaction zones of the flame. Numbers on curves refer to the specific elementary reactions listed in the figure. The total rate for production or removal is also plotted.

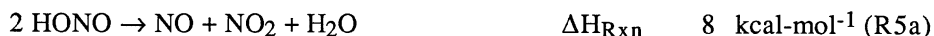
Using the production and removal rates for each of the molecular species, such as those given in Fig. 9, we can develop chemical reaction flow diagrams. In Fig. 10, we present the chemical reaction flow diagrams for the RDX flame. A similar diagram occurs for the ignition case.³¹ For both the ignition and flame conditions, we find that the chemistry takes place in three stages, involving decomposition and two oxidation stages. In the decomposition stage, the dominant net reactions are



and



During the first oxidation stage, the dominating net chemical reactions are



and



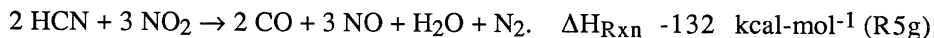
Following these reactions, we observe the remaining removal of NO_2 via



and



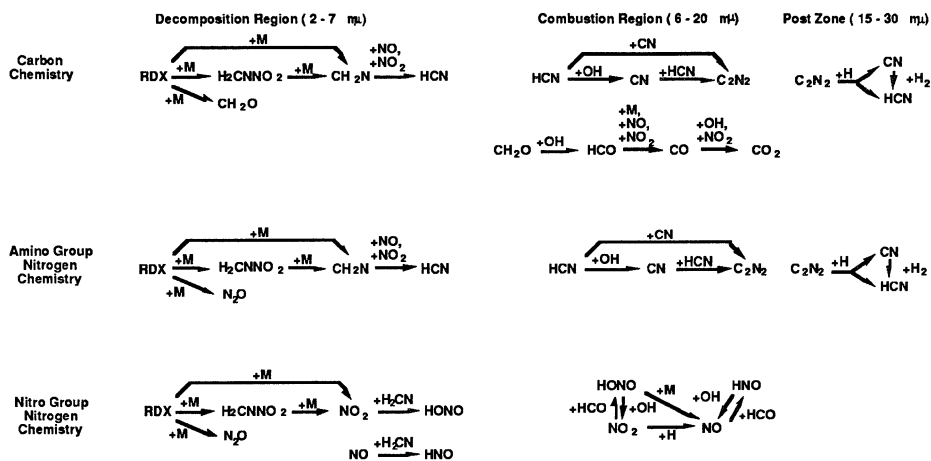
while at higher ignition temperatures, reactions (R5e) and (R5f) are replaced by



During the second stage of oxidation, the dominant net reactions are

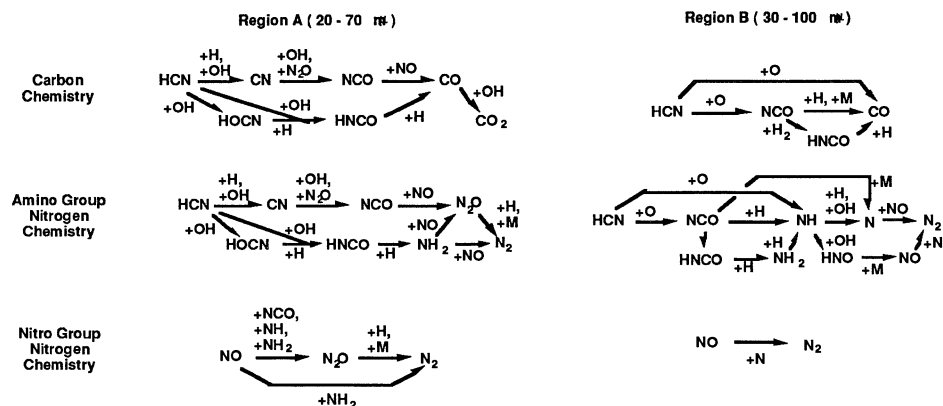


Primary Flame Zone of an RDX Flame



(a)

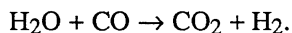
Secondary Flame Zone of an RDX Flame



(b)

Fig. 10. Chemical reaction flow diagrams for the (a) primary and (b) secondary stages (or zones) in the RDX flame at 17 atm. The spatial extent of the zones is indicated by the distances given in μm . We have separately indicated the reaction chemistry of the carbon species, the nitrogen species of the amino group of the RDX ring, and the nitrogen chemistry of nitro group of RDX. A similar reaction flow diagram exists for other flame pressures except that the distances must be scaled. Thick arrows indicate major pathways, while thin arrows indicate minor pathways.

and



$$\Delta H_{\text{Rxn}} \quad -10 \text{ kcal-mol}^{-1} \text{ (R6d)}$$

HONO plays an analogous role to CH_3OH in nitromethane by providing a temporary source of heat for the first stage ignition. The HONO is formed from NO_2 by reactions with weakly bound hydrogenated species, such as H_2CN , CH_2O , and HCO (see Fig. 10). HONO then regenerates NO_2 along with NO via the net reaction (R5a).

Since the C-H bond in HCN is very strong, the majority of HCN remains until the second oxidation stage zone. Note that the N_2O formed during the initial decomposition stage also remains relatively inert until the high temperature second oxidation stage. The secondary oxidation zone itself has two interdispersed reaction regions (see Fig. 10), which differ by their reaction path mechanisms, due to the higher temperature available later in the secondary flame, producing more O and N atoms.

The NO_2 acts as an inhibitor to the second stage chemistry. It is much more reactive than NO toward radicals. In particular, it reacts rapidly with H atoms, thereby reducing the H atom concentration. The OH radical dominates the primary zone chemistry. Unlike normal oxidation flames in which the $\text{H} + \text{O}_2$ reaction dominates, we find no significant chain branching mechanism. The thermal decomposition of HONO therefore provides the source of OH radicals in the primary flame. We find C_2N_2 contributing to the removal of NO_2 by providing H atoms, after which the C_2N_2 is converted back to HCN (see Fig. 10).

Another tool available to the modeler is sensitivity analysis of the results. The normalized sensitivity coefficient s for some property P (such as burn rate, species concentration, or temperature) due to variation in some parameter α (such as a rate constant) is given by

$$s = (\partial P / \partial \alpha) / (P / \alpha) \quad (18)$$

Having applied sensitivity analysis to the flame model results, in Fig. 11 we present the most important chemical reactions governing the burn velocity. One can see from the reaction flow diagram of Fig.10 and the sensitivity analysis in Fig. 11 that there are no dominant chain branching steps that control the flame chemistry. Thus, it is the thermal decomposition of N_2O which provides the source of radicals in the secondary stage flame for nitramines. Sensitivity analysis of RDX ignition also indicated that N_2O decomposition is the dominating reaction in ignition.

For the RDX flame, we can also use sensitivity analysis to determine the importance of condensed phase physical properties in affecting the burn velocity. The results are shown in Fig. 12. As expected, one sees that the burn rate is very sensitive to the initial temperature of the propellant. Similarly, one also sees a strong dependence on pressure.

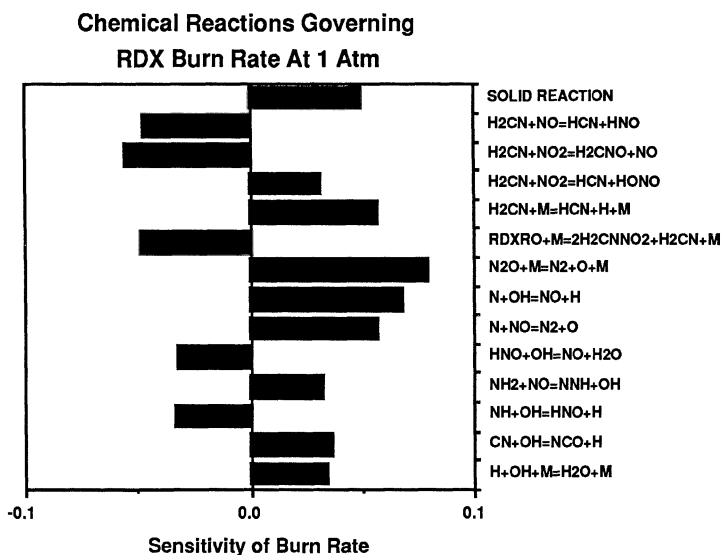


Fig. 11. Sensitivity analysis of the flame speed to changes in the pre-exponential rate constant for the elementary chemical reactions. A negative dependence means that increasing its rate constant would slow the burn rate. Shown in the figure are the most sensitive reactions affecting the burn rate to the RDX flame.

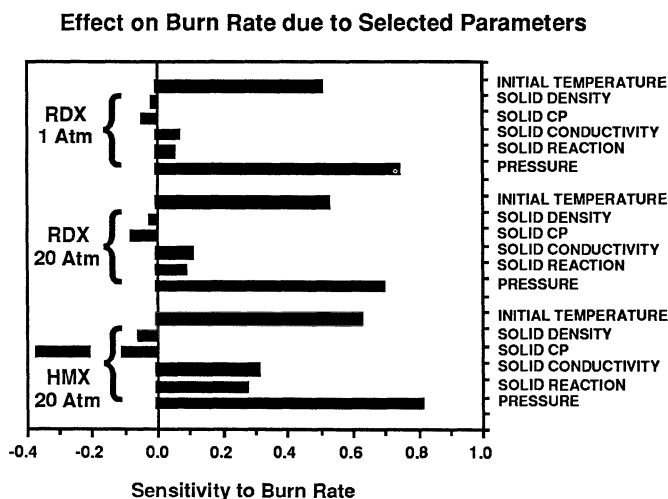


Fig. 12. Sensitivity analysis of the flame speed to changes in values of properties of the solid phase RDX, including initial temperature, density, heat capacity, and thermal conductivity. Also given are the rate constant for condensed phase decomposition and for the pressure.

Conclusions

We have presented a set of theoretical modeling techniques, involving detailed chemical kinetics combined with mass and energy diffusion, which can be used to gain insight into the chemical processes of energetic materials. We have provided examples for both the zero-dimensional ignition problem and the one-dimensional steady state flame. We have shown how the output of these models can be used to determine reaction mechanisms involved in energetic materials. We have illustrated these techniques for nitromethane ignition and for nitramine ignition and combustion.

As the power of computers continues to increase in the future, these modeling approaches will include more and more fundamental processes. The combustion community is currently extending these techniques to handle multiply dimensioned systems, such as diffusion flames. Progress is also being made in extending these techniques to time-dependent spatial problems, such as forced ignition (e.g., the heating of a propellant surface leading to combustion). Efforts are also being made to improve the condensed phase chemistry aspects of these computer models. As these models progress, the need for detailed knowledge of the chemistry and physics of molecular processes in energetic materials as input to the codes will continue to increase.

References

- ¹For a general survey of ignition and combustion issues of propellants, see the various articles in Fundamentals of Solid Propellant Combustion, M. Summerfield and K. Kuo, Eds., 1984, and references therein.
- ²N. Kubota, Nineteenth Symp. (Internat.) on Comb., p. 777, The Comb. Inst. (1983); Eighteenth Symp. (Internat.) on Comb., p. 187, The Comb. Inst. (1981).
- ³T. L. Boggs, in Fundamentals of Solid Propellant Combustion, M. Summerfield and K. Kuo, Eds., 1984, Chapter 3, p. 121, and references therein.
- ⁵R. A. Fifer, in Fundamentals of Solid Propellant Combustion, M. Summerfield and K. Kuo, Eds., 1984, Chapter 4, p. 177, and references therein.
- ⁶R. Zimmer-Galler, AIAA 11, 2107 (1968).
- ⁷G. Lengelle and J. Duterque, AGARD/PEP Specialists' Meeting on Smokeless Propellants, Florence, Italy, September 1985.
- ⁸M. Ben-Reuven, L. H. Caveny, R. J. Vichnevetsky, and M. Summerfield, Sixteenth Symp. (Internat.) on Comb., p. 1223, The Comb. Inst. (1977).
- ⁹M. Ben-Reuven and L. H. Caveny, AIAA 19, 1276 (1981).
- ¹⁰N. E. Ermolin, O. P. Korobeinichev, L. V. Kuibida, and V. M. Fomin, Fiz. Goreniya Vzryva 22, 54 (1986) and data presented therein by O. P. Korobeinichev et al. in Mass Spectrometry and Chemical Kinetics, Moscow (1984).
- ¹⁰D. M. Parr and T. P. Parr, 20th JANNAF Combustion Meeting, p. 281, October, 1983.
- ¹²B. N. Kondrikov, V. M. Rakkova, and B. S. Samsonov, Fiz. Goreniya Vzryva 9, 84 (1973).
- ¹³R. L. Hatch, Proceedings of the 24th JANNAF Combustion Meeting, October 1987.
- ¹⁴T. Parr and D. Hanson-Parr, WSSI/CI 87-8, April 1987; T. Parr and D. Hanson-Parr, 24th JANNAF Combustion Meeting, October 1987.

- 15T. Edwards, D. P. Weaver, D. H. Campbell, and F. Frederick, 23rd JANNAF Combustion Meeting, p. 181, October 1986.
- 16T. Edwards, Proceedings of the 24th JANNAF Combustion Meeting, October 1987, and references therein.
- 17V. M. Mal'tsev, A. G. Stasenke, V. A. Selezner, and P. F. Pokhil, Fiz. Goreniya Vzryva 9, 220 (1973).
- 18R. Fifer and H. E. Holmes, Proceedings of the 16th JANNAF Combustion Meeting, Vol.2, p. 35, December 1979.
- 19M. A. Schroeder, BRL Technical Report BRL-TR-2659, June 1985, and references therein.
- 20M. A. Schroeder, BRL Technical Report BRL-TR-2673, September 1985, and references therein.
- 21T. B. Brill and Y. Oyumi, J. Phys. Chem. 90, 6848 (1986) and references therein.
- 22A. Perche, J. Tricot, and M. Lucquin, J. Chem. Res.(S), p. 304 (1979); *ibid.*, p. 306 (1979).
- 23D. S. Y. Hsu and M. C. Lin, J. Ener. Mat., 3, 95 (1985).
- 24R. Guirguis, D. Hsu, D. Bogan, and E. Oran, Comb. and Flames 61, 51 (1985).
- 25R. Fifer, Seventeenth Symp.(Internat.) on Comb., p. 587, The Comb. Inst. (1978).
- 26R. L. Hatch, Proceedings of the 23rd JANNAF Combustion Meeting, Vol. I, p. 157, October 1986.
- 27C. F. Melius and J. S. Binkley, Twenty-first Symp.(Internat.) on Comb., in press.
- 28C. F. Melius, J. de Physique Colloque C4, Vol. 48, p. 341 (1987).
- 29C. F. Melius, Proceedings of the 23rd JANNAF Combustion Meeting, Vol. I, p. 241, October 1986.
- 30C. F. Melius, paper I in Chemistry and Physics of the Molecular Processes in Energetic Materials, NATO ASI Series, S. N. Bulusu, ed., Kluwer Academic Publishers.
- 31C. F. Melius, Proceedings of the 24th JANNAF Combustion Meeting, October 1987.
- 32C. F. Melius, Proceedings of the 25th JANNAF Combustion Meeting, Vol. II, p. 155, October 1988.
- 33R. J. Kee and J. A. Miller, Sandia Report SAND86-8841 (1988).
- 34R. J. Kee, J. A. Miller, and T. J. Jefferson, Sandia Report SAND80-8003 (1980).
- 35R. J. Kee, J. Warnatz, and J. A. Miller, Sandia Report SAND83-8209 (1983).
- 36R. J. Kee, F. M. Rupley, and J. A. Miller, Sandia Report SAND87-8215 (1987).
- 37S. Gordon and B. J. McBride, NASA SP-273 (1971).
- 38P. Glarborg, R. J. Kee, J. F. Grcar, and J. A. Miller, Sandia Report SAND86-8209 (1986).
- 39M. E. Coltrin, R. J. Kee, and J. A. Miller, J. Electrochem. Soc. 131, 425 (1984); J. Electrochem. Soc. 133, 1206 (1986).
- 40R. J. Kee, J. F. Grcar, M. D. Smooke, and J. A. Miller, Sandia Report SAND85-8240 (1985).
- 41R. J. Kee and J. A. Miller, Physica D 12, 198 (1984).
- 42J. F. Grcar, R. J. Kee, M. D. Smooke, and J. A. Miller, 21st Symp. (Internat.) on Comb., (1986).

- ⁴³G. Dixon-Lewis, T. David, S. Gaskell, P. H. Fukutani, H. Jinno, J. A. Miller, R. J. Kee, M. D. Smooke, N. Peters, E. Effelsberg, J. Warnatz, and F. Behrendt, Twentieth Symp. (Internat.) on Comb., p. 1893, The Comb. Inst. (1984).
- ⁴⁴R. E. Mitchell R. J. Kee, Sandia Report SAND82-8205 (1982).
- ⁴⁵K. Kuo, "Principles of Combustion".
- ⁴⁶A. E. Lutz, R. J. Kee, and J. A. Miller, Sandia Report SAND87-8248 (1987).
- ⁴⁷M. Caracotsios and W. E. Stewart, Comp. and Chem. Eng. 9, 359 (1985).
- ⁴⁸L. R. Petzold, SIAM J. Scientific and Stat. Comp. 3, 367 (1982b); Sandia Report SAND83-8673 (1983).
- ⁴⁹P. Glarborg, J. A. Miller, and R. J. Kee, Comb. and Flame 65, 177 (1986), and references therein.
- ⁵⁰J. A. Miller, M. C. Branch, W. J. McLean, and D. W. Chandler, Twentieth Symp. (Internat.) on Comb., p. 673, The Comb. Inst. (1984).
- ⁵¹L. R. Thorne, M. C. Branch, D. W. Chandler, R. J. Kee, and J. A. Miller, Twenty-first Symp. (Internat.) on Comb., p. 965, The Comb. Inst. (1986).
- ⁵²O. I. Smith and L. R. Thorne, WSS/CI 86-34, October, 1986.
- ⁵³W. A. Hepler and O. I. Smith, WSS/CI 87-23, April, 1987.
- ⁵⁴J. E. Shepherd and C. F. Melius, unpublished results.
- ⁵⁵C. Y. Lin, H. T. Wang, M. C. Lin, and C. F. Melius, J. Phys. Chem., in press.
- ⁵⁶R. A. Yetter and H. Rabitz, in press.

FUNDAMENTAL PHYSICS AND CHEMISTRY BEHIND MOLECULAR CRYSTAL DETONATIONS AT A MICROSCOPIC LEVEL

Simone Odier

Université Pierre et Marie Curie,
Département de Recherches Physiques-Laboratoire associé au CNRS
Tour 22, 4 Place Jussieu
75252 Paris Cedex 05
France.

The main results presented here were obtained with Michel Peyrard (OSC, Dijon), and Elaine Oran, Sam Lambrakos (NRL) and, for a long time, the technical collaboration of Monique Blain (DRP).

ABSTRACT. In these two review lectures, we combine Quantum Chemistry, Crystalline structure analyses and Molecular-Dynamics simulations to obtain an insight into the Physics and Chemistry of shock induced detonation wave propagation mechanisms in energetic molecular crystals in order to help define a microscopic theory of detonations. By "*numerical experiments*" on 1-D and 2-D models with variable physical and chemical parameters, the way to divide the complicated problem of detonation into simpler steps will be shown. We present the microscopic models for chains of molecules as the support of molecular dissociation propagations in a condensed energetic material and discuss the role of molecular and crystal structures, energy transfers (dissipation) and the effects of different chemical steps on detonation wave propagation. Some crystal structure conditions are defined which allow accentuating, in a series of more or less energetic crystals, the characteristic crystal "architecture" of an explosive compound.

INTRODUCTION

The extreme conditions of temperature and pressure, the ultra fast reaction phases with distinct and characteristic times (very short times 10^{-6} 10^{-9} 10^{-12} s, but very large execution phase ratio times 10^3 to 10^6), involved in "the science of detonations", submit its evolution to that of the technics. Nowadays, from both the experimental and the theoretical point of views, the sharpness of microscopic information together with their interpretations to induce a new manner of observing macroscopic detononic manifestations, allow us to develop the first steps of induced shock detonation theory in a molecular crystal.

These two lectures are devoted to a microscopic view of the phenomena involved in a shock induced detonation process in an energetic molecular crystal.

The question arises:

What is a detonation wave in this microscopic approach and which are the problems to be analyzed in order to define the molecular and crystalline conditions which characterize a molecular crystal as an explosive?

In other words, more directly, in order to bring some answer to the question: *"why does an explosive explode"* or if you prefer why could it not explode?

In order to improve our knowledge on possible detonation mechanisms, we analyze energetic and electronic characteristics of an explosive molecule by **quantum chemistry calculations and spectroscopy data**, the crystalline structure of energetic crystals by **visualization on micro computers**, their effects on experimental detonation parameters, while energy transfer processes are defined and their efficiency, if possible is estimated by **molecular dynamics and numerical simulations**.

The aim of this study is to suggest some ways to **control** detonation phenomena.

This **interdisciplinary** subject allows us to take a two-hour walk among the dream-filled fields of Chemistry and of Physics.

Chimie Quantique Fonction Détonique

C Q F D

PLAN

PART I FUNDAMENTAL PHYSICS BEHIND A MICROSCOPIC APPROACH TO MOLECULAR CRYSTAL DETONATIONS

THE MOLECULE

- 1 - Electronic **Molecular** Parameters
- 2 - Energetic Electronic Molecular States and **Excited State** Geometries by Quantum Chemistry and Resonance Raman Spectroscopy

THE CRYSTAL

- 3 - **Crystalline** Structure - Chain Structures

ENERGETIC COMPOUND WHO ARE YOU?

- 4 - Conclusions **Status of the problems** on a microscopic scale

PART II MOLECULAR DYNAMIC MODELS FOR DETONATION WAVE PROPAGATION

- 1 - **1-D Model** Definition-Results-Comparison to Experiments
- 2 - **Dissipation Energy**: **2-D Model** Definition-Results-Comparison to Experiments
Come back to crystalline structure analysis.
- 3 - **Chemical Energy**: **2-D Model** and Elementary Chemical Reactions
- 4 - **Excitation Electronic Molecular Energy**: **3-D Model**
- 5 - Conclusions and **Perspectives**

PART I

FUNDAMENTAL PHYSICS BEHIND A MICROSCOPIC APPROACH TO MOLECULAR CRYSTAL DETONATIONS

The view of the average human being

Under shock, the molecule breaks, the medium reacts chemically, the energy released transmitted to the next molecules emphasizes the shock till detonation. A very simple scheme in which an energetic material must be characterized, first, by the molecular ability to break chemical bonds, then to produce chemical energy in a medium which can induce a cooperative intermolecular energy transfer mechanism in very short times.

1. The molecule - Electronic Parameters

The view of the theoretical chemist

If the molecule is explosive, and if the detonation phenomenon begins in breaking chemical bonds, an explosive molecule will differ significantly from a stable one at its electronic structure level. As correlations between molecular electronic structure and shock sensitivity have been established, it is not the purpose of these lectures to discuss this vast subject studied in detail in 1987: *Sensitivity of Explosives*. Socorro N.M. USA . Two lectures given here by P. Politzer and by C.B. Storm, J.R. Stine are devoted to this subject. Correlations between theoretical bond polarities and sensitivities (see for a review on Cherville and Delpuech results, R. Cheret "La detonation des explosifs condensés" tome 1, chapitres IV, V, VI Masson 1989), are based on valence electron bond polarity calculations in the ground state and the electronic excited state which leads to the greatest lowering of the $X-NO_2$ ($X=C, N, O$) polarity value. In this scheme, the correlation between the relative bond polarity variations (ground - excited states) and shock sensitivities in the three series: nitroaromatic, nitramide and nitric ester, is excellent for a large number of molecules and allows prediction for new explosives. These works suggest that a privileged molecular bond in an excited electronic state is involved in shock-induced detonations.

Early simple work on nitroaromatic compounds at the π electronic system level suggested that the C-N bond was involved in detonation, in the first excited π electronic state. In Hückel approximations, bond-orders and bond-polarities have been calculated in ground and excited states, in non explosive nitrobenzene and toluene and in 20 explosive nitro compounds. This very simple method was suitable, as a starting point, for finding an evolution in a homogeneous series of compounds in order to suggest some idea. (The Hückel π system method (LCAOMO totally empirical method) introduced in 1931 has been extensively used in theoretical chemistry and allowed "hand calculations"; all the integrals, (Coulomb and Resonance) are empirical parameters. In these pioneer times, these integrals were very carefully fitted to experiments and appeared once and for all as specific parameters of an atom in a molecule and of a molecular bond between two atoms in referring respectively to the Carbon atom and Carbon-Carbon bond. This method, because of its excellent empiricism, introduces implicitly many of the desired features of the chemistry and electronic physical principles as long as it studies electronic variations in the π system

in a series of comparable molecules. Later it was successfully extended to the σ electronic system. After the arrival of computers the too great simplicity of the method did not convince younger referees of high level reviews to pay attention to Hückel calculations. Only ab initio results with a large basis set and correlation effect are up to date and credible. Semi-empirical calculations, CNDO, MINDO,...if the number of atoms and atomic orbitals is too high, are still now just "good enough to be published". However, if one uses this very simple well known method, it is necessary to be aware of its limits. With all its abilities in mind, Hückel method may be sometimes so easily useful).

Systematically, by substitution, we observed an effect on the π C-N bonds. It is reflected, Table 1, in 5 selected compounds. In this table, we report:

Hückel bond order: P_{CN} and C-NO₂ polarity: D_{C-NO_2} ; inside (), first excited state values.

Compared to the C-N bond order in nitrobenzene (N°1), methyl group (N°2) lowers significantly the meta C-N bond order while the para bond order increases. The same effect is observed by NO₂ substitution (N°4). In replacing the O by F atom (N°3, N°5), it is observed that the C-N(F₂) bond order lowers whatever the substitution site is; this last effect is so significant that it could explain by an electronic effect the great sensitivities of NF₂ compounds.

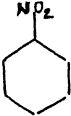
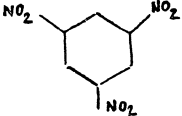
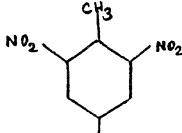
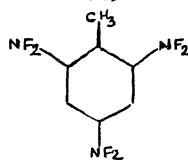
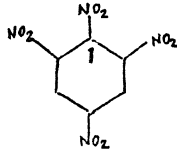
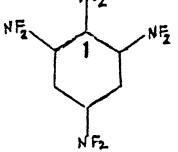
These results mean that the π bond order which reflects the strength of a bond in the Hückel frame, reflects a lowering of C-N bond energy in such an explosive molecule which would reflect its sensitivity.

In going from the ground state to the first π excited state, it has been observed that if the bond order remains about the same in nitrotoluene derivatives, in regard to the C-NO₂ bond polarities, the values increase from the ground state to the first π excited state e.g., values are given for toluene in Table 1. This important increase of a parameter which is not related to bond energy, like the bond order in the Hückel frame is, but to dipole moment suggested to us the idea that via multipolar interactions, the intermolecular potentials between C-NO₂ ... C-NO₂ groups in condensed phases will significantly increase by electronic excitation.

With all these different results in mind, and the idea that an excited state would be involved in the detonation mechanism in order to be in favor of an energy exchange of the C-N bond dissociation with the next one, we look at now the bond dissociation and the behaviour of the electronic excited states against the C-N bond lengthening, in a series of nitro compounds.

2. Energetic Electronic States

The Hückel method is evidently not adapted for doing such calculations. We calculated the section of the molecular potential hypersurfaces relative to the stretching C-N normal coordinate with the STO-3G method, correlation effect included, for ground state; then, we obtained the first 9 electronic excited states, for each normal coordinate C-N value, from the ground state energy value to which, one by one, we added the first 9 CNDO/S transition energy values, taking account of the correlation energy (Configuration

		P_{C-N}	D_{C-NO_2}
1		0,496	
		High degenerescence in Hückel frame	
2		0,231 o (0,220) 0,531 p (0,489)	0,067 (0,578)
3		0,173 o (0,127) 0,173 p (0,176)	
4		0,213 1 0,220 o. 0,491 p.	
5		0,204 1 0,189 o 0,189 p	

Bond order P_{C-N} and D_{C-NO_2} Polarity (in bracket excited state value)

TABLE I-1

π Hückel Parameters of 5 aromatic compounds

Interactions including single and double excitations) and of the symmetry of the molecular orbitals for respecting the possibility of crossing states. In spite of the accuracy of the principle of the technics used, the method is not sufficiently accurate to take into account multiconfigurational states at large distances and the pictures obtained are difficult to interpret.

Thus we chose to study two explosive compounds, **nitromethane** and **difluoramine**, whose decompositions appear respectively along a C-N and (or) N-H (N-F) bond. These two compounds were chosen 1/ because they are small enough to allow ab initio 4/31G with large Configuration Interactions (5 excitation classes), a total geometry optimization and singlet or triplet excited state calculations; 2/ because their detononic sensitivities are very different. If the dissociating process is correlated with initiation, these different electronic bonds must behave as differently in dissociating as the sensitivities are.

Fig. 1 (nitromethane) and 2a, 2b (difluoramine along (a)N-H or (b) N-F) show:

-for **nitromethane**, a predissociative **excited** exothermic state 1A_2 at 4.18 eV from the ground state

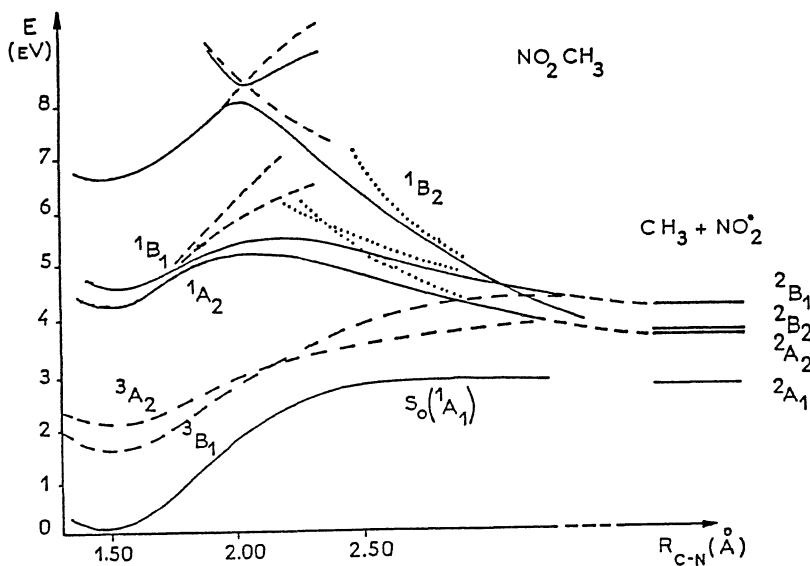
-for **difluoramine**, a predissociative endo or exothermic (we could not obtain further precision) **ground state** by cross section with the first triplet for both dissociation pathways.

These two results precisely give an account of the different sensitivities of these two compounds; it is well known that difluoramine is an extremely sensitive explosive.

In conclusion, the simple theoretical analysis of an explosive molecule suggest the existence of a privileged bond for dissociating in an excited or ground, predissociative, exothermic or perhaps not exothermic (see Part II) state. In energetic aromatic compounds, the increase of π polarities in the first excited state suggested such an excitation for increasing molecular interactions in a cooperative mechanism of detonation wave propagation. The clear electronic chemical bond behavior with detononic sensitivity between only two non aromatic compounds nitromethane and difluoramine, underlies the most important role of the electronic state level in the early steps of detonation initiation.

In order to improve the models for detonation wave propagation described in part II, it is necessary to improve the knowledge of the electronic excited states of the molecule after defining the dissociation coordinate: i.e. the geometry of the excited states, the molecular fragments involved in excitation, the behaviour of the state along vibrational coordinates, the force constants, the polarities of the bonds, and the variations induced in these results by the crystalline environment and by high dynamic pressure.

Information can be obtained in using Quantum Chemistry Calculations and Spectroscopy results. For instance, the previous calculations on nitromethane in ground and excited states have been supported favorably by interpreting Schnur and coll. (NRL) picosecond UV dissociation results. The perfect comparison with recent Vergoten (Lille) Raman results of the calculated rotation barrier of methyl group in nitromethane crystal underlies the good choice of a **particuliardimer** in representing the best environment of the crystal on the molecule (for rotation) and the necessity of **adopting in calculations the geometry of the molecule in the crystal** (table 2 and fig 3). Finally, the study of the increasing intensity band in UV Resonance Raman (in comparing theoretical and experimental spectra) for the excitation state geometry optimization, will indicate which coordinates of the molecule will vary during excitation and consequently will allow **selecting only these parameters in the**



Potential surfaces of the ground state S_0 , predissociative states $1A_2$, $1B_1$, $1B_2$ and the two first triplets $3B_1$, $3A_2$. The curves indicated by a solid line (—) correspond to the interpolation of the value of the energy in assuming that the NO_2 and CH_3 fragments for each value of $R_{\text{C-N}}$ are in an optimized geometry. The curves indicated by a broken line (---) correspond to the calculation of the variation in the energy as a function of $R_{\text{C-N}}$; the CH_3 and NO_2 fragments are in the equilibrium geometry of the ground state of the Nitromethane. The curves indicated by a dotted line (...) correspond to the calculation of the variation in the energy as a function of $R_{\text{C-N}}$; the CH_3 fragment is in the equilibrium geometry of its ground state, the geometry of the NO_2 fragment is adapted to the geometry of its excited state.

FIGURE I-1

Potential surfaces of Nitromethane

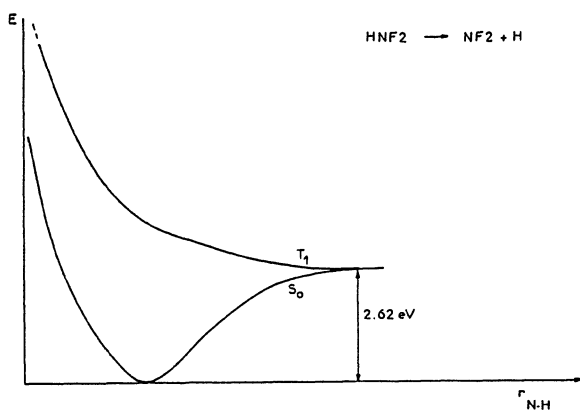


FIGURE I-2a

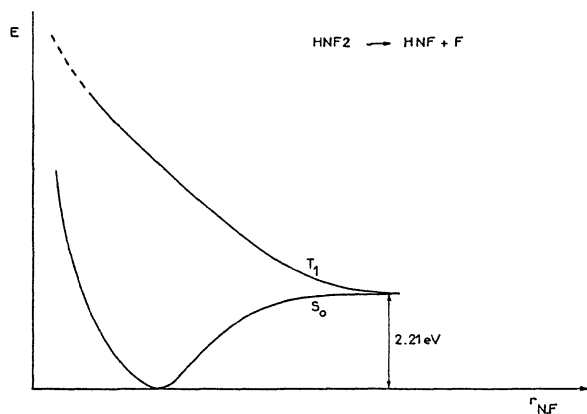


FIGURE I-2b

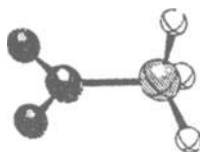
Ground state and first triplet state of difluoramide following two dissociation paths

FIGURE I-2

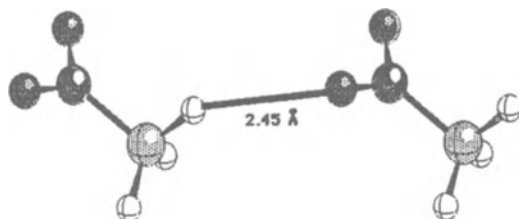
Potential surfaces of Difluoramide

a) vs $r_{\text{N-H}}$

b) vs $r_{\text{N-F}}$



a Monomer $\Delta E=60$ cal/mole



b Dimer $\Delta E=685$ cal/mole

FIGURE I-3

Methyl rotation barrier in Nitromethane

- a) Monomer in crystal structure
- b) Dimer in crystal structure

STO-3G ENERGIES (cal/mole)		
	crystal	gas *
monomer	60	8
dimer	685	1285
trimer (symmetric)	694	1580
trimer (asymmetric)	1229	1512
quadramer	931	

Experiment G.Vergoten 655 cal/mole

* : optimised geometry

TABLE I-2

Nitromethane - Methyl rotation barrier height

geometric optimization which can then be reached by calculations.

3. Crystalline Structure Chain Structure

In a crystal, the intermolecular forces involved in the breaking bonds between atoms or "atom groups" in lattice-fixed positions are thought to be the supports of energy transfers from one molecule to the next. **Moreover, they appear as a leading "designer" to lay out roads in the molecular crystal for a detonation wave propagation cooperative mechanism.**

Strange to observe, an excellent classification between explosive and non explosive nitro molecular crystals was obtained recently on 46 compounds (32 explosives), from a very simple criterium: the density in NO_2 defined as : $\rho \cdot N = Z \cdot M / V$ g.cm^{-3} with,

Z: number of molecules per cell,

M: nitro molecular mass / molecule = (number of NO_2 / molecule) $\cdot (m_N + 2 \cdot m_O)$

V: cell volume (the orthorhombic, monoclinic or triclinic lattice cell is defined by the three unit vectors \vec{a} , \vec{b} , \vec{c} and their angles α , β , γ),

N: Avogadro number.

Table 3 gives the list of the compounds classified in chemical series, and C-N(O_2),

N-N(O_2), O-N(O_2) bond types with their unit cell volumes V, NO_2 density $\rho \cdot N$, the sensitivity h_{50} , the detonation speed (gas phase value) D. A * marks the non explosive compounds, and ? the unknown one. Fig. 4 clearly distinguishes explosive compounds from the other ones.

Nitroguanidine, with a density of $\rho_0 N = 0.47$, defines the boundary-line between the two classes; above this value one finds without exception explosives, but perhaps in the crystal phase, nitromethane (see later why in our view, it would explode or not?), and under, the non explosive compounds. The ? compound would be non explosive.

The variations of detonation speed and sensitivity against the volumic NO_2 density have been reported on curves 1 and 2, no significant results with sensitivity (too sharp variations to be significant with experiments) are observed; one notes on curve 1 the appearance of two linear significant correlations with speed: one for C-N bond, another one, above, for N-N bond. In this C-N linear variation of the speed with the density, the methyl group (compare TNB, TNT, TNX) decreases the speed, while the amino group (compare TNB, TNA, DATB, TATB) is almost without effect. Note that, in this series, the amino group increases the π (CNDO) bond order values (curve 2, where bond orders are given in brackets) in nitroaromatic compounds as the sensitivity decreases strongly, while the velocity does not vary; methyl group increases the bond order and the sensitivity decreases. **Sensitivity** for a given C-N bond once more seems to be crudely correlated with **electronic bond density at a molecular level**, while the **velocity** for this same bond seems to be dependent on the **intermolecular environment at an overcrowding level**.

From this last point of view let us examine, *the view of an architect*, how the groups C- NO_2 are linked together in nitro molecular crystals along the three different cristallographic axes. We have chosen among several studies to present here in a homogeneous series, the most representative results i.e.

name (* = non explosive) (? = unknown)	formula	volume cell (Å ³)	pH (g/cm ³)	D (m/s)	h50 (cm)
NITRO-AROMATIC COMPOUNDS					
1) nitrobenzène at -30°C *	C ₆ H ₅ NO ₂	592.56	0.310		
2) m-dinitrobenzène,	C ₆ H ₄ (NO ₂) ₂	700.73	0.525	6000	
3) p-dinitrobenzène,	C ₆ H ₄ (NO ₂) ₂	338.11	0.544		
4) 1,3,5 trinitrobenzène (TNB),	C ₆ H ₃ (NO ₂) ₃	3377.72	0.653	7300	100
5) hexanitrobenzène (HNB),	C ₆ (NO ₂) ₆	1162.98	0.949	9300	15
6) p-nitroaniline *	NH ₂ C ₆ H ₄ NO ₂	643.15	0.286		
7) trinitroaniline (TNA),	C ₆ H ₂ (NO ₂) ₃ NH ₂	854.42	0.646	(7300)	177
8) diamino trinitrobenzène (DATB),	C ₆ H(NO ₂) ₃ (NH ₂) ₂	439.13	0.628	(7500)	320
9) trinitro triaminobenzène (TATB),	C ₆ (NO ₂) ₃ (NH ₂) ₃	442.48	0.623	(7500)	550
10) 2,3,4,6-tetranitro aniline (TENA),	C ₆ H ₃ N(NO ₂) ₄	975.02	0.754	(7630)	41
11) trinitrotoluène monoclinique (TNT-m),	C ₆ H ₂ CH ₃ (NO ₂) ₃	1826.63	0.604	6900	160
12) trinitrotoluène orthorhombique (TNT-o),	C ₆ H ₂ CH ₃ (NO ₂) ₃	1823.55	0.605		
13) 2,4,6-trinitro-m-xylène (TNX),	C ₆ H(CH ₃) ₂ (NO ₂) ₃	980.24	0.563	(6600)	
14) trinitro mésithylène (TNM),	C ₆ (NO ₂) ₃ (CH ₃) ₃	549.65	0.502		
15) trinitro chlorobenzène (PICL),	C ₆ H ₂ Cl(NO ₂) ₃	927.30	0.595	7200	105
16) trinitro dichlorobenzène (PICL2),	C ₆ H(Cl) ₂ (NO ₂) ₃	969.15	0.569		
17) trinitro trichlorobenzène (PICL3),	C ₆ (Cl) ₃ (NO ₂) ₃	1639.41	0.505		
18) (N,N-difluoroamino) trinitro-2,4,6-benzène,	C ₂ H ₂ (O ₂ N) ₃ NF ₂	922.33	0.598		
19) hexanitrostilbène (HNS),	(C ₆ H ₂ (NO ₂) ₃ CH) ₂	1713.67	0.644		
20) hexanitro azobenzène I (HANAB1),	(C ₆ H ₂ (NO ₂) ₃ N) ₂	836.40	0.659		
21) hexanitro azobenzène II (HANAB2),	(C ₆ H ₂ (NO ₂) ₃ N) ₂	1721.39	0.641		
22) 2,4,6-trinitro phénétol,	C ₂ H ₅ OC ₆ H ₂ (NO ₂) ₃	1096.24	0.503		
23) p-nitrobenzoic acid *,	NO ₂ C ₆ H ₄ COOH	1400.84	0.262		
24) o-nitrobenzoic acid *,	NO ₂ C ₆ H ₄ COOH	354.20	0.259		
25) o-nitrobenzaldehyde *,	C ₆ H ₄ (NO ₂)CHO	340.83	0.269		
26) N,N-diméthyl-p-nitroaniline *,	N(CH ₃) ₂ C ₆ H ₄ (NO ₂)	407.16	0.225		
27) p-nitrophénol (forme bêta) *,	NO ₂ C ₆ H ₄ OH	617.58	0.297		
28) p-nitrophénol (forme alpha) *,	NO ₂ C ₆ H ₄ OH	595.28	0.309		
29) 1,5-dinitronaphthalène *,	C ₁₀ H ₆ (NO ₂) ₂	458.67	0.401		
30) 1,8-dinitronaphthalène *,	C ₁₀ H ₆ (NO ₂) ₂	911.39	0.403		
31) 9-nitroanthracène *,	C ₁₄ H ₉ (NO ₂)	1067.77	0.172		
32) 9,10-dinitroanthracène *,	C ₁₄ H ₈ (NO ₂) ₂	278.45	0.330		
33) 1,5-dinitro-4,8-dihydroxyanthraquinone *,	C ₁₄ H ₄ O ₂ (OH) ₂ (NO ₂) ₂	639.66	0.288		
34) tri-p-nitrophényl méthyl ?,	(NO ₂ C ₆ H ₄) ₃ C	1668.42	0.330		
ALIPHATIC COMPOUNDS					
35) nitrométhane,	CH ₃ NO ₂	275.31	0.668	(6247)	
36) β-nitropropionic acid *,	NO ₂ CH ₂ CH ₂ COOH	995.37	0.369		
NITRAMINE COMPOUNDS					
37) nitroguanidine,	(NH ₂) ₂ CNNO ₂	1562.08	0.471	8200	320
38) nitramide,	NH ₂ NO ₂	231.47	0.794		
39) N-N'-dinitro éthylène diamine,	(NO ₂ NHCH ₂) ₂	583.43	0.630	7750	34
40) cyclotriméthylène-trinitramine (hexogène-RDX),	C ₃ H ₆ N ₃ (NO ₂) ₃	1633.85	0.675	8750	25
41) α-Cyclotétraméthylène tétranitramine (α-HMX),	C ₄ N ₄ H ₈ (NO ₂) ₄	2138.70	0.688		
42) β-Cyclotétraméthylène tétranitramine (β-HMX),	C ₄ N ₄ H ₈ (NO ₂) ₄	519.38	0.708	9100	26
43) γ-HMX,	C ₄ N ₄ H ₈ (NO ₂) ₄	1098.32	0.670		
44) δ-HMX,	C ₄ N ₄ H ₈ (NO ₂) ₄	1663.92	0.663		
NITRIC ESTER COMPOUND					
45) pentrite (PETN)	C(CH ₂ -O-NO ₂) ₄	589.49	0.624	*8400	12
MIXTE DERIVATE COMPOUND					
46) N-méthyl-N 2,4,6-tétranitroaniline (tétryl),	C ₇ H ₅ N(NO ₂) ₄	1101.51	0.668		

TABLE I-3

Explosive, Non Explosive Nitro compounds

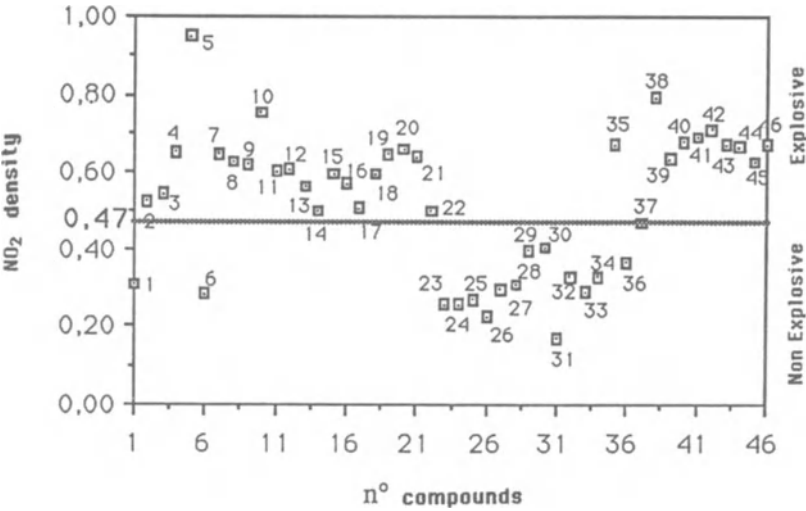
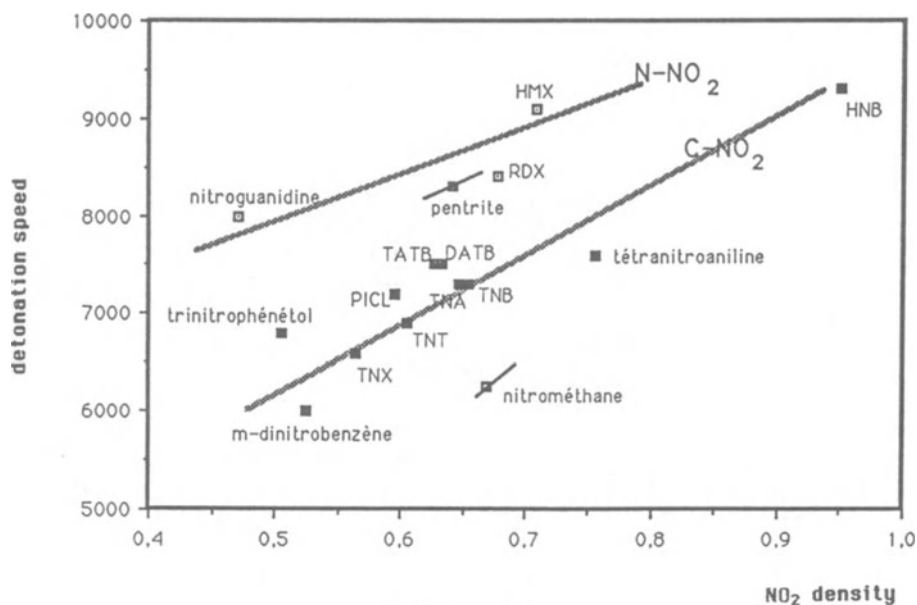
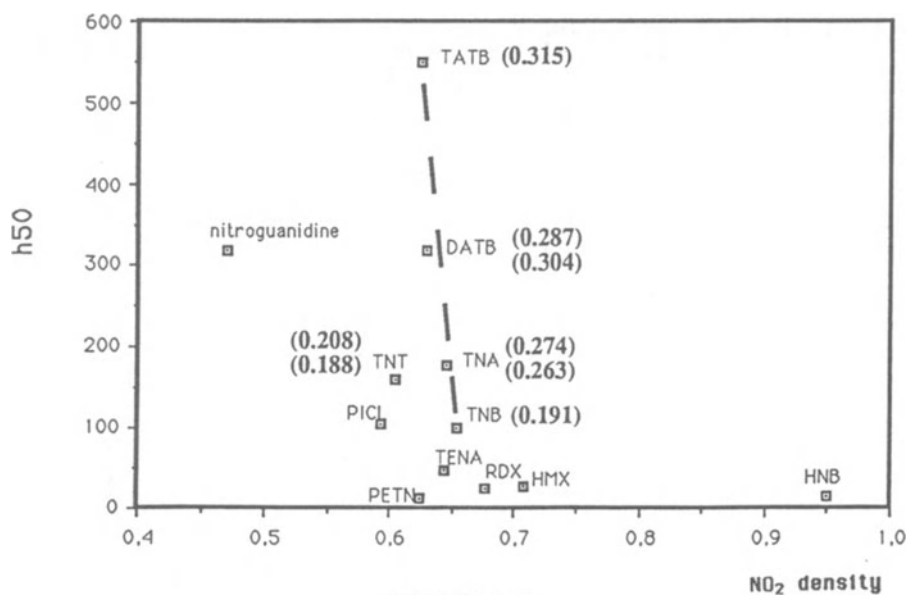


FIGURE I-4

Density of NO₂ for nitro crystal compounds



CURVE I-1

Detonation speed vs. NO_2 Density

CURVE I-2

Sensitivity vs. NO_2 Density

- (1) nitrobenzene, non explosive reference (4 molecules per cell, $D=0000$ m/s)
- (2) m dinitrobenzene (4 molecules per cell, $D=6000$ m/s.)
- (3) trinitrobenzene (16 molecules per cell, $D=7300$ m/s.)
- (4) hexanitrobenzene (4 molecules per cell, $D=9300$ m/s.)

The variations of the velocities are different enough in such a large scale of values to be regarded as significant.

From the literature crystalline structures, using the length and angular unit cell parameters, atomic coordinates of the first molecule, space group of the cell to generate by symmetry operations the atoms of the other molecules of the unit cell, after translations along \vec{a} , \vec{b} , \vec{c} , to create the crystal lattice, every N-N distance not farther than e.g. 6 Å, has been listed. They are visualized on the computer to observe a lattice of N...N...N... over the crystal lattice that we call the chain structure. Of course, due to the periodic crystal structure, chain structure will always appear, and they are never listed. Observations are the following:

In compounds 2, 3, 4, (fig. 5,6,7), nitrogen atoms (and carbon atoms) are linked in chains, they define more or less **privileged ways** to exchange energies through intermolecular potentials in a more or less **rigid architecture** (fig.5',6',7'), allowing as we shall see later, less or more atom transverse motions dissipating less or more energy useless for sustaining the detonation. In nitrobenzene (fig. 8), whatever the direction \vec{a} , \vec{b} , \vec{c} , no chains appear; if so, the inter N lengths are too far, $N...N > 6$ Å, moreover, the architecture around is smooth (non rigid). What can we say about the perfect architecture of hexanitrobenzene (fig. 7'), the most rigid one with triangle bridges to prevent transverse motions and favor longitudinal pathways along straight directions with the N very close to each other to make the transfer energy easier? Fantastic if we remember that its detonation velocity is very high, 9300m/s.

Adding another compound, nitromethane, (fig. 9), such chain structures appear; however another aspect must be underlined: the chains are regular **zig-zags**, and it has been observed that these zig-zags are amplified for low NO_2 density compounds, like m-dinitrobenzene or TNT-m (not given here) and consequently for low speed detonation.

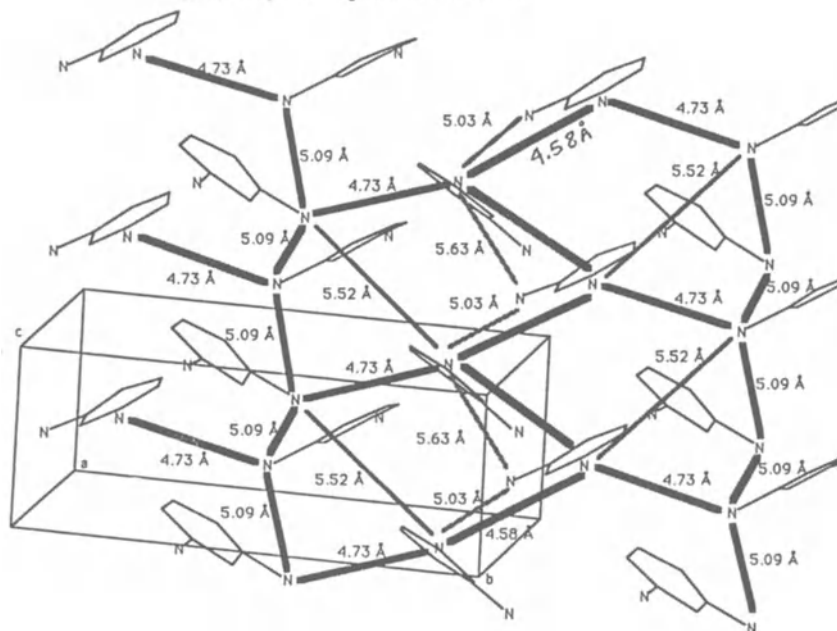
From these very simple observations, short distance chains, straight paths roads without zig-zag "fancy", rigid frame, appear to be the starting points to draw the scheme of the basic models for the numerical "experiments" on detonation wave propagations, studied in part II.

4. Conclusion Status of the Problems on a Microscopic Scale.

The thermodynamic model of a detonation, Hugoniot curve, and Equations Of State of final products, determines "a priori" the macroscopic characteristics, in the steady state, of a detonation: pressure and velocity. We have seen that microscopic contributions from chemical bond and crystalline structure may play a capital role to initiate, propagate and sustain a detonation in a molecular crystal. The problem now is to go further and to try to understand at this microscopic level how they can do it. The answer to this question does not yet belong to experiments but to "theoretical experiments" from numerical simulations of molecular dynamics governed by these microscopic factors, *the view of a physicist and a mathematician*, a new approach to understanding

m-dinitrobenzene, orthorhombic, $Pbn2_1$, 4 molecules per cell.
 $a=13.20 \text{ \AA}$, $b=13.97 \text{ \AA}$, $c=3.80 \text{ \AA}$.

J.Trotter, *Acta Cryst.* (1961) **14**, 244



it is observed in the (001) direction:

- a zig-zag chain with $N-N=5.09 \text{ \AA}$ and $C-C=6.24 \text{ \AA}$
- a zig-zag chain with $N-N=4.58 \text{ \AA}$ and $C-C=5.60 \text{ \AA}$

Note: in the other directions the benzenes rings prevent chain structures

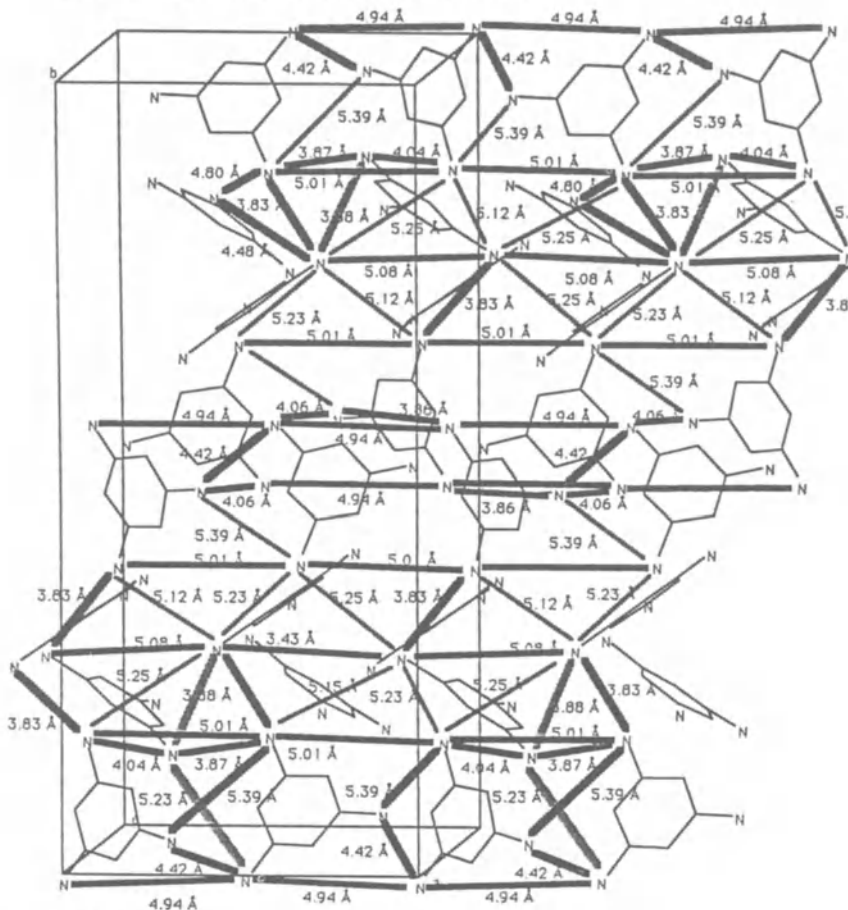
chains in direction (001)

FIGURE I-5

Chain structures in *m*-Dinitrobenzene

1,3,5-trinitrobenzene, orthorhombic, $Pbca$, 16 molecules per cell.
 $a=9.78 \text{ \AA}$, $b=26.94 \text{ \AA}$ et $c=12.62 \text{ \AA}$.

C.S.Choi and J.E.Abel , *Acta Cryst.* (1972) **B28**, 193



It is observed

- a zig-zag chain with $N-N = 4.94 \text{ \AA}$ $C-C = 5.24 \text{ \AA}$.
- a zig-zag chain with $N-N = 5.01 \text{ \AA}$ $C-C = 5.28 \text{ \AA}$.
- a zig-zag chain with $N-N = 5.08 \text{ \AA}$ $C-C = 5.82 \text{ \AA}$.

Note : In the other direction a steric effect prevent chain structures

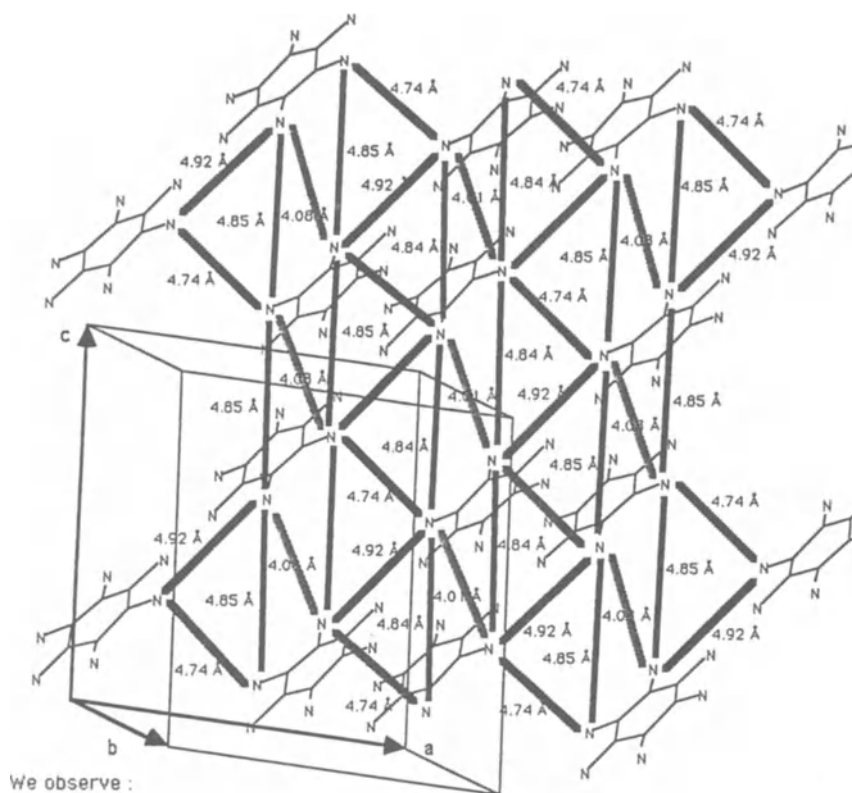
Chains in direction (100) :

FIGURE I-6

Chain structures in Trinitrobenzene

hexanitrobenzene, monoclinic, $12/c$, 4 molecules per cell
 $a=13.22 \text{ \AA}$, $b=9.13 \text{ \AA}$, $c=9.68 \text{ \AA}$, $\beta=95^\circ.50$.

Crystal Structure, XV, aVII, 9



- a chain with N-N = 4.84 \AA and C-C = 5.27 \AA
- a chain with N-N = 4.85 \AA and C-C = 5.29 \AA

Note : in the other directions the benzene- rings prevent chain structures

direction (001)

FIGURE I-7

Chain structures in Hexanitrobenzene

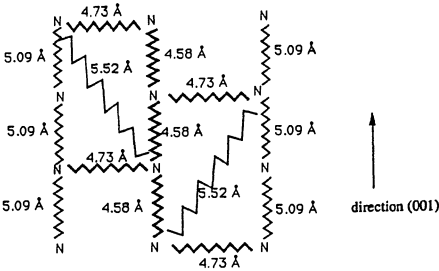


FIGURE I-5'

Intermolecular bonds in m-Dinitrobenzene

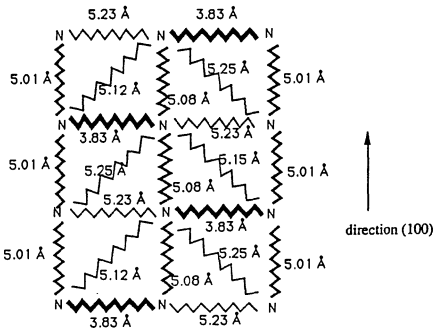


FIGURE I-6'

Intermolecular bonds in Trinitrobenzene

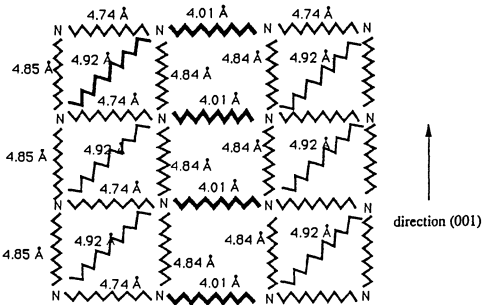
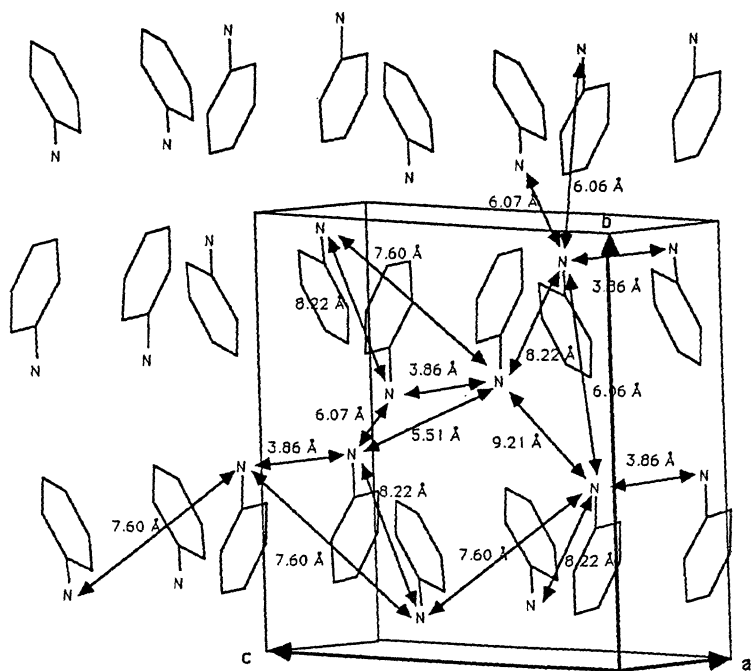


FIGURE I-7'

Intermolecular bonds in Hexanitrobenzene

nitrobenzene at -30°C , monoclinic, $P2_1/c$, 4 molecules per cell.
 $a=3.86\text{ \AA}$, $b=11.65\text{ \AA}$, $c=13.24\text{ \AA}$, $\beta=95^{\circ}35'$.

J.Trotter, *Acta Cryst.* (1959) 12, 884



It is observed longer distances N-N, thus there are no chain structures in this crystal.

FIGURE I-8

Chain structures in Nitrobenzene 3-D representation

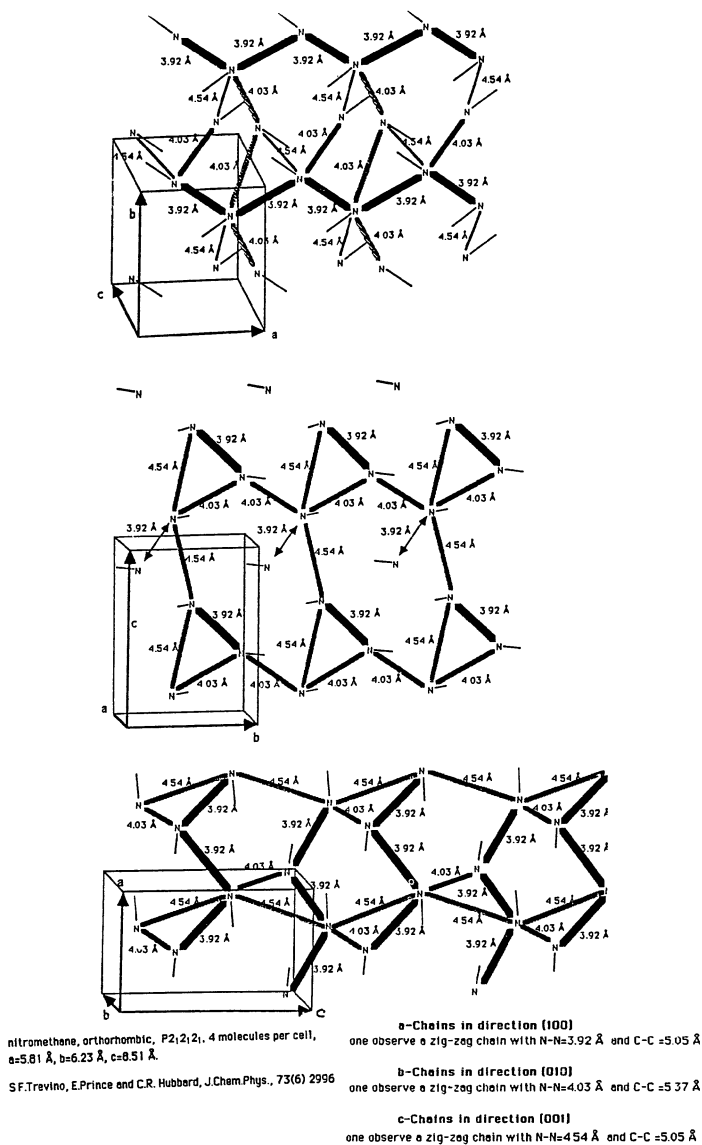


FIGURE I-9

Chain structures in Nitromethane

a) (100)

b) (010)

c) (001)

dynamics of shocked non linear systems (Fermi, Pasta, Ulam,... Ford, Zabuski and Kruskal...Toda then, Walker, Wasley, and Karo, Hardy,...). This interface subject, chemistry, physics, may be reduced to three questions:

I- Can we systematically find an electronic state of a privileged chemical bond in these explosive molecules capable of dissociating more or less easily with more or less exothermic energy?

II- If so, how may such a state be shock populated if it is not the ground state, by which energy transfer mechanism between shock, crystal lattice and molecule?

III- Once this state is populated, which collective phenomenon is at the origin of the explosive reaction?

Points I and III involve the shock induced detonation wave **propagation** point II concerns **initiation**, and our next lecture concerns only **propagation**

Initiation is a topic studied by Cherville and Delpuech and Dufort in France, by Zerilli and Toton, Walker and Karo, Coffey and Bardo.... in USA; **propagation** has been and is currently studied by Manvi and Duvall and Lowel, Tasi, Tsai and Bekett and Trevino and Mac Donald, Lambrakos and Oran and Boris, Holian and Straub, Batteh and Powell, Karo and Hardy and Walker....., in USA; Dremin and Klimenko in URSS.

We have chosen to restrict our study to propagation by modelling of a crystal like **nitromethane**. This choice of this compound was determined by interest in the diversity of behaviors as regards detonations (e.g. in the liquid vs. solid phases; sensitivity modified by some traces of additives), and the richness of experimental other physical and chemical data as well as the simplicity of the chemical formula which allow both, the interpretation of experiment and the accuracy of the calculations of the electronic structure in the different electronic states... A body of conditions which gives a heuristic character to this compound and, consequently, an opening to new ideas.

PART II

MOLECULAR DYNAMICS MODELS FOR DETONATION WAVE PROPAGATION INTRINSIC INSTABILITY OF ENERGETIC CRYSTALS

A great deal of theoretical work has been done in the area of detonation physics mainly by macroscopic-fluid-dynamics approaches and thermodynamic techniques. They allow with experimental data to depict precisely the structure of a detonation wave front as well as its coherence and instability.

The view of a shock wave taking a walk in molecular crystals

In a solid, the intermolecular interactions that play a large role in shock-wave propagation are coherent. Thus, in solids, strong coherent nonlinear excitations can exist and several molecular-dynamics studies of shock waves in solids have shown the importance of such nonlinear excitations in the coherence of the structure of the shock. Because of the large atomic displacements which occur in detonations in solids, coherent excitations play an important role in the structure of the detonation waves. The shock front is narrow on an atomic scale, about some intermolecular lengths, as we know from recent measures in condensed phase and thermal equilibrium does not occur in a large domain behind the shock front. At this level, an approach seeing the molecular crystal as a continuous matter is inadequate and a microscopic: molecular, crystalline, approach is necessary.

A detailed molecular interpretation for the propagation of detonations in energetic crystals is then proposed and discussed at three approximation levels: 1-D, 2-D, 3-D.

1. 1-D Model (1)

1.1.THE MODEL

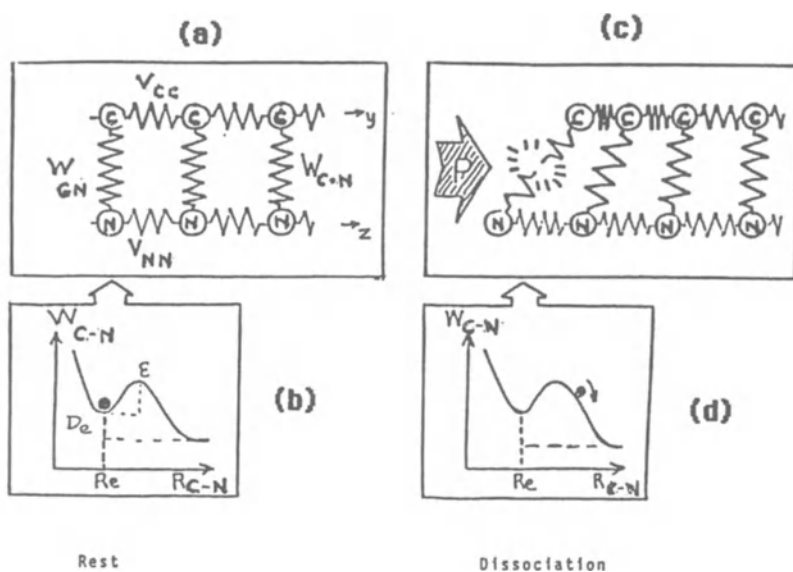
This model is based on three hypotheses:

1- the molecule is broken along a privileged C-N bond (C, N may be atoms or group of atoms like H_3C and NO_2 in nitromethane molecule H_3C-NO_2) in an excited electronic predissociative exothermic state: "active state" described by an intramolecular W_{CN} potential (fig.1b), fitted as the difference of two Morse type potentials:

$$W_{CN}(y_n - z_n) = D_1(e^{-K_1(y_n - z_n)} - 1) - D_2(e^{-K_2(y_n - z_n)} - 1) \text{ with } D_2 > D_1 \text{ and } K_2 < K_1.$$

2- the molecules C-N in the crystal are bonded in asymmetric chains along C.... C.... C... and N.... N.... N.... by intermolecular Morse type potentials:

i.e., $V_{CC}(y_{n+1} - y_n) = D_C(e^{-K_C(y_{n+1} - y_n)} - 1)^2$ where D_C and K_C are, respectively, the



Monodimensional Model. P : Shock wave; $\text{H}_3\text{C} - \text{N}_2$: $(\text{C}-\text{N})$; \bullet : the molecule
 E correlated to detonation threshold : P .
 D_e correlated to detonation velocity.
 These two parameters are independent.

FIGURE II-1

1-D model

dissociation energy of the bond and its anharmonicity coefficient.

3- this lattice (fig 1a), initially at rest, has fixed boundary conditions on one end, while a mechanical shock is applied to the other end as a constant force F applied to the first C_1 and N_1 particles during a time t_1 ; then this end of the chain is left free for t greater than t_1 . The impulse $P = F \cdot t_1$ is the intensity of this initial excitation.

To study a shock induced detonation in this model, one determines the response of the system to the mechanical shock. The main questions that we want to answer are the following:

- how does this dissociation propagate as a detonation wave in the lattice?
- how can we relate the results to experiments at a macroscopic level?
- finally, what is the dependence of the detonation on molecular and crystalline parameters?

The equations of motions are obtained easily, see table 1, where f is a unique function, derivative of the Morse potentials which expresses all of the coupling intra and inter potentials. Its general expression is the following:

$$f(x) = \delta V(x) / \delta x = -2KD(e^{-Kx} - 1) e^{-Kx} \text{ with the appropriate } K \text{ and } D \text{ values.}$$

The impulse P on the first molecule will push it. C is supposed to be less massive than N and because $C...C...$ is a much less rigid chain than $N...N...$, C will be displaced and the $C-N$ bond will increase in length to the point of rupture, see fig. 1c, in the repulsive part of the intramolecular potential, fig. 1d. The exothermic dissociation energy ($D_2 - D_1$), will be transferred to the next molecule via the intermolecular potentials, converted into kinetic energy: **We call the detonation wave this transmission of dissociation along the lattice**; the dissociation process is accelerated to infinity in such a simple model where no dissipative energy is implicitly included. Thus, in order to produce a steady state, a damping term proportional to the velocity with a γ empirical coefficient is explicitly introduced; it will be adjusted to the detonation velocity and we must always remember that **such a model is nothing more than a certain way of thinking**, namely,

- as regards the nature of a detonation wave propagation
- as concerns the relevant molecular and crystalline parameters included in the model
- on how these parameters may be correlated with the experimental data.

The set of coupled non linear equations cannot be solved analytically in the current state of knowledge of non linear equations. They have to be solved numerically. A lattice of 450 $C-N$ molecules has been considered. Since the lattice spacing does not appear explicitly in the equations, the velocity of the excitations propagating along the lattice are expressed in unit cells per time units, 10^{-14} s.

1.2. 1-D RESULTS

1- Depending on the values of P , a dissociation threshold P_1 and a detonation threshold P_2 will appear to exist. (fig. 2)

Between P_1 and P_2 after some chemical dissociations, the propagation of breaking of the $N-C$ bonds dies alone. *It has been currently observed that under shock some*

$$m_A \frac{d^2 y_n}{dt^2} = f_A(y_{n+1} - y_n) - f_A(y_n - y_{n-1})$$

$$- \gamma_1 (y_n - z_n) + \gamma_2 (y_n - z_n)$$

$$- \gamma \frac{dy_n}{dt}$$

$$m_B \frac{d^2 z_n}{dt^2} = f_B(z_{n+1} - z_n) - f_B(z_n - z_{n-1})$$

$$+ \gamma_1 (y_n - z_n) - \gamma_2 (y_n - z_n)$$

$$- \gamma \frac{dz_n}{dt}$$

avec : $f(x) = -2KD (e^{-kx} - 1) e^{-kx}$

γ empirical parameter Energy dissipation

TABLE II-1

2-D Equations

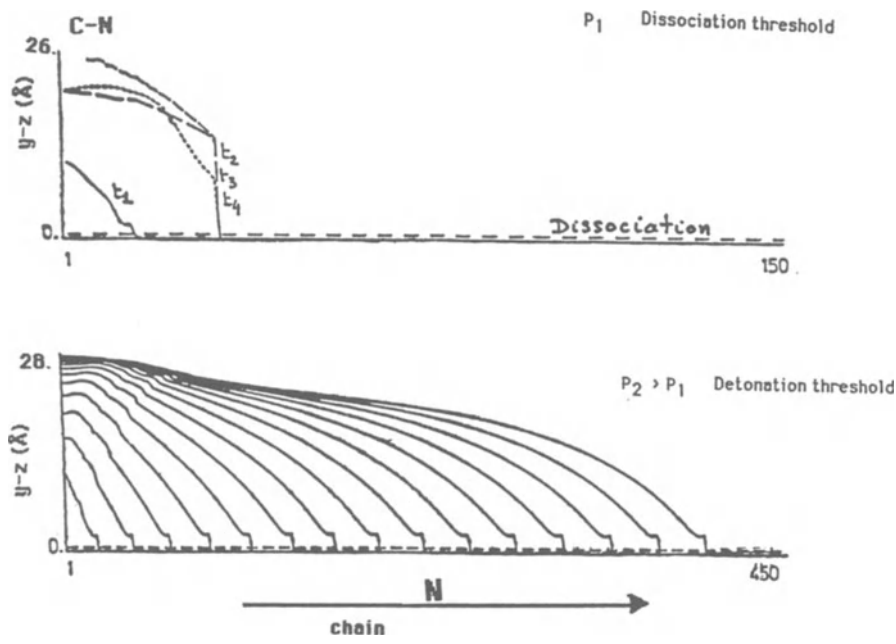


FIGURE II-2

Detonation wave propagation

smoke may appear and disappear.

For P values above P_2 , the detonation wave keeps on propagating along the lattice and reaches a steady state, with a limit velocity value independent of the P excitation values but it must be ,

$$P > \text{or} = P_2.$$

Note that if P is much larger than P_2 , the same limit velocity is reached by decreasing values. (fig.3)

This existence of a detonation threshold correlated with the intrinsic sensitivity of the explosive, the establishment of a steady state detonation, the independence of the velocity with shock intensity are well known experimentally.

2- In the absence of any energy loss, dissipation energy process, the speed of the wave front increases more and more and no steady state can be reached. But due to the damping term, γ , the chemical dissociation energy is balanced by an energy loss included in γ . Every detonation phenomenon seems to be understood with such an energetic balance. Later we shall show that it is not sufficient. Within inter and intra molecular potential models of nitromethane crystal, it is easy to fit γ to some reasonable values of the detonation velocity. It has been shown that γ is a very important parameter and that a very small variation of γ gives a large variation of the velocity.

It seems very important to study accurately energy dissipation, its origins, and their respective effects on the phenomenon. This will be done in the next 2-D models.

3- The role of the intramolecular bond potential (fig. 4) is crucial, and two parameters characterize it, 1- the potential barrier height ϵ to dissociate the molecule, 2- the dissociation energy D_e ; *the first one is shown to be correlated with the threshold detonation, the sensitivity of the material, the second with the velocity, once the value of γ has been fixed.* It is interesting to note that ϵ and D_e are two independent parameters in the description of the potential that means a certain independence of the two detononic parameters: velocity and sensitivity, *and the difficulty of finding some detononic characteristics mixing both together*

4- In order to propagate a detonation through the lattice, it is necessary that the N chain acts as a semirigid support for the repulsive force; this is the case if the mass ratio m_N / m_C is larger than one (remember that C and N may be "atom groups") or (and) if the N....N.... bond is stronger than the C....C... bond. Numerical results show that, contrasting with γ and D_e , the masses or the coupling coefficients along C or N chains play little role in determining the final velocity. The values of the intermolecular potential are not important as long as they are **large enough** to transmit energy from one molecule to the other one and that the rigidity of the N chain in consideration of the C chain is sufficient.

In conclusion, the numerical simulations performed for various parameters of the model allow us to point out some microscopic conditions which are required in a real solid to have a material which can explode according to the proposed mechanism: the

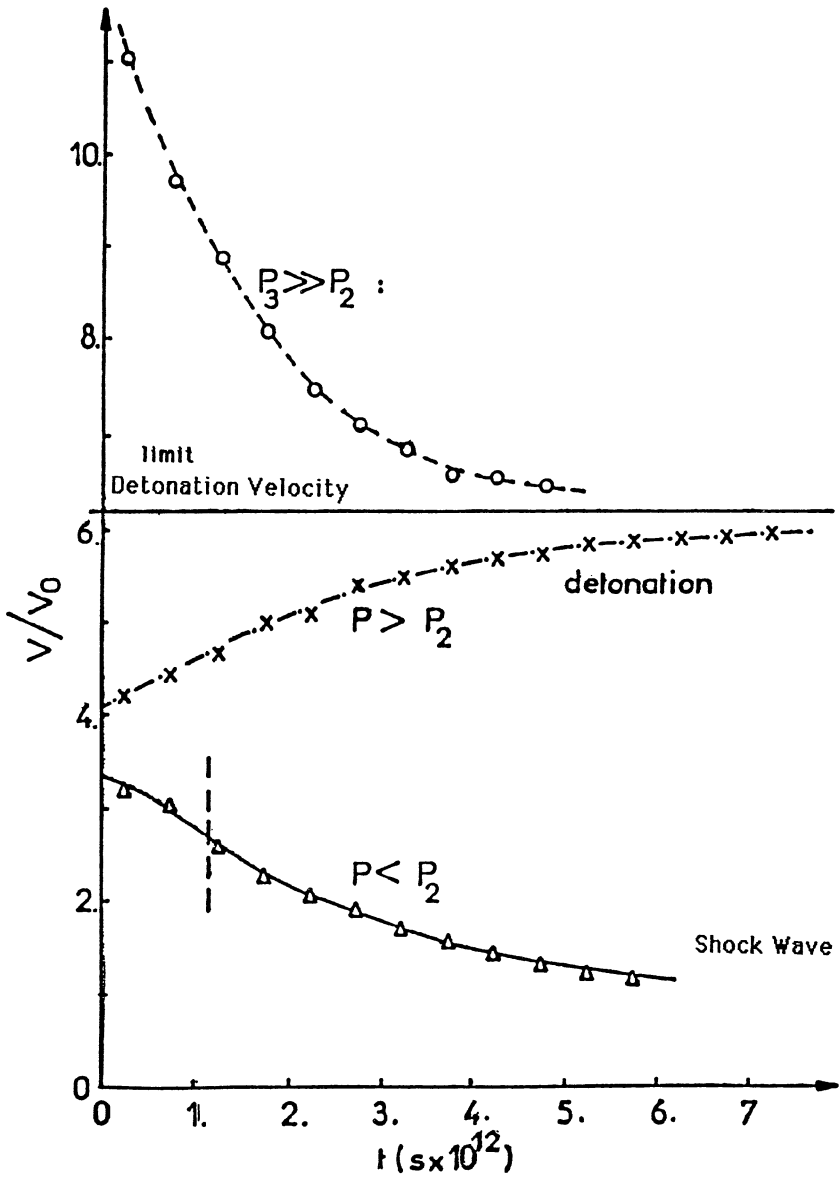


FIGURE II-3

Limit detonation velocity

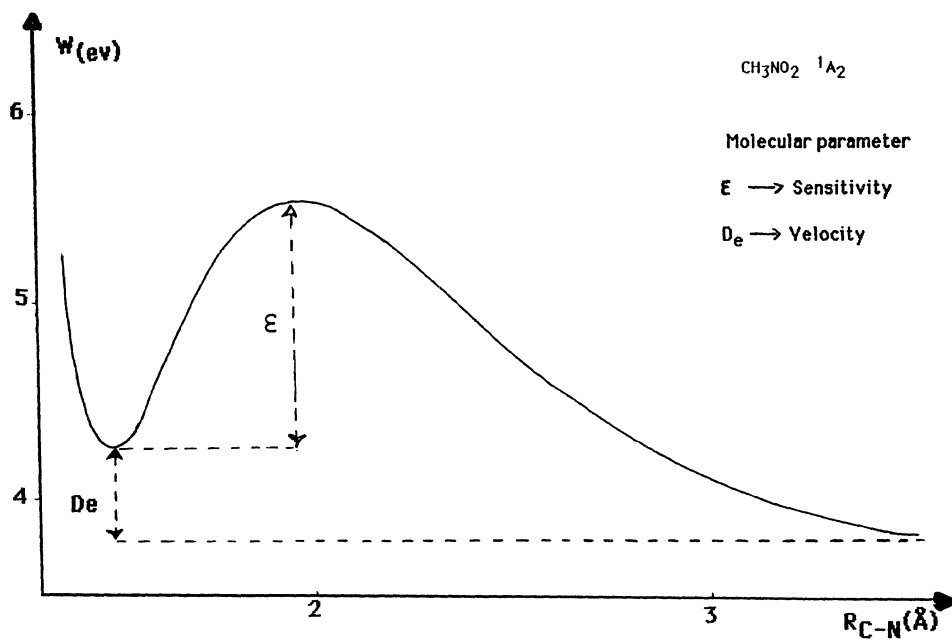


FIGURE II-4

Intramolecular potential - CH₃NO₂ ¹A₂

existence of an intramolecular bond with a predissociative exothermic potential is indeed an essential feature in a model where other sources of energy do not appear, but it is not sufficient. The two parts of the molecule connected with this predissociative potential

must also be coupled to the corresponding parts of neighbouring molecules to form paths along which a large amplitude mechanical wave can propagate and induce dissociation on the next molecules. These two paths so formed must be largely unequivalent, i.e., one of the two is rather "soft" whereas the second one is "hard". This can be achieved both by variation of the masses of the groups involved or by variation of the strength of the bonds which connect them.

Although 1-D model is restricted to one spatial dimension, it can explain several important features of detonations in energetic compounds:

- 1- The detonation speed is characteristic of the material and not of the initial excitation.
- 2- There are two unequal dissociation and detonation thresholds
- 3- The relative independence of the sensitivity to shock and the detonation velocity of the material.

Finally it invites us to take care of **dissipation** and its origin. A quantum mechanical study of the dissociation of nitromethane molecule in the "active" excited electronic state 1A_2 indicated that 96% of the dissociation energy is transferred as kinetic energy in the dissociation fragments, while only 6% is taken away by vibrations and rotations. Consequently, no dissipation energy due to internal molecular motions will be considered in detonation models here.

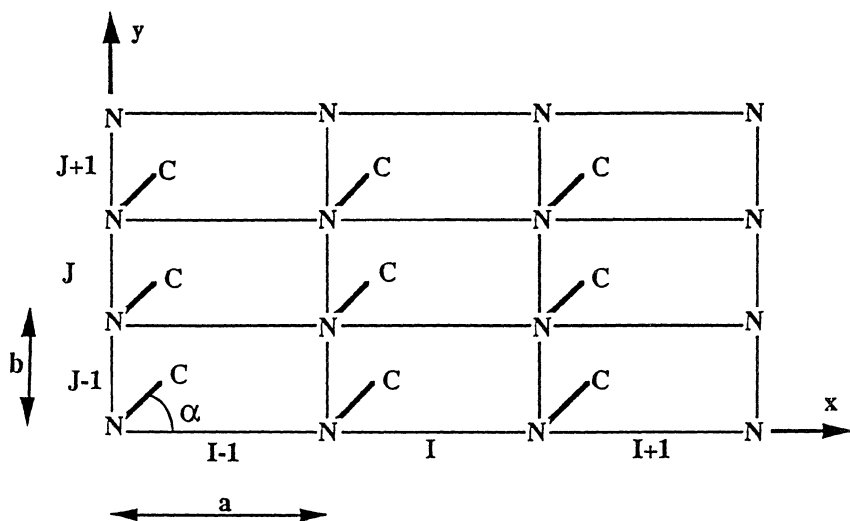
2. Dissipation Energy 2-D Model (2,3)

2.1. 2-D MODEL

The 1-D model could not describe the energy transferred from the longitudinal compressive shock wave into transverse motions.

In order to study the problem of the dissipation energy involved in transverse motions and to determine the microscopic conditions that a solid must have in order to sustain a detonation, the previous microscopic study of shock-induced detonations is extended to include both longitudinal and transverse motions.

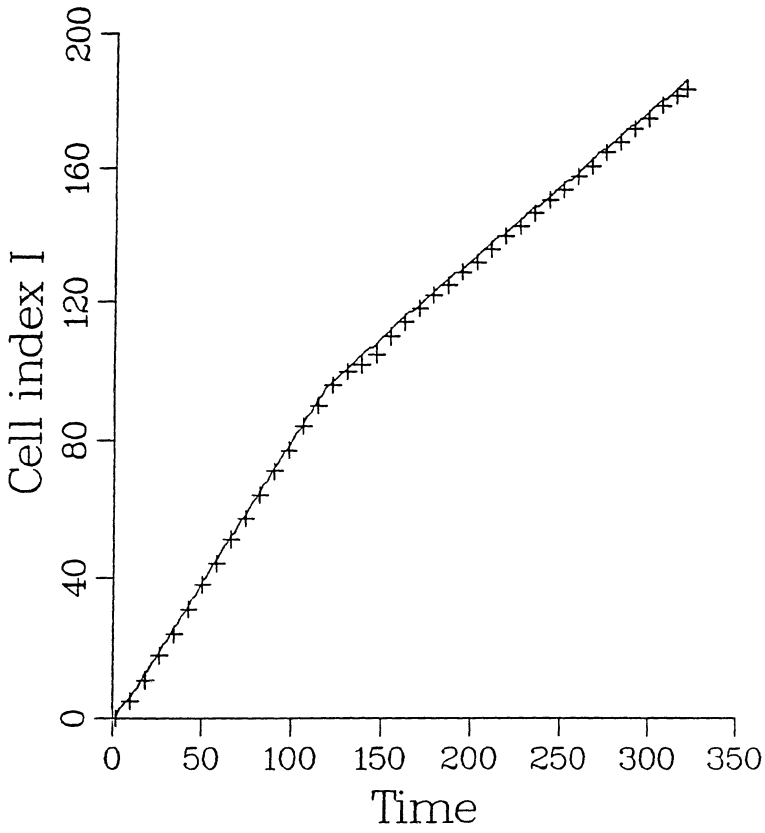
The structure of the model lattice is schematically shown in fig.5. It consists of an array of the two-component molecules, N-C. The previous conditions on masses and chains: "soft" and "hard" remain the same. The detonation propagates along the X axis. The mode of excitation is the same as previously. The parameters which characterize the lattice are the dimensions a and b of the unit cell of the model along the X and Y axes, the equilibrium length d_{NC} of the N-C bond, and the angle α between the N-C molecule and the X axis. Forces acting on an atom are computed by atom-atom potential pairs, and by considering all other atoms within a given distance. P. Maffre shows us in a poster the model and the manner of computing on a lattice with about $N_y=20$ molecules in the transverse Y array with cyclic boundary conditions and $N_x=48$ to 128 molecules, inside a window which moves like the shock front in the X direction and allows us to follow the detonation propagation on several hundred cells. He will also give a new more realistic model to take account of the atoms moving far from their original cells by shock.



bidimensional model: basic lattice
 x : shock wave propagation

FIGURE II-5

2-D model



Position of the shock front (solid line) and of the last bond broken (crosses) as a function of time when a detonation propagates in the two-dimensional lattice at zero initial temperature

FIGURE II-6

Position of the shock front

2.2. 2-D RESULTS

Fig.6 shows the position of the shock front (solid line) and of the last intramolecular C-N bond broken (crosses) which defines the detonation front as a function of time at zero initial temperature. Note that dissociation follows the shock front with very little delay; the distance between the front and the most recently broken bond is only 2 or 4 cells. Two coherent propagation regimes with different speeds appear. The high speed regime corresponds to the propagation of almost purely longitudinal motions; a compression in the N sublattice, a rarefaction wave in the C one. These two motions stretch the N-C bond till rupture, the atomic motions in this regime are very regular, all the atoms in the same column of cells orthogonal to the X axis have exactly the same motion and the detonation wave propagates in the X direction as a plane wave. The regime is perfectly coherent and the detonation speed depends on the energy of the initial shock but *this result is contrary to both the experiments and macroscopic fluid model results*; consequently this perfect coherent regime does not interpret real systems.

The structure of the detonation wave which propagates in the lower-speed regime is much less regular than the previous one. Because the N-C molecular bond is oblique with respect to the direction of the detonation propagation, the repulsive forces between the 2 components N, C, are oblique and lead to transverse motions in addition to longitudinal motions (compression and rarefaction). A significant part of the dissociation energy is thus transferred into transverse motions that do not contribute to motions in the direction of propagation and it can be understood by this simple analysis how the obliquity of the CN bond will play an important role in detonation inside a molecular crystal. Rupture between the two regimes, high and low speed, corresponds to the appearance of these transverse motions. The coherence is not destroyed in the low speed-regime where it has been shown *that its detonation speed is independent of the initial intensity excitation as expected* (the transition regime does exist but cannot be seen experimentally, of course.) Later, some simulations have shown that this coherence is not destroyed at high initial temperatures.

The 1-D model results remain the same in the 2-D model which justifies some of its principle; e.g. fig.7 studies the variation of the detonation speed as a function of the energy released when an N-C bond breaks; the speed increases with the amount of energy released by dissociation, thus the 2-D result shows that the simple hypothesis of a dissipation energy proportional to velocity, introduced in 1-D model gives a reasonably accurate picture of the energy transferred into transverse motions.

But, evidently, more is learnt about the crystalline parameter effects on detonations.

1- Fig.8 gives the variation of the detonation threshold as a function of the angle α of the N-C bond fixed in the crystal with the X axis of the shock wave propagation; note that this angle will vary with the molecular crystal face attacked by the shock and will describe *the anisotropy of the detonation*, if necessary. While variation of α is not too important when $> 90^\circ$, reducing it below 90° drastically increases the detonation threshold; no stable detonation has been observed under 30° . For this value, very large transverse motions appear to absorb too much energy, the detonation dies without reaching the stable state. With that in mind, an analysis of the crystalline chain structure in a monocrystal of pentrite may explain *the observed experimental velocity anisotropy in this crystal*: (fig 9, 9'; fig. 10, 10' and table 2)

In nitromethane crystal, with four molecules per unit cell, we have noted the appearance of zig zag chains (fig. I-9) which could prevent detonation. Numerical

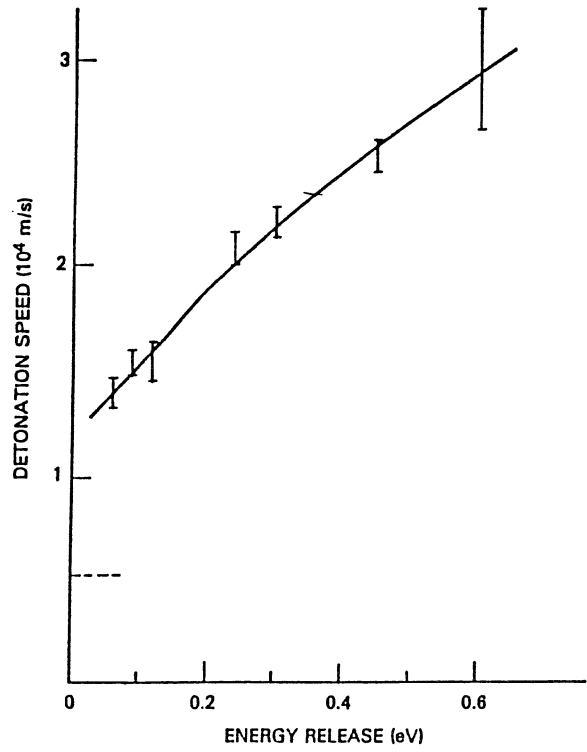
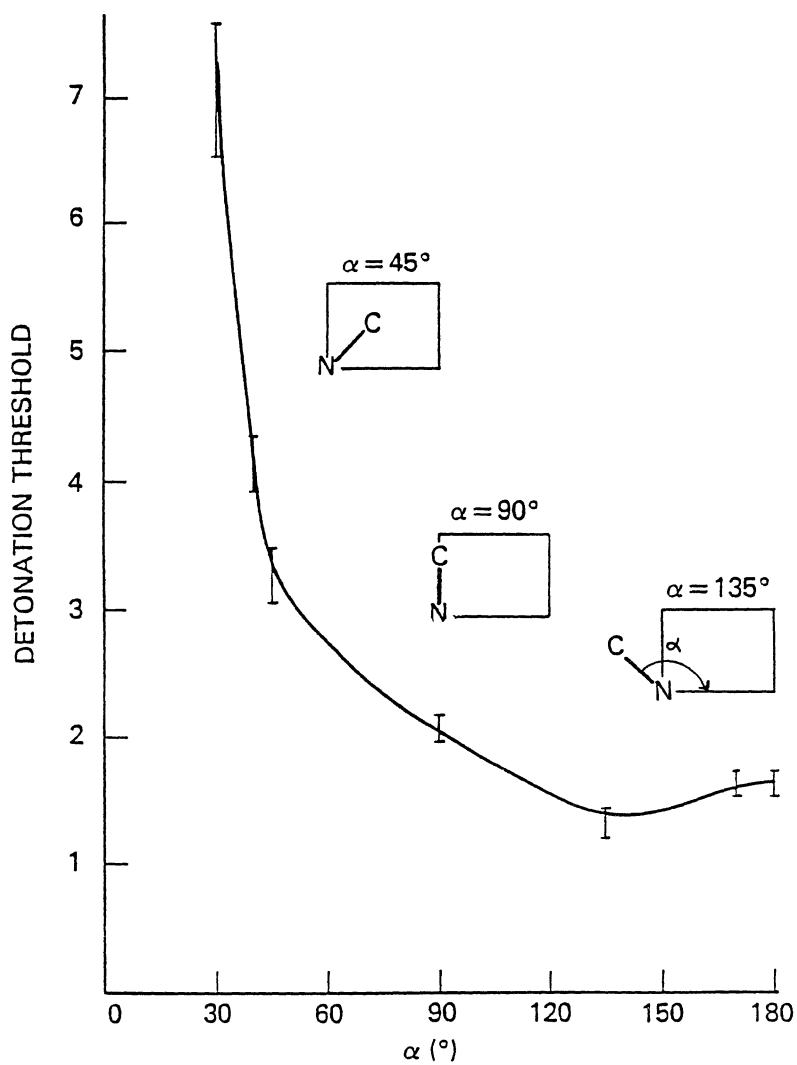
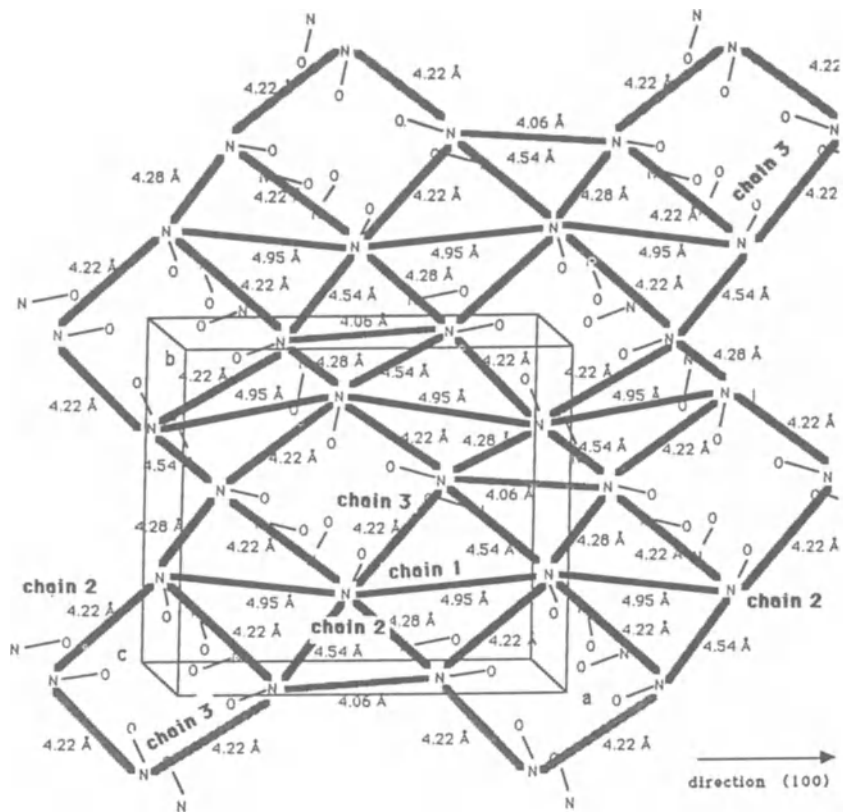


FIGURE II-7

Detonation speed vs energy release

**FIGURE II-8**

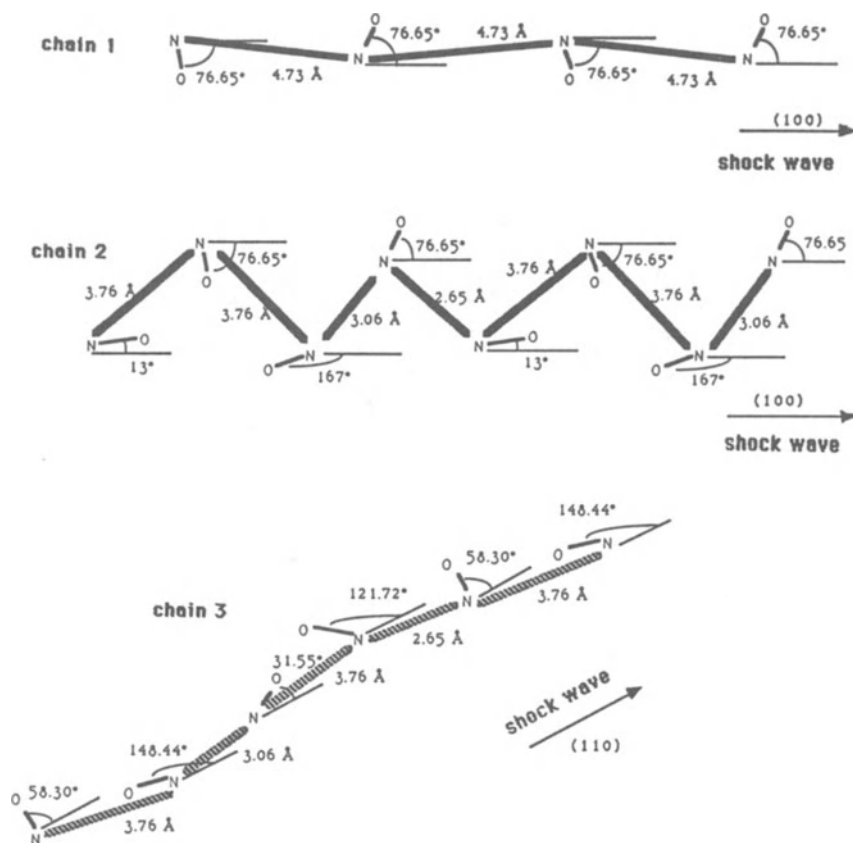
Detonation threshold vs α angle between N-C bond and the X axis



We observe in the (100) direction :
a chain with N-N=4.95 Å chain 1
a zig-zag chain with N-N=4.22 Å+4.22 Å+4.54 Å+4.28 Å chain 2

We observe in the (110) direction :
a chain with N-N=4.22 Å+4.54 Å+4.22 Å+4.28 Å chain 3

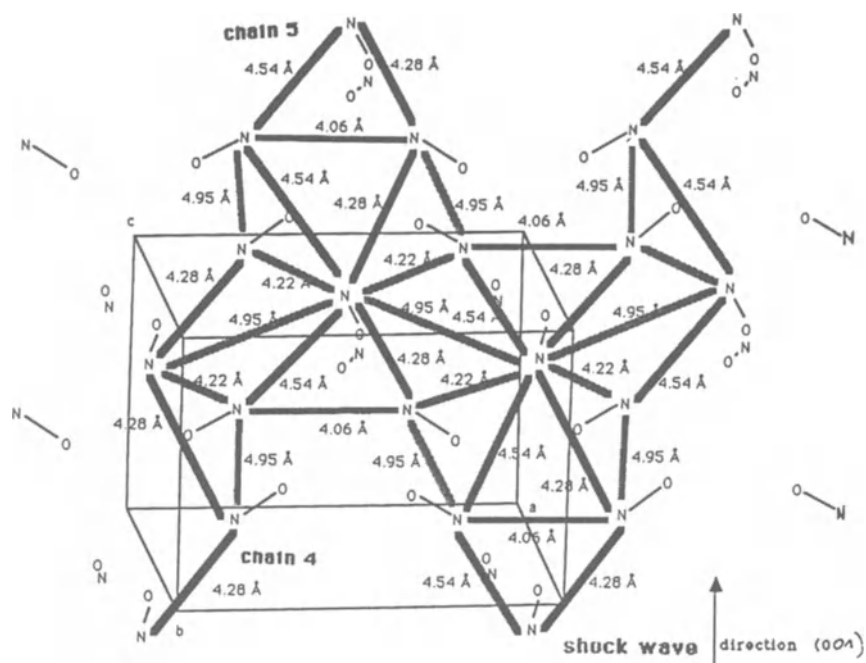
FIGURE II-9
(100) Chain structure in Pentrite



the (110) direction is more favourable to a detonation wave than the (100) direction
(see α angles and (or) N-N lengths)

FIGURE II-9'

(100) and (110) : 2-D (a,b) Projection chain structure in Pentrite

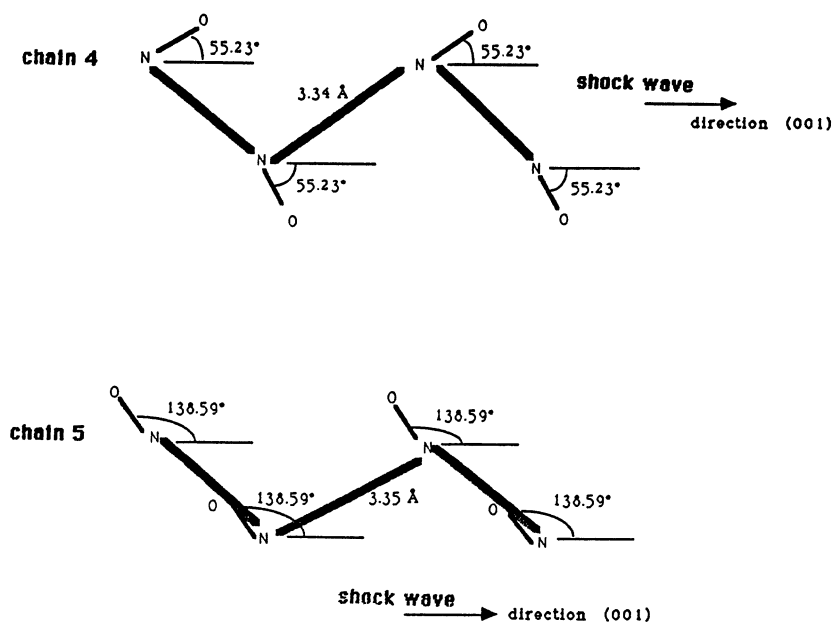


We observe in the (001) direction :
 a zig-zag chain with N-N=4.28 Å
 a zig-zag chain with N-N=4.54 Å

chain 4
 chain 5

FIGURE II-10

(001) Chain structure in Pentrite



the (001) direction is favourable to a detonation wave

(see \angle angles and N-N lengths)

FIGURE II-10'

(001) : 2-D (b-a,c) Projection chain structure in Pentrite

direction	Samirant exp.	Dick exp.	Rudel chain structure
(100)	(oui ?)	non	non favorable
(110)	---	oui	favorable
(001)	oui	oui	favorable
(101)	---	non	non
(111)	oui	---	---

TABLE II-2

Detonation anisotropy in a mono crystal of Pentrite

simulations on (\vec{a}, \vec{b}) plane projection with a more realistic chain structure of nitromethane crystal, i.e. (fig. 11), with 2 molecules in the lattice, are indeed not able to give stable detonation whatever the initial excitation intensity is. However, (fig. 11'a, 11' b), show in direction \vec{a} (100) or \vec{b} (010) a non rigid architecture of the lattice atoms which can easily raise transverse motions. Thus, by dissipating too much energy, these intermolecular environments may be another cause of preventing detonation propagation than zig zag chains. In fig. 11'c, we can see that the "architecture" is rigid and prevents energy from dissipating in transversal atomic motions; because a same chain zig zag pattern occurs we have to do a numerical simulation in the \vec{c} direction (001) in (\vec{a}, \vec{c}) plane in order to know if crystalline nitromethane does explode or does not.

Till now no shock induced detonation has been experimentally obtained in solid nitromethane.

2- In fig.12, the increase of the detonation speed with the ratio a/b of the cell parameters, when a/b is > 1.2 emphasizes the role of crystal symmetry in determining whether a solid can sustain a detonation: if this ratio is < 1.2 , no stable detonation can be found, the first coherent state is obtained, but when transverse motions appear, they dissipate too much energy (Note that a, b are the basic lattice parameters of fig.5 and do not have the same signification as $\vec{a}, \vec{b}, \vec{c}$ unit vectors of the unit cell in the real crystal lattice).

3- Detonation wave structure : We define 4 zones in the detonation.

zone a: a very narrow *shock front* (about 2 - 5 intermolecular lengths) followed by

zone b: *an induction zone* where shocked molecules are not yet dissociated, then,

zone c: *a reaction zone* where dissociations are produced, followed by,

zone d: *a chemical zone* where dissociated products react.

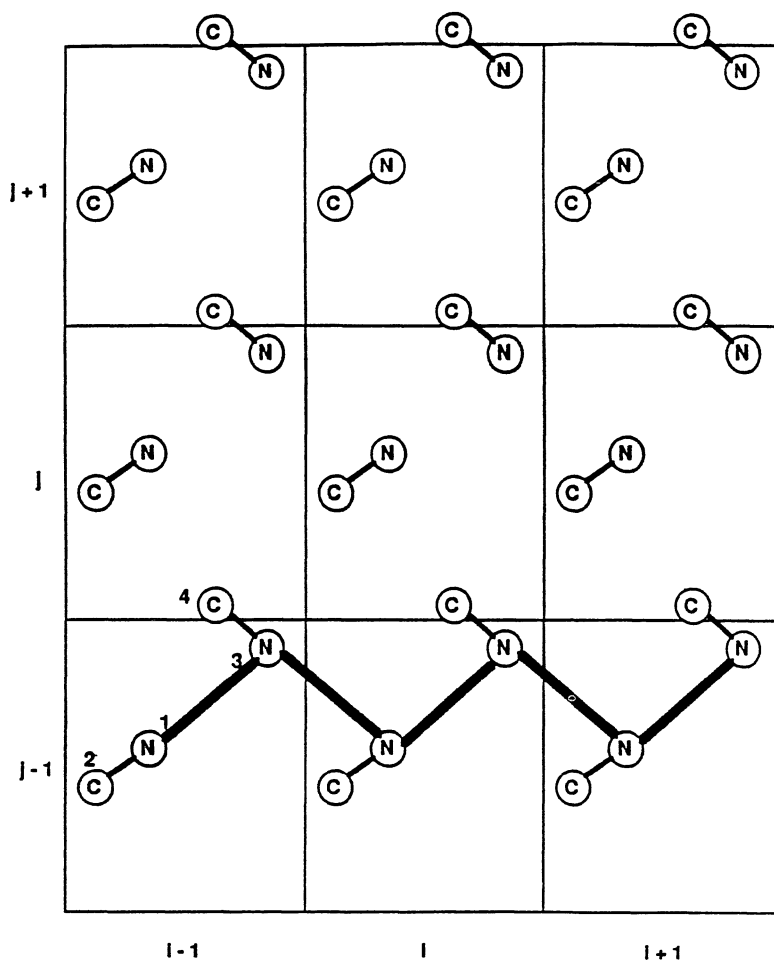
The detonation propagates through the lattice as coherent excitation which keeps its form when the steady state is reached. However, experiments show that very often in fluid phases, a plane detonation wave is instable. Some transverse waves appear and their intersections with main longitudinal wave give triple points and then a complex detonation cell structure appears. Some observations have also been done in solid phase with microscopic lengths. Numerical simulations agree with the fact that the detonation wave does not always behave as a plane wave, perpendicular to its propagation direction, and that the formation of transverse waves depends on the crystalline geometry and specially on the asymmetry of interatomic bonds (fig. 13), as can be obtained in the case of intermolecular hydrogen bonds in many energetic compounds.

Doesn't this demonstrate the first microscopic origin of cellular detonation structure?...

3. Chemical Energy 2-D Model ⁽³⁾

3.1. CHEMICAL MODEL

In the chemical zone, in the gas phase behind the reaction zone some chemistry occurs



Nitromethane type lattice
 -Projection on (a,b) plane shortest chain bonds N-N

FIGURE II-11

2-D Nitromethane type lattice $((a,b)$ plane)

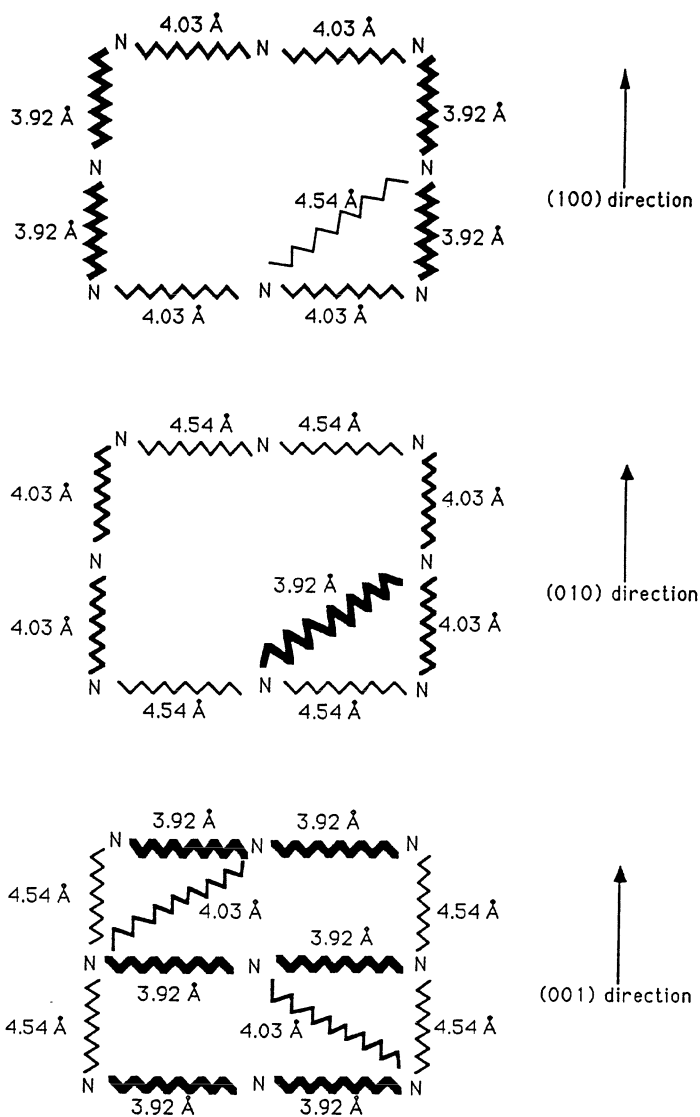


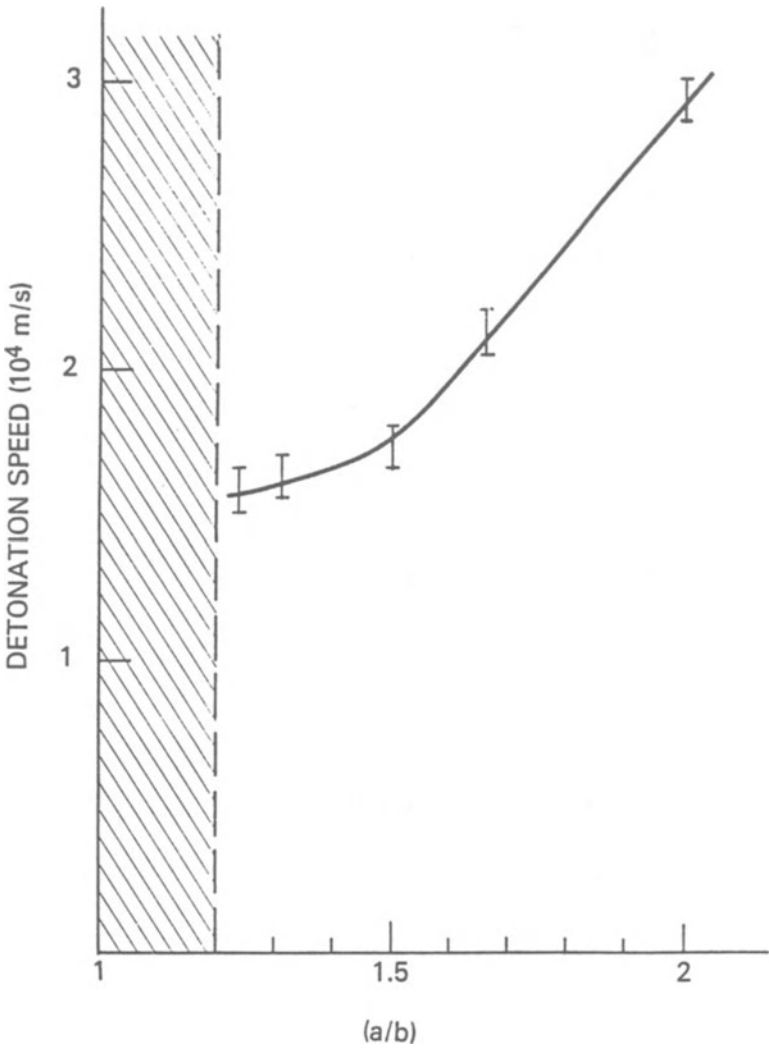
FIGURE II-11'

Intermolecular bond architecture in Nitromethane

(100)

(010)

(001)



Variation of the detonation speed as a function of the ratio a/b of the 2D basic lattice (fig.II 5). No stable detonation has been found when $a/b < 1.2$ (shaded area).

FIGURE II-12

Detonation speed vs a/b ratio of the 2-D basic lattice

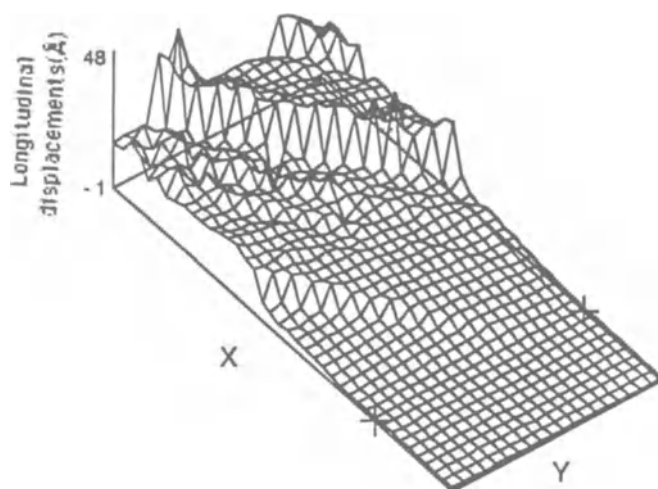


FIGURE II-13

Detonation in an asymmetric intramolecular environment

with exothermic and endothermic elementary reactions. In a simple energetic balance they may bring more energy to the system than the only one which has been considered, i.e. dissociation intramolecular bond energy. It is difficult to take account of this complex chemistry in these numerical simulation experiments.

However it seems possible to ask the following question, *what is the relative effect on detonations of a same amount of dissociation and chemical energy transfers which occur in two different locations, one in the reaction zone very near the solid phase inductive zone, and the other in the chemical zone, much farther from the detonation front in the gas phase, depending on the chemical reaction time, in other words on the kinetics?* **Could a simple energetic balance determine the detononic phenomenon?**

In order to examine this point, the exothermic reactions between the fragments are very simply described by a mean power q , given to one fragment N or C. q for a given material depends on the energy released by each elementary reaction and on their number per unit time that is to say on kinetics, once more. q will be a parameter in the dynamic model. It is used to raise the kinetic energy of the fragments in the reaction zone, after a delay time following the dissociation in order to take care of an induction time in the exothermic reactions. Once the process has started on a particular fragment, it is maintained during the time t_f it remains inside the calculation window.

The mean energy Q given per molecule is: $Q = 2q \cdot t_f$ (2 means that there are two fragments N and C supposed with a same q value).

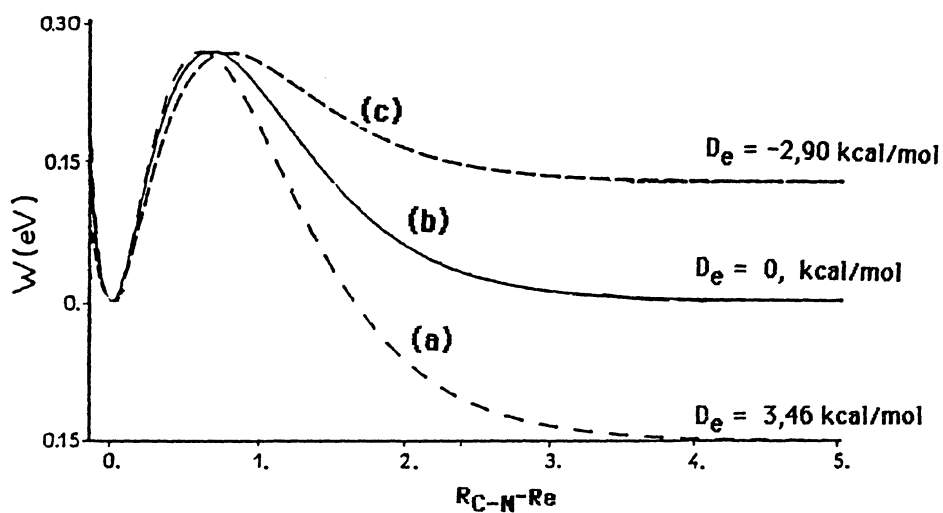
3.2. RESULTS

In order to study the relative effect of the two energy transfers, dissociation and elementary chemistry, on detonation velocity, we report the variations of the velocity vs. q for three potentials: (a) exothermic: $D_e = 3.46 \text{ kcal/mole}$, (b) neutral: $D_e = 0$, (c) endothermic: $D_e = -2.90 \text{ kcal/mole}$ (fig. 14).

The velocity increases with q (fig. 15). For a given q value, i.e. $= 0.1 \text{ eV/u.t.}$ ($Q = 59 \text{ kcal/mole}$), the velocity increases 1000 m/s if D_e varies from 0 (potential (b)) to $+3.46 \text{ kcal/mole}$ (potential (a)). To obtain a same velocity variation, keeping $D_e = 0$ for instance, it is necessary to raise Q from 59 to 90 kcal/mole . Thus, a variation of **3.45 kcal/mole** in dissociation energy near the detonation front is equivalent for the detonation velocity to a chemical reaction variation of **30 kcal/mole** far the detonation front. For greater q values it can be seen on the figure that the relative effect must be even more important. Now we have to pay attention to the accuracy of bond dissociation energy calculations. A little change in D_e will have a big effect on detonations.

In conclusion, an energetic balance is not sufficient to interpret detonation effects, *(detonation speeds measured in different materials vary in smaller proportions than the chemical energies released in these materials)*, but the manner, the location, how energy transfers occur, appear to play a very important role that, in particular, imply to study with attention the kinetics of elementary chemical reactions together with their exothermic or endothermic properties.

In a poster (dimer formation enthalpies), E. Vauthier will discuss the accuracy of the X_α method presented by S. Fliszar for the calculations of reaction enthalpies.

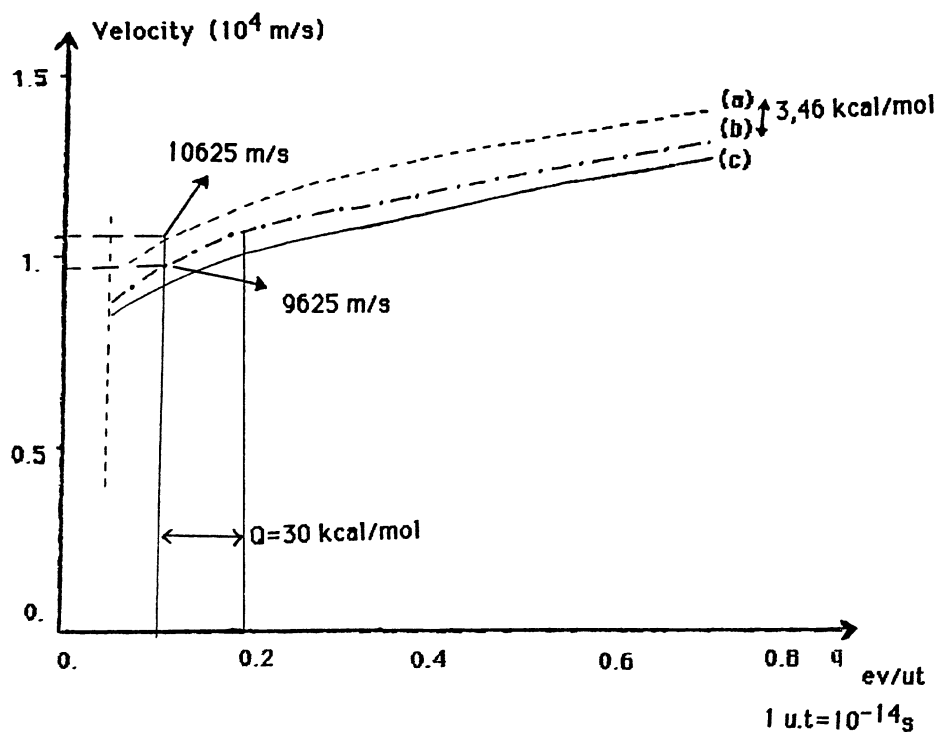


Different intramolecular predissociative Potentials

- a) exothermic
- b) neutral
- c) endothermic

FIGURE II-14

Intramolecular predissociative potentials



Detonation velocity against exothermic chemical reaction mean power q for different intramolecular potentials

(a) exothermic

(b) neutral

(c) endothermic

FIGURE II-15

Detonation velocity vs chemical mean power

4. Excitation Electronic Molecular Energy 3-D Model (4)

Recently, in a new simulation technique, a 3-D model has been proposed by S.Lambrakos and coll. and we just mention the originality introduced in it by the authors, especially at the intramolecular C-N bond level which is not described by an internal potential but which is supposed to be rigid as long as an energetic threshold is reached after an induction time necessary to induce the breaking of the bond and the release of the dissociation energy. Something like a quantum effect is thus introduced to take account of the initiation in the early phase of detonation i.e., an energy transfer from the shock on lattice crystal directly to the molecule. Through the induction time, the model allows the investigation of the effects of a characteristic response time of dissociative molecules to the shock. The intermolecular forces are treated in the conventional way. The results previously found in 1-D and 2-D models remain the same in 3-D (with evidently, more dissipation) so that we may think that they are model independent and could reflect some reality.

The authors note that in some cases, "the leading shock front can promote a transition from one crystal structure to another one "(....)" which is able to inhibit the detonation."

When the minimum delay for breaking the intramolecular bond increases, the wave detonation structure is qualitatively preserved but the induction zone increases and the velocity is affected. It is another piece of new information, *known in fluids from hydrodynamic simulations*.

The model of the intramolecular rigid bond excited and dissociated by quanta of energy, together with the new numerical simulation techniques, is full of promise.

5. Conclusions Perspectives

Perhaps a microscopic approach to detonations has provided some perception of the origins of the detonic phenomenon, of the factors which, on the microscopic scale, define the detonic characteristics of an energetic crystal, helping to pose the first basic data towards a microscopic detonation theory in the condensed phase. The next step is to extend this information to less rigid compounds and to liquids. Can we understand the difference between the liquid and solid state?

In analyzing each of the factors introduced in the simulation experiments, other simulation experiments can be done, not in order to supply real experiments, but to suggest a new one or an original interpretation of macroscopic effects. Moreover, a systematic study of relative chemical bond weaknesses in a compound, together with its elementary chemical reaction analysis submitted to **high pressure and temperature** and to the study of possible chain restructuration, may define its more or less detonic characteristics. Other information can be obtained in adding inhomogeneities in the crystal simulation experiments, see P.Maffre poster. It implies improving the dynamics models and, concurrently, not only the numerical simulation techniques but our accurate knowledge of molecule response to shock which implies exploring more the molecular electronic excited states in connection with modified environments of the molecule by microscopic picosecond spectroscopy, Resonance Raman UV spectroscopy and ab initio Quantum Mechanics calculations.

But other important things will be really understood in unexpected explosions if we study in such dissipative non linear systems, the effect, on a long time scale of a small perturbation on the molecular crystal, that is to say, *the view of the historian of the distant past*, in the numerical simulation "experiments", what does appear on detonation if some initial conditions change little, little...? the chaos, *the view of insatiable curiosity !!!*

It is really true that "the Science of Detonations" is a multidisciplinary one which implies all our joint efforts in fruitful international, interdisciplinary, sympathetic collaboration and frequent meetings like this one.

Many thanks to Dr. Bulusu, to NATO and to "La Sicile, un des hauts lieux de la civilisation"

Acknowledgments: We are grateful to Pascal Rudel for his original contribution in simple classification of explosive-non explosive compounds in terms of NO₂ density and in analysing the crystalline structure of energetic compounds in relation to their ability to detonate and velocity anisotropy.

- (1) M.Peyrard, S.Odiot, E.Lavenir. C.R. Acad. Sci. **199**, 917 (1984)
M.Peyrard, S.Odiot, E.Lavenir, J.M.Schnur. J. of Appl. Phys. **57**, 7 (1985)
- (2) M.Peyrard, S.Odiot, E.Oran, J.Boris, J.Schnur. Phys. Rev. B, **33**, 2350 (1986)
- (3) M.Peyrard, S.Odiot, M.Blain. J. Chim. Phys., **85**, 759 (1988)
- (4) S.G.Lambrakos, M.Peyrard, E.S.Oran, J.P.Boris. Phys. Rev. B **39**, 993, (1988)

ON THE $X\alpha$ LOCAL SPIN DENSITY APPROXIMATION IN THE STUDY OF ORGANIC MOLECULES

S. FLISZAR

Département de Chimie

Université de Montréal

C.P. 6128, Succ. A

Montréal (Qué.) Canada H3C 3J7

ABSTRACT. While the familiar wave function methods meet with considerable success in numerous applications to chemistry, they involve formidable computational demands in any evaluation of thermochemical data at a level approaching chemical accuracy. By far the most useful non-empirical alternatives to configuration interaction calculations are the methods rooted in density functional theory (DFT). Building on their success in applications to inorganic chemistry, we examine here the applicability of DFT to the "simpler" organic systems, with the hope of retrieving good-quality thermochemical information (atomization energies, enthalpies, and the like). Namely, we examine here the local spin density (LSD) approximation and treat exchange and correlation in the $X\alpha$ approach where α is a variable parameter. The tentative hypothesis is that the $X\alpha$ (LSD) method basically meets the required demands of accuracy, i.e., that the energy should be right, if α is properly selected. This is where the problem lies: ever since the appearance of the $X\alpha$ method, the way of selecting α has been a fundamental problem. On the basis of regularities which are observed for exchange-correlation energies, we develop a recipe permitting valid estimates of α . The at least approximate validity of this procedure is illustrated by the accuracy of calculated atomization energies, thus paving the way to accurate evaluations of dissociation energies. Examples include alkanes, alkyl radicals, amines and chloroalkanes, as well as weaker interactions (hydrogen bonds), showing that the theoretical results obtained in this approach are well within experimental accuracy. Bond dissociation energies in compounds N_xH_y were also investigated, with a direct application to the explosive decomposition of HN_3 .

Introduction

Important applications of quantum mechanical methods concern the thermochemistry accompanying chemical transformations $A + B + \dots \rightarrow \text{Products}$. On the laboratory scale, of course, the final results are a blend of energy changes pertaining *i*) to molecules at equilibrium (i.e., molecules in their hypothetical vibrationless state at 0 K) and *ii*) to contributions arising from vibrational, rotational and translational energies. The evaluation of the latter contributions – which requires, namely, calculation of the fundamental vibrational frequencies of both the reactants and the products – clearly represents a problem which should be treated in isolation. Here we concentrate on the equilibrium properties of molecules at 0 K.

The success of "good" SCF calculations (by this we mean conventional *ab initio* approaches using reasonably extended basis sets) largely depends on the type of chemistry which is investigated. Indeed, a great number of questions can be adequately

answered at the SCF level, e.g., those pertaining to conformational analysis, rotational barriers, and others, in essence because of important (though occasionally equivocal) error cancellations. As the demand for more sophisticated information grows, namely, for thermochemical information on the unforgiving scale set by taking atoms as reference marks (e.g., in form of the energies of the isolated atoms or, in an equivalent approach, in terms of their standard enthalpies of formation), the limitations of SCF methods become all too evident. A case in point concerns atomization energies

$$\Delta E_a^* = \sum_i E_i^{\text{atom}} - E \quad (1)$$

which measure by how much the ground-state energy of a molecule, E , differs from the sum of the individual ground-state energies of the atoms making up that molecule. Theoretical improvements are sought in configuration interaction (CI) calculations. These too have their limitations, however. A full CI calculation of pentane, for example, using the STO-3G minimal basis set, requires the construction of 10^{19} determinants. Although, admittedly, one is generally not asked to go to this extreme limit, at this point we face a serious problem of computer financing technology. Yet, the need for accurate thermochemical information persists.

By far the most useful non-empirical alternatives to configuration interaction calculations are the methods rooted in density functional theory (DFT)^{1,2}. Building on their success in numerous applications to inorganic chemistry³, an area where the familiar wave function methods rapidly sink under the burden of formidable computational demands, we examine here the applicability of DFT to the "simpler" organic systems, particularly to the study of their atomization energies, Eq. 1, keeping in mind that any presently known density functional approach involves approximations. The tests are meaningful in that they are conducted at a very demanding level, that approaching experimental accuracy. E is the target of our theoretical calculations. ΔE_a^* is convenient for comparisons with experimental results.

Outline of LCGTO-X α (LSD) Calculations

Here we use the local spin density (LSD) approximation⁴ and expand the molecular orbitals as a linear combination of gaussian type orbitals (LCGTO) for solving the LSD equations. The specific form of the latter depends on the treatment of exchange and correlation in electron-gas calculations. The X α approach yields the following exchange energy^{2,5}

$$E_{X\alpha} = - \frac{3}{4} \alpha \left(\frac{81}{8\pi} \right)^{1/3} \int \rho(1)^{4/3} dv_1 \quad (2)$$

where α is treated as a variable parameter. The LCGTO-X α (LSD) calculations^{6,7} were performed using the program developed by Dunlap, Connolly and Sabin⁷, with the help of reasonably extended basis sets^{8,11}. In this X α method it is necessary to fit the charge density and the exchange potentials to sets of auxiliary Hermite gaussian

functions. The $X\alpha$ exchange potentials were fitted to the auxiliary functions following the criterion given by Dunlap *et al.*⁷, i.e.,

$$\int \rho(\widetilde{\rho}^{1/3}) d\tau = \int (\rho^{1/3})^4 d\tau$$

where the tilde represents a fitted quantity. The sampling points for the exchange potentials were determined by taking each tenth point of the Herman-Skillman radial mesh¹² and an angular mesh consisting of the twelve vertices of a regular icosahedron¹³ – an approach which may require future attention. Two s -type bond-centered auxiliary functions were also used, as suggested by Dunlap *et al.*⁷.

So much for the method. Now we step in with applications to organic molecules with the hope of calculating their total energies with a reasonable degree of confidence. The tentative hypothesis is that the LCGTO- $X\alpha$ (LSD) method basically meets the required demands of accuracy. In other words, we assume that the energy should be right if the parameter α , Eq. 2, is properly selected. This is where the problem lies. Ever since the appearance of the $X\alpha$ method, the way of selecting α has been a fundamental problem. Here we focus attention on this particular topic.

The Selection of α

Slater's original treatment¹⁴ of the exchange potential amounts to taking $\alpha = 1$ but Gáspár⁵ and later Kohn and Sham² showed that $\alpha = 2/3$ is more appropriate. The more recent treatment of the exchange-correlation potential by Gáspár and Nagy¹⁵ represents a generalization of the Slater and Gáspár-Kohn-Sham approaches and contains those as special cases. The theoretical α 's deduced by Gáspár and Nagy are intermediate between $2/3$ and 1 . They offer a justification for the value $\alpha \approx 0.7$ advocated by Baerends and Ros¹⁶ for molecular calculations and bear some resemblance to our own results^{9,11}, $\alpha \approx 0.76$ - 0.78 . The familiar exchange parameters given by Schwarz¹⁷, e.g. 0.77725 for H and 0.75928 for C, obtained from an adjustment of the statistical total energies to the Hartree-Fock total energies of the isolated atoms, also fall in that range.

All this is fine, but for the calculation of accurate atomization energies "approximate" α values are clearly insufficient. The final value obtained for E , the energy of a molecule, strongly depends on α . Indeed, it follows from Eq. 2 that $\partial E/\partial \alpha = \partial E_{X\alpha}/\partial \alpha$ and

$$\partial E/\partial \alpha = E_{X\alpha}/\alpha \quad (3)$$

The $\partial E/\partial \alpha$ terms are large (between -8.87 and -100 au for the molecules considered here). In consequence, even a relatively minor error ($\Delta\alpha$) accompanying the selection of α results in a sizeable error, $\Delta\alpha(\partial E/\partial \alpha) = \Delta\alpha(E_{X\alpha}/\alpha)$, in the evaluation of E . For example, with $\partial E/\partial \alpha = -40$ au, an error of 0.001 in the estimate of α translates into a discrepancy of ~ 25 kcal mol⁻¹ and would put a stop to our hopes of doing thermochemistry using $X\alpha$ (LSD) calculations.

Though serious, the situation is not desperate. We examine first the α values which would duplicate the experimental energies, Eq. 1, and look for regularities, namely as regards exchange-correlation energies. These energies are implicitly treated in one lump, in a brute-force approach, although alternate ways of effectively incorporating correlation in LSD exist¹⁸. Second, we examine the possibility of constructing these α 's in a simple manner on the basis of structural features. Finally, taking advantage of regularities which are, indeed, observed for exchange-correlation energies, we develop a recipe permitting valid estimates of α and, thus, an assessment of the possibilities offered by LCGTO-X α (LSD) calculations. Our approach is illustrated by means of a representative collection of molecules (Table 1). For each molecule we have calculated the total X α (LSD) energy using an initial guess, α° , for α . This yields an approximate value of E , namely $E^\circ = E^\circ(\alpha^\circ)$. Next, we have estimated an improved α value, $\alpha = \alpha^\circ + \Delta\alpha$, using the experimental E of Table 1 and the formula

$$E = E^\circ + \Delta\alpha(\partial E/\partial\alpha) \quad (4)$$

and repeated the procedure until convergence was attained. In practice, with a little experience as regards the initial guess, two calculations suffice. We tentatively proceed with the idea that, under proper circumstances, X α (LSD) calculations effectively mimic correlated calculations, although there is presently no formal justification for this contention.

At first glance, the results suggest that the α 's are all alike, ranging from ~ 0.774 to ~ 0.781 . This is a deceitful illusion, however. In fact, the α 's obtained for the individual molecules listed in Table 1 differ significantly from one another. For example, a recalculation using one single α value for the alkanes and the alkyl radicals, namely the best possible one, 0.778, leads to sizeable errors, averaging 13.5 kcal mol⁻¹ for the alkanes and 10.7 kcal mol⁻¹ for the radicals. Similarly, with $\alpha = 0.7746$, the average error for the chloroalkanes amounts to ~ 25 kcal mol⁻¹. Clearly, we have to account for the variations of α in these classes of compounds, even though they may seem small at first sight.

With this in mind, we now examine the X α (LSD) values obtained for $\partial E/\partial\alpha$, Eqs. 2 and 3. Inspection of the results (Table 1) indicates that the $\partial E/\partial\alpha$ derivatives linearly depend on the numbers of atoms of each species found in the molecule. In writing

$$\partial E/\partial\alpha = \sum_i n_i (\partial E_i/\partial\alpha) \quad (5)$$

we express the idea that $\partial E/\partial\alpha$ is, at least to a good approximation, the sum of individual atomic contributions⁸, $\partial E_i/\partial\alpha$. Equation 5 is, indeed, satisfied with $\partial E_H/\partial\alpha = -0.437$, $\partial E_C/\partial\alpha = -7.098$, $\partial E_N/\partial\alpha = -9.105$, and $\partial E_{Cl}/\partial\alpha = -38.309$ au. Additional $\partial E_i/\partial\alpha$ results¹¹ include oxygen, -11.362 , and fluorine, -13.862 a.u. On the other hand, it appears that our exchange-correlation energies, $E_{X\alpha} = \alpha(\partial E/\partial\alpha)$, are also linearly related to the n_i 's, i.e.,

$$\alpha (\partial E/\partial\alpha) = \sum_i n_i \alpha_i (\partial E_i/\partial\alpha) \quad (6)$$

TABLE 1. Experimental energies (Hartree) and corresponding α and $\partial E/\partial\alpha$ values of selected molecules^{8,10}

Molecule	E	α	$\partial E/\partial\alpha$
Methane	-40.5239	0.781456	-8.872
Ethane	-79.8439	0.779431	-16.833
Propane	-119.1675	0.778775	-24.774
Pentane	-197.8163	0.778257	-40.665
Neopentane	-197.8223	0.778250	-40.789
Cyclopropane	-117.9236	0.777459	-23.899
Cyclobutane	-157.2503	0.777488	-31.900
Cyclopentane	-196.6066	0.777323	-39.927
Cyclohexane	-235.9408	0.777466	-47.789
Spiropentane	-195.3208	0.776547	-38.991
Methyl Radical	-39.8465	0.780721	-8.361
Ethyl Rad.	-79.1721	0.778869	-16.354
Propyl Rad.	-118.4967	0.778313	-24.346
<i>tert</i> -Butyl Rad.	-157.8342	0.778009	-32.345
Cyclopropyl Rad.	-117.2432	0.776944	-23.443
Chloromethane	-501.3673	0.774497	-46.724
Chloroethane	-540.6916	0.774839	-54.701
1-Chloropropane	-580.0151	0.775100	-62.684
1-Chlorobutane	-619.3378	0.775346	-70.669
1-Chloropentane	-658.6640	0.775551	-78.654
Dichloromethane	-962.2087	0.773827	-84.549
1,1-Dichloroethane	-1001.5370	0.774068	-92.517
1,3-Dichloropropane	-1040.8652	0.774330	-100.519
Ammonia	-56.5858	0.776920	-10.426
Methylamine	-95.8945	0.776901	-18.378
Ethylamine	-135.2187	0.776944	-26.353
Dimethylamine	-135.2077	0.776917	-26.342
Isopropylamine	-174.5482	0.776945	-34.334
<i>tert</i> -Butylamine	-213.8778	0.776949	-42.320
Diethylamine	-213.8587	0.776940	-42.304
Azirane	-133.9696	0.775816	-25.435
Pyrrolidine	-212.6500	0.776112	-41.413
Piperidine	-251.9848	0.776270	-49.413

where each α_i ($\partial E_i/\partial\alpha$) plays the role of a local "atomic" contribution to $\alpha(\partial E/\partial\alpha)$, that of atom i , α_i being the corresponding "atomic" α . The genuine X α (LSD) results are well given by Eq. 6 with $\alpha_H(\partial E_H/\partial\alpha) = -0.357$, $\alpha_C(\partial E_C/\partial\alpha) = -5.484$, $\alpha_N(\partial E_N/\partial\alpha) = -7.011$, and $\alpha_{Cl}(\partial E_{Cl}/\partial\alpha) = -29.629$ au. Briefly, both $\partial E/\partial\alpha$ and $\alpha(\partial E/\partial\alpha)$ satisfy, in a first approximation, simple atom-by-atom additivity rules. As a consequence, it follows from Eqs. 5 and 6 that

$$\alpha = \sum_i n_i \alpha_i (\partial E_i / \partial \alpha) / \sum_i n_i (\partial E_i / \partial \alpha) \quad (7)$$

meaning that the molecular α can be understood as a weighted average governed by the composition of the molecule. Eq. 7 is a genuine product of X α (LSD) energy analyses. It has been found appropriate as a source of sufficiently accurate α 's for use in X α (LSD) calculations of molecular energies at a level approaching experimental accuracy⁸. Let us look at the results.

Applications

The first question concerns the appropriate selection of basis sets. The results discussed here were obtained using Huzinaga's (9s5p) basis¹⁹ for carbon and nitrogen and a (12s8p) basis²⁰ for chlorine. Hydrogen was described by a (5s) basis obtained from Dunning's (3s) basis set²¹. The selected auxiliary functions were (9s5p3d) for carbon and nitrogen, (7s3p4d) for chlorine, and (5s5p) for hydrogen. Attempts made with smaller basis sets resulted in occasionally erratic results and were abandoned. At times, larger basis sets were also used, namely in the study of hydrogen bond formation¹¹ involving H₂O, NH₃ and HF. Indications are that improvements in the basis set description lead to a small decrease of α (with a minor but noticeable effect on the results) and that at one point any further improvement has virtually no bearing on the final outcome. Our selection of basis sets represents a reasonable compromise which ensures stability of the results. Attempts were also made to circumvent the use of Dunlap's bond-centered auxiliary functions⁷, but had to be abandoned because of the relatively poor results obtained in this manner. Briefly, up to a point there is a perceptible basis set effect on α , but this effect seems to vanish with no evil consequences when reasonably large basis sets are used.

We can now proceed with comparisons between calculated and experimental results. In order to examine the true merits of Eq. 7 and to assess how closely X α (LSD) energies match their experimental counterparts, it is most convenient to express the results in terms of atomization energies, Eq. 1, using experimental values for the isolated atoms, namely, -0.5(H), -37.8558(C), -54.6121(N), and -461.3823 hartree (Cl). (E_i^{atom} is taken, with the appropriate change in sign, as the sum of its ionization potentials²³, with 1 hartree = 27.2106 eV.) This gives the X α (LSD) atomization energies reported in Table 2, to be compared with experimental ΔE_a^* 's. The latter are deduced from Eq. 8

$$\Delta E_a^* = \sum_i n_i \left[\Delta H_f^\circ(A_i) - \frac{5}{2} RT \right] + ZPE + (H_T - H_0) - \Delta H_f^\circ \quad (8)$$

where ΔH_f° is the standard enthalpy of formation of the molecule in the gas phase and $\Delta H_f^\circ(A_i)$ that of the isolated atom A_i , with n_i = number of atoms A_i found in the molecule. We have used²⁴ $\Delta H_f^\circ(\text{H}) = 52.09$, $\Delta H_f^\circ(\text{C}) = 170.89$, $\Delta H_f^\circ(\text{N}) =$

TABLE 2. Predicted α values, Eq. 7, and a comparison of the corresponding X α (LSD) atomization energies with their thermochemical counterparts^a

Molecule	α	ΔE_a^* , kcal mol ⁻¹	
		X α (LSD)	Thermochem.
Methane	0.781263	418.17	419.24
Ethane	0.779446	710.69	710.54
Propane	0.778797	1004.42	1004.08
Pentane	0.778262	1592.31	1592.18
Neopentane	0.778262	1596.25	1595.94
Cyclopropane	0.777429	850.58	851.0
Cyclobutane	0.777429	1145.35	1146.5
Cyclopentane	0.777429	1462.25	1460.6
Cyclohexane	0.777429	1759.71	1760.80
Spiropentane	0.776559	1281.53	1281.23
Methyl Radical	0.780699	307.77	307.89
Ethyl Rad.	0.778922	603.28	602.73
Propyl Rad.	0.778309	896.82	896.88
<i>tert</i> -Butyl Rad.	0.777998	1198.94	1199.16
Cyclopropyl Rad.	0.776912	737.36	737.83
Chloromethane	0.774482	394.39	394.83
Chloroethane	0.774856	689.40	688.82
1-Chloropropane	0.775135	983.67	982.30
1-Chlorobutane	0.775351	1275.51	1275.29
1-Chloropentane	0.775524	1569.14	1570.47
Dichloromethane	0.773812	368.36	369.16
1,1-Dichloroethane	0.774091	666.99	665.66
1,3-Dichloropropane	0.774326	961.85	962.10
Ammonia	0.776900	297.18	297.26
Methylamine	0.776925	581.72	581.45
Ethylamine	0.776934	875.22	875.38
Dimethylamine	0.776934	868.77	868.47
Isopropylamine	0.776939	1172.50	1172.62
<i>tert</i> -Butylamine	0.776943	1469.77	1469.94
Diethylamine	0.776943	1458.03	1457.96
Azirane	0.775604	715.71	719.09
Pyrrolidine	0.776124	1327.32	1327.01
Piperidine	0.776259	1627.25	1627.60

^a The ΔE_a^* values are indicated with a precision which is in many cases not warranted by our actual knowledge, particularly as regards the radicals²². They are used here primarily to facilitate recalculations without being continually bothered by rounding-off errors. The results are extracted from Refs. 8 and 10.

113.0, and $\Delta H_f^\circ(\text{Cl}) = 28.92 \text{ kcal atg}^{-1}$. ZPE is the zero point energy of the molecule (usually evaluated in the harmonic oscillator approximation) and $(H_T - H_O)$ its heat content. The appropriate $ZPE + (H_T - H_O)$ and ΔE_a^* results considered here are conveniently tabulated elsewhere^{10,22,25}. The most important source of possible errors accompanying the evaluation of ΔE_a^* originates in the experimental uncertainty associated with ΔH_f° . Possible errors associated with $ZPE + (H_T - H_O)$ are expected²⁵ not to exceed $\sim 0.2 \text{ kcal mol}^{-1}$. Equations 1 and 8 indicate how any error in the $X\alpha(\text{LSD})$ computation of the total energy E reflects in the estimate of ΔH_f° . Too negative E 's translate into too negative ΔH_f° 's, by the same amount. No test of Eq. 7 can be any more severe than that presented here because the reference energies are those of the isolated atoms.

A statistical data analysis carried out for the hydrocarbons indicates that the α 's of Table 1 are best reproduced with the use of $\alpha_H = 0.816235$ and $\alpha_C = 0.772651$ in Eq. 7, together with the $\partial E_i / \partial \alpha$ values given previously (i.e., those satisfying Eq. 5). The final α values thus recalculated from Eq. 7 (Table 2) are those used in our $X\alpha(\text{LSD})$ computations of E and ΔE_a^* . The comparison between calculated and experimental ΔE_a^* results indicates that Eq. 7 certainly represents a valid source of sufficiently accurate α 's for use in $X\alpha(\text{LSD})$ calculations of molecular energies. A good insight is offered by the cycloalkanes C_3H_6 to C_6H_{12} . Their thermochemical stabilities reflect an important destabilizing effect, the strain energy, accompanying the shrinking of a ring. Because all these cycloalkanes have the same composition, $(\text{CH}_2)_n$, they also have the same α , Eq. 7. The quality of the results (Table 3) strongly suggests that the very strained cyclopropane and the strain-free cyclohexane are, indeed, to be treated in precisely the same manner in applications of Eq. 7. This, of course, implies the persistence, even in highly strained systems, of simple additivity as far as exchange-correlation energies are concerned. Spiropentane is another good example. Similar conclusions hold true also for the nitrogen-containing small cycles. Applications of these observations regarding, namely, the constancy of α as long as the composition of

TABLE 3. A comparison between theoretical and experimental strain energies⁸

Molecule	Strain energy, kcal mol ⁻¹	
	$X\alpha(\text{LSD})$	Exptl.
Cyclohexane	0	0
Cyclopentane	4.2	6.7
Cyclobutane	27.8	27.4
Cyclopropane	29.3	29.4
Spiropentane	59.2	60.2
Piperidine	0	0
Pyrrolidine	6.8	7.1
Azirane	31.7	28.1

a system does not change, are found²² in X α (LSD) analyses of reorganizational energies accompanying radical formation – a field of interest pertaining to the study of bond dissociation energies.

A difficulty arises with radical-carbon, nitrogen, and chlorine containing molecules, as if the parameters determined for the hydrocarbons were not exactly transferable to other classes of compounds. This may be so on physical grounds or only appear that way because of *i*) possible superposition errors like those discussed for conventional *ab initio* calculations of ammonia and alkylamines²⁶ and, more generally, for computations involving hydrogen basis sets which are not adequately balanced²⁷ or, more likely, *ii*) as a result of approximations involved in the present form and use of X α (LSD) theory. Indeed, it has appeared¹¹, namely for H₂O, NH₃ and HF, that the numerical fittings depend, in our calculations, on how the reference axes are selected for the molecules under study – a circumstance which should not occur and which causes slight but importunate uncertainties in the search for the most appropriate α 's. Our present calculations of structurally related compounds carefully avoided internal inconsistencies which could result from this imperfection, which is not there to stay. Temporarily leaving things as they are, we proceed with what we have. Using $\alpha_{C^\bullet} = 0.774589$, $\alpha_N = 0.771777$, and $\alpha_{Cl} = 0.773852$ in Eq. 7, as well as the α_H and α_C values of the alkanes, we multiply the α 's thus obtained by 0.99951 (radicals), 0.999513 (chloroalkanes) or 0.999392 (amines). The averages of the errors which are normally distributed, meaning that do they not follow any trend, are 1.35, 0.79 and 0.17 kcal mol⁻¹ for the radicals, the chloroalkanes, and the aliphatic amines, respectively. This fine-tuning is important if we desire to approach experimental results as closely as possible. On the other hand, considering the smallness of the required correction, it is also clear that Eq. 7 basically represents a valid approximation for α .

This is best illustrated by the following example. The "correct" α values¹¹ of monomeric H₂O and NH₃ differ from one another by as much as ~ 0.005 ; approximately the same difference is found between HF and H₂O and, finally, the difference between NH₃ and HF is as high as ~ 0.01 . Under these circumstances, how can we pick the appropriate α values for the various possible hydrogen-bonded complexes involving H₂O, NH₃, and HF? In each case we have to make a choice: we tentatively select a common α value, α° , and calculate the energies E_1° , E_2° , and E_{12}° for the monomers (1 and 2) and the complex (12), respectively. The corresponding *correct* energies are, from Eq. 4,

$$E_1 = E_1^\circ + (\alpha_1 - \alpha^\circ)(\partial E_1 / \partial \alpha)$$

$$E_2 = E_2^\circ + (\alpha_2 - \alpha^\circ)(\partial E_2 / \partial \alpha)$$

$$E_{12} = E_{12}^\circ + (\alpha_{12} - \alpha^\circ)(\partial E_{12} / \partial \alpha)$$

Had we used the correct α 's throughout our calculations (i.e. α_1 and α_2 for monomers 1 and 2, respectively, and α_{12} for the complex), the correct energy difference (i.e. the dimerization energy) would amount to $\Delta E = E_{12} - E_1 - E_2$. Using our selected α° , we find $\Delta E^\circ = E_{12}^\circ - E_1^\circ - E_2^\circ$ instead. Hence, an error, $\Delta E - \Delta E^\circ$, should be anticipated, namely

$$(\alpha_{12} - \alpha^\circ)(\partial E_{12}/\partial \alpha) - (\alpha_1 - \alpha^\circ)(\partial E_1/\partial \alpha) - (\alpha_2 - \alpha^\circ)(\partial E_2/\partial \alpha)$$

Now we ask what happens if our tentative choice had been exactly that appropriate for the complex, i.e., if $\alpha^\circ = \alpha_{12}$. In that event, a zero error would result provided that $(\alpha_1 - \alpha^\circ)(\partial E_1/\partial \alpha) + (\alpha_2 - \alpha^\circ)(\partial E_2/\partial \alpha) = 0$, i.e., $\alpha_1(\partial E_1/\partial \alpha) + \alpha_2(\partial E_2/\partial \alpha) = \alpha^\circ[(\partial E_1/\partial \alpha) + (\partial E_2/\partial \alpha)]$, which is precisely the result given by Eq. 7. There is no viable substitute for it. (Note that this reasoning involves only the use of Eq. 4.) Thus, it comes as no surprise that $X\alpha$ (LDS) dimerization energies calculated with the help of Eq. 7 are of excellent quality¹¹.

In more general terms, proper use of LCGTO- $X\alpha$ (LSD) theory, coupled with Eq. 7, is expected to provide valuable predictive information at a level approaching experimental accuracy, thus giving access to good-quality enthalpies of formation, Eq. 8. Even in these early stages, useful applications have found their way in the laboratory, namely in the calculation of HN_3 , and of the radicals NH , NH_2 , and N_3 which are intermediates in the explosive decomposition of HN_3 , in good general agreement with recent experimental results pertaining to detonation theory⁹.

We can reasonably conclude that it should not take too long (but this still requires intensive work) before $X\alpha$ (LSD) theory enters the reign of organic chemistry, not only as a highly accurate but also as a practical, efficient tool.

ACKNOWLEDGEMENTS

I sincerely thank all the people (and friends) involved in this project, namely Dr. E.C. Vauthier and Prof. S. Odier (Paris), Prof. V. Barone (Napoli) and Prof. C. Minichino (Potenza), as well as Prof. S. Salahub and Dr. J. Andzelm for their valuable suggestions. Financial support given by the Natural Sciences and Engineering Research Council of Canada is gratefully acknowledged, as well as the financial assistance offered by DRET (France). Finally, I thank the Nato Advanced Study Institute and in particular Dr. Surya N. Bulusu for letting us share our results under the most pleasant conditions offered by Sicily.

REFERENCES

1. P. Hohenberg and W. Kohn, *Phys. Rev.* **136**, B864 (1964).
2. W. Kohn and L.J. Sham, *Phys. Rev.* **140**, A1133 (1965).
3. D.R. Salahub, *Adv. Chem. Phys.* **69**, 447 (1987); J.P. Dahl and J. Avery (Editors). *Local density approximations in quantum chemistry and solid state physics*. Plenum, New York, 1984; S. Lundqvist and N.H. March (Editors). *Theory of the inhomogeneous electron gas*. Plenum, New York, 1983.
4. U. von Barth and L. Hedin, *J. Phys. C.: Solid State Phys.* **5**, 1629 (1972).
5. R. Gáspár, *Acta Phys. Acad. Sci. Hung.* **3**, 263 (1954).
6. H. Sambe and R.H. Felton, *J. Chem. Phys.* **62**, 1122 (1975).
7. B.I. Dunlap, J.W.D. Connolly, and J.R. Sabin, *J. Chem. Phys.* **71**, 3386 (1979); **71**, 4993 (1979).
8. S. Fliszár, S. Rioux, J. Andzelm, C. Minichino, and E.C. Vauthier, *Can. J. Chem.* **66**, 3166 (1988).

9. E.C. Vauthier, S. Fliszár, G. Dupré, and C. Paillard, Actes du Congrès commun des sections britannique et française du Combustion Institute: Groupement français de combustion, Rouen, 18-21 avril 1989.
10. E.C. Vauthier and S. Fliszár, to be published.
11. V. Barone, S. Fliszár, C. Minichino, and E.C. Vauthier, manuscript in preparation.
12. F. Herman and S. Skillman, *Atomic structure calculations*, Prentice-Hall, Englewood Cliffs, NJ, 1963.
13. A.H. Stroud, *Approximate calculation of multiple integrals*, Prentice-Hall, Englewood Cliffs, NJ, 1971.
14. J.C. Slater, *Phys. Rev.* **81**, 385 (1951); J.C. Slater, *Adv. Quantum Chem.* **6**, 1 (1972); J.C. Slater, *The self-consistent field for molecules and solids*, Vol. 4. McGraw-Hill, New York, 1974.
15. R. Gáspár and Á. Nagy, *Theor. Chim. Acta* **72**, 393 (1987). Á. Nagy, *Int. J. Quantum Chem.* **31**, 269 (1987); R. Gáspár, *Acta Phys.* **35**, 213 (1974).
16. E.J. Baerends and P. Ros, *Chem. Phys.* **2**, 52 (1973).
17. K. Schwarz, *Phys. Rev.* **B5**, 2466 (1972).
18. H. Stoll, E. Golka, and H. Preuss, *Theoret. Chim. Acta* **55**, 29 (1980).
19. S. Huzinaga, *J. Chem. Phys.* **42**, 1293 (1965).
20. S. Huzinaga, Technical Report, University of Alberta, Edmonton, Alberta (1971).
21. T.H. Dunning, *J. Chem. Phys.* **55**, 716 (1970).
22. S. Fliszár and C. Minichino, *Can. J. Chem.* **65**, 2495 (1987).
23. C.E. Moore, *Nat. Stand. Ref. Data Ser. (US Nat. Bur. Stand.) NSRD-NBS* **34**, 1 (1970).
24. D.R. Stull and G.C. Sinke, *Adv. Chem. Ser.* **18** (1956); J.D. Cox and G. Pilcher, *"Thermochemistry of Organic and Organometallic Compounds"*, Academic Press, New York, 1970.
25. S. Fliszár, *"Charge Distributions and Chemical Effects"*, Springer-Verlag, New York, 1983; S. Fliszár, F. Poliquin, I. Bădilescu, and E.C. Vauthier, *Can. J. Chem.* **66**, 300 (1988).
26. G. Del Re, S. Fliszár, M. Comeau, and C. Mijoule, *Can. J. Chem.* **63**, 1487 (1985).
27. W. Kolos, *Theor. Chim. Acta* **54**, 187 (1980); W.A. Sokalski, *J. Chem. Phys.* **77**, 4529 (1982); J.G.M. Van Duijneveldt-van de Rijdt and F.B. van Duijneveldt, *J. Mol. Struct. Theochem.* **89**, 185 (1982).

ON THE DISSOCIATION OF CHEMICAL BONDS

S. FLISZAR
*Département de Chimie
Université de Montréal
C.P. 6128, Succ. A
Montréal (Qué.) Canada H3C 3J7*

ABSTRACT. The equilibrium ground-state energy of a molecule with fixed nuclei can be exactly expressed in terms of the total molecular electrostatic potentials at the nuclei. Application of the Hellmann-Feynman theorem achieves a partitioning into atomic terms, from which energy expressions can be derived for the individual chemical bonds from an appropriate pairing of atomic terms. The energies associated with the individual bonds depend markedly on the electronic charges carried by the bond-forming atoms (e.g., in a range of ~ 15 kcal mol⁻¹ for CC single bonds), hence on the molecular environment which determines the equilibrium charge densities at the atoms in a molecule. These intrinsic bond energies, ϵ_{ij} , measure their contribution to the thermochemical stability of their host molecule at equilibrium. Here we address the problem of bond dissociation, $R_1R_2 \rightarrow R_1^\bullet + R_2^\bullet$, and that of the bond dissociation energy, D_{ij} , accompanying such a cleavage. Our approach accounts for the important fact that the molecular fragments R_1 and R_2 may not be individually electroneutral while they are part of the host molecule R_1R_2 , whereas each product resulting from the cleavage of the R_1 - R_2 bond is certainly electroneutral. The novelty lies in the straightforward application of this electroneutrality constraint *via* a relatively simple energy balance involving the charge-dependent intrinsic bond energy terms, ϵ_{ij} . Our discussion centers on the relationship between dissociation and intrinsic theoretical (as opposed to empirical) bond energies in order to learn how much of the physics governing dissociation processes can be extracted from a theoretical description of the reactant, thus going beyond a mere description of its ground-state bond energies. The emphasis is on the fundamental concepts involved and on an, admittedly incomplete, assessment of future possible developments and applications of the novel views revealed by the present theory.

Introduction

To put things in a realistic perspective, the whole of chemistry rests on "small events" from an energetic point of view. Even brutal phenomena, such as explosions, are ultimately triggered by relatively minor causes although the victim (or the beneficiary) of such an event may well think differently. The point is that we should pay diligent attention to any minor change which may occur locally in a molecule and which may decisively affect the outcome of a reaction and not necessarily anticipate spectacular causes at the molecular level simply because the final result is excessively spectacular in our perception. Here we discuss local properties at a microscopic level *i*) in terms of the energies of chemical bonds in ground-state molecules in order *ii*) to gain access to the energetics accompanying bond dissociation. The whole gives an idea regarding the

nature of the local microscopic causes which affect the overall outcome of a macroscopic event.

Energy Partitioning. The Chemical Bond

Under laboratory conditions, molecules contain vibrational, translational and rotational energies which are not fairly partitionable among chemical bonds. For convenience, our analysis considers the molecules at their potential minimum, i.e., with reference to their hypothetical vibrationless state at 0 K; the role of vibrational energies is treated as a separate problem. The measure for what holds the atoms together in a molecule is thus offered by the difference

$$\Delta E_a^* = \text{energy of all the isolated ground-state atoms} \\ \text{minus the ground-state energy of the molecule} \quad (1)$$

which is the energy required for breaking up that molecule into its constituent atoms. The atomization energy, ΔE_a^* , includes the annihilation of all interactions between atom pairs which are not chemically bonded to one another in the conventional sense, ΔE_{nb}^* , and the destruction of all chemical bonds ij , represented by their energies ϵ_{ij} , i.e.,

$$\Delta E_a^* = \sum_{i < j} \epsilon_{ij} + \Delta E_{nb}^* \quad (2)$$

It turns out that nonbonded interactions are minor^{1,2}, ~0.02-0.05% of ΔE_a^* , so that the study of ΔE_a^* essentially reduces to a consideration of bond energies, $\Delta E_a^* \simeq \sum_{i < j} \epsilon_{ij}$. Each ϵ_{ij} represents the part of the total atomization energy which is contributed by a particular ij bond. This contribution is dictated by actual properties in the molecule (internuclear distance and local charge density) and should not be mistaken for the energy, D_{ij} , required to break that bond. The all-important relationship between D_{ij} and ϵ_{ij} is described in the next Section. Let us first review the concepts involved in an approximate, but accurate, description of bond energies.

Use of the Hellmann-Feynman theorem³ in the evaluation (at constant electron density ρ) of the derivative

$$\left(\frac{\partial E}{\partial Z_i} \right)_\rho = \langle \psi^{\text{mol}} | \frac{\partial \hat{H}^{\text{mol}}}{\partial Z_i} | \psi^{\text{mol}} \rangle \\ = - \int \frac{\rho(\mathbf{r})}{|\mathbf{r} - \mathbf{R}_i|} d\mathbf{r} + \sum_j Z_j / R_{ij}$$

of the equilibrium total energy of a molecule with respect to the nuclear charge of atom i achieves *i*) a partitioning into atomic parts and *ii*) reduces the problem to a "simpler" electrostatic calculation because the kinetic and interelectronic repulsion terms have disappeared¹. It follows that

$$\sum_i Z_i \left(\frac{\partial E}{\partial Z_i} \right)_\rho = V_{ne} + 2V_{nn} \quad (3)$$

where V_{ne} and V_{nn} are the nuclear-electronic and nuclear-nuclear potential energies, respectively. With the virial theorem, $2E = V_{ne} + V_{ee} + V_{nn}$ (where V_{ee} is the interelectronic repulsion energy), Eq. 3 becomes

$$2E - \sum_i Z_i \left(\frac{\partial E}{\partial Z_i} \right)_\rho = V_{ee} - V_{nn} \quad (4)$$

On the other hand, we obtain from the Hartree-Fock formula $E = \sum \epsilon^{\text{orb}} - (V_{ee} - V_{nn})$ and Eq. 4 that

$$(3 - \gamma)E = \sum \epsilon^{\text{orb}} \quad (\text{sum of occupied orbital energies}) \quad (5)$$

and, using also Eq. 3, that

$$E = \frac{1}{\gamma} (V_{ne} + 2V_{nn}) \quad (6)$$

Equations 5 and 6 represent an identity in Hartree-Fock theory provided, of course, that all quantities are evaluated at equilibrium geometry^{4,5}. The particular interest offered by Eq. 6 lies in the fact that $\gamma = \frac{7}{3}$ appears to be the characteristic homogeneity of both Thomas-Fermi⁶ and local density functional theory⁷, in which case Eq. 5 gives the Ruedenberg approximation⁸, $E = \frac{3}{2} \sum \epsilon^{\text{orb}}$, while Eq. 6 gives the Politzer formula⁹

$$E = \frac{3}{7} (V_{ne} + 2V_{nn}) \quad (7)$$

This formula, which has been scrutinized in detail⁵, is pivotal in the evaluation of bond energies. It represents a valid approximation in our intended applications to real molecules. Let us now temporarily switch to another subject.

At this point it becomes practical to use common sense and a simple example in order to clarify things without engaging in lengthy calculations. Suppose we know ϵ_{CH} for methane. (This is easy: we could obtain it from Eq. 2 using the experimental ΔE_a^* value with a small correction for ΔE_{nb}^* , estimated^{1,2} at $-0.09 \text{ kcal mol}^{-1}$.) Its actual value is irrelevant at this stage. What matters is that this particular ϵ_{CH} reflects the properties of methane, namely its electron distribution. If a (yet unspecified) population analysis assigns non-zero net charges $-\delta$ to H, and thus $+4\delta$ to C, the exact transfer of methane CH bonds to ethane amounts to constructing a molecule with a $+2\delta$ total net charge. This is not acceptable. The lesson to be learned is the following. If we select a set of reference bond energies ϵ_{ij}° defined for reference electron populations N_i° and N_j° assigned to atoms i and j , respectively, the simple sum,

$\sum \epsilon_{ij}^p$, of these reference energies does not yield a correct ΔE_a^* for any molecule other than that used for deriving the ϵ_{ij}^p 's because the sum $\sum \epsilon_{ij}^p$ does not ensure electroneutrality, except for the reference molecule. The gap between $\sum \epsilon_{ij}^p$ and ΔE_a^* requires explicit consideration of charge normalization. This involves changes in electron populations (with respect to those in the reference molecule) provoking changes in nuclear-electronic potential energies. The key is in ΔV_{ne} , i.e., the total change of V_{ne} occurring when the valence-electron population of each atom i changes from N_i° (the value in the reference molecule) to $N_i = N_i^\circ + \Delta N_i$, with the constraint that $\sum_i N_i$ should satisfy molecular electroneutrality. Where appropriate, we also take into account possible changes in bond distances through $\Delta V_{nn} = V_{nn} - V_{nn}^\circ$. Briefly, we evaluate $\Delta(V_{ne} + 2V_{nn})$. This is where the Politzer formula, Eq. 7, comes in: the energy change accompanying charge normalization to fill the gap between $\sum \epsilon_{ij}^p$ and ΔE_a^* is approximated as

$$\frac{3}{7} \Delta(V_{ne} + 2V_{nn})$$

In the spirit of the Politzer-Parr core-valence separation¹⁰, we write^{1,2}

$$\Delta V_{ne} = - \sum_i Z_i^{\text{eff}} [N_i \langle r_i^{-1} \rangle - N_i^\circ \langle r_i^{-1} \rangle^\circ + \sum_{j \neq i} (N_j \langle r_{ij}^{-1} \rangle - N_j^\circ \langle r_{ij}^{-1} \rangle^\circ)] \quad (8)$$

where the Z_i^{eff} s are "effective" nuclear charges (e.g., 4 for carbon, 5 for nitrogen, etc.). The quantities appearing in the square brackets are defined in terms of a suitable partitioning of the molecular electron density into atomic contributions ρ_i and of the equilibrium coordinates, \mathbf{R}_i , of the nuclei, i.e.,

$$\begin{aligned} \int \frac{\rho_i(\mathbf{r})}{|\mathbf{r} - \mathbf{R}_i|} d\mathbf{r} &= N_i \langle r_i^{-1} \rangle \quad \text{with} \quad \int \rho_i(\mathbf{r}) d\mathbf{r} = N_i \\ \int \frac{\rho_j(\mathbf{r})}{|\mathbf{r} - \mathbf{R}_i|} d\mathbf{r} &= N_j \langle r_{ij}^{-1} \rangle \quad \text{with} \quad \int \rho_j(\mathbf{r}) d\mathbf{r} = N_j \end{aligned} \quad (8a)$$

Thus, $\langle r_i^{-1} \rangle$ and $\langle r_{ij}^{-1} \rangle$ can be interpreted as the average inverse distances from Z_i^{eff} to the centers of the electron populations N_i and N_j , respectively; the superscript zero in Eq. 8 indicates the corresponding expressions for the reference molecule. The accompanying change in nuclear repulsion can be added to ΔV_{ne} in the form

$$2(V_{nn} - V_{nn}^{\circ}) = \sum_i \sum_j Z_i^{\text{eff}} Z_j^{\text{eff}} [(R_{ij}^{-1}) - (R_{ij}^{-1})^{\circ}] \quad (9)$$

where the summation extends over all bonded atom pairs. Inspection of Eqs. 8 and 9 indicates that all the terms appearing in $\frac{3}{7} \Delta(V_{ne} + 2 V_{nn})$ lend themselves to a bond-by-bond partitioning. Thus we can write out a bond energy formula featuring the effects of charge normalization.

The final results deduced in this fashion^{1,2} are most conveniently expressed in terms of net atomic charges $q_i = Z_i^{\text{eff}} - N_i$, and their changes, $\Delta q_i = q_i - q_i^{\circ}$. They are:

$$\epsilon_{ij} = \epsilon_{ij}^{\circ} + a_{ij} \Delta q_i + a_{ji} \Delta q_j \quad (10)$$

where the a_{ij} and a_{ji} parameters measure the effect of unit charge variations at atoms i and j , respectively. It follows from Eqs. 8 and 9 that

$$a_{ij} = \frac{3}{7} \cdot \frac{\gamma_i}{v_i} \left(\frac{\partial E_i^{\text{vs}}}{\partial N_i} \right)^{\circ} - \frac{3}{7} Z_j / R_{ij} \quad (11)$$

where v_i = number of atoms bonded to i . The term $\gamma_i (\partial E_i^{\text{vs}} / \partial N_i)^{\circ}$ comes from an application of Eq. 6 to the valence state of atom i , $\gamma_i E_i^{\text{vs}} = N_i \langle r_i^{-1} \rangle$ (= nuclear-electronic potential energy between N_i and Z_i^{eff}), and the Taylor expansion $N_i \langle r_i^{-1} \rangle = N_i^{\circ} \langle r_i^{-1} \rangle^{\circ} + (\partial N_i \langle r_i^{-1} \rangle / \partial N_i) \Delta N_i + \dots$ used in the evaluation of the $N_i \langle r_i^{-1} \rangle - N_i^{\circ} \langle r_i^{-1} \rangle^{\circ}$ part of Eq. 8. γ_i is always close to $\frac{7}{3}$, except for H where $\gamma = 2$ because of the virial theorem. Finally, it follows from Eqs. 8-11 and Eq. 2 that

$$\Delta E_a^* = \sum \epsilon_{ij}^{\circ} + \sum_i \sum_j a_{ij} \Delta q_i + F + \Delta E_{\text{nb}}^* \quad (12)$$

where

$$F = -\frac{3}{7} \sum_i \sum_j Z_i^{\text{eff}} q_j \left(\langle r_{ij}^{-1} \rangle - \langle r_{ij}^{-1} \rangle^{\circ} \right) - \frac{3}{7} \sum_i \sum_j Z_i^{\text{eff}} Z_j^{\text{eff}} \left[(R_{ij}^{-1}) - (R_{ij}^{-1})^{\circ} - \left(\langle r_{ij}^{-1} \rangle - \langle r_{ij}^{-1} \rangle^{\circ} \right) \right]$$

contains information regarding orbital shapes and internuclear distances. F is negligibly small if the charge centroids are located at their nuclear positions. When this is not the case, it is always possible to incorporate the appropriate parts of F in newly defined reference ϵ_{ij}° 's and thus render $F = 0$ again¹¹. What really matters is

$\sum_i \sum_j a_{ij} \Delta q_i$ which describes the energy associated with the changes, Δq_i , of the net atomic charges with respect to the reference molecule.

So much for the theory. Its quality is best illustrated by comparisons of Eq. 12 with experiment (Fig.1). We now wish to take advantage of it and examine an important part of the microscopic effects capable of orienting the dynamics of bond dissociation. To do this, we examine selected a_{ij} values obtained from Eq. 11 (Table 1).

FIGURE 1. Frequency of deviations between calculated and experimental atomization energies. This error distribution survey covers alkanes² (including cycloalkanes constructed from chair and (or) boat cyclohexane rings), simple ethylenic² and polyunsaturated hydrocarbons^{12b}, both conjugated and nonconjugated, as well as ethers, aldehydes, and ketones². Similar results were also obtained for ~40 benzenoid hydrocarbons^{12a}, including graphite^{12c}. (Reproduced from Ref. 12a.)

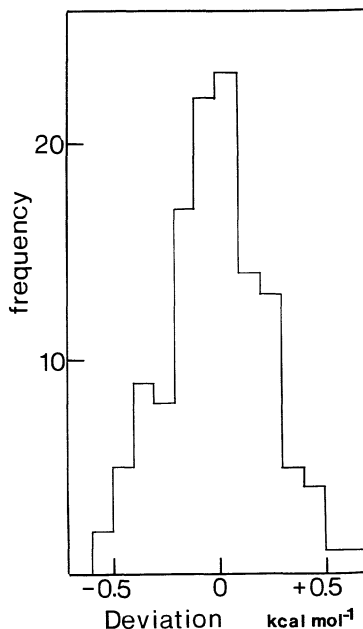


TABLE 1. Selected a_{ij} values for single bonds and the bond weakening due to the loss of 1 me at both atoms.

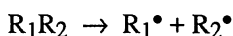
Bond	a_{ij} , kcal mol ⁻¹ me ⁻¹		Bond weakening
HC	$a_{\text{HC}} = -0.632$	$a_{\text{CH}} = -0.247$	0.879
HN	$a_{\text{HN}} = -0.814$	$a_{\text{NH}} = -0.200$	1.014
HO	$a_{\text{HO}} = -1.013$	$a_{\text{OH}} = -0.229$	1.242
CC	$a_{\text{CC}} = -0.488$		0.976
CN	$a_{\text{CN}} = -0.593$	$a_{\text{NC}} = -0.441$	1.034
CO	$a_{\text{CO}} = -0.712$	$a_{\text{OC}} = -0.505$	1.217

The results for the HC, CC and CO bonds are given in Ref. 2. For the HN, CN and OH bonds we have used $R = 1.0027, 1.489^{13}$ and 1.03 \AA , respectively, where the latter is the calculated distance between the charge centroid of oxygen and the H nucleus, with an internuclear distance of 0.943 \AA . $(\partial E / \partial N)^\circ$ was taken at -0.29 au for oxygen² and at -0.28 au for nitrogen, using the results of Ref. 14.

These a_{ij} 's indicate, for example, that the loss of 1 millielectron (1 me = 10^{-3} electron) at H, i.e., $\Delta q = +1$ me, lowers the energy of a CH bond by 0.632 kcal mol $^{-1}$. The results of Table 1 suggest the following rule of thumb: "*the loss of 1 millielectron at each atom forming a single bond translates into a bond weakening of ~ 1 kcal mol $^{-1}$* ". Surely, microscopic changes in local charge densities produce sizeable thermochemical effects. We shall keep this in mind and examine how these changes in bond energies ultimately affect the dissociation of chemical bonds.

Bond Dissociation Energies

The problem is now to find how D_{ij} , the bond dissociation energy, depends on ϵ_{ij} , the intrinsic energy of that bond. The cleavage



of the bond linking R_1 and R_2 to one another in the R_1R_2 molecule involves the dissociation energy

$$D_{R_1R_2} = \Delta E_a^*(R_1R_2) - \Delta E_a^*(R_1^\bullet) - \Delta E_a^*(R_2^\bullet) \quad (13)$$

where the ΔE_a^* 's are atomization energies, Eq. 1. The following partitioning of $\Delta E_a^*(R_1R_2)$ can be made by reference to Eq. 2. Here we consider all the bonds occurring in R_1 (except the one linking R_1 to R_2) and the nonbonded interactions confined within R_1 . The sum of all these contributions gives $\Delta E_a^*(R_1^{\text{mol}})$. This is the part of $\Delta E_a^*(R_1R_2)$ which is associated with the group of atoms R_1 as it exists in that particular molecule R_1R_2 . We proceed similarly with R_2 and obtain $\Delta E_a^*(R_2^{\text{mol}})$. The sum $\Delta E_a^*(R_1^{\text{mol}}) + \Delta E_a^*(R_2^{\text{mol}})$ thus collects the energies of all the bonds found in the molecule except one, that linking R_1 to R_2 , which is $\epsilon_{R_1R_2}$, and all the nonbonded interactions except those occurring between the atoms of R_1 and those of R_2 , i.e., $\Delta E_{\text{nb}}^*(R_1 \cdots R_2)$. The energy balance satisfying Eq. 2 is

$$\Delta E_a^*(R_1R_2) = \Delta E_a^*(R_1^{\text{mol}}) + \Delta E_a^*(R_2^{\text{mol}}) + \epsilon_{R_1R_2} + \Delta E_{\text{nb}}^*(R_1 \cdots R_2) \quad (14)$$

When R_1 and R_2 are identical in the molecule (as in $\text{CH}_3\text{-CH}_3$, for example) each of these groups is necessarily electroneutral. Electroneutral groups, taken exactly as in RR , are identified by the superscript zero. Under these circumstances, it follows from Eq. 14 that

$$\Delta E_a^*(R^0) = \frac{1}{2} \left[\Delta E_a^*(\text{RR}) - \epsilon_{\text{RR}} - \Delta E_{\text{nb}}^*(R \cdots R) \right] \quad (14a)$$

which is a useful formula in applications requiring the knowledge of $\Delta E_a^*(R^0)$. The energy formulas 13 and 14 are straightforward representations of first-principle energy balances. Eq. 13 features the dissociation energy, $D_{R_1R_2}$, and Eq. 14 the

corresponding intrinsic bond energy, $\epsilon_{R_1R_2}$. Now we examine how these bond terms are related to one another.

Our central argument rests on a simple but crucial observation¹⁵ concerning any dissociation $R_1R_2 \rightarrow R_1^\bullet + R_2^\bullet$. The individual fragments (R_1 and R_2) are in general not electroneutral while they are part of the unperturbed host molecule whereas the corresponding radicals certainly satisfy electroneutrality. This, of course, is not a new idea. The novelty lies in the theoretical exploitation of this charge reneutralization constraint. Our strategy rests on a comparison of R_1^{mol} and R_2^{mol} with their electroneutral counterparts, R_1° and R_2° , respectively. The selection of the $\Delta E_a^*(R^\circ)$'s as references is only one of the possible choices. It is arbitrary but convenient because it is the only one agreeing with the idea that it makes sense to first get the number of electrons right, then relax everything else. The sum $\Delta E_a^*(R_1^{\text{mol}}) + \Delta E_a^*(R_2^{\text{mol}})$ differs (in principle) from that of the corresponding electroneutral fragments, $\Delta E_a^*(R_1^\circ) + \Delta E_a^*(R_2^\circ)$. The difference between these sums is *CNE*, the charge neutralization energy, i.e.,

$$\Delta E_a^*(R_1^{\text{mol}}) + \Delta E_a^*(R_2^{\text{mol}}) = \Delta E_a^*(R_1^\circ) + \Delta E_a^*(R_2^\circ) + CNE \quad (15)$$

Using the energy balance, Eq. 14, it follows that

$$CNE = \Delta E_a^*(R_1R_2) - \epsilon_{R_1R_2} - \Delta E_{\text{nb}}^*(R_1 \cdots R_2) - \Delta E_a^*(R_1^\circ) - \Delta E_a^*(R_2^\circ) \quad (16)$$

The electroneutral (R°)'s selected once and for all as convenient references differ, of course, from the genuine radicals R^\bullet ; this difference is represented by the reorganizational energy

$$RE = \Delta E_a^*(R^\circ) - \Delta E_a^*(R^\bullet) \quad (17)$$

Equation 16 is the key equation for the description of bond dissociation energies. Indeed, using the definition of $D_{R_1R_2}$, Eq. 13, and that of the reorganizational energy, Eq. 17, it follows from Eq. 16 that

$$D_{R_1R_2} = \epsilon_{R_1R_2} + CNE + \Delta E_{\text{nb}}^*(R_1 \cdots R_2) + RE(R_1) + RE(R_2) \quad (18)$$

This new energy formula is general and suffers from no approximations in that all the appropriate bonded and nonbonded contributions are taken care of. It is seen that *CNE*, Eq. 16, should not be regarded as just a correction term. Quite on the contrary, this particular form of electroneutrality constraint is all that is required for deducing the relationship between bond dissociation and intrinsic bond energies. Eq. 18 is exact. Incidentally, application of Eqs. 17 and 18 to the calculation of step-wise dissociations consisting in an atom-by-atom removal of all the atoms of a polyatomic molecule, with dissociation energies D_1, D_2, \dots, D_i , gives $\sum_i D_i = \Delta E_a^*$. The energy balance is correct.

Applications

The merits of Eq. 18 are revealed by a survey of the leading terms governing bond dissociations when the cleavage occurs *i*) in the "interior" of the molecule, *ii*) in its peripheral region or *iii*) when it concerns "exterior" bonds formed by a molecule, such as hydrogen bonds or, more generally, as a result of weak interactions accompanying cluster formation or adsorption on a catalyst. (Only dissociations yielding electroneutral products are considered because the formation of ions, $AB \rightarrow A^+ + B^-$, can be treated along the same lines, with final corrections involving the ionization potential of A and the electron affinity of B.)

Let us first examine the effects of charge neutralization accompanying the cleavage of a bond located in the "interior" of a molecule, i.e., a bond linking polyatomic groups. The electron loss by one group weakens its bonds, an effect which is largely counteracted by the bond strengthening in the group gaining that electronic charge. As a result of this important cancellation, it appears that the dissociation of chemical bonds embedded between sufficiently large molecular fragments involves relatively minor *CNE* contributions, as compared to the important structure related changes affecting $\epsilon_{R_1R_2}$ energies. On the other hand, nonbonded contributions are also almost negligible¹⁵, so that $CNE + \Delta E_{nb}^* \simeq 0$. Numerical calculations and comparisons with experiment fully confirm the validity of these general expectations^{15,16}. Our approximation, Eq. 18a, typically represents a bond in the "interior" of a molecule. (This equation has the same form as the formula considered by Sanderson¹⁷ on an empirical basis, but differs in conceptual content: Eq. 18a commands the use of theoretical bond energies, Eq. 10.)

$$D_{R_1R_2} \simeq \epsilon_{R_1R_2} + RE(R_1) + RE(R_2) \quad (18a)$$

In contrast, bond dissociations occurring at the edge of a molecule are accompanied by important *CNE* contributions. Abstraction of an electroneutral atom, X, which carried a partial charge while part of the host molecule affects only the bond energies of the polyatomic fragment left behind, because the abstracted atom forms no bonds and, hence, cannot compensate for the bond energy changes induced in the other fragment: any cleavage of a C-X bond, for example, involves a significant *CNE* energy^{15,16} (e.g., ~6-13 kcal mol⁻¹ for CH bonds). On the other hand, the individual C-X bonds also differ considerably from one another, depending on what is attached to X. The remarkable feature is that $\epsilon_{C-X} + CNE + \Delta E_{nb}^*$ is nearly constant for each type of bond^{15,16}. Hence, contrasting with the cleavage of a chemical bond well embedded in a molecule, which is sensitive to any change affecting its intrinsic energy, the cleavage of "peripheral" bonds is essentially described by the approximation

$$D_{C-X} \simeq \text{constant} + RE \quad (X = H, Cl, Br, I) \quad (18b)$$

meaning that D_{C-X} is primarily determined by the type of bond (CH or CCl, etc.) and *RE*. Structure related modifications of intrinsic C-X bond energies, though occasionally large, have little say in the abstraction of an atom from a molecule. (Other types of bonds, e.g. O-X and N-X, are currently under investigation.)

Our approach has revealed fundamental differences between the "interior" of a molecule, Eq. 18a, and its peripheral bonds, Eq. 18b. Let us now explore processes involving the "exterior" of a molecule, such as the formation of hydrogen bonds or its adsorption onto a surface. This is done on a tentative basis, primarily justified by the fact that Eq. 18 is an exact description of any dissociation process. When two ground-state molecules, A and B, associate without loss of their chemical identities (as in $\text{HOH}\cdots\text{OH}_2$), some charge transfer is generally to be expected in AB. The *CNE* part accompanying the dissociation $\text{AB} \rightarrow \text{A} + \text{B}$ is given by Eq. 15. The $\Delta E_a^*(R^0)$'s are now simply the atomization energies of A and B and we have zero reorganizational energies. The linkage between A and B should certainly not be considered as a "normal" chemical bond. More appropriately, it should be included in the computation of $\Delta E_{\text{nb}}(\text{A}\cdots\text{B})$ although it may differ from a "usual" nonbonded interaction. $\Delta E_{\text{nb}}(\text{A}\cdots\text{B})$ is a sum of pair-wise (intermolecular) interactions between the atoms of A and those of B and it is a matter of taste whether or not we single out any particular interaction, e.g., that between the O and H atoms engaged in the hydrogen "bond" $\text{HOH}\cdots\text{OH}_2$. The form of Eq. 18 describing the cleavage of a molecular association is thus

$$D_{\text{A}\cdots\text{B}} = \text{CNE} + \Delta E_{\text{nb}}(\text{A}\cdots\text{B}) \quad (18\text{c})$$

Equation 18c discriminates, in a way, between intramolecular (*CNE*) and intermolecular contributions to $D_{\text{A}\cdots\text{B}}$. It would be instructive to learn about their relative importance in light of this equation, e.g., *via* calculations of *CNE*. Eq. 10 offers access to *CNE*: we calculate the ϵ_{ij} 's of all the bonds found in the complex and subtract those of the isolated molecules A and B. The difference is $\text{CNE} = \sum_i \sum_j a_{ij} \Delta q_i$, where Δq_i is the difference between the net charge of atom *i* in the complex and that of the same atom in the isolated molecule. As regards the calculation of $\Delta E_{\text{nb}}(\text{A}\cdots\text{B})$, the answer is in Eq. 12, namely in the change of *F* accompanying complex formation. This change represents an intermolecular contribution (atoms *i* and *j* belong to different molecules), so that $\langle R_{ij}^{-1} \rangle = \langle r_{ij}^{-1} \rangle = 0$ at infinite separation of A and B. Under these circumstances, the change in \bar{F} accompanying complex formation reduces exactly to $\frac{3}{7}$ of minus the intermolecular contribution ($V_{\text{ne}} + 2V_{\text{nn}}$), as it should. Applications of Eq. 18c require a good knowledge of atomic charges, in both the complex and the monomers, as well as accurate calculations of charge centroids. This is a challenging task. (Current work¹⁸ on the dimerization of water indicates that *CNE* is certainly negative, of the order of -10 (or perhaps -20) kcal mol^{-1} , with a large positive $\Delta E_{\text{nb}}(\text{A}\cdots\text{B})$ compensation). The point is that complex formation depends on two energy components with a *CNE* part which should be considered at its true merits.

The Involvement of "Weak Interactions"

Let us review, in light of the present theories, the sequence of events accompanying "weak" interactions between molecules, starting with their "exterior" and working our way back to their "interior". This is done on a tentative and admittedly incomplete basis, with the intent of offering a fresh and more general view about the microscopic factors involved in bond dissociation and, thus, hopefully generate new ideas on old problems.

The dissociation of the complex, $AB \rightarrow A + B$, is described by Eq. 18c. The complex may well be "weak", i.e., $D_{A...B}$ small. This does not imply that CNE itself is negligibly small, only that it is the order of magnitude of its companion, $\Delta E_{nb}(A...B)$, with a change in sign. This CNE may result from an intramolecular charge transfer during complex formation or from more subtle electronic rearrangements occurring in neutral molecules which become part of a crystal. Now all depends on which atoms have gained or lost electrons.

The effect on bond energies is given by Eq. 10. If complex formation causes the charges of atoms i and j to change by Δq_i and Δq_j , respectively, the corresponding change in bond energy is $\Delta \epsilon_{ij} = a_{ij}\Delta q_i + a_{ji}\Delta q_j$. If this bond is embedded in a molecule, Eq. 18a tells us that its dissociation energy varies like ϵ_{ij} , because the reorganizational energies do not change since the final products remain the same, i.e.,

$$\Delta D_{R_1R_2} \simeq a_{ij} \Delta q_i + a_{ji} \Delta q_j \quad (19)$$

Now we remember our rule of thumb: hence, a modest loss of 1 millielectron at the atoms forming a bond causes its dissociation energy to drop by ~ 1 kcal mol $^{-1}$. Moreover, as explained by S. Odier¹⁹, in the kinetic course of an explosion such a modest change may well provoke a tenfold energetic enhancement of the overall process. Briefly, a story which started with a relatively small perturbation may find its conclusion on a scale which seems disproportional with respect to its origin. The conclusion is that apparently minor effects, as they are revealed by appropriate charge analyses, are important. The response of the "interior" properties of a molecule to modifications of its environment is now accessible to quantitative explorations through our energy partitioning permitting the study of local properties, namely bond energies and bond dissociation energies, in terms of local charge densities.

Equation 19 describes why a lowering of the intrinsic energy associated with a given bond brought about by an external perturbation ultimately lowers the energy required for its dissociation. It must be made clear, however, that this parallelism is not generally valid, namely in comparisons between *different* bonds. Examples are offered in Table 2. As regards the CH bonds, both the H atom and the carbon attached to it gain electronic charge in going from CH₃-H to *tert*-butyl-H. This, of course, corresponds to what one would normally expect from a consideration of the familiar inductive effects and is, indeed, well reflected by theoretical charge analyses.² These charge effects, in turn, translate into increasingly larger intrinsic CH bond energies, eq. 10. The corresponding dissociation energies (eq. 18b), however, exhibit the opposite trend because the reorganizational energies of the alkyl radicals¹⁵ decrease in going from methyl ($RE = 12.45$ kcal/mol), ethyl (10.05), *n*-propyl (9.19), isopropyl (6.99), to *tert*-butyl (2.45 kcal/mol): the physical reason rests with the almost planar geometry of the methyl radical (meaning that its carbon resembles an sp^2 hybridized C atom) whereas, at the other end, the geometry of the *tert*-butyl radical closely approaches that found in isobutane. The same arguments apply to the CC bonds, eq. 18a. These conclusions also hold for dissociation enthalpies.¹⁵

TABLE 2. Intrinsic bond energies (ϵ), dissociation energies (D) and bond dissociation enthalpies DH of selected CH and CC bonds, kcal mol⁻¹.

Bond	ϵ	D	DH
CH ₃ -H	104.86	111.42	103.45
C ₂ H ₅ -H	106.81	107.81	101.05
<i>n</i> C ₃ H ₇ -H	107.13	107.41	100.19
<i>i</i> C ₃ H ₇ -H	108.72	104.61	97.99
<i>t</i> C ₄ H ₉ -H	110.89	100.86	93.45
CH ₃ -CH ₃	69.63	94.76	88.63
C ₂ H ₅ -C ₂ H ₅	72.38	92.64	86.58
<i>i</i> C ₃ H ₇ - <i>i</i> C ₃ H ₇	73.71	87.80	81.79
<i>t</i> C ₄ H ₉ - <i>t</i> C ₄ H ₉	73.87	78.77	72.87

Additional results are given in Ref. 15.

These numerical examples illustrate that any argument constructed in terms of local bond properties necessarily requires the clear distinction between intrinsic bond energies – i.e., those responsible for the thermochemical stability of isolated ground-state molecules, eq. 2 – and bond dissociation energies, eq. 18, which depend on both the intrinsic bond energies and the nature of the dissociation products. The important role of local charge effects, introduced by the constraint requiring preservation of electroneutrality in both the reactant and the reaction products, contributes a conceptually simple novelty permitting a straightforward description of the physics involved in any dissociation process. The present approach which adds to our arsenal of investigative tools hopefully opens new horizons and paves the way to a better insight into the complex problems accompanying "weak" interactions.

ACKNOWLEDGEMENTS

I wish to thank the Nato Advanced Study Institute and in particular Dr. Surya N. Bulusu for this opportunity to meet with my esteemed colleagues in the benevolent shadow of one of the most remarkable men in History – Frederick von Hohenstaufen.

REFERENCES

1. S. Fliszár, *J. Am. Chem. Soc.* **102**, 6946 (1980).
2. S. Fliszár, "Charge Distributions and Chemical Effects", Springer-Verlag, Heidelberg, New York, 1983.
3. R.P. Feynman, *Phys. Rev.* **56**, 340 (1939); T. Berlin, *J. Chem. Phys.* **19**, 208 (1951).
4. R.G. Parr and S.R. Gadre, *J. Chem. Phys.* **72**, 3639 (1980).

5. S. Fliszár, M. Foucrault, M.-T. Béraldin, and J. Bridet, *Can. J. Chem.* **59**, 1074 (1981).
6. N.H. March, *Adv. Phys.* **6**, 1 (1957).
7. R.G. Parr, S.R. Gadre, and L.J. Bartolotti, *Proc. Natl. Acad. Sci. USA.* **76**, 2522 (1979).
8. K. Ruedenberg, *J. Chem. Phys.* **66**, 375 (1977).
9. P. Politzer, *J. Chem. Phys.* **64**, 4239 (1976); **69**, 491 (1978).
10. P. Politzer and R.G. Parr, *J. Chem. Phys.* **61**, 4258 (1974); P. Politzer and R.G. Parr, *J. Chem. Phys.* **64**, 4634 (1976); S. Fliszár, *J. Chem. Phys.* **79**, 3874 (1983).
11. S. Fliszár, G. Del Re, and M. Comeau, *Can. J. Chem.* **63**, 3551 (1985).
12. S. Fliszár, G. Cardinal, and N. Baykara, *Can. J. Chem.* **64**, 404 (1986). S. Fliszár and G. Cardinal, *Can. J. Chem.* **62**, 2748 (1984). A. Peluso and S. Fliszár, *Can. J. Chem.* **66**, 2631 (1988).
13. A.P. Cox and S. Waring, *J. Chem. Soc. Faraday Trans. 2*, 5071 (1966).
14. D.A. Case, M. Cook, and M. Karplus, *J. Chem. Phys.* **73**, 3294 (1980).
15. S. Fliszár and C. Minichino, *Can. J. Chem.* **65**, 2495 (1987).
16. S. Fliszár and C. Minichino, *J. Phys. Colloque C4, Supp.9*, 367 (1987).
17. R.T. Sanderson, *J. Org. Chem.* **47**, 3835 (1982). R.T. Sanderson, "Chemical Bonds and Bond Energy", 2nd ed., Academic Press, New York, 1976.
18. V. Barone, C. Minichino, and S. Fliszár, manuscript in preparation.
19. S. Odier, "Fundamental Physics and Chemistry behind Molecular Crystal Detonations at a Microscopic Level", this volume. M. Peyrard, S. Odier, and M. Blain, *J. Chim. Phys.* **85**, 759 (1988).

STRUCTURE-SENSITIVITY RELATIONSHIPS IN ENERGETIC COMPOUNDS

J. S. MURRAY AND P. POLITZER

*Department of Chemistry
University of New Orleans
New Orleans, LA 70148*

ABSTRACT. Considerable progress has been made in understanding factors influencing the sensitivities of energetic molecules to outside stimuli such as shock, impact and heat. In this chapter, we discuss correlations between molecular properties and impact/shock sensitivity and also special cases that do not follow sensitivity relationships. For nitramines and nitroaliphatics, taken separately, we have shown that the strengths of all N-NO₂ linkages in these systems, in conjunction with overall molecular size, are important factors in determining their shock sensitivities. For nitroaromatics (excluding hydroxy derivatives) we have found a relationship between impact sensitivity and the electrostatic potential at the midpoint of the C-NO₂ bond, as approximated by atomic charges. We suggest that the high sensitivities of hydroxynitroaromatics may be due to the formation of small quantities of unstable nitronic acid tautomers.

1. Introduction

During the last two decades, there has been an accelerating effort to develop and understand the relationships between the molecular structures of energetic compounds and their sensitivities to specific stimuli, such as impact or shock. The driving force behind this effort has been a movement toward less sensitive munitions. Ideally, an explosive should be sensitive to a predetermined level of intentional stimuli, and completely insensitive to unwanted stimuli. Identifying intrinsic molecular features which correlate with the wide range of measured sensitivities provides a framework for the development of less sensitive systems through chemical modification of conventional explosives and the design and synthesis of non-conventional energetic materials.

In this chapter we will briefly survey some of the most commonly used measures of sensitivity, as well as some earlier correlations between sensitivity and molecular properties. This will provide a basis for further discussion of factors affecting sensitivities and the subsequent presentation of correlations developed in our laboratory. It is often the exceptions to structure-sensitivity relationships that offer the greatest promise in broadening our understanding of the reactivities of energetic compounds. Studies of several exceptional systems will be presented and discussed in the light of unique structural or reactive features which can account for their observed behavior.

2. Measures of Sensitivity

The sensitivity of an energetic molecule to external stimuli is a key property used in determining its potential applications and handling safety. It is defined in general terms as the ease with which a substance subjected to one of these stimuli can be made to undergo detonation. Many different kinds of sensitivity can and have been identified, depending on the nature of the stimulus causing detonation [1]; among these are heat, friction, impact, shock, and electrostatic charge. For example, thermal sensitivity refers to the combination of temperature and rate of heating that results in ignition. Differential scanning calorimetry measurements of some nitroaromatics have been made, and demonstrate that there is no simple relationship between their thermal stabilities and shock/impact sensitivities [2].

Impact and shock sensitivity are by far the most commonly used measures of an explosive's tendency to detonate. Impact tests (of which there are several, differing in detail but similar in principle) involve subjecting a sample of explosive material to the impact of a standard weight falling from varying heights [3,4]. The sensitivity is inversely proportional to the height at which there is a 50% probability of causing an explosion (50% impact height or h_{50}). Shock sensitivity is normally measured by a standard small scale gap test [5]. It is interpreted as being directly proportional to the maximum gap width through which a given shock wave generated by another explosive (e.g. RDX) will detonate the compound 50% of the time.

3. Some Earlier Correlations of Sensitivity and Molecular Properties

Correlations between impact sensitivity and chemical composition reported earlier by Kamlet and Adolph [3,4] are probably the most widely applied in the area of energetic materials research. These demonstrate that for families of high energy molecules with similar decomposition mechanisms (e.g. trinitromethyl, N-nitro and gem-dinitro compounds and nitroaromatics with and without α -CH linkages), there are approximately linear relationships between $\log h_{50}$ and OB_{100} ; the latter is a measure of "oxygen balance" in C-H-N-O explosives, as defined by eq. (1):

$$OB_{100} = \frac{100 (2n_O - n_H - 2n_C - 2n_{COO})}{M} \quad (1)$$

n_O , n_H and n_C represent the numbers of atoms of the respective elements in the molecule, n_{COO} is the number of carboxyl groups, and M is the molecular weight. The term "oxygen balance" refers to the amount of oxygen available for the combustion of the C and H atoms in the molecule to CO and H_2O . In these correlations, $\log h_{50}$ increases as OB_{100} decreases for any one family of molecules. Thus, the more impact sensitive explosives have the more positive OB_{100} values.

Numerous studies have been carried out with the aim of more specifically identifying molecular properties that relate to measures of sensitivity; many of these support the idea that the C-NO₂ and N-NO₂ bonds are of key importance in determining the sensitivities of nitro-containing energetic systems [6-13]. Nitroaromatics have been the focus of most of these studies [6,8-12]. Nitramines, however, are in general the more sensitive [1], and efforts are in progress to better understand the relationship between their structures and sensitivities.

Recent studies of secondary nitramines suggest that competing mechanisms of

decomposition are operative in these systems [13-19]. For example, in the thermolysis of RR'N-NO₂ systems, N-NO₂ bond cleavage is clearly the dominant process in some molecules, while competing reactions appear to be quite significant in other instances [13,15]. An infrared multiphoton dissociation study of hexahydro-1,3,5-trinitro-1,3,5-triazine (RDX) has reported that a concerted ring bond rupture is the dominant initial step in its thermal decomposition [16]. In contrast, a recent computational study of the thermal decomposition of 1,3-dinitro-1,3-diazacyclobutane using a vibrational analysis approach suggests that N-NO₂ bond breaking may be the preferred decomposition pathway [19].

In nitroaromatics, a striking structural correlation that has been observed is the decreasing sensitivity that accompanies an increase in the number of amine groups [4,20]. Though this effect was originally interpreted as being due to a strengthening of the ring carbon-carbon bonds [20], more recent theoretical studies suggest that the electron-donating amine groups actually strengthen the C-NO₂ bonds [9,21]. It has been shown in a group of trinitroaromatics that measures of both the total donating effect of the non-nitro substituents and the estimated bond strength of the weakest R-NO₂ bond correlate with impact sensitivity and with each other [9].

An interesting feature of aromatic C-NO₂ bonds that has been pointed out earlier is the presence of a buildup of positive electrostatic potential above and below the C-NO₂ bond region, the magnitude of which depends on the nature of the other substituents on the ring [21-24]. It has been shown (for nitrobenzene [22]) that this region can serve as an initial site for nucleophilic attack and thus may be a key factor in determining nitroaromatic chemical stabilities. A somewhat related parameter, V_{mid} , the electrostatic potential at the midpoint of the C-NO₂ bond as obtained from calculated atomic charges, has been empirically correlated with the sensitivities of a group of six nitroaromatics toward impact and shock [10]. V_{mid} is invariably positive for nitroaromatic C-NO₂ bonds, as a consequence of the calculated charges of the carbon and nitrogen atoms forming these bonds usually being positive. This suggests a certain degree of instability inherent in these bonds. It is also consistent with the rigorously computed buildups of positive electrostatic potential that are associated with C-NO₂ bond regions. That V_{mid} increases with increasing sensitivity toward shock and impact suggests that the properties of the C-NO₂ bonds are important in determining the stabilities of nitroaromatics to shock and impact.

Further supporting the idea that C-NO₂ and N-NO₂ bonds in energetic molecules are key factors in determining sensitivities to shock and/or impact are correlations between impact sensitivity and (a) the bond dissociation energy (E_{bond}) of the weakest bond, and (b) E_{bond} divided by detonation temperature in a group of nitroaromatics and nitramines [25]. The latter correlation is actually relating impact sensitivity to a quotient which can be viewed as the logarithmic term in a rate equation.

4. Factors Affecting Sensitivity

In view of the important role that the C-NO₂ and N-NO₂ bonds appear to play in triggering the decomposition of energetic materials [6-13,18,26,27], it may be anticipated that sensitivity will increase as the stability or strength of one or more of these bonds decreases. Within this framework, we have found it best to treat nitroaromatics, nitramines and nitroaliphatics separately, in our ongoing effort to develop relationships between molecular properties and sensitivities.

Looking first at nitroaromatics, we have extended our earlier work correlating V_{mid} and shock/impact sensitivity [10] to include a larger number of molecules. V_{mid} , the electrostatic potential at the midpoint of the C-NO₂ bond, is approximated by equation (2),

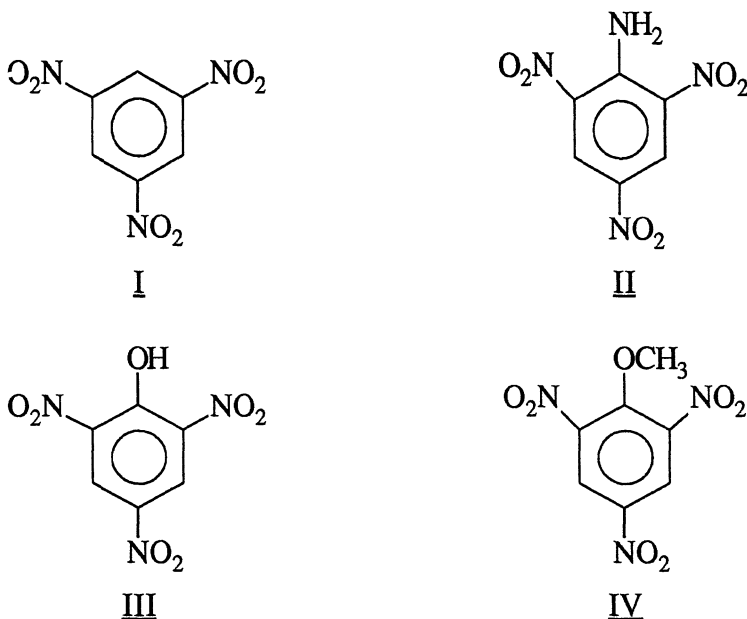
for a bond A-B:

$$V_{\text{mid}} = \frac{Q_A}{0.5R} + \frac{Q_B}{0.5R} \quad (2)$$

Q_A and Q_B are the charges on atoms A and B, obtained from the Mulliken population analysis [28] of the molecular orbital wave function; R is the A-B bond length in Å. The V_{mid} values for the C-NO₂ bonds in nitroaromatic molecules are taken to be indicative of the relative instabilities of the respective bonds; indeed eq. (2) is closely related to a bond energy expression that has been developed by Fliszar [29,30].

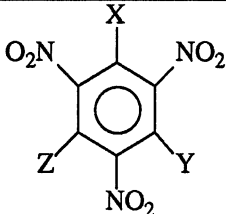
The GAUSSIAN programs [31-33] have been used to compute SCF-MO wave functions for twenty-six polynitroaromatics at the STO-5G level, using crystallographic geometries. The largest V_{mid} , or $V_{\text{mid,max}}$, of each of these molecules is listed in Table 1 along with its impact sensitivity. $V_{\text{mid,max}}$ does not invariably correspond to the longest C-NO₂ bond. Also included in Table 1 is $(1/R)_{\text{ave}}$, the average of the 1/R values of all the C-NO₂ bonds.

It is shown in Table 1 that trinitroaromatics with substituents that are strong resonance donors, such as -NH₂, -OH, -OCH₃ and -OC₂H₅, have $V_{\text{mid,max}}$ values that are less than that of 1,3,5-trinitrobenzene (**I**), which can be viewed as a reference molecule (since it has



only hydrogens as non-nitro substituents). This is consistent with the view that resonance donors strengthen C-NO₂ bonds by donating electronic density through resonance mechanisms, thereby diminishing the positive charges of the carbon and nitrogen atoms. There is an accompanying shortening of the C-NO₂ bonds, as indicated by structures **IIA** - **IIC** and by the increase in $(1/R)_{\text{ave}}$ compared to 1,3,5-trinitrobenzene, **I**. (See Table 1.) However the dominant effect is the decrease in the carbon and nitrogen charges, so that the net result is a lower $V_{\text{mid,max}}$ value.

TABLE 1. Properties of some nitroaromatics.

		Impact Drop Height ^a (cm)	V _{mid,max}	$\left(\frac{1}{R}\right)_{\text{ave}}, \text{Å}^{-1}$	Reference for Structure
X,Y,Z					
OH, OH, OH	(VI)	27	.143	.692	b
NH ₂ , OH, OH		32	.142	.698	c
CHO, H, H		36	.217	.675	c
NH ₂ , NO ₂ , H		41	.240	.683	d
OH, OH, H	(V)	43	.170	.685	b
CH ₂ Cl, H, H		44	.214	.675	b
CH ₂ OH, H, H		52	.217	.679	b
C ₂ H ₄ OH, H, H		68	.210	.678	b
OCH ₃ , Cl, Cl		75	.202	.677	b
Cl, H, H		79	.234	.672	e
COCH ₃ , H, H		79	.210	.678	b
OH, H, H	(III)	87	.203	.684	f
COOCH ₃ , H, H		90	.223	.680	b
H, H, H	(I)	100	.208	.675	g
COOH, H, H		109	.205	.675	h
OH, NH ₂ , NH ₂		112	.125	.699	i
OH, NH ₂ , H		138	.151	.688	h
CN, H, H		140	.213	.675	b
CH ₃ , H, H		160	.209	.678	j
NH ₂ , H, H	(II)	177	.174	.681	k
OC ₂ H ₅ , H, H		190	.198	.681	l
OCH ₃ , H, H	(IV)	192	.187	.679	m
OCH ₃ , OCH ₃ , H		251	.185	.678	b
NH ₂ , NH ₂ , H		320	.146	.689	n
OCH ₃ , NH ₂ , H		>325	.165	.685	b
NH ₂ , NH ₂ , NH ₂		>325	.103	.705	o

^a Impact sensitivity is measured as the height from which a given weight must be dropped on a compound to produce detonation fifty percent of the time. Thus, the smaller the value given, the more sensitive is the compound toward impact. These data are taken from reference 4.

^b Pierce-Butler, M. A. (1982) Acta Cryst. B38, 3097.

^c Gilardi, R., George, C. and Flippen-Anderson, J., Naval Research Laboratory, Washington, D.C.

^d Dickinson, C., Stewart, J. M. and Holden, J. R. (1966) Acta Cryst. B21, 663.

^e Willis, J. S., Stewart, J. H., Ammon, H. L., Preston, H. S., Gilyab, R. E. and Harris, P. M. (1971) Acta Cryst. B27, 786.

^f Duesler, E. N., Engelmann, J. H., Curtin, D. Y. and Paul, I. C. (1978) Cryst. Struct. Comm. 7, 449.

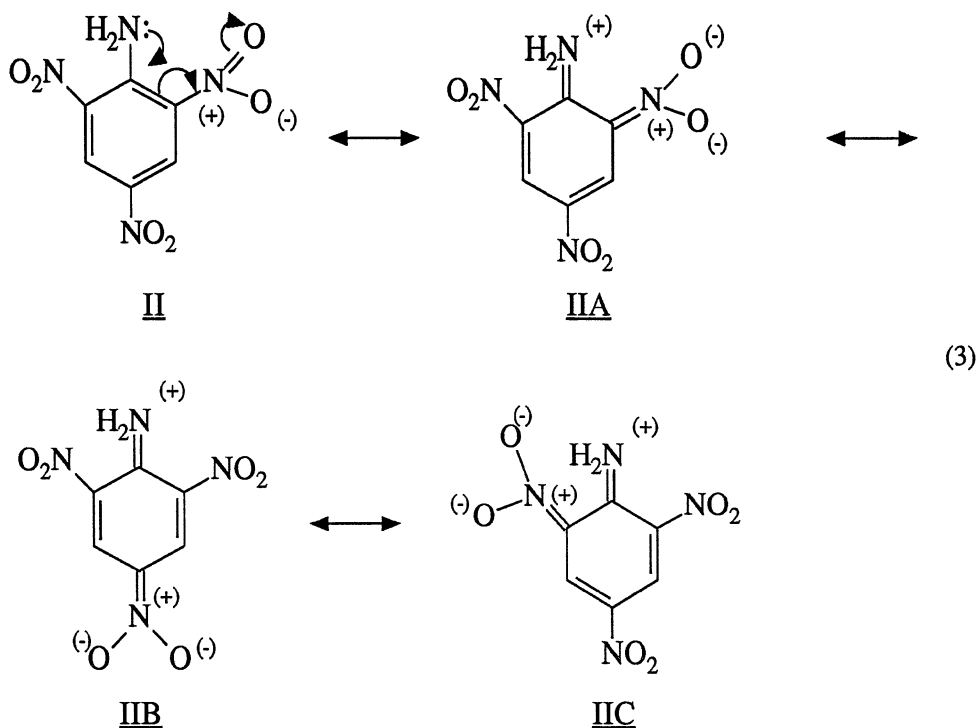
^g Choi, C. S. and Abel, J. E. (1972) Acta Cryst. B28, 193.

^h Rheingold, A. L., Department of Chemistry, University of Delaware.

(continued)

Footnotes for TABLE 1. (continued):

- i Bhattacharjee, S. K. and Ammon, H. L. (1981) *Acta Cryst.* B37, 2082.
 j Carper, W. R., Davis, L. P. and Extine, M. W. (1982) *J. Phys. Chem.* 86, 469.
 k Holden, J. R., Dikenson, C. and Bock, C. M. (1972) *J. Phys. Chem.* 76, 3597.
 l Gramaccioli, C. M., Destro, R. and Simonetta, M. (1968) *Acta Cryst.* B24, 129.
 m JBarnes, J. C., Chudek, J. A., Foster, R., Jarrett, F., Mackie, F., Paton, J. and Twiselton, D. R. (1984) *Tetrahedron*, 40, 1595.
 n Holden, J. R. (1967) *Acta Cryst.* B22, 545.
 o Cady, H. H. and Larson, A. C. (1965) *Acta Cryst.* B18, 485.



Amine substituents and alkoxy groups diminish the sensitivities of nitroaromatics toward impact (Table 1). Hydroxy nitroaromatics, however, are found to be very sensitive, even though -OH is a strong resonance donor and structures analogous to IIA - IIC can be drawn for III and the di- and trihydroxy derivatives, V and VI. This increase in sensitivity may reflect the formation of unstable nitronic acid tautomers [34]. We will elaborate upon this idea in the following section.

When the measured impact sensitivities are plotted against $V_{\text{mid,max}}$ for the molecules in Table 1, excluding those with one or more hydroxyl groups, the calculated correlation coefficient is 0.86 [35]. (The hydroxy derivatives have not been included because of their anomalous sensitivities.) This relationship suggests that the C-NO₂ bond with the greatest instability, as indicated by $V_{\text{mid,max}}$, may be a key bond involved in initiating detonation in

nitroaromatics subjected to impact. This is in agreement with the previously mentioned correlation between shock and/or impact sensitivity and the bond dissociation energy of the weakest C-NO₂ (or N-NO₂) bond [25]. It is noteworthy that nitroaromatics bearing α -CH linkages do not need to be treated separately, as was necessary in Kamlet's OB₁₀₀ correlations [4]. As a final point of interest, neither the quantity $(1/R)_{ave}$ nor $1/R_1$, where R_1 is the length of the longest C-NO₂ bond, is found to correlate with impact sensitivity for the eighteen molecules included in Figure 1. This is suggestive of $V_{mid,max}$ representing a more fundamental property related to instability of C-NO₂ bonds than simply their bond distances.

In considering the sensitivities of nitramines, the overall consensus is that cleavage of the N-NO₂ bond plays an important role in their decomposition [7,13,15], although alternative pathways exist and in some cases appear to predominate [13,16-18]. A qualitative relationship has been reported between the length of the N-N bond, the average frequency of the NO₂ asymmetric stretching vibration, and the amount of NO₂ evolved during rapid thermolysis [13].

Table 2 lists shock sensitivities and certain structural properties for a group of seven nitramines. As for the nitroaromatics, no relationship exists between shock sensitivity and either R_1 or R_{ave} , where R_1 is the longest N-NO₂ bond and R_{ave} is the average length of all the N-NO₂ bonds.

A good correlation can be obtained, however, by (a) explicitly accounting for each N-NO₂ bond, and (b) recognizing that the effectiveness of each in initiating decomposition is "diluted" as the molecule becomes larger [36]. These considerations are presented in a straightforward manner below:

$$\text{Sensitivity} \sim \frac{1}{M} \sum_{i=1}^n \frac{1}{R_i} = \frac{1}{M} \sum_{i=1}^n R_i = \frac{n}{M} (R_{ave}) \quad (4)$$

n is the number of N-NO₂ linkages in the molecule, having N-N distances R_i , and M is the molecular weight, which is taken as a measure of molecular size.

A plot of measured shock sensitivity versus the quantity $(n/M) R_{ave}$ for the seven molecules listed in Table 2 has been presented elsewhere [36]. A good linear relationship was found, with a correlation coefficient of 0.94. The wide variety of structural types included in this correlation is encouraging; they include both cyclic and aliphatic systems, with differing numbers of N-NO₂ groups.

The success of this nitramine shock sensitivity relationship [Table 2 and eq. (4)] prompted us to investigate whether eq. (4) would serve also for nitroaliphatics. Table 3 lists shock sensitivities and some structural parameters for five nitroaliphatics. Again, no correlation was found to exist between shock sensitivity and either R_1 or R_{ave} , where R_1 and R_{ave} are, respectively, the longest C-NO₂ distance and the average of all C-NO₂ (and N-NO₂) bond lengths in the molecule. However, an excellent correlation between shock sensitivity and the quantity $(n/M)R_{ave}$ was found, with a linear correlation coefficient of 0.98 [36].

The correlations that have been discussed [eqs. (2) and (4)] reflect our current views on factors affecting the sensitivities of nitroaromatics, nitramines and nitroaliphatics. Our results suggest that the strengths of all the N-NO₂ and C-NO₂ bonds in nitramines and nitroaliphatics, respectively, taken in conjunction with the overall size of the molecule, help to determine their shock sensitivities [see eq. (4)]. Nitroaromatics, however, must be treated differently; their impact sensitivities do not follow eq.(4). With the exception of hydroxynitroaromatics, a reasonable correlation is found between $V_{mid,max}$ and impact

TABLE 2. Some Nitramine Properties.

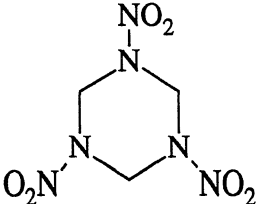
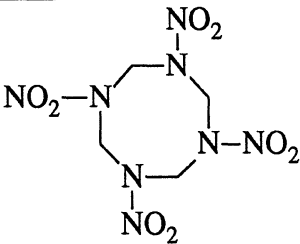
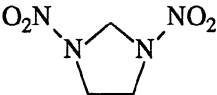
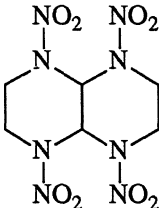
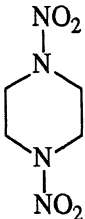
Molecule	Shock Sens. ^a	M g/mole	R ₁ ^b , A	R _{ave} , A	$\frac{n}{M} R_{ave} \times 10^2$
<u>VII.</u>					
	2.5	222	1.393 ^c	1.379	1.86
<u>VIII.</u>					
	2.23	296	1.373 ^d	1.362	1.84
<u>IX.</u>					
	2.17	162	1.410 ^e 1.346 ^f	1.354 1.344	1.67 1.66
<u>X.</u>					
	2.02	322	1.417 ^g	1.414	1.76
<u>XI.</u>					
	1.64	176	1.373 ^f	1.373	1.56

TABLE 2 Some nitramines properties (continued).

Molecule	Shock Sens. ^a	M g/mole	R ₁ ^b , Å	R _{ave} , Å	$\frac{n}{M} R_{ave} \times 10^2$
XII.					
(NC-CH ₂) ₂ N-NO ₂	1.35	140	1.371 ^f	1.371	0.98
XIII.					
(NC-CH ₂ CH ₂) ₂ N-NO ₂	<0.5 ^h	168	1.355 ^f	1.355	0.81

^a Spivak, T., Betancourt, D., O'Connor, J., NSWC TR 88-282, in press. The report will be available from Defense Technical Information Center, Cameron Station, Alexandria, VA 22134. The values are given in inches, and refer to the maximum distance over which a given shock wave will cause detonation. The greater the distance, the more sensitive is the compound.

^b R₁ is the longest N-NO₂ (or C-NO₂) bond length in the molecule.

^c Crystal structure: Choi, C. S. and Prince, E. (1972) Acta Cryst. B28, 2857.

^d Crystal structure (β-HMX): Choi, C. S. and Boutin, H. P. (1970) Acta Cryst. B26, 1235.

^e Crystal structure: Personal communication, Rheingold, A. L. (Department of Chemistry, University of Delaware).

^f 3-21G optimization.

^g Crystal structure: Naval Weapons Center Report TP 6681 (China Lake, CA).

^h The experimentally-determined shock sensitivity was given as <0.5. In preparing Figure 1, we used 0.5 as the value.

sensitivity. This suggests that the instability of the weakest C-NO₂ linkage in nitroaromatics is essential in initiating decomposition induced by impact.

5. Special Cases

5.1. HYDROXYNITROAROMATICS

The contrasting effects of -NH₂ (and -OR) and -OH groups on the impact sensitivities of nitroaromatics have been mentioned earlier and can be seen in Table 1. For example, 1,3,5-trihydroxy-2,4,6-trinitrobenzene (**VI**) is the most sensitive compound listed, while its triamino analogue is so insensitive that its impact height cannot even be measured by the standard impact test.

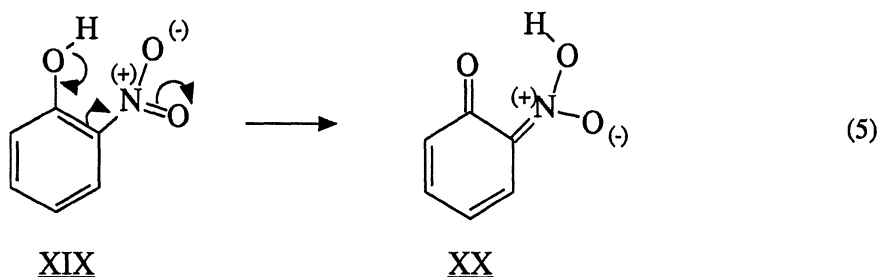
The anomalous observed sensitizing effect of the hydroxyl group in nitroaromatics has been the focus of a recent computational study [34]. It is indicated by crystallographic data that hydrogen bonding occurs between the hydroxyl and an ortho nitro group in picric acid, **III** [37]. The O - - O separation of 2.55 Å is near the shorter end of the range that is typical of O-H - - O hydrogen bonds (2.50 - 2.80 Å) [38]. We have accordingly used an *ab initio* self-consistent-field approach (GAUSSIAN 86 [32]) to investigate the possibility of some significant probability of hydrogen migration occurring in o-nitrophenol, **XIX**, which is

TABLE 3. Properties of some nitroaliphatics

Molecule	Shock Sens. ^a	M g/mole	R _l ^b , Å	R _{ave} , Å	$\frac{n}{M} R_{ave} \times 10^2$
<u>XIV</u>					
$[C(NO_2)_3CH_2O]_2C=O$	2.30	388	1.543 ^c	1.514	2.34
<u>XV</u>					
$ \begin{array}{c} NO_2 \quad CH_3 \\ \quad \\ H_3C-C-CH_2-N-NO_2 \\ \\ NO_2 \end{array} $	2.11	208	1.506 (C-N) ^d 1.418 (N-N) ^d	1.477	2.13
<u>XVI</u>					
$ \begin{array}{c} OH \\ \\ C(NO_2)_3CH_2CH_2C=O \end{array} $	2.03	223	1.556 ^e	1.534	2.06
<u>XVII</u>					
$[H_3CC(NO_2)_2CH_2O]_2C=O$	1.51	326	_____	1.514 ^f	1.86
<u>XVIII</u>					
$ \begin{array}{c} OH \\ \\ H_3CC(NO_2)_2CH_2CH_2C=O \end{array} $	1.30	192	_____	1.534 ^f	1.60

^a See footnote a, Table 2.^b R_l is the longest C-NO₂ (or N-NO₂) bond length in the molecule.^c Crystal structure: Personal communication, Rheingold, A. L. (Department of Chemistry, University of Delaware).^d 3-21G optimization.^e Crystal structure: Bock, C. M. (1970) Amer. Cryst. Assoc. (Winter), 41.^f The R_{ave} values for XVII and XVIII are taken from XIV and XV, respectively. We have found in earlier work that C-NO₂ distances in aliphatic compounds are very little affected by geminal substituents. See, for example, Politzer, P. and Lane, P., Struct. Chem., in press.

taken as a model for III [34]. This tautomerism is shown in equation (5). XX is a nitronic acid; these are known to be reactive and unstable [39]. Recent experimental

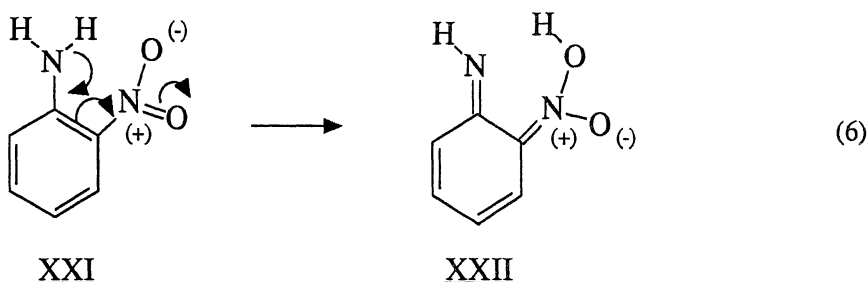


studies have linked the sensitization and decomposition of nitroalkanes to the presence of nitronate anions [40-43].

At the 3-21G level, the nitronic acid tautomer XX is calculated to be 15 kcal/mole higher in energy than XIX [34]. We speculate that the corresponding energy difference for picric acid (III) and its nitronic acid tautomer may be slightly smaller than this; the presence of three strongly electron-withdrawing nitro groups in III makes the hydroxyl hydrogen more positive than in XIX, and likely to be more easily transferred.

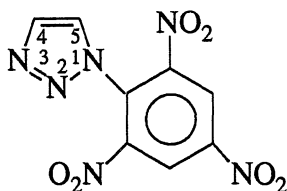
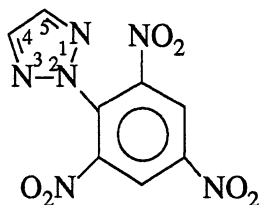
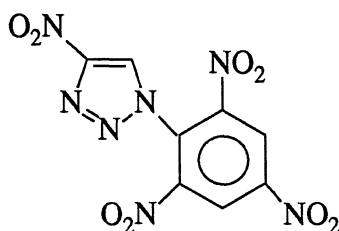
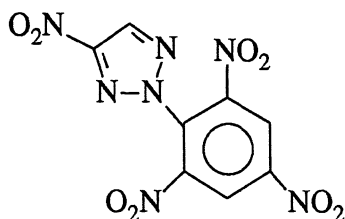
Our calculated structural data indicate that the hydroxyl proton in XIX has to move only a relatively short distance (<1.0 Å) to reach its position in XX. Such a positional transfer could result from a vibrational excitation of the O-H bond. We suggest that the anomalously high and increasing sensitivities of III, V, and VI may be due to some significant fraction of each forming unstable nitronic acid tautomers. These could presumably result from the energy input associated with shock or impact being transferred to vibrational modes.

The possibility of a proton transfer analogous to eq. (5) occurring for o-nitroaniline (XXI) has also been investigated, in light of the contrasting effects of -OH and -NH₂ groups on sensitivity. Despite exhaustive computational efforts, an energy minimum corresponding to XXII was not found [34]. This suggests that there is no tendency for nitronic acid tautomers to form in aminonitroaromatics, and points out a major difference between the amino- and hydroxynitroaromatics that may in part account for their contrasting sensitivities.



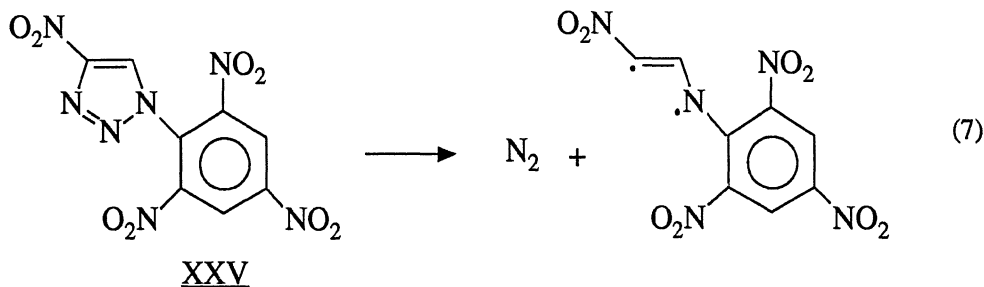
5.2. PICRYL TRIAZOLES

The isomeric pairs 1-picryl-1,2,3-triazole (XXIII), 2-picryl-1,2,3-triazole (XXIV) and 4-nitro-1-picryl-1,2,3-triazole (XXV), 4-nitro-2-picryl-1,2,3-triazole (XXVI) show a wide

XXIII (11 cm)XXIV (200 cm)XXV (9 cm)XXVI (67 cm)

range of impact sensitivities, but have fairly similar detonation properties [44,45]. (The measured impact heights for XXIII - XXVI are given under each structure and are compatible with those in Table 1.) Clearly, a stoichiometric sensitivity relationship such as Kamlet's OB₁₀₀ correlation [4] would predict the same sensitivity for each member of these and other isomeric pairs. A recent experimental/theoretical study by Storm et al [45] has assessed the likely basis for the differences in sensitivities of XXIII and XXIV, and XXV and XXVI, as being structural.

Storm et al report that the primary structural difference between the 1-picryl and 2-picryl isomers is in the various N₁-N₂-N₃-C₄ bond lengths of the triazole rings. The N₂-N₃ bond distances in XXIII and XXV are both experimentally and computationally found to be about 0.03 Å shorter than those in XXIV and XXVI [45], suggesting that the loss of nitrogen may conceivably be a possibility in the decomposition of the 1-picryl isomers.



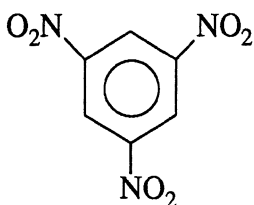
Indeed, AM1 calculations for the reaction of XXV to form N_2 and the biradical shown in equation (7) report a heat of reaction significantly less than that for C- NO_2 bond cleavage [44]. It has therefore been suggested that a facile loss of N_2 in the 1-picryl isomers XXIII and XXV, but not the 2-picryl, may account for their differing impact sensitivities.

5.3. ALKYL-SUBSTITUTED NITROAROMATICS: THERMAL STABILITY VERSUS IMPACT SENSITIVITY

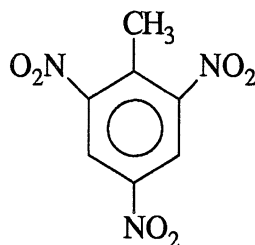
The thermal decomposition of 2,4,6-trinitrotoluene (TNT, XXVII) has been a subject of interest in energetic materials research for more than half a century [4,12,46-58]. It is known that XXVII is thermally unstable relative to 1,3,5-trinitrobenzene (I), which can be viewed as a reference molecule [4]. The former self-ignites between 200 and 210°C, while the latter is stable at 300°C for extended periods of time [4].

In spite of the numerous studies carried out so far, there is as yet no simple or definitive explanation of the presumably complex processes occurring during the thermal decomposition of XXVII. The overall consensus, however, is that C- NO_2 bond breaking, which appears to be the main decomposition pathway in many nitroaromatics, is not the primary process for XXVII [4,12,46-58]. In agreement with this, a recent single-pulse shock tube study reports that the primary decomposition pathway in o-nitrotoluene, as yet not elucidated, does not involve C- NO_2 bond breaking [57]. This is consistent with other studies which support the conclusion that the thermal instability of XXVII is due to a distinct change in reaction mechanism [4,53,54,56-58], possibly involving the methyl group and its labile α -hydrogens [4,54,56,58].

The difference in the thermal stabilities of XXVII and I is quite intriguing, particularly because it is the reverse of their impact sensitivities; XXVII is less sensitive to impact than I! In fact, it is found in general that unsubstituted alkyl groups have a desensitizing effect on the trinitrobenzene framework. The impact heights of I, 2,4,6-trinitrotoluene (XXVII), 2,4,6-trinitrocumene (XXVIII) and 1-picrylpropane (XXIX) increase in the order listed, denoting decreasing sensitivity. (The measured impact heights are given under each structure. These were not measured with the same test as those in



I (39 cm)



XXVII (72 cm)

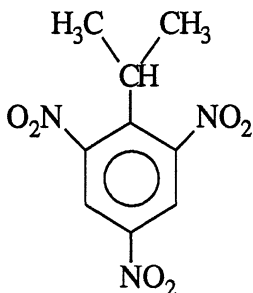
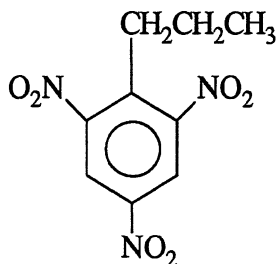
XXVIII (93 cm)XXIX (222 cm)

Table 1 and the two sets of results should not be compared to each other; 222 cm is the upper limit of this impact height test [59].)

Alkyl groups are generally thought to be slightly electron-donating in aromatic systems, as indicated for example by Taft's substituent constants [60]. Thus, that XXVII - XXIX are less sensitive than I is consistent with the observation that electron-donating groups (with the exception of -OH) are in general desensitizing. However, the pronounced decrease in impact sensitivity in the n-propyl substituted molecule, XXIX, is likely due to other factors, not yet identified.

This discussion has pointed out that the thermal stabilities and the impact sensitivities of 1,3,5-trinitrobenzene and alkyl-substituted nitroaromatics do not follow the same trends. While alkyl groups tend to desensitize the trinitrobenzene ring toward impact, they also increase its sensitivity to heat and subsequent thermal decomposition. We are currently investigating the basis for these opposing tendencies.

6. Summary

The search for a better understanding of which molecular properties are important in determining the sensitivities of energetic materials to outside stimuli is an important aspect of high energy materials research, and reflects a movement toward the development of less sensitive munitions. Although the likelihood of establishing an unequivocal universal structure-sensitivity relationship covering all types of energetic materials is indeed questionable, considerable progress has been made in understanding factors which influence sensitivity within separate classes of highly energetic systems.

Kamlet's correlations between $\log h_{50}$ and OB_{100} for families of high energy molecules with similar decomposition mechanisms [3,4] provide a stoichiometric means of assessing the impact sensitivities of a wide range of systems. Our recent shock sensitivity relationship for nitramines and nitroaliphatics [36] permits a broad predictive capability and also gives insight into how factors such as the number of N-NO₂ and C-NO₂ linkages, their relative strengths and the overall molecular size influence shock sensitivity. The relationship presented between $V_{mid,max}$ and impact sensitivity for a group of eighteen nitroaromatics suggests that the instability associated with the weakest C-NO₂ linkage in nitroaromatics may be a key factor involved in the initiation of decomposition by impact.

These two correlations reflect the importance, in general, of C-NO₂ and N-NO₂ bonds in determining sensitivity to impact and shock.

Molecules which do not fit the existing correlations suggest starting points for further investigations aimed at elucidating the basis for their exceptional behavior. This, in fact, has been the driving force for studies of hydroxynitroaromatics and picryl triazoles. From the results of a computational analysis, we have suggested that the high sensitivities of hydroxynitroaromatics may be due to the formation of small quantities of unstable nitronic acid tautomers [34]. The differing impact sensitivities of the isomeric pairs 1-picryl- and 2-picryl-1,2,3-triazole and 4-nitro-1-picryl- and 4-nitro-2-picryl-1,2,3-triazole have been attributed to a structural difference between the 1-picryl and 2-picryl pairs which allows for a facile loss of nitrogen in the 1-picryl isomers but not the 2-picryl [45]. The basis for the opposing trends in thermal stability and impact sensitivity between 1,3,5-trinitrobenzene and alkyl-substituted nitroaromatics is the focus of current research and remains to be elucidated.

7. Acknowledgements

We greatly appreciate the financial support provided by the Naval Surface Warfare Center, Dalgren, VA, through contract #N60921-86-C-0217, the Army Armament Research Development and Engineering Center, through the Battelle Scientific Services Program, Delivery Order # 1219, the Air Force Armament Laboratory, Eglin AFB, through contracts FO8635-87-C-0090 and FO8635-87-C-0127 and the Office of Naval Research through contract # N00014-85-K-0217.

8. References

1. Iyer, S. and Slagg, N. (1988) Structure and Reactivity (Molecular Structure and Energetics); Liebman, J. F.; Greenberg, A., eds.; VCH Publishers: New York, Ch. 7.
2. Weinstein, D. and Owens, F. J. unpublished data.
3. Kamlet, M. J. (1976) The Relationship of Impact Sensitivity with Structure of Organic High Explosives. I. Polynitroaliphatic Explosives, Proceedings 6th Symposium (International) on Detonation, San Diego, CA, Aug. 24-27, ONR Report ACR 221, p. 312.
4. Kamlet, M. J. and Adolph, H. G. (1979) Propellants Explosives Pyrotech. 4, 30.
5. Price, D. and Liddiard, Jr., T. P. (1966) 'The Small Scale Gap Test: Calibration and Comparison with Large Scale Gap Test,' NOLTR 66-87.
6. Sharma, J. and Owens, F. J. (1979) Chem. Phys. Lett. 61, 280.
7. Dubovitskii, F. I. and Korsunskii, B. L. (1981) Russ. Chem. Rev. 50 (10), 958.
8. Sharma, J., Garrett, W. L., Owens, F. J. and Vogel, V. L. (1982) J. Phys. Chem. 86, 1657.
9. Owens, F. J. (1985) J. Mol. Struct. (THEOCHEM) 121, 213.
10. Owens, F. J., Jayasuriya, K., Abrahmsen, L. and Politzer, P. (1985) Chem. Phys. Lett. 116, 434.
11. Owens, F. J. and Sharma, J. (1985) J. Appl. Phys. 51, 1494.
12. Gonzalez, A. C., Larson, C. W., McMillen, D. F. and Golden, D. M. (1985) J. Phys. Chem. 89, 4809.
13. Brill, T. B. and Oyumi, Y. (1986) J. Phys. Chem. 90, 2679.

14. Bulusu, S., Weinstein, D. I., Autera, J. R. and Velicky, R. W. (1986) *J. Phys. Chem.* 90, 4121.
15. Oyumi, Y. and Brill, T. B. (1988) *Propellants, Explosives and Pyrotechnics* 13, 69.
16. Zhao, X., Hints, E. J. and Lee, Y.T. (1988) *J. Chem. Phys.* 88, 801.
17. Sumpter, B. G. and Thompson, D. L. (1988) *J. Chem. Phys.* 88, 6889.
18. Saxon, R. P. and Yoshimine, M. (1989) *J. Phys. Chem.* 93, 3130.
19. Grodzicki, M., Seminario, J. M. and Politzer, P. unpublished work.
20. Dodson, B. W. and Graham, R. A. (1982) in Nellis, W. J., Seaman, L. and Graham, R. A. (eds.) *Shock Waves in Condensed Materials*, American Institute of Physics, New York.
21. Politzer, P., Abrahmsen, L. and Sjoberg, P. (1984) *J. Amer. Chem. Soc.* 106, 855.
22. Politzer, P., Laurence, P. R., Abrahmsen, L., Zilles, B. A. and Sjoberg, P. (1984) *Chem. Phys. Lett.* 111, 75.
23. Politzer, P., Jayasuriya, K., Sjoberg, P. and Laurence, P. R. (1985) *J. Amer. Chem. Soc.* 107, 1174.
24. Murray, J. S., Lane, P. and Politzer, P. unpublished results.
25. Nielsen, A. T. (1987) in Report on Working Group Meeting on Sensitivity of Explosives, Army Research Office, Socorro, NM, March 15-18, p. 256.
26. Gonzalez, A. C., Larson, C. W., McMillen, D. F. and Golden, D. M. (1985) *J. Phys. Chem.* 89, 4809.
27. Tsang, W., Robaugh, D. and Mallard, W. G. (1986) *J. Phys. Chem.* 90, 5968.
28. Mulliken, R. S. (1955) *J. Chem. Phys.* 23, 1833.
29. Fliszar, S. (1980) *J. Am. Chem. Soc.* 102, 6946.
30. Fliszar, S. (1983) *Charge Distribution and Chemical Effects*, Springer-Verlag, Heidelberg, New York.
31. Binkley, J. S., Frisch, M. J., DeFrees, D. J., Krishnan, R., Whiteside, R. A., Schlegel, H. B., Fluder, E. M. and Pople, J. A. GAUSSIAN 82, Carnegie-Mellon Quantum Chemistry Publishing Unit, Pittsburgh, PA, 15213.
32. Frisch, M. J., Binkley, J. S., Schlegel, H. B., Raghavachari, K., Melius, C. F., Martin, R. L., Stewart, J. J. P., Bobrowicz, F. W., Rohlfing, C. M., Kahn, L. R., DeFrees, D. J., Seeger, R., Whiteside, R. A., Fox, D. J., Fleuder, E. M. and Pople, J. A. (1984) Carnegie-Mellon Quantum Chemistry Publishing Unit, Pittsburgh, PA.
33. Frisch, M. J., Head-Gordon, M., Schlegel, H. B., Raghavachari, K., Binkley, J. S., Gonzalez, C., Defrees, D. J., Fox, D. J., Whiteside, R. A., Seeger, R., Melius, C. F., Baker, J., Martin, R., Kahn, L. R., Stewart, J. J. P., Fluder, E. M., Topiol, S. and Pople, J. A., (1988) GAUSSIAN 88, Gaussian Inc., Pittsburgh, PA.
34. Politzer, P., Seminario, J. M. and Bolduc, P. R. (1989) *Chem. Phys. Lett.* 158, 463.
35. Murray, J. S., Lane, P., Politzer, P. and Bolduc, P. R. unpublished work.
36. Politzer, P., Murray, J. S., Lane, P., Sjoberg, P. and Adolph, H., *J. Phys. Chem.*, submitted.
37. Duesler, E. N., Engelmann, J. H., Curtin, D. Y. and Paul, I. C. (1978) *Cryst. Commun.* 7, 449.
38. Pauling, L. (1960) *The Nature of the Chemical Bond*, 3rd. Ed. Cornell Univ. Press, Ithaca, section 12-6.

39. Nielsen, A. T. (1969) in Feuer, H., (ed) *The Chemistry of the Nitro and Nitroso Groups*, Part 1, Interscience, New York, Ch. 7.
40. Engelke, R., Earl, W. L. and Rohlfing, C. M. (1986) *J. Chem. Phys.* 84, 142.
41. Engelke, R., Earl, W. L. and Rohlfing, C. M. (1986) *Int. J. Chem. Kinetics* 90, 545.
42. Engelke, R., Earl, W. L. and Rohlfing, C. M. (1986) *Int. J. Chem. Kinetics* 18, 1205.
43. Engelke, R., Schiferl, D., Storm, D. B. and Earl, W. L. (1988) *J. Phys. Chem.* 92, 6815.
44. Neuman, P. N. (1971) *J. Heterocycl. Chem.* 8, 51.
45. Storm, C. B., Ryan, R. R., Ritchie, J. P., Hall, J. H. and Bachrach, S. M. (1989) *J. Phys. Chem.* 93, 1000.
46. Robertson, R. (1921) *J. Chem. Soc.* 119, 1.
47. Urbanski, T. and Rychter, S. (1939) *C.R.Acad. Sci.* 208, 900.
48. Robertson, A. J. B. (1948) *Trans Faraday Soc.* 44, 977.
49. Cook, M. A. and Abegg, M. T. (1956) *Ind. Eng. Chem.* 48, 1090.
50. Wenograd, J. (1961) *Trans. Faraday Soc.* 57, 1612.
51. Zinn, J. and Rogers, R. N. (1962) *J. Phys. Chem.* 66, 2646.
52. Enig, J. W. and Petrone, F. J. (1966) *Phys. Fluids* 9, 398.
53. Rogers, R. N. (1967) *Anal. Chem.* 39, 730.
54. Dacons, J. C., Adolph, H. G. and Kamlet, M. J. (1970) *J. Phys. Chem.* 74, 3035.
55. Shackelford, S. A., Beckmann, J. W., and Wilkes, J. S. (1977) *J. Org. Chem.* 42, 4201.
56. Turner, A. G. and Davis, L. P. (1984) *J. Amer. Chem. Soc.* 106, 5447.
57. Tsang, W., Robaugh, D. and Mallard, W. G. (1986) *J. Phys. Chem.* 90, 5968.
58. Cox, J. R. and Hillier, I. H. (1988) *Chem. Physics* 124, 39.
59. These data were obtained from the Air Force Armament Laboratory, Eglin, AFB (FL).
60. Charton, M. (1981) in Taft, R. W. (ed) *Progress in Physical Organic Chemistry*, Wiley, New York, Vol. 13, p. 119.

COMPUTATIONAL STUDIES OF ENERGETIC NITRAMINES

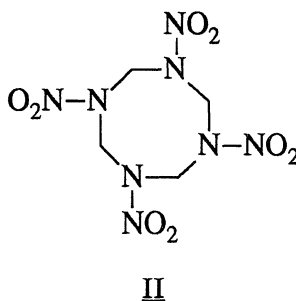
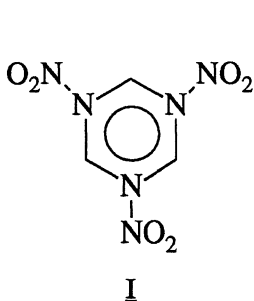
J. S. MURRAY AND P. POLITZER

*Department of Chemistry
University of New Orleans
New Orleans, LA 70148*

ABSTRACT. Computed properties of secondary nitramines are surveyed with regard to fundamental interest and possible relation to impact/shock sensitivity and thermal stability. An *ab initio* SCF approach was used to compute optimized structures and properties. The replacement of carbons by nitrogens in aliphatic and alicyclic systems is found to provide added stability, attributed to lone pair σ -conjugation; this is amplified by NO_2 substitution on these nitrogens. The negative electrostatic potentials characteristic of amine lone pairs are greatly weakened in nitramines; these changes increase as the amine nitrogens approach planarity and the $\text{N}-\text{NO}_2$ bonds become shorter (presumably stronger). A good correlation with nitramine shock sensitivity was obtained, based on the strengths of all $\text{N}-\text{NO}_2$ bonds and overall molecular size. An analysis of dissociation pathways for 1,3-dinitro-1,3-diazacyclobutane shows $\text{N}-\text{NO}_2$ bond cleavage favored over ring opening. While the thermal, shock and impact sensitivities may be determined primarily by decomposition pathways requiring the least energy input, e.g. $\text{N}-\text{NO}_2$ bond breaking, energetic performance may depend upon channels with energy barriers, e.g. ring opening.

1. Introduction

Energetic secondary nitramines are currently a subject of increasing interest in high energy materials research [1-15]. This surely reflects the fact that two of the most effective (yet highly sensitive) military secondary explosives are nitramines, namely 1,3,5-trinitro-1,3,5-triazacyclohexane (RDX, **I**) and 1,3,5,7-tetranitro-1,3,5,7-tetraazacyclooctane (HMX, **II**)



[16,17]. Of particular importance are efforts aimed at gaining insight into how molecular features of nitramines influence their detonation properties and sensitivities to stimuli such as heat, shock and impact. A better understanding of such key properties will provide a

framework for the design and development of systems with improved performance and/or reduced sensitivities.

Computational approaches play an important role in the study of energetic molecules, since they permit both existing and proposed systems to be analyzed and evaluated. In this chapter we will initially discuss methodology as related to our general computational approach. Our focus thereafter will be on specific calculated properties of particular importance in our study of energetic nitramines: (a) the significance and properties of amine nitrogen lone pairs; (b) the effect of nitro groups upon amine lone pairs; (c) the added stability imparted by aza nitrogens and N-nitro groups in aliphatic and alicyclic systems; (d) the geometries of amine nitrogens (pyramidal versus planar); and (e) properties of N-NO₂ bonds. Finally, we will discuss how some of these factors relate to measures of sensitivity and recent studies of thermal decomposition.

2. Computational Methods

2.1. GENERAL

In our ongoing study of energetic systems, we use primarily an *ab initio* self-consistent-field (SCF) molecular orbital approach utilizing the GAUSSIAN programs [18-20] to compute wave functions and specific properties of interest. In this section we will discuss geometry optimizations and the importance of understanding basis set effects in computational work.

Geometry optimizations are carried out for molecules of interest to obtain structural data. Gradient methods [21-24] are currently used for this purpose by the GAUSSIAN programs. From an initial geometry and wave function, the forces on the nuclei are computed by taking partial derivatives of the energy with respect to the nuclear coordinates. Then from this knowledge of the forces on the nuclei and using force constants obtained as second derivatives of the energy with respect to distance and angle, predicted changes in all geometrical parameters being varied are determined, and made simultaneously. This procedure is repeated until the net forces on all nuclei are essentially zero, as must be the case at equilibrium. The resulting optimized geometry does depend somewhat on the nature of the basis set used in the optimization, as shall be discussed.

The GAUSSIAN programs contain sets of internally stored standard basis sets, which can be classified into three main categories [25]: (1) minimal, (2) split valence, and (3) split valence plus polarization. Minimal basis sets contain one Slater-type function per atomic orbital; to simplify the computations, it is expanded in terms of gaussian functions. The designation used is STO-nG, an abbreviation for "Slater-type orbital approximated by a linear combination of n gaussian functions". The split valence basis sets, written as n-lmG, represent each valence atomic orbital by two sets of gaussian functions, designated as outer and inner, and each core atomic orbital by one set. n, l and m are the numbers of gaussians in the core, outer and inner valence sets of functions, respectively. The coefficients of the inner and outer valence basis functions are varied independently during construction of the molecular orbitals in the SCF procedure, allowing the size of the atomic orbitals that contribute to the molecular orbitals to vary. This feature is not possible with a minimal basis set.

The addition of "polarization" functions, which are d-orbital type basis functions, permits greater flexibility in the calculated charge distribution and can be added to both minimal and split valence basis sets. Their inclusion is designated by an asterisk. They are most commonly added to split valence basis sets; the most widely used of these is the 6-31G*.

Since the number of integrals evaluated in an SCF calculation increases as N⁴, where N is the number of gaussian functions, the choice of a basis set for any specific project must be made with accuracy, computational cost and speed in mind. For very large systems, a

minimal basis set is the only option. The STO-3G basis has been shown to give fairly good geometries for many classes of molecules [26]; its major limitation is that it and other minimal basis sets do not have the flexibility to properly represent all resonance interactions, such as those involving amine and nitro groups [25].

The simplest split valence basis set, the 3-21G, is in general quite effective for providing good geometries [27,28]. We have used it extensively for geometry optimizations in our studies of nitramines [10,13,14]. However, split valence basis sets tend to overestimate bond angles around atoms having lone pairs of electrons, such as nitrogen and oxygen [28,29]. An extreme example of this effect is seen in the case of nitramide (H_2NNO_2), which the 3-21G basis predicts erroneously to have a planar equilibrium structure [30,31]. Addition of polarization functions corrects this overestimation of bond angles [28,29,31], but can be computationally impractical for large molecules. It is important to note, however, that the 3-21G basis does show a range of pyramidal characters for amine nitrogens in other noncyclic and cyclic nitramines [10,13,14].

One cannot assume that a basis set which gives an improved energy will also be better for calculating structural properties [28,32,33]. For example, it is found that the addition of polarization functions to split valence basis sets results in decreased bond lengths, often to distances considerably shorter than what is found experimentally [28]. It is therefore important to carefully consider what the key properties of interest are for each particular study, and to choose the basis set accordingly within the limitations set by the computational facilities.

2.2. CALCULATED PROPERTIES

2.2.1. The Electrostatic Potential. The nuclei and electrons of a molecule create a potential $V(\mathbf{r})$ in the surrounding space, expressed rigorously by equation (1):

$$V(\mathbf{r}) = \sum_A \frac{Z_A}{|\mathbf{R}_A - \mathbf{r}|} - \int \frac{\rho(\mathbf{r}') d\mathbf{r}'}{|\mathbf{r}' - \mathbf{r}|} \quad (1)$$

Z_A is the charge on nucleus A, located at \mathbf{R}_A , and $\rho(\mathbf{r})$ is the electronic density function, which we compute from the molecular wave function. $V(\mathbf{r})$ is commonly termed the "electrostatic" potential, as molecular systems are most practically treated as static distributions of electronic charge around rigid nuclear frameworks. It is a real physical property which expresses the net electrical effect of the nuclei and electrons at each point in space \mathbf{r} , and it has emerged as an effective tool for studying molecular reactive behavior [34-37]. An important feature of $V(\mathbf{r})$ is that it can be determined experimentally by diffraction methods [37-39], as well as computationally.

The first term on the right of equation (1) represents the contribution of the nuclei, which is positive; the second term brings in that of the electrons, which is negative. An approaching electrophile will initially be attracted to those regions where $V(\mathbf{r})$ has its most negative values (the local minima), where the effects of the electrons are dominant. $V(\mathbf{r})$ has indeed been used extensively in the past two decades as a guide to electrophilic processes [36, 40], and also as a useful analytical tool in the study of biological recognition interactions [36, 40, 41].

While negative regions of $V(\mathbf{r})$ are indicative of sites favorable for electrophilic attack, a positive potential does not necessarily imply a tendency to react with nucleophiles. The positive charges of atomic nuclei are very highly concentrated (in contrast to the negative charges of the dispersed electrons); one consequence of this is that $V(\mathbf{r})$ around a free neutral atom is positive everywhere. The electronic rearrangements that occur when atoms interact to form a molecule produce the regions of negative potential. Each such region

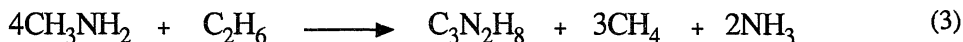
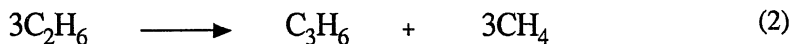
must necessarily have one or more local minima, to which an electrophile would be initially attracted. Positive regions, on the other hand, normally have maxima only at the positions of the nuclei. These reflect the magnitudes of the nuclear charges and cannot be assumed to indicate relative affinities for nucleophiles. We have, however, developed techniques that allow the electrostatic potential to be used to interpret nucleophilic processes [42,43]. One of these involves computing $V(r)$ for a molecule in a distorted conformation corresponding to some early stage in its reaction with a nucleophile [42]. In a more recent approach, we have found that when the potential is examined on an appropriate three-dimensional surface of the molecule in its equilibrium geometry (rather than being plotted in planes above or through the molecule), then positive regions do indicate relative reactivities toward nucleophiles [43]. This promising method is currently being further developed and investigated.

Equation (1) is an exact formula for the electrostatic potential due to a set of nuclei $\{Z_A\}$ and an electronic density $\rho(r)$. The latter, however, is usually obtained from an *ab initio* or semi-empirical molecular wave function, and is accordingly approximate. Given $\rho(r)$, $V(r)$ can be evaluated either rigorously [as with eq. (1)] or approximately [36].

In our present work, $V(r)$ is in most instances determined from an *ab initio* STO-5G SCF molecular orbital wave function, using the GAUSSIAN programs [18-20], with all integrals in equation (1) evaluated rigorously. It has been shown that electrostatic potentials obtained even from SCF wave functions that are not near Hartree-Fock quality are generally reliable [33, 44-49]. Many alternative procedures for computing $V(r)$ have been discussed and analyzed in depth elsewhere [35,36,50].

The electrostatic potential reflects the net electrical effect of the nuclei and electrons of a molecule in some fixed state. It does not, however, account for changes that can occur in a molecule as it begins to interact with some approaching species. These include charge polarization, distortion of geometry and charge transfer. $V(r)$ also does not reflect in any way the nature of the other reactant. Because of these inherent limitations, the electrostatic potential is most useful as a guide to the early stages of a reaction and in recognition processes, where the effects of polarization, distortion and charge transfer are relatively minor.

2.2.2. Anomalous Energy Effects. The isodesmic reaction procedure [25,51] is a means of studying anomalous energy effects in molecules. An isodesmic reaction is a hypothetical chemical process in which the number of bonds of each formal type remains the same on each side of the equation, but their mutual relationships are changed. Representative isodesmic reactions for cyclopropane (C_3H_6) and imidazolidine (**III**; $C_3N_2H_8$) are given in equations (2) and (3), respectively. The ΔE values for reactions such as these reveal any

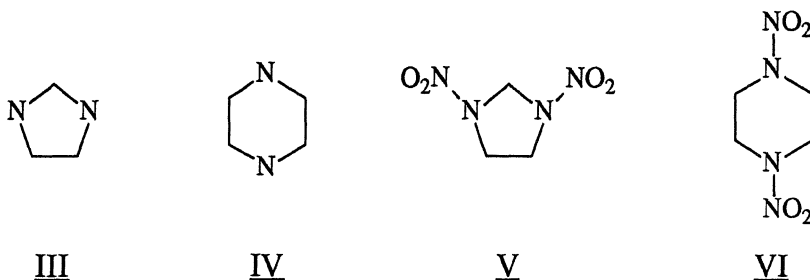


deviations from bond energy additivity, and are interpreted as being due to special energy effects associated with the molecule being investigated, e.g. strain, resonance stabilization, etc. Positive ΔE values are regarded as reflecting destabilizing factors, such as strain. For example, the 3-21G isodesmic reaction energy of cyclopropane [eq. (2)] is 31 kcal/mole [52], which is close to its widely cited strain energy of 28 kcal/mole [53]. Negative ΔE 's, on the other hand, indicate the presence of stabilizing factors. SCF methods have been shown to give satisfactory results for isodesmic energy differences, when viewed on a relative basis [25,54].

3. Computed Properties of Energetic Nitramines

3.1. ELECTROSTATIC POTENTIALS

An inherent characteristic of an amine molecule is what is commonly viewed as an unshared pair of electrons, or "lone pair". The electrostatic potentials of amines are in general dominated by strongly negative regions attributed to these lone pairs [13, 14, 36, 55-57]. These are indicative of sites attractive to electrophiles, and are consistent with the basic character of amines. An example is given by the $V(r)$ of piperazine (**IV**), shown in Figure 1; each amine lone pair region has a most negative value, or $V_{\min}(N)$, associated



with it. Their values are -93.8 kcal/mole [14], compared to -109.3 kcal/mole for that of ammonia [57]. The $V_{\min}(N)$ of NH_3 is, in fact, the most negative that we have found in our studies of nitrogen-containing systems. The $V_{\min}(N)$ values for ammonia, piperazine and various other aliphatic and alicyclic aza systems are listed in Table 1.

In an earlier study, we have shown that the $V_{\min}(N)$ values of $\text{NH}_2\text{-X}$ molecules reflect the total electron-attracting tendencies of the substituents X [57]. The decrease in magnitude of $V_{\min}(N)$ relative to NH_3 was viewed as an indication of the degree to which the nitrogen lone pair electronic density is redistributed or "delocalized" throughout the remainder of the molecule. We interpret the $V_{\min}(N)$ values in Table 1 in a similar manner.

The substitution of nitro groups on amine nitrogens to form nitramines diminishes the sizes and magnitudes of their characteristic lone pair potentials, indicating these nitrogens to be less likely sites for electrophilic attack, and presumably decreasing their basicities relative to the parent molecules. All of this is fully consistent with the strong electron-withdrawing power of the nitro group. The varying extent of this tendency is seen in Table 1, which includes $V_{\min}(N)$ values for a few nitramines. For example, the $V_{\min}(N)$ of 1,4-dinitropiperazine (**VI**) is -31.6 kcal/mole (compared to -93.8 kcal/mole for **IV**), while that of 1,4-dinitroimidazolidine (**V**) is -5.5 kcal/mole (compared to -95.3 kcal/mole for **III**). Factors influencing the extents of these observed decreases will be elaborated upon in a later discussion of the geometries of amine nitrogens in nitramines.

3.2. ANOMALOUS ENERGY EFFECTS

An especially interesting feature of aliphatic and alicyclic amines is brought out by looking at their isodesmic reaction energies. As seen in Table 2 the presence of nitrogens is found to confer added degrees of stability to these molecules; in all instances, the aza systems have more negative $\Delta E_{\text{isodesmic}}$ values than their hydrocarbon analogues. We attribute this to σ -conjugation of the nitrogen lone pairs [14, 58, 59]. This extra stabilization occurs to a greater extent in the cyclic than noncyclic systems, and increases even more strikingly when there are fused rings. We find that within any particular aliphatic or alicyclic series of molecules with the same number of first row atoms, the stabilization is greater as the

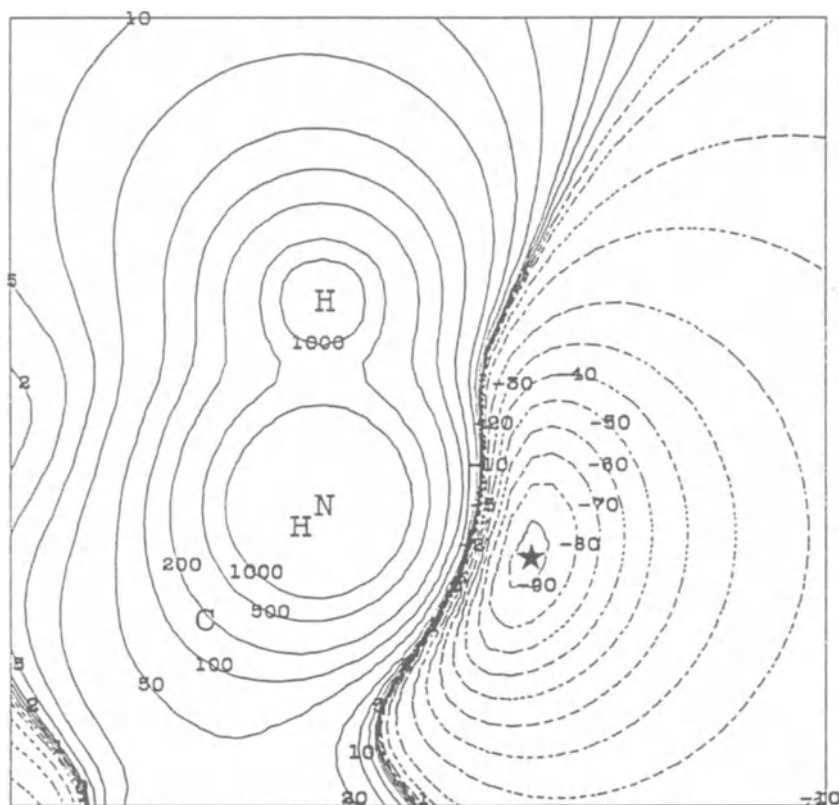


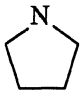
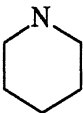

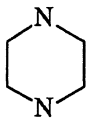
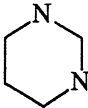
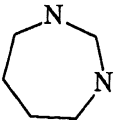
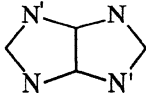
Figure 1. Calculated electrostatic potential of piperazine (**IV**), in kcal/mole, in a plane containing an amine nitrogen and hydrogen and the most negative potential [$V_{\min}(\text{N})$] associated with this nitrogen. Dashed contours correspond to negative potentials. The position of the most negative potential is indicated; the value is: ★ -93.8.

number of nitrogens increases. This is shown even more strikingly by the relative $\Delta E_{\text{isodesmic}}$ values in Table 2.

The 1,3-diaza systems in Table 2 show a greater degree of stabilization than do their 1,4-diaza isomers. (This can be viewed as an example of the anomeric effect [58, 60].) The fused ring systems have calculated ΔE values that are surprisingly large in magnitude (more than twice the ΔE 's of **III** and **IV**). This may be due to the additional 1,3-diaza groupings that occur in each by virtue of being fused.

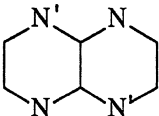
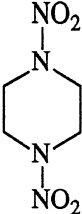
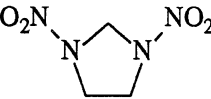
Our $V_{\min}(\text{N})$ data in Table 1 support the view that the extra stability provided by replacing carbons by nitrogens in aliphatic and alicyclic systems is largely due to lone pair σ -conjugation. In general, the $V_{\min}(\text{N})$ values decrease in magnitude as the isodesmic reaction energies of the corresponding molecules become more negative. (This trend holds rigorously within the five- and six-membered cyclic systems taken separately.) Thus, increased delocalization of the nitrogen lone pairs, as measured by decreases in the magnitudes of the $V_{\min}(\text{N})$ values, roughly parallels an increase in stabilization.

TABLE 1. Calculated Electrostatic Potentials [$V_{\min}(\text{N})$] of Aza Nitrogens

Molecule		$V_{\min}(\text{N})$, [kcal/mole] ^a
NH ₃		-109.3
NH(CH ₃) ₂		-100.0
		-97.2
		-95.5
	(III)	-95.3
	(IV)	-93.8
		-93.5
		-88.9
		-88.2 (N)
		-86.0 (N')

(continued)

TABLE 1. Calculated Electrostatic Potentials [$V_{\min}(\text{N})$] of Aza Nitrogens (continued).

Molecule		$V_{\min}(\text{N})$, [kcal/mole] ^a
		-98.5 (N)
		-88.9 (N')
	(VI)	-31.6
	(V)	-5.5
(CH ₃) ₂ NNO ₂		none

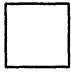





^a The $V_{\min}(\text{N})$ for NH₃ is taken from reference 57. The $V_{\min}(\text{N})$ data for III -VI are from reference 13. All other $V_{\min}(\text{N})$ data are taken from reference 14.

Isodesmic reaction energies for some nitramines are listed in Table 3. The $\Delta E_{\text{isodesmic}}$ values for these systems are more negative (or less positive, in the case of the azacyclobutanes) than those for the corresponding unsubstituted systems, indicating that the substitution of nitro groups on the amine nitrogens has an overall stabilizing effect. This additional stabilization may be due to enhanced delocalization of the σ -electrons, particularly the amine lone pairs, resulting from the strong electron-withdrawing power of the nitro group [14].

3.3. STRUCTURAL PROPERTIES

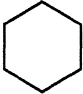
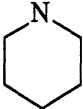
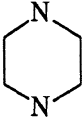
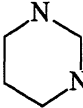
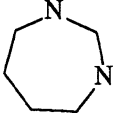
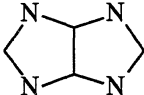
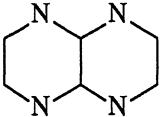
Amine nitrogens in most aliphatic and alicyclic aza systems are pyramidal. However, strongly electron-withdrawing substituents and geometrical constraints can lessen the degree of pyramidal character of these nitrogens. An extreme example of this is dimethylnitramine (VII); the methyl carbons and the -NO₂ group are found, both experimentally [61] and computationally [10], to be coplanar. This and the unusually short N-N bond distance of 1.323 Å [61] suggest that structure VIIB contributes significantly in this system. (An average experimentally-determined N-N single bond length is 1.425 Å [62]).

Table 2. Calculated 3-21G Isodesmic Reaction Energies^a

MOLECULE	$\Delta E_{\text{isodesmic}}$ (kcal/mole)	Relative $\Delta E_{\text{isodesmic}}^b$ (kcal/mole)
<chem>C3H8</chem>	-1.4	0.0
<chem>NH(CH3)2</chem>	-2.3	-0.9
<chem>NH2CH2NH2</chem>	-10.5	-9.1
<chem>NH2(CH2)2NH2</chem>	-8.8	---
<chem>NH2CH2NHCH3</chem>	-11.2	---
	+23.4 ^c	0.0
	+19.5 ^c	-3.9
	+16.7 ^c	-6.7
	+3.0	0.0
	-5.7	-8.7
 (III)	-11.3	-14.3

(continued)

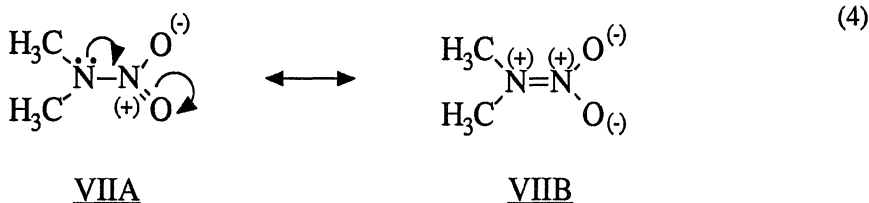
Table 2. Calculated 3-21G Isodesmic Reaction Energies^a (Continued).

MOLECULE	$\Delta E_{\text{isodesmic}}$ (kcal/mole)	Relative $\Delta E_{\text{isodesmic}}^b$ (kcal/mole)
	-9.1	0.0
	-13.0	-3.9
 (IV)	-16.7	-7.6
	-20.1	-11.0
	-16.3	---
	-41.1	---
	-44.5	---

^a With the exception of the cyclobutanes, data are taken from references 13 and 14.

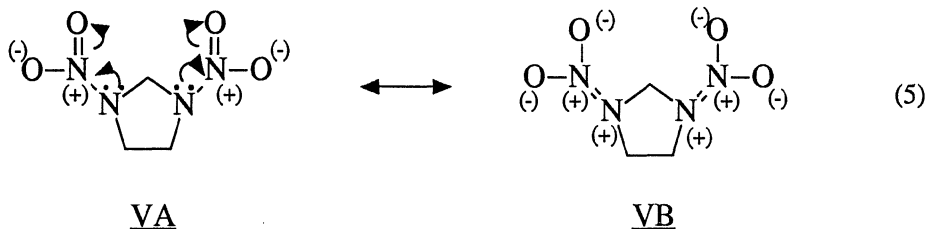
^b Relative isodesmic reaction energies are referred to the corresponding hydrocarbon.

^c Data are from: J. S. Murray, P. Lane and P. Politzer, unpublished results.



The introduction of N-nitro groups in aza systems has a varying effect on the geometries of the amine nitrogens. As has been mentioned earlier, nitramide has a pyramidal amine nitrogen [63], while that of dimethylnitramine is planar [61]. The alicyclic diaza molecules imidazolidine (**III**) and piperazine (**IV**) and their dinitro derivatives **V** and **VI** further emphasize the range of effects that nitro substitution has upon amine nitrogen geometries [13]. In order to point out some interesting features of these systems, we will discuss our calculated 3-21G structures of **III** - **VI**, which are given in Table 4.

Both **III** and **V** have puckered geometries, while the most stable conformers of **IV** and **VI** are chairs [13]. It can be seen from Table 4 that imidazolidine (**III**) and piperazine (**IV**) have pyramidal amine nitrogens; the CNH angles of **III** and **IV** are 112° and 113°, respectively, while the CNC angles are, in the same order, 107° and 113°. The substitution of N-nitro groups results in a significant ring flattening in 1,3-dinitroimidazolidine (**V**), as evidenced by a decrease in the ring atom dihedral angles of **V** relative to **III** (Table 4). This is accompanied by a concurrent reduction in pyramidal character of the amine nitrogens in **V**. We attribute these geometry changes to the introduction of the strongly electron-withdrawing nitro groups and suggest that structure **VB** contributes significantly to the

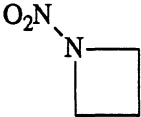
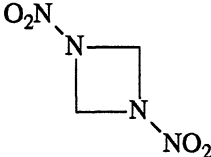
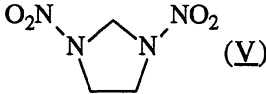
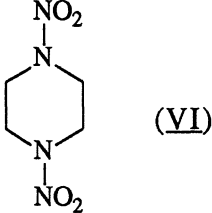


geometry of **V**. Consistent with this interpretation are our calculated N-N bond distances of 1.343 Å. (The planar amine nitrogen and N-N bond distance of 1.323 Å in **VII** [61] suggest that the degree of conjugation of the amine lone pair is greater in **VII** than **V**).

The 1,4-dinitropiperazine chair is flattened somewhat relative to piperazine, as seen by the decrease in the calculated NCCN and CNCC dihedral angles of **VI** relative to **IV** (Table 4). In addition, its calculated N-N bond distance is 1.38 Å. These data are consistent with a lesser degree of conjugation of the nitrogen lone pair in **VI** than in **V** and **VII**, which may be because the six-membered ring framework is less able to accommodate nearly planar C-N(NO₂)-C groupings.

It is interesting to note that the electrostatic potential of dimethylnitramine, which is planar, has no negative regions associated with its amine nitrogen (Table 1). 1,3-dinitroimidazolidine, with its ring framework approaching planarity and relatively short N-N bond distances of 1.343 Å, has extremely weak $V_{\min}(\text{N})$ values of -5.5 kcal/mole, compared to -31.6 kcal/mole in 1,4-dinitropiperazine, which has more pyramidal nitrogens and longer N-N bond distances than V and VII. This trend in $V_{\min}(\text{N})$ data further indicates that a greater degree of delocalization of the amine lone pair toward the nitro group [as in eqs. (4) and (5)] goes together with both a decrease in pyramidal character of the C-N(NO₂)-C portion of the molecule and a decrease in N-NO₂ bond distance.

Table 3. Calculated 3-21G Isodesmic Reaction Energies for Some Nitramines.

MOLECULE	$\Delta E_{\text{isodesmic}}$ (kcal/mole)	Relative $\Delta E_{\text{isodesmic}}^a$ (kcal/mole)
$(\text{CH}_3)_2\text{NNO}_2$	-11.3 ^b	-9.0
$\text{NO}_2\text{NH}(\text{CH}_2)_2\text{NHNO}_2$	-13.1 ^b	-4.3
	+10.2 ^c	-9.3
	+9.5 ^c	-7.2
 (V)	-22.9 ^b	-11.6
 (VI)	-31.4 ^b	-14.7

^a Relative isodesmic reaction energies are referred to the $\Delta E_{\text{isodesmic}}$ values of the unsubstituted parent molecules, which are given in Table 2.

^b Data are taken from reference 14.

^c Data are from: J. S. Murray, P. Lane and P. Politzer, unpublished results.

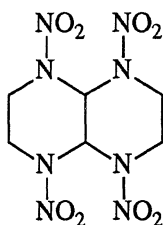
The N-NO₂ bonds in nitramines vary considerably in length. This has been pointed out earlier for dimethylnitramine (VII), 1,3-dinitroimidazolidine (V) and 1,4-dinitropiperazine (VI), which have reported N-NO₂ bond distances of 1.323 Å [61], 1.343 Å and 1.380 Å [13], respectively. The longest N-NO₂ bonds in RDX (I) and β-HMX (a polymorph of II) are given by crystallographic studies as having lengths of 1.393 Å [64] and 1.373 Å [65], respectively. This range of N-NO₂ bond distances appears to reflect largely the varying degrees of delocalization of the aza nitrogen lone pairs [as depicted for VII and V in eqs. (4) and (5)] [13]. Brill and Oyumi have pointed out in a recent experimental study that the lengths of the N-NO₂ bonds in RR'NNO₂ systems qualitatively correlate with both the average frequency of the NO₂ asymmetric stretching vibration and also the amount of NO₂ evolved during rapid thermolysis [4]; nitramines with longer N-NO₂ bonds tend to liberate more NO₂ during this process than those with short ones. This study and intuitive arguments invoking delocalization of the amine lone pair density suggest that a reasonable index of N-NO₂ bond strength is the N-NO₂ bond distance.

An interesting exception to the qualitative trend observed by Brill and Oyumi is 1,3-dinitroimidazolidine (V), which has relatively short N-N bond lengths but is found to liberate significant amounts of NO₂ during rapid thermolysis [4]. This behavior is believed to reflect an anomalously high stability of the imidazolidine ring [9], and is consistent with the stabilization shown for this molecule (III) in Table 2 and for its 1,3-dinitro derivative (V) in Table 3.

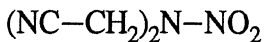
4. Discussion

Nitramines can be induced to decompose by stimuli such as heat, shock or impact. Their thermal decomposition is, in fact, currently a subject of considerable interest [1-12]. The breaking of the N-NO₂ bond is considered a key step in this process, although there appear to be important competing pathways which may even predominate in some cases [4,7,11,12].

Because of the evidence that the cleavage of the N-NO₂ bond plays an important role in nitramine decomposition [1,2,4,8,11], we have investigated whether there exist any relationships between shock sensitivity and the quantities R_1 and R_{ave} for a group of seven nitramines, I, II, V, VI and VIII - X. (R_1 is the longest, and presumably weakest, N-NO₂ bond and R_{ave} is the average length of all the N-NO₂ bonds.) Crystal data were used to obtain the N-NO₂ distances in I, II, V and VIII; for VI, IX and X, these data were taken



VIII



IX



X

from optimized 3-21G structures [13,15]. No correlations were found between shock sensitivity and the quantities R_1 and R_{ave} .

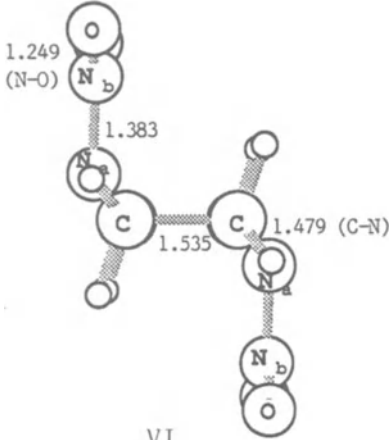
We have, however, obtained a good correlation with shock sensitivity (correlation coefficient = 0.94) by (a) explicitly taking into account each N-NO₂ bond, and

TABLE 4. Calculated 3-21G Structures of III - VI^a.

Molecule and Distances (Å) ^a	Angles and Dihedral Angles (degrees)
<p style="text-align: center;"><u>III</u></p>	NCN 107 CNC 107 NCC 103 CCH 110 - 114 NCH 110 HCH 109 CNH 112 NC _a NC _b 11 C _a NCC 29 NCCN 35 NCNH 112
<p style="text-align: center;"><u>IV</u></p>	CCN 108 (110) CNC 113 (109) NCH 109 - 112 CCH 108 - 110 HCH 109 CNH 113 NCCN 58 CCNC 61 CCNH 170
<p style="text-align: center;"><u>V</u></p>	NCN 98 CNC 116 NCC 101 CCH 112-113 NCH 110 HCH 110 C _a N _a N _b 119 C _b N _a N _b 120 N _a N _b O _a 116 N _a N _b O _b 117 O _a N _b O _b 127 N _a C _a N _a C _b 9 C _a N _a CC 23 N _a CCN _a 25 N _a C _a N _a N _b 164 C _a N _a N _b O _a 14 C _b N _a N _b O _b 13

(continued)

TABLE 4. Calculated 3-21G Structures of III - VI^a (Continued).

Molecule and Distances (Å) ^a	Angles and Dihedral Angles (degrees)
 <p style="text-align: center;"><u>VI</u></p>	CCN
	108
	CNC
	117
	NCH
	107 - 109
	CCH
	110 - 112
	HCH
	110
	CN _a N _b
	115
	N _a N _b O
	117
	NCCN
	53
	CCNC
	58
	CN _a N _b
	80

^a Calculated 3-21G structures for III - VI are taken from reference 13. Experimental parameters for piperazine (IV) from a gas electron diffraction study are given in parentheses. The reference is: Yokozeki, A. and Kuchitsu, K. (1971) Bull. Chem. Soc. Japan 44, 2352.

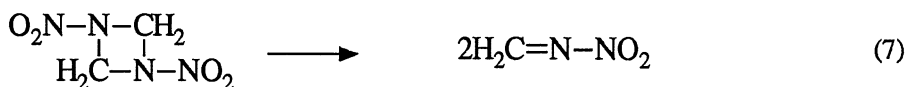
(b) recognizing that their effectiveness in triggering decomposition is "diluted" as the molecule becomes larger [15]. These considerations are presented in a straightforward manner by,

$$\text{Sensitivity} \sim \frac{1}{M} \sum_{i=1}^n \frac{1}{R_i^{-1}} = \frac{1}{M} \sum_{i=1}^n R_i = \frac{n}{M} (R_{\text{ave}}) \quad (6)$$

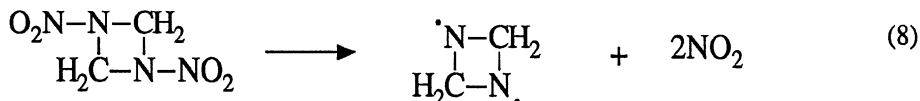
where n is the number of N-NO₂ linkages in the molecule, having N-N distances R_i . M is the molecular weight, taken as a measure of molecular size. The variety of structural types represented by molecules I, II, V, VI and VIII - X is especially encouraging; they include both aliphatic and alicyclic nitramines. This relationship suggests that the strengths of all the N-NO₂ bonds, taken in conjunction with the overall size of the molecule, do help to determine the shock sensitivities of nitramines, and provides support for the idea that rupture of the N-NO₂ bond is a key step in shock-induced nitramine decomposition.

In a recent computational study focusing on possible initial steps in the unimolecular thermal decomposition of 1,3-dinitro-1,3-diazacyclobutane (XI), a vibrational analysis has pointed to two modes that clearly support bond rupture and molecular dissociation [66].

One is a ring mode, while the other involves a stretching of the N-N bonds. The bond-breaking processes corresponding to these modes are indicated by eqs. (7) and (8):



XI



XI

(It is interesting to note that the pathway depicted in eq. (7) is analogous to the concerted symmetric ring opening that has been proposed as the "dominant primary channel" in the thermal decomposition of RDX [7].) An important difference between the processes given in eqs. (7) and (8) is that the former has an activation barrier, while the latter, N-NO₂ bond scission, does not. The energetics analysis in this study has led us to the qualitative conclusion that N-N bond breaking is favored over ring opening as an initial dissociation step in the unimolecular thermal decomposition of XI [66].

That ring-opening processes, such as that indicated by eq. (7), have activation barriers means that some of the energy required to initiate decomposition will be subsequently released and could be used to induce further decomposition steps. Thus, while the thermal, shock and/or impact sensitivity of a nitramine molecule may be determined primarily by the pathway requiring the smallest input of energy, ie. N-N bond breaking [15,66], its energetic performance may depend upon decomposition channels with energy barriers. This suggests that if the N-N bonds could be strengthened without greatly affecting the activation barriers of other pathways, then it might be possible to reduce sensitivity without any substantial change in energetic performance. As has been pointed out earlier, such N-N bond strengthening can result from a decrease in the pyramidal character of the aza nitrogen and the concurrent increase in the delocalization of its lone pair [13].

5. Summary

A survey of computed properties of secondary nitramines has been presented and discussed in light of both their fundamental interest and also their possible relation to impact/shock sensitivity and thermal stability. Our overall computational approach has used the ab initio self-consistent-field molecular orbital GAUSSIAN programs to calculate optimized structures (primarily at the 3-21G level), molecular energies and STO-5G electrostatic potentials for molecules of interest.

The replacement of carbons by nitrogens in aliphatic and alicyclic aza systems is found to provide an added degree of stability, which we attribute to lone pair σ -conjugation. This stabilization is further amplified by the substitution of nitro groups on these nitrogens, presumably due to increased delocalization of the amine lone pairs. The magnitudes of the most negative electrostatic potentials of the amine nitrogens, which can be viewed as indicating the degrees of delocalization of the nitrogen lone pairs, in general decrease as the added stability increases.

The characteristic large and strongly negative regions of electrostatic potential associated with nitrogen lone pairs are greatly diminished, both in size and magnitude, when amine hydrogens are replaced by nitro groups to form nitramines; this is fully consistent with the strong electron-withdrawing power of the $-\text{NO}_2$ substituent. These changes become greater as the geometries of the normally pyramidal amine nitrogens approach planarity and the lengths of the $\text{N}-\text{NO}_2$ bonds become shorter (and presumably stronger).

The relatively wide range of $\text{N}-\text{NO}_2$ bond lengths in nitramines reflects the varying degrees of delocalization of the aza nitrogen lone pairs in these systems [as depicted for VII and V in eqs. (4) and (5)], and suggests that these bonds differ accordingly in strength. A good correlation with shock sensitivity in nitramines has been obtained by taking into account the strengths of all $\text{N}-\text{NO}_2$ bonds (as measured by the inverse of the bond distance), in conjunction with the overall size of the molecule. This relationship supports the general consensus that the $\text{N}-\text{NO}_2$ bond plays a key role in determining the overall stabilities of nitramines.

An analysis of two possible dissociation pathways for 1,3-dinitro-1,3-diazacyclobutane has indicated that $\text{N}-\text{NO}_2$ bond cleavage is favored over ring opening. While the thermal, shock and impact sensitivities of nitramines may be determined primarily by pathways requiring the smallest input of energy, such as $\text{N}-\text{NO}_2$ bond breaking, energetic performance may depend upon decomposition channels with energy barriers, e.g. ring opening.

6. Acknowledgement

We greatly appreciate the support of this work by the Office of Naval Research through contract #N00014-85-K-0217.

7. References

1. Dubovitskii, F. I. and Korsunskii, B. L. (1981) Russ. Chem. Revs. 50, 958.
2. Lloyd, S. A., Umstead, S. E. and Lin, C. M. (1985) J. Energ. Mater. 3 187.
3. Oyumi, Y., Brill, T. B. and Rheingold, A. L. (1986) J. Phys. Chem. 90, 2526.
4. Brill, T. B. and Oyumi, Y. (1986) J. Phys. Chem. 90, 2679.
5. Bulusu, S., Weinstein, D. I., Antera, J. R. and Velicky, R. A. (1986) J. Phys. Chem. 90, 4121.
6. Melius C. F. and Binkley, J. S. (1986) Proc. 23rd JANNAF Combustion Mtg., CPIA, Vol. I, 241.
7. Zhao, X., Hints, E. J. and Lee, Y.T. (1988) J. Chem. Phys. 88, 801.
8. Sumpter, B. G. and Thompson, D. L. (1988) J. Chem. Phys. 88, 6889.
9. Oyumi, Y. and Brill, T. B. (1988) Propellants, Explosives and Pyrotechnics 13, 69.
10. Politzer, P., Sukumar, N., Jayasuriya, K. and Ranganathan, S. (1988) J. Amer. Chem. Soc. 110, 3425.
11. Stewart, P. H., Jeffries, J. B., Zellweger, J. -M., McMillen, D. F. and Golden, D. M. (1989) J. Phys. Chem. 93, 3557.
12. Saxon, R. P. and Yoshimine, M. (1989) J. Phys. Chem. 93, 3130.
13. Murray, J. S., Redfern, P. C., Lane, P., Politzer, P. and Willer, R. L. J. Mol. Struct. (THEOCHEM) submitted.
14. Murray, J. S., Redfern, P. C., Seminario, J. M. and Politzer, P. J. Phys. Chem., in press.
15. Politzer, P., Murray, J. S., Lane, P., Sjoberg, P. and Adolph, H., J. Phys. Chem., submitted.

16. Urbanski, T. (1984) Chemistry and Technology of Explosives, Pergamon Press, New York, Vol. 4, Ch. 13.
17. Iyer, S. and Slagg, N. (1988) Structure and Reactivity (Molecular Structure and Energetics); Liebman, J. F.; Greenberg, A., eds.; VCH Publishers: New York, Ch. 7.
18. Binkley, J. S., Frisch, M. J., DeFrees, D. J., Krishnan, R., Whiteside, R. A., Schlegel, H. B., Fluder, E. M. and Pople, J. A. GAUSSIAN 82, Carnegie-Mellon Quantum Chemistry Publishing Unit, Pittsburgh, PA, 15213.
19. Frisch, M. J., Binkley, J. S., Schlegel, H. B., Raghavachari, K., Melius, C. F., Martin, R. L., Stewart, J. J. P., Bobrowicz, F. W., Rohlfing, C. M., Kahn, L. R., DeFrees, D. J., Seeger, R., Whiteside, R. A., Fox, D. J., Fleuder, E. M. and Pople, J. A. (1984) Carnegie-Mellon Quantum Chemistry Publishing Unit, Pittsburgh, PA.
20. Frisch, M. J., Head-Gordon, M., Schlegel, H. B., Raghavachari, K., Binkley, J. S., Gonzalez, C., DeFrees, D. J., Fox, D. J., Whiteside, R. A., Seeger, R., Melius, C. F., Baker, J., Martin, R., Kahn, L. R., Stewart, J. J. P., Fluder, E. M., Topiol, S. and Pople, J. A., (1988) GAUSSIAN 88, Gaussian Inc., Pittsburgh, PA.
21. Fletcher, R. and Powell, M. J. D. (1963/64) Comput. J. 6, 163.
22. Murtaugh, B. A. and Sargent, R. W. H. (1970) Comput. J. 13, 185.
23. Poppinger, D. (1975) Chem. Phys. Letts. 34, 332.
24. Schlegel, H. B. (1982) J. Chem. Phys. 77, 3676.
25. Hehre, W. J., Radom, L., Schleyer, P. v. R. and Pople, J. A. (1986) Ab Initio Molecular Orbital Theory, John Wiley and Sons, New York.
26. Radom, L., Wathan, W. A., Hehre, W. J. and Pople, J. A. (1971) J. Amer. Chem. Soc. 93, 5339.
27. Binkley, J. S., Pople, J. A. and Hehre, W. J. (1980) J. Amer. Chem. Soc. 102, 939.
28. Boggs, J. E. and Niu, Z. (1985) J. Computat. Chem. 6, 46.
29. Pulay, P., Fogarasi, G., Pang, F. and Boggs, J. E. (1979) J. Amer. Chem. Soc. 101, 2550.
30. Ritchie, J. P. (1985) J. Amer. Chem. Soc. 107, 1829.
31. Ritchie, J. P. (1989) J. Amer. Chem. Soc. 111, 2517.
32. Wiberg, K. B. and Wendoloski, J. J. (1982) J. Amer. Chem. Soc. 104, 56749.
33. Rall, M., Harmony, M. D., Cassada, D. A. and Staley, S. W. (1986) J. Amer. Chem. Soc. 108, 6184.
34. Scrocco, E. and Tomasi, J. (1973) in Topics in Current Chemistry, Springer-Verlag, Berlin, No. 42, p. 95.
35. Scrocco, E. and Tomasi, J. (1978) Adv. Quantum Chem. 11, 115.
36. Politzer, P. and Daiker, K. C. (1981) in B. M. Deb (ed), The Force Concept in Chemistry, Van Nostrand Reinhold, New York, p. 294.
37. Politzer, P. and Truhlar, D. G. (eds.), (1981) Chemical Applications of Atomic and Molecular Electrostatic Potentials, Plenum Press, New York.
38. Stewart, R. F. (1979) Chem. Phys. Lett. 65, 335.
39. Bentley, J. (1979) J. Chem. Phys. 70 159.
40. Politzer, P., Laurence, P. R. and Jayasuriya, K. (1985) Environ. Health Perspect 61, 191 (Special Issue on Structure-Activity Correlation in Mechanism Studies and Procedure Toxicology).
41. Politzer, P. and Murray, J. S. (1989) in Beveridge, D. L. and Lavery, R. (eds.), Theoretical Biochemistry and Molecular Biophysics: A Comprehensive Survey, Adenine Press, in press.
42. Politzer, P., Landry, S. J. and Warnheim, T. (1982) J. Phys. Chem. 86, 4767.
43. Sjoberg, P. and Politzer, P., J. Phys. Chem., submitted.

44. Bonaccori, R., Pullman, A., Scrocco, E. and Tomasi, J. (1972) *Chem. Phys. Lett.* 12, 622.
45. Ghio, C. and Tomasi, J. (1973) *Theor. Chim. Acta* 30, 151.
46. Almlof, J. and Stogard, A. (1974) *Chem. Phys. Lett.* 29, 418.
47. Perahia, D., Pullman, A. and Berthod, H. (1975) *Theor. Chim. Acta* 40, 47.
48. Catalon, J. and Yaney, M. (1978) *J. Amer. Chem. Soc.* 100, 1398.
49. Petrongolo, C., Preston, H. J. T. and Kaufman, J. J. (1978) *Int. J. Quantum Chem.* 13, 457.
50. Tomasi, J. (1982) 'Electrostatic Molecular Potential Model and Its Application to the Study of Molecular Aggregations' in Ratajczak, H. and Orville-Thomas, W. T. (eds.), *Molecular Interactions*, Wiley, New York, Vol. 3, p. 199-181.
51. Hehre, W. J., Ditchfield, R., Radom, L., and Pople, J. A. (1970) *J. Amer. Chem. Soc.* 92, 4796.
52. Politzer, P. and Lane, P., *Struct. Chem*, in press.
53. Greenberg, A. and Liebman, J. F. (1978) *Strained Organic Molecules*; Academic Press: New York.
54. Hinchliffe, A. (1988) *Computational Quantum Chemistry*, John Wiley and Sons, New York, Chap. 5.
55. Politzer, P., Abrahmsen, L. and Sjoberg, P. (1984) *J. Amer. Chem. Soc.* 106, 855.
56. Politzer, P., Elminyaw, I. M., Lane, P. and McKenney Jr., R. L., *J. Mol. Struct. (THEOCHEM)*, in press.
57. Murray, J. S. and Politzer, P. (1988) *Chem. Phys. Lett.* 152, 364.
58. Dewar, M. J. S. (1984) *J. Amer. Chem. Soc.* 106, 669.
59. Minkin, V. I., Glukhovtsev, M. N. and Simkin, B. YA (1988) *J. Mol. Struct. (THEOCHEM)* 181, 93.
60. Romers, C. Altona, C., Buys, H. R. and Havinga, E. (1969) *Top. Stereochem.* 4, 39.
61. Filhol, A., Bravic, G., Rey-Lafon, M. and Thomas, M. (1980) *Acta Crystallogr.* B36, 575.
62. Allen, F. H., Kennard, O., Watson, D. G., Brammer, L., Orpen, A. G. and Taylor, R. (1987) *J. Chem. Soc. Perkin II*, S1.
63. Tyler, J. K. (1963) *J. Mol. Spectrosc.* 11, 39.
64. Choi, C. S. and Prince, E. (1972) *Acta Cryst.* B28, 2857.
65. Choi, C. S. and Boutin, H. P. (1970) *Acta Cryst.* B26, 1235.
66. Grodzicki, M., Seminario, J. M. and Politzer, P., *J. Chem. Phys.*, submitted.

MOLECULAR DYNAMICS APPROACH TO DETONATION STUDIES AND RELATED PROBLEMS IN THE CONDENSED PHASE

D. H. TSAI
10400 Lloyd Road,
Potomac, MD 20854,
U. S. A.

ABSTRACT. Molecular dynamics is capable of providing important dynamical details at the atomic level in studies of detonation and related problems in the condensed phase. In this report I discuss our molecular dynamics investigations of the propagation of heat waves, the thermal relaxation in the shock compression of a crystalline lattice, the modeling of a "chemically" driven detonation wave, and some new results on the mechanisms of heating of "hotspots" in a lattice containing vacancy clusters. Our focus in these investigations has been on the energy propagation, energy sharing and energy equilibration processes. We found that the details of the atomic motion provided a systematic method for investigating the energy relaxation processes, and led to a better understanding of some of the mechanisms involved. In the study of heat waves our results not only agreed well with experimental measurements but also clarified their interpretation.

1. Introduction

Detonation in a chemically reactive system has been extensively studied from the viewpoint of continuum hydrodynamics. One of the basic assumptions in these studies is that there is local equilibrium in all thermodynamic parameters except chemical composition. This means that the various energy relaxation processes in the detonation wave, i.e., energy exchange among the molecules following chemical reaction, would have to occur at a speed equal to the local sound speed. The time scale for achieving local equilibrium is therefore assumed to be in the range of picoseconds, which is fast and difficult to verify by experiments. Also, there are other problems involving motion of the atoms, e.g., the mechanisms of structural and thermal relaxation under shock loading, the motion of dislocations, the mechanism of heating of "hotspots," etc., that are difficult to investigate by the continuum approach or by experiment.

With the development of high-speed computers, the method of molecular

dynamics (MD) also has been applied to detonation studies in recent years. MD is concerned with the motion of individual atoms and molecules, instead of the averaged motion of a volume element in continuum hydrodynamics. This molecular viewpoint is important because the properties of the atoms and molecules, and their arrangements and their motion, determine many of the static and dynamic properties of the materials they make up. At this time MD is the only general (numerical) method available for studying condensed systems, because these systems always involve non-linear, many-body interactions, and analytical solutions are not available. From the motion of the atoms and molecules, MD is capable of providing a detailed description of the energy transport and energy equilibration processes, as well as the associated atomistic mechanisms, on the time scale of 10^{-13} s. For detonation studies, these are precisely the problems about which we need more information. Also, because the model is flexible and completely under our control, it is relatively easy to introduce special conditions in isolation and study their effects without ambiguity. For example, we can introduce a single vacancy cluster or an impurity in a lattice model and investigate its effect on the generation of a "hotspot" under shock loading. These are important advantages of the MD method.

There are, however, important limitations in the application of MD: First, practical considerations limit the model system to relatively small sizes of 10^3 to 10^5 atoms. This makes it difficult to extrapolate the results of MD, and to compare them with those of macroscopic systems consisting of 10^{23} atoms. Second, our knowledge of the interaction potentials among various kinds of atoms is seriously deficient. It is therefore difficult to compare MD results directly with real experiments. Moreover, chemical reactions are basically controlled by quantum mechanics, not classical mechanics. This imposes additional difficulties in MD simulations of chemical detonation. Third, only numerical solutions are available, and from these it is difficult to develop a broad theoretical understanding of the particular effect under study. Great care must be exercised in the interpretation of the numerical results, and in making certain that they are physically realistic, and are not simply an idiosyncrasy of the numerical model or the assumed boundary conditions.

We have employed the method of MD in a range of investigations related to the shock compression of condensed systems and to detonation. In these investigations, we have attempted to ascertain the validity of the model, as discussed above, by comparing its dynamical characteristics with experiments under conditions in which we have reasonably clear experimental results. As an example, since all materials exhibit thermal conduction in a temperature gradient, we must require that our model support a heat current when a temperature gradient is imposed. The computed value of thermal conductivity might not correspond to the measured value, because of errors in the assumed interaction potential and other simplifying assumptions. But there must be qualitative agreement,

or the validity of the model would be in doubt. This procedure of checking is tedious, but it has proved successful so far in showing results in good qualitative agreement with experiments under a variety of conditions. In fact, in some cases, the MD results have helped clarify the interpretation of experimental results and hence also our understanding of certain theoretical details of the energy relaxation processes in condensed systems. These results demonstrate the utility of MD and increase our confidence in the method of modeling.

In this paper, I shall discuss four problems related to detonation which we have studied by the method of MD: (1) Pulsed heating of a lattice. (2) Thermal relaxation in the shock compression of a lattice. (3) Profiles of a detonation wave. (4) Some preliminary results from a new study of the mechanism of heating of vacancy clusters in a lattice under shock compression. From these results I wish to show how the MD method complements the continuum method by providing details of many atomistic processes which would be difficult to investigate by theoretical or experimental means.

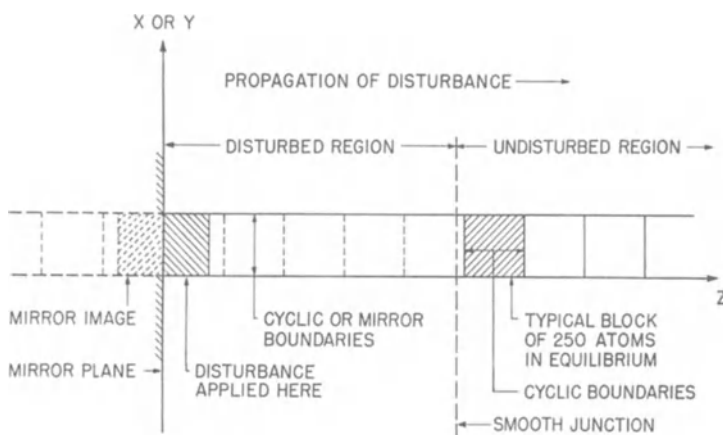


FIG. 1. Lattice model.

2. Molecular Dynamical Model

All four problems employed essentially the same lattice model shown in Fig. 1. The model was a semi-infinite filament in two or three dimensions arranged in X - Z or X - Y - Z directions, Z being along the length of the filament. One-dimensional models were excluded because they were found not to obey Fourier's law of thermal conduction, i.e., they could not sustain a heat current in a temperature gradient [1-4]. Two-dimensional motion was obtained by calculating all the interactions among neighbors

in the full three-dimensional model and by setting the velocities in the Y direction to zero on account of the assumed symmetry in the Y direction. In this way the stability of the lattice was preserved. The filament was further divided into periodic blocks each consisting of a number of cells (128 to 288 bcc or fcc unit cells). This was done so that the equilibrium condition of the filament (and of the entire semi-infinite half space), before it was disturbed, could be represented by that of a single block, for purpose of reducing numerical computation. The disturbance, i.e., heating or shock compression, was introduced at the free surface at $Z=0$ where the boundary condition was assumed to be mirror reflection. As the disturbance propagated along the filament, the periodic boundary condition in the Z direction on the various blocks affected by the disturbance was not imposed. But ahead of the disturbance, the filament was still undisturbed so that it could be joined smoothly to a single block still at equilibrium, through the periodic boundary in the Z direction. This block thus served to terminate the computation at each time step. As the disturbance advanced, we would move this block, keeping it just ahead of the disturbance. In this way we were able to preserve the periodic boundary condition of the terminating block while at all times ensure a smooth junction between the disturbed and the undisturbed parts of the filament. With this scheme we were able to save numerical computation almost by 50% for a long computation. We chose the mirror boundary at $Z=0$ because we wished to examine the relaxation processes in the entire profile. For the detonation problem, this boundary condition also corresponded to that of the "piston problem" discussed by Fickett and Davis [5]. Other boundary conditions have been used [6-9]. Peyrard *et al.* [7-9], for example, employed a window through which they could monitor the motion of the reaction front of the detonation wave. As the detonation wave propagated, they would move the window to keep the reaction front in view, and allow the reaction products to leave the window to the rear. Their boundary condition corresponded to the ejection of the reaction products into vacuum at a fixed distance from the reaction front.

The interatomic potentials used in the four problems are shown in Fig. 2. Potential A (Fig. 2a) was constructed by Chang and Graham [10a] for α -iron to fit the elastic constants. This was used in problem (1) for pulsed heating. Potential B was constructed by Tsai and MacDonald [11] for α -iron to fit both the elastic properties and the pressure-induced phase transition from the α (bcc) to the ϵ (hcp) phase. This was used in problem (2) for studying the thermal relaxation in the shock profile. For both problems, (1) and (2), the unit of distance was taken to be the lattice parameter of α -iron, equal to 1.43 angstroms. The unit of time was taken to be the time it took longitudinal sound waves to travel unit distance, or 0.264×10^{-13} s. A third potential C for α -iron is also shown. This was constructed by Johnson [10b] to fit radiation damage data and was not used here. The differences in these potentials, nominally all for α -iron, showed our incomplete knowledge of the interatomic potential: each could represent only a limited set of properties of the system. This was

not a serious deficiency for our purpose because we were not so much interested in studying the energy transport and energy equilibration in α -iron as we were in the mechanisms of energy transport and energy equilibration in a typical lattice.

Fig. 2b is a compound Morse potential for simulating the exothermic dissociation of a *hypothetical* diatomic molecular crystal of A_2 : $A_2 = A + A + \text{energy}$. A form of this potential was used in problem (3) for studying the profile of a detonation wave. In this potential:

$$V_1(R) = \epsilon \{ \exp[-2a_1(R-R_1)] - 2\exp[-a_1(R-R_1)] \}, \quad R \geq R_{\text{dis}}, \quad (1)$$

$$V_2(R) = b_2 \epsilon \{ \exp[-2a_2(R-0.15R_1)] - 2\exp[-a_2(R-0.15R_1)] \} + Q\epsilon, \quad R < R_{\text{dis}}. \quad (2)$$

Here $R=R_{ij}$ is the separation distance between atoms i and j . The units of

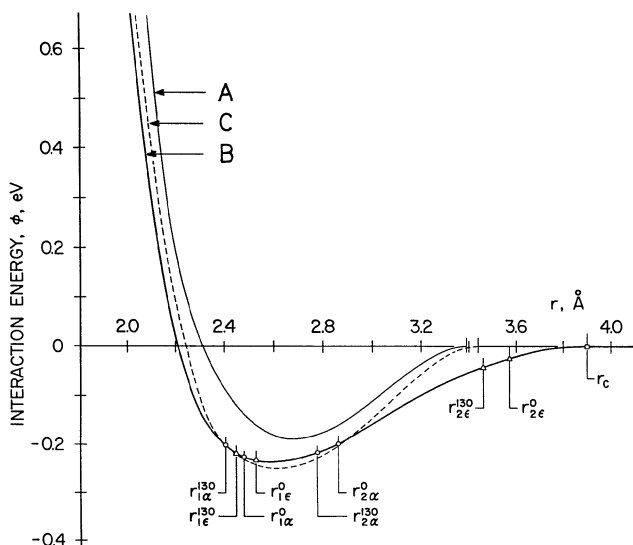


FIG. 2a. Comparison of three interatomic potentials for iron [11]. A was constructed by Chang and Graham [10a] to fit the elastic constants C_{11} , C_{12} and C_{44} of α -iron. B was constructed by Tsai and MacDonald [11] to fit the elastic properties of α -iron and the phase transition from the α -phase (bcc) to the ϵ -phase (hcp) at 130 kbar. $r_c = 3.90$ angstroms, superscript 0 and 130 refer to pressures in kbar, sub-scripts 1 and 2 refer to first and second neighbor separations. C was constructed by Johnson [11b] to fit radiation damage data for α -iron.

distance R_1 , energy ϵ , atomic mass M , and time τ in natural units, all were taken to be unity for convenience. a_1 , a_2 , b_2 and Q were constants: $a_1 = \ln 2 / 0.255$, $a_2 = \ln 2 / 0.05$, $b_2 = 0.4$, and $Q = 32$. With these values, $V_1 = V_2$ at $R_{dis} = 0.2983$. Atoms i and j were assumed to form a molecule in its predissociative state when $R_{ij} < R_{dis}$, equation (2). Dissociation was assumed to occur when $R_{ij} \geq R_{dis}$, equation (1). To simplify the model, we further assumed that once the molecule ij was formed, the bond ij would become saturated, such that other neighbors k of atom i would now interact with i through V_1 , even when $R_{ik} < R_{dis}$. V_1 thus represented the interaction between i and all neighbors except j , when ij formed a molecule. V_1 was also the potential to hold the molecules A_2 together as a molecular crystal. The range of interaction (cutoff) for V_1 was set at $R_c = 1.2$. At the cutoff, $V_1 = 0.8241\epsilon$. The zero axis of V_1 and V_2 was then shifted by this amount so that $V_1 = 0$ for $R \geq 1.2$. We chose the parameters a_1 , a_2 , and b_2 so as to make the vibrational frequency of A_2 only slightly higher (by a factor of three or four) than the intermolecular frequency. This increased the coupling and the energy transfer between the intermolecular

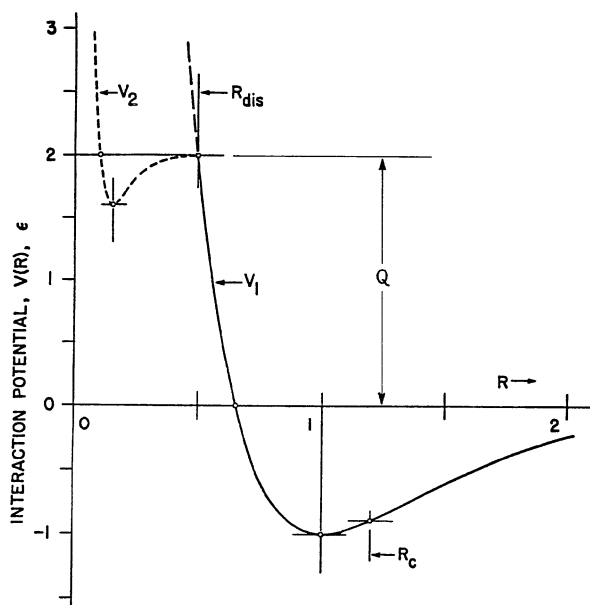


FIG. 2b. Compound Morse potential V_1 and V_2 , equations (1) and (2), for simulating exothermic molecular dissociations. V_1 and V_2 in units of ϵ , R in units of $R_1 = 1.0$. Other parameters in equations (1) and (2) are given in the text. For the detonation study discussed here, Q was set equal to 32, but this figure was drawn with $Q = 2$ to reduce the height. At $Q = 2$, $R_{dis} = 0.4929$, at $Q = 32$, $R_{dis} = 0.2983$. From references [36,38].

and the internal modes of the molecules, and hence made the dissociation reactions occur more easily. The increased coupling was not expected to affect the basic mechanism of energy exchange which was one of the objectives of our investigation.

V_1 was also used in problem (4) for studying the mechanism of heating around vacancy clusters in a monatomic lattice under shock loading. For this problem it was necessary to include the interactions of more attractive neighbors in order to stabilize the vacancy clusters and prevent them from breaking up and diffusing thermally into the lattice. This was accomplished by making the potential steeper and by increasing the range of interaction at the same time: $a_1 = \ln 2 / 0.10$ and $R_c = 1.7$ at the cutoff.

The disturbance was imposed at $\tau=0$ with the filament initially at thermal equilibrium. In problems (1) and (3), heat was added to the lattice in the first few lattice planes next to the mirror boundary at $Z=0$. In problems (2), (3), and (4), the shock wave was generated by giving the entire filament a uniform mass average velocity U_p toward the mirror plane, and compressing the filament against its mirror image. In some cases, U_p was imposed gradually over a time period (τ_1) during which the mass average velocity changed from zero to U_p over a half period of a cosine curve.

3. Pulsed Heating: Second Sound in a Lattice

Second sound refers to the wave-like propagation of a temperature disturbance. This subject has been studied by many authors from two different points of view: heat propagation in an isotropic continuum (solid), and Boltzmann's equation for a phonon gas. The literature has been discussed in a recent review by Joseph and Preziosi [12]. In the continuum picture, second sound may be described by adding a second derivative term of temperature with respect to time to the equation for thermal diffusion, changing it to a wave equation. In the phonon picture, second sound in a crystalline lattice is a temperature wave which results from phonon scattering by normal (N) processes, before the wave is damped out by umklapp (U) processes [13]. These conditions require a crystal of high purity and at low temperature for second sound to be observable in experiments. McNelly, *et al.* [14] and others [15] showed that under these conditions a heat pulse indeed propagated as a wave in NaF and other crystals. But the identification of the wave with second sound was uncertain because the velocity of the wave was found to depend on the temperature of the crystal, not predicted by theory [16]. This discrepancy prompted further theoretical investigations [17].

In our study of the heat pulse propagation [18], we approached the problem from the viewpoint of MD. Our objectives were twofold: to investigate the mechanisms of energy flow and thermal relaxation when a condensed system is driven far from equilibrium, and to test our method

of modeling under what we thought was a stringent set of conditions. The results proved rather satisfactory, and enhanced our understanding not only of the processes of energy transport, but also of the role of MD in this type of investigations.

We used the filament of Fig. 1 in three dimensions. Each periodic block consisted of $5 \times 5 \times 5$ bcc unit cells. The initial temperature of the lattice was set either to zero or to a low temperature. The transverse boundary condition was periodic as described above, but mirror boundary was also used for purpose of comparison. Heat was added to the first 10 lattice planes by scaling the velocities of the atoms in these planes by a constant factor. The heat pulse was approximately a square temperature pulse (about 800 K) which lasted 40 time units. After that the lattice was isolated from further disturbance.

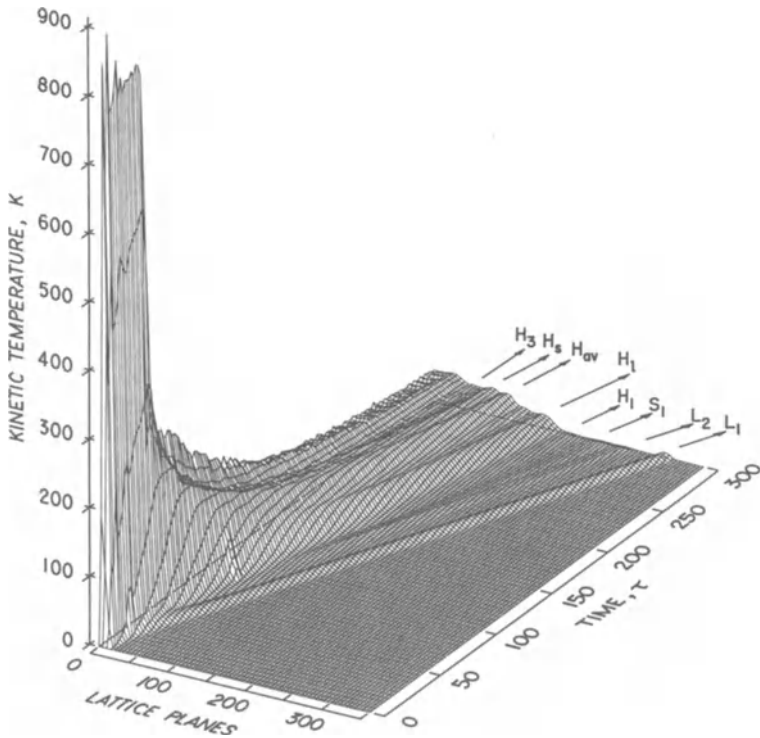


FIG. 3. Evolution of the kinetic temperature profile as a function of lattice plane number and time τ for $T_i=0$ K in a three-dimensional lattice with mirror boundary conditions in transverse directions. L_1 , L_2 , S_1 , etc., label features in the profile moving with constant velocities. From reference [18].

Fig. 3 shows the kinetic energy distribution following the heat pulse plotted as functions of time and lattice position. The interaction potential was assumed to be A of Fig. 2a for α -iron. The observable features L_1 , L_2 , etc., are indicated. These features were superimposed on a surface which described the diffusive part of energy transport. This surface could be fitted to the continuum theory of thermal diffusion with a thermal diffusivity of $4.8 \times 10^{-6} \text{ m}^2 \text{ s}^{-1}$ (thermal conductivity of $11.3 \text{ W m}^{-1} \text{ K}^{-1}$) for the lattice of α -iron. The latter value may be compared with the estimated lattice thermal conductivity of $28.2 \text{ W m}^{-1} \text{ K}^{-1}$ for Fe(99.5%)Ni-(0.05%) at 75 K [19]. In view of the fact that the interatomic potential for iron is not accurately known, we consider this result satisfactory.

The linear trajectories of L_1 , L_2 , etc., indicated that these were waves of various types. From the elastic properties of the lattice and from the stresses associated with these waves, we identify L_1 and L_2 as longitudinal stress waves generated by the expansion and contraction of the heated layers of the lattice near $Z=0$, and S_1 as the transverse shear wave accompanying L_1 . These waves propagated respectively with the longitudinal (C_L) and shear (C_S) sound velocities (first sounds). Analyses of the velocity distributions of the atoms in the region from L_1 to S_1 showed that thermal equilibrium was not attained in this region. But in the region from H_1 to H_3 and to the mirror plane at $Z=0$, local thermal equilibrium was attained. Between H_1 and H_3 , the temperature was above the diffusive background, and this excess temperature profile also propagated as a wave (see below). In fact, this wave was a composite wave made up of three wavelets: H_L , H_{av} , and H_S . H_L propagated with the velocity of $C_L/\sqrt{3}$; H_S propagated with the velocity of $C_S/\sqrt{3}$; and H_{av} propagated with the velocity of $C_{av}/\sqrt{3}$, where C_{av} is average of the longitudinal and transverse first sound velocities of a Debye solid [16]. Thus we see that the individual excitations (L_1 , S_1 , heat pulse) generated their individual second sounds, in accordance with theory [13,20]. This was an important result and we shall return to it later. Note that H_3 actually propagated with a velocity somewhat lower than that of H_S , probably due to the spreading of H_S (and/or H_{av} , H_L) rearward by thermal diffusion. If it was diffusion, the trajectory of H_3 would not be linear, but our data were too limited for us to be certain. Thermal diffusion then would damp out the second sound pulses at long times.

Fig. 4a shows several kinetic temperature profiles as a function of time "measured" at a fixed station in the lattice. Curve C is the average kinetic temperature of planes 71 to 75 taken from Fig. 3. Other curves are explained in the figure caption. The general rise of these curves beyond S_1 was due to thermal diffusion (curve D), as discussed above. These results may be compared with the experimental measurements of McNelly *et al.* [14]. The similarities between our results and McNelly's are striking, especially our profile A and McNelly's at 14.3 K in their Fig. 1b: our first sound pulses L_1 and S_1 corresponded to their "ballistic" phonon pulses L and T , and our heat pulse H_1H_3 to their "new" pulse. Our second sound velocities, viz., $C_L/\sqrt{3}$, etc., were also in agreement with

theory. The question, therefore, is how we are to understand McNelly's data (Fig. 2 of [14]) which showed a dependence of the arrival time of their "new" pulse on the initial temperature T_i of the crystal.

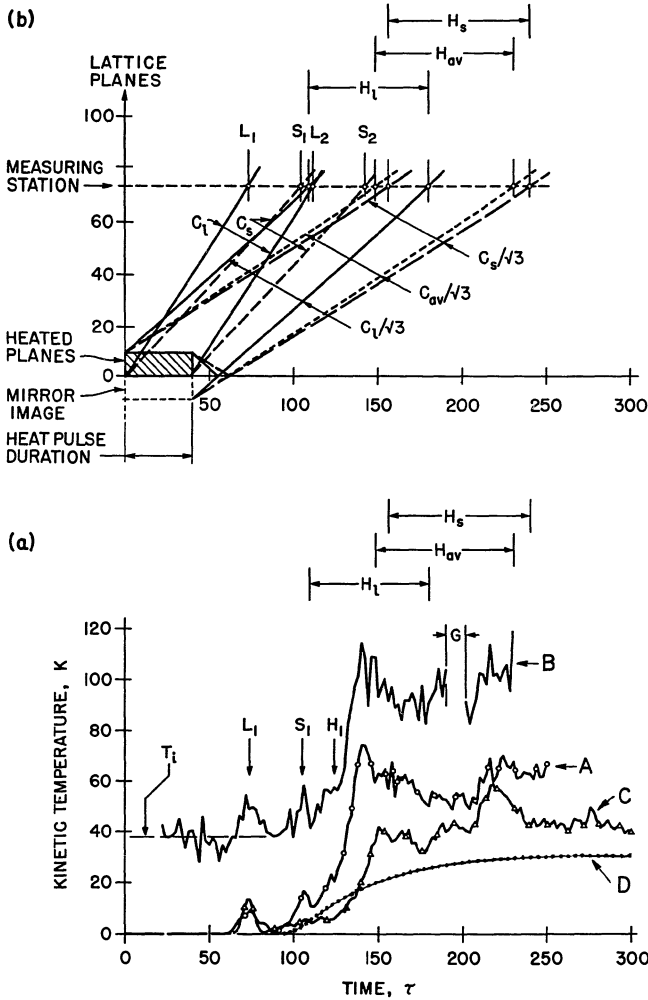


FIG. 4. (a) Kinetic temperature vs time τ at station 15 (average of planes 71 to 75) in the lattice of Fig. 3. G marks a gap in the data. A: cyclic boundary conditions in transverse directions, $T_i=0$ K; B: cyclic boundary conditions, $T_i=38$ K; C: mirror boundary conditions, $T_i=0$ K; D: theoretical estimate of the diffusive profile. (b) Wave front construction: plane number vs time τ , to show the development of various pulses. Ranges H_ℓ , H_{av} and H_s mark the heat pulse components. From reference [18].

The arrival times of L_1 , S_1 , etc., at the measuring station may be obtained by constructing a wave diagram as in Fig. 4b. Because of the finite duration of the heat pulse, the second sound signals H_ℓ , H_{av} , and H_s overlapped to some extent. Now the first sound velocities did not change with T_i or with different boundary conditions, but the amplitudes of the individual second sound pulses did change (see Fig. 4a). Thus we expect that the arrival time of the individual heat pulses would remain the same, but that the shape of H_1H_3 might change with T_i and with other conditions such as damping, etc., owing to the overlap noted above. If this expectation is correct, then McNelly's results would simply mean that their "new" pulse was also a composite wave like our H_1H_3 , and that they were measuring the arrival time of different parts of H_1H_3 , rather than a real dependence of second sound velocity $C_{av}/\sqrt{3}$ on T_i . We see evidence of the composite nature of their "new" pulse. For example, at the low temperature around 8 K (Fig. 2 of [14]), the arrival time of the "new" pulse was 4.3×10^{-6} s, which was close to $\sqrt{3}$ times the arrival time of the longitudinal pulse. But their data (Fig. 1b of [14] at 8.1 K) also showed a small signal at 7×10^{-6} s, which was close to $\sqrt{3}$ times the arrival time of the transverse pulse. This interpretation is appealing because of its naturalness and simplicity. It is different from other theoretical explanations [17] of the temperature dependence of second sound velocity of T_i .

As a further check, we also calculated the heat pulse propagation in a two-dimensional model. We again obtained three second sounds, with velocities equal to $1/\sqrt{2}$, instead of $1/\sqrt{3}$, times C_ℓ , C_{av} , and C_s .

The close correspondence between our MD results for a high temperature heat pulse in α -iron and McNelly's experimental results for a low temperature heat pulse in NaF indicates that the mechanisms of energy transport and energy equilibration in the two systems were basically similar. In both cases, energy propagated as waves of different frequencies, and thermalization of the disturbance required the attainment of a local equilibrium distribution of both the kinetic and the potential energies through wave interactions. And in both cases, both second sound and diffusive heating were observed. This also indicated that damping of second sound was comparable: damping was kept small in our case by the short time of calculation, and in their case by the careful choice of the experimental conditions to reduce the U -processes compared to the N -processes. Had we extended our calculations to longer times, we would expect the second sound signals to be damped out. Note also that when the initial temperature T_i was high (Fig. 4a, case B, $T_i=38$ K), all the signals became noisier. We expect that at still higher T_i , it would be more difficult to detect the signals from the noise. Whether or not the observed comparability in damping might be fortuitous, the results demonstrate rather nicely, we think, the flexibility and the utility of modeling: It is easy to adjust the conditions of the model in order to study a particular phenomenon. And it is relatively easy to interpret the results because detailed information on the atomic motion is available.

In the present case, the MD results have proved not only to be in good qualitative agreement with experiments, despite the large differences (factor of 10^6) in the time and distance scales, but they have also suggested a more straightforward and rational interpretation of the details of the physical measurements. These considerations provide powerful arguments in favor of using the MD method for investigation of energy relaxation processes in condensed systems. These processes basically result from the discrete nature of the system. By ignoring the discreteness, the continuum approach cannot give the correct description of the relaxation processes except by a *a priori* assumption or by phenomenology.

4. Thermal Relaxation in the Shock Compression of a Lattice

Energy transfer and energy relaxation processes in the shock wave profile are important to our understanding of the initiation and propagation of chemical reactions in a detonation wave. The shock compression of a fluid has long been studied from a continuum viewpoint which pictures the shock front as a moving surface of discontinuity. The profile behind the shock front is assumed to be steady. The conditions across the shock front are then given by the Hugoniot equations. In numerical calculations with a finite difference method, it is found that the discretization procedure gives rise to unwanted oscillations between the mass points behind the shock front, making the shock profile unsteady. This difficulty can be circumvented by introducing a pseudo-viscosity into the energy and momentum equations [21]. Then the computation can be carried smoothly through a continuous shock front, and the tedious procedure of matching the conditions across a moving discontinuity is avoided. It is found that even a small pseudo-viscosity would damp out the oscillations behind the shock front.

The discretization procedure transforms the fluid to a one-dimensional lattice of mass points. The shock compression of such a system has been studied analytically in the special case with harmonic interactions [22], and both analytically and numerically in the more general case with non-linear interactions [23,24]. From these studies, it is known that the shock front indeed was not a sharp discontinuity but a region spanning about ten mass points in the direction of shock travel. In this region the various properties changed rapidly but continuously. These rapid changes would excite oscillations which would persist but with diminishing amplitudes farther away from the shock front. If the mass points were atoms, the oscillations would be analogous to a kind of thermal agitation, and the energy associated with the oscillations would represent the rise in internal energy due to shock compression, as Peierls had early pointed out [21]. Thus when we use a pseudo-viscosity to damp out the oscillation, we prescribe, in effect, the process of energy conversion behind the shock front. This is risky, because we do not have a rational criterion

for specifying the magnitude of the pseudo-viscosity. But this objection is moot, because the one-dimensional model is inherently unsatisfactory for studying problems of energy propagation and energy sharing, as we have already noted in Section 2. Lastly, as we have seen in Section 3, thermalization of a longitudinal stress (shock) wave in a three-dimensional lattice occurs with the speed of longitudinal second sound, which is lower than the speed of the shock wave by a factor of $1/\sqrt{3}$. Thus the kinetic energy profile behind the shock front should be time-dependent. There could also be other slower relaxation processes such as structural relaxation.

For the reasons given above, a number of authors [23-28] have applied MD to shock wave studies in an effort to obtain details of the various shock compression processes that are not easily available from the conventional continuum method. We have carried out calculations of the shock compression of one-, two- and three-dimensional systems in both solid and liquid phases [29,30], using essentially the same model as in Fig. 1. Here I shall first summarize the general features of the shock profile from our studies, then I shall discuss one representative case, with special reference to the thermal relaxation problem, as an illustration of some of the general results.

4.1. GENERAL RESULTS

(1) The shock front is thin but not discontinuous. Its thickness extends about ten lattice spacings, independent of the dimensionality of the model. The steepening effect of the shock front results from the anharmonicity of the interaction potential which makes sound wave propagate faster in the lattice under greater compression. But the steepening also excites higher frequency oscillations within the shock front, and these propagate more slowly in the lattice (dispersion) and tend to flatten the profile. When these two effects are in balance, the shock front has the shape of a sigmoid. Averaged over time and space, the shock front profile is smooth and its velocity steady. The steepness of the rise of the shock front seems to be controlled by the inertial effect of the atomic mass acted on by the finite interatomic forces [30], not by the effects of viscosity or heat conduction. This conclusion is supported by the observation that shape of the shock front (or rise time) in a two- or a three-dimensional model is essentially the same as in a one-dimensional model, and the latter model does not have any viscous effect or heat conduction effect in the conventional sense. The high frequency oscillations within the shock front thickness are predominantly in the direction of shock front travel. They are shed from the shock front due to dispersion and are not immediately in equilibrium with the rest of the shock profile [29-31]. See discussion below.

(2) The velocity of the shock front (U_s) varies with the amount of compression, or the particle velocity (U_p) behind the shock front. At a given U_p , U_s is sensitive to the assumed interatomic potential. With a

reasonably realistic potential, the relationship between U_s and U_p is approximately linear, in agreement with experiments.

(3) Behind the shock front various relaxation processes occur in the potential and the kinetic energies. The potential energy relaxation is associated both with thermal relaxation (see below) and with structural rearrangement within the system. Structural relaxation generally occurs at a speed considerably lower than that of the shock front (e.g., plastic flow), but it may be as fast as the shock front (e.g., martensitic transformation). It is accompanied by stress relaxation which occurs at the appropriate speed of first sound.

(4) Thermal relaxation occurs behind the shock front to restore thermal equilibrium. In a condensed system, this involves the reestablishment of the equilibrium distribution of both the frequencies and the velocities of the particles, i.e., their potential and kinetic energy distributions. In the simplest case without structural relaxation and the accompanying stress relaxation, we expect this process to occur at the appropriate second sound velocity. In the fully relaxed region the kinetic and potential energy distributions are in equilibrium. In the relaxing region these distributions are not steady. The shock profile as a whole is therefore unsteady.

(5) The mass density profile adjusts to the stress and the kinetic energy profiles. Since the kinetic energy profile is unsteady, the mass density profile is also unsteady, even though the stress profile may be uniform.

4.2. THERMAL RELAXATION IN THE SHOCK PROFILE

Fig. 5 shows a number of kinetic energy and longitudinal stress profiles at $\tau=100$ for a three-dimensional filament (Fig. 1) with the periodic blocks again made up of $5 \times 5 \times 5$ bcc unit cells. The interaction potential was B of Fig. 2a, also for α -iron. The lattice was initially at an equilibrium temperature of 38 K. U_p expressed in its longitudinal Mach number was 0.1. The different cases, A to F, corresponded to different initial conditions characterized by two parameters (τ_0, τ_1) , with τ_0 denoting the initial position of the phase space trajectory of the uncompressed lattice, and τ_1 the half-period over which U_p was changed from zero to its final value (see Section 2 above). $\tau_1=0$ corresponded, for example, to instantaneous compression.

Case A (instantaneous compression) showed a large increase in the kinetic energy at the tail end of the profile. Further investigation revealed the reason for this increase: The assumed bcc structure with potential B was metastable with respect to a slightly distorted structure. When the lattice was suddenly compressed from the bcc configuration, there was not enough time for the lattice to transform to the more stable configuration, so that a large amount of the compressive work was first stored as potential energy. When the lattice later relaxed to the more stable configuration, the stored potential energy was partly converted to

kinetic energy, and caused the rise as observed in case A. When the compression was more gradual, cases B to F, there was more time for structural rearrangement, and the ensuing overshoot of the kinetic energy was smaller. The stress profiles (Fig. 5) were steady, indicating that the stress relaxation propagated in this lattice at the velocity of the shock wave. The overshoot of the kinetic energy at the tail end tended to obscure the process of thermal relaxation behind the shock front, which was the subject of our study. Therefore, we extended the calculations only in those cases of gradual compression, D, E, and F. The stress profiles of Fig. 5 are similar to that obtained by Paskin, *et al.* (Fig. 2 of [25a] and Fig. 1 of [25b]). Fig. 6 shows the average kinetic temperature profiles of cases D, E, and F extended to $\tau=212$. These profiles are generally similar to those obtained earlier for one- and two-dimensional models [31,32]. But for the one-dimensional case, the kinetic energy pro-

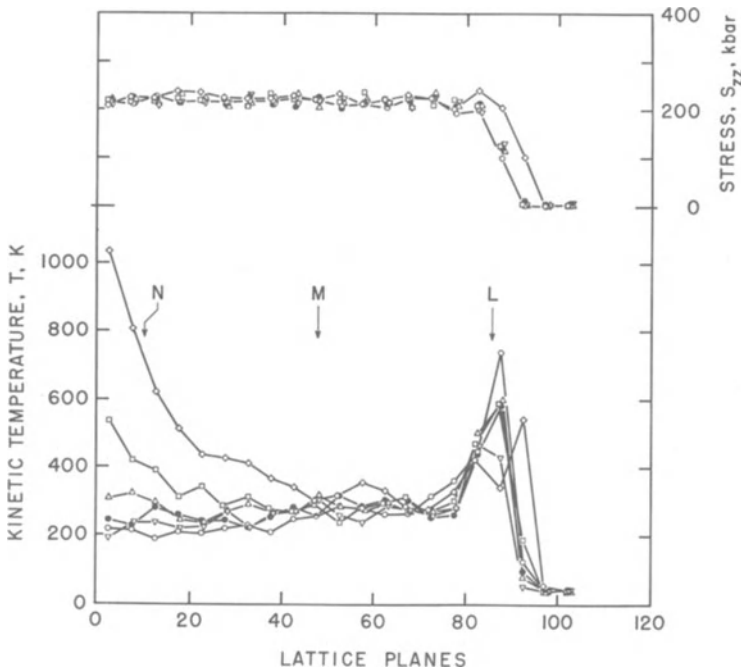


FIG. 5. Kinetic temperature and stress S_{zz} vs lattice plane number of the undisturbed lattice for six cases labeled A to F at $\tau=100$: A(36,0), (\diamond); B(44,2), (\square); C(20,2), (\bullet); D(44,3), (∇); E(20,3), (Δ); F(20,4), (\circ). The numbers in parentheses denote the starting conditions (τ_0, τ_1) discussed in the text. Three-dimensional bcc lattice with cyclic boundary conditions in transverse directions. Interatomic potential fitted to α -iron [11]. $U_p=0.10$, $T_i=38$ K. From reference [29].

file decreased from L toward M with oscillations, because of lack of scattering in the transverse direction, whereas for the two- and three-dimensional cases, the average kinetic energy decreased without oscillations. The average kinetic energy as well as the average stress and density in region MN were steady. In addition, there was also equipartition of the kinetic energy in this region. Therefore, there was thermal equilibrium in region MN. The temperature in MN was 260 K. The position of M at any given time could not be determined precisely. In Fig. 6, the slope of the line MM was chosen to give the maximum velocity consistent with thermal

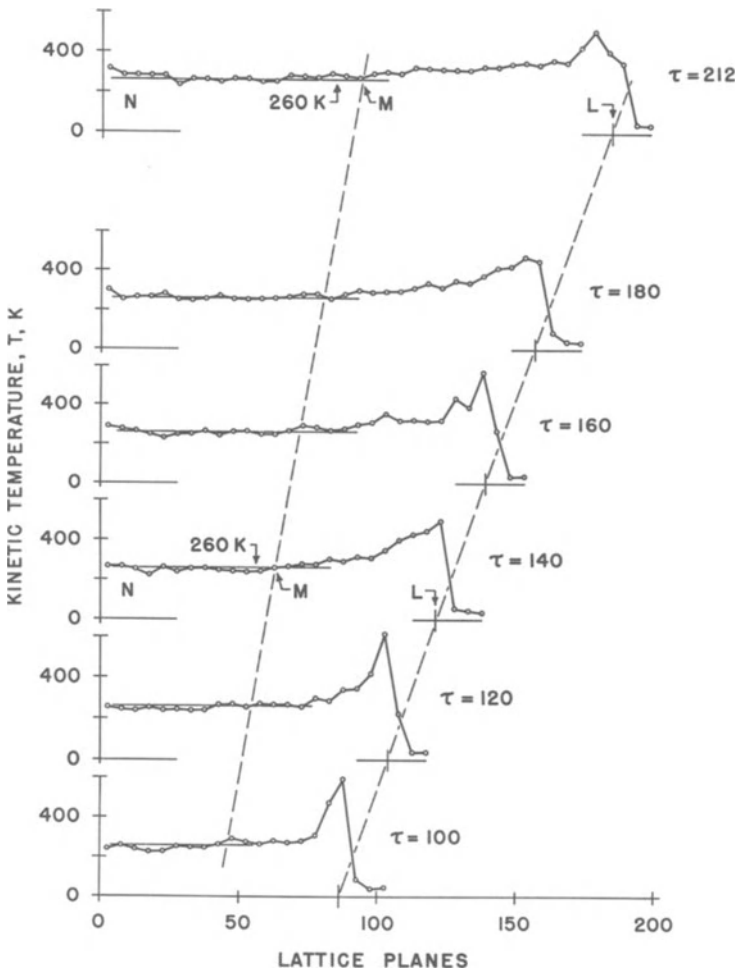


FIG. 6. Kinetic temperature T averaged over cases D, E and F in Fig. 5 vs lattice plane number at several times. From reference [29].

equilibrium behind this line throughout the calculation. From this construction we find that M moved into the lattice at a velocity approximately equal to $U_s/\sqrt{3}$. The region LM was clearly a region of thermal relaxation. In this region, the high frequency oscillations excited by the steep shock front and the interplanar oscillations between L and M interacted and exchanged energies with the thermal oscillations of the lattice. This process was closely analogous to the second sound generated by a displacement field investigated by Kwok and Martin and by Sham [20], except that the displacement field was large in shock compression and small in [20]. It was also analogous to the thermalization of the stress wave L_1 in Fig. 3, leading to the second sound pulse H_ℓ . Thus we identify M as the longitudinal second sound generated by the longitudinal stress wave which in this case was a shock wave. In this picture, L would move with velocity U_s and M with $U_s/\sqrt{3}$. Therefore M would trail farther behind L with increasing time, and the shock profile as a whole would not be steady as assumed in the continuum theory.

4.3. DISCUSSION

The foregoing results showing an unsteady shock wave profile apply to the thermal equilibration in the shock profile in condensed systems. If structural relaxation also occurs behind the shock front (as in cases A , B , C in Fig. 5, and in Ref. [33]) and if the relaxation process is slow compared with the propagation of the shock wave, then we would expect to observe additional energy exchange processes accompanied by further thermal relaxation in the shock profile. Even in a dense Lennard-Jones liquid, we found that the liquid structure did not relax quickly to a hydrostatic state under shock compression, and we observed thermal relaxation similar to that displayed in Fig. 6, but with a smaller overshoot in the kinetic energy after the shock front [30].

This unsteady shock profile from MD is not in full agreement with the assumed steady profile in the conventional hydrodynamic treatment of the shock wave. This does not mean that the results from MD are in violation of the conservation equations of mass, momentum and energy, for both MD and continuum hydrodynamics are based on the same set of classical equations of motion. Rather, the steady profile follows from the implicit assumption that the potential energy is small compared with the kinetic energy of the system, as in gasdynamics. The system then adjusts to a shock disturbance with the speed of sound. With complex molecules, energy relaxation may require many collisions. However, the molecules are of finite size, so that the required number of collisions and hence the relaxation time should remain constant on average, i.e., the shock profile remains steady. When the potential energy is large compared with the kinetic energy, as in condensed systems in which all the molecules are closely coupled, thermal equilibration requires the establishment of the proper distribution of the frequencies of the system, i.e., proper distribution of both the potential and the kinetic energies, and this is

achieved at the speed of second sound.

The effect of an unsteady shock profile may be small or large depending on the information being sought. For example, the unsteady profile does not have much effect on the nearly linear relationship between U_s and U_p . On the other hand, for given U_s and U_p (the quantities actually measured), the derived pressure at a given density may be in considerable error.

In a review by Maddox [34] of the review by Joseph and Preziosi [12], the author asked why we do not more often encounter wave-like propagation of heat. Our results in Section 3 indicated that under high temperature conditions second sound generated by pulsed heating would be quickly damped out. But the results here suggest that second sound generated by a shock wave, as a consequence of thermal relaxation, should last as long as the shock wave propagates and therefore should be observable. But we must note that there is no general agreement at this time on the conclusions we have reached here. Dynin [28], for example, has emphasized this point, and we agree with him. The final answer on the shock wave structure must await experimental measurements. These are difficult because of the high temperature, high stresses, and the highly transient and non-equilibrium conditions involved. For example, the temperature profile of the shock wave remains rather uncertain today, despite the great amount of effort devoted to its measurement [35]. Moreover, there might be other relaxation processes occurring simultaneously to confound simple interpretation. This is where MD should be able to help, by providing detailed information on atomic processes, and thereby aiding the interpretation of experiments and the formulation of theories.

5. Energy Profile in a Detonation Wave

A number of investigators have employed MD in detonation studies [6-9]. Our own work is still at a preliminary, learning stage. Our approach differed from those of the others mainly in the following ways: (1) Our chemical model of $A_2=A+A$ +energy, equation (1) and (2) above, was for a hypothetical diatomic molecular system; (2) we used a relatively long three-dimensional filament (about 400 lattice planes) which has enabled us to investigate the shock and thermal initiation processes in the entire detonation profile, from the mirror plane (the "piston problem" of [5]) to the shock front; and (3) the vibrational, rotational, and translational degrees of freedom of the molecules were fully considered, so that the dissociation and the energy exchange processes were described by the dynamics of the atoms and molecules, and not arbitrarily prescribed. We have previously determined [36,37] (see summary in the next paper) that the dynamical characteristics of the model in both endothermic and exothermic dissociations were realistic. For example, under endothermic conditions, we found that the results were in good agreement with both thermodynamic considerations and kinetic considerations based on the Arrhenius relation. On the bases of these results and those for the heat

pulse, shock wave, etc., we extended our modeling to the investigation of the energy transfer processes in a detonation wave.

The filament (Fig. 1) was built up with periodic blocks of crystallites each containing 128 molecules (256 atoms in $4 \times 4 \times 4$ bcc unit cells) [38a, 38b]. The system was prepared in its predissociative molecular form and held in equilibrium with an average kinetic energy per atom of 0.26ϵ , just below the threshold of spontaneous dissociation. We shall limit our discussion to one case (Figs. 7 and 8) in which the lattice was initially at rest ($U_p=0$, no impact), and the first six lattice planes of the filament were heated rapidly for 80 time steps by scaling the velocities of the atoms in these planes by a factor of 1.03526 per time step (at $\Delta\tau=0.01$). After heating the system was allowed to evolve without interference. We have also investigated cases with simultaneous heating and impact, at $U_p=1.6$ and 2.4 [38b]; and with impact alone, at $U_p=3.75$ to 6.0 , but without heating [39]. For all these cases, the exothermicity factor Q in equation (2) was 32.

Figs. 7a to 7e show the results obtained under the conditions stated above at $\tau=20.05$. Fig. 7a shows the average of the normal stress components as a function of distance from the mirror plane. Fig. 7b shows the number of atoms per plane, and as molecules and as free (dissociated) atoms. Fig. 7c shows the average kinetic energy of the atoms and the molecules per degree of freedom. Figs. 7d and 7e similarly show the average kinetic energies of only the atoms (7d) and only the molecules (7e). In these figures the shock front was at $N_a=330$, and the main reaction front was at $N_a=150-170$. The motion of the reaction front is shown in Fig. 8 which is a series of plots of Fig. 7b from $\tau=6$ to 20 , plotted as the relative number density ρ/ρ_0 of the free (dissociated) atoms.

The initial heating of the first six planes caused the molecules in these planes to dissociate. The energy thus released caused further heating and expansion of this part of the lattice, as may be seen from the higher E_k (Fig. 7c) and lower density (Figs. 7b and 8) near the mirror plane. This process of heating advanced into the lattice and caused further dissociation and expansion. By $\tau=6$ a reaction front was well formed and had acquired a propagation velocity of $U_r=4.0$, (Fig. 8). The reactions in this region between the mirror plane and the reaction front were thermally initiated. Meanwhile, the expansion of the dissociated region compressed the lattice ahead of it, as would a moving piston, and generated a shock wave propagating into the filament. The trajectory of the shock front is shown by the dashed lines in Fig. 8. Its velocity, $U_s=7.5$, was obtained from the stress profiles which are not shown here (but see [38b]). The compression may be seen from the trajectories of a few reaction sites ahead of the reaction front (dotted line with velocity $U_m=2.0$ in Fig. 8). The reactions at these sites were clearly initiated by shock compression. Once initiated, the dissociation would tend to grow, as Fig. 8 shows, because of heating by the dissociated molecules and because the local disorder would tend to reduce the effect of "caging" and

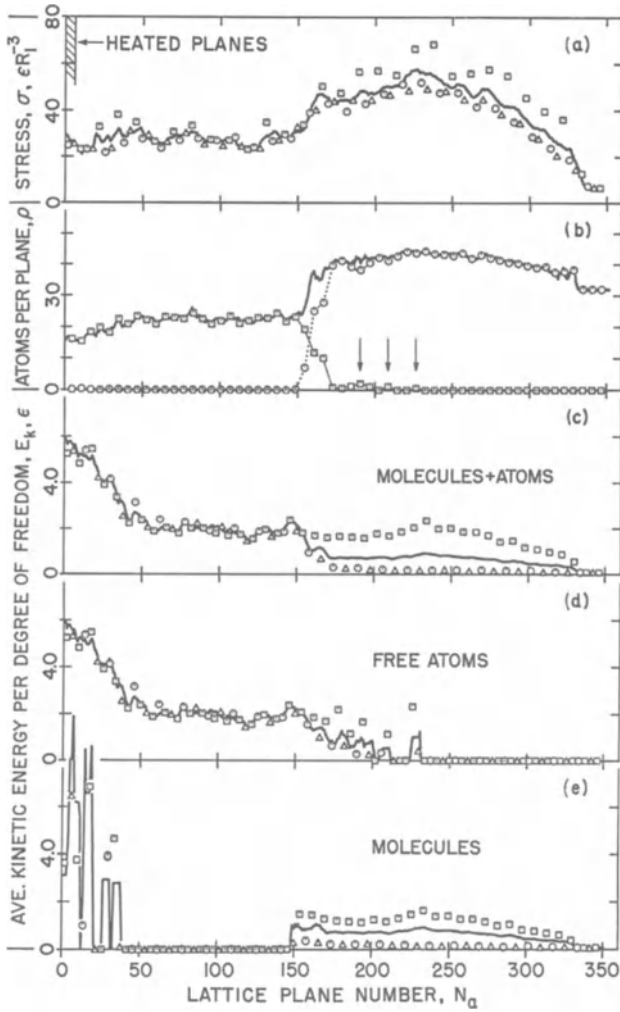


FIG. 7. Profiles of the detonation wave at time $\tau=20.05$, vs lattice plane number of the undisturbed lattice spaced at 0.5455 between planes. (a) Normal stress components $X(O)$, $Y(\Delta)$, $Z(\square)$ and their average (heavy curve). (b) Number of atoms per plane (heavy curve), and number of dissociated (\square) and associated (O) atoms per plane. (c) Average kinetic energy per degree of freedom E_k (heavy curve) of the molecules and dissociated atoms, and kinetic energies associated with velocities in the $X(O)$, $Y(\Delta)$, $Z(\square)$ directions. (d) Same as (c), but of dissociated atoms only. (e) Same as (c), but of associated molecules only, in $T(\square)$, $R(O)$, $V(\Delta)$ degrees of freedom. Data have been smoothed by averaging over neighboring planes: (a) ± 4 ; (b) ± 1 ; (c), (d), (e) ± 2 ; and over ± 15 time steps. From reference [38a].

increase the chance of further dissociation [36]. The growth of these sites would then cause additional compression in this region, as may be seen in Figs. 7a-7c.

In the present case, U_r was higher than U_m (Fig. 8), and we see the main reaction front overtake the shock initiated reaction sites, causing small wavelets to be generated in the main reaction front as well as in the region behind it. But U_r was lower than U_s , so that the profile of the detonation wave as a whole was not steady in this case. Between $\tau=14$ and 22, the amplitude of the shock front profile decreased by about 16%. This decrease could also slow down the propagation speed of the reaction front, but more data are needed to determine this point. In this connection, note

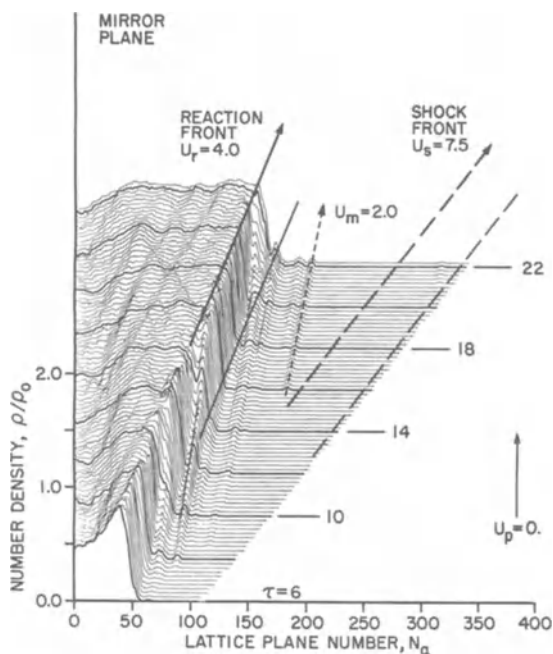


FIG. 8. Profiles of the density of dissociated atoms, ρ/ρ_0 , (b) of Fig. 7, vs lattice plane number at different times. Data have been smoothed by averaging over ± 2 neighboring planes ahead of the reaction front, and ± 6 behind the reaction front, and over ± 15 time steps. Solid lines are the steady-state trajectories of the head and foot of the reaction front. Dashed lines are the corresponding trajectories of the shock front obtained from a similar plot of the stress profiles vs time and distance. Dotted line marks the trajectories of some local reaction sites initiated by shock compression. Velocities refer to the stationary mirror plane. From reference [38b].

that the wavelets (sound waves) behind the reaction front propagated at a higher speed than the reaction front. The latter therefore was at a subsonic speed with respect to the reaction products.

If we increased the mechanical compression, we could increase the shock initiated reactions relative to the thermally initiated reactions. Their combined effect would make the main reaction front propagate at a higher speed. For this model, with the same amount of heating but with $U_p=2.4$ [38b], the reaction front trailed the shock front only by a small distance of about 10 lattice planes, and both fronts traveled at the same supersonic speed with respect to the reaction products. Comparable results were obtained without heating but with greater compression at $U_p=6$ [39], but at lower U_p (3.5 to 4.0) the results were more like those of Figs. 7 and 8. Behind the reaction front, Figs. 7a, 7c, 7d show that the stress components and E_k in the various degrees of freedom were well equilibrated. But in the region between the reaction front and the shock front the stress components and E_k among the translational, rotational, and vibrational degrees of freedom of the molecules (Figs. 7c, 7e) were not equilibrated. These results are consistent with those obtained earlier for pulsed heating and shock compression (Figs. 3 to 6).

The results discussed here contain a wealth of dynamical details of the detonation wave profiles under different conditions. In particular, they show both thermal initiation and shock initiation of dissociation reactions, as well as the coupling of the reactions front, the shock front, and the thermoelastic properties of the lattice, all under highly non-equilibrium conditions. It is true that our hypothetical molecular model and the simulation of the "chemistry" of dissociation are too simple and perhaps simplistic. Nevertheless, because we were able to demonstrate by separate tests [36,37] that this model system was well behaved, we believe that many of the details, especially those relating to the mechanisms and rates of energy transfer and energy sharing, should have their counterparts in reality. As we further develop our techniques of modeling chemical reactions, we should be able to apply the MD method to the study of these details which are not easily accessible by any other method.

6. Heating Around Vacancy Clusters in a Lattice Under Shock Loading

Lastly, we discuss some preliminary results of a study of the energy distribution around defects in a monatomic lattice under shock compression. Many investigators have studied the initiation of chemical reaction in condensed explosives by the mechanism of "hotspots," both experimentally [40] and theoretically [41]. Because of experimental difficulties, few quantitative measurements on "hotspots" have been reported. From the theoretical side, various mechanisms have been postulated, but not completely verified. MD investigations [42] thus far have focused on energy distributions and structural configurations in non-reactive systems in the condensed phase, some containing defects. In our first attempt

[43], we were interested in studying the energy distribution around vacancy clusters and its effect on detonation. We used a two-dimensional reactive molecular model similar to that of Section 5 above. Unfortunately, in that model, we had set the cutoff of the range of interaction to $R_c=1.2$ in the interest of reducing the amount of computation. And that made the attractive part of equation (1) too weak to stabilize the vacancy clusters, so that the vacancies diffused easily throughout the lattice, defeating our purpose.

6.1. TWO-DIMENSIONAL MODEL

In the present case, we reverted to a two-dimensional monatomic (non-reactive) model with a stiff Morse potential ($a_1=\ln 2/0.10$, equation (1)), and with the cutoff extended to $R_c=1.7$. The filament (Fig. 1) was made up of periodic blocks of $12 \times 12 \times 1$ bcc unit cells, each block containing a vacancy cluster which ranged from a di-vacancy to a cluster of ten vacancies. The case of a perfect lattice without any vacancy was also studied as the reference case. Under these conditions the vacancy clusters were stable. They did not move about easily either before or after shock compression. Since the density of a substance in the solid phase is much greater, by a factor of 1000 or more, than that in the gas phase, and since the vacancy clusters in our model contained no more than ten vacancies, it was convenient to assume that these vacancy clusters were empty, containing no gas particles at all.

We shall only summarize here the results concerning the mechanisms of heating around defects under shock compression.

6.2. SUMMARY OF RESULTS

The results are shown in Figs. 9-11, for a case in which each cluster contained ten vacancies, $U_p=1.0$, initial $E_k=0.035\epsilon$, and initial stress $\sigma_{av}=0.571\epsilon/R_1^3$. The positions of the atoms in the two lattice planes of each cell at time step $J=3220$ ($\tau=16.1$) are plotted in Fig. 9. In the transverse direction (ordinate) there were 12 rows of unit cells, each containing two lattice planes. In the longitudinal direction (abscissa) the position is given in terms of lattice plane number (N_a) of the uncompressed filament, folded three times starting at the mirror plane, $N_a=0$. Two vertical lines at $N_a=263$ and $N_a=287$ mark a periodic block, containing one vacancy cluster. The shock front was at $N_a=249$. The vacancy clusters behind the shock front were deformed but remained identifiable all the way back to the mirror plane. These deformations, under the periodic boundary condition in the transverse direction, produced many misalignments of the lattice planes which have the appearance of dislocations. Two sets running in two diagonal directions are shown around $N_a=40-90$. Two more sets running in the transverse direction are shown around $N_a=150-190$. In fact, for this model, it appeared that two or more dislocations eventually would be formed at the site of a vacancy cluster after it came under shock

compression. These dislocations were rather stationary, although they did move small distances over time, especially along diagonal lines where the shear stresses were the highest under the uniaxial loading by the shock compression. We shall come back to this point later in this section. At higher compression, $U_p=3.0$, the vacancy clusters closed up almost completely a short distance from the shock front, and the disorder of the lattice structure increased, extending beyond the original sites of the vacancy clusters in some regions. In the cases investigated here, we did not observe any spalling of the interior surface of the vacancy clusters during the passage of the shock front.

Fig. 10a shows the local potential energy distribution in the filament at time step $J=3200$. The height of each grid point above the base plane gives the potential energy per atom (E_p) in a cell, obtained by averaging over 41 time steps ($J=3180-3220$), and over a small region of 3×3 unit cells with this cell at the center. Fig. 10b shows the distributions of E_p (solid curve) and the total energy E_T (solid curve with crosses) along

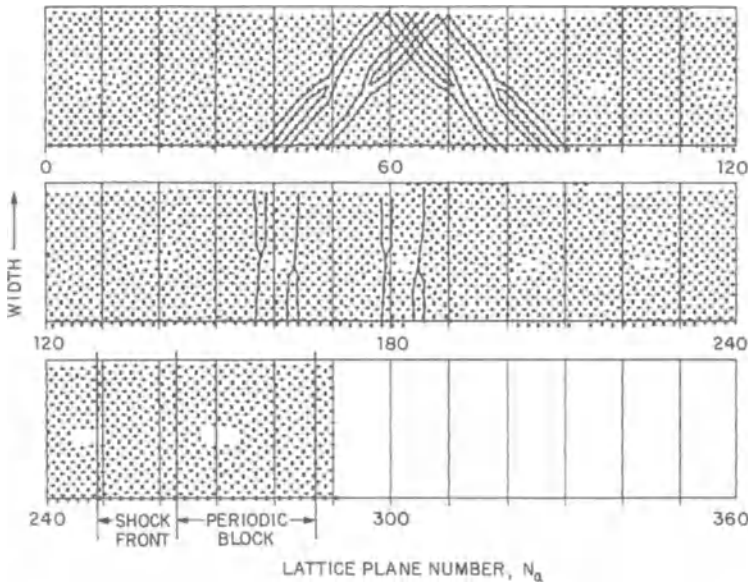


FIG. 9. Configuration of a two-dimensional lattice filament (Fig. 1) under shock compression at time step $J=3220$. Each periodic block contained 12×12 bcc unit cells, one unit cell thick. Each block contained a cluster of ten vacancies. Morse potential (equation (1)) with $a_1 = \ln 2 / 0.10$, $R_c = 1.7$. Other conditions as described in the text. Points (rectangles and crosses) mark the positions of the atoms in the two lattice planes of the unit cell. Solid lines joining the atoms show the misalignments (dislocations) in the deformed lattice under shock loading.

row $L=6$ of the filament from the transverse boundary. The average E_p of the whole surface (Fig. 10a) between $N_a=0$ and the shock front is shown by the dotted horizontal line. The points are the local averages of E_p across the width of the filament. Fig. 10c shows the distribution of atoms of $L=6$, and the local averages (points) across the width of the filament. These figures show that the effect of the vacancy clusters was to raise the local potential energy (strain energy) around the defects. Note that the strain energy was larger ahead of the shock front than behind it. In addition to the strain energy along $L=6$, the E_p surface (Fig. 10a) also showed a waviness along the transverse boundaries. This resulted from the greater strain energy in those regions where the lattice was weakened in the neighborhood of the vacancies. At higher compression, $U_p=3.0$, the lattice became more closely packed behind the shock front, and the peaks and valleys in the E_p surface were relatively less prominent. In the lattice without defects, the E_p surface showed only local thermal fluctuations and was relatively smooth.

Fig. 11a shows the kinetic energy surface E_k , and Fig. 11b the distribution of E_k for $L=6$, corresponding to the distributions of E_p of Figs. 10a and 10b. Fig. 11c gives the normal stress components. The stress profile was the average of nine profiles at time steps $J=3180-3220$ in five-step

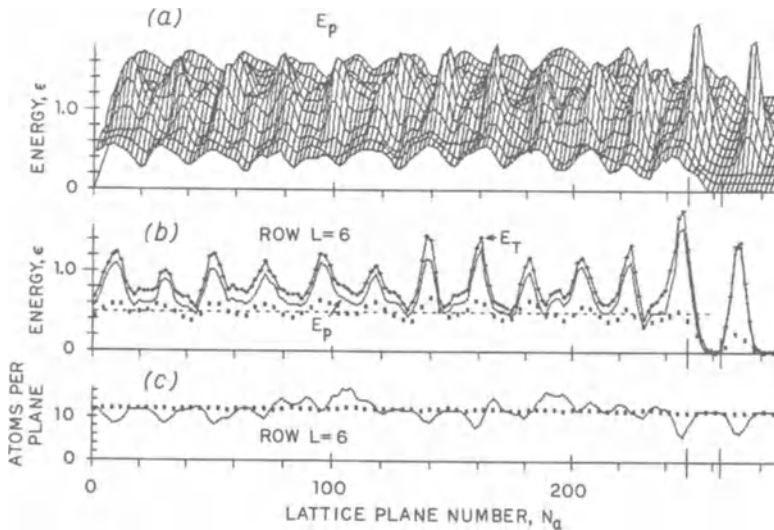


FIG. 10. (a) Distribution of potential energy E_p in the lattice of Fig. 9. (b) Distribution of E_p and total energy E_T along row $L=6$. Rectangular points are planar averages of E_p across the width of the filament. Dotted line is the overall average of E_p up to the shock front. (c) Density (atoms per plane) along row $L=6$ (solid curve) and planar average density (rectangular points) across the width of the filament, as in (b).

increments. At the shock front E_k would overshoot the average rise behind the shock front, but would usually return to around the average value after the shock front had passed. Then the overshoot would indicate an "elastic" response of the lattice. This was the case observed here: There was not enough time for the lattice to deform plastically at the shock front, and even the vacancy cluster remained largely intact. Thus the high value of E_k here would not be considered a "hotspot."

When we compare Fig. 11b with Fig. 10b, we find that for $L=6$, the peaks of E_k , when they occurred, tended to coincide with the peaks of E_p due to the vacancy clusters. These peaks in E_k resulted from two mechanisms: First, since the strain energy next to the vacancy cluster was high (Figs. 10a and 10b), the conversion of the strain energy to E_k as the lattice underwent relaxation also must be high. Second, during this relaxation atoms next to a vacancy cluster would tend to have higher E_k because the vacancies would offer smaller resistance to the atoms moving toward them. This may be considered as a kind of a "hotspot," if the higher E_k did not

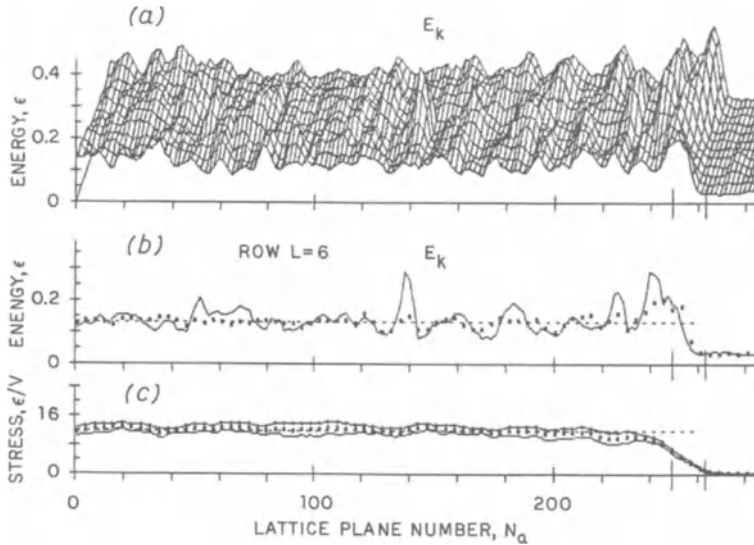


FIG. 11. (a) Distribution of kinetic energy E_k in the lattice of Fig. 9. (b) Distribution of E_k along row $L=6$. Rectangular points are planar averages of E_k across the width of the filament. Dotted line is the overall average of E_k up to the shock front. (c) Profiles of the stress components (σ_{xx} , solid curve, σ_{zz} , solid curve with crosses) behind the shock front. Rectangular points are planar averages of the stress. Dotted line is the average stress up to the shock front, as in (b). Position of the shock front is defined as that point along the filament where the stress is one-half of the average stress in the shock profile.

leave the region, but had time to thermalize locally.

The E_k surface in Fig. 11a turned out to be more irregular than the E_p surface in Fig. 10a. The peaks in the E_k surface were not limited only to the locations of vacancy clusters. There were also suggestions of ridges of E_k peaks, for example, in the neighborhood of $N_a=175-195$. These E_k peaks again must have occurred from the relaxation of the lattice under load, resulting in the conversion of E_p to E_k . This can be seen from the changes in the stress components in Fig. 11c, where a smaller-than-average difference in the stress components would indicate an adjustment in the lattice. The adjustment here was not so localized as in Fig. 11b, and the E_k peaks not so prominent. In addition, some of these peaks lasted over long periods of time. For example, the peak in the neighborhood of $N_a=180$, $L=4-6$, (shown only in Fig. 11b for $L=6$ at $J=3200$) first appeared at $J=2800$ and was still visible at $J=3400$ when the computation was stopped. During this time the shock front had advanced from $N_a=220$ to $N_a=265$. If the kinetic energy in this peak was thermalized, then this would be a genuine "hotspot." In this case, the kinetic energy of the "hotspot" was about twice that of the average kinetic energy behind the shock front.

The mechanisms discussed above were also observed at higher compression, $U_p=3.0$. But because the lattice was now more tightly packed, and lattice relaxation occurred with greater difficulty, fewer "hotspots" were observed, and the E_k surface was relatively smooth.

One more mechanism may be identified. When a lattice contains a distribution of defects, such as the vacancy clusters in the present model, the average elastic constant for the entire lattice is lowered, and the lattice becomes more compressible. Hence, a given compressive force would do more work on a lattice with defects than on one without defects, and the temperature rise in the lattice with defects would be higher. In consequence, the "hotspots" in the lattice with defects would be hotter. With the present model, at $U_p=3.0$, the rise in the average E_k across the shock front was from 0.034ϵ to 1.153ϵ for a perfect lattice, and from 0.036ϵ to 1.253ϵ for a lattice with vacancy clusters containing 10 vacancies each, as in Fig. 9.

If the vacancy cluster were large enough to contain some gas molecules, then the collapse of the volume of the cluster under load would heat up the gas. But the heating would be non-adiabatic, because of the good thermal contact between the gas and the lattice. Moreover, the total energy content of the gas would be small, because of its small mass, as noted above. Thus we would not expect much heating of the surroundings.

Finally, as we have noted, the non-uniform distribution of the difference in the stress components in Fig. 11c indicated that structural relaxation was occurring locally in the shock profile. From a time sequence of these profiles, it was possible to determine that the relaxation process was slow compared with the motion of the shock front. At higher compression, structural relaxation occurred with greater difficulty and therefore more slowly, because of the greater barriers to atomic motion with increased compression. Thus we observed that the dislocations

did not move easily in our model during the time of computation. The results for a three-dimensional model might be different, but it is unlikely that a dislocation would be able to move as fast as the speed of sound in any model, because the mechanisms for dislocation motion and for sound propagation are basically different. On the other hand, since we can identify the vacancy clusters (and presumably other forms of defects) with the generation of dislocations under shock compression, as in Fig. 9, we should expect that a group of defects would generate a band of dislocations which perhaps could be identified as a shear band, and the rate of dislocation generation would be proportional to the rate of shock front propagation.

7. Conclusion and Prospects

We have discussed the application of MD to several problems related to detonation in the condensed phase. These include thermal conduction and diffusion, heat wave propagation, thermal relaxation in the shock profile, initiation of "chemical" reactions in a hypothetical energetic crystal leading to detonation, and the mechanisms of heating of "hotspots" under shock loading. From our viewpoint, the MD method employed in these studies and in the next paper, on energy sharing in a molecular system, has two important features in common: First, it provides a method for treating dynamical phenomena without requiring the existence of thermal equilibrium. Second, it provides details of atomic motion from which atomistic mechanisms may be investigated. These are unique advantages of the MD method. The application of MD, however, is limited by our lack of knowledge of the interaction potential and by the lack of computing facilities. For these reasons, we have chosen to employ simple models and simple potentials. This strategy has been advantageous, although it has also required additional work to determine the validity of the models. On balance, we have been able to demonstrate that the dynamics of the simple models were realistic, and we have learned more about modeling in the process. In fact, in heat pulse propagation, we found that the MD results not only were in good agreement with experiments, but they actually suggested a better explanation of the experimental results. This in turn has led us to a clearer understanding of the thermal relaxation process in the shock profile. Also, the simplicity of the model has made it possible to do fairly extensive computations with inexpensive microcomputers. Thus we believe that at this time a useful role of MD is in the provision of qualitatively correct results that are not obtainable by any other means. In this way, MD may serve as a complement to the conventional continuum approach.

To illustrate this point of view, we may outline an MD problem for testing the assumption of equilibrium in the continuum model, as follows. We start with a hypothetical energetic system, as in Section 5 above, and calculate, by means of MD, the dynamical behavior of the system as it

undergoes detonation. We calculate next, again by means of MD, the equation of state of this system before reaction, the equation of state of the products after reaction, and the reaction rates of the system under conditions which simulate how real reaction rates would be measured. With the equilibrium and kinetics data thus obtained we now calculate the detonation characteristics of a continuum model by means of the conventional continuum method. The results from the two methods may be compared without ambiguity. If they agree, then we would have a proof that non-equilibrium effects, for this simple system, are not important. If they do not agree, then we would have to investigate the reasons for the discrepancies, and this could lead to a better understanding of the detonation process at a molecular level. In view of our MD results which show thermal relaxation effects in the shock profile and in fast dissociation reactions (Figs. 6 and 8 above), it seems important that we should determine if these effects would in fact make a difference in the continuum model.

In their review of the propagation of heat waves, Joseph and Preziosi [12] suggested that the MD approach should be further developed. We agree with this assessment, but suggest that the MD approach is more broadly applicable than to the problems of energy transport in condensed systems, as we have discussed here. MD also should be capable of providing useful information on changes in the structure of materials under dynamic loading on an atomic scale. The mechanisms of dislocation motion and fracture mechanics are examples of this class of problems.

ACKNOWLEDGEMENTS

I thank R.W. Armstrong, F.A. Bandak, C.S. Coffey, D.D. Joseph, M. Peyrard and S.F. Trevino for helpful discussions.

REFERENCES

1. E. Fermi, J.R. Pasta and S.M. Ulam, *Studies of Non-linear Problems*, Los Alamos Report LA-1940 (1955); also in *Collected Works of Enrico Fermi*, Vol II, (University of Chicago, Chicago, 1965) p. 978; E.A. Jackson, *J.Math.Phys.* 4, 551, 686 (1963); J. Ford and J. Waters, *J.Math.Phys.* 4, 1293 (1963).
2. D.N. Payton, III, M. Rich and W.N. Visscher, *Phys.Rev.* 160, 706 (1967); E.A. Jackson, J.R. Pasta and J. Waters, *J.Comp.Phys.* 2, 207 (1968); W.M. Visscher, *Methods in Comp.Phys.* 15, 371 (1973).
3. N. Ooyama, H. Hirooka and N. Saito, *J.Phys.Soc.Japan* 27, 815 (1969), K. Ishii and H. Matsuda, *Progr.Theor.Phys.Suppl.* 45, 56 (1970), H. Nakazawa, *Progr.Theor.Phys.Suppl.* 45, 231 (1970).

4. R.A. MacDonald and D.H. Tsai, *Phys.Rep.* **46**, 1 (1978), and references cited therein.
5. W. Fickett and W.C. Davis, *Detonation*, (University of California, Berkeley, 1979) p. 14.
6. A.M. Karo, J.R. Hardy and F.E. Walker, *Acta Astronaut.* **5**, 1041 (1978); A.M. Karo, F.E. Walker, T.M. Deboni and J.R. Hardy, in *Proc. Ninth International Colloquium on the Dynamics of Energetic and Reactive Systems*, edited by J.R. Bowen, N. Manson, A.K. Oppenheim and R.I. Soloukin (American Institute of Aeronautics and Astronautics, New York, 1984) pp.405-415; A.M. Karo, M.H. Mehlman and J.R. Hardy, in *Proc. Eighth Symposium (International) on Detonation, Albuquerque, July 1985*, edited by J.M. Short, NSWC MP 86-194 (US GPO, Washington, 1986) pp. 864-869.
7. M. Peyrard, S. Odier, E. Oran, J. Boris and J. Schnur, *Phys.Rev. B* **33**, 2350 (1986); M. Peyrard, S. Odier and M. Blain, *J. de Chimie Physique*, to be published; M. Peyrard, S. Odier and E. Oran, *J. de Physique Colloq.* **48**, C4-291 (1987).
8. S. Odier, *J. de Physique Colloq.* **48**, C4-225 (1987); S. Odier and M. Peyrard, *ibid.* C4-393.
9. S.G. Lambrakos, M. Peyrard, E.S. Oran and J.P. Boris, *Phys.Rev. B* **39**, 993 (1989).
- 10a. R. Chang and L.J. Graham, *Phys.Stat.Sol.* **18**, 99 (1966).
- 10b. R.A. Johnson, *Phys.Rev.* **134**, A1329 (1964).
11. D.H. Tsai and R.A. MacDonald, in *Proc. Symposium on Mechanism of Phase Transitions*, *Trans.Amer.Crystal.Assoc.*, **7**, 107 (1971).
12. D.D. Joseph and L. Preziosi, *Rev.Mod.Phys.* **61**, 41 (1989).
13. J.C. Ward and J. Wilks, *Phil.Mag.* **43**, 48 (1952); M. Chester, *Phys.Rev.* **131**, 2013 (1963); E.W. Prohofsky and J.A. Krumhansl, *ibid.* **133**, A1403 (1964); R.A. Guyer and J.A. Krumhansl, *ibid.* **133**, A1411 (1964); **148**, 766 (1966).
14. T.F. McNelly, S.J. Rogers, D.J. Channin, R.J. Rollefson, G.E. Schmidt, J.A. Krumhansl and R.O. Pohl, *Phys.Rev.Lett.* **24**, 100 (1970).
15. C.C. Ackerman, B. Bertman, H.A. Fairbank and R.A. Guyer, *Phys.Rev. Lett.* **16**, 789 (1966); C.C. Ackerman and R.A. Guyer, *Ann.Phys.(NY)* **50**, 128 (1968); C.C. Ackerman and W.C. Overton, *Phys.Rev.Lett.* **22**, 764

- (1969); S.J. Rogers, Phys.Rev. 3, 1440 (1971); V. Narayanamurti and R.C. Dynes, Phys.Rev.Lett. 28, 1462 (1972); V. Narayanamurti, R.C. Dynes and K. Andres, Phys.Rev. B 11, 2500 (1975).
16. J.A. Sussman and A. Thellung, Proc.Phys.Soc.Lond. 81, 1122 (1963).
 17. J. Ranninger, Phys.Rev. B 5, 3315 (1972); H. Beck and R. Beck, *ibid.* 8, 1669 (1973); H. Beck, Z.Physik B 20, 313 (1975).
 18. D.H. Tsai and R.A. MacDonald, Phys.Rev. B 14, 4714 (1976).
 19. C.Y. Ho, M.W. Ackerman, K.Y. Wu, S.G. Oh and T.N. Havill, *Thermal Conductivity of 10 Selected Binary Alloys*, CINDAS (Purdue University, Fayette, 1975) T.P.R.C. Report No. 30.
 20. P.C. Kwok and P.C. Martin, Phys.Rev. 142, 495 (1966); L. Sham, *ibid.* 156, 494 (1967); 163, 401 (1967).
 21. R.D. Richtmyer and K.W. Morton, *Difference Methods for Initial Value Problems*, 2nd ed. (Wiley-Interscience, New York, 1967) Chap. 12.
 22. T.H. Havelock, Phil.Mag. (6), 19, 160 (1910); E. Schroedinger, Ann. der Physik (4), 44, 916 (1914).
 23. R. Manvi and G.E. Duvall, Br.J.Appl.Phys. Ser 2, 2, 1389 (1969); R. Manvi, G.E. Duvall and S.C. Lowell, Int. J.Mech.Sci. 11, 1 (1969).
 24. J. Tasi, J.Appl.Phys. 43, 4016 (1972); 44, 2245 (1973); 47, 5336 (1976); M.J.P. Musgrave and J. Tasi, J.Mech.Phys.Solids 24, 19 (1976); J. Tasi and M.J.P. Musgrave, *ibid.* 24, 43 (1976).
 - 25a. A. Paskin and G.J. Dienes, J.Appl.Phys. 43, 1605 (1972).
 - 25b. A. Paskin, A. Gohar and G.J. Dienes, J.Phys.C: Solid St. Phys. 10, L563 (1977).
 26. B.L. Holian and G.K. Straub, Phys.Rev. B 18, 1593 (1978); J.H. Batteh and J.D. Powell, J.Appl.Phys. 49, 3933 (1978); W.G. Hoover, Phys.Rev. Lett. 42, 1531 (1979); G.K. Straub, B.L. Holian and R.G. Petschek, Phys.Rev. B 19, 4049 (1979); B.L. Holian and G.K. Straub, Phys.Rev. Lett. 43, 1598 (1979); B.L. Holian, W.G. Hoover, B. Moran, and G.K. Straub, Phys.Rev. A 22, 2798 (1980); J.D. Powell and J.H. Betteh, J.Appl.Phys. 51, 5066 (1980).
 27. V.Yu. Klimenko and A.N. Dremin, in *Detonatsiya Chernogolovka*, edited by O.N. Breusov *et al.* (Akad. Nauk, Moscow, 1978), p.79; Sov.Phys.Dokl. 25, 288 (1980).

28. E.A. Dynin, *Fiz. Goreniya Vzryva* **19**, 111 (1983).
29. D.H. Tsai and R.A. MacDonald, *J.Phys.C: Solid St. Phys.* **11**, L365 (1978).
30. D.H. Tsai and S.F. Trevino, *Phys.Rev. A* **24**, 2743 (1981).
31. D.H. Tsai, in *Accurate Characterization of the High Pressure Environment*, edited by E.C. Lloyd, Natl.Bur.Stds (US) Spec.Publ. No. 326 (US GPO, Washington, DC, 1971) pp. 105-123.
32. D.H. Tsai and C.W. Beckett, in *Behaviour of Dense Media Under High Dynamic Pressures, Symposium HDP, IUTAM, Paris, Sept. 1967*, (Gordon and Breach, New York, 1968) pp.99-108.
33. D.H. Tsai and R.A. MacDonald, *High Temp.-High Pres.* **8**, 403 (1976).
34. J. Maddox, *Nature* **338**, 373 (1989).
35. S.B. Kormer, M.V. Sinitsin, G.A. Kirillov and V.D. Urtin, *Sov.Phys. JETP* **21**, 689 (1965); I.M. Voskoboinikov and Bogomolov, *Zh.Eksp.Teor. Fiz. Pisma Red.* **7**, 338 (1968); P.A. Urtiew and R. Grover, in *Temperature, Its Measurement and Control in Science and Industry*, Vol. 4, edited by H. Preston-Thomas, T.P. Murray and R.L. Shepard, H.H. Plumb, Editor-in-Chief (Instrum. Soc. of Amer., Pittsburgh, 1972) pp. 677-684; *J.Appl.Phys.* **45**, 140 (1974); R. Grover and P. Urtiew, *ibid.* **45**, 146 (1974); D.D. Bloomquist and S.A. Sheffield, in *Proc. Seventh Symposium (International) on Detonation, Annapolis, June 1981*, edited by J.M. Short, NSWC MP 82-334 (US GPO, Washington, 1982) pp.1004-1009; W.G. Von Holle, in *Shock Waves in Condensed Matter — 1983, Proc. Amer.Phys. Soc. Topical Conference, Santa Fe, July 1983*, edited by J.R. Assay, R.A. Graham and G.K. Straub (North-Holland, Amsterdam, 1984) pp. 283-291; S.C. Schmidt, D.S. Moore and J.W. Shaner, *ibid.* pp. 293-302.
36. D.H. Tsai and S.F. Trevino, *J.Chem.Phys.* **79**, 1684 (1983).
37. S.F. Trevino and D.H. Tsai, *J.Chem.Phys.* **81**, 248 (1984).
- 38a. D.H. Tsai and S.F. Trevino, *J.Chem.Phys.* **81**, Pt.I, 5636 (1984).
- 38b. S.F. Trevino and D.H. Tsai, in *Proc. Eighth Symposium (International) on Detonation, Albuquerque, New Mexico, July 1985*, edited by J.M. Short, NSWC MP 86-194 (US GPO, Washington, 1986) pp. 870-877.
39. S.F. Trevino and D.H. Tsai, "The simulation of condensed matter chemistry," in *Proc. Army Science Conference, West Point, New York, 1986*, to be published.

40. A.W. Campbell, W.C. Davis, J.B. Ramsay and J.R. Travis, *Phys.Fluids*, **4**, 511 (1961); R.E. Winter and J.E. Field, *Proc.R.Soc. Lond. A* **343**, 399 (1975); W.G. Von Holle and E.L. Lee, in *Behaviour of Dense Media Under High Dynamic Pressures, Proc. Symposium HDP, IUTAM, Paris, August 1978*, (Commissariat a l'Energie Atomique, Paris, 1978) pp. 425-438; W.G. Von Holle and C.M. Tarver, in *Proc. Seventh Symposium (International) on Detonation, Annapolis, June 1981*, edited by J.M. Short, NSWC MP 82-334 (US GPO, Washington, 1982) pp.993-1003; J.E. Field, G.M. Swallowe and S.N. Heavens, *Proc.R.Soc. Lond. A* **382**, 231 (1982); R.E. Setchell, in *Proc. Eighth Symposium (International) on Detonation, Albuquerque, July 1985*, edited by J.M. Short, NSWC MP 86-194 (US GPO, Washington, 1986) pp. 15-25.

41. F.P.Bowden and A.D. Yoffe, *Initiation and Growth of Explosion in liquids and Solids*, (Cambridge, 1952); *Fast Reactions in Solids*, (Academic, New York, 1958); P.H. Thomas, *Combust.Flame* **9**, 369 (1965); P. Gray and P.R. Lee, in *Oxidation and Combustion Reviews*, edited by C.F.H. Tipper (Elsevier, Amsterdam, 1967) pp. 1-183; M.J. Frankel and D.J. Pastine, in *Proc. Seventh Symposium (International) on Detonation, Annapolis, June 1981*, edited by J.M. Short. NSWC MP 82-334 (US GPO, Washington, 1982) pp. 523-528; C.L. Mader and J.D. Kershner, in *Proc. Eighth Symposium (International) on Detonation, Albuquerque, July 1985*, edited by J.M. Short, NSWC MP 86-194 (US GPO, Washington, 1986) pp. 42-51; P.K. Tang, J.N. Johnson and C.A. Forest, *ibid.* pp. 52-61; C.S. Coffey, *ibid.* pp. 62-67; J.N. Johnson, *Proc.R.Soc. Lond. A* **413**, 329 (1987).

42. A.N. Dremin, V.Yu. Klimenko and I.Yu. Kosiriva, in *Proc. Eighth Symposium (International) on Detonation, Albuquerque, July 1985*, edited by J.M. Short, NSWC MP 86-194 (US GPO, Washington, 1986) pp.678-687; A.M. Karo, M.H. Mehlman and J.R. Hardy, see [6]; G. Liu, R. Zhang and W. Yu, *J. de Physique Colloq.* **49**, C3-387 (1988); M.A. Mogilevsky, *ibid.* C3-467.

43. D.H. Tsai, *J. de Physique Colloq.* **48**, C4-303 (1987).

MOLECULAR DYNAMICAL STUDIES OF ENERGY TRANSPORT AND ENERGY SHARING IN MOLECULAR DISSOCIATION

D. H. TSAI

10400 Lloyd Road, Potomac, MD 20854, U. S. A.

S. F. TREVINO

*Energetics and Warheads Division,
U. S. Army Research Development and Engineering Center,
Picatinny Arsenal, NJ 07806-5001, U. S. A., and
Reactor Radiation Division,
National Institute of Standards and Technology,
Gaithersburg, MD 20899, U. S. A.*

ABSTRACT. We discuss our simulation studies of the dissociation of a diatomic molecular crystal by the method of molecular dynamics. Our objectives were to determine the dynamical properties of the model, to ascertain that they were realistic, and to investigate the mechanisms of energy transfer and energy sharing in such a system. The results showed that when the energy release was endothermic, the kinetics of the model followed the Arrhenius relation, consistent with thermodynamic considerations. These results, moreover, remained consistent when three-body interactions were introduced. When the energy release was exothermic, the dissociation reaction proceeded rapidly to completion, and the results showed the details of thermal initiation and various energy transfer processes among the molecules and the products, as well as other effects such as induction time, "caging," etc. We were also able to examine the energy relaxation process when the vibrational degree of freedom alone was heated. These results suggest that molecular dynamics may be further developed into a tool for detonation research from an atomistic viewpoint.

1. Introduction

In the preceding paper [1] we have discussed the application of molecular dynamics (MD) to the study of energy relaxation and energy equilibration in the shock compression of a condensed material and in the detonation profile in a dense, "chemically" reactive system. For the latter study we employed a hypothetical diatomic molecular model: $A_2 = A + A + \text{energy}$. We assumed that the interaction potentials were represented by equations (1)

and (2) of [1], which we reproduce here for convenience:

$$V_1(R) = \epsilon \{ \exp[-2a_1(R-R_1)] - 2\exp[-a_1(R-R_1)] \}, \quad R \geq R_{\text{dis}}, \quad (1)$$

$$V_2(R) = b_2 \epsilon \{ \exp[-2a_2(R-0.15R_1)] \} - \\ - 2\exp[-a_2(R-0.15R_1)] \} + Q\epsilon, \quad R < R_{\text{dis}}. \quad (2)$$

We further prescribed an arbitrary set of rules for the interactions between a pair of atoms when they were bonded as one molecule, and when the molecule dissociated into two free atoms. Specifically, we assumed that atoms i and j would form a molecule when their separation distance $R=R_{ij}$ was less than R_{dis} ; then they would interact through V_2 . Once an A_2 was formed, the molecular bond would become saturated, so that another atom k , either free or as a member of another molecule, would now interact with atom i through V_1 , even if $R_{ik} < R_{\text{dis}}$. These rules were imposed for convenience, to prevent atoms from aggregating to form trimer, etc. Nevertheless, we thought it important to determine if such an arbitrary system would still obey thermodynamics and show Arrhenius behavior. Should the answer be "yes," then it would be worthwhile to study other properties of the model, such as the rate of energy relaxation among the internal degrees of freedom of the molecules, and the effect of three-body forces, etc. In this way we may hope to develop not only our understanding of modeling, but also insight into the problems of energy exchange in condensed systems under the highly non-equilibrium conditions of detonation.

We have carried out the first few steps of this program. We began with a study of the energy exchange in the exothermic dissociation of A_2 [2]. This was followed by an investigation of the kinetics of endothermic dissociation of A_2 [3]. Next, we studied the structure of a detonation wave in a system of exothermic A_2 under conditions of thermal initiation alone, combined thermal and shock initiation, and shock initiation alone [4], as discussed in [1]. At about the same time, colleagues at the Institute of Mechanics of the Chinese Academy of Sciences in Beijing initiated a study of the rate of energy exchange among the internal degrees of freedom in the A_2 system without dissociation [5]. Lastly, we have obtained preliminary results in which V_2 of equation (2) was modified by the introduction of three-body forces during the reaction $A_2 + A = A + A + A$ (dissociation of A_2 in the presence of a third A). Other possible reactions, such as $A_2 + A = A + A_2$ and $A_2 + A_2 = A_2 + A_2$ (exchange of partner(s)), etc., also were allowed. In Section 2 below we first describe the model used in these studies. In Sections 3, 4, and 5 we summarize the results of [2], [3] and [5], the results of [4] having been discussed in [1]. In Section 6 we discuss the preliminary results of our three-body calculations. In Section 7 we conclude with some remarks on the application of MD to detonation studies.

2. Model

The model used in [2], [3], and [5] was similar to the periodic block described in [1], and consisted of $4 \times 4 \times 4$ bcc unit cells and a total of 128 diatomic molecules (256 atoms). The model for the three-body calculations consisted of $5 \times 5 \times 5$ bcc unit cells and 250 molecules (500 atoms). The two-body potentials used in [2] were similar to those of equation (1) and (2) above, and shown in Fig. 2b of [1], except Q was equal to 8. Two sets of these potentials were used in [3], designated as systems A and B and

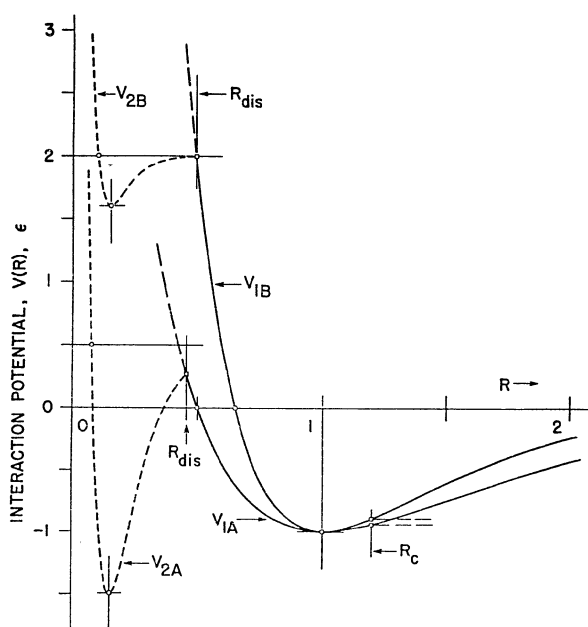


FIG. 1. Compound two-body potentials of equations (1) and (2) used in Section 3. V_1 and V_2 are in units of ϵ , R in units of $R_1=1.0$. Other parameters are listed below. R_c is cutoff for V_1 . From reference [3].

Potential	a_1	a_2	b_2	Q	R_{dis}	R_c	Sound ^a Velocity R_1/τ
System A	$\ln 2/0.5$	$\ln 2/0.075$	2.0	0.5	0.4556	1.2	2.27
System B	$\ln 2/0.35$	$\ln 2/0.05$	0.4	2.0	0.4929	1.2	3.27
Ref. [1]	$\ln 2/0.35$	$\ln 2/0.05$	0.4	8.0	0.3019	1.2-1.35	3.27

^a At density of $1.54 \text{ molecule}/R_1^3$ and zero temperature.

shown in Fig. 1 here. In [5], the values of a_1 , a_2 , b_2 as well as the minimum position of V_2 were adjusted over a range to study their effect on the energy relaxation processes. In the problem of Section 6, the two-body potentials were the same as system A of Fig. 1 except V_{1A} and V_{2A} were joined together by a polynomial interpolation curve ($V_{2i}=\sum_n C_n R^n$) between $R=0.40$ and 0.50 , with continuous first and second derivatives at both ends. This is shown in Fig. 2. The coefficients of the polynomial are given in the figure caption. The maximum ($V_{2i}=0.2043\epsilon$) of the polynomial occurred at $R=0.4409$, which was taken as R_{dis} . For the three-body potential, we followed Murrell, *et al.* [6] and used an arbitrary

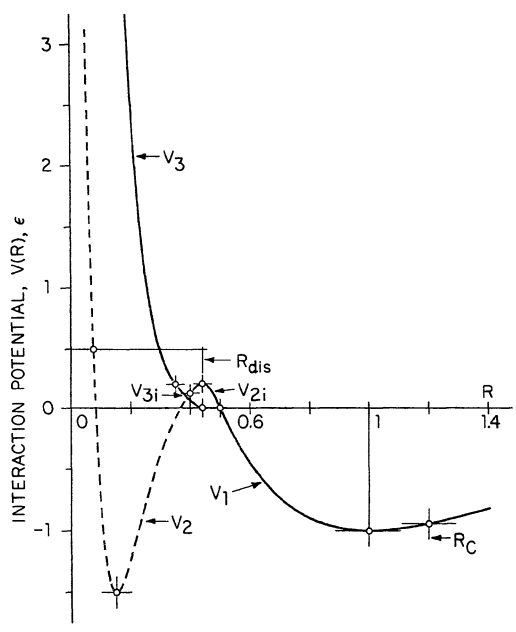


FIG. 2. Two-body and three-body potentials used in Section 6. V_1 and V_2 are the same as V_{1A} and V_{2A} in Fig. 1. $V_{2i}=\sum_n C_n R^n$ is an interpolation polynomial with coefficients C_n for V_{1A} and V_{2A} between $R=0.4$ and 0.5 . $R_{dis}=0.4409$ at maximum of $V_{2i}=0.2043\epsilon$. $R_b=3.8$, $b_3=76.9117$, $a_3=0.058803$. $V_{3i}=\sum_n D_n R_3^n$ is an interpolation polynomial with coefficients D_n for V_3 between $R_3=0.35$ and 0.4409 . The coefficients C_n and D_n are:

n =	5	4	3	2	1	0
C_n	18656.02	-37654.28	29927.51	-11718.35	2264.30	-173.111
D_n		3227.803	-4985.139	2890.881	-748.548	73.3593

"range function" V_3 :

$$V(R_{ij}) = V_2(R_{ij}) + V_3(R_3), \quad (3)$$

$$\text{where } R_3 = (R_{ij} + R_{jk} + R_{ki})/R_b, \quad (4)$$

$$\text{and } V_3(R_3) = b_3 \epsilon \exp[-R_3/a_3], \quad \text{for } R_3 \leq 0.35, \quad (5a)$$

$$V_{3i}(R_3) = \sum_n D_n R_3^n, \quad \text{for } 0.35 < R_3 \leq R_{dis}, \quad (5b)$$

and R_b , b_3 , a_3 , and the coefficients D_n 's are constants. Equation (5a) is an exponentially repulsive potential, passing through $V_3=0.2\epsilon$ at $R_3=0.35$. Equation (5b) is another interpolation polynomial to connect to equation (5a) at $R_3=0.35$ with continuous first and second derivatives and to the zero energy axis at $R_{dis}=0.4409$ with continuous first derivative. The values of R_b , b_3 , a_3 , and D_n 's, etc. are also given in the figure caption of Fig. 2.

3. Exothermic Dissociation of A_2 : Energy Exchange in Rapid Reactions

The exothermic dissociation of $A_2=A+A+\text{energy}$ was studied in a number of cases in [2] under different conditions: with different interaction potentials, different exothermicity parameter Q , different crystal structures, and at different pressures, etc. Although these were only specific case histories, and their number were too few to provide valid ensemble averages, the dynamical results under these different conditions were in fact qualitatively similar. And these results contained details of the molecular motion such that it was possible to draw quite general conclusions regarding the energy distribution and exchange within the system, the attainment of equilibrium, the mechanisms of dissociation, etc. Due to space limitations here, we shall describe only our general approach and summarize the main results in Figs. 3 to 8 for one single case history.

In [2], the system was first prepared in its metastable molecular form below the threshold of dissociation under a given set of conditions in thermal equilibrium at $E_k=0.187\epsilon$. The system was then heated by scaling the velocity components of all the atoms by a common factor, to increase their kinetic energy by 0.005ϵ to 0.010ϵ per time step for 10 to 40 steps ($\Delta\tau=0.01$). After heating, the system was allowed to evolve for several thousand time steps without interference, until all the molecules had dissociated. The dynamical quantities of all the molecules and free atoms, their positions, time of dissociation, and energies and energy distributions, etc., i.e., the complete case history of the dissociation process, were continuously monitored.

The main results may be summarized as follows: (1) Fig. 3 shows the number of free atoms during the course of dissociation in one case history

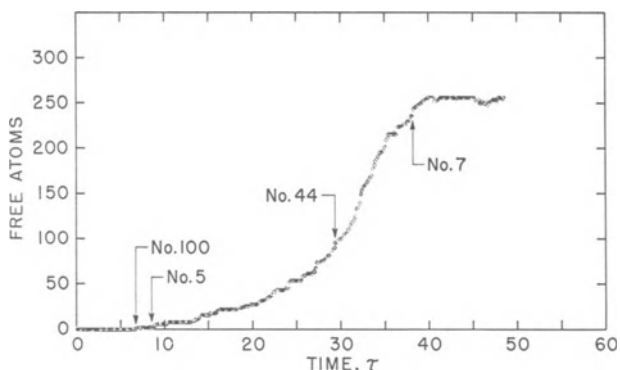


FIG. 3. Number of dissociated free atoms during a dissociation process at constant volume, $V=83.10 R_1^3$, total energy (per atom) before heating= 3.526ϵ , energy added per time step= 0.005ϵ , for 25 steps, at $\Delta\tau=0.01$, total energy after heating= 3.651ϵ , kinetic energy after heating $E_{k0}=0.260\epsilon$, induction time $\tau_d=27$. Arrows with numbers point to the times of dissociation of the numbered molecules discussed in the text. From reference [2].

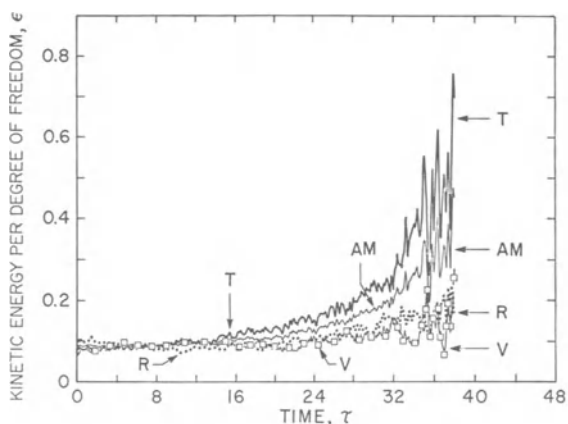


FIG. 4. Distribution of the average kinetic energy per degree of freedom of the molecules during the dissociation process of Fig. 3. T is kinetic energy in the translational degrees of freedom, R the rotational degrees of freedom, and V the vibrational degrees of freedom. AM is the weighted average of T, R, and V per degree of freedom of all molecules. The data have been smoothed by averaging over 25 time steps ($\Delta\tau=0.01$), 12 on each side. From reference [2].

discussed in [2]. The first molecule to dissociate was one labeled No. 100, this was followed by No. 5, etc. No. 7 was one of the last molecules to dissociate. We note here that these three molecules actually were nearest neighbors to one another. Their dissociation at different times showed the combined effects of local heating, local disruption of crystal-line order, and the caging effect. These will be discussed below.

(2) Before the start of dissociation, the system was at equilibrium and the average kinetic energy for the molecules (and atoms) was the same for each degree of freedom (Fig. 4). But the kinetic energies for individual molecules may fluctuate considerably from the average, owing to the inefficient energy exchange among the vibrational (V), rotational (R) and translational (T) degrees of freedom of the molecules. This difference may persist over many molecular vibrations. Fig. 5a gives an example of this situation for molecule No. 5. We observed in Fig. 5a and other similar figures that dissociation occurred only if the vibrational energy of the molecule was equal to or higher than the binding energy of the molecule (i.e., b_2 in equation (2)), and then only if the surroundings were able to accommodate the products of dissociation (i.e., the cage effect was absent). These favorable conditions for dissociation occurred by chance, and hence an induction time was always required for the start of thermal dissociation. We found that the logarithm of the induction time increased approximately linearly with the inverse of the initial temperature of the system (Fig. 6).

(3) The dissociation caused the potential energy of the molecule to be released and redistributed to the surroundings, changing both the potential and the kinetic energies of the system, without affecting its total energy (Fig. 7). The potential energy increase manifested itself as an increase in the pressure of the system, which equilibrated in two or three transit times of sound waves in the system. The potential energy released per molecule was determined mainly by the difference in the height of the potential energy wells in equations (1) and (2), and was not much affected by the pressure of the system. If the system were harmonic, the released potential energy would have been redistributed equally between the potential and kinetic energies of the system. For the anharmonic system here, the redistribution was approximately 62% to the potential energy and 38% to the kinetic energy at the end of dissociation.

(4) The kinetic energy from the dissociated molecule was first distributed among the T degrees of freedom, and eventually among all degrees of freedom of the surrounding particles. This was the basic mechanism of "heating." The heating, however, was not uniform in all the degrees of freedom, and thus there was not an equilibrium temperature in this case of rapid dissociation (Fig. 4). The efficiency of the energy exchange was determined by the coupling of the eigen vectors of the molecules to the surroundings in some complicated manner. We found that the energy exchange among the T degrees of freedom of the molecules and the free atoms was quite efficient (Fig. 5b). But the energy exchange between the V-R, V-T, and R-T degrees of freedom was inefficient (Figs.

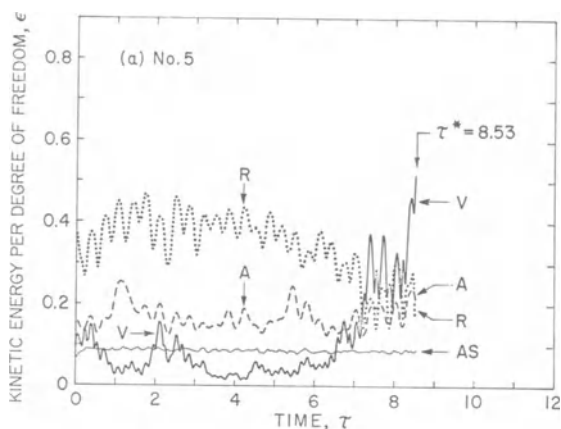


FIG. 5a. Distribution of the kinetic energies per degree of freedom in V and R of molecule No. 5 before dissociation at $\tau^*=8.53$. A is the weighted average of V, R, and T per degree of freedom. AS is the average kinetic energy per degree of freedom of the whole system of molecules and atoms. V, R, and A have been smoothed, as in Fig. 4, except the average was over 11 time steps, 5 on each side. From unpublished data of reference [2].

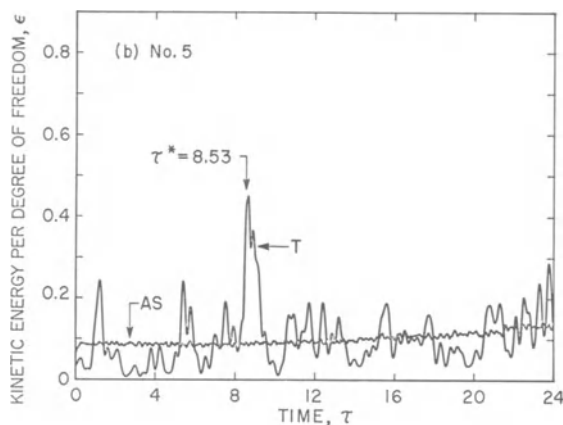


FIG. 5b. The average kinetic energy per degree of freedom in T of molecule No. 5 before dissociation at $\tau^*=8.53$, and of its products after dissociation. AS and the smoothing of data are the same as in Fig. 5a. From unpublished data of reference [2].

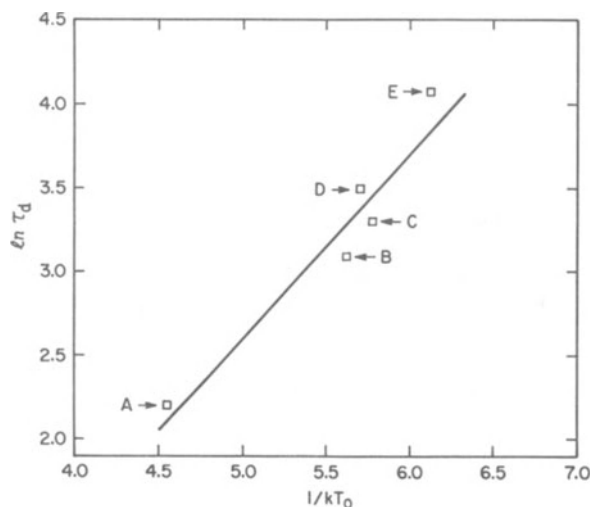


FIG. 6. A plot of the logarithm of the induction time τ_d vs $1/kT_0$, with $kT_0 = (2/3)E_{k0}$, T_0 is the temperature and E_{k0} the kinetic energy of the system at the start of dissociation, after heating. Run C corresponds to the run in Figs. 3 to 8. From reference [2].

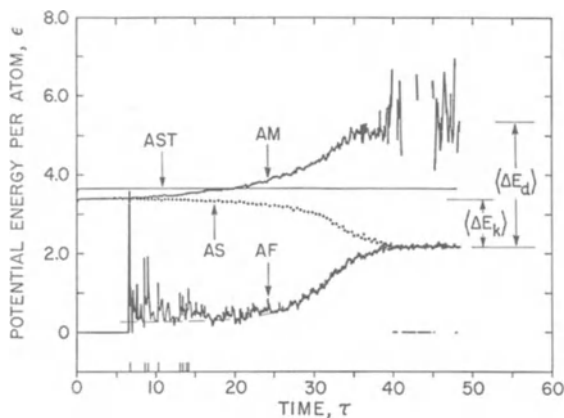


FIG. 7. Distribution of the potential energy during the dissociation process of Fig. 3. AST is the average total energy, AS the average potential energy, per atom, of the whole system, AM the average potential energy per atom of the molecules, AF the average potential energy per atom of the dissociated free atoms. ΔE_d is the average potential energy given up by the dissociated molecules, ΔE_k the average change of the kinetic energy of the system. Marks on the time axis correspond to the first few events of dissociations. From reference [2].

4 and 5a). This was so despite our effort to improve the coupling among the various degrees of freedom by making the molecular potential (equation (2)) softer than usual in comparison with the intermolecular potential of equation (1).

(5) The dissociation also would cause a disruption of the local structural order and a decrease of the caging effect. Both the heating and the disruption of structural order tended to increase the chance of dissociation in the neighborhood of the previous dissociation. In this way we observed the growth of the region of dissociation. The rate of growth was initially slow due to the effect of induction time. As the region heated up, the rate of dissociation also increased. At the same time, the increase of pressure would have a retarding effect because of increased caging effect. This is shown in Fig. 8 for molecule No. 7. Note that despite the higher energy barrier at R_{dis} , the energy change in the last part of the trajectory just before dissociation was approximately b_2 . Toward the end of the process, the rate of dissociation again was low due to the decrease in concentration of the undissociated molecules. Thus a plot of the number of dissociations vs time showed the characteristic shape of a sigmoid, as in Fig. 3.

(6) The above results are in fair qualitative agreement with experimen-

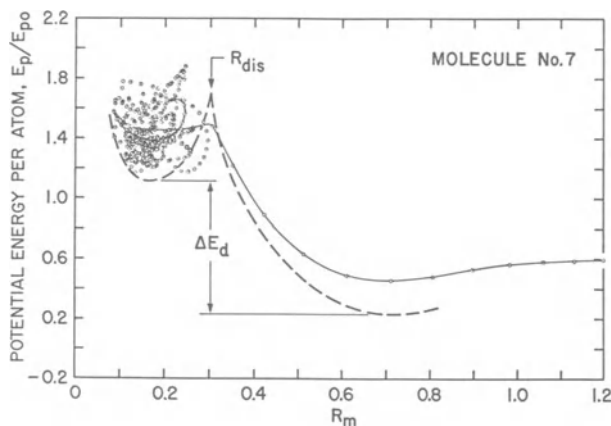


FIG. 8. The potential energy per atom, E_p/E_{p0} , of molecule No. 7 before and after dissociation as a function of the intramolecular separation R_m . After dissociation, E_p and R_m are those associated with the fragments of the molecule. $E_{p0}=3.391\epsilon$ is the average potential energy of the system before any dissociation had occurred. A portion of the trajectory of E_p/E_{p0} just before and just after dissociation (when R_m passed through R_{dis}) is shown as a thin solid curve through the data points. Heavy dashed curves show the outlines of the potential wells with the barrier at R_{dis} . ΔE_d is taken from Fig. 7. From unpublished data of reference [2].

tal results, for example, those of reference [7]. They show that the method of MD is indeed capable of providing information on energy transport and energy relaxation in dense systems, especially information on the intra- and intermolecular energy exchange. The atomistic details contained in these results should be particularly useful for studying the mechanisms of energy sharing processes under highly transient and non-equilibrium conditions such as those encountered in picosecond chemistry and in detonation. These conditions present serious difficulties to both theoretical and experimental studies. For these reasons, we were encouraged to extend the investigation to other cases with a view to developing insight into the proper application of MD to this class of problems.

4. Endothermic Dissociation of A_2 : Equilibrium Kinetics

For the dissociation reaction of A_2 , we may write



where k_1 is the rate constant for the forward reaction and k_2 the rate constant for the reverse reaction. By changing the parameters in equations (1) and (2), it was easy to change from the exothermic dissociation of Section 3 to endothermic dissociation. We studied two endothermic cases [3]: In system A, we set $a_1 = \ln 2 / 0.5$, $a_2 = \ln 2 / 0.075$, $b_2 = 2.0$ and $Q = 0.5$, in equations (1) and (2). In system B, we set $a_1 = \ln 2 / 0.35$, $a_2 = \ln 2 / 0.05$, $b_2 = 0.4$, and $Q = 2.0$. These potentials are shown in Fig. 1. Our objectives here were twofold: (1) We wished to determine the overall equilibrium kinetics of the model and to compare the qualitative features of our results with those of real chemical systems. The latter have been well studied for more than one hundred years. Thus unless we obtained satisfactory agreement, the validity of our model would be in doubt. (2) If we could obtain good agreement, then it would be important to establish the relationship between the "measured" parameters of our results and the "molecular" parameters of the model. By measured parameters we mean the rate constants k_1 and k_2 , the equilibrium constant $K = k_1 / k_2$ (equation (6)), the activation energy change ΔE , and the activation volume change ΔV , etc. By molecular parameters we mean the pair potential, the kinetic and potential energies of the molecules and atoms, and the V , R , and T energies of the molecules, the mechanisms of dissociation, etc. These objectives make up a stringent set of tests on the validity of the model and on our understanding of its dynamical characteristics. If all the results should be favorable, despite the simplicity of the model, our confidence in the model and in the MD method naturally would be enhanced.

4.1. RATE CONSTANTS AND EQUILIBRIUM CONSTANT

The dependence of the rate constants k_1 and k_2 on temperature is given by the Arrhenius equation:

$$k_1 = B_1 \exp(-E_1/kT), \quad (7)$$

where B_1 is a frequency factor, and E_1 is the activation energy corresponding to k_1 . Similarly for k_2 . Then for equation (6) at equilibrium,

$$K = k_1/k_2 = B \exp(-\Delta E/kT), \quad (8)$$

where $B=B_1/B_2$, and $\Delta E=E_1-E_2$.

In equation (6) if we denote the concentration of A_2 at $\tau=0$ by N and the concentration of A_2 at time τ by $N-x$, then the concentration of the dissociated free atoms at time τ would be $2x$, and [8]

$$dx/d\tau = k_1(N-x) - k_2x^2. \quad (9)$$

At equilibrium, $dx/d\tau=0$, $x=x_\infty$, therefore

$$K = k_1/k_2 = (x_\infty)^2/(N-x_\infty). \quad (10)$$

We can also define an equilibrium constant K_x [9] in terms of the mole-fraction concentration: If $a=x_\infty/N$, then

$$K_x = 4a^2/(1-a^2). \quad (11)$$

The temperature dependence of K_x is similar to that of K in equation (8).

To determine the kinetic behavior of the model, we first prepared the system in its molecular form in thermal equilibrium at a low temperature. Then we rapidly heated the system, in 10 to 40 time steps, at constant volume, to raise the temperature to the desired level. After heating, we allowed the system to evolve without interference, while we continuously monitored the energies of the system, the number of dissociated molecules, etc., until the dissociation reached an equilibrium state in several thousand time steps (6,000 to 10,000). In some cases we also applied a correction to keep the total energy of the system constant to within narrow limits (0.0005ϵ). The cumulative corrections in 2000 or more time steps (at $\Delta\tau=0.01$ per time step) were found to remain small, typically under 0.3% of the total energy of the system. We obtained constant pressure conditions by adjusting the volume of the system by trial and error.

4.2. DISCUSSION OF RESULTS

With the potentials of system A, the molecular dissociations in the

initial stage would raise the potential energy and lower the kinetic energy of the system. This was the origin of the endothermicity of the reaction. The decrease in the kinetic energy, however, was not large, because of the efficient energy transfer in the T degrees of freedom of the free atoms, and because of the pressure rise in the system as the dissociation continued. Also, because the dissociations tended to occur singly, and sometimes in the reverse direction, the effect of the dissociating molecules on the average of the kinetic energy of the system was small. Thus the dissociation appeared to occur under a condition of thermal equilibrium within the system. This condition is usually assumed

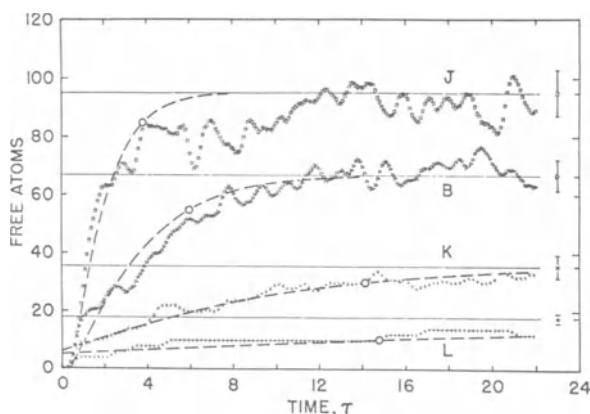


FIG. 9. Endothermic dissociation of system A (Fig. 1) at four temperatures under conditions listed below. Each data point is the average of 5 time steps ($\Delta\tau=0.01$), and is further smoothed by averaging over 5 points, 2 on each side. Dashed curves, equation (12), are fitted to the computed data at the points (O) indicated. The rate constants k_1 and k_2 are obtained from the fit on the assumption that they followed equation (8). Horizontal lines are the averages over the time interval $\tau=30-60$ when the system was assumed to have reached equilibrium. Vertical bars at the right indicate the standard deviation of the averages at equilibrium. From reference [3].

Run	Volume R_1^3	<u>Point of Fit</u>		E_k	$1/kT$	x_∞	$\ln k_1$	$\ln k_2$
		Free atoms	τ					
J	83.10	85.0	3.4	0.990	1.515	47.53	-1.71	-5.05
B	83.10	55.0	5.6	0.746	2.011	33.31	-2.82	-5.29
K	83.10	15.0	17.0	0.546	2.747	17.69	-4.55	-5.59
L	83.10	10.0	26.0	0.434	3.456	8.95	-6.36	-5.97

in the theoretical treatment of chemical kinetics. Our results were consistent with this assumption.

Fig. 9 shows the dissociation processes at four temperatures in one series of constant volume runs at $V=83.10 R_1^3$ (volume per molecule=0.649). The horizontal lines are the averages over the time interval $\tau=30$ to 60, when the system has reached an equilibrium state of dissociation. They give the values of x_∞ in equation (10) from which the values of K and K_x may be determined. The results indicate that the equilibrium state was maintained dynamically by molecular dissociation and recombination proceeding in opposite directions at comparable rates. The values of k_1 and k_2 may be determined by fitting the data of Fig. 9 to the solution of equation (9) at one point. The solution of equation (9) is given by [8]:

$$\tau = (1/2mk_2) \ln\{[N + x(m/K - 1/2)]/[N - x(m/K + 1/2)]\}, \quad (12)$$

where $m=(KN+K^2/4)^{1/2}$. Curves obtained from equation (9) are shown as dashed curves in Fig. 9. The small circle on each curve is the point of the fit to the MD data. The values of k_1 and k_2 obtained this way are tabulated in the caption of Fig. 9. We see from Fig. 9 that equation (12) represents the computed MD data well. This was found to be the case also for the other runs in [3].

Fig. 10 shows the equilibrium constant K_x plotted as $\ln K_x$ vs $1/kT$ for four series of runs, three at constant volumes and one at constant pressure. For all four runs, the relationship between $\ln K_x$ and $1/kT$ was linear to within one standard deviation of the data shown by the vertical and horizontal bars. This indicates that the equilibrium constants for this system, under different conditions, follow the Arrhenius relation.

Fig. 11 plots $\ln K_x$ vs pressure from the same data as in Fig. 10. The standard deviations of the pressure data were large, but we were able to sketch three constant volume curves (dashes and dots) and four constant temperature curves (dashes) from the data of Fig. 10 to give a consistent set of P - V - T data to within one standard deviation in most cases. From the constant temperature curves, we also obtained the slope $(\partial \ln K_x / \partial P)_T$ at different temperatures and at constant pressure (solid straight lines, $P=5.53$). It can be shown from thermodynamics [9,10] that this slope is related to ΔV , the volume change associated with the process:

$$\Delta V = -kT(\partial \ln K_x / \partial P)_T. \quad (13)$$

Now, under constant pressure condition, ΔE in equation (8) refers to the enthalpy change in the dissociation process:

$$\Delta E = (\Delta \epsilon + P\Delta V). \quad (14)$$

Here $\Delta \epsilon$ is the change in the internal energy associated with the process. In the present case, $\Delta \epsilon$ is equal to the change in the potential energy from that of the associated molecules to that of the dissociated free

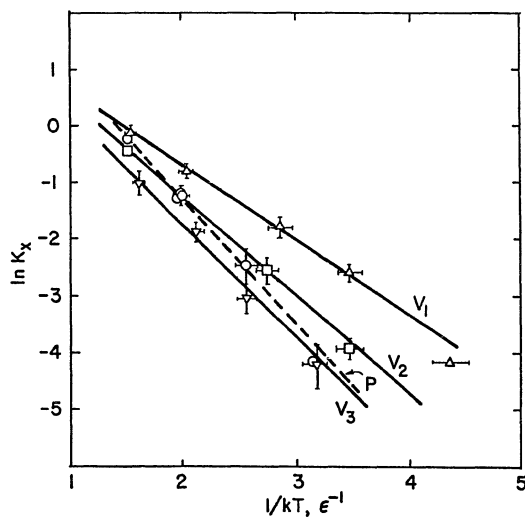


FIG. 10. $\ln K_x$ vs $1/kT$ for various runs of reference [3] at constant volume: $V_1=94.82$, $V_2=83.10$, $V_3=74.09 R_1^3$; and at constant pressure: $P=5.53 \epsilon/R_1^3$.

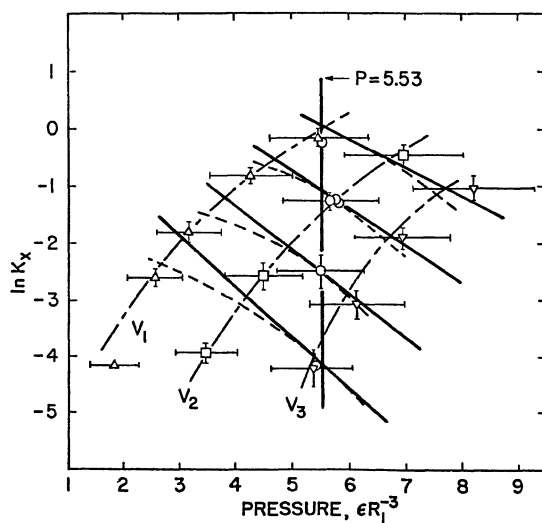


FIG. 11. $\ln K_x$ vs pressure for the runs of Fig. 10. Dashed curves are constant temperature curves, and their slopes at $P=5.53 \epsilon/R_1^3$ are shown by the straight lines and listed in Table 1. From reference [3].

atoms (E_{pm} to E_{pa}), because the kinetic energy of the free atoms was the same as that of the molecules (rapid equilibration), as noted earlier. With ΔV determined from equation (13) and $\Delta\epsilon$ determined from the MD data, ΔE can be evaluated directly from equation (14). The results are tabulated in Table 1. They show that ΔE obtained from the molecular data with the aid of equations (13) and (14) was in good agreement with that obtained from the "measured" data of Fig. 10. Although our data were limited in scope, this agreement shows that there was satisfactory consistency of the MD results with equilibrium kinetics based on thermodynamic considerations.

In a separate series of calculations with the interaction potentials of system B (Fig. 1), we obtained substantially similar results as those of system A, i.e., the dissociation in system B was also endothermic and the equilibrium constant also showed the typical Arrhenius dependence on temperature. At first sight, these results were puzzling because in system B the potential well of V_2 was higher than that of V_1 , so that the dissociation of an isolated molecule (in the gas phase) should be exothermic, not endothermic. The reason for this behavior was the positive ΔV for the dissociation reaction studied here. Each dissociation would do $P\Delta V$ amount of work on the surroundings. We expect this $P\Delta V$ term to be much larger in a condensed system than in a system at low density because of the higher potential energy in the former. Indeed, for system A, the data of Table 1 show that $P\Delta V$ was several times larger than $\Delta\epsilon$. Therefore if $\Delta\epsilon$ was not sufficiently negative in system B to make ΔE negative, as our results suggest, then the dissociation would be endothermic. In Section 3, we had set $Q=8$, and there the reaction was decidedly exothermic.

To summarize, we have found that the kinetics of our model in endothermic dissociation is entirely consistent with standard theories of chemical kinetics. For example, the temperature dependence of the equilibrium constant K or K_x followed closely the Arrhenius relation, and the computed

TABLE 1. Calculation of ΔE for constant pressure at $P=5.53\epsilon/R_1^3$

Run	τ	kT ϵ	$\left[\frac{\partial \ln K_x}{\partial P}\right]_T$	$\frac{\Delta V}{R_1^3}$	$\frac{P\Delta V}{\epsilon}$	$\frac{E_{pm}}{\epsilon}$	$\frac{E_{pa}}{\epsilon}$	$\frac{\Delta\epsilon}{\epsilon}$	$\frac{\Delta E}{\epsilon}$
A	35-75	0.655	-0.50	0.328	1.841	0.216	0.449	0.233	2.05
B	30-60	0.498	-0.65	0.324	1.792	0.059	0.456	0.397	2.19
C	30-70	0.390	-0.78	0.304	1.681	-0.122	0.422	0.544	2.23
D	30-80	0.318	-0.90	0.286	1.582	-0.248	0.396	0.644	2.23

Average $\Delta E = 2.18 \pm 0.09$

Negative slope of $\ln K_x$ vs $1/kT$ from Fig. 10 = 2.21

rate of dissociation agreed with that given by equation (12). The results also revealed information on the energy distribution within the system during dissociation, and confirmed that the process of dissociation occurred under thermal equilibrium, as commonly assumed. In addition to these qualitative features, we have been able to relate the molecular parameters of the model to the kinetic parameters of the system in a natural and satisfactory way based on general thermodynamic considerations. These results, therefore, tend to enhance our confidence in the MD method and in modeling.

5. Vibrational Energy Relaxation in a Diatomic Molecular Crystal

Chen and Ding [5] have carried out a series of MD calculations to investigate the vibrational energy relaxation process in a diatomic molecular model that was substantially the same as that studied in Section 4 here. They were interested in examining the relationship between the relaxation time and the parameters of the potentials (equations (1) and (2)) when only the vibrational degree of freedom of the molecules was heated. They kept $a_1 = \ln 2 / 0.35 = 1.9804$ in equation (1), but modified equation (2) to change the stiffness of the intramolecular potential as follows: they varied a_2 and b_2 over a range of values and changed the position of the bottom of the potential well from 0.15 to $c_2 = a_1 / a_2$. They also set $Q=0$. The values used are shown in Table 2 along with the main results. In Table 2, the square of α_v is the factor by which the kinetic energy of the molecules in the vibrational degree of freedom was increased (heated) without disturbing the kinetic energies in the R and T degrees of freedom; τ_r is the equilibration time (step size $\Delta\tau=0.01$), and f_{21} is a frequency factor, equal to the ratio of the natural frequency of the intramolecular potential of equation (2) to the natural frequency of the intermolecular potential of equation (1):

$$f_{21} = (1/c_2)b_2^{1/2} = (a_2/a_1)b_2^{1/2}. \quad (15)$$

TABLE 2. Conditions of six runs and their equilibration times

Run	a_1	a_2	b_2	c_2	α_v	f_{21}	τ_r
1	1.9804	6.0331	0.66	0.3283	1.7321	2.475	2.80
2	1.9804	6.8950	0.66	0.2872	2.0000	2.828	3.00
3	1.9804	6.8950	0.66	0.2872	1.7321	2.828	3.00
4	1.9804	5.6015	1.00	0.3536	2.2500	2.828	3.00
5	1.9804	9.7509	0.66	0.2031	1.4142	4.000	8.50
6	1.9804	9.7509	1.32	0.2031	3.0000	5.657	29.00

f_{21} is an approximation of the ratio of the intra- to intermolecular vibrational frequencies with the effects of other neighbors neglected. Fig. 12 shows the energy relaxation process for run 6 after heat addition at point A. Fig. 13 is a plot of $\ln \tau_r$ vs f_{21} for all six runs. The data are well represented by a straight line. The data show that the equilibration time was longer for larger f_{21} , that the different amounts of heating did not affect the equilibration time (*cf.* runs 2 and 3), and that the effects of b_2 and a_2 on the equilibration time was compensatory. They also found that the V-R relaxation was more efficient than the V-T relaxation. These features are in accord with our expectation. They suggest

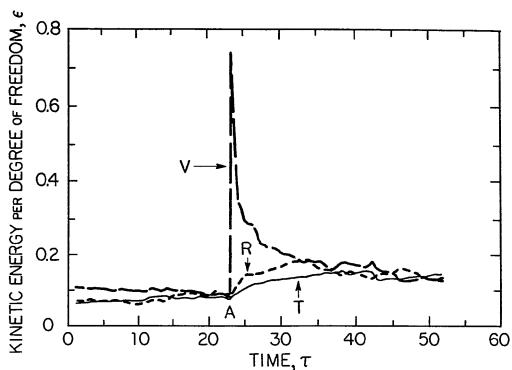


FIG. 12. Energy relaxation processes for run No. 6 in reference [5] at $f_{21}=5.657$. Point A was the time of heat addition. Time step $\Delta\tau=0.01$.

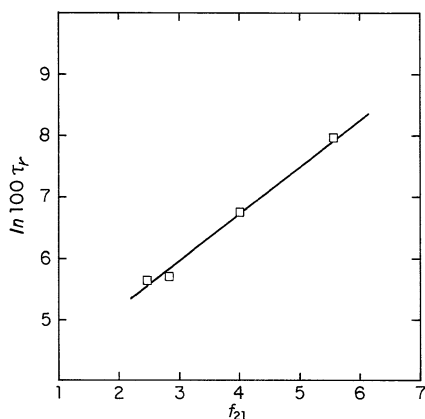


FIG. 13. Equilibration time vs frequency factor f_{21} from reference [5].

that the MD approach may be further developed for studying this class of problems, in connection, for example, with energy relaxation studies in picosecond laser experiments. Here the unique advantage of the MD method is that it gives rather complete dynamical information on the flow and the distribution of energy along different paths of energy exchange.

6. Simulation of Three-Body Interactions

As we have discussed earlier, with the two-body potentials of equations (1) and (2), it was necessary to invoke a special set of rules to allow only free atoms and diatomic molecules in the system, and not trimers, quadrumers, etc. These rules were arbitrary, and may not give a proper phenomenological description of the dissociation and the formation of diatomic molecules. It was of interest to introduce three-body interactions, following Murrell, *et al.* [6], as described in Section 2, to see what difference they would make in the dissociation and association processes.

With the potentials of equations (3) to (5), we may calculate the motion of the atoms under the combined effects of two- and three-body interactions. Figs. 14a and 14b show two sample trajectories for the reaction $A_2 + A$ in the gas phase, in reaction coordinates R_{12} vs R_{31} , where R_{12} is the distance between atoms 1 and 2, and R_{31} that between atoms 3 and 1. The potential energy surfaces, V of equation (3), are shown in contours of constant energy. The parameters of these surfaces and the initial conditions of the two trajectories are given in the figure caption. In Fig. 14a, the potential energy surface was for the case in which atom 3 approached molecule (1-2) along the perpendicular bisector of the latter, all three particles being in the plane $Z=0$; but at the start of the trajectory, the triangle 1-2-3 was slightly warped from the plane $Z=0$. This trajectory corresponded to the reaction $A_2 + A = A + A + A$: molecule (1-2) dissociated after some interaction with atom 3; the three free atoms stayed around a while longer and then flew apart. In Fig. 14b, both the potential energy surface and the trajectory were for the case in which atom 3 was colinear with molecule (1-2) along the X -axis. This trajectory corresponded to the reaction $A_2 + A = A + A_2$: molecule (1-2) dissociated after about ten intramolecular oscillations, and a new molecule (3-1) was formed, leaving atom 2 a free atom. If the interactions were limited only to the two-body potential of equation (2) and if the above-mentioned arbitrary rules applied, then the trajectories of Figs. 14a and 14b would not have been able to penetrate the region inside of R_{dis} , and molecule (3-1) could have formed only from outside the region, after molecule (1-2) had dissociated into free atoms.

Fig. 15 shows the dissociation process in the condensed phase at constant volume at six temperatures with both the two- and three-body interactions taken into account. The system was similar to that of Fig. 9, except it contained 250 molecules, and the volume per molecule was

$0.653 R_1^3$. The average number of free atoms, x_∞ , was taken in the interval between $\tau=35$ and 50. The standard deviation shown at $\tau=35$ corresponds to the scatter of the primary data in this interval. The results are similar to those of Fig. 9. The values of $\ln K_x$ obtained from x_∞ are plotted against $1/kT$ in Fig. 16. The data for V_2 (volume per molecule $=0.649 R_1^3$) in Fig. 10 are reproduced for comparison. With both two- and three-body interactions the equilibrium constants were slightly lower than those for the two-body case. Also, $\ln K_x$ vs $1/kT$ for the three-body case showed a curvature whereas for the two-body case it was nearly linear.

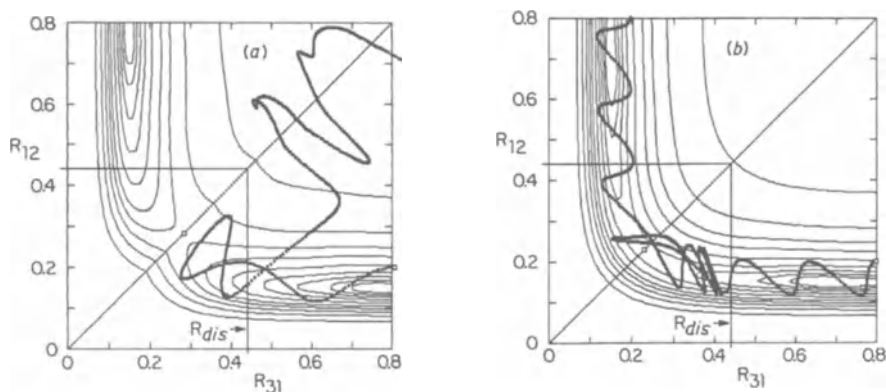


FIG. 14. Two trajectories of the reaction $A_2 + A$ in the gas phase with the two- and three-body interactions of equations (2-5) taken into account. The parameters of system A were used in equation (2), $R_{dis}=0.4556$, $R_b=3.8$ in equation (4). $V_3=76.91166\epsilon\exp(-R_3/0.05880282)$, for $R_3 \leq 0.35$; and $V_{31}=\epsilon(34.4941R_3^3 - 25.58808R_3^2 + 1.833879R_3 + 1.213748)$, for $0.35 < R_3 \leq R_{dis}$. R_{12} is the distance between atoms 1 and 2, R_{31} that between atoms 3 and 1. The potential energy surfaces (equation (3)) are shown in contours of constant energy at $V/\epsilon=2.0, 1.0, 0.5, 0.2, 0.0, -0.2, -0.34, -0.42, -0.47, -0.50$, starting from $V/\epsilon=2.0$ closest to the zero axes. In Fig. 14a, the saddle point (open square on diagonal) was at $R=0.284$, with energy of 0.224ϵ . In Fig. 14b, the saddle point was at $R=0.230$, with energy of -0.376ϵ . The trajectories start from the points marked by open squares on the right with initial conditions listed below:

Atom	Fig. 14a						Fig. 14b					
	X	Y	Z	U_x	U_y	U_z	X	Y	Z	U_x	U_y	U_z
1	-0.10	0.00	-0.019	0.00	0.50	0.00	0.10	0.00	0.00	0.20	0.00	0.00
2	0.10	0.00	0.00	0.00	0.50	0.00	-0.10	0.00	0.00	0.20	0.00	0.00
3	0.00	0.80	0.019	0.00	-1.00	0.00	0.90	0.00	0.00	-0.40	0.00	0.00

The probable reason for this curvature is that equilibrium had not been attained in these runs. Some support for this conjecture may be noted from the data for runs *E* and *F* (Fig. 15) which indicate that the number of free atoms was still rising at $\tau=50$. On the other hand, in runs *B*, *C*, and *D*, the free atoms actually overshoot their average values for long periods before $\tau=35$. The reason for the overshoot is seen from Fig. 17 which shows the kinetic energy per atom vs time for the six runs. The initial sharp rise was due to the rapid heating. At the end of heating, E_k was at its maximum, but dropped to the average value (both are marked

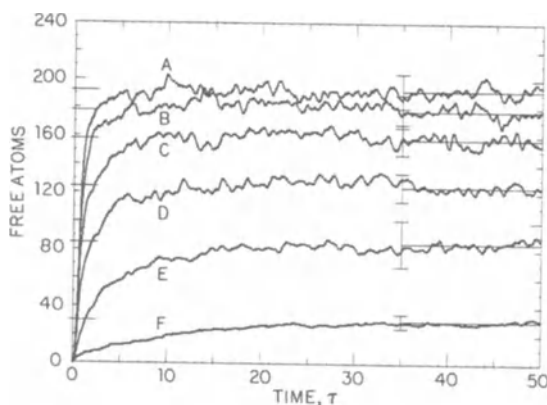


FIG. 15. Endothermic dissociation of the system of Fig. 2 with 250 molecules at 6 temperatures, with two- and three-body interactions taken into account. Conditions for the runs and the results are listed below. Each curve is the average of 4 to 7 cases, started from different points in phase space at constant total energy of $-0.63775 \pm 0.00002\epsilon$. The primary data for each case were taken at every 5th time step, $\Delta\tau=0.005$. Data from the various cases were averaged and were further smoothed at each time step by averaging over 21 steps, 10 on each side. Steady-state averages were obtained between $\tau=35$ -50. Error bar indicates the scatter of the primary data of the steady-state values.

Run	Volume R_1^3	E_k	x_∞	$1/kT$	$\ell n K_x$
A	163.14	1.474	96.36	1.018	-0.360
B	163.14	1.192	89.19	1.259	-0.539
C	163.14	0.949	79.19	1.580	-0.807
D	163.14	0.757	62.49	1.982	-1.322
E	163.14	0.616	42.57	2.436	-2.125
F	163.14	0.452	15.11	3.316	-4.222

by horizontal lines on the $\tau=0$ axis) in 5 to 10 units of time. The overshoot of E_k was due to the endothermicity of the reaction and subsequent equilibration, as discussed in Section 4 above. The point to note is that the overshoot was not uniform, but was large in runs *B* through *E*, especially in *C* and *D*. Because the dissociation was the most rapid during the initial period (Fig. 15), the larger overshoot must have

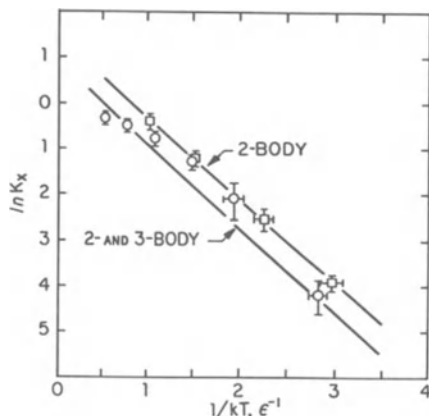


FIG. 16. Comparison of $\ln K_x$ vs $1/kT$ obtained from Figs. 9 and 15. For the two-body case (Fig. 9), volume= $83.10 R_1^3$ (0.649 per molecule), intercept=2.33, slope=-1.80. For the three-body case (Fig. 15), volume= $163.14 R_1^3$ (0.653 per molecule), intercept=1.79, slope=-1.72.

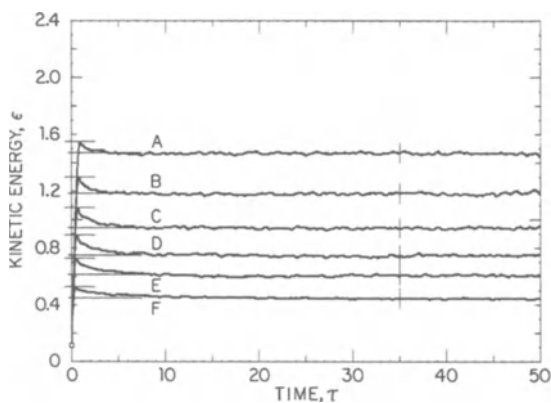


FIG. 17. Kinetic energies E_k of the system of Fig. 15 during the various dissociation processes. Maximum and average values (averaged between $\tau=35$ -50) are shown on the $\tau=0$ axis.

caused more dissociations during the initial stage than was normal. Once the overshoot had occurred, equilibrium would likely require a long time to establish, on the time scale of our calculations, because molecular association would now depend on mass diffusion of the free atoms to the site of the reaction. The foregoing considerations, if valid, should tend to reduce the curvature observed in Fig. 15. But more work is needed to determine the merit of these arguments. A linear least squares fit to the data gives a slope of -1.72 for the three-body case and -1.80 for the two-body case, for two comparable constant-volume series of runs, at approximately the same volume per molecule. These results indicate that the addition of three-body interactions made the molecular dissociation and association processes more realistic (Figs. 14a and 14b), and the equilibrium constants lower, than in the case of two-body interactions alone. The relationship of $\ln K_x$ vs $1/kT$, however, remained similar to the Arrhenius equation (Fig. 15).

7. Conclusions

We have discussed several MD studies dealing with both the exothermic and the endothermic dissociations of a hypothetical diatomic molecular crystal. We found that the dynamics and the kinetics of the system were well simulated under rather diverse conditions. Moreover, the results revealed such details of the motion of the atoms and their energies that we were able to obtain a fairly complete description of the energy transport and energy sharing, as well as other atomistic mechanisms, on the time scale of picoseconds for molecular processes. In the exothermic case, we found that the sharing of the potential energy, and of the kinetic energies among the dissociated free atoms and between the free atoms and molecules in the T degrees of freedom, was efficient. But the intra- and intermolecular energy exchange between the T - R , T - V , and V - R degrees of freedom was inefficient. During a rapid dissociation process the molecules were not in thermal equilibrium, either with themselves or with the rest of the system. Dissociation would occur only in molecules with vibrational energy higher than the binding energy of the molecules and then only if the caging effect was absent. The chance occurrence of these events was responsible for the observed induction time which showed an exponential dependence on the inverse of the initial temperature. Finally, because the dissociation of a molecule increased the local kinetic energy at the site of dissociation, and disrupted the local structural order, the probability of the next dissociation occurring in the neighborhood was enhanced. In this way the results showed the growth and propagation of the dissociation reaction.

In the endothermic case, the mechanism of dissociation remained the same, but thermal equilibrium was quickly established because the disturbance was small, and because energy sharing among the dissociated free atoms and with the molecules in the T degrees of freedom was

efficient. The equilibrium concentration was maintained dynamically, and the data allowed the determination of the rate constants k_1 and k_2 and the equilibrium constants K and K_x which were found to follow the Arrhenius equation with temperature change. The data also allowed the determination of $P\Delta V$ and ΔE from thermodynamic considerations, and we obtained good agreement of the MD results with thermodynamics.

Chen and Ding [5] obtained quantitative results on the rate of energy transfer between the V, R, and T degrees of freedom for this model, when only the V degree was heated. Their data showed a linear relationship between the equilibration time and the frequency factor f_{21} . Their study could be extended to yield quantitative information on the rate of energy redistribution among all the degrees of freedom. This kind of information would be useful in picosecond laser experiments, not only for interpreting experimental results, but also for checking the validity of the MD method.

By introducing three-body interactions, we were able to modify the potential energy surface on which the dissociation and recombination processes occurred. The addition of three-body interactions made the dissociation and association processes more realistic, without changing the basic Arrhenius relationship of $\ln K_x$ vs $1/kT$ obtained for two-body interactions. These comparisons — against different models and against experimental results when the latter are available — are especially useful for checking the MD results. They tend to increase our understanding of the modeling method, and when we obtain satisfactory agreement, increase our confidence in modeling.

The MD method has been applied to detonation studies by other investigators and by us [1]. In our view, the main limitation of the method is in our rudimentary knowledge of the interaction potentials, so that simulation of real energetic materials may be out of reach at this time. But even with this limitation, many problems may be studied from the MD viewpoint to develop our qualitative understanding of the detonation process on an atomic scale. Problems of energy exchange under the non-equilibrium conditions of detonation are especially suited to MD studies, because at the high temperatures involved classical mechanics of the MD method is valid, and because many parameters such as f_{21} , temperature, pressure, etc., may be adjusted over a wide range without difficulty. Moreover, powerful microcomputers are now available for doing large-scale computations at low cost. For example, most of the work of Section 6 was performed on MicroVAX II type of personal computers, and the work of Section 5 on an AT type of computer. In these circumstances, we expect that applications of MD to detonation research will increase both in scope and in importance in the future, alongside the chemical and hydrodynamic research in detonation being actively pursued in many laboratories.

ACKNOWLEDGEMENTS

We thank Chen Zhiying and Ding Jiaqiang, Institute of Mechanics, Chinese

Academy of Sciences, Beijing, S. Odier, Universite Pierre et Marie Curie, Paris, and M. Peyrard, Laboratoire ORC, Universite de Dijon, for helpful discussions. A part of the work on the three-body interactions was performed in the summer of 1987 by DHT at the Universite Pierre et Marie Curie, with financial support from the CNRS, Paris.

REFERENCES

1. D.H. Tsai, "Molecular dynamical approach to detonation studies and related problems in the condensed phase," preceding paper in this volume.
2. D.H. Tsai and S.F. Trevino, *J.Chem.Phys.* **79**, 1684 (1983).
3. S.F. Trevino and D.H. Tsai, *J.Chem.Phys.* **81**, 348 (1984).
4. D.H. Tsai and S.F. Trevino, *J.Chem.Phys.* **81**, Pt.I, 5636 (1984); S.F. Trevino and D.H. Tsai, in *Proc. Eighth Symposium (International) on Detonation, Albuquerque, July 1985*, edited by J.M. Short, NSWC 86-194 (US GPO, Washington, 1986) pp. 870-877; S.F. Trevino and D. H. Tsai, "The simulation of condensed matter chemistry and detonation," in *Proc. Army Science Conference, West Point, 1986*, to be published.
5. Chen Zhiying, Ding Jiaqiang, and D.H. Tsai, *Acta Mechanica Sinica*, (in English) **4**, 373 (1988); (in Chinese) **21**, 35 (1989).
6. J.N. Murrell, S. Carter, S.C. Farantos, P. Huxley, and A.J.C. Varandas, *Molecular potential energy functions*, (Wiley, New York, 1984) Chap.3.
7. For example, our results showing slow vibrational relaxation may be compared with the slow vibrational relaxation of nascent iodine molecules in liquid CCl_4 observed in experiments and discussed by D.J. Nesbitt and J.T. Hynes, *J.Chem.Phys.* **77**, 2130 (1982); see also, P.H. Berens and K.R. Wilson, in *Picosecond Phenomena II*, edited by R. Hochstrasser, W. Kaiser, and C.V. Shank (Springer, New York, 1980) pp.246-248; *J.Chem.Phys.* **74**, 4872 (1981).
8. W.J. Moore, *Physical Chemistry*, 2nd ed. (Prentice-Hall, New Jersey, 1955) p.539.
9. W.J. Moore, *Physical Chemistry*, 3rd ed. (Prentice-Hall, New Jersey, 1962) Chap.8.
10. S.D. Hamann, in *High Pressure Physics and Chemistry*, edited by R.S. Bradley (Academic, London, 1963) Chap.7, ii, pp.131-162.

FAST THERMOLYSIS-FOURIER TRANSFORM INFRARED SPECTROSCOPY METHODS TO STUDY ENERGETIC MATERIALS

THOMAS B. BRILL
Department of Chemistry
University of Delaware
Newark, DE 19716
USA

ABSTRACT. The philosophy and methods behind high heating rate thermolysis techniques combined with rapid-scan FTIR spectroscopy to diagnose thermal decomposition chemistry of energetic materials are discussed. One-dimensional methods are described that provide only the relative percent concentration of the gas products as a function of time. Two-dimensional techniques provide, in addition to the gas products, a real-time measurement of the temperature of the condensed phase. These are the Temperature Profiling/FTIR and Fast-Heat-and-Hold/FTIR methods. The three-dimensional technique called SMATCH/FTIR gives a simultaneous real-time measurement of the weight change and temperature change of the condensed phase and FTIR spectroscopy of the gas products while heating at 100°C/sec or faster. Acoustic levitation as a nonintrusive method to investigate droplets and bubbles spectroscopically is also described. Application of these techniques to advancing the fundamental understanding of physicochemical condensed phase and near surface processes in situations approaching combustion or explosion is given.

1. Introduction

Fourier transform infrared (FTIR) spectroscopy has the advantage where high energy throughput, rapid data acquisition and broad IR spectral band pass are required [1]. These facts were not lost on us in designing the studies described in this article nor on others when conducting investigations of complex thermal decomposition processes. In early studies of the kinetics of solid-solid phase transitions [2], the nature of the RDX and HMX melt phase [3], and the structure of the β -polymorph of RDX [4], FTIR methods made the difference between success and failure. Others have had similar success. For instance, the products and kinetics of RDX [5], HMX [6] and NO [7] thermolysis have been investigated successfully in a diamond anvil cell. The complex events during fast pyrolysis of coal particles has undergone a new level of analysis by FTIR methods [8].

The problem focused on in our laboratory has been the behavior of energetic materials (propellants and explosives) at fast heating rates. This subject requires the description of complex physicochemical processes in the condensed phase and the near surface regime. New sample cells and experimental methods needed to be developed that simulate the dynamic

conditions of combustion and explosion chemistry, where fast heating rates and elevated pressures are normal. Considerable success has been realized in the chemical descriptions, especially at the phenomenological level. At the instrument development level, these experimental methods have become a newly commercialized subfield of analytical spectroscopy.

We term this broad area Fast Thermolysis/FTIR Spectroscopy [9]. Variations on this basic theme include Temperature Profiling/FTIR Spectroscopy [10], in which the temperature changes of the condensed phase are also measured; Fast-Heat-and-Hold/FTIR Spectroscopy [11], in which isothermal decomposition is studied following rapid heating to a selected temperature; and SMATCH/FTIR [12], in which the mass change and temperature change are measured simultaneously at high heating rates. This chapter describes the methods and gives selected examples of each. The companion article of this Institute describes selected physicochemical results in more detail.

2. Historical Development

To emphasize the importance of coworker contributions, the history of our work in this area can be traced. Fast Thermolysis/FTIR Spectroscopy originated in our proposal to the Aerospace Sciences Directorate of the Air Force Office of Scientific Research in the Spring of 1982. At that time the Nicolet 60SX FTIR spectrometer, the first truly rapid-scanning FTIR spectrometer, was about to be introduced, and was needed to make the program viable.

An inventive graduate student, Richard J. Karpowicz, undertook the project. Toward the end of his doctoral program, Karpowicz developed the cell that was the forerunner of that used today for rapid gas evolution studies [13]. The project passed to a remarkably organized and hard-working new graduate student, Yoshio Oyumi, who in the next 3.3 years, using a simplified version of the cell [9], performed extensive studies designed to develop structure/property/decomposition relationships for a wide range of energetic materials. Oyumi and another graduate student, Stephen F. Palopoli, did much work to calibrate and parameterize the cell. Oyumi's name appeared on 27 papers, 23 of which dealt directly with the structure/property/decomposition theme. James T. Cronin, continued making innovations in the project. As he advanced, Cronin, with the aid by a new student, Thomas P. Russell, made a major improvement by adding real-time temperature profiling of the condensed phase to the real-time gas evolution studies [10]. For this and the development of acoustic levitation as an IR spectroscopy sampling technique [14], Cronin received a national Tomas Hirschfeld Student Award. Cronin and another new student, Peter J. Brush, also made the filament modifications that permitted fast-heat-and-hold experiments [11].

I refer to the experiments of Karpowicz, Oyumi and Palopoli, as "one-dimensional" because only one parameter of fast thermolysis, that of the gas species, was detected in real-time. I refer to the experiments of Cronin, Russell and Brush as "two-dimensional" because in addition to the gas species, a second important variable, the real-time temperature change of the condensed phase, is measured simultaneously with the evolved gases. The task of developing the first "three-dimensional" experiment, in which, in addition to real-time species and temperature change measurements, the

real-time mass change is simultaneously measured, was given to a post-doctoral student, Mark D. Timken. Timken, with later stage help from a beginning graduate student, Jangkang Chen, developed a technique which we call the SMATCH/FTIR method [12]. Chen is using the technique for fast thermolysis of polymer binders in his doctoral research. These fast thermolysis/FTIR methods add a new dimension to combined thermal analysis and spectroscopy. The methods are described below.

3. Near Real-Time FTIR Spectra of Gases from Fast-Heated Compounds

One can confidently state that no ideal experimental methods exist to characterize the condensed phase chemistry and physics and the near surface processes during combustion or an explosion. Trade-offs occur with respect to temporal resolution, the size and position of the spectral window, the number of species probed at one time, the configuration of the sample, the method of heating, the temperature, the pressure, etc. In designing our experiments we chose to optimize the amount of spectral information first and then to heat as rapidly as possible. Thus, our heating rates are one or two orders of magnitude slower than combustion heating rates, but are one or two orders of magnitude faster than conventional thermal analysis techniques. However, a great deal of new insight is gained with this faster heating rate range.

3.1 CELL DESIGN AND METHODS

To achieve our goal, a fast-thermolysis cell [9,13] was developed and its principles of operation [9] described and updated [10,15]. Figure 1 gives the essential design features. The anti-reflection coated 0.5" x 1" diameter ZnSe windows are held in a 3" diameter aluminum cylinder by brass end caps. ZnSe was used because it has good mid-IR throughput and has a high bursting pressure. The cell was designed to withstand a static pressure of 5000 psi, but is used only in the 1-1000 psi range. The filament is a creased nichrome IV ribbon (2.5 x 0.6 x 0.012 cm) supported on pressure-tight feed through insulators. Although studies were not conducted on a variety of compounds, a detailed study of a liquid gun propellant LGP1845 expected to be especially sensitive to catalysis revealed little dependence of the thermolysis products on the filament material [16]. Typically, 1-2 mg of sample (solid, liquid or mixture) was heated using a Foxboro 40 Pyrochem controller. The constant voltage-variable current feature of the controller has special value in the temperature profiling experiments discussed below. In principle, any reasonable heating rate of the sample could be achieved, but $<400^{\circ}\text{C}/\text{sec}$ was chosen because the spectral collection rate does not distinguish processes at higher heating rates. True combustion heating rates are thousands of degrees per second. The argon gas pressure in the cell was adjusted as desired in the 1-1000 psi range. Because of the importance of collecting IR spectra at high temporal resolution, the rapid-scan mode of a Nicolet 60SX FTIR spectrometer was used in all of these studies. With the beam focused several mm above the filament surface, the IR active gas products from the fast heated sample can be detected in near real-time. No significant change in the pressure occurred from the evolved gases because of the small sample size. If smoke or an aerosol forms during

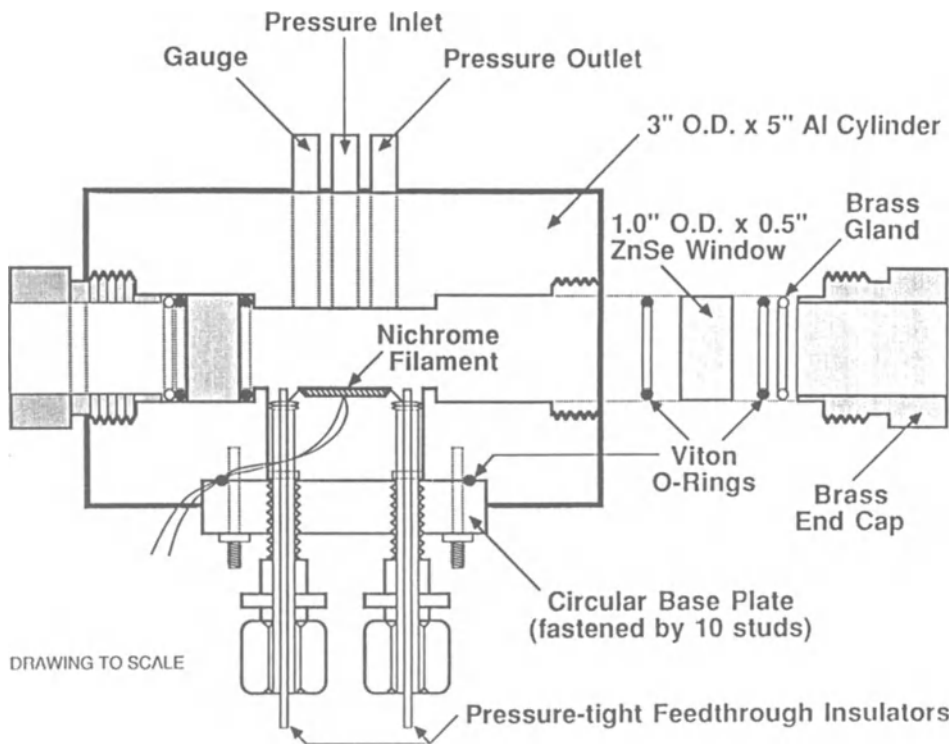


Figure 1. A sketch of the basic Fast Thermolysis/FTIR cell. The pressure ports and gauge are drawn in abstraction.

thermolysis, wavelength dependent dispersion causes the baseline to slope. However, the gas product concentrations usually still can be calculated. This basic cell is currently being developed by Spectra Tech around the CDS/Autoclave Engineers Model 2000 Pyroprobe for use in any IR spectrometer.

3.2 AN EXAMPLE OF THE RESULTS

In the above experiment there is no significant time delay between thermolysis and the detection of the evolved gases because the gases need only diffuse several mm from the sample to reach the IR beam. The gases rise into the cool Ar atmosphere of the cell where they are momentarily quenched during the detection stage. Based on the relative intensities of the P and R branches, the gases are in their ground state by the time they reach the IR beam. Argon was used as the atmosphere so that the intrinsic thermolysis characteristics of the parent compound are measured. If, for example, the thermolysis is performed in air, then the intrinsic thermolysis is intermixed with the reactions with O_2 and H_2O . N_2 was

initially used as the atmosphere, but it was discarded because of its potential to shift equilibria involving N_2 .

Figure 2 illustrates for a sample of RDX the good quality spectra that can be obtained. When heated at $dT/dt \approx 170^\circ\text{C}/\text{sec}$ from room temperature, the initial gases from RDX are first detected in about 1.15 sec because

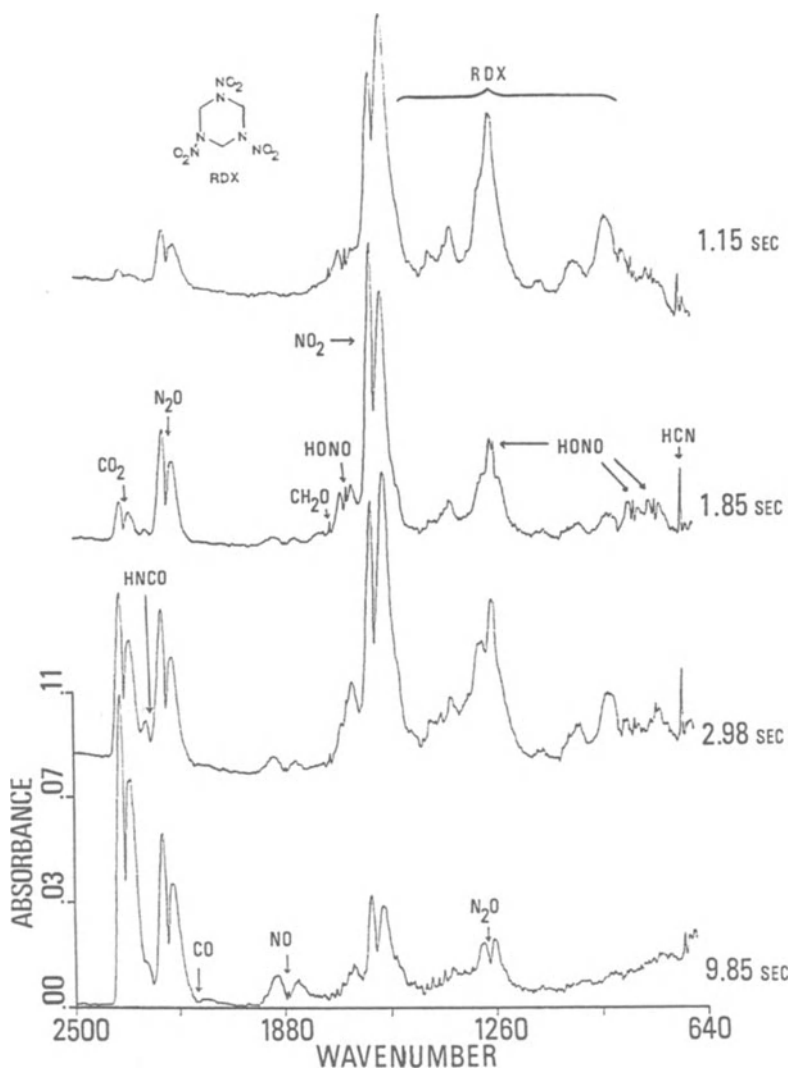


Figure 2. Selected absorption spectra of the gas products, along with a small amount of RDX aerosol, when 2 mg of RDX is heated at $170^\circ\text{C}/\text{sec}$ under 15 psi N_2 . The times given are those following the onset of heating. Note the good quality of spectra.

the thermal decomposition occurs at about 200°C. By using the IR intensities, it is possible to convert the observed absorbances to relative percent composition of the IR active gases [9] (*vide infra*). Figure 3 shows relative composition vs time profiles for RDX. In effect, these are percent concentrations based on volume. H₂O, IR inactive molecules, and any species for which the IR intensities are unknown (i.e., HNCO) are not included. The importance of near real-time analysis of the gas products in fast thermolysis research is evident from Figure 3. NO₂ is the dominant early decomposition product of RDX, but, because of secondary redox reactions, decreases rapidly in concentration, while NO increases. Note that NO is negligible at the onset of decomposition. As a result, if the time delay between the analysis and the onset of thermolysis were to exceed five seconds, then different and potentially incorrect conclusions about the thermal decomposition process of RDX could be drawn. The changes in the gas concentrations with time give an indication of secondary reactions among the gases, while the initial gas concentrations are most closely related to the thermolysis of the parent molecule. Based on extensive studies of the thermolysis of nitramines in various reactive atmospheres, the evidence is very strong that the processes leading to the initial gas products occur in the condensed phase [17]. Thus, condensed phase processes are largely separated from any gas phase processes in this experiment.

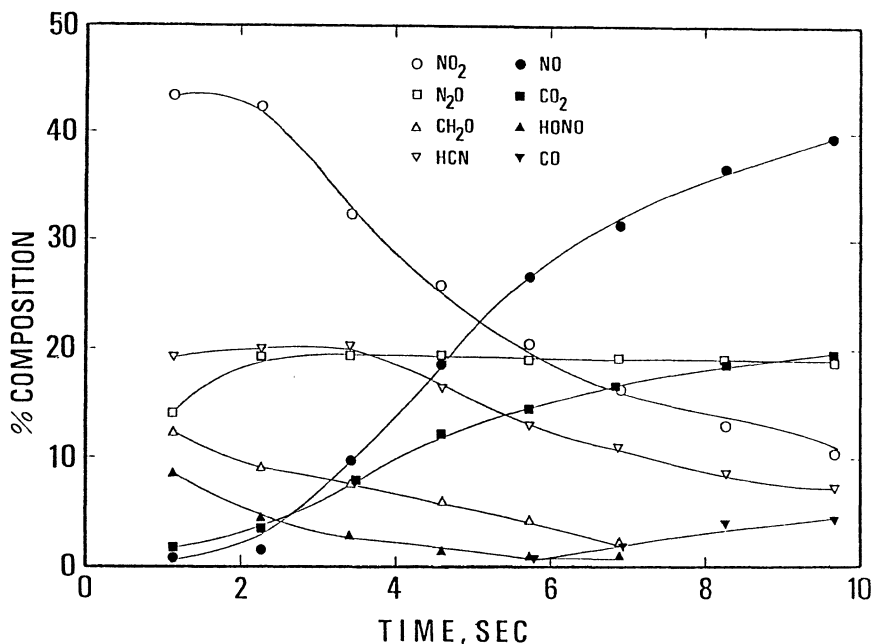


Figure 3. The relative percent concentration vs. time profile of the quantified gas products from RDX in Figure 2. Any H₂O, HNCO, IR inactive products and RDX aerosol are not included. Note the strong time dependence of several products.

3.3 A SUMMARY OF THE QUANTITATION PROCESS

The relative percent concentrations of the gas products were obtained by a procedure employing the effective width factors and absolute intensities of non-interfering absorbances for each product [9]. The effective width factors were determined from a greatly expanded, 2 cm^{-1} resolution spectrum of the decomposition gases. For most of the products, the area of the absorption of interest (Q branch only for NH_3 and HCN) was measured by using a planimeter and divided by the peak height. This gave an effective width factor for the absorption which was then divided by the absolute intensity to obtain a scaling factor. The scaling factor for each of the gases was then divided by that for CO_2 to obtain the relative percent concentrations based on CO_2 as the standard. Several known mixtures of gases were compared to the scaling factors derived in this way and gave similar results. For all subsequent studies, this scaling factor needed only to be multiplied by the peak height for the gas in question to obtain the relative percent concentration of that gas.

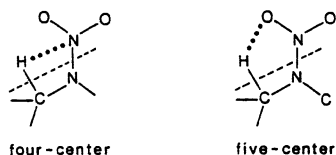
There are several potential sources of error. Pressure broadening can change the peak height. Experimentally, it was found that HCN was most affected by pressure and so a correction was needed at higher pressures. Occasionally, the desired absorption overlapped another absorption. This was overcome by estimating the curve profiles of each component and using the desired one. Given the uncertainty in some of the literature values for absolute intensities and the other approximations in this quantitation procedure, there is an absolute error of about $\pm 10\%$ in the concentrations, but the relative changes in concentration within a given plot, such as Figure 3, have lower error.

Because of the rotation-vibration fine structure, H_2O is difficult to quantify and, therefore, has not been included in the concentration-time profiles in our work. Homonuclear diatomics and any molecules for which IR intensities are unknown are also not included.

3.4 A COMPOSITION-DECOMPOSITION RELATIONSHIP REVEALED

Studies of the formation of HONO from secondary nitramines, $\text{R}_2\text{N}(\text{NO}_2)$ ($\text{R} = -\text{CH}_2-$), illustrate an advance made possible by Fast Thermolysis/FTIR methods [18]. HONO has been considered to be an important intermediate in the thermal decomposition of nitramines [19], but, because of its reactivity, was proposed based on indirect evidence [20,21] until this Fast Thermolysis/FTIR technique was applied. Cis- and trans- HONO are both present in the IR spectrum of the gas from RDX (see the PQR pair at $700\text{--}900\text{ cm}^{-1}$ in Figure 2), but as shown in Figure 3, HONO is transient under the conditions of the experiment. The initial concentration most closely reflects its relationship to the composition of the parent molecule. Figure 4 shows the quantity of HONO as a percentage of the initial gas products for various nitramines [18] versus the H/NO_2 ratio in the parent molecule. The general trend suggests that HONO arises from adventitious bimolecular encounters of $\text{H}\cdot$ and $\text{NO}_2\cdot$ radicals in the condensed phase [18], rather than concerted decomposition of the 4- and 5-center unimolecular intermediates shown below that may contribute in the gas phase [22].

Fast Thermolysis/FTIR has so far also made key contributions to uncovering relationships between the parent molecular structure and



decomposition gases in addition to HONO, such as NO_2 [23], CH_2O [24,25] and NH_3 [26]. These gases are important in determining the ignition and flame chemistry as well as the hazards of the parent compounds at elevated temperature.

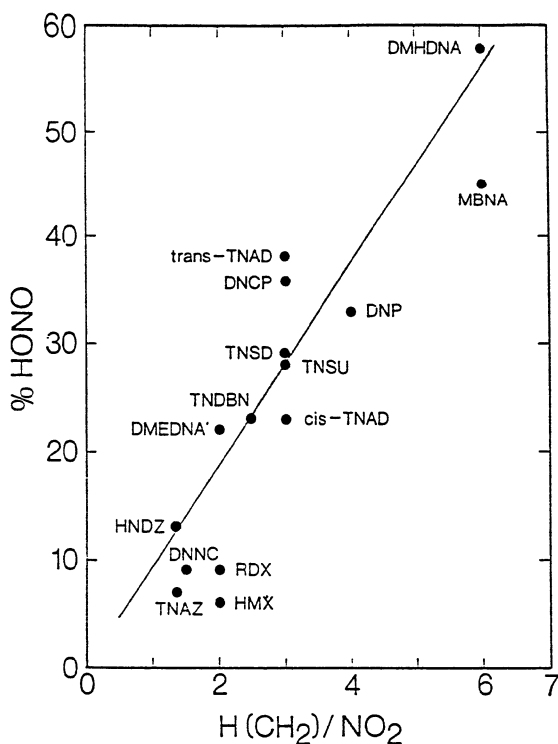


Figure 4. A plot of the initial relative percent concentration of HONO vs. the H/NO_2 ratio in the parent molecule for a series of nitramine compounds. See reference [18] for the names of the compounds.

4. Temperature Profiling/FTIR Spectroscopy

In the Fast Thermolysis/FTIR method discussed above, the final temperature and heating rate of the filament were established by spot-welding a type J thermocouple to the filament and recording its output on a digital oscilloscope. Subsequently, it was found that positioning a type E thermocouple on the underside of the filament opposite the sample and

leaving it in place during the thermolysis experiment enabled the endothermic and exothermic events of the condensed phase to be tracked simultaneously with detection of the gas products. This led to the Temperature Profiling/FTIR technique [10]. It proved to be straightforward to develop this technique because the heating of the filament is achieved by constant voltage-variable current control. Figure 5 shows a block diagram of the circuit used for this temperature profiling experiment.

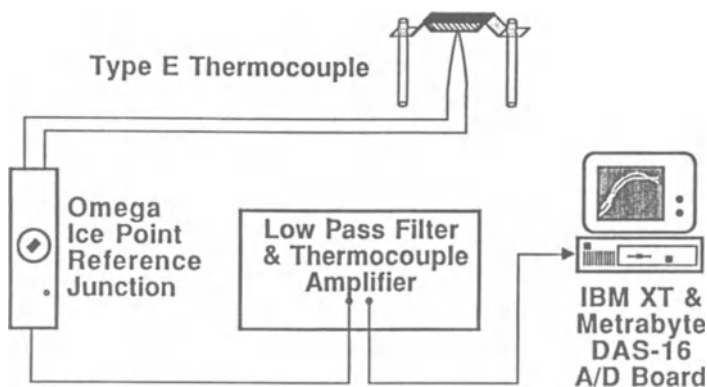


Figure 5. The block diagram of the circuit used for real-time filament temperature measurements in Temperature Profiling/FTIR Spectroscopy.

The 60Hz noise on the filament was removed by a low pass filter, and the signal amplified by about 100X with a differential amplifier. The analog output was processed through a Metrabyte DAS-16 AD convertor to an IBM-PC. The "take data" cycle of the interferometer triggered the heating of the filament so that there is a direct correlation between the time, temperature and interferogram. Four hundred data points were collected in the ten-second temperature measurement.

Figure 6 for ethylenediammonium dinitrate (EDD) shows a reference thermal trace (filament with no sample present) and a sample thermal trace (filament with 2 mg of EDD evenly and thinly spread on the center portion) superimposed on the difference trace (sample trace minus reference trace). Most of the endotherms and exotherms are evident in the sample thermal trace, but the difference trace clearly shows an endotherm preceding an exotherm in the 300-330°C range.

The temperature signature in Figure 6 needs to be explained for EDD, but, before doing so, it is worthwhile to mention several sources of endotherms and exotherms in the fast heating conditions used. Common origins of endotherms are melting, sublimation or evaporation, decomposition off-gasing, and endothermic chemical reactions in the condensed phase. Sources of exotherms are exothermic chemistry in the condensed phase and filament "catch up." Exothermic gas phase chemistry

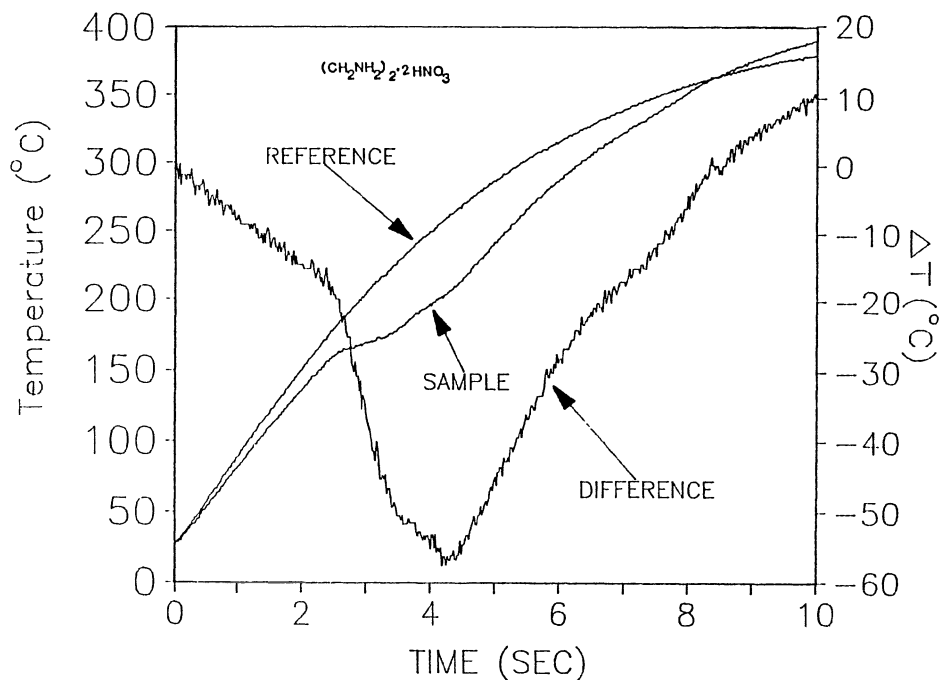


Figure 6. The filament temperature trace without sample (reference), the filament trace with 2 mg of ethylenediammonium dinitrate (EDD) spread on it (sample), and the difference thermal trace (sample trace minus reference trace). The initial heating rate is about 70°C/second and the atmosphere is 15 psi Ar.

makes a negligible contribution to the filament temperature in this experiment. Filament "catch up" arises from the fact that the portion of the filament in contact with the sample and thermocouple can have a lower temperature than regions away from the sample. This is because the sample may leave the filament by endothermic decomposition off-gasing, evaporation or sublimation. Toward the end of this process heat can flow rapidly from the hotter regions of the filament toward the cooler thermocouple area resulting in a rapid temperature rise. Therefore, an apparent exotherm is sensed which may not be connected to an exothermic chemical event in the sample. A true sample exotherm is a temperature rise that drives the sample thermal trace above that of the reference trace. An apparent exotherm that leaves the filament temperature below the reference trace may or may not be due to exothermic chemistry, because a chemical event cannot be readily distinguished from "catch up" by a single thermocouple measurement in this case. At this stage detailed quantitation of the thermal trace, as is done in DSC and DTA measurements, is difficult because of the complexity of the heat transfer phenomena at these high heating rates. However, the qualitative information produced is great.

Returning to the description of the thermal decomposition of EDD, Figure 7 shows the quantified gas products from EDD superimposed on the

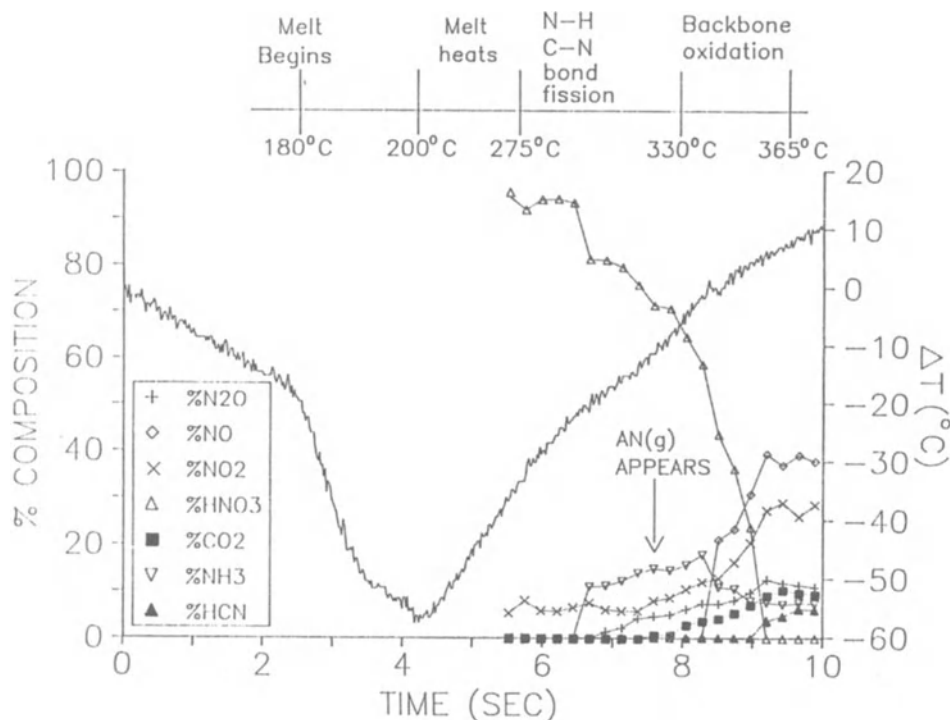


Figure 7. The difference thermal trace superimposed on the quantified gas products from EDD. H_2O , NH_4NO_3 aerosol and any IR inactive gases are excluded.

difference thermal trace [27]. This permits chemical and physical events to be attached to the temperature deflections. The initially negative slope of the difference thermal trace results from the additional heat capacity of the filament with the sample present. The melting endotherm occurs at about 175–180°C. At about 200°C, melting is complete (not isothermal because of the rapid heating rate) and the liquid phase continues to heat to about 275°C without evidence of decomposition off-gassing. At 275°C, the first gas products are detected. These are $\text{HNO}_3(\text{g})$ formed by proton transfer and desorption, and a small quantity of $\text{NO}_2(\text{g})$, probably from thermal decomposition of HNO_3 . $\text{NH}_3(\text{g})$ then appears perhaps from C–N bond heterolysis. The lag in the thermal trace shows that this stage of decomposition is, as might be expected, overall endothermic. However, above 330°C, CO_2 from backbone oxidation and the more reduced nitrogen oxide products, NO and N_2O , become detectable. The appearance of these products is accompanied by exothermic events in the condensed phase as evidenced by the increased heating rate of the filament. Thus, the combination of a real-time temperature record and near real-time observation of the gas products provides a mapping of the overall reaction sequence during the fast thermal decomposition of a complex material.

5. Pressure as a Variable

Apart from its practical value for suppressing sublimation and evaporation of the sample when so needed, pressure is a useful research variable. Since the initial pressure in the cell can be set as desired, we found that performing thermolysis with the initial pressure as the major variable gives additional insight [28]. Pressure differences affect gas diffusion rates. That is, the decomposition gases are forced to remain in contact with the condensed phase for different lengths of time. Figure 8 illustrates the effect of pressure on the initial relative percent of gas products from RDX. At lower pressure the most reactive gases (NO_2 , HONO)

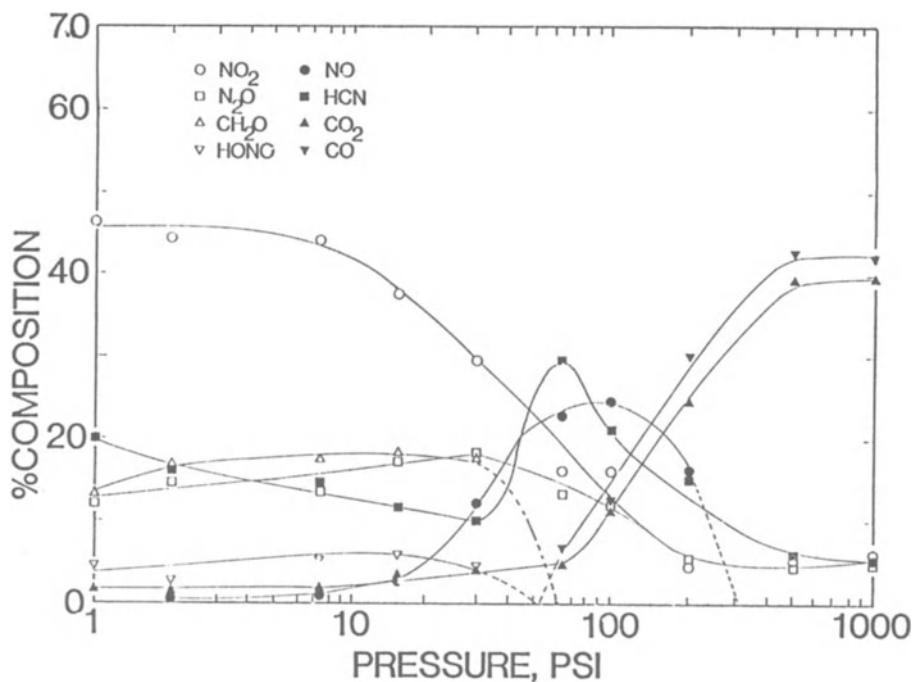


Figure 8. The pressure dependence of the initially detected gas products from RDX when the sample is heated at a similar rate at each pressure of Ar.

remain in high concentration because they are able to diffuse away from the reaction zone. When the applied pressure is increased, the gases remain in the reaction zone longer and react to the extent that products of intermediate stability dominate (NO, HCN). At the highest pressures studied, the most thermally stable products dominate (CO, CO_2 and, undoubtedly, N_2). We do not believe that a change in the decomposition mechanism of RDX is implied by these results, but simply that the order of reactivity of the nitrogen compounds ($\text{NO}_2 > \text{NO} > \text{N}_2$) and carbon compounds

(CH_2O , CO , CO_2) in this environment is reflected in the length of time the gases remain in the reaction zone.

The thermal trace can also display pressure dependence. If the position of the exotherm is insensitive to pressure, it suggests that the exotherm is driven by condensed phase reactions with little participation of the gas phase [29]. Conversely, a significant temperature shift of the exotherm with pressure, as occurs with nitrate salts [27], implies that heterogeneous gas phase-condensed phase chemistry is important.

6. Isothermal Decomposition Studies Following Rapid Heating

The uniformity and efficiency of heat transfer to the sample is enhanced and the complication of filament "catch up" is reduced by employing a much smaller filament (5.0 x 1.2 x 0.02 mm), smaller sample mass (200-300 μg), and a higher percent coverage of the filament by the sample [11]. The modified filament and sample holder are shown in Figure 9. The center one-

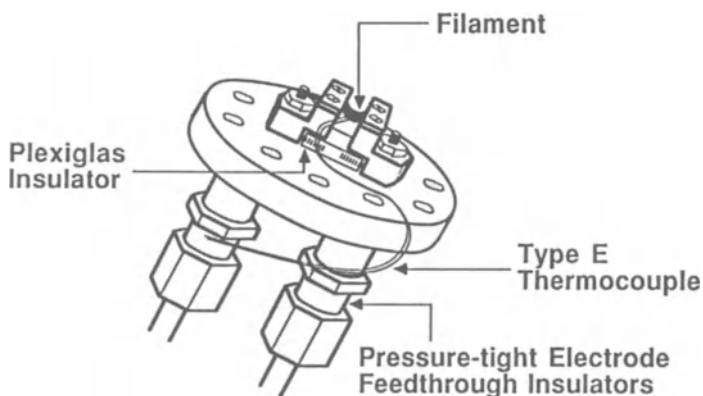


Figure 9. A sketch of the modified filament and filament holder used for the Fast-Heat-and-Hold/FTIR experiment.

third of the filament was covered by a thin layer of sample about 0.2 mm thick. Upon melting, the sample layer becomes much thinner, which further enhances the efficiency of heat flow. The smaller filament is also much more responsive to the heater circuit. This modification permits rapid heating to a specified temperature and then holding at that temperature. As before, the IR spectrum of the gas phase is monitored simultaneously with the temperature of the condensed phase.

The experiments were termed Fast-Heat-and-Hold/FTIR and can be used to simulate time-to-explosion tests of explosives [11]. Hence, Fast Thermolysis/FTIR can be used to study the explosion hazard of materials directly. Engineering tests, such as Henkin [30] and one-dimensional time-to-explosion (ODTX) [31], measure the time-to-explosion as a function of the sample temperature. As shown in Figure 10 for HMX, a similar measurement, the time-to-exotherm, is made in the Fast-Heat-and-Hold experiment [11]. An apparent activation energy can be calculated from

these data. In addition, however, the IR spectra of the gas products are obtained simultaneously making the cell a spectroscopically instrumented thermal explosion test. Figure 11 shows the relative percent concentrations of the gases from HMX for two time-to-exotherm profiles. First, it is important to note that thermal decomposition gases appear in advance of the exotherm indicating that autocatalysis must occur to achieve the exotherm. Second, N_2O and NO_2 are the first detected gases and their appearance precedes the appearance of CH_2O . The formation of N_2O and CH_2O from HMX has frequently been considered to be a coupled process [32].

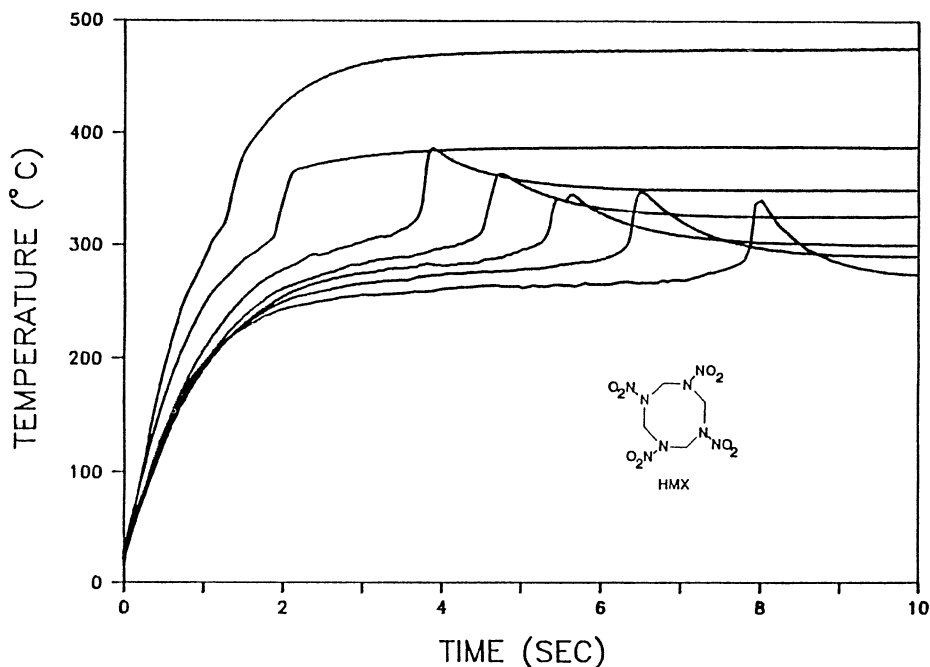


Figure 10. The temperature profile of 200 μ g of HMX showing the times-to-exotherm as a function of the sample temperature using the Fast-Heat-and-Hold filament design.

Figure 11 suggests that their formation is not necessarily coupled. Third, the difference in the gas profiles is relatively small and consistent with the higher temperature conditions (more extensive reactions) in the data on the left. There is no evidence of a change in the decomposition mechanism between the two sets of conditions shown.

7. SMATCH/FTIR Spectroscopy

If more than one decomposition step occurs upon rapid heating, then there is a question about how much of the compound is involved in each step. To address this question we have recently developed a technique termed SMATCH/FTIR spectroscopy (Simultaneous Mass and Temperature Change)/FTIR

which, as the name implies, permits the mass and temperature change to be measured at high heating rates [12]. Figure 12 shows the essential features of the sample holder for SMATCH/FTIR. The sample is coated onto a stainless steel end tip attached to a quartz capillary tube. The tube

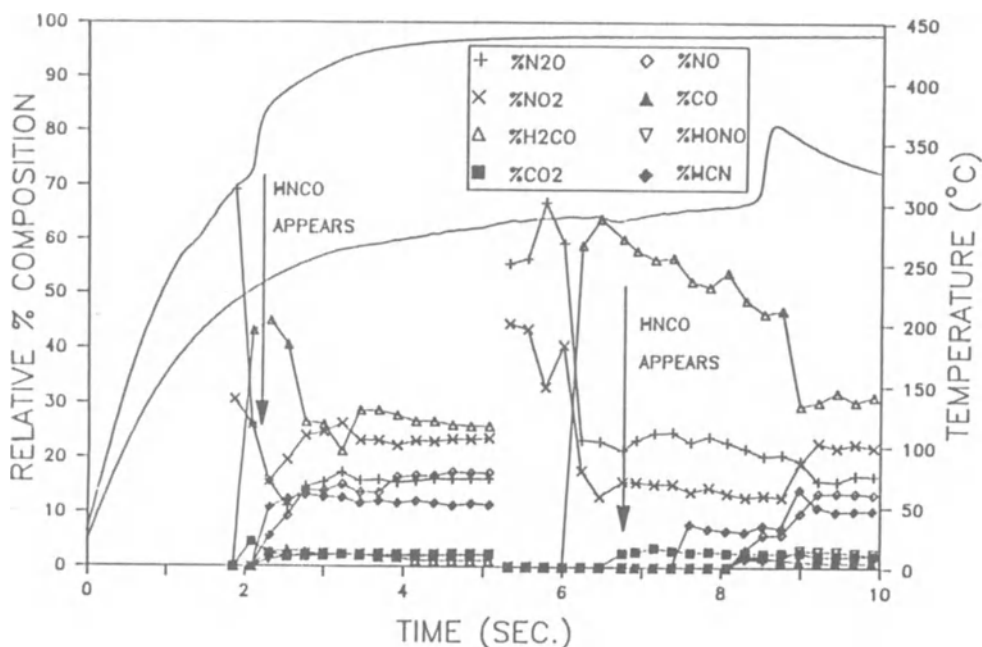


Figure 11. Selected time-to-exotherm data for HMX superimposed on the quantified gas products. The atmosphere is 15 psi Ar.

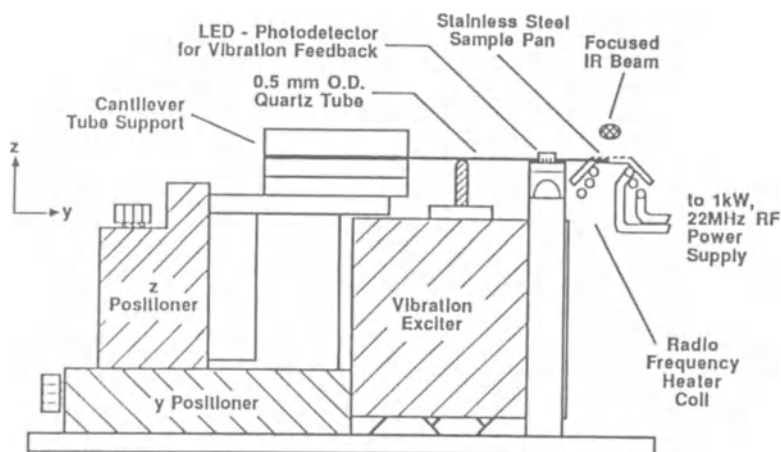


Figure 12. A sketch of the sample holder and cell region for SMATCH/FTIR.

is set into 130 Hz motion by the exciter piston. Heating of the metal end tip is effected by a 1 kW RF power source. The measurement of the mass change is based on the change in the vibrational frequency of the capillary tube as measured by the output of a photo-transistor that senses the motion. Some of the essential features of the design of this vibrator have been described by others [33]. The temperature change is measured by a type E thermocouple attached to the metal end tip. The gas products are evolved into a cell and are detected by the IR spectrometer beam focused about 1 cm above the metal end tip. The essential electronic features are given in Figure 13 for the temperature and mass change measurement. While

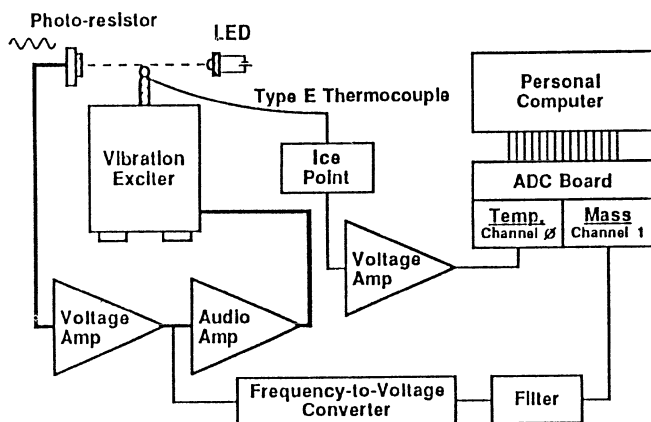


Figure 13. The circuit for the temperature and mass change measurement in SMATCH/FTIR.

this experiment is more complicated than the other Fast Thermolysis/FTIR experiments, it gives the most detailed information about the fast thermolysis process. The newness of the SMATCH/FTIR method precludes discussion of detailed experimental data at this time. However, Figure 14 shows a composite plot of the weight change, temperature change and gas products all measured simultaneously from 13.4% N nitrocellulose. SMATCH/FTIR has considerable power to characterize the fast thermal decomposition of energetic materials.

8. Acoustic Levitation/FTIR Spectroscopy of Droplets and Bubbles

Although not directly related to the fast thermolysis/FTIR spectroscopy techniques discussed above, it is worthwhile to include a different type of sampling technique that was developed around FTIR spectroscopy to investigate materials nonintrusively in the droplet state. Droplets are the state of the energetic matter in applications such as liquid gun propellants and diesel engines, yet droplets do not appear to have been investigated previously by dynamic FTIR. With this as an objective, an acoustic levitator was constructed in an optical bench external to the FTIR interferometer [14]. Figure 15 shows the essential features of the levitator itself. A titanium driver cone was powered at 22.4 KHz by using

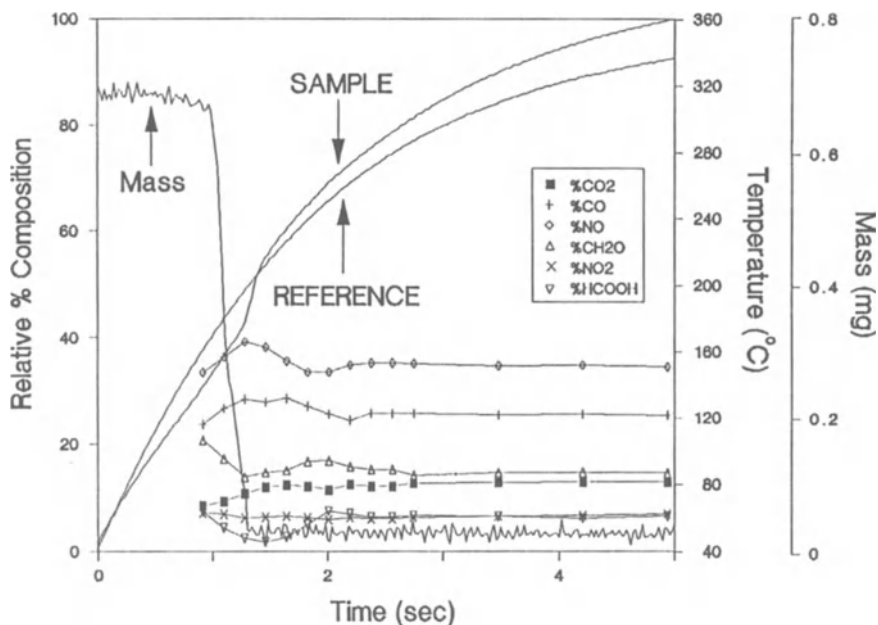


Figure 14. SMATCH/FTIR Spectroscopy of 13.4% N nitrocellulose showing the simultaneous measurement of the weight change, sample temperature and gas products.

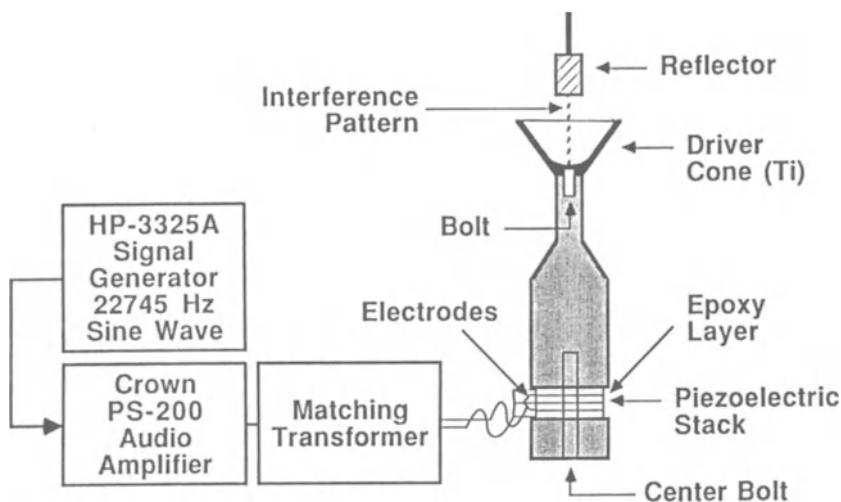


Figure 15. A diagram of the acoustic levitator assembly. A droplet or a bubble could be situated in the modes of the sound wave interference pattern.

a piezoelectric crystal stack. Although the sound wave is above the human auditory range, earmuffs were used because the power level was often high. When surrounded by a Plexiglas shell to reduce air currents, droplets and bubbles of up to 5 mm diameter could be stably levitated in the modes of the sound wave. The optical bench shown in Figure 16 was used to condense the IR beam by 6X and focus it on the droplet.

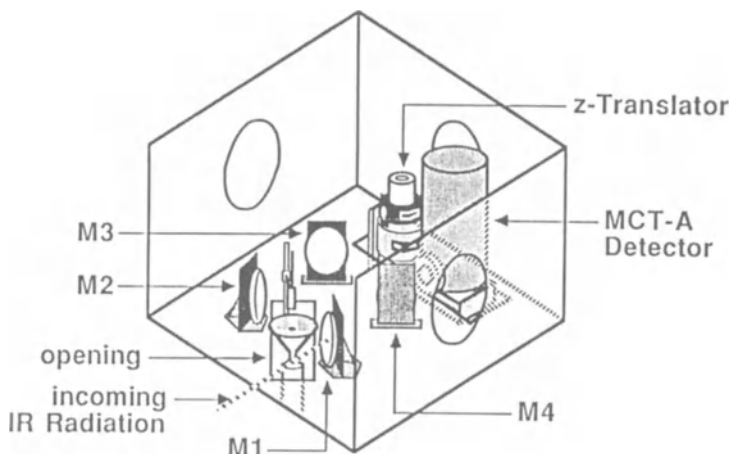


Figure 16. A drawing of the external IR optical bench used for studying acoustically levitated droplets.

The best results were obtained on bubbles, rather than droplets, because the pathlength was much shorter. Even with bubbles, the long pathlength requires that the studies be conducted on the weakest absorptions in the spectrum. Figure 17 illustrates this point using the mid-IR spectrum of a bubble of the liquid gun propellant LGP1845 along with a short pathlength spectrum obtained by using a Circle Cell [14]. The bubble can be heated in various ways, including a CO₂ laser, and investigated by the changes in the FTIR spectrum. The problem encountered with CO₂ laser heating is that the 10.6 μm line saturates the interferometer. A notch filter could be used to exclude this wavelength. This project ended before we had a chance to advance on this phase of the problem. However, after preliminary transmission experiments were conducted, it appears that more successful measurements might be performed in the emission mode. Nevertheless, acoustic levitation provides a novel approach to investigate the droplet or particle state of matter nonintrusively.

9. Conclusions

Fast Thermolysis/FTIR Spectroscopy gives considerable new mechanistic insight into the chemical and physicochemical processes that occur in materials undergoing rapid heating. The pressure and the composition of the atmosphere can be set as desired to gain an additional variable.

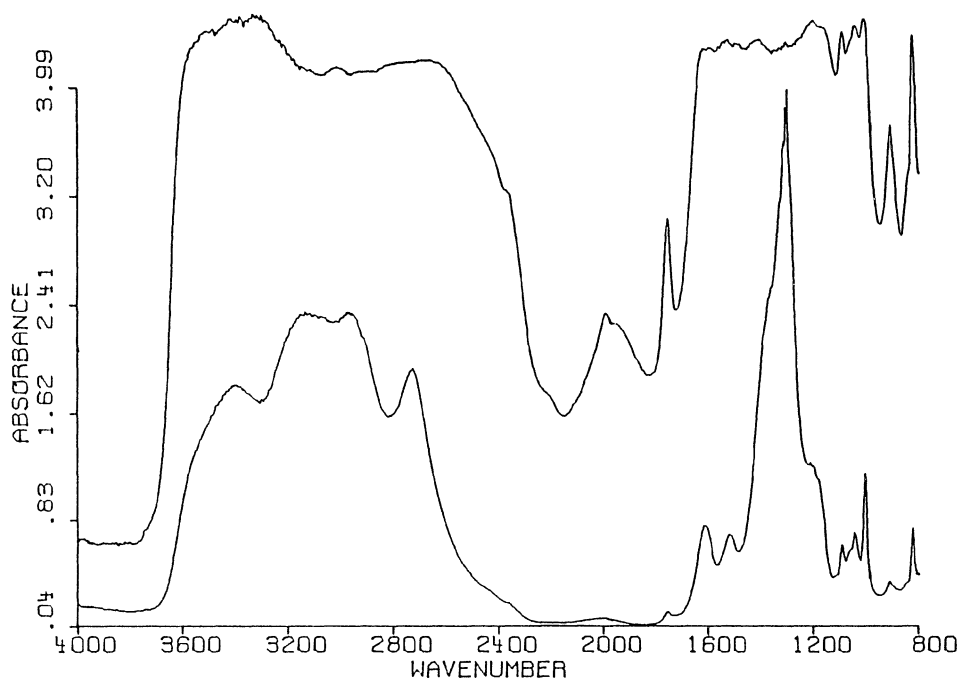


Figure 17. (Top) The absorbance spectrum of a levitated bubble of LGP1845. (Bottom) The Circle Cell spectrum of LGP1845. Because of the longer pathlength, the bubble spectrum is more intense, but the spectral features match well between the two.

The conditions of the experiment relate to fire and other combustion situations and explosions. The small sample size permits studies to be performed safely and on scarce research materials. The sample can be a mixture, a pure material, a solid or a liquid.

The methods also have application to quality control and routine analysis. Samples can be studied with reasonably rapid turnover. Once established on an authentic sample, the gas product distribution is frequently characteristic and distinguishable among various materials. Hence, Fast Thermolysis/FTIR has broad applications extending beyond the study of energetic materials. Its commercial availability will make advances possible in a wide range of applications in the future.

10. Acknowledgments

Doctoral students Richard J. Karpowicz, Yoshio Oyumi, Stephen F. Palopoli, James T. Cronin, Thomas P. Russell, Peter J. Brush and Jangkang Chen, and post-doctoral student Mark D. Timken took this field from dream to reality. The Air Force Office of Scientific Research (AFOSR-80-0258, AFOSR-85-0353, AFOSR-87-0033), the Army Research Office (DAAG29-84-K-0198), the Air Force Armament Test Laboratory (F08635-87-C-0130), and Morton-Thiokol, Inc., supported chemistry programs during which most of the methods described here were developed.

11. References

- [1] Griffiths, P.R. and DeHaseth, J.A. (1986) Fourier Transform Infrared Spectroscopy, John Wiley and Sons, New York.
- [2] Brill, T.B. and Karpowicz, R.J. (1982) 'Solid Phase Transition Kinetics. The Role of Intermolecular Forces in the Condensed Phase Decomposition of Octahydro-1,3,5,7-tetranitro -1,3,5,7-tetrazocine' Journal of Physical Chemistry 86, 4260-4265.
- [3] Karpowicz, R.J. and Brill, T.B. (1984) 'In situ Characterization of the 'Melt' Phase of RDX and HMX by Rapid-Scan FTIR Spectroscopy' Combustion and Flame 56, 317-325.
- [4] Karpowicz, R.J., Sergio, S.T. and Brill, T.B. (1983) ' β -Polymorph of Hexahydro-1,3,5-trinitro-s-triazine. A Fourier Transform Infrared Study of an Energetic Material' I & EC Product Research and Development 22, 363-365.
- [5] Miller, P.J., Piermarini, G.J., and Block, S. (1984) 'An FT-IR Microspectroscopic Method for Kinetic Measurements at High Temperatures and High Pressures' Applied Spectroscopy 38, 680-686.
- [6] Piermarini, G.J., Block, S. and Miller, P.J. (1987) 'Effects of Pressure and Temperature on the Thermal Decomposition Rate and Reaction Mechanism of β -Octahydro-1,3,5,7-tetranitro-1,3,5,7-tetrazocine' Journal of Physical Chemistry 89, 1678-1682.
- [7] Agnew, S.F., Swanson, B.I., Jones, L.H., and Mills, R.L. (1985) 'Disproportionation of Nitric Oxide at High Pressure' Journal of Physical Chemistry 89, 1678-1682.
- [8] Solomon, P.R., Sergio, M.A., Carangelo, R.M. and Markam, J.R. (1986) 'Very Rapid Coal Pyrolysis' Fuel 65, 182-194.
- [9] Oyumi, Y. and Brill, T.B. (1985) 'Thermal Decomposition of Energetic Materials 3. A High-Rate, In Situ, FTIR of the Thermolysis of RDX and HMX with Pressure and Heating Rate as Variables' Combustion and Flame 62, 213-224.
- [10] Cronin, J.T. and Brill, T.B. (1987) 'Thermal Decomposition of Energetic Materials 26. Simultaneous Temperature Measurements of the Condensed Phase and Rapid-Scan FT-IR Spectroscopy of the Gas Phase at High Heating Rate' Applied Spectroscopy 41, 1147-1151.
- [11] Brill, T.B. and Brush, P.J. (1990) 'Chemical Phenomena Associated with the Initiation of Thermal Explosions' Proceedings of the Ninth Symposium (International) on Detonation, Portland, OR, in press.
- [12] Timken, M.D., Chen, J.-K., and Brill, T.B. (1990) 'Thermal Decomposition of Energetic Materials 37. Simultaneous Mass Change

Temperature Change and FTIR Measurements at High Heating Rates (SMATCH/FTIR)' Applied Spectroscopy, submitted.

- [13] Karpowicz, R.J. (1984) Ph.D. Dissertation, University of Delaware, Newark, DE.
- [14] Cronin, J.T. and Brill, T.B. (1989) 'Acoustic Levitation as an IR Spectroscopy Sampling Technique' Applied Spectroscopy 43, 253-257.
- [15] Cronin, J.T. and Brill, T.B. (1989) 'Thermal Decomposition of Energetic Materials 33. The Thermolysis Pathway of the Azidodinitromethyl Group' Applied Spectroscopy 43, 650-653.
- [16] Cronin, J.T. and Brill, T.B. (1988) 'Thermal Decomposition of Energetic Materials 29. The Fast Thermal Decomposition Characteristics of a Multicomponent Material: Liquid Gun Propellant 1845' Combustion and Flame 74, 81-89.
- [17] Palopoli, S.F. and Brill, T.B. (1990) 'Thermal Decomposition of Energetic Materials 43. Mechanistic Features of HMX Decomposition Inferred from the Effect of the Gas Environment on the Products' to be published.
- [18] Brill, T.B., Oyumi, Y. (1986) 'Thermal Decomposition of Energetic Materials 17. A Relationship of Molecular Composition to HONO Formation: Bicyclo and Spiro Tetranitramines' Journal of Physical Chemistry 90, 6848-6853.
- [19] Melius, C.F. (1987) 'Molecular Decomposition Mechanisms of Energetic Materials' Journal de Physique 48, C4-341-352.
- [20] Bulusu, S., Axenrod, T. and Milne, G.W.A. (1970) 'Electron-Impact Fragmentation of some Secondary Aliphatic Nitramines. Migration of the Nitro Group in Heterocyclic Nitramines' Organic Mass Spectrometry 3, 13-21.
- [21] Farber, M. and Srivastava, R.D. (1979) 'Mass Spectrometric Investigation of the Thermal Decomposition of RDX' Chemical Physics Letters 64, 307-310.
- [22] Shaw, R. and Walker, F.E. (1977) 'Estimated Kinetics and Thermochemistry of Some Initial Unimolecular Reactions in the Thermal Decomposition of 1,3,5,7-Tetranitro-1,3,5,7-tetraazaacyclooctane in the Gas Phase' Journal of Physical Chemistry 81, 2572-2576.
- [23] Brill, T.B. and Oyumi Y. (1986) 'Thermal Decomposition of Energetic Materials 10. A Relationship of Molecular Structure and Vibrations to Decomposition: Polynitro-3,3,7,7-tetrakis (trifluoromethyl)-2,4,6,8-tetraazabicyclo[3.3.0]octanes' Journal of Physical Chemistry 90, 2679.

- [24] Oyumi, Y., Brill, T.B. and Rheingold, A.L. (1986) 'Thermal Decomposition of Energetic Materials 9. Polymorphism, Crystal Structures and the Thermal Decomposition of Polynitroazabicyclo [3.3.1]nonanes' *Journal of Physical Chemistry* 90, 2526-2533.
- [25] Oyumi, Y. and Brill, T.B. (1988) 'Thermal Decomposition of Energetic Materials 28. Prediction and Results for Nitramines of Bis-imidazolidinedione: DINGU, TNGU and TDCD' *Propellants, Explosives and Pyrotechnics* 13, 69-73.
- [26] Oyumi, Y. and Brill, T.B. (1987) 'Thermal Decomposition of Energetic Materials 25. Shifting of the Dominant Decomposition Site by Backbone Substitution of Alkylammonium Nitrate Salts' *Journal of Physical Chemistry* 91, 3657-3661.
- [27] Russell, T.P. and Brill, T.B. (1989) 'Thermal Decomposition of Energetic Materials 31. Fast Thermolysis of Ammonium Nitrate, Ethylenediammonium Dinitrate and Hydrazinium Nitrate and the Relationship to the Burning Rate' *Combustion and Flame* 76, 393-401.
- [28] Oyumi, Y. and Brill, T.B. (1987) 'Thermal Decomposition of Energetic Materials 22. The Contrasting Effects of Pressure on the High-Rate Thermolysis of 34 Energetic Compounds' *Combustion and Flame* 68, 209-216.
- [29] Brill, T.B. and Subramanian, R. (1990) 'Thermal Decomposition of Energetic Materials 35. A Mechanism Study of Decomposition of the Transition to Ignition-Like Behavior in Trinitromethyl Alkyl Compounds' *Combustion and Flame*, in press.
- [30] Henkin, H. and McGill, R. (1952) 'Rates of Explosive Decomposition of Explosives' *Industrial and Engineering Chemistry* 44, 1391-1395.
- [31] McGuire, R.R. and Tarver, C.M. (1981) 'Chemical Decomposition Models for the Thermal Explosion of Confined HMX, TATB, RDX and TNT Explosives' *Proceedings of the Seventh Symposium (International) on Detonation* US Naval Academy, Annapolis, MD 56-64.
- [32] For example, see reviews by Schroeder, M.A. (1979) 'Critical Analysis of Nitramine Decomposition Results: Some Comments on Chemical Mechanisms' *Chemical Propulsion Information Agency Publication* 308, 17-34; (1981) 'Critical Analysis of Nitramine Decomposition' *Chemical Propulsion Information Agency Publication* 347, 395-413.
- [33] Price, E.W., Sigman, R.K., Powers, R.J., Markou, C., and Sambamurthi, J.K. (1986) 'Combustion Mechanisms of Solids' *Final Report*, N00014-79-C-0764, Office of Naval Research, Arlington, VA 22217.

STRUCTURE-THERMOLYSIS RELATIONSHIPS FOR ENERGETIC MATERIALS

THOMAS B. BRILL
Department of Chemistry
University of Delaware
Newark, DE 19716
USA

ABSTRACT. Rapid thermal decomposition studies ($dT/dt \geq 70^\circ\text{C/sec}$) under static pressures of 1-1000 psi provide new insight into the behavior of energetic materials in the condensed phase. The connection between the parent molecular structure of nitramines and the tendency to liberate NO_2 , HONO , NO , N_2O , CH_2O , HCN , and hydrocarbons is discussed. Many important differences are found between the results of gas phase decomposition studies and those herein for the condensed phase which points out the hazards of transferring gas phase notions to the condensed phase. In addition to nitramines, selected correlations for C-NO_2 , O-NO_2 , N-NO , azide, furazan, and furoxan containing compounds, energetic metal complexes, and nitrate salts are presented. The effect of applied pressure and the thermolysis of mixtures are addressed. Various solid phase phenomena are described in the context of energetic materials. Some application of these physicochemical phenomena to explosives and propellant ignition and combustion are discussed.

1. Introduction

The physicochemical events that take place during the fast thermal decomposition and pre-ignition of energetic materials are among the more poorly understood molecular aspects of the propulsion and explosion process. This is partly because it is extremely difficult to gather information about this regime under realistic conditions. Figure 1 shows a very simple, generalized, one-dimensional view of the main zones. Of greatest interest to us has been the approximately $100\ \mu\text{m}$ thick region that constitutes endothermic breakup of large molecules to form smaller species that go on to feed the exothermic decomposition flame. The overall process of combustion is extremely complicated when one blends the details of this thin zone with the detailed chemistry of the gas phase and the fluid mechanics of turbulent diffusion.

Given the thinness and complexity of the interface between the condensed phase and near surface gas region, there are no ideal methods to probe the chemistry directly. At present, one must resort to experiments that simulate some or all of the conditions of combustion or explosion. The most relevant experiments employ rapid heating, realistic pressures, and allow gases, liquids and solids to be present simultaneously.

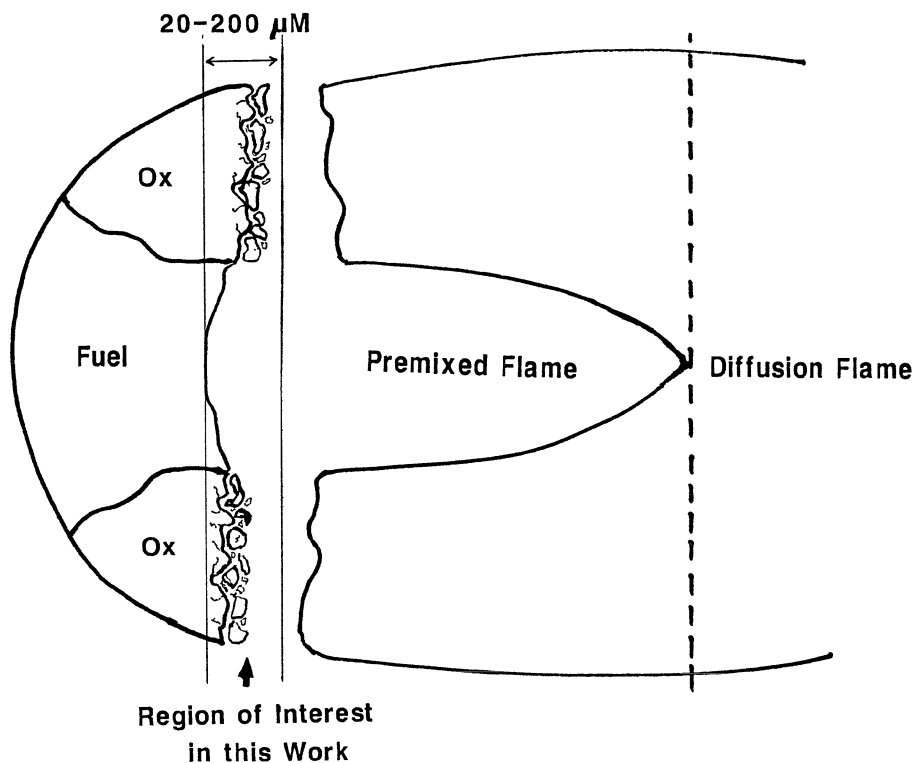


Figure 1. A simplified one-dimensional view of propellant combustion showing the region of interest in the studies described in this article.

Real-time diagnostics are needed because the processes take place dynamically. If such simulation experiments are successful, then major practical advances are possible toward understanding the pre-ignition and ignition of solids, and at least parts of the combustion process of energetic materials. The enormous complexity of the chemistry and physics mitigate against attempting to specify the events quantitatively at this time. In most cases, even a qualitative phenomenological description is valuable because this level of chemical understanding is frequently not even available from experiment.

Toward filling these voids, we have developed several fast thermolysis/Fourier transform infrared spectroscopy techniques that permit near real-time studies of energetic materials heated at 70-400°C/sec under selected pressures in the 1-1000 psi range. These techniques are described in the companion article for this Institute.

We have a number of objectives for our research effort. First, we have sought to discover structure/property/decomposition correlations that connect the parent molecular structure and composition to the evolved gases near the surface. This is a step toward coupling the formulation of the material to its combustion and explosion characteristics. An inert atmosphere (Ar), rather than a reactive atmosphere (air), is used during

the thermolysis process so that the decomposition gases reflect the intrinsic thermolysis behavior of the compound rather than its thermolysis augmented by primary and secondary reactions with the air. Second, since pressure is such a ubiquitous variable, we wanted to uncover the effect of pressure on the overall processes. Third, we are interested in the behavior of mixtures of energetic materials because this is frequently the "real world." Fourth, we have continued to investigate the solid phase behavior of energetic materials since this can influence their manufacture, use and efficacy. Fifth, we have attempted to relate our findings to the physicochemical effects that could be important in explosions and propellant combustion.

I wish to stress that all of these subjects are on-going studies in our laboratory. This article should be viewed as a progress report expected to be constantly updated. Some of the conclusions could even change as we gain further insight. It is also important to emphasize that the research summarized in this article deals mostly with the condensed phase. Much work has been conducted by others on the thermal decomposition of energetic molecules in the gas phase. It will soon be evident that many of the observations and conclusions we draw from our work are partly or entirely at variance with the gas phase data. We believe that this points out (once again) that gas phase kinetics and mechanism studies do not routinely describe the reaction behavior of energetic materials in their neat condensed phase.

2. A Comment on Other Structure/Property/Decomposition Studies

Much of the research on reactivity in the field of chemistry can be classified as attempts to uncover structure-reactivity relationships. This very broad categorization is narrowed considerably in this article to those studies where a relatively large number of related compounds are systematically subjected to the same technique for the purpose of extracting correlations between the parent molecular structure and a thermal decomposition characteristic. At the risk of excluding important and relevant papers (entirely unintentional), a few studies of this kind are noted here in the spirit of emphasizing that we are neither the first nor the only workers in this field.

Correlations of the oxygen balance of a parent energetic compound and its impact sensitivity (a thermal decomposition phenomenon) are well known [1-3]. Hammett correlations with the explosive sensitivity in arylammonium perchlorate salts have been uncovered [4]. Relationships between the composition [5] and decomposition [6,7] of explosives and their detonation velocity are known. Extensive studies have been made relating molecular structure to the kinetics and thermolysis trends for aliphatic nitro compounds [8], azides [9,10], and nitramines [11]. Correlations of the melting point with burn-rate [12], functional group with decomposition temperature [13], and various structural parameters with stability [14] have been proposed.

Our research is mainly focused on reactions of energetic materials at high heating rates, under sub- and super-atmospheric pressures, and with near real-time detection of the gas products and the temperature changes. Because of this particular focus, no attempt whatsoever is made to review the field of decomposition of energetic materials. This is because most

other studies have been carried out under conditions that are very different from ours. An encyclopedic compilation [15] and various more specialized reviews are available [8,11,16-18] as a guide to other work.

3. Correlations of the First Detected Gases with Structure and Composition of the Parent Molecule

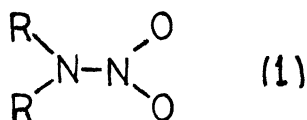
A determined effort has been made through fast thermolysis studies in the past seven years to establish the relationships between the structure and composition of the parent energetic molecule and the near surface gases. These gases dominate the pre-ignition and ignition chemistry of the gas phase. In turn, their products control the flame chemistry. If such connections can be uncovered, then the work of the synthesis chemist could be guided by the combustion and explosives scientist. In truth, however, the connections have been elusive because (1) the gas evolution data must be acquired under reasonably realistic and representative conditions, and (2) ignition, burn-rate and other ballistic data on a wide range of energetic materials have not been available. The first requirement is the objective of our work. The second is not a capability in our laboratory and has, therefore, hampered progress toward making these connections. However, confidence that the thermolysis results are at least approaching the right goal comes from the fact that our findings for nitramines qualitatively resemble many aspects of the theoretical gas products profiles of Melius [19] and bear some resemblance to the results of microprobe-mass spectrometry [20] and planar laser induced fluorescence [21] studies of nitramine flames.

Cells and an experimental protocol were developed to provide near real-time detection of the gas products and the physicochemical phenomena of fast heated energetic materials and fuels. We use the heating rate, final sample temperature and pressure as the main variables. Through the generosity of many synthetic organic chemists and hard-won syntheses of our own, a wide variety of compounds have been assembled containing the energetic functional groups R_2NNO_2 , $RHNNO_2$, $=NNO_2$, R_2NNO , $RONO_2$, R_3CNO_2 , $R_2C(NO_2)_2$, $RC(NO_2)_3$, $RC(NO)_2F$, $RC(NO_2)_2Cl$, $RC(NO_2)_2N_3$, alkynes, guanidines, furazans, furoxans, tetrazoles, triazoles and salts of NO_3^- and ClO_4^- . Some of the compounds contain more than one energetic site enabling competition studies to be performed. Solid and liquid physical states, monomers and polymers, and pure and mixed components were investigated. The compounds were grouped into sets as we saw appropriate so that the relative percent composition of the first detected gases could be correlated with the structure and composition of the parent molecule. These gas products were detected several mm above the surface of 1-2 mg of thinly spread sample. The heating rates were in the range of 70-400°C/sec. The buffer gas was a cool Ar atmosphere. The pressure was set as desired in the 1-1000 psi range. The gas products were monitored in time, which frequently gave some insight into the decomposition reaction sequence and/or the secondary reaction behavior of the product gases. However, the initial gas product composition is often the most useful for correlations with the parent molecular structure. These gases are generated mostly by condensed phase reactions [22]. Therefore, the discussion in this article is largely focused on issues of the condensed phase.

This section summarizes the structure/decomposition correlations found in our work for various classes of energetic compounds. More details and justification for most of the results are contained in the original articles.

3.1 NITRAMINE (N-NO₂)-CONTAINING COMPOUNDS

One of the most important classes of energetic materials is that containing the nitramine function group. We have made an extensive study of nitramines and the work is continuing. For a secondary nitramine, the six



atom framework of unit (1) tends toward planarity in most nitramines where the C-N-C angle is unstrained. The planarity of the unit and the N-N bond order, which is intermediate between a single and double bond, suggests that significant electron delocalization exists in the NNO₂ fragment [23]. The small excursions from planarity at the amine nitrogen atom follow no systematic pattern, which implies that packing and steric requirements are predominately responsible for distortions. In fact, the RDX molecule in RDX-sulfolane contains one planar, one *exo* and one *endo* NNO₂ group [24] clearly showing that a low barrier to distortion exists. For this reason, we have discounted a previous attempt to explain the rate of NO₂ production from gaseous nitramines on the basis of planar and pyramidal distortions of the amine nitrogen atom [25].

The nitramine functional group can be the source of NO₂(HONO) and HCN or N₂O and CH₂O depending on the temperature and structure of the molecule. These and other issues are now addressed.

3.1.1. Tendency to form NO₂(g). The formation of NO₂ is of major importance in nitramine combustion because it is an oxidizer in the primary flame. Although not previously discussed as such, it seemed plausible to us that the length of the N-N bond in secondary nitramines might be an important factor in the tendency of the N-N bond to homolyze and liberate NO₂ upon fast thermolysis. Because of the reactivity of NO₂, it is necessary to draw these conclusions from rapidly heated samples and to employ near real-time detection (IR spectra recorded at 50-100 msec intervals) of the initial gas products. Otherwise, secondary reactions of NO₂ disguise any relationships between its concentration and the structure of the parent molecule. Of course, it must be emphasized that even the simple homolysis of the N-N bond in the condensed phase is, overall, a complicated process. Bimolecular activity is possibly present. At the very least, the NO₂ must diffuse through and desorb from the heterogeneous environment before it is detected. The most severe complication would be for N-N bond homolysis to follow or to compete with another decomposition route, such that the initial N-N bond distance would no longer be the controlling factor. If this were the case, then any general structure-decomposition relationship involving NO₂ could be futilely disguised. We

hoped for better luck, but chose to look for general patterns rather than absolute quantitation at this time.

The crystal structures of many nitramines needed to be determined and combined with the structures already available to build the database for this comparison. Putting these together, Figure 2 [26,27] shows a plot of

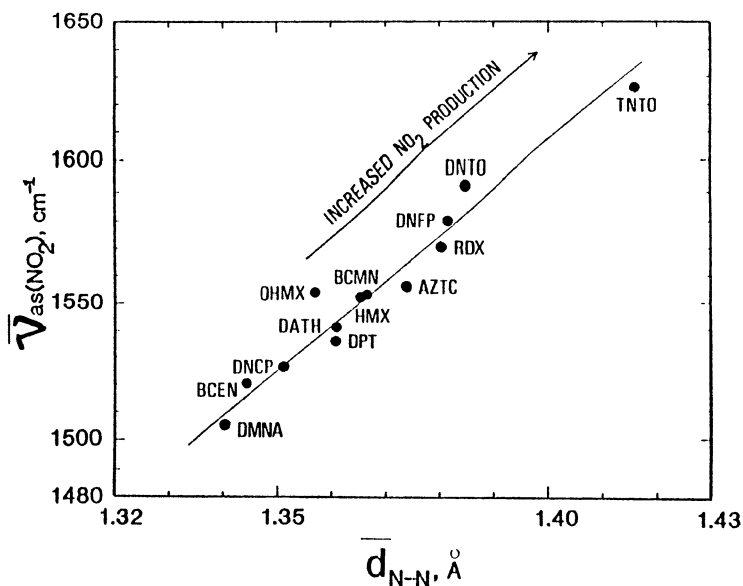
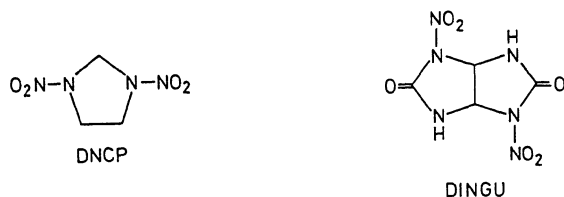


Figure 2. The average asymmetric NO_2 stretching frequency compared to the average N-N bond distance in secondary nitramines. Compounds to the right tend to be strong NO_2 generators upon fast thermolysis.

the average N-N bond distance versus the average asymmetric NO_2 stretching frequency from the infrared spectrum of a series of secondary nitramines, R_2NNO_2 . The compound identities are given elsewhere [26,27]. A reasonably good trend exists between these two parameters, suggesting that the force constant of $-NO_2$ stretching depends markedly on the amount of electron density that $-NO_2$ shares with the adjacent N-N bond. From fast thermolysis it was found that NO_2 is the dominant, initially detected product for compounds on the right side of this plot. NO_2 was either not detected or was detected as a lesser abundant product from compounds on the left side. Thus, long N-N bonds favor N-N scission. Hence, with reasonable confidence one can predict the amount of NO_2 likely to be generated by fast thermolysis of a given secondary nitramine compound from its IR spectrum or crystal structure.

The simple connection in Figure 2 could be expected to, and does, have exceptions. Several potential causes were mentioned above. Most thermal decomposition processes of complex molecules are a balance of competitive reactions [28]. For instance, a different degree of stability of the backbone could shift the balance from one mechanism to another [29]. If

the backbone is especially stable, as would be expected of the five-membered 1,3-dinitroimidazolidine (DNCP) ring, then the rate of ring



opening would be slowed relative to N-NO₂ homolysis. This could cause NO₂ to be a major product despite the relatively short N-N bond. This is what is observed for DNCP [30]. NO₂ (and HONO) are among the dominant, initially detected gas products even though the N-N bond distance is 1.35 Å. Conversely, a compound with a relatively long N-NO₂ bond distance might produce much less NO₂ than Figure 2 suggests if the backbone is especially unstable. This is because the decomposition rate might be controlled by the backbone fission route causing the N-NO₂ bond to break more slowly or to be retained in favor of N₂O generation. 1,4-Dinitroglycoluril (DINGU) [31] illustrates this behavior. The average N-NO₂ bond distance is 1.375 Å and $\nu_{\text{as}}(\text{NO}_2)$ is 1565 cm⁻¹ suggesting that NO₂ should be a significant product. NO₂ is not detected under 15 psi Ar, but, instead, N₂O dominates. We attribute this departure from expectation to the fact that the backbone is thermally unstable toward the loss of stable products, such as HNCO, and that the N-N bond is preferentially retained in the fragmentation process of the backbone.

Despite some exceptions that can be qualitatively rationalized on the basis of competitive or separately preferred decomposition pathways, it is encouraging that most secondary nitramines thermolize in the condensed phase in a systematically predictable way. Thermal reactions in the neat condensed phase are complex, but the result above gives hope for uncovering and refining patterns that can be applied in practice to propellant combustion and explosives.

3.1.2. Tendency to Form HONO(g). Closely related to NO₂ is the formation of HONO. At least one additional process, that of H· participation, is required before HONO(g) is detected. Kinetic modelling indicates that HONO formation plays a key role in the N-N bond fission process [32]. The formation of HONO has been used in many previous studies of nitramines to rationalize products, but it was not detected directly before Fast Thermolysis/FTIR Spectroscopy was applied. HONO is a reactive and, thus, transient molecule which is not observed without rapid heating and near real-time product detection. However, both the *cis* and *trans*-HONO isomers can now be routinely observed from nitramines [30].

After examining a large number of nitramines heated at 145–180°C/sec under 15 psi Ar, it was discovered that the initial relative percent composition of HONO depended strongly on the parent secondary nitramine [30]. In one instance, HONO represented nearly 60% of the first detected gas products. A broad relationship was discovered between the ratio of the H atoms to NO₂ groups in the parent molecule and the initial percentage of HONO detected as shown in Figure 3. The leveling off at the higher percent

values is attributable to dilution of the HONO by other gases. Insight into the processes by which HONO is formed from the condensed phase is contained in the pattern of Figure 3. The concentration of HONO must

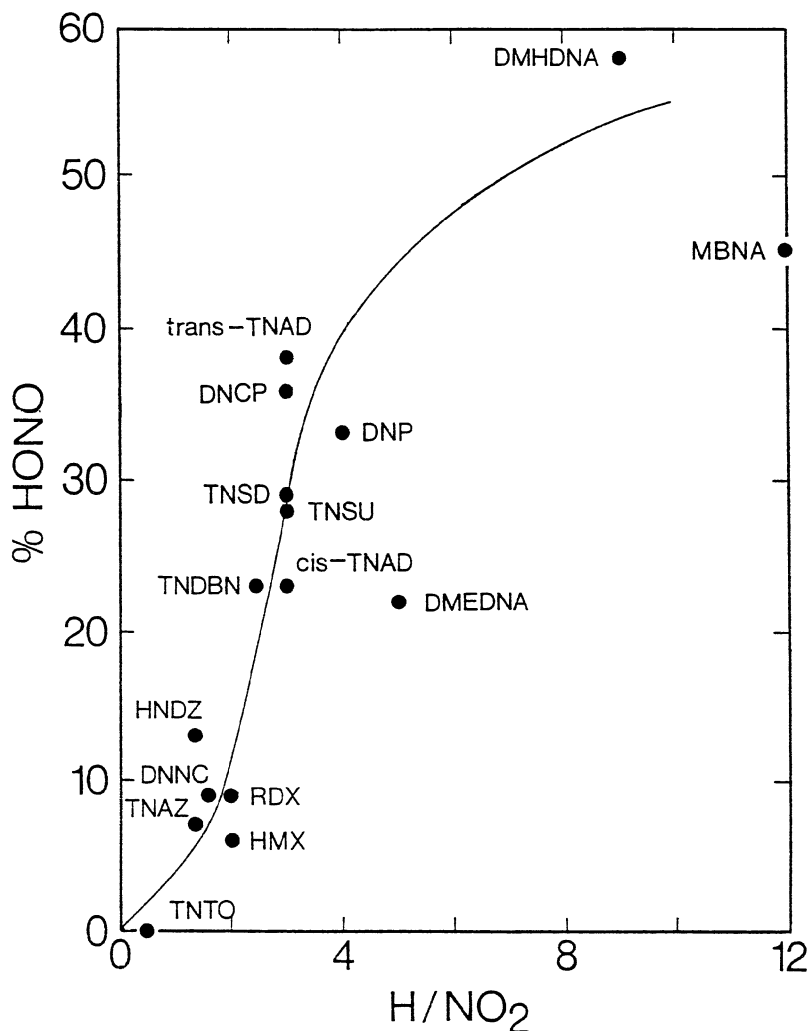
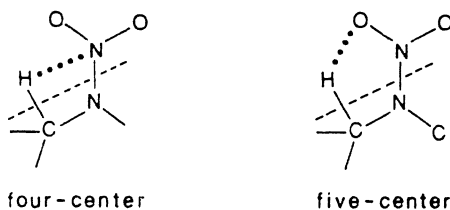


Figure 3. The relative percent of HONO initially detected on fast-thermolysis of secondary nitramines compared to the H/NO₂ ratio in the parent molecule.

depend on the adventitious encounter of H· (or an H· source) and NO₂· (or an NO₂· source) in the condensed phase. Statistically increasing the chance for contact enhances the HONO concentration. The molecularity, the nature of the transition state and any other aspects of the reaction

mechanism are beyond the extension of these condensed phase data. Many species could liberate $H\cdot$, but it is interesting to note that C-H bond fission has been proposed to be rate-determining in nitramine decomposition [33,34] and combustion [35]. H_2O has also been suggested to assist possibly in HONO formation [36], but the pattern in Figure 3 would still need to be accommodated if this were the case. Compounds producing the largest amounts of HONO are not the ones expected to produce the largest amounts of H_2O because of their low oxygen content. Also, the four- and five-center concerted reactions that could be important in the gas phase [37], do not appear to dominate in the condensed phase. If they did, only



a $-CH_2-$ fragment adjacent to the nitramine would be required to produce HONO. All nitramines having this linkage should produce the same amount of HONO, which they do not.

The most plausible explanation for HONO formation remains the chance contact between $H\cdot$ and $NO_2\cdot$. In keeping with this notion, steric crowding of H and NO_2 groups in a molecule enhances the initial HONO concentration [30]. It is interesting to note that when the H/NO_2 ratio is calculated using only the H atoms from secondary carbon atoms ($-CH_2-$), the fit is slightly more linear as shown in Figure 4. This suggests that $-CH_2-$ groups are somewhat more efficient $H\cdot$ sources than primary carbon atoms ($-CH_3$). Nitramines having only tertiary carbon atoms ($\equiv CH$) do not produce HONO [26,31].

3.1.3. Tendency to Form $NO(g)$. NO plays a role in the secondary flame chemistry of compounds containing NO_2 groups [38]. It is very rare not to detect NO during the fast thermolysis of secondary nitramines. The initial amount of NO is variable, but almost always increases during the ten seconds of the thermolysis experiment. The relative amounts of NO_2 and HONO decrease nearly monotonically as the NO increases. This pattern implies that a major source of NO is secondary reactions of NO_2 and HONO in the gas phase or, possibly, in the heterogeneous condensed phase. In keeping with this, NO becomes a higher percentage of the total gas when the thermolysis is performed at super-atmospheric pressures (30-300 psi), but at a pressure below the range where N_2 usually dominates (>500 psi Ar).

Because the majority of the NO appears to emanate from later stage reactions, especially in the gas phase, its relationship to the parent molecular structure in the condensed phase is primarily through the concentrations of NO_2 and HONO produced in the primary decomposition steps. First, a major source of NO is the equilibrium (1) which favors NO at

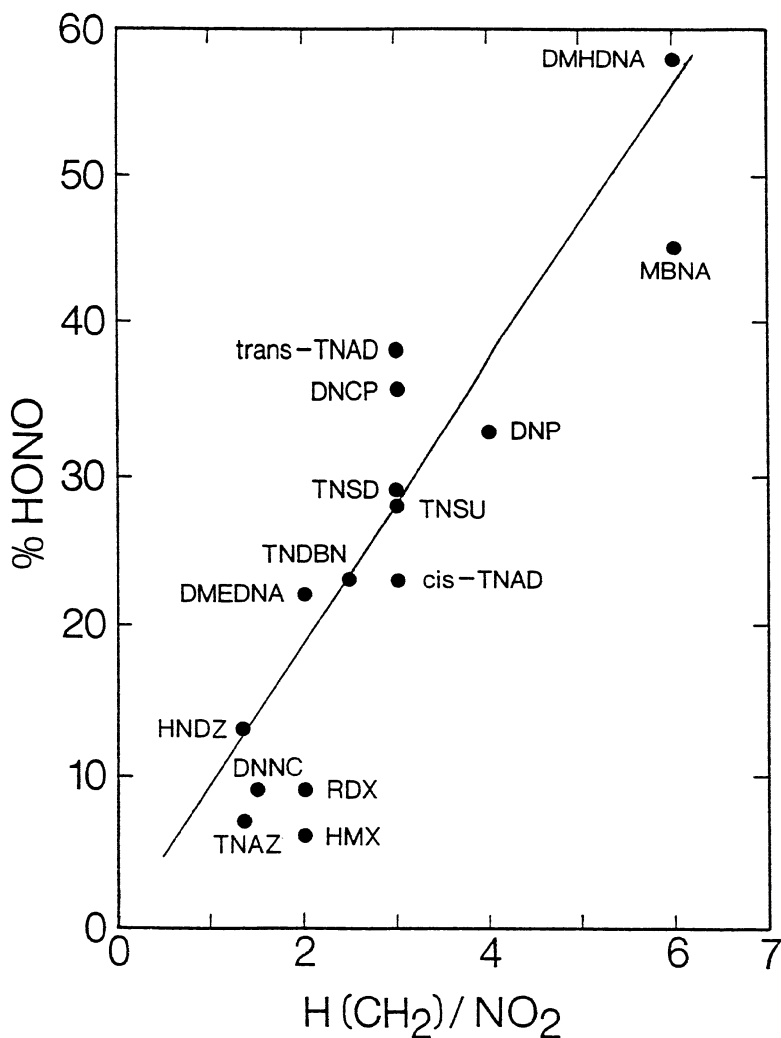
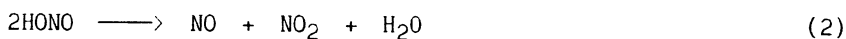


Figure 4. The same plot as in Figure 3 except using only the H from the CH₂ groups in the H/NO₂ ratio.

higher temperature. Thus, the concentration of NO₂ should decrease and the concentration of NO should increase with increasing temperature, which they are always found to do in our work. Second, a source of NO is the decomposition of HONO by reaction (2).



This reaction can account for the high initial abundance of NO found when the initial HONO concentration is also high [30]. Third, some nitramines we have studied also contain aliphatic C-NO₂ groups. C-NO₂ compounds are found to generate a considerable amount of NO [39,40], perhaps because of the approximately thermally neutral C-NO₂ to C-ONO isomerization [41]. CO-NO homolysis leading to NO is facile in this isomerized state. Fourth, there is evidence that nitramines can form nitrosamines (R₂N-NO) upon thermal decomposition in the condensed phase [42-44]. Fast thermal decomposition of nitrosamines also liberates NO [45].

3.1.4. Tendency to Form N₂O. It is not readily obvious what governs the N₂O/NO₂ branching ratio during the thermal decomposition of nitramines in the heterogeneous reaction state. A few secondary nitramines liberate a high amount of N₂O compared to NO₂(HONO) [46-50]. Conversely, other nitramines generate N₂O as only a few percent of the total gases liberated [30,39,51,52], while still others produce no N₂O at all [27,31].

Although the N₂O/NO₂ branching ratio could be partly phase dependent, the physical state of the compound is not likely to be the sole determining factor. Temperature may play a role. The N₂O/NO₂ branching ratio for the gas phase decomposition of RDX is temperature dependent and reaches unity at about 375°C [53]. However, from our work on the thermal decomposition of nitramines in the condensed phase where the decomposition temperatures range from 100°C to 300°C, there is rarely a correlation of the temperature with the N₂O/NO₂ ratio. However, it should be mentioned that there is a notable exception found when comparing the fast thermolysis of HMX to that of RDX. HMX and RDX have the same empirical formula but are simply telomers of methylene nitramine, CH₂=NNO₂. RDX produces relatively more NO₂ than N₂O initially, whereas N₂O and NO₂ have similar concentrations from HMX [50]. This difference might be attributed to the higher melting temperature of HMX which causes more of the decomposition chemistry to take place in the solid phase for HMX than is the case for RDX [50]. In general and considering all of the data at hand, our studies suggest that the reactions of nitramines have several mechanisms leading to N₂O and NO₂ in the condensed phase and that the gas phase results do not necessarily generalize to the condensed phase behavior.

All of the compounds liberating N₂O have in common a -CH₂- group straddled by two nitrogen atoms as shown by unit (2). No compounds lacking structural unit (2) produce N₂O upon fast thermolysis. This feature appears to be the only structure/decomposition relationship pertaining to N₂O formation.



Three secondary nitramines that liberate virtually all of their nitramine nitrogen atoms as N₂O are DPT [47], AZTC [46] and DATH [48]. The N-N bond distances in these compounds (1.355-1.375 Å) suggest that NO₂ and N₂O should be competitive thermolysis products [26,27] based on Section 3.1.1. DATH produces this result at temperatures slightly above its

(2) being present. Possibly ring strain plays a role that favors C-N bond homolysis and facilitates oxygen transfer.

In fact, the long held notion that CH_2O and N_2O form from a coupled process in the condensed phase decomposition of nitramines should be viewed with some skepticism. Recent work on HMX using Fast-Heat-and-Hold thermolysis techniques coupled with FTIR diagnostics [54], and slow thermolysis coupled with time-of-flight mass spectrometry [43] reveal that N_2O (and NO_2 [54]) reach the gas phase distinctly ahead of CH_2O . Figure 5 shows the gas sequencing from HMX under rapid heating conditions. At the

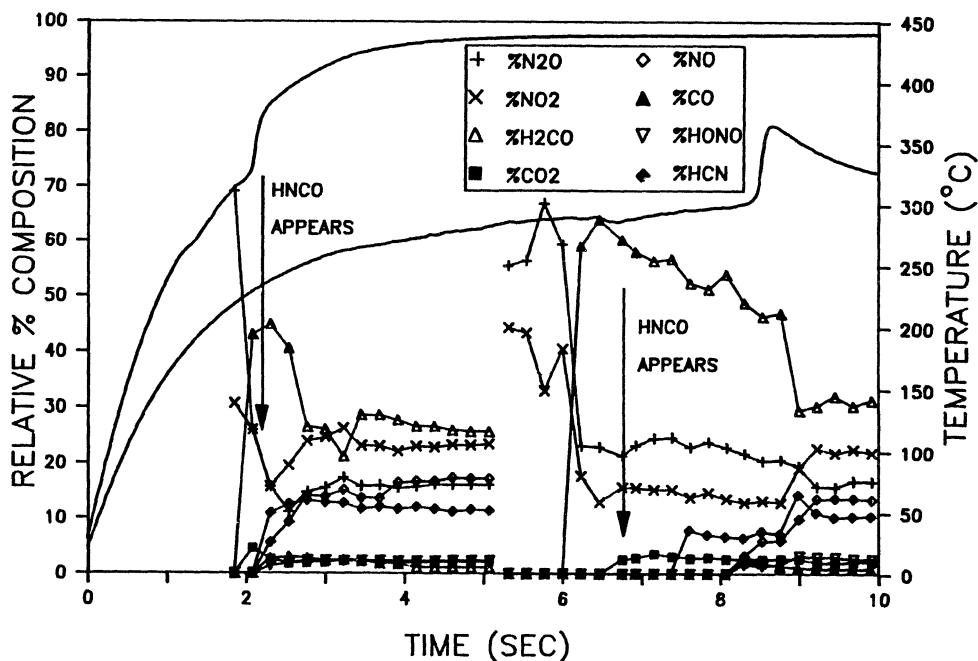


Figure 5. The gas products superimposed on the simultaneously acquired thermal trace in a Fast-Heat-and-Hold/FTIR study of HMX. Note NO_2 and N_2O precede CH_2O to the gas phase and that HNCO is also a later stage product.

temperatures used, N_2O and CH_2O should appear in the IR beam at the same time if they are being formed in the condensed phase from the same reaction at the same rate. The difference in their time of detection suggests a somewhat more complex reaction scheme than the customary oxygen transfer process is taking place under these experimental conditions. A further comment on this is given Section 3.1.6.

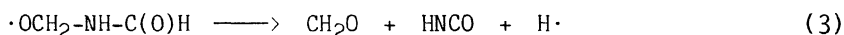
If unit (2) usually is required in the molecule to assure the formation of CH_2O , then it is of interest to learn how the $\text{>NCH}_2\text{CH}_2\text{N}<$ unit behaves in a nitramine molecule. This unit is present in many nitramines that we have studied. Ethylene straddled by two nitrogen atoms does not lead to CH_2O [29,52]. When C-N bond homolysis occurs in this fragment, the C-C bond probably strengthens so that CH_2O is not produced. No products

containing a carbon-carbon bond were detected perhaps because NO_2 oxidized any olefins present.

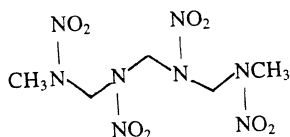
3.1.6. Tendency to Retain the C-N Bond. HCN is a ubiquitous product from most nitramines. Its concentration ranges from negligible to high under 15 psi depending on the compound. HCN is not detected unless NO_2 is also present, suggesting that the long held notion of a coupled reaction sequence producing these two products is true. The decomposition of the CH_2NNO_2 fragment leading to H_2CN and NO_2 is the most commonly cited reaction. Decomposition of H_2CN produces HCN.

HCN has a high degree of thermal stability under the conditions of our experiment and this results in its being found in the highest relative percent concentration in the middle pressure ranges (50-300 psi). All of the more reactive gases have decomposed leaving HCN and other reasonably stable gases, like NO, to dominate. If a nitrile group is present in the parent molecule, thermolysis directly to HCN occurs upon fast thermolysis [27].

HNCO is frequently detected in the decomposition gas of nitramines (see Figure 5), but its relative amount cannot be measured because no IR intensities are available. HNCO polymerizes to cyanuric acid so that its concentration is difficult to establish. In DINGU where the backbone connectivity is already set up to liberate HNCO directly, the quantity of HNCO is very large [31] and it is detected among the first gases. In most other nitramines, less HNCO is produced, and it appears in the gas phase after the initial products are detected (Figure 5). This suggests that HNCO may be evolved from the nonvolatile residue that forms while the initial gas generation is taking place. This residue is undoubtedly a mixture of components, but it contains various amides and polymerized products [55-58]. An amide, such as the radical of hydroxymethyl formamide, could yield HNCO and CH_2O upon thermolysis by reaction (3) [22]. This could help explain the later stage appearance of CH_2O shown experimentally in Figure 5.



3.1.7. Tendency to Form Hydrocarbons, CO, and CO_2 . Normally, hydrocarbon fragments originate in the fuel or binder component of the propellant or explosive formulation. The hydrocarbon portion of the oxidizer is oxidized to CH_2O or CO and CO_2 upon fast thermolysis. However, if built into the backbone in the appropriate way, hydrocarbon fuel molecules can appear in the products. Worthy of mention in the nitramine category is the formation of CH_4 from the terminal methyl groups of the open chain analog of HMX called OHMX [49]. Alkane, alkene and alkyne molecules are among the



OHMX

products of fast thermolysis of azide-containing polymers [59]. This is because no oxygen is present.

CO and CO₂ are reaction products of oxidizers. Their concentrations can be expected to relate more to the oxygen balance in the parent molecule than the original structure or decomposition mechanism. Therefore, we have not attempted to correlate CO or CO₂ concentrations with the parent molecular structure because these products are merely the final, thermodynamically stable sinks for carbon. Indeed, the CO/CO₂ ratio in the product gases of a range of energetic molecules has been shown to correlate with the oxygen balance of the parent molecule [12]. Carbon burning increases with increased oxygen balance. If the atom connectivity is already set up to eliminate CO₂, as in carboxylic acids or carbonates, then the CO₂ concentration produced by rapid thermolysis is anomalously high [40].

An ongoing program exists in our laboratory to learn more about the fast thermolysis of binders and fuel materials. It is too early to provide results that are being obtained in this effort.

3.1.8. Primary Versus Secondary Nitramines. Primary nitramines, RN(H)NO₂ are found experimentally to be strong N₂O generators compared to most secondary nitramines upon fast thermolysis [29]. It is possible that a rearrangement to the aci form (3) is favored at higher temperatures such



that the N-N bond is preferentially strengthened. Upon thermolysis, a nitrosamine and OH radicals could form [32]. Nitrosamines liberate a large amount of N₂O when rapidly thermolyzed [45] (Section 3.6.2). A second factor is that intermolecular hydrogen bonding involving the H atom and neighboring nitro groups could influence the ease of H transfer and preference for N-N bond reaction. A third factor is that the N-N bond in the parent primary nitramine is intrinsically shorter than that in secondary nitramines [60], which would favor N-N bond retention during thermolysis.

The general pattern is that, while certain secondary nitramines are found to generate N₂O in preference to NO₂ (see Section 3.1.4), the balance is tipped in favor of NO₂. The balance is tipped toward N₂O production from primary nitramines.

3.1.9. Comparison of Cyclic and Acyclic Pairs Upon Thermolysis. It is not possible for a cyclic and acyclic pair of nitramine compounds to exist with the same connectivity and composition. Thus, it is unclear if a difference in the thermolysis pattern of a closely related cyclic and acyclic pair of nitramines should be ascribed to the composition and connectivity differences or to cyclization. Despite this question, several compositionally similar pairs of cyclic and acyclic nitramine compounds

were thermalized [29,49]. Within the limited scope of this work, the gas product ratios are similar. This study suggests that the usual N-N bond homolysis leading to NO_2 and ring depolymerization occurs without regard to whether the structure is cyclized or not.

AZTC and DATH are a similar pair of mixed azidomethyl nitramines, one of which is cyclic and the other acyclic. Both compounds decompose similarly (and somewhat anomalously for nitramines) liberating N_2O and CH_2O as the vastly dominant nitramine products [46,48]. Neither produces much NO_2 . From these results we conclude that cyclization has little effect on the gas product distribution, but it could influence the temperature at which thermal decomposition begins.

3.1.10. The Effect of Metal Ions on Nitramine Thermolysis. In an ongoing study, the influence on the thermolysis process of coordination of energetic organic molecules to metal ions and the formation of salts of energetic functional groups is being investigated. The work completed to date has dealt mostly with nitramines and its motivation has been to develop potential burn-rate catalysts for nitramines.

Attempts to dope RDX and HMX crystals homogeneously with energetic Cu(II) and Ni(II) coordination complexes were stimulated by the possibility of modifying the burn rate by placing catalytic sites homogeneously in the crystal lattice. By using energetic metal complexes, the energy of the crystal would not be diluted. Attention was paid to the ways that polar organic molecules are incorporated into the RDX and HMX lattice and interact with nitramines [24,61,62]. Numerous metal complexes with the appropriate structural features to optimize success were prepared. Despite these considerations, all attempts at co-crystallization failed [63]. However, by using a slightly different route, a Cu(OH)_2 -ethylenediamine-RDX mixture in H_2O did yield crystals of "blue RDX" [63]. This preparation was difficult to reproduce and appears to be very sensitive to the conditions. "Blue RDX" was proven to contain 300-500 ppm of Cu. Although many techniques were applied, the mode of incorporation of Cu(II) was never discovered. However, the incorporated Cu(II) did give some evidence of achieving the original goal of decreasing the decomposition temperature and enhancing the condensed phase reactions of RDX. By DSC "blue RDX" displayed an additional decomposition exotherm below the exotherm of pure RDX. Careful studies proved that more CH_2O and N_2O were generated from the doped state than from pure RDX [63].

New coordination complexes of Cu(II) , Ni(II) and Pd(II) using nitramine molecules as ligands resulted in the discovery of the ambidentate properties of nitramines [64]. The most conspicuous structure/decomposition relationship was found with the $\text{M(NH}_3)_2[\text{N(NO}_2)_2\text{CH}_2\text{CH}_2\text{N(NO}_2)_2]$ complexes, $\text{M}=\text{Cu, Pd}$. NH_3 is an excellent source of $\text{H}\cdot$, which facilitates combustion and explosion reactions. The Pd-NH_3 bond is stronger than the Cu-NH_3 bond causing NH_3 to be retained in the condensed phase to a greater extent with the Pd complex where it reacts extensively with the nitramine ligand. Hence, the decomposition gases from the Pd complex are much closer to the final, thermodynamically stable combustion products than those of the Cu complex [65]. The dominance of N_2O over NO_2 during the fast thermal decomposition of metal nitramine complexes [65] is consistent with the fact that the N-N bond distance is very short (1.25 - 1.275 Å) compared to the typical purely organic

nitramine compound (see Figure 2) [64]. Upon thermolysis, N_2O , which retains the N-N bond, should be, and is, the dominant product of the nitramine linkage.

3.1.11. Gas Product Predictions Based on Structure/Property/ Decomposition Relationships. The relationships described above have qualitative predictive value for anticipating the thermal decomposition characteristics of imagined or newly synthesized energetic nitramines. This point will be illustrated with a new energetic molecule, TDCD.

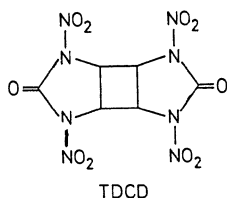


Table 1 lists some observations (causes) for the TDCD molecule and the resulting predictions (effects) about the decomposition gases from fast thermolysis based on these observations.

TABLE 1. Observations and predictions about TDCD thermolysis

<u>Cause</u>	<u>Effect</u>
$\nu_{as}(NO_2) = 1590cm^{-1}$	a) Much NO_2 generated; therefore, b) Much HCN and HNCO, c) NO grows as NO_2 is lost
Few H atoms (only $\equiv C-H$)	No HONO
No $-CH_2-$ straddled by N	a) No CH_2O , b) No N_2O

As shown in Figure 6, the qualitative predictions in Table 1 about the decomposition gases are borne out in experiment when TDCD is heated at $110^\circ C/sec$ under 15 psi Ar [31]. NO_2 is indeed the dominant, initially detected product and no HONO is formed. The high initial concentration of NO_2 leads to increased NO formation with time. HNCO (not quantified) and HCN are major products. Note that after N-N bond homolysis, the NCO radical and HCN are already set up by connectivity in the backbone to split out. Neither N_2O nor CH_2O is produced.

Admittedly, the structure/property/decomposition relationships described in Sections 3.1.1 - 3.1.10 for nitramines do not always give as reliable a prediction as they do for TDCD, but frequently they work well for many products. As mentioned already, discrepancies arise when other

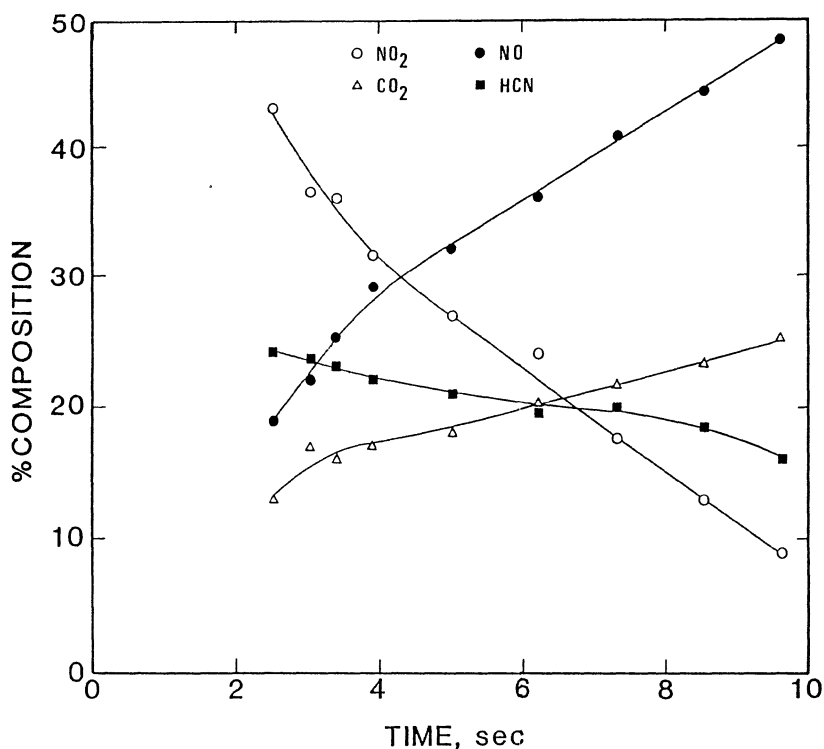


Figure 6. The quantified products from TDCD heated at 100°C/sec under 15 psi Ar. HNCO is a significant product also, but cannot be quantified.

reaction pathways compete with or override the one on which the structure/decomposition relationship is based. The central point is that structure/property/decomposition relationships can be uncovered for any class of energetic materials if and when one particular reaction pathway dominates over the others. Competitive reactions, or the occasionally unique and obscure reaction pathway, can lead to a breakdown in the prediction.

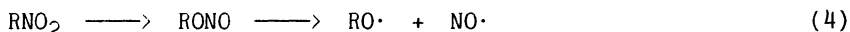
3.2 ALIPHATIC C-NO₂ COMPOUNDS

Most of our work to date on energetic C-NO₂ compounds has dealt with aliphatic *gem*-dinitromethyl and trinitromethyl-containing compounds. Detailed studies of aromatic nitro compounds are planned for the future.

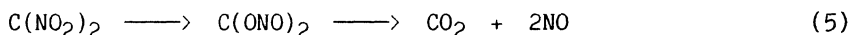
A number of reactions involving the C-NO₂ group appear to contribute in aliphatic nitro compounds. Because NO₂ is a major product upon fast thermolysis [28,39,40,51,66], C-NO₂ homolysis is an important reaction. It has been considered by others to be rate-determining [8]. Recently, a case for C-C heterolysis as the rate-determining step has been made for trinitromethylalkyl compounds [67]. Although the spectroscopic techniques that we have developed were not intended for kinetic measurements, the

order of stability of $[(\text{NO}_2)_3\text{CCH}_2\text{O}]_x\text{CH}_{4-x}$, $x = 2-4$, is consistent with C-C heterolysis [68]. However, NO_2 is still the first detected and dominant initial gas product. Thus, the data are consistent with parallel C- NO_2 homolysis and C-C(NO_2)₃ heterolysis reactions occurring under fast heating conditions. HONO is also known to form under certain conditions from C- NO_2 compounds [8], but we have detected it only when an N- NO_2 group is also present.

Another well-known reaction of the C- NO_2 group is the thermally neutral [41] and low activation energy isomerization reaction (4). Thus, NO should be, and is, a major product of most C- NO_2 containing



compounds that we have studied. Gem-dinitromethyl compounds might undergo a double isomerization reaction (5), which would help explain



the large amount of CO_2 detected early in the thermolysis of such compounds [39,40].

Trinitromethylalkyl compounds are interesting from the standpoint of their tendency to produce NO_2 exclusively in an induction-like phase and then to transit sharply to an ignition-like or explosion phase. Figure 7 shows this behavior for TEFO ($x = 2$ in compounds above). We first interpreted this finding to originate from the $\text{NO}_2(\text{g})$ initially produced returning to attack the hot condensed phase residue and igniting it [51,66]. However, because of the lack of a pressure dependence to the ignition-like exotherm [68], it now seems unlikely that this description is correct. The lack of pressure dependence implies that the initially produced $\text{NO}_2(\text{g})$ is not playing a role, but, instead, the ignition-like exotherm is caused by the decomposition of the condensed phase residue alone [68].

3.3 NITRATE ESTER (O- NO_2) COMPOUNDS

Work conducted to date on the fast thermolysis of nitrate ester compounds reveals significant differences in the initially detected decomposition gases [69]. While NO_2 may actually be the dominant gas in all cases, this is not manifested in the gases detected. That is, mechanistically, the initial decomposition step may be the same in all cases, but, in practice, the gases leaving the surface can differ dramatically because of the interplay of various secondary reactions.

Three categories of nitrate esters appear to exist based on the gas product distributions produced by fast thermolysis [69]. Highly nitrated, low molecular weight nitrate esters, such as PETN and TMETN, liberate mostly the side-chain fragments, NO_2 and CH_2O , under a sub-atmospheric Ar pressure. These side-chain dominated compounds (category 1) differ from a compound like 14% nitrocellulose (category 2). While NO_2 and HONO are the major products at sub-atmospheric pressure from nitrocellulose, NO and CO are also present in significant abundance. Thus, NC and the other category 2 compounds released both side-chain and backbone decomposition products in competitive concentrations implying that more condensed phase

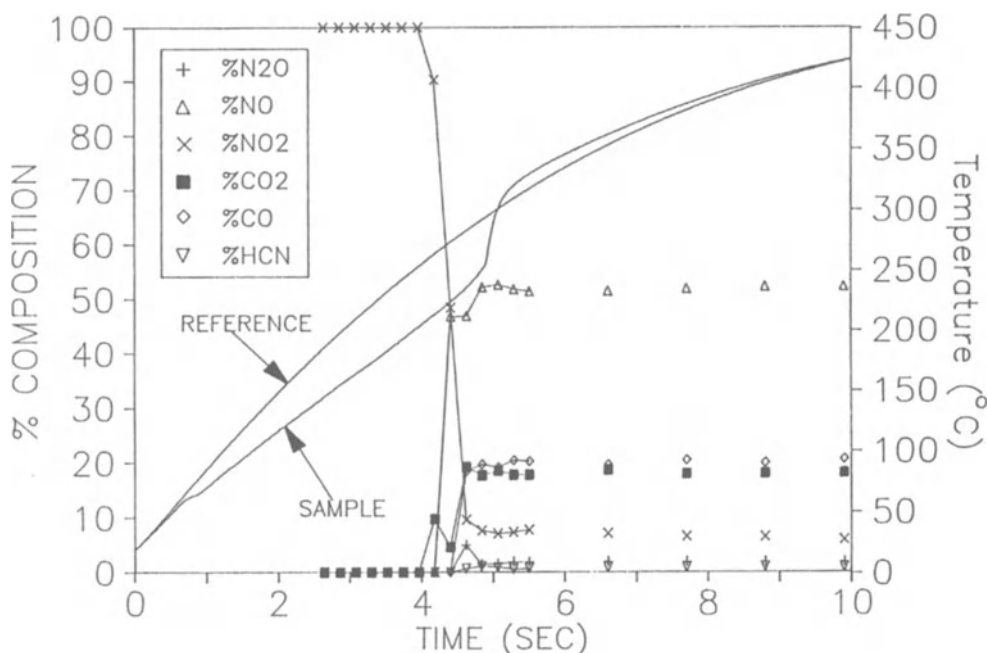
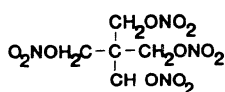
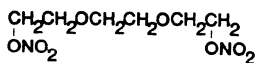


Figure 7. Temperature Profiling/FTIR Spectroscopy of TEFO showing the transition from induction phase decomposition to an ignition-like exotherm in 4.7 sec. Note the melting endotherm at 70-80°C.

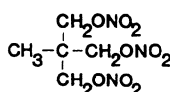
reactions of NO_2 occur. Category 3 contains compounds like NMMO polymer and TEGDN where little or no NO_2 is detected under the same thermolysis conditions used in categories 1 and 2. Instead, carbon-containing backbone



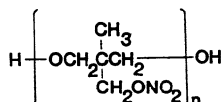
PETN



TEGDN



TMETN



NMMO POLYMER

products and NO dominate. The implication is that at high heating rates, any NO_2 produced is consumed in backbone degradation reactions before it leaves the sample. Hence, secondary reactions in the condensed phase dominate during fast thermolysis.

The progression from the detection of the dominance of reactive, primary side chain products to more thermally stable secondary products of the side chain and backbone, qualitatively correlates with the oxygen and nitrogen content of the parent nitrate ester. As shown in Figure 8, as the oxygen and nitrogen contents decrease, there is a tendency to move from category 1 to category 3.

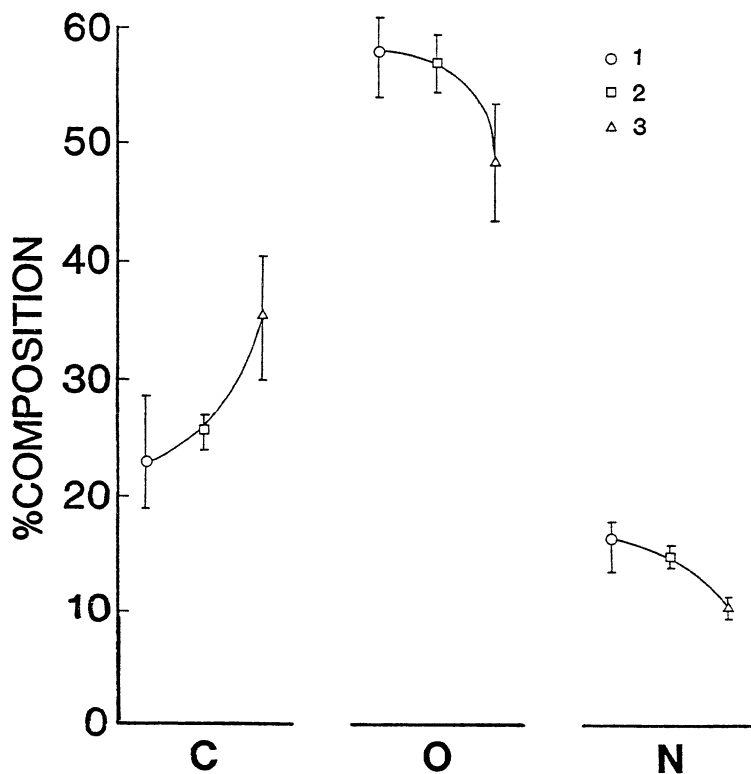
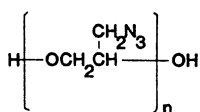


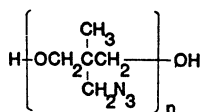
Figure 8. The average percent of N, C, and O in nitrate esters corresponding to categories 1, 2, and 3.

3.4 AZIDOMETHYL ($-\text{CH}_2\text{N}_3$) CONTAINING COMPOUNDS

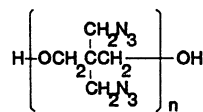
Studies of poly(oxetanes) containing the azidomethyl group, AMMO and BAMO, and the glycidyl azide polymer, GAP, reveal a mixture of hydrocarbon and oxycarbon fragments along with some NH_3 and HCN [59]. Presumably IR silent



GAP



AMMO



BAMO

N_2 is also present. No doubt, the decomposition process begins in the methylazide group [10]. Fast thermolysis of the azidomethyl oxetane monomers that polymerize to form AMMO and BAMO yields products that are

expected of the thermolysis of an alkylazide and an oxetane. These two units are the main components of the monomers. Poly(AMMO) is more thermally stable than the other polymers. This may explain why the product distribution from poly(AMMO) differs much more from that of its monomer than is the case for BAMO and GAP.

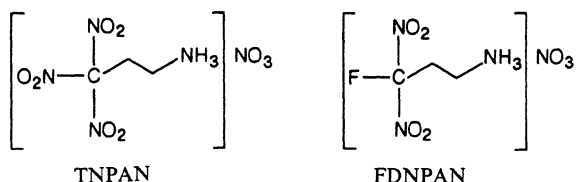
The thermolysis of two azidomethyl nitramines, DATH and AZTC, was discussed above in the context of the nitramine portion of the molecule. Both DATH and AZTC initially liberate HN_3 [46,48]. There is little doubt that the main decomposition pathway of the azidomethyl group leads to N_2 and the nitrene, but the presence of HN_3 in this work proves that C-N₃ scission with hydrogen migration (perhaps a bimolecular process in the neat condensed phase) also occurs early in the thermolysis reaction. The decomposition of DATH and AZTC appears to be initiated at the azide site rather than the nitramine site in keeping with the somewhat lower activation energy for decomposition of $-\text{CH}_2\text{N}_3$ (38-44 kcal mol⁻¹) compared to R_2NNO_2 (45-55 kcal mol⁻¹) [48].

3.5 ALKYLAMMONIUM NITRATE SALTS

Relatively extensive studies of the fast thermolysis of related classes of alkylammonium nitrate salts have been conducted that permit the gas products from fast thermolysis to be correlated with the composition of the parent salt. Classes of compounds for which data have been gathered are $[(\text{CH}_3)_n\text{NH}_{4-n}]\text{NO}_3$, $n = 1-3$ [70], $[(\text{CH}_3\text{CH}_2)_n\text{NH}_{4-n}]\text{NO}_3$, $n = 1-4$ [70], $[\text{CH}_3(\text{CH}_2)_n\text{NH}_3]\text{NO}_3$, $n = 0-3$ [70], $[\text{H}_{3-n}\text{N}(\text{CH}_2\text{CH}_2)\text{NH}_{3-n}]\text{NO}_3$, $n = 0-2$ [71], $[\text{H}_3\text{N}(\text{CH}_2)_n\text{NH}_3]\text{NO}_3$, $n = 1-4, 6$ [72] and a series of five N-methyl substituted ethanediammonium dinitrate salts [73].

The primary and secondary alkylammonium nitrate salts release $\text{HNO}_3(\text{g})$ as the initial gas product. In fact, the deneutralization reaction leading to HNO_3 appears to be the initiation step of thermal decomposition. The temperature at which $\text{HNO}_3(\text{g})$ is first detected qualitatively correlates with the basicity of the amine [70]. As the base strength increases, $\text{HNO}_3(\text{g})$ appears at a higher temperature. Hence, the decomposition temperature follows the trend $[\text{R}_2\text{NH}_2]\text{NO}_3 > [\text{RNH}_3]\text{NO}_3$. The basicity of longer chain alkanediamines is higher than that of the monoamine series because of the cyclization process (unit (3)). The only tertiary alkylammonium nitrate salt that liberates $\text{HNO}_3(\text{g})$ is $[(\text{CH}_3)_2\text{HNCH}_2\text{CH}_2\text{NH}-(\text{CH}_3)_2](\text{NO}_3)_2$, but it does so only to a small extent and at a relatively high temperature [73]. Because of their high basicity, the other tertiary alkylammonium nitrate salts studied retain the nitrate ion in the condensed phase for further reactions, as will be discussed in a moment.

Many primary alkylammonium nitrate salts, such as pentaerythrityltetrammonium tetranitrate [74], TNPAN [28] FDNPAN [28] and $[\text{H}_3\text{N}(\text{CH}_2)_n\text{NH}_3](\text{NO}_3)_2$, $n = 1-4, 6$ [71], release $\text{NH}_3(\text{g})$ as a result of C-N bond fission. However, this reaction is not general to primary ammonium nitrate salts because NH_3 appears only for $n = 3$ in the series $[\text{CH}_3(\text{CH}_2)_n\text{NH}_3]\text{NO}_3$, $n = 0-3$ [70]. Qualitatively, it seems that the most important factor in determining whether $\text{NH}_3(\text{g})$ is released from an alkylammonium nitrate salt is the ability of the residue to stabilize itself. If four or more carbons atoms are present in the alkyl portion, then there appears to be sufficient stabilizing reactions following C-N bond fission to enhance the release of $\text{NH}_3(\text{g})$. Alkanediammonium dinitrate salts readily release $\text{NH}_3(\text{g})$ upon rapid



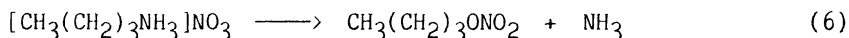
heating perhaps because lone pair delocalization can stabilize the residue following a C-N bond fission step [71]. Not surprisingly, secondary and tertiary alkylammonium salts do not produce NH_3 .

If the alkylammonium salt does not produce NH_3 upon thermolysis, then the alkylamine is evolved to some degree [70]. Irrespective of whether it is NH_3 or the alkylamine that is released, $\text{HNO}_3(\text{g})$ reacts with the base in the gas phase to form an aerosol of the salt.

In a reaction that appears to be general to the secondary and tertiary alkylammonium nitrate salts, secondary alkyl nitrosamines are formed upon fast thermolysis [70,72]. There is considerable precedent for the formation of nitrosamines from nitrate salts [75,76]. Trialkylamines rearrange to dialkyl nitrosamines, in part because of the driving force of multiple bond formation in the N-NO unit of the nitrosamine. For instance, when heated, the bicyclic salt $[\text{HN}(\text{CH}_2\text{CH}_2)_3\text{NH}](\text{NO}_3)_2$, rearranges to the cyclic nitrosamine, $\text{ONN}(\text{CH}_2\text{CH}_2)_2\text{NNO}$, with the aid of α -carbon oxidation [72]. CH_2O is liberated in the α -carbon oxidation step. Nitrosamine formation greatly increases the potential health risks when formulations containing secondary and tertiary alkylammonium nitrate salts are heated.

There is no evidence that alkylammonium nitrate salts convert to nitrosamines via the nitramine intermediate [70,72]. Studies of authentic samples of the respective nitramines indicate that they would volatilize and be detected by infrared spectroscopy if they had formed. No nitramines were detected from any salt studied.

Methylammonium nitrate salts undergo α -carbon oxidation leading to amides, such as formamide and N,N-dimethylformamide [70]. On the other hand, the longer chain alkylammonium nitrates release alkyl nitrates. This reaction for n-butylammonium nitrate is straightforwardly represented by equation (6) based on the gas products evolved [70].



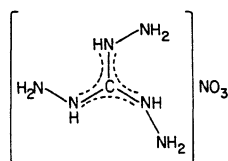
N-Methyl substitution of ethanediammonium dinitrate yields compounds whose thermal decomposition could possibly be intermediate between the alkylammonium nitrate salts and the alkanediammonium dinitrate salts. Indeed, the thermal decomposition behavior of all the compounds and isomers with one, two or three methyl groups substituted at the nitrogen sites have thermal decomposition temperatures that more closely parallel the alkylammonium mononitrate salts than the alkanediammonium dinitrate salts [73]. If four N-methyl groups are present giving N,N,N',N'-tetramethylethanediammonium dinitrate, then the decomposition temperature is similar to the diammonium series because of the higher basicity of the tertiary amine [73]. Relatively large molecular fragments from both C-C

and C-N bond fission are clearly evident in the gas phase from the thermal degradation reactions in the condensed phase.

The temperature at which the higher temperature exotherm occurs with many of these compounds is quite sensitive to the applied pressure in the cell [77]. Because the fast thermolysis/FTIR spectroscopy experiment largely involves the condensed phase, the only way the static pressure in the cell can affect the temperature of the exotherm is by influencing the heterogeneous condensed phase/gas phase chemistry. Thus, we conclude from the pressure sensitivity that the thermal decomposition of alkylammonium nitrate salts involves an extensive amount of heterogeneous gas phase/condensed phase chemistry. This notion is consistent with many of the comments in this section, especially with regard to the participation of HNO_3 in the degradation chemistry.

Studies of several alkylammonium nitrate salts in which a second type of energetic functional group is present in the cation reveal that the energetic site that triggers the decomposition reaction can switch [28]. When the more thermally stable $\text{F}(\text{NO}_2)_2\text{C}-$ functional group is present, then the $-\text{NH}_3^+\text{NO}_3^-$ site triggers the decomposition reaction. When the more thermally labile $(\text{NO}_2)_3\text{C}-$ group is present, then this group initiates the decomposition reaction rather than the $-\text{NH}_3^+\text{NO}_3^-$ site. Hence, the order of stability is $\text{F}(\text{NO}_2)_2\text{C}- > \text{NH}_3^+\text{NO}_3^- > (\text{NO}_2)_3\text{C}-$ in a closely related set of compounds [28].

Several ammonium nitrate salts without alkyl groups have been studied by fast thermolysis. These are ammonium nitrate [77], triaminoguanidinium nitrate (TAGN) [78], hydroxylammonium nitrate (HAN) [79], and hydrazinium nitrate [77]. HNO_3 is the initially detected gas product in all cases. All but HAN produce NH_3 . HAN is conspicuous and unusual because of the



TAGN

oscillation in the gas product concentrations when HAN is heated at 130 K/sec or more under at least 100 psi Ar [79]. The period of these oscillations is affected by the amount of H_2O present in the sample. The oscillation frequency is lower as the H_2O content is reduced. The oscillations disappear with concentrations below 12 M HAN.

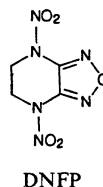
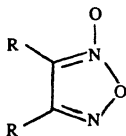
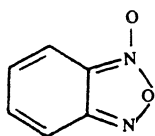
An additional feature of aqueous nitrate salt solutions that is interesting is the different degree of ion association as a function of temperature. As the temperature and pressure approach or exceed the critical point of pure water, the extent of contact ion pair formation increases [80]. Thus, salts in H_2O become increasingly molecular at high temperature. This fact has implications for the chemical initiation step (proton transfer leading to HNO_3) of liquid gun propellants [81]. At higher temperature and pressure, the increasingly molecular nature of salts

in H_2O increases the ease of H^+ transfer and, thus, favors the initiation of the ignition process.

3.6 MISCELLANEOUS ENERGETIC FUNCTIONAL GROUPS

Several studies of other types of energetic functional groups have been undertaken. These are grouped here because less comprehensive studies of them were conducted owing to the unavailability of extensive sets of compounds. Selected studies merit mention even though the structure/decomposition relationships found are not especially broad. Studies are currently in progress on tetrazoles and triazoles, but the data are not sufficiently complete to discuss here.

3.6.1. Furazan and Furoxan Containing Compounds. These energetic functional groups are interesting in their own right, but have also been identified in the thermal decomposition and sensitization of TATB [82]. Structure/decomposition relationships for benzofuroxan compounds were not decipherable in the set of compounds studied [83]. However, the results reveal distinctly different decomposition pathways for benzofuroxans and dialkylfuroxans. With benzofuroxans the benzene ring holds the furoxan

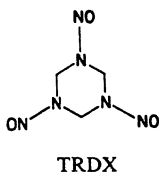


ring in place so that its decomposition characteristics depend on the substituents on the benzene ring. Small molecule, combustion-like fragments are the first detected gas products [83]. On the other hand, without the stabilizing template of the benzene ring, the dialkylfuroxans cleave to two alkyl nitrile-N-oxide (RCNO) molecules [83].

Only one furazan compound, DNFP, has been investigated in detail to date [52]. DNFP contains both a furazan ring and nitramine groups. The nitramine groups appear to trigger the thermal decomposition of the molecule. Further work on furazans and metal complexes of furazans is under way at the present time [84].

3.6.2. Nitrosamine (R_2NNO) Containing Compounds. Nitrosamines are receiving attention in the explosives and propellants field, not so much for their value as primary materials, but from the fact they have been identified among the slow and fast thermal decomposition products of nitramines [42-44] and alkylammonium nitrate salts [70,72,73].

The nitrogen atoms of trinitroso-s-triazine (R-Salt or TRDX) have been shown to wind up as NO, N_2O and HCN upon fast thermolysis [45]. The formation of NO is in keeping with the expected N-NO bond fission thermal

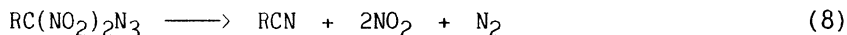


decomposition reaction (7) of a secondary nitrosamine. Once this reaction occurs at one site, the CN bonds of the ring weaken and it becomes facile



to release N_2O from other sites. Even without this effect, the C-N bonds of a secondary nitrosamine are weaker than those of nitramines [32], which favors N_2O formation. Of course, not enough oxygen is present to produce CH_2O upon C-N bond fission as occurs with many nitramines, such as RDX, but otherwise the N-N bond homolysis/C-N bond homolysis scenario of TRDX can be thought of as resembling that of RDX.

3.6.3. Compounds Containing $-C(NO_2)_2X$; $X=N_3, F, Cl$. The fast thermolysis process of the azidodinitromethyl functional group is perhaps the simplest of any energetic functional group in an organic molecule. Certainly it is the simplest of any that we have studied. Reaction (8) summarizes the process [85]. An alkylnitrile and NO_2 are the only IR active gas products



detected, and they appear simultaneously at about $180^\circ C$ [85]. Because N_2 is IR inactive, it can only be presumed to be present, but the presumption is very safe because of the unequivocal assignment of the other two products [85].

Fluorodinitromethyl compounds are less exothermic upon fast thermolysis than the corresponding trinitromethyl compounds [86] in keeping with their greater thermal stability [2]. The resting place of the F atoms after thermolysis has been revealed by IR spectroscopy to be FNO [86]. The chlorodinitromethyl functional group decomposes to release ClNO [86].

3.6.4. Alkynes and Nitroxides. Alkyne-containing compounds might be interesting fuels because the $-C\equiv C-$ bond stores about 110 kcal/mol more energy than a C-C bond. Reasonably simple alkynes seem most likely to yield interpretable thermolysis data. Metal propiolates, $M[O_2CC\equiv CH]$, were chosen for this reason. Moreover various metal propiolate salts have been reported to decompose explosively when heated [87]. A detailed study of the thermolysis was performed for the Na^+ , K^+ , Rb^+ , Co^{2+} , Ni^{2+} and Zn^{2+} salts by TGA, DSC and various IR spectroscopy methods at slow and rapid heating rates [88]. All of the salts are intumescent, but to different

degrees and rates. The Rb^+ salt is the least intumescent while the Co^{2+} salt is the most. The putative explosive behavior of the Co^{2+} salt is attributed to this high rate of gas generation, perhaps because of redox reactions not available to the other cations. The thermal decomposition of these salts was found to occur by competitive pathways depending on the temperature [88]: decarbonylation leading to CO , C_2H_2 , C , and carbonate salts; decarboxylation leading to CO_2 , C , C_2H_2 and either carbonates; or coupling leading to an acetylenedicarboxylate salt. The balance of these three reactions is determined by the lattice energy of the original salt and its temperature of thermal decomposition. When the decomposition temperature and lattice energy are on the low side, then decarboxylation and polymer products form (Rb^+ , Co^{2+} , Zn^{2+} salts). When the decomposition temperature and lattice energy are on the high side, then decarbonylation and carbonate products are favored (Na^+ , K^+ , Ni^{2+}). Confinement of the sample between two BaF_2 plates during slow thermolysis accentuates the coupling reaction in all cases.

Thermolysis of compounds containing alkyne and nitroxide energetic sites led to destruction of both the nitroxide group and the acetylene linkages [89], rather than polymerization and the generation of a rare example of bulk ferromagnetism in a purely organic compound, as had been proposed by others [90].

4. The Effect of Pressure on the First Detected Products

Pressure is such a profoundly important variable in propellant and explosive applications that we have attempted not only to understand its effects, but to use it to advantage to uncover relationships between the parent molecular structure and decomposition, and to probe physicochemical processes. Because the temporal resolution of the interferometer and the spacial resolution of the IR beam precluded observation of differences in the gas product compositions at pressures above 1000 psi, we conducted all studies of the effect of pressure on thermolysis with pressures in the 1-1000 psi range.

Two categories of general behavior emerge when the relative percentages of the first detected gas products from many of the compounds above are plotted against the applied Ar pressure [91]. A separate thermolysis experiment was performed at each pressure. The first category, which contains various nitramines, aliphatic nitro compounds and nitrate esters, displays a strong pressure dependence in several or all of the gas products. This category contains compounds that tend to release highly reactive gases, such as NO_2 , HONO , and CH_2O , in the lower pressure range. Figure 9 illustrates this behavior for RDX. In the middle pressure range of 40-200 psi, a different set of products dominates. These products are those of intermediate stability, such as NO and HCN , and result, in part, from further reactions of the gases that dominate at lower pressure. At pressures above 200 psi combustion-like products, CO , CO_2 , H_2O and (probably) N_2 dominate because of still more extensive reaction chemistry.

The second general category contains compounds that produce gases exhibiting only a minor dependence on pressure [91]. As with the first category, more than one type of energetic functional group is represented: nitramines, aliphatic nitro compounds, and azides. Thus, the behavior results from a general situation rather than the particular reaction

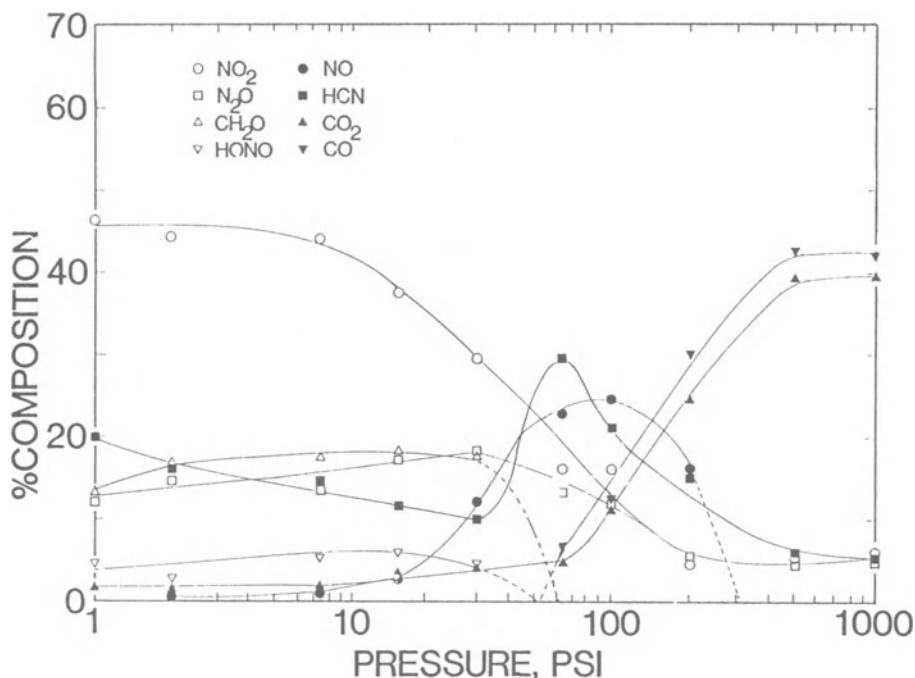


Figure 9. The effect of the Ar pressure on the initially detected gas products from RDX, heated at approximately the same rate at each pressure. Note the three-zone behavior of the dominant gas products.

mechanism of a functional group. Present are compounds that produce a reactive gas, such as NO_2 , but that do not also liberate another product with which NO_2 can react. Also present are compounds that liberate relatively unreactive products initially, such as N_2 or N_2O , and compounds in which extensive condensed phase chemistry appears to have occurred before the gases reach the IR beam. Condensed phase chemistry is not especially pressure dependent. Figure 10 illustrates the composition-pressure dependence of this category of compounds for nitroguanidine [92].

The source of the strong effect of pressure on the first category compounds has been demonstrated to result from the difference in the diffusion rates of the gases (and, thus, their residence time with the condensed phase) as a function of the applied pressure [91]. The gases must percolate through the condensed phase. As the pressure is raised, the extent of heterogeneous gas phase/condensed phase reactions increases because the time of percolation and residence increases. Thus, the yield of increasingly stable gas products increases with pressure. The three-zone behavior shown in Figure 9 simply reflects the natural progression in the nitrogen chemistry [$\text{NO}_2(\text{HONO}) \longrightarrow \text{NO} \longrightarrow \text{N}_2$] and carbon chemistry ($\text{CH}_2\text{O} \longrightarrow \text{CO}, \text{CO}_2$) toward the more thermodynamically stable products. There is no implication of a change in the decomposition mechanism as a function of pressure for these compounds in the 1-1000 psi range. It is interesting to note that this broad pattern of reaction behavior resembles

the theoretically derived [19] and experimentally measured [20,21] flame structure of nitramines as a function of distance from the surface.

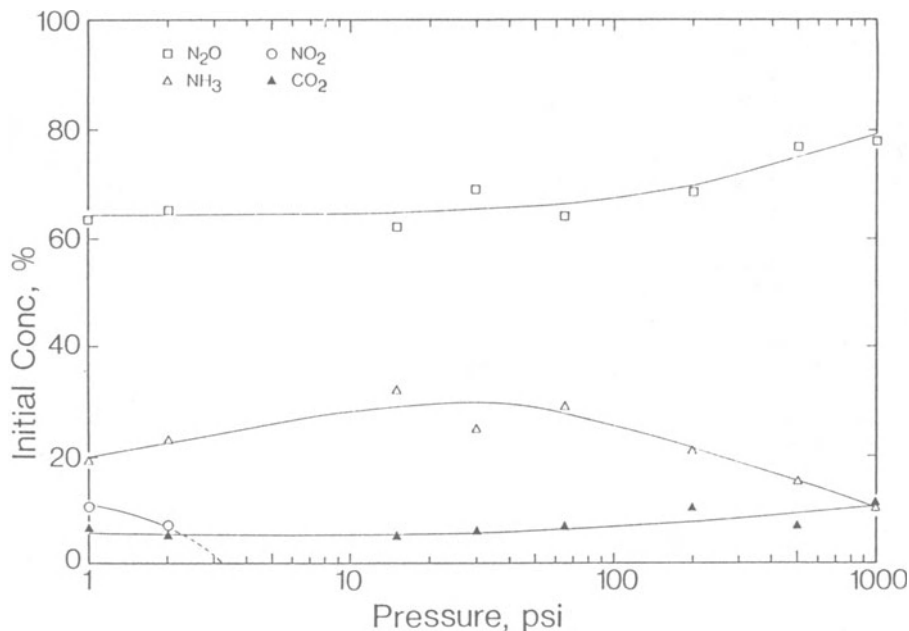


Figure 10. The effect of the Ar pressure on the initially detected gas products from nitroguanidine. Note the relative independence of the gas products on pressure in this range.

The above explanation for the source of the pressure dependence of the first-detected gases implies that initial pressure differences can be used to advantage. Recall that Fast Thermolysis/FTIR data mostly reflect condensed phase processes [22]. In the Temperature Profiling/FTIR method, the temperature deflections caused by the condensed phase processes are measured simultaneously with the gas products [93]. Thus, the pressure dependence of the gas product distribution and the temperature deflection can be used to distinguish decomposition process involving the heterogeneous gas/condensed phase from those that are solely associated with the condensed phase. The gas products and temperature deflections of alkylammonium nitrate salts are dependent on pressure as noted in Section 3.5 [77]. Therefore, heterogeneous gas/condensed phase processes are important during their fast thermal decomposition. On the other hand, the temperature deflections of trinitromethyl compounds discussed in Section 3.2 are mostly caused by reactions of the condensed phase alone without participation of the gas products [68], because the deflection is independent of pressure.

5. Fast Thermolysis of Mixtures

Energetic materials are usually used as mixtures of several components. Since Temperature Profiling/FTIR Spectroscopy [93] permits several variables of the thermal decomposition process to be measured simultaneously, useful data on decomposition synergism among the components might be extracted with this technique.

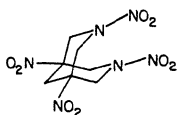
Considerable success has been achieved in understanding the thermolysis reaction sequence in the liquid gun propellant LGP1845 [94]. LGP1845 contains 63.2% $[\text{NH}_3\text{OH}]\text{NO}_3$ (HAN), 19.9% $[(\text{HOCH}_2\text{CH}_2)_3\text{NH}]\text{NO}_3$ (TEAN) and 16.8% H_2O by weight. To understand this mixture, the thermolysis of each component was first characterized separately [79,94], including the behavior of H_2O . From these data, and the effect of pressure on the overall process, a description of the sequential thermolysis process of LGP1845 was developed [94]. The first step is the endothermic evaporation of H_2O , which concentrates the solution further. The second step in the endothermic deprotonation of the NH_3OH^+ ion by NO_3^- to produce $\text{HNO}_3(\text{g})$. This process occurs in the 160–170°C range. The third step is partial decomposition of TEAN beginning in the 240–250°C range and is, perhaps, the result of reactions with the decomposition products of HAN. An ignition exotherm then occurs at about 260°C. Likewise, HAN decomposition appears to initiate the decomposition of a mixture of HAN and hydrazinium nitrate [77].

In other mixtures of nitrate salts, such as NH_4NO_3 with butanediammonium dinitrate [95] and NH_4NO_3 with ethanediammonium dinitrate [77,96], considerable additivity exists in the thermolysis behavior. That is, the gas products and temperature deflections of the mixture resemble the physical sum of those of the pure components. Of course, physical effects, such as melting point depression, occur in the mixture that are not reflected in the pure components, but the decomposition behavior of the mixtures studied to date has considerable additivity. One difference is that NH_4NO_3 sublimation is suppressed in the mixture implying that the liberation of NH_3 is retarded compared to the pure components. This retention of NH_3 in the condensed phase would have a stabilizing effect on the mixture, as is found to be the case in practice [97].

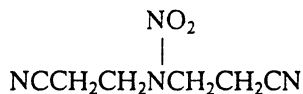
6. Solid State Effects

While not necessarily exerting a profound influence of the thermal decomposition of energetic materials, many solid state and condensed phase phenomena occur with energetic materials that play a role in the manufacture, use, and efficacy of energetic materials. HMX and NH_4NO_3 are notorious for the problems created by their tendency toward polymorphism. Some of the condensed phase phenomena newly observed for energetic materials are described in this section.

Complex schemes of polymorphism have been uncovered for TNDBN [47], DNFP [52], TNPAN [28], DPT [47] and OHMX [49]. The asymmetric unit of one of the polymorphs of TNDBN and also DNNC [98] contains two molecules having different conformations. This is a variation on the notion of conformational polymorphism which is well known with HMX. The polymorphism of TNPAN causes the compounds to have two different melting points [28]. Despite a careful look at many compounds, no clues were ever revealed about



TNDBN



BCEN

how to predict polymorphism at this level. However, there is some consolation in the fact that such predictions have also eluded researchers of other classes of compounds.

High temperature plastic crystal phases were found for DNFP [52,99] and TRDX [99]. The plastic phase of TRDX was determined by solid state NMR to be best described as a "crystal liquid" [100]. That is, the TRDX crystals retain their shape in the plastic phase, but translational mobility of the molecules exists in the solid giving it the essential feature of a liquid. In TAGN, melting of the NO_3^- sublattice was found to occur prior to thermal decomposition [78]. The ClO_4^- ion of NH_4ClO_4 exhibits this same type of behavior slightly in advance of massive thermal decomposition [101]. Both DATH [48] and BCEN [27] can be stabilized as amorphous solids which gradually transform to the crystalline state at room temperature within an hour.

Despite considering an extensive amount of data, only one generalization emerged from this work that relates the structure of the molecule to thermal properties of the solid state. It was observed that the sum of the ΔH value for the solid-solid phase transitions and melting, and the ΔS values for melting fall into statistically different ranges for cyclic and acyclic compounds [99]. The $\Sigma \Delta H$ and ΔS values for seven cyclic nitramines and nitrosamines are $35 \pm 4 \text{ cal g}^{-1}$ and $0.06 \pm 0.03 \text{ cal deg}^{-1} \text{ g}^{-1}$, respectively. For ten acyclic nitramines, the values are 66 ± 18 and 0.17 ± 0.07 , respectively. Therefore, more energy is required to mobilize a linear molecule than a cyclic molecule into the molten phase. ΔS is smaller for the cyclic compounds because the cyclic molecules are more internally constrained and, thus, have fewer degrees of freedom than the acyclic compounds [99].

7. Application to Explosives

7.1 CORRELATIONS WITH IMPACT SENSITIVITY

The impact sensitivity of a material has long been known to be related to the thermal decomposition process [102]. We have not yet had a chance to develop fully how the fast thermolysis studies here might relate to impact sensitivity. Only one study has touched on this subject.

Hydrogen bonding has been proposed to influence the impact sensitivity strongly by providing a mechanism to absorb the impact energy [103,104]. Thus, hydrogen bonded solids often have low impact sensitivity. While this mechanism is consistent with the data for selected compounds [103,104], a comparison of the data for nitroguanidine (NQ) and (trinitroethyl)nitroguanidine (TNENG) indicates that this broad generality

has exceptions [92]. The extent of hydrogen bonding in NQ and TNENG is similar, but TNENG has a high impact sensitivity ($H_{50} = 15$ cm) while NQ does not ($H_{50} > 320$ cm). Thus, the sensitivity imparted by the trinitroethyl group overrides any stabilizing influence provided by the hydrogen bonding.

7.2 TIME-TO-EXOTHERM STUDIES

Recently, a research project was undertaken to elucidate some of the chemistry associated with the initiation of thermal explosions [54]. This study involves Fast-Heat-and-Hold/FTIR measurements of the times-to-exotherm in which the IR spectra of the near surface gases were recorded simultaneously. The Fast-Heat-and-Hold/FTIR technique is described in the companion article. By measuring the time-to-exotherm as a function of the sample temperature, an apparent activation energy can be calculated from a plot of $\ln(t_{\text{exo}})$ versus $1/T$. Figure 11 shows such a plot for RDX. All

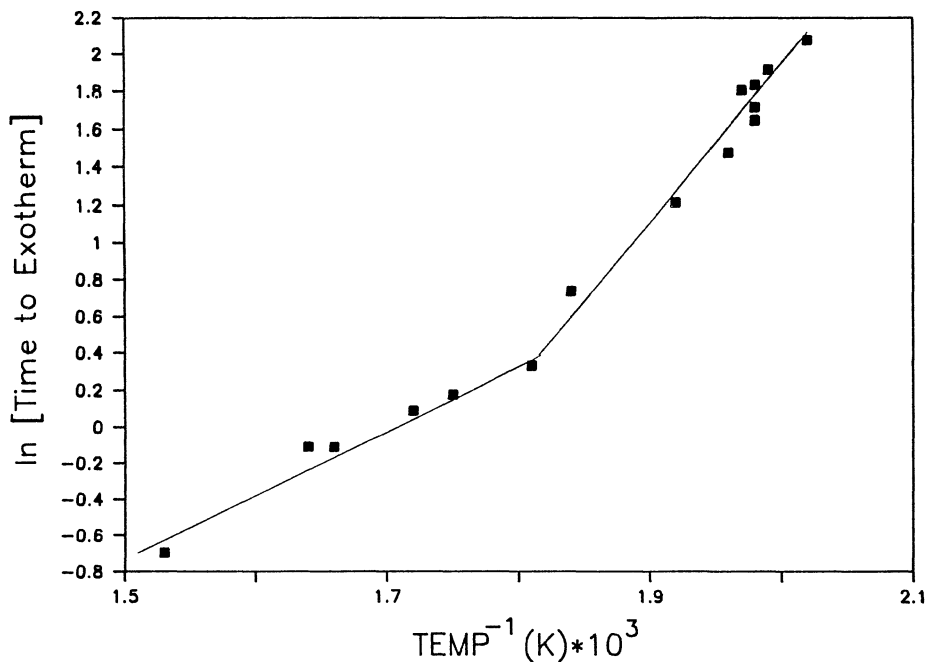


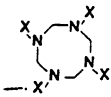
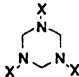
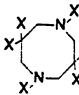
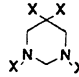
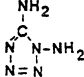
Figure 11. The apparent activation energy for the time-to-exotherm as a function of the sample temperature for RDX.

compounds studied to date display a slope break somewhere in their decomposition temperature range. We have not established the source of the slope break, but it is reproducible and different for each compound. It does not appear to be an experimental artifact because it occurs at a different temperature with each compound. Note that the temperature range

covered extends well above that which is considered to be the temperature of the onset of decomposition.

Table 2 summarizes the apparent activation energies for some of the compounds studied to date by this method. The values are usually small and definitely below the values for the activation of chemical, thermally-

TABLE 2. Apparent activation energies for times-to-exotherm

	Compound ^a	Pressure, psi Ar	Apparent Activation Energy, Kcal/mol	
			Low temperature ^b	High temperature ^b
HMX		15	15.1 (276-317)	10.4 (318-431)
RDX		40	15.2 (222-280)	7.2 (281-381)
EDNA	$\text{HNCH}_2\text{CH}_2\text{NH}$ with X substituents on the nitrogen atoms	50	13.9 (175-267)	5.0 (268-348)
HNDZ		40	18.3 (265-318)	14.8 (319-422)
DNNC		50	25.2 (209-237)	10.0 (238-314)
PETN	$\text{C}(\text{CH}_2\text{Y})_4$	200	18.1 (196-231)	7.8 (232-317)
AMMO	$\text{HO}-\left[\text{CH}_2\text{CH}(\text{CH}_3)\text{CH}_2\text{N}_3\right]_n-\text{H}$	15	22.7 (265-297)	6.7 (298-479)
TZL4		15	14.6 (248-347)	2.8 (348-431)
AP	NH_4ClO_4	50	47.5 (468-491)	14.8 (492-554)

^a X=NO₂; Y=ONO₂

^b Parenthetical numbers are the temperature range in °C.

induced decomposition. The most satisfactory interpretation of these low apparent activation energies comes from extending the model for one-dimensional time-to-explosion (ODTX) measurements [105]. The two main contributions to the apparent activation energy in this model are chemical activation energy and heat flow. At lower temperatures the chemical terms dominate and produce higher apparent activation energy values. At higher temperatures the heat flow becomes more important in determining the time to reach an exotherm and so the apparent activation energy becomes smaller. As yet, we have not determined the reasons for why the values in Table 2

depend so strongly on the compound. However, this is an ongoing research program and much more work is planned.

One of the features that distinguishes this study from previous time-to-explosion studies [102,105,106] is the opportunity to detect the near surface gas products simultaneously with the temperature or thermal measurement. Figure 12 shows the relative percent concentrations of the

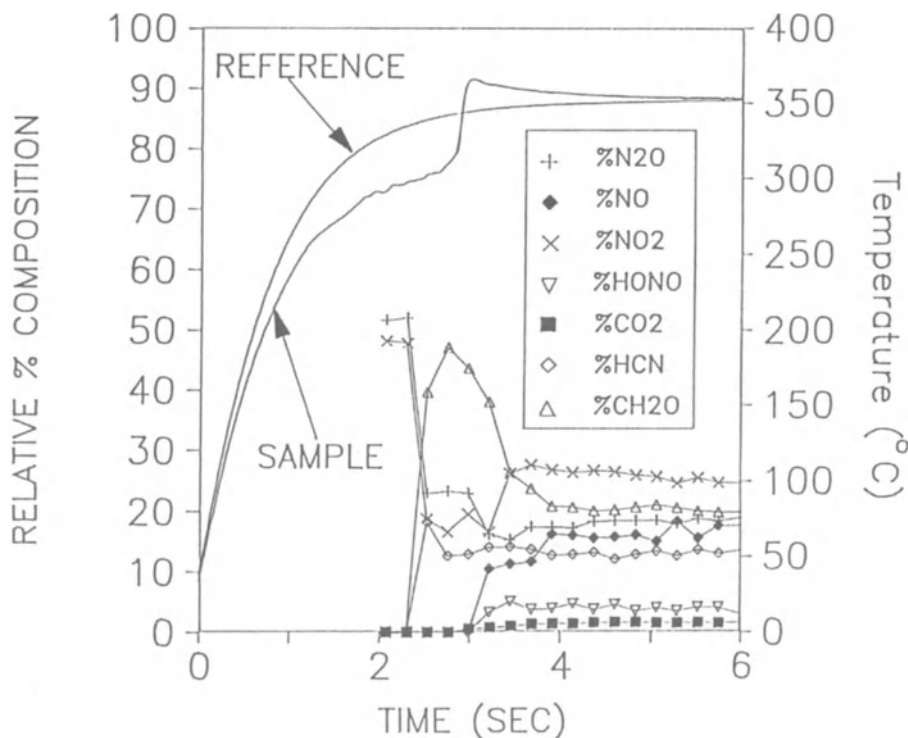


Figure 12. The relative percent of the quantified gas products from HMX superimposed on their simultaneously acquired temperature traces in Fast-Heat-and-Hold/FTIR spectroscopy. Two sets of data are shown.

gas products from HMX superimposed on the corresponding time-to-exotherm temperature traces of HMX. There is clearly an induction period before the exotherm during which extensive chemistry occurs. It is interesting to note that N_2O and NO_2 precede CH_2O in reaching the gas phase. Thoughts on this observation were given in Sections 3.1.5 and 3.1.6. Based on the similarity of the gas products, there does not appear to be much difference in the thermal decomposition process of HMX under the two heating conditions shown in Figure 12.

8. Additional Applications to Propellants

Some of the aforementioned comments on the application of fast thermolysis to explosives extend to the ignition and combustion processes of propellants and *vice versa*. Because a considerable amount of our effort has been directed at understanding the sub-surface and near super-surface processes of energetic materials, this article will conclude with some further generalities that can be drawn about fast heated materials in relation to their pre-ignition, ignition, and combustion-like state.

8.1 THERMOLYSIS MECHANISMS

Combustion chemistry strongly depends on the gas molecules that leave the surface of the propellant. Section 3 of this article summarized most of the findings to date. Many of the small molecule products detected in our measurements are likely to be important in feeding the early flame zone. A practical use of the structure/decomposition relationships might then be to connect the synthetic organic chemist and propellant formulator to the combustion scientist. By knowing the flame characteristics of various gas combinations from the work of the combustion scientist, the desirable and undesirable combustion features could be tailored in and out by the synthetic organic chemist and formulator to produce the desired gas combinations.

Figure 7 in Section 4 of the companion article of this Institute deals with the sequencing of physical and chemical events from the fast thermolysis of ethanediammonium dinitrate. Figure 5 of this article shows the same type of results for HMX. Both figures illustrate the opportunity to sequence some of the main events and establish the temperatures of the processes that take place when energetic materials are rapidly heated.

8.2 LIQUEFACTION AT HIGH HEATING RATES

The Temperature Profiling/FTIR method has revealed that most compounds display an endotherm corresponding to the known melting temperature, even when they are heated at the fastest rates used in this technique (400°C/sec) [93]. Thus, most oxidizers formulated into a propellant and undergoing thermal decomposition during combustion probably have a thin liquid layer on the surface. However, as the pressure is raised in our experiment, the melting endotherm becomes less evident or is absent. This could mean either that liquefaction no longer occurs at high pressure or that the thermocouple is no longer able to detect the temperature deflection caused by the phase change. It is known that the liquid layer on the surface of HMX-containing propellants becomes smaller at higher pressures [107].

We attempted to learn more about the liquid phase of HMX and RDX by recording the FTIR spectrum of rapidly heated samples [57]. The fresh melt of RDX is composed almost entirely of RDX molecules. It requires several seconds before the decomposition products build up to the level where they become detectable by IR spectroscopy. HMX gives evidence of decomposition in advance of "melting" and, therefore, we [57] and others [108] prefer to think of HMX as passing into a liquefaction phase because it is no longer a pure material when the solid lattice transits to the molten state.

Decomposition products are evident in molten HMX from the outset, but most of the sample in the fresh molten state still consists of HMX molecules [57].

8.3 EVIDENCE OF OSCILLATING PROCESSES

Chemical oscillations may or may not be a factor in combustion instability. There is little evidence of oscillations in the product concentrations in any of the energetic materials that we have studied by fast thermolysis. However, in the case of hydroxylammonium nitrate under certain conditions of pressure and heating rate, the relative product composition reproducibly changes in an oscillating manner [79]. Figure 13 shows this behavior for

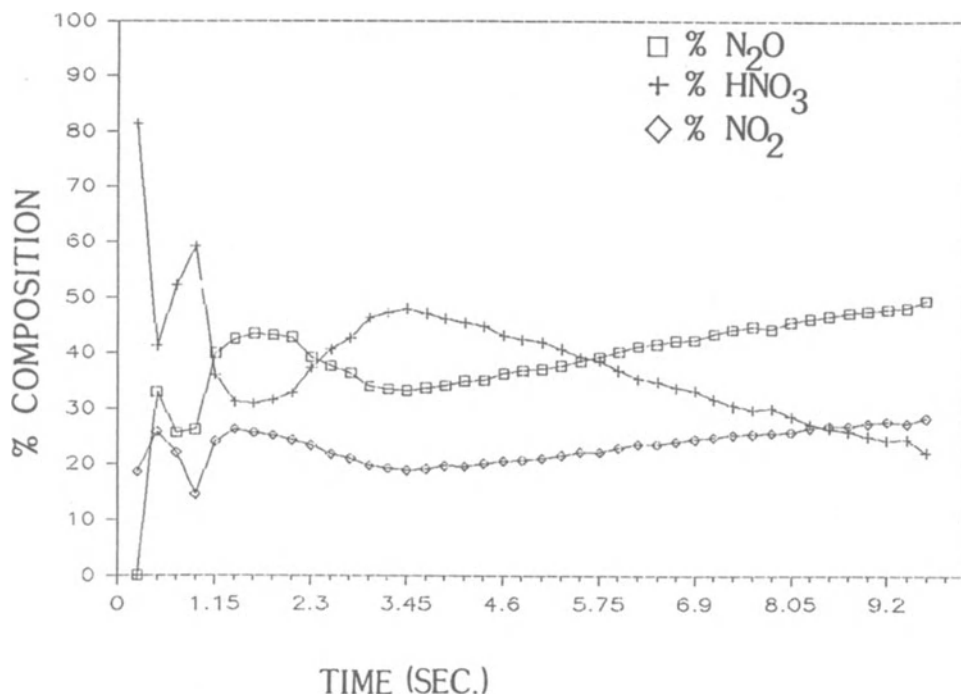


Figure 13. The temporal oscillations in the gas product concentration from 1 mg of solid HAN heated at $dT/dt = 130^{\circ}\text{C/sec}$ under 500 psi Ar.

HAN heated at 130°C/sec under 500 psi Ar. Pressures above 100 psi Ar and heating rates exceeding 130°C/sec are required to induce such oscillations. The oscillations continue, but with an increasingly lengthened period, when HAN is diluted with H_2O . Therefore, we have not referred to HAN decomposition as an oscillating chemical reaction. Perhaps a better term is simply that the decomposition is an oscillating process. If the concentration of HAN is lowered to about 12 M, then the oscillation essentially ceases. Since this concentration is in the range of that used

for liquid gun propellants, it is unlikely that chemical oscillations are responsible for instabilities and pressure oscillations observed in regenerative liquid gun fixtures. However, as new oxidizers and fuels are tested in propulsion formulations, the potential for oscillations in the gas product concentrations should not be overlooked. The number of examples of this behavior uncovered by fast thermal decomposition studies is small, but the fact that one exists under certain experimental conditions is cause for concern.

8.4 CHEMISTRY IN THE THERMAL WAVE OF THE CONDENSED PHASE

The temperature in the condensed phase of a burning propellant drops from a high value at the burning surface to the cool material within about 100 μM . The gradient is exponentially steep near the surface and the depth of penetration of the thermal wave depends on factors such as the thermal conductivity and diffusivity of the propellant, the pressure at the burning surface, and the burn-rate [109].

Chemical reactions begin to occur along the thermal wave in the condensed phase beginning at the depth where the decomposition temperature of the material is reached. They occur at increasing rates from this point out to the surface, where the temperature is highest. However, the chemical reactions and the heat flow rates are merged in this near surface region so that an understanding of the physicochemical aspects of this process is difficult to acquire. By using the Fast-Heat-and-Hold technique described in the companion article, we believe that we have found a way to probe the heat flow/chemistry interface in this narrow and difficult-to-study regime. The results discussed in Section 7.2 for the time-to-exotherm are applicable to this problem as well. As the temperature becomes higher (closer to the surface), the apparent activation energy to achieve the exotherm becomes smaller because of the fact that heat flow becomes increasingly important relative to the chemical activation energies. Figure 14 illustrates this notion. The apparent activation energy values from this work on HMX at each temperature are shown superimposed on the temperature (thermal wave) profile for HMX at 15 psi adapted from the literature [109]. The distance axis represents the distance from the surface (0 μM) into the material. The dark line representing the experimental global apparent activation is the line that must be fit by the sum of heat flow and chemical activation energy terms when modelling the behavior of the condensed phase during combustion. In effect, the time to achieve exothermic chemistry is controlled by diffusion near the surface, and chemical activation energies further below the surface. As far as we know, this apparent activation energy "wave" is the only experimentally determined, chemically related variable available to model the physicochemical processes taking place in the condensed phase near the burning surface.

8.5 DECOMPOSITION FACTORS DIRECTLY CONNECTED TO THE BURN-RATE

It is, of course, highly unlikely that the global burn-rate of a propellant can be routinely traced to some characteristic of the decomposition of the oxidizer in the condensed phase. Burn-rate is simply a function of too many other variables. However, the absence of burn-rate data for a wide

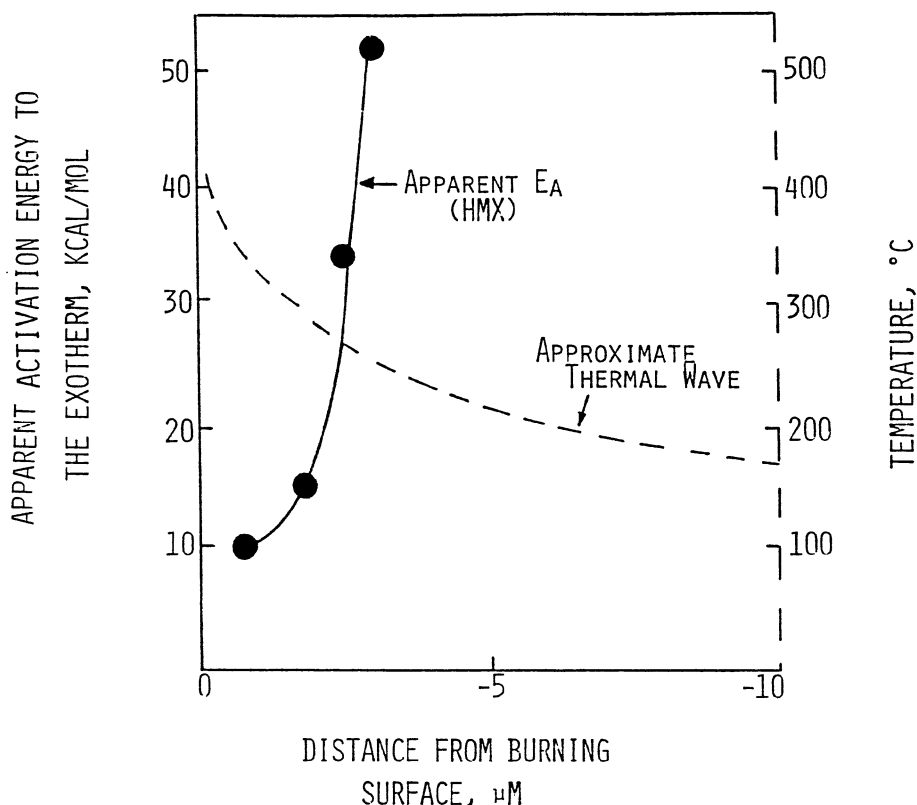


Figure 14. A plot of the estimated temperature wave in a crystal of burning HMX superimposed on the apparent activation energy to the exotherm at the corresponding temperatures. Note that the apparent activation energy (heat flow plus chemical activation energy) decreases with increasing temperature (that is, the apparent activation energy is less when the process occurs closer to the surface).

range of "research-type" materials makes it difficult to access the possibility. We were excited to find that there was a potential connection in one instance where all the required data are available. Burn-rate data have become available for several of the nitrate salts and their mixtures mentioned in Sections 3.5 and 5 where we have fast thermolysis data. These systems we studied were pure NH_4NO_3 (AN), hydrazinium nitrate, ethylenediammonium dinitrate (EDD), 50/50 AN/EDD, and 67/33 HAN/AN and other mixtures [77]. We found that fast thermolysis produced a large quantity of AN in the gas phase in all cases irrespective of whether AN was present in the original material or not [77]. This means that NH_3 and HNO_3 are significant early thermolysis products in all cases. That is, in the course of heating, the low AN-content or non-AN-containing mixtures first decompose to produce significant quantities of NH_3 and HNO_3 in the gas phase before combustion takes place. The combustion characteristics are,

therefore, likely to be controlled by the NH_3/HNO_3 flame. These data suggested to us the possibility that the burn-rate of mixtures of nitrate salts might be leveled to about the burn-rate of pure AN. The burn-rates of several propellants prepared from nitrate oxidizers are tabulated in Table 3 [110]. Unfortunately, all of the formulations contained some AN, but the amount is small in several of the mixtures. Note that the burn rates are similar to AN within experimental error. This suggests that, in

TABLE 3. Strand burner data for nitrate salt propellants at 1000 psi

<u>Nitrate salt component^a</u>	<u>Burn-rate, in/sec</u>
AN	0.11 ± 0.03
50/50 AN/EDD	0.15 ± 0.03
20/40/40 AN/HAN/HN	0.17 ± 0.03
25/75 AN/HAN	0.18 ± 0.03

^a Equal quantity of Al and binder in each formulation

certain instances, a simple decomposition step of the parent oxidizer may be a major factor in determining the burn-rate of the material.

9. Acknowledgments

Numerous student coworkers have executed the experiments described in this article. Without their help and doing the work myself, I would be stumbling along somewhere in Section 3. In alphabetical order they are Peter Brush, Jangkang Chen, James Cronin, Frank Goetz, Thomas Haller, Richard Karpowicz, Yoshio Oyumi, Stephen Palopoli, Thomas Russell, Peter Spohn, Charles Stoner, Rajeevi Subramanian, and Mark Timken. Also, the very valuable collaborations with my colleagues Arnold Rheingold on x-ray crystallography and Cecil Dybowski on solid state NMR are most appreciated.

I am very grateful to many researchers in the energetic materials field, now too numerous to mention by name, who asked me questions, reviewed our papers, sneered at the right moment, and so forth for giving us so much feedback. A research project like this one is a collage of ideas, false and true paths, and etherial insights that come from discussions and meetings with others, and time to think alone.

Without compounds to study, my students and I would have gotten nowhere. In alphabetical order I am sincerely grateful for this generosity to Horst Adolph, Bill Anderson, Kurt Baum, Joe Boyer, Jeff Bottaro, Surya Bulusu, Mae Chan, Mike Chaykovsky, Mike Coburn, Cliff Coon, Milt Frankel, Bob Fifer, John Fisher, Bruce Foxman, Ev Gilbert, Ron Henry, Bill Koppes, Ray McGuire, Bob McKenney, Ross Millar, Fred Myers, George Naufflett, Arnie Nielsen, Jim Weber, Rod Willer, Dean Woolery, and Walt Zajac. (I hope my memory is accurate).

Finally, none of us would be able to carry out our research without agency and industrial funding. Each organization listed here supported a different aspect of our work. They are the Air Force Office of Scientific Research, Aerospace Sciences, on AFOSR-80-0258, AFOSR-85-0353, and AFOSR-87-0033. Program managers through this period were Len Caveny, who recommended support for the original proposal in this field, Bob Vondra, Julian Tishkoff, and Mitat Birkan. The Army Research Office supported the project on DAAG29-84-K-0198. The program managers were Bob Ghiradelli and Dick Paur. Morton-Thiokol, Inc. provided support on an IR & D program overseen by Dave Flanigan, Tom Davidson, Ernie Sutton, and Win Brundage. The Air Force Armament Laboratory supported the project on F08635-87-C-0130. Bob McKenney was the monitor. Two small projects were also supported by Aerojet Solid Propulsion Company and Battelle.

10. References

- [1] Kamlet, M.J. and Adolph, H.G. (1979) 'The Relationship of Impact Sensitivity with Structure of High Explosives. II. Polynitroaromatic Explosives' *Propellants and Explosives* 4, 30-34.
- [2] Kamlet, M.J. and Adolph, H.G. (1981) 'Some Comments Regarding The Sensitivities, Thermal Sensitivities and Explosive Performance Characteristics of Fluorodinitromethyl Compounds' *Proceedings of the Ninth Symposium (International) on Detonation, Annapolis, MD*, 84-92.
- [3] Sundararajan, R. and Jain, S.R. (1983) 'Structure and Impact Sensitivity Relation in Organic Explosives' *Indian Journal of Technology* 21, 474-477.
- [4] Jain, S.R., Rao, M.V. and Pai Verneker, V.R. (1979) 'Structure and Explosive Sensitivity Relation in Ring Substituted Arylammonium Perchlorates' *Combustion and Flame* 35, 289-295.
- [5] Sundararajan, R. and Jain, S.R. (1982) 'A Simple Method of Estimating the Detonation Velocity from Chemical Composition of Organic Explosives' *Combustion and Flame* 45, 47-52.
- [6] Zeman, S., Fedak, J. and Dimun, M. (1982) 'The Relationship Between DTA Data and the Detonation Characteristic of Thermodynamically Unstable Aliphatic Series Compounds' *Zbornik Radova* 18, 119-135.
- [7] Zeman, S. (1981) 'Kinetic Data from Low-Temperature Thermolysis in the Study of the Microscopic Initiation Mechanism of the Detonation of Organic Polynitrate Compounds' *Thermochimica Acta* 49, 219-246.
- [8] Nazin, G.M., Manelis, G.B. and Dubovitskii (1968) 'Thermal Decomposition of Aliphatic Nitro Compounds' *Russian Chemical Reviews* 37, 603-612.
- [9] Bock, H. and Dammel, R. (1987) 'The Pyrolysis of Azides in the Gas Phase' *Angewante Chemie International Edition (English)* 26, 504-526.

- [10] Lee, A., Law, C.K. and Randolph, A.L. (1988) 'Aerothermochemical Studies of Energetic Liquid Materials 2. Combustion and Microexplosion of Droplets of Organic Azides' *Combustion and Flame* 71, 123-136.
- [11] Dubovitskii, F.I. and Korsumskii, B.L. (1981) 'Kinetics of the Thermal Decomposition of N-Nitro Compounds' *Russian Chemical Reviews* 50, 958-978.
- [12] Flanagan, J.E., Frankel, M.B., Weber, J.F., and Woolery, D.O. (1987) 'Basic Research in the Chemistry and Combustion of Nitroform Compounds' *Proceedings of the AFOSR/ONR Meeting on Combustion and Rocket Propulsion*, Pennsylvania State University, University Park, PA, 251-254.
- [13] Kilmenko, G.K. (1977) 'Thermal Stability and Chemical Structure of Polynitro and Nitrato Compounds' *Gorenie i Vzryu*, 585-593.
- [14] Nielsen, A. (1987) 'Correlation of Chemical Structure of Organic High Explosives and Sensitivity' *Proceedings of the Working Group Meeting on Sensitivity of Explosives*, Socorro, NM 256-278.
- [15] Fedoroff, B.T. *Encyclopedia of Explosives and Related Items*, Vols 1-10, Picatinny Arsenal, Dover, NJ.
- [16] Schroeder, M.A. (1979) 'Critical Analysis of Nitramine Decomposition Results: Some Comments on Chemical Mechanisms' *Chemical Propulsion Information Agency Publication* 308, 17-34; (1981) 'Critical Analysis of Nitramine Decomposition Data: Product Distributions from RDX and HMX Decomposition' *Chemical Propulsion Information Agency Publication* 347, 395-413.
- [17] Boggs, T.L. (1984) 'The Thermal Behavior of RDX and HMX' *Progress in Astronautics and Aeronautics* 9, 121-175.
- [18] Fifer, R.A. (1984) 'Chemistry of Nitrate Ester and Nitramine Propellants' *Progress in Astronautics and Aeronautics* 9, 177-237.
- [19] Melius, C.F. (1987) 'Molecular Decomposition Mechanisms of Energetic Materials' *Journal de Physique* 48, C4-341-352.
- [20] Korobeinichev, O.P., Kuibida, L.V. Orlov, V.N., Tereshchenko, A.G., Kutsenogii, K.P., Mavliev, R.A., Ermolin, N.E., Fomin, V.M. and Emel'yanov, I.D. (1985) 'Mass Spectrometric Probe Study of the Flame Structure and Kinetics of Chemical Reactions in Flames' *Mass Spectroscopy and Chemical Kinetics*, 73-93.
- [21] Parr, T.P. and Hanson-Parr, D.M. (1986), 'The Application of Imaging Laser Induced Fluorescence to the Measurement of HMX and Aluminized Propellant Ignition and Deflagration Flame Structure' *Chemical Propulsion Information Agency Publication* 457, Vol. 1, 249-261.

- [22] Palopoli, S.F. and Brill, T.B. (1990) 'Thermal Decomposition of Energetic Materials 43. 'Mechanistic Features of HMX Decomposition Inferred from the Effect of the Gas Environment on the Products' to be published.
- [23] Politzer, P., Sukumar, N. Jayasuriya, K. Ranganathan, S. (1988) 'Computational Evaluation and Comparison of Some Nitramine Properties' *Journal of the American Chemical Society* 110, 3425-3430.
- [24] Haller, T.M., Brill, T.B. and Rheingold, A.L. (1984) 'Structure of the 1:1 Complex between Hexahydro-1,3,5-trinitro-1,3,5-triazine (RDX) and Tetrahydrothiophene 1,1-dioxide (Sulfolane)' *Acta Crystallographica C* 40, 517-519.
- [25] Burov, Yu. M. and Nazin, G.M. (1982) 'Influence of Structure on the Rate of Decomposition of Secondary Nitramines in the Gas Phase' *Kinetics and Catalysis* 23, 5-10.
- [26] Brill, T.B. and Oyumi, Y. (1986) 'Thermal Decomposition of Energetic Materials 10. A Relationship of Molecular Structure and Vibrations to Decomposition: Polynitro-3,3,7,7-tetrakis (trifluoromethyl)-2,4,6,8-tetraazabicyclo[3.3.0]octanes' *Journal of Physical Chemistry* 90, 2679-2682.
- [27] Oyumi, Y., Rheingold, A.L., Brill, T.B. (1987) 'Thermal Decomposition of Energetic Materials 18. Bis(cyanomethyl) nitramine and Bis(cyanoethyl)nitramine' *Propellants, Explosives and Pyrotechnics* 12, 1-7.
- [28] Oyumi, Y. and Brill, T.B. (1987) 'Thermal Decomposition of Energetic Materials 25. Shifting of the Dominant Decomposition Site by Backbone Substitution of Alkylammonium Nitrate Salts' *Journal of Physical Chemistry* 91, 3657-3661.
- [29] Oyumi, Y. and Brill, T.B. (1987) 'Thermal Decomposition of Energetic Materials 21. The Effect of the Backbone Composition of the Products Evolved upon Rapid Thermolysis of Linear Nitramines' *Combustion and Flame* 67, 121-126.
- [30] Brill, T.B. and Oyumi, Y. (1986) 'Thermal Decomposition of Energetic Materials 17. A Relationship of Molecular Composition to HONO Formation: Bicyclo and Spiro Tetranitramines' *Journal of Physical Chemistry* 90, 6848-6853.
- [31] Oyumi, Y. and Brill, T.B. (1988) 'Thermal Decomposition of Energetic Materials 28. Predictions and Results for Nitramines of Bis-imidazolidinedione. DINGU, TNGU and TDGD' *Propellants, Explosives and Pyrotechnics* 13, 69-73.
- [32] Melius, C.F. and Binkley, J.S. (1986) 'Thermochemistry of the Decomposition of Nitramines in the Gas Phase' *Proceedings of the Twenty-First Symposium (International) on Combustion*, 1953-1463.

- [33] Shackelford, S.A., Coolidge, M.B., Goshgarian, B.B., Loving, B.A., Rogers, R.N., Janney, J.L. and Ebinger, M.H. (1985) 'Deuterium Isotope Effects in Condensed-Phase Thermochemical Decomposition Reactions of Octahydro-1,3,5,7-tetranitro-1,3,5,7-tetrazocine' *Journal of Physical Chemistry* 89, 3118-3126.
- [34] Bulusu, S., Weinstein, D.I., Autera, J.R. and Velicky, R.W. (1986) 'Deuterium Kinetic Isotope Effect in the Thermal Decomposition of 1,3,5-Trinitro-1,3,5-triazacyclohexane and 1,3,5,7-Tetranitro-1,3,5,7-tetrazacyclooctane: It's Use as an Experimental Probe for Their Shock-Induced Chemistry' *Journal of Physical Chemistry* 90, 4121-4126.
- [35] Shackelford, S.A. (1987) 'In-situ Determination of Exothermic Transient Phenomena: Isotopic Labelling Studies' *Journal de Physique* 48, C4-193-207.
- [36] Melius, C.F. (1988) Sandia National Laboratory, personal communication.
- [37] Shaw, R. and Walker, F.E. (1977) 'Estimated Kinetics and Thermochemistry of Some Initial Unimolecular Reactions in the Thermal Decomposition 1,3,5,7-tetranitro-1,3,5,7-tetraazacyclooctane in the Gas Phase' *Journal of Physical Chemistry* 81, 2572-2576.
- [38] Fogel'zang, A.E., Svetlov, B.S., Adhemyan, V. Ya, Kolyasov, S.M. and Sergienko, O.I. (1974) 'The Combustion of Nitramines and Nitrosamines' *Doklady Akademii Nauk USSR* 216, 603-606.
- [39] Oyumi, Y. and Brill, T.B. (1985) 'Thermal Decomposition of Energetic Materials 4. High-Rate, In Situ, Thermolysis of Four, Six, and Eight Membered, Oxygen-Rich, Gem-Dinitroalkyl Cyclic Nitramines, TNAZ, DNNC and HNDZ' *Combustion and Flame* 62, 225-231.
- [40] Oyumi, Y. and Brill, T.B. (1986) 'Thermal Decomposition of Energetic Materials 11. Condensed Phase Structural Characteristics and High Rate Thermolysis of Di- and Trinitroaliphatic Carboxylic Acids and Carbonates' *Combustion and Flame* 65, 103-111.
- [41] Gray, P. (1955) 'Bond Dissociation Energies in Nitrites and Nitro Compounds and the Reaction of Free Radicals with NO_2 ' *Transactions of the Faraday Society* 51, 1367-1374.
- [42] Hoffsommer, J.C. and Glover, D.J. (1985) 'Thermal Decomposition of 1,3,5-Trinitro-1,3,5-triazacyclohexane (RDX): Kinetics and Nitroso Intermediates Formation' *Combustion and Flame* 59, 303-310.
- [43] Behrens, R. (1987) 'Simultaneous Thermogravimetric Modulated Beam Mass Spectroscopy and Time-of-Flight Velocity Spectra Measurements: Thermal Decomposition Mechanisms of RDX and HMX' *Chemical Propulsion Information Agency Publication* 476, I, 333-342.

- [44] Hoffssommer, J.C., Glover, D.J. and Elban, W.L. (1985) 'Quantitative Evidence for Nitroso Compound Formation in Drop-Weight Impacted RDX Crystals' *Journal of Energetic Materials* 3, 149-167.
- [45] Oyumi, Y. and Brill, T.B. 'Thermal Decomposition of Energetic Materials 5. High-Rate, In Situ, Thermolysis of Two Nitrosamine Derivatives of RDX by FTIR Spectroscopy' *Combustion and Flame* 62, 233-241.
- [46] Brill, T.B., Karpowicz, R.J., Haller, T.M. and Rheingold, A.L. (1984) 'A Structural and Fourier Transform Infrared Spectroscopy Characterization of the Thermal Decomposition of 1-(azidomethyl)-3,5,7-tetrazacyclooctane' *Journal of Physical Chemistry* 88, 4138-4143.
- [47] Oyumi, Y., Brill, T.B. and Rheingold, A.L. (1986) 'Thermal Decomposition of Energetic Materials 9. Polymorphism, Crystal Structures and Thermal Decomposition of Polynitroazabicyclo [3.3.1] nonanes' *Journal of Physical Chemistry* 90, 2526-2533.
- [48] Oyumi, Y., Rheingold, A.L. and Brill, T.B. (1987) 'Thermal Decomposition of Energetic Materials 19. Unusual Condensed Phase and Thermolysis Properties of a Mixed Azidomethyl Nitramine: 1,7-Diazido-2,4,6-trinitro-2,4,6-triazaheptane' *Journal of Physical Chemistry* 91, 920-925.
- [49] Oyumi, Y., Brill, T.B. and Rheingold, A.L. (1987) 'Thermal Decomposition of Energetic Materials 20. A Comparison of The Structure Properties and Thermal Reactivity of an Acyclic and Cyclic Tetramethylenetetranitramine Pair' *Thermochimica Acta* 114, 209-225.
- [50] Oyumi, Y. and Brill, T.B. (1985) 'Thermal Decomposition of Energetic Materials 3. A High-Rate, In Situ, FTIR Study of the Thermolysis of RDX and HMX with Pressure and Heating Rate as Variables' *Combustion and Flame* 62, 213-224.
- [51] Oyumi, Y., Brill, T.B. and Rheingold, A.L. (1985) 'Thermal Decomposition of Energetic Materials 7. High-Rate FTIR Studies and The Structure of 1,1,1,3,6,8,8,8-Octanitro-3,6-diazaoctane' *Journal of Physical Chemistry* 89, 4824-4828.
- [52] Oyumi, Y., Rheingold, A.L. and Brill, T.B. (1986) 'Thermal Decomposition of Energetic Materials 16. Solid-Phase Structural Analysis and the Thermolysis of 1,4-Dinitrofurazano [3,4-b] piperazine' *Journal of Physical Chemistry* 90, 4686-4690.
- [53] Melius, C.F. (1987) 'Theoretical Studies of The Chemical Reactions Involved in the Ignition of Nitramines' *Chemical Propulsion Information Agency Publication* 476, Vol. I, 359-366.

- [54] Brill, T.B. and Brush, P.J. (1990) 'Chemical Phenomena Associated with the Initiation of Thermal Explosions' Proceedings Ninth Symposium (International) on Detonation, Portland, OR, in press.
- [55] Cosgrove, J.D. and Owen A.J. (1974) 'The Thermal Decomposition of 1,3,5-Trinitro Hexahydro-1,3,5-Triazine (RDX) - Part II: Effects of the Products' Combustion and Flame 22, 19-22.
- [56] Kimura, J. and Kubota, N. (1980) 'Thermal Decomposition of HMX' Propellants and Explosives 5, 1-8.
- [57] Karpowicz, R.J. and Brill, T.B. (1984) 'In Situ Characterization of the 'Melt' Phase of RDX and HMX by Rapid-Scan FTIR Spectroscopy' Combustion and Flame 56, 317-325.
- [58] Snyder, P.A., Kremer, J.H., Liebman, S.A., Schroeder, M.A. and Fifer, R.A. (1989) 'Characterization of Cyclotrimethylene trinitramine (RDX) by N,H Isotope Analysis with Pyrolysis-Atmospheric Pressure Ionization Tandem Mass Spectroscopy' Organic Mass Spectrometry 24, 15-21.
- [59] Oyumi, Y. and Brill, T.B. (1986) 'Thermal Decomposition of Energetic Materials 12. Infrared Spectral and Rapid Thermolysis Studies of Azide-Containing Monomers and Polymers' Combustion and Flame 65, 127-135.
- [60] Turley, J.W. (1968) 'A Refinement of the Crystal Structure of N,N'-Dinitroethylenediamine' Acta Crystallographica B24, 942-946.
- [61] Haller, T.M., Rheingold, A.L. and Brill, T.B. (1985) 'Structure of the 1/1 Complex between Octahydro-1,3,5,7-tetranitro-1,3,5,7-tetrazocine (HMX) and N-Methyl-2-Pyrrolidinone (NMP)' Acta Crystallographica C41, 963-965.
- [62] Haller, T.M., Rheingold, A.L. and Brill, T.B. (1983) 'The Structure of the Complex Between Octahydro-1,3,5,7-tetranitro-1,3,5,7-tetrazocine (HMX) and N,N-Dimethylformamide (DMF). A Second Polymorph' Acta Crystallographica C39, 1559-1563.
- [63] Palopoli, S.F. and Brill, T.B. (1988) 'Thermal Decomposition of Energetic Materials 27. Synthesis, Characterization and Thermolysis of Cu(II)-Doped "Blue RDX"' Combustion and Flame 72, 153-158.
- [64] Palopoli, S.F., Geib, S.J., Rheingold, A.L. and Brill, T.B. (1988) 'Synthesis and Modes of Coordination of Energetic Nitramines Ligands in Copper (II), Nickel (II) and Palladium (II) Complexes' Inorganic Chemistry 27, 2963-2971.
- [65] Palopoli, S.F. and Brill, T.B. (1988) 'Thermal Decomposition of Energetic Materials 30. Thermolysis of Energetic Metal-Nitraminato Complexes Under Conditions that Simulate Combustion' Inorganic Chemistry 27, 2971-2976.

- [66] Oyumi, Y. and Brill, T.B. (1986) 'Thermal Decomposition of Energetic Materials 15. Evidence that Decomposition Initiates Deflagration: High-Rate Thermolysis of FEFO, TEFO and DITEFO' *Propellants, Explosives and Pyrotechnics* 11, 35-39.
- [67] Adolph, H.G. (1987) 'Evidence of Rate Determining C-C Bond Heterolysis in the Condensed Phase Thermal Decomposition of Polynitroethyl Compounds' *Combustion and Flame* 70, 343-347.
- [68] Brill, T.B. and Subramanian, R. 'Thermal Decomposition of Energetic Materials 35. A Mechanism Study of Decomposition and the Transition to the Ignition-Like State in Trinitromethyl Alkyl Compounds' *Combustion and Flame*, in press.
- [69] Oyumi, Y. and Brill, T.B. (1988) 'Thermal Decomposition of Energetic Materials 14. Selective Product Distributions Evidenced in Rapid, Real-Time Thermolysis of Nitrate Esters at Various Pressures' *Combustion and Flame* 66, 9-16.
- [70] Russell, T.P. and Brill, T.B. (1990) 'Thermal Decomposition of Energetic Materials 39. Fast Thermolysis Patterns of Poly (Methyl), Poly(ethyl), and Primary alkylammonium Mononitrate Salts' *Propellants, Explosives and Pyrotechnics*, in press.
- [71] Russell, T.P. and Brill, T.B. (1990) 'Thermal Decomposition of Energetic Materials 40. Fast Thermolysis Patterns of Alkane Diammonium Dinitrate Salts $[H_3N(CH_2)_nNH_3](NO_3)_2$, $n = 1-4,6$ ' *Propellants, Explosives and Pyrotechnics*, in press.
- [72] Russell, T.P. and Brill, T.B. (1990) 'Thermal Decomposition of Energetic Materials 41. Fast Thermolysis of Cyclic and Acyclic Ethanediaammonium Dinitrate Salts and their Oxonium Nitrate Double Salts, and the Crystal Structure of Piperazinium Dinitrate' *Propellants, Explosives and Pyrotechnics*, in press.
- [73] Russell, T.P. and Brill, T.B. (1990) 'Thermal Decomposition of Energetic Materials 42. Fast Thermal Decomposition of Five N-Methyl Substituted Ethanediaammonium Dinitrate Salts' *Propellants, Explosives and Pyrotechnics*, in press.
- [74] Oyumi, Y., Brill, T.B., Rheingold, A.L. and Lowe-Ma, C. (1985) 'Thermal Decomposition of Energetic Materials 2. The Thermolysis of NO_3^- and ClO_4^- Salts of the Pentaerythrityltetrammonium Ion, $C(CH_2NH_3)_4^{4+}$, by Rapid-Scan FTIR Spectroscopy. The Crystal Structure of $[C(CH_2NH_3)_4](NO_3)_4$ '. *Journal of Physical Chemistry* 89, 2309-2315.
- [75] Fridman, A.L., Mukhametshin, F.M., and Novikov, S.S. (1971) 'Advances in the Chemistry of Aliphatic N-Nitrosamines' *Russian Chemical Reviews* 40, 34-50.

- [76] Scanlan, R.A. and Tannenbaum (Eds.) (1981) 'N-Nitroso Compounds' ACS Symposium Series 174, 117-289.
- [77] Russell, T.P. and Brill, T.B. (1989) 'Thermal Decomposition of Energetic Materials 31. Fast Thermolysis of Ammonium Nitrate, Ethylenediamine Dinitrate and Hydrazinium Nitrate and the Relationship to the Burning Rate' Combustion and Flame 76, 393-401.
- [78] Oyumi, Y. and Brill, T.B. (1985) 'Thermal Decomposition of Energetic Materials 6. Solid-Phase Transitions and the Decomposition of 1,2,3-Triaminoguanidinium Nitrate' Journal of Physical Chemistry 89, 4325-4329.
- [79] Cronin, J.T. and Brill, T.B. (1986) 'Thermal Decomposition of Energetic Materials 8. Evidence of an Oscillating Process during the High-Rate Thermolysis of Hydroxylammonium Nitrate, and Comments on the Ionic Interactions' Journal of Physical Chemistry 90, 178-181.
- [80] Spohn, P.D. and Brill, T.B. (1989) 'Raman Spectroscopy of the Species in Concentrated Aqueous Solutions of $\text{Zn}(\text{NO}_3)_2$, $\text{Ca}(\text{NO}_3)_2$, $\text{Cd}(\text{NO}_3)_2$, LiNO_3 and NaNO_3 up to 450°C and 30MPa' Journal of Physical Chemistry.
- [81] Brill, T.B., Spohn, P.D., and Cronin, J.T. (1989) 'Thermal Decomposition of Energetic Materials 32. On the Instantaneous Molecular Nature of Aqueous Liquid Gun Propellants at High Temperatures and Pressures Before Thermal Decomposition' Journal of Energetic Materials, in press.
- [82] Sharma, J., Forbes, J.W., Coffey, C.S., and Liddiard, T.P. (1987) 'The Physical and Chemical Nature of Sensitization Centers Left from Hot Spots Caused in Triaminotrinitrobenzene by Shock or Impact' Journal of Physical Chemistry 91, 5139-5144.
- [83] Oyumi, Y. and Brill, T.B. (1986) 'Thermal Decomposition of Energetic Materials 13. High-Rate Thermolysis of Benzofuroxans and 3,4-Dimethylfuroxan' Combustion and Flame 65, 313-318.
- [84] Stoner, C.E., Jr., and Brill, T.B. unpublished results.
- [85] Cronin, J.T. and Brill, T.B. (1989) 'Thermal Decomposition of Energetic Materials 33. The Thermolysis Pathway of the Azidodinitromethyl Group' Applied Spectroscopy 43, 650-653.
- [86] Brill, T.B. and Subramanian, R. (1990) 'Thermal Decomposition of Energetic Materials 36. Fast Thermolysis of Overoxidized Nitro and Halonitro Nitramines', Propellants, Explosives and Pyrotechnics, in press.
- [87] Booth, C.A., Foxman, B.M. and Jaufmann, J.D. (1987) 'Design of a Solid-State Reaction: Crystal Structure and Solid-State Polymerization of Bis(propiolato)tetraaquo zinc (II)' ACS Symposium Series 337, 95-105.

- [88] Stoner, C.E., Jr., and Brill, T.B. (1989) 'Thermal Decomposition of Energetic Materials 34. Decarbonylation, Decarboxylation and Coupling Reactions of Metal Propiolate Salts, $M[O_2CC\equiv CH]$ ' Inorganic Chemistry, in press.
- [89] Miller, J.S., Glatzhofer, D.T., Laversanne, R., Chittipeddi, S., Vaca, P., Brill, T.B., Timken, M.D., O'Conner, C.J., Zheng, J.H., Calabrese, J.C., and Epstein, A.J. (1989) 'Structural and Magnetic Characterization of α - and β -4,4'-(Butadiene-1,4-diyl)-bis-(2,2,6,6-tetramethyl-4-hydroxypiperidin-1-oxyl) and Its Thermal Degradation Product' submitted.
- [90] Korshak, Yu., Medvedeva, V., Orchinnikov, A.A., Spektor, V.N. (1987) 'Organic Polymer Ferromagnet' Nature 326, 370-372.
- [91] Oyumi, Y. and Brill, T.B. (1987) 'Thermal Decomposition of Energetic Materials 22. The Contrasting Effects of Pressure on the High-Rate Thermolysis of 34 Energetic Compounds' Combustion and Flame 68, 209-216.
- [92] Oyumi, Y. Rheingold, A.L. and Brill, T.B. (1987) 'Thermal Decomposition of Energetic Materials 24. A Comparison of the Crystal Structures, IR Spectra, Thermolysis and Impact Sensitivities of Nitroguanidine and Trinitroethylnitroguanidine' Propellants, Explosives, and Pyrotechnics 12, 46-52.
- [93] Cronin, J.T. and Brill, T.B. (1987) 'Thermal Decomposition of Energetic Materials 26. Simultaneous Temperature Measurements of the Condensed Phase and Rapid-Scan FT-IR Spectroscopy of the Gas Phase at High Heating Rate' Applied Spectroscopy 41, 1147-1151.
- [94] Cronin, J.T. and Brill, T.B. (1988) 'Thermal Decomposition of Energetic Materials 29. The Fast Thermal Decomposition Characteristics of a Multicomponent Material: Liquid Gun Propellant 1845' Combustion and Flame 74, 81-89.
- [95] Brill, T.B. and Russell, T.P. (1988) 'Characterization of the Thermal Degradation of Selected Energetic Materials and Mixtures by Rapid-Scan FTIR Spectroscopy' Air Force Armament Laboratory, Technical Report 88-85, 1-44.
- [96] Brill, T.B. and Russell, T.P. (1989) 'Characterization of the Thermal Decomposition of Selected Energetic Materials and Mixtures by Rapid-Scan Fourier Transform Infrared Spectroscopy' Air Force Armament Laboratory TR-89-55, 1-21.
- [97] Dobratz, B.M. (1983) 'Ethanediimine Dinitrate and Its Eutectic Mixtures' LA-9732H, UC-45, Los Alamos National Laboratory, Los Alamos, NM.

- [98] Oyumi, Y., Brill, T.B., Rheingold, A.L. and Haller, T.M. (1985) 'Crystal Structure and Molecular Dynamics of the Energetic Nitramine 1,3,3,5-Tetranitrohexahydropyrimidine and a Comparison with 1,3,3,5,7,7-Hexanitro-1,5-diazacyclooctane and 1,3,3-Trinitroazetidine' *Journal of Physical Chemistry* 89, 4317-4324.
- [99] Oyumi, Y. and Brill, T.B. (1987) 'Thermal Decomposition of Energetic Materials 23. Thermochemical Differentiation of Cyclic and Acyclic Nitramines by Their Phase Transitions' *Thermochimica Acta* 116, 125-130.
- [100] Mesaros, D.V., Oyumi, Y., Brill, T.B. and Dybowski, C. (1986) 'NMR Investigation of the Premelt Phase of Hexahydro-1,3,5-trinitroso-s-triazine' *Journal of Physical Chemistry* 90, 1970-1973.
- [101] Brill, T.B. and Goetz, F. (1976) 'Laser Raman Studies of Solid Oxidizer Behavior' *Progress in Astronautics and Aeronautics* 63, 3-19.
- [102] Wenograd, J. (1961) 'The Behavior of Explosives at Very High Temperatures' *Transactions of the Faraday Society* 57, 1612-1620.
- [103] Rogers, J.W., Jr., Peebles, H.C., Rye, R.R., Houston, J.E. and Binkley, J.S. (1984) 'A Carbon Auger Line Shape Study of Nitroaromatic Explosives' *Journal of Chemical Physics* 80, 4513-4520.
- [104] Ritchie, J.P., Cromer, D.T., Stewart, R.F., Wasserman, H.J., Ryan, R.R. (1985) 'Electron Density Distribution Analysis for Nitroguanidine' Los Alamos Scientific Laboratory, NM, LA-UR-85-1088.
- [105] McGuire, R.R. and Tarver, C.M. (1981) 'Chemical Decomposition Models for the Thermal Explosion of Confined HMX, TATB, RDX and TNT Explosives' *Proceedings of the 7th Symposium (International) on Detonation*, US Naval Academy, Annapolis, MD, 56-64.
- [106] Henkin, H. and McGill, R. (1952) 'Rates of Explosive Decomposition of Explosives' *Industrial and Engineering Chemistry* 44, 1391-1395.
- [107] Derr, R.L., Boggs, T.L., Zurn, D.E. and Dibble, E.J. (1974) 'The Combustion Characteristics of HMX' *Chemical Propulsion Information Agency Publication* 261, 231-241. Taylor, J.W. (1962). 'A Melting Stage in the Burning of Secondary Explosives' *Combustion and Flame* 6, 103-107.
- [108] Kraeutle, K.J. (1981) 'The Thermal Decomposition of HMX: Effect of Experimental Conditions and of Additives' *Chemical Propulsion Information Agency Publication* 347, 383-394.
- [109] Kubota, N. (1984) 'Survey of Rocket Propellants and Their Combustion Characteristics' *Progress in Astronautics and Aeronautics* 90, 1-50.

- [110] Campbell, J.A. (1987), Aerojet Solid Propulsion Co., personal communication.

THE APPLICATION OF SIMULTANEOUS THERMOGRAVIMETRIC MODULATED BEAM MASS SPECTROMETRY AND TIME-OF-FLIGHT VELOCITY SPECTRA MEASUREMENTS TO THE STUDY OF THE PYROLYSIS OF ENERGETIC MATERIALS*

RICHARD BEHRENS

*Sandia National Laboratories
Combustion Research Facility
Livermore, CA 94551-5000
USA*

ABSTRACT. The use of mass spectrometry to collect data on the decomposition chemistry of nitramine compounds and the relevance of the data to the processes occurring in these materials when they are used in actual propellant and explosive applications is discussed. The simultaneous thermogravimetric modulated beam mass spectrometry (STMBMS) and time-of-flight (TOF) velocity-spectra techniques and their application to the study of energetic materials are discussed. The means by which these techniques enhance the amount of information obtained from more conventional mass spectrometric experiments is illustrated with studies on the evaluation of the use of appearance energy measurements to study the thermal decomposition of HMX and on the identification of the HMX pyrolysis products and the determination of their gas formation rates.

Introduction

To obtain the most information from experiments on energetic materials, the experimental technique should address both the uses and behaviors of the materials. Energetic materials are used in both propellant and explosive formulations. Most of the work on the behavior of these materials addresses their combustion and sensitivity. The majority of the work on their combustion addresses parameters that cause variations in the burn rate and its pressure dependence.^{1,2} The sensitivity of the energetic materials to external stimuli have addressed areas that include: mechanical, electrical, and thermal forms of initiation.

The overall goal of experiments with energetic materials is to establish a correlation between the behaviors and the properties of the materials. Analysis of the extensive database on energetic materials has led to correlations between both combustion behaviors (i.e. burn rates and detonation velocities) and sensitivities and the properties of the materials. The material properties that have been or can be correlated with behaviors of energetic materials in order of more detailed effects are:

heat content	
density	
physical properties	-- melting point
	-- thermal diffusivity
physical features	-- particle size
	-- grain size, defects
atomic composition	
molecular structure.	

As the effects of more microscopic and specific features of the energetic material on the behaviors are probed, a more fundamental understanding of the material properties that effect the energetic material behavior will be achieved.

The difficulty in obtaining meaningful experimental results, which can be used to obtain a better understanding of the behavior of these materials, is illustrated in Figure 1. The overlap between the parameter space in which it is easiest to acquire the most meaningful data and the operational parameter space of the materials is small. Experiments that are conducted under the operating conditions of the materials give much less detailed information than experiments that are conducted outside the operation region. To make a connection between the experimental and operational parameter space, it is important to know the conditions under which the experimental results are obtained and to link these conditions with the experimental results and the conditions used in the normal application of these materials.

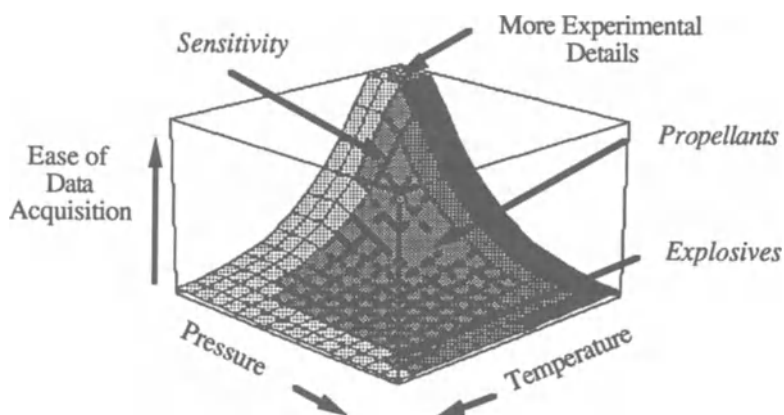


Figure 1. The ease of data acquisition in temperature and pressure space illustrates the lack of overlap between the conditions under which the most detailed experimental information is easiest to acquire and the conditions under which the materials are typically used.

In a similar manner, it is also important to assess how much information is actually determined from an experiment. The extent of the correlation between the observations (e.g., heat or reaction products) and the reaction region conditions that lead to the observations need to be determined in order to draw appropriate conclusions from the observations. The ultimate goal of an experiment would be to observe the reaction progression of each molecule under its operational conditions.

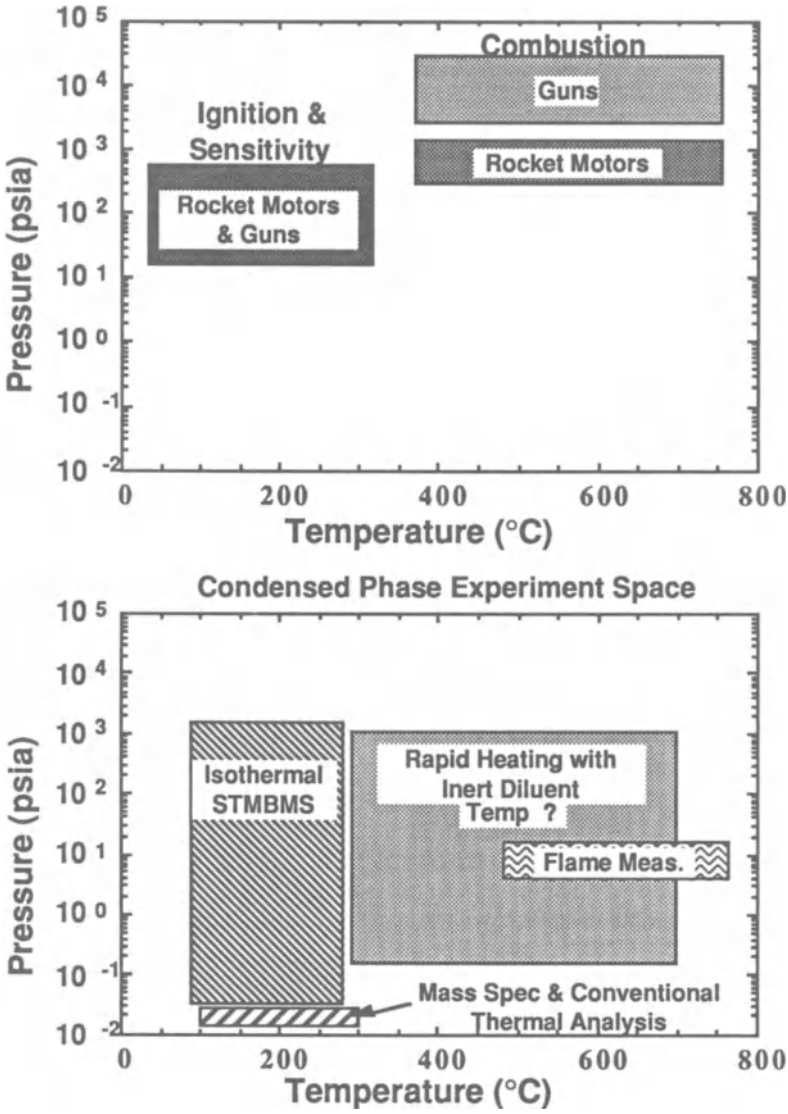


Figure 2. a) Operational space for early stage processes of ignition, sensitivity, and combustion for rocket and gun applications; b) experimental space for different techniques that can be applied to the study of early stage processes.

The diagnostics used for in situ measurements of the products formed during the initial stages of the combustion in energetic material propellant applications overlap different regions of operational space as illustrated in Figure 2. The species formed in the higher temperature regions during the early stages of the decomposition have been measured in low pressure flames by planar laser induced fluorescence (PLIF) imaging and under an inert atmosphere by rapid scan Fourier transform infrared (RSFTIR) spectroscopy. These techniques detect the lower molecular weight products generated during the decomposition, such as NO_2 and CH_2O . Conventional mass spectrometry and thermal analysis methods have explored the behaviors of energetic materials at lower pressure and temperature conditions. The simultaneous thermogravimetric modulated beam mass spectrometry (STMBMS) measurements usually explore the same parameter space as conventional mass spectrometry experiments. However, with at least one energetic material, HMX, the nature of the decomposition allows the decomposition at higher pressures to be explored.

This paper will review the advantages and limitations of conventional mass spectrometry for the study of energetic materials, describe the STMBMS and time-of-flight (TOF) velocity-spectra measurement techniques, and illustrate the use of these techniques to obtain information on the decomposition of HMX. The following paper³ will present the results on the decomposition of HMX along with a qualitative model of the processes occurring during the low temperature decomposition of HMX.

Conventional Mass Spectrometry

A number of studies^{4,5,6} of nitramine decomposition have been made using conventional mass spectrometry techniques. The configuration for a typical experiment is shown in Figure 3. The sample is decomposed either within the vacuum chamber housing the mass spectrometer (1) or in an external vessel followed by transport of the volatile gases into the mass spectrometer via an inlet system (2). A small fraction ($\sim 10^{-4}$) of the molecules are then ionized (by either electron bombardment or chemical ionization), the positive ions are then separated according to their m/z values, the ions are detected and the resulting signal is recorded for each different m/z value. The advantages of using mass spectrometry for the study of energetic materials are its high sensitivity and its ability to detect all of the different species that may be generated during a decomposition. Consequently, the higher molecular weight species that may be the initial products from the decomposition of a nitramine can be detected.

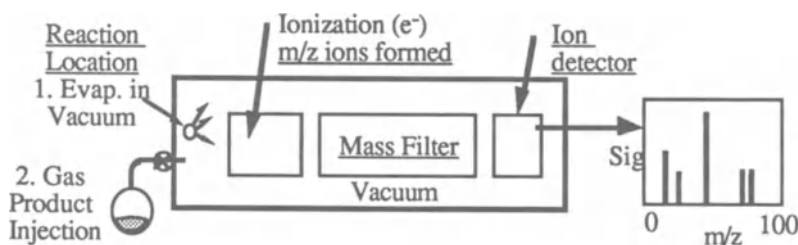
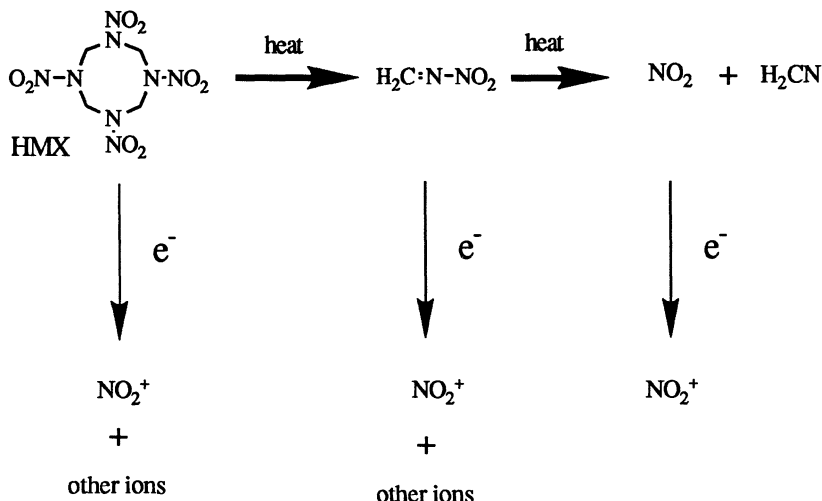


Figure 3. Configuration of a conventional mass spectrometry experiment used for the study of energetic materials.

Although these advantages make the use of mass spectrometry very attractive for the study of the decomposition of energetic materials, there are a number of disadvantages that have limited its use. These disadvantages include the following:

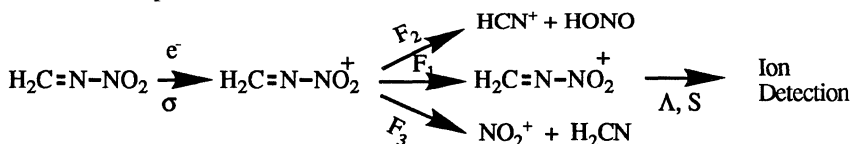
- 1) interference from background species
- 2) the product identification in mixtures of gases is ambiguous
- 3) quantitative results are difficult to obtain
- 4) the reactions usually occur in a very low pressure environment
- 5) correlation between the reaction products and the reaction conditions that produced the products can be ambiguous.

The problem associated with using mass spectrometry to identify products from a mixture of gases may be illustrated with the following hypothetical example for HMX decomposition:



in which the HMX thermally decomposes into methylenenitramine ($\text{H}_2\text{C}=\text{NNO}_2$), NO_2 , and other products. The mixture is then introduced into the mass spectrometer and the ions are formed from the gas products in the mixture. Because of the excess energy introduced into the molecule during the ionization process, the HMX and methylenenitramine ions can undergo subsequent fragmentation, thus, producing NO_2^+ . Since the mass spectrometer detects the signal at $m/z = 46$ (corresponding to NO_2^+), it is not possible to tell from the mass spectrometry data alone which type of molecule lead to the formation of the NO_2^+ ion. Note that even though NO_2^+ is detected with the mass spectrometer, no NO_2 may actually be formed during the thermal decomposition.

Another difficulty associated with conventional mass spectrometry is making quantitative measurements. Determining the rates of gas formation from mass spectrometry data is difficult because for each product either a sensitivity factor must be known or calculated or calibration standards must be measured. For example, from methylenenitramine the factors that must be determined for the detection process



are the electron current density, the ionization volume, the ionization cross section, σ , the cracking factors, F , the quadrupole transmission, Λ , and the ion detector sensitivity, S . For simple molecules, such as NO or N₂, it is possible to determine these factors. However, even for these types of molecules calibration standards are often used. For more complicated molecules in which the cracking factors, F , become important, it is more difficult to calculate the factors and calibration standards are necessary. Unfortunately, for many of the products that may be formed during the nitramine decomposition, it is not possible to obtain calibration standards. Furthermore, even if calibration standards are available, the method of introducing the standards into the apparatus must simulate the way in which the gas is produced during the actual decomposition in order for the calibration to be accurate.

Finally, it is important to control the reaction environment when using mass spectrometry to study the decomposition of energetic materials. Most organic compounds evaporate prior to decomposing in a vacuum environment. So to study reactions occurring in the condensed phase it is necessary to reduce the vaporization rate sufficiently to allow the material to decompose in the condensed phase prior to evaporation.

The Simultaneous Thermogravimetric Modulated Beam Mass Spectrometer

A schematic of the STMBMS apparatus, which is described in detail elsewhere,^{7,8,9} is shown in Figure 4. Basically, this instrument allows the concentration of each gas phase species in a reaction cell to be measured as a function of time by correlating the ion signals at different m/z values measured with the mass spectrometer with the force measured by a microbalance at any instant. The thermal decomposition products are distinguished from the ion dissociation products in two ways. First, an autocorrelation analysis of all the ion signals at different m/z values measured during one thermal decomposition experiment is made to determine the temporal correlation between the m/z values. Second, time-of-flight (TOF) velocity spectra at the different m/z values are measured to determine the molecular weights of the thermal decomposition products leading to the formation of the ion signals at each m/z value.

To conduct an experiment, a sample is placed in an alumina reaction cell that is placed on a DTA sample probe. The sample probe is inserted in a microbalance which has a sensitivity of 5 μg . The balance chamber and the furnace chamber are evacuated by turbomolecular pumps. The reaction cell is radiatively heated by a bifilar wound tungsten wire on an alumina tube. The molecules exiting from the reaction cell traverse two beam defining orifices before entering the mass spectrometer. The ionizer of the mass spectrometer is located in a separate vacuum chamber which is pumped by a 600 l/s ion/titanium sublimation pump. The ions traverse a quadrupole mass filter, are extracted by a set of electrostatic lenses and detected by a Daly detector¹⁰. The beam path defined by the orifices is modulated by a chopping wheel that is driven by a hysteresis synchronous motor. The reference signal for collecting the modulated waveform comes from an optical switch. The distance between the reaction cell and the ionizer is varied by moving the detector chamber assembly on a drive plate. The background pressure in the ionizer vacuum chamber is $< 10^{-9}$ torr during an experiment.

The features that make the STMBMS apparatus unique are the controlled reactor environment, direct sampling of products released from the reaction environment, the use of TOF velocity spectra to help identify pyrolysis products, and the ability to make real-time quantitative measurements on mixtures of products.

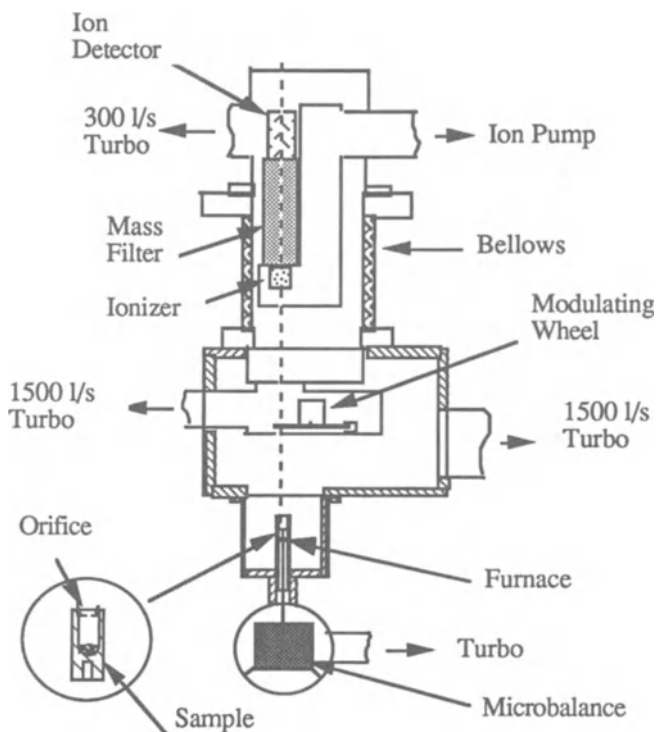


Figure 4. Schematic diagram of the simultaneous thermogravimetric modulated beam mass spectrometer (STMBMS) apparatus.

The reaction cell used in the experiments is shown in Figure 5. A balance between the vaporization and decomposition rates is achieved by adjusting the orifice size and sample mass for the desired experiment temperature. Measurement of the TOF velocity spectra for each m/z value gives the approximate molecular weight of each pyrolysis product that is contributing to each m/z value. This technique is illustrated in Figure 6 for the hypothetical decomposition of HMX discussed previously. The rotating TOF wheel admits a short pulse of the mixture of gaseous products to the flight path between the TOF wheel and the ionizer of the mass spectrometer. The ion signal for a selected m/z value is recorded as a function of time after the mixture of products is first admitted to the flight path. The major portion (> 99%) of the flight time is due to neutral molecules traversing the path between the TOF wheel and the ionizer. Therefore, the time of arrival is inversely proportional to the velocity of the molecules. For effusive flow conditions in the reaction cell, the time of arrival is proportional to the square root of the mass of the molecules. As shown in Figure 6, the arrival times of NO_2^+ can be due to the three different pyrolysis products NO_2 , $\text{H}_2\text{C}=\text{NNO}_2$, or HMX.

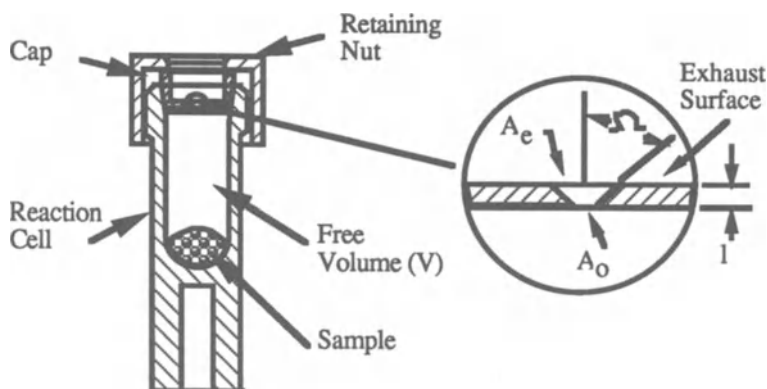


Figure 5. Cross section of the reaction cell. The gas produced during the decomposition of the sample escapes through the orifice whose area is A_o .

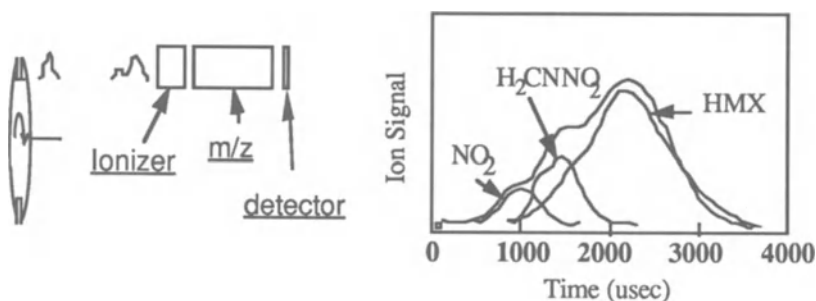


Figure 6. Illustration of the TOF velocity-spectra technique used to determine the molecular weights of the pyrolysis products contributing to the ion signals at $m/z=46$ from a hypothetical decomposition of HMX.

After all of the pyrolysis products from the decomposition are identified, the STMBMS data are used to determine the rate of formation of each pyrolysis product by the general procedure illustrated in Figure 7. In this procedure the time-dependent mass spectrometry and microbalance data are used in conjunction with the reaction cell flow conditions to determine the time-dependent gas formation rates of the different products in the reaction cell. The gas formation rate is defined

as the rate that each product appears in the free volume of the reaction cell. Possible sources of the products that may contribute to the gas formation rate are gas phase reactions in the free volume of the cell and release of products from the solid into the free volume of the cell. Figure 7 also illustrates the necessity of determining the sensitivity factors for each product, in that the ion signal for product 1 is less than product 2 in the mass spectrometer data but the actual rate of formation of product 1 is larger than product 2.

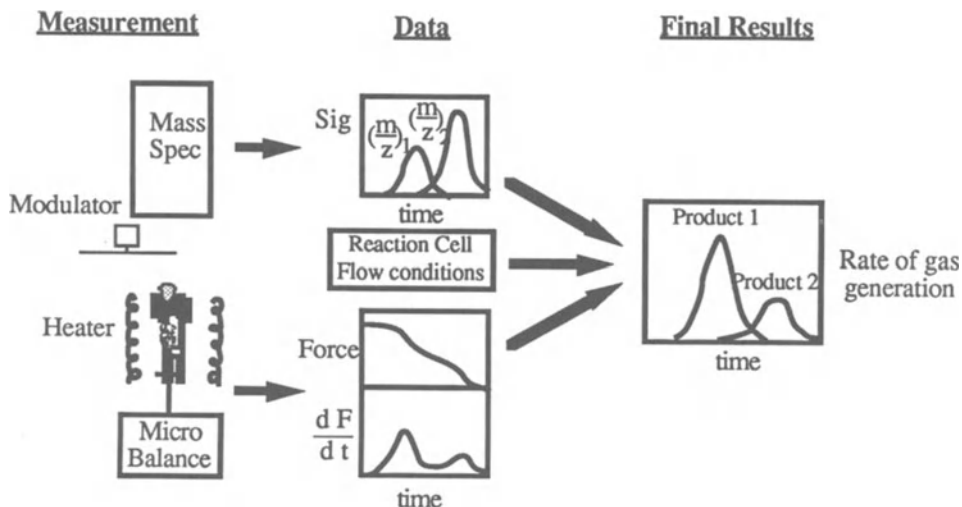


Figure 7. Illustration of the procedure used to collect and analyze the STMBMS data to determine the time-dependent rates of gas formation of the different products produced during a thermal decomposition.

The STMBMS apparatus is also designed to increase the signal to noise ratio so that products with low concentrations in the reaction cell can be detected. With the ion counting detection system used in the mass spectrometer and modulating the path between the reaction cell and ionizer, the signal to noise ratio is given by

$$\text{Signal/Noise} = \frac{st}{\sqrt{st + Bt}} \quad (1)$$

where s is the rate of detection of modulated products from the reaction cell and B is the rate of detection of products from the background in the vacuum system. The signal to noise ratio in the system is increased by lengthening the period that the signals are collected and using differential pumping in the vacuum system to reduce the contribution of the background, B , in the ionization region of the mass spectrometer.

The time-dependent measurements are made possible through use of computer control of the data acquisition process.⁷

Data Analysis

The analysis of both the TOF velocity spectra and the STMBMS data are dependent on the geometric parameters of the apparatus and reaction cell as shown in Figure 8.

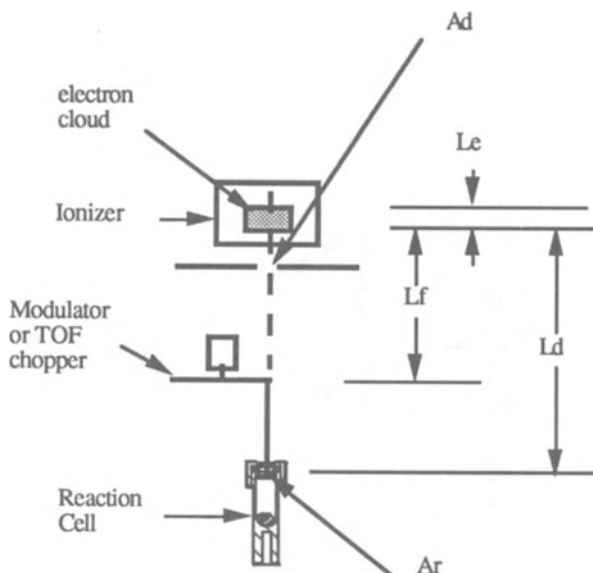


Figure 8. The apparatus and reaction cell geometric parameters used in the TOF velocity spectra and STMBMS data analysis.

TOF VELOCITY SPECTRA ANALYSIS

The TOF measurements are made by measuring the waveform that results from a pulse of neutral molecules generated by the TOF wheel.¹¹ The TOF pulse is generated by rotating a 7.62 cm radius disk with two equally spaced 0.30 cm wide slots past a 0.30 cm square orifice at a frequency of 167 Hz. This produces a triangular gate pulse $g_p(t^*)$, centered about $t^* = 0$, with a base width of 74 μsec and a period of 3000 μsec . After subtracting the transit time of ions through the quadrupole and ion detector, the TOF spectra $I(t_0)$ are obtained where t_0 is measured from the center of the gate pulse and is related to the neutral velocities by

$$t_0 = t^* + \frac{L}{v} \quad (2)$$

where L is the flight path of the neutrals. Thus, the TOF spectra $I(t_0)$ are a convolution of the velocity distribution $I(v)$ with the gate pulse $g_p(t^*)$ and the flight path distribution $g_L(L)$ and expressed as

$$I(t_0) = \int_0^\infty G(t_0, v) I(v) dv \quad (3)$$

where

$$G(t_0, v) = \int_0^\infty g_L(L) g_p(t_0 - \frac{L}{v}) dL$$

and

$$\int_0^\infty G(t_0, v) dt_0 = 1$$

Since the objective of the analysis is to determine the mass of the neutral decomposition products that contribute to an ion signal at an m/z value, a sum of velocity distributions with a functional form appropriate for an isentropic expansion is used

$$I(v) = \sum_{i=1}^n \frac{C_i v^3}{\alpha_i^2} \exp \left[-\frac{(v - u_i)^2}{\alpha_i^2} \right] \quad (4)$$

where n is the total number of different neutral species that contribute to the ion signal at the m/z value being measured, $\alpha_i = \sqrt{RT_i/M_i}$, R is the gas constant, M_i is the molecular weight of species i , T_i is the temperature of the gas in the isentropic expansion from the reaction cell after the transition to molecular flow has been obtained, u_i is the flow velocity of the isentropic expansion and C_i is a coefficient. A modified version¹² of the Levenberg-Marquardt nonlinear least squares algorithm is used to optimize the variables in Eq. 3. The general procedure used to identify the neutral mass or masses is as follows: 1) The molecular weights used in the fit are selected from a set of plausible decomposition products. The fitting procedure does not optimize the molecular weight; 2) Several fits with only one velocity distribution for a number of different molecular weights are made and the results are evaluated based on visual examination and a χ^2 calculation. The variables C_i , T_i , and u_i are optimized subject to the constraint that the translational energy in the beam falls within a range expected for an isentropic expansion based on a temperature band centered about the temperature of the reaction cell; 3) If the single velocity distribution fits are not satisfactory, then combinations of molecular weights are used. In these fits only C_i and T_i are varied and the velocity of the isentropic flow, u_i , is recalculated to maintain the energy of the beam consistent with the reaction cell temperature. Again, visual examination and a χ^2 calculation are used to evaluate the results.

QUANTIFICATION PROCEDURE

The STMBMS quantification procedure has been described extensively elsewhere.^{7,9} The expressions for the rate of force change, $dF_i(t)/dt$, measured with the microbalance and the ion signals, $N_{K^+}^+(t)$, measured with the mass spectrometer for each species i can both be expressed in terms of the number density in the reaction cell for each species, $n_i(t)$. The expression for the rate of force change consists of two terms.

$$\frac{dF_i(t)}{dt} = -g \frac{dm_i(t)}{dt} + \frac{d\tau_i(t)}{dt} \quad (5)$$

The first term represents the force change due to mass loss from the reaction cell and the second term represents the thrust generated due to the gas in the reaction cell. The rate of force change may be expressed as a function of number density, n_i , reaction cell geometry, G_1 , and the flow conditions in the reaction cell.

$$\frac{dF_i(t)}{dt} = F(n_i, G_1, \text{FLOW}) \quad (6)$$

Similarly, the expressions for the signals measured with the mass spectrometer can be expressed as functions of the number density, reaction cell and apparatus geometry, G_2 , the ionization and fragmentation processes in the mass spectrometer, IFP, and the reaction cell flow conditions.

$$\dot{N}_{k_i}^+(t) = F_2(n_i, G_2, \text{IFP}, \text{FLOW}) \quad (7)$$

These two functions are combined for each pyrolysis species to produce the following expression relating the rate of force change and the ion signals.

$$\frac{dF(t)}{dt} = \sum_{i=1}^m X_i \left[K_{0_i}(t) \dot{N}_{k_i}^+(t) + K_{1_i}(t) \frac{d\dot{N}_{k_i}^+(t)}{dt} \right] \quad (8)$$

The terms $K_{0_i}(t)$ and $K_{1_i}(t)$ are calculated from the geometric parameters of the instrument and the flow conditions in the reaction cell. $F(t)$ and $\dot{N}_{k_i}^+(t)$ are measured in the experiment. An overdetermined system of equations is generated from the data at different times during the experiment. This set of equations is then solved in a least squares sense to determine the coefficients X_i . By using the determined coefficients, the number density of the different species in the reaction cell can be calculated as a function of time

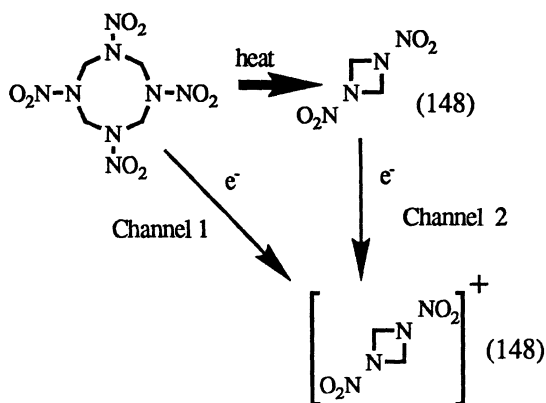
$$n_i(t) = (\text{FLOW}) X_i \dot{N}_{k_i}^+(t) \quad (9)$$

From the time-dependent number densities the rates of gas generation of each different species in the reaction cell can also be calculated.

Application of the Techniques

EVALUATION OF APPEARANCE ENERGY MEASUREMENTS

The TOF velocity-spectra measurements can be used to evaluate the application of appearance energy measurements in mass spectrometry experiments to determine the initial products of HMX decomposition. In appearance energy measurements the energy of the ionizing electrons is lowered so that fragmentation of the ions is eliminated. For example, in experiments with HMX this would allow the 148 pyrolysis product to be observed from the following reaction



because the ion fragmentation pathway to form $m/z=148$ from HMX is eliminated. Therefore, if $m/z=148$ is detected it indicates that the 148 species is a pyrolysis product. To test the basic assumption of appearance energy measurements (i.e., fragment ions are eliminated) for HMX, the m/z values formed in the mass spectrometer from evaporating HMX are measured at low electron energies. The results from an experiment with HMX in which the sample temperature is 225°C , the orifice diameter is .098 cm, and the electron energy is 12.4 eV are shown in Figure 9. The three largest ion signals are at m/z values of 128, 148, and 222. All of the ion signals at the different m/z values are temporally correlated. This high degree of temporal correlation suggests that the signals at the different m/z values are either fragment ions of HMX or molecular ions of HMX pyrolysis products that are formed at constant ratios throughout the decomposition. The TOF velocity spectra measured under the same conditions used for the STMBMS experiment are shown in Figure 10 for m/z values of 75, 128, 148, and 222. Analysis of the spectra shows that each m/z value arises from a compound with a molecular weight of 296 and consequently the signals are fragment ions from HMX and not molecular ions from HMX pyrolysis products. Therefore, these results show that the basic assumption of appearance energy measurements (i.e. that the molecular ion once formed will not undergo fragmentation) does not apply to the nitramine compound, HMX.

HMX THERMAL DECOMPOSITION PRODUCTS AND THEIR FORMATION RATES

By reducing the net vaporization rate of HMX from that used in the appearance energy measurements, the HMX is contained longer and decomposition occurs. This is evident from the ion signals at the various m/z values and the autocatalytic-like behavior of the weight loss as shown in Figure 11 for an experiment conducted at 212°C , with an orifice diameter of 0.014 cm, and an electron energy of 18.4 eV. The ion signals at m/z values of 120, 128, and 148 remain approximately constant throughout the decomposition, whereas the ion signals at the lower m/z values, such as 18, 30, and 44, exhibit a large variation in their intensity through the decomposition.

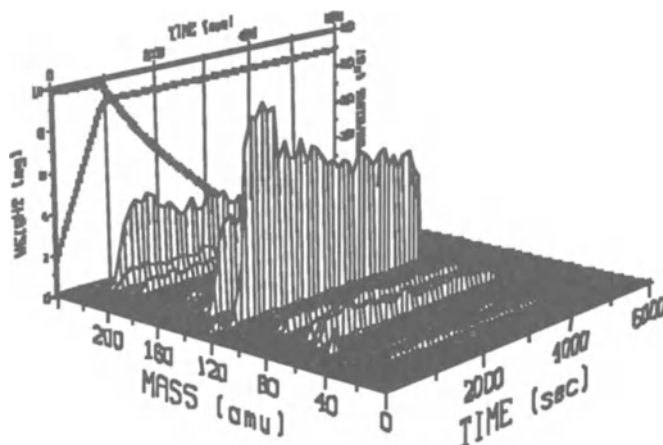


Figure 9. The ion signals formed from the gas products evolving from the reaction cell held at 225°C, with a .098 cm diameter orifice, and containing HMX. The two plots on the rear graph show the weight of the HMX sample and the temperature of the reaction cell during the experiment.

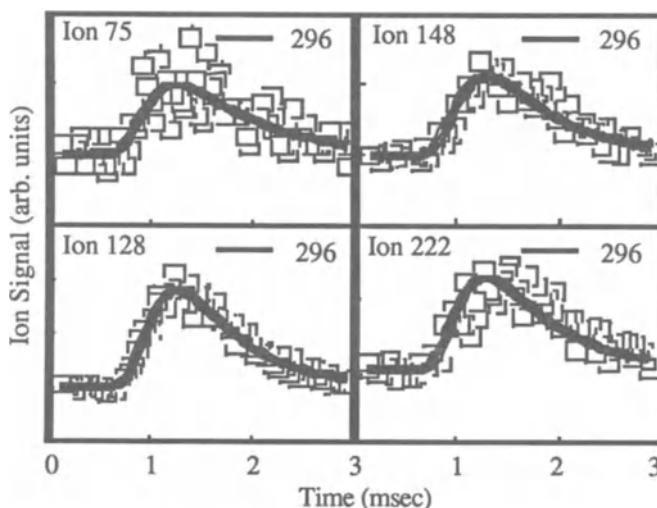


Figure 10. TOF velocity spectra of the HMX fragment ions formed by 12.4 eV electrons. The error bars show the one-sigma standard deviation. The solid lines show the best convoluted velocity distribution fit to the data. The molecular weight used in the velocity distribution is shown on each plot.

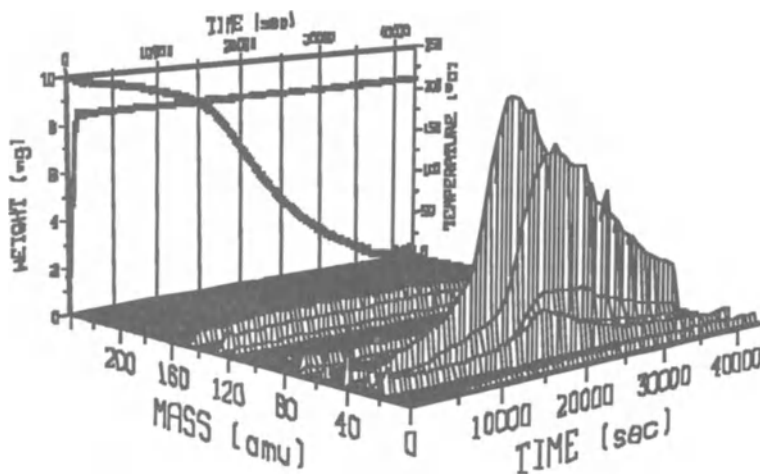


Figure 11. The ion signals from HMX and its pyrolysis products. The sample weight and temperature are shown in the rear. The orifice diameter of the reaction cell is 0.014 cm.

To identify the pyrolysis products leading to the ion signals at each of the different m/z values, TOF velocity spectra were recorded. Several of the spectra are presented in Figure 12. The TOF velocity spectra indicate $m/z = 18$ is from water and $m/z = 29$ is from formaldehyde (CH_2O). The $m/z = 46$ signal, which could originate from NO_2 , comes from two species, one has a molecular weight of ~ 74 and the other is HMX. The $m/z = 74$ signal originates from a pyrolysis product that has a molecular weight of 74. This suggests that the product may be methylenenitramine ($\text{H}_2\text{C}=\text{NNO}_2$). However, further experiments with isotopically labelled HMX show that this is not correct as discussed below. The $m/z = 132$ signal originates from a product that has a molecular weight of 280. Although a molecular weight of 296 (HMX) also gives a reasonable fit to the $m/z = 132$ data, the 280 gives a better fit. This information, along with ion signals at m/z values of 159, 189, and 206 (each is 16 amu lower than the corresponding HMX fragment ion) that are temporally correlated with the $m/z = 132$ signal in the STMBMS data, indicates that this pyrolysis product is 1-nitroso-3,5,7-trinitro-1,3,5,7-tetrazocine (ONTNTA). The last ion signal shown in Figure 12 at $m/z = 148$ originates from HMX and not a pyrolysis product.

To further establish the identity of the HMX pyrolysis products, the experiments were also run with isotopically labelled HMX. The results from deuterium and $^{15}\text{NO}_2$ labelled HMX are listed in Table I. Together with the TOF velocity spectra this shows that the decomposition products formed during the experiments include: H_2O , CO , CH_2O , NO , N_2O , $\text{C}_2\text{H}_5\text{NO}$, $\text{C}_2\text{H}_6\text{N}_2\text{O}$, and ONTNTA. The $\text{C}_2\text{H}_6\text{N}_2\text{O}$ stoichiometry of the pyrolysis product with a molecular weight of 74 is an interesting result in that it shows that it is not methylenenitramine, a product that has been suggested from previous mass spectrometric work.⁶

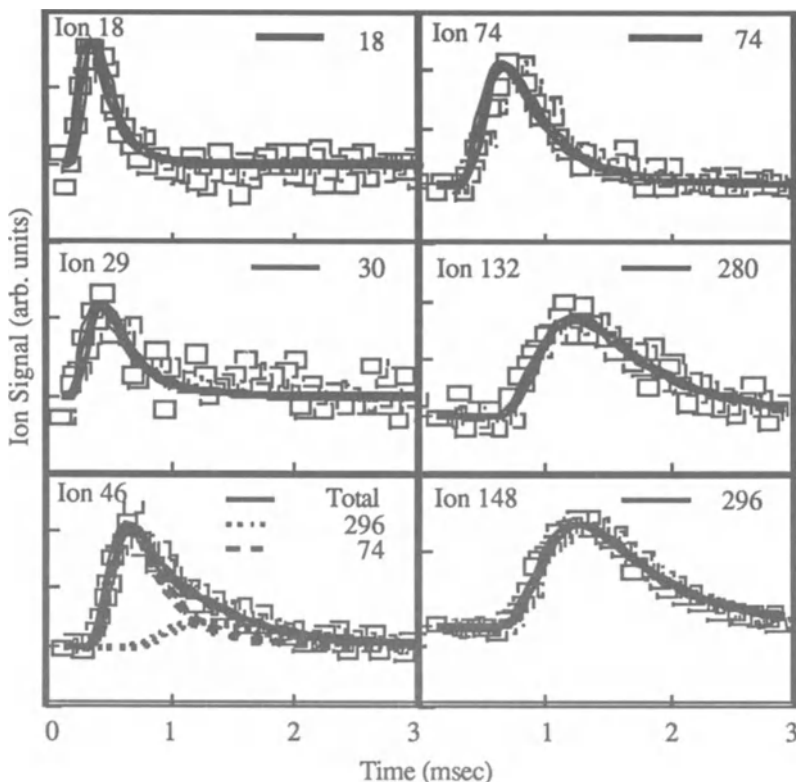


Figure 12. TOF velocity spectra recorded during the acceleratory stage of the decomposition of HMX at 212°C using a 0.014 cm diameter orifice on the reaction cell. The symbols represent the data for the m/z value listed in the upper left corner of each graph. The solid curves are the best convoluted fits to the data. The molecular weights of the products used in each fit are listed on each plot.

The ion signals representing each of the pyrolysis products are extracted from the data and used in the quantification procedure. A comparison between the measured rate of force change and the rate of force change calculated from the quantification procedure is shown in Figure 13. The fit to the data is very good. The results of the best fit to the rate of force change data for reasonable relative ion formation probabilities are listed in Table II. The results show that N_2O , CH_2O , and H_2O are the most abundant products, CO , NO , and HCN are less abundant, and the amounts of C_2H_5NO , $C_2H_6N_2O$, and $ONTNTA$ are the smallest. The elemental mass balance shows that at least 98 percent of each element in the starting material is accounted for in the results from the analysis.

Table I. Gaseous Products from the Pyrolysis of HMX and Their Associated Mass Spectrometric Ion Signal m/z Values^a

Ions				Pyrolysis Products	
	m/z values from Labelled HMX				
Formula	HMX-hg	HMX-d8	HMX- ¹⁵ NO ₂	Mol. Weight ^b	Formula
H ₂ O	18	20	18	18	H ₂ O
HCN	27	not obs.	27	27	HCN
CO	28	28	28	28	CO
HCO	29	30	29	30	CH ₂ O
NO	30	30	31	30	NO
N ₂ O	44	44	45	44	N ₂ O
C ₂ H ₄ NO	58	62	58	~116	(CH ₃ NHCHO) ₂
C ₂ H ₅ NO	59	64	59	not meas.	(CH ₃ NHCHO) ₂
C ₂ H ₆ N ₂ O	74	80	75	74	H ₆ C ₂ N ₂ O
CH ₃ N ₂ O ₂	75	78	76	296	HMX
C ₂ H ₄ N ₄ O ₃	132	136	134	280	H ₈ C ₄ N ₈ O ₇
C ₂ H ₄ N ₄ O ₄	148	152	150	296	HMX

^a A detailed presentation of the correlation between all of the different m/z values measured in the mass spectra of each isotopomer of HMX is given in Ref. 8.

^b The approximate molecular weights of the gaseous products from the pyrolysis of HMX was determined by the time-of-flight velocity spectra method described in Ref. 8

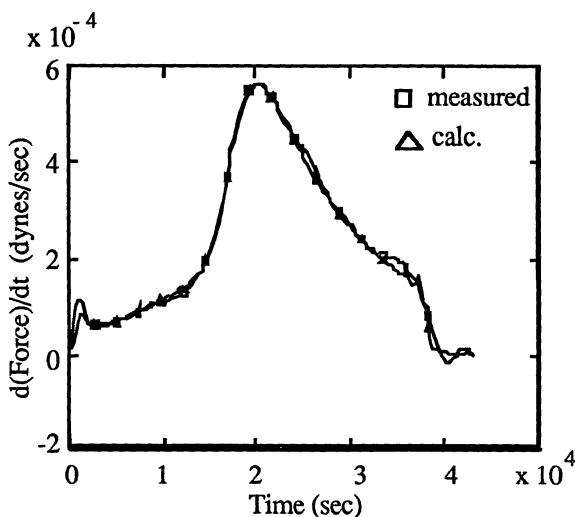


Figure 13. The measured and calculated rate of force change data for the fit parameters listed in Table II.

Table II. HMX fitting parameters and results.^a

Ion Mass	Neutral Product	RIFP ^b band	RIFP	Amount (mg)	Weight Percent	Mole frac ^c
18	H ₂ O	.4 - .68	.40	.553	5.6	1.15
27	HCN	.38 - .75	.38	.256	2.6	.36
28	CO	.4 - 1.0	.4	.641	6.4	.86
29	H ₂ CO	.3 - .5	.5	1.485	14.9	1.85
30	NO	.91 - 1.83	1.83	.498	5.0	.62
44	N ₂ O	.94 (REF)	.94	3.485	35.0	2.97
74	C ₂ H ₆ N ₂ O	.48 - 1.46	1.46	.148	1.5	.07
58	C ₄ H ₁₀ N ₂ O ₂	.6 - 1.2	1.2	.082	.8	.03
132	C ₄ H ₈ N ₈ O ₇	.2 - 2.0	.67	.399	4.0	.05
148	HMX	no band	.69	2.058	20.7	
	Residue ^d			.351	3.5	.13
Euclidean Norm:		1.27 x 10 ⁻⁵				
Mass Balance	Percent H:	98.6				
	C:	99.5				
	N:	97.9				
	O:	102.1				

^a The experimental conditions are as follows: Initial sample weight = 9.956 mg, isothermal temperature = 210.5°C, orifice diameter = 0.0137 cm.

^b RIFP is the relative ion formation probability

^c mole fraction of decomposed HMX.

^d Stoichiometry from elemental analysis of residue: C_{3.3}H_{2.7}N_{1.8}O₂

When the sensitivity factors calculated from the quantification procedure are combined with the time-dependent ion signals representing each of the pyrolysis products, the gas formation rates are determined as a function of time during the decomposition of the sample. The results of this quantification procedure are shown in Figure 14. The implications of the temporal behaviors of the gas formation rates will be discussed in the following paper, however, the more obvious features are noted here. First, under isothermal conditions the rates of gas formation (i.e. the rate of appearance in the free volume of the reaction cell) varies by up to a factor of 40 during the decomposition. Second, the temporal behaviors of the gas formation rates are not all temporally correlated with each other. This is most apparent during the acceleratory stage of the decomposition when the gas formation rates of H₂O and N₂O are approximately equal and the ratio of the N₂O to CH₂O gas formation rates is 2.5. Finally, the rate of exhaust of HMX from the reaction cell remains approximately constant throughout the decomposition, which is expected for the quasi-equilibrium conditions between the gas and solid phase HMX in the reaction cell.

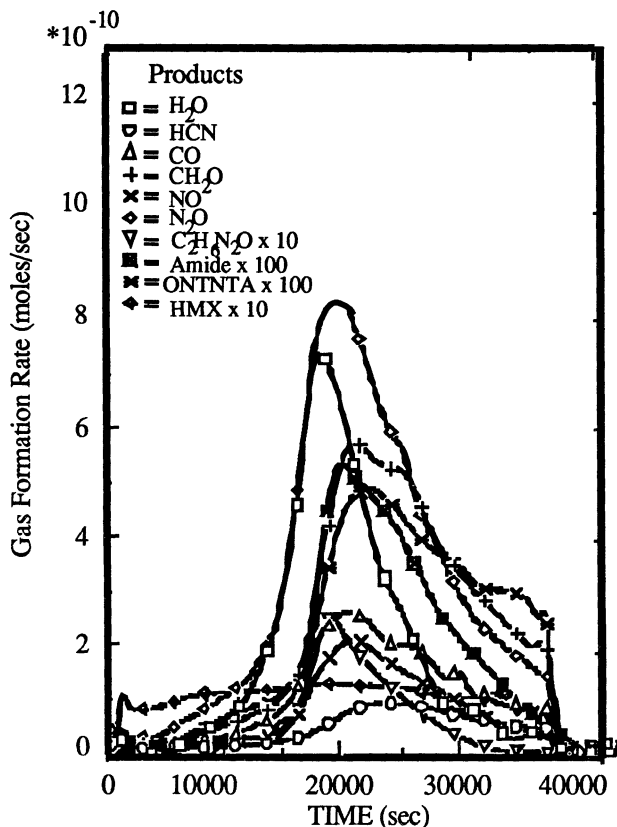


Figure 14. Gas formation rates of the pyrolysis products during the decomposition of HMX in a reaction cell with a 0.014 cm diameter orifice and at 212°C. The HMX sample size is 9.956 mg.

Summary

The STMBMS and TOF velocity spectra techniques enhance the use of mass spectrometry in the study of the decomposition of energetic materials. The careful control of the reaction environment in these experiments allows the identification of the pyrolysis products and accurate measurement of their gas formation rates to be made. Correlation between the observed products and the macroscopic and microscopic processes occurring within the reaction cell will allow qualitative models to be created that may explain the processes leading to the formation of the various products. Hopefully, these results may be correlated with the more limited results gathered from experiments conducted under more severe conditions (i.e. shock initiated reactions or quenched combustion experiments) to provide further insight into the mechanisms controlling the combustion of these materials under their operational conditions.

The design principles of the STMBMS apparatus that allow high sensitivity measurements to be made on energetic materials have been presented. The use of TOF velocity spectra to enable the

pyrolysis products in a mixture of gases to be identified from the mass spectrometric data has been illustrated with an evaluation of the applicability of appearance energy measurements to the study of the pyrolysis of HMX and also a determination of the pyrolysis products formed during a decomposition of HMX below its melting point. The method of using the simultaneous measurement of the rate of force change of the reaction cell and the mass spectrometric data to determine the quantitative gas formation rates within the reaction cell has been discussed. These two techniques combined with the use of automated data acquisition to determine the time-dependent features of a decomposition provide valuable data that can be used to further the understanding of nitramine decomposition chemistry.

* Research supported by a joint Memorandum of Understanding between the U.S. DOE and the U.S. Army.

- ¹ Boggs, T.L., "The Thermal Decomposition Behavior of Cyclotrimethylene - trinitramine (RDX) and Cyclotetramethylene - tetranitramine (HMX) in "Fundamentals of Solid-Propellant Combustion," Kuo, K.K. and M. Summerfield eds.; Progress in Astronautics and Aeronautics Vol. 90., p. 121, AIAA Inc., New York, NY, 1984.
- ² Fifer, R.A., "Chemistry of Nitrate Ester and Nitramine Propellants," in "Fundamentals of Solid-Propellant Combustion," Kuo, K.K. and M. Summerfield eds.; Progress in Astronautics and Aeronautics Vol. 90., p. 177, AIAA Inc., New York, NY, 1984.
- ³ Behrens, Jr., R., (1990), 'Thermal Decomposition of HMX and RDX: Decomposition Processes and Mechanisms Based on STMBMS and TOF Velocity-Spectra Measurements', S. Bulusu (ed.), 'Proceedings of the NATO Advanced Study Institute', ***
- ⁴ Bulusu, S. and Graybush, R.J., "Proceedings of the 36th International Congress on Industrial Chemistry", Brussels, Belgium, 1967; C. R. Ind. Chim. Belge, 1967, **32**, 647.
- ⁵ a) Goshgarian, B.B., (1978), 'The Thermal Decomposition of Cyclotrimethylenetrinitramine (RDX) and Cyclotetramethylenetetranitramine', AFRPL-TR-78-76; b) Pfau, J.P., Rocchio, J.J., and Wires, R.A., (1979), 'New Aspects of HMX and Thermal Decomposition as Studied by Pyrolysis/Mass Spectrometry', 'Proceedings of the 15th JANNAF Combustion Meeting', CPIA Publ. No. 297, pp. 267-293.
- ⁶ a) Farber, M. and Srivastava, R.D. , (1979), 'Mass Spectrometric Investigation of the Thermal Decomposition of RDX', Chem. Phys. Lett., **64**, pp. 307-310; b) Farber, M. and Srivastava, R.D. , (1981), 'Mass Spectrometric Studies of the Thermal Decomposition of 1,3,5,7-Tetranitro-1,3,5,7-tetraazacyclooctane (HMX)', Chem. Phys. Lett., **80**, pp. 345-349.
- ⁷ Behrens, Jr., R., (1986), 'A New Simultaneous Thermogravimetry and Modulated Molecular Beam Mass spectrometry Apparatus for Quantitative Thermal Decomposition Studies', Rev. Sci. Instrum., **58**, pp. 451- 461.
- ⁸ Behrens, Jr., R., (1989), 'Identification of Octahydro-1,3,5,7-tetranitro-1,3,5,7-tetrazocine (HMX) Pyrolysis Products by Simultaneous Thermogravimetric Modulated Beam Mass Spectrometry and Time-of-Flight Velocity Spectra Measurements, to be published in Int. J. Chem. Kinetics.
- ⁹ Behrens, Jr., R., (1989), 'Determination of the Rates of Formation of Gaseous Products from the Pyrolysis of Octahydro-1,3,5,7-tetranitro-1,3,5,7-tetrazocine (HMX) by Simultaneous Thermogravimetric Modulated Beam Mass Spectrometry', to be published in Int. J. Chem. Kinetics.
- ¹⁰ Daly, N.R., (1960), Rev. Sci. Instrum., **31**, p. 264.
- ¹¹ Parr, T.P., Freedman, A., Behrens Jr., R., and Herm, R.R., (1977), 'Crossed Molecular Beams Kinetics: BaO Recoil Velocity Spectra from Ba + N₂O', J. Chem. Phys., **67**, pp. 2181-2190.
- ¹² Brown, K.M. and Dennis, J.E. , (1972), Numerische Mathematik, **18**, 289.

THERMAL DECOMPOSITION OF HMX AND RDX: DECOMPOSITION PROCESSES AND MECHANISMS BASED ON STMBMS AND TOF VELOCITY-SPECTRA MEASUREMENTS*

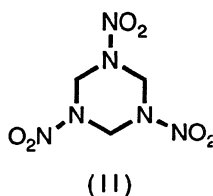
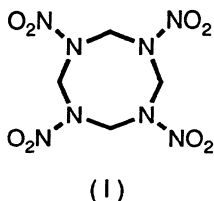
RICHARD BEHRENS
*Sandia National Laboratories
Combustion Research Facility
Livermore, CA 94551-5000
USA*

ABSTRACT. A brief history of the decomposition of HMX and RDX is presented to illustrate the development of the mechanisms that are used to explain the decomposition of these two nitramines. The results from simultaneous thermogravimetric modulated beam mass spectrometry (STMBMS) and time-of-flight (TOF) velocity-spectra measurements on HMX and RDX are used to identify the decomposition products and to determine their gas formation rates as a function of time during the decomposition of the samples. Both nitramines form H_2O , N_2O , CH_2O , NO , and $(\text{CH}_3)\text{NHCHO}$ during the decomposition. RDX forms NO_2 and hydroxy-s-triazine (HST), products associated with N-N bond breaking, whereas HMX forms $\text{C}_2\text{H}_6\text{N}_2\text{O}$, CO , and a nonvolatile residue (NVR). A mononitroso analogue of the parent compound is formed during the decomposition of both materials. The rates of gas formation of the various pyrolysis products along with the macroscopic and microscopic features of the NVR that is generated during the decomposition of HMX suggest that a major process involved in the decomposition of HMX below its melting point is the formation of bubbles containing pyrolysis products within the HMX particles. The pressure of the gas within the bubbles may range up to 35000 psi.

Possible reaction mechanisms that include both the physical location of the reactions and the possible chemical reaction pathways are presented. The results from the STMBMS experiments are consistent with initial fragmentation of the N-N bond of the molecule to form NO_2 and the subsequent unravelling of the remaining ring to form N_2O and CH_2O . Secondary reactions of the primary decomposition products that occur within the particles are important in determining the identity and the relative rates of gas release of the products from the solid particles. The possible bimolecular reactions between pyrolysis products and HMX are also presented.

Introduction

The cyclic nitramines, octahydro-1,3,5,7-tetranitro-1,3,5,7-tetrazocine HMX (I) and hexahydro-1,3,5-trinitro-s-triazine RDX (II),



are energetic ingredients that are used in various propellants and explosives. Understanding the complex physicochemical processes that underlie the combustion of these materials can lead to methods for modifying the propellant and explosive formulations in order to obtain better ignition, combustion, or sensitivity properties. A number of new experimental and diagnostic techniques, such as planar laser induced fluorescence (PLIF), coherent anti-stokes raman spectroscopy (CARS), and infrared multiphoton dissociation (IRMPD), are available to probe the gas phase processes and further the understanding of the gas phase chemistry. Similarly, the development of simultaneous thermogravimetric modulated beam mass spectrometry (STMBMS) and time-of-flight (TOF) velocity-spectra techniques^{1,2,3} have enhanced the application of mass spectrometry to probe processes in the condensed phase using evolved gas measurements.

An important goal of these new experiments is to develop a link between the physical properties and molecular structures of different nitramines and their combustive behavior. The motivation of the work on the condensed phase is to obtain a better understanding of the physical processes and reaction mechanisms that occur, so that the identity and rate of release of the pyrolysis products can be predicted, as a function of pressure and heating rate, based on the physical properties and molecular structure of the material. This information can then be used along with the gas-phase reaction models to correlate modifications of the nitramine ingredients with variations in the overall combustion.

Over the past 40 years many studies have been conducted on the decomposition of HMX and RDX under various conditions. Recent reviews of the decomposition and combustion,^{4,5} thermal decomposition,⁶ and summaries of possible decomposition mechanisms,^{6,7} have been published for these materials. Based on many of these results and the structural similarities of HMX and RDX, the same decomposition mechanisms have been proposed for both materials.

Robertson's⁸ results on the decomposition of RDX show that in solutions of dicyclohexylphthalate and trinitrotoluene (TNT) the decomposition exhibits a unimolecular behavior, whereas, neat RDX and HMX show an effect of neighboring molecules. Post analysis of the gases evolved in his experiments show the presence of: NO, N₂O, N₂, CO, CO₂, CH₂O, and H₂O. This work provides the initial evidence that the decomposition of HMX and RDX occurs by transfer of an oxygen atom from the NO₂ group to the CH₂ group.

Subsequent mass spectral analysis of the decomposition products from HMX below its melting point, by Bulusu and Graybush,⁹ show the same products as observed by Robertson.⁸ In addition, they found that the rate of formation of the products varied during isothermal decomposition experiments in a way that can be explained by either the characteristic induction, acceleratory, and decay stages associated with solid-phase decompositions or by invoking autocatalytic behavior. Furthermore, ¹⁵N-tracer studies¹⁰ indicate that the N₂O is formed without N-N bond breaking, thus, suggesting that oxygen atom transfer to the CH₂ group and C-N bond rupture is an important step in the decomposition. However, since the total nitrogen is not accounted for in these experiments, N-N bond breaking cannot be ruled out as the initial step in the decomposition.

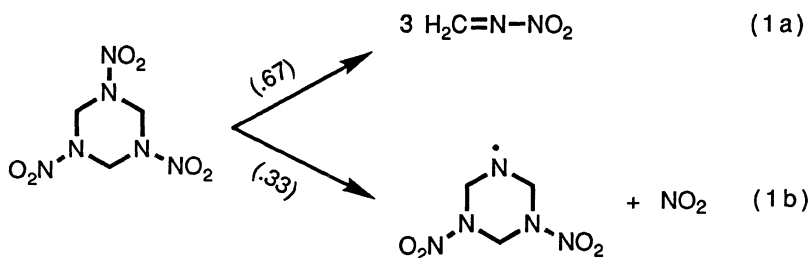
A deviation from the oxygen atom transfer mechanism comes from the RDX experiments of Rauch and Fanelli¹¹ in which they observe the formation of NO₂ in addition to the products observed by Robertson⁸ and Bulusu.⁹ Their results suggest that the NO₂ is formed in the gas-phase decomposition of RDX.

More recent work on the decomposition of RDX¹² and HMX¹³ report additional decomposition products. These products include formic acid, ammonia, and hydroxymethyl formamide from RDX¹² and HMX.¹³ Observations of these products imply that the decomposition mechanism leading to the formation of the pyrolysis products is more complicated than only unimolecular

decomposition. Several studies of autocatalytic effects^{14,15} on RDX decomposition find that formaldehyde and hydroxymethyl formamide both have a catalytic-like effect on the decomposition. It is not clear whether this is from catalysis of the RDX decomposition or from liquefaction of the RDX that, in turn, increases the release rate of the products from the condensed phase.

Higher temperature and higher heating rate experiments¹⁶ conducted at atmospheric pressure and at nominal temperatures of 300, 600, and 800°C on HMX and RDX show that the relative amounts of HCN and NO produced, compared to N₂O and CH₂O, are greater at 600°C and 800°C than they are at 300°C. In light of previous work,¹¹ this suggests that evaporation and subsequent gas-phase decomposition of the RDX and HMX is favored over condensed-phase decomposition at atmospheric pressure and higher heating rates. This effect is also observed in planar-laser-induced-fluorescence (PLIF) measurements on HMX¹⁷ and coherent-antistokes-raman-spectroscopy (CARS) measurements on RDX¹⁸ low pressure flames in which NO₂ and HCN are measured close to the surface of the burning propellant. In addition, mass spectrometric measurements on low pressure flames of RDX¹⁹ and HMX²⁰ also show substantial fractions of HCN in the gas above the burning propellant surface. The steps leading to the pyrolysis products under these low-pressure high-heating-rate conditions appear to be different than those in the slow-heating-rate thermal decomposition experiments.

Several studies to determine the initial steps in the decomposition of HMX and RDX have been conducted using Langmuir and Knudsen cell evaporation with appearance-energy-mass-spectrometric measurements²¹ and infrared multiphoton dissociation (IRMPD) in a molecular beam.²² The appearance-energy-mass-spectrometric measurements indicate that the stoichiometry of the initial gaseous products from the pyrolysis of RDX and HMX are the same as several of the fragment ions found in the mass spectra of these materials. However, subsequent mass spectrometric work on HMX² shows that HMX fragmentizes in the mass spectrometer at low electron energies. Therefore, appearance-energy measurements cannot differentiate between fragment ions from the HMX molecule and molecular ions from its pyrolysis products that occur at the same *m/z* values. Hence, these experiments²¹ did not determine the initial products from the pyrolysis of HMX. The collision-free IRMPD experiments show that RDX molecules dissociate via both concerted symmetric triple fission and N-N bond scission channels.



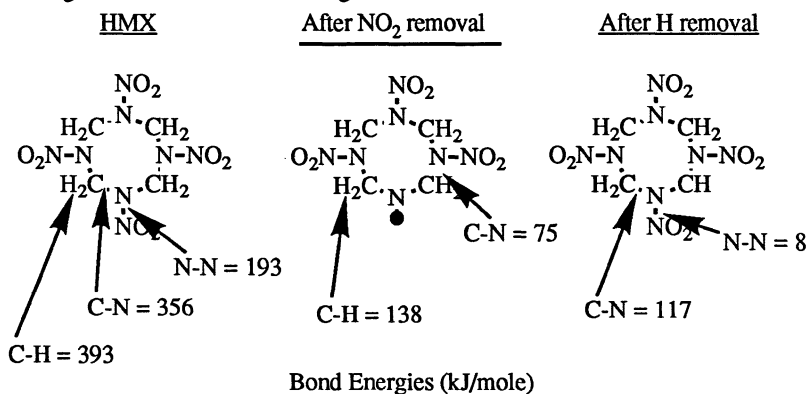
These primary products dissociate further to form HCN, HONO, N₂O, and CH₂O. Whether these reactions control the decomposition of RDX and HMX in the condensed phase and whether reactions between adjacent molecules are important, as originally suggested by Robertson, are still in question.

A number of studies show that decomposition reactions occur in the condensed phase of these materials. High-pressure studies of the β -HMX to δ -HMX phase transition²³ between 190°C and 240°C show evidence of formation of decomposition products within the 175 μ diameter particles used in the experiments. In other experiments with deuterium labelled analogues of HMX,²⁴ a

primary deuterium kinetic isotope effect (DKIE) is observed in the rate of decomposition of the solid phase and is attributed to C-H bond breaking in the rate-controlling step. In the liquid phase, a secondary kinetic isotope effect is observed, suggesting that C-N bond breaking becomes important. This work emphasizes the importance of the state of the material in which the reactions occur, and suggests that the decomposition mechanism is linked to the physical processes occurring in the material. This linkage has been suggested previously, by Oyumi and Brill,²⁵ in their high heating rate experiments on RDX and HMX in which they found larger fractions of N_2O and CH_2O in experiments under higher pressure conditions where evaporation of the reactant is reduced. Thermogravimetric analysis (TGA) and shock sensitivity experiments on deuterium labelled HMX and RDX²⁶ both show a DKIE. The large A-factors found in these TGA experiments rule out a cyclic transition state and suggest that chain reactions are important in the condensed-phase decomposition. The lower shock sensitivities of the deuterium labelled analogues of HMX and RDX in the exploding foil experiments suggest that hydrogen also plays a role in the shock initiated decomposition chemistry of these materials.

Two studies^{27,28} on the products formed during shock initiated decomposition of RDX have shown the formation of products not previously observed in thermal decomposition experiments. The presence of the nitroso derivatives of RDX, (1,3,5-trinitroso-1,3,5-triazacyclohexane, 1,3-dinitroso-5-nitro-1,3,5-triazacyclohexane, and 1-nitroso-3,5-dinitro-1,3,5-triazacyclohexane) were found in residues formed during drop weight impact experiments.²⁷ The presence of nitroso derivatives of RDX as well as compounds with a melamine functionality were also found with x-ray photoelectron spectroscopy (XPS) measurements in post analysis of RDX subject to drop weight impact and underwater shock at levels close to ignition.²⁸ If similar products can be identified in thermal decomposition experiments and the mechanisms leading to their formation explained, then a connection between shock-initiated decomposition chemistry and processes that occur during thermal decomposition may be established.

The quantum chemical Bond-Additivity-Corrected Moller-Plesset fourth order perturbation theory method (BAC-MP4)²⁹ has been used to calculate the heats of formation, the free energies, and the thermochemical properties of the transition states of the activated complexes for the nitramines H_2NNO_2 and CH_3NHNO_2 as well as of the molecular radical species that might arise from the decomposition process. The bond energies and dissociation energies from these calculations are used to estimate the bond energies and decomposition pathways of HMX and RDX. The following estimates of the bond energies in HMX



suggest that N-N bond fission should play an important role in the initial decomposition and that subsequent rupture of the C-N bond should occur. In addition, the calculations also show that if a hydrogen atom is removed through a bimolecular reaction (i.e., a reaction of a decomposition product and the HMX) then the adjacent N-N bond becomes very weak and loss of NO_2 is expected.

From all of the studies on HMX and RDX decomposition, it is still not possible to predict the identity and rate of formation of the pyrolysis products under different heating and pressure conditions. The underlying reason is that in all experiments (with the exception of the IRMPD molecular beam experiments) many different physicochemical processes occur simultaneously and it has not been possible to associate any set of products with the processes leading to their formation. For example, when gas-phase and condensed-phase decomposition occur simultaneously, it has not been possible to quantitatively associate the measured products with the phase in which they were formed. Although experiments such as the IRMPD on RDX provide valuable mechanistic information on the decomposition of the isolated molecules, the behavior of the nitramines in a combustion environment may involve more complicated processes. Such processes may include: follow-up bimolecular reactions of the initial decomposition products, autocatalytic reactions between decomposition products and the reactant, stress-induced reactions between molecules along slip planes, and preferential reactions at the reactant surfaces. A key to understanding how the nitramines decompose lies in relating the observed species and their rates of formation to the different processes that lead to their formation.

Experimental Results and Discussion

PRODUCT IDENTIFICATION

The thermal decomposition experiments are conducted with 10 mg to 30 mg samples of RDX and HMX whose median particle diameters range from $40\text{ }\mu\text{m}$ to $150\text{ }\mu\text{m}$. During the experiment the samples are contained in an alumina reaction cell that has a $50\text{ }\mu\text{m}$ to $100\text{ }\mu\text{m}$ diameter exit orifice as shown in Figure 1. The experiments with HMX are isothermal and are carried out in the temperature range from 190°C to 250°C . This range is 30°C to 90°C below the melting point of HMX. The RDX experiments are thermal ramp experiments using a heating rate of $1^\circ\text{C}/\text{min}$. The decomposition of RDX occurs over a temperature range of 187°C to 210°C , which spans the melting point of RDX (203°C). The differences in the temperatures of the experiments with respect to the melting points of the materials affects the processes occurring within the reaction cell as illustrated in Figure 1. For HMX the sample does not melt and gas products that may form within the HMX particles may be contained in cavities under very high pressures. For RDX the samples will melt and gases formed within the condensed phase will form bubbles that can easily expand within the liquid phase. This implies that gas contained within the RDX will be at lower pressures than gas contained within the HMX.

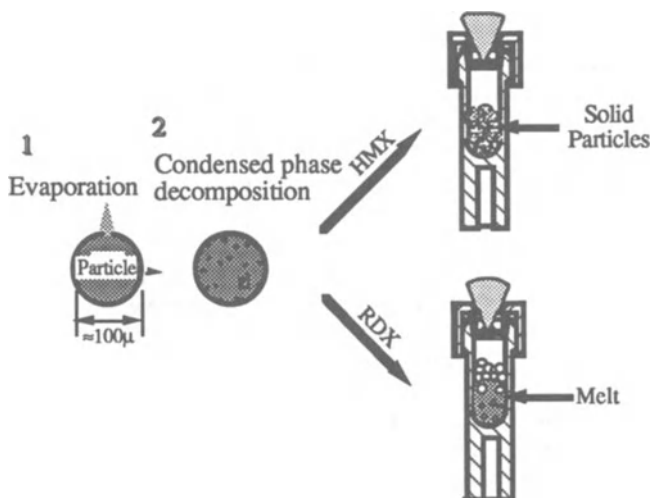


Figure 1. The behavior of the HMX and RDX particles differs during the decomposition in the reaction cell. The HMX remains a solid whereas the RDX melts and forms a frothy mixture.

<u>Common</u>		
<u>HMX Only</u>		<u>RDX Only</u>
$\begin{array}{c} \text{NO} \\ \\ \text{H}_3\text{C}-\text{N}-\text{CH}_3 \end{array}$	H_2O	NO_2
$\begin{array}{c} \text{NO} \\ \\ \text{O}_2\text{N}-\text{N} \quad \text{N}-\text{NO}_2 \\ \quad \quad \\ \text{N} \quad \quad \text{N} \\ \quad \quad \\ \text{NO}_2 \end{array}$	N_2O	$\begin{array}{c} \text{OH} \\ \\ \text{N} \quad \text{N} \\ \diagup \quad \diagdown \\ \text{N} \quad \text{N} \end{array}$
∞	CH_2O	
	NO	
	CH_3NHCHO	
RESIDUE		$\begin{array}{c} \text{NO} \\ \\ \text{O}_2\text{N}-\text{N} \quad \text{N}-\text{NO}_2 \\ \quad \quad \\ \text{N} \quad \quad \text{N} \end{array}$

Figure 2. The products formed during the decomposition of HMX and RDX.

The products that have been identified from the STMBMS and TOF velocity-spectra measurements are listed in Figure 2. There is one set of products that is common to the decomposition of both HMX and RDX and two other sets of products that are unique to each material. The products common to both materials are H_2O , N_2O , CH_2O , NO , and CH_3NHCHO .

The TOF velocity spectra show that the molecular weight of the CH_3NHCHO product is ~ 118 , suggesting that this product leaves the reaction cell as a dimer. However, it is possible that this product has a structure that is somewhat different from N-methylformamide (e.g. acetamide). The two unique sets of products each have a mononitroso derivative of the parent compound. Experiments conducted under conditions in which RDX and HMX only evaporate and do not decompose show no evidence of the nitroso derivative, thus, this product is formed during the decomposition and is not a contaminant in the starting material. The other products that are unique to the RDX decomposition are NO_2 and hydroxy-s-triazine (HST). These two products indicate that rupture of the N-N bond is an important reaction path way in RDX. The products that are unique to the decomposition of HMX are CO, $\text{C}_2\text{H}_6\text{N}_2\text{O}$, and a nonvolatile residue (NVR).

The NVR that remains after an isothermal decomposition of HMX is orange-brown in color and has a macroscopic structure similar to the original sample; (i.e., the shape of the original HMX particles is still discernible). A transmission electron micrograph (TEM) of the residue that remains after an isothermal decomposition at 224°C is shown in Figure 3. The residue consists of fractured ellipsoidal shells whose diameters range from 0.3μ to 5μ and whose wall thicknesses are about 0.1μ . The residue that remains after the decomposition consists of agglomerates of the fractured ellipsoidal shells that retain the shape of the original particles. The sizes and structures of these shells suggest that as the sample decomposes the gaseous products are contained in bubbles within the solid particles as illustrated in Figure 4. Within the bubbles, the gases react to form a polymeric residue on the wall of the bubble. When the bubble intersects the surface of the shrinking particle, the polymer film ruptures and releases the gas from within the bubble. During the initial stages of the decomposition, shrinkage of the particle is primarily due to evaporation of HMX, and, during the later stages, it is due to both evaporation of HMX and release of gaseous products formed previously during the decomposition and retained within the particle. The elemental analysis of a typical NVR shows that the mole percent composition is 33.9% carbon, 27.5% hydrogen, 18.6% nitrogen, and 20% oxygen. It is enriched in carbon and hydrogen relative to HMX.

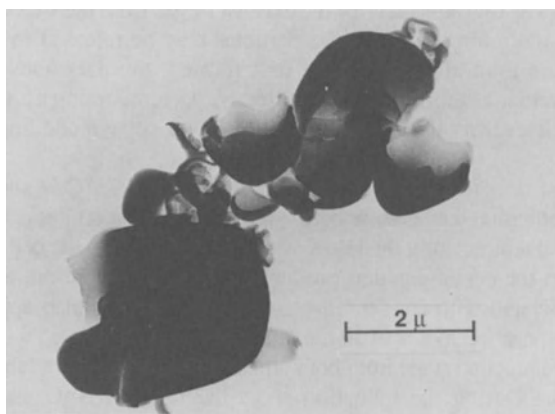


Figure 3. Transmission electron micrograph of the NVR remaining after an isothermal decomposition of HMX.

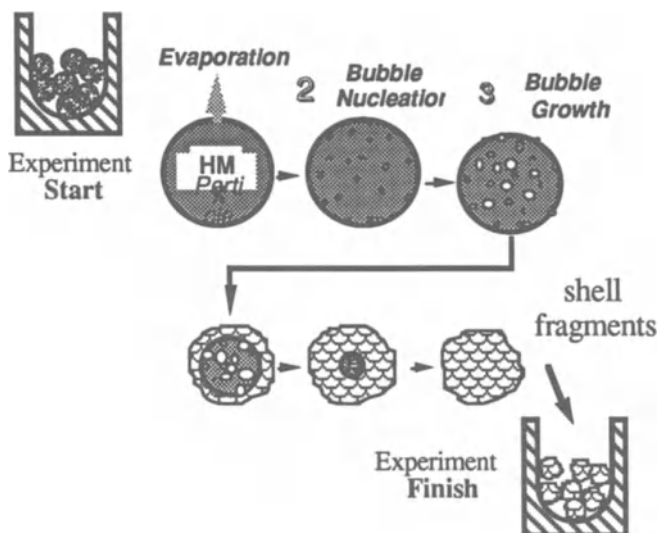


Figure 4. Illustration of the change of an HMX particle from the start to finish of an isothermal decomposition below its melting point. At the end of the decomposition the NVR has the same morphology as the starting HMX sample.

GAS FORMATION RATES

The gas formation rates are defined as the rates that gaseous products appear in the free volume of the reaction cell. The time constant for the exhaust of gas from the free volume of the cell is 0.2 sec. Since gases that are formed within the particles may be released to the free volume of the reaction cell at some time after they were first formed, the data does not provide the time-dependence of the actual gas formation rates directly. Determination of the actual gas formation rates within the particles from the data will depend on properly modelling the release processes from the particles.

The gas formation rates for the decomposition of HMX at 235°C is shown in Figure 5. The HMX reaches its isothermal temperature before little decomposition has occurred. Once the HMX reaches its isothermal temperature, the HMX vapor pressure within the cell remains approximately constant. However, the decomposition products exhibit the induction, acceleratory, and decay stages that are associated with condensed-phase reactions. It is also apparent from the data in Figure 5 that the temporal behaviors of all the products are not correlated with each other.

The details of the induction stage from both unlabelled and deuterium labelled HMX samples are shown in Figure 6. During the induction stage the rates of N_2O and CH_2O formation are approximately equal and their ratio remains constant. The H_2O detected during the induction stage from the unlabelled HMX is probably from absorbed water on the sample or reaction cell since the experiment with the deuterium labelled HMX shows no evidence of D_2O during the first part of the induction stage. The slow growth of D_2O near the end of the induction stage appears to indicate the onset of the acceleratory stage. The factor of 4 difference in the duration of the induction stage

between the unlabelled and deuterium labelled HMX shows that there is a strong DKIE. At the transition from the induction stage to the acceleratory stage there is an increase in the rates of water, CH_2O , and N_2O formation. However, the increase in the rates of formation are larger for N_2O and H_2O than for CH_2O .

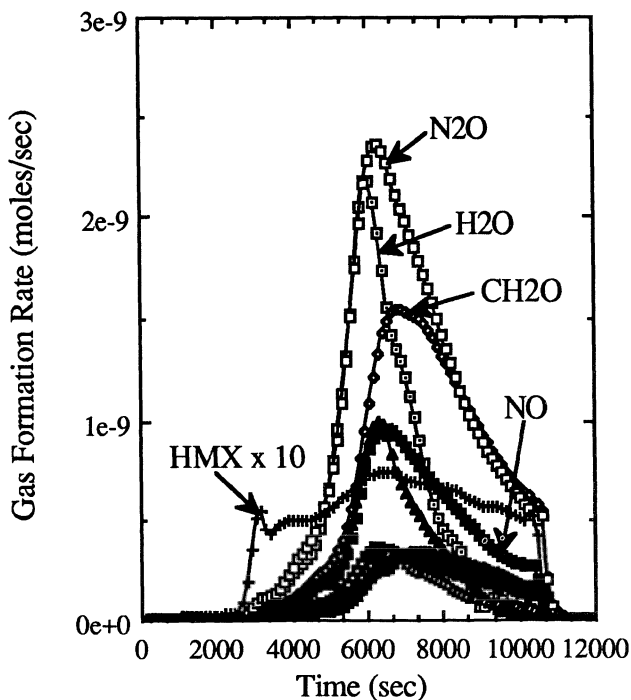


Figure 5. Gas formation rates of the more abundant pyrolysis products formed during the decomposition of HMX. The sample reaches its constant temperature of 235°C at the first peak in the HMX signal.

This trend in the rates of formation of water, N_2O , and CH_2O persists through most of the acceleratory stage as can be seen from Figure 7 in which the gas formation rates for the major products are plotted versus the extent of the sample decomposition X . During the sample decomposition the gas formation rates vary by up to a factor of 40. The rates of formation of H_2O and N_2O remain approximately equal through most of the acceleratory stage. In contrast, the ratio of the gas formation rates of N_2O to CH_2O vary between 1 and 2.5 during the decomposition. When the ratio of the N_2O to CH_2O gas formation rates is highest, the formation rate of water is the largest. During the decay stage, as the amount of HMX remaining goes to zero, the rate of water

formation goes to zero, whereas the rates of formation of N_2O and CH_2O become equal and approach a non-zero value.

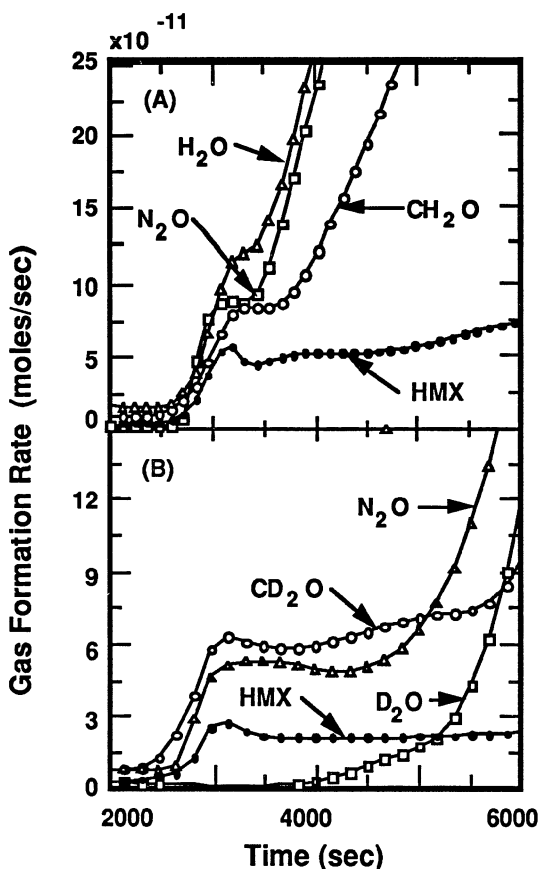


Figure 6. Gas formation rates of H_2O , CH_2O , N_2O , and HMX and their isotopic analogues during the induction period of the decomposition of unlabelled and deuterium labelled HMX. The HMX gas formation rate is determined by the HMX vapor pressure and the exhaust rate from the reaction cell.

The temporal behaviors of the less abundant pyrolysis products produced at lower formation rates are shown in Figure 8. The formation rate of $\text{C}_2\text{H}_6\text{N}_2\text{O}$ increases rapidly during the acceleratory stage in a manner similar to H_2O . The rates of formation of N-methylformamide and ONTNTA on the other hand increase gradually during the acceleratory stage. The rate of formation of N-methylformamide falls to zero as the amount of HMX approaches zero.

A comparison of the gas formation rates of the major pyrolysis products for sample sizes of 8.6 mg and 27.9 mg, shown in Figure 9, indicates that the gas formation rates are proportional to the

size of the sample. The length of time for each sample to decompose is approximately the same. This indicates that the reactions occur in the condensed phase. If unimolecular decomposition of HMX in the gas phase is responsible for the formation of the pyrolysis products, then the gas formation rates should remain constant and the larger sample should last for longer period of time since the gas phase HMX concentration within the reaction cell remains constant under the isothermal conditions of the experiment. One difference in the results from the experiments with different sample sizes is that the relative formation rate of H_2O with respect to N_2O is smaller in the larger sample. This may be indirectly due to the slower surface regression rates of the larger sample.

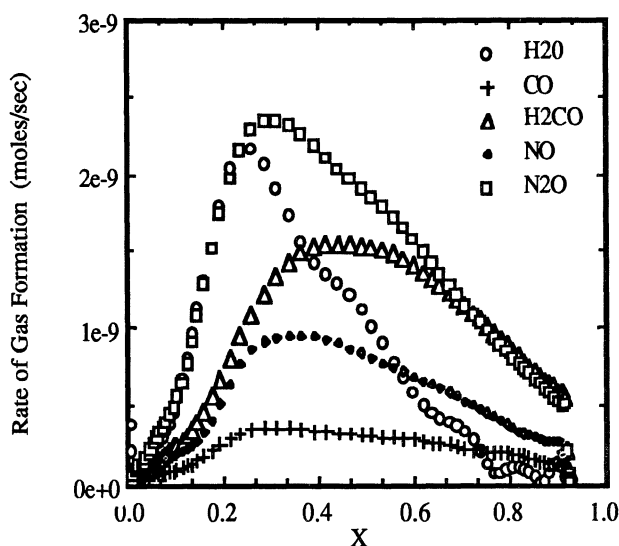


Figure 7. Gas formation rates of the more abundant pyrolysis products during the isothermal decomposition of HMX as a function of the extent of decomposition X .

A comparison of the gas formation rates of the major pyrolysis products for unlabelled and deuterium labelled HMX, shown in Figure 10, indicates that the ratio of the N_2O gas formation rates from the unlabelled and the deuterium labelled HMX is 1.6. The results also show that the relative rates of formation of water and NO are less from HMX-dg.

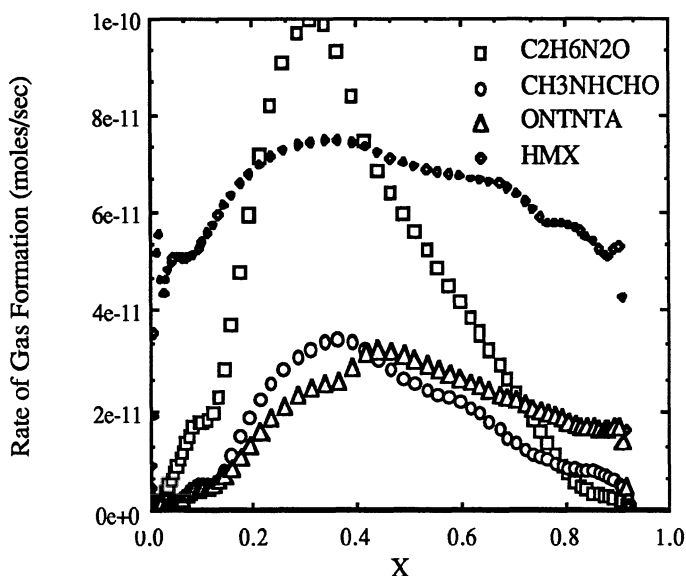


Figure 8. Gas formation rate of the less abundant pyrolysis products formed during the decomposition of HMX as a function of the extent of sample decomposition X .

The ion signals at various m/z values formed during the thermal decomposition of the NVR that were produced during the isothermal decomposition of unlabelled and deuterium labelled HMX are shown in Figure 11. The temporally correlated ion signals at the different m/z values produced from the unlabelled and deuterium labelled samples show that the products produced during the decomposition are NH_3 , HCN , HNCO , H_2NCHO , and $(\text{CH}_3)\text{NHCHO}$ and their deuterium analogues. The HNCO and amide products are the predominant products in the 250°C to 500°C temperature range, whereas, NH_3 and HCN are the main products formed between 500°C and 800°C .

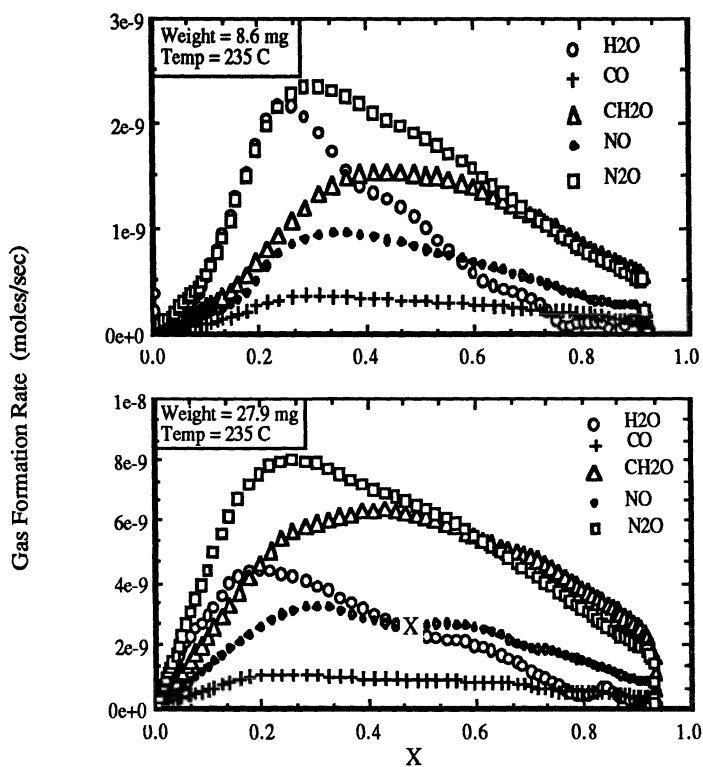


Figure 9. Gas formation rates of the pyrolysis products formed during the isothermal decomposition of HMX for two different size samples as a function of the extent of sample decomposition X .

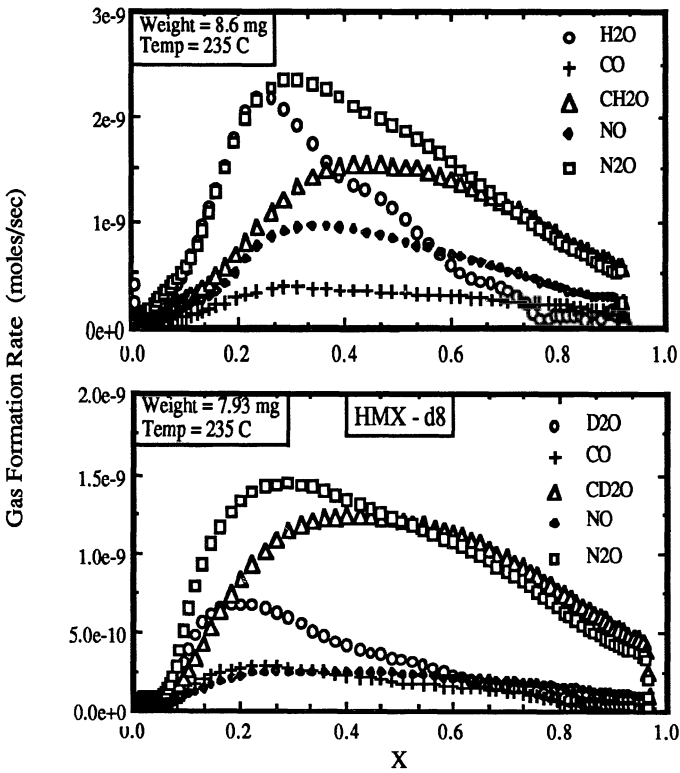


Figure 10. Gas formation rates of pyrolysis products from the isothermal decomposition of unlabelled and deuterium labelled HMX as a function of the extent of HMX decomposition X.

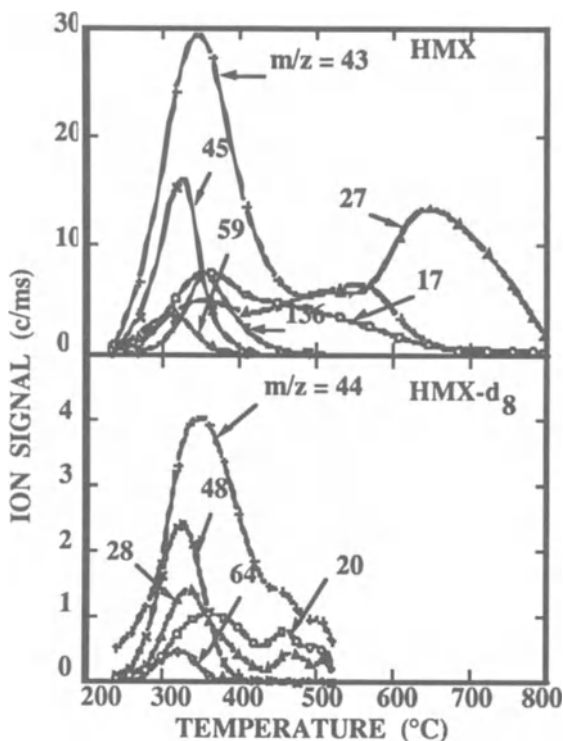


Figure 11. The ion signals formed at different m/z values from the decomposition of the NVR formed during the decomposition of HMX and HMX-d₈. The ion signals are representative of different pyrolysis products. The stoichiometry of the products associated with the different m/z values are: NH_3 (17,20), HCN (27,28), HNCO (43,44), H_2NCHO (45,48), $(\text{CH}_3)\text{NHCHO}$ (59, 64).

QUALITATIVE DECOMPOSITION MODEL

The processes involved in the decomposition of HMX below its melting point are complex. An illustration of several of the processes that may play a role in HMX decomposition are shown in Figure 12. Three important processes are evaporation of the HMX from the particle, nucleation of bubbles within the particles, and growth and coalescence of the bubbles. The gaseous pyrolysis products are released from the particles as the bubbles intersect the receding surface of the HMX particle. During the early stages of the decomposition the bubbles are smaller and they are uncovered due to evaporation of HMX from the particle surface, whereas, during the later stages of the decomposition coalescence and channel formation can provide additional pathways for gas release. During the course of the formation and growth of the bubbles within the particles, the

NVR is formed at the gas-HMX interface of the bubble. As the bubble intersects the particle surface the gas fractures the NVR shell releasing its gas from the particle.

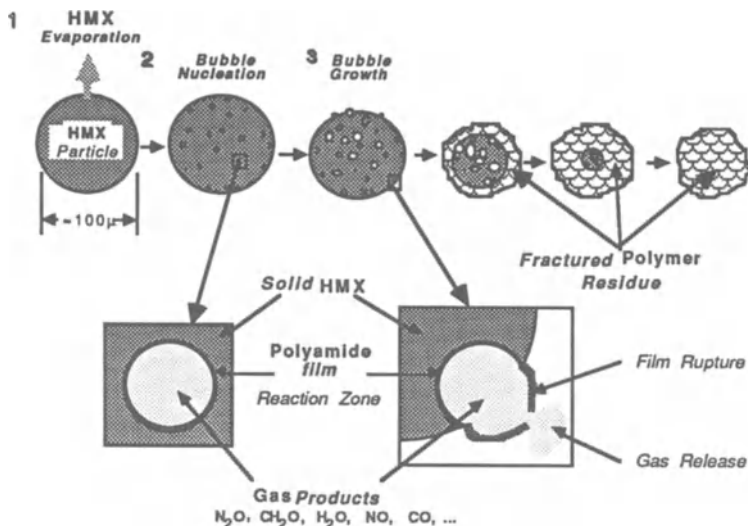
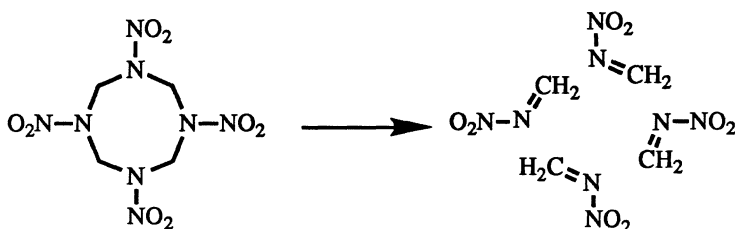


Figure 12. The processes occurring during the decomposition of a HMX particle. The processes transforming a HMX particle into a NVR with the same shape are: HMX evaporation, bubble nucleation and growth, reactions within the bubble, and release of gaseous products from the bubbles.

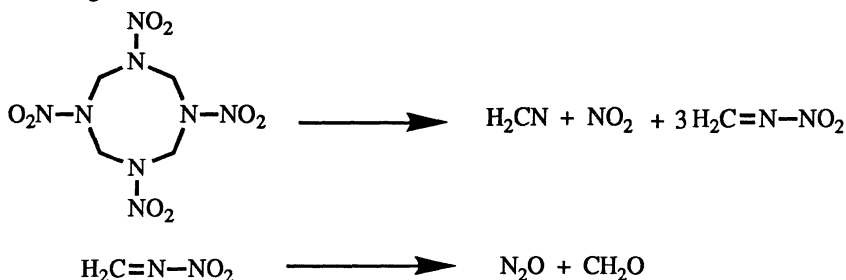
The pressures of the gases contained in the bubbles within the particles are much higher than in the free volume of the reaction cell. If the condensed phase HMX is assumed to be compressible, the pressure within the bubble is determined by its surface free energy, and using the diameters of the NVR shell fragments, the pressures may range from 0.5 to 9 MPa. On the other hand if the condensed phase HMX is assumed to be incompressible then the pressure within the bubbles could be as high as 240 MPa.

Although the bubble formation process that occurs in condensed phase HMX makes the interpretation of the evolved gases in terms of chemical reaction pathways difficult, it also provides the opportunity to examine the decomposition processes that occur under much higher pressure conditions than are achievable in typical laboratory experiments. The results show that it is important to consider several different reaction locations when analyzing the results from thermal decomposition experiments. The reaction environments include: the low density gas phase reactions in the free volume of the reactions cell, reactions at the gas/surface interface, reactions in the bulk at grain boundaries or defects, high density gas phase reactions within the bubbles, and reactions of the NVR. Reactions that may be influenced by the NVR include: the decomposition of the NVR itself, interaction of the NVR with the HMX, interaction of the NVR with the gases within the bubbles, and the effect of the NVR as a barrier between the gases contained within the bubbles and the surrounding HMX.

Although low density gas phase reactions or reactions at the gas surface may be occurring during the experiments as evidenced by the approximately equal formation rates of the N_2O and CH_2O products observed during the induction stage of the decomposition, the majority of the products are formed within the condensed phase of the HMX. As a starting point for interpreting the results of our experiments, we consider the decomposition steps observed in the IRMPD experiments with RDX.²² By analogy with the IRMPD results for RDX the HMX may undergo a quadruple fission to four methylenenitramine molecules

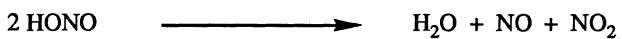
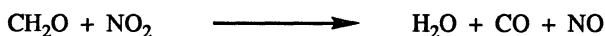


and the methylene nitramine may undergo decomposition to either N_2O and CH_2O or HONO and HCN . The fact that 3 moles of N_2O are observed for each mole of decomposed HMX can be explained by either a branching ratio of the methylene nitramine of 3:1 for the $\text{N}_2\text{O}/\text{CH}_2\text{O}$ and HCN/HONO channels or, more likely, the domination of the N-N bond dissociation pathway for the first step in the decomposition, followed by ring fragmentation and decomposition to N_2O and CH_2O of the remaining molecule.



The facts that no NO_2 is observed and that H_2O , CO , and NO are observed indicate that secondary reactions are important in determining which products are released from the condensed phase.

Water formation indicates the importance of secondary reactions. Possible reactions that may produce water include



However, these reactions will not produce as much water as observed in our experiments. An additional pathway for the formation of water is by condensation reactions such as

decomposition of the sample nears completion, the surface area of the HMX should approach zero and not a finite value as indicated by the N_2O and CH_2O gas formation rate behaviors. Thus, it seems more likely that the HMX may be interacting with the NVR that is formed during the decomposition and remains in the reaction cell.

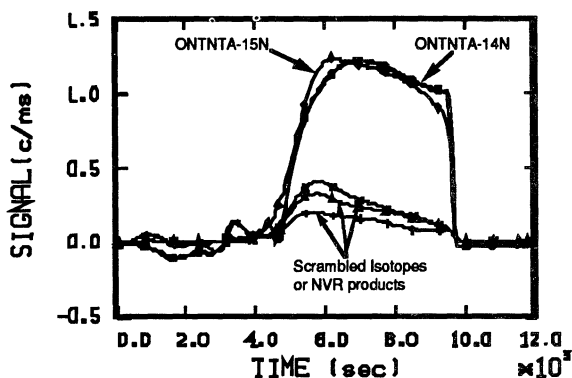


Figure 13. The ion signals from $m/z = 132$ (f) to $m/z = 136$ (ϕ) that are formed in the mass spectrometer from the ONTNTA pyrolysis product. The ONTNTA products are formed during the decomposition of HMX formed from a mixture of ^{15}N -HMX and unlabelled HMX.

In summary, the bubble model for the HMX is supported by a number of observations. These observations include: the temporal behaviors of the release rates of the gaseous products, the formation of the polymeric NVR, the macroscopic and microscopic structure of the NVR, the observed DKIE, and the sample size dependence of the decomposition. The model can account for many of the observations of previous experimenters in addition to the results obtained in our experiments. However, it also brings forth a number of new questions regarding the decomposition of HMX and other solid nitramines such as: What controls the nucleation and growth of the bubbles? Is the formation of ONTNTA associated with the bubble formation? Does the stress generated by the high pressures within the bubbles lead to the formation of ONTNTA in the surrounding HMX lattice? Are similar mechanisms applicable when the bubbles are formed in a liquid under a high pressure environment? Under what conditions will bubble growth and polymer formation fail? How closely are bubble growth and NVR formation related to the physical properties and molecular structure of the materials? These and other questions need to be addressed to obtain a more fundamental understanding of the physical processes and reaction mechanisms that control the decomposition of nitramine compounds.

Summary

A brief history of the decomposition of HMX and RDX has been presented to illustrate the development of the mechanisms used to explain the decomposition of these two nitramines. The history spans the initial low temperature thermal decomposition experiments by Robertson up to more recent high heating rate and shock initiated decomposition studies.

The results from STMBMS and TOF velocity spectra measurements on HMX and RDX have identified the decomposition products and determined their rates of gas formation. Both nitramines formed H_2O , N_2O , CH_2O , NO , and $(\text{CH}_3)\text{NHCHO}$ during the decomposition. RDX was found to form NO_2 and hydroxy-s-triazine, products associated with N-N bond breaking, whereas HMX formed $\text{C}_2\text{H}_6\text{N}_2\text{O}$, CO , a nonvolatile residue. A mononitroso analogue of the parent compound was formed during the decomposition of both materials. The rates of gas formation of the various pyrolysis products along with the macroscopic and microscopic features of the NVR generated during the decomposition of HMX suggest that a major process involved in the decomposition of HMX below its melting point is the formation of bubbles containing pyrolysis products within the HMX particles. The pressure of the gas within the bubbles may range up to 240 MPa.

Possible reaction mechanisms that include both the physical location of the reactions and the possible chemical reaction pathways have been presented. The results from the STMBMS experiments are consistent with initial fragmentation of the N-N bond of the molecule to form NO_2 and the subsequent unravelling of the remaining ring to form N_2O and CH_2O . Secondary reactions of the primary decomposition products that occur within the particles are responsible for the identity and the relative rates of gas release of the various products from the solid particles. The possible bimolecular reactions between pyrolysis products and HMX are also presented.

* Research supported by a joint Memorandum of Understanding between the U.S. DOE and the U.S. Army.

- ¹ Behrens, Jr., R., (1986), 'A New Simultaneous Thermogravimetry and Modulated Molecular Beam Mass spectrometry Apparatus for Quantitative Thermal Decomposition Studies', *Rev. Sci. Instrum.*, **58**, pp. 451- 461.
- ² Behrens, Jr., R., (1989), 'Identification of Octahydro-1,3,5,7-tetranitro-1,3,5,7-tetrazocine (HMX) Pyrolysis Products by Simultaneous Thermogravimetric Modulated Beam Mass Spectrometry and Time-of-Flight Velocity Spectra Measurements, submitted to *Int. J. Chem. Kinetics*.
- ³ Behrens, Jr., R., (1989), 'Determination of the Rates of Formation of Gaseous Products from the Pyrolysis of Octahydro-1,3,5,7-tetranitro-1,3,5,7-tetrazocine (HMX) by Simultaneous Thermogravimetric Modulated Beam Mass Spectrometry', submitted to *Int. J. Chem. Kinetics*.
- ⁴ Boggs, T.L., "The Thermal Decomposition Behavior of Cyclotrimethylene - trinitramine (RDX) and Cyclotetramethylene - tetranitramine (HMX) in "Fundamentals of Solid-Propellant Combustion," Kuo, K.K. and M. Summerfield eds.; Progress in Astronautics and Aeronautics Vol. 90., p. 121, AIAA Inc., New York, NY, 1984.
- ⁵ Fifer, R.A., "Chemistry of Nitrate Ester and Nitramine Propellants," in "Fundamentals of Solid-Propellant Combustion," Kuo, K.K. and M. Summerfield eds.; Progress in Astronautics and Aeronautics Vol. 90., p. 177, AIAA Inc., New York, NY, 1984.
- ⁶ (a) Schroeder, Michael A. "Critical Analysis of Nitramine Decomposition Data: Product Distributions from HMX and RDX," BRL-TR-2659, 1985. (b) Schroeder, Michael A., "Critical Analysis of Nitramine Decomposition Data: Activation Energies and Frequency Factors for HMX and RDX Decomposition," BRL-TR-2673, 1985.
- ⁷ Shaw, R. and Walker, F.E., (1977), "Estimated Kinetics and Thermochemistry of Some Initial Unimolecular Reactions in the Thermal Decomposition of 1,3,5,7-Tetranitro-1,3,5,7-tetraazacyclooctane in the Gas Phase", *J. Phys. Chem.*, **81**, pp. 2572-2576.
- ⁸ Robertson, A.J.B., (1949), "The Thermal Decomposition of Explosives", *Trans. Faraday Soc.*, **45**, pp. 85-93.
- ⁹ Bulusu, S. and Graybush, R.J., (1967), "Thermal Decomposition of 1,3,5,7-Tetranitro-1,3,5,7-tetraazacyclooctane (HMX): A Mass Spectrometric Study of the Products from β -HMX", "Proceedings

- of the 36th International Congress on Industrial Chemistry", Brussels, Belgium, C. R. Ind. Chim. Belge, 32, pp. 1 - 4.
- 10 Suryanarayana, B., Graybush, R.J., and Autera, J.R., (1967), "Thermal Degradation of Secondary Nitramines: A Nitrogen-15 Tracer Study of HMX", Chem. Ind., London, pp.2177 - 2178.
 - 11 Rauch, F.C. and Fanelli, A.J., (1969), "The Thermal Decomposition Kinetics of Hexahydro-1,3,5-trinitro-s-triazine above the Melting Point: Evidence for Both a Gas Phase and Liquid Phase Decomposition", J. Phys. Chem., 73, pp. 1604 - 1608.
 - 12 Cosgrove, J.D. and Owen, A.J., (1974), "The Thermal Decomposition of 1,3,5-Trinitro-hexahydro-1,3,5-triazine (RDX) -- Part I: The Products and Physical Parameters", Comb. Flame, 22, pp. 13 - 18.
 - 13 Kimura, J. and Kubota, N., (1980), "Thermal Decomposition Process of HMX", Propellants and Explosives, 5, pp. 1 - 8.
 - 14 a) Batten, J.J. and Murdie, D.C., (1970), "The Thermal Decomposition of RDX at Temperatures Below the Melting Point I. Comments on the Mechanism", Aust. J. Chem, 23, pp 737 - 747; b) Batten, J.J. and Murdie, D.C., (1970), "The Thermal Decomposition of RDX at Temperatures Below the Melting Point II. Activation Energy", Aust. J. Chem, 23, pp. 749 - 755; c) Batten, J.J. , (1971), "The Thermal Decomposition of RDX at Temperatures Below the Melting Point III. Towards the Elucidation of the Mechanism", Aust. J. Chem, 24, pp. 945 - 954; d) Batten, J.J. , (1971), "The Thermal Decomposition of RDX at Temperatures Below the Melting Point IV. Catalysis of the Decomposition by Formaldehyde", Aust. J. Chem, 24, pp. 2025 - 2029; e) Batten, J.J. , (1972), "The Thermal Decomposition of RDX at Temperatures Below the Melting Point V. The Evolution of Occluded Volatile Matter Prior to the Decomposition, and the Influence of Past History of the Sample on the Rate of Decomposition", Aust. J. Chem, 25, pp. 2337 - 2351.
 - 15 Cosgrove, J.D. and Owen, A.J., (1974), "The Thermal Decomposition of 1,3,5-Trinitro-hexahydro-1,3,5-triazine (RDX) -- Part II: The Effects of Products", Comb. Flame, 22, pp.19 - 22.
 - 16 a) Axworthy, A.E., Flanagan, J.E., and Woolery, D.O., (1978), "High Temperature Pyrolysis Studies of HMX, RDX, and TAGN", CPIA Publ. No. 297, "Proceedings of the 15th JANNAF Combustion Meeting," , Vol. 1, pp. 253 - 265;
b) Axworthy, A.E., Flanagan, J.E., Woolery, D.O., and Gray, J.C., (1979), "Kinetics - Combustion Interactions of Nitramines", CPIA Publ. No. 308, "Proceedings of the 16th JANNAF Combustion Meeting," Vol. III, pp. 289 - 306.
 - 17 Parr, T. and Hanson-Parr, D., (1987), "Temperature and Species Profiles in Propellant Ignition and Combustion", CPIA Publ. No. 476, "Proceedings of the 24th JANNAF Combustion Meeting", 1, 367 - 382.
 - 18 Aron, K. and Harris, L.E., (1983), "CARS Studies of Nitramine LOVA Propellants," ARLCD-TR-83045: SBI-AD-E401101, AD-A13581314,.
 - 19 Korobeinichev, O.P. , Kuibida L.V., Orlov, V.N. , Tereshchenko, A.G., Kutsenogii, K.P. , Mavliev, R.A., Ermolin, N.E., Fomin, V.M., Emel'yanov ,I.D., in: "Mass Spectrometry and Chemical Kinetics" [in Russian], 1985, 73-93.
 - 20 Korobeinichev, O.P. , Kuibida, L.V., and Madirbaev, V.Zh., Fiz. Goreniya Vzryva, 20, 1984, 3, 43.
 - 21 a)Farber, M. and Srivastava, R.D. (1979), "Mass Spectrometric Investigation of the Thermal Decomposition of RDX", Chem. Phys. Lett., 64, pp. 307 - 310; b) Farber, M. and Srivastava, R.D., (1981), "Thermal Decomposition of HMX", Chem. Phys. Lett., 80, pp. 345 - 349.
 - 22 Zhao, X., Hints, E.J., Lee, Y.T., (1988), "Infrared Multiphoton Dissociation of RDX in a Molecular Beam", J. Chem. Phys., 88, pp. 801 - 810.
 - 23 Karpowicz, R.J. and Brill, T.B., (1982), "The $\beta \rightarrow \delta$ Transformation of HMX: Its Thermal Analysis and Relationship to Propellants", AIAA Journal, 20, pp. 1586 - 1591.

- ²⁴ Shackelford, S.A., Coolidge, M.B., Goshgarian, B.B., Loving, B.A., Rodgers, R.N., Janney, J.L., and Ebinger, M.H., (1985), "Deuterium Isotope Effects in Condensed-Phase Thermochemical Decomposition Reactions of Octahydro-1,3,5,7-tetranitro-1,3,5,7-tetrazocine", *J. Phys. Chem.*, **89**, pp. 3118 - 3126.
- ²⁵ Oyumi, Y. and Brill, T.B., (1985), "Thermal Decomposition of Energetic Materials 3. A High-Rate, In Situ, FTIR Study of the Thermolysis of RDX and HMX with Pressure and Heating Rates as Variables", *Comb. and Flame*, **62**, pp. 213 - 224.
- ²⁶ Bulusu, S., Weinstein, D.I., Autera, J.R., and Velicky, R.W., (1986), "Deuterium Kinetic Isotope Effect in the Thermal Decomposition of 1,3,5-Trinitro-1,3,5-triazacyclohexane and 1,3,5,7-Tetranitro-1,3,5,7-tetraazacyclooctane: Its Use as an Experimental Probe for Their Shock-Induced Chemistry", *J. Phys. Chem.*, **90**, pp. 4121 - 4126.
- ²⁷ Hoffsommer, J.C., Glover, D.J., and Elban, W.L., (1985), "Quantitative Evidence for Nitroso Formation in Drop-Weight Impacted RDX Crystals", *J. Ener. Mat.*, **3**, pp 149 - 167.
- ²⁸ Sharma, J., Hoffsommer, J.C., Glover, D.J., Coffey, C.S., Forbes, J.W., Liddiard, T.P., Elban, W.L., and Santiago, F., (1985), "Sub-Ignition Reactions at Molecular Levels in Explosives Subjected to Impact and Underwater Shock", *Proceedings of the Eighth Symposium (International) on Detonation*, Albuquerque, New Mexico, 725.
- ²⁹ Melius, C.F. and Binkley, J.S., "Thermochemistry of the Decomposition of Nitramines in the Gas Phase", *Twenty-first Symposium (International) on Combustion/ The Combustion Institute*, 1986, 1953-1963.

THE DIAMOND ANVIL CELL FOR PHYSICAL AND CHEMICAL INVESTIGATIONS OF ENERGETIC MATERIALS AT HIGH PRESSURES

Gaspar J. Piermarini and Stanley Block
Institute for Materials Science and Engineering
National Institute of Standards and Technology
Gaithersburg, MD 20899

and Philip J. Miller
Naval Surface Warfare Center
White Oak, MD 20910

ABSTRACT. Brief descriptions of the five generic types of diamond anvil high pressure cells are given with an assessment of their strengths and weaknesses for various kinds of scientific measurement applications. Three techniques applied successfully to the study of energetic materials, optical polarizing microscopy, infrared absorption spectroscopy, and energy dispersive x-ray powder diffraction, are described along with examples of some relevant data and results.

1.0 INTRODUCTION

Scientific advances can be made either in a dramatic and revolutionary way, or, as in the case of the diamond anvil cell (DAC), in a slow and evolutionary manner over a period of years. For more than two decades the DAC has developed, stepwise, from a rather qualitative instrument to the sophisticated quantitative research tool that it is today, capable of routinely reaching static pressures in the megabar range and readily adapting to many scientific measurement techniques.

In recent years the amount of research with diamond cells has greatly expanded with new applications being reported in the literature frequently. In an article of this scope and magnitude we cannot hope to cover all aspects. Instead, we intend to focus on the applications of the DAC to the study of energetic materials. To achieve this, we present four topics: (1) descriptions of five basic generic models of the DAC, (2) the ruby fluorescence pressure measurement method, (3) pressure transmitting media for specific applications, and (4) high- and low-temperature capability. This is followed by descriptions of three DAC applications which have been found especially useful in the study of energetic materials. These applications are: (1) optical polarizing microscopy for detecting high pressure polymorphism and measuring phase transition pressures, (2) Fourier transform infrared

spectroscopy (FTIR) for obtaining kinetic data on thermal decomposition reactions at high pressures, and (3) energy dispersive x-ray diffraction for confirming the existence of polymorphism and identifying the new phases crystallographically. These techniques were used to obtain the data reported in another presentation in this proceedings entitled, " Effects of Pressure on the Thermal Decomposition Kinetics, Chemical Reactivity and Phase Behavior of β HMX, RDX and Nitromethane" given by the same authors.

2.0 DIAMOND CELLS

The basic principle of the DAC is very simple. As was first reported in 1959 in the description of the original opposed-anvil diamond high pressure cell developed at the National Institute of Standards and Technology (NIST) (formerly the National Bureau of Standards) [1], two miniature diamond anvils (single-crystal, gem-quality diamonds about 1/3 carat each) are in an opposed-anvil configuration as shown in Fig. 1, similar in concept to Bridgman anvils.

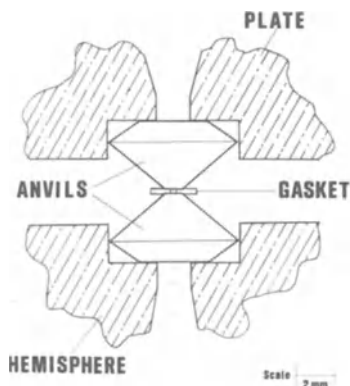


Figure 1. Enlarged cross-section drawing of the opposed diamond anvil configuration in a typical NIST diamond cell showing details of the sample confining gasket.

The sample is contained between the flat parallel faces of the anvils and is usually confined by a metal gasket containing a small diameter hole ($\approx 250 \mu\text{m}$). Pressure is generated on the sample when an applied force pushes the two opposed anvils together so that the metal gasket plastically deforms to produce a decrease in volume. Variations in the mechanical design of the DAC have arisen from different ways of generating the applied force and of aligning the diamonds to make them parallel and on axis. Five basic types of DAC's have evolved and each design has its own unique advantages for various applications.

2.1 NIST DAC

A recent model [2] of the original opposed-anvil DAC (180°

transmission) developed at NIST in 1959, is shown in Fig. 2.

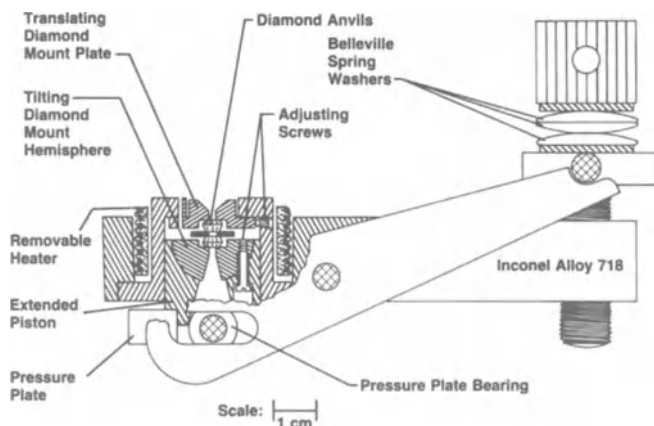


Figure 2. This cut-away cross section shows the essential components of the NIST DAC including the anvil support alignment design, lever-arm assembly and spring washer loading system. For high temperature experiments the entire cell, except for the spring washers, is fabricated from Inconel 718*, a high-temperature high-strength superalloy which permit sample temperatures as high as 1073 K to be maintained routinely.

In this design the principle employed to generate force is a spring-loaded lever-arm assembly, where the applied force is produced by the simple rotation of a large screw which compresses Belleville spring washers each having 272 kgf capacity when fully compressed to the flat position. The spring lever-arm arrangement generates a uniform and continuously varying force as the screw is rotated, a feature which has proved, in practice, to be highly desirable because it eliminates distortions in the anvil assembly and also unwanted large changes in pressure. Use of spring washers has also proved to be highly useful because they can be stacked either in series, in parallel, or in combinations of both, to alter sensitivity and load characteristics as desired. It is control of these parameters which is desired because they can be tailored to the peculiarities of the sample under investigation.

The applied load, magnified by 2 through the lever arm system, is transmitted to the pressure plate which bears against the extended piston containing one of the diamond anvils. The opposing anvil is fixed in its position and acts as an entablature for the piston anvil. The fixed anvil or entablature is supported by a translating diamond mount plate which permits the two anvil faces to be aligned with respect to the axis along the direction of the load. The piston anvil is supported in a tilting diamond mount hemisphere and permits parallel

adjustment of the opposing faces. With these simple adjustment features, anvil alignment can be accomplished with ease and precision and is also permanently maintained. Both diamond mount supports contain conical cut-outs which permit 180° optical access and can be modified to accommodate the particular requirements of the measurement of interest.

A readily removable bifilar-type resistance coil heater, sheathed in Inconel* alloy and electrically insulated with MgO powder, is inserted in a cavity surrounding the anvil-piston assembly for heating as shown in Fig. 2. In effect, the sample is located at the center of an external, coiled, resistance furnace. The maximum temperature obtainable is limited by the properties of the diamonds. In the open air, the temperature is limited by thermal etching of the diamonds which initiates at ≈ 1073 K. Sustained higher temperatures can be reached when the DAC is placed in a chemically inert environment. For low temperatures, the furnace can be replaced with a cooling coil for the passage of liquid nitrogen permitting temperatures as low as 77 K to be obtained depending on the degree of insulation and heat flow loss.

We favor the spring-loaded lever-arm design over others because of the ease in control and sensitivity of pressure, characteristics found to be critical to the accurate determination of phase boundaries. Other advantages include simple arrangement for static heating with resistance coil heaters and ease in loading with gasketed samples. We note, however, that regardless of the mechanism employed for generating the force, the criteria for producing very high pressures remain the same: (1) the ability to align the anvil faces accurately and (2) maintaining this alignment rigidly under the loads necessary to produce high pressures. The NIST cell has been adapted for x-ray powder [3] and single crystal [4] diffraction, FTIR absorption [5] and Raman spectroscopy [6], and optical polarizing microscopy [7].

2.2 BASSETT DAC

The force generating mechanism in this cell (Fig. 3) consists of a driving nut in a threaded stainless steel cylinder with relatively massive walls to provide strength and rigidity [8]. The anvil assembly consists of a stationary anvil whose support is threaded from one end of the cylinder and a movable anvil in a sliding piston arrangement is driven from the opposite end of the cylinder as shown in Fig. 3. Rotation of the driving nut advances the piston pushing the anvil against the stationary entablature. Anvil alignment is achieved with two half-cylinder rocker anvil supports whose axes are rotated by 90° in the plane normal to the load direction. Forces generated by this mechanism tend to be discontinuous and in relatively large steps rather than continuous, as is the case provided by spring washers, because the pitch of the thread determines the magnitude of the load generated for a given fraction of a rotation. In cells of this kind, the thread pitch

is necessarily small in order to sustain the large forces needed to produce high pressures particularly because there is no mechanical magnification factor as in the case of the lever-arm system.

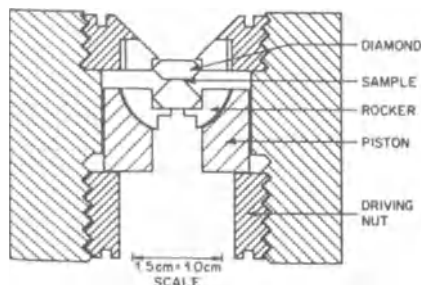


Figure 3. Cross-section drawing of the Bassett cell showing the hemi-cylinder hardened rocker supports for anvil alignment and the very simple force generating mechanism of a driving nut pushing against a movable piston in a guiding cylinder [8].

The design is inconvenient for static heating with resistance coil furnaces. This cell has been used extensively for high pressure x-ray powder diffraction studies and with laser heating of samples to very high temperatures for phase diagram studies [9]. Pressures as high as 40 GPa have been reported with samples in the ungasketed configuration using 0.3 mm anvil flats.

2.3 MAO-BELL DAC

Based on the NIST cell, this DAC [10] uses a spring-loaded lever-arm mechanism for generating the force, but is considerably larger and is used in an inverted configuration as shown in Fig. 4a. For stable anvil alignment this cell uses a long 60-70mm detachable piston-cylinder assembly (Fig. 4b).

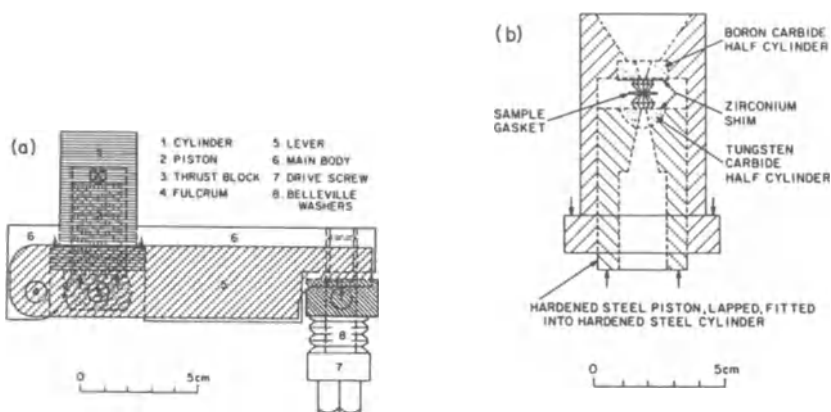


Figure 4. (a) Cross-sectional view of the Mao-Bell DAC showing the massive cell body (5) and the inverted thrust mechanism. (b) shows the elongated piston-cylinder design with the anvils mounted in tungsten carbide hemi-cylinders

rotated 90° from one another in the plane normal to the thrust direction [10].

Anvil alignment involves translating and tilting two hardened half-cylinder rockers. Basically a scaled-up version of the NIST DAC, this cell facilitates the generation of very large forces to produce pressures in the megabar range. Originally intended for the study of materials of geological interest, this cell has continued to break records in achieving the highest static pressures in the laboratory [11]. It also has been used extensively to study the condensed noble gases, as well as other gases, which are loaded in a large cryostat at low temperatures [12]. In fact, the recent discovery of metallic hydrogen was made with a diamond cell of this design using this low temperature loading technique [13]. Its relatively large size makes it inconvenient to adapt to measurement techniques where limited space is available.

2.4 HOLZAPFEL DAC

Another DAC design based on a knee mechanism to generate force [14] is shown in Fig. 5. Two parallel threaded rods which connect the two larger levers shown in Figure 5 are synchronously rotated with a special gear-set wrench pulling the lower ends of the levers together.

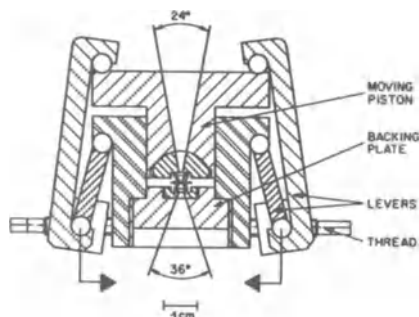


Figure 5. Cross-section of the Holzapfel DAC [14]. The thrust for the piston is generated by moving the opposed knee-type lever arms closer together when the threads are advanced synchronously without distortion. A tilting hemispherical diamond mount and a translating plate are used to align the diamonds similar to the NIST design.

A force is exerted on the moving piston which generates the pressure. This knee mechanism results in a large force multiplication factor which permits pressures in the 50 GPa range to be reached. This cell uses the NIST mechanism of a tilting hemisphere and a translation plate for anvil alignment. The cell has been adapted for x-ray powder and single crystal diffraction, Raman, Brillouin and other optical studies at high pressure [15]. The special geometry of the knee mechanism including the levers and threaded rods require precision machined components which must all fit together with great accuracy. Otherwise, the thrust will not act strictly parallel to the cylindrical axis of the instrument, and problems may arise in maintaining anvil alignment under applied loads.

2.5 MERRILL DAC

This DAC [16] is the simplest of all designs. As shown in Fig. 6,

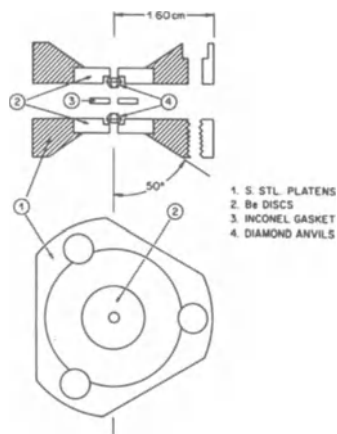


Figure 6. Miniature Merrill cell for single crystal x-ray diffraction studies [16]. Beryllium backing plates are used to support the diamonds because of the materials low absorption to x-rays. The thrust is applied by tightening the three symmetrically located pulling screws. Maintaining diamond alignment may be a problem if the screws are not tightened at the same rate.

three screws pull two platens together. When tightened synchronously with a special gear-set wrench, diamond alignment is maintained and pressures are generated. Of all the DACs, this device is the most compact, rendering it useful for single crystal x-ray diffraction measurements because it can be mounted directly on the circle of an automated x-ray goniometer using standard goniometer heads. For this application Be supports are required for the diamond anvils because they are relatively transparent to x-rays and provide wide-angle windows for the incident and diffracted x-ray beams. Unlike steel, however, Be is relatively weak which limits the support it can provide to reach very high pressures. The lack of a positive guidance mechanism for the diamond anvils is a concern in maintaining alignment. Pressures in excess of 10 GPa are rarely reached with this DAC.

3.0 GASKETED AND UNGASKETED SAMPLES

The diamond cell can be used in either of two sample configurations, gasketed and ungasketed. Originally, the ungasketed sample was used when the DAC first came into use [1]. Later, the gasketed mode was developed increasing the possible scientific applications of the DAC [17].

3.1 UNGASKETED

Initially the cells were used in the ungasketed configuration where the sample, usually in the form of a powder, was squeezed between the two parallel anvil flats. The sample pressure was uniaxial and resulted in a parabolic profile with the maximum at the center of the flat [18].

Samples prepared in this way were studied by x-ray diffraction, infrared absorption and optical polarizing microscopy and errors in the accuracy of the results were always present because of the large pressure gradient. In this ungasketed configuration, sample pressures not much greater than 30 GPa were reached before cracks developed in the diamond anvils ultimately leading to failure.

3.2 GASKETED

The development of the gasket technique came later [17]. As deficiencies in the ungasketed method, such as the large parabolic gradient in pressure, the relatively small volume of sample (a thin layer between the anvil flats), and the upper limit of 30 GPa became more apparent with use, the need for improvement was obvious [18]. A metal gasket was first used to contain a liquid such as ethanol in order to measure its freezing pressure at room temperature [19]. It was quickly recognized that if liquids could be confined under pressure in a DAC, then other materials in the form of powders and single crystals could be included and the liquid would act as a hydrostatic pressure transmitting medium as long as it remained a fluid [18]. Not only did this improve existing x-ray powder diffraction studies by providing a well characterized pressure environment, but it also led to single crystal x-ray diffraction under high pressure, a revolutionary development in high pressure techniques [4]. Advances were made in other areas also. For example, the gasket permitted the study of viscosity of liquids as a function of pressure and also the detection of the glassy state in liquids by line broadening measurements of the ruby fluorescence lines [18,20,21]. It also led to the discovery of new hydrostatic pressure transmitting liquids such as methanol:ethanol:water mixtures as will be discussed later.

Today, the sample is generally prepared in the gasketed configuration as shown in Figure 1. Metal gaskets, in addition to prolonging the life of the anvils and extending their pressure range, permit the sample to be encapsulated in a fluid pressure transmitting medium, thus providing a truly hydrostatic environment for the sample. The hydrostatic state is highly desirable because it eliminates the presence of shear stresses of unknown magnitude which often lead to serious difficulties in the interpretation of the desired measurement. Thus, the maintenance of the hydrostatic environment is a prime consideration for achieving error-free results in any high pressure experiment.

4.0 PRESSURE MEASUREMENT

In most of the earlier work with the DAC, sample pressures were estimated from the applied load. Such estimates yielded an average pressure over the sample in the nongasketed case, but are even less reliable using a gasketed sample, because the gasket absorbs an unknown amount of the load. Losses in load due to friction both in the sample and in the instrument were also unknown. The lack of a rapid reliable

pressure measurement procedure seriously hampered research using the DAC, because one could not prescribe and then produce a desired pressure condition and thus could not give meaningful in situ direction to an experimental study.

4.1 FIXED POINTS AND EQUATIONS OF STATE

In gasketed samples with pure liquids as pressure transmitting media, the freezing points were used as calibration markers because the freezing pressures for many of these liquids were known from large press experiments. For example, anisotropic and volume compressibilities as well as phase transition behavior of several azides including α - and β -lead azide, barium azide, potassium azide, sodium azide and thallium azide were measured by a single crystal x-ray diffraction precession method using this approach [22]. Measurements on these azides were made at the freezing pressures of n-hexane, n-decane, chloroform and ethanol at room temperature with both solid and liquid pressure transmitting medium in equilibrium. This method of pressure determination is cumbersome and time consuming because the cell has to be reloaded each time a different pressure point is needed for a different liquid is required.

4.2 RUBY FLUORESCENCE PRESSURE MEASUREMENT

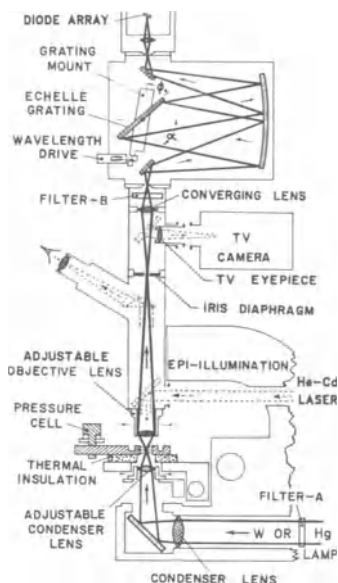
With the development of the rapid, accurate, routine and convenient ruby fluorescence method of pressure measurement at NIST in 1972, the problem of pressure calibration and measurement, a major obstacle to widespread use of the DAC, was removed [7]. As a result of this development, the DAC experienced an unprecedented expansion in its use and acceptance by the high pressure community as a tool for physical and chemical investigations.

The optical system for rapid routine pressure measurement shown in Fig. 7, utilizes a pressure shift in the sharp R-line fluorescence spectrum of ruby. The pressure dependent shift was calibrated against the volume compression of NaCl using an equation of state to calculate pressures [23]. For the first time pressures could be measured in the DAC with an accuracy and speed hitherto unachieved. The precision of the measurement in a hydrostatic environment is 0.05 GPa.

In our work, a small ruby sphere ($\approx 5\mu\text{m}$ diameter) is placed in the gasket hole along with the sample. Fluorescence is excited with a He-Cd 40 mw laser line or some other source of intense light such as a Hg arc lamp and the fluorescent spectrum is recorded digitally using a diode array detector. The spectrum is then transferred to a computer via a data acquisition controller interface. The spectrum is immediately processed either by a peak shift calculation or a line-shape model (or both) to evaluate the pressure. Measurements can be

made repeatedly in as little time as every 3 sec. The computer also performs a temperature correction calculation which is used in the determination of the pressure, thereby permitting measurements as a function of temperature.

Figure 7. Schematic diagram of the optical features of the ruby fluorescence pressure measuring and optical polarizing microscopy systems.



The most important consideration for the line shape analysis is the specification of the model itself [24]. The R lines form a pair of overlapping bell-shaped curves (Fig. 8).

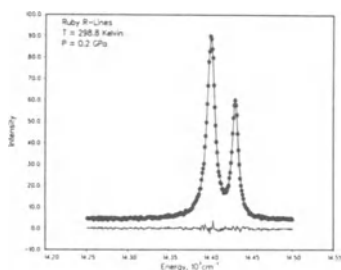


Figure 8. Comparison of model (solid line) and data (discrete points) for the ruby fluorescence R-lines at 298 K and 1 atm. The line oscillating about zero intensity is the difference between experiment and model.

At room temperature and 1 atm the two peaks are separated by about 29.5 cm^{-1} and have line-widths of about 13 and 10 cm^{-1} for R_1 and R_2 , respectively. The most widely known bell-shaped functions, Gaussian and Lorentzian, can be adjusted to represent the major features of the R lines, but they fail to represent adequately the outer wings, the

central overlap region, and/or the peak intensities. Furthermore, both functions become worse models with increasing temperature. In general, Gaussians are too sharply peaked, while Lorentzians are too broadly peaked. A third function, the Voigt profile, resolves this problem through a convolution of the Gaussian and Lorentzian functions, and this profile can be adjusted to give a good representation of the R line spectrum. However, optimization of the parameters in the Voigt profile exhibits slow convergence owing to their apparent insensitivity to the details of the ruby spectrum. Consequently, an alternative model to the Voigt profile is desirable which is more appropriate and mathematically convenient for the line-shape analysis.

An admixture of the Gaussian and Lorentzian forms with constraints on peak position, relative amplitudes, relative linewidths and background (black body radiation profile) was derived which gives very good representations of the observed R line spectrum even at temperatures as high as 400° C. Without the model an error as large as 0.6 GPa can occur in pressure at this temperature. The principle advantage of line-shape analysis is improved precision in pressure measurements at higher temperatures. Below 300° C similar precision can be obtained from a properly calibrated peak shift calculation. The model also produces two other enhancements to the utility of the ruby method. Under hydrostatic conditions temperatures can be determined with an estimated accuracy of 5%-10%. Under nonhydrostatic conditions a quantitative estimate of the distribution of pressure across a sensor can also be made.

4.3 OPTICAL POLARIZING MICROSCOPY

The optical system is mechanically unified and the critical optical alignment is readily made and permanently maintained. A high pressure Hg light source is placed at the rear of the base of the microscope for convenience. It is normally positioned as shown in Fig. 7 for transmission illumination, but can be positioned also for EPI (reflection) illumination, where normally a He-Cd laser beam is located for exciting fluorescence in the ruby sensor. To visually study the sample using polarized light in the normal manner, a standard tungsten microscope illumination lamp is also provided at the rear base of the microscope and can be optically inserted in place of the Hg lamp by means of a movable mirror. The pressure cell is firmly mounted on a massive x-y-z positioning device for both positioning the cell on the optic axis of the instrument (x,y) and focusing (z) the sample. Appropriate light filters are placed in the optical path to isolate the wavelength range of the fluorescent radiation thus preventing masking of the fluorescence.

A television camera and monitor are built into the system to eliminate eye fatigue during extended experiments involving visually observed phase changes and to allow simultaneous viewing of the sample by several individuals. Often, pressure-induced phase changes occur within fractions of a second following a pressure and/or temperature change, and the constant visual concentration on microscopic detail

over periods of time can cause serious eye fatigue. The light image is transmitted to the television camera by inserting a movable mirror which contains a very small circular noncoated area for transmission of the fluorescent radiation to the monochromator permitting simultaneous visual observation of the sample (via the television system) and pressure measurements. At very low fluorescent intensity levels, the background signal from the tungsten light increases and may eventually become so great that it interferes with the pressure measurement. This potential problem is eliminated by using the Hg light source which is far removed from the fluorescent wavelength, and, therefore, does not contribute background to the spectrum.

The pressure cell can be mounted in an insulating box for experiments requiring heating of the cell. Pressure measurements are reliable to temperatures up to about 300°C and perhaps to 400°C when the model is used. At higher temperatures, line broadening effects, very low fluorescent intensity levels, and a poor temperature correction all contribute to give an increasingly more unreliable pressure measurement.

The calculated pressures (both peak shift and model values), the measured temperature, the measured and calculated model R-line spectra and the differences between them, and the time and date are displayed on a color monitor every 6 seconds next to the real-time image of the sample. All of the displayed information can be recorded on video tape. As a result, a complete record of the experiment can be referred to at future times with all of the relevant information visible as the experiment is replayed.

An illustration of optical polarizing microscopy is provided by Fig. 9 which shows a photograph of a sample of powdered RDX compacted in a gasketed DAC at 2.0 GPa and room temperature in a Pt-Rh gasket.

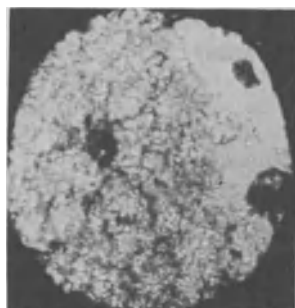


Figure 9. Photograph of a sample of RDX in a gasketed DAC at an average pressure of 2 GPa at 20°C prior to undergoing thermal decomposition. The powder was packed into a Pt-Rh gasket $\approx 250 \mu\text{m}$ in diameter and $150 \mu\text{m}$ in thickness. Two small ruby chips are included, one near the center and the other at the edge. The sample pressure is very nonhydrostatic with a large uncertainty associated with it.

Two small ruby chips used as pressure sensors are visible, one near the center of the sample and the other adjacent to the gasket edge. The sample is homogeneous. The products of decomposition exhibit interesting behavior and require further discussion. Thermal decomposition of RDX at 4.0 GPa and 516 K produced the products shown

in Fig. 10 after the DAC was cooled to room temperature. The pressure measured 0.9 GPa.

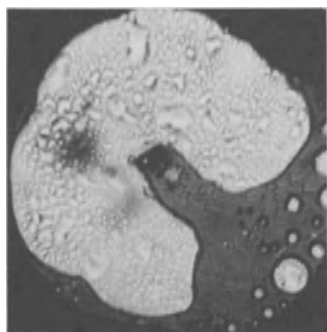


Figure 10. Photograph of the decomposition products of RDX in the DAC produced at about 4 GPa and 516 K. The sample shown here is at 0.9 GPa and room temperature. A brownish liquid is present dispersed with clear circular regions. The sample has measurable ir absorption under these conditions.

Both a solid region, showing strong birefringence with polarized light with some evidence of crystalline morphology, and a liquid region are visible. Also visible are large regions of gas as indicated by the bubble structure in the photograph. Infrared spectra indicate the presence of H_2O , CO_2 , and N_2O chemical species. As the pressure was lowered on this sample at room temperature, gases evolved from the liquid in the pressure range of about 0.3 GPa. At 1 atm only the solid residue shown in Fig. 11 was observed.

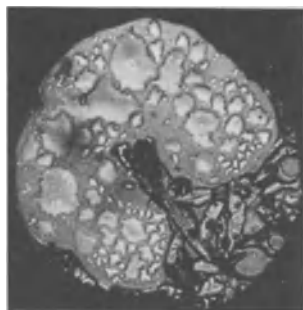


Figure 11. Photograph of solid residue after decomposition of RDX. System has been lowered to 1 atm and room temperature. Crystal morphology and the absence of the liquid seen in Fig. 10 are evident. On pressure reduction, gas evolution was detected and the liquid was no longer visible. The sample under this condition has no measurable ir absorption.

Some crystalline morphology remains in the solid and is visible under polarized light. The material gives no infrared spectrum. At present the solid material is unidentified.

The α - γ phase boundary of RDX was also determined by optical polarizing microscopy of single crystals of RDX in a quasihydrostatic environment. Fig. 12 shows two single crystals of RDX at about 3.5 GPa at room temperature in a Fluoroinert (chemically inert fluorinated hydrocarbon) pressure transmitting medium which provides a hydrostatic environment up to about 4.0 GPa at room temperature. At constant pressure, as the temperature is increased the hydrostatic limit increases because temperature reduces the viscosity of the liquid. This

accounts for less scatter in the data points at the higher temperatures for the line defining the α - γ transition. The two crystals shown in Fig. 12 are under polarized light so that the smaller diamond shaped

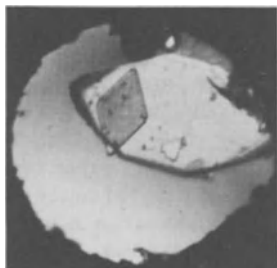


Figure 12. Two single crystals of α RDX at about 3.5 GPa and room temperature in a Fluoroinert pressure transmitting medium. The orthorhombic crystals exhibit weak birefringence with the smaller crystal showing more intense color than the larger under polarized light.

crystal, rotated approximately 90° from the larger crystal, shows slightly different birefringent properties. As the pressure is increased to approximately 3.8 GPa the α crystals undergo a transition to the γ phase shown in Fig. 13. The γ crystals exhibit very different birefringent properties and this change is used to detect when the transformation takes place. Note that the crystal does not break up on going through the transition. This indicates that the transformation may be displacive rather than a major rearrangement of the structure and accounts for the retention of the orthorhombic crystal class. The β - γ transformation was not observed visually under polarized light.

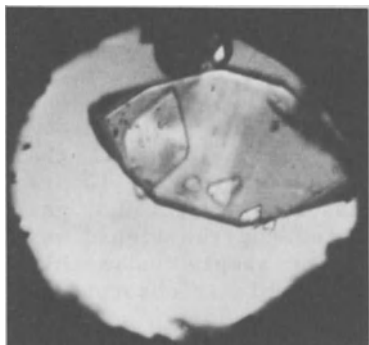


Figure 13. The same two crystals after transformation to γ RDX at about 3.8 GPa at room temperature. Both crystals are highly birefringent and the larger crystal shows parallel bands running perpendicular to the long axis of the crystal.

5.0 INFRARED ABSORPTION SPECTROSCOPY

We have developed a Fourier transform infrared microspectroscopic method for obtaining kinetic data on the thermal decomposition of energetic materials as a function of pressure and temperature [5]. The method utilizes a diamond-anvil high pressure cell basically of the NIST design described earlier, but with essential modifications to permit heating and appropriate optical access for infrared absorption measurements. The modifications over the earlier design are significant and require further discussion here. A cross-sectional schematic diagram of the cell used for the present infrared measurements was shown in Fig. 2. This cell is fabricated almost completely from a high-

strength/high-temperature corrosion resistant alloy, Inconel 718*, a nickel-base alloy retaining its high-strength mechanical properties to temperatures up to 973 K. The only components not made of this alloy are the Belleville spring washers (spring steel, type 1075), and the threaded bolt (Vascomax 300*).

For heating, a commercially available high output heating element consisting of a bifilar wound nichrome wire resistance coil ($\approx 70\Omega$) sheathed in Inconel* with MgO insulation, is inserted in the cavity around the anvil assembly. Sustained sample temperatures up to 1073 K have been reached with this heating arrangement. The anvils used in this cell are a pair of type II diamonds ($\approx 1/3$ carat each), specially selected for optimum transmission in the $600\text{--}5000\text{ cm}^{-1}$ range. To utilize maximum beam energy, the translation plate and piston-hemisphere assemblies contain relatively large conical apertures (35° apex angle). With non-converging beam ir instruments, the pressure cell must be used in conjunction with a matched pair of on-axis reflecting objective lenses (Cassegrain-type), in order to focus the beam to permit utilization of maximum beam energy. In converging beam instruments these reflecting objectives are unnecessary and the cell can be mounted directly in the infrared beam as shown in Fig. 14.

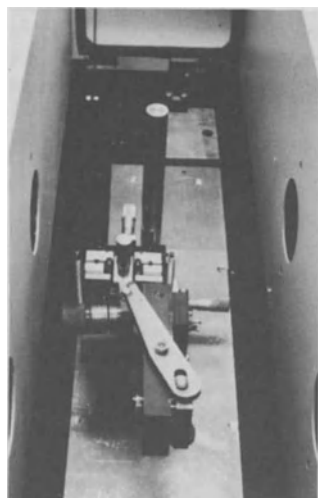


Figure 14. Micrometer positioning device for the DAC in an FTIR Nicolet* instrument. The ample available space permits inclusion of the micrometer instrument, the heater and thermocouple leads with ease.

Power to the heating element is controlled by a thyristor controller, a silicon-controlled rectifier, which permits automatic control of heating with proportional, integral, and derivative features for adjusting the heating rate. The system features also time-proportional heating temperature overshoot inhibition, thermocouple input, and direct temperature readout. The temperature probe is a chromel-alumel thermocouple with the bead in direct contact with the sample gasket. Temperatures measured with this system have been calibrated with the use of a series of pure materials with fixed known melting points. At 473 K, for example, temperatures can be maintained to within ± 2 K. At

573 K the uncertainty in temperature is larger, about ± 5 K.

Samples for infrared transmission measurements must be on the order of 0.01-0.05 mm in thickness in order to get useful spectra. This is not a trivial task to accomplish because gaskets of that thickness are not easily made. Moreover, pressures determined by the ruby technique are subject to great error because the ruby sphere often is pinched between the two closely-spaced diamond flats giving an incorrect shift as well as severe broadening to the ruby R-lines. To avoid these potential sources of error in the pressure measurement, gaskets are made in the usual thicknesses, i. e., ≈ 0.25 mm, and then packed with dry NaCl containing one ruby sphere ($\approx 10\mu\text{m}$ in diameter) as the pressure sensor. A 0.01-0.05 mm layer of NaCl is removed from the gasket plug and is replaced with the sample to be studied. This procedure gives a thin sample of material in the form of a thin disk suitable for ir absorption experiments.

In our most recent experiments, the DAC is mounted on a micrometer positioning device, as shown in Fig. 14, inside the sample chamber of a Nicolet* 7000 FTIR spectrometer equipped with an enhanced sensitivity MCT "A" detector and a Nicolet* 1280 data acquisition system. Unlike in our previous experiments, where a matched pair of Cassegrain beam condensing mirrors were employed to achieve sufficient energy throughput with a DAC, in the present system this arrangement is unnecessary. The f/5 sample optics and enhanced sensitivity detector combine to increase the overall sensitivity of the present system by a factor of approximately 27 over the previous system, thereby eliminating the need for the beam condensing apparatus.

Rate measurements can be made with this system by monitoring the infrared absorption spectra at various pressures and temperatures as a function time. The decomposition reaction of RDX was monitored in this way. The assembled pressure cell was mounted in the path of the infrared beam (see Fig. 14) and consisted of two opposed diamond anvils (type IIa with low birefringence) separated by an Inconel X750* gasket. The computerized system recorded the infrared spectra as shown in Fig. 15, in which the spectra for α (bottom) and β (top) RDX are shown.

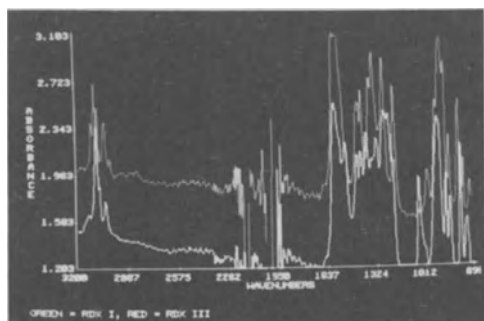


Figure 15. Infrared absorbance spectra for α RDX (bottom) and β RDX (top) as observed on the CRT of the ir instrument. These patterns are displayed for comparison of the α and β phases.

6.0 ENERGY DISPERSIVE X-RAY DIFFRACTION

The requirement of containment in a high pressure vessel imposes severe restrictions on a x-ray powder diffraction system [25]. In order to achieve maximum pressure, the x-ray entrance and exit ports must be relatively small and this greatly limits the angular diffraction range. The basic relationship between the interplanar spacings of a crystal and the wavelength of the diffracted beam is $\lambda_H = 2d_H \sin\theta$. Generally the wavelength is held constant and the sample and/or detector are rotated over a large range to bring the various planes into diffraction position. As this is not feasible in a constrained environment, the energy dispersive technique is used [26,27,28]. Here, the sample is held in a constant position and white radiation is used in conjunction with a solid state detector (Si_{Li} , Ge_{Li} , or intrinsic Ge) and a multichannel analyzer. All the data are collected simultaneously. The diffraction relationship combined with $E=h\nu$ becomes $Ed_H = h/2\sin\theta = 6.19905/\sin\theta$ where E is in keV units. When E vs $1/\sin\theta$ is plotted for the various interplanar spacings in a crystal a series of straight lines is obtained. Any fluorescence, characteristic tube x-ray lines or absorption edges are at a fixed energy. The observed intensities of the lines are proportional to: a) distribution of the white radiation from the x-ray source (tube or synchrotron), b) absorption through the diamonds (very high below 10 keV), c) specimen transparency, and d) scattering power decreasing as $1/E^2$. Based on the number of lines desired, the resolution, the avoidance of interfering fixed lines, and the constraints of the particular system, i.e., diamond greatly absorbs radiation below 10 keV and the Tungsten x-ray tube has little output above 55 keV, the appropriate diffraction angle is chosen. Table I gives the energy for 3 fixed diffraction angles of RDX.

Table I

Diffraction Energy (keV) of d Spacings of RDX for three 2θ Angles

<u>d Spacing</u>	<u>4°</u>	<u>6°</u>	<u>8°</u>
6.73	26.39	17.60	13.21
4.95	35.88	23.93	17.95
4.32	41.12	27.42	20.57
4.00	44.41	29.61	22.22
3.48	51.04	34.04	25.54
3.29	-----	36.00	27.01
3.03	-----	39.09	29.33

In this example, too few lines were available at 4° and the lines were too close together, i.e., resolution was poor at 8°. Therefore, a two theta angle of 6° was chosen for all diffraction experiments on RDX.

To conduct the energy dispersive x-ray diffraction experiments, the DAC described above is mounted in the beam of the diffractometer by

attachment to a micrometer positioner device with 3 mutually perpendicular independent motions as shown in Fig. 16. The x- and z-motions are used to place the sample in the x-ray beam. This can be done by using either the difference in absorption between the sample and the gasket or optically using a microscope with micrometer eyepiece. Optically, the x, y coordinates of the exit hole in the collimator are determined under illumination with visible light, and the sample is then placed at the appropriate position. The optical technique is preferable because of its speed and greater range of use.



Figure 16. Photograph of the energy dispersive x-ray diffraction system showing the horizontal goniometer with the DAC mounted on an x-y-z positioning device to facilitate sample alignment.

The absorption technique, in contrast, is useless if the absorption of the sample and gasket are similar. However, the optical technique requires an additional microscope to view the collimator and sample. The y motion is used to place the center of the sample on the diffractometer axis. As the sample center is dependent on the size of the diamonds and their mountings, the y position must be redetermined whenever the diamond anvils are changed. Two slits are used in this system. One is at the detector and serves to define the diffraction angle. The other is close to the DAC and serves to remove much of the scattering from the diamonds. Because of its greater range in energy and the property that it is not harmed by being at room temperature, an intrinsic germanium detector is often used. However there is a disadvantage in that for intense lines there is an escape peak at 9.87 keV below the line which can confuse the analysis.

Fig. 17 is a photograph of the display of the x-ray patterns of α

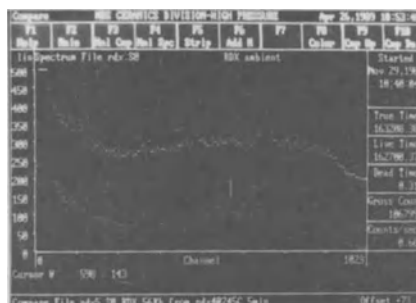


Figure 17. CRT display from the computer assisted energy dispersive x-ray apparatus showing typical patterns for α RDX (bottom) and γ RDX (top) demonstrating the differences between the two patterns.

RDX (bottom) at ambient conditions and γ RDX (top) at 5.6 GPa. The difference in the number of peaks and their positions clearly demonstrates that the phases are different.

REFERENCES

* Trade names mentioned are to specify experimental procedures. In no case does this imply endorsement by NIST.

1. Weir, C, E. Lippincott, E. R. Van Valkenburg, A. and Bunting, E. N. (1959) "Infrared studies in the 1-to-15 micron region to 30,000 atmospheres", J. Res. Natl. Bur. Stand., Sec. A 63, 55-62.
2. Piermarini, G. J. Block, S. (1975), "Ultrahigh pressure diamond-anvil cell and several semiconductor phase transition pressures in relation to the fixed point pressure scale", Rev. Sci. Instrum. 46, 973-979.
3. Walrafen, G. E. Abebe, M. Mauer, F. A. Block, S. Piermarini, G. J. and Munro, R. (1982) "Raman and x-ray investigations of ice VII to 36.0 GPa", J. Phys. Chem. 77, 2166-2174.
4. Piermarini, G. J. Mighell, A. D. Weir, C. E. and Block, S. (1969) "Crystal structure of benzene II at 25 kbar", Science 165, 1250-1255.
5. Miller, P. J. Piermarini, G. J. and Block, S. (1984) "An FTIR microscopic method for kinetic measurements at high temperatures and high pressures", Appl. Spectros. 38, 680-686.
6. Weinstein, B. A. and Piermarini, G. J. (1975) "Raman scattering and phonon dispersion in Si and GaP at very high pressure", Phys. Rev. 12, B 1172-1186.
7. Barnett, J. D. Block, S. and Piermarini, G. J. (1973) "An optical fluorescence system for quantitative pressure measurement in the diamond-anvil cell", Rev. Sci. Instrum. 44, 1-9.
8. Bassett, W. A. Takahashi, A. T. and Stook, P. W. (1967) "X-ray diffraction and optical observations on crystalline solids up to 300 kbar", Rev. Sci. Instrum. 38, 37-42.
9. Bassett, W. A. and Takahashi, T. (1974) in Advanced High Pressure Research, edited by R. H. Wentorf, Jr. (Academic, New York), Vol. 2, p.75.
10. Mao, H. K. and Bell, P. M. (1978) in Carnegie Institution of Washington Year Book 77, 904.
11. Mao, H. K. and Bell, P. M. (1978) "High pressure physics: Sustained static generation of 1.36 to 1.72 Megabars", Science 200, 1145-1147.

12. Mao, H. K. and Bell, P. M. (1979) in Carnegie Institution of Washington Year Book 78, 659.
13. Mao, H. K. and Hemley, R. J. (1989) "Optical studies of hydrogen above 200 Gigapascals: Evidence for metallization by band overlap", Science 244, 1462-1465.
14. Huber, G. Syassen, K. and Holzapfel, W. B. (1977) "Pressure dependence of 4f levels in europium pentaphosphate up to 400 kbars", Phys. Rev. B 15, 5123-5128.
15. Hirsch, K. R. and Holzapfel, W. B. (1981) "Diamond anvil high-pressure cell for Raman spectroscopy", Rev. Sci. Instrum. 52, 52-55.
16. Merrill, L. and Bassett, W. A. (1974) "Miniature diamond anvil pressure cell for single crystal x-ray diffraction studies", Rev. Sci. Instrum., 45, 290-294.
17. Van Valkenburg, A. (1965) "Visual observations of single crystal transitions under true hydrostatic pressures up to 40 kbars", Conference Internationale Sur-les Hautes Pressions, LeCreusot, Soane-et-Loire, France, August 2-6, 1965.
18. Piermarini, G. J. Block, S. and Barnett, J. D. (1973) "Hydrostatic limits in liquids and solids to 100 kbar", J. Appl. Phys. 44, 5377-5382.
19. Van Valkenburg, A. (1970) "High pressure optics", Applied Optics 9, 1-4.
20. Piermarini, G. J. Forman, R. A. and Block, S. (1978) "Viscosity measurements in the diamond anvil pressure cell", Rev. Sci. Instrum. 1061-1066.
21. Munro, R. G. Piermarini, G. J. and Block, S. (1980) "Viscosities and glass transitions in liquids at high pressures", Rev. Phys. Chem. Japan 50, 79-96.
22. Weir, C. E. Block, S. and Piermarini, G. J. (1970) "Compressibility of inorganic azides", J. Chem. Phys. 53, 4265-4269.
23. Piermarini, G. J. Block, S. Barnett, J. D. and Forman, R. A. (1975) "Calibration of the pressure dependence of the R_1 ruby fluorescence line to 195 kbar", J. Appl. Phys. 46, 2774-2780.
24. Munro, R. G. Piermarini, G. J. Block, S. and Holzapfel, W. B. (1985) "Model line-shape analysis for the ruby R lines used for pressure measurement", J. Appl. Phys. 57, 165-169.
25. Mauer, F. A. Block, S. and Piermarini, G. J. (1979) Paper G3,

American Crystallographic Association Program and Abstracts of Summer Meeting, Boston University, Boston MA, August 12-17.

26. Giessen, B. C. and Gordon, G. E. (1968) "X-ray diffraction: new high speed technique based on x-ray spectroscopy", *Science* 159, 973-975.

27. Albritton, L. M. and Margrave, J. L. (1972) "Polychromatic x-ray diffraction: a rapid and versatile technique for the study of solids under high pressure and high temperature", *High Temperatures-High Pressures* 4, 13-19.

28. Buras, B. Staun Olsen, J. Gerward, L. Selsmark, B. and Lindegaard Andersen, A. (1975) "Energy-dispersive spectroscopic method applied to x-ray diffraction in single crystals", *Acta Cryst.* A31, 327-333.

EFFECTS OF PRESSURE ON THE THERMAL DECOMPOSITION RATES, CHEMICAL REACTIVITY AND PHASE BEHAVIOR OF HMX, RDX AND NITROMETHANE

Gaspar J. Piermarini and Stanley Block
Institute for Materials Science and Engineering
National Institute of Standards and Technology
Gaithersburg, MD 20899

and Philip J. Miller
Naval Surface Warfare Center
White Oak, MD 20910

ABSTRACT. The effects of pressure on the thermal decomposition kinetics, chemical reactivity and phase behavior of β HMX, RDX and nitromethane have been studied by a combination of measurement techniques in conjunction with a high pressure diamond anvil cell. These techniques include: (1) Fourier transform infrared (FTIR) spectroscopy, (2) energy dispersive x-ray powder diffraction, (3) optical polarizing microscopy, and (4) Raman scattering. Studies were generally limited to the region where decomposition rates could be measured within reasonable laboratory time, i. e., below 10 GPa and 573K. The P-T phase diagram for RDX was determined to 573K and 7.0 GPa, delineating the stability fields of three solid phases, α , β and γ , and the liquidus. The α and β phases of RDX were found to thermally decompose, while the γ phase transformed to either α or β before reaching decomposition temperatures. The decomposition rate of α phase was found to increase with increasing pressure suggesting a bimolecular-type mechanism. Conversely, β HMX decomposition rates decrease with increasing pressure suggesting a unimolecular-type reaction mechanism. Activation energies, volumes and entropies for the thermal decomposition reactions are calculated from the observed data for β HMX and α RDX. The decomposition mechanism for nitromethane appears to be complex and varies over large changes in pressure. A mechanism is proposed which explains the bimolecular nature of the reaction and also accounts for the observed pressure dependence of the decomposition rate and products.

1. INTRODUCTION

The thermophysical and thermochemical properties of HMX (octahydro-1,3,5,7-tetranitro-1,3,5,7-tetrazocine), RDX (1,3,5-trinitrohexahydro-1,3,5-triazine) and nitromethane at elevated pressures are of

interest because these compounds are used extensively as monopropellants and explosives. Considering the importance of understanding the chemical decomposition of these materials, it would be useful to study the pressure dependence of their thermal decompositions. Parameters in the Arrhenius equation which characterize the reaction rate such as activation energy, usually are derived from ambient pressure studies and then extrapolated to the detonation regime. Published results [1,2] indicate that these ambient pressure kinetic parameters are not applicable to the high pressure regime. Generally, investigations of the reaction kinetics were experimentally performed by thermo-gravimetric or differential scanning calorimetry [3-8]. Quite significantly, different results were obtained when the experiments were carried out in either a confined or unconfined state. The discrepancies were thought to be due to either the autocatalytic or pressure dependent nature of the reaction mechanism. Consequently, applicable high pressure data is critically needed to increase our understanding of the reaction mechanism under detonation conditions and to improve the accuracy of the mathematical modelling procedures for combustion and explosive behavior.

In the pressure regime above 1 GPa, few published methods are currently available for kinetic measurements particularly for decomposition reactions of energetic materials where microvolume samples are necessary for the safety of the investigators. In a companion paper in this same issue, we describe a number of experimental methods utilizing a miniature high pressure diamond anvil cell (DAC) applicable to the study of energetic materials. Some of the methods described in that paper were used to obtain data in the present studies.

Here, we report the results of FTIR absorption kinetic measurements on the thermal decomposition of β HMX, α RDX and nitromethane confined in a DAC as a function of pressure and temperature. Through a combination of the measured pressure effects on the thermal decomposition kinetics, and, in the case of nitromethane, the identification of decomposition products, we propose possible reaction mechanisms for the thermal decomposition process in β HMX and nitromethane at high pressures. The chemical reactivity and phase stability of these materials at high pressures and elevated temperatures are also reported.

2. EXPERIMENTAL

As noted above, a combination of high pressure diamond anvil techniques, all utilizing the ruby fluorescence method of pressure measurement, were used to carry out these experiments. These include: (1) Fourier transform infrared (FTIR) spectroscopy for the kinetic measurements [9-11], (2) energy dispersive x-ray powder diffraction for crystallographic identification of the observed polymorphic forms and also compression measurements [12], (3) optical polarizing microscopy

for visually detecting phase transformations to delineate the stability fields in the equilibrium pressure-temperature phase diagrams of the various phases found, as well as for confirming the observed phase transitions, particularly for the α - γ phase transition which is subtle in the x-ray data [13], and (4) Raman scattering for measuring the pressure dependence of the shifts in the vibrational modes in liquid nitromethane, including the super-compressed state to 2.0 GPa [14]. The FTIR kinetic measurements were limited generally to pressures below 10 GPa and to temperatures below 573K, where decomposition could be measured within reasonable laboratory time spans. Detailed descriptions for these four methods along with some relevant illustrations of their application are given in the companion article in this Proceedings.

A combination of high pressure diamond anvil techniques was used to determine the equilibrium P-T phase diagram for RDX. In all of the methods employed, the ruby fluorescence method of pressure measurement calibrated for a temperature correction was used [13]. Optical polarizing microscopy observations of single crystals of RDX in a quasi-hydrostatic environment using Fluorinert as the pressure transmitting medium were used to measure the RDX α - γ phase boundary as a function of P and T by observing large discontinuous changes in birefringence between the two phases. This optical method was also used to measure the pressure dependence of the melting point by observing melting in compacted RDX powders. The γ - β transition could not be detected by this optical polarizing technique. Energy dispersive x-ray diffraction measurements of RDX powders in the same hydrostatic environment confirmed the structural changes associated with the three different polymorphs. Observed changes in the FTIR spectra obtained for the three solid phases provided additional confirmation for the phase transitions.

3. RESULTS AND DISCUSSION

3.1 β HMX

There are four known polymorphs of HMX, α , β , γ and δ [15]. The stabilities and densities of the four forms at 300K are: $\beta > \alpha > \gamma > \delta$. The β form was found to decompose at elevated temperatures in the pressure range 0.2 to 6.5 GPa. At very low pressures (< 0.2 GPa), the β form transforms to the δ form in the temperature range 453-493 K [10].

FTIR kinetic measurements on β HMX were made over the temperature range $528 \leq K \leq 583$ in 5K increments, and $1.0 \leq \text{GPa} \leq 6.5$ in 1.0 GPa increments, but not all combinations possible in this P,T regime were studied because, in some cases, excessively long times were required for the reaction to go to completion. Typical extent of reaction (α) vs. time curves for β HMX decomposition at 3.6 GPa are illustrated in Fig. 1 for several temperatures.

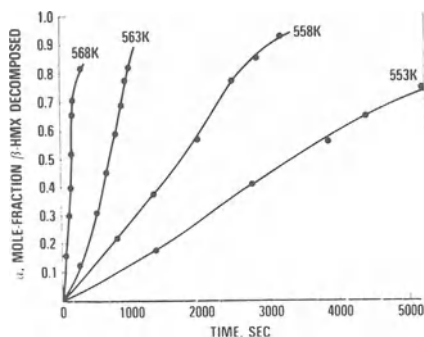
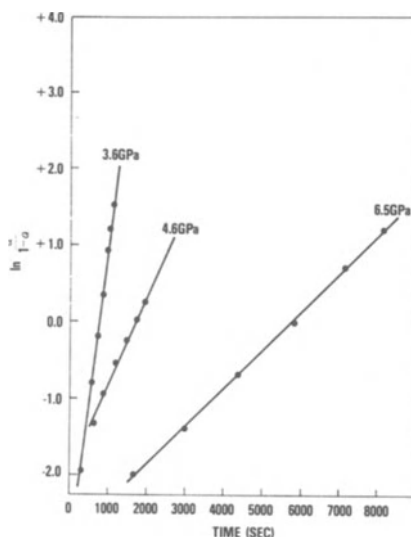


Figure 1. Typical α vs. time curves for the thermal decomposition of β HMX at 3.6 GPa for the various temperatures indicated. Sigmoid curves such as those shown here are characteristic of autocatalytic decomposition reactions of a single solid.

These sigmoid-type curves can be identified with thermal decomposition of a single solid in an autocatalytic-type reaction having an initial ($\alpha < 0.2$) induction period and an intermediate ($0.2 \leq \alpha \leq 0.9$) acceleratory or normal growth stage with the final ($\alpha > 0.9$) decay or deceleratory stage absent [8,9].

The rate of decomposition of a single solid material is governed by the formation of nuclei. The Prout-Tompkins rate equation, $\ln[\alpha/(1-\alpha)] = kt + C$, which is based on the chain theory of nucleation and allows for branching interference, was applied to our data in Fig. 1, and gave remarkable linearity over the range $0 \leq \alpha \leq 0.8$, as shown in Fig. 2.

Figure 2. Linearization of the α data at 3.6 GPa for the decomposition temperatures shown using the Prout-Tompkins rate equation, $\ln[\alpha/(1-\alpha)] = kt$.



The slopes of these lines, determined from least-squares fits, give the overall rate constant for the reaction. These data show typical Arrhenius temperature behavior with the overall rate constant

increasing with increasing temperature at 3.6 GPa. The rate constant, k , is pressure dependent and decreases with increasing pressure at constant temperature as illustrated in the $\ln[\alpha/(1-\alpha)]$ vs time curves in Fig. 3. This behavior is typical of data taken at $P \geq 3.6$ GPa. Measurements made below this pressure do not appear to fit the trend established by the higher pressure data and has been attributed to either or both of two sources: (1) at lower pressures the decomposition products may form as liquids and/or gases thereby complicating the decomposition mechanism and greatly influencing the overall rate constant, and (2) gases confined in a DAC at low pressures are known to leak through the pressure seal producing a significant decrease in the sample pressure thereby affecting the kinetics of the reaction.

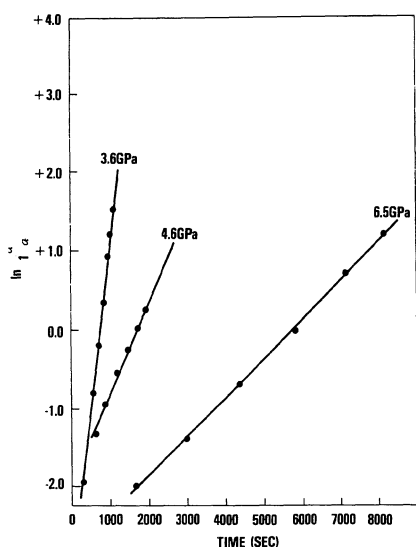


Figure 3. (above) Plots of $\ln[\alpha/(1-\alpha)]$ vs. time showing least-squares linear fits to data obtained at 563K for the three pressures indicated. Here the rate constant, k , decreases with increasing pressure.

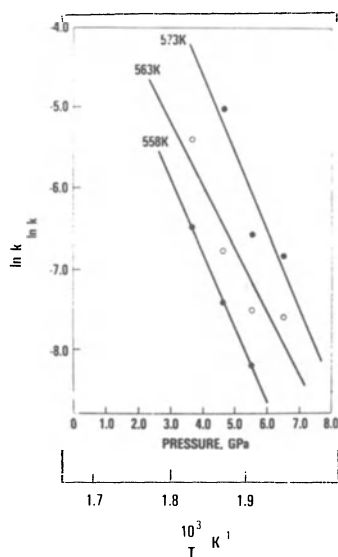


Figure 4. (above, right) Arrhenius plots [$\ln k$ vs. $10^3/T$] for β HMX decomposition at four different pressures (least-squares fits). The fits for the 3.6 GPa and 4.6 GPa data both have linear correlation coefficients of 0.996. The 5.5 GPa and 6.5 GPa data are less well-fitted to a straight line with correlation coefficients of 0.91 and 0.96, respectively.

From the rate constant for the overall decomposition reaction, thermodynamic terms and the effect of P and T on them can be determined. Fig. 4 shows linear plots of $\ln k$ vs. $1/T$ for the various

pressures indicated. As described in reference 10, the total differential of the natural logarithm of k is:

$$d \ln k = (\delta \ln k / \delta T)_P dT + (\delta \ln k / \delta P)_T dP,$$

where it can be shown that the partial derivatives are equal to:

$$(\delta \ln k / \delta 1/T)_P = - \Delta H^* / R$$

$$(\delta \ln k / \delta P)_T = - \Delta V^* / RT,$$

where ΔH^* and ΔV^* are experimental enthalpy and volume of activation, respectively. They are functions of P and T . Therefore, the slopes of these lines shown in Fig. 4 obtained from least-squares fits, yield the activation enthalpy (ΔH^*) which decreases with increasing pressure as shown in Fig. 5. At a temperature in the vicinity of 543K, near the melting point of δ HMX, the β form has a measurable, but very slow, decomposition rate regardless of the pressure.

Figure 5. (right) Pressure dependence of the enthalpy (ΔH^*) and internal energy (ΔE^*) of activation for β HMX decomposition. Curves are drawn to illustrate the sharp drop-off in the region above 5.5 GPa. Straight-line fits had poor correlation coefficients.

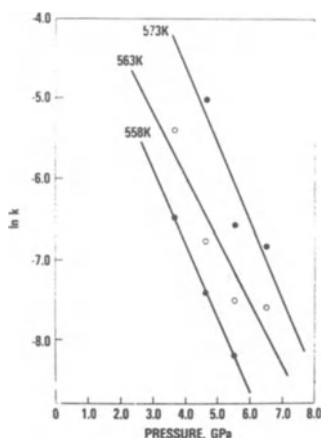
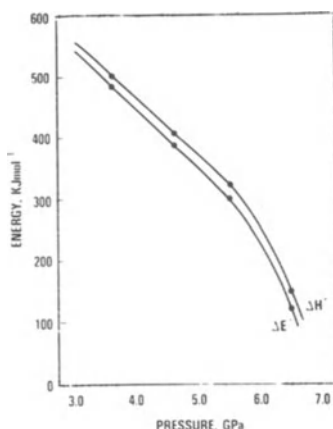


Figure 6. (left) Pressure dependence of $\ln k$ for β HMX decomposition at various temperatures. These are linear regression fits with the following correlation coefficients: 558K (1.00), 563K (0.93), 573K (0.91). Within the experimental error of our measurements, the slopes of these lines are the same.

Similarly, $\ln k$ can be plotted as a function of pressure at constant temperature as shown in Fig. 6, where the result is a series of almost parallel lines (least-squares fits) at the temperatures indicated. The slopes of these lines, -0.91 GPa^{-1} (558K), -0.76 GPa^{-1} (563K) and -0.94 GPa^{-1} (573K), are equal to $-\Delta V^*/RT$, so that the volume of activation can be determined for these temperatures. Because the lines have almost equal slopes, ΔV^* appears to be independent of temperature and pressure and has a positive average value of approximately $4.1 \text{ cm}^3/\text{mol}$. The rate determining step in the reaction mechanism is probably unimolecular at these high pressures because the activated complex occupies a larger volume than the volume of the reactants and its entropy is also greater than that of the reactants. The decomposition mechanism in β HMX at these high pressures probably proceeds through a bond scission process of the expanded bonds in the complex.

3.2 RDX

In reporting the kinetic results for RDX, it is first necessary to present our latest results on the P-T phase equilibrium diagram because we have found that our measured rates are phase dependent, so that one has to know what phase is undergoing decomposition at a particular pressure and temperature.

3.2.1 P-T EQUILIBRIUM PHASE DIAGRAM

Previously, it was known that RDX had one metastable conformer (β RDX) [16,17], in addition to the room temperature stable orthorhombic form (α RDX, space group Pbca) [18,19]. α RDX was also known to undergo a phase change at approximately 4.0 GPa at room temperature with a 1.6% reduction in volume. The high pressure phase was in the same crystal system (orthorhombic) as the ambient α RDX, but a definite structure was not reported [20].

Our recently determined equilibrium phase diagram for RDX as a function of pressure and temperature is shown in Fig. 7.

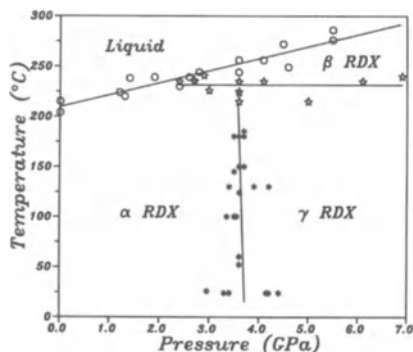
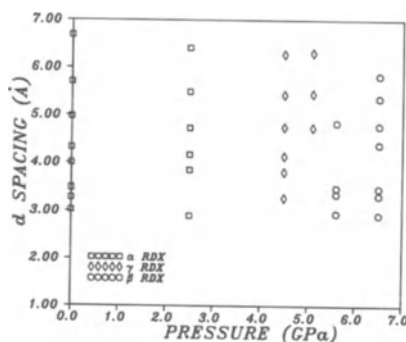


Figure 7. Equilibrium phase diagram for RDX showing the stability fields for three solid phases, α , β and γ and the liquidus or melting point.

Three solid polymorphs, identified as α , β , and γ were found. In keeping with phase equilibria convention, we label the phases with Greek letters. The stable ambient orthorhombic phase, α , the high pressure phase, γ , stable above 3.8 GPa, and the high temperature-high pressure phase, β , stable above 2.7 GPa and 488K. α RDX, stable at ambient P and T, was observed to transform to another orthorhombic phase, γ , at about 3.8 GPa at room temperature. The transition is very rapid, reversible and involves no break-up of the single crystals that were studied in a hydrostatic environment. The α - γ phase boundary was found to be essentially independent of temperature to about 488K, where the boundary abruptly ends. A sharp change in birefringence is accompanied by the transformation and serves as a detection marker along the entire α - γ boundary. The phase boundary lines are the result of least-squares linear fits to the data points, except for the α - γ transition line which is parallel to the temperature axis. Nonhydrostatic effects arising from the Fluoroinert pressure transmitting medium increased the scatter in the data points at the lower temperatures in the diagram introducing unwanted bias in the fit of the line. Until better data points are obtained, we prefer to show the boundary in this way. The scatter in the data points at the lower temperatures is due to sample strain arising from the shear stresses produced in the Fluoroinert liquid used as a chemically inert pressure transmitting medium [21]. The glass transition in Fluoroinert is about 4.2 GPa at room temperature and shear stresses produced in the medium at these pressures will effect the transition pressure in RDX. At higher temperatures the viscosity of Fluoroinert decreases significantly and shear stress plays almost no role in initiating the α - γ transition accounting for less scatter in the data points.

Our observed x-ray data for γ RDX, shown in Fig. 8 and 9, are in agreement with published results.

Figure 8. Diagram showing crystallographic "d" spacings versus pressure for the different RDX solid phases. For α RDX, the normal orthorhombic pattern is shown at 2.6 GPa (squares). At 4.5 and 5.1 GPa, another orthorhombic pattern is shown (diamonds) for the γ phase. The circles indicate the "d" spacings found for the β phase at 5.6 and 6.7 GPa. All the data were measured at room temperature.



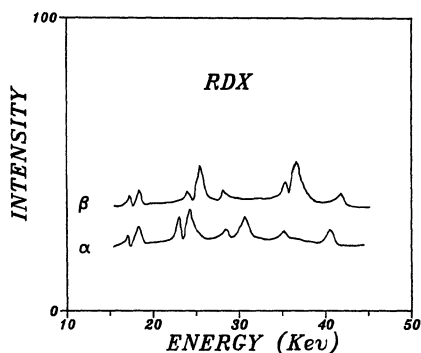


Figure 9. Energy dispersive powder x-ray diffraction patterns of α and β RDX showing the differences between the two phases.

No change in the crystal system was found. The pressure dependencies of the orthorhombic lattice parameters decrease monotonically with increasing pressure. However, near 4 GPa both a and c continue to decrease, but b abruptly increases resulting in a small decrease in volume of about 1.6%. This 1st order phase transition agrees with our optical observations where a discontinuous change in the birefringence of a single crystal is observed along the α - γ phase boundary shown in Fig. 7. Above about 488K, a new solid phase, β , exists which, at higher temperatures, is the phase in equilibrium with liquid. The β phase has not been identified crystallographically. Unlike the γ phase, β RDX cannot be detected by visual observation under polarized light. The only means of detection so far are (1) a change in the ir pattern (see Fig. 10 and 11), and (2) a change in the x-ray powder diffraction pattern (see Fig. 8 and 9). Both infrared and x-ray measurements show that the β phase can be metastably retrieved to room temperature conditions at elevated pressures. As the pressure is lowered at room temperature, β phase remains metastable to almost 1 atm where it rapidly reverts to the stable α phase. The measured pressure dependence of the liquidus or melting point is essentially linear to 7.0 GPa and, as expected, increases with increasing pressure. The scatter in the data points is an indication of (1) the effect of shear stress on the melting point because compacted powders were used in order to maintain sample purity, [21], and (2) the increased inaccuracy of our ruby pressure measurement at these higher temperatures [15].

The infrared spectra of α and γ RDX, shown in Fig. 10 and 12, indicate that the molecular structure of the respective RDX molecules is very similar, because only slight changes between the two spectra are observed. The γ -to- β transformation, however, results in a significant change in the molecular spectra of the two phases (see Fig. 11 and 12). In particular, the bands at $\approx 1060\text{ cm}^{-1}$ and at $\approx 1400\text{ cm}^{-1}$ that are observed in the α and γ phases are not seen in the β phase. The 1060 cm^{-1} bands have been assigned to cyclic vibrations coupled to deformations of the NO_2 groups through the C-N-N bond angle [22]. The

1400 cm^{-1} bond results from a CH_2 wagging motion. In addition, two prominent bands are observed in α phase in the CH stretching region, $\approx 3100 \text{ cm}^{-1}$. However, in the β phase at least five bands are observed in this region. A detailed assignment of the vibrational spectra for α RDX and its isotopes has been reported and will not be presented here [22]. A detailed analysis of the vibrational spectra of β RDX found in the present study is not given at this time because it requires additional isotopic study and structural information.

It is of interest to note that infrared spectra of a metastable RDX phase, obtained by the evaporation of a thymol-RDX solution, have been reported [17]. The ir spectra appear to be very similar to the spectra that we obtain for our β phase at different conditions of pressure and temperature. There appears to be strong evidence, because of the great similarity in the ir spectra, that the two phases are the same and that we have, in fact, determined the equilibrium stability field of this phase.

Figure 10. (right) Infrared absorbance spectra of α RDX at 1.4 GPa and γ RDX at 4.1 GPa, both at room temperature. Since only slight changes between the molecular spectra are observed, the molecular structure for the RDX molecule must be very similar for the two phases.

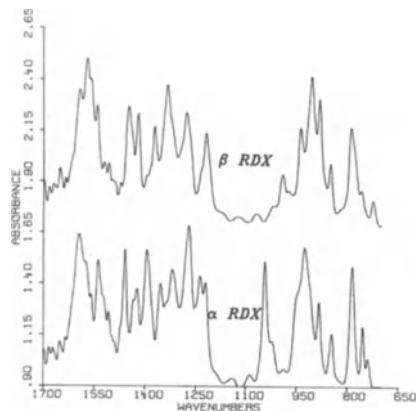


Figure 12. (right) Infrared absorbance spectra for α and β RDX taken at the same conditions stated in Fig. 8. The spectrum for the γ phase was taken at 4.1 GPa at room temperature.

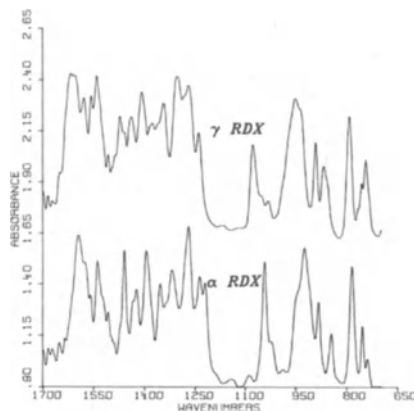
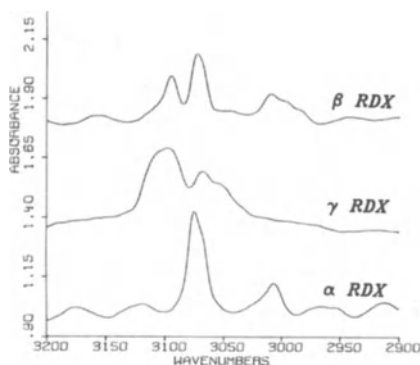


Figure 11. (left) Infrared absorbance spectra for α and β RDX taken at 2.4 GPa and 508K. The spectra show significant differences in the wavenumber range indicated.



3.2.2 THERMAL DECOMPOSITION RATE

Thermal decomposition in RDX was observed to occur in α and β phases only. No decomposition in γ phase was detected in the pressure-temperature regime studied, i.e., $1.4 < \text{GPa} < 6.9$ and $478 < K < 508$, because it always transformed to β phase before decomposition initiated.

The thermal decomposition rate for α RDX was measured by monitoring the infrared absorbance spectra labelled α RDX shown in Figs. 10, 11 and 12. The infrared bands in the region of 1050, 800 and 3000 cm^{-1} were used to determine $1-\alpha$, the concentration of α RDX (concentration is proportional to the measured absorbance) at any given time during the decomposition. Kinetic measurements were made over the temperature range $478 \leq K \leq 508$ in 10K increments at pressures of 1.4, 1.8, 2.1 GPa. α vs. time curves are not as sigmoid in character as those found for β HMX, except for P,T conditions where the reaction proceeded rapidly. In those cases α curves can be identified with the initial and intermediate stages of a sigmoid curve.

As in Figure 13, the data plotted as $\ln(1-\alpha)$ vs. time showed straight-line behavior indicating a diffusion limited reaction mechanism. Using this procedure, of course, is an oversimplification of rather complex rate expressions involving rate constants for nucleation, growth and termination of reaction in the solid. It does, however, permit the extraction of a rate constant, k , for a given observed reaction even though the true physical meaning may be unknown. Despite the above caveats, if we have a measure of the overall rate constant for the reaction, then we can estimate ΔH^* and ΔV^* from the dependence of k on the pressure and the temperature.

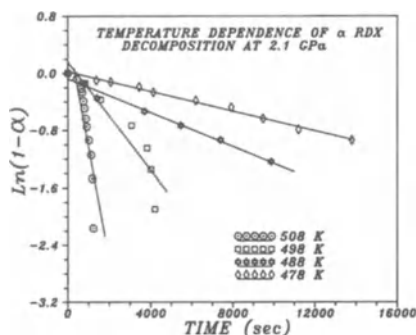


Figure 13. Linearization of the α data using a diffusion limited function $\ln(1-\alpha)$.

A plot of $\ln k$ vs $10^3/T$ is shown in Fig. 14 for the decomposition of α RDX. The observed rate increases with increasing temperature as expected and within our experimental error the change in rate is independent of pressure in the region of concern here. The slopes of these lines permit us to compute an Arrhenius activation energy of 51 kcal/mol for the decomposition reaction.

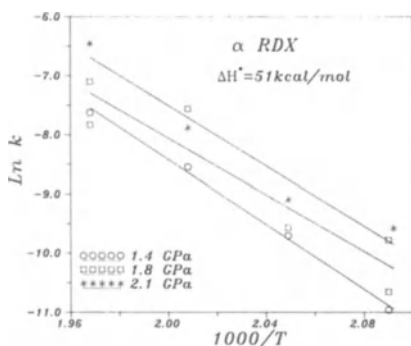
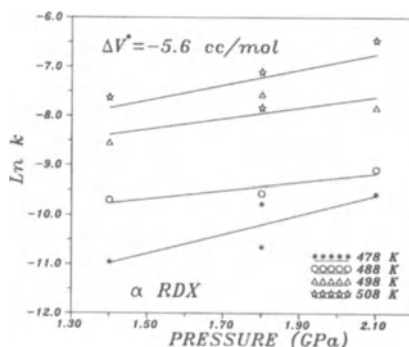


Figure 15. (right) Pressure dependence of the rate constant of α phase decomposition.



For comparison, values reported in the literature vary over a range of about 35-70 kcal/mole, with most of them within a few kcal/mole of 50. Generally, these values were obtained from thermo-gravimetric or differential scanning calorimetry experiments. Quite significantly, different data were obtained when the experiments were carried out where the RDX was in a confined and unconfined state. This was thought to be due to the autocatalytic or pressure dependent nature of the reaction mechanism.

A plot of $\ln k$ vs. pressure is shown in Fig. 15, and confirms that the rate of thermal decomposition of α RDX increases with increasing pressure in the range of concern here. Within our experimental error, the slopes of these lines are independent of temperature. From activation theory, the slopes of these lines permit us to calculate a volume of activation of $-5.6 \text{ cm}^3 \text{ mole}^{-1}$ for the decomposition reaction. Reactions with positive pressure dependence of the rate constant indicate a bimolecular-type reaction mechanism, where two or more molecular entities combine to form an activated complex whose combined molar volume is less than the separate entities. In this case the volume decrease is $5.6 \text{ cm}^3/\text{mole}$.

Under the P,T conditions used here to study the α RDX decomposition, the reaction products formed appear to be mainly H_2O , CO_2 and N_2O in the form of liquids. These liquids begin to transform to gases when the pressure is lowered to approximately 1.2 GPa and are lost completely at

Figure 14. (left) Temperature dependence of the rate constant of α phase decomposition.

1 atm (see Fig. 16).

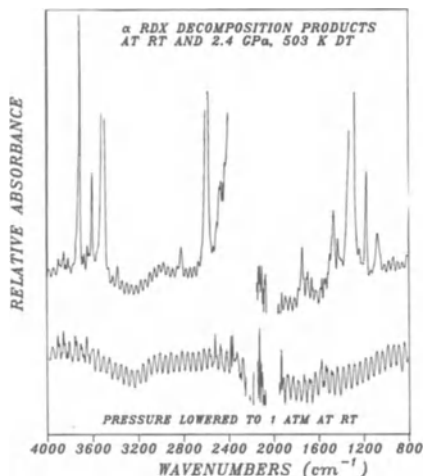


Figure 16. Infrared absorbance spectra of the thermal decomposition products of α RDX. The decomposition took place at 2.4 GPa and 503 K. The spectra were obtained after cooling to room temperature.

A number of reports investigated the decomposition products of the α RDX decomposition reaction. The major decomposition products, H_2O , CO , CO_2 , N_2O and N_2 were found to vary greatly with pyrolysis rate and temperature. Also a number of possible reaction mechanisms have been proposed. These include for the initial step N-NO_2 cleavage, C-N cleavage and an elimination step giving HONO . The overall reaction is thought to have both unimolecular and bimolecular reaction steps. At this point in our studies, we are unable to propose a reaction mechanism for the decomposition because of insufficient data available in the limited stability range of α RDX. However, we intend to remeasure the kinetics using deuterated RDX to determine if more information about the mechanism can be obtained through a possible isotopic effect. RDX under ambient pressure is known to give a kinetic isotope effect [23].

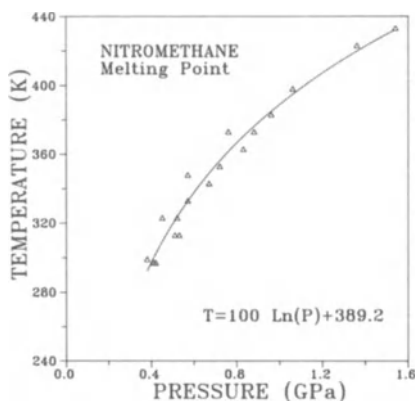
3.3 NITROMETHANE

The chemical reactivity and melting point of nitromethane as a function of pressure and temperature was observed optically with the aid of a polarizing microscope as described earlier [11]. The pressure dependence of the melting point is shown in Fig. 17 to about 1.54 GPa. Above 1.54 GPa and 433K, thermal decomposition initiates and is readily observed by darkening of the liquid and crystal producing ultimately brown solid residue, liquid, and gases.

Upon release of pressure, only the solid residue remains, which has been analyzed by mass spectrometry in order to determine its chemical constituents. The major products of decomposition up to 7 GPa, are ammonia, formic acid or its salt and water. The residue was originally reported to be the oxalate salt based on the similarity of the ir

absorption spectra, but that result had never been confirmed [24].

Figure 17. Pressure dependence of the melting point of nitromethane.



Pressure tends to increase the chemical reactivity of nitromethane as well as the rate of thermal decomposition. It was observed, quite accidentally, that a pressure-induced spontaneous explosion of single crystals of nitromethane at room temperature can occur. Further study revealed that single crystals grown from the liquid with the (111) and either the (001) or the (100) crystal faces perpendicular to the applied load direction in the DAC, if pressed rapidly to over 3 GPa, explode instantaneously accompanied by an audible snapping sound. The normally transparent sample becomes opaque instantly. Visual examination of the residue revealed a dark brown solid which was stable when heated to over 300°C. Subsequent x-ray analysis showed the material to be amorphous. Mass spectral analysis of the residue was inconclusive because no well defined spectra were observed. Because most of the sample is recovered as solid residue after the explosion and is stable to over 300°C, the material may be amorphous carbon. This stress-induced explosion occurs only in protonated nitromethane because similar attempts on the deuterated form did not result in explosion. Shock experiments on oriented pentaerythritol (PETN) crystals have shown similar type behavior [25]. In this case it was suggested that the sensitivity of shock pressures to crystal orientation is the result of the availability of slip planes or system of planes in the crystal to absorb the shock, thereby increasing the threshold to explosion. A similar explanation may be applicable to the nitromethane crystals as well. The deuteration effect must play a role in the initiation chemistry. An isotope effect has been observed previously in the sensitivity of HMX and RDX to shock and thermal conditions [23].

At elevated pressures, the thermal decomposition of nitromethane is expected to behave differently from HMX and RDX. Previously reported time-to-explosion measurements on nitromethane up to 5 GPa indicate that pressure decreases the time required to achieve an explosion [26]. As a result of this behavior, pressure is expected to increase the thermal decomposition rate in nitromethane.

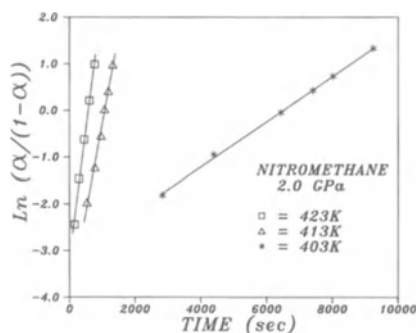
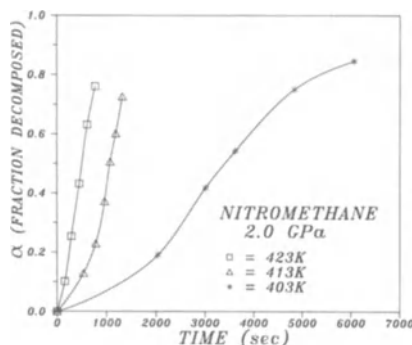


Figure 18. (above, left) α vs. time curves for data obtained at 2.0 GPa for the temperatures indicated. Curves shown are logarithmic fits to the data points.

Figure 19. (above, right) Linear fits of $\ln[\alpha/(1-\alpha)]$ vs. time for data obtained at 2.0 GPa for the decomposition temperatures indicated. The rate increases with increasing temperature.

Kinetic measurements were made over the ranges $2.0 \leq P \leq 7.1$ and $393 \leq T \leq 453$ with the following results. As in the case of HMX, the α vs. t curves can be identified with the initial and intermediate stages of a sigmoid (s-shaped) type curve characteristic of thermal decomposition of a single solid in an autocatalytic type reaction [27,28]. With increasing temperature the s-character diminishes to where the curve is almost linear at 423K as shown in Fig. 18. A plot of $\ln[\alpha/(1-\alpha)]$ vs. t (Fig. 19) gives linear dependence which supports a decomposition mechanism consistent with nuclei formation with branching interference similar to the HMX result. The slopes of these lines give typical Arrhenius temperature behavior with the overall rate increasing with temperature.

Unlike HMX, however, the decomposition rate in nitromethane was found to increase with increasing pressure, but the overall trend in the data was not consistent. Some interesting qualitative observations can be made on the basis of reaction times at the various P,T conditions measured and these are as follows:

- (1) To 5 GPa at least two different reaction mechanisms are involved in the decomposition and both have a positive pressure dependence on the overall rate of decomposition.
- (2) Mechanism (1) is dominant below 4 GPa and $T \leq 130^\circ \text{C}$.
- (3) Mechanism (2) operates at all measured temperatures at 5 GPa and at $T \geq 140^\circ \text{C}$ at 4 GPa (see Fig. 20).
- (4) The mechanism crossover temperature appears to be 140°C . At $T \leq 140^\circ \text{C}$ at 2 GPa mechanism (1) is operative, but at $T \geq 140^\circ \text{C}$ either

mechanism (2) or a mixture of both are operative.

(5) Mechanism (1) is linearly dependent in $\ln[\alpha/(1-\alpha)]$ vs. time, similar to that found earlier for β HMX, while mechanism (2) is linear in $\ln(1-\alpha)$ vs. time. The type of predominant chemical mechanism of the decomposition reaction determines the mathematical functionality of α with respect to time [5]. The fact that we find two different time dependencies indicates that we are dealing with two separate and distinct kinetic processes. Recently, it was reported that the aci or enol form of nitromethane can play an important role in the thermal decomposition of nitromethane by acting as a catalyst [29]. The results obtained here cannot rule out the possibility of this form affecting our observed kinetic data.

(6) Finally, a third mechanism operates at pressures greater than 5 GPa.

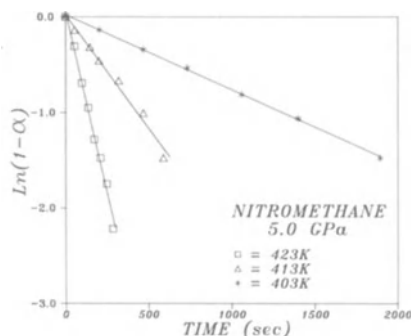


Figure 20. Linear fits of $\ln(1-\alpha)$ vs. time for data obtained at 5.0 GPa at three decomposition temperatures. The linearity of the fit with this function indicates a reaction mechanism different from the one found for the data plotted in Fig. 19.

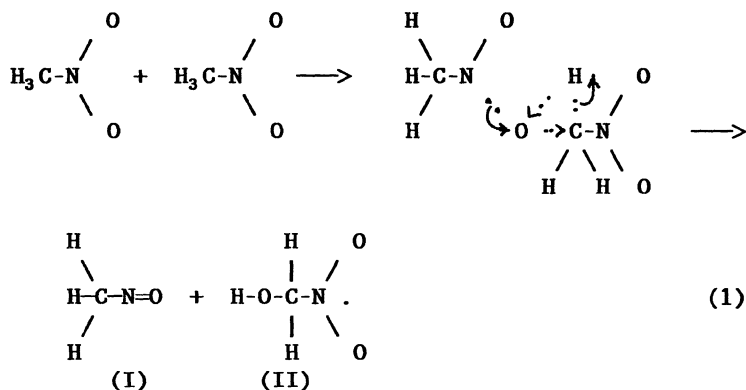
The results illustrate the complexity of the nitromethane thermal decomposition reaction. More than one kinetic mechanism and/or catalytic effect may be present. However, the results show definitely a positive pressure enhancement of the reaction rate. As described in reference 10, from the expression:

$$d \ln k = \Delta H^* / RT^2 dT - \Delta V^* / RT dP,$$

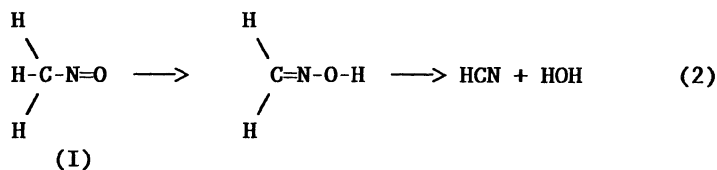
for small increases in pressure with all other terms being equal, only a negative ΔV^* will cause increases in $\ln k$. Therefore, the thermal decomposition rate of nitromethane shows a negative volume of activation in the P-T regime studied in the present experiments. This result directly implies that the nitromethane decomposition reaction in the solid state is bimolecular in character. This result differs from recent mass spectra studies of molecular reactions in the gas phase [30-32], where the reaction is found to be unimolecular. The disagreement in the results is not surprising because different decomposition mechanisms can be expected between the crystalline and gaseous phases of nitromethane. The intermolecular collision probability, for example, is much higher in the condensed phase.

3.3.1 Chemical Mechanism of Nitromethane Decomposition

Considerable work has been reported on the possible chemical reaction pathways for both pyrolysis and detonation processes in nitromethane [30-34]. Most of these proposed mechanisms are based upon a unimolecular process. As far as we can determine, only this work and one other (see reference 26) show experimentally that the reaction under pressure results from a bimolecular process, although the results reported in reference 26 were derived from the effect of pressure on time-to-explosion measurements. Based on theoretical electronic orbital calculations a bimolecular process has been proposed [32] as follows:



The reaction of nitrosomethane (I) proceeds rapidly to form HCN and finally NH_3 and HCOOH as shown below in equations 2 and 3.



At elevated P and T, HCN hydrolyzes very fast to yield:



The remaining product (II) from reaction (1), rapidly decomposes (reaction 4, not shown) into the following possible gaseous compounds: H_2O , N_2O , CO_2 , CO , NO , H_2 , and solid C. Reaction (1) is rate controlling with a calculated activation energy of $32.5 \text{ Kcal mole}^{-1}$. Reactions (2), (3), and (4) are relatively fast compared with reaction (1). Reactions (3) and (4) provide the pathways for the production of NH_3 , HCOOH and H_2O via chemical reaction with HCN which is known to be

a major pyrolysis product of nitromethane [33]. Our experiments confirm the presence of NH_3 , HCOOH , and H_2O along with volatile gases as the major products of thermal decomposition of nitromethane under high pressures.

This proposed reaction scheme for nitromethane decomposition at elevated pressures suggests a strong intermolecular interaction of nitromethane in the condensed phase. If this is indeed the case, then it is important to investigate the effect of pressure on the vibrational bands in nitromethane and to analyze the observed shifts in light of intermolecular coupling between the $-\text{NO}_2$ and $\text{H}_3\text{C}-$ groups of interacting molecules.

4. CONCLUSIONS

4.1 β HMX

Pressure was found to decrease the rate of thermal decomposition of β HMX, while temperature increased the rate in typical Arrhenius behavior. The decomposition reaction followed a Prout-Tompkins equation, $\ln[\alpha/(1-\alpha)] = kt$, which is based on the theory of nuclei formation with branching interference characteristic of the decomposition of single solid materials. Activation energies decrease with increasing pressure in a linear fashion with the value tending toward zero at very high pressures. The volume of activation is positive for the decomposition and essentially constant over the P,T domain studied. The reactants undergo a 3% increase in volume to achieve the activated state prior to decomposition. The reaction mechanism is unimolecular and probably involves a ring expansion of about 3% before bond scission. The entropy of activation is positive, but with a negative linear pressure dependence indicating that the activated complex, although more disordered than the initial reactants, is becoming less disordered with increasing pressure. The free energy of activation increased linearly to 5.5 GPa. Above this pressure it decreased indicating a positive effect on the reaction rate. Thus, the reaction mechanism above 5.5 GPa, which is in the regime of detonation pressures, may be significantly different from those dominating the reaction in the 3.6-5.5 GPa regime.

4.2 α RDX

The equilibrium phase diagram of RDX has been determined to 7.0 GPa and 573K. Three solid phases, α , β and γ , have been found and their stability fields delineated. The pressure dependence of the melting point has also been defined. The α and β phases were found to thermally decompose in the P, T regime of concern here. Pressure enhances the rate of decomposition of the α phase and probably reacts through a bimolecular-type mechanism. The activation volume, ΔV^* , for the reaction is $-5.6 \text{ cm}^3/\text{mole}$ and is temperature independent. The

activation energy, ΔH^* , is pressure independent and was found to be 51 kcal/mole in agreement with previously reported values. The reaction followed a rate expression, $-\ln(1-\alpha)=kt$, which is based on a diffusion limited mechanism.

4.3 Nitromethane

Nitromethane decomposes under pressure when heated to temperatures above 440K at pressures greater than 1.6 GPa. Both pressure and temperature accelerate the rate of decomposition. The condensed product residues are mainly ammonium formate and water in addition to nonretrievable volatile gases. More than one reaction mechanism appears to be present as indicated by the complex kinetic results. A proposed bimolecular decomposition mechanism is presented that can account for the observed positive pressure dependence of the reaction rate and the experimentally detected reaction products. Nitromethane undergoes a catastrophic reaction under certain dynamic stress conditions in the DAC at room temperature. The sensitivity level to the initiation of this reaction appears to be crystal orientation dependent with respect to the applied stress in the DAC. The resulting opaque solid residue is amorphous and carbonaceous and stable to temperatures in excess of 573 K. Deuterated nitromethane was not observed to undergo this catastrophic reaction.

ACKNOWLEDGEMENTS

We wish to acknowledge the U.S. Army Research Office and the Naval Surface Warfare Center, Independent Research Program for financial support for these projects.

REFERENCES

1. Bardo, R. D. Hall T. N. and Kamlet M. J. (1982) "Energies and volumes of activation for condensed detonating explosives", J. Chem. Phys. 77, 5858-5859.
2. Bardo, R. D. Hall T. N. and Kamlet M. J. (1979) "Volume of activation in the shock initiation of explosives", Combustion and Flame 35, 259-265.
3. Kishore, K. (1977) "Thermal decomposition studies on Hexahydro-1,3,5-trinitro-s-triazine (RDX) by differential scanning calorimetry", Propellants and Explosives 2, 78-81.
4. Robertson, A. J. B. (1949) "The thermal decomposition of explosives Part II Cyclotrimethylene trinitramine and cyclotetramethylene tetranitramine", Trans Faraday Soc. 45, 85-93.

5. Rogers, R. N. (1974) "Determination of condensed-phase kinetics constants", *Thermochem-Acta* 9, 444-446.
6. Rogers, R. N. and Daub, G. W. (1973) " Scanning calorimetric determination of vapor-phase kinetics data", *Anal.Chem.* 45, 596-600.
7. See for example, A.E. Axworthy, *Proceedings of the 15th JANNAF Combustion Meeting*, 1979, pp. 253-265.
8. Shaw, R. and Walker, F. E. (1977) "Estimated kinetics and thermochemistry of some initial unimolecular reactions in the thermal decomposition of 1,3,5,7-tetranitro 1,3,5,7-tetraazacyclooctane in the gas phase", *J. Phys. Chem.* 81, 2572-2576.
9. Miller, P. J. Piermarini, G. J. and Block, S. (1984) "An FTIR Microscopic Method For Kinetic Measurements At High Temperatures and High Pressures", *Appl. Spectrosc.* 38, 680-686.
10. Piermarini, G. J. Block, S. and Miller, P. J. (1987) "Effects of pressure and temperature on the thermal decomposition rate and reaction mechanism of β -octahydro-1,3,5,7-tetranitro-1,3,5,7-tetrazocine", *J. Phys. Chem.* 91, 3872-3878.
11. Piermarini, G. J. Block, S. and Miller, P. J. (1989) "Effects of pressure on the thermal decomposition rate and reaction mechanism of Octahydro-1,3,5,7-tetranitro-1,3,5,7-tetrazocine", *J. Phys. Chem.* 93, 462-466.
12. Walrafen, G. E. Abebe, M. Mauer, F. A. Block, S. Piermarini, G. J. and Munro, R. (1982) "Raman and x-ray investigations of ice VII to 36.0 GPa", *J. Chem. Phys.* 77, 2166-2174.
13. Barnett, J. D. Block, S. and Piermarini, G. J. (1973) "An optical fluorescence system for quantitative pressure measurement in the diamond-anvil cell", *Rev. Sci. Instrum.* 44, 1-9.
14. Miller, P. J. Piermarini, G. J. and Block, S. (1989) "Effects of pressure on the vibrational spectra of liquid nitromethane", *J. Phys. Chem.* 93, 457-462.
15. Goetz, F. and Brill, T. B. (1979) "Laser Raman spectra of α -, β -, γ -, and δ -Octahydro-1,3,5,7-tetranitro-1,3,5,7-tetrazocine and their temperature dependence", *J. Phys. Chem.* 83, 340-346.
16. McCrone, W. C. (1950) "RDX (Cyclotrimethylenetrinitramine)", *Anal. Chem.* 22, 954-955.
17. Karpowicz, R. J. Sergio, S. T. Brill, T. B. (1983) " β -Polymorph

of hexahydro-1,3,5- trinitro-s-triazine. A Fourier transform infrared spectroscopy study of an energetic material", Ind. Eng. Chem. Prod. Res. Rev. 22, 363-365.

18. Choi, C. S. and Prince, E. (1972) "The crystal structure of Cyclotrimethylene-trinitramine", Acta Cryst. B28, 2857-2862.
19. Cady, H. H. Larson, A. C. Cromer, D. T. (1963) "The crystal structure of α -HMX and a refinement of the structure of β -HMX", Acta Cryst. 16, 617-623.
20. Olinger, B. (1988) private communication
21. Piermarini, G. J. Block, S. Barnett, J. D. and Forman, R. A. (1975) "Calibration of the pressure dependence of the R_1 ruby fluorescence line to 195 kbar", J. Appl. Phys. 46, 2774-2780.
22. Rey-Lafon, M. Trinquescoste, C. Cavagnat, R. and Forel, M. (1971) "Etude des spectres de vibration de la Trinitro-1,3,5,-hexahydro-s-triazine", J. Chim. Phys. 68, 1533-1542.
23. Bulusu, S. Weinstein, D. I. Autera, J. R. and Velicky, R. W. (1986) "Deuterium kinetic isotope effect in the thermal decomposition of 1,3,5-trinitro-1,3,5-triazacyclohexane and 1,3,5,7-tetranitro-1,3,5,7-tetrazacyclooctane: Its use as an experimental probe for their shock-induced chemistry", J. Phys. Chem. 90, 4121-4126.
24. Brasch, J. W. (1980) "Irreversible reaction of nitromethane at elevated pressure and temperature", J. Phys. Chem., 84, 2084-2085.
25. Dick, J. J. (1984) "Effect of crystal orientation on shock initiation sensitivity of pentaerythritol tetranitrate explosive", Appl. Phys. Lett., 44, 859-861.
26. Lee, E. R. Sandborn, R. H. and Stromberg, H. D. (1970) "Thermal Decomposition of High Explosives At Static Pressures to 50 Kbar", Proceedings of the 5th Symposium (International) on Detonation", p. 331-337,
27. Jacobs, P. W. M. and Tompkins, F. C. in W. E. Garner (ed.), "Chemistry of the Solid State", chap. 7, Butterworth & Co. (Publishers), Ltd., London, 1955.
28. Dollimore, D. Dollimore, J. and Nicholson, D. (1961) in J. H. deBoer (ed.), "Reactivity of Solids", p. 627, Elsevier Publishing Co., Amsterdam.
29. Engelke, R. Earl, W. L. Rohlffing, C. M. (1986) "Production of the nitromethane Anion by UV irradiation: Its effect on

- detonation sensitivity", J. Phys. Chem. 90, 545-547.
30. Dewar, M. J. S. Ritchie, J. P. and Alster, J. (1985) "Thermolysis of molecules containing NO₂ groups", J. Org. Chem., 50, 1031-1036.
31. Wodtke, A. M. Hints, E. J. and Lee, Y. T. (1986) "The observation of CH₃O in the collision free multiphoton dissociation of CH₃NO₂", J. Chem. Phys. 84, 1044-1045.
32. Bardo, R. D. (1989) "Calculated Reaction Pathways for Nitromethane and Their Role in the Shock Initiation Process", in Proceedings of the Eighth Symposium (Int.) on Detonation, Office of Naval Research, Washington, DC, to be published. Private Communication.
33. Brower, K. (1989) Private Communication.
34. Schroeder, M. A. (1985) "Critical Analysis of Nitramine Decomposition Data: Product Distributions From HMX and RDX Decomposition"; Technical Report BRL-TR-2659, U.S. Army Ballistic Research Laboratory, Aberdeen Proving Ground, MD, June 1985.

MECHANISTIC INVESTIGATIONS OF CONDENSED PHASE ENERGETIC MATERIAL DECOMPOSITION PROCESSES USING THE KINETIC DEUTERIUM ISOTOPE EFFECT

SCOTT A. SHACKELFORD
F.J. Seiler Research Laboratory (AFSC)
Directorate of Chemical Sciences
USAF Academy, CO 80840-6528
USA

ABSTRACT. The condensed phase kinetic deuterium isotope effect (KDIE) approach directly reveals the rate-controlling mechanistic step that ultimately determines the rate at which energy is released by an energetic material's thermochemical decomposition process. This paper reviews the KDIE concept and discusses previous condensed phase KDIE mechanistic investigations conducted during the thermochemical decomposition process of various nitroaromatic (TNT, HNBB, TATB) and nitramine (HMX, RDX) compounds using isothermal DSC and TGA analyses. Isothermal DSC evaluation methods used for obtaining an energetic compound's KDIE and in determining its rate-controlling step are outlined, and the possible dependence of the rate-limiting step on an energetic compound's physical state during the thermochemical decomposition process is considered.

1. Introduction

Thermally initiated decomposition of an energetic material is an extremely complex process involving numerous sequential and parallel chemical reactions. Of all the chemical reactions contributing to the thermochemical decomposition process, one reaction will progress more slowly than all others. This slowest chemical reaction is perhaps the most important one taking place because it contains the rate-controlling mechanistic step. It is this rate-controlling step that ultimately determines the overall rate at which an exothermic decomposition proceeds by kinetically regulating an energetic compound's rate of energy release. By using the kinetic deuterium isotope effect (KDIE) approach, this slow rate-controlling step is selectively identified during the thermochemical decomposition itself, despite the presence of the numerous other participating chemical reactions, and is observed only if the deuterium labeled site of a compound or a position in the near vicinity of the deuterium atom, participates in the slowest chemical reaction's rate-controlling step along a given mechanistic pathway. The KDIE is observed by comparing differences in reaction rates between a normal hydrogen atom containing energetic compound and this same compound's isotopically substituted deuterium analogue.

Although mainly used in more easily defined gas phase and solvolyzed

chemical reaction systems, application of the KDIE approach to neat condensed phase (solid, mixed melt, liquid) energetic compounds permits the direct, non-intrusive, in-situ identification of the rate-controlling mechanistic step during the thermochemical decomposition process itself. Sometimes also referred to as the rate-determining step or rate-limiting step, the mechanistic rate-controlling step results from the dissociation of chemical bonds or attractive interactions; but, it is necessary to realize in the case of a chemical bond rupture, that the rate-controlling mechanistic step may not be the first chemical bond dissociation to occur along a given mechanistic pathway. The first chemical bond rupture in an energetic compound may affect the specific mechanistic pathway a decomposition process will follow; however, the rate-controlling chemical bond rupture occurs somewhere along the mechanistic pathway and determines the energy release rate and overall velocity of the thermochemical decomposition process. Condensed phase KDIE investigations of various energetic materials selectively reveal two new mechanistic insights about the thermochemical decomposition process. First, the rate-controlling step can be dependent upon an energetic compound's predominant physical state; and secondly, extension of condensed phase KDIE investigations into more hostile high energy incidents suggest the thermochemical decomposition process can mirror the mechanistic rate-controlling steps present in more drastic rapid pyrolytic decomposition/deflagration, combustion, thermal explosion, and detonation incidents.

This paper addresses the concept of the KDIE itself and outlines the use of the condensed phase KDIE approach for determining the mechanistic rate-controlling step in thermochemical decomposition process of various energetic compounds and their deuterium labeled analogues. Instrumental methods employed and isothermal DSC data evaluation techniques used with these condensed phase KDIE mechanistic investigations are also discussed. The second companion paper, "Mechanistic Relationships of the Decomposition Process to Combustion and Explosion Events from Kinetic Deuterium Isotope Effect Investigations," reviews extensions of the condensed phase KDIE into more hostile higher pressure/temperature/rate incidents wherein mechanistic comparisons can be made with the thermochemical decomposition process using the KDIE determined rate-controlling step as a common experimental parameter.

2. Discussion

2.1 KINETIC DEUTERIUM ISOTOPE EFFECT (KDIE) CONCEPT

When a normal hydrogen atom is replaced by a heavier deuterium atom in a given chemical compound, a difference in reaction rate is observed if the newly labeled chemical bond, or a bond in the near vicinity, ruptures during the slowest chemical reaction step. This rate variation between the normal and deuterium labeled compound originates from the difference in ground state or zero-point vibrational energy between a compound's carbon-hydrogen (C-H) and identical but stronger carbon-deuterium (C-D) bond as illustrated by the normal HMX and perdeuterio-substituted HMX-d₈ chemical structures (Figure 1). Note the C-D bond has a lower zero-point vibrational energy level than the analogous C-H bond; this zero-point vibrational energy difference at approximately 2.3

Kcal/mol¹, is a direct consequence of the deuterium atom's higher mass compared to the lighter hydrogen isotope.^{2,3} During a single stepwise chemical reaction, or during a chemical reaction that is one of many sequential reactions during a complex chemical process, dissociation or rupture of the lower energy C–D bond proceeds in a less facile manner than its analogous higher energy C–H bond. Because the C–D bond initially begins at a 2.3 Kcal/mol lower zero-point vibrational energy, it requires a higher energy of activation to reach the reaction's transition state; this results in a slower reaction rate (k_d) for the deuterium labeled compound so that k_h/k_d defines a KDIE greater than one.

DISSOCIATION BOND ENERGY: C–D > C–H

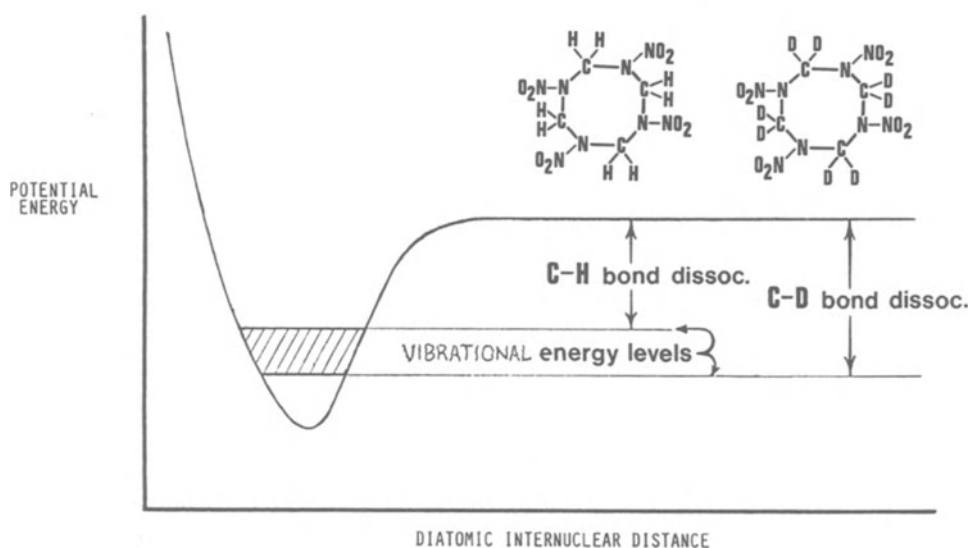


Figure 1. Potential energy curve for the C–H and C–D bond with HMX and HMX–d₃ chemical structures.

The KDIE value normally is expressed as a ratio between reaction rate constants of the normal C–H compound and its C–D labeled analogue. While k_h/k_d rate constants are most often used, inverse induction period times t_d/t_h ^{5,6} critical temperature T_{ch}/T_{cd} ^{6,7} burn rates r_{bh}/r_{bd} ⁸, and impact sensitivity V_d/V_h ^{9,10} can be used since they all are dependent upon the global decomposition rate of the given energetic compound. This is especially important in chemical reactions or processes when one cannot directly obtain an experimental rate constant (k).^{5,7-10} There are three characteristics regarding the KDIE which one must remember, especially as it might apply to the complex thermochemical decomposition process of an energetic material:

(1) A KDIE is observed only during the slowest step in a given chemical reaction; or in the slowest chemical reaction of a multi-reaction process; therefore, a KDIE defines the rate-controlling step of a chemical reaction or process;

(2) The rate-controlling step may not be the first step in a chemical reaction sequence or mechanistic pathway; but, the rate-controlling step is often mistakenly assumed to be the initial step;

(3) The magnitude of the KDIE generally decreases with increasing reaction temperature; KDIE values ranging from 2.5 to 8 are normally seen at standard temperature.^{1, 3, 11}

There are three types of KDIE possible, and these are illustrated using the HMX molecular structure (Figure 2). Direct C-H/C-D bond rupture during the rate-controlling step produces a primary (1°) KDIE where the ratio of HMX/HMX- d_8 rate differences would give a value greater than the theoretically minimum 1.41 value at an infinitely high temperature limit²; however, a value of 1.35 is an acceptable experimental lower limit for a 1° KDIE.^{3, 12-14} Rupture of either bond adjacent to the C-H/C-D bond or one bond further away respectively provides an alpha or beta secondary (2°) KDIE whose values theoretically could lie between 1.01 and 1.34. Normally α 2° KDIE values range

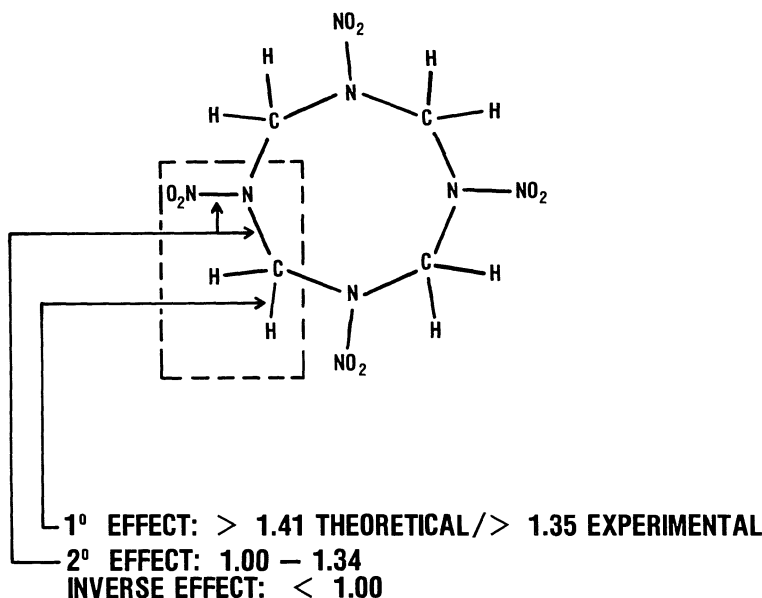


Figure 2. Possible KDIE types illustrated with the HMX chemical structure or structural fragment.

from 1.15 to 1.25 at standard temperature (298K) while β 2° KDIE values stay around a 1.1 ratio.³ The minimum infinitely high temperature value for a 2° KDIE would be one (1.00).^{3, 4} Collectively, the 1° KDIE and 2° KDIE are sometimes referred to as normal or positive isotope effects because their magnitudes are greater than one (1.00). Finally, a third type of KDIE can occur where a KDIE value less than 1.00 indicates an inverse KDIE (i -KDIE). While the theory describing KDIE behavior can be quite complex; generally, both 1° and 2° KDIE values decrease with higher reaction temperatures²⁻⁴ when the

rate-controlling step involves a covalent bond dissociation or rupture proceeding through in a fairly linear transition state^{2,10,15}. The condensed phase KDIE investigations described for energetic material thermochemical decomposition differ greatly from more traditional mechanistic KDIE investigations in two main respects. First, much higher temperatures are encountered; and secondly, the energetic compounds react in the complex multi-reaction condensed phase process rather than under simpler, more easily controlled solvolyzed or gas phase reaction conditions. Application of the condensed phase KDIE to the high temperature thermochemical decomposition process occurs in a much more hostile chemical environment; and, in this respect, reaches into a new relatively unexplored experimental regime.

2.2 NITROAROMATIC CONDENSED PHASE KDIE STUDIES

The first mechanistic application of the condensed phase KDIE approach to the thermochemical decomposition of an energetic material was conducted with liquid 2,4,6-trinitrotoluene (TNT) and its α , α , α -trideuteriomethyl labeled analogue (TNT-d₃) using isothermal differential scanning calorimetry (IDSC) analysis. This study revealed the first direct experimental evidence that covalent

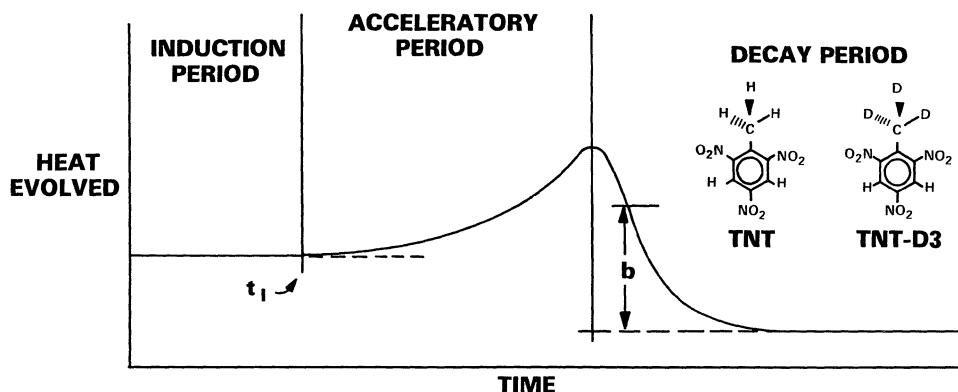


Figure 3. Generalized isothermal DSC curve for either the liquid TNT or liquid TNT-d₃ thermochemical decomposition process.⁵

homolytic C-H bond rupture in the TNT methyl group constitutes the rate-controlling step of its thermochemical decomposition process.⁵ Figure 3 displays a generalized IDSC curve for the TNT thermochemical decomposition in which the heat evolved (y-axis) is measured against time (x-axis) at constant temperature. Because this ambient pressure liquid phase decomposition (mp TNT = 81–82°C) follows pseudo first order kinetics, the IDSC curve's deflection height (b) above the base line at any given time (t) is directly proportional to the rate of TNT heat energy evolution, which in turn, is directly proportional to TNT's rate of reaction or rate of disappearance as TNT converts to other decomposition products. This means that $\ln b = kt$ takes on the form of a first

order rate equation and shows that the rate constant of a TNT or TNT- d_3 decomposition can be obtained directly from a linear plot of $\ln b$ vs time where the rate constant ($-k$) is the slope of the line.¹⁶ This simplified determination of rate constants by IDSC, however, is valid only in cases where a decomposition follows first order or pseudo first order kinetics.¹⁷

Following IDSC data analysis convention, the TNT and TNT- d_3 rate constants evaluated during the decay phase of the thermochemical decomposition process (Figure 3), provides an averaged k_h/k_d KDIE value of 1.35 ± 0.02 at temperatures ranging from 245 – 269°C (518–542 K).⁵ From this borderline 1° KDIE value, several important observations emerge. TNT forms mainly condensed phase decomposition products (Figure 4); these remain in the liquid melt phase and undergo further decomposition themselves^{18, 19}. Some of these isolated products 5, 6, do not involve a potential rate-controlling C–H bond rupture. Because IDSC measures the total rate of all contributing chemical

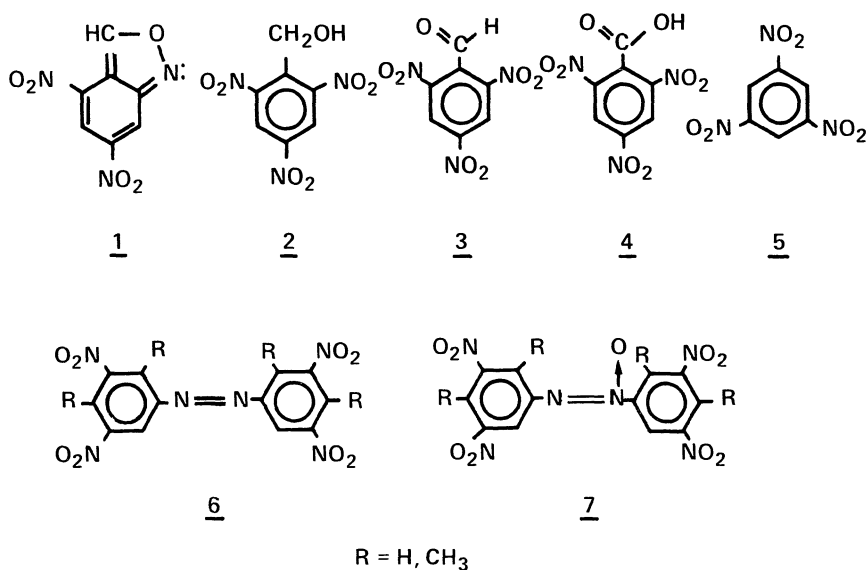


Figure 4. Isolated condensed phase products from the liquid TNT thermochemical decomposition process.^{5, 18}

reactions during the TNT decomposition process, and because those reactions not involving a rate-controlling C–H bond rupture would contribute a factored k_h/k_d KDIE ratio of 1.00 to the overall measured k_h/k_d KDIE of 1.35, the 1.35 KDIE value is diluted or masked from its true higher value.⁵ Therefore, the TNT rate-controlling step is detected earlier in the decomposition process before other subsequent condensed phase reactions could interfere with the true KDIE value. This early detection is justified by two other observations. First, a high pressure liquid chromatography (HPLC) analysis of TNT samples quenched during the seemingly innocuous induction period (Figure 3), reveals trace level formation of a new compound 1 from TNT. Secondly, when this unidentified

trace compound I is combined with a fresh TNT sample, it catalyzes TNT's autocatalytic decomposition and reduces the induction period (t_i) nearly 2.5 times.⁵ Condensed phase KDIE evaluation of the early induction period cannot be done using k_h/k_d rate constants because rate constants must be evaluated from the IDSC curve's baseline deflection represented by the height of b (Figure 3). The horizontal induction period generates no measureable deflection; however, induction times (t_i) can be used and are conveniently measured from the IDSC curve.⁵ The t_i value even can be used to determine the energy of activation (E_{a_i}) for formation of the catalytic unidentified compound I .²⁰ Two mathematical approximations are invoked to provide equation 1 where k is the rate constant and i_i the small mole fraction of compound I formed at any given induction time, t_i .²⁰ Equation 2 represents the natural logarithmic form of the Arrhenius

$$k = i_i / t_i \quad (1)$$

equation, and equation 3 results from setting equation 2 equal to equation 1's logarithmic form. Equation 3 serves as the starting point for determining TNT's KDIE using induction times of TNT (t_{ih}) and TNT- d_3 (t_{id}). Equation 3 is

$$\ln k = E_{a_i} / RT + \ln Z \quad (2)$$

$$\ln k = \ln i_i - \ln t_i = E_{a_i}/RT + \ln Z \quad (3)$$

rearranged to give equation 4. Assuming the mole fraction (i_i) of compound I must reach a specific threshold concentration²¹ during the induction period

$$\ln i_i = \ln k + \ln t_i \quad (4)$$

(t_i) in order to catalyze TNT's thermochemical decomposition process into its exothermic acceleratory phase (Figure 3), only t_i and k may vary between the normal TNT compound and deuterium labeled TNT- d_3 during the decomposition process. Because i_i reaches a constant threshold concentration,^{5, 21} equation 5 can be written from equation 4, and then simplifies into equation 6, to finally provide equation 7. Equation 7 establishes the necessary relationship between

$$\ln k_h + \ln t_{ih} = \ln i_i = \ln k_d + \ln t_{id} \quad (5)$$

constant

$$\ln k_h + \ln t_{ih} = \ln k_d + \ln t_{id} \quad (6)$$

$$\frac{k_h}{k_d} = \frac{t_{id}}{t_{ih}} \quad (7)$$

the k_h/k_d rate constant ratio and inverse t_{id}/t_{ih} induction time ratio for determining the induction period's KDIE, where a chemical reaction proceeds, but at a small enough extent that its heat release is not detected.⁵ The inverse relationship exhibited by equation 7 makes sense when one notes that a larger rate constant (k_h) represents a faster chemical reaction with a smaller (shorter) induction time (t_{ih}).

A 1° KDIE equal to 1.66 results during the induction time portion of the TNT thermochemical decomposition process. This 1° KDIE value reveals covalent C—H bond rupture in TNT's methyl group is the rate-controlling step; and ultimately, this rate-controlling C—H bond dissociation determines the rate at which the entire exothermic TNT decomposition proceeds and releases its energy.⁵ Most importantly, the induction period KDIE comes only from the decomposition of TNT itself. Further verification comes from a proton nmr analysis of a TNT sample quenched at the maximum energy output of the IDSC curve where the acceleratory phase ends and the decay phase begins. Although only 64% of the total heat was released at this point, 97% of the original TNT is consumed.²² The remaining melt is primarily condensed phase TNT products undergoing further decomposition themselves to form more products during the decay phase (Figure 4). In this case, the decay phase k_h/k_d KDIE and its associated kinetics have little to say about decomposition of TNT itself since most of the TNT is reacted by the time the decay phase of the IDSC curve begins. A study of hydrogen atom versus ionic proton donation to the TNT molecule using hydroquinone and benzoic acid respectively, suggests the TNT methyl group C—H bond rupture is homolytic, involving transfer of a hydrogen atom since a 2% mixture of hydrogen atom donating hydroquinone reduces the induction time to zero, while proton donating benzoic acid has little affect.⁵ Further verification of homolytic C—H bond rupture is found in electron spin resonance (epr) investigations.²³⁻²⁵

The thermochemical decomposition of TNT is controlled by a homolytic, covalent C—H bond rupture in its methyl moiety, and this rate-controlling step occurs very early in its overall thermochemical decomposition process. An intramolecular transfer of a hydrogen atom via the rate-controlling C—H bond rupture to the ortho-nitro group followed by the elimination of H_2O , would provide the isolated 4,6-dinitroanthranil product **1** (Figure 4). An intermolecular hydrogen atom transfer from one TNT molecule during this rate-controlling C—H bond dissociation step would provide a 2,4,6-trinitrobenzyl radical and protonated TNT radical wherein the para-nitro group²⁴ picks up the hydrogen atom (Figure 5). An intermolecular coupling of these two radical species could produce the epr observed 3',5'-dinitro-4'-methyl-2,4,6-trinitrobenzyl nitroxyl radical **9**^{24, 25} (Figure 5) via radical OH elimination, or possibly via the analogous benzyl oxonitroxyl radical **8** which readily converts to the nitroxyl radical at the temperatures needed for the thermally initiated TNT decomposition²⁶. Further reaction of the nitroxyl radical by oxidative cleavage, continued reaction by the 4,6-dinitroanthranil, or progressive oxidation of the trinitrobenzyl radical itself, could produce the other monoaryl products previously isolated and characterized (Figure 4).^{18, 19} Several concepts emerge from this TNT condensed phase KDIE mechanistic investigation that have a general applicability to the thermochemical decomposition process. First, a KDIE can be detected during the complex high temperature thermochemical decomposition process and identifies the specific mechanistic feature that ultimately constitutes the overall process's rate-controlling step. Secondly, this rate-controlling step can occur very early in the thermochemical decomposition process and can involve a slow chemical reaction sequence that proceeds to a minor extent. In other words, the mechanistic rate-controlling step may not occur in the most obvious reaction proceeding to the greatest detectable percentage or extent. Thirdly, KDIE values can be determined by comparing experimental data of the normal and analogous

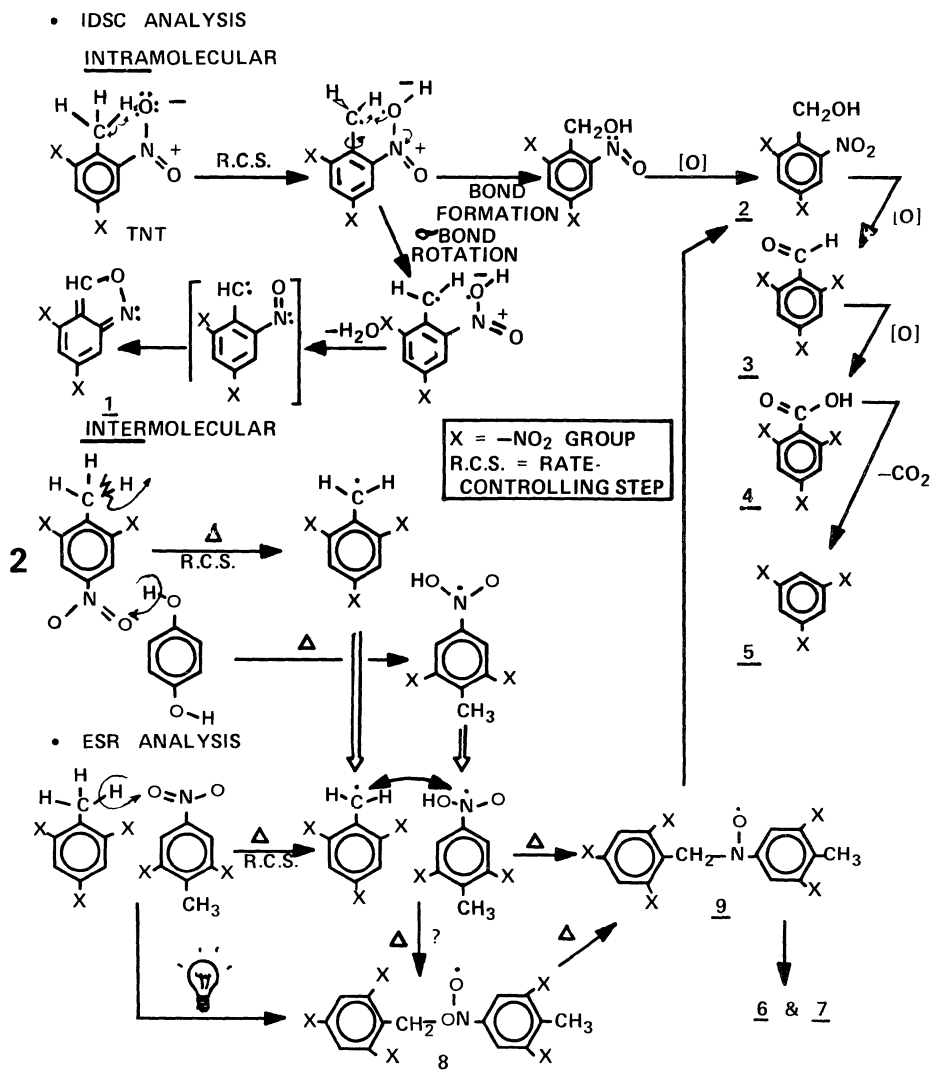


Figure 5. Possible mechanistic aspects of the liquid TNT thermochemical decomposition process.

deuterium labeled energetic compounds which are related to rate constants and reaction rates; that is, other comparative data like induction time ratios can be used in place of conventional rate constant ratios when rate constants cannot be obtained.

Finally, in cases where condensed phase products may be generated from the original decomposing compound, the early stage of the decomposition process is particularly important because further decomposition of these condensed phase products begins interfering with the decomposition reactions of the original compound under investigation; and, this can mask a true 1° KDIE even when it is present.

The compound, 2,2',4,4',6,6'-hexanitrobibenzyl (HNBB), is related in its molecular structure (Figure 6) to TNT, and displays a similar mechanistic behavior in its IDSC analysis. Liquid HNBB and HNBB-d₄ produced a 1° KDIE

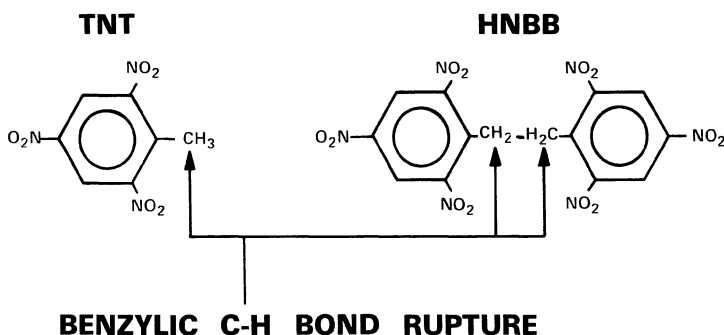


Figure 6. The chemical structures of TNT and HNBB.

equal to 2.44 ± 0.35 during the induction period as well as from its decay phase (2.35 ± 0.41).²⁷ These 1° KDIE values appear over a 248–269°C temperature range and suggest covalent C–H bond rupture at the benzylic position constitutes the rate-controlling step in the liquid HNBB thermochemical decomposition process. This is the same structural position of TNT's rate-controlling C–H rupture.

The highly insensitive 1,3,5-triamino-2,4,6-trinitrobenzene (TATB) and its deuterium labeled amino group analogue (TATB-d₆) have also been studied by IDSC at ambient pressure in a 570–655K temperature range.⁶ Because TATB decomposes in its solid state within this temperature range, a more complex thermochemical decomposition process is encountered (Figure 7). This complexity is reflected in its IDSC curve which displays two consecutive autocatalytic reaction sequences, each with its own maximum peak energy release.^{6, 22} Pseudo first order kinetics are not unsuitable for evaluating this IDSC curve, and an autocatalytic rate plot (Figure 8) must be used where $d\alpha/dt$ is plotted against $\alpha(1-\alpha)$, with α representing the mole fraction of decomposed energetic material (TATB) at any given time (t).²⁸ The term α is found as the progressive Simpson's Rule summation of $\Delta\alpha/\Delta t$ (Figure 7) to provide the partial area (a) under the IDSC curve of TATB divided by the total area (A) or:

$$\alpha = \text{area at time } t / \text{total area} = a/A$$

Because the IDSC measures the total heat evolved by an energetic material, and because this heat evolution is proportional to the global rate at which an energetic material chemically reacts during its decomposition process, the overall

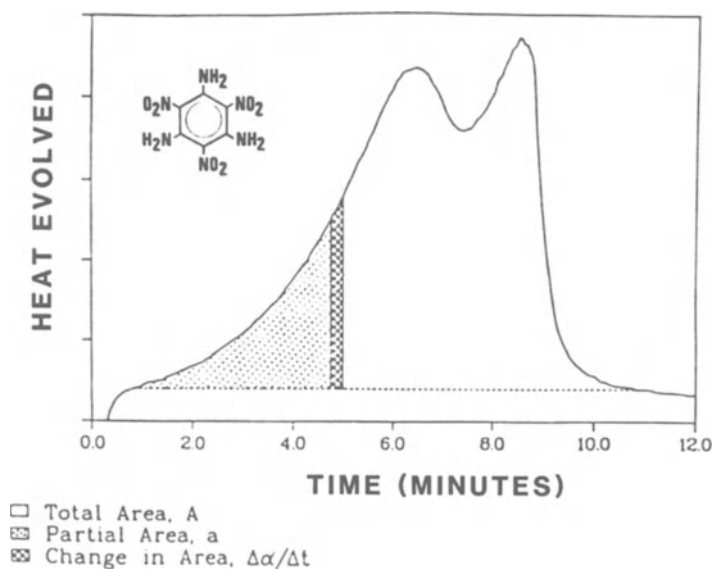


Figure 7. Isothermal DSC curve for either the solid state TATB or solid state TATB- d_6 thermochemical decomposition process^{6, 28} with TATB and TATB- d_6 chemical structure.

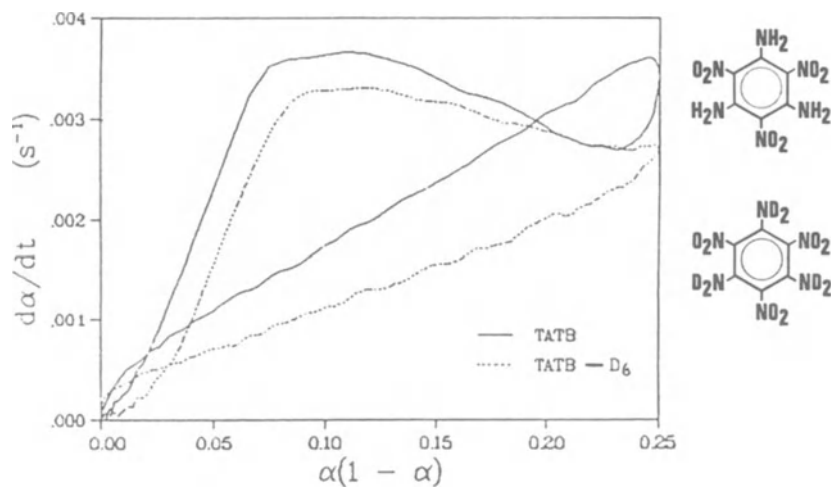


Figure 8. Folded autocatalytic rate plot for both the solid state TATB and the solid state TATB- d_6 thermochemical decomposition process.^{6, 28}

rate of decomposition at any given time (t) is described by the following approximation: $d\alpha/dt = \text{height (h) above baseline at } t/\text{total area} = h @ t/A$, because h is proportional to a very small $\Delta\alpha/\Delta t$ segment,²⁸ especially if one chooses a very small Δt value. The autocatalytic rate plot (Figure 8) for TATB is based upon the specific rate equation⁶ where the slope of any linear segment

$$d\alpha/dt = k\alpha(1 - \alpha) \quad (8)$$

provides the rate constant (k). Two segments of linearity are seen in this type of rate plot where the curve folds back on itself at $\alpha(1 - \alpha) = 0.25$. The two linear segments define a consistent component reaction where a single mechanism likely predominates during the linear portion of the complex decomposition process. Further verification of a consistent mechanism in this portion of the IDSC curve would be achieved if this linear portion remains when separate isothermal IDSC decomposition runs are conducted over a wide temperature range.⁶ An early linear segment occurs during the first autocatalytic solid state reaction sequence prior to reaching the first energy release maximum. This first linear segment displays a difference in slope between TATB and TATB- d_6 where k_h/k_d is about 1.5 and reveals a 1° KDIE.⁶ The second linear segment occurs in the decay period of the second autocatalytic reaction sequence beyond the second energy release maximum and shows no TATB/TATB- d_6 slope difference ($k_h/k_d = 1.00$), and no KDIE. The 1° KDIE suggests that solid state covalent N-H bond rupture in TATB's amino moiety constitutes the rate-controlling step early in its global thermochemical decomposition process. This finding is supported by elemental analysis showing the decomposed TATB residue is nearly devoid of hydrogen atoms during this final decomposition curve portion where no KDIE is observed.⁶ More recent thin-layer chromatography (TLC) elution of the decomposed TATB, followed by chemical ionization mass spectral (CEMS) and x-ray photoelectron spectroscopy (XPS) analyses of the TATB decomposition products, reveal three compounds in which hydrogen atoms are lost.²⁹ These three furazan products apparently form by the loss of H_2O with cyclization of adjacent amino and nitro pendant groups (Figure 9). This loss of H atom by amino group again is consistent with the 1° KDIE and rate-controlling step N-H bond rupture found in the early portion of the solid state TATB decomposition process.

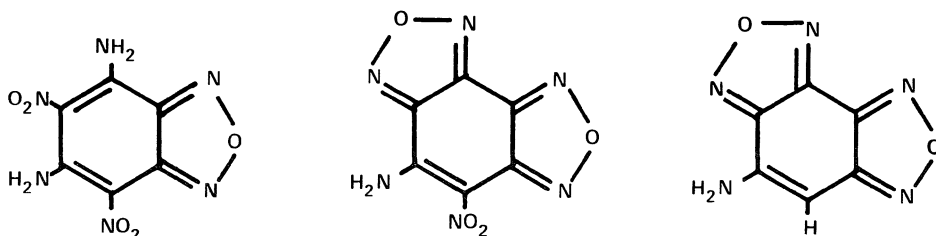


Figure 9. Isolated furazan products of the TATB thermochemical decomposition process showing loss of H atoms by N-H bond rupture.²⁹

2.3 NITRAMINE CONDENSED PHASE KDIE STUDIES

The thermochemical decomposition process followed by the two most prominent nitramines, octahydro-1,3,5,7-tetranitro-1,3,5,7-tetrazocine (HMX) and its six-membered cyclic analogue, hexahydro-1,3,5-trinitro-1,3,5-triazocine (RDX) is still not well understood and continues to be a matter of spirited mechanistic discussion. Recent condensed phase KDIE investigation of the HMX thermochemical decomposition process by IDSC possibly reveals one reason why.⁷ An examination of the HMX molecular structure reveals several different positions where bond rupture during a rate-controlling step would provide a different type of KDIE (Figure 2). Indeed, when HMX and HMX-d₈ are investigated by IDSC, three dissimilar KDIE values are found over the entire decomposition process; and each occurs in a different physical state (Figure 10, top).⁷

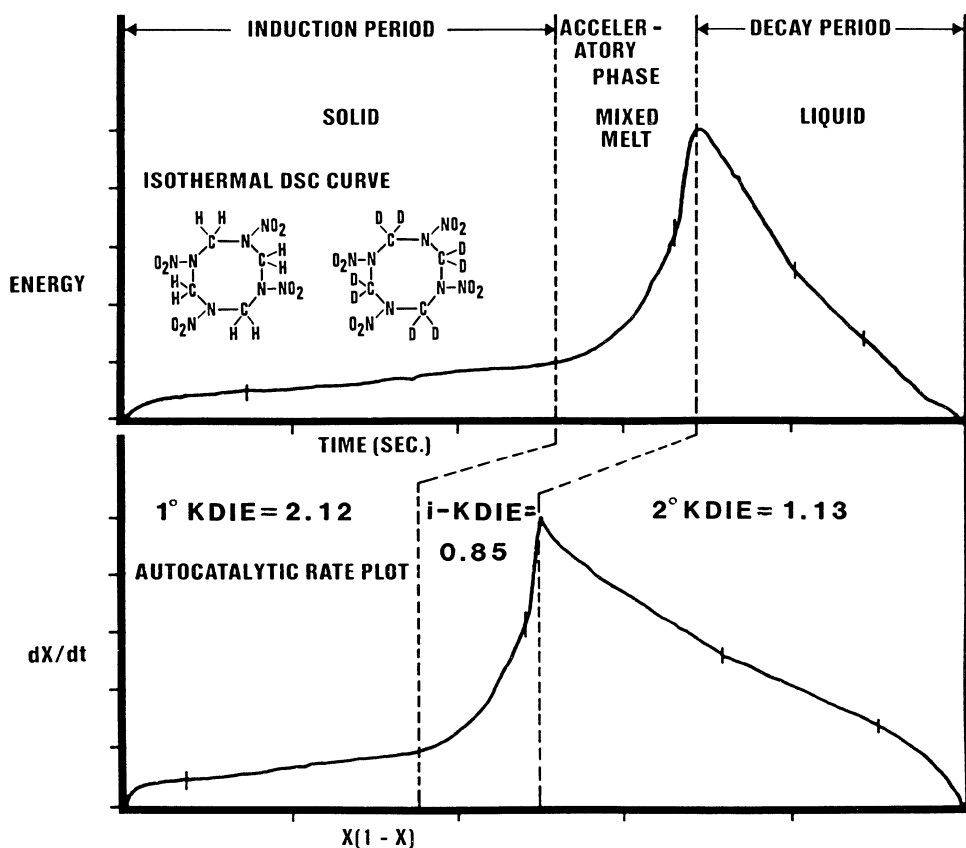


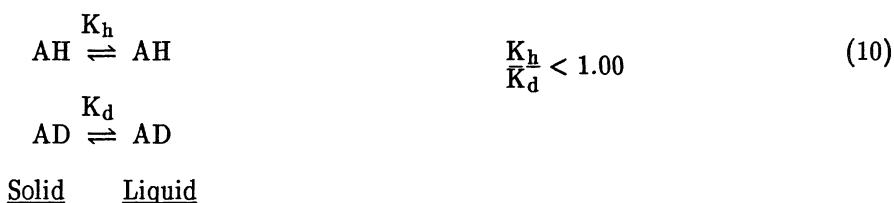
Figure 10. (TOP) Isothermal DSC curve of the HMX thermochemical decomposition process. (BOTTOM) Unfolded autocatalytic rate plot of the HMX thermochemical decomposition curve.⁷

Like TATB, the HMX thermochemical decomposition curve (Figure 10, top) fits an autocatalytic rate plot (Figure 10, bottom), which in this case is an unfolded representation. This unfolded autocatalytic rate plot [$x = \alpha =$ the mole fraction of decomposed HMX at various times (t)] displays three linear segments that likely represent a consistent mechanistic feature for each. Like liquid TNT and HNBB, the HMX IDSC curve consists of an induction period, acceleratory phase, and decay period, but unlike, liquid TNT, HNBB, or solid TATB where the decomposition was investigated in one physical state, HMX decomposition progresses through three different physical states, each of which correlate with one of the linear autocatalytic rate plot segments. These three physical states were verified visually by observing liquid N_2 quenched IDSC samples with a microscope and with scanning electron microscope pictures. The induction period corresponds to solid state HMX decomposition and contains the first linear segment in the autocatalytic rate curve (Figure 10, bottom). Induction time ratios of HMX and HMX- d_8 over a 278–280°C (551–553K) temperature range (mp HMX = 282°C)³⁰ provide a t_{id}/t_{ih} equal to 2.12. This 2.12 KDIE value corresponds to a high temperature 1° KDIE and indicates that covalent C–H bond rupture is the rate-controlling step of solid state HMX decomposition.⁷

The acceleratory phase results when HMX begins melting and ends at the maximum point of heat energy release where the HMX sample is totally liquefied. The acceleratory phase exhibits a short linear segment just before the peak of its heat energy release, and the HMX/HMX- d_8 slopes of this linear segment exhibit a KDIE value less than one (0.85).⁷ Because the KDIE results from force constant changes between the ground state and activated complex in a chemical reaction,³¹ this inverse KDIE suggests the C–D bond's force constant is increasing at a faster rate than the C–H force constant as the highly oriented intermolecular crystal lattice forces are thermally overcome to produce liquefaction. Because the C–D with its heavier deuterium atom is already at a lower vibrational energy than its analogous C–H bond, one would expect the C–D bond would contract more readily as its force constant increases and provide the observed i -KDIE.^{7,32} Among the many attractions intermolecular in the HMX crystal lattice,³³ the inverse KDIE is specific only to its solid state intermolecular hydrogen bonds³⁴ and results from a shortening of the C–D or C–H bond as the highly oriented solid state intermolecular hydrogen bonds are thermally weakened.⁷ From a qualitative viewpoint³, the heavier deuterium atom concentrates itself at a molecule's site where it is most strongly bonded and where its force constant is largest. In the case of an actual chemical reaction, the deuterium atom favors the reactant where the force constant is larger, while the higher energy hydrogen atom, relative to the deuterium atom, prefers the transition state where the force constant is lower. Therefore, the normal unlabeled compound will proceed faster through the chemical reaction to reach the transition state and give a positive KDIE. For an equilibrium reaction,³ the deuterium isotope still prefers the situation where its more strongly bonded. If its force constant is higher in AD than in BD, the deuterium isotope prefers AD. Relative to its deuterium isotope, the hydrogen atom, however, prefers BH where force constants are lower, and K_h/d will be greater than one (positive KDIE).³



This same equilibrium reasoning applies to a melting organic compound. The portion of HMX or HMX- d_8 molecules not yet undergoing decomposition during liquifaction, would possess C-H or C-D bonds with higher force constants in the liquid phase where opposing intermolecular hydrogen bonding attractions would be weaker than in the rigid, highly ordered solid state crystal lattice.⁷ In this situation, the force constant of the C-D bonds in AD would be higher in the liquid state from bond contraction than in the solid phase; but, because the heavier D atom concentrates itself where it is most strongly bonded, relative to the lighter H atom, the stronger C-D bond would favor the more strongly bonded AD liquid state to a greater degree than the weaker C-H bond prefers A-H. Therefore, liquid AD would form more readily than liquid AH at any given instant in time and the K_h/K_d ratio will be less than one (*i*-KDIE) because K_d would be larger than K_h .



Upon achieving complete liquefaction, the HMX decomposition enters the decay period where the autocatalytic rate curve reveals a third linear segment. A 2° KDIE with a k_h/k_d ratio equal to 1.13 results and provides evidence that covalent ring C-N bond rupture constitutes the rate-controlling step in liquid phase HMX decomposition.⁷ Assignment of the rate-controlling ring C-N bond rupture as a true 2° KDIE and not as a masked or diluted 1° KDIE, as in TNT's decay period, is confirmed by comparative HPLC determined HMX concentration and HMX weight loss measurements on liquid N₂ quenched IDSC samples taken at different times along the decomposition curve. The visual absence of any condensed phase decomposed product in the IDSC sample pan at the completion of the decomposition run also supports this 2° KDIE assignment.⁷

The appearance of three different types of KDIE, each during the HMX thermochemical decomposition in dissimilar condensed phases (solid, mixed melt, liquid), shows that HMX does not decompose by a single mechanistic pathway; rather, HMX thermochemical decomposition is a chemical process consisting of at least three different mechanistic pathways, each with its own rate-controlling step that is dependent upon the predominant HMX physical state. The rate-controlling step in solid state decomposition is covalent C-H bond rupture (1° KDIE); the mixed melt phase apparently is controlled by the rate at which the attractive intermolecular crystal lattice forces are weakened by thermal activation (*i*-KDIE), and covalent ring C-N bond rupture is the rate-controlling step (2° KDIE) for the liquid phase. Further verification of the HMX's rate-controlling solid state C-H bond rupture comes from an HMX/HMX- d_8 thermochemical decomposition investigation using the isothermal thermal gravimetric analysis (TGA) method¹⁰. TGA assumes the reaction rate is proportional to a compound's weight loss as a function of time, and is valid for compounds like HMX or RDX where decomposition produces gaseous rather than condensed phase products. Induction period I_d/I_h ratios determined by TGA over a 235–254°C (508–527 K) temperature range for HMX and HMX- d_8 gives

an average KDIE value equal to 1.91 and defines a 1° KDIE. TGA rate constant ratios (k_h/k_d) taken between 235–282°C (508–555K) at the 25 percent sample decomposition point also produce an average 1° KDIE (2.07) value.¹⁰

The two dimensional chemical structure of the eight-membered cyclic HMX/HMX- d_8 molecule and its six-membered cousin RDX/RDX- d_6 are similar (Figure 11), but their chemical behavior sometimes differs. One

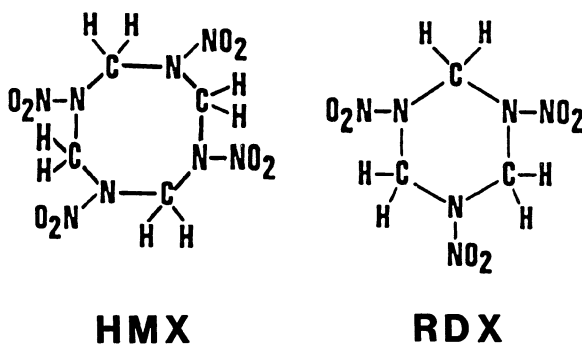


Figure 11. The HMX and RDX chemical structures.

difference is displayed in its thermochemical decomposition. Both TGA¹⁰ and IDSC³⁵ have been used in mechanistic KDIE investigations of RDX and its RDX- d_6 deuterium labeled analogue. Isothermal TGA provides an average 1° KDIE value of 1.54 between 206–216°C (429–489 K) for the liquid phase RDX thermochemical decomposition (mp RDX = 203°C or 476 K), and a 1° KDIE value of 1.51 for apparent solid state RDX decomposition between 199–202°C (392–475 K).¹⁰ This suggests both the RDX solid and liquid thermochemical decomposition processes have covalent C–H bond rupture as the rate-controlling mechanistic step. Mechanistic IDSC investigation of liquid phase RDX and RDX- d_6 at 237°C (510K) produces a pseudo first order rate whose k_h/k_d rate constant ratio gives a 1° KDIE equal to 1.74 ± 0.2 and again confirms that covalent C–H bond rupture is the rate-controlling step for RDX liquid state decomposition.³⁵ This result from both TGA¹⁰ and IDSC³⁵ investigations contrasts with the IDSC⁷ determined HMX result. While covalent C–H bond rupture seems to be the rate-controlling step in the liquid phase RDX decomposition process,^{10,35} covalent ring C–N ring bond rupture is the rate-controlling step for liquid phase HMX.⁷ Both HMX and RDX appear to exhibit the same rate-controlling C–H bond rupture in their solid state thermochemical decomposition process.^{7,10}

3. Conclusion

The kinetic deuterium isotope effect (KDIE) selectively identifies the slowest rate-controlling mechanistic step amid the numerous chemical reaction sequences that drive the complex thermochemical decomposition process followed by energetic materials. This kinetically based rate-controlling mechanistic step ultimately determines the rate at which the overall thermochemical

decomposition process and its associated energy release may proceed. Condensed phase KDIE mechanistic investigations of various energetic materials (TNT, HNBB, TATB, HMX, RDX) and their analogous deuterium labeled compounds, (TNT-d₃, HNBB-d₄, TATB-d₆, HMX-d₈, RDX-d₈), are easily accomplished using isothermal differential scanning calorimetry (IDSC) and isothermal thermogravimetric analysis (TGA) methods. Condensed phase KDIE investigations conducted by IDSC analysis reveal that covalent chemical bond rupture, or in one case, destruction of attractive intermolecular crystal lattice forces, cause this rate-controlling mechanistic step in the thermochemical decomposition process. The rate-controlling step can show a mechanistic dependence on an energetic compound's physical state and change as the energetic compound moves from one physical state to another. This demonstrates that thermochemical decomposition should not be pictured as having a single mechanistic pathway; rather it is a complex chemical process that may involve several potential mechanistic pathways, each with its own rate-controlling step. Various kinetically determined experimental parameters can be used to identify the KDIE from which one identifies the rate-controlling step in an energetic compound's thermochemical decomposition process. These include rate constants, induction times, critical temperatures, burn rates, and impact sensitivities which are all related directly or indirectly to kinetic reaction rates. The condensed phase KDIE approach can be extended from the milder thermochemical decomposition process into more drastic high energy incidents that all likely involve a rapid pyrolytic decomposition/deflagration of an energetic material. The KDIE determined rate-controlling step, therefore, provides a common experimental feature for comparing mechanistic similarities or differences among various drastic high energy phenomena represented by rapid pyrolytic decomposition/ deflagration, combustion, thermal explosion and detonation. This is addressed in the follow-on paper entitled, "Mechanistic Relationships of the Decomposition Process to Combustion and Explosion Events from Kinetic Deuterium Isotope Effect Investigations".

4. Acknowledgements

The Air Force Office of Scientific Research/Directorate of Chemical and Atmospheric Sciences (Director, Dr Don L. Ball) is gratefully acknowledged for funding the portions of research described herein conducted at the F.J. Seiler Research Laboratory (1975-78) and Astronautics Laboratory (1981-85) by the author and his referenced colleagues. Long-time scientific colleague Raymond N. Rogers generously has provided valuable guidance and advice on IDSC kinetic data evaluation techniques for many years. Mrs Linda Pukajlo and the USAF Academy's Directorate of Audio Visual Services assisted in camera-ready manuscript preparation; Mr J.E. Pflug and Dr Clay M. Sharts assisted with manuscript review. The author wishes to thank the Director of NATO ASI on Chemistry and Physics of the Molecular Processes in Energetic Materials, Dr Surya N. Bulusu, for this lectureship opportunity and partial financial support which made presentation of this paper possible.

5. References and Notes

1. N.L. Allinger, M.P. Cava, D.C. DeJongh, C.R. Johnson, N.A. Lebel, C.L. Stevens, *Organic Chemistry*, Worth Publishers, Inc., 1971, pp. 300–301.
2. J. Bigeleisen, M. Wolfsberg, "Theoretical and Experimental Aspects of Isotope Effects in Chemical Kinetics", in *Advances in Chemical Physics*, Vol 1, Ed I., Prigogine, Interscience Publishers, Inc., New York, 1958, pp. 15–31.
3. T.H. Lowry, K.S. Richardson, *Mechanism and Theory in Organic Chemistry*, Harper and Row, 2d ed, New York, 1981, pp. 206–208, 211–212.
4. J. Bigeleisen, private communication (Jun 1989).
5. S.A. Shackelford, J.W. Beckmann, J.S. Wilkes, "Deuterium Isotope Effects in the Thermochemical Decomposition of Liquid 2,4,6–Trinitrotoluene: Application to Mechanistic Studies Using Isothermal Differential Scanning Calorimetry Analysis", *J. Org. Chem.*, **42**, 4201–4206, (1977).
6. R.N. Rogers, J.L. Janney, M.H. Ebinger, "Kinetic Isotope Effects in Thermal Explosions", *Thermochim. Acta*, **59**, 287–298, (1982).
7. S. A. Shackelford, M.B. Coolidge, B.B. Goshgarian, B.A. Loving, R.N. Rogers, J.L. Janney, M.H. Ebinger, "Deuterium Isotope Effects in Condensed–Phase Thermochemical Decomposition Reactions of Octahydro–1,3,5,7–tetranitro–1,3,5,7–tetrazocine", *J. Phys. Chem.*, **89**, 3118–3126 (1985).
8. S.A. Shackelford, B.B. Goshgarian, R.D. Chapman, R.E. Askins, D.A. Flanigan, R.N. Rogers, "Deuterium Isotope Effects during HMX Combustion: Chemical Kinetic Burn Rate Control Mechanism Verified", *Prop., Explos., Pyrotech.*, **14**, 93–102 (1989).
9. S. Bulusu, J.R. Autera, "Initiation Mechanism of TNT: Deuterium Isotope Effect as an Experimental Probe", *J. Energetic Matls.*, **1**, 133–140 (1983).
10. S. Bulusu, D.I. Weinstein, J.R. Autera, R.W. Velicky, "Deuterium Kinetic Isotope Effect in the Thermal Decomposition of 1,3,5–Trinitro–1,3,5–triazacyclohexane and 1,3,5,7–tetranitro–1,3,5,7–tetrazacyclooctane: Its Use as an Experimental Probe for Their Shock–Induced Chemistry", *J. Phys. Chem.*, **90**, 4121–4126 (1986).
11. G.W. Klumpp, *Reactivity in Organic Chemistry*, Wiley–Interscience, New York, 1982, p. 262.
12. A. Streitweiser, R.H. Jagow, R.C. Fahey, S. Suzuki, "Kinetic Isotope Effects in the Acetolyses of Deuterated Cyclopentyl Tosylates", *J. Am. Chem. Soc.*, **80**, 2326–2332 (1958).
13. G. Herzberg, *Molecular Spectra and Molecular Structure*, Vol II, Van Nostrand Co., Inc., New York, 1950, pp. 217.

14. E.K. Thornton, E.R. Thornton, "Origin and Interpretation of Isotope Effects", in *Isotope Effects in Chemical Reactions*, Eds. C.J. Collins and N.S. Bowman, Van Nostrand Reinhold Co., New York, 1970, pp. 215–216.
15. H. Kwart, D.A. Benko, M.E. Bromberg, "Geometry of Transition States Involving Allylic Hydrogen Abstraction Elucidated by Isotope Effect Studies", *J. Am. Chem. Soc.*, **100**, 7093–7094 (1978).
16. R.N. Rogers, "Simplified Determination of Rate Constants by Scanning Calorimetry", *Anal. Chem.*, **44**, 1336–1337 (1972).
17. R.N. Rogers, private communication (May 1989).
18. R.N. Rogers, "Combined Pyrolysis and Thin Layer chromatography: A Method for the Study of Decomposition Mechanisms", *Anal. Chem.*, **39**, 730–733 (1967).
19. J.C. Dacons, H.G. Adolph, M.J. Kamlet, "Some Novel Observations Concerning the Thermal Decomposition of 2,4,6-Trinitrotoluene", *J. Phys. Chem.*, **74**, 3035–3040 (1970).
20. J.W. Beckmann, J.S. Wilkes, R.R. McGuire, "2,4,6-Trinitrotoluene Thermal Decomposition: Kinetic Parameters Determined by the Isothermal Differential Scanning Calorimetry Technique", *Thermochim. Acta*, **19**, 111–118 (1977).
21. E. Swinborn, *Analysis of Kinetic Data*, Appleton–Century–Crofts, New York, 1971, p. 47.
22. J.L. Janney, R.N. Rogers, "Experimental Thermochemical Observations of Condensed-Phase Reactions", *Proceed. 11th No. Am. Thermal Anal. Soc. Conf., Vol II*, 643–649 (Oct 1982).
23. E.G. Janzen, "Spontaneous Free-Radical Formation in the Pyrolysis of Nitroaromatic Compounds", *J. Am. Chem. Soc.*, **87**, 3531–3532 (1965).
24. J.T. Swanson, L.P. Davis, R.C. Dorey, W.R. Carper, "An EPR Study of the Thermal Decomposition of 2,4,6-Trinitrotoluene and its Isotopic Analyses", *Mag. Res. Chem.*, **24**, 762–767 (1986).
25. T.M. McKinney, L.F. Warren, I.B. Goldberg, J.T. Swanson, "EPR Observation of Nitroxide Free Radicals during Thermal Decomposition of 2,4,6-Trinitrotoluene and Related Compounds", *J. Phys. Chem.*, **90**, 1008–1011 (1986).
26. J.A. Menapace, J.E. Marlin, "Photochemical Decomposition of Energetic Materials: Observation of Arylbenzyloxynitroxyl and Arylbenzylinitroxyl Radicals in Solutions of 1,3,5-Trinitrotoluene and Toluene and their Deuteriated Analogues at 200 K", *J. Phys. Chem.*, in press.

27. S.A. Shackelford, J.W. Beckmann, J.S. Wilkes, M.L. Gunziger, "Deuterium Isotope Effects in the Thermochemical Decomposition of Liquid Nitroaromatics: Application to Mechanistic and Synthetic Considerations in Energetic Materials", 7th Nitroaromatic Seminar, ARDEC, Picatinny Arsenal, NJ (Oct 1977).
28. R.N. Rogers, "Quantitative Evaluation of Thermal Hazards", RCEM Report A-04-87, 15-65 (4 Nov 1987); RCEM, New Mexico Tech, Socorro, NM 87801, USA.
29. J. Sharma, J.C. Hoffsommer, D.J. Glover, C.S. Coffey, F. Santiago, "Comparative Study of Molecular Fragmentation in Sub-Initiated TATB caused by Impact, UV, Heat and Electron Beams", in *Shock Waves in Condensed Matter*, Eds. J.R. Asay, R.A. Graham, G.K. Straub, Elsevier Science Publishers, Amsterdam, 1983, pp. 543-546.
30. In reference 3, the DSC instrument was calibrated using 555K (282°C) as the HMX melting point.
31. W.A. Van Hook (1970) "Kinetic Isotope Effects: Introduction and Discussion of Theory", in *Isotope Effects in Chemical Reactions*, Eds. C.J. Collins, and N.S. Bowman, Van Nostrand Reinhold Co., New York, pp. 39.
32. R.N. Rogers, J.L. Janney, "The Thermal Decomposition of HMX: Kinetic-Isotope-Effect Observations", Proceed. 12th No. Am. Thermal Anal. Soc. Conf., 474-477 (Sep 1983).
33. T.B. Brill, R.J. Karpowicz, "Solid Phase Transition Kinetics. The Role of Intermolecular Forces in the Condensed-Phase Decomposition of Octahydro-1,3,5,7-tetranitro-1,3,5,7-tetrazocine", J. Phys. Chem., **86**, pp. 4260-4265 (1982).
34. H.H. Cady, A.C. Larson, D.T. Cromer, "The Crystal Structure of α -HMX and a Refinement of the Structure of β -HMX", Acta Crystallogr., **16**, 617-623 (1963).
35. S.A. Shackelford, S.L. Rodgers, M.B. Coolidge, "Deuterium Isotope Effects in RDX Decomposition and Combustion Processes: A Progress Report", CPIA Publ. 412, II, 615-621 (Oct 1984).

MECHANISTIC RELATIONSHIPS OF THE DECOMPOSITION PROCESS TO COMBUSTION AND EXPLOSION EVENTS FROM KINETIC DEUTERIUM ISOTOPE EFFECT INVESTIGATIONS

SCOTT A. SHACKELFORD
F.J. Seiler Research Laboratory (AFSC)
Directorate of Chemical Sciences
USAF Academy, CO 80840-6528
USA

ABSTRACT. The condensed phase kinetic deuterium isotope effect (KDIE) approach directly determines the overall rate-controlling mechanistic step of an energetic material's complex thermochemical decomposition process. This second paper discusses extending the KDIE approach into progressively more drastic high temperature/pressure/rate regimes encountered with pyrolytic decomposition/deflagration, combustion, thermal explosion, and detonation incidents in order to determine the rate-controlling step of each. This rate-controlling step provides a common basis for comparing the mechanistic similarities or differences among these high energy incidents; and possible relationships between the thermochemical decomposition process and higher order combustion or explosion incidents are described for HMX, RDX, TATB, and TNT. The KDIE determined rate-controlling step between a pure nitramine compound and a formulated energetic material also is compared.

1. Introduction

The condensed phase kinetic deuterium isotope effect (KDIE) approach directly identifies the rate-controlling mechanistic step of an energetic material's thermochemical decomposition process.¹⁻⁴ The usefulness of this condensed phase KDIE approach not only applies to thermochemical decomposition studies, it also can be extended into mechanistic investigations of progressively more drastic high energy incidents like rapid pyrolytic decomposition/deflagration³, combustion⁵, thermal explosion^{2,3} and detonation.^{4,6} Extension of the KDIE into these higher pressure/temperature/rate regimes provides the rate-controlling step as a common experimental parameter and permits a direct comparison of mechanistic similarities or differences that promote or generate these high energy incidents.⁷ Because the kinetically regulated rate-controlling mechanistic step ultimately determines the overall or global rate at which a high energy incident proceeds, it inherently must be an important consideration for computationally modeling or experimentally tailoring an energetic material's energy releasing behavior.

For this discussion, the five high energy incidents cited are defined in two categories. Thermochemical decomposition and rapid pyrolytic decomposition/deflagration are referred to as energetic processes driven by many complex chemical reactions proceeding in parallel and sequentially. Combustion, thermal explosion, and detonation are referred to as energetic events where an event is composed of at least two different interactive energetic processes. A high energy incident is a collective term for either a chemically driven high energy process or event. The pyrolytic decomposition/deflagration process is defined here as an

Process.	comprised of many chemical reactions
Event.	comprised of more than one process
Incident	either a process or event

extremely fast, thermally activated conversion of a condensed phase energetic material into gaseous decomposition products without a visual flame; this contrasts with the slower and milder thermochemical decomposition process found in isothermal differential scanning calorimetry (IDSC) or thermal gravimetric analysis (TGA) studies which proceeds over visually discernable seconds or minutes. Because both processes can convert condensed phase energetic materials like TNT, TATB, RDX, and HMX into the gaseous products needed for promoting or sustaining combustion, thermal explosion, and detonation events, they likely play a role in these three energetic high pressure/temperature events.

The previous paper, "Mechanistic Investigations of Condensed Phase Energetic Material Decomposition Processes Using the Kinetic Deuterium Isotope Effect," discusses applying the condensed phase KDIE approach to the slow ambient pressure thermochemical decomposition process of specific energetic nitroaromatic and nitramine materials. It covers the KDIE concept itself and reviews previous condensed phase KDIE investigations in order to illustrate the various analytical methods and evaluation techniques used to detect the KDIE. The earlier paper further illustrates how the KDIE identifies the kinetically regulated rate-controlling mechanistic step; and with HMX, it demonstrates that thermochemical decomposition is a complex chemical process whose rate-controlling step may change as a compound's physical state is altered. This paper addresses extending the condensed phase KDIE approach beyond the slow ambient pressure thermochemical decomposition process into the progressively more drastic, higher rate/temperature/pressure regimes represented by the pyrolytic decomposition/deflagration process, plus combustion, thermal explosion, and detonation events. Because the condensed phase KDIE approach has been used most extensively in mechanistic investigations with HMX, and because HMX apparently displays a mechanistic dependence on its physical state, KDIE investigations of HMX's high energy incidents will be reviewed first and the rate-controlling step found in each event will be compared. Following the HMX discussion, the energetic compounds RDX, TATB and TNT are also addressed to illustrate the mechanistic relationships which possibly exist between their thermochemical decomposition process and higher order combustion, thermal explosion, and detonation events.

2. Discussion

2.1 HMX KDIE-DETERMINED MECHANISTIC RELATIONSHIPS

The slow ambient pressure thermochemical decomposition process of HMX may involve more than one mechanistic pathway and specific rate-controlling step. Isothermal DSC (IDSC) investigation of the HMX and deuterium labeled HMX- d_8 compounds over a 551–553 K temperature range (mp HMX = 555 K), reveal three dissimilar KDIE values (Figure 1), and each occurs in a different physical state (Figure 2).³ The early induction period reveals a 1⁰ KDIE which indicates covalent C–H bond rupture of the HMX molecule, or C–H bond

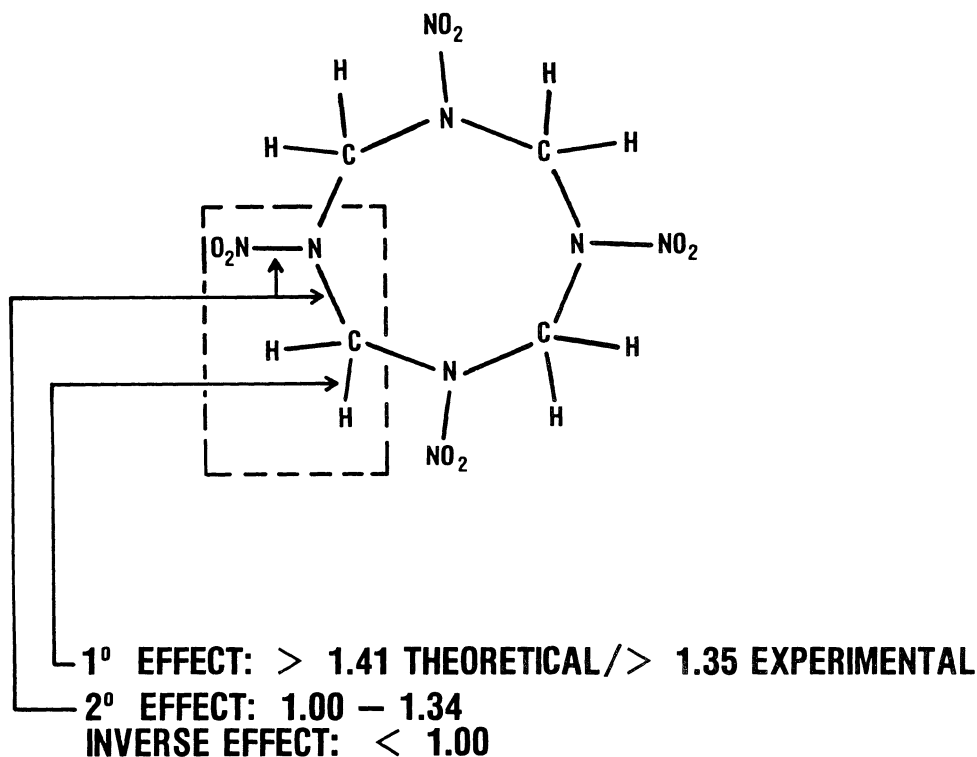


Figure 1. Possible KDIE types in the HMX molecule or structural fragment.^{3, 5}

dissociation in an HMX condensed phase derivative, is the rate-controlling mechanistic step in solid state decomposition. Solid state C–H bond rupture as a rate-controlling step is also indicated by HMX and HMX- d_8 isothermal TGA analysis.⁴ As the IDSC decomposition of HMX enters a short-lived mixed melt phase, an apparent inverse KDIE ($\dot{\gamma}$ -KDIE) results possibly caused by the C–H or C–D bond contracting; this suggests that a thermal weakening of the attractive intermolecular crystal lattice forces constitutes the mixed melt phase's rate-controlling step.³ Upon complete liquification, a 2⁰ KDIE shows ring C–N

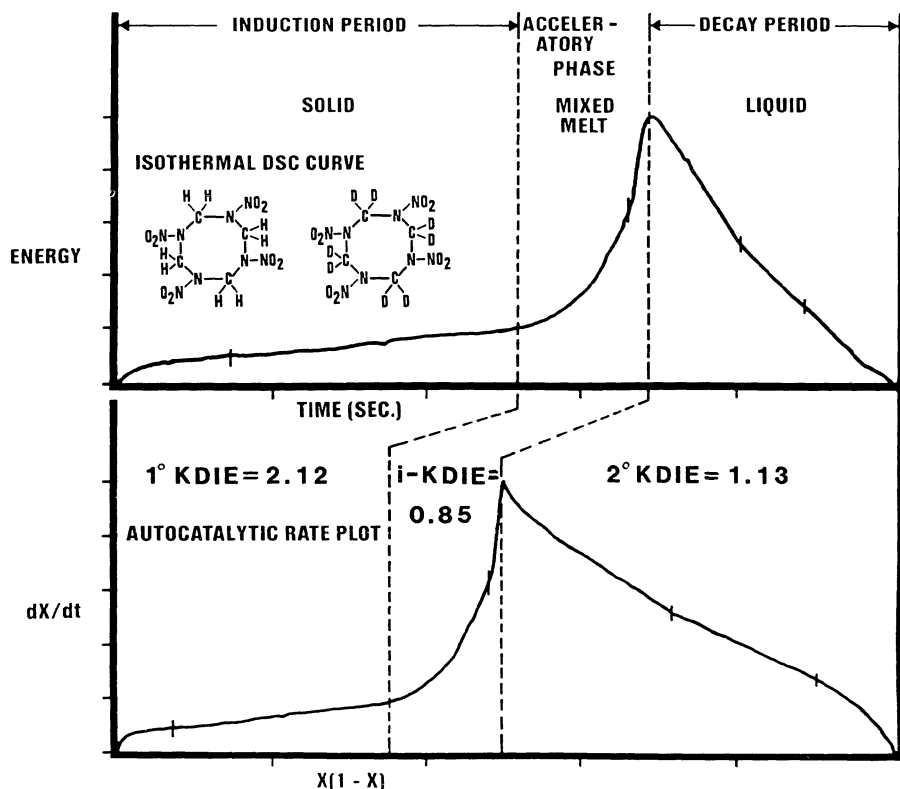


Figure 2. (TOP) Isothermal DSC curve of the HMX thermochemical decomposition process. (BOTTOM) Autocatalytic rate plot of the HMX-thermochemical decomposition curve for HMX and HMX-d₈.³

bond rupture or C-N bond rupture in a liquid phase ring fragment, as being the liquid state's rate-controlling step.³ These results (Table 1) reveal HMX thermochemical decomposition is not a single mechanistic pathway with one rate-controlling step; rather, it is a complex process consisting of at least three different mechanistic pathways. Each mechanistic pathway has its own unique rate-controlling step, and this rate-controlling step is dependent upon the

Table I. HMX Thermochemical Decomposition KDIE Values³

<u>Solid State</u>	<u>Mixed-Melt</u>	<u>Liquid State</u>
2.21 ± 0.2	0.85 ± 0.2	1.13 ± 0.1
1°KDIE	$i\text{-KDIE}$	2°KDIE

predominant physical state of HMX.³ The appearance of three different HMX physical states during the IDSC investigation likely results from the boat pan configuration used.^{7a, b} The sample pans are covered, but are not sealed and gaseous products generated during the HMX decomposition can gradually escape (Figure 3). During the early portion of the HMX decomposition (Figure 2), the

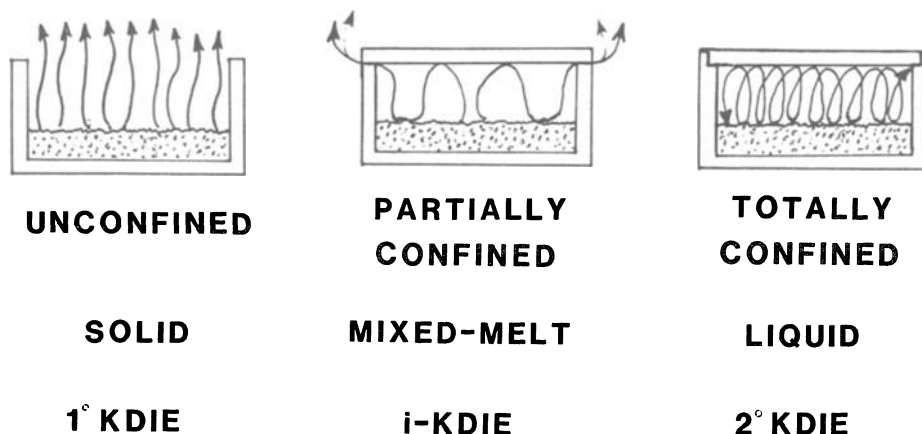


Figure 3. Illustration of possible HMX gaseous and solid state heterogeneous phase interactions during the thermochemical decomposition process.

small amount of gaseous products generated can escape; but as the concentration of gaseous products increase more rapidly with time, not all immediately escape. The gaseous HMX decomposition products build up and begin to act as impurities with the solid HMX sample causing a physical melting point lowering, and bring the HMX sample into the mixed melt phase even though the decomposition is conducted isothermally slightly below the HMX melting point.^{3, 5b} As the decomposition progresses, an even higher concentration of gaseous products is generated in the sample pan, and complete HMX liquification results to form the HMX liquid phase during the latter portion of the IDSC curve. Two other condensed phase KDIE experiments involving a pyrolytic decomposition/deflagration process and the thermal explosion event support this mechanistic chemical scenario.³

An ambient pressure, isothermal pyrolytic decomposition/deflagration of HMX and HMX-d₈ conducted with a high heating rate pyroprobe gun at 21 degrees (534 K) below the HMX melting point (555 K), produces a 1° KDIE with a value slightly over 3.00 (Table II).³ Lightly pressed HMX or HMX-d₈ powder disks are placed into an experimental pyroprobe apparatus where gaseous

Table II. HMX Pyrolytic Decomposition/Deflagration KDIE Values³

Run	Temp (K)	KDIE	Type
A	534	3.02 ± 0.6	1°
B	534	3.06 ± 0.5	1°

decomposition products are rapidly carried away so that gaseous decomposition products do not build up, or interact with the solid HMX sample and cause a physical melting point lowering (Figure 4). The solid HMX and HMX- d_8 samples instantaneously convert to gaseous products with no visible flame (Figure 5). By induction time comparison,¹ a 1° KDIE ($t_{id}/t_{ih} > 3.00$) shows that solid state covalent C-H bond rupture is the mechanistic rate-controlling step for this rapid pyrolytic decomposition/deflagration,³ just as it is in the slow thermochemical decomposition process studied by IDSC³ and TGA.⁴

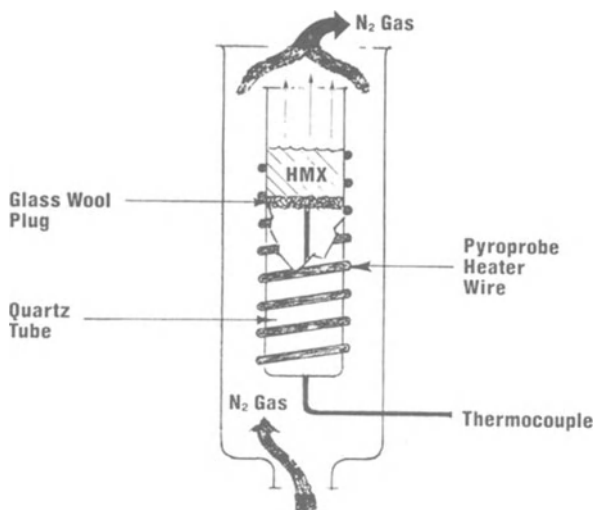


Figure 4. Rapid high heating rate pyroprobe apparatus and assembly for HMX and HMX- d_8 .³

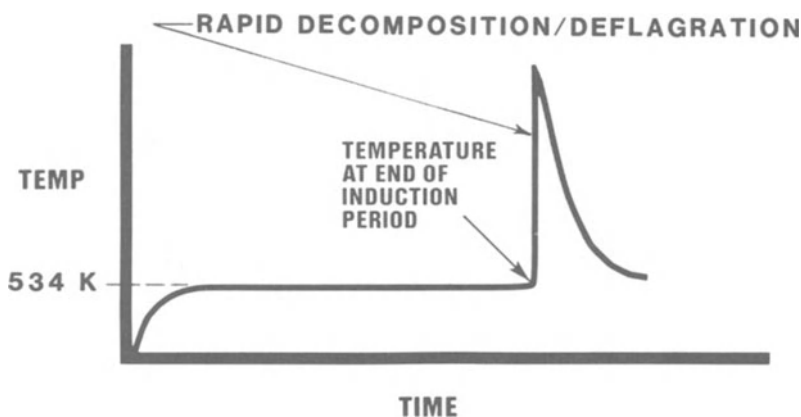


Figure 5. Isothermal rapid pyrolytic decomposition/deflagration curve of HMX and HMX- d_8 .³

The thermal explosion event produced during HMX and HMX- d_8 time-to-explosion experiments reveals an *i*-KDIE. This *i*-KDIE suggests the rate-controlling mechanistic step results from the rate at which the attractive HMX intermolecular crystal lattice forces are weakened by thermal activation.³ Isothermal time-to-explosion experiments with a normal and deuterium labeled compound show a correlation between the two energetic compounds' critical temperature difference and the type of KDIE the same compounds display in an IDSC thermochemical decomposition experiment.² Critical temperature (T_c) represents the lowest constant surface temperature at which a given energetic material of a specific size and shape will self-heat catastrophically to a thermal explosion event in a modified Henkin Test apparatus.^{2,3,8} The first KDIE study relating mechanism with energetic material sensitivity² discloses that energetic compounds producing a higher critical temperature with their deuterium labeled analogue (T_{cd}), correlate with a positive (1^0 or 2^0) KDIE determined during an IDSC analyzed thermochemical decomposition process. Normal or unlabeled compounds that have a critical temperature (T_{ch}) equal to or greater than its deuterium labeled analogue, apparently correlate with an *i*-KDIE observed in the complementary IDSC investigation (Table III).² This relationship apriori seems

Table III. Thermal Explosion and Thermochemical Decomposition KDIE Comparison

Thermal Explosion Event	Thermochemical Decomp. Process (IDSC)
$T_{cd}/T_{ch} > 1.00$	1^0 or 2^0 KDIE
$T_{cd}/T_{ch} < 1.00$	inverse KDIE

justified since a higher T_c would indicate the kinetically regulated chemical reactions promoting or generating the thermal explosion event occur more slowly (smaller overall rate constant, k) at a lower temperature; and thus, $k_h/k_d \propto T_{cd}/T_{ch} \propto t_{id}/t_{ih}$. HMX affords a critical temperature (257^0C) that is 15 degrees above HMX- d_8 (242^0C) as illustrated by Figure 6.³ This correlates to the *i*-KDIE found during the mixed-melt phase in the IDSC thermochemical decomposition investigation, and suggests the thermal explosion event occurs with HMX predominantly in the mixed melt phase.³ Because the HMX or HMX- d_8 sample is totally confined during the time to explosion test, a rapid high pressure build-up occurs, and the gaseous decomposition products cannot escape. Instead, these gaseous impurities interact with the solid HMX sample and apparently produce a rapid melting point lowering to quickly bring the HMX into the mixed-melt phase where the thermal explosion event occurs before liquefaction is completed. Heterogenous gas-condensed phase interactive reactions have been observed to increase with higher pressure⁹ and take on a greater importance in a nitramine's rapid thermoanalysis.¹⁰ As revealed by the *i*-KDIE and possible C-H/C-D bond contraction, the rate-controlling mechanistic step in a highly confined HMX thermal explosion event depends upon the rate at which the HMX intermolecular molecular crystal lattice forces are overcome by thermal activation. In contrast, the unconfined, ambient pressure HMX pyrolytic decomposition/deflagration process where appreciable solid state HMX/gaseous product interactions are avoided, shows solid state C-H bond rupture as the rate-controlling mechanistic step (Figure 3).

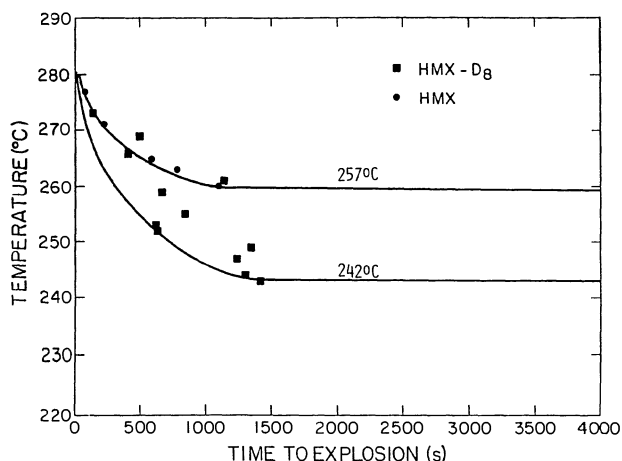


Figure 6. Critical temperature of HMX and HMX-d₈ determined from isothermal time-to-explosion tests.³

Sample confinement apparently represents one external boundary condition that directly influences the predominant HMX physical state present during a given energetic process or event; this in turn, dictates the rate-controlling mechanistic step. It appears there is a mechanistic correlation with the KDIE-determined rate-controlling steps observed in the ambient pressure, slow thermochemical decomposition process with both the rapid pyrolytic decomposition/deflagration process and the thermal explosion event. This causes one to wonder if a correlation exists between the high pressure combustion event and the ambient pressure thermochemical decomposition process.

Combustion represents an intermediate pressure/temperature/rate regime between the rapid pyrolytic decomposition/deflagration process and thermal explosion event. When the condensed phase KDIE approach is applied to the static high pressure combustion of pressed HMX and HMX-d₈ solid pellet samples, a significant KDIE results and verifies a substantial degree of chemical kinetic control for this event.⁵ The combustion event undoubtedly is a very complex phenomenon involving both interactive chemical and physical processes proceeding among various condensed and gaseous physical states. All three HMX condensed phase physical states (solid, mixed-melt, liquid) could be present during combustion, and the far more extensively investigated gaseous flame consists of several flame stages and reaction zones.¹¹⁻¹⁴ Some conceptual simplification is necessary to address the relevant mechanistic points revealed by the KDIE combustion study of HMX. The combustion event may be viewed as consisting of two interacting processes: (1) a condensed phase rapid decomposition/deflagration process that produces the gaseous decomposition products needed to feed and sustain the second process; (2) a gas phase flame oxidation process that converts these gaseous decomposition products to the final combustion products^{5,7} (Figure 7). Each complex process considered separately

has many chemical reactions, and each has its own rate-controlling mechanistic step; but, of the two, one rate-controlling step will occur more slowly than the other. This slower rate-controlling mechanistic step ultimately determines the overall or global HMX burn rate.^{5, 7}

The combustion KDIE is determined from the burn rate ratios (r_{bh}/r_{bd}) of the cylindrical HMX and HMX- d_8 pellets made from identically synthesized^{3, 5, 15, 16} HMX and HMX- d_8 powders. The HMX and HMX- d_8 pellet samples are pressed to 96–97 percent of the HMX single crystal density assuring any burn rate

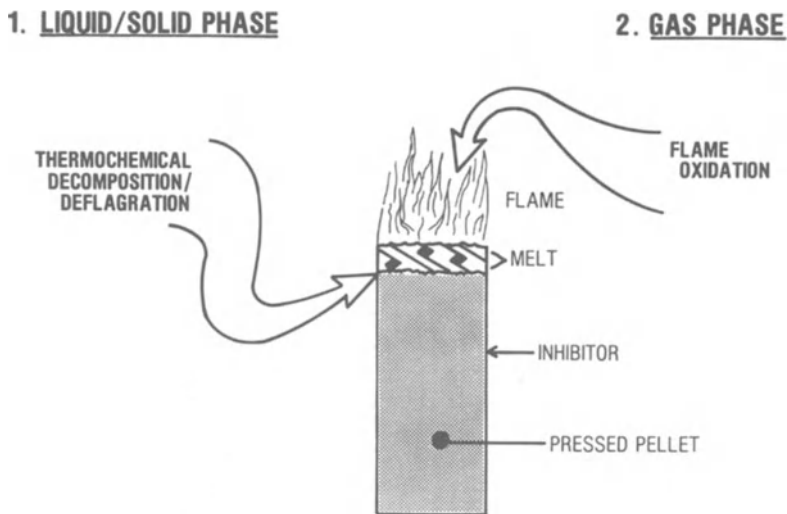


Figure 7. Representation of the HMX and HMX- d_8 pressed pellet combustion event.⁵

differences that cause a KDIE result solely from the deuterium isotope substitution and not from sample history, purity, particle size or void distribution. This is a necessary condition for KDIE validity. High pressure window bomb combustion produces a significant KDIE over a 500 psig (3.55 MPa) to 1500 psig (10.4 MPa) pressure range (Table IV). A 1^0 KDIE results at 500 psig (3.55 MPa) and 1000 psig (6.99 MPa) pressures indicating C–H bond rupture is this event's rate-controlling step. The KDIE value at 1500 psig (10.4 MPa) at first glance, appears low for a 1^0 KDIE; but, it is within the experimentally accepted minimum 1^0 KDIE value of 1.35^{18–20} at a statistical 95% confidence level range. The possibility the KDIE at 1500 psig (10.4 MPa) represents a very large 2^0 KDIE involving a sudden mechanistic change from a rate-controlling C–H bond rupture to a ring C–N bond rupture also should be considered;^{5a} but, when the experimental KDIE values are mathematically extrapolated to standard temperature, a 1^0 KDIE still remains plausible. When one considers the maximum 2^0 KDIE value at standard temperature theoretically would be 1.74 squared or 3.03²¹ and that a true 2^0 KDIE value of only 1.13 is seen in the 551–553 K temperature range for the HMX thermochemical decomposition process³ which calculates to 1.32 at standard temperature^{5a, 7a}, a

Table IV. HMX and HMX-d₈ Burn Rates (in/s) and KDIE (r_{bh}/r_{bd}) Values.⁵

500 psig (3.55 MPa)		1000 psig (6.99 MPa)		1500 psig (10.4 MPa)	
HMX(r_{bh})	HMX-d ₈ (r_{bd})	HMX	HMX-d ₈	HMX	HMX-d ₈
0.257	0.167	0.464	0.306	0.716	0.604
0.253	0.219	0.505	0.311	0.690	0.596
0.284	0.183	0.529	0.320	0.698	0.502
	0.192		0.308		
<u>Ave. r_b:</u>					
0.265±.02	0.193±.03	0.499±.03	0.331±.01	0.701±.01	0.576±.06
<u>Expl. KDIE*</u> (553 K) ¹⁷ :					
1.37±0.2 (1 ⁰)		1.60±0.2 (1 ⁰)		1.24±0.2 (?)	
<u>Std. KDIE</u> (298K) ¹⁸ :					
3.26		3.80		2.95	

*Error limits for KDIE values are shown at the 95% confidence level

masked 1⁰ KDIE remains a possibility. The KDIE generally shows a temperature dependence and decreases with increasing temperature; so, KDIE values semi-quantitatively can be extrapolated mathematically to standard temperature using appropriate equations.¹⁸ It should also be pointed out, true 1⁰ KDIE values can be diluted or masked to appear as a 2⁰ KDIE because of other interfering reaction pathways which have their own rate-controlling mechanistic step. In such a case, the true 1⁰ KDIE would appear as a larger number if its specific reaction pathway were the only one occurring or were the only one being detected. An example of masking appears in the IDSC thermochemical decomposition of TNT and TNT-d₃.¹ This possible masking of the KDIE value at 1500 psig (10.4 MPa) is discussed in greater detail elsewhere;⁵ but, the appearance of significant KDIE values from over the 500 psig (3.55 MPa) to 1500 psig (10.4 MPa) pressure range verifies a substantial degree of kinetic control for the combustion event.⁵ The 1⁰ KDIE values at 500 psig (3.55 MPa) and 1000 psig (6.99 MPa) reveal covalent C-H bond rupture as being the rate-controlling mechanistic step for the global or overall HMX burn rate in this pressure range. It further suggests this kinetically regulated rate-controlling C-H bond rupture may occur in the portion of the combustion event that involves the solid state rapid decomposition/deflagration process (Figure 7).⁵ While the gas phase flame oxidation process has its own rate-controlling mechanistic step, past studies with the HMX and RDX decomposition process within a similar temperature range, show a decomposition rate increase as one proceeds from the solid to liquid to gaseous state.²² This suggests the observed kinetic rate-controlling C-H bond rupture step could occur most slowly in the condensed phase's decomposition/deflagration process; and since the 1⁰ KDIE has been observed for HMX only in the solid state³, it follows that covalent solid state C-H bond dissociation ultimately may exercise a substantial kinetic control over the global HMX burn rate. Control of the HMX burn rate by condensed phase reactions recently has also been postulated from other experimental findings^{10, 13, 23-24} and micro-thermocouple studies reveal a solid phase temperature gradient profile that is

high enough to produce a rapid HMX decomposition/deflagration in either HMX¹³ or in an HMX based propellant.²⁴ The appearance of a significant KDIE in the HMX combustion event and its implication of a kinetically based rate-controlling solid state C–H bond rupture, strongly indicate that mechanistic condensed phase combustion characteristics can no longer be ignored as they have been in the past. While previous theoretical and experimental mechanistic studies of the gas phase chemical process abound, only by understanding the mechanistic features of both the condensed phase decomposition/deflagration process, and gas phase flame oxidation process, plus their interaction with one another, will adequate computational codes be developed which accurately describe and predict the combustion behavioral characteristics of a specific energetic material.

The mechanistic importance of kinetically controlled condensed phase reaction contributions in determining the overall or global burn rate of a pure energetic compound is further illustrated by the KDIE investigation of laboratory scale HMX and HMX–d₈ based propellant formulations. Parallel window bomb combustion experiments conducted at 1000 psig (6.99 MPa) with pure HMX and HMX–d₈ samples, as well as an HMX/CW5²⁵ propellant and its HMX–d₈/CW5 analogue, give essentially the same KDIE value (Table V).²⁶ These samples are prepared in a No. 3 gelatin capsules (Eli Lilly Co) at a density of 1.62 g/cm³. The appearance of the same probable 1⁰ KDIE value for the pure HMX and HMX/CW5 propellant samples strongly suggests the same solid state covalent C–H bond rupture found in pure HMX is also the rate-controlling mechanistic step which kinetically regulates the formulated, urethane cured propellant burn rate.^{7a, 26}

Table V. HMX and HMX/CW5 Propellant KDIE Values at 1000 psig (6.99 MPa).²⁶

	<u>HMX/HMX–d₈</u>	<u>HMX/CW5&HMX–d₈/CW5</u>
Expl KDIE (553 K) ¹⁷	1.30 ± .05	1.29 ± .09
Std KDIE (298 K) ¹⁸	3.09	3.07

Max Theo. 2⁰ KDIE (298 K) = 3.03²¹

While the KDIE values in Table V fall slightly below the experimental 1.35 value for a pure compounds minimum high temperature value, and are somewhat lower than those in the pressed pellet combustion study of the pure pressed pellet HMX samples (Table IV), the KDIE possibly is masked by interfering reactions from combustion of the gelatin capsules which could have a different rate-controlling mechanistic step from the HMX or HMX/CW5 propellant formulation itself. Still, the 95% confidence level statistical variation places these presumed 1⁰ KDIE values within the same confidence level range as the earlier HMX pressed pellet KDIE combustion results. When mathematically normalized to standard temperature using a 1⁰ KDIE equation,¹⁸ the standard temperature KDIE values in Table V also slightly exceed the maximum theoretical 2⁰ KDIE value of HMX at 298 K and are, therefore, considered plausible representations of a 1⁰ KDIE. This 1⁰ KDIE assignment is further supported by the fact that the only

confirmed 2^0 KDIE seen around 552 K for an energetic compound, is 1.13 for HMX during its liquid phase thermochemical decomposition³ and equates only to a 1.32 2^0 KDIE value¹⁸ at standard temperature (298 K).^{7a}

The first mechanistic KDIE correlation of the thermal decomposition process with explosive sensitivity was accomplished with the thermally initiated nonsteady-state thermal explosion event.² The HMX thermal explosion event has been discussed³ and represents an intermediate temperature/pressure regime between the less drastic combustion event and the high order steady-state detonation event. Mechanistic KDIE detonation investigations recently have been conducted and provide the first correlation between the thermochemical decomposition process and shock-induced detonation using an exploding foil driven flyer plate test.^{4, 6}

The shock-induced KDIE detonation of HMX and HMX- d_8 detects a KDIE as the difference between flyer plate velocity (V) needed to shock initiate normal HMX (V_h) and its deuterium labeled HMX- d_8 analogue (V_d). The HMX- d_8 demonstrates a small but definitive positive KDIE ($V_d/V_h > 1.00$) where the rate-controlling mechanistic step of HMX- d_8 proceeds more slowly (lower k_d) than that of HMX (higher k_h). Thus, k_h/k_d has a proportional correlation to V_d/V_h because a larger flyer plate velocity (V_d) is needed to bring the overall slower k_d value to the same value as k_h (Table VI), and $k_h/k_d \propto t_{id}/t_{ih}$,^{1, 3} t_{cd}/t_{ch} ,^{2, 3} $\propto r_{bh}/r_{bd}$ ⁵ $\propto V_d/V_h$,^{4, 6}.

Table VI. Exploding Foil Shock Detonation KDIE Values.⁴

<u>Sample</u>	<u>Flyer Plate Vel.(mm/μs)</u>	<u>Std Dev</u>	<u>KDIE Type</u>
HMX	2.37	.028	Positive — <u>ie.</u>
HMX- d_8	2.27	.046	(1^0 or 2^0)

The indirect nature of this KDIE does not permit a quantitative differentiation between a solid state C—H bond rupture (1^0 KDIE) or liquid state ring C—N bond rupture (2^0 KDIE) as the rate-controlling mechanistic step, assuming δ -HMX and β -HMX will display the same mechanistic pathways in their thermochemical decomposition process. Certainly, an i -KDIE like that apparently produced in the thermally initiated HMX thermal explosion event³ does not occur. Recent high pressure diamond anvil cell/FTIR decomposition experiments have been conducted with β -HMX in the GPa pressure range to simulate the pressures closer to that experienced by the detonation event. This study reveals β -HMX decomposition at GPa pressures occurs solely in the solid state.²⁷ This finding might favor the solid state process as housing the detonation event's rate-controlling mechanistic step where the exploding flyer plate's shock produces an adiabatic compression, which in turn, initiates a rapid pyrolytic solid state β -HMX decomposition/deflagration process that generates or promotes the detonation event before liquefaction can occur.^{7a} Interestingly, the high pressure GPa HMX decomposition process provides a linear autocatalytic kinetic plot;²⁷ this is the same kinetically based autocatalytic behavior found with the ambient pressure IDSC thermochemical decomposition process where a 1^0 KDIE reveals covalent solid state C—H bond rupture as being the rate-controlling mechanistic step for δ -HMX.³ For a totally adequate rate-controlling step correlation to be shown between the ambient pressure thermochemical decomposition process's solid state C—H bond dissociation (δ -HMX) and the shock induced detonation

event (likely β -HMX), a high pressure KDIE investigation of β -HMX and β -HMX- d_8 is needed.

In all HMX high energy incidents, significant kinetic control is observed using the condensed phase KDIE approach. Most notably, the same physical state dependent rate-controlling mechanistic steps found in the mildest HMX high energy incident, the ambient pressure thermochemical decomposition process, also are mirrored in the more drastic high energy incidents (Table VII). This

Table VII. Summary of HMX High Energy Incident Rate-Controlling Steps^{7a}

	¹⁰ KDIE (solid state) (C-H bond)	<i>i</i> -KDIE (mixed melt) (cryst forces)	²⁰ KDIE (liquid state) (C-N bond)
Thermochemical Decomp	X	X	X
Pyrolytic Decomp/ Deflagration	X		
Combustion	X		
Thermal Explosion		X	
Detonation	(X)	or	(X)

suggests that with careful consideration, mechanistic results obtained from slow ambient pressure, thermochemical decomposition KDIE investigations can be extrapolated and used as a preliminary guide for planning future mechanistic studies in the higher order combustion, thermal explosion, and possibly detonation events.^{7a} In support of this statement are other extensions of the condensed phase KDIE approach from the ambient pressure thermochemical decomposition process into these more drastic energetic events using energetic compounds other than HMX.

2.2 RDX KDIE-DETERMINED MECHANISTIC RELATIONSHIPS

The slow thermochemical decomposition process of both liquid and solid state RDX produces a ¹⁰ KDIE indicating that C-H bond rupture is its rate-controlling mechanistic step (Figure 8).^{4, 28} The same rate-controlling

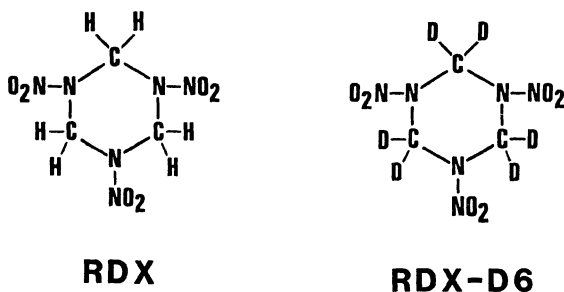


Figure 8. Chemical structure of RDX and RDX- d_8 .

C—H bond rupture is also present in the RDX static combustion event at 500 psig (3.55 MPa) and 1000 psig (6.99 MPa).²⁸ Identically synthesized cylindrical pressed RDX and RDX-d₆ pellets were burned in a window bomb and provide a 1⁰ KDIE when their burn rates ratios are calculated (Table VIII). For the same reasons that solid state C—H bond rupture might be the rate-controlling step in the HMX combustion event, the rate-controlling C—H bond rupture in RDX

Table VIII. RDX Burn Rates (in/s) and Combustion KDIE (r_{bh}/r_{bd}) Values²⁸

	500 psig (3.55 MPa)		1000 psig (6.99 MPa)	
	RDX(r_{bh})	RDX-d ₆ (r_{bd})	RDX	RDX-d ₆
Ave r_b	0.297 ± 030	0.217 ± 012	0.567 ± 069	0.387 ± 032
<u>Expl KDIE*</u>	1.37 ± 0.2		1.46 ± 0.2	

*Error limits for KDIE values are shown at the 95% confidence level

combustion could also come from the solid or liquid state during the pyrolytic decomposition/deflagration process. While there is less data to support RDX condensed phase C—H bond rupture as housing the rate-controlling step that determines its burn rate, both isothermal TGA and IDSC analyses show RDX can undergo significant decomposition even below its melting point.^{4, 29} A KDIE mechanistic combustion study of the RDX/CW5 and RDX-d₆/CW5 propellant²⁵ reveals C—H bond rupture to be the rate-controlling step for the urethane cured propellant formulation as well as for the pure RDX energetic compound (Table IX).²⁶ The samples are prepared in the same No. 3 gelatin capsules used for the analogous HMX/CW5 propellant KDIE combustion experiment; the density of the pure RDX and RDX/CW5 samples is 1.48 g/cm.³ Again it appears the pure

Table IX. RDX and RDX Propellant KDIE Values at 1000 psig (6.99 MPa).²⁶

	Pure RDX/RDX-d ₆	RDX/CW5 & RDX-d ₆ /CW5
Expl KDIE (673 K) ³⁰	1.31 ± .04	1.24 ± .05
Std KDIE (298 K) ¹⁸	3.73	3.53
Max Theo 2 ^o KDIE (298 K) = 3.03 ²¹		

nitramine component's rate-controlling mechanistic step is also that which determines a formulated propellant's burn rate.

Impact initiation experiments conducted with a 10 kg weight on RDX just below its ignition threshold and subsequently analyzed by x-ray photoelectron spectroscopy (XPS), suggest both nitroso and triazine type products form within the hot spots created by mechanical impact.³¹ The very rapid pyrolytic decomposition/deflagration that causes the hot spots in the RDX sample, converts the RDX to the nitroso and triazine type products on the hot spot surface. The thermally initiated hot spots caused by physical impact could be a prelude to either a thermal explosion,³² or if shocked stringently enough with an exploding foil plate,⁴ a detonation event. It appears the nitroso compounds may form first enroute to the triazine type products.³¹ Formation of triazine type products requires a C—H bond rupture to generate the ring C=N double bond

structure for this type of chemical compound and would be consistent with C–H bond rupture as the rate-controlling step. Consistent also with the RDX rate-controlling C–H bond rupture step is a shock-induced KDIE detonation experiment with RDX and RDX-d₆. Already described for the HMX/HMX-d₈ system, the RDX-d₆ demonstrates a small but definitive positive KDIE ($V_d/V_h > 1.00$) as shown in Table X.⁴

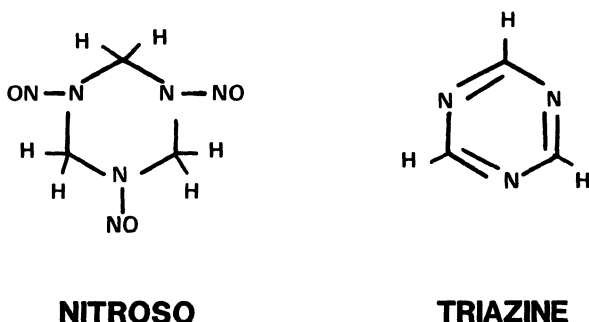


Figure 9. Chemical structure of nitroso and triazine type compounds.

Table X. Exploding Foil Shock Detonation KDIE Values.⁴

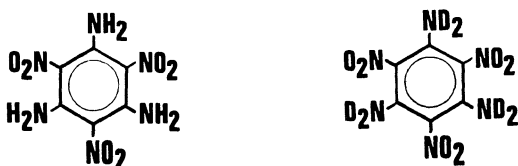
<u>Sample</u>	<u>Flyer Plate Vel.(mm/μs)</u>	<u>Std Dev</u>	<u>KDIE Type</u>
RDX	2.323	0.061	Positive – <u>ie</u>
RDX-d ₆	2.402	0.028	(1 ⁰ or 2 ⁰)

The appearance of a positive KDIE could be consistent with C–H bond rupture as the rate-controlling mechanistic step that significantly promotes or generates the detonation event. It appears that the same rate-controlling mechanistic step found in KDIE investigations of the RDX thermochemical decomposition process,^{4,28} may be present in the higher order combustion event²⁶ and possibly in the process that initiates or promotes the impact induced³¹ thermal explosion and shock initiated⁴ detonation events.

2.3 TATB KDIE–DETERMINED MECHANISTIC RELATIONSHIPS

The slow thermochemical decomposition process of solid TATB produces a 1⁰ KDIE indicating amino group N–H bond rupture is its rate-controlling mechanistic step (Figure 10).² This decomposition is a complex autocatalytic process involving two sequential reaction pathways. The 1⁰ KDIE and rate-controlling N–H bond rupture appear in the first reaction pathway early in the process; and, nmr proton analysis of the condensed phase products found in the second reaction pathway show little or no hydrogen atoms present.² The same rate-controlling mechanistic step may be present in TATB's thermal explosion event since TATB-d₆ displays a 12 degree higher critical temperature than its normal hydrogen substituted analogue.² This higher TATB-d₆ critical temperature correlates to a positive KDIE (1⁰ or 2⁰) with isothermal DSC

analysis. If one assumes the accepted kinetic generality that a reaction rate doubles for each 10 degree temperature rise and that it applies to the kinetically regulated reactions promoting or generating TATB's thermal explosion event, its rate-controlling step would be displaying a 1^0 KDIE approximately equal to a 2.4 value.



TATB

TATB-D6

Figure 10. Chemical structure of TATB and TATB-d₆.

Thermally decomposed TATB condensed phase products have been isolated by repeated thin layer chromatography (TLC) elution, and chemical ionization mass spectrometry (CIMS) analysis reveals at least three furoxan products formed by the loss of H₂ and cyclization of adjacent amino and nitro groups (Figure 11).³³ This must involve N–H bond rupture and is consistent with it being the same

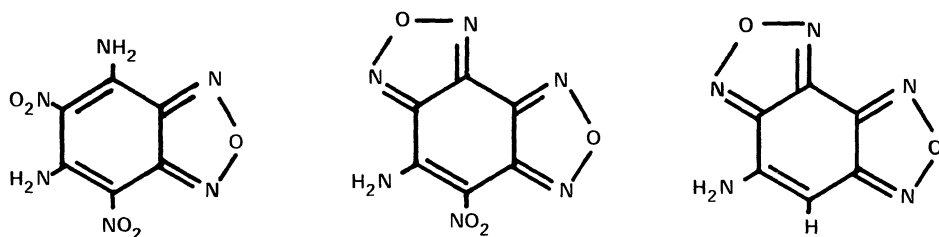


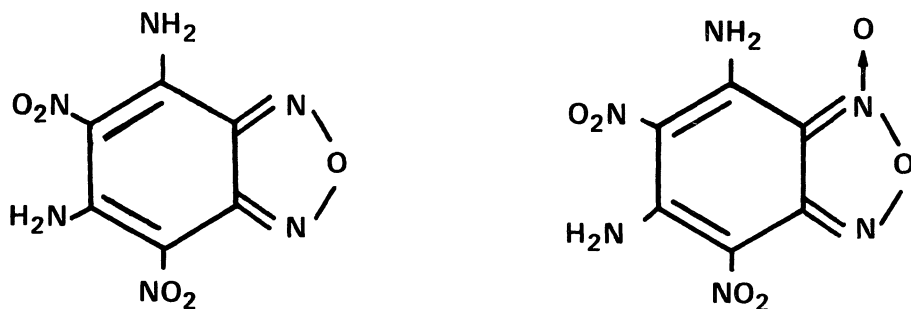
Figure 11. Isolated furoxan products from the TATB thermochemical decomposition process.³³

rate-controlling mechanistic step found in the IDSC decomposition experiment.² Impact initiation experiments conduct just below the ignition point of TATB and subsequent XPS, plus CIMS analysis of the rapidly decomposed surface products in the hot spots, show both furoxan **4** and furoxan **5** derivatives form from the loss of H₂ and H₂O respectively (Figure 12).³⁴ Again, these products are consistent with N–H bond rupture as being the same rate-controlling mechanistic step found by the IDSC analysis of the TATB's slow ambient temperature decomposition process,² and likely could be the same rate-

controlling step for both the TATB thermally induced thermal explosion event,² and impact initiated³⁴ thermal explosion event.

2.4 TNT KDIE—DETERMINED MECHANISTIC RELATIONSHIPS

The slow thermochemical decomposition process of liquid TNT produces a 1^0



MONOFURAZAN

MONOFUROXAN

Figure 12. Furazan and furoxan products formed from sub-ignition of TATB by mechanical impact.³⁴

KDIE very early in the IDSC analysis decomposition curve and indicates methyl group C—H bond rupture is the rate-controlling mechanistic step (Figure 13).¹ A catalytic product forms in trace amounts by this rate-controlling C—H bond dissociation from the TNT itself and initiates the exothermic portion of the TNT thermochemical decomposition process. Product isolation studies^{35,36} and electron paramagnetic resonance (epr) analysis^{37,38} identify a number of condensed phase products and a stable nitroxyl radical, formed via methyl group C—H bond rupture during TNT's slow thermochemical decomposition process (Figure 13); an apparent 1^0 KDIE also has been detected in a TNT and TNT- d_3 epr study by comparing the rate of nitroxyl radical formation.³⁹ Further evidence possibly supporting this C—H bond dissociation as the possible rate-controlling step leading to thermal explosion by impact, or a detonation by shock initiation, also has emerged. Impact initiation experiments conducted just below the ignition point of TNT with a 10 kg weight, and subsequent XPS analyses of SEM identified microscopic hot spot sites, reveal melting occurs at these sites and that three condensed phase products are present.^{31,40} These three products (Figure 14) correspond to 4,6-dinitroanthranil, 2,4,6-trinitrobenzaldehydoxime, and 2,4,6-trinitrobenzyl nitrile derived from TNT with the benzyl nitrile possibly formed by loss of H₂O from the benzaldehyde oxime. In all three cases, these intermediate hot spot products involve methyl group C—H bond rupture. A KDIE detonation study of TNT and TNT- d_3 shock initiated by an exploding foil method, demonstrates a small but positive KDIE ($V_d/V_h > 1.00$) where the flyer plate velocity for the deuterium labeled compound is higher (Table XI).⁶ While the indirect nature of this study does not permit a KDIE

ratio to be determined quantitatively, the appearance of a positive KDIE is significant and could be caused by the same rate-controlling C-H bond rupture⁶ as that seen in the slow ambient pressure IDSC investigation¹ of TNT

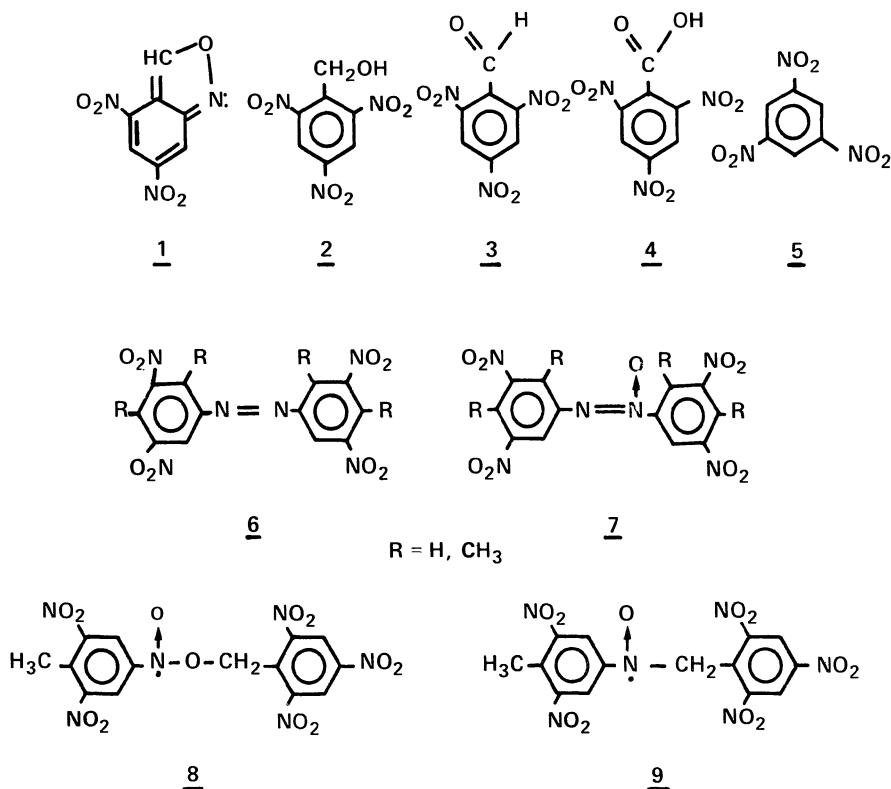


Figure 13. Isolated products and nitroxyl radical species from the TNT thermochemical decomposition process.^{1, 35, 36}

Table XI. Exploding Foil Shock Detonation KDIE Values.⁶

Sample	Flyer Plate Vel.(mm/ μ s)	Std Dev	KDIE Type
TNT	3.381	0.127	
TNT	3.237	0.170	Positive — <u>ie.</u>
TNT- <u>a</u> -d ₃	3.681	0.155	1 ⁰ or 2 ⁰

and TNT-a-d₃. When one considers both the products isolated from TNT in the sub-ignition impact study and the positive KDIE observed in the shock induced detonation study of TNT and TNT-d₃, it is plausible that the same liquid state

TNT methyl group C–H bond rupture observed in the earlier KDIE condensed phase thermochemical decomposition process,¹ also constitutes the overall rate–controlling mechanistic step for these higher order incidents.

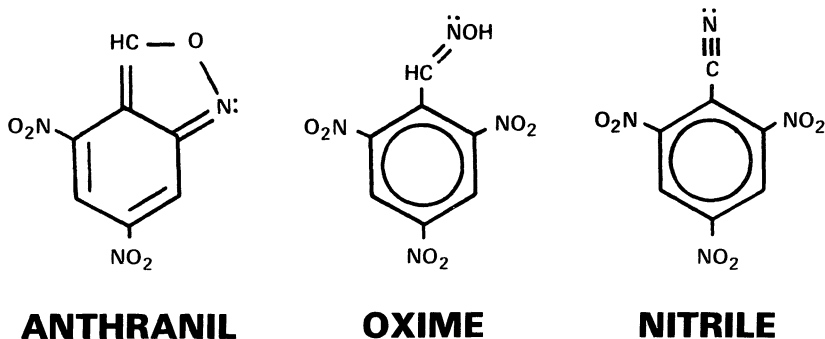


Figure 14. Products formed from sub-ignition of TNT by mechanical impact.^{31, 40}

3. Conclusions

A review of various mechanistic investigations of both nitroaromatic (TNT, TATB) and nitramine (HMX, RDX) energetic compounds using the condensed phase kinetic deuterium isotope effect (KDIE) approach demonstrates a finite and significant degree of chemical kinetic control in all high energy incidents. Whether the high energy incident is a mild slow ambient pressure thermochemical decomposition process, a more rapid pyrolytic decomposition/deflagration process, a progressively more drastic higher pressure/temperature combustion, thermal explosion, or detonation event, discernable KDIE values appear with thermal, impact, or shock initiation methods. These KDIE values show rupture of the covalent C–H/C–D bond (N–H/N–D bond for TATB) or a bond in its immediate vicinity, generally constitutes the overall or global rate–controlling step of the high energy incident. In one case, the rate–controlling step apparently results from a thermal weakening of a solid compound's attractive intermolecular crystal lattice forces in the short-lived HMX mixed melt phase. When an energetic compound's rate–controlling mechanistic step may vary with different physical states as shown by HMX, the type of KDIE observed can strongly hint at the predominant physical state present during a given high energy incident; and in such a case, suggests the rate–controlling step controlling the global rate of energy release, may reside in the condensed phase process of high order events like combustion, thermal explosion or detonation. The condensed phase chemical processes, therefore, must be computationally modeled in order to develop acceptable computer codes that accurately predict energy releasing behavior. The presence of condensed phase products formed during these various high energy incidents by chemical pathways that are consistent with KDIE determined rate–controlling mechanistic steps, suggest the same rate–controlling step seen in the mild thermochemical decomposition process often mirrors those found in the

faster pyrolytic decomposition/deflagration process or in the progressively more drastic higher pressure/temperature/rate combustion, thermal explosion, detonation events. This apparent KDIE determined mechanistic relationship between the decomposition process and both combustion or explosion events suggests that condensed phase KDIE data obtained from the mild thermochemical decomposition process, can serve as a valuable guide in designing or planning mechanistic investigations of higher order energetic incidents, and that the condensed phase KDIE approach constitutes a valuable experimental tool for making mechanistic comparisons among them.

4. Acknowledgements

The Air Force Office of Scientific Research/Directorate of Chemical and Atmospheric Sciences (Director, Dr Don L. Ball) is gratefully acknowledged for funding the portions of research described herein conducted at the F.J. Seiler Research Laboratory (1975–78) and Astronautics Laboratory (1981–85) by the author and his referenced colleagues. Long-time scientific colleague Raymond N. Rogers generously provided valuable guidance and advice on IDSC kinetic data evaluation techniques for many years. Mrs Linda Pukajlo and the USAF Academy's Directorate of Audio Visual Services assisted in camera-ready manuscript preparation. Mr J. Lloyd Pflug and Dr Clay M. Sharts assisted with manuscript review. The author wishes to thank the Director of NATO ASI on Chemistry and Physics of the Molecular Processes in Energetic Materials, Dr Surya N. Bulusu, for this lectureship opportunity and partial financial support which made presentation of this paper possible.

5. References and Notes

1. S.A. Shackelford, J.W. Beckmann, J.S. Wilkes, "Deuterium Isotope Effects in the Thermochemical Decomposition of Liquid 2,4,6-Trinitrotoluene: Application to Mechanistic Studies Using Isothermal Differential Scanning Calorimetry Analysis", *J. Org. Chem.*, **42**, 4201–4206, (1977).
2. R.N. Rogers, J.L. Janney, M.H. Ebinger, "Kinetic Isotope Effects in Thermal Explosions", *Thermochim. Acta*, **59**, 287–298, (1982).
3. S. A. Shackelford, M.B. Coolidge, B.B. Goshgarian, B.A. Loving, R.N. Rogers, J.L. Janney, M.H. Ebinger, "Deuterium Isotope Effects in Condensed-Phase Thermochemical Decomposition Reactions of Octahydro-1,3,5,7-tetranitro-1,3,5,7-tetrazocine", *J. Phys. Chem.*, **89**, 3118–3126 (1985).
4. S. Bulusu, D.I. Weinstein, J.R. Autera, R.W. Velicky, "Deuterium Kinetic Isotope Effect in the Thermal Decomposition of 1,3,5-Trinitro-1,3,5-triazacyclohexane and 1,3,5,7-tetranitro-1,3,5,7-tetrazacyclooctane: Its Use as an Experimental Probe for Their Shock-Induced Chemistry", *J. Phys. Chem.*, **90**, 4121–4126 (1986).

5. (a) S.A. Shackelford, B.B. Goshgarian, R.D. Chapman, R.E. Askins, D.A. Flanigan, R.N. Rogers, "Deuterium Isotope Effects during HMX Combustion: Chemical Kinetic Burn Rate Control Mechanism Verified", Prop., Explos., Pyrotech., **14**, 93–102 (1989).

(b) S.A. Shackelford, M.B. Coolidge, B.B. Goshgarian, R.N. Rogers, J.L. Janney, M.H. Ebinger, D.A. Flanigan, R.E. Askins, "Deuterium Isotope Effects in HMX Thermochemical Mechanisms: Decomposition, Deflagration, and Combustion", 20th JANNAF Combustion Meeting, Monterey, CA, 17–20 Oct 1983; [Proc.], CPIA Publ. 383, Vol I, 571–580 (Oct 1983).

6. S. Bulusu, J.R. Autera, "Initiation Mechanism of TNT: Deuterium Isotope Effect as an Experimental Probe", J. Energetic Matls., **1**, 133–140 (1983).

7. (a) S.A. Shackelford, P.C. Trulove, R.D. Chapman, "Deuterium Isotope Effects in Combustion and Explosion: Impact of Chemical Mechanism and Physical State on Energy Release", 19th Annual International ICT Conference: Combustion and Detonation Phenomena, Karlsruhe, Fed Rep of Germany, 29 Jun – 1 Jul 1988; [Proc] Fraunhofer – Institut fuer Chemische Technologie, 1988, D-7507 Pfinztal/Berghausen, FRG, pp 40.1 – 40.14.

(b) S.A. Shackelford, "In-Situ Determination of Exothermic Transient Phenomena: Isotopic Labeling Studies", National Workshop, Micro- and Macroscopic Approaches on Detonations, Megeve, France, 1–5 Jun 1987, [Proc], J. de Physique, **48** (C4), 193–207 (Sep 1987).

(c) S.A. Shackelford, M.B. Coolidge, S.L. Rodgers, B.B. Goshgarian, B.A. Loving, R.N. Rogers, J.L. Janney, M.H. Ebinger, R.E. Askins, D.A. Flanigan, "Mechanistic Condensed Phase Deuterium Isotope Effect Analysis in Decomposition, Explosion, and Combustion: In-Situ Rate-Controlling Step Identification", 17th Annual International ICT Conference: Analysis of Propellants and Explosives – Chemical and Physical Methods, Karlsruhe, Fed Rep of Germany, 25–27 Jun 1986; [Proc] Fraunhofer-Institut fuer Treib- und Explosivstoff, 1986, D-7507 Pfinztal/Berghausen, FRG, pp 23.1–23.10.

(d) Ibid., "In-Situ Mechanistic Elucidation of High Energy Thermochemical Reaction Processes Using the Deuterium Isotope Effect: Decomposition, Explosion, Combustion", NATO Advanced Study Institute, Advances in Chemical Reaction Dynamics, Iraklion (Crete) Greece, 25 Aug – 7 Sep 1985.

8. R.N. Rogers, "Quantitative Evaluation of Thermal Hazards", RCEM Report A-04-87, 15–65 (4 Nov 1987); RCEM, New Mexico Tech, Socorro, NM 87801, USA.

9. Y. Oymi, T.B. Brill, A.L. Rheingold, "Thermal Decomposition of Energetic Materials. 20. A Comparison of the Structural Properties and Thermal Reactivity of an Acyclic and Cyclic Tetramethylenetetranitramine Pair", Thermochim. Acta, **114**, 209–225 (1987).

10. Y. Oymi, T.B. Brill, "Thermal Decomposition of Energetic Materials. 22. The Contrasting Effects of Pressure on the High-Rate Thermolysis of 34 Energetic Compounds", Combust. Flame, **68**, 209-216 (1987).
11. G. Lengellé, A. Bizot, J. Duterque, J.F. Trubert, "Steady-State Burning of Homogeneous Propellants", Fundamentals of Solid-Propellant Combustion, Vol 90 of Progress in Astronautics and Aeronautics, Eds. K.K. Kuo and M. Summerfield, AIAA, Inc., 1984, pp 361-407.
12. J. Duterque, J. Hommel, G. Lengellé, J.F. Trubert, "Experimental Study of Double-Base Propellants Combustion Mechanisms", Prop., Explos., Pyrotech., **10**, 18-25 (1985).
13. N. Kubota, S. Sakamoto, "Combustion of HMX", Prop., Explos., Pyrotech., **14**, 6-11 (1989).
14. T.B. Brill, "Condensed Phase Issues Related to Combustion", ONR Workshop, Energetic Material Initiation Fundamentals and Reaction Processes of Pure Materials, Livermore, CA (Dec 1988).
15. M.D. Coburn, D.G. Ott, "A Convenient Synthesis of Nitrogen-15 and Deuterium Labelled Octahydro-1,3,5,7-tetranitro-1,3,5,7-tetrazocine", J. Labelled Compd. Radiopharm., **18**, 1423-1427 (1980).
16. V.I. Siele, M. Warman, J.L. Leccacorvi, R.W. Hutchinson, R. Motto, E.E. Gilbert, T.M. Benzinger, M.D. Coburn, R.K. Rohwer, R.K. Davey, "Alternative Procedures for Preparing HMX", Propellants Explos., **6**, 67-73 (1981).
17. Because 553 K represents the highest temperature in ref. 3 for which a 1° KDIE was observed in the solid state HMX, this temperature was chosen as a reference point for calculating the 1° KDIE at standard temperature as described in ref. 18.
18. T.H. Lowry, K.S. Richardson, Mechanism and Theory in Organic Chemistry, Harper and Row, 2d ed, New York, 1981, pp. 206-208, 211-212.
19. A. Streitweiser, R.H. Jagow, R.C. Fahey, S. Suzuki, "Kinetic Isotope Effects in the Acetolyses of Deuterated Cyclopentyl Tosylates", J. Am. Chem. Soc., **80**, 2326-2332 (1958).
20. G. Herzberg, Molecular Spectra and Molecular Structure, Vol II, Van Nostrand Co., Inc., New York, 1950, pp. 217.
21. J. Bigeleisen, M. Wolfsberg, "Theoretical and Experimental Aspects of Isotope Effects in Chemical Kinetics", in Advances in Chemical Physics, Vol 1, Ed I., Prigogine, Interscience Publishers, Inc., New York, 1958, pp. 15-31.
22. (a) R.A. Fifer, "Cage Effects in the Thermal Decomposition of Nitramines and Other Energetic Materials", 19th JANNAF Combustion Mtg., Greenbelt, MD, Oct 1982; [Proc], CPIA Publ. 366, Vol I, 311-319 (Oct 1982).

(b) Ibid., "A Hypothesis of the Phase Dependence of the Decomposition Rate Constants of Propellant Molecules, Jt. ONR/AFOSR/ARO Workshop: Fundamental Directions for Energetic Material Decomposition Research, Berkeley, CA, 20-22 Jan 1981, [Rept], ONR, Arlington, VA, pp 153-168.

23. Y. Oyumi, T.B. Brill, "Thermal Decomposition of Energetic Materials. 3. A High-Rate, In-Situ, FTIR Study of the Thermolysis of RDX and HMX with Pressure and Heating Rate as Variable", Combust. Flame, **62**, 213-224 (1985).

24. Y. Yano, N. Kubota, "Combustion of HMX-CMDB Propellants (II)", Prop., Explos., Pyrotech., **11**, 1-5 (1986).

25. The HMX/CW5 laboratory propellant composition is as follows: Nitramine (73.2%), Hydroxy-terminated R-18 binder (8.5%), TMETN plasticizer (16.9%), IDPI curative (1.4%) and DBTDA cure catalyst (0.01%).

26. P.C. Trulove, R.D. Chapman, S.A. Shackelford, "Deuterium Isotope Effects in the Combustion of Formulated Nitramine Propellants", 24th JANNAF Combustion Mtg., Monterey, CA, Oct 1987; [Proc], CPIA Publ. 473, Vol I, 303-308 (Oct 1987).

27. G. J. Piermarini, S. Block, P.J. Miller, "Effects of Pressure and Temperature on the Thermal Decomposition Rate and Reaction Mechanism of β -Octahydro-1,3,5,7-tetranitro-1,3,5,7-tetrazocine", J. Phys. Chem., **91**, 3872-3878 (1987).

28. S.A. Shackelford, S.L. Rodgers, M.B. Coolidge, "Deuterium Isotope Effects in RDX Decomposition and Combustion Processes: A Progress Report", 21st JANNAF Combustion Mtr., Laurel, MD, Oct 1984; [Proc.], CPIA Publ. 412, Vol.II, 615-621 (Oct 1984).

29. K. Kishore, "Thermal Decomposition Studies on Hexahydro-1,3,5-trinitro-s-triazine (RDX) by Differential Scanning Calorimetry", Propellants Explos., **2**, 81-84 (1979).

30. The 673 K temperature was selected as the reference point for calculating the 1° KDIE at standard temperature because it is the maximum condensed phase temperature experimentally measured during combustion of a nitramine propellant formulation (see ref 24).

31. J. Sharma, J.C. Hoffsommer, D.J. Glover, C.S. Coffey, J.W. Forbes, T.P. Liddiard, W.L. Elban, F. Santiago, "Sub-Ignition Reactions at Molecular Levels in Explosives Subjected to Impact and Underwater Shock", [Proc.], Symposium (International) on Detonation, 8th, U.S. Government Printing Office, Washington, DC, MP 86-194 1987; pp 725-733.

32. R.N. Rogers, private communication, Apr 1988. An impact machine (drop hammer apparatus) initiates a thermal explosion event and does not cause a steady state detonation.

33. J. Sharma, J.C. Hoffsommer, D.J. Glover, C.S. Coffey, F. Santiago, A. Stolovy, S. Yasuda, "Comparative Study of Molecular Fragmentation in Sub-Initialed TATB Caused by Impact, UV, Heat and Electron Beams", in *Shock Waves in Condensed Matter*, Eds. J.R. Asay, R.A. Graham, G.K. Straub, Elsevier Science Publishers, Amsterdam, 1983, pp 543–546.
34. J. Sharma, J.W. Forbes, C.S. Coffey, T.P. Liddiard, "The Physical and Chemical Nature of Sensitization Centers Left from Hot Spots Caused in Triaminotrinitro–benzene by Shock or Impact", J. Phys. Chem., 91, 5139–5144 (1987).
35. R.N. Rogers, "Combined Pyrolysis and Thin Layer Chromatography: A Method for the Study of Decomposition Mechanisms", Anal. Chem., 39, 730–733 (1967).
36. J.C. Dacons, H.G. Adolph, M.J. Kamlet, "Some Novel Observations Concerning the Thermal Decomposition of 2,4,6–Trinitrotoluene", J. Phys. Chem., 74, 3035–3040 (1970).
37. J.T. Swanson, L.P. Davis, R.C. Dorey, W.R. Carper, "An EPR Study of the Thermal Decomposition of 2,4,6–Trinitrotoluene and its Isotopic Analysis", Mag. Res. Chem., 24, 762–767 (1986).
38. T.M. McKinney, L.F. Warren, I.B. Goldberg, J.T. Swanson, "EPR Observation of Nitroxide Free Radicals during the Thermal Decomposition of 2,4,6–Trinitrotoluene and Related Compounds", J. Phys. Chem., 90, 1008–1011 (1986).
39. J.T. Swanson, private communication, Sep 1987.
40. J. Sharma, J.W. Forbes, C.S. Coffey, J.P. Liddard, "The Nature of Reaction Sites and Sensitization Centers in TATB and TNT", in *Shock Waves in Condensed Matter*, Eds. S.C. Schmidt, N.C. Holmes, Elsevier Science Publishers, Amsterdam, 1987, pp 565–568.

KIVA REACTIVE HYDRODYNAMICS CODE APPLIED TO DETONATIONS IN HIGH VACUUM

N. ROY GREINER
Chemical and laser Sciences Division
Los Alamos National Laboratory
Los Alamos, NM 87545

ABSTRACT. The KIVA reactive hydrodynamics code has been adapted for modeling detonation hydrodynamics in a high vacuum. Adiabatic cooling rapidly freezes detonation reactions as a result of free expansion into the vacuum. After further expansion, a molecular beam of the products is admitted without disturbance into a drift tube, where the products are analyzed with a mass spectrometer. This paper explains how the model is used for interpretation and design of experiments for detonation chemistry. Modeling of experimental hydrodynamic characterization by laser-schlieren imaging and model-aided mapping that will link chemical composition data to particular volume elements in the explosive charge are also discussed.

1. Introduction

We have used the KIVA reactive hydrodynamics code (1,2) to provide a computational model of our experiments in frozen detonation chemistry (3-5). By constraining the model with the known essential features of the experiments, we hope to gain insight about the behavior of the experimental system that will aid in interpretation of experimental results and will provide a basis for the design of new experiments.

Briefly, the experiments involve the detonation of condensed explosives in a high-vacuum environment (Fig.1), where the products expand freely and cool adiabatically (to 300 K) in a very short time (2 μ s) after the shock arrival. Additional (extensive) expansion after the short freezing step allows the mean free path of the product molecules to increase into the free molecular flow regime so that a molecular beam of the products can be admitted without disturbance to a drift tube through a 1-mm-diam skimmer. As the frozen product beam is passing freely down the drift tube, a portion is ionized and its chemical composition is analyzed with a mass spectrometer. Further details are provided in another lecture at this conference (5).

A detailed picture of this process is desired so that the chemical information in the time-resolved mass spectral data can be related to the detonation process. The modeling has provided a picture that has proved useful for the highly interactive process of interpretation

and design of experiments. For example, laser-schlieren movies (or sequences of time-delayed snapshots) provide information-laden images of the early expansion of the exploding charge. These images cover the time during the passage of the detonation wave through the explosive pellet and the subsequent early expansion while the products are freezing. The modeling suggested the feasibility and usefulness of the experiment, and the successful acquisition of good quality schlieren images stimulated the development of a subroutine to compute expected schlieren images, such as explosive characteristics and starting conditions, while the code was under various constraints. The similarities in the computed and experimental images give confidence in our picture of the hydrodynamic history, and the search for constraints that closely reproduce experimental features leads to insights about the process. Discrepancies between output from the model and observations from experiment stimulate closer examination and refinement of both modeling and experiment.

An example of the application of KIVA is the computed interval of time for the arrival at the mass spectrometer of material from specific (and identifiable) volume elements in the unexploded charge. To the degree that material does not mix between volume elements by processes such as diffusion or turbulence, the time-of-arrival interval can be mapped to specific volume elements, for which a hydrodynamic history is available, with the aid of the model. If this enterprise is successful, we will obtain a sequence of mass spectra for a series of volume elements with model-generated (and experimentally validated) hydrodynamic histories, which include the detonation and quenching processes.

2 . The KIVA Code

Our version of the KIVA code has been described (1), and further developments in the code have been made (6). It is an arbitrary Lagrangian-Eulerian (ALE) finite-element code (2) for modeling chemically reactive fluids containing condensed droplets. Modifications for modeling free-expansion experiments have been minimal. The principal modifications are the equations of state of the fluids, the reaction models, the schlieren subroutine, the introduction of rezoning and artificial viscosity to smooth shocks, and the selection of input-output features. The code provides a file of images of the expanding fluid, including mesh configurations (Figs. 2, 10, 15, and 16); velocity fields (Figs. 3-9, 11-14, and 16); and contours of values for various fluid parameters such as density (Figs. 3-10), pressure, and temperature. Other graphics display parameter values for chosen volume elements as functions of time; among these parameters are density, pressure, temperature, diffusion lengths, mean-free-path, and measures of reaction progress (Figs. 20-23). Examples are presented below.

3 . Modeling

The modeling of detonation, which is a reactive shock, requires a number of tricks to make an assembly of finite elements behave acceptably when the parameters are evaluated and advanced with finite time steps. The two major variations involve artificial viscosity and rezoning, both discussed in the descriptions of KIVA (1) and its predecessor ALE (2).

Numerous trials were done to arrive at a compromise between adequate stability and minimal adverse effects on the calculation, but these details will not be elaborated here.

To illustrate our current capability in modeling free-expansion experiments with the KIVA code, we present a selection of results from a single calculation. The parameters chosen were for a nominal case of a right circular cylindrical pellet of RDX (or PETN, approximately) at a loading density of 1.61 g/cm³. Other details of the calculation are given in Table I.

TABLE I. Initial conditions and the governing equations

Charge Geometry:	Right circular cylinder 0.3 cm diam × 0.3 cm high
Initial Density:	$d \text{ (g/cm}^3\text{)} = 1.61$
Pressure* of Detonation Products:	$P_p \text{ (dyne/cm}^2\text{)} = 2.53 \times 10^{10} d^{2.8}$ $+ 8.73 \times 10^9 d^{1.4}$
Pressure of Unreacted Explosive:	$P_r \text{ (dyne/cm}^2\text{)} = [7.3 \times 10^{10} X$ $+ 4.7 \times 10^{11} (1 - X)]$ $\times (d - 1.61),$
where	$X = (2.38 - d/0.77)^{0.4}$
Pressure of Mixture:	$P \text{ (dyne/cm}^2\text{)} = WP_r + (1 - W)P_p$
Temperature:	$T \text{ (K)} = 2287 [(1 - W)d]^{0.4}$
Burn Rate:	$R \text{ (1/s)} = 2.5 \times 10^{-25} P^3$ $+ (1 - W)d[\exp(-5000/T)]$
Fraction of Explosive Unreacted:	$W = W_{old} [\exp(-R \times dt)],$
where	W_{old} is the fraction unreacted from the previous time step and dt is the time step.

$$*10^{11} \text{ dyne/cm}^2 = 100 \text{ kbar} = 10 \text{ GPa.}$$

Some of the issues to be addressed by the model are time-of-arrival mapping to location in the charge (Figs. 17 and 18), degree of scrambling of material by turbulence and diffusion (Figs. 20-23), and freezeout or quenching as a function of location in the charge (Figs. 20-23). In effect, what we seek in the model is a plausible (and approximately quantitative) picture of the hydrodynamic history of the detonating material as a function of location in the charge. To validate the model, we compare predictions based on

hydrodynamics with observations such as time-resolved schlieren images (Figs. 11-15 and 24) and time-of-arrival profiles (Figs. 17-19). With the modeling results presently in hand, we can assign mass spectra to volume elements with computed hydrodynamic histories.

4 . Design of Experiments

We have mentioned the role of modeling in the development and interpretation of the schlieren (Figs. 11-15 and 24) and shadowgraph imaging. Estimates of time and space dependence of fluid densities (Figs. 17-19, for example) have been helpful in designing the new firing chamber, molecular beam drift tube, and mass spectrometer. The scaling of confinement times with charge size and geometry gives estimates of reaction time scales accessible with this technique, which are useful in choosing experiments for particular explosives.

5 . Conclusions

Modeling with KIVA is an indispensable adjunct to the free-expansion experiments. Without the modeling, we would have no grasp of the hydrodynamic histories behind the chemical compositions of the frozen reaction products. The model also provides a quantitative mathematical synthesis of the features believed to be important in the overall process of detonation so that the consequences of that synthesis can be foretold, examined, and compared with observation. Discrepancies between model results and experimental observations generate questions that stimulate and direct further investigation.

6 . Future Plans

Future plans include a study of chemical reaction models that mimic both observed hydrodynamic phenomena and time-dependent chemical composition. It is also desirable to model the leading edge of the expanding products more realistically (compare Figs. 17 and 19). Reduction of artificial numerical contamination of the modeling results is a continuing concern.

We expect that results from our new apparatus (currently under construction) will have considerable influence on future modeling. For instance, if we see significant molecules with a molecular weight higher than the present size limit of 60 amu, their identities and time-dependent quantities must be considered when choosing models for computation. The greatly improved mass spectral data acquisition system expands the opportunities for investigating the effects of the many extrinsic parameters, such as those determined by charge microstructure (e.g., crystal structure, crystal size, void size, and void distribution). High-speed schlieren and other imaging will afford extensive hydrodynamic characterization of each charge and will provide confidence in linking the chemistry to hydrodynamic history for each shot fired.

Clearly, this technique may have application to a widening variety of systems that involve exploding materials, such as propellants, laser-heated materials, electrically heated materials, and materials that are simply shock heated. For example, propellant burn chemistry might be quenched at a desired point in the burn process by firing the propellant in a container sealed with a suitable burstable diaphragm properly aimed at the skimmer. The technique has even been applied to cryogenically prepared samples of energetic materials (7,8).

Acknowledgments

Discussions with my colleagues Norm Blais, Peter O'Rourke, Tony Amsden, Scott Murray, Jack Jacobson, and Frank Harlow were indispensable in the pursuit of this work.

References

1. Amsden, A. A., Ramshaw, J. D., O'Rourke, P. J., and Dukowicz, J. K. (1985), "KIVA: A Computer Program for Two- and Three-Dimensional Fluid Flows with Chemical Reactions and Fuel Sprays," Los Alamos National Laboratory report LA-10245-MS.
2. Hirt, C. W., Amsden, A. A., and Cook, J. L. (1974), "An Arbitrary Lagrangian-Eulerian Computing Method for All Flow Speeds," *J. Comput. Phys.* **14**, 227-253.
3. Greiner, N. R., and Blais, N. C., "Free-Expansion Experiments and Modeling in Detonation: Chemistry and Hydrodynamics on a Laboratory Scale," The Ninth Symposium (International) on Detonation, Portland, Oregon, August 28-September 1, 1989, Preprints, pp. 377-383.
4. Greiner, N. R. (1988), "Freely Expanding Detonation Products: Scaling of Rate Processes," in *19th International Annual Conference of ICT--Combustion and Detonation Phenomena*, Fraunhofer-Institut fuer Chemische Technologie, Karlsruhe, Federal Republic of Germany, pp. 36-1 to 36-13.
5. Blais, N. C., "Detonation Chemistry Studies of Energetic Materials Using Laboratory-Scale Samples," this conference.
6. Amsden, A. A., O'Rourke, P. J., and Butler, T. D. (1989), "KIVA-II: A Computer Program for Chemically Reactive Flows and Sprays," Los Alamos National Laboratory report LA-11560-MS.
7. Greiner, N. R., and Blais, N. C. (1986), "Real-Time Analysis of the Chemical Products from Shocked Nitric Oxide," in *17th International Annual Conference of ICT--Analysis of Propellants and Explosives*, Fraunhofer-Institut fuer Treib- und Explosivstoffe, Karlsruhe, Federal Republic of Germany, pp. 33-1 to 33-10.

8. Blais, N. C., and Greiner, N. R. (1988), "Real-Time Analysis of the Reaction Products of Shocked Solid Nitric Oxide," *J. Energetic Materials* 6, 255-281.

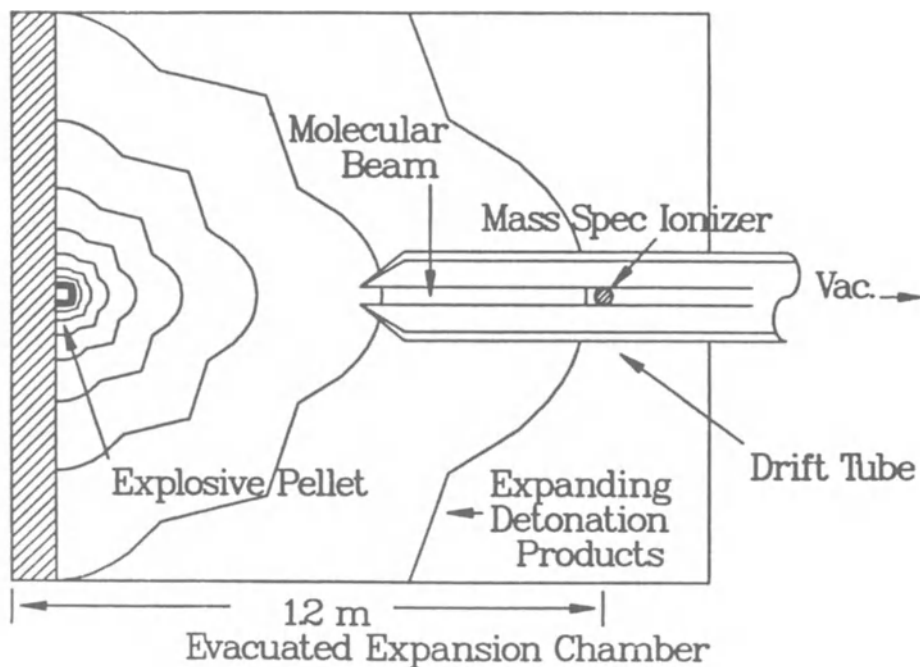


Figure 1. Schematic of the free-expansion experiment. The skimmer is the cone with the tip missing at the left end of the drift tube. Other features are noted.

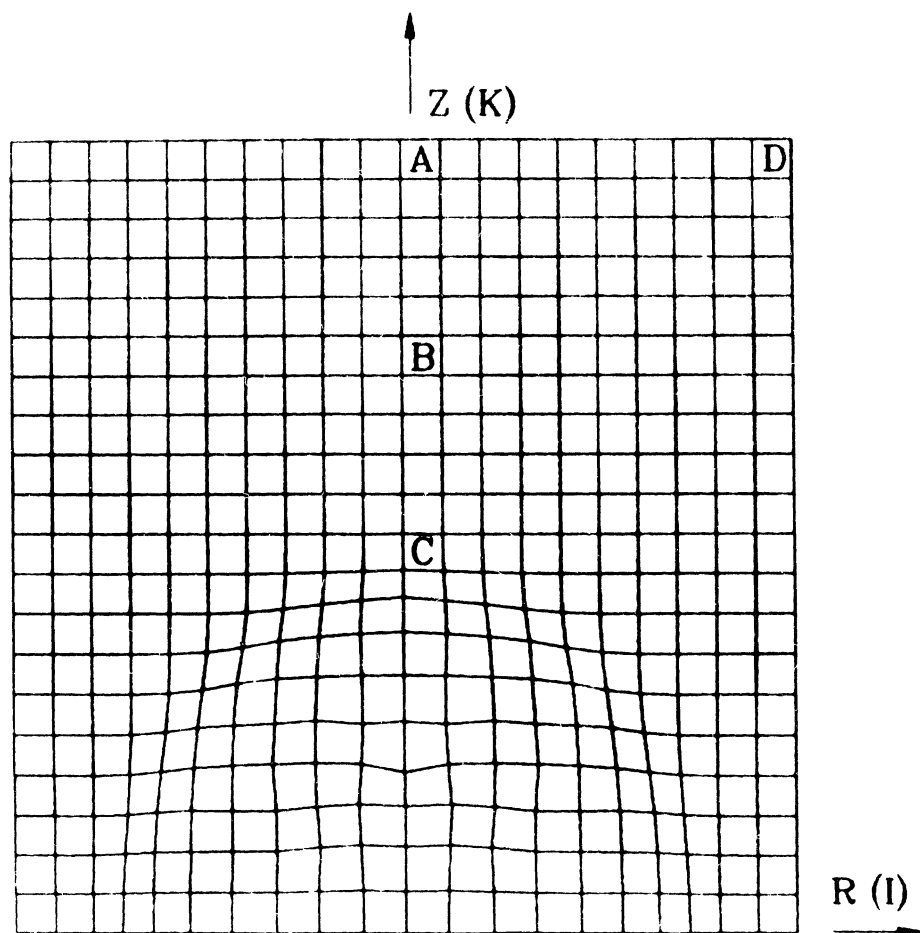


Figure 2. Computational mesh at $0.17 \mu\text{s}$. K indexes the cells in the Z direction starting with 1 at the bottom of the cylinder, and I indexes the cells in the R direction, starting with 1 next to the cylinder axis. Other cells referred to in the text, along with their (I,K) indices, are $A(1,20)$, $B(1,15)$, $C(1,10)$, and $D(10,20)$. The initial dimensions of the cylinder are $Z_{\text{top}} = 3.0 \text{ mm}$ and $R = 1.5 \text{ mm}$. This figure can be compared with Fig. 5, which is also for $0.17 \mu\text{s}$. The compressed cells indicate the position of the detonation wavefront.

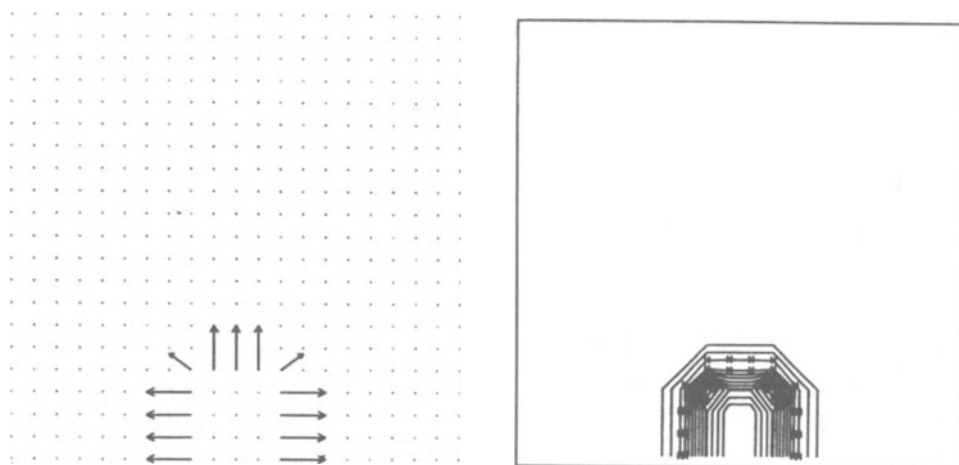


Figure 3. This and the following figures show the progression of the detonation wave through the 3-mm-diam \times 3-mm-high cylindrical pellet with parameters that approximately simulate RDX (or PETN). Initial velocity field and density contours are at 1.5 ns. Vectors originate on cell vertices and length is proportional to velocity. Maximum velocity in the R direction, u , is 0.04 mm/ μ s and maximum velocity in the Z direction, w , is 0.05 mm/ μ s. Density is 1.61 g/cm³ everywhere. The gradients in the initiated cylinder at the bottom are insignificant at this time.

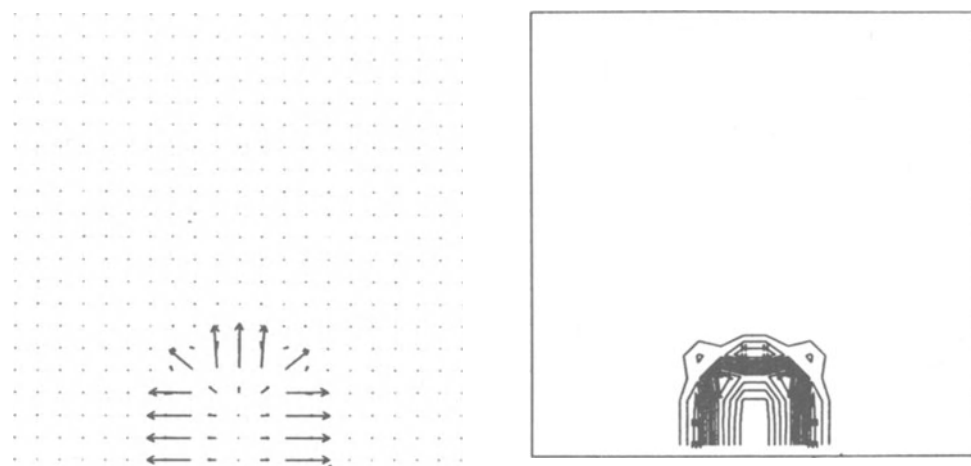


Figure 4. Time = 0.033 μ s, $Z_{\text{top}} = 3.00$, $u = 1.06$, and $w = 1.08$. (Here and in the following figures, Z_{top} units will be in mm, velocity units will be in mm/ μ s and density units will be g/cm³.) The density contours are based on a logarithmic density scale. Densities on intermediate contours differ by a factor (Q) = 0.966. Maximum density (d_{max}) = 1.830, density on the H-contour (d_H) = 1.768, and density on the L-contour (d_L) = 1.344.

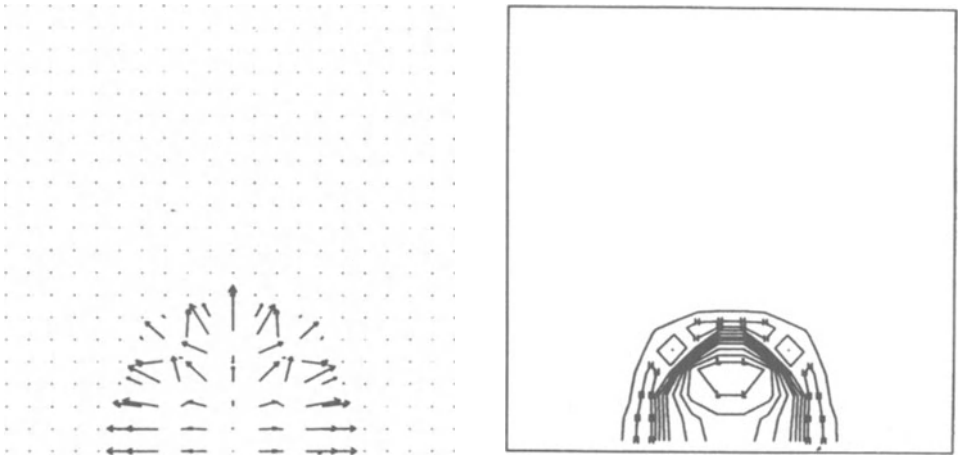


Figure 5. Time = $0.085 \mu\text{s}$, $Z_{\text{top}} = 3.00$, $u = 1.20$, $w = 1.54$, $Q = 0.927$, $d_{\text{max}} = 1.995$, $dH = 1.847$, and $dL = 1.011$.

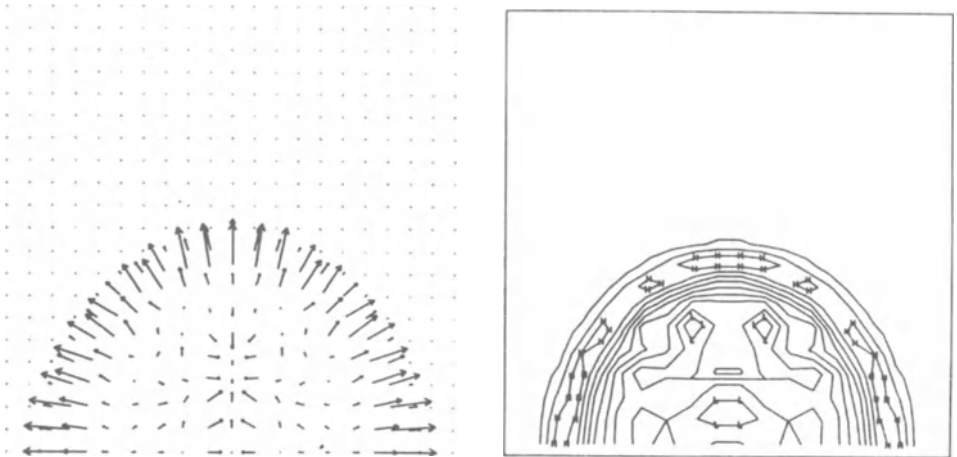


Figure 6. Time = $0.171 \mu\text{s}$, $Z_{\text{top}} = 3.00$, $u = 1.93$, $w = 1.81$, $Q = 0.935$, $d_{\text{max}} = 2.089$, $dH = 1.953$, and $dL = 1.1395$.

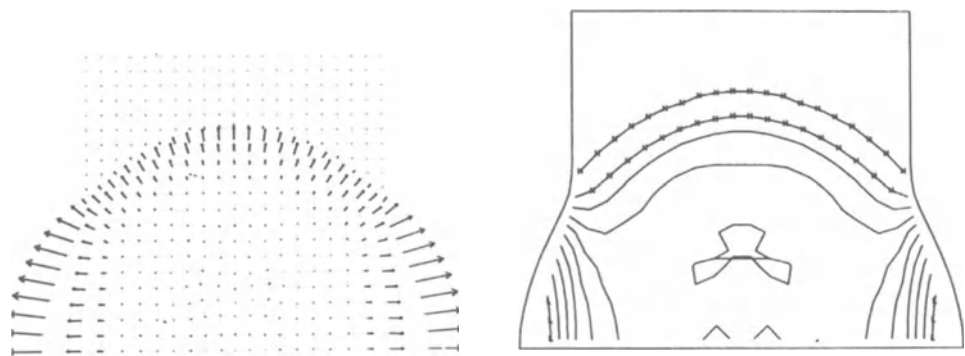


Figure 7. Time = $0.306 \mu\text{s}$, $Z_{\text{top}} = 3.00$, $u = 6.62$, $w = 2.17$, $Q = 0.854$, $d_{\text{max}} = 2.161$, $dH = 1.844$, and $dL = 0.520$. The detonation wave has broken out of the bottom half of the charge surface.

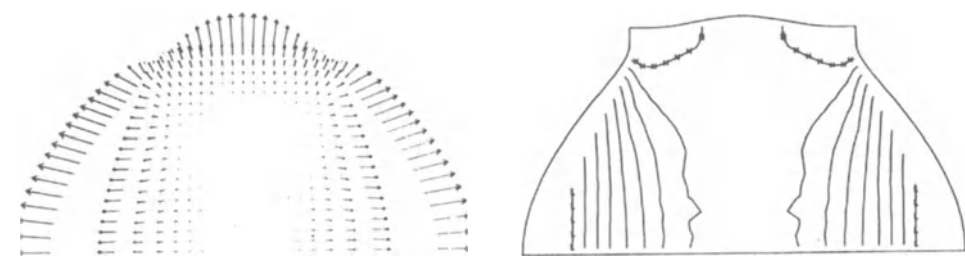


Figure 8. Time = $0.447 \mu\text{s}$, $Z_{\text{top}} = 3.14$, $u = 7.01$, $w = 5.62$, $Q = 0.746$, $d_{\text{max}} = 2.174$, $dH = 1.622$, and $dL = 0.156$.

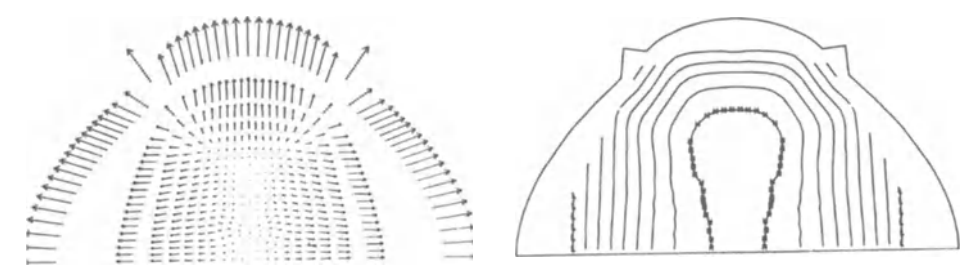


Figure 9. Time = $0.639 \mu\text{s}$, $Z_{\text{top}} = 4.51$, $u = 7.11$, $w = 7.45$, $Q = 0.709$, $d_{\text{max}} = 1.268$, $dH = 0.899$, and $dL = 0.057$. At this time, the detonation wave has broken out of all of the charge surfaces.

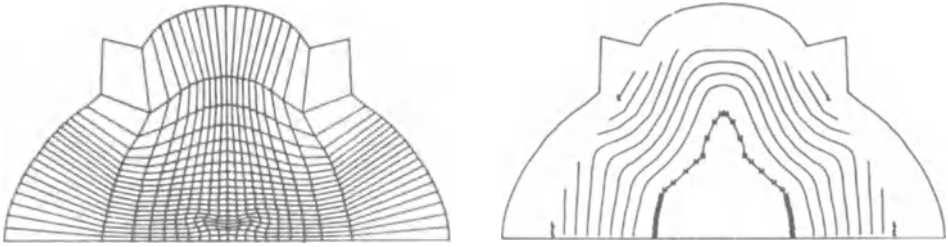


Figure 10. Computational mesh and density map. Time = $1.003 \mu\text{s}$. $Z_{\text{top}} = 7.28$, $Q = 0.675$, $d_{\text{max}} = 0.420$, $dH = 0.283$, and $dL = 0.012$.

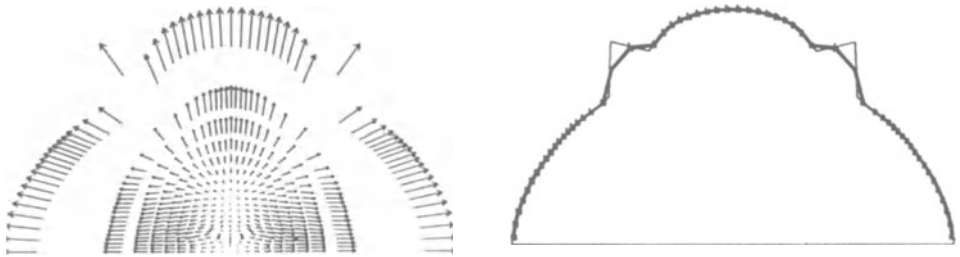


Figure 11. Time = $1.003 \mu\text{s}$, $Z_{\text{top}} = 7.28$ (same as Fig. 10), $u = 7.13$, and $w = 7.71$. This begins a sequence showing computed schlieren-image profiles (right) as contours of deflection angles defined by the schlieren aperture and the Gladstone-Dale constant of the expanding fluid. All schlieren contours overlap in this figure.

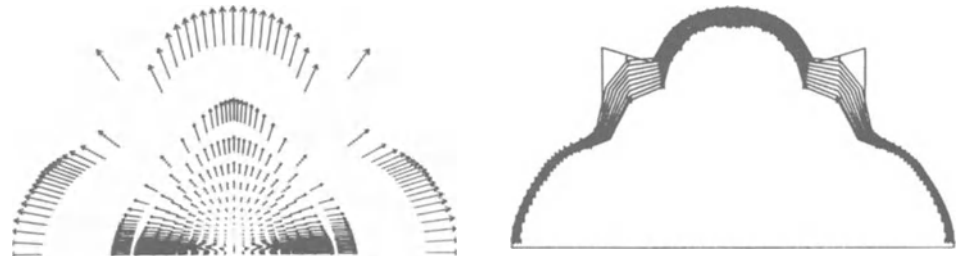


Figure 12. Time = $2.000 \mu\text{s}$, $Z_{\text{top}} = 15.00$, $u = 7.04$, and $w = 7.74$. Schlieren-image contours correspond to different Gladstone-Dale constants for a fixed aperture size. The L contour is that for very complex molecules, and the fifth one from the top is for pure nitrogen gas. The H contour is for a system with a larger aperture than the one used in our experiments. Schlieren contours have the same meaning in Figs. 13-15.

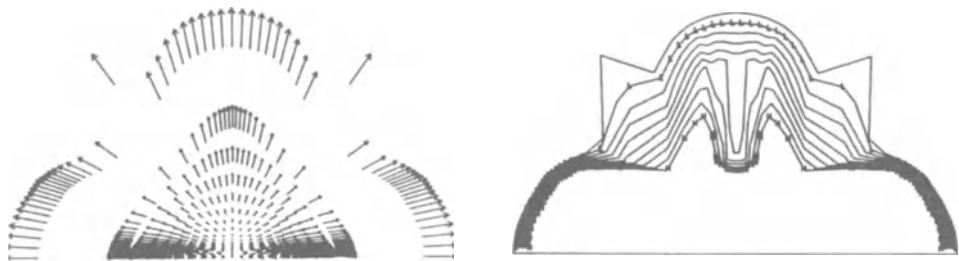


Figure 13. Time = 3.011 μs , $Z_{\text{top}} = 22.81$, $u = 6.92$, and $w = 7.70$.

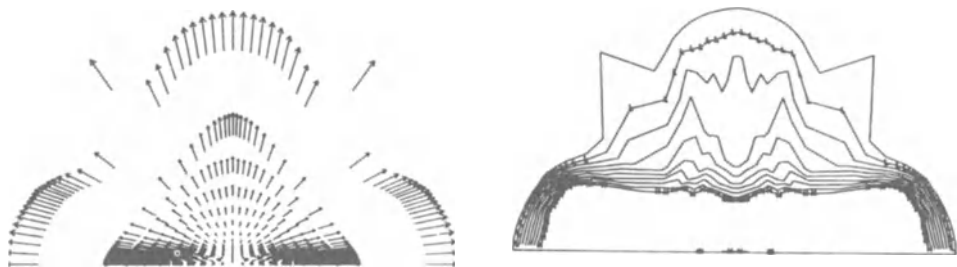


Figure 14. Time = 4.001 μs , $Z_{\text{top}} = 30.43$, $u = 6.81$, and $w = 7.67$. Comparison of velocity fields up to this time show that self-similar flow is established by 4 μs .

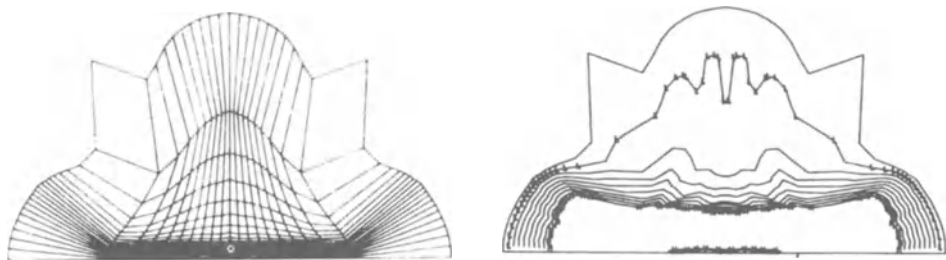


Figure 15. Time = 5.035 μs , $Z_{\text{top}} = 39.34$. In comparison with Fig. 2, the computational mesh (left) shows distortion caused by the detonation and expansion processes.

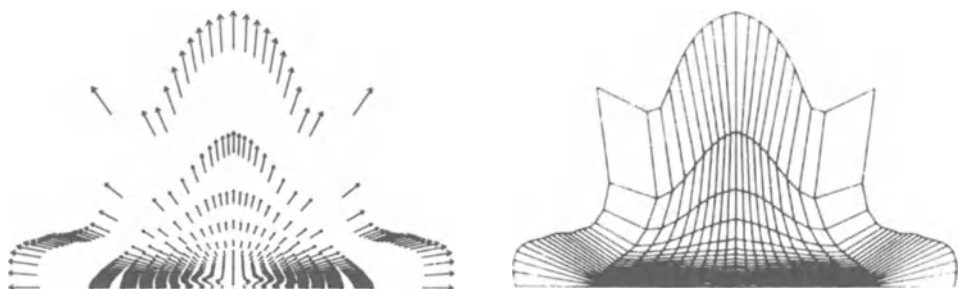


Figure 16. Time = 1006.0 μs , $Z_{\text{top}} = 7.259$ m, $u = 5.79$, and $w = 7.14$. Comparison of this velocity field with that in Fig. 13 shows the long-time cumulative effects of numerical stability functions on the velocities. Comparison of the computational mesh here with that in Fig. 14 shows the effect of the stability controls on the mesh shape.

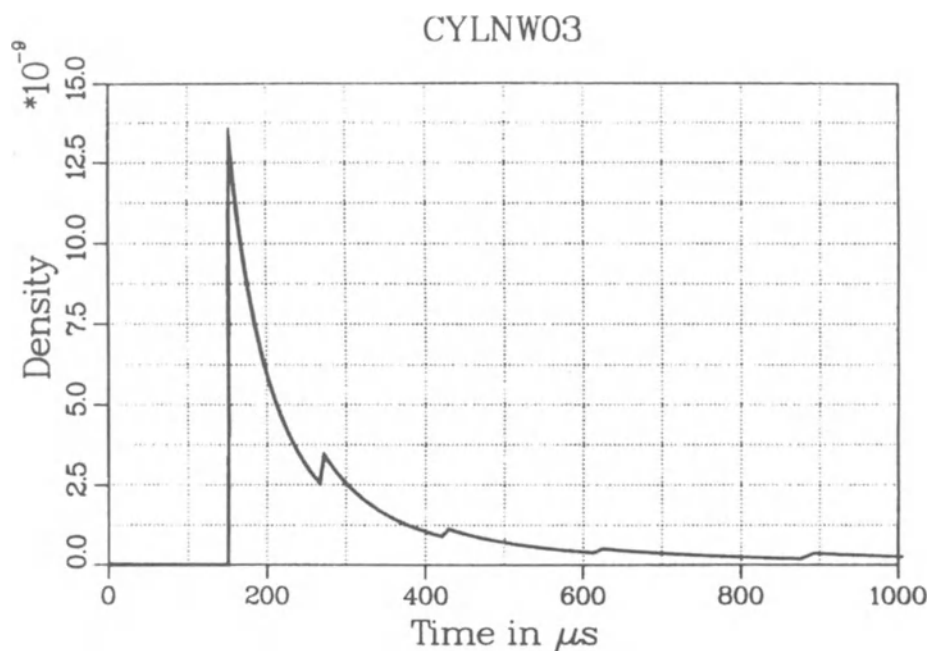


Figure 17. Total fluid density vs time-of-arrival at the mass spectrometer located at $Z = 1.130$ m from the base of the unexploded charge. The points of the sawtooth conveniently mark the times when the leading edge of a new volume element reaches the spectrometer, the earliest being element A in Fig. 1 and the later ones being those shaded cells below A on the cylinder axis. This plot gives information on the mapping of time-of-arrival to volume element, which allows assignment of an observed chemical composition to a particular volume element in the original charge.

Arrival Time Corresponds to Position in Charge

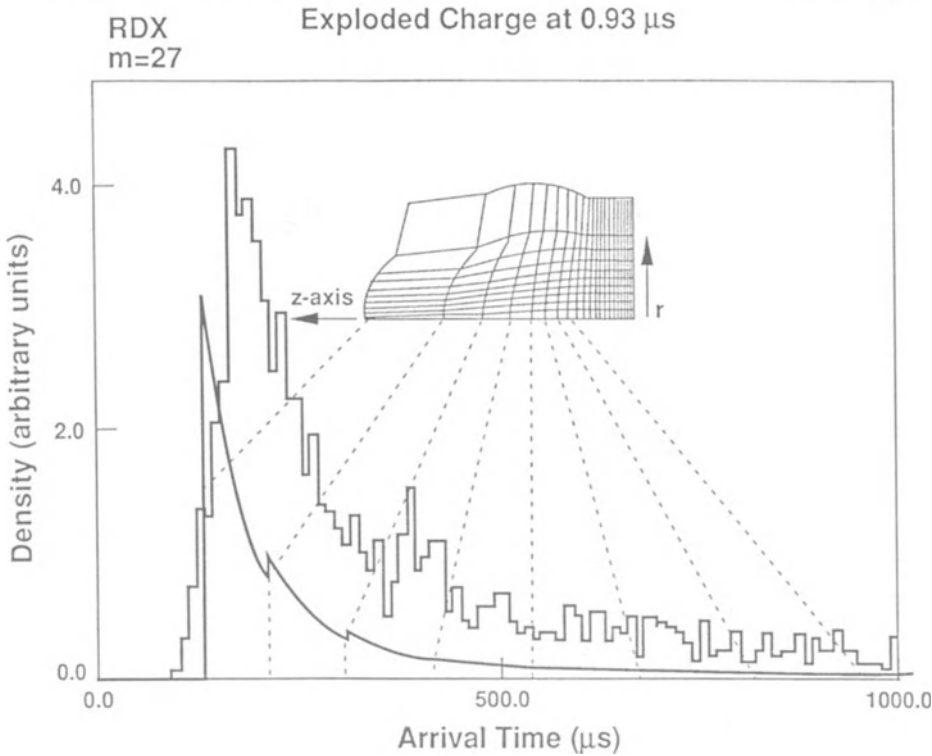


Figure 18. Mapping of experimental time-of-arrival data for mass 27 (HCN) to volume elements in the charge. The experimental data (the series of rectangular bars) in arbitrary units, the calculated total fluid density in g/cm^3 (sawtooth curve), and the mapping of time intervals back to volume elements (dotted lines) are shown. This calculation is an earlier one that started with somewhat less realistic conditions than those used in the most recent calculations.

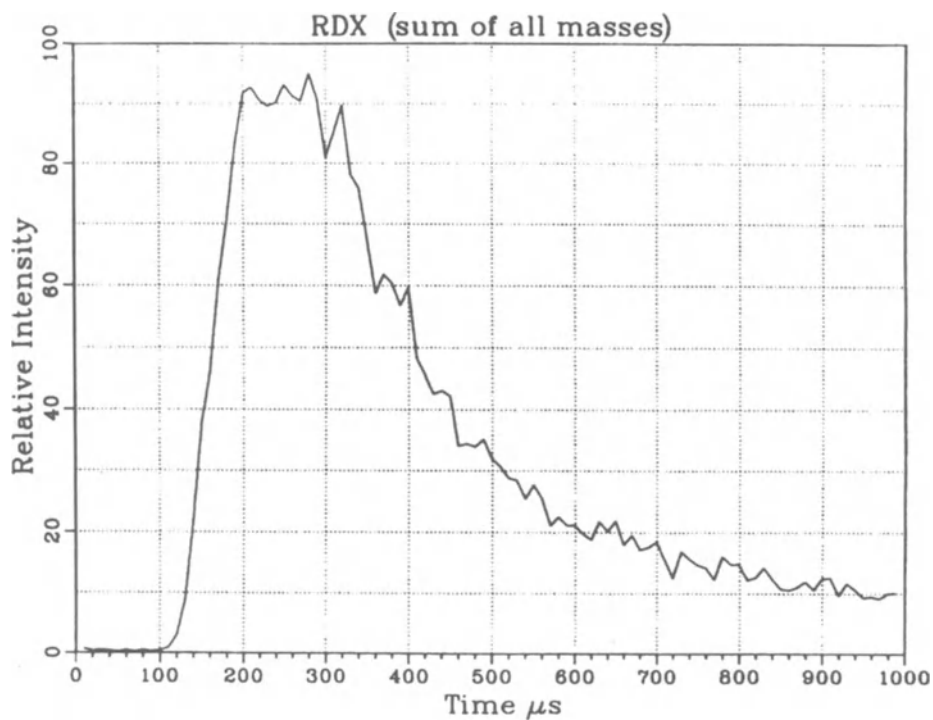


Figure 19. Time-of-arrival plot for sum of intensities of all masses for RDX. This is the experimental data to be compared with the computed density vs time-of-arrival in Fig. 17.

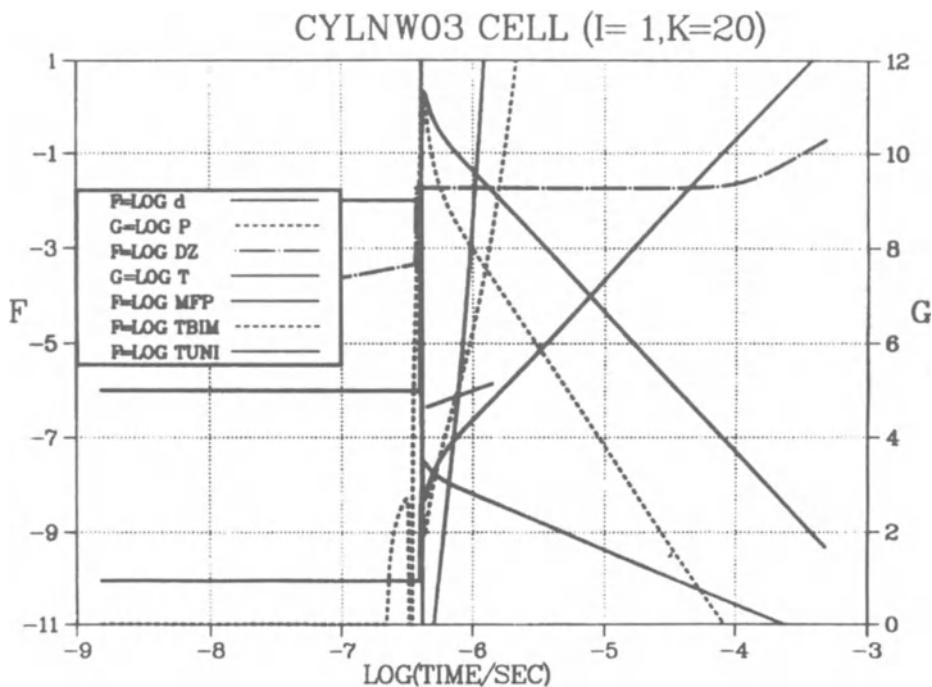


Figure 20. The first of a set of plots showing parameter values that describe the hydrodynamic history of selected volume elements. This plot is for element A in Fig. 1. The units in this figure and the following ones are centimeter-gram-second units, d = density, P = pressure, DZ = time-integrated diffusion distance, T = temperature in K, MFP = mean-free-path of a nitrogen molecule, $TBIM$ = characteristic reaction time for a bimolecular reaction with arrhenius activation energy of 10 000 cal/mol and arrhenius bimolecular frequency factor of 10^{12} cm³/mol-s, $TUNI$ = characteristic reaction time for a unimolecular reaction having arrhenius activation energy of 40 000 cal/mol and arrhenius frequency factor of 10^{16} /s. The sharp vertical group of lines marks the arrival of the detonation wave at the cell. Curves at earlier times are minimally meaningful and will not be discussed here. To identify the meaningful part after the detonation wave, we note the markings starting from the topmost and working down: d (solid), P (dotted), DZ (dot-dash), T (solid), MFP (solid), $TBIM$ (dotted), $TUNI$ (solid). The small line segment marks where the reaction-time curves cross the quench line, which is the point where reaction time equals time after initiation. The crossing point is roughly where the reaction quenches. In this case these reactions quench about 0.4 μ s after the arrival of the detonation wave. The integrated mean diffusion distance, DZ , is less than 0.1 cm (equivalent to 0.2 μ s difference in arrival time) by the time the fluid reaches the mass spectrometer at $Z = 1.130$ m (at 150-270 μ s). This result demonstrates the very small scrambling effect of molecular diffusion.

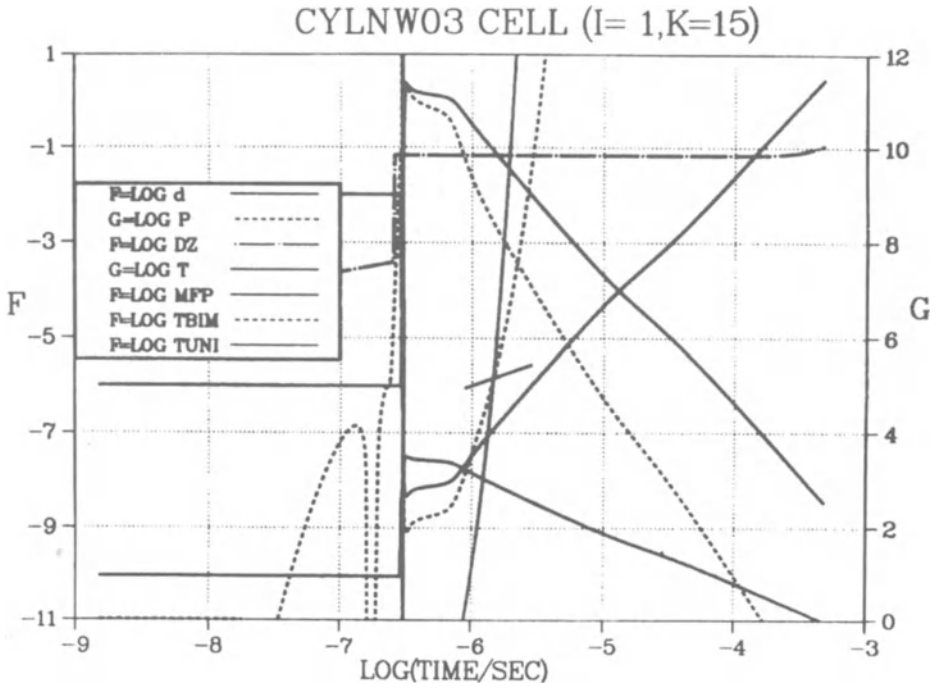


Figure 21. Hydrodynamic history for Cell B, Fig. 1. Curve identifications are the same as in Fig. 17. Quench comes $1.2 \mu\text{s}$ after the detonation wave. This cell is expected to be closer to equilibrium than Cell A.

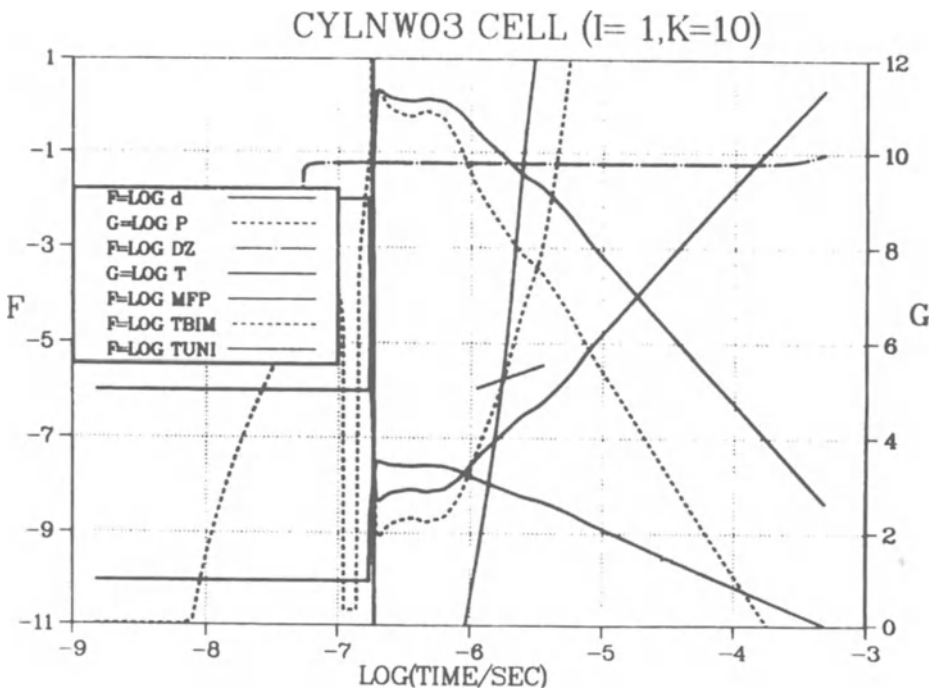


Figure 22. History for Cell C. Quench at 1.6 μ s after detonation. This cell should be even closer to equilibrium than Cell B. Cells A, B, and C are among those sampled in the present experimental configuration.

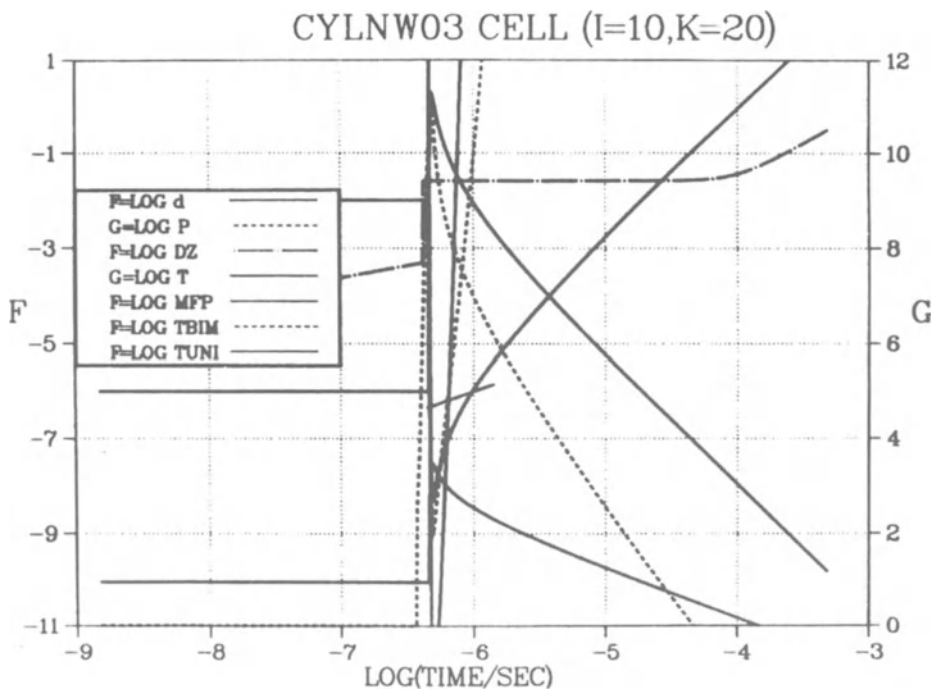


Figure 23. History for Cell D. Quench comes $0.2 \mu\text{s}$ after detonation, which is faster than in Cell A. This result suggests that the corner is a good place to sample for the most rapidly quenched material.

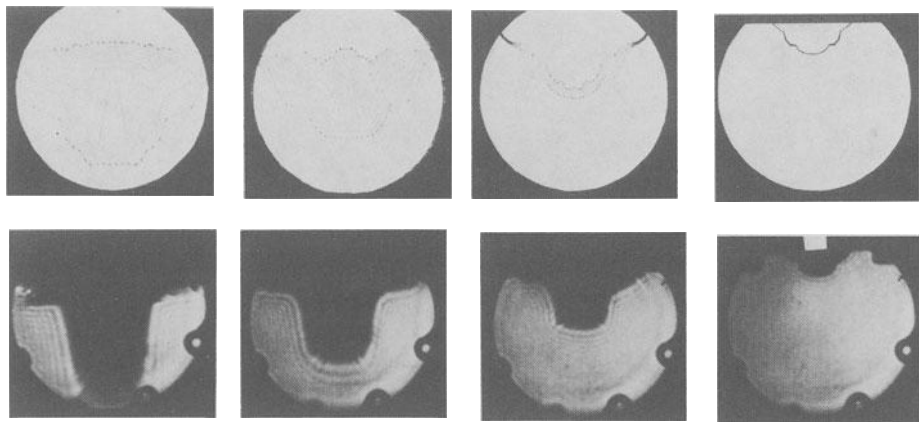


Figure 24. Comparison of computed and experimental sequences of time-delayed laser-schlieren snapshots for detonation of RDX pellets.

DETONATION CHEMISTRY STUDIES OF ENERGETIC MATERIALS USING LABORATORY SCALE SAMPLES

N. C. Blais, N. R. Greiner and W. J. Fernandez
Mail Stop G738
Los Alamos National Laboratory
Los Alamos, NM 87545

ABSTRACT. We describe an apparatus by which the detonation products of an explosive can be identified and whose relative concentrations can be determined quantitatively. These measurements can be made on products that have been formed in less than one microsecond after the passage of the detonation wave. The technique is based on the rapid quenching of chemical reactions by virtue of the free expansion of the products into vacuum. Of course, products that have been formed over a longer period of time and under different pressure/temperature conditions can also be studied. Time resolved molecular-beam mass spectrometry is used, so that whether detonation occurred or not in forming the products can be determined. We describe optical techniques, principally Schlieren photographs, that also confirm detonation. We report measurements made on six standard explosives, PETN, RDX, HMX, HNS, TNT and TATB, and one research explosive, nitric oxide. For none of the standard explosives do we measure product distributions that agree with model predictions based on equilibrium assumptions. A computer model of the free expansion is described briefly and its importance to the interpretation of the data is emphasized.

INTRODUCTION

The apparatus that we are going to describe and the experiments performed thereon are intended to provide, in the long term, data that lead to the identification of the important chemical reaction

mechanisms or pathways that are responsible for the propagation of detonation waves in explosive materials. The convening of this conference is evidence that this is an important goal to some people, at least. But we know that this chemistry remains, in large part, a mysterious process except that in very general terms it is an oxidation process or a "flame" initiated by a shock.¹ In our view, the mystery arises because the chemistry involves reactions that are a direct consequence of what are now called "many-body interactions," a subject that is not well understood and which only now is being tentatively probed by chemists. Because it is a relatively new subject, it promises to be an exciting time for some of us.

In the shorter term, as a necessary step to studying the chemistry of detonations, we want to know what the products of those chemical reactions are. We already know the identity of the reagents in detail, because analytical and crystal structure fields are well established disciplines and have long been applied in explosive studies. But the reaction products are not so easy to identify. The equilibrium products can be inferred from thermodynamic considerations, and very careful measurements have confirmed that these are the products one finds some time after the Chapman-Jouget (CJ) conditions have been attained.² For many applications, this is all the information that one needs. Very successful models of the detonation wave propagation in specific explosives are being developed using only the heats of formation of the explosives and their bulk physical properties. These successes don't provide much insight into the chemistry that drives the process, however, because their successes seem to be insensitive to any input about chemistry. As kineticists, we are impressed by the hydrodynamic models and shock wave measurements, but we very much would like to know what the products of the reaction are in the region between the CJ point and the detonation front, and their relative concentrations. We know of no experiments that have provided information of this kind for any explosive, although one or two molecular species have been identified spectroscopically.³ In the following presentation, we will describe an apparatus and some

experiments which we feel attain the goal of providing the desired reaction product spectrum.

EXPERIMENTAL ARRANGEMENT

The idea behind our experimental arrangement is to take advantage of the rapid cooling of the detonation products that occurs if these products are allowed to expand freely without impediment to the stage where they become isolated molecules. So the apparatus is designed to be able to look at those reaction products for which the expansion and the subsequent cooling is maximized, the free surface at which the detonation wave ends.

We use small, generally cylindrically shaped explosive charges having a mass of about 20 mg to 100 mg in weight. The charges are shocked to detonation from one end of the cylinder so that the detonation wave ends at the other end of the cylinder. The material at this far end subsequently expands away from the body of the now hot, still very dense products of detonation, with a velocity close to that of the detonation wave. The expansion is sufficiently rapid that the effective temperature of those products is reduced to the point that chemical reactions are quenched in a time that we calculate is less than a microsecond. This time, then, determines the time duration between the passage of the detonation wave and our ability to examine the product concentrations. For some explosives, such as TNT, our data suggests that some of the products are from that region of detonation wave propagation called the "reaction zone." During our experiments, the time over which measurements are made is considerably longer than one microsecond, but these times are not relevant except for those products that can change their states spontaneously, for example by radiation.

Our "work-horse" method of identifying the reaction products is electron impact ionization mass spectrometry. We feel that this method is one of the most generally universal for all chemical species and sufficiently adaptable for fast measurements to be the central focus in the instrument design. It is now a well developed technique developed by chemical kineticists during the

1970s that is ideal to examine those detonation products at the leading edge of the expanding gases, that of molecular beam mass spectroscopy. By the time that the gases have expanded to about ten times the original pellet dimensions, the temperature is low enough that there are scarcely any collisions at all. Thus the molecules are now moving in unison, and we can utilize molecular beam forming techniques to direct them into a mass spectrometer designed especially for molecular beam detection. This allows us to obtain a mass spectrum of the products that reflect directly the concentrations they had at the time that the expansion quenched the reactions that formed them. Moreover, by allowing the molecules to drift, collisionlessly, over a measured path length we can measure their velocities with reasonable accuracy and obtain a time history of the density of a product in the expanding gases.

Figure 1 is a diagram of the apparatus we use which has the characteristics to do what we have described above. It consists of three principal parts: the detonation vacuum chamber, the molecular beam skimmer and differential pumping chambers, and the quadrupole mass spectrometer detector.

The detonator vacuum chamber is large compared to the other parts of the apparatus, and contains the apparatus to detonate the charges and sometimes optical components for spectroscopic studies. Its dimensions are determined by several considerations, the first being that the pressure rise that occurs in it following the detonation of the explosive charge does not adversely affect the other parts of the apparatus. Having a volume of about 280l, detonating a 100-mg charge gives rise to a pressure increase of about 100-200 mPa (1-2 micron). But in determining its dimensions it is also important to consider that no surfaces are located in a position to intersect and reflect molecules back into the drift region of the molecules to be formed into the molecular beam. These considerations also determine where we locate a rotatable carousel that supports and aligns the detonator stations. We can fire a charge every 5 minutes, which is the time that we normally need after each shot to evacuate the chamber to a pressure of 10^{-4} Pa (10^{-6} torr). At these pressures, the mean free path for

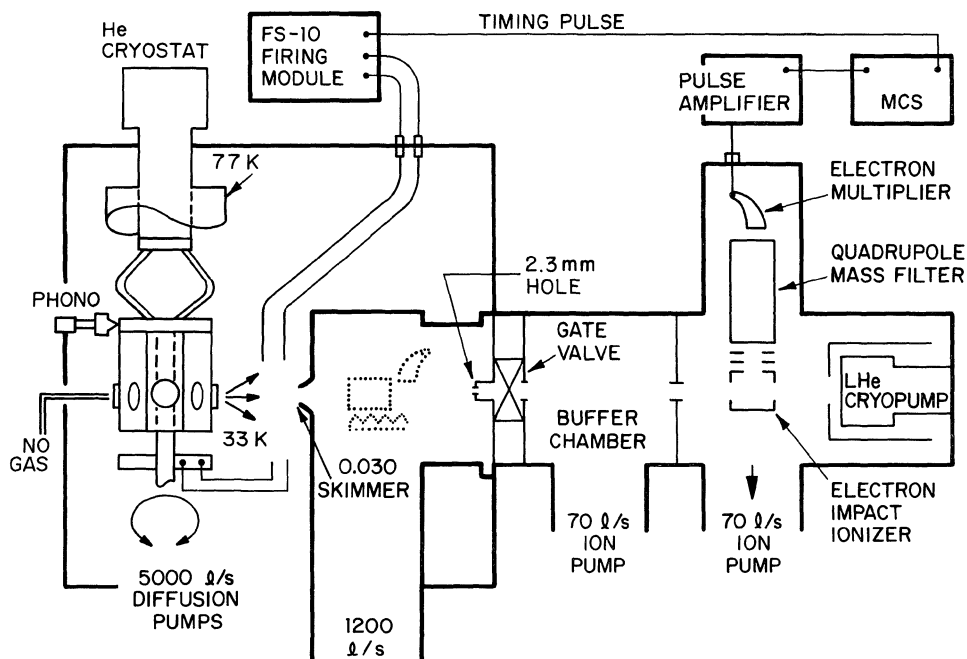


Figure 1. Schematic arrangement showing essential features of the apparatus for the mass spectrometric examination of the reaction products from detonation. The figure is not to scale, and the text has a more complete description of the design considerations. Also reference 15 and others therein contain more details.

collisions in the ambient gas is several meters, so that the detonation product expansion is a "free expansion."

The skimmer serves the function of forming a molecular beam of those products that we want to examine under the collision-free conditions we discussed above. Its design is somewhat critical because the density of the gases are high when they arrive at the skimmer. If many molecules collide with the edges of the skimmer aperture, they can be reflected back into the oncoming particles that follow in time and cause a shock to be formed that distorts the velocity and temperature of the beam. Our skimmer is designed to minimize these types of collisions by virtue of a very sharp cone angle (15 degrees) and a very thin edge (1/40 mm).⁴ The skimmer aperture is 1 mm, and we estimate that about 1% of the molecules that are intercepted by the skimmer are scattered back into the path of oncoming molecules. Two stages of differential pumping follow the skimmer that serve to effectively isolate the mass spectrometer detector from the large pressure variations of the detonation chamber.

We detect the molecular beam with a quadrupole mass spectrometer.⁵ The combination electron impact ionizer-mass filter-electron multiplier is estimated to have an overall efficiency of detection between 10^{-7} and 10^{-8} for a nozzle beam of argon atoms. The vacuum chamber in which it is housed never rises in pressure above 10^{-7} Pa (10^{-9} torr), and a cryopump is located so that any neutral molecules that escape the detector are trapped in the cryopump. Except for very low mass signals, all of the detonation signals are very large compared to background. Pulse counting electronic signal processing is used in conjunction with a multichannel scaler (MCS) so that a time history of the product density arriving at the detector is obtained as standard data. Time of flight velocity analysis is routine over the 110-cm drift path taken by the products from the detonation point to the ionizer. Actually an apparatus preceded ours with design characteristics that were very similar in many respects⁶ but our apparatus was developed independently. A mass spectrum of PETN, one of the

explosives we will discuss here, was reported. However, no other work has appeared subsequently.

Figure 2 shows an example of the way our data looks from the molecular beam detector. The number of counts recorded in each channel of the MCS is plotted as a function of the arrival time at the detector. For convenience we have converted the ordinate from the channel number to the time elapsed to reach the center of each channel. Each channel is proportional to the number density of product molecules with the indicated mass at the indicated time after the explosive charge was detonated. The data shown is from PETN and the ion masses are for $M=15$ and $M=44$, the latter being scaled by a factor of 0.4. Since it is unlikely that $M=15$ is a fragment of $M=44$, the figure serves to emphasize that the threshold for the arrival of products at the detector is independent of mass, so that the higher mass has about three times the energy of the lighter mass. To show that the time history of the arrival of products at the detector contains information about the chemistry, in Fig. 3 we show times-of-arrival averaged over all of the masses for two explosives, RDX and TNT. They are clearly much different from each other, and we are tempted to speculate that the difference at the shorter times arises because of the difference in the length of the reaction zones of the two explosives. TNT has a longer reaction zone than does RDX, and thus some of the products originate deeper in the TNT pellet than it does for RDX and so arrives later at the detector. Unfortunately reaction zone data is not very common, especially for pure explosives we show here, and considerable differences of opinion exists about the meaning of their measurements. We point out that only one mass at a time can be examined for each detonation of a pellet of explosive. The reproducibility of the signal intensity for several trials at one mass depends very much on the particular explosive being studied, sensitivity and homogeneity apparently being important factors. For this reason, we always rely on at least six trials or more at masses with large signal intensities, and at least two or three for masses with little or negligible intensity. We are examining the use of time-of-flight mass spectrometers, and an ion-trap device to obtain the entire mass spectrum at one trial.

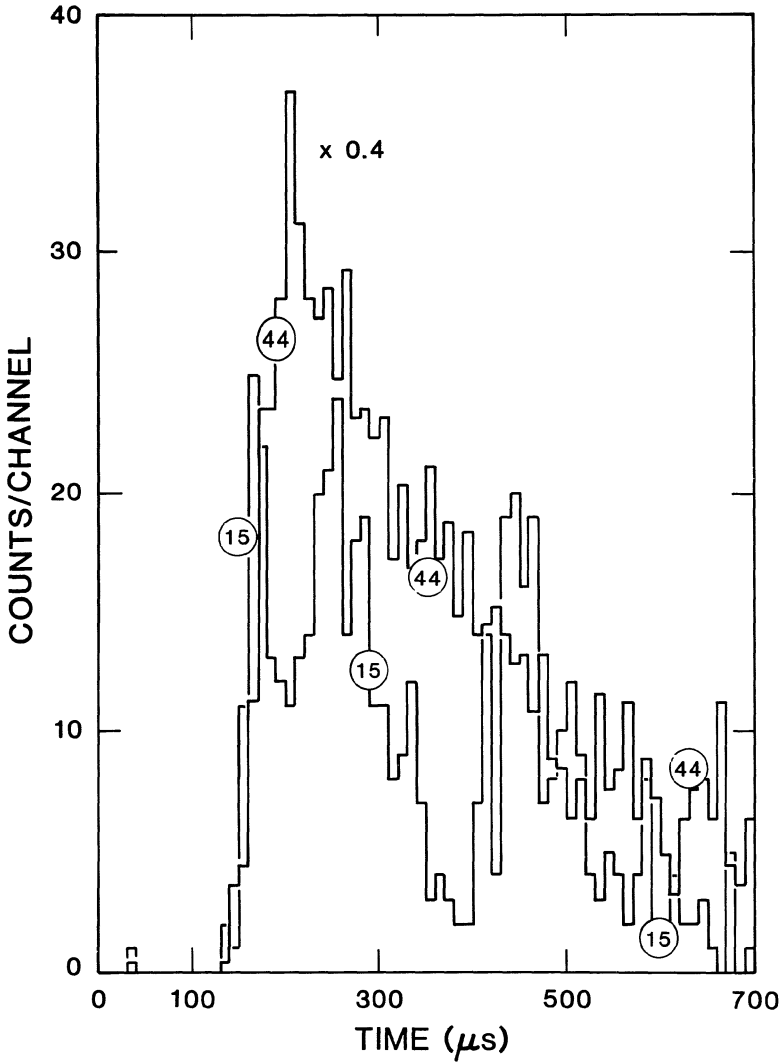


Figure 2. An example of data obtained with the quadrupole mass filter. The vertical axis is the number of ions counted while the multichannel scaler was in a particular channel. For convenience the horizontal axis has been converted from channel number to the elapsed time from detonator excitation to the time that a particular channel number was being filled. Two sets of data are shown, one with the mass spectrometer set at $M=15$ and the other at $M=44$. The latter was scaled by a factor of 0.4

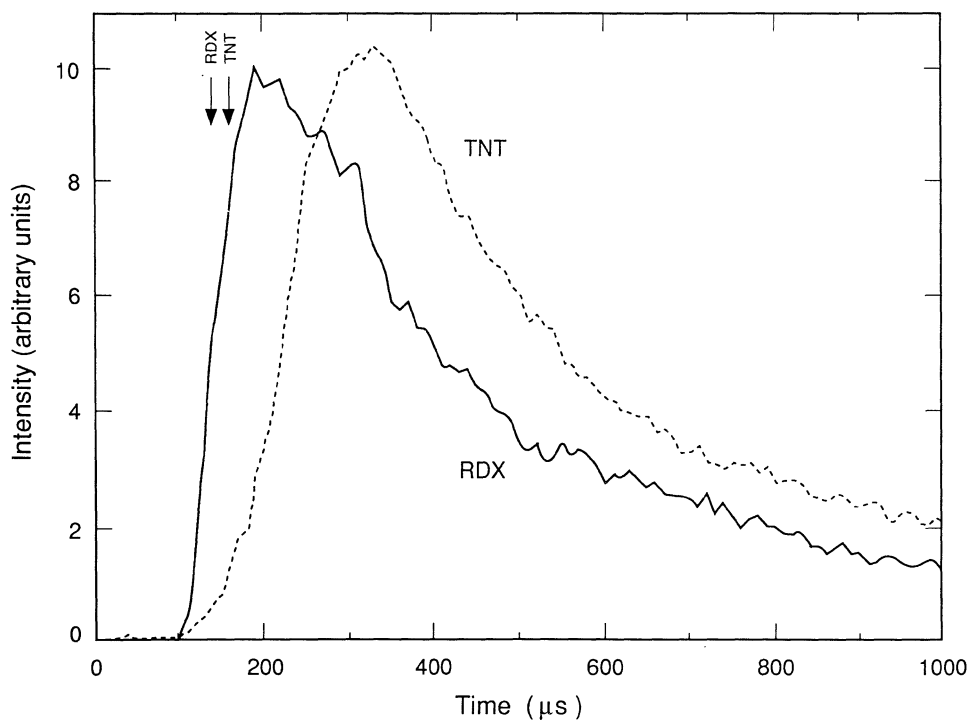


Figure 3. Time of flight spectra for two explosives averaged over all of the masses contained in the mass spectrum. RDX and TNT are being compared. The respective detonation velocities are shown with arrows, with that for RDX on the left.

All of our explosive samples that we've used so far, with the exception of solid nitric oxide, contain 0.1 g or less. With NO, quantities of 25-35 mmole are used to ensure detonation. The densities are relatively low so that pure explosives can be detonated without booster charges. Kapton slappers driven by deposited copper bridges detonate all but the solid NO and TNT. For these, PETN booster charges are required.

A rotatable carousel allows us to load and fire up to 30 charges in the large detonation chamber without the need to vent the high vacuum for replacements. We can also use a carousel which has only 10 charges, but which can be cooled to 30 K to study explosives such as nitric oxide or to perform more exotic experiments some of which we will describe later.

COMPUTER MODELING

An indispensable part of the work connected with our program is the modeling of the detonation of the charges being studied and the subsequent free expansion of the detonation products. We will not discuss this aspect in detail in this lecture because the subject will be discussed by our coworker in another lecture. The interpretation of the data is very difficult without such modeling of the relevant events, and we will mention only a few points that bear directly on the experiments themselves.

A computer code called KIVA is being developed for the modeling process which can incorporate reaction kinetics during the gas phase portion of the expansion, after the detonation wave has reached the far surface of the pellet. Realistic equations of state of products are used, and the starting conditions include approximate conditions of a Taylor wave. The code has been used to simulate some of the optical diagnostics, such as Schlieren photography, that are a part of the experimental techniques we use. It accurately represents the leading edge velocity profile of the products as being closely the velocity of the detonation wave in the explosive material, and it predicts the density-vs-time profiles we observe experimentally. We use it to model the temperature distribution in the free expansion as a function of the stage of the

expansion, and it confirms that for some explosives, we should be able to distinguish products that originate in the reaction zone as the detonation arrives at the surface of the pellet in the field of view of the mass spectrometer detector. Figure 4 is a plot showing some of the relevant parameters that characterize the small volume near the surface of an explosive pellet. The temperature of the gas, the density, the pressure and the mean free path are included in this busy set of graphs, but we particularly want to call attention to the estimates of inverse of the rate constants for bimolecular exchange reactions and also for unimolecular process. A bimolecular reaction with an activation energy of 10 kcal/mole and an A factor of $10^{12} \text{ cm}^3 \text{ mole}^{-1} \text{ s}^{-1}$ is seen to reduce its rate a thousand fold and is effectively quenched in less than a microsecond after the detonation wave has reached the surface of that volume.

One of the assumptions of the code that we hope to examine in more detail is that there is very little mixing of the products that originate at different depths of the explosive charge during expansion. Preliminary studies have not yet refuted that assumption, but the experiments have not been very definitive on the mixing point. Should this assumption be borne out, then the model suggests that the time dependence of the arrival of each species in the products reflects directly the depth in the pellet at which the species was formed. Furthermore, the pressure and thermal history experienced by the products in each increment of depth in the pellet is also different, and calculations of the kind shown in Fig. 4 can be made for any distance from the pellet surface. Therefore, we should also pay attention to the experimental distribution of products for various time slices in a three dimensional plot of intensity as a function of mass and time-of-arrival.

ARE WE STUDYING DETONATION?

This question arises often enough that we are devoting at least a short section to its discussion. In our opinion the explosive charges for which we acquire data are detonating. It may be

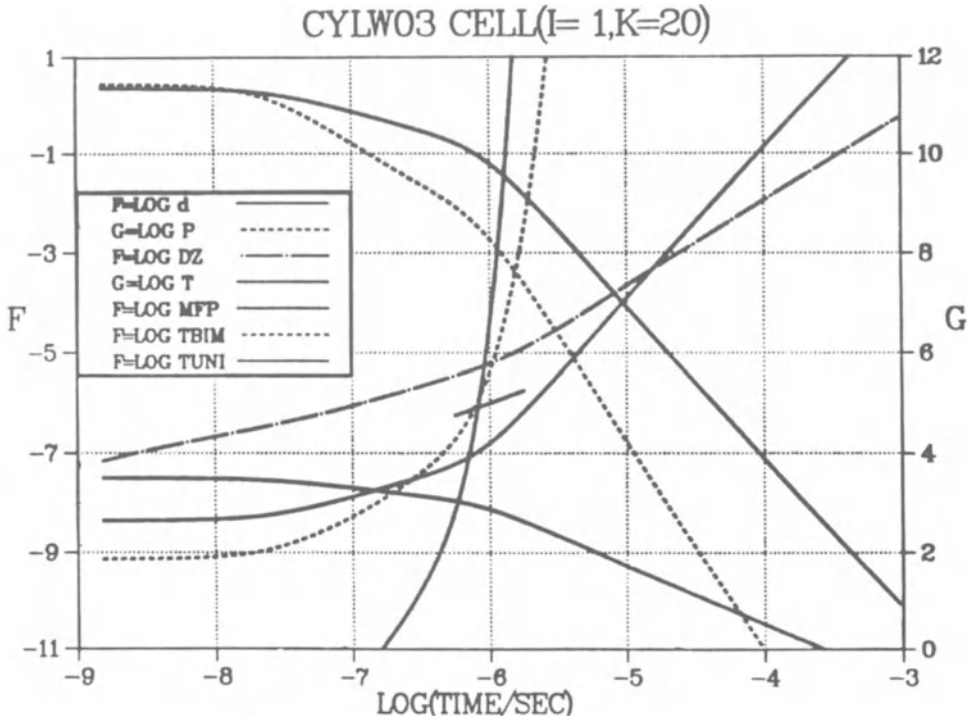


Figure 4. A log-log plot of some of the important reaction product external variables calculated using a modeling program to represent the free expansion of those products from a pellet 3mm diameter and 3 mm high. The products have been given an equation of state somewhat characteristic of PETN. The particular mathematical cell considered here is at the cylinder end opposite to the detonation point. In the legend d stands for density, p for pressure, T for gas temperature, MFP for the mean free path for collisions in the gas, TBIM is the inverse of the rate for bimolecular exchange reactions, TUNI is the inverse of the rate for unimolecular decomposition. For the TBIM curve an activation energy of 10 kcal/mole and an A factor of 10^{12} was used. The short section of line that intersects TBIM and TUNI indicates the time at which quenching occurs.

suggested that this should not be a matter of opinion, but that we should be able to establish it unequivocally. Unfortunately, the matter is not that simple. The statement has been made that since a detonation is a steady state wave phenomenon, then a large amount of detonating material in an ideal geometry is necessary to ensure that a steady wave is established. Our sample sizes are sufficiently small that it becomes questionable if a steady wave forms for some explosives, especially for example in TATB where the reaction zone is measured to be of the order of the pellet size. With this strict definition of a detonation, there is perhaps some justification in the question. However, we have made various kinds of tests or measurements which indicate that our experimental conditions demonstrate some of the important characteristics of detonation. If ideal detonation is not occurring, then a high order process is occurring which has enough features in common with detonation to be of chemical interest to us. We discuss below some of the relevant test and measurements we look for to establish detonation.

Dent tests, or witness plate tests are made for each of the explosive materials that we study. We do this so that we can determine the slapper electrical energy, or the slapper size that is needed for the explosive pellet to reliably produce a dent larger in diameter than the pellet in a steel plate or rod held in contact with the pellet. Not only does this convince us that the pellet is detonating, but we are assured that we have minimized conditions that lead to variability we sometimes find in mass spectral intensity.

Schlieren and shadowgraph photographs are made of the freely expanding gases for most of the explosive materials that we've studied. The Schlieren images are particularly useful because we can make the sensitivity of the method high enough to locate the leading edge of the expanding products. With several photographs made at well timed intervals, the velocity of that leading edge can be determined with a simple ruler measurement. These measurements indicate that even in the early stages of expansion, within a few millimeters of the initial explosive surface, the

velocity is approximately the detonation velocity. Our KIVA model and other theoretical models⁷ indicate that this should be the case.

Time-of-flight measurements of the molecular products with the mass spectrometer are part of the data collection procedure, and velocity determinations are often made. Under conditions that have been determined by the dent tests and by Schlieren photographs to give detonation, the velocities of the early arriving products have velocities close to the detonation velocity of the explosive. This feature is very reliable, so reliable that if it is clear that the time history of the ion signal during a particular measurement does not have this high initial characteristic velocity, we assume that detonation was incomplete and discard the data. In just about every case that this happens there are other characteristics of the data that make it suspicious.

COMPARISON OF HYDRODYNAMIC DATA WITH THE MODEL

Figure 5 is a diagram of the optical arrangement that can simultaneously take a photograph in the Schlieren mode and in the shadowgraph mode, transverse to the direction of the expansion of the products. In the Schlieren mode, which effectively puts the image plane at infinity, a ray of light which is refracted by density gradients in the expanding gases by one milliradian or more is stopped by the aperture at the focus of the last concave telescope mirror. A dark region appears in the photographic image where that ray would have been in the absence of the refracting medium. On the other hand, the shadowgraph mode gives a different image for every finite image plane distance, and only at infinity does the Schlieren and shadowgraph look alike. In this mode we can look inside the dark regions of the Schlieren image.

Figure 6 is a set of slides of Schlieren and shadowgraph images taken with the apparatus of Fig. 5 with RDX. Each slide is a set of a Schlieren image and a shadowgraph image taken at the indicated delay after the detonator was triggered. Very striking to us is the highly directional characteristic of the expansion process seen most clearly in the Schlieren image. There is no resemblance to a hemispherical expanding cloud of gases that one might expect if

Optical Apparatus

Telescope Reflection Angles Exaggerated: 4-5°Max.

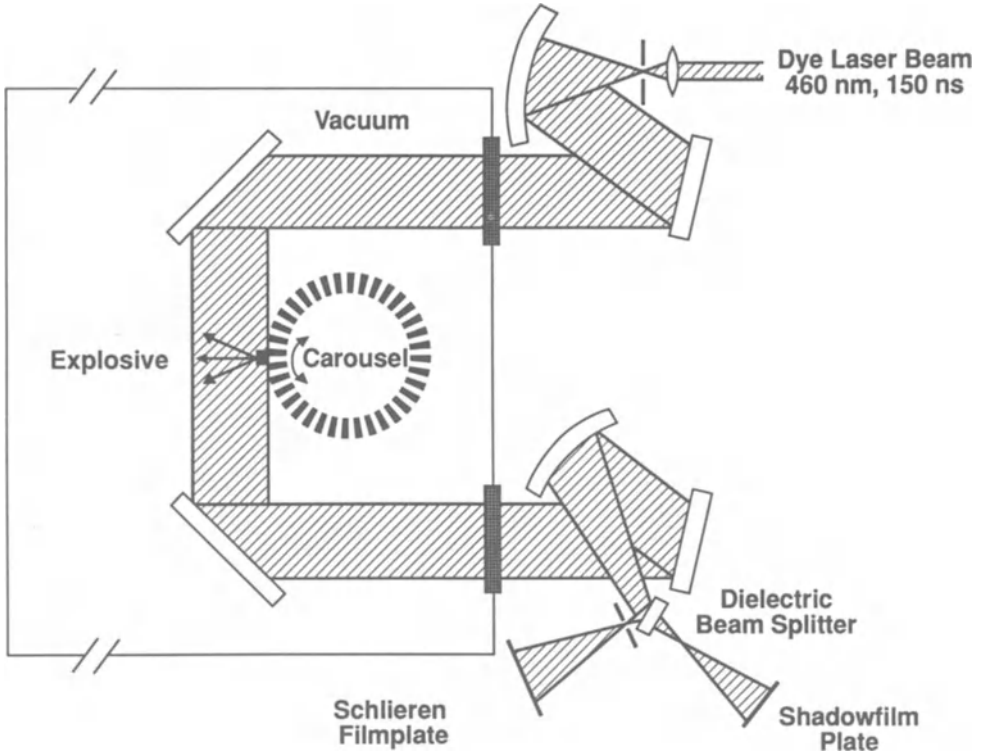


Figure 5. A schematic of the optical telescope arrangement for taking Schlieren and shadowgraph photographs transverse to the motion of the freely expanding products of a detonating pellet. The beam diameter at the pellet is about 35 mm. The Schlieren aperture is slightly less than 1/3 mm (0.015 inches). The angles are exaggerated in the figure, the maximum angle of reflection from the curved mirrors being about 4-5 degrees.

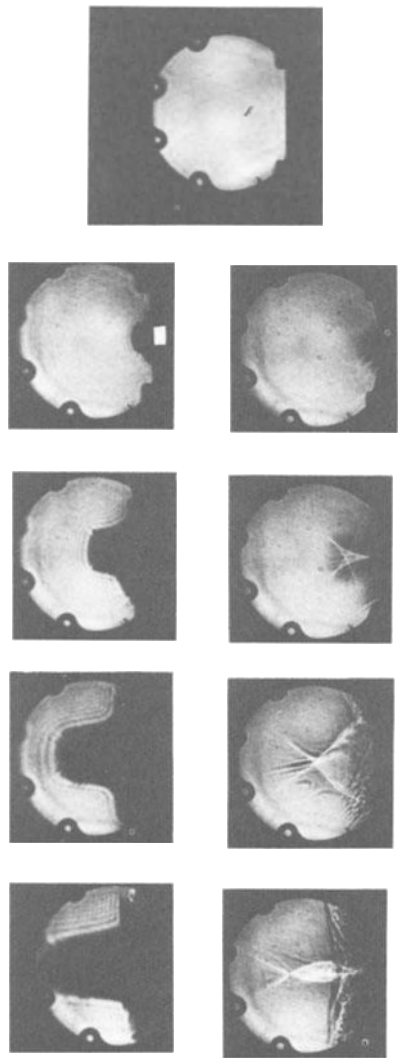


Figure 6. Contains four slides of pairs of photographs consisting of a Schlieren photograph and a shadowgraph. The top single photo is of the field of view without a detonating pellet. The first pair is taken 2 microseconds after initiation, the second pair at 3, the third pair at 4 and the fourth pair at 5. The pellet was RDX. The small protrusions on the periphery of the circular window are caused by retaining rings that hold the windows in place.

one pictures the pellet explosion as being a conversion from a solid to a high temperature, high density gas. One sees the remnants of the detonation wave in the shape of the pellet expansion. Also, there is a clear difference between the Schlieren and the shadowgraphs. The fact that the shadowgraph is looking inside the Schlieren image indicates that it is refraction arising from an index of refraction gradient that causes the difference in the images. The bright geometrical portions in the shadowgraphs are probably caused by lensing effects similar to the rings one sees on the bottom of pan of water if waves are set up.

If we do the same photography with PETN pellets, the images are much the same as for RDX. However, the explosive TNT, HNS and TATB give very much different shadowgraph images from PETN or RDX. The shadowgraphs look so nearly as dark as the Schlieren images that they are indistinguishable. Evidently, the dark regions of the images do not arise from refraction for these three explosives, but from absorption of the light. As we will discuss later, carbon clusters are observed in the product distribution for these three explosives, and these clusters may be responsible for the absorption of light but we haven't established this yet. The only evidence we have to support the statement is that the shadowgraphs do not become completely opaque until one microsecond or so after the expansion starts, and large carbon clusters are relatively slow to form as compared to the production of other products.

A different slapper and support design was required to study the mass spectra of TATB and HMX, and we needed to use larger pellets. We found that the steering optics near the detonating pellets of the optical arrangement of Fig. 5 did not hold up for as many shots as were needed for a complete sequence of photographs. We were able to borrow a fast framing camera that took a sequence of 8 images that covered the complete range of the expansion⁸ with only one pellet firing. Figure 7, which is another slide, is a set of motion picture "stills" taken at one microsecond frame intervals, with an illumination time per frame of 200 nanoseconds. Instead of a

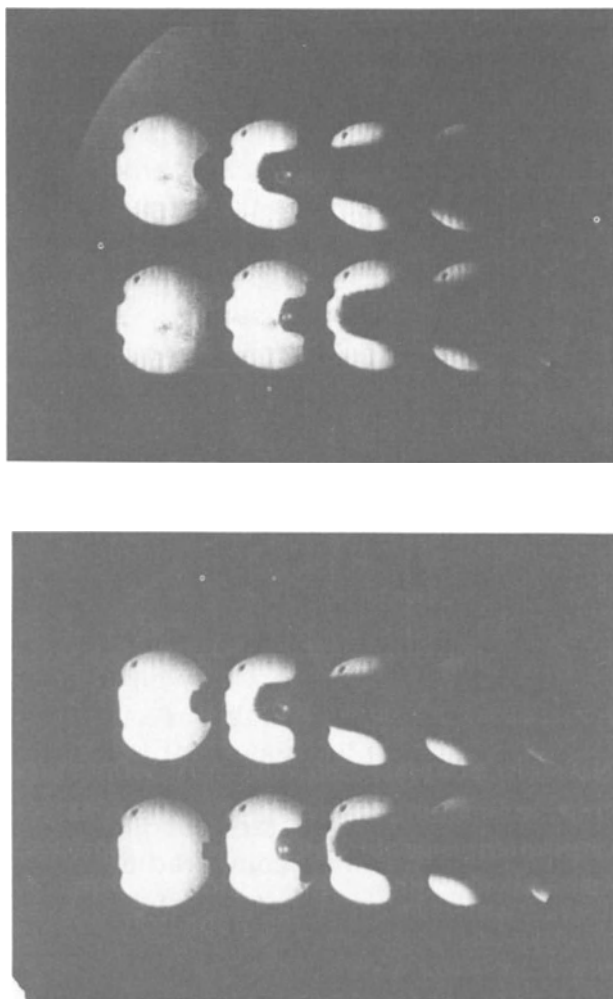


Figure 7. Schlieren photographs of TATB, but these were taken with a fast framing camera. The sequence of each frame is from the bottom frame to the top frame, which is then repeated after being shifted from left to right. Each frame is one microsecond apart, and was exposed for 0.2 microseconds. A cw laser was used for illumination, at 514.5 nm and 1/2 watt.

pulsed dye laser, the light source was an argon ion laser operating at about 1/2 watt of energy at 514.5 nm.

Firing an identical TATB pellet and detonator arrangement in air gives a much different expansion pattern than the one shown in Fig. 7. We show the effect that an ambient pressure of air at atmospheric pressure has in Fig. 8, which was also obtained using a fast framing camera.

MASS SPECTRUM OF DETONATION PRODUCTS

A composite plot of the mass spectra of six of the explosives that we have studied is shown in Fig. 9. For each of the explosives, the plots were obtained by summing up all of the counts in the channels of the MCS, up to channel 40,400 μ s after detonation of the pellet. The sum for each mass was then compared to that at a standard mass, several shots of which were always recorded for each run of from 17 to 26 shots. Thus provided with an intensity ratio, several instrumental variables were eliminated between runs made on different days. It is these ratios that we show in the plot, and, as we mentioned earlier each mass point is actually an average of several of these ratios. An adjustment is included in the plot to account for the mass transmission of the quadrupole mass filter, but no correction is made to the intensity for the ionization sensitivity of the electron bombardment ionizer. Thus the relative ion mass ratios of Fig. 9 are almost raw data of the mass spectrum. Making the more difficult corrections would necessitate having the identity of the parent molecule that gives ions at each mass. We have not progressed to that point yet. Truncating the sum at 400 μ s is arbitrary, but our intention is to eliminate from our analysis molecules that may appear at late times because they were directed into the detector by collisions with parts of the apparatus.

We estimate that the accuracies of the relative intensities shown in Fig. 9 are about 30%. Some of the more intense signals are perhaps more accurate than that with respect to each other, but we don't want to suggest that these spectra have the quality obtainable using refined analytical mass spectrometer instruments. For example, we do not obtain a good atom inventory for those explosives in the first column of Fig. 9, but we will discuss this

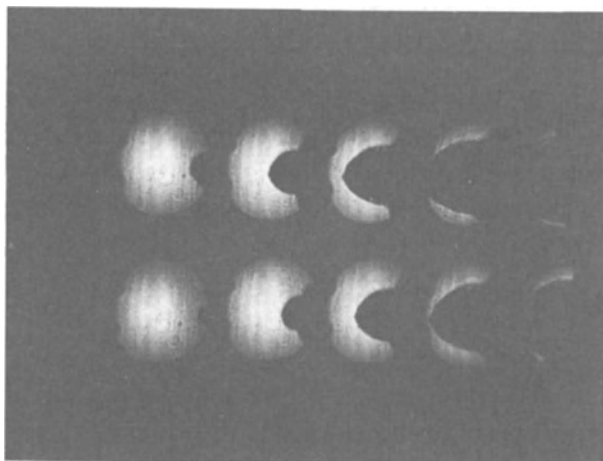


Figure 8. The same as Fig. 7 except that the pellet was detonated with the ambient pressure at one atmosphere instead of at high vacuum.

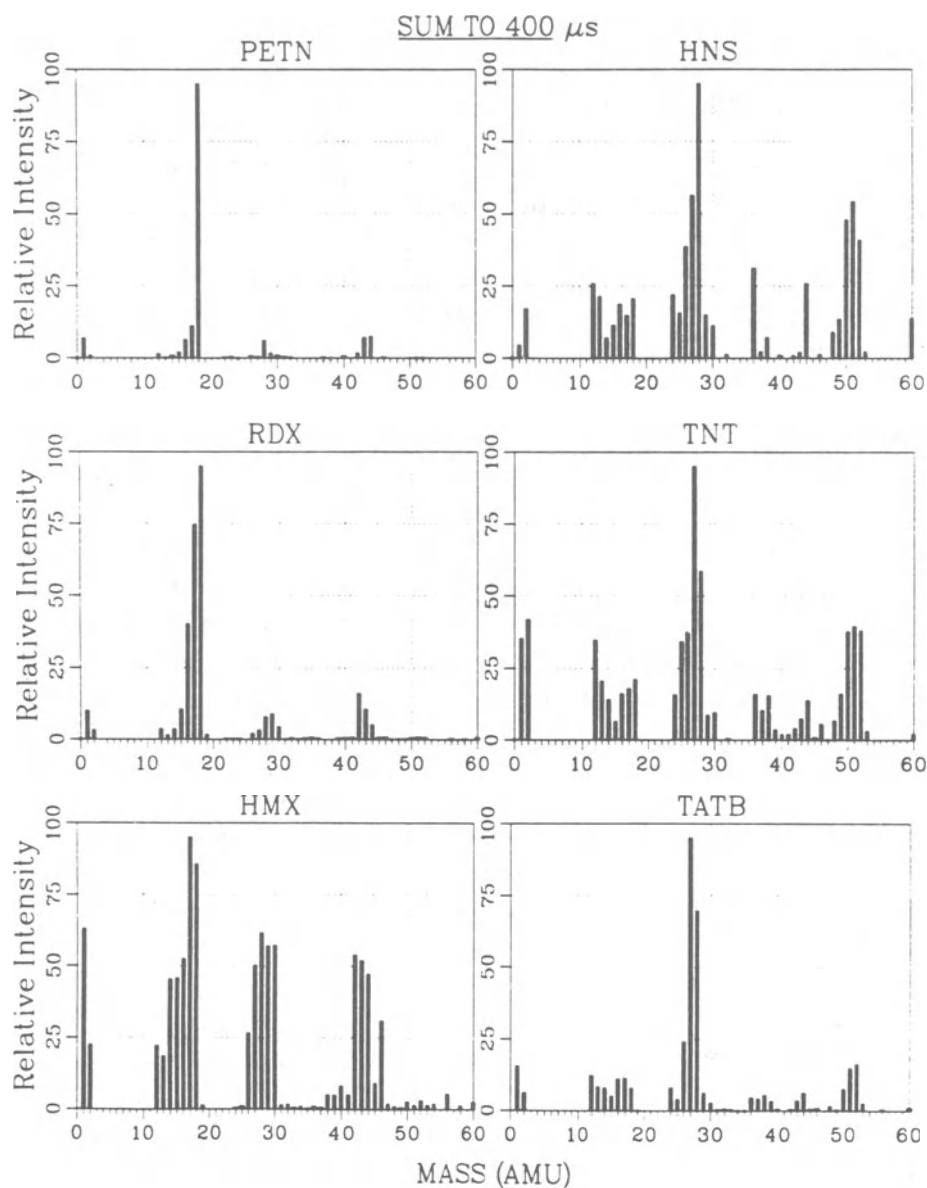


Figure 9. A composite of the mass spectra obtained for the six explosive substances indicated. The vertical scale is relative to the most intense peak in each of the spectra, and are not scaled with respect to the other materials on the plot.

more later. We intend these data to show important qualitative features about the detonation products and how they compare to other information about them.

By comparing the two columns of Fig. 9, it is clear that there are at least two different classes of explosives represented. For PETN and for RDX, on the left, the mass 18 ion, which is almost certainly largely from H_2O , is the dominant product. Those explosives on the right, TNT, HNS, and TATB, have the predominant intensities around mass 28 with very little mass 18 contributing to the spectrum. Mass 28 is a mixture of ions from CO and N_2 , and if we assign about a 20% N_2 -80% CO, the atom inventory from those spectra on the right are reasonably good. Mass 27, which is also fairly intense, must arise largely from HCN. We recognize that the right hand group consists of explosives which are considered to be oxygen poor, i.e., the ratio of oxygen to carbon is low for the formation of CO_2 . Those explosives on the left are oxygen balanced, with both RDX and HMX having almost identical chemical formulas. HMX, although it is placed in the left hand column, has a spectrum which has characteristics of both the oxygen balanced and the oxygen poor explosives. The mass 18 ion and the masses 27 and 28 are almost of equal intensity. Thus the expectation that its spectrum should look nearly the same as that of RDX because of its similar chemical formula is not borne out. The popularly used codes that calculate the detonation velocities, etc. of explosives at the CJ condition, such as BKW and Tiger, long have been known to require input parameters that can be grouped as RDX-like or TNT-like to reflect the fact that there are two groups of explosives based on relative oxygen content. Therefore our observations coming from Fig. 9 is not unexpected. What is unexpected is the way that this grouping manifests itself in the mass spectrum by the predominance of $M=18$ for one group and $M=27$ and 28 for the other.

There is no similarity between our observed product distribution and those predicted by the codes however. In Figs. 10 and 11 we have plotted several synthesized mass spectra obtained from experiments that quench the product distributions of detonations at near-equilibrium conditions at temperatures of about 1500 K to

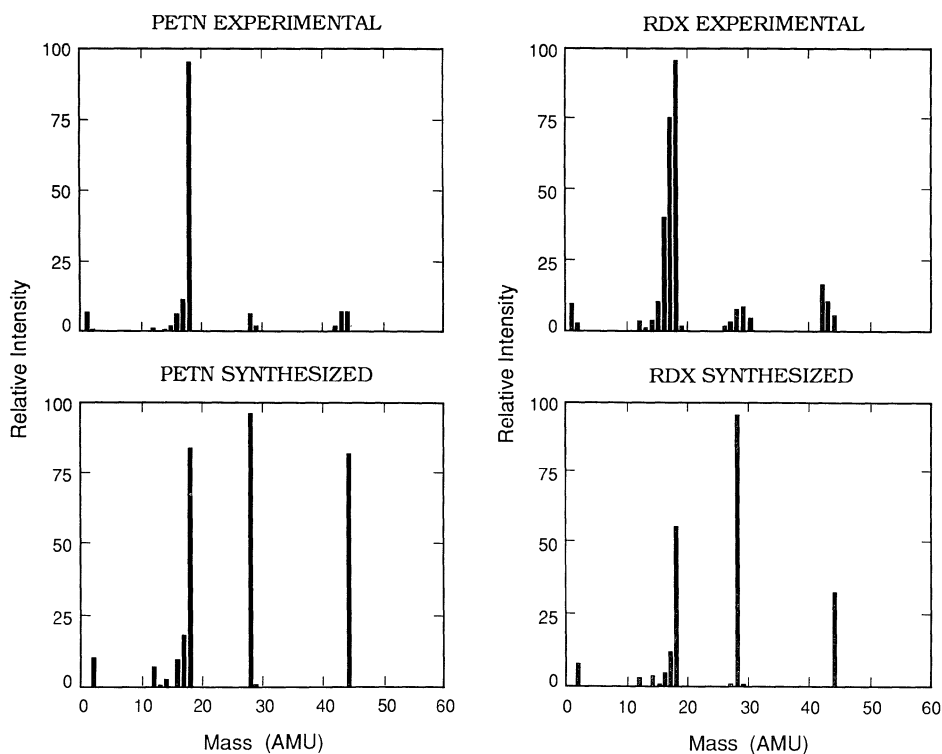


Figure 10. This plot compares the experimental mass spectra for PETN and RDX with a set synthesized from equilibrium data.² Ion fragments expected for the given parent molecules are included in the synthesized plots, and we have omitted very small values for ease of plotting.

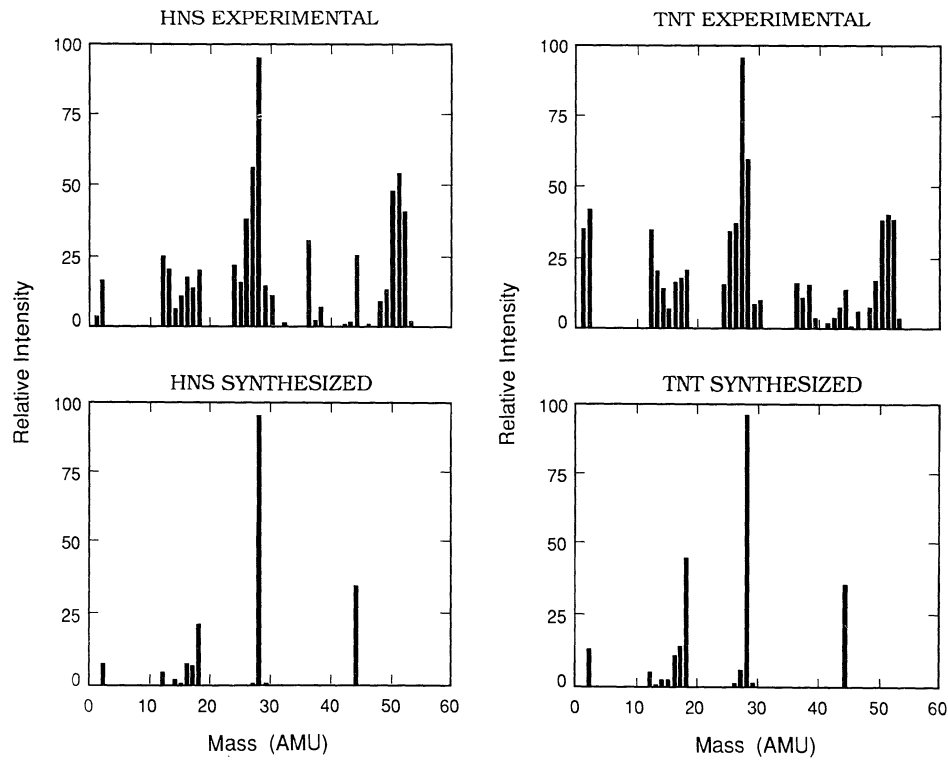


Figure 11. Same as Fig. 10, but for the explosives HNS and TNT.

2000 K.² Except for some differences arising because of a higher temperature at the CJ point, these sorts of distributions are what the computer codes would also predict because they make the assumption of equilibrium between product states throughout the computations. To make the comparison to our mass spectra more appropriate, we have included the fragmentation pattern for the known products.⁹ For convenience, the figure also has our mass spectrum for the same explosive. It is clear that there are many differences between the equilibrium products distributions and those that we obtain. Conspicuously absent from the experimental results is a sizable intensity at $M=44$ coming from CO_2 or N_2O and an absence of a dominant product in the synthesized distribution. There is also evident a much richer distribution of products in the measured spectrum, and although some of ions are the result of electron impact dissociation in the ionizer, most of them have only a small fractional contribution from fragments of heavier parent molecules. Unfortunately we have not been able to reconstruct the neutral molecule product distribution that leads to the experimentally observed ion distribution.

All of the plots in Fig. 9 end at $M=60$. This is because we find no significant intensity above that mass. For each explosive, we searched at higher masses to convince ourselves that we hadn't missed an important product contribution. The mass at the molecular weight of the explosive molecule was always examined as well as masses below that value at which one would expect to see an ion if the parent explosive molecule were present in the products. What we found was that there were traces of ions at many of these masses, all the way down to the lower masses where the intensities rise for M less than 60. But it is difficult to do anything quantitatively with these traces of product, and we feel that their presence may account for the difficulty of getting a good atom inventory or mass balance from some of our spectra. From Fig. 10 it is clear that the measured spectrum of PETN has a lot of argon and nitrogen missing as compared to the synthesized spectrum. The problem of mass balance becomes much less acute for the explosives other than PETN and RDX.

In previously reported work,^{10,11} we've looked for comparisons with other types of studies related to explosives. Experimental studies such as thermal decomposition, laser irradiation decomposition (LIMA), impact induced decomposition, and even unimolecular decomposition have been examined to see if there is a common thread between decomposition and detonation products. Almost all of the products that we observe, which of course are gaseous, are in the list of products that some of these other experiments report. But quantitatively we don't find much in common, although that may be partly because not all of their products were reported in enough detail for a good comparison. Water seems to be especially difficult to measure in some of the methods and is only reported as being present. We conclude that the product distributions that we find, and which we are certain are closely related to the chemistry driving the detonation process, are not well represented by any other process at work in these other experiments.

Because we work on such a small scale, we can be somewhat venturesome in making measurements. We want to describe briefly some measurements of species that have not been reported in explosives by any other method, namely carbon clusters. The problem of soot formation is certainly a long standing one in any hydrocarbon combustion study as well as in modeling detonations. For example, neglecting the heat release from soot formation in BKW calculations of TNT can lead to serious errors,¹² sometimes even leading to the process being endoergic. In addition, the recent discoveries of small diamonds in the residue of contained explosions¹³ provides more encouragement to trying to understand the role of solid carbon in detonation products. The details of soot formation are still not well understood, but one of the mechanisms is thought to be an accretion process of atoms and small clusters to form clusters of increasing size as the process continues and the temperature of the product gases cool.¹⁴ So we examined the distribution of carbon cluster sizes under various conditions of detonation of HNS. In Fig. 12 we plot the relative intensities of products observed from HNS at the masses $M=12n$,

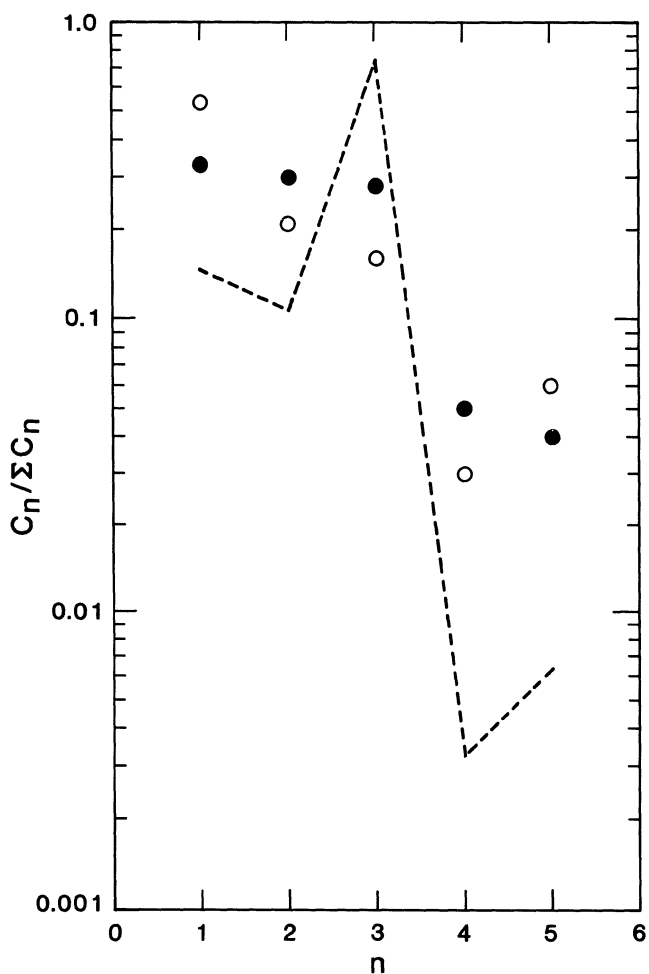


Figure 12. The relative intensities of carbon clusters of size n , that is C_n , observed in products from HNS. Two different sets of conditions were used to obtain the data. The closed circles are for room temperature, unconfined expansion of the products after detonation. The open circles were obtained at 30 K with an overlayer of Xe covering the pellet to tamp the expansion. The dashed line represents an equilibrium distribution of carbon clusters at 3400 K and 0.01 atmospheres partial pressure of carbon vapor.

where n is an integer. We plot the intensities as if they represented the number densities of carbon clusters with n carbon atoms in each cluster. Up to $n=5$ were observable with our mass spectrometer, but we were expecting larger n values because we found HNS to leave copious quantities of solid carbon in the detonation chamber. We then repeated the cluster size intensity measurements while detonating the HNS under very different conditions. We cooled the detonator station holding the HNS pellets to a temperature of 30 K. A layer of solid Xe of about 20 to 30 mg was deposited by condensation on the pellet surface. This acts as a tamper to the surface layer of HNS about equal to half the thickness of the pellet to prevent its rapid initial expansion, and the intent was to see what the effect was of confinement. These results are also shown in Fig.12, and they are disappointing in that the resulting distribution is not really very different than the room temperature one. An equilibrium distribution of carbon clusters is also shown for comparison.

Evidently the products we examine from HNS at the early arriving times has not had sufficient time to accumulate many clusters to sizes much larger than $n=5$. We extended our search of carbon clusters to higher masses than $M=60$ for HNS also, even going as high as $M=720$ ($n=60$, the so-called Bucky-ball) without seeing large enough counts to distinguish from background.

OTHER EXPLOSIVE MATERIALS AND EXPERIMENTS

This section is a catch-all that we will use to describe work that we've done on unusual explosives and with techniques other than mass spectrometry.

We were able to shock solid nitric oxide with sufficient intensity that we observed the detonation products in our mass spectrometer.¹⁵ Fig.13 shows a sample of the data that we obtained with our cryocooled detonator-carousel upon which we vapor deposited nitric oxide to a solid. N_2 and O_2 mass peaks having all of the characteristics of velocity and intensity that we normally find for the usual detonation products of explosives were

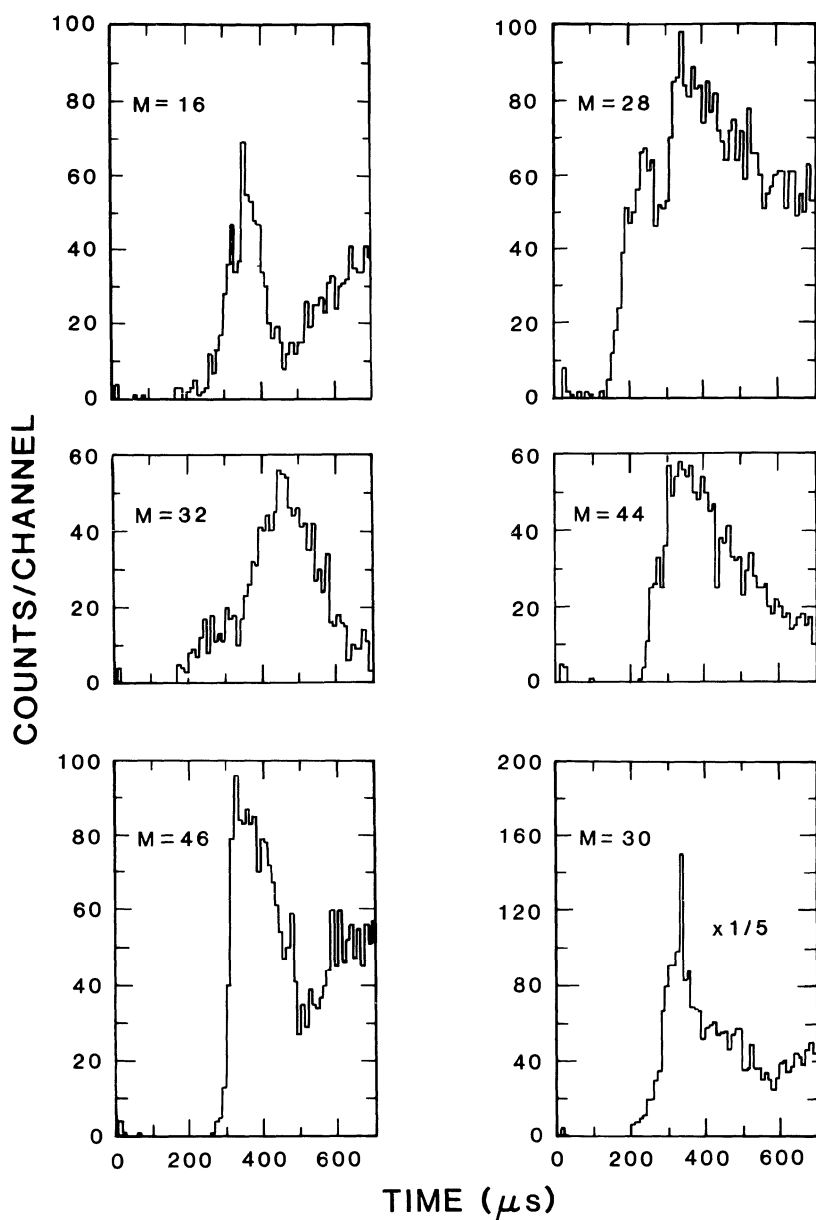


Figure 13. Sample data obtained by shocking solid nitric oxide with a PETN booster. These are all of the ions that were observed with any significant intensity. About 65% of the NO was consumed in the detonation, about 19% through the production of N_2 and O_2 .

seen, along with ions from the simple oxides of the material, namely NO, N_2O and NO_2 . These results confirmed what was inferred from equation-of-state measurements, that N_2 and O_2 were the principal products after detonating NO, and that some oxides of NO were also present. The oxides did not have quite the high velocities that N_2 and O_2 had, indicating that they were not formed as early in the process of the expansion of the product gases. For this particular study, the final atom inventory was quite good in that we were able to account for all of the atoms to within 5% with the suggested reaction mechanism. We also obtained an absorption spectrum of NO_2 from which we obtained an internal molecular temperature. This is the first time that we know of in which both a kinetic and a molecular temperature were measured for a detonation.

From a chemistry point of view, this reaction is very important because it exemplifies well the view expressed in the first paragraph of this article. That is to say that the intermolecular potential must be considered as having a many-body character to it. In gas phase, the reaction of NO that leads to the formation of N_2 and O_2 is known to proceed by an atomic mechanism, and requires temperatures of 4000 K to be measurable. At the densities and temperatures behind the shock that initiates liquid and also presumably solid NO, the concentrations of N and O atoms must be negligible. Therefore the reaction must occur in a concerted molecular fashion, and reactions of this kind have not been well studied so far. Simulations that we've done with very crude connections to the NO system indicate that if three or more molecules are involved, the concerted reactions between molecules become reasonably facile.

Experiments with isotopically labeled explosives can be done to good advantage with our apparatus. We hope to obtain some mass spectra with isotopically substituted constituents to resolve the indeterminacy of some of the mass peaks, such as $M=17,18$ and $M=27,28,44$. Deuterated PETN is available and we hope to obtain ^{15}N substituted TNT. But besides such standard uses, there are

other applications which are intriguing. Consider another application that we found which relies on isotopically substituted constituents. $^{15}\text{N}^{18}\text{O}$ was used in the NO studies to examine the question of mixing of products from various depths in the explosive charge. Layered deposits of solid NO were made with several alternating layers of normal NO and the isotopically substituted compound. We then examined the N_2 signal at masses 28, 29 and 30 to see if the time of arrival was representative of the layers that we had deposited. The results indicated that extensive mixing did not occur, but unfortunately they were not as definitive as we would have liked. We plan to repeat these kinds of measurements under different conditions.

As we mentioned earlier, spectroscopic methods have already been applied to identify and probe some of the species in the free expansion. We hope to expand on the use of optical methods with Transient Infrared Absorption (TRISP)¹⁶ and laser-induced fluorescence. Because the CJ temperatures are only 2000-3000 K, most of the molecular products are in the ground electronic state. Emission spectroscopy looks selectively at only a few extraordinary molecules which are scarcely representative of most of the products. Infrared absorption, on the other hand is ideal for probing the vibrotational states of the ground state molecules, and the fast response time of TRISP makes it ideal for detonations. The technique has not been applied extensively and is difficult to implement, but our preliminary attempts have shown that we can do it with the proper laser apparatus. Broadband CARS is an alternative approach if the instrumental difficulties of TRISP cannot be overcome.

Laser-induced fluorescence is, by now, a fairly well used technique for the quantitative probing of gaseous species. The advantage of using LIF is that it can detect very low concentration products whose presence in the detonation products is suspected but that cannot be reliably detected with mass spectroscopic methods. The sensitivity advantage can sometimes be offset by its specificity, so that only a limited amount of data can be accumulated during one trial.

To summarize, we have developed an apparatus of considerable versatility of measurement by which we can examine the products of detonation of small laboratory scale explosives. We have considerable evidence that the chemistry we are probing is characteristic of what is occurring in the reaction zone in some of the explosives, while for others the mass spectra we obtain is on a time scale as nearly characteristic of the detonation process as any other experimental measurements. The spectra that we report are considerably at variance with what model calculations predict, which suggests that the assumptions of equilibrium amongst the products is doubtful.

REFERENCES

- 1 J.O. Hirschfelder, C.F. Curtis, and R.B. Bird (1954, "Molecular Theory of Gases and Liquids," John Wiley and Sons, New York, see p. 797.
2. Ornellas, D.L., (April 5,1982), "Calorimetric Determinations of the Heat and Products of Detonation for Explosives: October1961 to April 1982." UCRL- 52821, Lawrence Livermore National Laboratory, 94550.
3. Renlund, A. and Trott, W. (1987) `Spectroscopic Studies of Shocked and Detonating Explosive's, Shock Waves in Condensed Matter, Schmidt, S.C. and Holmes, N.C. editors. Elsevier Science Publishers B.V. 1988 p. 547. Most notable in the emission observed in the "breakout- out" light was that of the diatomic species CN.
4. The skimmer is a chemically vapor deposited nickel structure sold by Beam Dynamics Inc. 708 East 56th St. Minneapolis, MN 55417.
5. Extranuclear Laboratories, P.O. Box 11512, Pittsburgh, PA 15238.
6. Hoh, A. and Aulinger, F., "Mass Spectrometric and Time-of-Flight Analysis of Gaseous Detonation Products in High Vacuum," Dynamic Mass Spectrometry, V5, p. 165,(1977)
7. Ahrens, T.J., Allen, C.F. and Kovach, R.L., (1971) "Explosive Gas Blast: The Expansion of Detonation Products in Vacuum," J. Appl. Phys. V42 pp. 815-829

8. Imacon model 790, Hadland Photonics, Limited. United Kingdom.
9. Cornu, A. and Massot, R. (1975), "Compilation of Mass Spectral Data," Heyden & Son, London, New York and Rheine, 2nd Ed., V1
10. Blais, N.C. (1987), "Real-Time Analysis of HNS Detonation Products: Carbon Clusters," J. Energetic Materials V6, p. 255.
11. Blais, N.C. (1988), "Real-Time Analysis of the Detonation Products of RDX," J. Energetic Materials V
12. Mader, C.L., (1979), "Numerical Modeling of Detonations," Univ. of Calif. Press, D.H. Sharp and L.M. Simmons, Jr., Editors, see pp. 125-131.
13. Greiner, N.R., Phillips, D.S., Johnson, J.D., and Volk, F., (1988), "Diamonds in Detonation Soot," Nature V333, pp. 440-442.
14. Shaw, M.S. and Johnson, J.D., (1987), "Carbon Clustering in Detonations," J. Applied Phys. V62 pp. 2080-2085
15. Blais, N.C. and Greiner, N.R., (1988), "Real-Time Analysis of the Reaction Products of Shocked Solid Nitric Oxide," J. Energetic Materials, V6, p. 255.
16. Bethune, D.S., Lankard, J.R., Loy, M.M.T. and Sorokin, P.P., (1979), "Time-Resolved Infrared Spectral Photography: A New Technique," IBM Journal of Research and Development v5 pp. 557-575.

ANALYSIS OF REACTION PRODUCTS OF PROPELLANTS AND HIGH EXPLOSIVES

F. VOLK

Fraunhofer-Institut für Chemische
Technologie, ICT, 7507 Pfinztal, FRG

ABSTRACT. The reaction products of propellants and high explosives are dependent on the pressure and therefore also on the confinement under which the combustion or detonation reaction proceeds. In order to evaluate this influence, different propellants were burned under atmospheric pressure and heavy confinement in a closed vessel.

In addition, high explosives containing TNT were initiated in an evacuated metal container under an atmosphere of argon. In all cases, the products were analyzed to find out the completeness of the combustion and detonation reaction. The gaseous products were analyzed by mass spectrometry and gas-chromatography, the residues by CHN-analysis and high performance liquid chromatography. The combustion of propellants at atmospheric pressure formed incomplete reaction gases with a high content of NO.

The investigation of the detonation products of unconfined high explosives has shown that unreacted TNT could be found in the solid residue and analyzed when the initiating booster was not optimized.

1. INTRODUCTION

The knowledge of the reaction products of combustion and detonation processes is important for several reasons:

- a. To learn more in the field of the reaction kinetics and about equilibrium or non-equilibrium burning.
- b. To study the heat output.
- c. To evaluate the completeness of reactions and to find out if components of the original propellant or high explosives can still be found in the residue.
- d. In connection with the disposal of energetic materials, it is also of interest, if the combustion leads to toxic or carcinogenic reaction products.

The last point of main interest for the disposal of ammunition, whereas in the case of c, the analysis of explosive residue allows us to find out the kind of explosive which was used, for example, in criminal acts.

2. AIM

It is the aim of this investigation to analyze the reaction products of some propellants with different heats of explosion. In each case the combustion reaction was started under a different confinement: a) low pressure resp. unconfined, and b) under heavy confinement which leads to a high combustion pressure.

When high explosives were investigated, a container of steel was used, which could be evacuated. So it was possible to analyze the detonation products formed under vacuum or under a different pressurization. Additionally, the influence of different initiating booster explosives on the completeness of the detonation reaction could be analyzed.

3. COMBUSTION EXPERIMENTS

3.1 Combustion at Ambient Pressure

For the low pressure experiments a 1.5 l glass vessel was used in which air was replaced by argon after prior evacuation. About 1 g of the propellant was ignited using a filament igniter. After the combustion, the gaseous products were analyzed by mass spectrometry.

Typical reaction gases consist of: H_2 , N_2 , CO , CO_2 , NO , N_2O , HCN , H_2O , and CH_4 with small amounts of NH_3 , C_2H_2 . Usually solid reaction products such as carbon were formed.

3.2 Combustion in Confinement

For the combustion in confinement, a high pressure vessel was used in which the heat of combustion of substances could also be measured when placed into a calorimeter. The volume of the calorimetric bomb was 25 cm³. Up to 2.5 g of the propellant were ignited, also by using a filament. Because of the heavily confined reaction, in all cases an equilibrium burning took place, which produced gases such as H_2 , CO , CO_2 , H_2O , and CH_4 . Carbon was formed in high pressure vessel only when propellants were burned with a very negative oxygen balance. The above mentioned gases, with the exception of H_2O , could be analyzed by gas-chromatography.

3.3 Propellants Investigated

For measuring the combustion products, the following propellants were taken into consideration:

- a. Black Powder (75% KNO_3 /15% Charcoal, 10% Sulfur).
- b. A gun propellant with a low heat of explosion: Single base gun propellant A 5020.
- c. A gun propellant with a high heat of explosion: Double base propellant H 518.

4. DETONATION EXPERIMENTS

The detonation experiments were carried out in a container of stainless steel with a volume of 1.5 m^3 , which could be evacuated in order to detonate under vacuum or to replace air by an inert gaseous atmosphere such as argon.

Cylindrical high explosive charges of about 300 g were used. The high explosive charges were initiated by a detonator cap No. 8 together with an RDX booster of 10 g.

In order to determine the influence of the booster strength on the completeness of the reaction, in some cases an additional booster was used (18 g) having the same diameter as the main explosive charge (50 mm). After the detonation, gas samples were taken for the mass spectrometric analysis. In addition, the solid residue was collected to analyze it for the CHN-content and for unreacted explosive components such as TNT.

Two different kinds of experiments have been conducted: (1) Measuring the influence of the initiation strength on the completeness of the detonation reaction, and (2) Measuring the influence of pressurization on the detonation products.

4.1 High Explosives Investigated for Measuring the Influence of Initiation Strength on the Completeness of the Detonation Reaction

The following high explosives were investigated:

a. Composition B and several cast high explosives charges consisting of:

- b. 60% TNT/40% Nitroguanidine (NQ).
- c. 50% TNT/30% Nitroguanidine/20% MG.
- d. 50% TNT/50% Ammonium nitrate (AN).
- e. 60% TNT/40% Nitroguanidine (NQ).
- f. 50% TNT/50% Nitroguanidine (NQ).
- g. 50% TNT/50% Triaminotrinitrobenzene (TATB).

4.2 High Explosives Investigated for Measuring the Influence of Prepressurization on the Detonation Products

The influence of prepressurization was tested by the initiation of unconfined charges in: Vacuum; 0.5 bar argon; and 1.0 bar argon.

Additionally, three charges of the same size and the same composition, but in a glass confinement with a thickness of 9 mm were investigated under the same conditions.

For all these tests, the composition of the explosive charges was as follows: 45% TNT/55% Nitroguanidine (NQ).

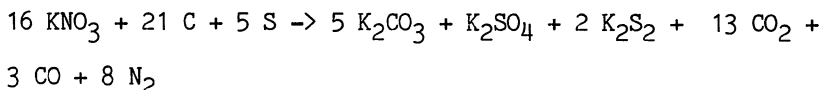
5. RESULTS

5.1 Combustion Processes

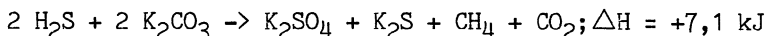
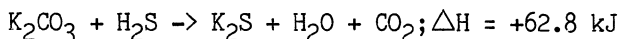
5.1.1 Black Powder. The black powder, which has been tested, consisted of: 75% potassium nitrate (KNO_3); 15% charcoal (79%); 10% sulfur.

The heat of explosion of this type of black powder was about 2850 kJ/kg. A mass of 2.5 g of black powder was burned in the closed bomb. The reaction gas was analyzed by using a double focusing mass spectrometer of Varion MAT.

Black powder burns basically according to the following empirical formula [1]



About 43 wt% of gases and 57 wt% of condensed reaction products are developed during this burning process. Depending on the development of the burning and on test conditions, the following reactions will take place in a more or less complete form:



An incomplete equilibrium will have no strong effect on the heat balance because of the low reaction enthalpy, however, it gives rise to a change of the reaction products.

The composition of the reaction products without H_2O may be seen from Table 1. The first column contains the result of a very low loading density 25 g/l. The next three columns are the result of the higher loading densities 100 g/l, 200 g/l, and 300 g/l.

As the most important result of our investigation it should be stressed that between loading density 100 g/l and 300 g/l the burning of the black powder is almost independent of the loading density. In contrast with this result, however, it is found that in the lower range of loading densities (25 g/l) the composition of gas is different from that in the higher range of loading densities.

With regard to the solid residue, the formation of solid products such as potassium carbonate, potassium sulfate, and potassium sulfide is characteristic for black powder.

5.1.2 Gun Propellant A 5020

The gun propellant A 5020, which exhibits a heat of explosion of about 3584 kJ/kg and an oxygen balance of -42.2 g O_2 /100 g propellant was tested under a very low loading density which was 0.33 g/l. The propellant was burned in glass vessel of 1.5 l, containing argon as an inert gas.

In addition, the same propellant was ignited in a stainless steel vessel of only 25 cm^3 burning volume. By using 2.5 g of the propellant, the loading density was 0.1 g/ cm^3 or 100 g/l. The results of both tests may be seen in Table 2. For the loading densities mentioned very different reaction gases were formed. Very large amounts of nitric oxide (NO) in the lower range and nearly no nitric oxide in the higher loading density. The different gases are responsible for the different heat outputs (Q_{ex} = heat of explosion).

TABLE 1. Reaction Products of Black Powder

Load Density g/l	25	100	200	300
Combustion Condition	Closed Vessel	Closed Vessel	Closed Vessel	Closed Vessel
Products in Vol %				
H ₂	0.7	3.5	2.9	4.1
N ₂	32.9	27.7	30.7	28.9
CO	4.6	10.6	10.2	9.2
CO ₂	52.4	52.5	50.4	53.3
H ₂ S	8.2	5.5	5.9	5.6
SO ₂	0.1	0.1	0.1	0.1
COS	1.1	0.2	0.2	0.2
CS ₂	0.04	-	-	-
CH ₄	0.04	-	-	-
Residue analysis in wt%				
C		3.6	3.6	3.5
K ₂ CO ₃	not	56.6	56.1	54.5
K ₂ SO ₄	analyzed	16.5	17.4	17.1
K ₂ S + others		23.3	22.9	24.9

TABLE 2. Reaction Products of Single Base Gun Propellant
A 5020

TLP A 5020	Experiment		Calculation	
			w/o CH ₄	incl CH ₄
O2-Balance [%]	-42.2	-42.2	-42.2	-42.2
Load Density [g/1]	0.33	100	100	100
Comb Condition	1 bar	Closed Vessel	-	-
Products [Mol %]				
H ₂	1.8	18.4	19.2	15.8
CH ₄	0.6	0.1	-	2.1
CO	17.0	42.7	42.4	40.2
CO ₂	7.0	12.6	12.5	14.7
N ₂	4.4	10.1	10.4	10.9
N ₂ O	-	-	-	-
NO	11.1	-	0.0018*)	-
HCN	0.2	-	0.013	0.01
C ₂ H ₄	-	-	-	-
NH ₃	-	0.85	0.14	0.10
H ₂ O	30.3	15.2	15.4	16.2
C s	27.6	-	-	-
Qex [J/g]	2696	3360	3472	3679
Kp (T)	40.88	2.799	2.72	2.80

*) (NO)x - Analyzer

As we see, the reaction gases at the loading density of 100 g/l agree very well with the equilibrium gases, which were thermodynamically calculated [2] using the ICT-computer-program.

The formation of carbon was only seen by burning the propellant in the lower pressure range. But there was no other residue which could be characteristic for detection of the original propellant.

5.1.3 Gun Propellant H 518

The gun propellant H518, which contains a high amount of nitroglycerine, exhibits a very high heat of explosion of 5132 kJ/kg. The oxygen balance is $-22.5 \text{ g O}_2/100 \text{ g propellant}$. It was tested under the same conditions as A 5020. At first it was burned in an argon atmosphere of about 1 bar; secondly, heavily confined in a closed bomb (see the results in Table 3).

Compared with the cooler propellant A 5020, the nitric oxide content of the low pressure burning experiment is clearly higher: 19.3 mol %. But the carbon formation is lower because of the higher oxygen content. On the other hand, the combustion in the closed bomb leads to high contents of CO_2 and H_2O ; both values are responsible for the very high heat of explosion of the propellant H 518. It is understandable that no solid residue has been formed.

5.2 Detonation Processes

The first part of these investigations has the objective to determine the influence of the initiation strength on the effectiveness of the detonation reaction. This means, it should be found out if it is possible to analyze explosive components in the detonation residue under the precondition that the initiating booster was too small or not optimized.

The second part has to examine what kind of influence on the reaction products of TNT containing high explosives will cause a detonation in vacuum, in argon atmosphere or if the explosive is confined in a glass tube.

5.2.1 Influence of Initiation Strength

For all the experiments described, we used high explosive charges of about 300 g with 50 mm in diameter and 80 to 90 mm in length. For the initiation different boosters were used:

a. A booster with a low initiation strength which consisted of 10 g RDX (Type I). The cylindrical shape of this booster had a diameter of about 20 mm and a length of about 20 mm.

In this connection it should be pointed out that the diameter of the RDX-booster is much smaller than the diameter of the explosive charge, see Figure 1.

b. The second booster type consisted on 18 g explosive sheets (Type II) with the same diameter as the main charge explosive. We expect that the increased initiation strength of both types of boosters gives rise to a more complete detonation reaction with the result that

TABLE 3. Reaction Products of Double Base Gun Propellant H518

TLP H518	Experiment		Calculation	
O2-Balance [%]	-22.5	-22.5	-22.5	
Load. Density [g/1]	0.33	100	100	
Comb. Condition	1 bar	Closed Vessel	-	
Products [Mol %]				
H ₂	1.9	10.2	10.0	
CH ₄	0.4	-	0.2	
CO	22.5	28.5	26.9	50.8
CO ₂	6.3	22.3	23.9	
N ₂	3.4	14.4	14.6	
N ₂ O	-	-	-	
NO	19.3	0.09	-	
HCN	0.6	0.03	0.002	
C ₂ H ₄	-	-	-	
NH ₃	-	-	0.05	
H ₂ O	28.8	24.4	24.4	
C s	16.8	-	-	
Qex [J/g]	2548	5044	5219	
Kp (T)	54.1	3.06	2.75	



Fig. 1

a = RDX - booster

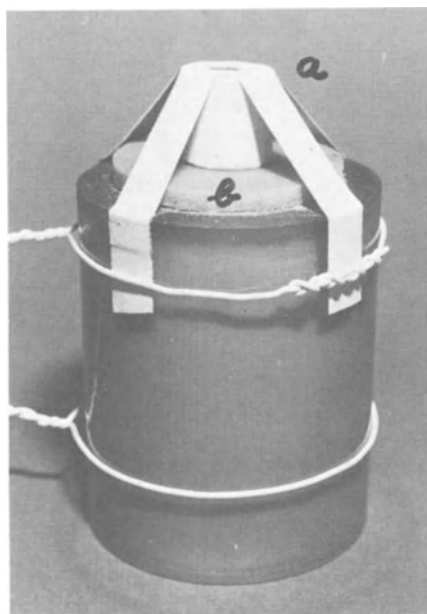


Fig. 2

a = RDX - booster

b = Detonation Sheets - booster

no more explosive components can be identified in the post-blast residue, see Figure 2.

The results of the examination of the initiation strength of the two different boosters may be seen from the following table. In the post-blast residues, which contain a large amount of carbon, TNT was determined quantitatively by high performance liquid chromatography (HPLC).

<u>Initiating Booster</u>		<u>High Explosive Charge</u>	<u>TNT in Residue wt%</u>
Type I 10 g RDX	Type II 18 g Expl. Sheets		
a) +	-	40% TNT/60% RDX (Compound B)	-
b) +	-	60% TNT/40% NQ	1.5
c) +	-	50% TNT/30% NQ/20% Mg	6.0
d) +	-	50% TNT/50% AN	2.0
e) +	+	60% TNT/40% NQ	-
f) +	+	50% TNT/50% NQ	-
g) +	+	50% TNT/50% TATB	-

In this Table it is shown that Compound B, which is much more easy to initiate, reacts completely by using the booster Type I alone. In contrast to this, NQ and ammonium nitrate (AN), containing high explosive charges which need a higher initiation strength, leave unreacted TNT. The same holds for the charge containing additional magnesium (Mg). On the other side, a complete detonation reaction is shown by using both types of boosters. No TNT could be analyzed.

5.2.2 Influence of Ambient Gas on the Detonation Products

When detonating high explosives in different atmospheric conditions, it is of interest to know if the energy output will change. In order to investigate this behavior, we analyzed the reaction products of explosive charges consisting of 45% TNT and 55% NQ initiated in different pressures of argon and in vacuum. Argon was used as an inert gas to avoid a reaction of the detonation products with air. The results of the unconfined charges are recorded in Table 4.

From Table 4 we see that the detonation products change very clearly going from vacuum to 1.0 bar of argon (0.1 MPa). The contents of H_2 and CO decrease, whereas CO_2 , H_2O , and carbon increase. The heat of detonation increases in the same direction. This means that a detonation under a pressure of 1 bar is much more powerful than vacuum or at low pressures.

In order to evaluate the influence of a confinement, three charges of the same composition and the same weight were cast into glass tubes of 9 mm wall thickness. The results are listed in Table 5.

It is shown that glass confined charge exhibits very different products from the unconfined charges if we compare the detonation in vacuum. The confined charge produces in vacuum nearly the same reaction

TABLE 4. Detonation Products of the Unconfined Charges of 45% TNT/55% NQ

Sample No.	1450/1c	1450/2c	1450/3c
Ar pressure, Mpa	Vac.	0.05	0.01
Composition	45% TNT/55% NQ		
O2-Balance, %	-47.6		
Charge Weight, g	331	332	331
H _f , kJ/kg	-661	-662	-657
<u>Products, Mol %:</u>			
H ₂	20.7	8.3	5.0
CH ₄	0.04	0.1	0.24
CO	32.1	17.9	14.3
CO ₂	3.7	7.9	10.3
N ₂	27.5	26.1	25.6
NO	0.1	0.1	0.13
HCN	0.3	3.2	3.6
C ₂ H ₂	0.02	0.03	0.1
NH ₃	0.5	3.0	4.9
H ₂ O	10.7	19.6	20.0
C _s	4.4	13.8	15.9
H _{det} , kJ/kg	2999	3653	3763
C in Residue [% of total C]	10.8	32.2	35.7
Gas formation [mol/Kg]	44.5	37.9	35.7

TABLE 5. Detonation Products of the Glass Confined Charges of 45% TNT/55% NQ in Different Argon Pressures and in Vacuum

Sample No.	1451/1	1451/2	1451/3
Ar pressure, Mpa	Vac.	0.05	0.01
Composition	45% TNT/55% NQ		
O ₂ -Balance, %	-47.6		
Charge Weight, g	332	335	332
H _f , kJ/kg	-656	-658	-658
<u>Products, Mol %:</u>			
H ₂	8.7	4.2	3.1
CH ₄	0.02	0.4	0.44
CO	15.9	10.2	9.3
CO ₂	7.9	11.9	12.7
N ₂	27.3	26.0	25.6
NO	0.06	0.05	0.14
HCN	1.35	2.4	1.1
C ₂ H ₂	0.07	0.1	0.13
NH ₃	1.15	4.7	5.3
H ₂ O	20.5	20.7	21.0
C _s	16.8	19.2	21.3
H _{det} , kJ/kg	3779	3960	4003
C in Residue [% of total C]	39.8	43.3	47.2
Gas formation [mol/Kg]	37.1	34.4	33.0

products as the unconfined explosive charge at 0.5 and 1.0 bar argon. The same holds also for the enthalpy of detonation. The conclusion which can be drawn from these experiments is that ambient argon behaves as a confinement.

6. CONCLUSION

Black powder and two gun propellants with different heats of explosion were burned under different pressures. Only black powder produces solid reaction products which can be used for the identification of the propellant.

The initiation of high explosives with different boosters has shown that components of the original explosive charges could be detected in the post-blast residue, when the initiating booster was not optimized.

The influence of an ambient atmosphere and of confinement could be demonstrated by examining the reaction products in vacuum, under 0.5 bar and 1.0 bar respectively, of argon. It was found that 1.0 bar argon behaved as a confinement.

7. REFERENCES

[1] Schwarzpulver, R. Escales and Sprengsalpeter, Leipzig 1514, Verlag von Veit u. Comp.

[2] Bathelt, H. and Volk, F., "Computer Program for Performance Calculation of Rocket and Gun Propellants and Gaseous Explosives," ICT Report 4/85.

[3] Volk, F., Bathelt, H., Schedlbauer, F., and Wagner, J., "Detonation Products of Insensitive Cast High Explosives," Proc. 8th Symp. (Int.) on Detonation, July 15-19, 1985, Albuquerque, NM, USA, p. 577-586.

[4] Vol, F., "Detonation Gases and Residues of Composite Explosives," Journal of Energetic Materials, 4, p. 93-113, (1986).

[5] Volk, F. and Schedlbauer, F., "Detonation Products of Less Sensitive High Explosives Formed Under Different Pressures of Argon and in Vacuum," Preprints of papers to be presented at the 9th Symp. (Int.) on Detonation, Portland, Oregon, USA, August 28-September 1, 1989.

CHEMICAL SENSITISATION IN NITRO, NITRAMINE AND NITRATE EXPLOSIVES

DR J CONNOR

Royal Armament Research and Development Establishment
Fort Halstead
Sevenoaks, Kent
TN14 7BP
UK

ABSTRACT Work has begun at RARDE to attempt to elucidate the complex chemistry of reacting explosives using molecular orbital calculations to describe possible potential energy surfaces for decomposition. The well-known sensitising effect of amines on nitromethane is modelled by studies of the nitromethane/ammonia system. The calculations lead to a new proposal for a mechanism for decomposition. This mechanism is supported by experimental data.

1. INTRODUCTION

Classical descriptions of the detonation process ignore reaction chemistry. While such descriptions are adequate for many purposes, they cannot be used to model important phenomena such as the ignition and subsequent growth of reaction to detonation in energetic materials. Further, there is concern about the extension of the classical detonation model to less sensitive explosives where the detonation reaction zone is of significant depth, to composite explosives where inter-molecular reactions contribute to the energy release supporting detonation and to explosives with energetic binder systems where it is hoped that both the explosive and the binder contribute to the energy in the detonation front.

Because of the short time-scales involved and the high temperatures and pressures, these are difficult areas to study experimentally. Consequently, in the last decade a number of more or less empirical approaches have been adopted to provide tools to describe the ignition and growth phase of detonation and to attempt to elucidate some of the important factors controlling this phase. The Forest Fire model (Ref 1) falls in the former category while typical of the latter group would be Lee and Tarver's ignition and growth model (Ref 2).

Neither of these approaches addresses the chemistry of decomposition in energetic materials in any fundamental way. In Forest Fire, the decomposition kinetics are subsumed within the

experimentally generated plot of shock pressure against the reciprocal of the run distance to detonation, the so-called Pop plot. Lee and Tarver assume a simple kinetic scheme and carry out a parameter fitting exercise to match existing data.

At the Royal Armament Research and Development Establishment (RARDE) in recent years we have begun a programme of theoretical and computational studies aimed at improving understanding of the initial decomposition reactions in energetic materials. We are using ab-initio molecular orbital codes to calculate ground state geometries and potential energy surfaces for possible decomposition modes. The activation energies for key reaction steps can then be employed in molecular dynamics simulations to provide reaction rates.

In this paper the intention is to review the techniques for theoretical studies which are now available and to provide some illustrations of their use based on current RARDE studies. It should be stressed that this review is carried out from the perspective of an explosives formulator or hazard assessment expert rather than that of a theoretical chemist. The aim is to challenge the theoreticians to employ the powerful techniques now at their disposal in attempts to describe the chemistry of explosives decomposition which will provide new insights to explosives formulators and novel answers to the need for higher performance, reduced hazard explosive systems.

2. BACKGROUND

Only a few years ago many would have considered accurate modelling of the fundamental chemistry of explosive events to be unrealistic. Computer codes have been available for perhaps the last twenty or so years which could predict the geometry of simple isolated molecules (Ref 3), but even their use demanded the most powerful computers of their era to perform these tasks. In the last few years the situation has changed dramatically. With the introduction of faster, more powerful supercomputers combined with advances in ab-initio molecular orbital codes, the possibility of accurately modelling reactions of energetic materials has become a reality. Furthermore, advances in chemical kinetic codes (Refs 4,5) during the last decade have also increased the ability of chemists to describe quantitatively the kinetics of complex systems. Such kinetic modelling techniques have already been applied with considerable success to characterisation of the pyrolysis of hydrocarbons (Refs 6-8), flame chemistry (Refs 9-11), soot formation and premature ignition in internal combustion engines (Ref 12). It is only a matter of time before these techniques are applied to reactions in energetic materials.

This paper will concentrate on the application of quantum mechanical molecular orbital codes to the modelling of energetic molecules and their decomposition reactions. The examples chosen to illustrate the use of these techniques will involve nitro compounds, but this should not be taken to mean that other classes of compounds

are not receiving attention. The nitramines, in particular, are under study at RARDE. It is also worth mentioning the use of molecular orbital codes to model the intermolecular forces between detonation products such as nitrogen, carbon monoxide, carbon dioxide, and water. The many-body contribution to intermolecular forces has received specific attention (Ref 13) and will be very briefly described here. This work is of direct relevance to the construction of theoretical equations of state for detonation products. It is hoped that these studies will enable equations of state derived from pair potentials to be corrected for many-body effects.

3. MOLECULAR ORBITAL CALCULATIONS

There are, in essence, three levels of theory that are available with which to simulate the molecular and electronic structure of chemical systems. These range from the most accurate ab-initio methods, through semi-empirical approaches, to force-field techniques using analytic potential gradients. Normally, each technique is used separately, but together they can prove an extremely powerful tool with which to explore complex chemical systems. For example, the use of ab-initio calculations on small molecules to provide parameters required to describe the subsequent potential energy functions necessary for the simulations of the dynamics of large biomolecules has proven to be a valuable technique. Such approaches could easily be extended to the modelling of energetic systems, and it is our intention to pursue this path in the near future. In the following sections we will discuss each of these techniques separately.

3.1 AB-INITIO METHODS

Ab-initio methods based on solution of the Hartree-Fock equations are well established (Ref 14), and are used in routine molecular and electronic calculations on small organic and inorganic molecules. For such molecules, extremely accurate predictions of many spectroscopic properties can be made using methods such as CAS-CI, MCSCF, coupled-cluster theory, and multireference methods. Recent advances in supercomputer technology coupled with improved algorithms have made it possible to perform full CI calculations for small systems. Due to their size and complexity, such calculations have been limited mostly to diatomic molecules. However, where cost is not a problem, it is quite feasible to perform full CI calculations on quite large systems, and such calculations have been carried out on small energetic molecules by Haskins and Cook at RARDE (Ref 16).

Unfortunately, it is a sad fact of life that high-precision ab-initio calculations are expensive. This is because with all ab-initio methods the computational effort increases dramatically with increasing number of electrons and basis functions. As a general rule the time required for such calculations increases with the number of electrons to the power of three. Thus, to model a hydrogen atom at the highest level of accuracy is trivial, but to perform a

similar calculation on an atom such as iron is prohibitive. Despite these drawbacks, it is not often that such calculations need to be performed, and in many cases single-determinant theory will suffice. However, for organic molecules it is almost routine to optimise structures having 15-20 or more atoms using large high calibre basis sets, and to obtain other spectral data. Geometrical parameters are obtained to better than 1% of experimentally determined values, but harmonic frequencies are less accurate (within 10% of experiment). This deviation can be corrected because it is systematic (the lack of correlation leading to higher frequencies). One good feature of SCF calculations is that in general they give good relative energy differences, for example, between different isomeric forms. In order to calculate electron density related quantities, large good-quality basis sets need to be used. If this is done, then quite good dipole moments and polarisabilities can be obtained. If smaller basis sets are used much larger systems with up to 40 or so first row atoms may be considered. Such systems allow reasonably accurate modelling of real chemical events.

The problem with ab-initio codes is that as the number of electrons in the system increases, the computational effort rises dramatically. Increasing the size of the basis set, and/or adding CI calculations, only magnifies the problem. The computational effort required is not only in speed of performing the many calculations, but also the size of the memory and more specifically disk storage capacity for keeping the integrals. Methods have been developed over the last few years to overcome this problem of disk storage. These are direct approaches which do not store all of the integrals, but recalculate them when required. This method is quite efficient because memory is now relatively cheap and fast compared to disks. Furthermore, despite the extra effort in recalculating the integrals, fewer and fewer need to be evaluated as self-consistency is approached. The calculations are nearly always simplified by taking advantage of molecular symmetry wherever possible.

3.2 SEMI-EMPIRICAL METHODS

The current practical limit for ab-initio codes is around 50 first row atoms. With new algorithms and direct methods this should be extended to 100-200, or possibly more, first row atoms within the next few years. At the present time, the study of larger molecules requires some simplifications to be made. These can take the form of approximations to the Fock Matrix using simple mathematical descriptions of the physics or, alternatively, experimental data can be used to calibrate a parameterised form of the Fock matrix. This is the basis of the widely used MNDO, MINDO/3 and AM1 semi-empirical methods (Ref 15).

Such approaches have proved extremely useful for optimising molecular geometries, and even for studying reaction paths. They allow quite large systems (200+ atoms) to be modelled, generally with

good accuracy, and with quite modest demands of computational power. However, they suffer one main drawback in that they can only be used in the regime for which they were initially parameterised, hence they must be used with some caution.

3.3 FORCE-FIELD METHODS

Force-field methods form the basis of molecular dynamics. They use a parameterised quasi-classical description of interatomic forces to model the trajectory of systems typically composed of hundreds or even thousands of atoms. One good feature of these types of calculations is that with large systems the computational effort increases linearly with the size of the problem. This means that increased computational power allows considerably larger systems to be studied. Further gains can also be made by using parallel processors since energy calculations in molecular dynamics simulations are inherently parallel.

The application of molecular dynamics codes to energetic materials will not be discussed any further here. Suffice it to say that these types of calculation can lead on from ab-initio or semi-empirical calculations (which provide reaction pathways) to give reaction rates.

4. MANY-BODY CONTRIBUTIONS TO INTERMOLECULAR FORCES

Recently (Ref 17) Haskins and Cook have described work at RARDE on short range interactions in N_2 , CO and CO_2 in the context of the description of high pressure regimes such as detonation products. These studies are seen as a step on the road towards derivation of an ab-initio equation of state for explosive reaction products. The Coulomb interactions in atomic and molecular systems are additive. However, the readjustment of charge distributions which result when additional atoms or molecules are involved result in a loss of pairwise additivity. It is this loss of additivity which is the source of the many-body interaction in closed shell systems. For polar molecules other factors such as non-additivity of induction and exchange-induction energies could also be significant.

Haskins and Cook have carried out molecular orbital calculations on helium atoms in an equilateral triangle geometry to investigate the minimum size of basis set required, the significance of electron correlation effects and the effect of basis set superposition. They find little significant difference between the 6-31G and 6-311G** basis sets, that electron correlation effects are small and that basis set superposition errors are very small. However, the many body effects are significant, amounting to up to 20% of the pair potential for helium at short separations.

These methods have then been applied to three and four body studies of N_2 , CO and CO_2 using the Gaussian 86 code with a 6-31G basis set. A full description of this work is outside the scope of this review but some of the conclusions may be of interest. Firstly, three body energies can be highly significant, ranging for example from 2-11% for nitrogen atoms in an equilateral triangle at separations from 2.8 to 1.6 \AA . Four body energies are less significant but may not be negligible. Fortunately, the data are found to be well fitted at most separations by an exponential form, Figures 1 and 2. Clearly for dense fluids such as detonation products we need an averaging procedure to enable effective pair potential to be produced but the exponential form of the many body potentials will simplify evaluation of such procedures.

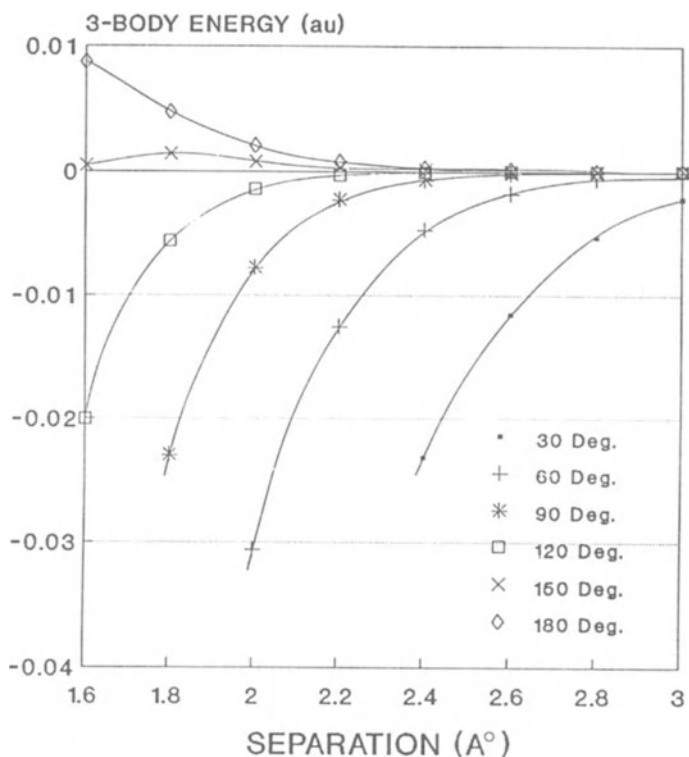


Fig 1. Nitrogen : 3-body energies

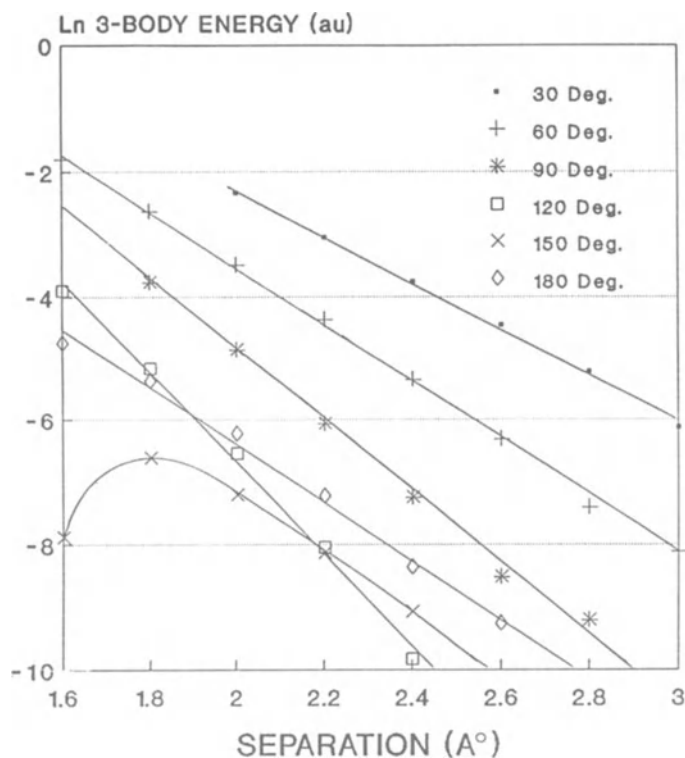


Fig 2. Nitrogen : Ln 3-body energies

5. DECOMPOSITION MECHANISMS

The objective of modelling the decomposition chemistry of energetic materials is to gain a better understanding of the detonation process itself. This in turn would allow better control to be achieved through design of new potential energetic molecules, modification of the properties of existing ones (eg through additives), and an increased predictive capability in the form of improved hydrocodes which incorporate important chemical features.

Attempting to understand the chemistry involved in initiation, growth of reaction, and detonation is a complex problem. Whilst it is desirable to model 'real' molecules (as employed in weapon systems) at the highest levels of accuracy, this is only just becoming feasible. Currently it is generally preferable to model relatively simple molecules which have all the pertinent features, yet are small

enough to carry out high accuracy calculations. typical model explosive molecules include nitromethane (and other nitroalkanes), methyl nitramine and methyl nitrate. Some of these materials are readily available and experiments can therefore be carried out to compliment the calculations.

The starting point for any chemical reaction is the equilibrium conformation of the molecule(s), hence it is normally the first calculation to be performed on a system. State-of-the-art ab-initio molecular orbital codes are capable of optimising all bond lengths and angles simultaneously with respect to energy. In general, very few convergence problems are experienced in such calculations, and the results, when compared with experimentally determined values, are excellent. An example of how good the agreement can be is illustrated by the results for nitromethane shown in Table 1.

TABLE 1. Comparison of experimental and calculated parameters of nitromethane.

<u>Parameter</u>	<u>Theory</u>	<u>Experimental</u>
C-N ($^{\circ}$)	1.479	1.489
N-O ($^{\circ}$)	1.192	1.224
C-H ($^{\circ}$)	1.078	1.088
ONC	117.1 $^{\circ}$	117.3 $^{\circ}$
HCN	107.5 $^{\circ}$	107.2 $^{\circ}$
Dipole(D)	4.033	3.46

Given the optimised geometry, possible reaction pathways can then be explored. There are essentially two types of reaction that can be investigated in the first instance. These are unimolecular reactions involving bond scission within a molecule (leading to either neutral radicals or ionic species), or bimolecular processes. Even for relatively simple molecules the potential energy surface for bimolecular processes can be very complex. There are also difficulties with many unimolecular reactions as SCF calculations are inadequate for modelling bond scission processes which lead to radical products. In such systems SCF calculations overestimate the ionic contribution and to describe them correctly it is necessary to include electron correlation effects. It is therefore very time consuming and costly to attempt to model the complete potential energy hypersurface for most reactions. For this reason, it is usually necessary to concentrate effort on particularly likely reaction paths. For example, the C-N bond in nitromethane is weaker

than the C-H or N-O bonds and is therefore more likely to be important in the initial chemistry. Similarly, the MeO-NO₂ bond in methyl nitrate is considerably weaker than the other bonds in this molecule, and therefore is likely to be involved with initial reaction steps.

Choosing appropriate reaction paths to study can be difficult and requires a considerable degree of chemical knowledge and intuition. An easier, and in some ways more direct, approach is to attempt to model chemical sensitisation/desensitisation effects on energetic molecules. Reaction pathways calculated with and without the sensitiser/desensitiser incorporated can then be compared and from the differences, the most likely mechanism deduced. This method has the advantage that computational time and effort is concentrated on a distinct problem which hopefully, will aid in understanding the decomposition mechanism of the pure explosive. This method has been used by Haskins and Cook (Refs 16-18) to investigate the initial steps in the decomposition of nitromethane.

It is well known that nitromethane is strongly sensitised by amines. Engelke (Refs 19,20,21) was probably the first to study such systems and recognise their significance in understanding detonation chemistry. He realised that the sensitisation of nitromethane by amines implied one of two things, either, new faster chemical pathways are afforded by the action of the amines or, the pathways already in effect without the amine present are enhanced, for example by the production of a higher concentration of a rate controlling species. Engelke has attempted to explain his observations on the sensitisation of nitromethane by amines in terms of the production of a new chemical species; the "aci-ion". At RARDE, Cook and Haskins have studied these sensitisation effects both theoretically and experimentally and have proposed an alternative mechanism for sensitisation. This work is summarised below.

5.1 POTENTIAL ENERGY CALCULATIONS

Theoretical studies have been based on ab-initio molecular orbital calculations performed using either the Gaussian 86 code or, earlier, Gaussian codes on a Cray 1 Computer. The majority of calculations employed a modestly sized basis set (6-31G) to save computational time but a few have been carried out using a larger (6-311G**) basis set and using Moller-Plesset (MP) many-body perturbation theory to second or fourth order.

The earlier calculations, reported at the Eighth Detonation Symposium, were carried out at the SCF level only and looked at C-N and C-H bond scission in nitromethane. However, this Hartree-Fock (HF) approach is inadequate on two grounds. Firstly, the single determinant wave function gives a poor representation of the ground state and of distorted species on the potential surface due to the significant bi-radical character of nitro compounds. Secondly, HF

calculations are poor in predicting the energetics of reactions involving rupture or formation of electron pair bonds. It is worth noting that the HF study of the C-N bond scission reaction predicts the formation of CH_3^+ and NO_2^- ions rather than the lower energy neutral radicals which are in fact formed. However, the activation energy for unimolecular scission to radical products can be estimated from UHF calculations on these products assuming, reasonably, that there is no significant barrier to radical recombination. The results of such calculations are shown in Figure 3 and indicate a bond dissociation energy of 46kcal/mol.

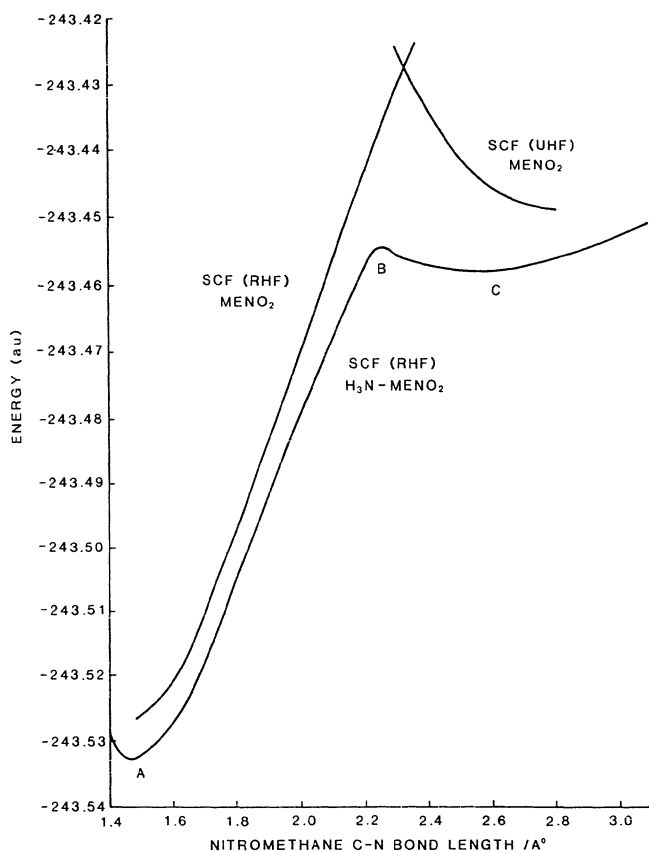


Fig 3. HF calculations on Nitromethane and an Ammonia-Nitromethane complex

These earlier calculations have now been improved with corrections for electron correlation at the MP2 and MP4 levels with HF optimised geometry and a more extended (6-311G**) basis set. The derived surfaces are at Figure 4. The MP2 level calculations still predict dissociation to CH_3^+ and NO_2^- . However, the MP4 calculations give a smooth curve from the ground state to the radical products, even predicting a small Van der Waals interaction between these radicals at 3.2 Å. The calculated bond dissociation energy is 65.6 kcal/mol compared with an experimental value of 60.3 kcal/mol. A full comparison of all of the calculated activation energies is given in Table 2.

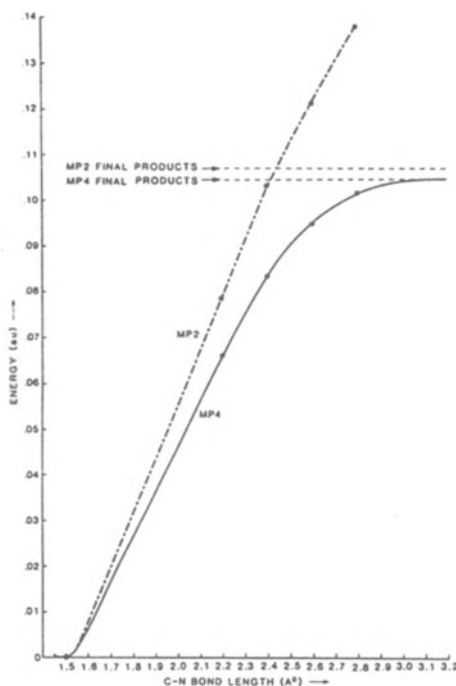


Fig 4. MP2 and MP4 Calculations on Nitromethane

TABLE 2. Activation Energies Calculated from Ground State and Radical Properties.

	MP2 HF Geometry	MP4 HF Geometry	MP2 Full optimisation
6-31G	68.1	66.7	57
6-311G**	67.1	65.6	

Energies in kcal/mol.

In studies of amine sensitisation, ammonia has been used as a model amine to reduce computational effort. Three geometries have been examined with the ammonia nitrogen atom aligned along the C-H and C-N bonds in nitromethane and a ring structure in which the ammonia nitrogen is adjacent to a methyl hydrogen and an ammonia hydrogen is adjacent to an oxygen atom. Calculations indicated hydrogen bonding in all cases with the ring structure energetically favoured, but only by a small margin.

C-H bond scission studies show that the presence of ammonia makes no difference. However, C-N scission calculations with ammonia aligned along the C-N bond give a markedly different potential energy surface as compared to the isolated nitromethane molecule, Figure 3. The regions labelled A, B and C correspond to the structures in Figure 5 where A is the ground state, B the transition state and C corresponds to the interacting products. The activation energy for C-N scission in the hydrogen bonded complex is calculated to be 50kcal/mole.

The potential surfaces have been recalculated using full optimisation of the MP2/6-31G level and at the MP4/6-31G level with SCF optimisation. The potential surfaces are similar to that of Figure 3 except that they show no minimum beyond the transition state. Calculated activation energies were 51 kcal/mol (MP2) and 49 kcal/mol MP4.

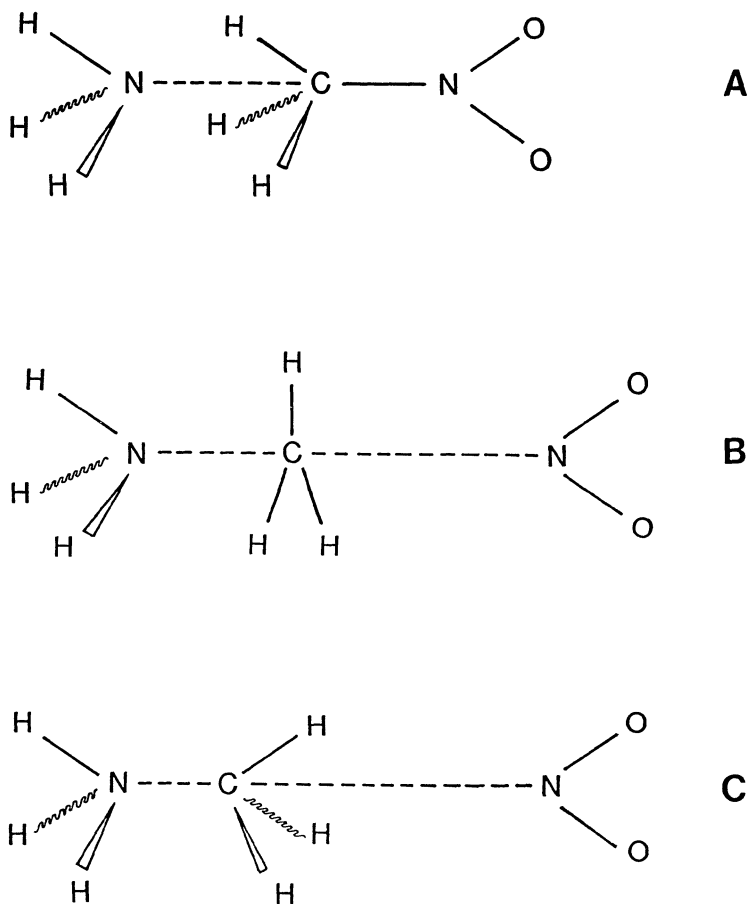


Fig 5. Illustration of structures on the potential surface for an Ammonia-Nitromethane complex

5.2 METHYL NITRATE AND METHYL NITRAMINE

Methyl nitrate and methyl nitramine have been chosen as models for two other important classes of energetic materials, nitrate esters and nitramines. The $X\text{-NO}_2$ bond dissociation energy for the nitrate was calculated to be 38 kcal/mol and that of the nitramine 47 kcal/mol, consistent with the well known trends in stability and sensitivity for nitro, nitrate and nitramine compounds. Assuming that $X\text{-NO}_2$ bond scission is rate determining, then neither nitrate nor nitramine decomposition is affected by the presence of ammonia.

6. EXPERIMENTAL STUDIES

To test these theoretical predictions a number of initiation experiments using both a modified version of the NOL large scale gap test and also the Rotter drop weight impact test have been conducted. The experimental details of these tests have been described in a previous publication (Ref 22).

The gap test has been used to examine the sensitisation effect of diethylene triamine on a series of nitroalkanes having progressively less readily abstractable α -hydrogens. These nitroalkanes were nitromethane, nitroethane, 2-nitropropane and 2-methyl-2-nitropropane. Gap test experiments showed that the pure nitroalkanes were all very insensitive, and with the exception of nitromethane all failed to detonate even with the donor charge in direct contact. Further gap test experiments on nitroalkane diethylene triamine (5% v/v) mixtures have shown that it is increasingly difficult to sensitise them along the series. A mixture of 2-methyl-2-nitropropane and 5% diethylene triamine failed to detonate even with the donor charge in direct contact. It should be noted that while both nitroethane and 2-nitropropane were sensitised their shock sensitivity is still considerably less than nitromethane.

Addition of diethylene triamine to both nitromethane and nitroethane gave straw-yellow solutions, addition of the same amine to 2-nitropropane gave a thick white precipitate which, if left, evaporated. No precipitate or colour change was noted when ethylene diamine was added to 2-methyl-nitropropane, and the mixture remained colourless.

In order to examine the effect of amines on a greater variety of explosives the Rotter drop weight impact test was used. This is more convenient than the gap test, and has the added advantage of only requiring a few grams of the explosive. The Rotter Test is an impact sensitiveness test, as compared with the gap test which measures the shock sensitivity of an explosive. With nitromethane the results from this test correlate well with those from the gap test experiments even to the extent that the test correctly predicts that ethylene diamine has a greater sensitisation effect than diethylene triamine. Unfortunately the other nitroalkanes failed to initiate at the highest drop heights available in the Rotter machine. This is a result of the low sensitiveness of these materials (even when sensitised) combined with a relatively low maximum available drop height.

Recently the Rotter test has been used to assess the sensitising effect of diethylene triamine on a number of crystalline explosives. The detailed results of these tests have been reported elsewhere (Ref 23), but the main points are summarised here as they provide additional support for the proposed sensitisation mechanism. The first crystalline explosive we studied in the Rotter test was 2,4,6-trinitrotoluene (TNT). This showed a marked sensitisation

effect on addition of ca 5% diethylene triamine. The TNT was also observed to change colour from pale yellow to dark purple on addition of the amine. This is indicative of a charge transfer complex. The Rotter test results are shown in Table 3.

TABLE 3. Drop weight impact results for explosives with and without 5% DETA.

Explosive	Drop Height (mm)	
	Pure_____	+5% DETA
Nitromethane	640	361
TNT	1570	1006
TNB	1610	986
RDX	1279	1386
PETN	1422	1555

The results with TNB and TNT are particularly relevant to the mechanism for nitro compound decomposition. Unlike TNT, TNB cannot form a resonance stabilised aci-quinone form, hence the aci-ion theory would not predict a sensitisation effect in TNB. The results of the Rotter sensitisation experiment on TNB showed not only that it was sensitised, but that the sensitisation was of the same magnitude as with TNT. TNB also underwent the same colour change as TNT on addition of the amine.

We have also carried out Rotter tests on RDX and PETN, both pure and with 5% diethylene triamine. For both these explosives no sensitisation effect was observed. This is consistent with our tentative hypothesis concerning nitramines and nitrates.

7. DISCUSSION

One of the major goals of explosives research currently is to develop compositions which are at the same time more powerful and less hazardous. We would expect such compositions to incorporate new energetic materials; perhaps new explosives molecules, certainly new

energetic binder systems. The introduction of these new materials into service presents a significant challenge to the energetic materials community.

Over the past several decades, military explosives have been based largely on the nitramines RDX and HMX, TNT and inert binders such as waxes or polyurethanes. New compositions have involved only relatively minor variations and a substantial base of empirical test data has been built up against which experts can assess the likely characteristics of a new formulation. The advent of new molecules in explosives compositions changes all of this. The same tests may be applied to the materials, but without knowledge of the fundamental physics and chemistry underlying the test responses how are these results to be extrapolated to the munitions scale?

At RARDE we have taken the view that it is essential to develop a quantitative understanding of the phenomena underlying ignition, initiation and growth of reaction in energetic materials and the propagation of detonation. Clearly this is a wide ranging programme and one which is beyond the scope of a single, small group of workers. Nevertheless, I believe we have been able to make some substantial progress. Our work on the nitromethane system, combining theory with experiment, seems to us to point the way ahead.

Our calculations on the nitromethane/ammonia system demonstrate a decrease in the activation energy for C-N bond scission of 27% in the presence of ammonia. Having identified the importance of scission of this bond in the decomposition mechanism, the effect of neighbouring nitromethane molecules is now being addressed. Hence we aim to piece together the full story of the detonation reaction mechanisms in pure and sensitised nitromethane. Knowledge from these studies can be applied to larger molecules such as trinitrotoluene and trinitrobenzene for it is known that these molecules are also sensitised by amines. The important point here from the viewpoint of the explosives formulator is that the study of a molecule of little practical interest can give a good insight into the chemistry of energetic materials which are in common usage.

Similarly, improved understanding of the physical and chemical factors controlling the ignition and growth of reaction in energetic materials is likely to prove to be the next major step forward in explosives hazard control. We know that hot spot formation and growth are vital features of explosives hazard responses but we currently have no quantitative models for these phenomena. Chemical descriptions must form part of such models and given the experimental difficulties, theoretical modelling must play an important role. While we must expect for the foreseeable future that practically useful ignition and growth models will be based on empirical kinetic schemes, we can at least attempt to provide some justification for these schemes.

In addition to our work on the nitromethane/ammonia system, we have begun to consider other possible explosive/additive combinations. We are, for example, carrying out calculations on the interactions between nitromethane and a range of organic compounds and we intend to extend this study to other energetic materials. One possibility of interest is that we may be able to determine what it is that makes an insensitive explosive insensitive and how such explosives might be made more sensitive by chemical techniques.

8. CONCLUSIONS

Clearly there is a long way to go before explosives science becomes an armchair occupation. However, significant progress is being made in developing understanding of the chemistry of detonation. This understanding is based on the development of powerful chemical codes and computers but also on the maintenance of a close link between computation and experiment.

The challenge now is to apply the techniques becoming available to the explosives chemist to the solution of the practical problems which we face. I believe we have the opportunity to radically improve our understanding of the chemistry of explosives and explosions and to use this knowledge.

If we can meet this challenge then we will witness a real renaissance in explosives science.

REFERENCES

1. Mader C L, Modelling of Detonation, Univ Calif Press 1979.
2. Tarver C M, Hallquist J O & Erikson L M, Modelling Short Pulse Duration Shock Initiation of Solid Explosives, 8th Symp (Int) on Detonation, Albuquerque, NM, 1985, preprints, p884.
3. Bingham R C, Dewar M J S & Lo D H, J.Amer.Chem.Soc., 97, (1975), 1285.
4. Hindmarsh A C, ODEPACK, A Systematic Collection of ODE Solvers in Scientific Computing, R S Stepleman et al., eds., North-Holland, Amsterdam, (1983) 55-64.
5. Kee R J, CHEMKIN: A General-Purpose, Problem-Independent, Transportable, FORTRAN Chemical Kinetics Code Package, Sandia National Laboratory Report, SAND80-8003 (1980).
6. Imbert F E & Marshall R M The Mechanism and Rate Parameters for the Pyrolysis of n-Hexane in the Range 723-823 K, Int.J.Chem.Kinet., 19, (1987), 81-103.
7. Ebert K H, Ederer H J & Isbarn, G, The Thermal Decomposition of n-hexane, Int.J.Chem Kinet., 15, (1983), 475-502.
8. Hillewaert L P, Dierickx J L & Froment G F, Computer Generation of Reaction Schemes and Rate Equations for Thermal Cracking, AIChE Journal, 34, (1988), 17-24.
9. Dean A M, Chou M S & Stern D, Nitrogen Chemistry in Flames: Observations and Detailed Kinetic Modelling, ACS Symposium Series No. 249, (1984), 71-86.
10. Thorne L R, Branch M C, Chandler D W, Kee R J & Miller J A Hydrocarbon/Nitric Oxide Interactions in Low Pressure Flames, Twenty-first Symposium (International) on Combustion, The Combustion Institute, (1986), 965-977.
11. Rogg B, Behrendt F & Warnatz J, Turbulent Non-Premixed Combustion in Partially Premixed Diffusion Flamelets with Detailed Chemistry, Twenty-first Symposium (International) on Combustion, The Combustion Institute, (1986), 1533-1541.

12. Frenklach M, Clary D W, Gardiner W C Jr & Stein S E, Effect of Fuel Structure on Pathways to Soot, Twenty-first Symposium (International) on Combustion, The Combustion Institute, (1986), 1067-1076.
13. Haskins P J & Cook M D, Short Range Interactions in Diatomic Molecules, in Shock Waves in Condensed Matter, ed Gupta (Plenum, New York, 1986), p 113.
14. Gaussian 86, M J Frisch, et al. Carnegie-Mellon Quantum Chemistry Publishing Unit, Pittsburgh PA, 1984.
15. MOPAC: Stewart J J P, QCPE # 455, Available from QCPE Dept of Chemistry, Indiana University, Bloomington, Indiana 47405, USA.
16. Cook M D & Haskins P J, Decomposition Mechanisms and Chemical Sensitisation in Nitro, Nitramine and Nitrate Explosives", accepted for inclusion in "The Ninth Symposium (International) on Detonation, to be held 28th August - 1st September 1989, Portland, Oregon, USA.
17. Haskins P J & Cook M D, Short Range Interactions of Detonation Products, Proceedings APS Conference on Shock Waves in Condensed Matter, Aug 1989.
18. Cook M D & Haskins P J, Decomposition of Nitromethane. A Critical Study of the Initial Steps, 12th Int Pyro Symp, Juan-les-Pins, 1987, 43-48.
19. Engelke R, Earl W L & Rohlfiing C M, "Production of the Nitromethane Aci Ion by UV Irradiation: Its Effect on Detonation Sensitivity", J.Phys. Chem., 90, (4), (1986), p 545.
20. Engelke R, Earl W L & Rohlfiing C M, The Importance of Enolate Anions in the High Pressure Kinetics of Nitroalkanes and Nitro-Aromatics", Int.J.Chem.Kinet., 18 (1986), p 1205.
21. Engelke W L, Earl W L & Rohlfiing C M, "Microscopic Evidence that the Nitromethane Aci Ion is a Rate Controlling Species in Detonation of Liquid Nitromethane", J.Chem.Phys. 84, (1) (1986), p 142.
22. SCC Manual of Tests, RARDE, Fort Halstead, 1988.
23. Cook M D & Haskins P J, "Chemical Sensitisation of Nitro Compounds", 19th International Annual Conference of ICT, Karlsruhe, FRG, (1988), pp. 85.1-85.8.

THE RESPONSE OF ENERGETIC MATERIALS TO PROJECTILE IMPACT

DR J CONNOR

Royal Armament Research and Development Establishment
Fort Halstead
Sevenoaks, Kent
TN14 7BP
UK

ABSTRACT RARDE work on the ignition or initiation of cased explosives and rocket propellants is reviewed. Attention is focussed on criteria to predict the threshold impact velocity for detonation. Critical energy and power concepts are considered. Experiments show that, for thin cases, a critical energy criterion is adequate but clear evidence is provided for a non-shock initiated detonation regime with thicker cases. Existing criteria cannot describe this phenomenon. The need for a quantitative description of hot spot formation and growth is highlighted.

1. INTRODUCTION

Modern, high performance weapon systems contain highly energetic propellants and explosives. Such materials are designed to explode or to burn violently when ignited and they pose a potential hazard to all those who handle and use them. Extensive testing is carried out to ensure that weapons are safe in normal peacetime environments. This testing, together with careful control of handling, transport and storage, has resulted in a general excellent safety record. However, in recent years the combat vulnerability of weapon systems has attracted increasing concern.

The basis for this concern is simple. Violent reactions of munitions subject to attack can destroy not only the weapon but also the platform which carries it. Ships, aircraft and tanks are expensive items and neither they nor their crews are easily replaced. Reducing munition vulnerability is therefore an important goal in increasing operational effectiveness.

There is a wide variety of potential threats to munitions. In this paper just one of these threats is considered. Impact by high velocity fragments or projectiles is a highly credible risk scenario for almost all munitions. Projectiles may be small or medium calibre

ammunition, metal fragments projected from other exploding munitions or spall or debris from the surroundings. Multiple hits may be important but consideration here is limited to single impacts.

The response of a weapon to projectile impact is a complex function of the nature of the input stimulus, system design features such as case materials and thickness and choice of energetic materials, environmental factors such as temperature and the previous history of the weapon. Responses may vary from detonation through violent deflagration to no reaction. Our understanding of these phenomena is limited and we have no adequate models or predictive small-scale tests which designers can use to ensure that munitions will meet vulnerability requirements. This is a major capability gap which represents a significant challenge to the energetic materials community.

This paper will briefly review experimental work with both cased explosives and propellants which illustrates the complexity of the phenomena involved and shows the importance of various system design parameters in determining responses. This will lead to the presentation of a protocol which is being developed to describe the response of munitions to fragment impact. The protocol helps to define the data required to generate a full model of the process. These data requirements vary from the macroscopic to the molecular level. Work now under way in our laboratories to begin to fill these requirements will be described.

2. PROPELLANT VULNERABILITY

At RARDE we have built up a considerable database on studies of rocket propellants in configurations which are representative of in-service motors. Much of the work has been carried out with the so-called model scale motor (1). This features heavy end blocks connected by tie bars to ensure that case damage is restricted to the motor tube. Propellant charges are filled in the desired configuration, for example as a cylindrical, cigarette burning charge or with a central conduit and may be fixed to the tube as required.

A 17g steel cylinder is used as the projectile and in the standard test this is fired at 530ms^{-1} or 920ms^{-1} . Targets may be conditioned at temperatures from $+18$ to -50°C . Projectile velocity is determined from timing screens and this, in conjunction with an enamelled wire wrapped around the tube circumference provides a measure of 'hit to split' time. Additionally, blast pressures and burning times are monitored. These observations, together with the degree of damage to the tube allow responses to be reported on a seven point scale from no reaction to explosion. Results for some typical propellants are shown in Figure 1.

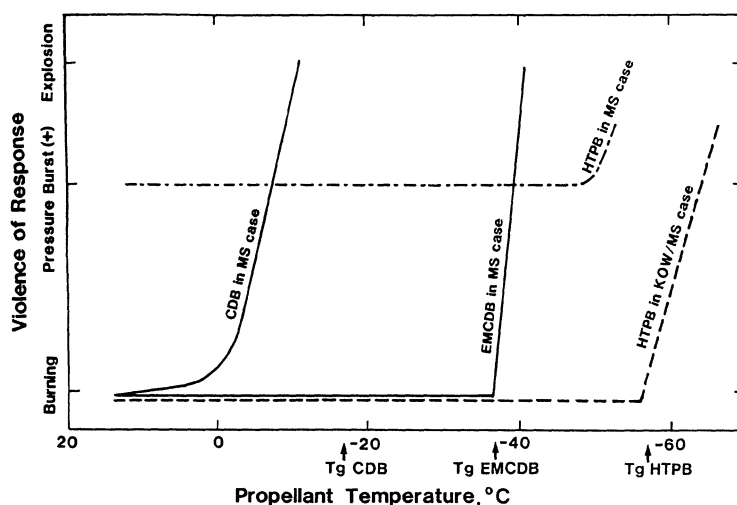


Fig. 1 Propellant fragment attack results, violence as a function of temperature

For present purposes the important feature of these results is that they show a correlation between violence of response and propellant brittleness as determined by strain rate adjusted glass transition temperature, Table 1.

TABLE 1. Glass Transition Temperature, T_g

Propellant type	CDB	EMCDB	HTPB
Strain rate			
1 min^{-1}	-50	-60	-83
10^6 min^{-1}	-16	-36	-56

These general findings have been confirmed by a large number of firings. However, these findings also show that responses vary with case material and propellant formulation. Given the essentially qualitative nature of the data, the relationships between the propellant chemistry, its mechanical properties, the properties of the case and the overall response are virtually impossible to

disentangle. Tests of this type are useful in that they provide guidelines for rocket motor designers. However, they do not provide designers with quantitative design data nor do they provide any predictive capability. The effects of changing propellant formulation or motor case design can only be assessed by further trials.

When gun propellant charges are considered the situation is even more complex. Rocket motor fillings are at least relatively homogeneous. Gun charges are made up from sticks or grains of propellant and contain significant voidage, adding heterogeneity to the list of parameters which may determine charge response. This perhaps did not matter when the maximum response anticipated from a gun propellant charge was burning but modern, high performance, propellants may explode if the input stimulus is sufficiently severe. The consequences of such an explosion could be disastrous and there is therefore a pressing need to identify those situations which may lead to explosion so that steps can be taken to avoid them.

3. EXPLOSIVES VULNERABILITY

Unlike propellants, explosives are designed to detonate. Reliable detonation is one of the keys to reliable performance and substantial effort is devoted to characterising the initiation characteristics of new explosives formulations. However, explosives may also burn or deflagrate, leading in some cases to violent but non-detonative explosions. Experience from many incident investigations suggests in fact that accidental detonations are rare. Most hazardous events involving explosives begin with an ignition and progress through a growth phase to a more or less violent deflagration. These phenomena are not described by tests to determine sensitivity to shock initiation. Performance tests have little or nothing to do with hazard.

In the UK we distinguish carefully between sensitivity, a measure of the probability of initiation by the design stimulus, and sensitiveness, a measure of the probability of ignition by accidental stimuli. Likewise, we must distinguish between the design performance, detonation, and the response to an accidental stimulus which we term explosiveness. The explosiveness is a function both of the chemistry of the composition and also of its environment. Generally, explosiveness will increase with, for example, confinement. On the whole propellants have greater sensitiveness but lower explosiveness than secondary explosives, Figure 2.

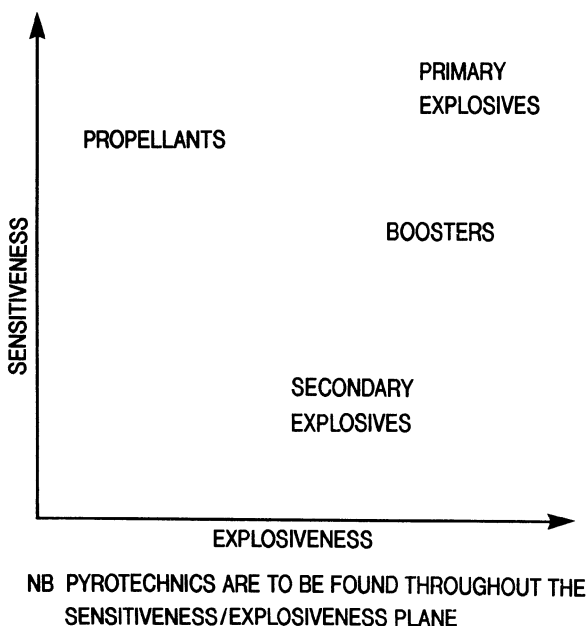


Fig 2. A schematic sensitiveness/explosiveness diagram

In assessing the vulnerability of explosives to fragment impact at RARDE we have attempted to determine the violence of response as a function of impact velocity. Thus we aim to determine thresholds not only for detonation but also for lower levels of reaction. The Fragment Attack Test (2) involves firing a 12.7mm diameter by 12.7mm long projectile weighing 13.5g at velocities up to $2,500\text{ms}^{-1}$ into a confined explosive sample. The steel test vehicle is closed by a 3mm thick mild steel or aluminium alloy cap through which the projectile enters. The explosive response is described in terms of reaction categories from 0 (no reaction) to 4 (detonation). Typical results are shown in Figure 3. Traditional, relatively brittle explosives such as RDX/TNT (60/40) show a steady rise in response with velocity until full detonative output is achieved. Plastic bonded explosives show rather different behaviour with little or no reaction until a threshold velocity is reached above which detonation is observed. This threshold can be interpreted as the velocity at which the shock transmitted to the explosive on impact exceeds the minimum level for initiation.

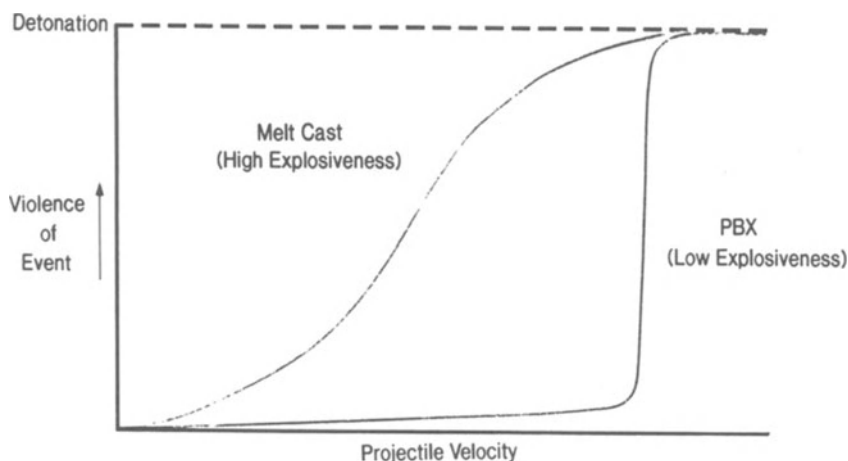


Fig 3. Projectile impact on cased explosives, typical responses

For unconfined explosives the only stimulus which can lead to initiation from impact is the shock in the explosive. For confined explosives the situation is different. Phenomena such as rapid plastic working of the explosive near the impact site due to projectile penetration and case distortion can lead to local ignition. The confinement then allows reaction to build up. Cased charges thus have a far greater complexity of responses than do bare charges.

4. A PROTOCOL FOR PROJECTILE IMPACT

Over the last three years, RARDE has been collaborating with laboratories in the USA, Canada and Australia to produce a format or protocol within which the hazards of munitions exposed to projectile impact can be assessed. Essentially, the protocol is a logic diagram which expresses the questions that must be answered if the response of a munition is to be predicted. These questions can only be answered by utilising experimental data fitted, where appropriate, to models of the systems of interest. The protocol serves principally to highlight acute deficiencies in both the data and the models.

Answering the questions posed by the protocol begins with a description of the stimulus. Assuming only a single fragment strikes the target, the fragment velocity, its material properties, including Hugoniot data, and its geometry are required together with similar information for the munition case in order to specify the shock in the case. Calculation of the shock in the energetic material then requires Hugoniot data for that material. For propellants the propellant geometry and configuration may also be important. Finally, to assess the possibility of detonation we need shock initiation criteria.

If there is no prompt shock detonation then further factors must be considered. For example, does the impact shock damage the energetic material? If so, is the damaged material more susceptible to ignition than undamaged material and, should ignition occur, is the reaction likely to grow in violence? Even if no shock is transmitted to the charge, the projectile may penetrate the case, setting in train a further chain of events which could lead to violent reaction.

From even such a cursory examination of the protocol as this several key factors quickly emerge. These include the need for good mechanical properties data on both undamaged and damaged material over a range of strain rates, the need for criteria for fracture and the need for codes to describe the penetration process. However, in the present context the most important requirements are for criteria to describe the conditions under which chemical reaction will begin in both shock and non-shock regimes and methods to predict whether these reactions will grow to violent explosions or detonations. It is in this area that we at RARDE have been concentrating our effort and it is this work which will be described in the next part of this paper.

5. DETONATION THRESHOLDS AND CRITERIA

Initially, we have concentrated on the detonation threshold although as already indicated, we regard less violent responses as being very important in overall hazard assessments. The target charges were 114mm long x 57mm diameter and were mainly of PE4 (a plastic explosive containing 88% RDX). Additional experiments have been carried out using both RDX/TNT (60:40) and Tetryl. The explosive was housed in a 9mm thick mild steel cylinder open at one end. This allows experiments to be carried out on the bare explosive or with varying thicknesses of barrier material. A total of three barrier materials have been employed in the studies to-date, namely aluminium, steel and PMMA. The projectiles were all of the same mass (27g) and manufactured from hardened steel (condition W). A variety of projectile geometries were investigated including flat-nosed rods, round nose rods, and sharply pointed rods. The projectiles were placed in a nylon sabot and fired from a 30mm rifled RARDEN gun. This system allows velocities of between 800-2000m/s to be achieved with

very few projectile stability problems. It appears from a limited number of comparison firings with a smooth bore RARDEN gun that projectile spin has a negligible effect on the detonation thresholds. The explosive target was back illuminated by flash bulbs and the event captured on film using a 1/4 height Fastax camera operating at ca. 30,000 fps. The film provided a permanent record of the event and the velocity of the projectile. The film record was also used to check projectile stability.

Theoretical analysis of the data is based on the critical energy criterion for bare explosives postulated by Walker and Wasley (3) and developed by James (4) to cope with projectiles such as flat-ended cylindrical rods. It is assumed that the theory is valid for covered explosives providing that:-

a) The initial impact shock can be transmitted into the explosive.

b) That the shock mechanism is the most efficient mechanism for initiating explosives within the region defined by a), ie it is not possible for a non-shock stimulus, produced by a projectile which is below the requirements for the shock threshold, to cause detonation.

If either a) or b) does not hold then the detonation threshold is not defined by a shock mechanism, and is not described by the theory given below.

The theory requires the explosive to have a critical value of energy-per-unit area (E_c) which, if exceeded by conditions within the initial shock, causes detonation. It is postulated that the value of E_c for a given explosive is constant regardless of whether the charge is bare, covered or cased. Hence to predict the detonation threshold the theory needs a value for E_c (from bare charge impacts), the values of shock parameters in the explosive and a knowledge of how quickly they are released by rarefactions from free surfaces. The importance of the latter requirement is that it determines the time at which the maximum shock energy is deposited in the explosive, which in turn is the time at which the energy-per-unit-area (E) is calculated (5). The detonation threshold for the covered explosive is theoretically determined by impacts which give E equal to E_c .

It should be noted that in bare charge experiments the E_c criterion has been found not to apply to some explosives (5), or to apply only over a limited impact velocity range in others (6). Obviously these limitations also apply to covered experiments. However, the criterion does apply to a sufficient number of commonly used explosives to make its adaptation to covered charges worthwhile.

The energy-per-unit-area deposited by the impact shock in the explosive is calculated in three stages. By knowing the Hugoniot for the projectile, barrier plate and charge material, and also by knowing the impact velocity, the shock parameters in the explosive can be calculated. These parameters, plus the barrier thickness and projectile diameter, allow the shock diameter at the case/explosive interface to be calculated at the start of shock transmission into the explosive. Finally by finding the main release mechanism for the shock volume in the explosive, the time at which the maximum shock energy is deposited in the charge is found. The value of E is calculated at this point and compared to E_c to predict the explosive's response.

Cook, Haskins and James have recently (7) discussed shock release mechanisms for cased charges. The major complicating factor is the effect of rarefactions in the barrier itself on the release waves within the explosive.

The critical energy criterion requires that the energy per unit area is calculated at the time when the shocked volume reaches a maximum (4).

The depth L of shock penetration is

$$L = (w_3 - u_3)t \quad (1)$$

where t is the time after the shock has reached the explosive interface, w and u are shock and particle velocities respectively and the subscripts 1, 2 and 3 refer to projectile, barrier and explosive respectively. The calculation of the radial shape of the volume is rather more complicated because of the two rarefactions involved. However, a study of the experimental evidence suggests that a simple approximation allows a reasonable estimate of E_c to be made for impacts at the initiation threshold.

Figure 4 shows experimental threshold data (8) for steel rods impacting bare and covered PBX9404. Shock pressure in the explosive (P) is plotted against the effective diameter of the projectile. The effective diameter is either the diameter of the projectile for bare explosive or the diameter of the initial shock in the explosive for covered explosive. It can be seen that to a first approximation the relationship between P and D_0 is the same as that between P and D_c .

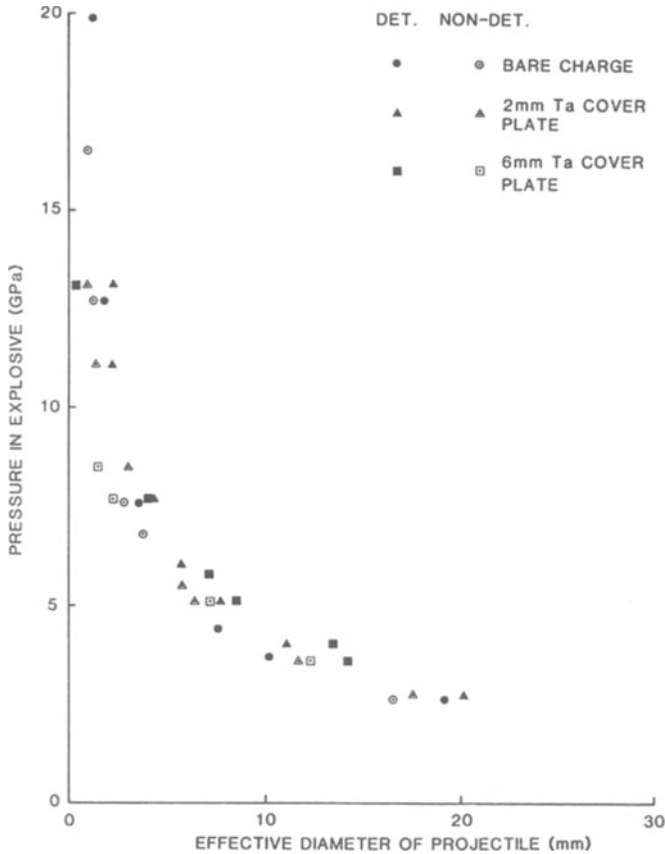


Fig 4. Threshold data for impact of steel rods on bare and covered PBX 9404

If the barrier rarefaction played a significant role in releasing the shock conditions in the explosive, it would be expected that the pressure/diameter relationships would differ between bare and covered impacts since the release mechanisms would be different. The fact that the relationships are so similar suggests that it is the rarefactions in the explosive that largely determine the explosive's response. This is reinforced by the experimental observation that materials that have high sound speeds do not necessarily provide the best protection against shock initiation resulting from projectile attack, for example references (9) and (10) show aluminium as not providing as good a protection as the same thickness of steel.

At the initiation threshold the critical energy criterion requires:-

$$E = E_c = P u_3 T \quad (2)$$

where T is the time to maximum shocked volume, relative to the arrival of the shock at the barrier/explosive interface. For bare impacts T has been shown to be $R_0 / (3c_3)$. As a result of the similarity between the bare and covered relationships it is assumed that to a first approximation:

$$T = R_c / (3C_3) \quad (3)$$

for covered impacts. Hence:

$$E = P u_3 R_c / (3C_3) \quad (4)$$

and $E = E_c$ for threshold impacts.

The shock pressure P can be calculated from Hugoniot data for explosive, barrier and projectile. Details of these data are included in reference (5). Figures 5-7 show both experimental and calculated plots of threshold impact velocity against barrier thickness.

The critical energy values used in the calculations are shown on each curve. It will be noted that a lower value, 1.70 MJ/m^2 , is required to give a good fit to the data with PMMA barriers than the value of 1.92 MJ/m^2 required with steel and aluminium values. This may be a consequence of the effects of rarefactions in the barrier materials.

The experimental curves are all similar in shape. For very thin barriers there is evidence of an increase in sensitivity to shock for both aluminium and PMMA barrier materials. Cook et al (7) explain this as being a consequence of the differing slopes of the projectile and barrier Hugoniots. Beyond this region, the threshold impact velocity increases in a roughly linear manner followed by a sharp rise in threshold velocity leading to a third region with a lower gradient.

The calculated curves can be fitted reasonably well to the experimental data in the linear region but the fit for thicker barriers is poor. This is shown most clearly in Figure 7 where detonations are observed experimentally at barrier thicknesses too great to allow the transmission of a primary shock into the explosive. We believe this to be clear evidence of a non-shock mechanism for detonation.

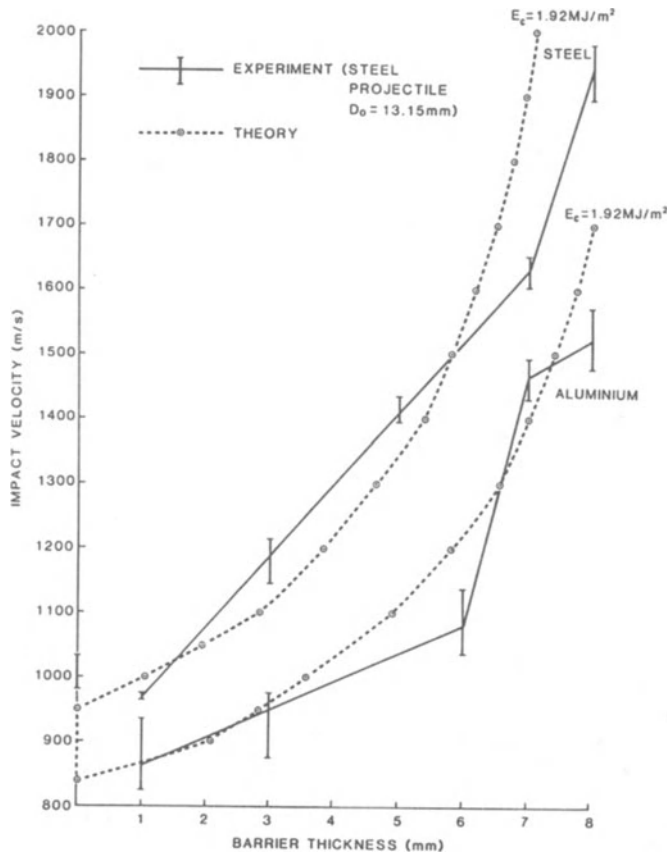


Figure 5. Steel and Aluminium Barriers Covering PE4

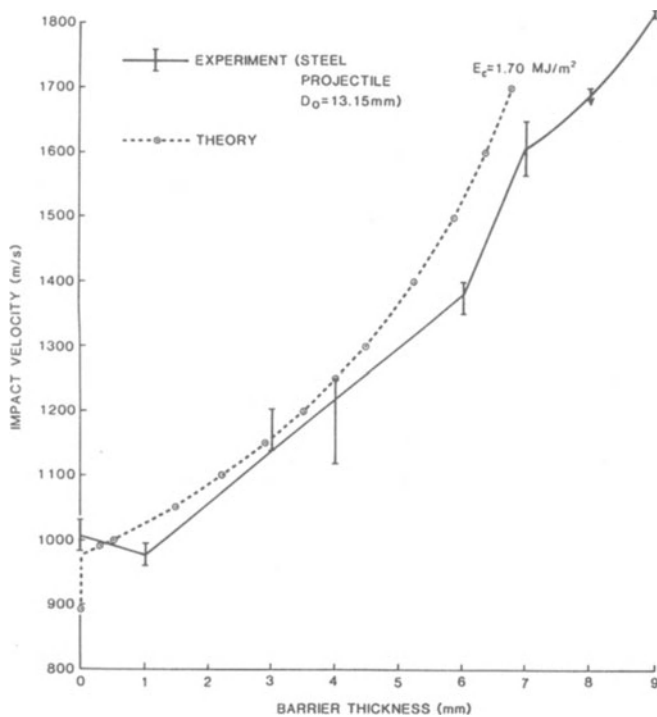


Figure 6. PMMA Barriers Covering PE4

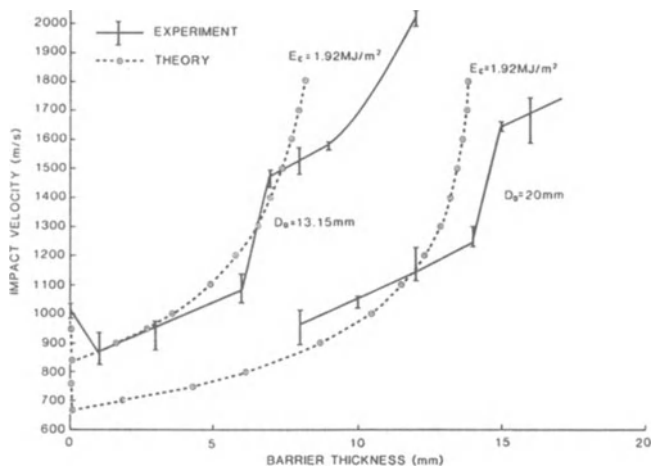


Figure 7. Steel and Aluminium Barriers Covering PE4, 13.15mm and 20mm Projectiles

Before giving consideration to such alternative mechanisms, it is worth considering if the Walker Wasley critical energy criterion really provides a worthwhile description of the shock initiation regime. Lee (11) has criticised such approaches which assume a critical energy for reaction. He argues, quite rightly, that the rate of energy input needs to be considered. There is an enormous difference between the response of an explosive to slow pressurisation in, for example, a press and to shock compression. Lee suggests that initiation criteria might more usefully be expressed in terms of power rather than energy.

It is clear that application of a large quantity of energy to an explosive will not result in reaction if the rate of application is sufficiently low. Energy will be dissipated, chiefly as heat, and the activation energy for reaction will not be exceeded. On the other hand, application of a very small amount of energy very rapidly will not cause any explosive response because, again, the activation energy is not exceeded despite the high power input. Lee proceeds essentially on this basis to propose an initiation criterion based on power density expressed at Watts kg^{-1} .

While this idea of power density is attractive, it must be recognised that it ignores the essential heterogeneity of explosive charges. This heterogeneity is at the very root of understanding of the deflagration and detonation processes since it is the source of the hot spots which propagate reaction. A more general criterion might be based on the assumption that initiation requires that the energy of a hot spot be raised above a threshold value. Use of the term hot spot does not necessarily imply a thermal decomposition mechanism but merely that a critical minimum amount of explosive must be involved if a self sustaining reaction is to occur. Calculation of the energy of a hot spot requires knowledge of the rates of both input and dissipation of energy. It is this latter factor which is ignored in the Walker Wasley approach.

At this stage in the argument it is not necessary to be concerned with the mechanisms whereby energy is concentrated into hot spots nor with identifying the critical minimum size of hot spot below which reaction will not propagate. Energy localisation may be assumed to be a natural consequence of heterogeneity while the critical size of hot spot is controlled by the balance between input and dissipative terms. For a sub-critical hot spot, dissipative processes are efficient so that the critical energy condition in the hot spot is never achieved.

Let ΔE be the energy acquired by the hot spot at time t after the arrival of a shock wave of duration T , $t < T$. $P_{\text{in}}(t)$ and $P_{\text{out}}(t)$ are the power input to the hot spot and dissipation respectively.

Then

$$\Delta E = \int_0^t (P_{in}(t) - P_{out}(t))dt \quad (5)$$

For simplicity, it is assumed that this energy is maximised when $t = T$. This is not true for all impact geometries but James (4) shows how various geometries can be related. Initiation occurs when the maximum value of ΔE reaches a critical threshold, ΔE_c , within the minimum size of hot spot from which reaction may propagate.

$$\Delta E_c = \int_0^T (P_{in}(t) - P_{out}(t))dt \quad (6)$$

The form of the power input term depends on the shock wave shape and duration. A simple case involves a square wave for which

$$P_{in}(t) = \begin{matrix} P_{in} & 0 < t < T \\ 0 & t < 0 \text{ and } t > T \end{matrix} \quad (7)$$

The simplest assumption to deal with the dissipative term is to assume that the losses are proportional to the excess energy.

$$P_{out}(T) = K \int_0^T (P_{in}(t) - P_{out}(t))dt \quad (8)$$

Substituting (7) into (8) gives

$$\begin{aligned} P_{out}(T) &= K \int_0^T (P_{in} - P_{out}(t))dt \\ &= KT P_{in} - K \int_0^T P_{out}(t)dt \end{aligned} \quad (9)$$

This equation has the solution

$$P_{out}(T) = P_{in}(1 - e^{-kT}) \quad (10)$$

which may be substituted into (5) to give

$$\Delta E_c = \int_0^T (P_{in} - P_{in}(1 - e^{-kt}))dt \quad (11)$$

$$= P_{in}(1 - e^{-kT}) k \quad (12)$$

Expanding the exponential and neglecting terms above second order in KT gives

$$\Delta E_c = P_{in} T \left(1 - \frac{kT}{2}\right) \quad (13)$$

The first term in (13) is simply the energy input to the system and is therefore equivalent to the Walker-Wasley criterion. This term will provide a good criterion for initiation provided $kT \ll 2$.

The constant k is the coefficient of proportionality between power loss and energy. If it is assumed that the energy dissipation mechanism is thermal then k can be related to the surface heat transfer coefficient of the hot spot, h .

$$k = hA/mc = 3h/r \quad c \quad (14)$$

where A , m , c , r and ρ are the surface area, mass specific heat, radius and density of the hot spot.

It is not proposed here to follow this argument further and to try to place values on these parameters. It is suggested simply that a critical energy criterion is likely to be valid for the shock to detonation transition where timescales are short. On the other hand such a criterion may not be valid for lower order reactions such as burning or deflagration where the timescales for ignition and growth of reaction are longer.

DISCUSSION

The work reported here indicates that a critical energy criterion as postulated by Walker and Wasley and modified by James can provide a useful model of prompt shock initiation in projectile impact experiments. However, it is important that the shocked volume is accurately estimated. It is at least likely that it is the failure to take into account rarefactions in the barrier material which account for the different critical energy values required to give the best fits to our data with metal and PMMA barriers, Figs 6-8.

However, major limitations in the applicability of the critical energy criterion are also apparent.

Firstly, a non-shock initiated detonation regime has been identified which cannot be described by the essentially shock-based Walker-Wasley criterion. Beyond this we must also recognise that impacts at lower velocities than those required to produce detonation can for many explosives nevertheless result in violent deflagrations. The description of such a complex phenomenon is unlikely to be possible in terms of single parameter. Finally, even when the Walker-Wasley criterion can be used, its value must be derived from experimental studies. We have no a priori methods for the estimation of the critical energy.

On the other hand, a qualitative picture of the processes occurring in an impacted explosive can readily be given based on the notion of the hot spot. Initially the stimulus produces within the explosive a more or less localised distribution of hot spots (12). These hot spots, which may represent only a small fraction of the total volume of the material, consist of locally heated regions where the energy of the stimulus is concentrated and where temperatures may

rise sufficiently because of this energy concentration to allow chemical reaction to begin. Once reaction begins, the history of a hot spot then depends on the balance between the rate of energy release as a result of the reaction and the rate of energy loss from the hot spot surface to the surrounding medium, the classical problem of thermal explosion theory. Hot spots which are large enough will produce more energy than they lose and will grow, propagating reaction; smaller hot spots will be extinguished. The critical hot spot size for any explosive depends upon the temperature attained and the duration, but for typical secondary explosives the critical values are around $1 \mu\text{m}$ for $1 \mu\text{s}$ at 700-800K (Ref 13).

Hot spots are formed in areas where energy is localised and such areas must be distinguished in some way from the surrounding medium. Since the energy localisation process is essentially physical, the distinguishing features of incipient hot spots are also likely to be physical. Thus hot spots might be expected to form at dislocations, at density discontinuities such as pores, cracks or inclusions of foreign material and at grain or crystal boundaries and interfaces. In a typical heterogeneous energetic material these features will be strongly influenced by factors such as the production process, final density, particle size and crystal geometry of the ingredients and by interactions with the binder. Such features are also important determinants of the bulk mechanical properties of the material, and to this extent correlations between these properties and the probability of ignition due to a particular stimulus are to be expected. However, quite minor variations in the physical characteristics of the energetic material or in the intensity of the stimulus may lead to a major change in the predominant hot spot formation mechanism and in such circumstances simple correlations with bulk properties are unlikely. Clearly, a complete description of the ignition process requires an understanding of the microscopic properties of energetic materials.

Once formed, hot spots which are sufficiently large will grow, generating thermal and pressure stresses in the surrounding material. The result of these stresses is the production of new hot spots, and if the rate of production exceeds the rate at which hot spots fail because their dimensions are too small to sustain growth, an accelerating reaction will ensue. As this growth phase continues, pressure waves from individual hot spots may coalesce to form a weak shock wave which may then itself develop through a strong shock to a detonation. Alternatively, the stresses produced in the material may exceed its strength so that fracture results. In cased or confined charges this fracture will produce a rapid increase in free surface area leading to accelerating burning and, in charges which are large enough and well enough confined, to transition to detonation. In uncased or lightly confined charges failure will result in break-up of the charge, separating reacting from unreacted material and preventing propagation.

Hot spot formation mechanisms have been studied in some detail by Field and his co-workers at Cambridge University (15-19), following on from the pioneering work of Bowden and Yoffe (13). Among the mechanisms proposed have been (i) fracture of explosive crystals (20,21), (ii) plastic flow with dislocation pile-up (22) and adiabatic shear flow (23-26), (iii) friction, (27,28), (iv) adiabatic compression of gas pockets (27) and (v) shock-void interactions (29). Chaudhri has very recently examined these possibilities (30) and concludes that intercrystalline friction and the interaction of strong shocks with voids producing fast jets are dominant mechanisms. Plastic flow can also be effective when the strain is high.

The complexity of hot spot formation is further compounded by the variation in the amount of explosive which may be ignited by the stimulus. High pressure shocks can result in 20-30% ignition (31) whereas low pressure may result in only a very small fraction being ignited (32). In the former case the violence of reaction is determined by whether or not build-up occurs but in the latter the ignition process itself may be the critical determinant.

Studies of the development of reactions within hot spots have been sparse but a recent report by Green, Pilling and Robertson (33) suggests a possible approach. They compare a simple deterministic kinetic model with a stochastic model. The latter may be applicable where hot spots are small so that the numbers of reactive species involved are also small. It is shown that the stochastic model can predict hot spot quenching under conditions where the deterministic model would suggest that reaction might propagate.

In another recent study, Spear and Nanut (34) have reviewed the physical processes involved in initiation and build up of reaction in heterogeneous explosives. They point out that the molecular processes occurring during shock initiation are not known and that there is disagreement as to whether grain burning or physical processes such as permeability, thermal conduction, convective and diffusivity are the key parameters controlling the subsequent build-up of reaction.

Spear and Nanut follow several previous authors in distinguishing between short and sustained shocks. The critical energy criterion is applicable in their view to short shocks only and, following Howe (35), they suggest that the criterion applies to situations where build-up dominates the response. However, James (4) suggests an alternative interpretation of the time factor in the calculation of the critical energy, equating it with the time to achieve maximum shock volume rather than the shock duration. James suggests that the critical energy might be regarded as a trigger energy, creating the right conditions for a self sustaining reaction. It should be stressed that both Spear and Nanut and James are concentrating on initiation of detonation and that violent reactions may still occur even if either or both of the ignition and subsequent build-up reactions are inadequate to lead to detonation.

Finally, we should consider the non-shock detonation regime which has been clearly identified, for example for PE4 covered by aluminium barriers. A considerable number of experiments have also been carried out with RDX/TNT (60:40) and tetryl using the 13.15mm projectiles. Although complete curves of the type shown in figures 2,4 and 5 are not yet available, detonations have again been observed outside the shock initiation regime. With RDX/TNT (open cast to a density of 1.65 Mg/m^3) detonations were observed with a 10mm thick steel barrier (threshold velocity ca. 2000 m/s) - clearly well outside the shock regime. Similarly, tetryl (pressed to a density of 1.58 Mg/m^3) has been detonated when covered by a 15mm steel barrier (threshold velocity: 1605-1537 m/s).

The experiments described above were all carried out on steel cased charges, as detailed in section 2. To see if this casing was influencing the detonation threshold in the non-shock regime an experiment was conducted on PE4 contained only in a light plastic tube, but covered with an 8mm aluminium barrier. Using a 13.15mm projectile detonation was achieved at ca. 1605 m/s. Whilst more experiments are needed this is sufficiently close to the threshold observed for the cased charges to suggest that the casing has not influenced the initiation to any significant extent. As a consequence of this result it would appear that neither interactions with the back plate nor the confinement afforded by the steel casing play a significant part in the initiation process. The lack of any apparent dependence on confinement suggests that onset of detonation must be reasonably prompt. The Fastax camera records show detonation occurring within 1 frame after projectile impact, which puts an upper bound on the delay before detonation of ca. 33us, but higher speed instrumentation will be needed to explore this question further.

Howe (26) has reviewed the evidence from earlier studies which have indicated that a non-shock process may be controlling the initiation of detonation. Howe concludes that a macroscopic shear process is probably the mechanism in many of these cases. The new results we have presented here are certainly consistent with such a mechanism but considerably more work is needed before any firm conclusions can be drawn.

Clearly, our understanding of projectile impact ignition of explosives is incomplete, even for simple geometries. In my view we will not make further progress towards improving this situation by looking for critical criteria based on bulk properties. We need instead to concentrate on hot spot ignition and growth.

Firstly we need to identify the hot spot formation mechanism so as to allow definition of the hot spot size, shape, temperature and distribution through the explosive; secondly the kinetics of the heat production and decay processes in the hot spot must be determined and finally the interactions between hot spots leading to self-sustaining

reaction must be described. These are challenging requirements but they are I believe within the scope of current experimental and modelling capabilities.

CONCLUSIONS

An experimental study of the projectile impact initiation of detonation in cased explosives has revealed both shock and non-shock regimes. The shock regime can be described by an empirical critical energy criterion for detonation. However, a full description of the processes leading to detonation or to violent reaction cannot be based on such a criterion and requires a full description of hot spot formation and growth mechanisms.

REFERENCES

1. SCC Manual of Tests, RARDE Fort Halstead, 1988, Test No 38.
2. Ibid, Test No 36.
3. F E Walker and R J Wasley, Explosivestoffe, 17, 9, 1969.
4. H R James, Propellants Explosives Pyrotechnics, 13, 35, 1988.
5. Y de Longueville, C Fauguignon & H Moulard, "Initiation of Several Condensed Explosives by a Given Duration Shock Wave", Sixth Symposium (International) on Detonation, San Diego, Ca., August 24-27, (1976), pp 105-114.
6. C A Honodel, J R Humphery, R C Weingart, R S Lee and P E Kramer, "Shock Initiation of TATB Formulations", Seventh Symposium (International) on Detonation, Annapolis, Md, June 15-19, (1981), pp 425-434.
7. M D Cook, P J Haskins and H R James, Ninth Symposium (International) on Detonation, Portland 1989, preprints, 615.
8. K L Bahl, H C Vantine & R C Weingart, "The Shock Initiation of Bare and Covered Explosives by Projectile Impact", Seventh Symposium (International) on Detonation, Annapolis, 1981, 325.
9. D C Slade & J Dewey, "High Order Initiation of Two Military Explosives by Projectile Impact", BRL Report 1021 Ballistic Research Laboratories Aberdeen Proving Ground, Md., (1957).
10. N Griffiths, R McN. Laidler & S T Spooner, "Some Aspects of the Shock Initiation of Condensed Explosives", Combustion and Flame, 7, 347, (1963).
11. P R Lee, Preprints, Ballistic Symposium, 1987.
12. Bowden F P, Yoffe A D, "Fast Reactions in Solids", Butterworth, London, 1958.
13. Rideal E K, Robertson A J B, Proc Roy Soc Lond, A195, 135, 1948.
14. Swallowe G M & Field J E, Seventh Symposium (International) on Detonation, Annapolis, 1981, 24.

15. Heavens S N & Field J E, Proc Roy Soc Lond, A382, 231, 1982.
16. Proc Roy Soc Lond, A382, 231, 1982.
17. Swallow G M & Field J E, Proc Roy Soc Lond, A379, 389, 1982.
18. Mohan V K & Field J E, Comb & Flame, 56, 269, 1984.
20. Copp J I, Napier, S E, Nash T, Powell W J, Skelly H, Ubbelohde A R & Woodward P, "The Sensitiveness of Explosives", Philosophical Transactions of the Royal Society, Vol 241, 1948, p 198-296.
21. Fox P G, "The Explosive Sensitivity of the Metal Azides to Impact", Journal of Solid State Chemistry, Vol 2, 1970, p 491-502.
22. Armstrong R W, Coffey C S & Elban W I, "Adiabatic heating at a dislocation Pile-up Avalanche", Acta Metallurgica, Vol 30, 1982, pp 2111-2116.
23. Afanas'ev G T & Bobolev V K, "Initiation of Solid Explosives by Impact", Israel Programme for Scientific Translations, Jerusalem, 1971.
24. Winter R E & Field J E, "The Role of Localised Plastic Flow in the Impact Initiation of Explosives", Proceedings of the Royal Society, Vol A343, 1975, pp 399-413.
25. Frey R B, "The Initiation of Explosive Charges by Rapid Shear" Proceedings of the Eighth Symposium (International) on Detonation, Naval Surface Weapons Center, White Oak, Silver Spring, Maryland, pp 36-42.
26. Howe P M, Gibbons G & Webber P E, "An Experimental Investigation of the Role of Shear in the Initiation of Detonation by Impact" Proceedings Eighth Symposium (International) on Detonation, Naval Surface Weapons Center, Silver Spring, Maryland, 1985, pp 294-301.
27. Bowden F P & Yoffe A D, "Initiation and Growth of Explosion in Liquids and Solids", Cambridge University Press, London, 1952, p 33.
28. Dienes J K, "Frictional Hot Spots and Propellant Sensitivity", in Proceedings Materials Research Society Symposium, Elsevier Science Publishing Co., 1984, p 373.

29. Campbell A W, Davis W C & Travis J R, "Shock Initiation of Detonation in Liquid Explosives", Physics of Fluids, Vol 4, No 6, 1961, pp 498-510.
30. Chaudhri M M, 9th Symposium (International) on Detonation, Portland, 1989, 331.
31. Tarver C M, Hallquist J O & Erikson L M, 8th Symposium (International) on Detonation, White Oak, Md, Preprints, 884, 1985.
32. Johnson J N, Tang P K & Forest C A, J.Appl.Phys., 57, 4323, 1985.
33. Green N J B, Pilling M J, Robertson S H, 9th Symposium (International) on Detonation, Portland, Preprints, 537, 1989.
34. Spear R J & Nanut V, J.Energetic Materials, 7, 77, 1989.

FUNDAMENTALS OF X-RAY PHOTOELECTRON SPECTROSCOPY(XPS) AND ITS APPLICATIONS TO EXPLOSIVES AND PROPELLANTS

J. SHARMA AND B.C. BEARD
Naval Surface Warfare Center
White Oak, Silver Spring
MD. 20903-5000
U.S.A.

Abstract: An introduction to x-ray photoelectron spectroscopy (XPS) is given. Its achievements as a powerful technique both for the study of bulk and surface in the field of solids and molecules has been described. Especial emphasis is put on the role of XPS in providing information about energetic materials, which could not be obtained by other methods of analyses.

1. Introduction

X-ray photoelectron spectroscopy(XPS) or electron spectroscopy for chemical analysis(ESCA), as it is often called, has developed into a powerful analytical technique which has found applications in many branches of physics and chemistry. It provides information about the electronic states and electronic structure in solids, liquids, and gases. In the last twenty five years since its birth, XPS has made fundamental contribution to the understanding of a large variety of phenomena and properties of matter. In the field of explosives and propellants also it has made significant contribution, some of which have been given in the accompanying article [1] while more will be discussed in the present one.

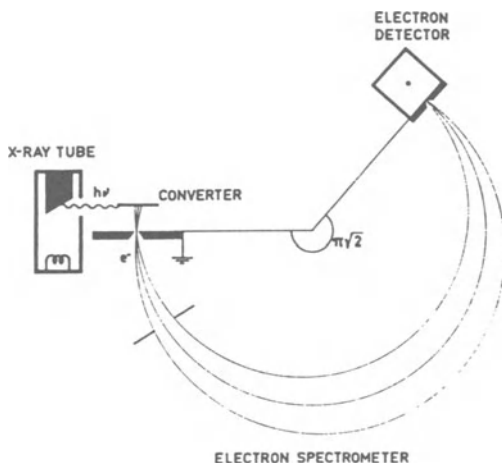


Figure 1. Schematic diagram of an x-ray photoelectron spectrometer, in which the electrons ejected from the sample (converter) by x-rays of known energy are analyzed for their kinetic energy.

Prof. Kai Siegbahn of Uppsala University, Uppsala, Sweden, is the person who gave birth to XPS and finessed it into a powerful technique in a short time, after his observation and discovery of chemical shift in sodium thiosulfate. The publications of his two books [2,3], one mainly on solids and the other on free molecules established XPS as a versatile analytical tool applicable to a large field of science. Every month more than a hundred publications appear in which XPS is used to elucidate the properties of the surface or bulk. Carlson [4] gives a comprehensive account of the XPS technique in his book. On account of the great impact XPS has made to scientific progress, Prof. K. Siegbahn was awarded the Nobel prize for Physics in 1981.

In the XPS experiment, the sample is irradiated with x-rays of precisely known energy and the photoelectrons ejected are analyzed for their kinetic energy with the help of an electrostatic or electromagnetic analyzer (Figure 1). From Einstein's photoelectric equation, if the energy of the incident photon is known, the kinetic energy with which the electron escapes can be used to measure the binding energy of the electronic orbit from which it has been ejected. Thus XPS can be used as a dip stick by which all the occupied electronic states accessible to the given photon energy, can be measured. Since the electrons and their levels are responsible for the material properties of matter, XPS has found applications in a large number of problems of physics and chemistry. It has become a versatile tool to investigate metals, semiconductors, organic materials, polymers and superconductors. The core level spectra provide information about the chemical state of the atom while the valence region spectra give the band structure and molecular orbital information.

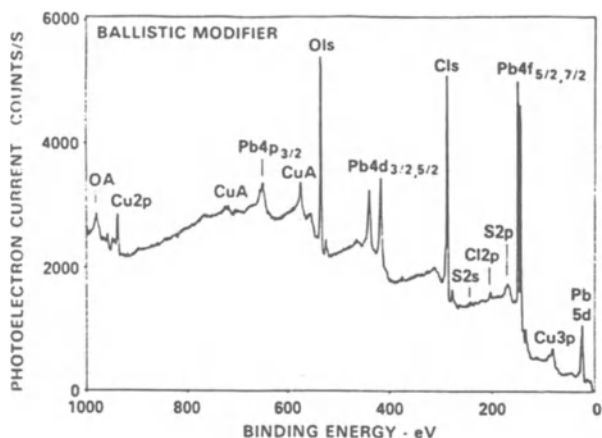


Figure 2. A typical, broad XP spectrum, showing lines from the different electronic levels of the constituent atoms, giving the elemental composition of the sample.

Only those photoelectrons that originate near the surface can escape out of the sample, consequently most information XPS gives is about the surface layer. Soon after the discovery of the technique it was realized

that it is essentially a surface probe and thereafter it became a versatile tool for the study of surfaces. In conjunction with other surface analytical probes such as Auger electron spectroscopy, Auger electron microscopy, XPS has proved to be a valuable tool. It has been widely used to investigate the surfaces of metals, adsorbed layers, semiconductors, polymers, superconductors and other materials. Since the electronic levels such as 1s, 2s, 2p of each atom have specific binding energy, a general survey spectrum readily leads to the elemental analysis of a given sample. The sensitivity of XPS as an analytical tool, is high. It has been demonstrated that it can detect and identify atoms even when they are present in parts per billion. The total list of lines for all the elements is not large either, in fact all the spectra for the elements can be listed in two or three pages. This adds simplicity to the identification problem. Furthermore, the various electronic levels for different atoms are so far apart that the superimposition of levels in the binding energy scale does not pose any serious problem. The relative cross-sections of the different levels have been calculated, and therefore it is quite straight forward to carry out semi-quantitative analysis of a given sample from a survey spectrum (Figure 2). Atomic composition of the material can readily be read out from the height or preferably the area of the peaks.

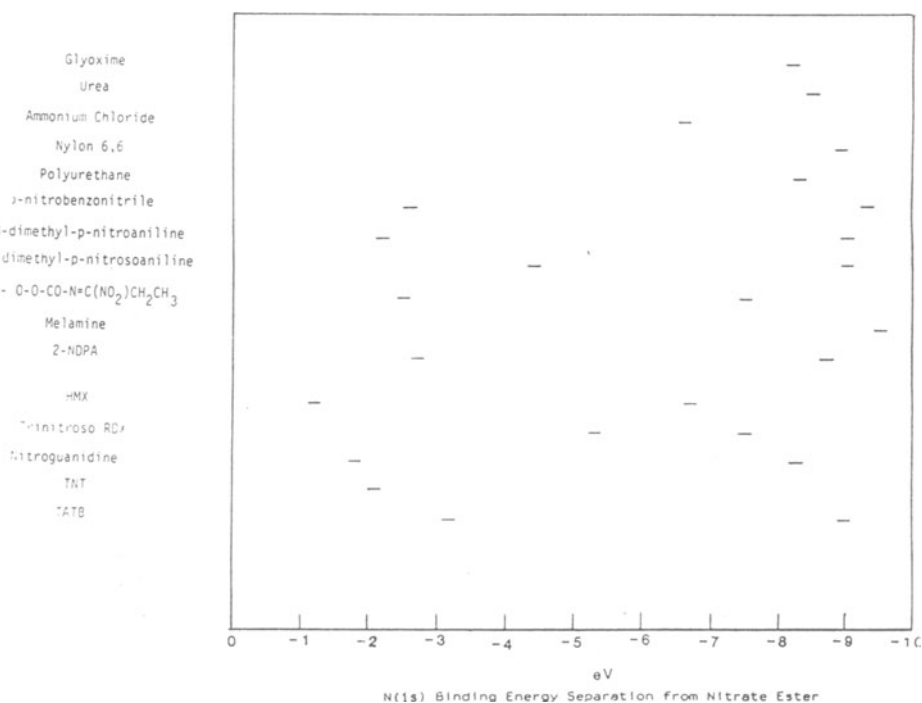


Figure 3. Chemical shift of the nitrogen 1s line in various explosives and organic compounds, measured relative to the position of the nitrate ester line of nitrocellulose, (408.0 eV).

The unique feature of XPS is that it not only gives information about the atoms present in the sample, like NMR it also gives information about the chemical states of the atoms. The core levels show a chemical shift over a range of 3-10 eV. The exact position of an electronic level of an atom depends on its chemical environment. If an atom is oxidized or loses (electronic) charge density, then the line shifts towards higher binding energy, while the opposite happens when the atom is in a reduced state. Picking up an example from explosives, for example, Figure 8 of [1] shows the N1s spectrum of HMX, where the nitro and the amine peaks are separated by 5.6 eV. The nitrogen in the nitro functional group is fairly oxidized, consequently it is located at higher binding energy than the amine nitrogen. If other products were present their position on this scale will be governed by the oxidation state. Nitroso functional groups will show up between the nitro and the amine peaks, while oximes or amides will show up on the lower binding energy side of the amine peak. This chemical shift exhibited by the core levels of the atoms, has been a great strength of XPS technique. It can be used to follow changes taking place in the molecule or solid. Figure 3 shows a chart giving the positions of nitrogen 1s line in various explosives and related molecules. This chart facilitates detection and identification of changes taking place in explosives and propellants due to various treatments. Similarly the XP spectrum of chlorine 2p line is shown in Figure 4, where the various products from the perchlorate family can be identified from simple shift with oxidation state of the chlorine atom. This principle can be applied to the other constituent atoms of the material being investigated, so that a comprehensive picture about the chemical changes taking place in a given sample can be obtained. As for example in some explosives when the nitrogen of the nitro functional group loses oxygen, the nitrogen shifts to the right, while the carbon spectrum shifts towards the left indicating oxidation.

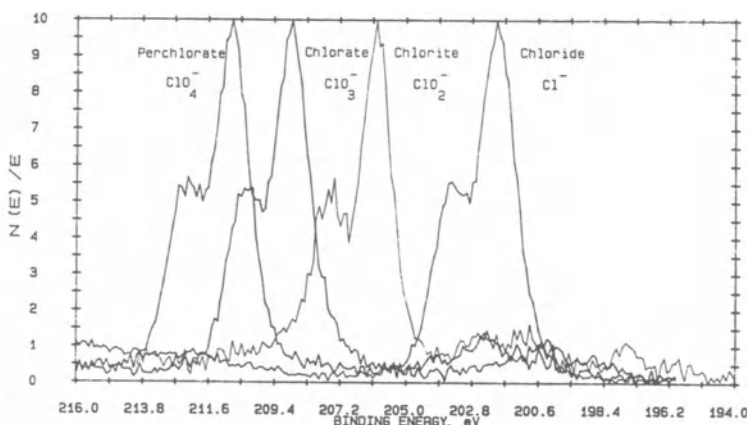


Figure 4. Chlorine 2p spectra, showing chemical shift with oxidation state of chlorine in different oxy-chlorides. (Charging 2 eV)

As mentioned earlier, the ejected electrons have a very short mean free path in a solid and consequently can escape from a depth of 50 Å only in an organic solid. This will correspond to the depth of ten to fifteen molecular layers. However approximately 40 % of the XPS signal arises from the very top molecular layer of the sample so that a major part of the information does deal with the very first few molecular layers. For molecular solids such as explosives, this prejudice in favor of the surface does not however misrepresent the bulk, as is illustrated by the spectrum of HMX, where the two peaks of nitrogen are precisely equal in area as they should be on the basis of the chemical formula of HMX. To the contrary, by virtue of its surface sensitivity, XPS has provided a singular advantage in the study of explosives. When explosives are subjected to shock, impact, friction, shear, or rapid fragmentation, the reaction mostly shows up on the surfaces of the particles. Thus the surface sensitivity, arising from the fact that the signals from the unaffected deeper bulk molecules stay at a minimum, boosts the relative signal of altered top molecules. That explains why XPS has been successful to follow changes taking place in explosives in the sub-ignition regime, which could not be detected by bulk analytical methods. The combination of two factors, chemical shift and the preferred picking up of the information from the surface molecules has given an advantage to XPS technique over bulk analytical techniques such as chromatography or optical spectroscopies for studying subtle changes taking place in explosives. This was brought home in a neat experiment. At NSWC, the very same samples of impacted RDX were analyzed by chromatography and by XPS, in order to determine the sub-ignition reactions caused by impact. Chromatographic analysis [5] showed a maximum of 5.6×10^{-3} % of nitroso products whereas XPS evidenced surface decomposition of as high as 10 % [6]. XPS reveals the solid state reactions manifest on the surface which would include the products which come out by diffusion and get settled on the surface. The products which do not stick will escape in the vacuum, so that they are lost to the XPS technique. Therefore, when an XP spectrum of an affected surface is obtained, it represents condensed phase reaction and shows what is retained by the surface.

A drawback of XPS technique is that it always shows a large signal for extraneous carbon and oxygen, besides that from the sample. Hydrocarbons and oxygen from the atmosphere readily settle on the surface of a given sample. On all samples, unless cleaned by ion-etching, carbon and oxygen from atmospheric contaminations are present. In order to obtain clean spectra it is common practice in the case of stable materials to remove the surface contamination by ion bombardment. However, in the case of explosives and related solids, this cannot be done without disrupting the sample. The existence of adventitious carbon on all samples can be profitably used to provide a reference line for correcting the charging shift of the spectra.

A precaution needed in the study of explosives is to get the spectra without beating the sample to death by x-ray damage of the instrument. Either by using monochromatic source and long time or by being satisfied with noisy spectra, the samples must be protected. Typical decomposition of the sample in an un-monochromatized XPS instrument is approximately a fractional percent for a period of five minutes giving a dose of about two Mrads. The special capability of XPS technique in detecting early reaction is shown in the example of the oxidizer, ammonium perchlorate (AP). Figure 5 shows the spectrum of control AP and that of AP impacted

in a drop test machine. The bunch of peaks on the right side of the parent peak shows that new products of lower oxidation state are being generated. By comparing with Figure 4, it is found that hypochlorite and chlorate are principal products of perchlorate decomposition prior to ignition. An estimate of the relative ratios of these products, can be made. For the first time the presence of hypochlorite as a prominent product is being demonstrated. Prior to the application of XPS the meager reactions and alterations of the sub-ignition regime caused by impact or shock could not be detected.

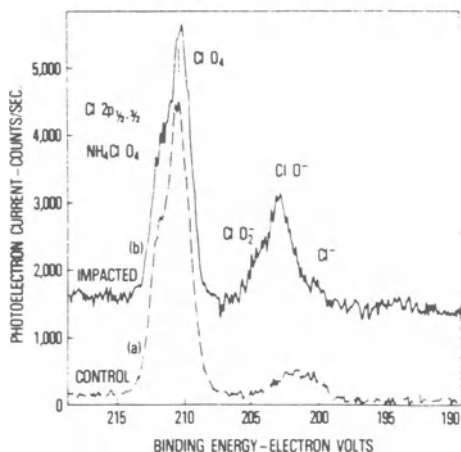


Figure 5. Chlorine 2p spectra of control and impacted ammonium perchlorate showing alteration of the molecule prior to ignition. The prominent product is hypochlorite (ClO^-), which is less stable than AP.

1.1 SPECTRAL RESOLUTION OF XPS:

In the early days of XPS, the full-width half maximum of a line was about 1 eV and the limitation was caused by the inherent width of the exciting line. Mg K emission consisted of alpha one and alpha two doublet, so that the spectra could not be better resolved. For the study of small chemical shift this became a serious difficulty. By 1975, [7] Siegbahn introduced the use of monochromatized x-rays, so that spectral resolution was pulled down to approximately 0.5 eV. Gelius in his new instrument Scienta, brought it down to 0.37 eV [8]. The latest development of instrumentation has been that of C.T.Chen [9] who has improved both the electron analyzer (to a resolving power of one in 10,000 from the normal value of one in 1000) and the x-ray monochromator. By using a synchrotron source and his improved instrument he has reported a resolution of the exciting line to 50 meV and shown a spectrum of the $\text{C}(1s)$ line of graphite to be as narrow as 0.243 eV, despite the inherent solid state broadening. This development will facilitate future work on explosives also, when more information from the chemical shift will be available. It is of interest to note that the XPS line width measurement also provides information on the ultimate line width of a core electronic

level. Previously it was believed that a core level has a energy width of 1 eV so that its life-time for transitions, from Heisenberg's uncertainty principal, would be 10^{-15} sec. The reduction in the observed line width would tend to increase the time taken for photoejection. In view of the recent results, it appears that the photoejection of a core level takes place in approximately 10^{-14} sec. The final state readjustment of molecules after photoemission, observable in many molecules, would take a bit longer time.

1.2 RELATED ELECTRON SPECTROSCOPIES:

Although the subject of electron spectroscopy came into existence with x-ray excited photoelectrons, soon other methods of excitation came into use and became valuable. The following modes are currently used:

1.2.1 Ultra Violet Photoelectron Spectroscopy

Ultra violet photoelectron spectroscopy (UPS), using He I and He II lines at 21 and 41 eV became very popular. This proved to be very useful to explore electronic levels in the valence region and yielded spectra with a resolution of about 20 meV, so that in the case of gas studies, even the vibrational spectra could be studied. UPS is now a standard technique used to understand the molecular orbitals of various gases and solids. It might be worthwhile to mention that the absolute cross-section of photo-electric effect is much larger for the UPS in the valence than that for x-ray excitation. In addition, the cross-sections increase in UPS is specific for the p-type orbitals, providing an avenue for determining orbital mixing in hybridization. By comparing X-ray, He I and He II excitation of the valence region it has been possible to determine the s-p character of the molecular orbitals in many gaseous and solid molecules [10]. Efforts are being made to apply UPS to the study of explosives. One of the recent triumphs of UPS has been the discovery of a superconducting electronic level in high temperature superconductors. Imer et al [11] have shown that a distinct electronic state associated with superconductivity exists at a depth of 23 meV below the conduction level.

1.2.2 Electron Beam Excitation

This mode of excitation by using an electron gun of a few kilovolts energy has led to the development of the whole subject of Auger Electron Spectroscopy and Auger electron microscopy, which has proved highly valuable in the field of surface science. Depth profiling with the help of ion bombardment has given an added capability for analyzing the materials. Elemental maps of the samples can also be obtained.

1.2.3 Synchrotron Source Photoelectron Spectroscopy

As mentioned earlier, the availability of synchrotron source radiation, has added a new dimension to photoemission research. By studying the valence levels with varying energy of the excitation photon, it has become possible to investigate the unoccupied states of the valence region. With the help of a synchrotron source the core and

valence spectra can be better resolved. Even photoelectron microscopy has become a possibility. Some of these new developments have not yet been applied to explosives studies.

1.2.4 Photoelectron Forward Scattering

Another versatile off-shoot from XPS is the study of surface crystallography carried out by using x-ray photoelectron and Auger electron forward scattering. In this, the XPS spectra of crystal surfaces are obtained as function of the polar and azimuthal angles corresponding to the directions connecting the emitting atoms with its neighbors. The photoelectrons are focussed or scattered by the presence of atoms through which they pass. The enhancement of intensities in different directions gives information about surface coverage of the crystal face. As shown in Figure 6, the addition of copper atoms gives enhanced peaks at 0° and 45° from Ni atoms. If the surface was covered with a diatomic molecule

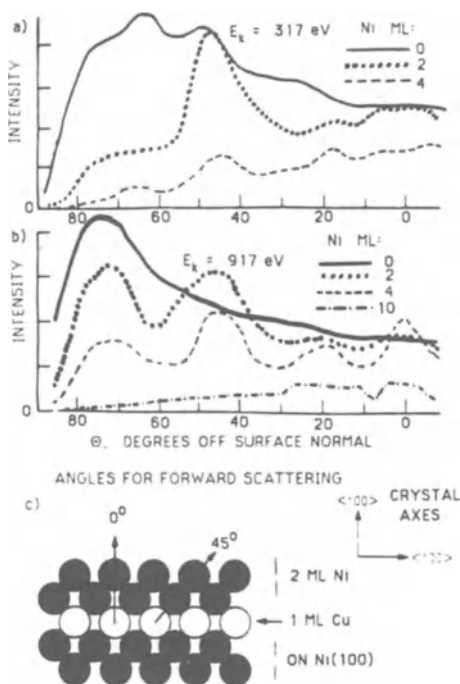


Figure 6. The angular dependence of the intensity of (a) the Cu $2p_{3/2}$ and (b) CVV Auger peaks for 1 ML of epitaxial Cu on Ni(100) and for subsequent deposition of epitaxial Ni over-layers on the 1-ML Cu (c). The variation in intensity demonstrates diffraction effects of the top layers of atoms on the angular dependant photoemission of the underlying layers. This approach presents an opportunity to study orientation of adsorbed molecules and segregation effects.

bonded at preferred vertical or other orientations, then the enhancement of the peak would take place corresponding to those directions. This method has been very profitably used to determine the orientation of small adsorbed molecules, epitaxial growth, segregation and diffusion effects. It has also been used to separate very closely spaced core level XPS lines without the need of high instrumental resolution. As described by Egelhoff [12], who has carried out a considerable amount of work on this technique, this form of XPS can act as an excellent compliment to EXAFS studies.

2. Application of XPS to Explosives and Propellants:

XPS has been very successfully applied to a number of problems in the field of explosives and propellants. A few of them are listed in the following:

2.1 DECOMPOSITION STUDIES OF EXPLOSIVES

Since explosives yield energy on decomposition, in order to understand the processes of molecular disruptions a very large number of studies on slow thermal decomposition has been carried out by many workers [13-15]. Such studies with XPS have been exceedingly profitable. XPS shows the solid products left on the sample at different stages of decomposition. By heating the samples in the XPS instrument to different temperatures and scanning XP spectra at different stages it is easy to follow the changes. Alternatively, samples recovered from high temperature treatment can be brought to room temperature and studied. It has been found that in TATB [16] the principal products are furoxan and furazan derivatives. In the case of TNT [17] the products are benzaldoxime, anthranil, and nitriles. In HMX and RDX nitroso derivatives and triazine are produced, along with nitrite ester. The latter is observed at low temperature, decomposing near room temperature. As described in the accompanying paper [1], some of the products are more sensitive than the original explosive, so that partial decomposition tends to sensitize the explosive. In general, decomposition is first identified by the loss of intensity of the nitro peak in the XPS spectra. When the nitro functional groups react, water and CO_2 are principle products, with nitrogen released as N_2 or incorporated into the solid residue in a reduced chemical state. Ultra violet, x-ray or electron beam irradiations cause decomposition reactions indistinguishable from those induced by heat. Careful analysis of the chemical changes that occur during extended irradiation in the XP spectrometer provide early reaction states that may not be isolated by thermal preparations.

2.2 FORENSIC INVESTIGATIONS

Since XPS picks up information from the few molecular layers of the material on the top, very little sample is needed to get the spectrum. Typically a milligram of sample is used, spread over an area of approximately one square centimeter. But spectra with a few micrograms of samples have been successfully obtained, by spreading the sample thinly over a substrate. This gives a great advantage for forensic investigations. In a typical explosion about one percent of the explosive

escapes decomposition, therefore XPS can be used to determine and identify the explosive from the debris. XPS not only identifies the atoms present in the sample, but also gives information about its chemical state. In one investigation, the nitrate ester of nitroglycerine was identified despite the presence of ammonium sulfate containing fertilizer, blown up in the background. Mass spectrometry or optical spectroscopy would detect the nitrogen but would not distinguish between the nitrogen of ammonium and that of nitroglycerine. In the XPS the ammonium nitrogen and the nitrate ester nitrogen are easily distinguishable.

2.3 MALFUNCTION INVESTIGATIONS OF MUNITIONS

Similar to the case of forensic work, XPS has been also used in malfunction investigations of weapons, pyrotechnic torches and rockets. The debris left following a violent failure have been used to identify the source of malfunction.

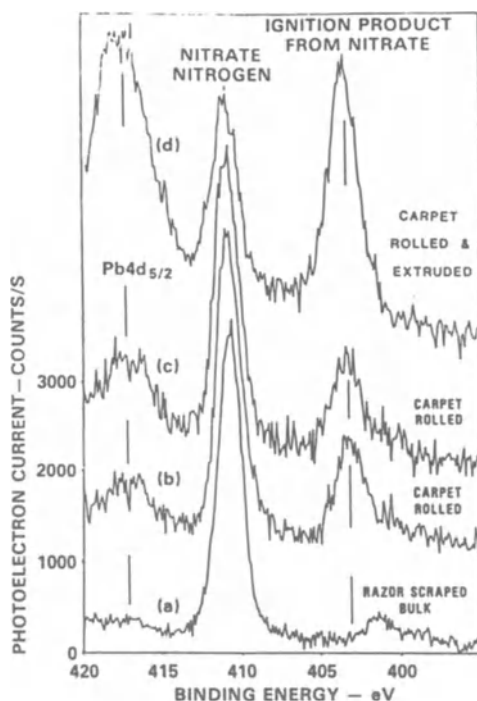


Figure 7. The XP spectra of control, carpet rolled and extruded double base rocket propellant in the spectral region of nitrogen and lead. Surface degradation of nitrate ester into oxime-like products and the emergence of lead to surface is observed.

2.4 MANUFACTURE AND PROCESSING CONTROL

In the case of double base rocket propellants, difficulties experienced during carpet rolling of the propellant and during extrusion have been investigated by XPS. Figure 7 shows the N1s spectrum of control, carpet rolled and harshly extruded propellant. The spectrum of control shows strong peak due to the nitrate ester while that of lead is hardly perceivable, as it should be on the basis of its low concentration. Carpet rolling is found to cause decomposition of the nitrate ester into oxime like products while concentrating lead on the surface. In cases where the extrusion required high pressure, samples demonstrate localized burning, a considerable loss of nitrate ester, and the build up of high concentrations of lead on the surface.

2.5 CATALYSIS OF DOUBLE-BASE ROCKET PROPELLANT

Lead is a well known catalyst for the increase and 'plateauing' of the combustion pressure in double-base propellants. By combining XPS and x-ray excited Auger electron spectroscopy it has been possible to show that it is the presence of lead in metallic phase on the surface of the propellant which produces the super burning rate. Lead plays two roles. Lead provides nuclei for the production of soot, while promoting the oxidation of carbon. The catalytic effects of lead are lost due to evaporation of lead from the surface of the propellant. (Figure 8) It has been found that the reaction zone in lead catalyzed propellant is approximately 30 microns, while that in unleaded propellant it is only 8 microns. XPS gives clear evidence of the fact that the reactions in the condensed phase control the burning rate. This fact so far has not been recognized by rocket designers.

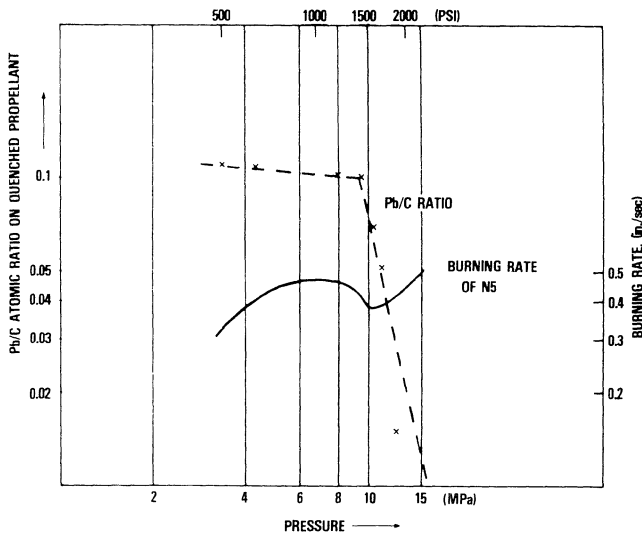


Figure 8. Concentration of lead on the surface of double-base rocket propellant extinguished from burning at different pressures. The burning rate shows a drop with the sudden decrease of the lead catalyst.

2.6 STUDY OF HOT SPOTS AND SUB-IGNITION REACTIONS

As described in the associated paper, XPS has been very useful in determining the chemical nature of quenched hot spots and giving a chemical basis to the sensitization of energetic materials. The historical difficulty in determining the formation of partial reaction products was that explosives undergo much less than 1% reaction prior to complete initiation. With the surface specificity of XPS it has revealed that the majority of these reactions occur at the surface of the materials, giving great advantage to this experimental approach [16]. Bulk techniques therefore were always at a disadvantage for detecting the reaction products. For the first time, reaction products forming at quenched hot spots resulting from sub-ignition damage to the explosive have been identified.

2.7 CARBON AUGER LINE-SHAPE STUDY OF NITROAROMATIC EXPLOSIVES

Rogers et al [18] have carried out Carbon (KVV) Auger lineshape studies in a series of amino-trinitrobenzene explosives and TNT. They have been able to correlate the effects of nitro and amino groups with pi level energy shifts. On the basis of charge withdrawing effects of nitro groups and charge donating effect of the amino group, they have been able to explain the variation of shock sensitivity of these explosives.

2.8 MOLECULAR ORBITAL STUDIES OF EXPLOSIVES

This is an on-going effort. By using XPS, the molecular orbitals of explosives in the valence region have been mapped. Figure 9 shows the valence region spectra for RDX. The observed features originate from the atomic 2s and 2p orbitals of C, N and O which form the molecular orbitals of the compound. The molecular orbitals have been measured for common explosives like HMX, RDX, TNT, TATB, DATB and TNB. The spectra are different for each case. These spectra have been to some extent explained and interpreted with the help of MO calculations. The principal difficulty in this approach lies in the fact that there are 30 to 50 orbitals crowded in the range of 0-40 eV. With resolution limited by the inherent x-ray linewidth, the discrete orbital peaks appear as broad composite peaks. This makes the identification and interpretation difficult. By using monochromatized x-rays, part of the difficulty is being overcome. Also this measurement is being combined with ultraviolet photoelectron spectroscopy (UPS), which has much higher resolving power (20 meV). As previously mentioned UPS favors p-type orbitals whereas XPS favors s-type, making the determination of the s-p hybridization a possibility. The motive behind this work is to understand explosives in terms of their electronic levels.

It is hoped that the energy of the explosive will be identified in terms of electronic levels. Each molecule stores about 18 eV/mole of energy, and so far electronic transitions that lead to this energy release between the reactants and products have not been identified. The MO picture will also aid in the explanation of explosives sensitivity. Description of the behavior of energetic materials on such a fundamental basis will put them on par with other materials like semiconductors that can be understood in terms of the electronic levels.

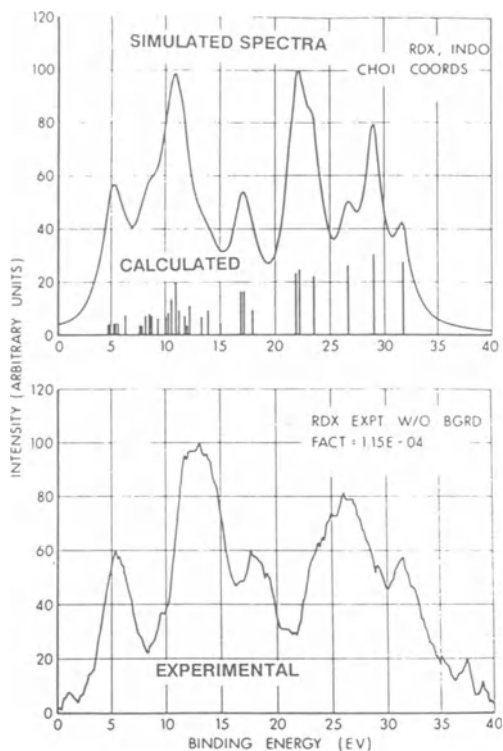


Figure 9. A comparison of INDO based simulated and experimental spectra of RDX in the valence region showing how the 33 molecular orbitals arising from the 2s and 2p atomic orbitals of C,N,and O (including 1s of H) bunch into five peaks.

2.9 SHAKE-UP SPECTRA OF EXPLOSIVES

When the core spectra of TATB, DATB and picramide are mapped, in all cases the nitrogen and the oxygen of the nitro group show multiple structure [19]. The nitro-nitrogen in TATB shows a satellite of one third intensity at 2.8 eV away on the high binding energy side, as shown in Figure 4a of [1]. Similarly the oxygen line shows a peak at 3.8 eV separated from the regular oxygen peak. These are known as Shake-up satellites, and considerable work has been done on such satellites both in the explosives as well as non-explosive solids [20-21]. The satellite separation decreases as one goes from TATB to TNB, becoming zero for TNB, which does not show any satellite structure. If a plot is made of the log of the 50 % drop height of these explosives against their satellite separation, a linear relation is evident. There seems to be a general relation of this kind for many compounds shown in Figure 10, although not

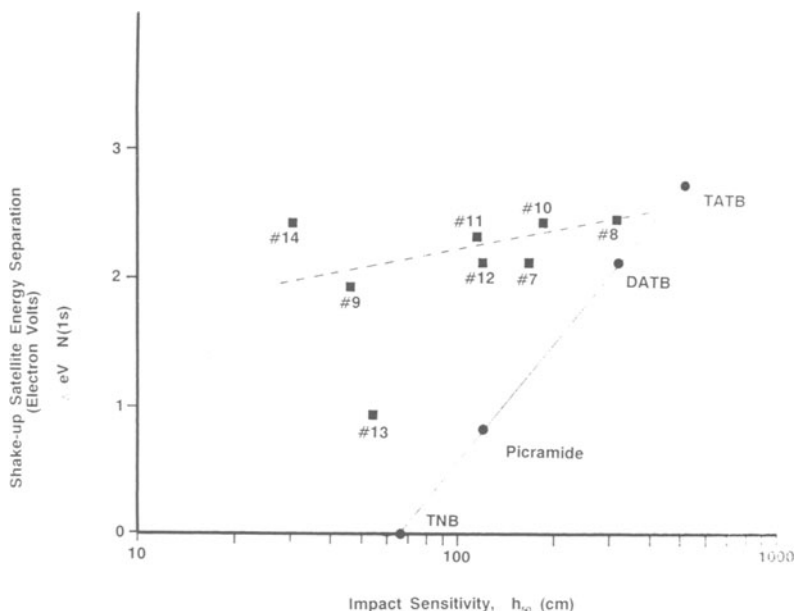


Figure 10. The shake-up satellite separation plotted against the log of the 50% drop height for TATB, DATB, Picramide and TNB show a perfectly linear relationship. TATB analog compounds having widely varying structure show a different slope.

The numbered compounds* in Fig. 10 are:

- #7 - N-Formyltrinitro-1,3,5-benzenetriamine
- #8 - Ureidotrinitro-1,3-benzenediamine
- #9 - 5-(2-Nitroguanidino)-trinitro-1,3 benzenediamine
- #10 - 1,2-Bis-(3,5-diaminotrinitroanilino)-ethane
- #11 - 3,5-Bis-(3,5-diaminotrinitroanilino)-1,2,4-triazole
- #12 - 3-(3,5-Diaminotrinitroanilino)-1,2,4-triazole
- #13 - 4-(3,5-Diaminotrinitroanilino)-1,2,4-triazole
- #14 - 5-(3,5-Diaminotrinitroanilino)-tetrazole

* Synthesis of these compounds described in NSWC-TR-83-22
M. Chaykovsky, and H.G. Adolph, March 1983

so dramatic as for the four compounds TATB to TNB, which happen to be structurally similar molecules. This result is highly significant, because for the first time the sensitivity of an explosive is being related to a measured electron transition of the molecule.

The shake-up phenomenon observed in XPS is by itself interesting. Normally the atoms of each functional group show only one line. This is explained on the basis of the sudden approximation described in Koopman's theorem whereby the photoejected electron escapes the vicinity of the

molecule before electronic changes occur due to the loss of the electron. However in the case where shake-up spectra appear the story is changed. In this class of molecules discussed here the HOMO resides with the electron donor portion of the molecule (amine) whereas the LUMO is with the acceptor, (nitro group). When photoemission occurs from the acceptor, electron density from the donor becomes available to compensate for the additional charge; this results in a decrease in the HOMO/LUMO separation, thereby increasing the probability of electron promotion from the HOMO to the LUMO. The energy for this promotion is stolen from the escaping photoelectron leading to a peak (the intensity of which is dependant upon the probability of shake-up promotion) shifted to lower kinetic energy, (higher binding energy).

It appears likely that the charge transfer leading to the shake-up process provide a mechanism for increased stability of ionized states. The amine groups that donate electron density into the aromatic system provide a buffer to compensate for the core holes that arise following photoemission. In molecules without donor groups or a means of rapid communication of electron density (conjugation) the ionized state could readily lead to the breaking of bonds. Experiments into the stability of energetic materials during x-ray irradiation support this claim [22]. The ability of certain energetic materials to compensate for ionization may also be important in their thermal stability.

2.10 NITRATION STUDIES OF CELLULOSE

Clark et al [23] at the University of Durham, U.K. have applied XPS to the study of cellulose nitrate and the step by step nitration of cellulose. They have shown which hydroxyl group is most easily accessible for nitration. They have observed sulfate ester from the nitration process at the surface of the nitro cellulose, this is suspected as an initiator of the degradation of N.C.

2.11 COMPATIBILITY PROBLEMS OF EXPLOSIVES AND PROPELLANTS

XPS is a very appropriate tool to study compatibility problems of explosives and propellants with respect to the materials with which they are in contact during formulation and storage. Surface reactions can be determined in very early stages. Degradation of the reactive components can easily be detected. XPS has been used to locate bond failure problems between different layers due to the extraneous presence of silicone grease and lubricants in rockets and missiles.

The above outline of XPS shows that the technique is very valuable to the study of energetic materials. Prior to the application of XPS the nature of hot spots was a mystery, now it is apparent that the hot spots containing more sensitive material in them can are potential sources of danger. In view of the forthcoming improvements in XPS, its value for the study of explosives and propellants will be further increased.

References:

1. Sharma, J., and Beard, B.C., (1990) "XPS Study of Hot Spots and Sensitization Centers in Energetic Materials". This Volume
2. Siegbahn, K., Nordling, C., Fahlman, A., Nordberg, R., Hamrin, K., Hedman, J., Johansson, G., Bergmark, T., Karlsson, S.E., Lindgren, I. and Lindberg, B., (1967) 'ESCA-Atomic, Molecular and Solid State Structure Studied by Means of Electron Spectroscopy', Nova Acta Regiae Soc. Sci., Upsaliensis, Ser. IV, Vol. 20.
3. Siegbahn, K., Nordling, C., Johansson, G., Hedman, J., Heden, P.F., Hamrin, K., Gelius, U., Bergmark, T., Werme, L.O., Manne, R. and Baer, Y. (1969) 'ESCA Applied to Free Molecules', North Holland Publishing Co. Amsterdam-London.
4. Carlson, T.A. (1975) Photoelectron and Auger Spectroscopy (Plenum, New York) 1975.
5. Hoffsommer, J.C. and Glover, D.J. and Elban, W.L. (1985) 'Quantitative Evidence of Nitroso Compound Formation in Drop-Weight Impacted RDX Crystals.' J. Energetic Materials, 3, (2) 149-167.
6. Sharma, J., Hoffsommer, J.C., Glover, D.J. Forbes, J.W., Liddiard, T.P., Elban, W.I. and Santiago, F. (1985) 'Sub-ignition Reactions at Molecular Levels in Explosives Subjected to Impact and Underwater Shock' Proc. Eighth (International) Detonation Symposium, Albuquerque, NSWC MP 86-164, 725-733.
7. Siegbahn, K. (1975) 'Electron Spectroscopy-An outlook' Uppsala University Report, UUIP-880, 7-10.
8. Gelius, U., Asplund, L., Basilier, E., Hedman, S., Helenlund, K and Siegbahn, K. (1984) 'A High Resolution Multipurpose ESCA Instrument with X-ray Monochromator' Nuclear Instruments and methods in Physics Research B1, 85-117.
9. Chen, C.T. (1987) 'Concept and Design Procedure for Cylindrical Element Monochromators For Synchrotron Radiation,' Nuclear Instruments and Methods in Physics Research A256, 595-604
10. Huang, J.J., Ellison, F.O., and Rabalais, J.W., (1974) J. Electron Spect. Rel. Phen. 3 339-344
11. Imer, J.M., Patthey, F., Dardel, B., Schneider, W.D., and Baer, Y., (1989) Phys. Rev. Lett. 62 336
12. Egelhoff, W.F., Jr. (1987), "Role of Multiple Scattering in X-ray Photoelectron and Auger Electron Diffraction in Crystals", Phys. Rev. Lett. 59(5), 559
13. Rogers, R.N. (1969), Anal. Chemistry 39, 730.

14. Dacons, R.N., Adolph, H.G. and Kamlet, M.J.(1970) J. Physical Chem. 74 730.
15. Shackelford, S.A., Beckman, J.W. and Wilkes, J.S. (1977) J. Org. Chemistry 42 4201.
16. Sharma, J., Hoffsommer, J.C., Glover, D.J., Coffey, C.S., Forbes, J.W., Liddiard, T.P., Elban, W.L., Santiago, F. (1987) Proceedings, Symposium(International) on Detonation, 8th, Naval Surface Weapons Center, Silver Spring, MD. U.S. Government Printing Office: Washington, DC, MP86-194, p 725.
17. Sharma, J., Forbes, J.W., Coffey, C.S. Liddiard, T.P.(1988) Shock Waves in Condensed Matter, S.C. Schmidt and N.C. Holmes(editors), Elsevier Science Publishers B.V.
18. Rogers, J.W., Peebles, H.C., Rye, R.R., Houston, J.E. and Binkley, J.S. (1984) 'A Carbon Auger Line Shape Study of Nitroaromatic Explosives,' J. Chem. Phys. 80(9) 4513-4520
19. Sharma, J., Garrett, W.L., Owens, F.J. and Vogel, V.L., 'XPS Study of Electronic Structure and Ultraviolet and Isothermal Decomposition of 1,3,5-triamino-2,4,6-trinitrobenzene,' J. Phys. Chem. 86, 1657-1661
20. Wang, J., Wu, W., Zeng, M. and Lang, H., (1988) 'XPS-Investigation of Intramolecular Charge Transfer in Polynitro-aminobenzenes' J. Electron Spectrosc. Relat. Phenom. 46, 363-372.
21. Nakagaki, R. Frost, D.C. and McDowell, C.A. (1980) 'The Intermolecular Charge-Transfer Interaction in X-ray Photoelectron Spectroscopy: The Charge Transfer Satellites Observed in p-Nitroaniline and Related Compounds', J. Electron Spectroscopy and Related Phenomena, 19, 355-370
22. Sharma, J., and Beard, B.C., (1989) J. Energetic Materials 7
23. Clark, D.T., Fowler, A.H.K., Stephenson, P.J. (1983) 'Applications of Modern Analytical Techniques to the Investigations of Cellulose Nitrate', J. of Macromolecular Science-Reviews in Macromolecular Chemistry and Physics, C23 (2), 217-286.

XPS STUDY OF HOT SPOTS AND SENSITIZATION CENTERS IN ENERGETIC MATERIALS

J. SHARMA AND B. C. BEARD
Naval Surface Warfare Center
White Oak, Silver Spring
MD. 20903-5000
U.S.A.

ABSTRACT. The physical and chemical nature of hot spots and sensitization centers caused by shock, impact or rapid shear in explosives have been investigated by using an SEM and XPS analysis. Micron size reaction sites in the crystallites were identified as hot spot remnants. Surrounding these reaction sites, deposits of new products containing altered molecules of the explosive were observed. Some products are more sensitive than the original explosive. This lends chemical basis to sensitization. Other products were from reactions involving the formation of water molecules, which would be associated with release of energy. Thus two major steps, one causing sensitization, the other providing energy for self-sustained reaction have been identified in the ignition process. This pattern of reaction is not confined to early stage only, it continues even when the parent explosive is appreciably consumed. The reaction products agree with the prominent products from slow thermal decomposition reported by earlier workers.

1. Introduction

When explosives are roughly handled, they get sensitized.[1] It is believed that dormant 'hot spots' cause sensitization. 'Hot spots' are believed to be tiny sites, where intense reaction started but was quenched leaving behind effected regions which can facilitate ignition at a much lower level of stimulus than before. The presence of hot spots has provided a ready explanation of many unanticipated and accidental ignitions. According to Bowden and Yoffe [2] the size of viable 'hot spots' is in the range of 10^{-3} - 10^{-4} cm in diameter. However, on account of their small size and sparseness hot spots have escaped physical detection. Very little is known about the physical and chemical nature of sensitization centers, created and left by the 'hot spots'. Proper detection and identification of sensitization centers (S-centers) in terms of their chemical or physical nature can contribute to making explosives more safe. It is important to know whether the chemical nature or morphological structure determines the sensitizing action.

Questions about hot spots are also related to the fundamental process of ignition of explosives. It is not known how an explosive with an infinite shelf-life starts on its path of fast and violent reaction. The first endothermic reactions which start the process of ignition and

the subsequent spontaneous exothermic steps are not exactly known. The investigation of S-centers can throw new light on the early steps of the ignition process.

In the present work, in order to understand the events of the sub-ignition regime, explosives have been imparted with various stimuli, such as underwater shock, impact, high rate shear, radiation damage or heat almost to the level of ignition. If the sample survived, it was recovered and investigated for minute changes. For the study of morphological changes a scanning electron microscope (SEM) has been used while the chemical changes have been detected and identified by x-ray photoelectron spectroscopy (XPS), chemical ionization mass spectrometry and chromatography. XPS is a surface analytical technique, and since most of the effects in explosives have been found to take place on the surfaces, this technique has proved to be singularly helpful. Chemical ionization (C.I.) mass spectrometry, identifies the molecular mass without the confusion arising from fragmentation of molecules as experienced with ionization.

In TATB, subjected to underwater shock or impact, SEM has revealed remnants of hot spots as holes with ragged edges in the smooth layered structures of TATB. The size of the holes ranges from 0.1 to 5 microns and the holes look like holes as in Swiss Cheese. Surrounding these holes, the area was found to be covered with reaction debris. The debris has been determined by XPS and C.I. mass spectrometry to contain reaction products of TATB, some of which are more sensitive than TATB. Thus micron size defects surrounded by deposition of more sensitive material, form the basis of sensitization centers. Reaction products in the form of furoxan and furazan derivatives of TATB were identified. The furoxan derivatives are known to be more sensitive than TATB. Furazan is produced by the loss of a water molecule from TATB. The formation of each furazan functional group would be associated with the exothermic release of 59 Kcal/mole of energy. These products signify two major steps essential for the propagation of reaction. The furoxan product makes the explosive more sensitive and facilitates continued reaction, the furazan product provides exothermic energy to sustain reaction. Similar trends have been observed in TNT and other explosives, although the reaction products are different. For the first time, localized reaction sites have been observed, which are recognized as hot spot remnants and sensitization centers.

1.1 BACKGROUND ON HOT SPOTS

The concept of hot spots was introduced to explain the start and build-up of ignition of explosives from mechanical effects. The work of Bowden and Yoffe,[2] and those of many others in the field has led to the belief that ignition from mechanical stimuli such as impact, friction, shock is of thermal origin. Calculations on models of hot spots have been given by Merzhanov [3], Freidman [4] and Mader [5]. Heat is believed to become concentrated in highly localized areas probably related to incipient defects, impurities, or structural inhomogeneities in the

crystallites. Thermal decomposition takes place at such hot spots, and because of the exothermic nature of the reactions, the hot spot can build into an explosion. In this development, generation of catalytic products or free radicals would accelerate the process. Some of the possible modes of hot spot generation as listed by Roth [6] are:

1. Adiabatic heating of compressed gas inclusions
2. Frictional hot spots
3. Inter-crystalline friction of the explosive
4. High shear, causing dislocations and decompositions
5. Viscous heating
6. Mutual reinforcement of relatively weak shocks
7. Spallation of particles
8. Micro-Munro jets.

The size of the hot spots, as mentioned earlier, has been estimated [2] to be in the range of a micron and the duration has been estimated to be of the order of 10^{-4} - 10^{-6} second. The minimum quantity of heat required to start an ignition center is believed 10^{-8} - 10^{-10} cal. Probably a certain minimum number of molecules of the explosive are needed to be decomposed before the reaction can build-up. This is very well brought out by the experiments of Cerny and Kaufman [7] who studied the effects of high energy pion tracks in explosives. It was argued that the pions can generate temperatures in the range of 10^6 K in their tracks due to intense ionization. However, no discernable effects were seen in terms of ignition or sensitization. The energy available from one molecule of an explosive is 4-8 times larger than the threshold energy required to break-up another molecule, consequently on principle a chain reaction can be started even at the disruption of one molecule. In the same sense one could argue that cosmic ray particles should ignite an explosive, but that is not known to have occurred. This leads to the conclusion that the size of hot spots that can lead to ignition has limits on either side. If the hot spots are too small, spatial dissipation of energy takes place. On the other hand if it is too large the rise of temperature is not enough. In the background of these speculations, any experimental information on the size and nature of hot spots should be valuable. With the application of XPS to the problem, for the first time, it has become possible to detect and identify chemical changes in the sub-ignited explosives. XPS can detect molecular changes and their modifications even when very few percentile of molecules are effected, as long as the reactions are preferably on the surfaces of the crystallites. Another technique which has great promise is laser ionization mass analyzer (LIMA), as demonstrated by Tang et al [8] for reaction sites produced by a laser beam.

2. Materials and Methods

XPS has been the work-horse in the present investigation. The probing depth of XPS is approximately 50 Å and 40 % of the signal arises from the top molecular layer. Since in explosives action seems to start on the surfaces, XPS provided an advantage of at least three orders of magnitude over bulk analytical techniques. The XPS studies of decomposition have been carried out by with a Kratos ES 3000 instrument as described by Sharma et al [9,10,11]. SEM investigation was carried out by using an AMR Model 1000A scanning electron microscope in which the current was kept at or less than 10^{-11} A in order to protect the sample from beam damage. For SEM studies, it was necessary to coat the samples with gold. A Finnigan 4000 GC/MS EI-CI mass spectrometer was used with methane plasma in the chemical ionization mode.

For studying the effects of underwater shock, the samples in the shape of pressed pellets of 5 mm diameter and one mm thick, were put in teflon plugs and placed at suitable distances from the donor charge in an aquarium test, as described by Liddiard [12]. Shock waves ranging over 4-18 kbars of pressure and a few microseconds duration could be imparted to the samples.

The effects of impact were studied by putting the pellets of explosives between sheets of heat-sensitive view-graph (3M) films, and impacting them in a drop weight impact machine as described earlier by Coffey and Jacobs [13]. A 10 kg weight was dropped from a predetermined height, whose effective value could be made as high as 3 meters, with the help of rubber bands. The impact pressure pulse was sinusoidal with a duration of 300-350 microseconds. The view-graph film gives a pattern of the impact showing regions of high temperatures. The central area is the region of maximum pressure and that of fracture and fragmentation of the particles. The rate of change of pressure is approximately 10^8 bars/s. However this is not the area where maximum reaction was observed. Pronounced reaction was shown in the outer area of the radial pattern created by the flow of material between the heat-sensitive films. In the latter area, maximum shear forces come into play, accompanied by pronounced decomposition and occasional development of ignition sites. In order to augment the effects of impact and cause larger decomposition by friction sometimes sand was added to the explosives powders.

The effects of high rate shear were studied by using an activator in which a piston of polyethylene was driven at 60 m/s. through a layer of an explosive at a pressure of 10 kbars, as described by Boyle.[14]. Decomposition in high shear experiments was found to be confined to a thin layer of the explosive on the surface of the plug that was pushed out.

For comparing the present results of fast reaction as in impact or shock, with those of slow thermal decomposition, thermally decomposed samples were prepared either by heating the samples in a furnace or by using proton beam heating.

Research grade TATB obtained from American Cyanamide was mostly used in underwater experiments, while micronized Pantex TATB, obtained from

Los Alamos National Laboratory, was used for impact experiments. The samples yielded smooth DTA and pyrolysis curves indicating no peaks or changes below their normal temperatures of decomposition. On washing the control TATB samples with acetone, no ragged holes or micro-cavities appeared under the SEM due to impurity extraction. The samples of TNT, HMX, RDX and other explosives used, were also the best samples available from various laboratories.

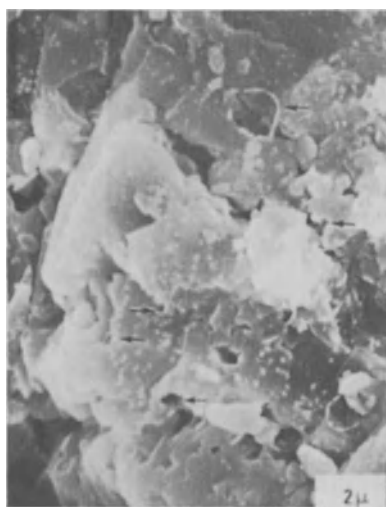
3. Results

3.1 TATB

SEM micrographs of control and underwater shocked TATB are shown in Figure 1. As pointed out by arrows in Figure 1b TATB has disappeared at many points leaving gaping holes similar to the holes seen in Swiss cheese. These holes have ragged edges and are 0.1-0.5 microns in size for the shocked samples, while they are somewhat larger (1-5 microns) for the



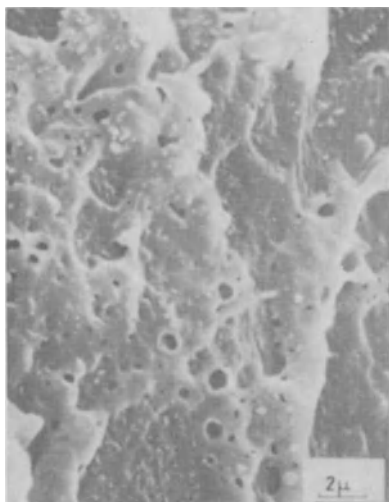
(a)



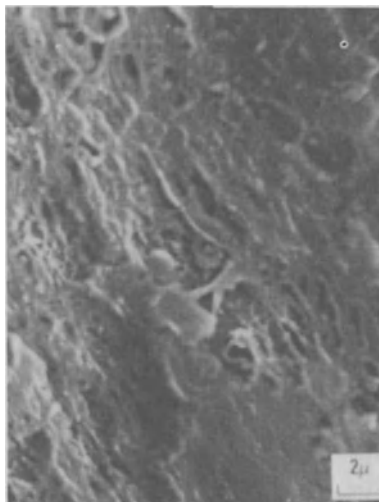
(b)

Figure 1. (a) SEM micrograph of (a) control TATB, showing smooth layered surfaces and smooth edges of the crystallites. The few holes with rounded appearance are incipient defects from crystal growth. (b) SEM micrograph of under-water shocked TATB, showing hot spots as holes with ragged edges located near the borders of the crystallites. The fine bead like deposits near the ragged holes are from reaction products. Figure from Ref. #9

impacted samples (Figure 2a). These holes are recognized as reactive sites. It is obvious that some material is disappearing at these reactive sites. Surrounding these holes, a deposit of material, in the form of beads is observable near the edges of the crystallites. In physical appearance these beads do not show the characteristic layered structure



(a)



(b)

Figure 2. SEM micrograph of (a) TATB impacted in a drop test machine, showing hot spots larger than those of underwater shock, (b) of impacted TNT giving string-like appearance of the effected TNT. Figures from Ref. #9 and #11

of TATB. The magnified image rather shows similarity with the sublime deposit from a sample of pyrolyzed TATB. (Figure 3.) The beady deposit disappeared on washing the samples with acetone or by heating to 220°C. indicating that it was not just TATB powder blown around by the impact. It might be noted that in the shocked TATB most of the deposit takes place near the edges of the crystallites and in fact seems to follow the edge. However, in the case of impacted samples it is more on the surface at random positions.

The chemical nature of the hot spots has been revealed by XPS. Spectra of control and impacted TATB are shown in Figure 4. A comparison of the two spectra shows that partial decomposition has taken place. The nitro peak with its shake-up satellite has dropped by about 50 %. Also the apparent separation between the nitro and amine peaks has decreased due to the development of a new peak close to the amine on its higher binding energy side and a small broadening of the nitro peak towards the lower binding energy side. These spectra were compared with those of chemically synthesized furoxan derivative of TATB, as shown in Figure 5 and it was found that the changes in the spectra of impacted sample could

be explained by the fact that about 6 % of furoxan and furazan each are produced. Since the drop in the nitro functional group was approximately 50 % (Figure 4), it has to be concluded that part of the explosive is disappearing, probably in gaseous form so that all of it does not show up in the new products. If the impacted TATB was washed with acetone, the acetone became slightly yellow in color, which when filtered and dried, left a residue yielding a spectrum similar to that of furoxan and furazan products. Thus, in the case of TATB it was possible to extract the reaction products for analysis, since TATB is insoluble in acetone,

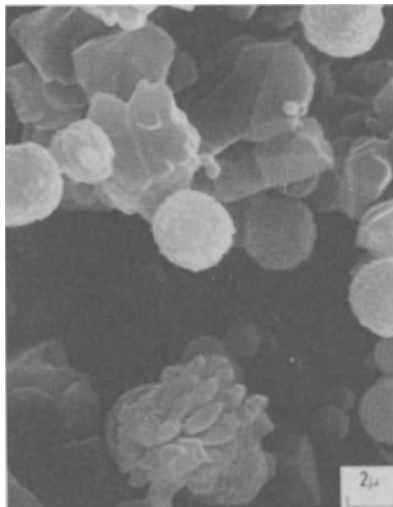


Figure 3. SEM micrograph of pyrolyzed TATB showing products of thermal decomposition having appearance like the deposits from shocked TATB.

whereas furoxan and furazan derivatives of TATB are soluble. When samples of diaminotrinitrobenzene (DATB), and monoaminotrinitrobenzene (picramide) were impacted, they showed spectra like those of impacted TATB. It appears that similar reaction is taking place, the nitro peaks drop and the furoxan and furazan derivatives are produced. This is expected because they are similar compounds. The trends of decomposition were the same, even when the samples of TATB, DATB and picramide were severely beaten up to the extent that the nitro peaks became smaller than the peaks due to the product molecules. In summarizing the results on TATB family of compounds, it can be said that furoxans and furazans (mono, di or tri derivatives), as shown below, are principal products of decomposition from impact or shock and represent the products from the first endothermic and exothermic reactions. The amount of decomposition observed in shocked TATB was less than that of impacted samples by a factor of five or so.

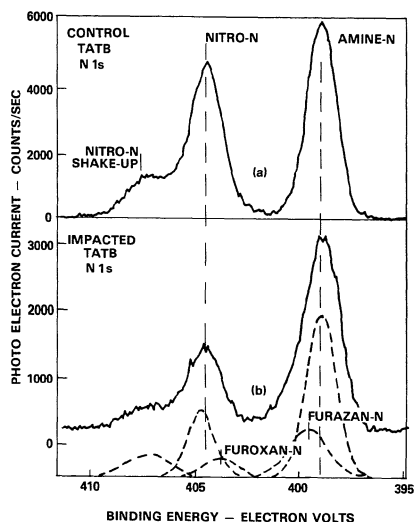


Figure 4. XPS spectra of (a) control TATB, (b) of impacted TATB, showing decrease of nitro peak and development of a small peak approximately 0.8 eV on the right side of the nitro peak due to furoxan formation, and another peak at 0.6 eV on the left side of the amine peak due to furazan formation. Figure from Ref. #9

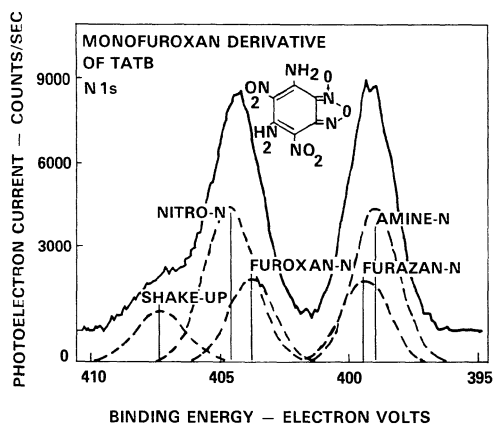
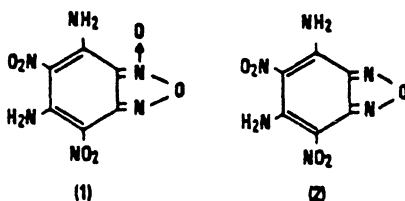


Figure 5. XPS spectrum of chemically prepared monofuroxan derivative of TATB indicating positions of the furoxan and furazan components, with respect to the amine and nitro peaks as observed in Figure 4. Figure from Ref. #9



MONOFUROXAN(1) AND MONOFURAZAN(2) DERIVATIVES OF TATB

3.2 TNT

Similar results on impacted TNT are available. The SEM micrographs of impacted TNT from area of high shear shows string like patterns (Figure 2b) associated with the generation of morphological defects. Probably melting and resolidification gives rise to the strings. The XPS spectra of impacted TNT, shown in Figure 6, gives evidence that new products are being generated. Unaffected TNT shows only one peak from nitro-nitrogen. The additional grouping of peaks, 5-7 eV away on the lower binding energy side in the impacted sample, belong to the new products and shows that reduced states of nitrogen compared to the nitro functional group are being produced. In order to calibrate the shift of nitrogen and interpret the results, XPS of known thermal products of TNT [15,16,17] were obtained.

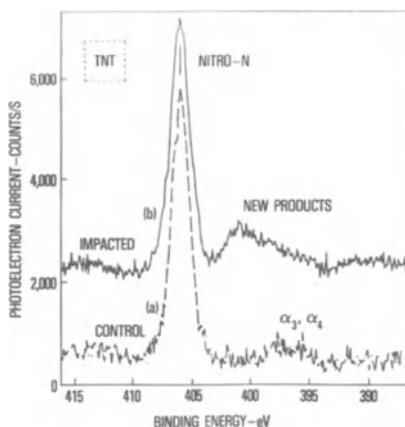


Figure 6. XPS spectra of (a) control TNT and (b) of impacted TNT in a drop weight machine. The bunch of peaks about 5-7 eV on the right side of the nitro-N peak are identified to be due to the production of benzaldoxime, anthranil and nitrile products. Figure from Ref. #10

The following compounds were considered, 4,6-dinitroanthranil; 2,4,6-trinitrobenzyl alcohol; 2,4,6-trinitrobenzaldehyde; 2,4,6-trinitrobenzoic acid; trinitrobenzene, tetranitroazoxytoluene; 2,4,6-trinitrobenzonitrile; picric acid; 5-nitroso-2-nitrotoluene; 3,5-dinitro-4-amino toluene and 2,4,6-trinitrobenzaldehyde oxime. From a comparison of the spectra it was concluded that benzaldoxime, anthranil and nitrile are being produced. Compounds such as trinitrobenzaldehyde, trinitrobenzoic acid and tribenzylalcohol did not show separate peaks from that of nitro

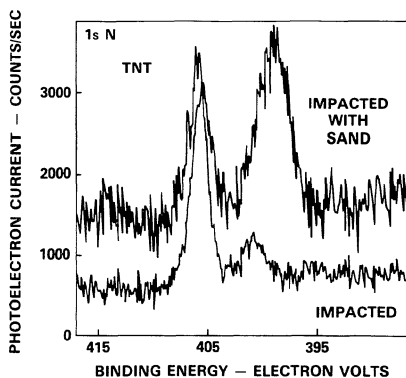


Figure 7. XPS spectra of TNT, impacted with and without sand. Sand augmentation increases the amount of nitrile produced and shows that the reaction path is same as in the beginning, even when major part of the TNT has been consumed in the reaction. Figure from Ref #11

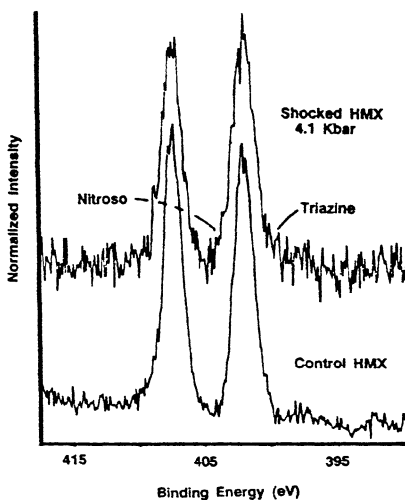


Figure 8. XPS spectra of shocked HMX shown along with that of control HMX. Distinct loss of the nitro groups and broadening due to formation of nitroso and triazine kind of products is evident.

nitrogen, except for slight broadening. Consequently it was not possible to be sure about these products, although impacted TNT also showed broadening. It is possible that these compounds were formed. None of the nitroso products were detectable. TLC studies of impacted TNT evidenced the presence of aldehyde, nitrile, and oxime. Thus in the case of TNT, it can be concluded that benzaldehyde, benzaldoxime and nitrile are principal products produced during impact.

Similar products are also shown by impacted trinitrobenzene (TNB) and impacted picric acid.

High rate shear experiments with TNT, carried out by using an activator, showed mainly benzaldoxime and anthranil with no evidence of any azoxy products. Decomposition, as high as 25 % was observed by XPS and was confined to a very thin layer on the surface of the plug pushed out by the piston.

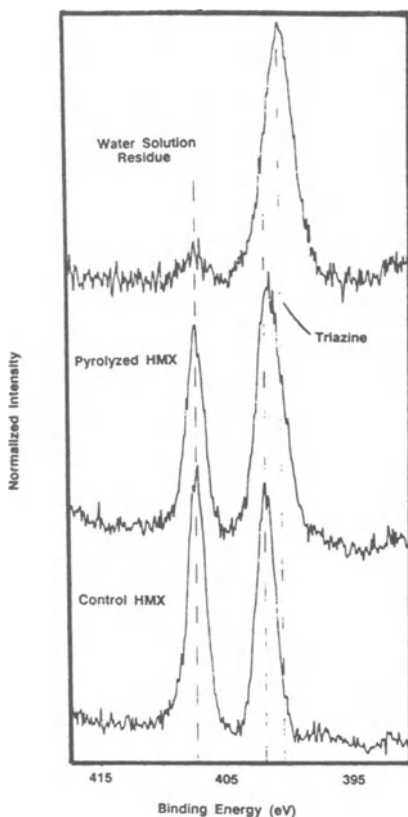


Figure 9. Comparison of XPS spectra from control, pyrolyzed and its water washed solution residue, indicating that the new products are more readily soluble in water and can be separated.

As in the case of TATB family, when TNT mixed with sand was impacted, more severe decomposition was observed, as shown in Figure 7. The products show a larger peak than the nitro peak of TNT itself. These results confirm that the same steps of decomposition, as observed in the early stages, are valid during the advanced stages of reaction.

3.3 Nitramines: RDX and HMX

The nitramines such as RDX and HMX are difficult to investigate, because they leave very little solid reaction product after they are subjected to shock or impact. Perhaps most of the reaction products disappear in gaseous form. As mentioned earlier [10], the principal effect in RDX is the loss of nitro group by about 20 %. The amine peak shows broadening to the high binding energy side as well as to low binding energy side. From a comparison of these shifts with chemically prepared samples it appears that the peak on the left, 1.4 eV away, is due to nitroso formation while that on the right side, 1.8 eV away, is ascribable to triazine-like products. Figure 8 shows a rare spectrum of HMX which has been subjected to an underwater shock of 4.1 kbars, the nitro group shows a loss of 16 % and there is broadening of the amine peak on either side conforming to what has been said about RDX. The existence of nitroso formation in thermally decomposed and in impacted RDX has been reported also by Hoffsommer et al[18,19]. In impacted RDX, by using newly acquired very sensitive detectors for their gas chromatographic equipment, they have observed nitroso products in the concentration of $5.6 \times 10^{-3} \%$, while in the very same samples, decomposition as measured by XPS was 20 %. These numbers demonstrate the superiority of XPS in this kind of investigation.

SEM micrographs do show differences between shocked and control HMX, but the results were rather strange. The control sample from pressed pellets, showed a large amount of porosity, perhaps from the voids left during pressing of the pellet. In the shocked HMX these seemed to have disappeared. The exact mechanism involved in this transformation is uncertain, it can be speculated that due to the long duration of the shock wave (a few microseconds) the sample might have melted and recrystallized. In the case of beam irradiation HMX was found to have melted, flowed and consolidated with the development of bubbles in it, without igniting. X-ray diffraction evidenced transformation of beta HMX into delta phase, which is known to be more sensitive [20] than beta HMX. Washing pyrolyzed HMX with water generated a solution which when dried left a residue that yielded an XPS spectrum exclusively representing triazine-like nitrogen. The spectra of pyrolyzed HMX, and its water extract are shown in Figure 9. In order to understand what is happening in nitramines, RDX was damaged with x-rays of the XPS instrument over long time and the changes in the spectra were followed at room temperature and at -50°C . The room temperature decomposition of RDX by x-rays confirmed the development of nitroso and triazine, as in shocked or impacted samples. Low temperature work showed an additional peak due to nitrite ester. On warming the irradiated sample to room temperature, the nitrite ester, and some nitroso

and triazine-like products are lost. This indicates the fragile nature of the intermediate products of RDX. The work on nitramines is continuing, so far a full picture of sensitizing products and exothermic steps has not emerged. Probably functional groups containing nitrite-ester contribute to sensitization.

4. Discussion

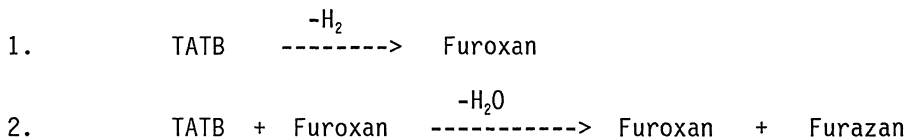
Referring to the SEM micrographs, the frequent occurrence of the reaction sites and the beady deposit of the products following the contour of the crystallite in shocked samples is noteworthy. Possibly the edges get exposed to high temperatures caused by adiabatic compression of entrapped gases. It is also possible that the reaction is concentrated on the edges because they are coincident with regions of shear, plastic deformation and piling up of dislocations which cause decomposition [22]. Some of the reaction sites may have originated at points of high free energy (defects and impurity sites) which can act as nuclei. In the case of impacted samples, the Swiss cheese holes were located on flat surfaces and may be related to energy concentration between particles. Thus the results conform to the hot spot theories of Bowden and Yoffe [2], who have suggested that concentration of energy from mechanical effects sites takes place at small sites. The size of hot spots observed in the present work agrees well with that suggested by Bowden and Yoffe.

The chemical nature of the products seen in the hot spots deserve comment. The 50 % drop height of aminodinitrofuroxan, synthesized as an explosive and tested by Hollins [21], is 56 cm and is comparable to that of TNT (54 Cm). TATB in his scale measures to 185 cm. Amino-nitrodifuroxan and benzotrifuroxan with drop heights of 33 and 56 cm respectively, are also sensitive. Friction, electrostatic and gap sensitivities are also greater for this family of compounds [21]. Thus the presence of furoxans implies that hot spots have left behind more sensitive products than the parent molecule. This fact identifies the hot spot with a sensitization center and explains why a roughly treated explosive can ignite at a lower threshold. Therefore, hot spots due to their chemical contents act as sensitization centers. This conclusion establishes a chemical basis of sensitization. It might be mentioned that the generation of a physical defect, like the ragged holes observed, can also contribute to sensitization by providing a ready site for further action, therefore its role should not be completely ignored.

Furazan derivatives of TATB have not been chemically produced in large amount, so the 50 % drop height has not been measured. However from Kamlets's oxygen balance relationship [23], furazan should not be more sensitive than TATB. It may therefore, not have any role in contributing to sensitivity. However furazan is produced by the separation of a water molecule from TATB. Thus the formation of each furazan group will be accompanied by the release of 59 kcal/mole of heat. This can be identified with the exothermic step needed to sustain the reaction. Thus the

generation of furoxan and furazan facilitates decomposition, one by making the material more unstable and the other by supplying needed energy.

It may be noted that a furoxan can react with a TATB molecule and convert it into a furoxan while itself it becomes a furazan, as shown below.



Therefore the furoxan can act as a catalyst without dropping in concentration. This is in agreement with the suggestion made by Bowden and Yoffe on p.5 in Reference [2], that some products of reaction can act as catalysts.

In the case of TNT, the product benzaldoxime could play a role like that of furoxan, in TATB. The material should be more sensitive than TNT on the basis of Kamlet's oxygen balance relationship, consequently its production would sensitize the material, so that remnants from hot spots can act as sensitization centers. (in Kamlet's scale, the drop height of TNT=160 cm, Trinitrobenzoic acid=109 cm, trinitrobenzene=100, tribenzyl alcohol=52 cm trinitrobenzaldoxime=42 cm and trinitrobenzaldehyde=36 cm). Anthranil is an exception it should be more like TNT in drop height but it will fill in like furazan, because it is produced by the separation of a water molecule from TNT and would be an energy giving step. Thus a combination of sensitizing action and release of energy are evident in the case of TNT as for TATB. The production of 2,4,6-trinitrobenzonitrile and 2,4,6-trinitrobenzaldehyde oxime suggests that intermolecular reactions between the products are also taking place.

Referring to Figures 7, which shows the XPS spectrum of severely impacted TNT sample, in which the reaction products are larger than the left over parent material, the nature of the peaks does not change. This means that the same reactions as seen in the early stage are in play even when the explosive is being appreciably consumed. Similar observations were made in relation to TATB, DATB and picramide. Thus the two principal steps, one making the material more vulnerable, the other feeding in exothermic energy may be a general basis of reactions in explosives.

5. Summary

From the present results it can be said that mechanical harm inflicted on energetic materials manifests itself in hot spots as chemical and physical changes. The physical changes are perhaps dependent on the melting, subliming characteristics, crystal habit and other properties of the material. They show up as holes in TATB but stringed structure in TNT. The explosive in the vicinity of hot spots becomes chemically

altered. Two types of reaction products are seen, one makes the material more sensitive and develops sensitization centers in the affected part of the sample, the other product involves exothermicity and ensures a supply of energy to continue the process of disruption. The smallest size of reaction sites so far observed has been 0.1 microns. This size is much larger than the molecules from which the action originates, probably future studies with scanning tunneling microscopy or atomic force microscopy will reveal finer structure. The present work gives a chemical basis to the nature of sensitization centers although the effects of defects produced in the crystals can not be completely ignored.

The fact that the reactions of early stage are continued even when most of the sample is consumed is very important. This means that the generation of intermediates observed, is not confined to the start up process only, it is also the basis of continued reaction. Thus generation of two kinds of products, an unstable one and another supplying exothermic energy may be a general feature of reactions in explosives.

If the XPS spectra of impacted TATB, TNT, RDX, HMX, TNB and other explosives are considered, a common feature is that the nitro nitrogen is reduced in all cases and products with intermediate oxidation state like furoxans, furazans, nitrosos, nitrites, triazines etc are produced. Simultaneously the carbon atoms in the molecules become oxidized and of course water is produced. It appears that these reactions represent the pattern of decomposition of explosives in general.

In view of the large amount of work on thermal decomposition, carried out by numerous workers [15,16,19], and the studies of kinetic isotope effects, [17,24] a question that has frequently been raised is whether the processes and products seen in slow decomposition are valid in fast reactions like those of impact or shock. Our results indicate that the principal products are the same, although a much larger number of products have been observed in thermal decomposition. The amount of decomposition observed in impacted or shocked samples is very minute, therefore one would not expect to see the minor products. The nature of products also points to the fact that both intra and intermolecular reactions are taking place.

6. References

1. Richter, H.P., Boyer, L.R., Graham, K.J., Lapie, A.H., and Zwierzchowski, N.G., (1989) 'Shock Sensitivity of Damaged Energetic Materials', Proc. of the Ninth Symposium (International) on Detonation, August 28-Sept.1. (In publication)
2. Bowden, F.B. and Yoffe, A.D., (1952) Initiation and Growth of Explosions in Liquids and Solids, Cambridge University Press, Cambridge, Gt. Britain.
3. Marzhanov, A.G. (1966) 'On Critical Conditions for Thermal Explosion of a Hot Spot', Combustion and Flame, 10, 341-348.
4. Friedman, M.H., (1967) 'A Generalized Thermal Explosion Criteria-Exposition and Interactive Applications' Combustion and Flame,

- 11, 239-246.
5. Mader, C.L. (1980) 'Numerical Calculations of Detonation Failure and Shock Initiation " Proc. 5th ONR Symposium. Detonation, 177-189.
6. Roth, J. (1975) 'Hot Spots', Encyclopedia of Explosives and Related items, Edited by Fedoroff, B.T. and Sheffield, O.E., Picatinny Arsenal, Dover, N.J. 7, H 170-175.
7. Cerny, J. and Kaufman, J.V.R. (1964) 'Consideration of "Spherical Hot Spots" Arising from Pion Capture in Explosives Using Thermal Initiation Theory' J.Chem. Phys. 40, (6), 1736-1744.
8. Tang, Tong B., Chaudhri, M.M., Rees, Caroline S. and Mullock, S.J. (1987) 'Decomposition of Solid Explosives by Laser Irradiation; a Mass Spectrometric Study', J. Material Science, 22, 1037-1044.
9. Sharma, J., Forbes, J.W., Coffey, C.S. and Liddiard, T.P. (1987) 'The Physical and Chemical Nature of Sensitization Centers Left from Hot Spots Caused in Triaminotrinitrobenzene by Shock or Impact' J. Phys. Chem., 91, 5139-5144.
10. Sharma, J., Hoffsommer, J.C., Glover, D.J., Forbes, J.W., Liddiard, T.P., Elban, W.I. and Santiago, F. (1985) 'Sub-ignition Reactions at Molecular Levels in Explosives Subjected to Impact and Underwater Shock', Proc. Eighth (International) Detonation Symposium, Albuquerque, NSWC MP 86-164, 725-733.
11. Sharma, J., Forbes, J.W., Coffey, C.S., and Liddiard, T.P. (1988) 'The Nature of Reaction Sites and Sensitization Centers in TATB and TNT' in S.C. Schmidt and N.C. Holmes (editors), Shock Waves in Condensed Matter, Elsevier Science Publishers B.V. pp. 565-568.
12. Liddiard, T.P. (1965) 'The Initiation of Burning in High Explosives by Shock Waves ', Proceedings of the Fourth (International) Detonation Symposium, Naval Ordnance Laboratory, White Oak, Md, U.S. Government Printing Office, Washington D.C., 487-495.
13. Coffey, C.S. and Jacobs, S.J. (1981) 'Detection of Local Heating in Impact or Shock Experiments with Thermally Sensitive Films' J. Appl. Phys. 52, 6991-6993.
14. Boyle, V., Pilarski, G.L., Blake, B.H. (1988) 'Combined Pressure Shear, Ignition Sensitivity Test', BRL Tech. Report. 2927.
15. Roger, R.N., (1967) 'Combined Pyrolysis and Thin Layer Chromatography -A Method for the Study of Decomposition Mechanism' Anal. Chemistry 39, 730-733.
16. Dacons, J.C., Adolph, H.G. and Kamlet, M.K. (1970) 'Some Novel Observations Concerning the Thermal Decomposition of 2,4,6-Trinitrotoluene ' J. Phys. Chemistry. 74, 3035-3040.
17. Shackelford, S.A., Beckman, J.W. and Wilkes, J.S. (1977) 'Deuterium Isotope Effects and the Thermochemical Decomposition of Liquid 2,4,6-Trinitrotoluene: Application to Mechanistic Studies Using Isothermal Differential Scanning Calorimetric Analysis' J. Org. Chemistry 42, 4201-4206.
18. Hoffsommer, J.C., Glover, D.J. and Elban, W.L. (1985) 'Quantitative Evidence for Nitroso Compound Formation in Drop-Weight Impacted RDX Crystals' J. Energetic Materials, 3, (2) 149-167.
19. Hoffsommer, J.C. and Glover, D.J. (1985) 'Thermal Decomposition of

- 1,3,5-trinitro-1,3,5- Triazacyclohexane (RDX): Kinetics of Nitroso Intermediates Formation' Combust. Flame, 59(3),303-310.
20. Cady, H.H. and Smith, L.C.(1962) 'Studies of the Polymorphs of HMX' Los Alamos National Laboratory tech. Report L&MS- 2652.
 21. Hollins, R. Naval Weapons Center, China Lake, CA, private communication.
 22. Coffey, C.S.(1985) 'Energy Localization in Rapidly Deforming Crystalline Solids' Phys. Rev B32 (8). 5335-5341.
 23. Kamlet, M.J. and Adolph, H.G, (1979) 'The Relationship of Impact Sensitivity with Structure of Organic High Explosives II. Polynitroaromatic Explosives', Propellants and Explosives,4, 30-34
 24. Bulusu, S. and Autera, J.(1983) 'Initiation Mechanism of TNT: Deuterium Isotope Effect as an Experimental Probe.' J. Energetic Materials, 1 (2),135-140.

SENSITIVITY RELATIONSHIPS IN ENERGETIC MATERIALS

C. B. Storm, J. R. Stine, and J. F. Kramer
Los Alamos National Laboratory
Los Alamos, NM 87545
USA

In searching for new explosives one is most concerned with performance (detonation velocity and pressure), thermal properties, and sensitivity. Whether a new candidate explosive is ultimately widely used may well be determined by other factors, such as cost, toxicity, melting point, etc., but the initial research effort is guided by the trinity of performance, thermal stability, and sensitivity. This presents a difficult multifactoral problem in assessing the various molecular properties that contribute to each of these principal selection criteria. For instance, detonation velocity is affected by density, elemental composition, and heat of formation. These factors must be varied together in such a way as to maximize the combined effect on performance.

Sensitivity is a complex problem and there is no single useful definition. Tests of the sensitivity of an explosive are devised with the idea of judging the potential safety of use in a particular application. This immediately raises two questions: 1) How do different molecules rank within any given sensitivity test? 2) How do different sensitivity tests compare in ranking molecules?

An understanding of sensitivity is in large part a chemical problem. The ease with which a detectable reaction of any kind can be initiated in an explosive; the tendency of a small reaction, once established, to grow to destructive proportions; and the ease with which a high-order detonation can be established in an explosive all contribute to the materials response to the stimulus in a sensitivity test. These properties are a consequence of the kinetics and thermodynamics of the thermal decomposition of the explosive.

Weston et al. [1] have considered relationships among various shock sensitivity tests and Price [2-4] has considered a variety of factors important in shock sensitivity tests. Among the more sensitive explosives, correlations tend to be satisfactory between tests that rely on shock initiation. It is important to understand the critical factors in each test (small scale gap test, large scale gap test,

radius of Extex primer in the minimum priming test, run distance to detonation in the wedge test (8.3 GPa), critical diameter for propagation in steady state detonation, critical flying plate kinetic energy fluence). In less sensitive explosives failure diameter effects appear to be the major problem in poor correlations.

Urizar et al. have considered the relations between four shock sensitivity tests [5] used at Los Alamos that initiate a detonation. These are the minimum priming charge, wedge, large scale gap and small scale gap tests. The tests reported in Ref. 5 were carried out on twenty one different materials made up under different conditions and in various compositions from seven pure explosives. They conclude "that the correlation is generally good, but that exceptions are numerous enough that no one test can be used with confidence as a measure of the detonation sensitivity of an explosive over a range of conditions of practical interest". Of the six possible cross-correlations among the four tests the poorest, surprisingly, was between the small-scale and large-scale gap tests.

By far the most commonly used measure of an explosive's sensitivity is the drop-weight impact test. This is convenient, easy-to-run, and inexpensive. An important question is whether this test is indicative of the explosive's behavior under other circumstances, i.e., a shock stimulus. In a typical drop-weight impact test the time constant for reaction is in the range of 200-250 μ s and the pressure is between 7-15 kbar. In a shock experiment the times range from 0.05-2.0 μ s and the pressures range from 30-200 kbar. Is the mechanism of decomposition of the explosive at all similar under these rather different conditions?

A problem that one immediately encounters in approaching these questions is that only a limited number of compounds have been studied under well-controlled and defined conditions. For shock initiated studies the largest collection of information has been gathered by the Naval Surface Warfare Center (NSWC) using the Navy Small Scale Gap Test [6,7]. For drop-weight impact tests a large collection of consistent data is available from NSWC [8-12] and from the Los Alamos National Laboratory (LANL) [13-15].

In Table 1 we give the drop-weight impact sensitivity ($h_{50,cm}$) and the shock sensitivity as measured by the NSWC small scale gap test (P_{90} the pressure in kbar required to initiate material pressed to 90% theoretical maximum density (TMD), $P_{95} = 95\%$ TMD, $P_{98} = 98\%$ TMD) for 21 explosives. The impact sensitivity given for TATB is estimated from oxygen balance correlations and will be discussed later.

If one selects from Table 1 a series of compounds that are closely related structurally, i.e. TNB, DIPAM, MATB, DATB, TATB, the correlation between the impact sensitivity and the shock sensitivity at 90% TMD ($h_{50} = 7.35P_{90}-27.44$, $R^2 = 0.99$) is excellent, Figure 1.

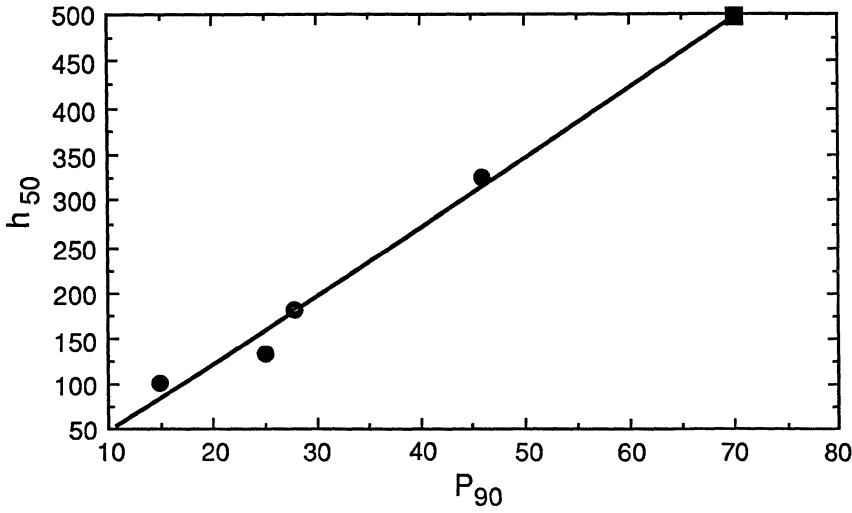


Figure 1. A plot of the drop-weight impact sensitivity (h_{50}) vs the NSW small scale gap test shock sensitivity at 90% TMD for TNB, DIPAM, MATB, DATB, and TATB. Data from Table 1.

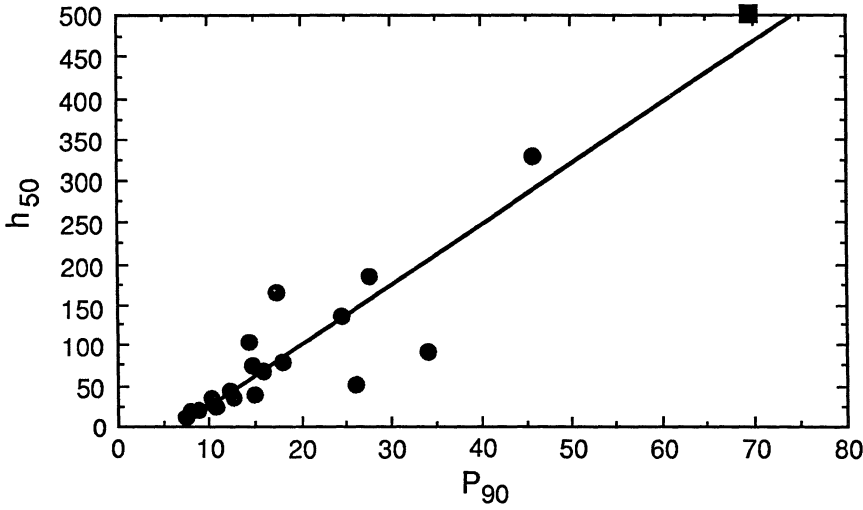


Figure 2. A plot of the drop-weight impact sensitivity (h_{50}) vs the NSW small scale gap test shock sensitivity at 90% TMD for the 21 explosives in Table 1.

TABLE 1. The impact and shock sensitivities of a variety of common explosives and their mixtures.

Compound	Composition	h_{50}^a (cm)	P_{90}^b (kbar)	P_{95}	P_{98}
PETN ^c	$C_5H_8N_4O_{12}$	12	7.47	10.76	13.69
Pentolite	50/50, PETN, TNT	18	8.21	11.73	15.18
TNETB ^d	$C_6H_6N_6O_{14}$	18	9.25	13.13	17.48
RDX ^e	$C_3H_6N_6O_6$	24	10.97	15.77	20.35
HMX ^f	$C_4H_8N_8O_8$	26	10.81	14.32	17.49
HNAB ^g	$C_{12}H_4N_8O_{12}$	32	12.77	18.11	22.48
Tetryl ^h	$C_7H_5N_5O_8$	32	10.64	15.14	19.42
Octol	75/25, HMX, TNT	42	12.62	19.23	25.98
Octol	65/35, HMX, TNT	42	12.30	18.50	26.02
HNS-I ⁱ	$C_{14}H_6N_6O_{12}$	47	26.26	30.15	32.90
HNS-II ^j	$C_{14}H_6N_6O_{12}$	39	15.03	20.29	24.70
Comp B	60/40, RDX, TNT	65	16.15	21.54	27.76
TNEDV ^k	$C_7H_9N_5O_{12}$	71	14.99	-----	-----
HNB ^l	$C_{12}H_4N_6O_{12}$	76	18.25	-----	-----
TACOT-z ^m	$C_{12}H_4N_8O_8$	85	34.43	41.26	-----
TNB ⁿ	$C_6H_3N_3O_6$	100	14.96	27.28	37.25
DIPAM ^o	$C_{12}H_6N_8O_{12}$	132	25.11	29.71	33.04
TNT ^p	$C_7H_5N_3O_6$	160	17.72	25.65	33.35
MATB ^q	$C_6H_4N_4O_6$	177	27.91	35.35	41.02
DATB ^r	$C_6H_5N_5O_6$	320	46.20	54.22	59.88
TATB ^s	$C_6H_6N_6O_6$	490 ^t	70.38	121.92	164.86

a. The impact sensitivity (h_{50} , cm) as measured at LANL and/or NSWC, using the Bruceton method, type 12 tools, 2.5 kg weight, 40 mg sample, 5/0 sandpaper, 25 trials. b. The shock sensitivity as measured by the

NSWC small scale gap test, P_{90} the pressure in kbar required to initiate material pressed to 90% theoretical maximum density (TMD), P_{95} =95% TMD, P_{98} =98% TMD. c. Pentaerythritoltetranitrate.

d. Trinitroethyltrinitrobutyrate. e. Cyclotrimethylenetrinitramine.

f. Cyclotetramethylenetetranitramine. g. 2,2',4,4',6,6'-Hexanitro-azobenzene. h. 2,4,6-Trinitrophenylmethylnitramine. i. Hexa-

nitrostilbene (0.2-2 μ particle size). j. No particle size

specification. k. Trinitroethyl-4,4-dinitrovalerate.

TABLE 1. (Continued)

l. 2,2',4,4',-6,6'-Hexanitrobiphenyl. m. 1,3,7,9-Tetranitrodibenzo-1,3a,4,6a-tetraazapentalene. n. Trinitrobenzene. o. 3,3'-Diamino-2,2',4,4',6,6'-Hexanitrobiphenyl. p. 2,4,6-Trinitrotoluene. q. 2,4,6,-Trinitroaniline. r. 1,3-Diamino-2,4,6-trinitrobenzene. s. 1,3,5-Triamino-2,4,6-trinitrobenzene. t. Estimated from oxygen balance of TNB, MATB, and DATB.

The correlation for this series between the shock sensitivity and 90% TMD and 95% TMD ($P_{95} = 1.74P_{90} - 10.44$, $R^2 = 0.92$) is good and the correlation between the shock sensitivity at 95% TMD and 98% TMD ($P_{98} = 1.40P_{95} - 7.79$, $R^2 = 0.99$) is excellent.

If one takes all 21 explosives listed in Table 1 and plots h_{50} vs P_{90} the correlation is not as good ($h_{50} = 7.23P_{90} - 50.0$, $R^2 = 0.87$), as one might expect, Figure 2. There are three main outliers off of the principal regression line, HNS-I, TACOT, and TNT. HNS-I is a special grade of hexanitrostilbene that has a 0.2-2 μ particle size distribution. HNS-II, which has no particle size specification, lies close to the regression line. It is well accepted that a small particle size can reduce shock sensitivity at high density. TNT lies off of the regression in the other direction, i.e. it is somewhat more shock sensitive than its impact sensitivity would suggest. TNT has an unusually low melting point and it has been suggested that melting in the impact test makes it appear to be less sensitive. TACOT, the third extreme outlier is a zwitterionic heterocycle, has not been extensively characterized, and may be a true structural anomaly.

If these three outliers are removed the remaining 18 explosives give an excellent correlation ($h_{50} = 7.83P_{90} - 54.25$, $R^2 = 0.99$), and this is the suggested regression for estimating the sensitivity of new materials. The shock sensitivity from 90% TMD to 95% TMD again correlates fairly well ($P_{95} = 1.55P_{90} - 3.03$, $R^2 = 0.94$) and the correlation between 95% TMD and 98% TMD is excellent ($P_{98} = 1.33P_{95} - 1.84$, $R^2 = 0.99$).

It is desirable to be able to estimate the sensitivity of proposed new materials. Even if only crude estimates can be made it is still useful for guidance for a synthetic effort. Kamlet [9-12] proposed a method for estimating impact sensitivity based on oxygen balance, which he defined as $OB_{100} = 100(2n_O - n_H - 2n_C - 2n_{COO})/\text{Molecular weight}$, where n_O , n_H , n_C , n_{COO} are the number of oxygen, hydrogen, carbon and carboxylate in the molecule. The problem has been considered by a number of other investigators [16-25]. Kamlet found reasonable correlations between OB_{100} and $\log h_{50}$ for broad classes of compounds, i.e. nitroaromatics, nitroaromatics with a ring methyl group, nitramines, nitroaliphatics, and dinitrofluoro compounds. It

was pointed out that individual impact measurements have a large scatter, but that when a large number of measurements are averaged reasonably consistent results are obtained. The regressions reported by Kamlet and Adolph [9,12] for the various classes are:

- 1) Nitroaromatic, $\log h_{50} = 1.73 - 0.32OB_{100}$
- 2) Nitroaromatic (alpha CH_3), $\log h_{50} = 1.33 - 0.26OB_{100}$
- 3) Nitroaliphatic, $\log h_{50} = 1.74 - 0.23OB_{100}$
- 4) Dinitrofluoro, $\log h_{50} = 2.14 - 0.30OB_{100}$
- 5) Nitramine, $\log h_{50} = 1.37 - 0.17OB_{100}$

Because of the multi-component nature of the sensitivity-performance problem in energetic materials it is highly desirable to have a system in which C,H,N,O explosives can be organized. Because the performance of an explosive is dependent only on relative composition, Stine [26] has proposed a system based on the geometric properties of a regular tetrahedron. The empirical formula for a $C_aH_bN_cO_d$ compound can be normalized so that:

$A+B+C+D=1$, where $A = a/n$, $B = b/n$, $C = c/n$, $D = d/n$, $n=a+b+c+d$ (Eq. 1).

This provides a convenient reference formula so different molecular compositions can be compared. A regular tetrahedron has the property that the sum of the four distances from any interior point to each of the four sides is a constant, which can arbitrarily be taken to be unity. Hence, every normalized chemical formula is represented by a unique point in a tetrahedron whose corners represent carbon, hydrogen, nitrogen and oxygen.

If the tetrahedron is centered at the origin of a cartesian coordinate system so that the four distances from any interior point to each of the four sides sum to unity, the coordinates on any interior point are: $X = \sqrt{2}(3D-1+C)/4$; $Y = \sqrt{6}(A-B)/4$; $Z = C-1/4$; where A,B,C, and D are as given in Eq. 1. Two oxygen balance planes can now be defined; one containing the normalized points for CO, H_2O , and N_2 and the other containing the points for CO_2 , H_2O , and N_2 . The two definitions of oxygen balance (balance to CO or CO_2) are then the perpendicular distances from the point to the respective plane. Illustrations of this tetrahedral representation are given in ref. 26.

We have chosen as an index of sensitivity the distance of a point from the CO oxygen-balance plane. This sensitivity index is then defined as $SI = 100(d-a-(b/2)-nCO)/5(a+b+c+d)$, where a,b,c,d are the coefficients of C,H,N,O, and nCO corresponds to the number of carbonyl groups in the molecule. This sensitivity index transforms to Kamlet's definition as $OBK = 0.87SI - 0.05$, $R^2 = 0.99$, for the 38 compounds in ref. 9.

In Tables 2-15 we have compiled the impact sensitivities for the compounds reported in Refs. 8-15. The compounds are grouped together by structural type. Table 2 reports nitroaromatic explosives (40 compounds); Table 3, nitroaromatic explosives with an alpha C-H

linkage (17 compounds); Table 4, nitropyridine explosives (6 compounds); Table 5, nitroimidazole explosives (10 compounds); Table 6, nitropyrzazole explosives (8 compounds); Table 7, nitrofurazan and nitrooxadiazole explosives (7 compounds); Table 8, nitro-1,2,4-triazole explosives (18 compounds); Table 9, nitro-1,2,3-triazole explosives (16 compounds); Table 10, nitropyrimidine explosives (4 compounds); Table 11, nitroaliphatic explosives (7 compounds); Table 12, nitroaliphatic explosives containing other functional groups (44 compounds); Table 13, nitramine explosives (61 compounds); Table 14, nitrate ester explosives (7 compounds); and Table 15, miscellaneous nitroheterocyclic explosives (13 compounds), providing impact sensitivity information on 258 pure explosives. Since the methods discussed here depend on having a close structural analogy, this wide variety of information is provided.

In Figure 3 the sensitivity index (SI) is plotted against the impact sensitivity ($\log h_{50}$) for 40 nitroaromatic compounds from Table 2. This is very much the same result as obtained by Kamlet [9]. The correlation for the original set of nitroaromatics reported by Kamlet and Adolph [9] of OB_{100} vs $\log h_{50}$ is $R^2 = 0.866$; for the correlation of SI vs $\log h_{50}$ R^2 is 0.836, essentially the same. The overall regression for the 40 compounds in Table 2 is $\log h_{50} = 1.72 - 0.19SI$, $R^2 = 0.639$.

If one considers groups of compounds that are structurally closely related the relation between impact sensitivity ($\log h_{50}$) and SI are excellent. In Figure 4 we plot $\log h_{50}$ vs SI for TNB, MATB and DATB (Table 2, Nos. 5,12,15). This series gives an excellent correlation. If this is extrapolated to the SI of TATB (Tables 2-18) an impact sensitivity of 490 cm is predicted. This is the value used in Table 1 and in Figures 1 and 2. A similar value would be predicted from the h_{50} vs P_{90} plots in Figures 1 and 2.

Several of the families of compounds in Table 2 have excellent correlations between $\log h_{50}$ and SI, i.e.

polynitroanilines (2-4,9,12), $\log h_{50} = 1.75 - 0.24SI$, $R^2 = 0.997$

polynitrobenzenes (2-1,3,5), $\log h_{50} = 1.70 - 0.13SI$, $R^2 = 0.938$

polyaminopolynitrobenzenes (2-1,2,5), $\log h_{50} = 0.58 - 0.84SI$, $R^2 = 0.998$

polynitrophenols (2-6,7,8,10,11,21,23,30,31), $\log h_{50} = 1.72 - 0.28 SI$, $R^2 = 0.895$.

The apparent scatter of points in Figure 3 is then the result of a series of families of crossing straight lines with rather different slopes and intercepts. If one wishes to estimate the impact sensitivity of a proposed explosive, and it is in any way related to known compounds, as closely related a series as possible should be chosen for interpolation or extrapolation to the appropriate SI value.

TABLE 2. The drop-weight impact sensitivities of nitroaromatic explosives.

No.	Compound	Formula	Mol. Wt.	SI	h_{50} (cm)	Ref.
1	Hexanitrobenzene	$C_6N_6O_{12}$	348	5.00	12	13
2	Benzotrifuroxan	$C_6N_6O_6$	252	0.00	50	13
3	1,2,4,5-Tetranitrobenzene	$C_6H_2N_4O_8$	258	1.00	27	13
4	2,3,4,5,6-Pentanitro-aniline	$C_6H_2N_6O_{10}$	318	2.50	15	9
5	1,3,5-Trinitrobenzene	$C_6H_3N_3O_6$	213	-1.67	100	9
6	Picric acid	$C_6H_3N_3O_7$	229	-0.53	87	9
7	2,4,6-trinitroresorcinol	$C_6H_3N_3O_8$	245	0.50	43	9
8	2,4,6-Trinitrophloro-glucinol	$C_6H_3N_3O_9$	261	1.43	27	9
9	2,3,4,6-tetranitroaniline	$C_6H_3N_5O_8$	273	0.45	41	9
10	2,4-Dinitroresorcinol	$C_6H_4N_2O_6$	200	-2.22	296	9
11	4,6-Dinitroresorcinol	$C_6H_4N_2O_6$	200	-2.22	>320	9
12	2,4,6-Trinitroaniline	$C_6H_4N_4O_6$	228	-2.00	177	9
13	2,4,6-Trinitro-3-amino-phenol	$C_6H_4N_4O_7$	244	-0.95	138	9
14	2,3,4,6-Tetranitro-aniline	$C_6H_4N_6O_8$	288	0.45	41	8
15	1,3-diamino-2,4,6-trinitrobenzene	$C_6H_5N_5O_6$	243	-2.27	320	9
16	1-Hydroxy-3,5-diamino-2,4,6-trinitrobenzene	$C_6H_5N_5O_7$	259	-1.30	120	8
17	Ammonium picrate	$C_6H_6N_4O_7$	246	-1.74	135	13
18	1,3,5-Triamino-2,4,6-trinitrobenzene	$C_6H_6N_6O_6$	258	-2.50	>320	8
19	2,4,6-Trinitro-benzonitrile	$C_7H_2N_4O_6$	238	-2.11	140	9
20	2,4,6-Trinitrobenzoic acid	$C_7H_3N_3O_8$	257	-1.43	109	9
21	2,4,6-Trinitroanisoie	$C_7H_5N_3O_7$	243	-2.27	192	9
22	3-Methoxy-2,4,6-trinitroaniline	$C_7H_6N_4O_7$	258	-2.50	>320	9
23	1,3-Dimethoxy-2,4,6-trinitrobenzene	$C_8H_7N_3O_8$	273	-2.69	251	9
24	2',2',2'-Trinitroethyl-2,4,6-trinitrobenzoate	$C_9H_4N_6O_{14}$	420	1.21	24	9

TABLE 2. (Continued)

No.	Compound	Formula	Mol. Wt.	SI	h_{50} (cm)	Ref.
25	2',2',2'-Trinitroethyl-3,5-dinitrobenzoate	C ₉ H ₅ N ₅ O ₁₂	375	-0.32	73	9
26	2',2',2'-Trinitroethyl-3,5-dinitrosalicylate	C ₉ H ₅ N ₅ O ₃	391	0.31	45	9
27	1,4,5,8-tetranitro-naphthalene	C ₁₀ H ₄ N ₄ O ₈	308	-3.08	100	8
28	2',2'-Dinitropropyl-2,4,6-trinitrobenzoate	C ₁₀ H ₇ N ₅ O ₁₂	389	-1.23	214	9
29	2,2',4,4',6,6'-Hexanitro-biphenyl	C ₁₂ H ₄ N ₆ O ₁₂	424	-1.18	85	9
30	3-hydroxy-2,2',4,4',6,6'-hexanitrobiphenyl	C ₁₂ H ₄ N ₆ O ₁₃	440	-0.57	42	9
31	3,3'-dihydroxy-2,2',4,4',6,6'-hexanitrobiphenyl	C ₁₂ H ₄ N ₆ O ₁₄	456	0.00	40	9
32	2,2',4,4',6,6'-Hexanitro-diphenylamine	C ₁₂ H ₅ N ₇ O ₁₂	439	-1.39	48	9
33	3,3'-Diamino-2,2',4,4',6,6'-hexanitrobiphenyl	C ₁₂ H ₆ N ₈ O ₁₂	454	-1.58	132	9
34	2,2',4,4',6-Pentanitro-benzophenone	C ₁₃ H ₄ N ₅ O ₁₁	407	-1.12	54	8
35	2,2',2'',4,4',4'',6,6',6''-nonanitro-m-terphenyl	C ₁₈ H ₅ N ₉ O ₁₈	635	-1.00	39	8
36	2,2'',4,4',4'',6,6',6''-Octanitro-m-terphenyl	C ₁₈ H ₆ N ₈ O ₁₆	590	-2.08	63	8
37	2,2',2'',4,4'',5',6,6''-Octanitro-p-terphenyl	C ₁₈ H ₆ N ₈ O ₁₆	590	-2.08	40	8
38	2,2',2'',4,4'',6,6',6''-octanitro-p-terphenyl	C ₁₈ H ₆ N ₈ O ₁₆	590	-2.08	59	8
39	Dodecanitroquater-phenyl	C ₂₄ H ₆ N ₁₂ O ₂₄	846	-0.88	40	8
40	Azo-bis-2,2',4,4',6,6'-hexanitrobiphenyl	C ₂₄ H ₆ N ₁₄ O ₂₄	874	-0.88	40	8

TABLE 3. The drop-weight impact sensitivities of nitroaromatic explosives with an alpha C-H linkage.

No.	Compound	Formula	Mol. Wt.	SI	h_{50} (cm)	Ref.
1	2,4,6-Trinitro-benzaldehyde	$C_7H_3N_7O_7$	271	-2.08	36	9
2	2,4,6-Trinitro-benzaldoxime	$C_7H_4N_4O_7$	256	-1.82	42	9
3	2,4,6-Trinitrotoluene	$C_7H_5N_3O_6$	227	-4.09	160	9
4	1-Dinitromethyl-3-nitrobenzene	$C_7H_5N_3O_6$	227	-4.09	105	8
5	2,4,6-Trinitrobenzyl alcohol	$C_7H_5N_3O_7$	243	-2.27	52	9
6	2,4,6-Trinitro-m-cresol	$C_7H_5N_3O_7$	243	-2.27	191	9
7	1-(2,2,2-Trinitroethyl)-2,4,6-trinitrobenzene	$C_8H_4N_6O_{12}$	376	1.33	13	9
8	2,4,6-Trinitrostyrene	$C_8H_5N_3O_6$	239	-3.41	32	8
9	1-(2,2,2-Trinitroethyl)-2,4 dinitrobenzene	$C_8H_5N_5O_{10}$	331	-0.36	31	9
10	3,5-Dimethyl-2,4,6-trinitrophenol	$C_8H_7N_3O_7$	257	-3.60	77	9
11	1-(3,3,3-trinitropropyl)-2,4,6-trinitrobenzene	$C_9H_6N_6O_{12}$	390	0.00	21	9
12	1-(3,3,3-trinitropropyl)-2,4-dinitrobenzene	$C_9H_7N_5O_{10}$	345	-1.61	31	8
13	3-Methyl-2,2',4,4',6,6'-hexanitrobiphenyl	$C_{13}H_6N_6O_{12}$	438	-2.16	53	9
14	3-Methyl-2,2',4,4',6,-pentanitrobiphenyl	$C_{13}H_7N_5O_{10}$	393	-3.71	143	9
15	Hexanitrostilbene	$C_{14}H_6N_6O_{12}$	450	-2.63	39	8
16	2,2',4,4',6,6'-Hexanitrobibenzyl	$C_{14}H_8N_6O_{12}$	452	-3.00	114	9
17	3,3'-Dimethyl-2,2',4,4',6,6'-hexanitrobiphenyl	$C_{14}H_8N_6O_{14}$	452	-1.90	135	9

TABLE 4. The drop-weight impact sensitivities of nitropyridine explosives.

No.	Compound	Formula	Mol. Wt.	SI	h_{50} (cm)	Ref.
1	2,4,6-Trinitropyridine-1-oxide	$C_5H_2N_4O_7$	230	1.11	20	13
2	3,3',5,5'-Tetranitro-2,2'-azopyridine	$C_{10}H_4N_8O_8$	364	-2.67	56	13
3	2,6-bis-(picrylazo)-3,5-dinitropyridine	$C_{17}H_5N_{13}O_{16}$	647	-1.37	33	13
4	2,6-bis-(picrylamino)-3,5-dinitropyridine	$C_{17}H_7N_{11}O_{16}$	621	-1.76	63	13
5	3,5-bis-(picrylamino)-2,6-dinitropyridine	$C_{17}H_7N_{11}O_{16}$	621	-1.76	92	13
6	2,6-bis(picrylamino)-pyridine	$C_{17}H_9N_9O_{12}$	531	-4.04	192	13

TABLE 5. The drop-weight impact sensitivities of nitroimidazole explosives.

No.	Compound	Formula	Mol. Wt.	SI	h_{50} (cm)	Ref.
1	2,4,5-Trinitroimidazole	$C_3HN_5O_6$	203	3.33	68	13
2	2,7-Dinitroimidazole	$C_3H_2N_4O_4$	158	0.00	105	13
3	Ammonium-2,4,5-trinitroimidazole	$C_3H_4N_6O_6$	220	0.88	50	13
4	Ammonium-4,5-dinitroimidazole	$C_3H_5N_5O_4$	175	-1.76	77	13
5	4,4',5,5'-Tetranitro-biimidazole	$C_6H_2N_8O_8$	314	0.83	37	13
6	Diammonium-4,4',5,5'-tetranitrobiimidazolate	$C_6H_8N_{10}O_8$	348	-1.25	105	13
7	2,4-Dinitro-1-picryl-imidazole	$C_9H_3N_7O_{10}$	369	-0.34	46	13
8	2-Nitro-1-picryl-imidazole	$C_9H_4N_6O_8$	324	-2.22	312	13
9	4-Nitro-1-picryl-imidazole	$C_9H_4N_6O_8$	324	-2.22	161	13
10	1-Picrylimidazole	$C_9H_5N_5O_6$	279	-4.40	314	13

TABLE 6. The drop-weight impact sensitivities of nitropyrazole explosives.

No.	Compound	Formula	Mol. Wt.	SI	h_{50} (cm)	Ref.
1	Ammonium 3,5-dinitropyrazole	$C_3H_5N_5O_4$	175	-1.76	158	13
2	4-Nitro-1-picryl-pyrazole	$C_9H_4N_6O_8$	324	-2.22	112	13
3	4-Nitro-3-picrylamino-pyrazole	$C_9H_5N_7O_8$	339	-2.41	>320	13
4	3,5-Dinitro-1-methyl-4-picrylpyrazole	$C_{10}H_5N_7O_{10}$	383	-1.56	118	13
5	3,5-Dinitro-1-methyl-4-picrylaminopyrazole	$C_{10}H_6N_8O_{10}$	398	-1.76	274	13
6	1,4-Dipicrylpyrazole	$C_{15}H_6N_8O_{12}$	490	-2.93	314	13
7	4-Nitro-1-picryl-3-picrylaminopyrazole	$C_{15}H_6N_{10}O_{14}$	550	-1.78	149	13
8	5-Nitro-1-picryl-4-picrylaminopyrazole	$C_{15}H_6N_{10}O_{14}$	550	-1.78	>320	13

TABLE 7. The drop-weight impact sensitivities of nitrofurazan and nitrooxadiazole explosives.

No.	Compound	Formula	Mol. Wt.	SI	h_{50} (cm)	Ref.
1	3-Amino-4-nitrofurazan	$C_2H_2N_4O_3$	130	0.00	27	13
2	4,4'-Dinitro-3,3'-bifurazan	$C_4N_6O_6$	228	2.50	13	13
3	3-Nitro-4-picrylamino-furazan	$C_8H_3N_7O_9$	341	-0.37	60	13
4	3-Amino-4-picrylamino-furazan	$C_8H_5N_7O_7$	311	-2.59	120	13
5	2-5-Dipicryl-1,3,4-oxadiazole	$C_{14}H_4N_8O_{13}$	504	-1.54	20	8
6	3,4-Bis-(picrylamino)-furazan	$C_{14}H_6N_{10}O_{13}$	522	-1.86	71	13
7	3,5-Bis-(picrylamino)-1,2,4-oxadiazole	$C_{14}H_6N_{10}O_{13}$	522	-1.86	95	13

TABLE 8. The drop-weight impact sensitivities of nitro-1,2,4- triazole explosives.

No.	Compound	Formula	Mol. Wt.	SI	h_{50} (cm)	Ref.
1	3-Nitro-1,2,4-triazole	$C_2H_2N_4O_2$	114	-2.00	>320	13
2	3-Nitro-1,2,4-triazole-5-one	$C_2H_2N_4O_3$	130	1.82	291	14,15
3	Ammonium 3-nitro-1,2,4-triazolate	$C_2H_5N_5O_2$	131	-3.57	>320	13
4	Ammonium 3,5-dinitro-1,2,4-triazolate	$C_2H_4N_6O_4$	176	0.00	110	13
5	4-Methyl-3,5-dinitro-1,2,4-triazole	$C_3H_3N_5O_4$	173	-0.67	155	8
6	5,5'-Dinitro-3,3'-bi-1,2,4-triazole	$C_4H_2N_8O_4$	226	-1.11	153	13
7	4-(2-Nitroethyl)-3,5-dinitro-1,2,4-triazole	$C_4H_4N_6O_6$	232	0.00	35	8
8	3-Nitro-1-picryl-1,2,4-triazole	$C_8H_3N_7O_8$	325	-1.15	68	13
9	1-Picryl-1,2,4-triazole	$C_8H_5N_5O_{10}$	280	-3.33	>320	13
10	3-Picrylamino-1,2,4-triazole	$C_8H_5N_7O_6$	295	-3.46	>320	13
11	4-Picrylamino-1,2,4-triazole	$C_8H_5N_7O_6$	295	-3.46	314	13
12	3-Amino-5-picrylamino-1,2,4-triazole	$C_8H_6N_8O_6$	310	-3.57	230	13
13	4-(2,4-Dinitrobenzyl)-3,5-dinitro-1,2,4-triazole	$C_9H_5N_7O_8$	339	-2.41	96	8
14	4-(4-Nitrobenzyl)-3,5-dinitro-1,2,4-triazole	$C_9H_6N_6O_6$	294	-4.44	>320	8
15	2-Picryl-3-picrylamino-1,2,4-triazole	$C_{14}H_6N_{10}O_{12}$	506	-2.38	>320	13
16	3,5-Bispicrylamino-1,2,4-triazole	$C_{14}H_7N_{11}O_{12}$	521	-2.50	240	13
17	N,N'Dipicryl-5,5'-dinitro-3,3'-bi-1,2,4-triazole	$C_{16}H_4N_{14}O_{16}$	648	-0.80	138	13
18	5,5'-Bispicrylamino-3,3'-bi-1,2,4-triazole	$C_{16}H_8N_{14}O_{12}$	588	-3.20	>320	13

TABLE 9. The drop-weight impact sensitivities of nitro-1,2,3-triazoles.

No.	Compound	Formula	Mol. Wt.	SI	h_{50} (cm)	Ref.
1	4-Nitro-1,2,3-triazole	$C_2H_2N_4O_2$	114	-2.0	25	13
2	Ammonium 4-nitro-1,2,3-triazole	$C_2H_5N_5O_2$	131	-3.57	235	13
3	4-Nitro-1-picryl-1,2,3-triazole	$C_8H_3N_7O_8$	325	-1.15	9	13
4	4-Nitro-1-picryl-1,2,3-triazole	$C_8H_3N_7O_8$	325	-1.15	67	13
5	1-(3',5'-dinitrophenyl)-4-nitro-1,2,3-triazole	$C_8H_4N_6O_6$	280	-3.33	56	13
6	1-(3',4'-dinitrophenyl)-4-nitro-1,2,3-triazole	$C_8H_4N_6O_6$	280	-3.33	51	13
7	1-Picryl-1,2,3-triazole	$C_8H_4N_6O_6$	280	-3.33	10	13
8	2-Picryl-1,2,3-triazole	$C_8H_4N_6O_6$	280	-3.33	200	13
9	1-(3'-Amino-2',4',6'-trinitrophenyl)-1,2,3-triazole	$C_8H_5N_7O_6$	295	-3.46	31	13
10	4-Picrylamino-1,2,3-triazole	$C_8H_5N_7O_6$	295	-3.46	103	13
11	4,6-Dinitro-1-picryl-benzotriazole	$C_{12}H_4N_8O_{10}$	420	-2.35	40	13
12	5,6-Dinitro-1-picryl-benzotriazole	$C_{12}H_4N_8O_{10}$	420	-2.35	35	13
13	1-Picryl-4-picrylamino-1,2,3-triazole	$C_{14}H_6N_{10}O_{12}$	506	-2.38	35	13
14	2,6-Dipicrylbenzo-[1,2-d:4,5-d']-bistriazole-4,8-dione	$C_{18}H_4N_{12}O_{14}$	612	-3.33	95	13
15	1,7-dipicrylbenzo-[1,2-d:4,5-d']-bistriazole	$C_{18}H_6N_{12}O_{12}$	582	-3.75	38	13
16	1,5-Dipicrylbenzo-[1,2-d:4,5-d']-bistriazole	$C_{18}H_6N_{12}O_{12}$	582	-3.75	40	13

TABLE 10. The drop-weight impact sensitivities of nitropyrimidine explosives.

No.	Compound	Formula	Mol. Wt.	SI	h_{50} (cm)	Ref.
1	2,4,6,2',4'',6''-heptanitro-4',6'-diazam-terphenyl	$C_{16}H_5N_9O_{14}$	547	-2.05	58	8
2	2,4,6,4',2'',4'',6''-heptanitro-2',6'-diazam-terphenyl	$C_{16}H_5N_9O_{14}$	547	-2.05	58	8
3	1-picryl-2-picrylamino-1,2-dihydropyrimidine	$C_{16}H_7N_9O_{12}$	517	-3.41	106	13
4	5-Nitro-2,4,6-tris-(picrylamino)-pyrimidine	$C_{22}H_9N_{15}O_{20}$	803	-1.97	201	13

TABLE 11. The drop-weight impact sensitivities of nitroaliphatic explosives.

No.	Compound	Formula	Mol. Wt.	SI	h_{50} (cm)	Ref.
1	1,1,1,3-tetranitro butane	$C_4H_6N_4O_8$	238	0.91	33	10
2	1,1,1,3,5,5,5-heptanitropentane	$C_5H_5N_7O_{14}$	387	4.19	8	10
3	1,1,1,6,6,6-hexanitro-3-hexyne	$C_6H_4N_6O_{12}$	352	2.86	7	8
4	1,1,1,6,6,6-hexanitro-3-hexene	$C_6H_6N_6O_{12}$	354	2.00	17	8
5	3,3,4,4-tetranitro-hexane	$C_6H_{10}N_4O_8$	266	-2.14	80	10
6	2,2,4,4,6,6-hexanitroheptane	$C_7H_{10}N_6O_{12}$	370	0.00	29	10
7	2,2,4,6,6-pentanitro-heptane	$C_7H_{11}N_5O_{10}$	325	-1.52	56	10

TABLE 12. The drop-weight impact sensitivities of nitroaliphatic explosives containing other functional groups

No.	Compound	Formula	Mol. Wt.	SI	h_{50} (cm)	Ref.
1	2,2,2-Trinitroethyl-carbamate	$C_3H_4N_4O_8$	224	2.11	18	10
2	2,2-Dinitro-1,3-propane-diol	$C_3H_6N_2O_6$	166	0.00	110	10
3	Methyl-2,2,2-trinitro-ethyl carbonate	$C_4H_5N_3O_9$	239	1.43	28	10
4	4,4,4-Trinitrobutyramide	$C_4H_6N_4O_7$	222	-0.95	40	8
5	Bis-(2,2,2-trinitro-ethyl)-carbonate	$C_5H_4N_6O_{15}$	388	4.67	16	10
6	Methylene-bis-N,N'-(2,2,2-trinitroacetamide)	$C_5H_4N_8O_{14}$	400	3.23	9	10
7	Bis-(trinitroethoxy)-methane	$C_5H_6N_6O_{14}$	374	3.87	17	8
8	N,N'-Bis-(2,2,2-trinitroethyl)-urea	$C_5H_6N_8O_{13}$	386	2.50	17	10
9	5,5,5-Trinitropentanone-2	$C_5H_7N_3O_7$	221	-2.27	125	10
10	Ethyl-2,2,2-trinitro-ethylcarbonate	$C_5H_7N_3O_9$	253	-0.42	81	10
11	N-(2-Propyl)-trinitroacetamide	$C_5H_8N_4O_7$	236	-2.50	112	8
12	Bis-(trinitroethyl)-oxalate	$C_6H_4N_6O_{16}$	416	3.75	15	8
13	2,2,2-Trinitroethyl-4,4,4-trinitrobutyrate	$C_6H_6N_6O_{14}$	386	2.50	18	10
14	Bis-(trinitroethyl)-oxamide	$C_6H_6N_8O_{14}$	414	1.76	13	8
15	Trinitroethyl-2,2-dinitropropylcarbonate	$C_6H_7N_5O_{13}$	357	1.61	15	8
16	N-Trinitroethyl-4,4,4-trinitrobutyramide	$C_6H_7N_7O_{13}$	385	1.52	18	8
17	1,5-Bis-(trinitroethyl)-biuret	$C_6H_7N_9O_{14}$	429	1.39	24	8
18	N-(t-Butyl)-trinitro-acetamide	$C_6H_{10}N_4O_7$	250	-3.70	110	8
19	Tris-(2,2,2-trinitroethyl)-orthoformate	$C_7H_7N_9O_{21}$	553	4.77	7	10

TABLE 12. (Continued)

No.	Compound	Formula	Mol. Wt.	SI	h_{50} (cm)	Ref.
20	1,1,1,7,7,7-Hexanitro-heptanone-4	C ₇ H ₈ N ₆ O ₁₃	384	0.59	34	10
21	Methylene-bis-(trinitro-ethyl)-carbamate	C ₇ H ₈ N ₈ O ₁₆	460	1.54	27	8
22	2,2-Dinitropropyl-trinitrobutyrate	C ₇ H ₉ N ₅ O ₁₂	355	-0.30	151	8
23	2,2,2-Trinitroethyl-4,4-dinitrovalerate	C ₇ H ₉ N ₅ O ₁₂	355	-0.30	70	10
24	Bis-(2,2-dinitropropyl)-carbonate	C ₇ H ₁₀ N ₄ O ₁₁	326	-1.25	300	10
25	2,2 Dinitropropyl-4,4,4-trinitrobutyramide	C ₇ H ₁₀ N ₆ O ₁₁	354	-1.18	72	10
26	Bis-(trinitropropyl)-urea	C ₇ H ₁₀ N ₈ O ₁₃	414	0.00	23	8
27	Bis-(1,1,1-trinitro-2-propyl)-urea	C ₇ H ₁₀ N ₈ O ₁₃	414	0.00	19	8
28	Bis-(trinitroethyl)-fumarate	C ₈ H ₆ N ₆ O ₁₆	442	1.67	14	8
29	Trinitroethyl-bis-(trinitroethoxy)-acetate	C ₈ H ₇ N ₉ O ₂₂	581	4.13	6	8
30	4,4,4-Trinitrobutyric anhydride	C ₈ H ₈ N ₆ O ₁₅	428	0.54	30	10
31	Bis-(2,2,2-trinitro-ethyl)-succinate	C ₈ H ₈ N ₆ O ₁₆	444	1.05	30	10
32	Bis-(2,2-dinitropropyl)-oxalate	C ₈ H ₁₀ N ₄ O ₁₂	354	-1.76	227	10
33	N,N'-Bis-(3,3,3-trinitro-propyl)-oxamide	C ₈ H ₁₀ N ₈ O ₁₄	442	-0.50	45	10
34	2,2,2 Trinitroethyl-4,4-dinitrohexanoate	C ₈ H ₁₁ N ₅ O ₁₂	369	-1.39	138	10
35	2,2 Dinitrobutyl-4,4,4-trinitrobutyramide	C ₈ H ₁₁ N ₅ O ₁₂	369	-1.39	101	10
36	2,2-dinitropropyl-4,4-dinitrovalerate	C ₈ H ₁₂ N ₄ O ₁₀	324	-2.94	>320	10
37	Nitroisobutyl-4,4,4-trinitrobutyrate	C ₈ H ₁₂ N ₄ O ₁₀	324	-2.94	279	10
38	Tetrakis-(2,2,2-trinitro-ethyl)-orthocarbonate	C ₉ H ₈ N ₁₂ O ₂₈	732	5.26	7	10
39	Methylene-bis-(4,4,4-trinitrobutyramide)	C ₉ H ₁₂ N ₈ O ₁₄	456	-1.40	113	10
40	Ethylene-bis-(4,4,4-trinitrobutyrate)	C ₁₀ H ₁₂ N ₆ O ₁₆	472	-0.91	120	10
41	N,N-Bis-(2,2 dinitro-propyl)-4,4,4-trinitro-butylamide	C ₁₀ H ₁₄ N ₈ O ₁₅	486	-1.28	72	10

TABLE 12. (Continued)

No.	Compound	Formula	Mol. Wt.	SI	h_{50} (cm)	Ref.
42	Bis-(2,2,2-trinitro-ethyl)-4,4-dinitro-heptanedioate	$C_{11}H_{12}N_8O_{20}$	576	0.39	68	10
43	2,2-Dinitropropane-1,3-1,3-diol-bis-(4,4,4-trinitrobutyrate)	$C_{11}H_{12}N_8O_{20}$	576	0.39	50	10
44	Bis-(2,2,2 Trinitro-ethyl)-4,4,6,6,8,8-hexanitro-undecanedioate	$C_{15}H_{16}N_{12}O_{28}$	812	0.85	32	10

TABLE 13. The drop-weight impact sensitivities of nitramine explosives.

No.	Compound	Formula	Mol. Wt.	SI	h_{50} (cm)	Ref.
1	N,N'-Dinitro-methanedi-amine	$\text{CH}_4\text{N}_4\text{O}_4$	136	1.54	13	10
2	N-Nitro-N-methyl-formamide	$\text{C}_2\text{H}_4\text{N}_2\text{O}_3$	104	-3.64	320	13
3	N,N'-Dinitro-1,2-ethanedi-amine	$\text{C}_2\text{H}_6\text{N}_4\text{O}_4$	150	-1.25	34	10
4	Methyl-2,2,2-trinitro-ethyl-nitramine	$\text{C}_3\text{H}_5\text{N}_5\text{O}_8$	239	2.38	9	10
5	Trinitroethyl-nitroguanidine	$\text{C}_3\text{H}_5\text{N}_7\text{O}_8$	267	2.17	15	8
6	Cyclotrimethylene-trinitramine	$\text{C}_3\text{H}_6\text{N}_6\text{O}_6$	222	0.00	26	10
7	N-Methyl-N,N'-dinitro-1,2-ethanedi-amine	$\text{C}_3\text{H}_8\text{N}_4\text{O}_4$	164	-3.16	114	10
8	Trinitroethyl-cyanomethyl-nitramine	$\text{C}_4\text{H}_4\text{N}_6\text{O}_8$	264	1.82	11	8
9	Bis-(2,2,2-trinitro-ethyl)-nitramine	$\text{C}_4\text{H}_4\text{N}_8\text{O}_{14}$	388	5.33	5	10
10	N-Methyl-N-nitro-(trinitroethyl)-carbamate	$\text{C}_4\text{H}_5\text{N}_5\text{O}_{10}$	283	2.08	17	8
11	N,N'-dimethyl-N,N'-dinitrooxamide	$\text{C}_4\text{H}_6\text{N}_4\text{O}_6$	206	-3.00	79	8
12	N-Nitro-N-(trinitro-ethyl)-glycinamide	$\text{C}_4\text{H}_6\text{N}_6\text{O}_9$	282	0.80	17	8
13	Cyclotetramethylene-tetranitramine	$\text{C}_4\text{H}_8\text{N}_8\text{O}_8$	296	0.00	29	10
14	N,N'-Dinitro-N-[2-(nitroamino)ethyl]-1,2-ethanedi-amine	$\text{C}_4\text{H}_{10}\text{N}_6\text{O}_6$	238	-2.31	39	10
15	1,3,3,5,5-Pentanitro-piperidine	$\text{C}_5\text{H}_6\text{N}_6\text{O}_{10}$	310	1.48	14	10
16	2,2,2-Trinitroethyl-3',3',3'-trinitropropyl-nitramine	$\text{C}_5\text{H}_6\text{N}_8\text{O}_{14}$	402	3.64	6	10
17	N,N'-Bis-2,2,2-trinitro-ethyl)-N,N'-dinitro-methanedi-amine	$\text{C}_5\text{H}_6\text{N}_{10}\text{O}_{16}$	462	4.32	5	10
18	Trinitroethyl-N-ethyl-N-nitro-carbamate	$\text{C}_5\text{H}_7\text{N}_5\text{O}_{10}$	297	0.37	19	8
19	Trinitroethyl-2-methoxy-ethyl-nitramine	$\text{C}_5\text{H}_9\text{N}_5\text{O}_9$	283	-0.36	42	8

TABLE 13. (Continued)

No.	Compound	Formula	Mol. Wt.	SI	h_{50} (cm)	Ref.
20	N-methyl-N'-trinitro-ethyl-N,N'-dinitro-1,2,-ethanediamine	$C_5H_9N_7O_{10}$	327	0.32	11	10
21	N,N'-3,3-Tetranitro-1,5-pentanediamine	$C_5H_{10}N_6O_8$	282	-1.38	35	10
22	N-nitro-N-(3,3,3-trinitropropyl)-2,2,2-trinitroethyl carbamate	$C_6H_6N_8O_{16}$	446	3.33	9	10
23	2,2,2-Trinitroethyl-N-(2,2,2-trinitroethyl)-nitramino acetate	$C_6H_6N_8O_{16}$	446	3.33	9	10
24	2,2,2-trinitroethyl-4-nitrazavalerate	$C_6H_9N_5O_{10}$	311	-1.00	35	10
25	Trinitropropyl-(2,2-dinitropropyl)-nitramine	$C_6H_9N_7O_{12}$	371	0.88	17	8
26	2',2',2'-Trinitroethyl-2,5-dinitrazahexanoate	$C_6H_9N_7O_{12}$	371	0.29	15	10
27	2,2,2-trinitroethyl-3,3-dinitrobutyl nitramine	$C_6H_9N_7O_{12}$	371	0.88	20	10
28	N-(2,2-Dinitropropyl)-N,2,2-trinitro-1-propanamine	$C_6H_{10}N_6O_{10}$	326	-0.63	29	10
29	1,7-dimethoxy-2,4,6-trinitrazaheptane	$C_6H_{14}N_6O_8$	298	-2.94	166	8
30	N,N'-Dinitro-N,N'-bis[2-(nitroamino)ethyl]-1,2-ethanediamine	$C_6H_{14}N_8O_8$	326	-2.78	53	10
31	Bis-(trinitroethyl)-2,4-dinitrazapentanedioate	$C_7H_6N_{10}O_{20}$	550	3.72	10	8
32	2,2-dinitropropyl-5,5,5-trinitro-2-nitrazapentanoate	$C_7H_9N_7O_{14}$	415	0.81	16	8
33	Trinitroethyl-5,5-dinitro-3-nitrazahexanoate	$C_7H_9N_7O_{14}$	415	0.81	25	8
34	2,2,2-Trinitroethyl-2,5,5-trinitro-2-azahexanoate	$C_7H_9N_7O_{14}$	415	0.81	22	10
35	N-nitro-N,N'-bis-(trinitropropyl)-urea	$C_7H_9N_9O_{15}$	459	1.25	21	8
36	2,2,2-Trinitroethyl-2,4,6,6-tetranitro-2,4-diazaheptaneoate	$C_7H_9N_9O_{16}$	475	1.71	18	10
37	Bis-(2,2,2-trinitroethyl)-3-nitrazaglutarate	$C_8H_8N_8O_{18}$	504	1.90	14	10
38	N,N'-Dinitro-N,N'-bis-3,3,3-trinitropropyl)-oxamide	$C_8H_8N_{10}O_{18}$	532	1.82	9	10

TABLE 13. (Continued)

No.	Compound	Formula	Mol. Wt.	SI	h_{50} (cm)	Ref.
39	Bis-(trinitroethyl)- 2,4,6-trinitraza- heptanedioate	$C_8H_8N_{12}O_{22}$	624	3.20	13	8
40	2,2,6,9,9-Pentanitro- 4-oxa-5-oxo-6-azadecane	$C_8H_{12}N_6O_{12}$	384	-1.58	47	10
41	1,1,1,3,6,9,11,11,11- nonanitro-3,6,9- triazaundecane	$C_8H_{12}N_{12}O_{18}$	564	1.60	12	10
42	N-(2-2-Dinitrobutyl)- N-2,2-trinitro-1- butanamine	$C_8H_{14}N_6O_{10}$	354	-2.63	80	10
43	N,N'-Dinitro-N,N'-bis-(3- nitrazabutyl)-oxamide	$C_8H_{14}N_8O_{10}$	382	-3.50	90	10
44	2,2,4,7,9,9,hexanitro- 4,7-diazadecane	$C_8H_{14}N_8O_{12}$	414	-1.43	72	10
45	N,N'-dinitromethylene- bis-(4,4,4-trinitro)- butyramide	$C_9H_{10}N_{10}O_{18}$	546	0.85	13	8
46	1,1,1,5,7,10,14,14,14- Nonanitro-3-12-dioxa- 4,11-dioxo-5,7,10- triazatetradecane	$C_9H_{10}N_{12}O_{22}$	638	2.26	11	10
47	Bis-(5,5,5-trinitro-3- nitrazapentanoyl)- methylenedinitramine	$C_9H_{10}N_{14}O_{22}$	666	2.18	15	8
48	1,1,1,4,6,6,8,11,11,11- Decanitro-4,8- diazaundecane	$C_9H_{12}N_{12}O_{20}$	608	1.89	11	10
49	1,1,1,3,6,6,9,11,11,11 Decanitro-3,9- diazaundecane	$C_9H_{12}N_{12}O_{20}$	608	1.89	10	10
50	Bis-(2,2,2-trinitroethyl) -4-nitrazo-1,7- heptanedioate	$C_{10}H_{12}N_8O_{18}$	532	0.00	29	10
51	Bis-(2,2,2-trinitroethyl) -3,6-dinitraza-1,8- octanedioate	$C_{10}H_{12}N_{10}O_{20}$	592	0.77	29	10
52	Bis-(trinitroethyl)-2,5, 8-trinitrazanonanedioate	$C_{10}H_{12}N_{12}O_{22}$	652	1.43	17	8
53	N,N'-Dinitro-N,N'-bis- (3,3-dinitrobutyl)- oxamide-triazatetradecane	$C_{10}H_{14}N_8O_{14}$	470	-2.17	37	10
54	1,1,1,3,6,9,12,14,14,14- Decanitro-3,6,9,12-tetraza- tetradecane	$C_{10}H_{16}N_{14}O_{20}$	652	0.67	19	10
55	Bis-(trinitroethyl)-5,5- dinitro-2,8-dinitraza- nonanedioate	$C_{11}H_{12}N_{12}O_{24}$	696	1.69	12	8

TABLE 13. (Continued)

No.	Compound	Formula	Mol. Wt.	SI	h_{50} (cm)	Ref.
56	2,2,4,7,7,10,12,12-Octanitro-4,10-diazatridecane	$C_{11}H_{18}N_{10}O_{16}$	546	-1.45	44	10
57	2,2,5,7,7,9,12,12-Octanitro-5,9-diazatridecane	$C_{11}H_{18}N_{10}O_{16}$	546	-1.45	37	10
58	1,4-Bis-(5,5,5-trinitro-2-nitrazapentanoate)-2-butyne	$C_{12}H_{12}N_{10}O_{20}$	616	0.00	16	8
59	1,1,1,18,18,18-Hexanitro-3,16-dioxa-4,15-dioxo-5,8,11,14-tetranitrazaoctadecane	$C_{12}H_{16}N_{14}O_{24}$	740	0.61	19	10
60	1,1,1,3,6,6,8,10,10,13,15,15,15-tridecanitro-3,8,13,-triazapentadecane	$C_{12}H_{16}N_{16}O_{26}$	800	1.71	23	10
61	2,2-Dinitropropanediol-bis-(5,5-dinitro-2-nitrazo-hexanoate)	$C_{13}H_{18}N_{10}O_{20}$	634	-1.31	138	8

TABLE 14. The drop-weight impact sensitivities of nitrate ester explosives.

No.	Compound	Formula	Mol. Wt.	SI	h_{50} (cm)	Ref.
1	1,2,3-Propanetriol trinitrate	$C_3H_5N_3O_9$	227	3.50	20	13
2	N-(2,2,2-Trinitroethyl)-nitraminoethyl nitrate	$C_4H_6N_6O_{11}$	314	2.96	7	10
3	2,2-Bis(nitroxymethyl)-1,3-propanediol dinitrate	$C_5H_8N_4O_{12}$	316	2.07	13	13
4	3-[N-(2,2,2-Trinitroethyl) nitramino]-propyl nitrate	$C_5H_8N_6O_{11}$	328	1.33	12	10
5	3,5,5-Trinitro-3-azahexyl nitrate	$C_5H_9N_5O_9$	283	0.36	21	10
6	1,9-Dinitrato-2,4,6,8-tetranitrazanonane	$C_5H_{10}N_{10}O_{14}$	434	2.05	10	8
7	4,4,8,8-Tetranitro-1,11-dinitrato-6-nitrazundecane	$C_{10}H_{16}N_8O_{16}$	504	-0.80	87	10

TABLE 15. The drop-weight impact sensitivities of miscellaneous nitroheterocyclic explosives.

No.	Compound	Formula	Mol. Wt.	SI	h_{50} (cm)	Ref.
1	Ammonium 5-Nitro-tetrazolate	$CH_4N_6O_2$	132	-1.54	30	13
2	Ethylenediammonium di-5-nitrotetrazolate	$C_4H_{10}N_{12}O_4$	290	-3.33	42	13
3	3,5-Dinitroisoxazole	$C_3H_4N_3O_5$	159	2.50	29	13
4	1,4-Dinitroglycoluril	$C_4H_4N_6O_6$	232	-2.0	100	13
5	1-Nitro-2,5-bis-(trinitromethyl)-pyrrolidine	$C_6H_6N_8O_{14}$	414	2.94	6	8
6	5-Picrylaminetetrazole	$C_7H_4N_8O_6$	296	-2.40	36	13
7	3,3,9,9-Tetranitro-1,5,7,11-Tetraoxaspiro-(5.5)-undecane	$C_7H_8N_4O_{12}$	340	0.65	66	10
8	N-(2,2,2-Trinitroethyl)-3,3,5,5-tetranitropiperidine	$C_7H_8N_8O_{14}$	428	1.62	18	10
9	N-(Trinitropropyl)-3,3,5,5-tetranitropiperidine	$C_8H_{10}N_8O_{14}$	442	0.50	29	8

TABLE 15. (Continued)

No.	Compound	Formula	Mol. Wt.	SI	h_{50} (cm)	Ref.
10	1,3,7,9-Tetranitrodibenzo -1,3a,4,6a-tetraazapentalene	$C_{12}H_4N_8O_8$	388	-3.75	85	8
11	3-6-Bis-(picrylamino)- s-tetrazine	$C_{14}H_6N_{12}O_{12}$	534	-2.27	61	13
12	1,3,5-Tris(1-oxo-5,5,5- trinitro-3-nitrazapentyl) s-triazacyclohexane	$C_{15}H_{18}N_{18}O_{27}$	882	0.00	13	8
13	Tripicryl-s-triazene	$C_{21}H_6N_{12}O_{18}$	714	-2.11	85	8

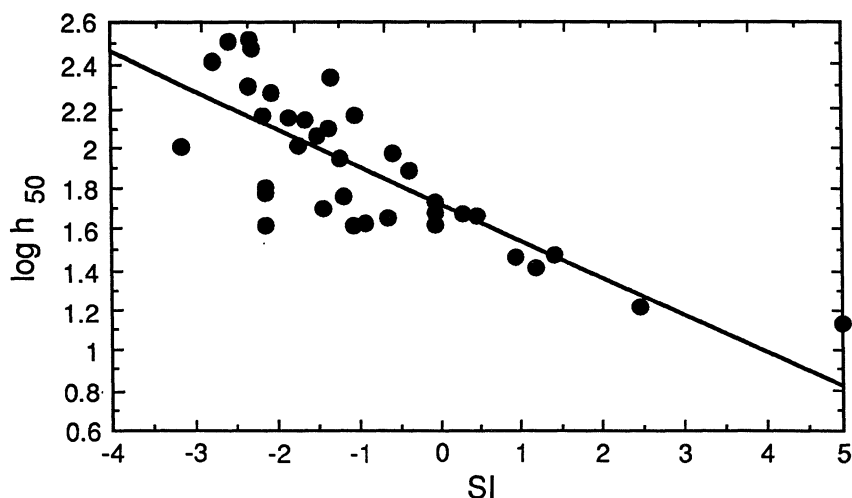


Figure 3. A plot of the impact sensitivity ($\log h_{50}$, cm) of the 40 nitroaromatic explosives in Table 2 vs the sensitivity index (SI). The regression is $\log h_{50} = 1.70 - 0.20 \text{ SI}$, $R^2 = 0.605$.

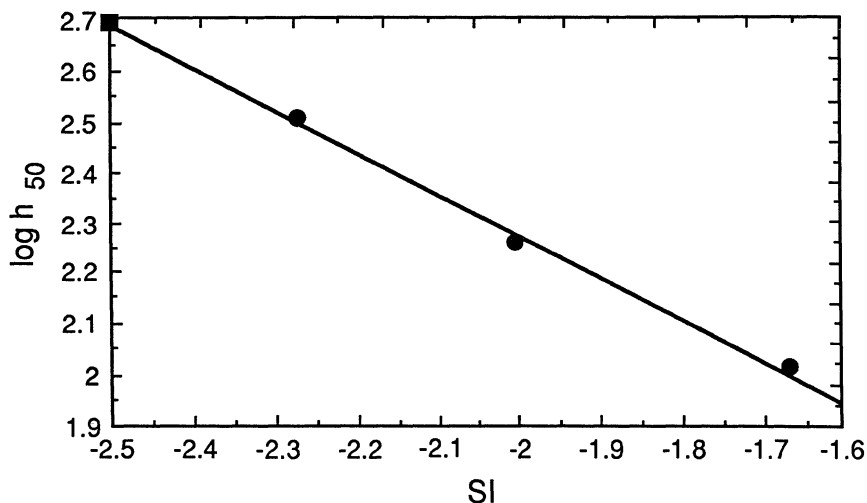


Figure 4. A plot of the impact sensitivity ($\log h_{50}$, cm) of TNB, MATB, and DATB vs the sensitivity index (SI), extrapolated to TATB. The regression is $\log h_{50} = 0.59 - 0.84 \text{ SI}$, $R^2 = 0.998$. See Table 2 - 5, 12, 15, 18 for values plotted.

An example of the use of the different families is given in Figure 5. Here we plot compounds 1,2,3,5,12,15,18,29 and 33 from Table 2, providing examples of the polynitrobenzene series, the polyaminotri-nitrobenzene series and benzotrifuroxan. To estimate the sensitivity of 5,7-diamino-4,6-dinitrobenzofuroxan (DADNBF) a tie-line between TATB and BTF is used, $\log h_{50} = 1.70 - 0.40SI$. This family relationship suggests a sensitivity of 268 cm for DADNBF. To estimate the impact sensitivity of 7-amino-4,6-dinitrobenzofuroxan (ADNBF) a tie line is constructed between DATB and BTF, $\log h_{50} = 1.70 - 0.36SI$. This estimates an impact sensitivity for ADNBF of 174 cm.

In Figure 6 we plot the impact sensitivity of the 18 1,2,4-triazoles given in Table 8. The 1,2,4-triazoles that have no other sensitive functional group generally lie above the regression observed for nitroaromatic explosives and thus form an inherently less-sensitive class of explosives.

The 1,2,3-triazoles also provide some interesting examples, Table 9. The very large difference in the impact sensitivities of 1-picryl-1,2,3-triazole compared to 2-picryl-1,2,3-triazole and 4-nitro-1-picryl-1,2,3-triazole compared to 4-nitro-2-picryl-1,2,3-triazole have been commented on previously [19]. Recent consideration of the problem [27] has ascribed the large difference in sensitivity to the facile loss of nitrogen in the 1-picryl isomers. This illustrates another use of the correlations, large exceptions point out important structural factors. This in turn suggests molecules that are interesting for detailed calculations and provides clues as to decomposition mechanisms.

Among explosives chemists the belief is widely held that ammonium salts are "unusually stable". When an acid is converted to its ammonium salt three extra hydrogens are added and the ammonium salt will certainly be more stable (i.e. less sensitive) than the parent acid. In Figure 7 we plot the SI vs $\log h_{50}$ for a variety of ammonium salts. The numbers in the figure refer to the table from which the data are taken. The solid line represents the general nitroaromatic regression and is for reference. The two extreme deviations in the sensitive direction (15-1,2) are nitrotetrazoles, an inherently sensitive class of materials. Seven of the ten ammonium salts follow the general nitroaromatic regression reasonably well. Ammonium 3,5-dinitro-1,2,4-triazolate appears to be rather more insensitive than expected. It has already been pointed out (Figure 6) that 1,2,4-triazoles are as a class less sensitive. It appears that an ammonium counter-ion provides no special "insensitivity".

In any energetic material one is pursuing a compromise between energy content and metastability. When a hot spot is formed it will grow if the rate of heat production is greater than the rate of heat loss [28,29]. In general as more nitro groups are added the available heat per molecule (Q) increases. For a homologous series, as a

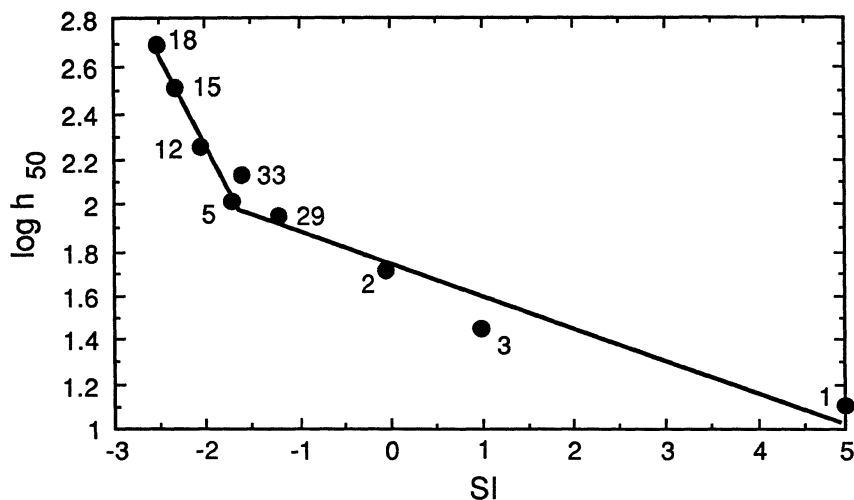


Figure 5. A plot of the impact sensitivity ($\log h_{50}$, cm) of compounds 1, 2, 3, 5, 12, 15, 18, 29 and 33 from Table 2 vs the sensitivity index (SI).

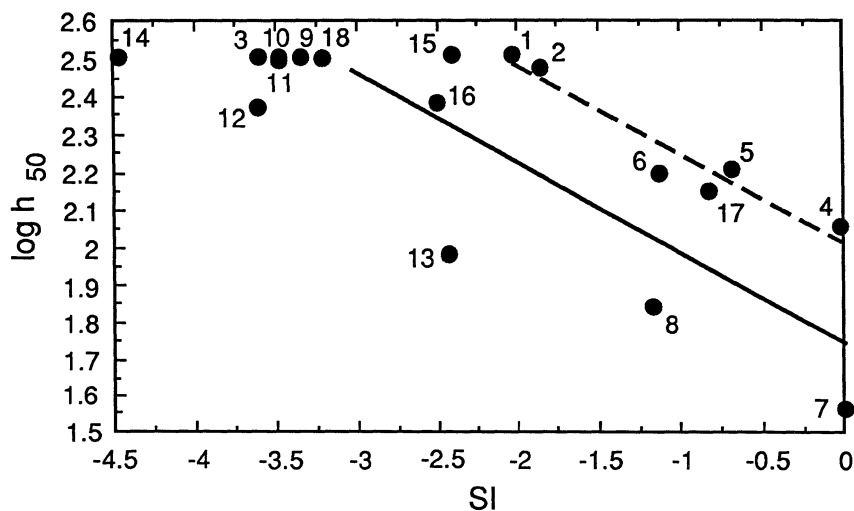


Figure 6. A plot of the impact sensitivity ($\log h_{50}$, cm) of the 18 nitro-1,2,4-triazoles in Table 8 vs the sensitivity index (SI). The regression for points 1, 2, 4, 5, 6, 17 is $\log h_{50} = 2.00 - 2.4\text{SI}$, $R^2 = 0.929$. The solid line is the regression for nitroaromatics from Table 2 and is for a reference comparison.

reaction becomes more exothermic the transition state leading to the products becomes lower (Hammond postulate) [30]. This leads to an increased rate of energy release at a given temperature. It is commonly observed in linear free energy relationships in homologous series that rate constants (k) and equilibrium constants (K) have linear relationships. So it is not surprising that the sensitivity index (an oxygen balance related number) relates in a systematic way to the impact sensitivity.

Based on an examination of the properties of various explosives tested for impact and/or shock sensitivity it would be desirable to identify the most important factors contributing to the decomposition. Kamlet and Adolph [12] suggested in 1981 "that impact sensitivities of explosives depend on the rates of thermal decomposition reactions which occur at the temperatures generated under the impact hammer, with the rate determining step usually being the homolytic cleavage of the weakest atom linkage (referred to as the "trigger linkage")." Their proposal was based in part on earlier work by Wenograd [31] which demonstrated that the time delay to explosion for most organic explosives could be described by $\tau = A \exp(B/RT)$, where τ is the delay time, T the absolute temperature, and A and B constants. This led Wenograd [31] to suggest that the important parameter in impact sensitivity is the temperature reached during the 250 μ s confinement interval under the impact hammer.

An explosive has a characteristic critical temperature, i.e. the lowest constant surface temperature at which a specific material of a specific size and shape will self-heat catastrophically. Below the critical temperature, energetic materials still decompose, but they fail to generate sufficient heat to become self-sustaining.

The critical temperature for the thermal explosion of an explosive may be calculated from the Frank-Kamenetskii equation [32]:

$$\frac{E}{T_m} = R \ln \frac{a^2 \rho Q Z E}{T_m^2 \lambda \delta R}$$

where R is the gas constant (1.99 cal mol⁻¹K⁻¹), a is the radius of a sphere or cylinder or the half-thickness of a slab, ρ is the density (g cm⁻³), Q₁ is the heat of explosion (cal g⁻¹), Z is the pre-exponential (s⁻¹) and E the activation energy (kcal mol⁻¹) from the Arrhenius expression, λ is the thermal conductivity (cal cm⁻¹sec⁻¹K⁻¹), and δ is a shape factor (0.88 for infinite slabs, 2.00 for infinite cylinders, and 3.22 for spheres). Rogers [32,33] has determined the kinetics constants for a variety of explosives (PETN, TETRYL, RDX, HMX, DIPAM, TNT, HNS, DATB, TACOT, TATB) for which shock sensitivity and impact sensitivity data are also available (Table 1). Using the kinetics constants and physical properties reported by Rogers [32,33], the heats of explosion given by Zeman et al. [34], and

the cylindrical dimensions of the NSWG small scale gap test [6] we calculate the critical temperatures for these explosives as given in Table 16.

In Figure 8 the calculated critical temperature (T_m) for the diverse set of explosives in Table 16 is plotted against the shock initiation pressure ($\log P_{90}$) taken from Table 1. The regression is $\log P_{90} = 0.007T_m - 2.03$, $R^2 = 0.848$. For these same explosives T_m plotted against the sensitivity index provides a R^2 correlation of 0.554, impact sensitivity ($\log h_{50}$) plotted against the sensitivity index for this series of explosives provides a R^2 correlation of 0.512. The critical temperature-shock sensitivity relationship is about as satisfactory at 95% TMD ($\log P_{95} = 0.007T_m - 1.87$, $R^2 = 0.823$) and at 98% TMD ($\log P_{98} = 0.007T_m - 1.76$, $R^2 = 0.808$). This relationship of calculated critical temperature and shock sensitivity is consistent with the hypothesis of Wenograd [31] and of Kamlet and Adolf [12] that the rate of thermal decomposition is a critical factor in shock and impact sensitivity.

A great deal of attention has been focussed on the notion of a critical "trigger linkage" in explosives. If such a bond could be identified, and avoided, less sensitive materials could be designed [12]. In more sensitive explosives it is likely that a single early dominant step can be identified. A detailed analysis of a series of picryl-1,2,3-triazoles has been made [27]. In less sensitive explosives complex chemistry is likely to precede a rate determining step and the insensitivity of the explosive is in fact the consequence of the chemistry preceding the rate determining step.

A good example is TATB. The thermal decomposition of TATB has been reported to consist of a slow endothermic stage followed by two slow exothermic stages, culminating in an explosive reaction above the critical temperature [35]. Sharma et al. [36] have observed the formation of furazans in impacted TATB and suggest that this is an important early decomposition step for the reaction of TATB. The heat of formation of TATB is -37 kcal/mole and for BTB it is 145 kcal/mole [37]. On converting an ortho-nitroamino functionality to a furoxan the ΔH is increased on average by 61 kcal/mole. The value for a furazan would be somewhat less, but still a substantial positive change. Thus the elimination of water (-58 kcal/mole) to form a furazan functionality is nearly a thermochemically neutral reaction. During the early stages of hot spot existence there is little early energy release to drive growth. This provides a favorable effect on sensitiveness (ease of initiating a reaction center) and on explosiveness (ease of transition to a violent explosion). Since the safety of an explosive is approximately the reciprocal of the product of these factors [38], TATB is a rather safe material (for an explosive) to work with. The inherent insensitive nature of the material resides in the thermochemically neutral chemistry required before exothermic decomposition ensues. It is difficult, in this scheme, to identify a "trigger linkage."

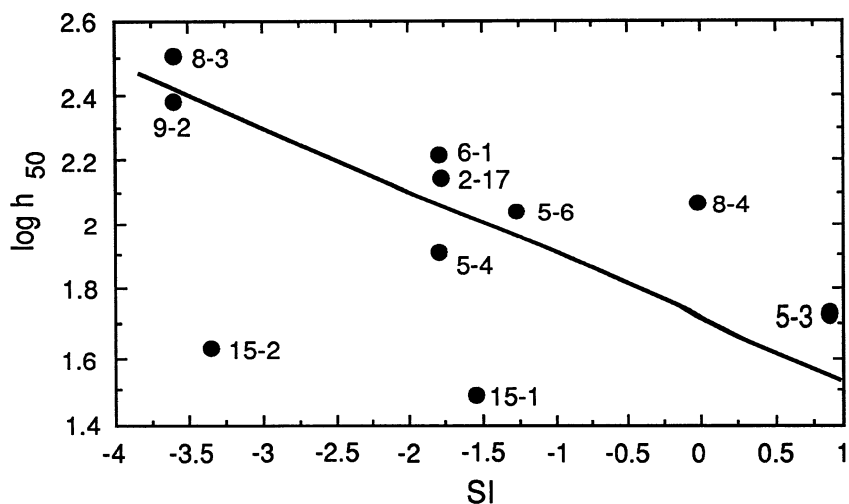


Figure 7. A plot of the impact sensitivity ($\log h_{50}$) for nine ammonium salts of nitroazole explosives and ammonium picrate. The numbers on the graph refer to the Table which is the source of the data. The solid line is the nitroaromatic regression (Table 2) and is for reference.

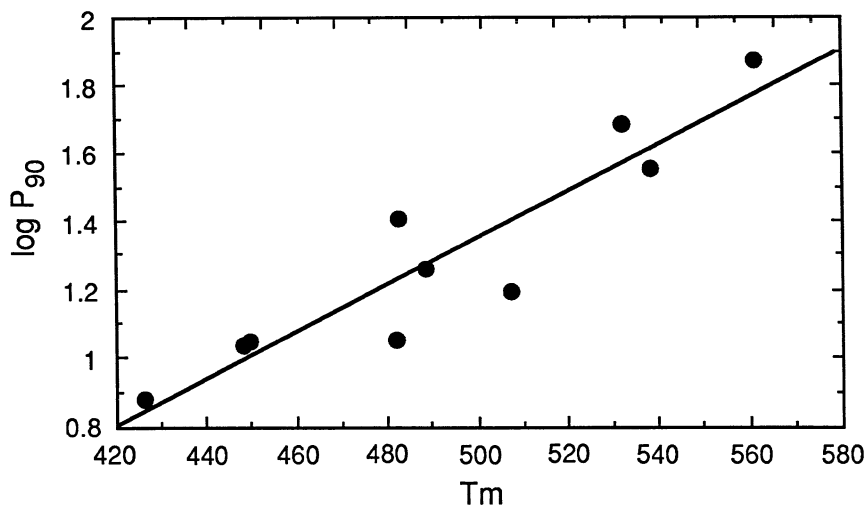


Figure 8. A plot of the calculated critical temperatures (T_m) vs the shock sensitivities ($\log P_{90}$) for the diverse set of explosives in Table 16. The shock sensitivities are from Table 1.

TABLE 16. The critical temperatures calculated from the Frank-Kamenetskii equation for a diverse set of explosives.

Compound ^a	T _m (K)	Compound	T _m (K)
PETN	427	TNT	491
TETRYL	449	HNS	508
RDX	450	DATB	533
HMX	483	TACOT	539
DIPAM	484	TATB	562

a. See Table I for abbreviations.

Nitromethane is another interesting case. Engelke et al. [39] have provided a variety of evidence that the early critical intermediate in nitromethane decomposition is the aci ion (CH_2NO_2^-). In pure nitromethane the driving force at high pressure is the electrostriction effect of the formation of the $\text{CH}_3\text{NO}_2\text{H}^+-\text{CH}_2\text{NO}_2^-$ ion pair. If this has a ΔV of -20 cc/mole one can very crudely estimate aci ion concentrations of 10^{-7} to 10^{-10} M at pressure conditions adequate to initiate homogeneous nitromethane. The aci ion is a very reactive species. It is known to be a good nucleophile, a precursor to fulminic acid, and a facile electron transfer agent. If these very small amounts of an intermediate are kinetically competent to bring about the violent exothermic decomposition of nitromethane it must indeed be very reactive. This is the basis for the arguments related to the amine sensitization of nitromethane [39]. Does one then view the C-H bond in nitromethane as the trigger linkage?

A third example is the dramatic difference in the impact sensitivity of 1-picryl-1,2,3-triazole and 2-picryl-1,2,3-triazole, as mentioned earlier in this article. An extensive structural and theoretical analyses [27] has been carried out on these isomers. It was concluded that the 1-picryl-1,2,3-triazole isomer loses nitrogen by a low activation energy, exothermic, process. This drives the propagation of the hot spot. In this case the N_2 loss is certainly a "trigger linkage".

We have shown a relationship between impact and shock sensitivity and illustrated how a sensitivity index based on oxygen balance can be used to estimate sensitivity in closely related series of molecules. It is shown that the critical temperature of an explosive calculated by the Frank-Kamenetskii equation correlates fairly well with the shock sensitivity of the material. This supports the idea that the shock or impact initiation of an explosive is primarily a thermal event and not dominated by pressure driven chemistry. The concept of the "trigger linkage" in explosives is discussed and it is pointed out that insensitive explosives will require early chemistry that is thermochemically neutral or endothermic and leads to the build-up of later strongly exothermic chemistry.

ACKNOWLEDGEMENT

This work was supported by the U.S. Department of Energy and by the U.S. Department of Defense, Office of Munitions.

REFERENCES

1. Weston, A.M., Kinkaid, J.F., James, E., Lee, E.L., Green, L.G. and Walton, J.R. (1981), "Correlation of the Results of Shock Initiation Tests", Seventh Symposium (International) on Detonation, Office of Naval Research, Washington, DC. pp. 887-897.
2. Price, D., and Liddard, T.E. (1966), "The Small Scale Gap Test: Calibration and Comparison with the Large Scale Gap Test", NOLTR pp. 66-87, White Oak, MD.
3. Price, D. (1985), "Examination of Some Proposed Relations Among HE Sensitivity Data", J. Energetic Materials, 3, pp. 239-254.
4. Price, D. (1986) "Gap Tests and How They Grow", Minutes of the 22nd Explosives Safety Seminar, Anaheim, CA, pp. 365-380.
5. Urizar, M.J., Peterson, S.W. and Smith, L.C. (1978), "Detonation Sensitivity Tests", LA-7193MS, Los Alamos, NM.
6. Ayres, J.N., Montesi, L.J. and Bauer, R.J. (1973) "Small Scale Gap Test Data Compilation; 1959-1972", Volume I, NOLTR 73-132, White Oak, MD.
7. Liddard, T.P., and Price, D. (1966) "The Small Scale Gap Test: Calibration and Comparison with the Large Scale Gap Test", NOLTR 66-87, White Oak, MD.
8. Adolph, H.G., Holden, J.R., and Chicra, D.A. (1981) "Relationships Between the Impact Sensitivity of High Energy Compounds and Some Molecular Properties Which Determine Their Performance", NSWC TR 80-495, White Oak, MD.
9. Kamlet, M.J., and Adolph, H.G., (1979) "The Relationship of Impact Sensitivity with Structure of Organic High Explosives. II. Polynitroaromatic Explosives", Propellants and Explosives, 4, pp. 30-34.
10. Kamlet, M.J. (1976) "The Relationship of Impact Sensitivity with Structure of Organic High Explosives. I. Polynitroaliphatic Explosives", Sixth Symposium (International) on Detonation, Office of the Naval Research, Washington, DC, pp. 312-322.

11. Kamlet, M.J. (1960) "Sensitivity Relationships", Third Symposium (International) on Detonation, Office of Naval Research, Washington, DC, pp. 13-34.
12. Kamlet, M.J., and Adolph, H.G. (1981) "Some Comments Regarding the Sensitivities, Thermal Stabilities, and Explosive Performance Characteristics of Fluorodinitromethyl Compounds", Seventh Symposium (International) on Detonation, Office of Naval Research, Washington, DC, pp. 84-92.
13. Stine, J.R. (1989) "A Pure Explosive Data Base", Los Alamos, NM; Coburn, M.D. (1989) private communication.
14. Lee, K-Y., Coburn, M.D. (1985) "3-Nitro-1,2,4-triazole-5-one, A Less Sensitive Explosive", LA-10302, Los Alamos, NM.
15. Lee, K-Y., Chapman, L.B. and Coburn, M.D. (1987), "3-Nitro-1,2,4-triazole-5-one, A Less Sensitive Explosive", J. Energetic Materials, 5, pp. 27-33.
16. Delpuech, A. and Cherville, J. (1978) "Relation Between Electronic Structure and Shock Sensitivity of Secondary Nitro Explosives: Molecular Criterion of Sensitivity. Part I. Nitroaromatics and Nitramines", Propellants and Explosives, 3, pp. 169-175.
17. Delpuech, A. and Cherville, J. (1979) "Part II, Nitric Esters", Propellants and Explosives, 4, pp. 121-128.
18. Delpuech, A., and Cherville, J. (1979) "Part III. Influence of Crystal Environment", Propellants and Explosives, 4, pp. 61-65.
19. Delpuech, A., Cherville, J. and Michaud, C. (1981) "Molecular Electronic Structure and Initiation of Secondary Explosives", Seventh Symposium (International) on Detonation, Office of Naval Research, Washington, DC, pp. 65-74.
20. Jain, S.R., Adiga, K.C. and Pai Verneker, V.R. (1981) "A New Approach to Thermochemical Calculations of Condensed Fuel-Oxidizer Mixtures", Combustion and Flame, 40, pp. 71-79.
21. Sundararajan, R., Adiga, K.C. and Jain, S.R. (1981) "Energetics of the Condensed Ternary Fuel-Oxidizer Systems", Combustion and Flame, 41, pp. 243-249.
22. Sundararajan, R. and Jain, S.R. (1983) "Structure and Impact Sensitivity Relation in Organic Explosives", Indian J. Technology, 21, pp. 474-477.
23. Brassy, C., Roux, M. and Ausanneau, M. (1987) "Reflexions on the Sensitivity of Polynitroaromatic Explosives", Propellants, Explosives, Pyrotechnics, 12, pp. 53-59.

24. Mullay, J. (1987) "A Relationship Between Impact Sensitivity and Molecular Electronegativity", *Propellants, Explosives, Pyrotechnics*, 12, pp. 60-63.
25. Mullay, J. (1987) "Relationships Between Impact Sensitivity and Molecular Electronic Structure", *Propellants, Explosives, Pyrotechnics*, 12, pp. 121-124.
26. Stine, J.R. (1989) "On predicting Properties of Explosives - Detonation Velocity", *J. Energetic Materials*, in press.
27. Storm, C.B., Ryan, R.R. Ritchie, J.P., Hall, J.H. and Bachrach, S.M. (1989) "Structural Bases of the Impact Sensitivities of 1-Picryl-1,2,3-triazole, 2-Picryl-1,2,3-triazole, 4-Nitro-1-picryl-1,2,3-triazole, and 4-Nitro-2-picryl-1,2,3-triazole", *J. Phys. Chem.*, 93, pp. 1000-1007.
28. Bowden, F.P. and Yoffee, A.D. (1952) "Initiation and Growth of Explosion in Liquids and Solids", Cambridge University Press, Cambridge, p. 64.
29. Dehui, L. and Yuming, X. (1987) "The Relationship Between Impact Sensitivity and Molecular Activity of High Explosives" in Jing, D. ed. *Proceedings of the International Symposium on Pyrotechnics and Explosives*, China Academic Pub., Beijing, China, pp. 800-807.
30. Hammond, G.S. (1955) "A Correlation of Reaction Rates", *J. Am. Chem. Soc.*, 77, pp. 334-338.
31. Wenograd, J. (1961) "The Behavior of Explosives at Very High Temperatures", *Trans. Faraday Soc.*, 57, pp. 1612-1620.
32. Rogers, R.N. (1975) "Thermochemistry of Explosives", *Thermochimica Acta*, 11, pp 131-139.
33. Rogers, R.N. (1988) private communication.
34. Zeman, S., Dimun, M. and Truchlik, S. (1984) "The Relationship Between Kinetic Data of the Low-Temperature Thermolysis and the Heats of Explosion of Organic Polynitro Compounds", *Thermochimica Acta*, 78, pp. 181-209.
35. Catalano, E. and Rolon, C.E. (1983) "A Study of the Thermal Decomposition of Confined Triaminotrinitrobenzene. The Gaseous Products and Kinetics of Evolution", *Thermochimica Acta*, 61, pp. 37-51.

36. Sharma, J., Hoffsommer, J.C., Glover, D.J., Coffey, C.S., Santiago, F., Stolovy, A. and Yasuda, S. (1984) "Comparative Study of Molecular Fragmentation in Sub-initiated TATB caused by Impact, UV, Heat and Electron Beams", in Asay, J.R., Graham, R.A. and Straub, G.K. eds., *Shock Waves in Condensed Matter-1983*, Elsevier Science Pub. B.V., pp. 543-546.
37. Dobratz, B.M. (1981) "LLNL Explosives Handbook", Lawrence Livermore National Laboratory, University of California, Livermore, CA.
38. Davis, W.C. (1977) "Sensitivity of TATB Explosives", LA-6676-MS, Los Alamos National Laboratory, Los Alamos, NM.
39. Engelke, R., Schiferl, D., Storm, C.B. and Earl, W.L. (1988) "Production of the Nitromethane Aci Ion by Static High Pressure", *J. Phys. Chem.*, 92, pp. 6815-6819, and references therein.

MOLECULAR ARCHITECTURE VERSUS CHEMISTRY AND PHYSICS OF ENERGETIC MATERIALS

JACK ALSTER, SURY IYER AND OSCAR SANDUS
U.S. ARMY ARDEC
PICATINNY ARSENAL, NJ 07806-5000

As part of a continuing effort to develop more powerful explosives and propellants, we are building compact molecular architectures of C-H-N-O atoms yielding energetic materials of high crystal density. These materials are expected to provide increased detonation energies as compared with currently available explosives.

In this paper, the properties of these new molecular structures will be discussed. Theoretical methods to estimate heats of formation, crystal densities and detonation properties will be presented. This will be followed by experimental results, as well.

INTRODUCTION:

When a column of explosive is subjected to an intense shock wave, a detonation wave progresses through the column (from left to right), as shown in Figure 1 (1). The shock front (Figure 1B) is followed by a chemical reaction zone where combustion of fuel-type molecular fragments by oxidizer-type fragments takes place. This process rapidly releases much gas and much energy known as detonation energy. Behind the chemical reaction zone, which is about 1mm wide are hot, dense gaseous detonation products that do work against the surrounding medium. In explosives like octanitrocubane that has no hydrogen atoms and is balanced to CO_2 , the detonation products are expected to be essentially the complete combustion gases, CO_2 and N_2 . Compared to H_2O which is a "soft" detonation gas among other gases in explosives containing hydrogen atoms, the hard molecules CO_2 and N_2 repel each other more strongly; thus are more efficient in pushing metal.

Theory helps in the design of new explosive molecules, which are likely to be more powerful (2,3). Theoretical analysis reveals that strained ring and cage molecules offer the possibility of achieving a significant increase in detonation energy. This comes from increased crystal densities and locked-in strain energies. There are good empirical methods to calculate densities for new molecules. In Stine's method (4), a least-square procedure is used to

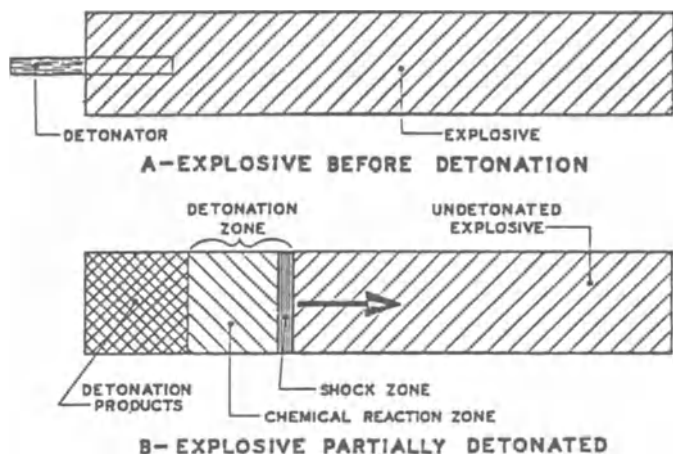


Figure 1. Progress of detonation through a column of explosive.

determine atomic volumes by minimizing the differences between observed and calculated volumes for 2051 compounds containing C, H, N, O and F atoms. This method is illustrated by calculation of the crystal density of TNT in Table 1. The agreement between calculated and experimental values is good. Using the same method, crystal densities were computed for polynitrocubanes; they are shown in Table 2 along with the experimental values.

For calculation of detonation properties, viz. detonation velocity and CJ-pressure, the Kamlet-Jacobs Simple Method (KJSM) and a more rigorous BKW - Thermo - Hydrodynamic Computer Code (Tiger Code) are available (5,6). Computed heats of formation values (7) are needed for these calculations for new explosives. By using bond contributions from known heats of combustion of many solid organic compounds and using the additivity rule, the heat of combustion is calculated for a proposed solid explosive. This value together with the equation for the combustion reaction yields the heat of formation. This procedure is illustrated in Exhibit 1 for TNT. The calculated and experimental values are in fair agreement. Exhibit 2 shows the equations for calculating detonation velocities and CJ pressures by KJSM. Table 3 shows the heats of formation as estimated above and the detonation properties for proposed polynitropolyhedranes.

Table 1. Calculation of the density of TNT by the Stine method (C H N O :
M.W.: 227.13) 7 5 3 6

NO. OF ATOMS	KIND OF ATOM	BOND CONTRIBUTION TO MOLAR VOLUME
6	C (AROMATIC)	72.570
1	C (ALIPHATIC)	13.390
3	N (NITRO)	31.104
6	O (NITRO)	76.524
2	H (BONDED TO AROMATIC C)	14.998
3	H (BONDED TO ALIPHATIC C)	17.943

$$\sum \text{ATOMIC CONTRIBUTIONS} = \text{MOLECULAR VOLUME} = 226.53 \text{ \AA}^3$$

$$\text{MOLECULAR VOLUME} = (226.53) (0.6023) = 136.44 \text{ cm}^3$$

$$\text{DENSITY} - \text{CALCULATED} = 1.66 \text{ gm/cm}^3$$

$$\text{EXPERIMENTAL} = 1.65 \text{ gm/cm}^3$$

Table 2. Calculated vs. experimental crystal densities of cubanes.

MOLECULE	CALCULATED (STINE) DENSITY (GM/CM ³)	CRYSTAL DENSITY (GM/CM ³)
CUBANE	1.37 (1.288)*	1.29
1,4-DINITRO	1.74 (1.66)*	1.66
1,3-DINITRO	1.74 (1.66)*	1.65
1,3,5-TRINITRO	1.84 (1.77)*	1.74
1,3,5,7-TETRANITRO	1.92 (1.86)*	1.81

* MODIFIED STINE USING CUBANE AS BASIS

Exhibit 1. Calculation of the heat of formation of TNT (C₇H₅N₃O₆).
7 5 3 6

$$\Delta H_{C,TNT}^{\circ} = F \left[3(C=C) + 4(C-C) + 5(C-H) + 3(C-NO_2)_{\text{AROM}} + \text{RESONANCE ENERGY OF BENZENE} \right]$$

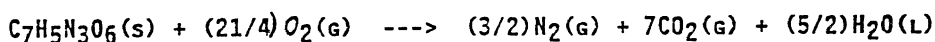
WHERE $\Delta H_{C,TNT}^{\circ}$ IS THE HEAT OF COMBUSTION OF TNT

$$\Delta H_{C,TNT}^{\circ} = -818.7 \text{ KCAL/MOL}$$

$$\Delta H_{F,TNT}^{\circ} = \sum_i N_I \Delta H_{F,I}^{\circ} - \Delta H_{C,TNT}^{\circ}$$

WHERE $\Delta H_{F,TNT}^{\circ}$ IS THE HEAT OF FORMATION OF THE EXPLOSIVE AND

$N_I = 7, 5/2$ IN THE COMBUSTION EQUATION BELOW.



$$\Delta H_{F,TNT}^{\circ} = -10.4 \text{ KCAL/MOL}$$

$$\text{EXPERIMENTAL } \Delta H_F^{\circ} = -16.0 \text{ KCAL/MOL}$$

Exhibit 2. Kamlet-Jacobs simple method (KJSM) equations.

$$D = 1.01 N^{1/2} M^{1/4} Q^{1/4} (1.00 + 1.30 \rho)$$

$$P_{CJ} = 15.58 N M^{1/2} Q^{1/2} \rho^2$$

$$Q = - \sum_I N_I \Delta H_{F,I}^{\circ} + \Delta H_{F, \text{EXP}}^{\circ}$$

D IS THE DETONATION VELOCITY IN MM/USEC

P_{CJ} IS THE CHAPMAN-JOUGET PRESSURE IN KBARS

N IS THE NUMBER OF MOLES OF GASEOUS PRODUCTS PER GM OF EXPLOSIVE

M IS THE AVERAGE MOLECULAR WEIGHT OF THE GASEOUS PRODUCTS

Q IS THE HEAT OF DETONATION IN CAL/GM

ρ IS THE DENSITY

ΔH_F° IS THE HEAT OF FORMATION

Table 3. Detonation properties of nitropolyhedranes and HMX calculated by KJSM.

COMPOUND	DENSITY GM/CM ³	ΔH_F KCAL/MOL	D MM/ μ SEC	P _{CJ} KBAR
HMX	1.90	17.4	9.12	382
OCTANITROCUBANE	2.09	81.0	9.82	467
HEXANITROTRIPRISMANE	2.14	80.0	10.04	493
TETRANITROTETRAHEDRANE	2.14	88.0	10.2	512
TETRANITROTETRAAZACUBANE	2.19	158.0	10.4	540
DINITRODIAZATETRAHEDRANE	2.19	133.5	10.9	590
UNDECANITROADAMANTANE	1.96	-136.7	9.06	383

For the more rigorous Tiger Code calculations (6), the following assumptions are made:

- 1) One dimensional flow.
- 2) Infinite reaction rate, which implies an infinitely small reaction zone length.
- 3) Chemical equilibria at the CJ-plane

and 4) C-J condition, viz. the particle velocity at the CJ plane is sonic with respect to the detonation front. This condition implies that only energy released by the explosive between the shock front and the CJ plane supports the detonation front, i.e., keeps it from attenuating. The BKW equation of state which is used to describe the hot, dense detonation gases used in this code is shown in Exhibit 3.

Thermohydrodynamic calculations yield the energy per unit volume released on detonation of the explosive (relative to TNT) as a function of V/V_0 the ratio of the volume of the expanding gases to the initial volume of the intact explosive. Figure 2 shows results for several proposed high energy density molecules. As can be seen, they are predicted to be substantially more powerful than HMX.

Exhibit 3. BKW equation of state.

$$P = RT/V [1 + \chi e^{\beta \chi}]$$

where,

$$\chi = K/V(T+\Theta)^{\alpha}$$

$$K = \delta \sum_i X_i k_i = \text{covolume}$$

X_i = mole fraction of i 'th product gas

and $\alpha, \beta, \Theta, \delta$ are adjustable parameters.

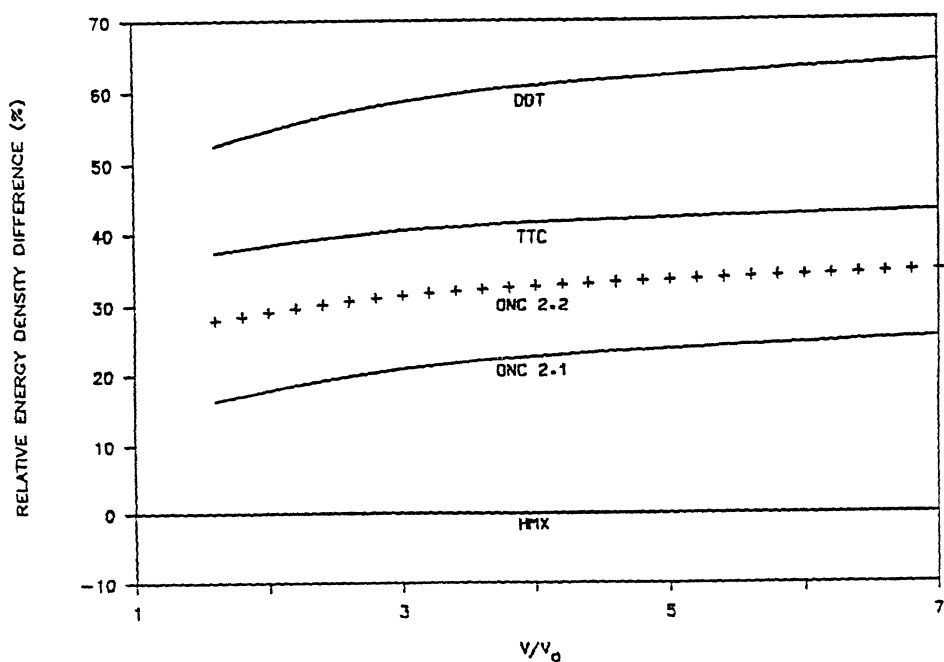


Figure 2. Calculated explosive output along the isentrope - relative to HMX (ONC: Octanitrocubane; TTC: Tetranitrotetrazacubane; DDT: Dinitro-diazatetrahedrane).

The compact cage molecules, octanitrocubane and tetranitro tetraazacubane and diazadinitro tetrahedrane, have molecular strain energy locked-in which is released along with the internal combustion energy when they explode. The strain energies in these molecules are high as demonstrated in Table 4 for the case of cubane.

Table 4. Calculated and experimental strain energies for cyclic systems (kcal/mole).

COMPOUND	THIS WORK	EXPERIMENTAL
CYCLOBUTANE	27.74	27.0
1,1-DINITROCYCLOBUTANE	27.2	-
1,2-DINITROCYCLOBUTANE	37.85	-
AZETIDINE	24.7	26.2
N-NITROAZETIDINE	21.1	IN PROGRESS
3,3-DINITROAZETIDINE	33.45	-
1,3,3-TRINITROAZETIDINE	38.9	37.0 ^A
CUBANE	163.3	161

(A). R. WILLER, MORTON THIokol INC., PRIVATE COMMUNICATION

SYNTHESIS OF MORE POWERFUL EXPLOSIVES:

ARDEC's more powerful explosives program focuses on the synthesis of two classes of energetic compounds, viz., carbocyclic/heterocyclic polynitro cage compounds and strained-ring compounds (3). Cage molecules have closed, compact three dimensional skeletal frames whose faces consist of carbocyclic or heterocyclic rings. The driving force behind the synthesis program is the observation that (a) cage molecules are inherently more compact than their open-structured molecular counterparts and (b) the maximum detonation pressure is a sensitive function of the crystal density of the explosive. Thus, the density of cubane, a cage molecule, is 1.288 g/cm^3 , as compared to a density of only 0.93 for the isomeric $(\text{CH})_8$ eight-membered, tub-shaped

ring compound, cyclooctatetraene.

Previous papers on this subject (2,3), reported on the concept of more powerful cage explosives and on target compounds of the carbocyclic cage variety whose syntheses constitute milestones toward optimally nitrated compounds. They included discussions of detonation performance calculations and approaches, both direct and indirect, to the synthesis of polynitrocage compounds. In this paper, we will trace the development of the program since then and cite specific accomplishments.

Theory of Stability:

A variety of cage systems which include propellane, bicyclopentane, and cubane are being investigated. The stability of these cage systems is derived from different factors. For example, a new type of bonding, the " σ -bridged π -bond," has been advanced to describe the central bond in the cage system (1.1.1) propellane (8). Essentially, propellanes are stable because they require a high activation energy for decomposition. This observation along with the recent discovery of σ -bridged

π -bond (8) strongly indicates that molecular configurations not previously considered possible or stable are indeed possible and stable in many cases. It is even possible to attach power-producing nitro groups to such strained, compact cage structures.

Polynitrocubanes:

Di-, tri- and tetranitrocubanes* have been successfully synthesized; their observed crystal densities are shown in Table 5. As predicted, the densities of nitrocubanes increase as a function of nitro group content.

Polynitro Cubane-Like Cage Systems:

New molecules of this cage type containing as many as six nitro groups have been synthesized and tested. Initial experiments suggest that D_3 -hexanitrotrishomocubane** and hexanitropentacycloundecane** (Figure 3) are less sensitive, and theoretical calculations show they are more powerful than TNT (Table 6). In Figure 4 the computed performance of these molecules, as a function of V/V_0 along the

* Synthesized by P.E. Eaton et al, U of Chicago

** Synthesized by A.P. Marchand et al, U of North Texas

Table 5. Observed crystal (xtal) densities of cubanes.

	<u>XTAL DENSITY (g/cc)</u>
CUBANE	1.29
1,3 DINITRO CUBANE	1.65
1,4 DINITRO CUBANE	1.66
1,3,5 TRINITRO CUBANE	1.74
1,3,5,7 TETRANITROCUBANE	1.81

isentrope, shows they are substantially more powerful than TNT. Also, hexanitropentacyclo undecane which, unlike the isomer, contains a strained four-membered ring is slightly more powerful than the isomer. The low sensitivity of the two molecules, is apparently related to the presence of geminal dinitro groups in these molecules. This opens the exciting prospect of building low sensitivity into a molecule even while endowing it with more power - a feat which defies conventional wisdom.

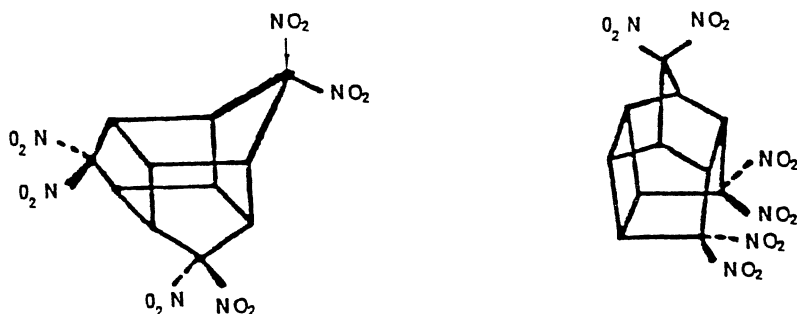


Figure 3. Hexanitro cubane-like cage molecules.

Table 6. Polynitro cubane-like cage molecules.

<u>Compound</u>	<u>Density</u>		H_f^O	<u>Computed detonation velocity</u>	<u>Computed detonation pressure</u>	<u>Sensitivity**</u>
	<u>Computed</u>	<u>Exptl</u>	<u>computed</u>			
D ₃ -hexanitro- trishomocubane(9)	1.836	1.827	-37.8	7.83	288	0.94
Hexanitropenta- cycloundecane (isomer of above)	1.836	1.827	-23.9	7.86	292	0.76

*Synthesized by A.P. Marchand et al, U of North Texas

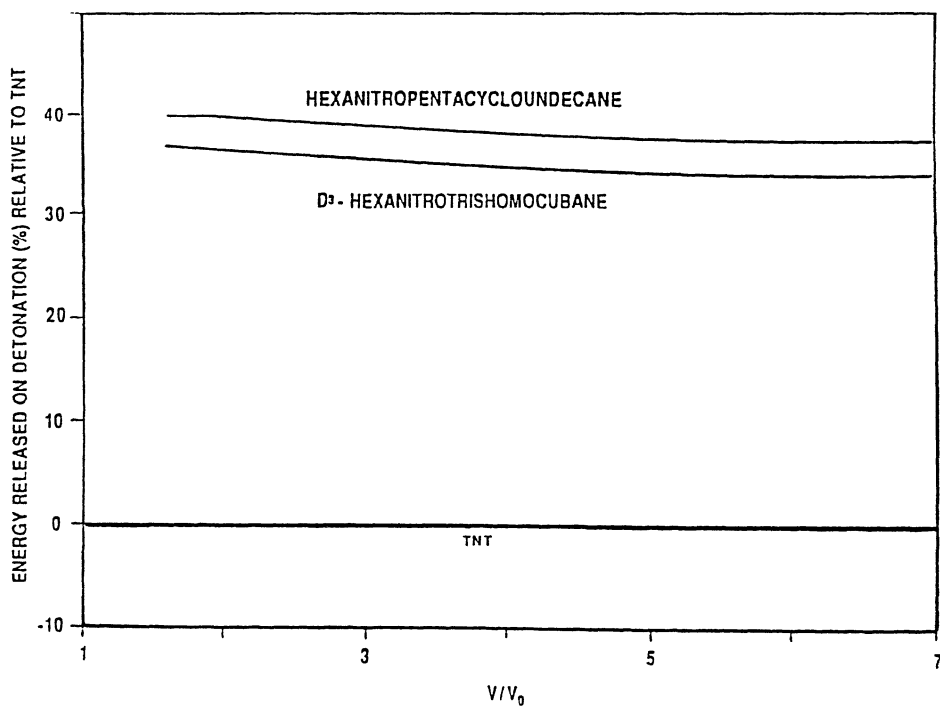
**Relative to TNT
=1.

Figure 4. Calculated explosive output along the isentrope - relative to TNT.

Table 7. Properties of 1,3,5,7-tetranitroadamantane (TNA)

<u>Property</u>	<u>Tetranitroadamantane</u>		<u>TNT</u>
	<u>Theoretical</u>	<u>Experimental</u>	<u>Experimental</u>
Density (g/cm ³)	1.59	1.61	1.65
5 sec explos temp (°C)	--	400	400
Impact sens. (cm)	--	Insensitive ^a	63
Det. velocity (mm/μs)	6.66 ^b	6.50	6.80
Det. press (kbar)	182	--	207, calc.

^a Impact of a 2.5 kg drop hammer from the maximum height of the machine (240 cm) failed to initiate 1,3,5,7-TNA.

^b $\Delta H_f = -76.8$ kcal/mole

^c 3/8 inch confined tube.

Polynitroadamantanes:

Polynitroadamantanes represent a class of potentially powerful explosives of low sensitivity. To date 1,3,5,7-tetranitro adamantane (1,3,5,7-TNA) was successfully synthesized* in multi-gram quantities and was tested for explosive properties. The data for 1,3,5,7-TNA and TNT are shown in Table 7. It should be noted that TNA is very insensitive to impact. In recent months, the 2,2,4,4-TNA isomer has been synthesized. The optimally nitrated adamantane as determined by theoretical calculations is undecanitro adamantane (11 nitro groups) predicted to be about 15% more powerful than HMX.

* By G.P. Sollott and E.E. Gilbert, ARDEC.

REFERENCES

1. Fickett, W. and Davis, W.C.: 1979, Detonation, U of California Press, CA.
2. Alster, J., Sandus, O., Gentner, R., Slagg, N., Ritchie, J.P., and Dewar, M.J.S.: Calculations of Molecular Properties for High Energy Polynitropolyhedrane Molecules, 1981, ARO Meeting on Synthesis of High Energy Molecules, Hilton Head, S.C.
3. Sollott, G.P., Alster, J., Gilbert, E.E., Sandus, O., and Slagg, N.: "Research Towards Novel Energetic Materials", 1986, J. Energ. Materials 4, p. 5.
4. Stine, J.R.: "Prediction of Crystal Densities of Organic Explosives by Group Additivity", 1981, LANL Report LA-8920.
5. Kamlet M.J. and Jacobs, S.J.: 1968, J. Chem. Phys. 48, p. 23.
6. Cowperthwaite, M. and Zwisler, W.H.: "Tiger Computer Program Documentation", 1973, SRI Publication No. Z-106.
7. Arthur D. Little, Inc.: "Study of Pure Explosive Compounds, Part II, Correlation of Thermal Quantities with Explosive Properties", 1947, Office, Chief of Ordinance. Contract NO. W-19-020-ORD-6436, Report # C-57625.
8. Jackson, J.E. and Allen, L.C.: 1984, J. Am. Chem. Soc. 106, p. 591.
9. Velicky, R.W., Iyer, S., Campbell, C., Sandus, O., Alster, J., Marchand, A.P., Sharma, G.V.M., and Annapurna, G.S.: 1988, J. Energ. Materials 6, p. 145.

EMISSION SPECTROSCOPY AS A TOOL TO DETECT DECOMPOSITION PRODUCTS OF LASER IRRADIATED EXPLOSIVES

B.J. van der Meer

Prins Maurits Laboratory TNO, P.O. Box 45, 2280 AA Rijswijk, The Netherlands

According to the scope of this Nato Advanced Study Institute the adjoining text reports on the investigations on explosives, which have been performed in recent years at the Prins Maurits Laboratory in the Netherlands, preceded by a brief review of the basic processes which may occur in laser irradiation of explosives. One of the main objectives of the research programme was, and still is, the detection of decomposition intermediates which are formed under explosive, or similar, conditions. Special attention was paid to the detection of the primary species formed during the first steps in the decomposition reaction. Because of the fast rates involved, unconfined explosive material was irradiated with a UV laser pulse of about 15 nsec time duration. The temperature of the irradiated layer increases within the time duration of the laser pulse to high a value, probably more than 1000 K, depending on several parameters, such as the laser intensity for example. The induced decomposition is accompanied by light, emitted by the decomposition products present in the plume of the irradiated explosive. The dispersed, emitted light, detected with a gated optical multichannel analyser, results in a spectrum characteristic for these products. The experiments show (i) that primary explosives are easily initiated by the laser light, while unconfined secondary explosives cannot be initiated; (ii) the prompt continuum-like emission of irradiated primary explosives show that the metal atom is initially present as a decomposition product. In the case of mercury fulminate other species show up about 350 nsec later, while the continuum is disappearing; (iii) The prompt emission spectrum of secondary explosives contains a continuum and, superposed on, it band and line emission which remain present in delayed emission spectra; (iv) Little influence was found of either the wavelength of the laser light on the sensitivity of lead azide or (v) on the species identified in the emission spectra of several explosives recorded after uv and after visible laser light irradiation. Though the variety of detected decomposition products is less than with the use of a mass spectrometer, it is believed that emission spectroscopy of laser irradiated explosives is a promising method to obtain insight into fast decomposition reactions. The capabilities thereof must be explored more extensively.

1. Introduction

The chemical decomposition mechanisms and pathways of explosives and the influence of the physical conditions thereon form a complex problem. The large molecules involved, which decompose into several reactive species at high temperature and pressure, make it difficult to obtain insight into the decomposition process. Mechanisms to interpret the experimental results have been drawn up only parsimoniously though the decomposition processes have been extensively investigated, mostly in so called slow thermal decomposition experiments (heating rate, let's say, on a second's or longer time scale). These experiments have revealed much information about the decomposition processes, but the results have sometimes led to various propositions of the decomposition pathways [1-4]. Many parameters, such as temperature, grain size, reaction volume, ambient pressure, reaction products, etc., as well as solid phase, liquid phase and gas phase decomposition, turn out to be important to (the rate of) the decomposition process.

Fast decomposition reactions have been investigated less extensively. However, with use of the recently available fast detection systems it is possible, in principle, to follow chemical reactions on a microsecond or shorter time scale. The first few steps in the decomposition reaction are of special interest. Due to the formation of, sometimes, reactive species (like NO_2 , OH, etc.), it is often difficult, if not impossible, to draw up these first steps from a long time scale product analysis of a slowly decomposing explosive. Furthermore, it has been stated that the reactions taking place in the various stages to detonation will probably be different [5]. As these stages will be passed through quickly, fast initiation and detection techniques are necessary.

Several techniques have been used to follow explosive reactions on a shorter time scale, such as mass spectrometry [6,7,31,46] and emission spectroscopy [11-14]. Mass spectrometry seems more universal as it can identify many species relatively easily. But due to the inherent instability of especially explosive molecules and some of the decomposition intermediates, the ionisation process can generate secondary species. This influence of the ionisation process is difficult to avoid. Also, the time resolution achieved in mass spectrometric techniques is not high enough, unless sophisticated and expensive techniques are used. On the other hand, emission spectroscopy is a fast, non-intrusive, sensitive detection technique. Furthermore, there is little spectroscopic information about the decomposition reactions of explosives. It is this technique (emission spectroscopy) that has been used in the experiments described below to investigate fast (explosive) decomposition reactions induced by a nanosecond laser light pulse.

Because of the established complexity of the decomposition process, it seems obvious to turn to a well defined and relatively simple system to investigate: the gas phase molecule under collision-free conditions

(for instance in a molecular beam). In these experiments, explosive molecules are seeded in an inert monoatomic gas (usually He) and forced to expand through an orifice into a vacuum. Only the molecular states close to the ground state are then populated (i.e. the temperature is only a few degrees from absolute zero while the molecules are still in the gas phase). Such experiments have been performed, among others, by Zuckermann [8] and Zhao [9], amongst others. Cold RDX and HMX molecules are selectively pumped, with the use of laser light, into a particular dissociative state. The dissociation products are probed using a second laser light pulse of the proper wavelength. In this way, Zuckermann et al. showed that OH was a primary decomposition product of both RDX and HMX, a molecule which is seldom reported to be observed in slow thermal decomposition experiments, with these explosives, as it is quite reactive. However, Zhao concluded from careful analysis of his experimental results, obtained with similar excitation equipment, that OH was not formed in the first few steps of the decomposition reaction. Another interesting observation made by Zuckermann [8] was the absence of OH emission by dimers of RDX or HMX. Apparently, the decomposition channels for single molecules do not necessarily coincide with those of an "interacting collection of molecules". It is known from cluster spectroscopy that clusters can reveal dissociation dynamics and channels which are different from single molecules [10]. So, on the one hand it is tempting to choose the more amenable gas phase to investigate the decomposition pathways of explosives, while on the other these pathways may appear to be determined on a more condensed level. In the experiments described below, granular (or powdered) explosives were used.

Laser irradiation of explosives is mostly used for investigating the initiation sensitivity for laser light [33,34,47,48,57]. However, it also offers the possibility to examine fast decomposition reactions. As the decomposition and the passing through the various stages to detonation occurs on a fast time scale, the initiation¹ mode must also be fast. Because shock initiation hampers the detection of emitted light, use of laser light to initiate the explosive is particular well suited. Not only because it offers the opportunity of fast initiation but also to simulate a variety of other initiation or ignition modes, such as heating (photothermal initiation), shock generation ("photoshock" initiation) or through specific chemical processes (photochemical initiation), by changing the pulse duration of the laser pulse, the intensity, the fluence (energy of the laser light per unit area), the wavelength, the power, etc.. These mechanisms are described in section 1.1.

1 The term initiation usually refers to either the process by which the reaction is started and grows to a detonation or it refers to the repeating process of regeneration of the reaction as it takes place in a detonation front [4]; the term ignition is more commonly used to indicate the inducement of burning, etc.

In addition to initiating the explosive, the decomposition products must be detected in order to approach our aim: to gain more insight into the first stage(s) of the decomposition reaction of explosives.

The decomposition of explosives, after laser irradiation, is accompanied by emission of light. This emission is a waste of energy for the performance of an explosive, but we gratefully make use of it. Light emission can be induced in two ways. Firstly, as a result of a physical law (Stefan-Boltzmann) stating that a body (a solid, a gas, etc), which is in thermal equilibrium with its (local) surroundings and has a temperature above zero Kelvin, has to emit light. The energy is gathered by the body through collisions or through light absorption. The second way is by the formation of reaction products in an excited state. Thermal equilibrium is not necessary. Excess energy can be given off by the emission of a photon.

The spectrum of the emitted light is characteristic for the atoms, ions, molecular fragments or even clusters of molecules present in the plume of the decomposing explosive. This allows for the detection of short living decomposition intermediates, such as radicals and other reactive species like NO_2 or HCN , which are frequently detected as decomposition products of RDX or HMX.

Due to the high temperature of a decomposing explosive (up to 3000-5000 K in the detonation front) a significant fraction of the light is emitted in the visible and ultraviolet part of the electromagnetic spectrum coincident with the sensitivity window of the optical detection system. An additional advantage of making use of the light emission is that reaction intermediates formed in, for instance, their ground state and therefore "invisible" for the detection system can be excited by light of the proper wavelength generated in its environment (radiation transfer) or through probe laser light and then become visible by the emission of a photon. The former process can be expected to take place shortly after the laser pulse has passed, as the initial light emission turns out to be a continuum and light of the proper wavelength is certainly present.

If the light detection system can be used in a time-gated mode, information about the evolution in time of the decomposition process can be obtained as well. As already mentioned above, different chemical reactions are expected to take place in the various stages to detonation. Detection systems, faster than the one used in the experiments described below, with the minimum time gate of 3.5 nanoseconds are commercially available. The detonation front has a velocity of, typically, 1 - 8 km/sec and in ideal situations a width of approximately 1 μm or less, which actually requires a picosecond time resolution to resolve decomposition products formed and, possibly, consumed closely at the detonation front. Chemical reactions on this time scale of decomposition products have been reported [55].

1.1. INITIATION/IGNITION MECHANISMS.

Our aim is not to obtain more insight into the interaction of laser light with the explosive material. Of course, there must be a mechanism that couples the laser light and the explosive. To understand the emission spectra that will be shown later, a brief survey will be given of a number of mechanisms through which an explosive can be ignited or initiated by laser light.

In this and later sections we will frequently refer to results and phenomena observed after laser irradiation of polymers, biological tissues, semiconductors, metals, etc., as there exists significant correlation between results obtained in similar experiments using these different kind of materials. Because much more has been published in recent years on laser irradiation of those materials than on laser initiation of explosives, it is worth the effort in following the progress made in that field of research. Especially illuminating are the experiments performed on biological tissues and organic polymers as these materials have similar molecular and spectroscopic properties to many explosives, except, of course, for the explosive property. Good introductory reports are [15-17] for the irradiation of polymers and biological tissues with uv lasers light. For a discussion of phenomena observed in irradiating metals we refer to [18-21].

1. An established method used to initiate explosives is to heat them. Using laser light, the intensity must be kept low, so that the evaporation rate is low. It is well known that absorbed (laser) light degrades rapidly, on a picosecond time scale, into heat. This way of heating is termed *photothermal*. The temperature of the irradiated surface layer of the explosive will rise to a final temperature which is depending on the heat capacity, the heat conduction and the linear absorption coefficient of the target. The coupling between laser light and a target is frequently expressed in a so-called *thermal coupling coefficient* [58], defined as the ratio of the deposited energy into the target (determined from the temperature rise of the irradiated material, the heated volume and the volume specific heat) to the energy in the laser pulse. Due to the temperature rise the decomposition rate enhances according to the well known Arrhenius term and eventually an explosive reaction takes place. For an irradiation fluence just below the ablation² threshold the temperature rise can be as large as a thousand degrees or more for a 10 mJ/cm², 20 nsec excimer laser light pulse [22,23].

Eggert [24] showed that the amount of light energy (millisecond exposure time to light of a flash lamp) needed to initiate nitrogen iodide decreased linearly with the initial temperature of the irradiated explosive and converges toward zero at the dark ignition temperature of the sample. Similar observations were obtained with lead azide and some other explosives. These results indicate a photothermal initiation mechanism. Roth [24] arrived at the same conclusion. The

² The process by which the material is blown off the surface by light irradiation is called ablation. Ablation encompasses cutting, melting, vaporisation, etc.

temperature rise of confined lead azide at room temperature, after argon flash-bomb irradiation (microsecond exposure time), as a result of a photochemical initiation mechanism, was estimated to be ca 35 °C, which is much too low to lead to a thermal explosion. However, recently, Chaudri [26] concluded from experiments with Nd:Yag laser light (nsec exposure time) irradiated lead azide films, that the temperature rise due to absorption of the laser light by the explosive (only 2K could not be responsible for the initiation. He concluded that the origin of initiation is formed by hot spots (i.e. small impurities (inclusions) which act as good light absorbers and which obtain a high enough temperature to initiate the explosive).

The theory on light induced thermal explosions is limited. Some theoretical analysis can be found in [27-30]. The photothermal initiation mechanism is complicated because of phase changes, melting, sublimation and vaporation processes, which are not usually taken into account. The same holds for the change of the absorption and reflection coefficient by these processes.

2. If the light intensity is high enough, the front layer of the explosive is rapidly heated to a temperature where significant vaporisation, melting, decomposition etc., (i.e. ablation), takes place. The thermal coupling coefficient, as a function of the laser pulse energy, decreases as a result of the transport of energy away from the surface by ablated products. The onset of ablation is accompanied by a shock pulse travelling into the explosive [32]. This process can be fast. Already during the laser pulse a high temperature, high pressure, gas layer of vaporized and decomposed material is formed in front of the explosive which subsequently expands away from the explosive's face. The impulse transfer can be characterized by a *mechanical coupling coefficient* C_m , which is defined as $C_m = P_a/I = J/E_1$ where P_a is the generated peak pressure, I the intensity of the laser light on the sample's surface, J the total momentum imparted to the target and E_1 the energy of the laser light. The larger the C_m , the larger the impulse transfer to the target. Typical values of the C_m are between 10^{-4} and 10^{-5} N/W for irradiation intensities larger than 10^8 W/cm² (C_m is a function of the intensity of the laser light). For these laser intensities a peak pressure of more than 100 MPa can be generated [35], a value that compares favourably with experimental results obtained with irradiating organic polymers with UV light. This peak pressure is high enough to initiate some explosives (*photo-shock initiation*).

It is expected here that the minimum intensity for initiation, the critical intensity (for a certain pulse duration), depends on the wavelength of the laser light. Many explosives show an increase in the linear absorption coefficient from the visible to the UV. Therefore, the absorption depth (defined as the inverse of the absorption coefficient) of the laser light decreases in that wavelength direction also. As the long wavelength absorption coefficient is relatively low, a large amount of material must be heated and, because of the fixed amount of energy in the laser light pulse, the temperature rise will be relatively low. Going to a shorter wavelength the absorption depth

decreases resulting in a higher temperature of the irradiated layer. Ablation processes are quite effective here. This, and the high temperature, will facilitate the initiation process [60]. At still shorter wavelengths (larger absorption coefficients), the now appreciably heated surface layer is very thin and a lot of energy will be lost to its surroundings. The critical intensity is expected to increase in this wavelength region. This agrees with the observations that unconfined PETN can be initiated with 266 nm [45], 308 nm and 355 nm [53], but not with 193 nm, 248 nm [39], 532 nm [53], 694.3 nm and 1064 nm [45] laser light.

The maximum laser-explosive matter interaction time is about 15 nsec, the time duration of the laser pulse, of course. However, it can be significantly shorter as the laser light can be absorbed by the rapidly formed gas layer (or plasma) of decomposition products. The light pulse is partially shielded from the surface of the explosive (laser pulse blocking) which therefore receives much less energy and the thermal coupling coefficient decreases. A plasma is a particularly good laser light absorber [61] if the laser frequency is below the plasma frequency, but molecular species and clusters ablated from the irradiated explosive can absorb the laser light as well. Such processes have been proposed to explain the observation of a fast peak in mass spectrometric experiments with laser irradiation of refractory and superconducting materials. This peak was composed of neutrals as well as of species ionised by the absorption of laser light [23,49]. It will be clear that the emission spectra recorded during the laser pulse can be disturbed by these processes. Carbon containing explosives (all secondary explosives) may have elemental carbon among their decomposition products, having a relatively strong transition at 248 nm. A broad emission line is observed at this position in the emission spectrum of the investigated secondary explosives when the 248 nm laser line of the excimer laser is used, while only a narrow emission line is observed after irradiation with 694.3 nm laser light, probably as a result of the above effect.

3. The third initiation mechanism to be mentioned, is a mechanism based on the capability of UV light to promote an electron to a higher electronic state, which is often of a dissociative character [16]. The dissociation products expand away from the surface with a high velocity. This *ablative photochemical decomposition* mechanism is frequently used in the integrated circuit industry to etch clean patterns in resists [62]. Due to the decoupling of the dissociation products from the explosive little energy absorbed in the irradiated layer is transferred into the rest of the material. The initiating power is provided by the shock pulse created by the expanding gases. The photochemical mechanism is usually accompanied by some photothermal heating. As far as I know, there is no conclusive evidence that an explosive can be initiated by a purely photochemical mechanism. However, based on the spectroscopic similarities with polymers, ablative photochemical decomposition can be expected to take place during irradiation of secondary explosives with UV laser light. Photochemical dissociation is observed only for UV light. (Hold your hand in the uv beam of a pulsed excimer laser and little will be felt.

The sensation will be quite different, however, when visible or IR laser light is used!) If this mechanism is operative, some influence of the laser wavelength on the initial decomposition products can be expected.

4. The initiation mechanisms discussed above all rely on the ability of the explosive to absorb the laser light. However, it is also possible to initiate an explosive, not because the frequency of the laser light is in resonance with a molecular or a solid state transition, but because the electric field strength of the laser light is so high that breakdown occurs. This phenomenon is often observed in experiments where metallic targets are irradiated. The plasma formed in front of the target absorbs the laser light which results in a high temperature detonation wave travelling through the ambient medium in the direction of the laser light. In air, ionised nitrogen and oxygen were observed [66]. The intense light, emitted by the shock front of the detonation wave, can cause initiation of an explosive. An enhanced thermal coupling coefficient is observed at the onset of plasma formation. As pressed primary explosives, like the metal azides, have a metallic-like surface, the light intensity must be kept below the detonation wave threshold if the recorded emission spectra may not be polluted with air species and reaction products of air species and explosive decomposition material.

It will be evident that this variety of initiation mechanisms can be used to induce various decomposition reactions of explosives. However, except for the thermal mechanism at low irradiation intensity, the initiation mechanisms do not appear single. Photoshock and photochemical initiation [62] is accompanied by a thermal contribution. The photochemical mechanism may give rise to an initial emission spectrum which is (somewhat) different from those recorded after shock initiated and thermally initiated explosives.

1.2. THE AMBIENT MEDIUM.

The ambient medium offers a possibility to influence the initiation threshold. The transfer of energy is determined by the residence time of this layer close to the surface of the explosive material. A high ambient pressure acts like a piston and prevents the gas layer expanding away "too quickly" from the explosive. Air is a good candidate. (It also accomplished a higher emission intensity of the decomposition products than vacuum [17]. Of the inert gases, helium induces a higher emission intensity than argon, probably because argon de-excites excited molecules more efficiently than helium).

Furthermore, the ambient pressure also influences the impulse transfer to the target [35]. An increase in the peak pressure of the shock wave in the target, with increase of the ambient pressure between 0.1 - 1 atmosphere, is observed after laser irradiation of cellulose acetate targets. Too high a pressure may reduce the peak pressure in the target due to decomposed material redeposited onto the surface of the explosive. An ambient pressure of about 1 atmosphere is used in the experiments described below.

2. Materials and Methods

2.1. SAMPLE PREPARATION

In each experiment an amount of 20 μ l of a solid explosive material was used to fill a cylindrical cup of 5 mm diameter and of 3 mm depth. It was considered that the characteristics of the sample holder were important [39] because they influence the critical energy. Therefore they will be described in detail here. The sample holder had a shaft drilled along the symmetry axis of a cylindrical metal sample holder, which had a total length of 20 mm and a diameter of 15 mm (see figure 1).

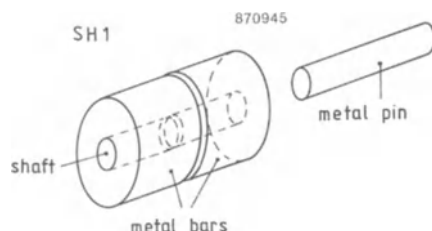


Figure 1. Sample holder used to record an emission spectrum at a distance from the explosives face.

A metal pin of 17 mm fitted this shaft, leaving the small cup of 3 mm depth and 5 mm diameter. This sample holder was used in experiments where the emission was sampled at a distance from the sample's face. The weight of the metal bar and of the metal pin was 27 gr. and 2.6 gr., respectively.

Another sample holder (weight 23 gr.) (see figure 2) had a symmetrical wedge-shaped notch cut in the middle of the sample holder, so that a 1-mm-wide slit was obtained, which allowed for the observation of light emitting species as close as possible to the surface of the irradiated explosive. The length of the pin fitting the shaft was 9.25 mm (weight 1.4 gr). To image the slit on the entrance slit of the spectrograph, a small hole (1 mm diameter) was drilled into the wall just facing the slit in the sample holder (see figure 2.). With the use of a He-Ne laser, the sample holder could be accurately positioned. The duplication of the position was assured by a small hole in the front side of the sample holder which fitted exactly into a pin in the base plate.

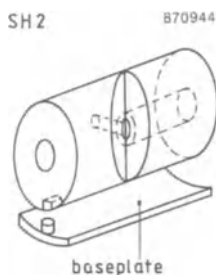


Figure 2. Sample holder used to record emission spectra close to the sample's face and the initial emission spectra.

2.2. THE LASER SYSTEM

UV laser light of a Lambda Physik excimer laser (EMG 200, pulse duration 15 nsec) was focussed onto the surface of an explosive material contained in the sample holder. The spot size was about $2 \times 4 \text{ mm}^2$. The ArF and KrF lines used, 193 nm and 248 nm respectively, delivered a maximum pulse energy of 400 mJ and 700 mJ, respectively, as measured with a Gentec Joule meter (model ED 500). This agreed with a fluence of 5 J/cm^2 and 9 J/cm^2 , respectively.

2.3. THE DETECTION SYSTEM

The light emitted by the flash at a distance z of the sample's surface was collected by two plano-convex quartz lenses ($f=100 \text{ mm}$ and $f=200 \text{ mm}$) and imaged onto the entrance slit of the spectrograph (Jobin Yvon, HRS-2) equipped with a 1200 lines/mm holographic grating (see figure 3). The used slit widths were no larger than $50 \text{ }\mu\text{m}$ in order to maintain the spectral resolution provided by the detector head of the Optical Multichannel Analyser (OMA, Spectroscopic Instruments, IRY 1024). An emission spectrum of about 30 nm was recorded per laser light pulse.

2.4. SPECTRUM RECORDING AND PROCESSING.

The OMA was equipped with an image intensifying microchannel plate and was used in the gated mode [38]. The maximum gate width 6 ms, the minimum is 180 nsec. The minimum time delay between a trigger pulse and the onset of the gate pulse of the OMA was 270 nsec. To circumvent this time delay, an additional delay generator was used for the recording of the initial spectra. In this way the laser pulse could be positioned at any point in time with respect to the gate of the OMA. Somewhat arbitrary, the prompt emission recorded from the start of the laser pulse until 180 nsec later will be referred to as "*initial emission spectrum*" [40]. The emission spectra recorded at later starting times

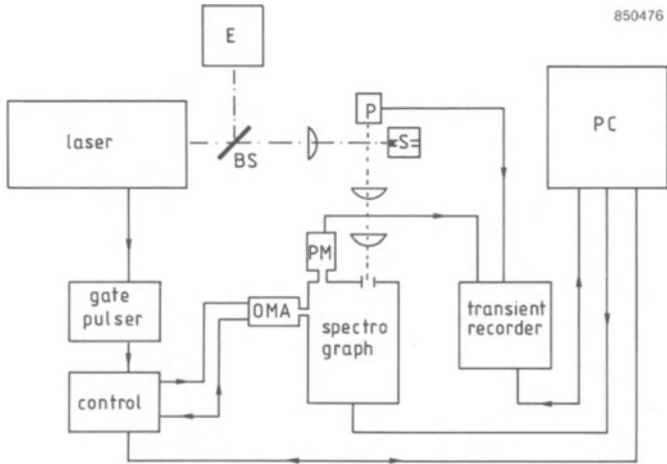


Figure 3. Block diagram of the experimental set-up for laser initiation. E=energy meter; BS=Beam splitter; S=sample; P=photodiode; PM=photomultiplier; PC=computer; OMA=Optical Multichannel Analyser.

or longer time gates will be called "*delayed emission spectra*".

The measured emission spectra were not corrected for the response function of the detection system. The total detection system was sensitive to radiation between 200 nm and 800 nm (the maximum sensitivity is between 200 nm and 400 nm). Since the intensity of the recorded spectra changed somewhat from shot to shot, the 30-nm-spectra were recorded with a certain overlap and normalized to each other.

3. Results

Experimental results, obtained with the use of an excimer laser which generates ultraviolet light at 193 nm or 248 nm will be described below. The reason for using UV laser light was the much larger absorption coefficient for wavelengths below 350 nm, for almost all the explosives used.

3.1. RELATION BETWEEN EMISSION SPECTRA OBTAINED AFTER IGNITION AND AFTER INITIATION.

For primary explosives the power or the energy in a nanosecond laser pulse is sufficient to initiate these explosives. For example, lead azide or silver azide require only a few mJ's in a nanosecond laser pulse, while most nanosecond pulse lasers deliver at least several tens

of mJ's. The minimum initiation intensity, *the critical intensity*, depends on laser parameters, such as pulse time duration, power, spot size etc. as well as on the properties of the explosives, such as density, grain size, confinement etc. The secondary explosives are harder to initiate [47, 48]. The critical intensity is often higher than delivered by the laser pulse used in the present experiments. Nevertheless, during, and some time after irradiation of the explosive, some decomposition took place, as witnessed by the light flash. Several of the mechanisms (maybe simultaneously) discussed in section 1.1 may be responsible for this. The question is, however, are the generated species different from those of an "explosive decomposition"? Or is the incipient initiation of the explosive just insufficiently strong to induce a self-sustaining reaction which nevertheless shows (perhaps almost) the salient features of the decomposition reaction under explosive circumstances? It is proposed here that the latter will be the case.

To verify this proposition to some extent, mercury fulminate was irradiated with a 75 mJ laser pulse, a value which is below the initiation energy threshold (for the used sample holder). The emission spectrum recorded 270 nsec after the start of the laser pulse does not reveal emission lines/bands or species different from those obtained after explosive irradiation [40], although some changes in the relative intensity of the emission lines were noticed. Although additional experiments to verify this proposal and to establish its limitations are needed, it is believed that the emission spectra of irradiated unconfined explosives give useful information about decomposition intermediates. This belief is supported by the observation of similar species in emission spectra recorded under various circumstances [14].

3.2. DELAYED EMISSION SPECTRA OF PRIMARY EXPLOSIVES

We start to present the delayed emission spectra to avoid, for the moment, the influence of the laser light on the emission behaviour and on the decomposition reaction. After a transient response as a result of the action of the laser light, the reaction will show features of the decomposing explosive.

3.2.1. Silver Azide

Silver azide (AgN_3) is one of the simplest explosive molecules with regard to the atomic content of the molecule. It has been established that it decomposes into a silver (Ag^+) and an azide ion (N_3^-). From several slow thermal decomposition experiments [4] the energy, giving rise to the explosive character of silver azide, as well as of some other azides, is thought to originate from the reaction of two azide molecules to give N_2 , $2\text{N}_3 \rightarrow 3\text{N}_2 + 880 \text{ kJ/mole}$. An investigation of the

fast decomposition reaction of AgN_3 with use of fast spectroscopic techniques has never been performed.

After laser irradiation, intense light emission (time duration several tens of microseconds) was observed close to the surface (within ca 1 cm). In figure 4 the emission spectrum is shown.

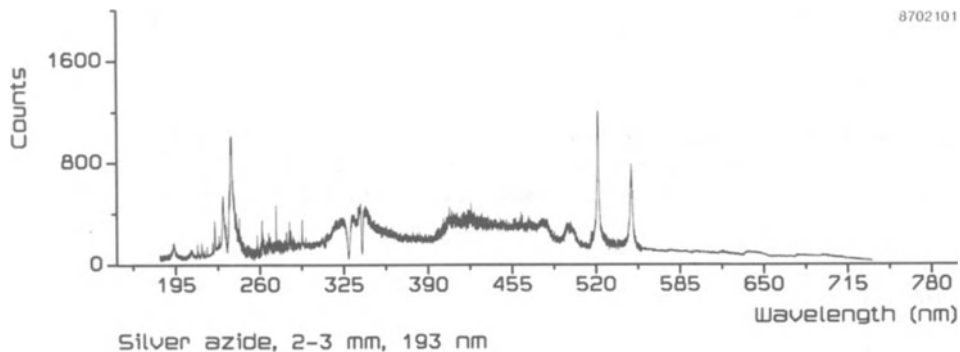


Figure 4. Emission spectrum of silver azide after irradiation with 200 mJ, 193 nm laser light at $z \approx 3$ mm.

Almost all emission lines between 200 nm and 400 nm could be attributed to neutral and singly ionised silver atoms, shown more clearly in figure 5. Ag^+ emission lines, particularly, are numerous. At the position of the strong silver lines at 328.1 nm and 338.3 nm, line inversion is observed (see figure 4). At wavelengths larger than 400 nm

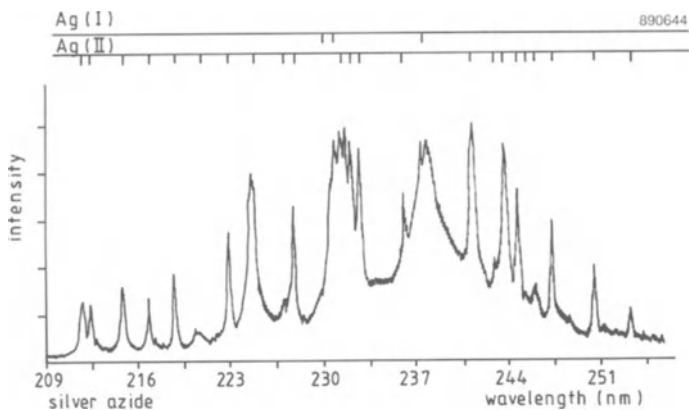


Figure 5. Emission spectrum of silver azide. Same conditions as in figure 4.

the emission spectrum revealed a continuum giving little information for the identification of reaction products. The origin of this continuum is not quite clear, but is probably associated with the occurrence of self-absorption and with free-electron-to-bound transitions [17].

As suggested above, emission of N_2 , N_3 and N_3^- was expected. It was reported [41,42] that N_3^- emits in the uv, around 230 nm and 190 nm, and N_3 around 272 nm. Though 190 nm is at the edge of transmission curve of quartz, no conclusive indication of the presence of the azide ion or the molecule was obtained. This was also the case for N_2 .

3.2.2. Lead Azide

Figure 6 shows the emission spectrum of lead azide, $Pb(N_3)_2$, recorded at $z \approx 3$ mm in front of the sample, after irradiation with 248 nm, 700 mJ, laser light.. All emission lines can be assigned to atomic

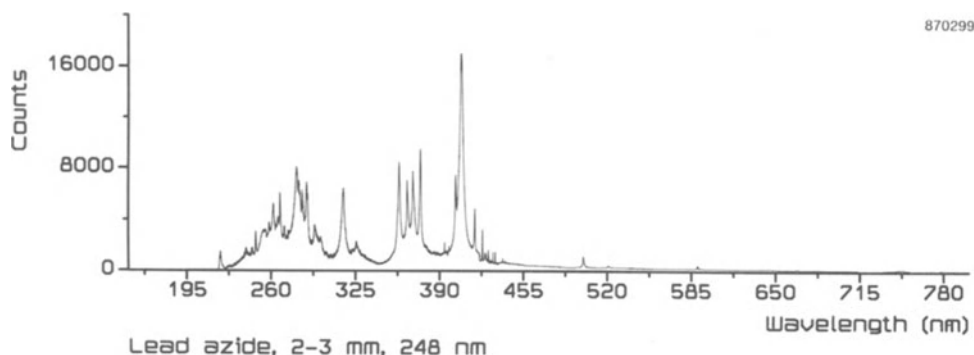


Figure 6. Emission spectrum of lead azide after irradiation with 248 nm laser light.

lead, except for some emission lines around 292 nm which are attributed to Wegener's B-system of Pb_2 [64]. In contrast to the emission spectrum of silver azide, no emission lines from ionised Pb were observed. Tables of spectral emission lines [65] show that Pb^+ has only a few emission lines in this spectral range.

Audubert [59] and Soullignac [43] reported the observation of light emission by N_2 . However, just as in the spectrum of silver azide, again no emission from N_3 , N_3^- , or N_2 could be conclusively identified.

3.2.3. Lead Styphnate

The emission spectrum of lead styphnate (gross formula $C_6H_3N_3O_9Pb$), recorded at $z \approx 3$ mm with 193 nm, 400 mJ laser light, is predominantly due to neutral lead atoms (see figure 7a) but some emission lines can be assigned to ionised lead atoms (figure 7b).

Weak emission of CN at 388 nm is observed (figure 7c). A few emission

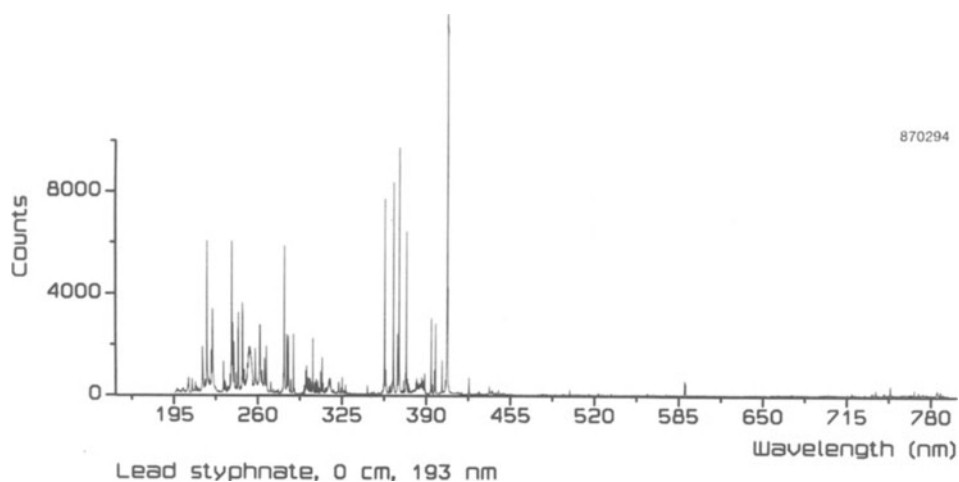


Figure 7a. Emission spectrum of lead styphnate after irradiation with 193 nm laser light recorded at $z \approx 0$ mm after a time delay of 270 nsec with respect to the laser pulse.

lines, such as a system around 304 nm and an unresolved emission band around 252 nm, have not yet been assigned.

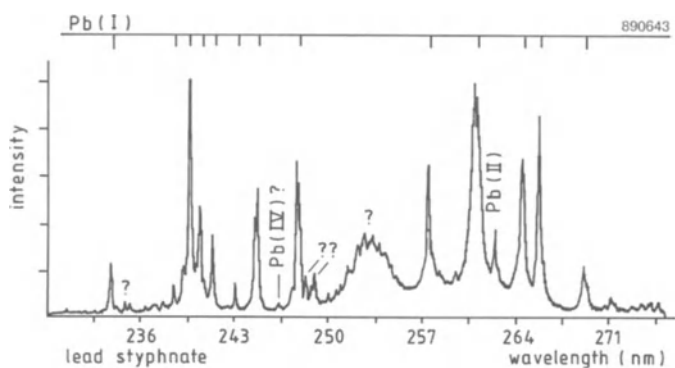


Figure 7b. Emission spectrum of lead styphnate.

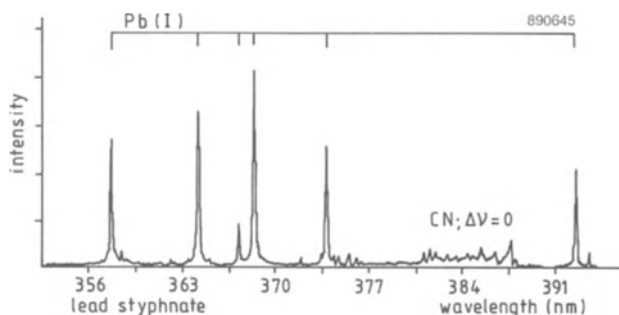


Figure 7c. Emission spectrum of lead styphnate.

3.2.4. Mercury Fulminate

Mercury fulminate, $\text{Hg}(\text{OCN})_2$, was found to have a rather peculiar effect. In one sample holder it does not explode at all; only a subdued report and a 6 msec induction time³ is noticed. However, in a different sample holder, irradiated at identical conditions, it explodes with a loud report and a simultaneous reduction of the induction time to less than a microsecond. The sample holders, though geometrically identical, have a different weight and therefore it is possible that the reflection of the laser generated shock wave by the walls of the sample holder initiated mercury fulminate instead of a direct initiation by the laser light. Nevertheless, the emission spectra of these

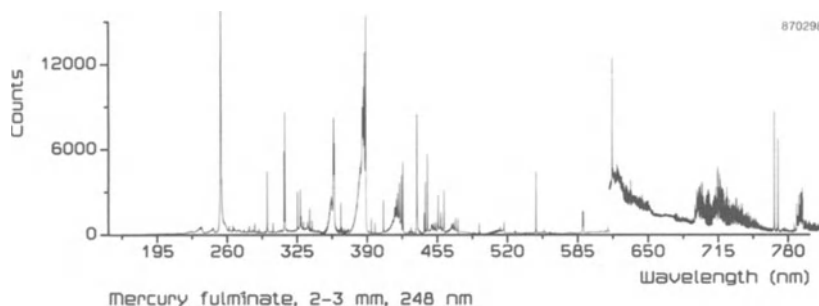


Figure 8. Emission spectrum of mercury fulminate.

³ The induction time is the time elapsed between initiation (by the laser pulse in this case) and the explosion (determined by the maximum intensity of the emitted light).

"explosions" resulted in the identification of the same decomposition species.

In figure 8 the emission spectrum of mercury fulminate is shown, recorded close to the sample's surface after irradiation with 248 laser light. All emission lines up to 600 nm can be assigned to Hg, CN, C₂ and to the impurities, Na, K, Ca and Ca⁺. The emission beyond 600 nm has not been identified.

3.3. EMISSION SPECTRA RECORDED AT A DISTANCE FROM THE SAMPLES FACE.

Emission spectra of mercury fulminate and of lead styphnate could be recorded relatively far away from the sample. This was probably due to an incomplete decomposition of the explosive material in the sample holder. The remniscent material obviously decomposed along the way and a relatively long plume was formed. While the conditions several centimetres from the explosive surface were different from those close to this surface, the various emission spectra showed only minor changes to the content of decomposition species. In the plume of irradiated mercury fulminate two emission bands appeared, around 555 nm and around 620 nm (see figure 9), growing in intensity relative to the other emission bands with increasing distance [39]. These bands were assigned to calcium monohydroxide (CaOH). The CN emission bands at 359 nm, 388.3 nm and 421.6 nm and the weaker emission band of C₂ at 517 nm were persistently present. Sometimes the 421.6 nm emission of CN disappeared, while the other two emission bands at 359 nm and 388 nm

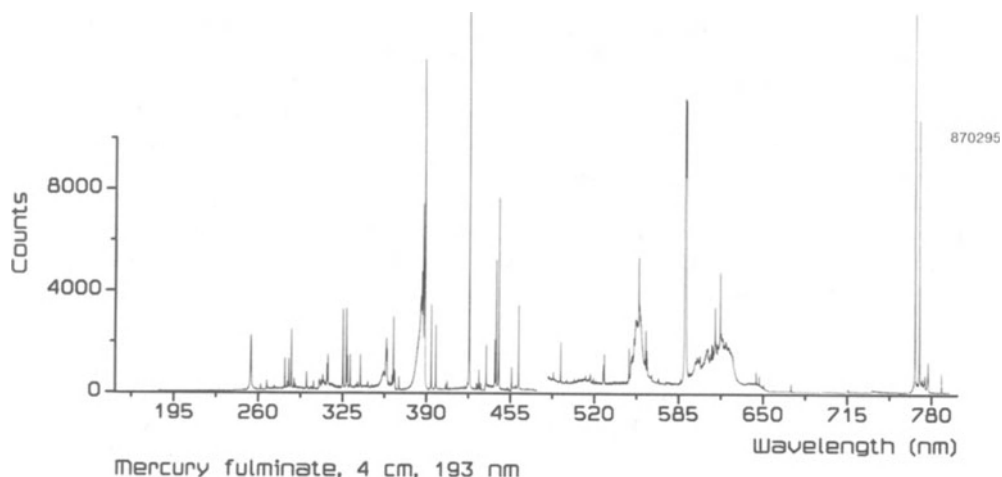


Figure 9. Emission spectrum of mercury fulminate recorded at 4 cm in front of the sample after irradiation with 193 nm laser light.

remained present. This is peculiar, because these three emission bands originate from the same upper vibronic levels of CN.

In the spectrum of lead styphnate [37], lead oxide appeared as an emitting species at about 5 cm from the sample, resulting in a reaction of atomic lead with oxygen present in the air. Flushing the explosion chamber with helium restrained the formation of lead oxide. No large fragments, sometimes observed in thermal decomposition analysis, were found.

The relatively stable content of reaction products in the emission spectra recorded at various circumstances did not support the expectation of different chemical reactions that take place in the various stages to detonation.

3.4. DELAYED EMISSION SPECTRA OF SECONDARY EXPLOSIVES.

As indicated above, attempts to initiate unconfined secondary explosives directly were not successful, not even with 700 mJ (6×10^8 W/cm², 15 nsec time duration) of UV laser light on PETN, a relatively sensitive secondary explosive. A similar conclusion was obtained in [44] using similar equipment. Successful initiation of confined secondary explosives have been frequently reported [53,54]. However, the emission spectra of confined explosives are structureless [39] providing little information about decomposition species. Recently Paisley [45] reported successful initiation of unconfined PETN with 266 nm of tripled Nd:Yag laser light, 10 nsec time duration and an intensity of 5×10^8 W/cm², as well as of HMX, a somewhat less sensitive explosive than PETN, which was initiated with 7×10^8 W/cm². HNS could not be initiated, not even with 50×10^8 W/cm². The discrepancy with our results could be due to different sample characteristics, such as mass density and grain size, but also to the effect of the absorption changing with the wavelength, as described in section 1.1 subdivision 2. Renlund [60] reported initiation of unconfined PETN irradiated with 308 nm and 355 nm excimer laser light.

As proposed in section 3.1, the emission spectrum obtained after low intensity laser irradiation gives (perhaps almost) similar information about the decomposition products as an emission spectrum taken from a real explosion would do.

3.4.1. RDX and HMX

The decomposition of the closely related RDX (gross formula $C_3H_6N_6O_6$) or HMX (gross formula $C_4H_8N_8O_8$) explosives is a complex process which appears to involve condensed phase as well as gas phase decomposition processes. A critical analysis of the decomposition data of both explosives can be found in [1-3].

A variety of small decomposition species was identified using gas chromatography, mass spectrometry and coherent anti-Stokes Raman scattering (CARS). Among these species are NO₂, N₂O, CH₂O, N₂, CO, CO₂ and HCN. Larger fragments, such as nitroso-compounds, or a

nitronitroxyl radical were detected with the use of gaschromatography/MS.

Of the smaller species, especially NO_2 , CH_2O (formaldehyde), N_2O and CO are frequently detected. NO_2 is considered to be formed in the first reaction step of the decomposition of RDX. Recently, a symmetric triple fission to produce $\text{CH}_2\text{N}_2\text{O}_2$ was proposed to be the predominant initial step in the decomposition of RDX under isolated conditions. Also, the elimination of OH was reported to be a primary process in the unimolecular dissociation of both RDX and HMX, although clusters do not emit OH . Except for OH and some impurity emissions due to Na , K , $\text{Ca}(\text{OH})$, none of these species could be seen in the emission spectra of RDX recorded at 4 mm in front of the samples surface, after irradiation with 700 mJ, 248 nm laser light. HMX showed, in addition, the emission bands due to CN and some unidentified emission lines below 400 nm (spectra not shown). As the intensity of the decomposition products of both explosives after irradiation was weak, emission spectra were recorded as close as possible to the surface of the explosives as well (see section 3.6).

3.4.2. PETN and Nitroguanidine

The emission spectrum of PETN (gross formula $\text{C}_5\text{H}_8\text{N}_4\text{O}_{12}$) and nitroguanidine (gross formula $\text{CH}_4\text{N}_4\text{O}_2$) were recorded at 4 mm in front of the explosive. Apart from impurity emissions from Na , K , Ca and CaOH , the spectrum of nitroguanidine revealed OH and CN , while the spectrum of PETN showed only OH (spectra not shown).

3.4.3. Tetryl and Picric acid

The emission spectra of tetryl (gross formula $\text{C}_7\text{H}_5\text{N}_5\text{O}_8$) and of picric

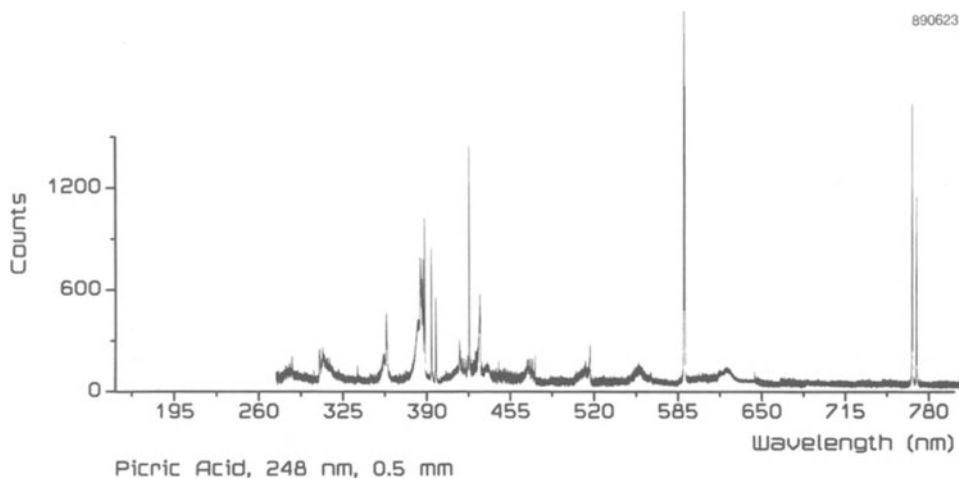


Figure 10. Emission spectra of Picric acid after irradiation with 248 nm laser light.

acid (gross formula C_6HNO) showed more structure than the spectra of PETN and RDX. The decomposition products of picric acid, particularly, are relatively good light emitters. The spectra of both explosives showed clear emissions of OH, CN, C_2 and of CH (see figure 10 and 11).

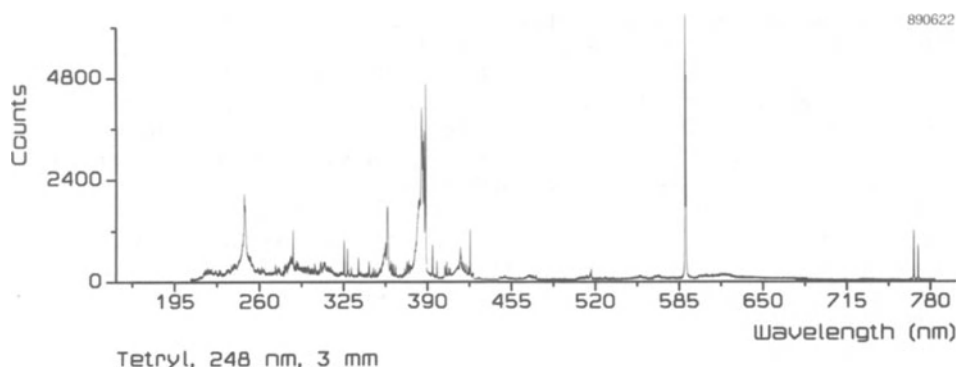


Figure 11. Emission spectrum of Tetryl after irradiation with 248 nm laser light.

3.5. INITIAL EMISSION SPECTRA OF PRIMARY EXPLOSIVES

As already mentioned above, the chemical reactions taking place in the different physical stages to detonation are themselves expected to be different. To probe the history of the explosion, several emission spectra of the plume of the explosion were recorded close to the surface of the explosive with the minimum time gate of the OMA and with various time delays with respect to the leading edge of the laser pulse. Though no thorough investigation with the various explosives has yet been performed, the results obtained showed no indication of an evolving emission spectrum, for instance reflected by the rise and fall of emission lines of species formed in the various stages to detonations.

The laser light might have some influence on the decomposition reaction [49] not only because of the promotion of specific reactions, but also as a result of the interaction of the laser light with the ablated and/or decomposed material. In the following sections the initial emission spectra will be discussed and compared with the delayed spectra.

In figure 12, 13 and 14 the initial emission spectra of silver azide, lead styphnate and lead azide, respectively, are displayed. A continuum emission is observed with self-absorption (line inversion) at the positions of 328.1 nm and 338.3 nm emission of neutral silver atoms (see figure 12) and at 357.3, 364.0, 368.3, 374.0, and 405.8 nm emission lines of neutral lead atoms, (see figures 13 and 14). Comparing these initial spectra with the

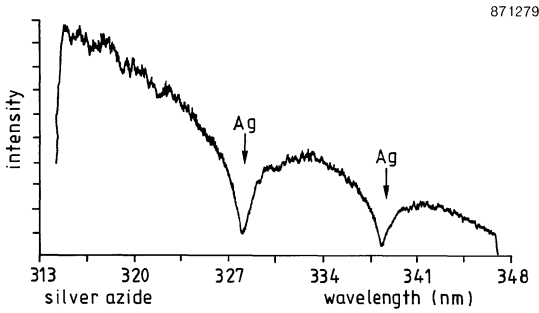


Figure 12. Initial emission spectrum of silver azide.

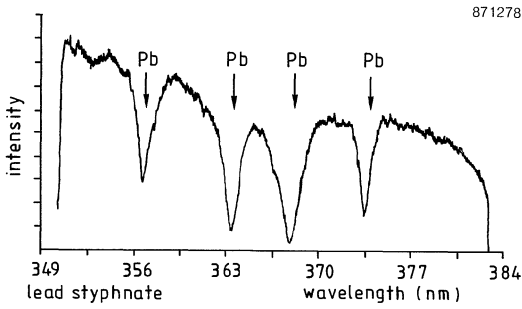


Figure 13. Initial emission spectrum of lead styphnate.

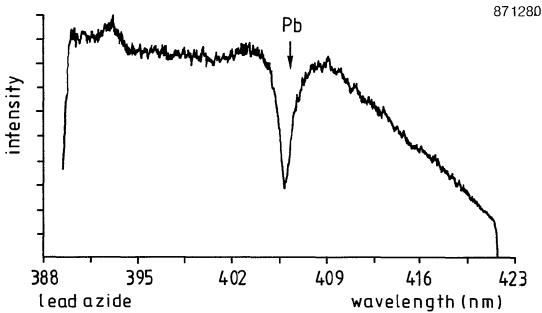


Figure 14. Initial emission spectrum of lead azide.

delayed spectra, it can be concluded that only the strong transitions of the neutral atoms showed selfabsorption. For instance, no Ag^+ self-absorption lines were found, though some of the numerous singly ionised transitions are strong enough to show this feature.

The broad continua and the line inversion shown in figures 12, 13 and 14 disappear when the light emission is recorded about 350 nsec after the start of the laser pulse. Then the laser pulse will have passed and the light emission is solely due to the decomposition process of the explosive. Particularly interesting are the initial and delayed emission spectra of mercury fulminate, shown in figure 15, which were recorded at $z = 0$ mm.

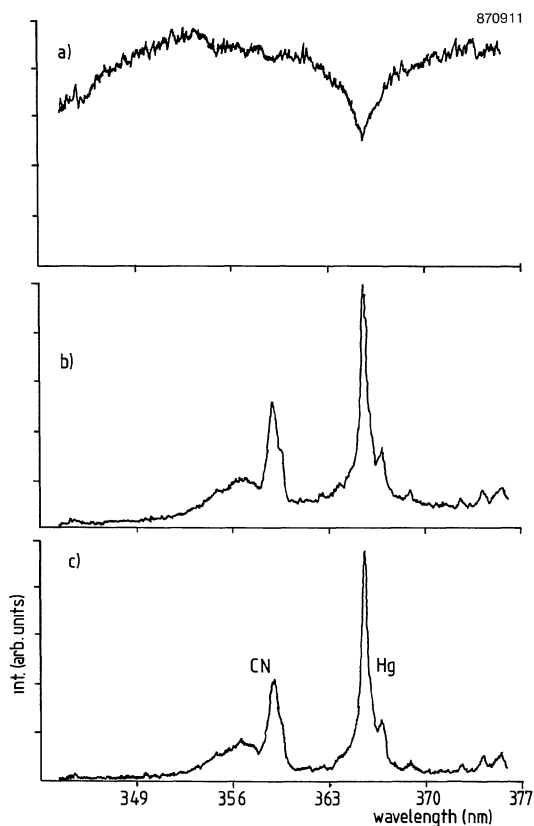


Figure 15. Emission spectrum of irradiated mercury fulminate. Time gate of the OMA is 180 nsec. a) start of the 180 nsec gate pulse coincides with the start of the laser pulse; no CN can be observed; b) 350 nsec delay of the gate pulse relative to the laser pulse; CN

emission is clearly present together with continuum emission; c) 700 nsec delay; CN is still present.

This spectrum also showed the self-absorption phenomenon, due to neutral Hg. However, no CN emission at 359 nm was present. Only after a delay of about 350 nsec did the CN emission show up and remain present from thereon. It appears that the laser light primarily eliminates the loose-bounded heavy metal atom out of the "explosive molecule". The low energy of the vibrational modes in which the metal atom is participating quickly receives enough energy to dissociate. A similar behaviour is expected for the appearance of C_2 .

3.6. INITIAL EMISSION SPECTRA OF HMX.

In figure 16 a portion of the initial (a) and delayed (b) emission spectra of HMX is shown after irradiation with 248 nm laser light. Emission spectra of RDX are similar [39]. In these initial spectra, CN could be identified superposed onto a continuum. This is in contrast with the emission characteristics of mercury fulminate, which showed CN only after a time delay. No line inversion was observed.

The delayed emission spectrum of HMX showed a continuum of weaker intensity, while the CN emission became more pronounced. No change in the light emitting decomposition products showed up. Obviously, within

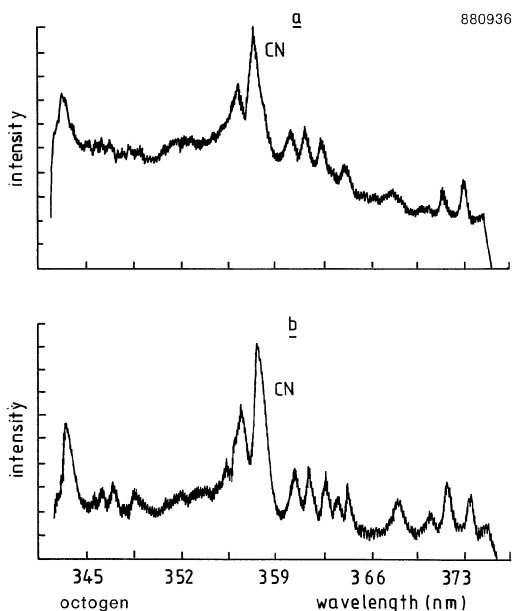


Figure 16. Initial (a) and delayed (b) emission spectrum of HMX after irradiation with 248 nm laser light.

the time resolution of the experiment, the explosive decomposed completely into its "final" decomposition products.

3.7. INFLUENCE OF THE WAVELENGTH ON THE DECOMPOSITION

With reference to the introduction, it is interesting to consider the initiation threshold as a function of the wavelength. The increase [4] in the absorption coefficient of lead azide (an explosive for which several initiation thresholds are determined), from the IR to the UV, suggests a decrease in the threshold sensitivity if linear light absorption is the basic physical initiation mechanism. In table 1 the minimum fluence (for laser pulses of comparable time duration), as reported in the literature, is tabulated, together with our result at 248 nm and at 694.3 nm.

TABLE 1. Critical energy density of lead azide

Reference	Pressure (kN/cm ²)	Energy density (mJ/cm ²)	Wavelength (nm)
This work	50	15	248
This work	50	4	694
50	50	10	694/1064
51	50	11	1064
52	150	8 and 5.5*	1064

* Depending on the laser pulse duration.

From this table it is clear that the sensitivity for laser light does not change systematically with the wavelength, but shows a more or less constant value.

A reservation must be made with respect to a correction for reflection losses. This aspect is considered by Paisley [45] in experiments with PETN. The reflection losses decreased with decreasing wavelength. Together with the increase in the absorption coefficient an decrease of the initiation threshold in the direction of the UV was expected and indeed observed for confined as well as unconfined PETN, as shown on Table 1 in [45].

The possible influence was also considered of the wavelength on the formation of species determined from emission spectra. The initial spectra, especially, may reveal some influence. Unfortunately, the bad timing characteristics of the Ruby-laser used did not allow for the recording of initial spectra. In figure 17 and 18 delayed emission spectra of picric acid and of RDX after irradiation with 248 nm and 694 nm laser light, recorded 270 nsec after the laser pulse, show identical emission spectra. If a different decomposition pathway was initiated by the Ruby laser pulse, then it apparently relaxes quickly to that

initiated by the UV laser pulse. However, it appears that the wavelength has little influence on the decomposition mode.

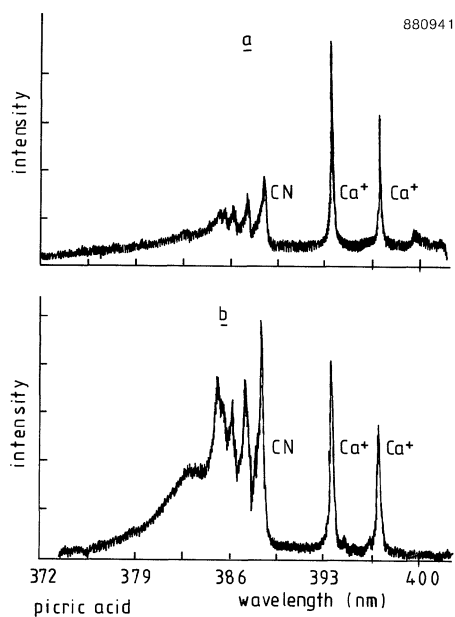


Figure 17. A portion of the emission spectrum of picric acid after irradiation with (a) 248 nm (b) 694 nm laser light.

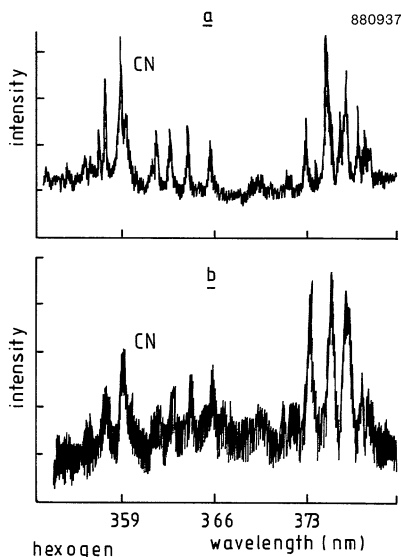


Figure 18. A portion of the emission spectra of RDX after irradiation with (a) 248 nm and (b) 694 nm laser light.

3.8. TEMPERATURE OF CN

The species created during the decomposition process can possess excess vibrational, rotational and/or translational energy with respect to their environment. Rotational and translational energy is thermalised quickly by collisions of the species. Vibrational energy survives this thermalisation process better, depending on the excited state of the molecule, the collision partners, etc.

In figure 19 and 20 the emission spectrum of the 0,0 and of the 0,1 band sequence of CN ($B^2\Sigma^+-X^2\Sigma^+$), respectively, obtained from irradiated tetryl, are displayed. Intensity distributions of the vibrational structure were calculated by J.T. Edwards [56] for 2500, 5000 and 7500 K. Comparing those results with the CN spectra shown in figure 19, a vibrational temperature of more than 7500 K can be inferred, a temperature which is much higher than regular detonation temperatures. A similarly high vibrational temperature, somewhat higher than 5000 K, but certainly lower than 7500 K, is estimated for the CN intensity

distribution in the emission spectrum of mercury fulminate (see figure 20).

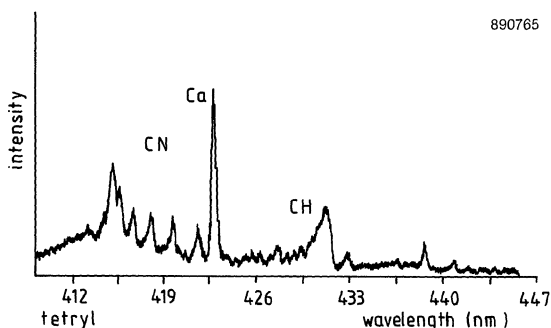


Figure 19. Intensity distribution of the (0,1) band sequence of CN ($B^2\Sigma^+-X^2\Sigma^+$) as observed in the emission spectrum of Tetryl.

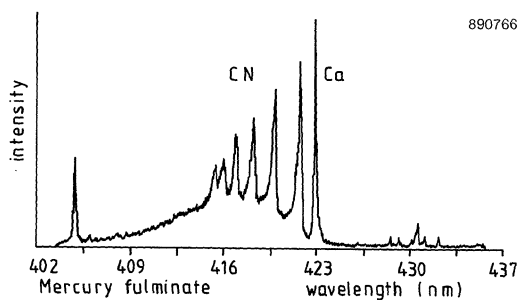


Figure 20. Intensity distribution of the (0,1) band sequence of CN ($B^2\Sigma^+-X^2\Sigma^+$) as observed for the emission spectrum of mercury fulminate.

4. Concluding remarks

The spectroscopic investigation of the decomposition process of laser irradiated (initiated or ignited) explosives has many possibilities that have to be developed and/or explored.

There is a paucity of emission spectra of decomposition products. The smaller fragments, such as OH and the stable radical CN, etc., are frequently observed, in contrast with the larger fragments which are hard to identify in emission spectra. Additional experiments are needed to probe these species. Furthermore, only the light emitting species

can be detected. It turned out, from a comparison with mass spectroscopic investigations, that more intermediates are formed during the decomposition than are detected with use of emission spectroscopy. Pump-probe laser experiments might resolve this problem. However, some conclusions can be drawn from the results presented above.

The investigated explosives are good UV light absorbers. Therefore, a thin layer of the explosive material is heated considerably. In the literature temperatures of 1000 K and higher have been reported for non-explosive materials. This hot thin layer decomposes quickly and forms a hot gas layer of decomposed, sometimes ionised, species. The residence time and the emission intensity of this layer can probably be manipulated somewhat by using different background gases and pressures. The expansion of the gas layer induces a shock wave travelling into the explosive. This shock wave is sometimes strong enough to initiate the explosive reaction. For instance, irradiating an aluminium film of 70 μm thickness, firmly pressed onto the surface, it was possible to initiate lead styphnate, indicating that the laser pulse is intense enough to generate strong enough shock waves.

It will be clear that little can be said about the character of the initiation process. Photothermal, mechanical and photochemical processes may contribute to the initiation process. Reflection of the shockwave, by the wall of the sample holder, can be important too. Evidence of this to play a role is the successful initiation of mercury fulminate in one sample holder, while it cannot be initiated in another, with the irradiation conditions being the same.

No influence of the wavelength on the variety of decomposition products was observed. The leading edge of the plume of irradiated primary explosives consists mainly of metal atoms. The high temperature and the high concentration of species resulted in self-absorption and line-broadening due to radiation transfer. Later, other reaction products did show up.

The emission spectra of irradiated secondary explosives reveal the immediate presence of the decomposition products which remain present at later times. This suggests for HMX and RDX that the N-N bond is broken upon decomposition rather than the C-N bond. The spectra very closely resemble the emission spectra and its characteristics which have been observed during and after irradiation of polymers and biological tissues such as vascular tissues, the myocardium etc. This ablation process induced by UV laser light has been explained by the promotion of an electron into a dissociative state through intersystem crossing or internal conversion. Similar mechanisms are probably also operative in explosives. To obtain more insight into the decomposition reactions of explosives, more experimental results are needed.

Acknowledgement

I would like to mention here E.A. Bal, M.W. Leeuw, W.Prinse, A.J.Th. Rooijers and A.C. van der Steen who have all contributed in recent years to the experiments described above. I would also like to thank the Air Force Office of Scientific Research, the US Air Force, who has supported this research through grant AFOSR-86-0348.

References

1. M.A. Schroeder, "Critical Analysis of Nitramine Decomposition Data: Product Distributions From HMX and RDX Decomposition", Technical Report, BRL-TR-2659, June 1985.
2. M.A. Schroeder, "Critical Analysis of Nitramine Decomposition Results: Some Comments on Chemical Mechanisms", Proceedings of the 16th JANNAF Combustion Meeting, CPIA Publications No. 38, volume II, p.17, September 1979.
3. T. Boggs, in: Fundamentals of Solid-Propellant Combustion, Progress in Astronautics and Aeronautics, vol 90, 1984, K. Kuo, M. Summerfield (eds.); "The Thermal Behaviour of Cyclotrimethylenetrinitramine (RDX) and Cyclotetramethylenetetranitramine (HMX)".
4. H.D. Fair and R.F. Walker (eds.), "Energetic Materials: Physics and Chemistry of Inorganics Azides", vol I, Plenum Press, New York, 1977.
5. F.P. Bowden and A.D. Yoffe, "Initiation and Growth of Explosions in liquids and solids", Cambridge University Press, 1952, p. 4.
6. H. Trinks and N. Schiff, Proceedings of the 7th ICOGER, Gottingen, p. 242.
7. T.B. Tang, G.M. Swallowe and V.K. Mohan, J. Solid State Chem. 55, 239, 1984.
8. H. Zuckermann, G.D. Greenblatt and Y. Haas, J. Phys. Chem. 91, 5159, 1987.
9. X. Zhao, E.J. Hints, Y.T. Lee, J. Chem. Phys. 88, 801, 1988.
10. V. Vaida, D.J. Donaldson, S.P. Sapers, R. Naaman and M.S. Child, J. Phys. Chem. 93, 513, 1989.
11. R.E. Setchell, Dynamics of Explosions, Progr. in Astronautics and Aeronautics, vol 106.
12. R.E. Setchell, in Shock Waves in Condensed Matter p. 553, 1987, S.C. Schmidt, N.C. Holmes (eds.), Elsevier Science Publishers B.V., 1988.
13. P.H. Stewart, J.B. Jeffries, J.M. Zellweger, D.F. McMillen, D.M. Golden, J. Phys. Chem. 93, 3557, 1989.
14. A.M. Renlund and W.M. Trott, Journal de Physique, Colloque C4, supplement au no. 9, Tome 48, septembre 1987.
15. B.J. Garrison, R. Srinivasan, J. Appl. Phys. 57, 2909, 1985.
16. R. Srinivasan, Science 234, 559, 1986.
17. G. Koren, J.T.C. Yeh, J. Appl. Phys. 56, 2120, 1984.
18. W.E. Maher, R.B. Hall, R.R. Johnson, J. Appl. Phys. 45, 2138, 1974.
19. A.N. Pirri, The Physics of Fluids, 16, 1435, 1973.
20. A.N. Pirri, R.G. Root, P.K.S. Wu, AIAA Journal, 16, 1296, 1978.
21. R.G. Root, Journal de Physique, Colloque C9, supplement au no. 11, Tome 41, novembre 1980.
22. G. Gorodetsky, T.G. Kayaka, R.L. Melcher, R. Srinivasan Appl. Phys. Lett. 46, 828, 1985.
23. D.R. Olander, S.K. Yagnik, C.H. Tsai, J. Appl. Phys. 64, 2680, 1988.
24. J. Eggert, J. Chem. Phys. 63, 11, 1959.
25. J. Roth, J. Chem. Phys. 41, 1929, 1964.

26. J.T. Hagan, M.M. Chaudri, J. of Materials Science 16, 2457, 1981.
27. B.L. Hicks, J. of Chem. Phys. 22, 414, 1954.
28. S.H. Lin, W.B. Richardson, H. Eyring, Proc. Natl. Acad. Sci. USA, 76, 4162, 1979.
29. A.L. Leu, C.S. Yen, Propellants, Explosives, Pyrotechnics, 12, 64, 1987.
30. R.J. Harrach, J. Appl. Phys. 47, 2473, 1976.
31. V.K. Mohan, T.B. Tang, J.Chem. Phys. 79, 4271, 1983.
32. R.J. Trainor, Y.T. Lee, Phys. Fluids 25, 1898, 1982.
33. A.A. Brish, I.A. Galeev, B.N. Zaitsev, E.A. Sbitnev, L.V. Tatarintsev, Fiz. Gor. I VZR. 5, 475, 1969.
34. A.A. Brish, I.A. Galeev, B.N. Zaitsev, E.A. Sbitnev, L.V. Tatarintsev, Fiz. Gor. I VZR. 2, 132, 1966.
35. R.E. Beverly III, C.T. Walters, J. Appl. Phys. 47, 3485, 1976.
36. N. Bloembergen, Appl. Optics, 12, 661, 1973.
37. M.W. Leeuw, "Laser initiation of primary explosives", PML-report no. 1986-61.
38. B.J. van der Meer, M.W. Leeuw, "Progress report (I) on decomposition reactions of laser-initiated explosives, PML-report 1987-C12.
39. B.J. van der Meer, M.W. Leeuw, "Progress Report (II) on decomposition reactions of laser-initiated explosives, PML report 1987-C125.
40. B.J. van der Meer, Progress Report (III) on decomposition reactions of laser-initiated explosives, PML report 1988-C123.
41. J.R. McDonald, J.W. Rabalais, S.P. McGlynn, J. Chem. Phys. 52, 1332, 1979.
42. R.A. Beaman, T. Nelson, D.S. Richards, D.W. Setser J. Phys. Chem. 91, 6091, 1987.
43. J.C. Soullignac, M. Destriau, Entropie 50, 31, 1973.
44. J.J. Dick, Report LA-9489-MS, Los Alamos National Laboratory, 1982.
45. D.L. Paisley, The Ninth Symposium (International) on Detonation, 1989.
46. H. Östmark, H. Nilsson, The Ninth Symposium (International) on Detonation, p. 65, 1989.
47. V.B. Ioffe, A.V. Dolgolaptev, V.E. Aleksandrov, A.P. Obraztsov, Fiz. Gor. I Vzryva, 21, 51, 1985.
48. L.C. Yang, V.J. Menichelli, Proc. of the 6th Symposium on Detonation, Coronado, 1976.
49. O. Eryu, K. Murakami, K. Masuda, Appl. Phys. Lett. 54, 2716, 1989.
50. Yu. F. Karabanov, V.K. Bobolev, Doklady Akad. Nauk SSSR, 256, 1152, 1981.
51. E.I. Aleksandrov, V.P. Tsipilev, Combustion, Explosives and Shock waves 18, 215, 1982.
52. E.I. Alexandrov, A.G. Voznyuk, Combustion, Explosives and Shock waves 14, 480, 1978.
53. A.M. Renlund, P.L. Stanton, W.M. Trott, The Ninth Symposium (International) on Detonation, 1989.
54. L.C. Yang, V.J. Menichelli, Appl. Phys. Lett. 19, 473, 1971.
55. R. Larciprete, M. Stuke, Appl. Phys. B 42, 181, 1987.
56. J.T. Edwards, "Solid Propellant Flame Spectroscopy", AFAL-TR-88-076, 1988.

57. H. Östmark, Reprint from Preprint of The Eight Symposium (International) on Detonation, p.46, 1985.
58. J.A. McKay, R.D. Bleach, D.J. Nagel, J.T. Schriempf, R.B. Hall, C.R. Pond, S.K. Manlief, J. Appl. Phys. 50, 3231, 1979.
59. R. Audubert, Trans. Farad. Soc., 35, 197, 1935.
60. A.M. Renlund, P.L. Stanton, W.M. Trott, The Ninth Symposium (International) on Detonation, p. 781, 1989.
61. R.G. Tomlinson, Phys. Rev. Lett., 14, 489, 1965.
62. P.D. Brewer, G.M. Reksten, R.M. Osgood, Solid State Techn., p. 273, April 1985.
63. P.E. Deyer, R. Srinivasan, Appl. Phys. Lett. 48, 445, 1986.
64. R.W.B. Pearse, A.G. Gaydon, "The Identification of Molecular Spectra", Chapman and Hall, 1976.
65. A.N. Zaidel', V.K. Prokof'ev, S.M. Raiskii, V.A. Slavnyi, E.Ya. Shreider, "Tables of Spectral Lines", IFI/Plenum, London, 1970.
66. P.S.P. Wei, R.B. Hall, W.E. Maher, J. Chem. Phys. 59, 3692, 1973.

TANDEM MASS SPECTROMETRY (MS/MS) AND COLLISION INDUCED DISSOCIATION (CID) - AN INTRODUCTION

J. YINON

Department of Isotope Research
The Weizmann Institute of Science
76 100 Rehovot, Israel

ABSTRACT. Tandem mass spectrometry (MS/MS) with collision induced dissociation (CID), is based on the fragmentation of mass selected primary ions in a reaction cell through collisions with an inert gas. The daughter ions thus obtained are mass analysed by the second mass analyser and are a "fingerprint" of the selected primary ion. A study of the MS/MS CID spectra of the molecular ion as well as of the fragment ions of a compound, will provide information leading to the determination of the fragmentation processes and pathways of that compound.

1. PRINCIPLE OF OPERATION

The MS/MS technique has been pioneered by John Beynon [1] in the United Kingdom and by Fred McLafferty [2], Graham Cooks [3] and Chris Enke [4] in the United States.

As can be understood from its name, MS/MS is a technique which is based on the combination of two mass spectrometers in tandem, with a reaction cell (collision cell) between them. A schematic illustration of an MS/MS is shown in Figure 1. The sample can be one single compound or a mixture. Accordingly one would use either electron impact (EI) or chemical ionization (CI) or any other ionization method.

The first mass analyser separates the ions produced in the source. The primary ion is selected and focused into the reaction cell. In the cell, the primary ion beam collides with an inert gas, such as helium, argon or nitrogen, resulting in collision induced dissociation (CID) or collisionally activated dissociation (CAD). The fragment ions produced in the collision cell are mass analysed by the second mass analyser and recorded. This secondary mass spectrum provides a "fingerprint" of the primary ion beam.

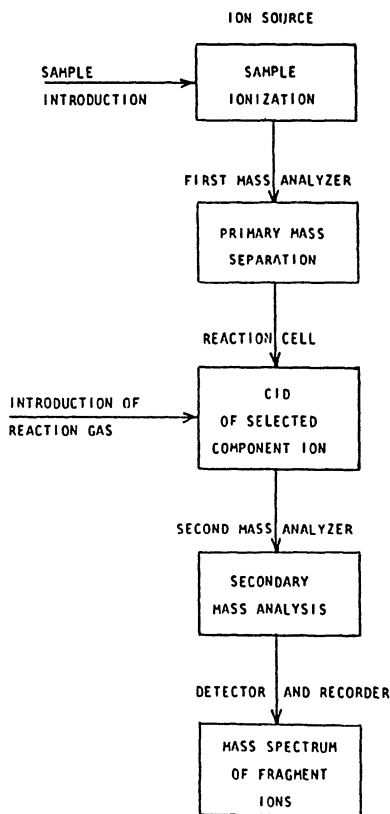


Figure 1. Schematic illustration of an MS/MS system.

There are two types of CID in the reaction cell, depending on the type of the first mass analyser:

- (1) High energy CID, if the first mass analyser is a magnetic sector analyser. The primary ion has then an energy of several keV.
- (2) Low energy CID, if the first mass analyser is a quadrupole analyser. In this case the primary ion has an energy of 0-100 eV.

In high energy CID, a beam of precursor ions having translational kinetic energies of several keV collides with an inert gas, which transforms some of the translational energy of the ions into internal excitation energy. The products of these high energy reactions arise from simple bond cleavages and are therefore useful for ion structure elucidation. The CID mass spectrum is related to the precursor ion structure in the same way as the EI mass spectrum is related to molecular structure.

In low energy CID, the transfer of momentum plays a more important role than the transfer of energy. Therefore larger molecules, such as nitrogen, are more effective than small atomic species such as helium, as collision gas.

There are several types of MS/MS configurations:

1.1. Two Sector Combinations

(a) Reversed-geometry double-focusing mass spectrometer or mass analysed ion kinetic energy spectrometer (MIKES)[5] (Figure 2). The magnetic field is used as the first analyser, while the electrostatic analyser is the second mass analyser. The mass scale of the fragment ions formed in a MIKE spectrum is a linear function of the electric sector voltage.

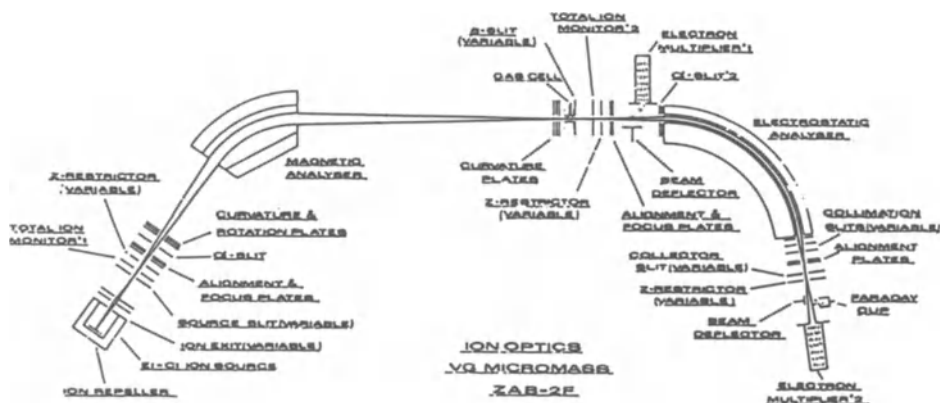


Figure 2. Ion optical system of a MIKE-CID spectrometer (reprinted from Ref. 5).

(b) B-B configuration (Figure 3).

This home-built instrument [6] consists of two magnetic sector analysers with a collision cell located in the region between the two analysers. The first stage consists of a Varian MAT CH7 analyser (90° , 21.4 cm radius), and the second stage is a home built 90° , 10.2 cm radius analyser. The precursor ion beam is monitored by the off-line electron multiplier detector No. 1. A voltage of 30 V applied to the deflection

plate deflects about 5% of the ion beam, while the other 95% continue their path into the collision cell. It is thus possible to monitor simultaneously the daughter ions on detector No. 2, and the precursor ion on detector No. 1.

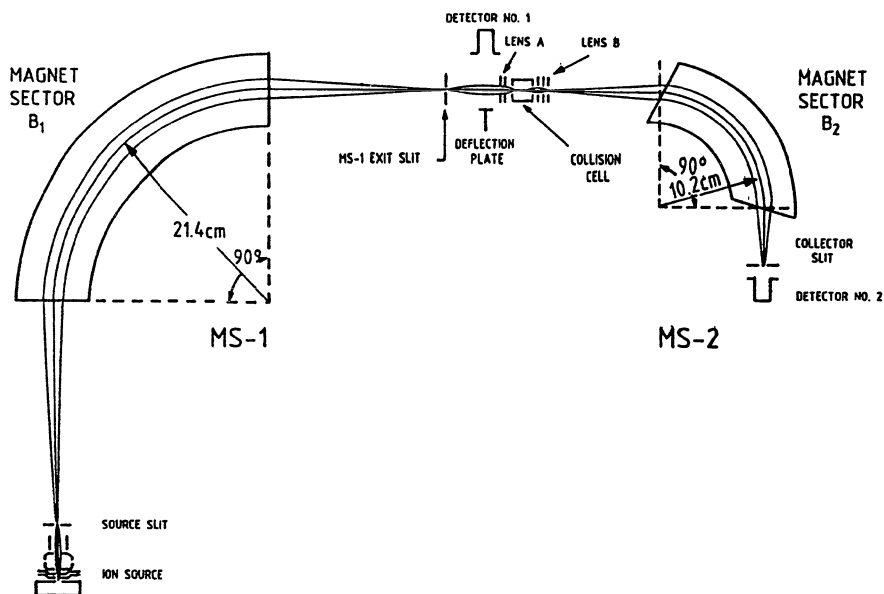


Figure 3. Schematic diagram of the tandem B-B mass spectrometer (reprinted from Ref. 6).

1.2. Triple Quadrupole System (Figure 4)

The triple quadrupole system consists basically of two quadrupole analysers (first and second quadrupole). The second quadrupole has only an R.F. voltage (without the D.C. component) and serves therefore as an ion focusing device [7]. The collision cell is located between the rods of this quadrupole. It has been found that when doing MS/MS with a tandem quadrupole mass analyser, an additional quadrupole focusing device is needed to focus the ions formed in the collision cell.

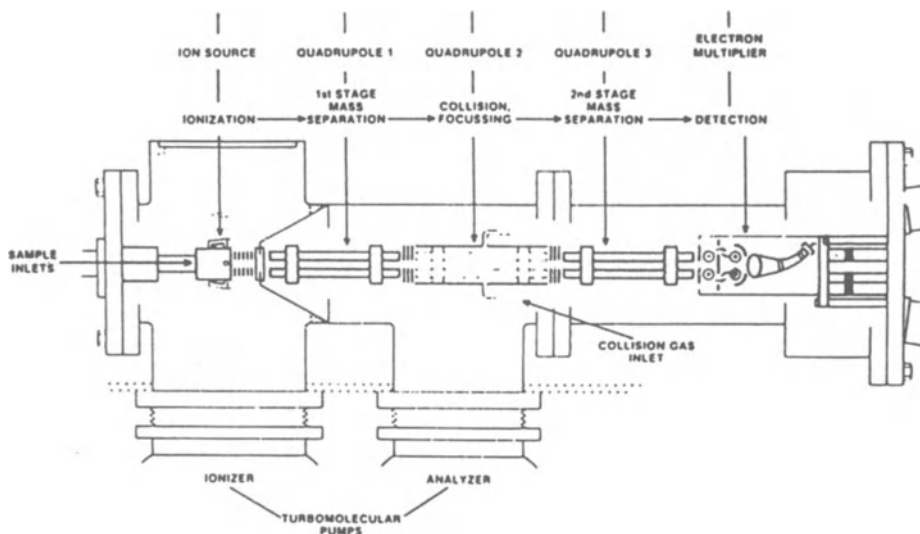


Figure 4. Triple quadrupole MS/MS system (reprinted from Ref. 7).

1.3 Magnetic Sector and Quadrupole Combinations (hybrid)

(a) BQQ configuration

(b) QBB configuration

Even in hybrid configurations, when a quadrupole analyser is used, an additional R.F.-only quadrupole focusing device is necessary for the collision cell.

1.4. Triple Sector Combinations

(a) BEQQ configuration

(b) EBQQ configuration

(c) BEB configuration

Figure 5 shows an example of a triple sector BEQQ MS/MS. This system has several collision cells at different locations, thus enabling a variety of experiments.

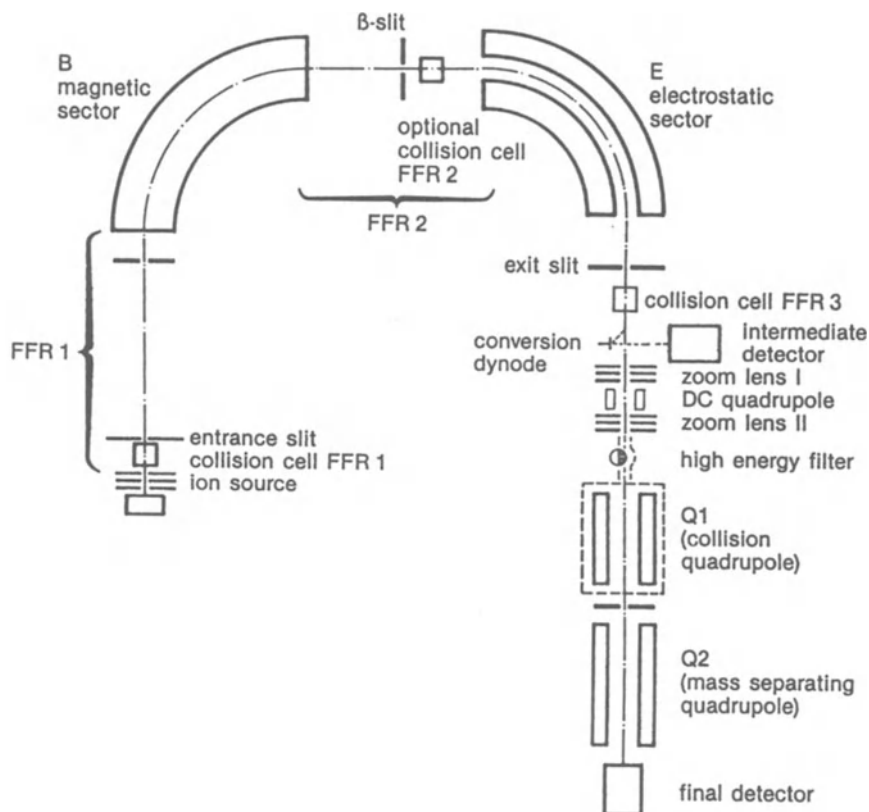


Figure 5. BEQQ hybrid MS/MS system (Finnigan-MAT H-SQ 30).

1.5. Four Sector Combination

Figure 6 shows the schematic diagram of a VG ZAB-4F MS/MS system, which is a tandem high-resolution mass spectrometer.

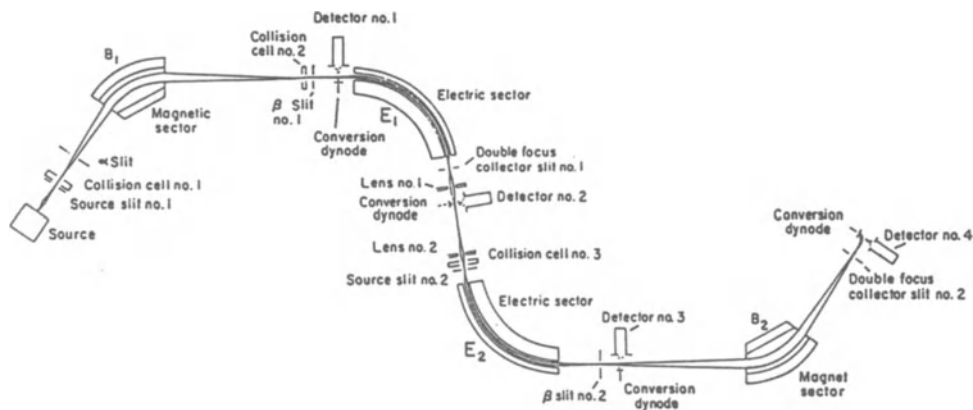


Figure 6. Four-sector MS/MS system (VG ZAB 4F).

Several experiments can be carried out with an MS/MS:

(1) Daughter experiment. This experiment allows a survey of specific compounds in complex mixtures. Each component of the mixture is represented by a characteristic ion (molecular ion or typical fragment ion). This ion undergoes CID in the collision cell and is identified by its CID mass spectrum obtained in the second mass analyser.

(2) Parent experiment. The first mass analyser is scanned while the second one is set at a specific mass. This experiment identifies all parent ions that dissociate to form a specific predetermined daughter (fragment) ion. For example, trinitroaromatic compounds could be identified by the NO^+ fragment ion, while nitrate esters by the NO_2^+ fragment ion.

(3) Neutral loss experiment. The two mass analysers are set to detect a constant neutral loss. For example, the first mass analyser is scanned from m/z 37 to 300, at the same time as the second mass analyser is scanned from m/z 20 to 283. In this example the neutral loss of 17 mass units may represent a series of nitrocompounds losing OH.

Another use of MS/MS is determination of fragmentation processes and pathways. A study of the MS/MS CID spectra of the molecular ion as well as of the fragment ions of a compound will provide information leading to the determination of the fragmentation pathways of that compound. Figure 7 shows such a hypothetical fragmentation pathways of a simple 4-atom linear ion.

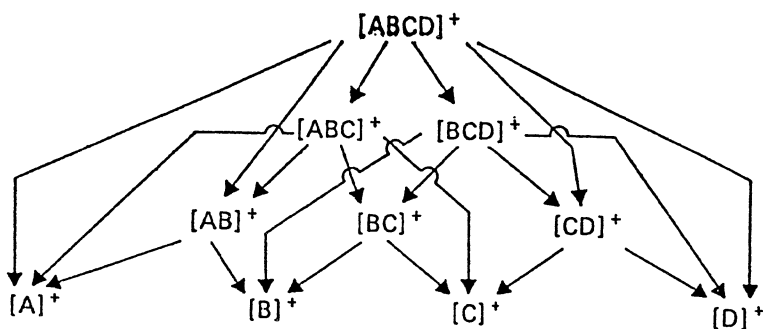


Figure 7. Hypothetical fragmentation pathways of a simple 4-atom linear ion (reprinted from Ref. 1).

2. REFERENCES

1. Bozorgzadeh, M. H., Morgan, R. P. and Beynon, J. H. (1978) 'Application of mass-analysed ion kinetic energy spectrometry (MIKES) to the determination of the structures of unknown compounds', *Analyst* 103, 613-622.
2. Bente, III, P. F. and McLafferty, F. W. (1980) 'Analytical applications of two-dimensional mass spectrometry', in: C. Merrit, Jr. and C. N. McEwen (eds.), *Mass Spectrometry*, Marcel Dekker, Inc., New York.
3. Cooks, R. G. and Glish, G. L. (1981) 'Mass spectrometry/mass spectrometry', *Chem. Eng. News* 59, 40-52.
4. Yost, R. A. and Enke, C.G. (1979) 'Triple quadrupole mass spectrometry for direct mixture analysis and structure elucidation', *Anal. Chem.* 51, 1251A-1264A.

5. Morgan, R. P., Beynon, J. H., Bateman, R. H. and Green, B. N. (1978) 'The MM-ZAB-2F double-focusing mass spectrometer and mike spectrometer', *Int. J. Mass Spectr. and Ion Phys.* 28, 171-191.
6. Yinon, J. (1987) 'Mass spectral fragmentation pathways in 2,4,6-trinitroaromatic compounds. A tandem mass spectrometric collision induced dissociation study', *Org. Mass Spectr.* 22, 501-505.
7. Slayback, J. R. B. and Story, M. S. (1981) 'Chemical analysis problems yield to quadrupole MS/MS', *Ind. Res. Devel.*, February 1981, 128-134.

MS/MS OF ENERGETIC COMPOUNDS: COLLISION INDUCED DISSOCIATION
(CID) STUDIES OF FRAGMENTATION PROCESSES IN ENERGETIC MOLECULES

J. YINON

Department of Isotope Research
The Weizmann Institute of Science
76 100 Rehovot, Israel

ABSTRACT. The application of MS/MS-CID in the study of fragmentation processes and pathways has been demonstrated in a series of energetic materials including well known explosives such as TNT, RDX and HMX as well as in novel energetic materials such as nitroadamantanes, polynitrobishomocubanes and polynitropolyamino compounds. Conclusions concerning various bond fragmentations have been discussed.

1. INTRODUCTION

A great deal of research has been done on the mass spectrometry of explosives [1] because of some interesting parallels between the early stages of decomposition by explosive shock and the fragmentation under electron impact (EI) in the mass spectrometer [2-6]. In EI mass spectrometry, the ions formed, containing excess energy, decompose into a series of fragments. The resulting mass spectrum indicates only the presence of the ions, but does not give any information on their routes of formation. A powerful tool for the study and determination of fragmentation processes and pathways of individual ions is tandem mass spectrometry (MS/MS) with collision induced dissociation (CID) [7]. Thus, we have studied the MS/MS CID spectra of a series of explosives such as trinitroaromatic compounds and RDX and HMX as well as of some novel energetic materials such as nitroadamantanes, bishomocubanes, polynitrobiphenyl-2-amines and some recently synthesized nitramines.

2. 2,4,6-TRINITROAROMATIC COMPOUNDS

The MS/MS CID spectra of compounds of type 1 were studied using a tandem BB mass spectrometer [8].



1

1,3,5-Trinitrobenzene (TNB)	(R ₁ =H, R ₂ =H)
2,4,6-Trinitrotoluene (TNT)	(R ₁ =CH ₃ , R ₂ =H)
2,4,6-Trinitro- <i>m</i> -xylene (TNX)	(R ₁ =CH ₃ , R ₂ =CH ₃)
2,4,6-Trinitrophenol (picric acid)	(R ₁ =OH, R ₂ =H)
2,4,6-Trinitro- <i>m</i> -cresol (TNC)	(R ₁ =CH ₃ , R ₂ =OH)
2,4,6-Trinitroanisole (TNA)	(R ₁ =OCH ₃ , R ₂ =H)
2,4,6-Trinitrophenetole (TNP)	(R ₁ =OCH ₂ CH ₃ , R ₂ =H)
2,4,6-Trinitroaniline (picramide)	(R ₁ =NH ₂ , R ₂ =H)
2,4,6-Trinitrochlorobenzene (picryl chloride)	(R ₁ =Cl, R ₂ =H)
2,4,6- <i>N</i> -Tetranitro- <i>N</i> -methylaniline (tetryl)	(R ₁ =N(NO ₂)CH ₃ , R ₂ =H)

Figure 1 shows an example, the CID spectrum of the M⁺ ion of TNX.

Table 1 lists the abundances of the major ions observed in the CID spectra of the molecular ions as well as of some highly abundant fragment ions.

In compounds where a methyl group is ortho to a nitro group, such as TNT, TNX and TNC, loss of OH due to an "ortho effect" [2] is the main decomposition route. This is followed in TNT and in TNX by loss of an additional OH group and by loss of NO₂, and in TNC by loss of NO. The major fragmentation route of picric acid and picramide is loss of NO due to formation of resonance - stabilized products. These two compounds contain the strong electron donating groups OH and NH₂ respectively. The major loss in tetryl is that of NO₂, where it is probably from the nitraminic group. This is followed by loss of OH due to an "ortho effect".

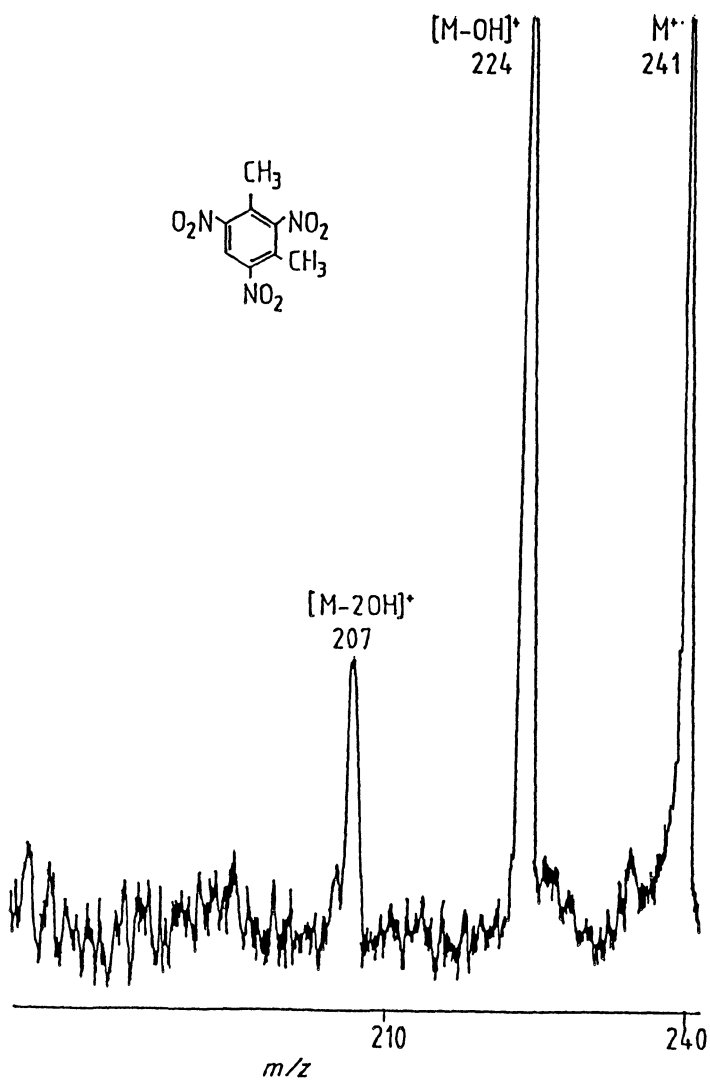


Figure 1. CID spectrum of the M^+ ion of TNX.

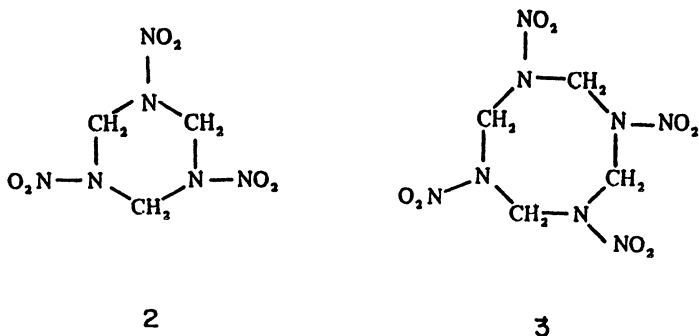
Table 1. CID ions of 2,4,6-trinitroaromatic compounds*

Mass units	Mass loss	Compound ^a	Precursor ion ^a	TNB	TNT	TNX	Picric acid	TNC	TNA	TNP	Picramide	Picryl chloride	Tetryl
				M ⁺	[M-OH] ⁺	M ⁺	M ⁺	[M-OH] ⁺	M ⁺	M ⁺	M ⁺	M ⁺	[M-NO ₂] ⁺
16	O												
17	OH ⁺			210 (100)	193 (100)	224 (100)	207 (99)	226 (100)					224 (100)
18	H ₂ O			209 (94)			196 (70)						
28	C ₂ H ₄												
28	NCH ₃												
30	CH ₂ O												
34	2OH ⁺												
44	C ₂ H ₂ O					207 (5)							
46	NO ₂			167 (100)	164 (30)		183 (7)	196 (100)	213 (100)	199 (100)	198 (100)		213 (20)
47	HNO ₂			180 (50)			171 (17)						211 (20)
58													
60	[NO ₂ + CH ₂] ⁺												
76	[NO ₂ + NO] ⁺						148 (100)						181 (22)
77							152 (12)						

* The abundances of the fragment ions are listed in parentheses alongside their *m/z* value.

3. RDX AND HMX

Fragmentation pathways of RDX (2) and HMX (3) have been determined by MS/MS CID, using a MIKE spectrometer [9].



CID spectra of the molecular ions and major fragment ions were recorded. Fragmentation maps of RDX and HMX were constructed and are shown in Figures 2 and 3 respectively.

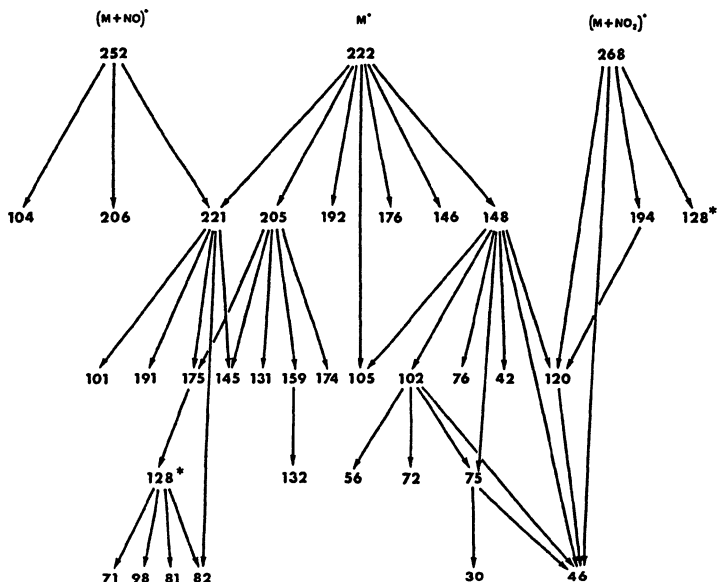


Figure 2. Fragmentation map of RDX.

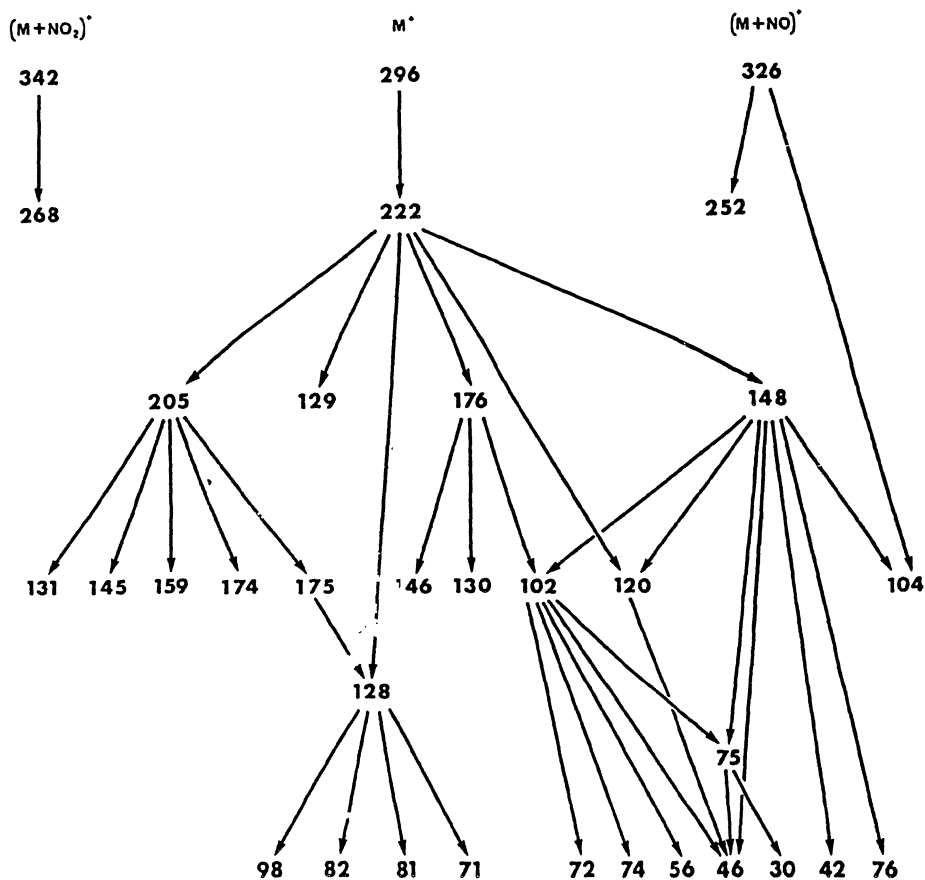


Figure 3. Fragmentation map of HMX.

The chemical composition of the ions in these maps is shown in Table 2.

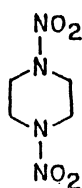
There is a similarity between the fragmentation pathways of RDX and HMX. Both compounds are characterized by typical losses of groups such as CH_2NNO_2 , CH_3NNO_2 , NO_2 , HNO_2 , NO and HNO . Mass spectral decomposition occurs by N-N bond fission and by C-N ring fragmentation and elimination of CH_2NNO_2 groups or parts of such groups, eventually followed by ring contraction in some cases.

Table 2. Chemical composition of ions in the CID spectra of RDX and HMX in EI

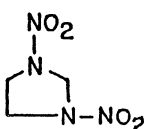
m/z	Chemical composition	Exact mass	Measured mass	m/z	Chemical composition	Exact mass	Measured mass
30	NO	29.9980		131	C ₂ H ₃ N ₄ O ₃	131.0205	131.0205
42	C ₂ H ₄ N	42.0344		132	C ₂ H ₄ N ₄ O ₃	132.0283	132.0287
46	NO ₂	45.9929		145	C ₃ H ₅ N ₄ O ₃	145.0361	145.0364
56	C ₂ H ₄ N ₂	56.0374	56.0361	146	C ₃ H ₅ N ₄ O ₃	146.0439	146.0416
71	C ₂ H ₃ N ₂ O	71.0246	71.0249	148	C ₂ H ₄ N ₄ O ₄	148.0233	148.0238
72	C ₂ H ₄ N ₂ O	72.0323	72.0317	159	C ₃ H ₅ N ₅ O ₃	159.0393	159.0398
74	CH ₂ N ₂ O ₂	74.0115	74.0114	174	C ₃ H ₄ N ₅ O ₄	174.0262	174.0255
75	CH ₃ N ₂ O ₂	75.0194	75.0183	175	C ₃ H ₅ N ₅ O ₄	175.0342	175.0342
76	CH ₄ N ₂ O ₂	76.0273	76.0292	176	C ₃ H ₅ N ₅ O ₄	176.0419	176.0406
81	C ₃ H ₃ N ₃	81.0327	81.0336	191	C ₃ H ₅ N ₅ O ₅	191.0290	191.0334
82	C ₃ H ₄ N ₃	82.0405	82.0413	194	C ₂ H ₄ N ₅ O ₆	194.0160	194.0146
98	C ₃ H ₄ N ₃ O	98.0354	98.0345	205	C ₃ H ₅ N ₆ O ₅	205.0321	205.0319
101	C ₂ H ₃ N ₃ O ₂	101.0225	101.0225	206	C ₃ H ₆ N ₆ O ₅	206.0399	206.0390
102	C ₂ H ₄ N ₃ O ₂	102.0303	102.0300	221	C ₃ H ₅ N ₆ O ₆	221.0270	221.0257
104	CH ₂ N ₃ O ₃	104.0097	104.0100	222	C ₃ H ₆ N ₆ O ₆	222.0348	222.0356
105	CH ₃ N ₃ O ₃	105.0175	105.0179	252	C ₃ H ₆ N ₇ O ₇	252.0327	252.0292
120	CH ₂ N ₃ O ₄	120.0044	120.0042	268	C ₃ H ₆ N ₇ O ₈	268.0277	268.0277
128	C ₃ H ₄ N ₄ O ₂	128.0334	128.0345	296	C ₄ H ₈ N ₈ O ₈	296.0465	
129	C ₃ H ₅ N ₄ O ₂	129.0412	129.0394	326	C ₄ H ₈ N ₉ O ₉	326.0445	326.0446
130	C ₃ H ₆ N ₄ O ₂	130.0490	130.0490	342	C ₄ H ₈ N ₉ O ₁₀	342.0392	342.0201

4. NITRAMINES

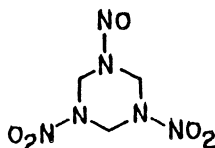
In an effort to improve the understanding of the fragmentation processes of heterocyclic nitramines, five nitramines were synthesized and their mass spectral pathways were studied using MS/MS CID [10]. Structures of these nitroamines are shown in schemes 4 to 8.



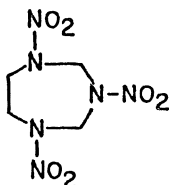
4



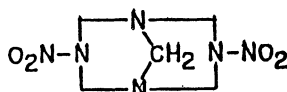
5



6



7



8

These are potential explosives. Like RDX and HMX they are thermally stable. But they are more oxygen deficient, therefore they have lower heats of detonation. The instrument used was a EBQQ type MS/MS (VG 7070 EQ) and was operated in the B/E linked scan mode. An example of a B/E-CID spectrum is shown in Figure 4, which shows the CID spectrum of the molecular ion of compound 6.

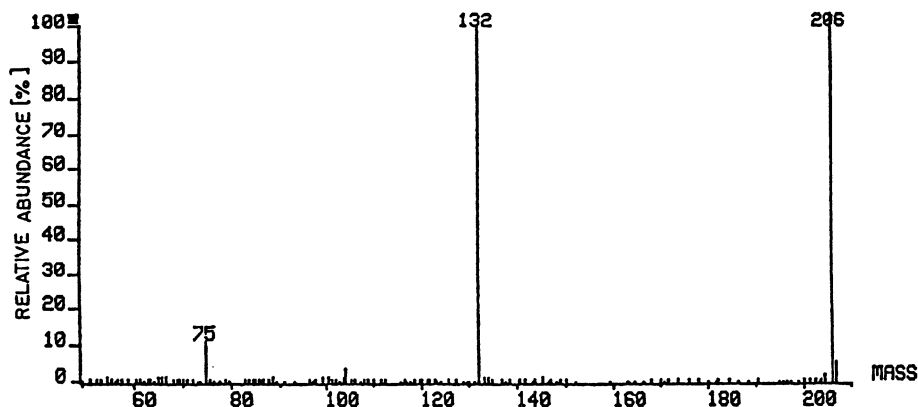
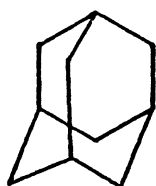


Figure 4. CID spectrum of the M^+ ion of compound 6.

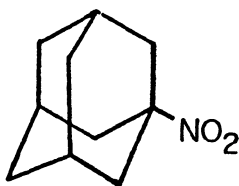
Results indicate that typical neutral eliminations include loss of OH, NO, NO_2 and HNO_2 as well as CH_2NNO and CH_2NNO_2 . In compounds 6 and 7, the N-N bond remains intact, they do not lose directly NO_2 , but lose CH_2NNO_2 as a main fragment, indicating that the C-N bond is broken. Compound 4 loses NO_2 but not CH_2NNO_2 . Here the N-N bond is broken, but the C-N bond remains intact. Compound 5 loses first NO_2 and then CH_2NNO_2 and compound 8 loses both NO_2 and CH_2NNO_2 simultaneously.

5. NITROADAMANTANES

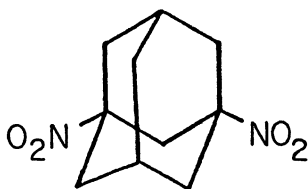
Several groups of novel energetic materials have been developed at U.S. Army ARDEC, Dover, N.J. One of these groups is the nitroadamantanes. The compounds included adamantane (9), 1-nitroadamantane (10), 1,3-dinitroadamantane (11) and 1,3,5,7-tetranitroadamantane (12).



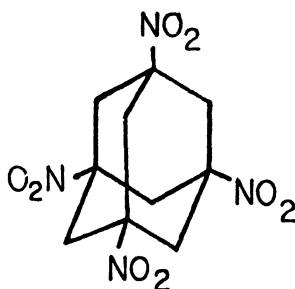
9



10



11



12

Mass spectral fragmentation pathways of these compounds were studied using CID [11]. The instrument used in this research was a four-sector VG ZAB-4F tandem high resolution mass spectrometer. Figure 5 shows an example of a CID spectrum, the CID spectrum of the ion at m/z 178 ($M-3NO_2$)⁺ in tetranitroadamantane. Fragmentation maps were determined for all 4 compounds studied. Figures 6-8 show the fragmentation maps of 1-nitroadamantane, 1,3-dinitroadamantane and 1,3,5,7-tetranitroadamantane respectively. Molecular ions were not observed; dashed arrows denote therefore presumed pathways. Results indicate that fragmentation of the C-N bonds takes place before the fragmentation of the C-C bonds. Only after the loss of all NO₂ groups will the hydrocarbon structure be broken.

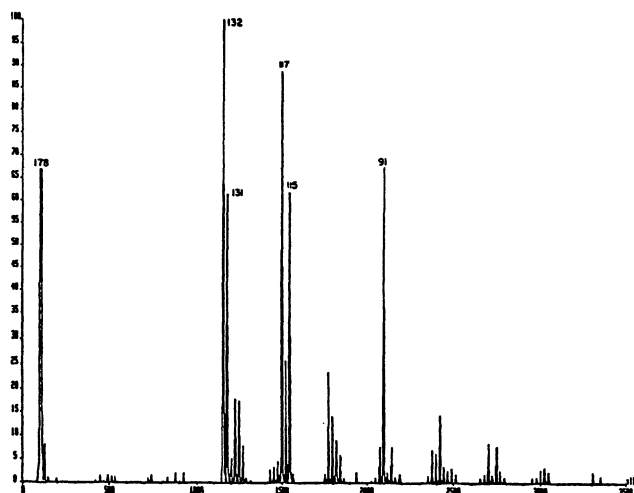


Figure 5. CID spectrum of the ion at m/z 178 ($M-3NO_2$)⁺ in tetranitrodamantane.

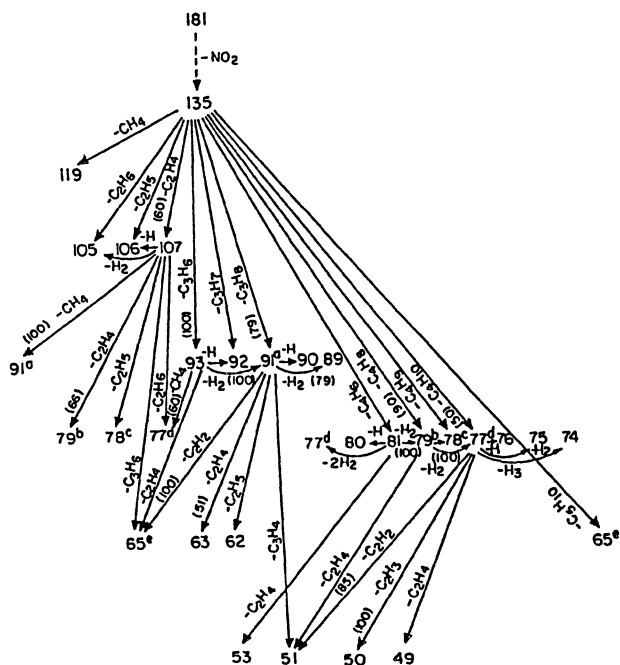


Figure 6. Fragmentation map of 1-nitroadamantane.

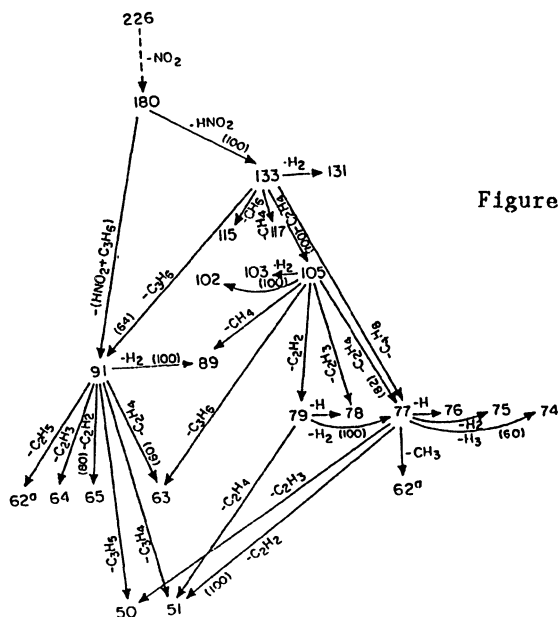


Figure 7. Fragmentation map of
1,3-dinitroadamantane.

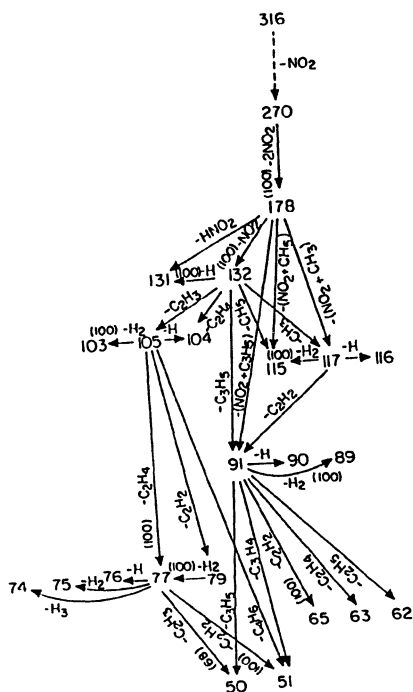
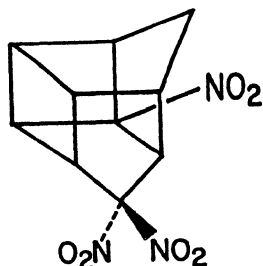


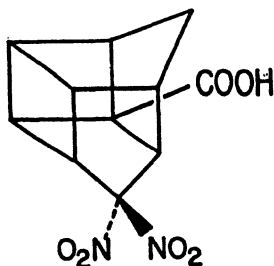
Figure 8. Fragmentation map of
1,3,5,7-tetranitroadamantane.

6. POLYNITROBISHOMOCUBANES

Another group of novel energetic compounds are the polynitrobishomocubanes. Two of these compounds, 3,5,5-trinitropentacyclodecane (TPCD) (13) and 5,5-dinitropentacyclodecane-3-carboxylic acid (DPCD-Acid) (14) were investigated by MS/MS CID [12].



13



14

Fragmentation maps were constructed from CID results using the VG ZAB-4F instrument. The fragmentation maps of TPCD and DPCD-Acid are shown in Figures 9 and 10 respectively.

Molecular ions were not detected. The dashed arrows in the fragmentation maps denote presumed pathways.

In both compounds we have first a loss of two NO_2 groups. In TPCD this is followed by loss of a third NO_2 group. Only then will the fragmentation of the hydrocarbon structure occur. Results indicate that fragmentation of the C-N bonds takes place before fragmentation of the C-C bonds.

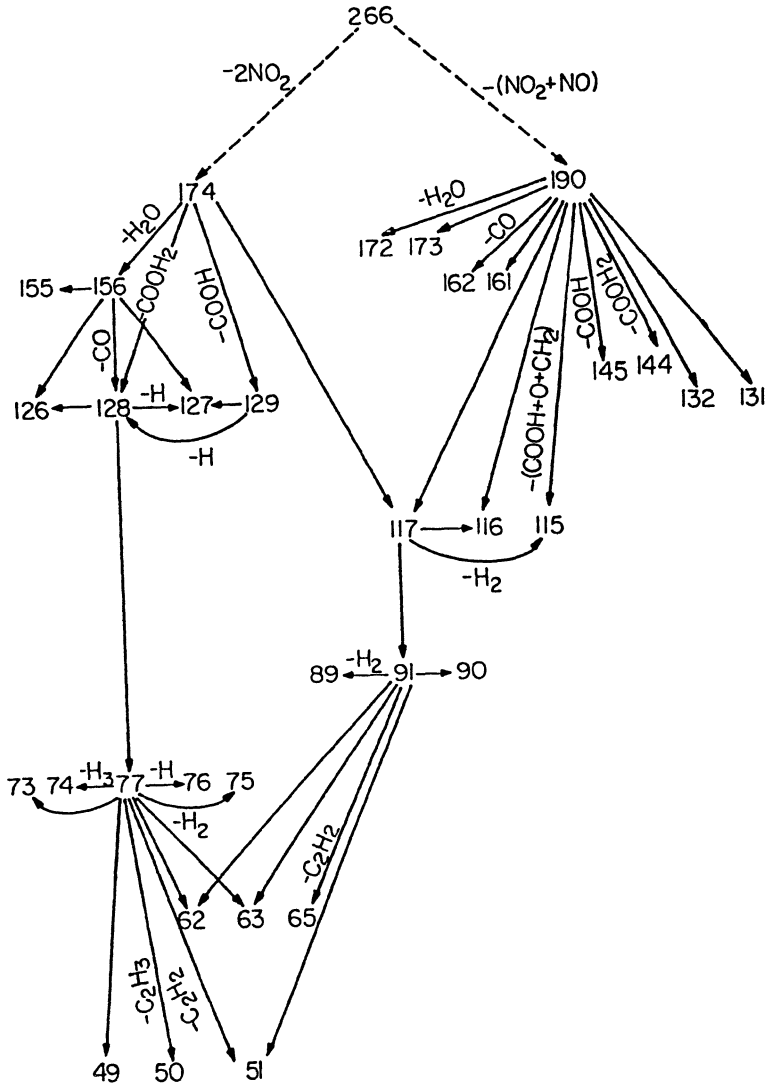
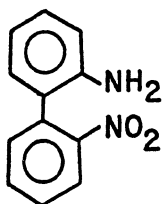


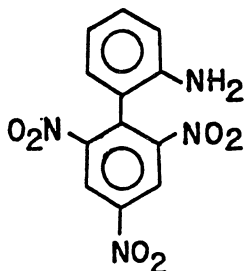
Figure 10. Fragmentation map of DPCD-Acid.

7. POLYNITROBIPHENYL-2-AMINES

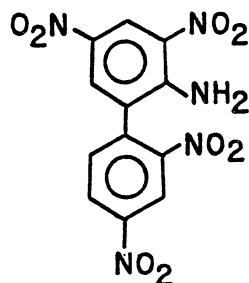
Another group of energetic compounds are polyaminopolynitrocompounds, which have become recently the subject of renewed interest. Amino substitution has been used as a way of modifying the properties of nitroaromatic compounds in an effort to decrease the impact sensitivity. As part of this effort, a series of polynitrobiphenyl-2-amines were synthesized [13]. The structure of these compounds are shown in schemes 15 to 20.



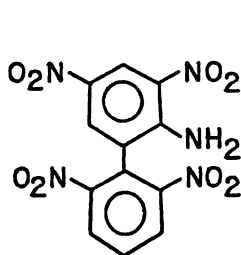
15



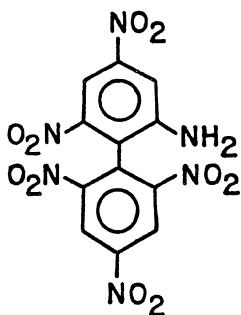
16



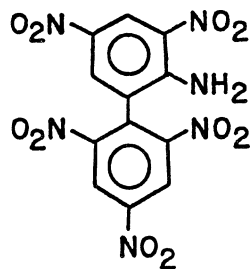
17



18



19



20

An MS/MS CID study of these compounds was carried out using the B-B tandem mass spectrometer [14]. Two examples of CID spectra are given in Figures 11 and 12 which show the CID spectra of the molecular ion of compound 15 and of the molecular ion of compound 18 respectively.

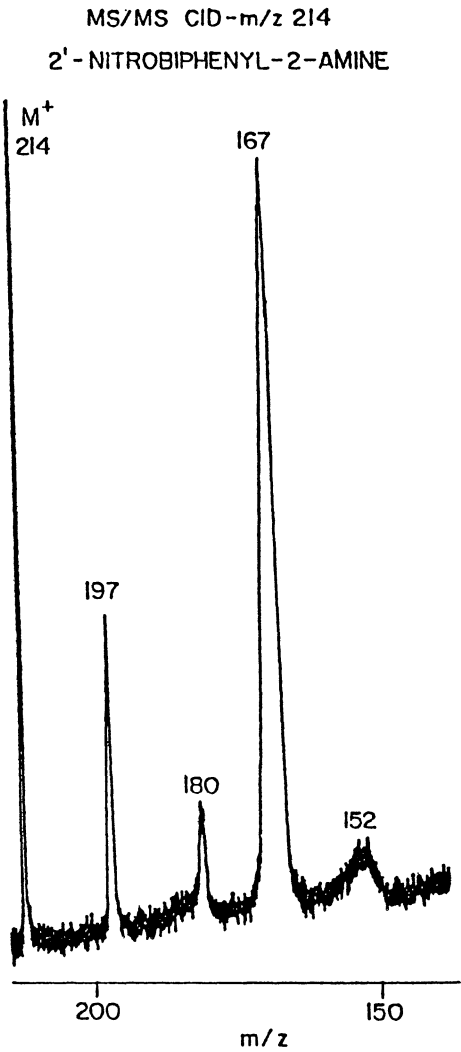


Figure 11. CID spectrum of the M^+ ion of compound 15.

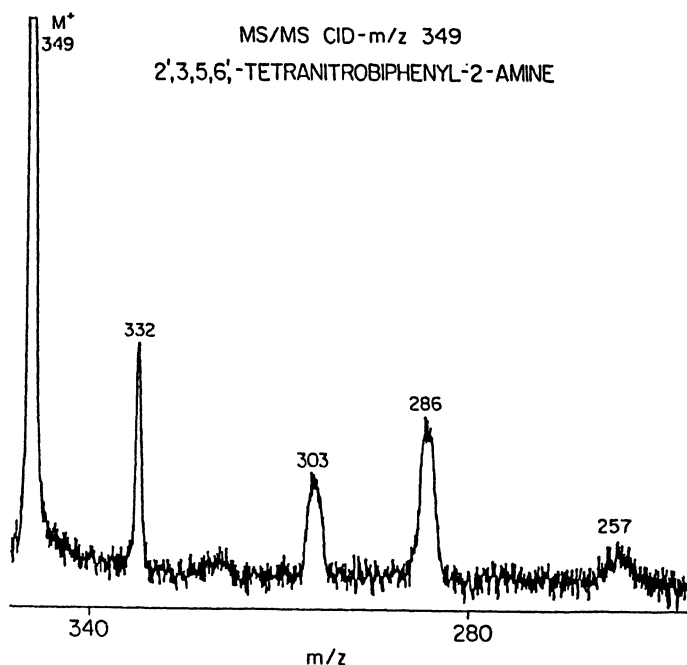


Figure 12. CID spectrum of the M^+ ion of compound 18.

Table 3 shows the abundances of the major ions observed in the CID spectra of the molecular ions as well as of the highly abundant fragment ions.

All six compounds are characterized by a molecular ion in their EI spectrum. Loss of OH is typical to all six compounds. Second loss of OH from the $(M-OH)^+$ ion occurs only in compounds 15 and 17. These two compounds are the only ones which do not have a nitro group in the 6' position, which might be the reason of the exclusion of this process in the other compounds. Loss of NO occurs sometimes after loss of OH as in 19, sometimes after loss of NO_2 as in 20, and sometimes after loss of both as in 17 and 18. The loss of NO could be a measure of the C- NO_2 to C-ONO rearrangement. Isotopic labeled compounds could give an indication concerning the origin of the NO loss. Loss of NO_2 (or HNO_2) is a major loss in these compounds, from the molecular ion as well as from $(M-OH)^+$. Loss of a second nitro group also occurs either simultaneously with the first, or consecutively after loss of the first one.

Table 3. CID ions of polynitrophenyl-2-amines

COMPOUND	PRECURSOR ION m/z	DAUGHTER IONS							
		(P-OH) ⁺	(P-NO) ⁺	(P-2OH) ⁺	(P-NO ₂) ⁺	(P-HNO ₂) ⁺	(P-OH-NO ₂) ⁺	(P-2NO ₂) ⁺	OTHER IONS
1 2'-NITROBIPHENYL-2-AMINE M.W. 214	214(M) ⁺⁺ 197(M-OH) ⁺ 167(M-HNO ₂) ⁺⁺	197(42) 180(100)		180(14)		167(100)			152(5) 166(5), 139(100)
2 2',4',5'-TRINITROBIPHENYL-2-AMINE M.W. 304	304(M) ⁺⁺ 287(M-OH) ⁺ 258(M-NO ₂) ⁺	287(100) 241(100)			258(71) 241(100) 212(73)		241(28)		
3 2',3,4',5'-TETRANITROBIPHENYL-2-AMINE M.W. 349	349(M) ⁺⁺ 332(M-OH) ⁺ 303(M-NO ₂) ⁺ 286(M-OH-NO ₂) ⁺	332(100) 315(35) 286(100)	256(100)		303(16) 286(100) 240(27)		286(12)	240(27)	
4 2',3,5,6'-TETRANITROBIPHENYL-2-AMINE M.W. 349	349(M) ⁺⁺ 332(M-OH) ⁺ 303(M-NO ₂) ⁺ 286(M-OH-NO ₂) ⁺	332(100) 286(100)	256(100)		303(42) 286(100) 257(11) 240(45)		286(68)	257(11) 240(10)	
5 2',4,4',5,6'-PENTANITROBIPHENYL-2-AMINE M.W. 394	394(M) ⁺⁺ 377(M-OH) ⁺	377(100)	347(100)		348(38)			302(11)	
6 2',3,4',5,6'-PENTANITROBIPHENYL-2-AMINE M.W. 394	394(M) ⁺⁺ 377(M-OH) ⁺ 348(M-NO ₂) ⁺	377(100)	364(21) 318(100)		348(25) 331(100) 302(80)		331(35)	302(9) 285(37)	

8. REFERENCES

1. Yinon, J. (1982) 'Mass spectrometry of explosives: Nitro compounds, nitrate esters, and nitramines', *Mass Spectr. Reviews* 1, 257-302.
2. Meyerson, S., Puskas, I. and Fields, E.K. (1966) 'Organic ions in the gas phase. XVIII. Mass spectra of nitroarenes', *J. Am. Chem. Soc.* 88, 4974-4980.
3. Fields, E.K. and Meyerson, S. (1969) 'Reactions of aromatic compounds at high temperatures', *Accounts Chem. Res.* 2, 273-278.
4. Stals, J. (1971) 'Chemistry of aliphatic unconjugated nitramines. Part 7. Interrelations between the thermal, photochemical and mass spectral fragmentation of RDX', *Trans. Farad. Soc.* 67, 1768-1775.
5. Bulusu, S., Axenrod, T. and Milne, G.W.A. (1970) 'Electron-impact fragmentation of some secondary aliphatic nitramines. Migration of the nitro group in heterocyclic nitramines', *Org. Mass Spectr.* 3, 13-21.
6. Fields, E.K. and Meyerson, S. (1972) 'Mass spectral and thermal reactions of dinitrobenzenes', *J. Org. Chem.* 37, 3861-3866.
7. Yinon, J. (1990) 'An introduction to tandem mass spectrometry (MS/MS) and collision induced dissociation (CID)', *Proc. of NATO Advanced Study Institute on Chemistry and Physics of the Molecular Processes in Energetic Materials, Sicily, Italy, September 3 to 15, 1989.*
8. Yinon, J. (1987) 'Mass spectral fragmentation pathways in 2,4,6-trinitroaromatic compounds', *Org. Mass Spectr.* 22, 501-505.
9. Yinon, J., Harvan, D.J. and Hass, J.R. (1982) 'Mass spectral fragmentation pathways in RDX and HMX. A mass analyzed ion kinetic energy spectrometric/collisional induced dissociation study', *Org. Mass Spectr.* 17, 321-326.
10. Yinon, J., Brumley, W.C., Brilis, G.M. and Bulusu, S. 'Mass spectral fragmentation pathways in nitramines. A collision induced dissociation study', *Org. Mass Spectr.* (in press).
11. Yinon, J. and Bulusu, S. (1986) 'Mass spectral fragmentation pathways in nitroadamantanes. A tandem mass spectrometric collisionally induced dissociation study', *Org. Mass Spectr.* 21, 529-533.

12. Yinon, J. and Bulusu, S. (1986) 'MS/MS of energetic compounds. A collisional induced dissociation study of some polynitrobishomocubanes', J. Energ. Materials 4, 115-131.
13. Bell, A.J. and Read, R.W. (1987) 'Synthesis of polynitro-substituted 2'-nitrobiphenyl-2-amines, analogues of polynitro benzo[c]cinnoline oxide derivatives', Aust. J. Chem. 40, 1813-1829.
14. Yinon, J. and Read, R.W. (1989) 'MS/MS of energetic compounds. A collision induced dissociation (CID) study of some polynitrobiphenyl-2-amines', Proc. of 3rd International Symposium on Analysis and Detection of Explosives, Mannheim-Neustadt, FRG, 1989.

NQR/NMR Studies of Solid Phase Energetic Materials

R. A. Marino
Department of Physics & Astronomy
Hunter College of CUNY
695 Park Avenue
New York, NY 10021

ABSTRACT. A review of NQR/NMR studies of solid phase energetic materials is presented. Work on structure and bonding and molecular dynamics in Trinitrobenzene, Ammonium Nitrate, Nitrocellulose, RDX, HMX and PETN is reviewed.

1. Background

The power of magnetic resonance techniques to elucidate structure and bonding has been well established in the half century since the development of nuclear magnetic resonance. This paper reviews studies of molecular structure and molecular dynamics, all in the solid state, for a few principal energetic materials. In addition to traditional NMR methods, the principal experimental technique used is nuclear quadrupole resonance (NQR), chosen because it enables observation of high resolution spectra rich in structural information, even for polycrystalline or amorphous materials^{1,2,3,4}.

Nuclear quadrupole coupling arises from the interaction of the electric quadrupole moment, eQ , of a nucleus, such as Nitrogen-14 (spin $I=1$, 100% abundant) and the electric field gradient, efg , at the nuclear site due to all other charges in the crystal. As depicted in Figure 1, electric field gradients arise principally from local electron distributions, with neighboring molecules contributing as much as 10%. Hence NQR frequencies are sensitive both to chemical bonding and to crystallography. External radio-frequency fields can couple to the nuclear magnetic moment, μ , in a manner completely analogous to NMR. In fact, detection of NQR levels is accomplished with spectrometers which are basically identical to those used for NMR.

The 3×3 electric field gradient tensor is traceless and symmetric, hence it contains only five independent parameters. Three of these convey the orientation of the principal axes of the efg with respect to the crystal axes, and could be obtained by single crystal experiments. The remaining two, with which we shall be principally concerned, are the quadrupole coupling constant, e^2qQ , a measure of the magnitude of the interaction, and the asymmetry parameter η , which measures the departure from cylindrical symmetry of the efg tensor:

$$e^2qQ = (eQ) (eq_{zz}) \quad (1)$$

$$\eta = (q_{xx} - q_{yy})/q_{zz} \quad (2)$$

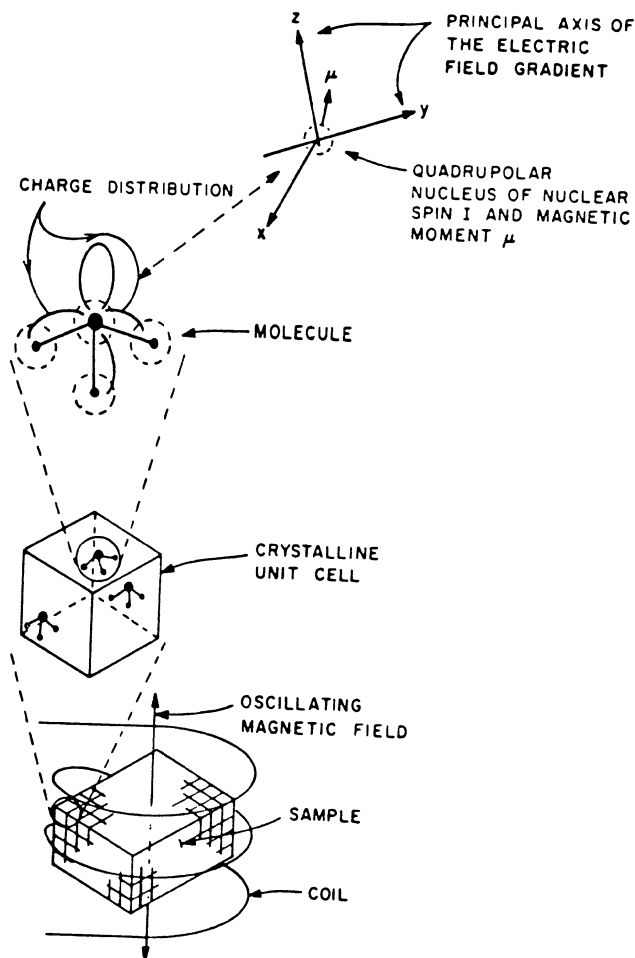


Figure 1. Schematic diagram for origin and detection of NQR

where the q_{ii} are the diagonal components of the electric field gradient, $\partial^2 V / \partial x_i^2$. V is the potential at the nucleus due to external charges, e is the electron charge, and Q is the nuclear quadrupole moment.

The NQR energy level diagram for the case of nuclear spin $I=1$, the only case of interest to us here, is shown in Figure 2. For Nitrogen-14 the resulting transition frequencies fall in the low MHz region. As shown in the figure, three transitions are possible. However, it is clear that knowledge of any two will determine the third. The quadrupole coupling constant and asymmetry parameter are related to the transition frequencies by

$$h\nu_{\pm} = e^2 q Q (3 \pm \eta) / 4 \quad (3)$$

In the following sections, NQR techniques, alone or in conjunction with NMR, are

employed to study structure and bonding of some energetic materials. While comprehensive NQR studies have not been attempted other than in TNT, what follows shows the kind of structural information that can be obtained by these experimental methods.

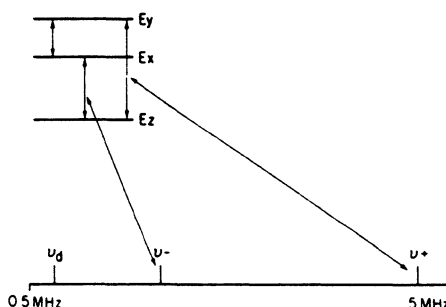


Figure 2. Energy level diagram for Nitrogen-14 NQR.

2. Trinitrotoluene, TNT

It has long been established that α -Trinitrotoluene can coexist^{5,6} as two different phases at ambient temperatures. A monoclinic form is the product of annealing cast TNT and has been studied by several workers,^{7,8,9}. A good crystal structure has recently been obtained by Carper et. al.¹⁰ Another possible crystal habit has orthorhombic symmetry^{9,11}. This phase can be formed by quickly chilling molten TNT as well as by recrystallization from cyclohexanol. A crystal structure of this phase also has been obtained¹⁰.

Samples of cast TNT, which commonly contain a mixture of these two phases, will often develop cracks and voids when orthorhombic microcrystals transform to the denser monoclinic phase upon annealing. The desire to learn more about the molecular structure and molecular dynamics of TNT in the two phases provided part of the rationale for this study.

2.1. SAMPLE PREPARATION AND NQR SPECTRUM

α -TNT was obtained from Eastman Kodak in the form of small flakes moist with 10% water. These flakes were gently dried under a heat lamp and recrystallized from acetone. The resulting very pale yellow crystals were used to prepare samples of solid TNT which were preferentially crystallized in one of its two crystal habits. Monoclinic TNT was obtained by seeding the melt^{12,13,14} with about $\frac{1}{2}$ of a percent of 2,2',4,4',6,6'-Hexanitrostylbene (HNS) allowing the complex $(\text{TNT})_2 \cdot \text{HNS}$ to form and then to nucleate the growth of monoclinic TNT.

The resulting polycrystalline material consisted of a mass of unoriented and very small crystallites, as expected. Orthorhombic TNT was prepared by quenching molten

Table 1. Nitrogen-14 NQR Spectra of Trinitrotoluene at 77°K. The spectral lines are assigned to one para (p) site and two ortho sites (oA,oB) for each of two inequivalent molecules (I and II). Data for the monoclinic phase are listed first, with corresponding lines of the orthorhombic phase shown in parentheses.

	ν_-	ν_+
<u>MOLECULAR SITE</u>	<u>kHz</u>	<u>kHz</u>
pII	792.1 (792.4)	869.4 (867.8)
pI	801.8 (803.2)	895.4 (897.9)
oAI	767.3 (766.5)	875.6 (875.7)
oBI	767.7 (768.5)	857.0 (858.6)
oAII	729.7 (727.4)	861.8 (862.3)
oBII	730.1 (732.5)	888.1 (885.6)

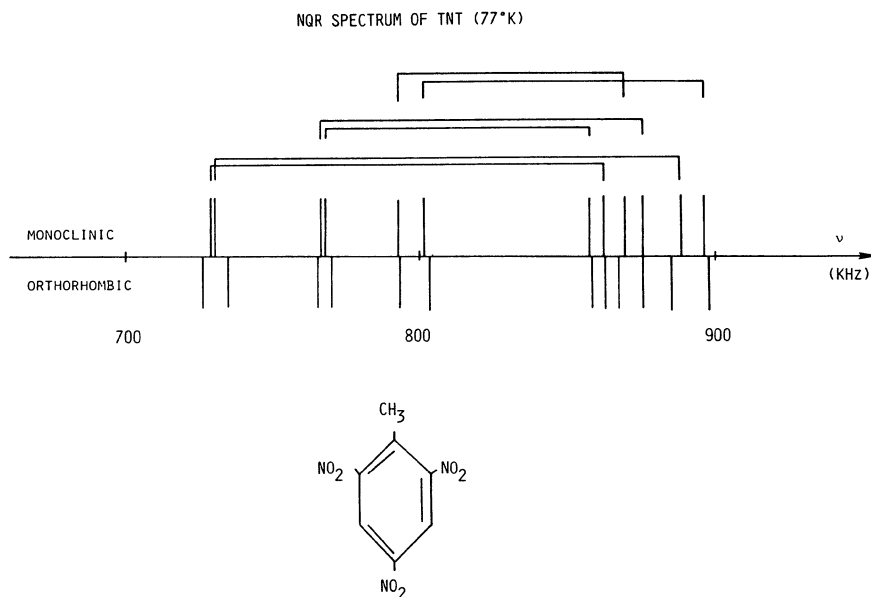


Figure 3. Nitrogen-14NQR Spectrum of TNT at 77 K. Brackets indicate paired lines.

TNT in small batches on a copper slab maintained at about 0°C.

The ^{14}N NQR spectrum of monoclinic TNT and of orthorhombic TNT is shown in Figure 3. The spectrum of each phase consists of twelve resonance lines, corresponding to six distinct nitrogen sites. Each site gives rise to a ν_- and a corresponding ν_+ line which are related to the quadrupole coupling constant, e^2qQ/h , and to the asymmetry parameter, η , by the equations (3).

For each corresponding pair of ν_- and ν_+ lines there also exists a "difference line" ν_d whose value is given by $\nu_d = \nu_+ - \nu_-$. In TNT the frequencies of these transitions fall below the lower operating point of our spectrometer and were not detected. Therefore, in order to compute e^2qQ/h and η for each site it is necessary to "match-up" the corresponding ν_+ and ν_- lines. This was done using a simple double resonance technique described elsewhere¹⁵. Table 1 shows the NQR frequencies matched and assigned to six crystallographic sites for both phases of TNT.

The similarity between the NQR spectra of the two phases of TNT as depicted in Figure 3 is remarkable. Experience with NQR spectra of other substances which undergo structural phase transition shows that the NQR frequencies undergo shifts of the order of 10%. Now, these structural phase transition shifts have been interpreted as giving a measure of the contribution of atoms and molecules other than those directly bonded to the resonant site to the total field gradient at that site. An independent

measurement of the same effect is the size of "crystal splitting", the difference in NQR frequencies corresponding to sites that are chemically equivalent, but which are made physically inequivalent by the crystal packing. These two measures of crystal field effects have been found generally in good agreement when they could be compared.

In the present case, we observe that the spectra of orthorhombic and monoclinic TNT are nearly identical to one another while at the same time each phase displays considerable physical inequivalence. This allows us to conclude with some confidence that the structure and conformation of each molecule in orthorhombic TNT and its relation to its immediate molecular neighbors must be remarkably similar to the case in monoclinic TNT.

Because of this great similarity, our discussion of structure and bonding of α -TNT will focus specifically on the temperature stable (monoclinic) phase of this material.

2.2. STRUCTURE AND BONDING OF TNT

For each crystal phase of TNT the observation of six ν_- lines and six ν_+ lines, indicating the presence of six Nitrogen NQR sites is in agreement with the x-ray crystallography work¹⁰. There are two crystallographically distinct molecules per unit cell, each with physically inequivalent nitro-groups.

The isolated molecule of trinitrotoluene (2-methyl-1,3,5-trinitrobenzene) has two chemically distinct nitro-groups which we could designate p and o for the groups which are para and ortho, respectively, to the methyl group. If the two ortho sites become physically inequivalent in the solid, and we label them oA and oB respectively, and if we now label the two crystallographically distinct molecules per unit cell I and II, we reach a nomenclature for the six sites which we will use for the remainder of this paper. Namely, pI, oAI and oBI for molecule I, and pII, oAII and oBII for molecule II.

The above considerations about the chemical and physical (in) equivalence of NQR sites is usually extremely useful in comparing these sites to their corresponding crystallographic sites. However, this is not the case in TNT as can be seen by the seemingly incongruous pairing of ν_- and ν_+ lines in Figure 3. In fact, it will be shown that the chemical inequivalence of "o" and "p" sites are not basically relevant to the interpretation of NQR spectrum of Figure 3. Rather, the determining factor in explaining the splitting of the NQR lines is the physical inequivalence of the six nitrogen sites in the solid state. Specifically, we will show that the parameter that makes the dominant contribution is the angle of twist of the nitro-group about the C-N bond.

In the following sections, we will first develop a set of equations (Townes-Dailey method) relating the observed NQR parameters to a bonding model of the nitro-group. Then we will use these equations to interpret the TNT data, and show how additional NQR data, much of it new, on molecules similar to TNT supports our interpretation.

2.2.1. Townes-Dailey theory. The Townes-Dailey (TD) method¹⁶ of relating measured field gradients to orbital occupation numbers is a first-order theory which works best when comparisons are made among similar molecules¹⁷. In our case, where we limit our discussion to C-nitro groups, we expect that the analysis will provide useful insights in the variation of structure and electron distribution among the various nitro groups under study.

The Townes-Dailey analysis of the C-nitro group begins with a choice of principal axes for the efg tensor. The presence of two local approximate mirror planes, and the

single crystal work by Cheng and Brown¹⁸ yield the following choice: The z-axis is along the N-C bond, the y-axis is perpendicular to the nitro group plane. The nitrogen site is assumed to be in a state of sp^2 hybridization: a sigma bonding orbital of occupation number σ_{NC} forms a bond to the ring carbon atom, while the two remaining hybrids, each with occupation number σ_{NO} , form sigma bonds to the oxygen atoms. A nitrogen p_y orbital, with occupation number π , takes part in the molecular $p\pi$ orbitals. The standard sp^2 hybridization is used in these equations even though the angle ONO is known to be larger than 120° by about four to five degrees. Although the TD method can easily accommodate this "refinement" it has been the experience of this and other workers that it does not result in a significant improvement of the final results.

Following Subbarao and Bray's notation¹⁹, the Townes-Dailey relations can be written in the following very useful form,

$$(\sigma_{NO} - \pi) = 4/3 \nu_d/q_0 \quad (4)$$

$$(\sigma_{NC} - \sigma_{NO}) = 2 \nu_-/q_0 \quad (5)$$

$$(\sigma_{NC} - \pi) = (2\nu_- + 4/3 \nu_d)/q_0 \quad (6)$$

Here q_0 is the magnitude of the coupling constant per p-electron in atomic nitrogen, a parameter estimated to be between -8 and -10 MHz. Although most of our conclusions will be insensitive to the particular choice of q_0 , we prefer the latter value, and shall use it when necessary.

2.2.2. Nitro group conformation. Equations (4) to (6) are the basis for the interpretation of the NQR data of α -TNT in terms of the structure and bonding of this molecule.

The first effect to be considered is the differential effect which the methyl-group will have on nitro-groups ortho and para to it. Fortunately, this general question of substituent effects on NQR parameters has been thoroughly investigated, most notably by Bray and coworkers¹⁷ and is well understood. The main results is that good correlations can be obtained between measured field gradients and Hammett σ constants. The latter are a measure of the ability of the substituent to withdraw or supply electrons to a reaction site. It should be noted, however, that these constants are determined in the liquid state. Thus it is not surprising that their correlation with NQR data obtained in solids breaks down when anisotropic interactions are strong.

In the case of α -TNT, considerations of the chemical inequivalence of the ortho and para nitro-groups using the correlations found by Subbarao and Bray¹⁹, lead to expectations of frequency shift less than 10 kHz. Clearly, these shifts are much less than the splittings of actual TNT frequencies. We conclude that chemical inequivalence due to the electron releasing property of the methyl group cannot even begin to explain the observed NQR data in α -TNT.

We now turn to a consideration of the possibility of strong physical inequivalence of the nitro-groups in nitrobenzenes. In fact crystallographic studies of these substances show that the plane of the NO_2 -group can exist in equilibrium in solids at relatively large angles of rotation from the plane of the benzene ring. This rotation occurs mainly about the CN bond, notwithstanding the large expected double bond character of this bond.

The crystallographic studies, taken together, indicate that this angle of twist generally increases with the number of neighboring substituents on the benzene ring. What is surprising is that even with no neighbors, angles of up to 10° or more are common. One substituent ortho to the nitro-group can lead to twist angles of the order of 30° to 40° , while rotations of up to 60° or 70° are found when both sites ortho to the nitro-group have a bulky substituent. In addition to the effect of steric hindrance from neighboring substituents, the details of crystal packing and of intermolecular interactions are responsible for further variations in the nitro-group twist angles.

When the plane of a nitro-group in a nitro benzene is constrained to be twisted away from the plane of the benzene ring by a rotation about the CN (for any of the reasons outlined above) it follows that at the same time there will be a decrease in the double bond character of the CN bond. Clearly, the overlap integral between the $p\pi$ orbitals of the ring carbon and of the nitrogen atom will show a strong dependence on the nitro-group twist angle. One would expect that this overlap integral would act as a gate which can modulate the otherwise strong electrophilic properties of the nitro-group. Thus, these first-order considerations lead us to the expectation that increasing the nitro-group twist angle would result in a decrease in the $p\pi$ electron population of the nitro-group.

Since quadrupole coupling constants are very sensitive to the electron densities local to the resonant nucleus, one expects that the Nitrogen-14 NQR spectra of nitrobenzenes would provide a good test of these hypotheses.

Analyses of the data reported in previous ^{14}N NQR studies of nitrobenzenes^{34,35} dealing mainly with planar molecules, disclose that of the three nitrogen occupation numbers, σ_{NO} , σ_{NC} , and π , variations in the first reflected variations in resonance as well as inductive effects of various substituents. On the other hand, the occupation number σ_{NC} is found to be insensitive to resonance effects. Thus of the Townes-Dailey relations, Equation (6) is the one to be used in a study of the nitro-group twist since it best separates resonance from inductive effects at the Nitrogen site. Figure 4 is a plot of $(2\nu_- + 4/3 \nu_d)$ for each of the six Nitrogen-14 NQR sites in monoclinic α -TNT vs. the nitro-group twist angle, θ , as measured by x-ray work¹⁰. Note that the figure shows a very suggestive relation between the NQR spectroscopic parameters and the structural parameter, θ . It is our contention that Figure 4 indicates that the unusually large scatter in the NQR spectrum of TNT, discernible in Figure 3, is explained in large part by shifts in orbital occupation numbers correlated with the conformation of the nitro group. The NQR data used in Figure 4 were obtained at 77 K. The assignment of crystallographic sites to NQR sites was done by matching sites with a higher value of the twist angle with sites with lower values of the occupation number π . Of course, this ensures that a curve connecting the points plotted in Figure 4 be monotonic. The argument that the correlation depicted in Figure 4 is real finally rests on the self consistency of the assignment and on its predictive value. In the next section we turn to an NQR study of other nitrobenzenes to test the predictive value of the relation discovered in Figure 4.

2.2.3. Supporting NQR Data. In the previous section we showed how the details of the NQR spectrum of α -TNT could be accounted for by considering the effect on the nitrogen $p\pi$ population due to the rotation of the plane of the nitro-group about the CN bond axis. Here we show how NQR data in other trinitrobenzenes support the model we developed.

The electronegativity of methyl groups is known to be much smaller in magnitude than the electronegativity of nitro groups. For that reason, of all the theoretical possibilities, s-trinitrobenzene (TNB), and s-trinitro-m-xylene (TNX) should be closest to TNT in electronic structure. They have, respectively, one less and one more methyl group than TNT. Since the crystal structure and molecular conformation of these

Table 2. Nitrogen-14 NQR spectral data for some trinitrobenzenes at 77 K. Also listed is the angle of twist of the NO₂-Group relative to the benzene ring

<u>COMPOUND/SITE</u>	ν_- <u>kHz</u>	ν_+ <u>kHz</u>	$2\nu_- + 4/3\nu_d$ <u>kHz</u>	Nitro twist Angle (degrees)
α -TNT (Monoclinic)				
pII	792.1	869.4	1687.3	30 ^a
pI	801.8	895.4	1728.4	24
oAI	767.7	857.0	1654.5	51
oBI	767.3	875.6	1679.0	43
oAII	729.7	861.8	1635.5	60
oBI	730.1	888.1	1670.9	45
Trinitrobenzene (TNB)	758.0	959.4	1784.5	3 ^b
	752.6	957.4	1778.3	5
	734.6	931.5	1731.7	10
	717.2	907.	1687.5	10
	668.6	884.	1624.4	8 bend
	704.0	832.	1578.7	28
Trinitro-m-Xylene (TNX)	759.	822.	1602.0	75.2 ^c
	759.	886.	1687	35.7
2, 4, 6-Trinitro-l-t- -Butyl-3,5-Dimethyl Benzene (TBDB)	752.8	825.1	1602.0	not available

a) Reference 10

b) Reference 20

c) Reference 21

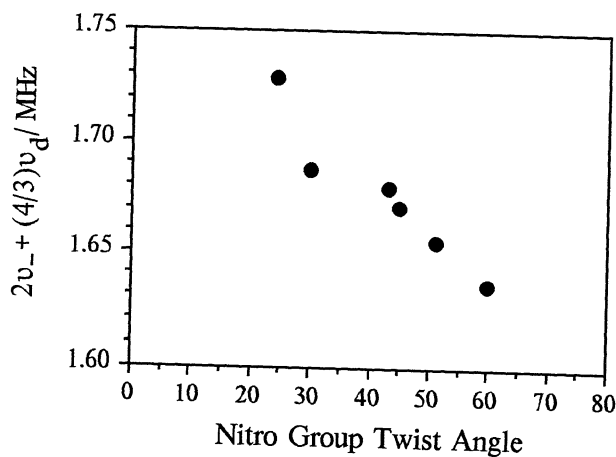


Figure 4. Plot of the spectral parameter $[2\nu_{-} + (4/3)\nu_d]$ for TNT as a function of the angle of twist of the Nitro group away from the plane of the benzene ring.

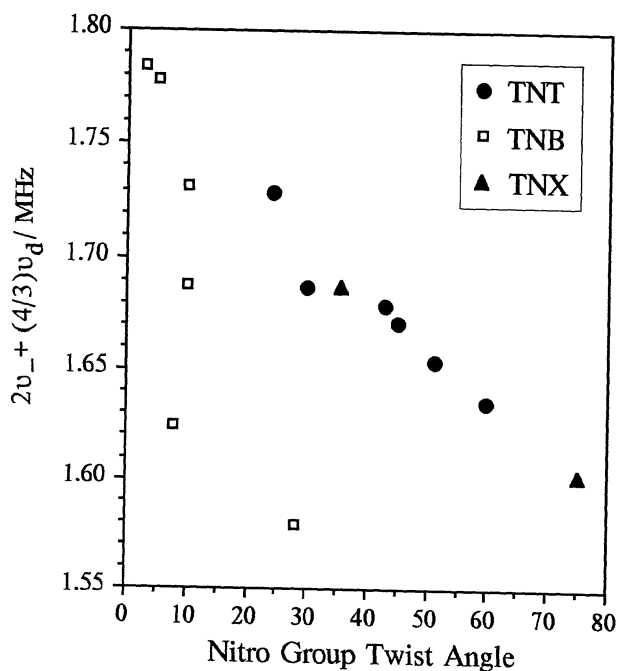


Figure 5. Plot of the spectral parameters $[2\nu_{-} + (4/3)\nu_d]$ for TNB, TNT and TNX as a function of the angle of twist of the Nitro group away from the plane of the benzene ring.

substances are known^{20,21}, we undertook a search for their NQR spectrum. The complete spectrum for both substances was found, and the ν_{\pm} lines corresponding to each site were paired up by double resonance methods¹⁵. The results are summarized in Table 2. Three of the 12 lines in TNB were previously reported by Subbarao and Bray¹⁹; we detected all 12 lines corresponding to the multiplicity expected from the results of the crystal structure study²⁰.

In Figure 5, plotted vs. the crystallographic twist angle θ is the experimental number $(2\nu_{-} + 4/3 \nu_{d})$ in kHz, which was shown previously to reflect the nitrogen $p\pi$ orbital occupation number, according to our model. Clearly, the six TNB sites do not fit so well, but the presence of considerable nitro group bending, as well as twisting, may be to blame. Further work may be necessary to include this complication into our model. It is encouraging, however, that in TNX, with its two large twist angles, there is indeed excellent agreement with the model we have developed.

3. Ammonium Nitrate, AN

3.1. BACKGROUND

The many commercial and military uses of ammonium nitrate (AN) have resulted in considerable attention by researchers to the interesting crystallographic phase transformations of this substance. Two problems in its applications, namely hygroscopicity and dimensional instability, are closely related to some of its temperature dependent phase transformations. Below its melting point at 169°C, AN exists in a succession of solid phases^{22,23} characterized by decreasing mobility of the ions. Transitions among these phases have been studied by several techniques in the past, including x-rays²⁴ and neutron diffractions²⁵ and Raman scattering^{26,27}. In previous NMR studies²⁸, translational and rotational diffusion of the ammonium ion has been studied in some detail by proton and deuteron spin relaxation times. On the other hand,

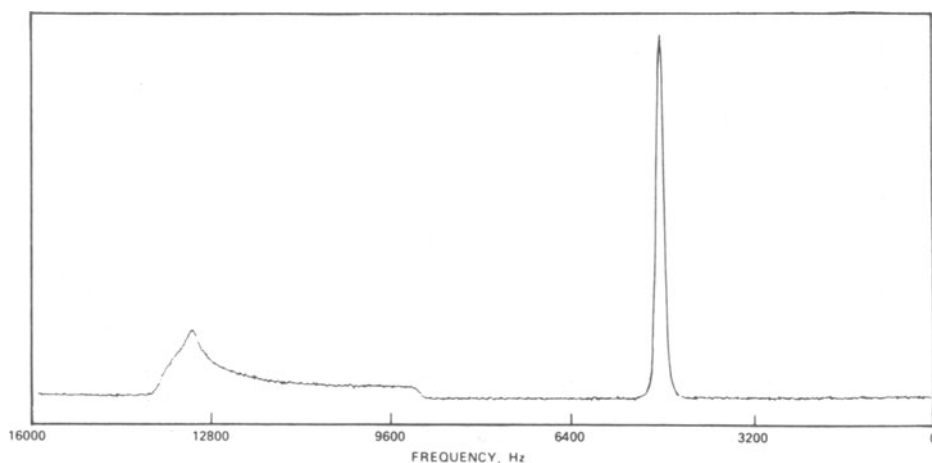


Figure 6. Nitrogen-15 NMR spectrum of polycrystalline N-15 labeled AN at room temperature.

the nitrate ion has received much less attention, probably because of the complications presented by the quadrupolar interaction present in the abundant species of nitrogen and the poor natural abundance of Oxygen-17. With the advent of MAS-NMR techniques, however, Nitrogen-15 NMR studies in solids have become more sensitive, and together with the commercial availability of ^{15}N -enriched ammonium nitrate they provide us with the primary means to undertake this study.

Table 3 summarizes the well-known characteristics of the phase transitions of AN for convenience in the following discussions.

TABLE 3. Polymorphism of Ammonium Nitrate

<u>Transition</u>	<u>Temperature, °C</u>	<u>Δ Volume, %</u>
V \rightarrow IV	-18	-0.9
IV \rightarrow III	32.1	+3.4
III \rightarrow II	84.2	-1.6
II \rightarrow I	125.2	+1.9
I \rightarrow Liquid	169.6	-

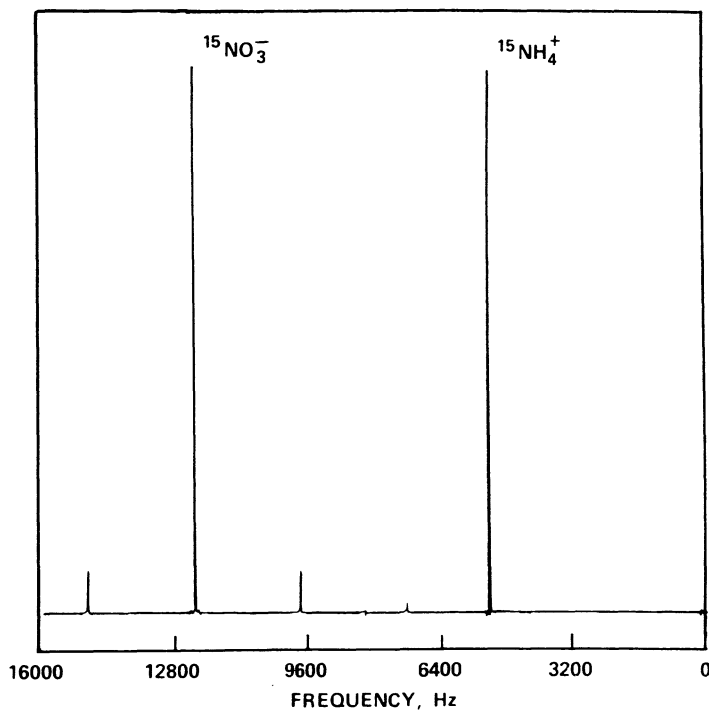


Figure 7. MAS Nitrogen-15 NMR spectrum of N-15 labeled AN at room temperature.

3.2. BROADBAND AND MAS NMR STUDIES

The Nitrogen-15 NMR spectrum of polycrystalline AN at room temperature is shown in Figure 6. It was obtained with the broadband probe of the Varian XL-200 spectrometer in a sample with 99% Nitrogen-15 enrichment by signal averaging 10,000 scans. Two well-resolved but broad features were observed, corresponding to the two chemically distinct nitrogen sites in AN. The lines were considerably broadened by the dipole interaction with the protons in the sample and, in the case of the planar nitrate ion, by considerable chemical shift anisotropy. Both of these sources of broadening could be drastically reduced by combining the techniques of sample spinning (MAS) and high power decoupling. The resulting spectrum is shown in Figure 7. The drastic reduction in linewidth for each line is to be noted as well as the appearance of sidebands at reduced amplitude at multiples of the sample spinning frequency. A consequence of the reduction in linewidth is an enhancement of the peak signal to noise (s/n) ratio. Figure 7 was the result of a single NMR scan, compared to 10,000 for Figure 6. Examination of the spectra shown in these two figures enables one to draw the following conclusions.

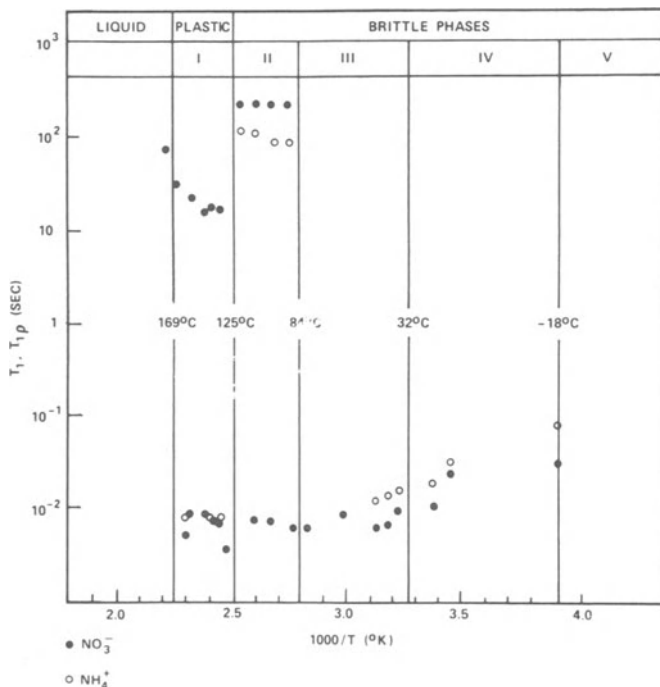


Figure 8. Nitrogen-15 NMR relaxation times for the nitrate and ammonium ion sites of AN plotted vs. reciprocal temperature.

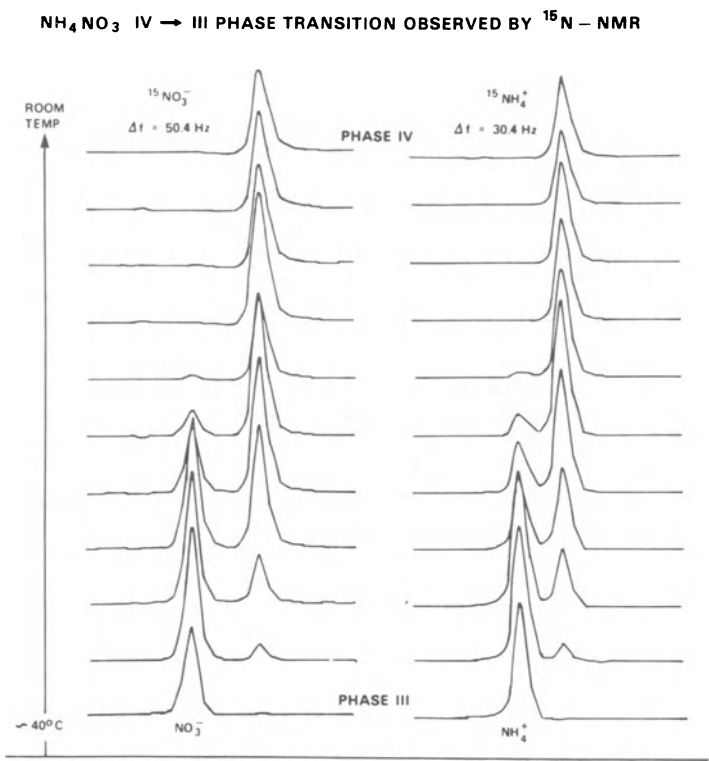


Figure 9. Observation of the melting phase transition in AN (III to IV) byMAS NMR>

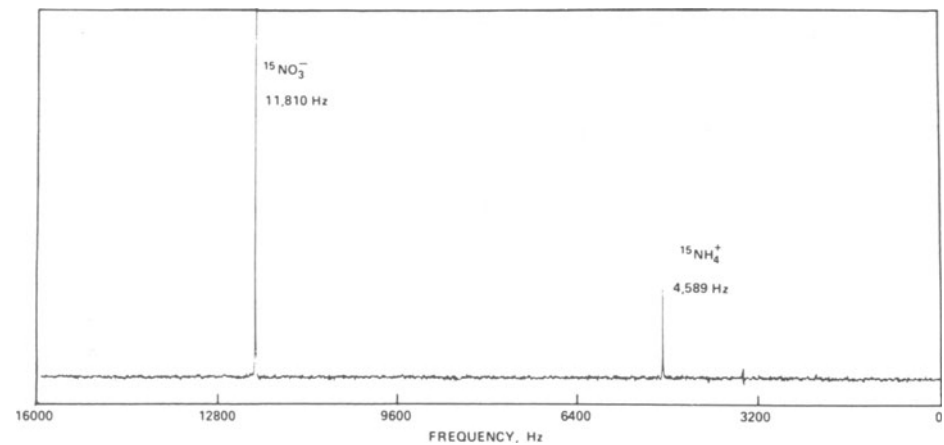


Figure 10. Nitrogen-15 broadband spectrum of N-15 labeled AN in its plastic phase.

First, the isotropic chemical shifts for the ammonium and nitrate ions in polycrystalline AN are not significantly different from those of the ions in solution. This result was not unexpected, but it implies that no particular insight about the structure of the solid is obtained from the isotropic chemical shift. Second, the anisotropy in the chemical shift of the nitrate ion obtained from Figure 6 is approximately 200 ppm. However, the $^{15}\text{NO}_3^-$ peak shows a shoulder on the down field side which indicates axial asymmetry.

The variation in the amplitude of spinning sidebands as a function of the sample spinning speed in a MAS experiment can yield an independent value of the chemical shift anisotropy²⁹. These measurements were undertaken and yielded the following results:

$$\begin{aligned}\sigma_{33} - \sigma_{12} &= 220 \pm 15 \text{ ppm} \\ \sigma_{11} + \sigma_{33} - 2\sigma_{22} &= 120 \pm 40 \text{ ppm}\end{aligned}$$

The temperature dependence of the relaxation times were measured over a limited temperature region. The results, shown in Figure 8 are mostly inconclusive. However, two interesting effects were observed. First, in the course of these relaxation time experiments, it was possible to observe simultaneously the high resolution MAS NMR spectrum of both phase IV and phase III material as they coexisted in the sample volume. These observations confirm the reports in the literature that the transition from the room temperature phase (IV) to the high temperature phase (III) is analogous to a "melting" transition. In fact, as the temperature of our NMR sample was allowed to drift from about 40° to room temperature over a 2 hour period, it was observed that the spectrum of one phase gradually decreased in amplitude as the spectrum of the other phase gradually increased. These results are shown in Figure 9. The thermal properties of AN have been well characterized by differential scanning calorimetry studies²² and it is presumed on that basis that the observations shown in Figure 9 represent "freezing" of phase III into phase IV material. This effect was easily reproducible in either direction by heating or cooling. Due to coarse temperature control, however, it was not possible to confirm the lack of hysteresis in the phase transition. As a consequence of these observations, it was possible to measure the difference in the isotropic chemical shift in the solid phases III and IV to considerable precision. The results indicate upfield shifts of the following magnitude in going from III to IV:

$$^{15}\text{NO}_3^- : 50.4 \text{ Hz}$$

$$^{15}\text{NH}_4^+ : 30.4 \text{ Hz}$$

The second interesting observation made in the course of temperature dependent studies, was the observation of the NMR spectrum of ammonium nitrate in its "plastic" phase, i.e., phase I. In this solid phase the ions are undergoing tumbling and diffusion sufficiently fast so that the NMR spectrum is motionally narrowed, as in a normal liquid. The spectrum of AN in Phase I is shown in Figure 10. The three spectra given in Figures 6, 7, and 10 together constitute an excellent example of the two methods for line narrowing: motional narrowing and high-power proton decoupling with magic-angle sample spinning.

3.3 NQR STUDIES

Crystallographic studies of AN^{24,30} show that the nitrate ion is found in an ordered state in phases IV and V. (See Section 3.1 for nomenclature of AN crystal phases.) Above 32 C, however, crystal structure studies indicate that the same nitrate ion exists in a state of orientational and positional disorder in an otherwise crystalline lattice^{31,32}. NQR results could make unique contributions to elucidating this type of disorder as well as to measure precise indices of electronic structure.

Preliminary results have been obtained by Smith³³ and by the author. Smith observed the room temperature spectrum (phase IV) using a sensitive field cycling double resonance method³⁴ whose major drawback is its poor resolution. NQR transitions are reported at 450 and 550 kHz, to yield a coupling constant of 666kHz and asymmetry parameter, η , of 0.301, respectively. It is rather surprising to observe such a large departure from zero for the asymmetry parameter, since the isolated ion's trigonal axis of symmetry would force a null value for η . The most likely cause for this is strong, anisotropic hydrogen bonding, which in turn could be further studied by NQR.

Very recently, the author detected two closely spaced resonances in AN at 77 K. The most remarkable features of these phase V resonances is their narrow linewidth. The observed transitions and their FWHM are 557.8 ± 0.45 kHz, and 554.4 ± 0.30 kHz. In fact, observation of narrow linewidths is consistent with the expected state of good crystal order in phase V of AN. Also consistent with the neutron diffraction data³⁰ is observation of two inequivalent nitrogen sites. Measurement of lineshape parameters in other phases or other compositions promises to develop into a sensitive probe of the order/disorder in these substances.

4. Nitrocellulose

4.1. BACKGROUND

The aim of the work described here was to use Nitrogen NMR and NQR techniques to make a contribution toward the study of the mechanism of degradation and autoignition in nitrocelluloses (NC). One might expect at the start that both the molecular and electronic structure, and the polymer chain dynamics be very relevant to a fundamental understanding of the general problem of degradation and autoignition. Given the apparently central role of nitrogen in nitrocellulose degradation, magnetic and quadrupole resonance techniques would appear to be well matched to the task.

4.2. NMR STUDY

4.2.1. *Theory.* A broadband Nitrogen-15 NMR study of nitrocellulose (NC) as a function of temperature was conducted in an attempt to investigate the dynamics of the polymer chains. This approach is justified by the assumption that an understanding of the onset of motion is prerequisite to fundamental understanding of any mechanism of degradation and autoignition.

The observable chosen in this experimental study to reveal the details of the motion is the chemical shift anisotropy. This parameter is the dominant feature of the broadband Nitrogen-15 NMR spectrum of solid nitrocellulose, and very recent theoretical advances have made its temperature dependence interpretable in terms of the slow motion associated with this polymer at environmental temperatures.

Nitrocellulose (NC) is known to undergo a glass-to-rubber transition at about 40°C,

so that at room temperature and above, progressively faster motions should be present to account for the mechanical properties. Yet, these motions are not nearly fast enough to provide motionally averaged high resolution NMR spectra, necessitating a broadband approach.

The conventional, and very convenient, index to describe the random motion associated with thermal processes is the correlation time, τ . This index measures the time scale over which noticeable motion occurs. In the limit of fast motion, i.e., short correlation times, such as occur in normal motionally averaged liquids, the well known theory of Bloembergen, Purcell and Pound³⁵ (BPP) allows calculation of the correlation time when a minimum is observed in a plot of relaxation time vs. (inverse) temperature. However, the motions relevant to the region of a glass-to-rubber transition are definitely not of the fast or motionally averaged variety, so that BPP-type theories are not applicable. Recently, Lee and Tang³⁶ developed an analytical theory for the slow orientational dynamic behavior of anisotropic ESR hyperfine and fine-structure centers. The theory holds for slow correlation times and is therefore applicable to the onset of polymer chain motions. Lee's theory was generalized to enable calculation of slow motion orientational correlation times from resolved NMR quadrupole spectra, as reported by Lee and Shetty³⁷ and it has now been expressed in terms of resolved NMR chemical shift anisotropy³⁸. It is this latter formulation of Lee's theory that shall be used to analyze our experimental results in what follows. The results of the theory are summarized below for the case of axially symmetric chemical shift anisotropy.

Let Δ be the rigid-lattice chemical shift anisotropy. This is the separation between the divergence and the shoulder in the typical power pattern NMR line shape, as shown for example Figure 11. Also, let τ be the correlation time of the slow-motion Brownian motion of the polymer chains. Then, with the onset of motion, it can be shown that the theory predicts that the two limiting powder pattern features, shoulder and divergence, will shift toward each other resulting in a narrowing of the powder pattern. The fractional shift is then found to be

$$\begin{aligned} \delta / \Delta &= [108^{1/4} + 50^{1/4}] (\tau \Delta)^{-1/2} \\ &= 0.68626 (\tau \Delta)^{-1/2} \end{aligned} \quad (7)$$

4.2.2. Experimental results and discussion. Samples of nitrocellulose (NC) isotopically enriched to 50% Nitrogen-15, and later to close to 100%, were prepared by Dr. Surya Bulusu of ARDEC. Broadband NMR spectra were obtained at 30.9 MHz with a 7 Tesla superconducting magnet and variable frequency high power NMR spectrometer at Hunter College, Department of Physics. Spin-lattice relaxation times for the Nitrogen-15 resonance were of the order of 50 sec, so that signal-to-noise problems were severe until samples enriched to close to 100% Nitrogen-15 were employed. Still, to obtain suitable signal-to-noise ratios it became a routine necessity to accumulate and signal average for 12 to 24 hours for each spectrum.

Figure 11 shows that Nitrogen-15 NMR spectrum of NC obtained at 25°C, well below the glass transition. The line shape is typical of the powder pattern expected from all possible orientations of resonant sites subject to an anisotropic chemical shift interaction. The "divergence" corresponds to those sites where the external magnetic field and the principal axis of the chemical shift tensor are perpendicular; the "shoulder" corresponds to parallel alignment of these two directions. The separation between these experimental features is measured to be,

$$| \sigma_1 - \sigma_2 | = 204 \text{ ppm}$$

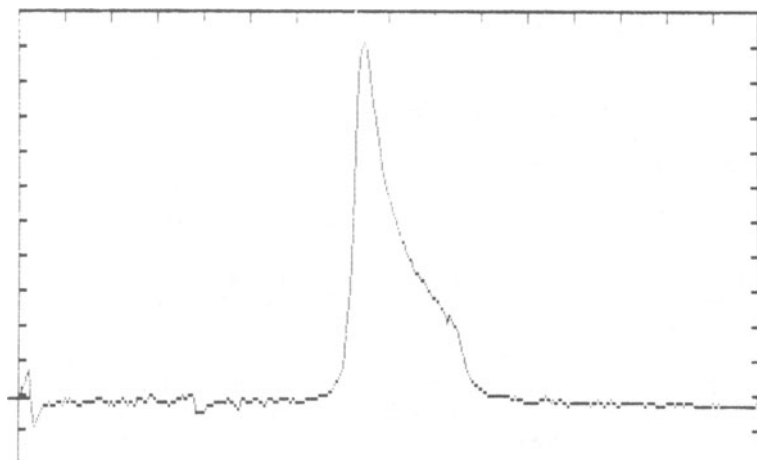


Figure 11. Broadband Nitrogen-15 NMR spectrum of NC at 25° C, taken at 30.9 MHz.

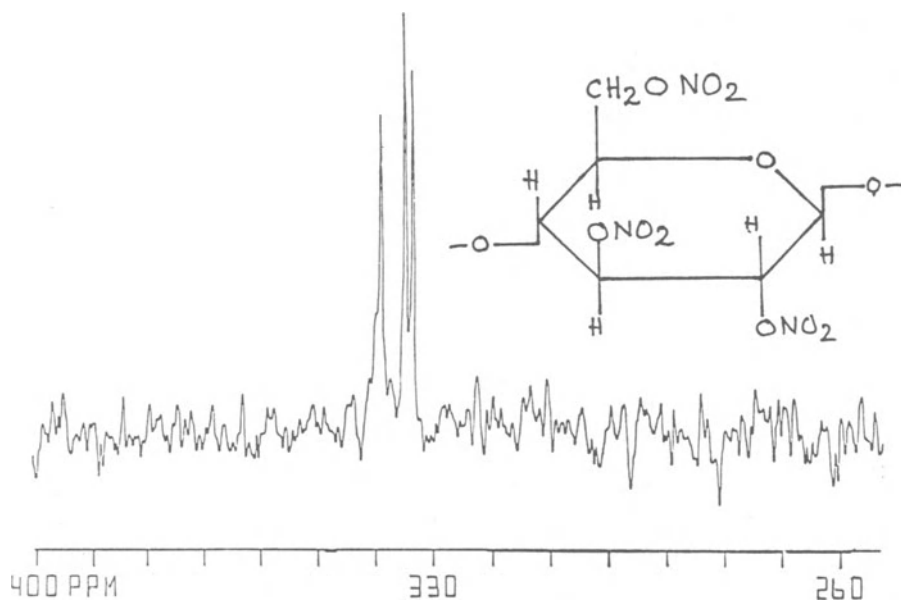


Figure 12. Nitrogen-15 NMR Spectrum of NC dissolved in DMSO-d₆. Spectrum obtained by S. Bulusu (ARDEC).

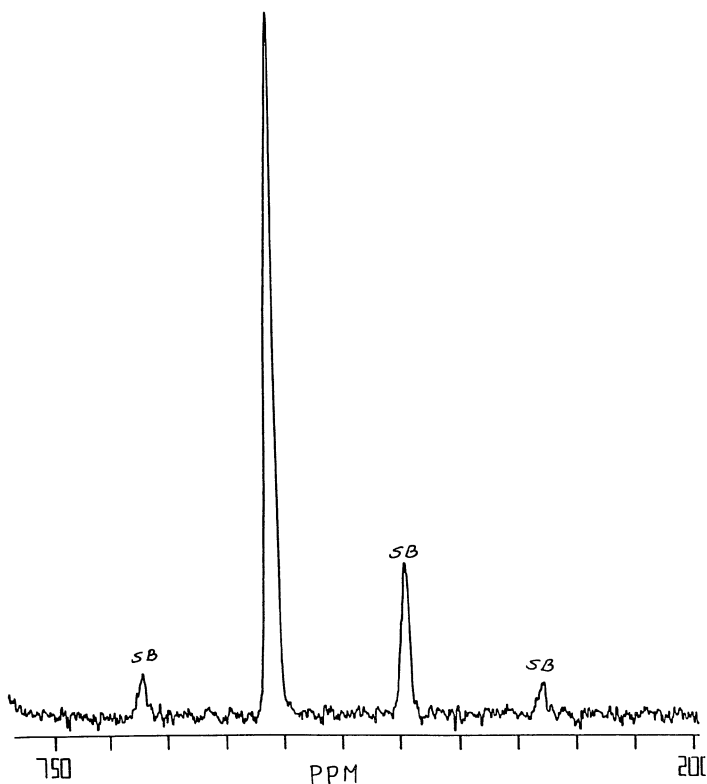


Figure 13. Nitrogen-15 MAS NMR spectrum of solid NC at room temperature. Spectrum taken by S. Bulusu (ARDEC).

We note here that the resonant site, a nitrate nitrogen, is surrounded by three oxygen atoms, two terminal and one bridging to the polymer chain. Thus, strictly speaking, the nitrogen site enjoys axial symmetry only to an approximate degree even considering only its nearest neighbors. Beyond that, there are three chemically distinct -ONO₂ sites on each dextrose ring forming the polymer chain, so that the question of chemical resolution must be addressed. Both these points can be satisfactorily explained by the following analysis on Nitrogen-15 high resolution NMR spectra obtained by S. Bulusu. Figure 12 shows the solution spectrum of NC. Note that the motional narrowing is sufficient to resolve the three chemically distinct nitrogen sites. The separation of the outer lines is about 5.6 ppm, so that on the scale of Figure 11, where the spectrum width is about 200 ppm, one would not expect to be able to resolve a triplet spectrum. To reinforce this conclusion, consider the MAS spectrum shown in Figure 13. It shows a single unresolved line of halfwidth 150 Hz, or about 7.4 ppm. Note that side-bands due to the sample rotation are labelled SB in the figure. Then,

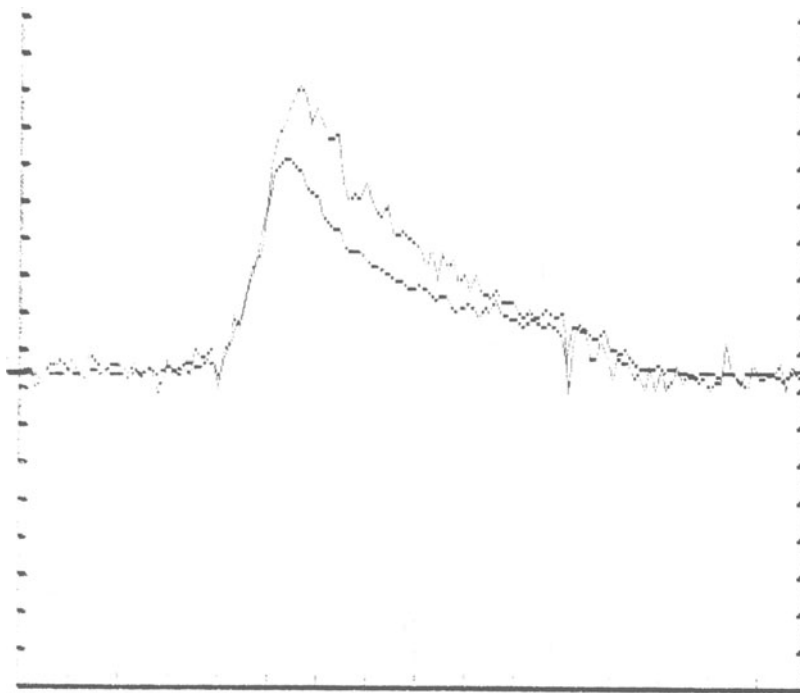


Figure 14. Superposition of broadband Nitrogen-15 NMR spectra of NC at 25° C and at 110° C. Spectra obtained at 30.9 MHz.

even at this level of resolution achieved by MAS-NMR, the chemical shift triplet, whose separation is only 5.6 ppm, is unresolved. With these considerations, it is clear why the broadband spectra, such as is shown in Figure 11, do not show any resolved structure due to the three chemically distinct nitro sites. Finally, it is reasonable to assume that the differences in the chemical shift anisotropy are of the same order (5.6 ppm) as the measured isotropic chemical shifts. Therefore, again no structure should be apparent at the level of resolution of the experiments reported here.

The next series of experiments consisted in measuring the variations in the line width parameters $|\sigma_1 - \sigma_2|$ as a function of temperature. Figure 14 shows the superposition of spectra at room temperature (25°C) and at 110°C. No filtering at all was used in these spectra, so that considerable improvement in signal-to-noise can be achieved by subsequent apodization and filtering. Still, it is clear that the trace corresponding to 110° has its two experimental features, the divergence and the shoulder, shifted inward with respect to the room temperature trace. The parameters obtained from these data are

$$\Delta = 2\pi \times 6.3 \times 10^3 \text{ sec}^{-1}$$

$$\delta = 2\pi \times 0.72 \times 10^3 \text{ sec}^{-1}$$

giving $\delta/\Delta = 11\%$, at the outer limit of applicability of the theory and implying a correlation time of 0.91 msec. Table 4 collects the data and the corresponding correlation times obtained between room temperature and 110°C as computed using the theory outlined earlier. Since the glass transition is known to occur in the vicinity of 40°C, the parameters at 25°C are taken to be the "rigid lattice" values. Then, the correlation times of the orientational Brownian motion of the polymer chains are found to decrease to the millisecond regime 40 to 70 Kelvins above the onset of the glass transition. It is interesting to contrast this with results obtained by Owens³⁹ who used ESR techniques to gauge the motion in the same temperature region as the NMR experiments reported here. Since NC itself is not paramagnetic, Owens dissolved paramagnetic probes of molecular weight comparable to NC monomers. He then found that the ESR data on his nitroxide probes yielded correlation times about two orders of magnitude smaller than our results shown in Table I. The picture that emerges is that as the polymer is warmed through the glass transition, the polymer chains enjoy motions roughly 100 times slower than is possible at the same temperature and in the same matrix for fragments of the order of a single dextrose ring. The consequences of these dynamical conclusions for degradation and autoignition mechanisms should be very interesting to pursue.

4.3. CONCLUSIONS

The NMR work reported here shows for the first time how the temperature dependence of the NMR chemical shift anisotropy can be used as a direct measure of ultraslow correlation times in polymers. The method is very general; it can be directly applied to Carbon and Hydrogen, as well as to Nitrogen, and it opens up a new and heretofore unexploited method of studying the fundamental motions of polymer systems. This method can easily be extended both to proton and to Carbon-13 NMR, and can be made to complement these broadband techniques with MAS/NMR using the method of Herzfeld and Berger²⁹ to obtain the anisotropy from side-band intensities. Furthermore, one should compare these results with those obtained, when possible by the more traditional, if more tedious, method of measuring rotating frame relaxation times vs. temperature as a function of radiofrequency field strength⁴⁰.

As for NQR experiments, they tend to be considerably more difficult to do successfully than NMR, but the additional resolution and sensitivity to chemical and physical inequivalence is unmatched. Higher sensitivity methods must be brought to bear on this problem, however, given the poor experience so far with non-crystalline samples.

TABLE 4. Temperature dependence of the Nitrogen-15 chemical shift anisotropy $\delta = 2\pi\gamma H_0 |\sigma_1 - \sigma_2|$ and the values of the orientational Brownian motion correlation times for NC, calculated as explained in the text.

T (Temperature)	$\delta/2$ (Frequency shift)	τ (Correlation time)
25°C		
90°C	0.27 kHz	6.5 m sec
110°	0.72 kHz	0.91 m sec

5. HMX, RDX, PETN

Table 5 summarizes the available NQR data in these substances. Only ring amine data is available in RDX and HMX, but their unusually large intensity has given impetus to schemes for outside-the-coil detection of these energetic materials⁴¹. RDX is seen to have three well resolved sites, indicating physical inequivalence of the three ring nitrogens. Similarly, β -HMX displays two NQR sites⁴², corresponding to the crystallographically inequivalent⁴³ equatorial and axial sites.

Other than the simple detection of the NQR transitions, summarized in Table 5, the only extended NQR study was the work by Landers, Brill and Marino⁴², LBM, who measured the temperature dependence of the transition frequencies in β -HMX from 77 K to 426 K. attempts to detect signals in δ -HMX, the phase thermodynamically favored under conditions of high pressure, such as in a rocket motor, were unsuccessful. However, LBM were able to draw the following conclusions:

- Each of the two NQR sites could be matched to its crystallographic site.

- The most important crystal stabilizing interaction in β -HMX both in terms of electrostatic energy⁴⁵, and molecular dynamics is known to be the O...CNC interaction between axial NO₂ groups in neighboring HMX molecules. This interaction is responsible for the existence of "chains" of HMX molecules in the solid state. As the temperature of the material is raised toward the β to δ transition, the NQR data show that a librational mode which disrupts this chain begins to grow toward a dominant role. In fact, disruption of the most important cohesive interaction is a prerequisite to the β to δ transition and this is found to take place.

Table 5. Nitrogen-14 NQR spectral data for RDX, HMX, and PETN at 77 K.

	ν_+/kHz	ν_-/kHz	ν_d/kz	η	$e^2qQ/h, kHz$
RDX	5118.0	3394.2	1724.2	0.608	5674.8
	5256.3	3413.5	1842.8	0.638	5779.9
	5319.0	3511.5	1807.3	0.614	5887.0
β -HMX	5336	3745	1591	0.5256	6054
	5091	3628	1462	0.5030	5813
PETN	904		400	0.855	936

6. Conclusions

Magnetic resonance offers a powerful tool for the study of structure, bonding and dynamics of solids. Because of its high resolution, Nuclear Quadrupole Resonance, in conjunction with Nuclear Magnetic Resonance has the potential to address problems of fundamental importance to the study of energetic materials. Examples were given in the foregoing on the conformation of C-nitro groups in trinitrobenzenes, and on molecular motions relevant to degradation in HMX and NC chains.

In most cases discussed above, it would appear that the most promising further studies for readers of these proceedings are of the temperature dependence of NQR and NMR parameters close to interesting phase transitions.

7. Acknowledgements

I am grateful to Drs. Surya Bulusu and Frank Owens for their continued encouragement and interest in my work and for what I have learned about the important problems in energetic materials research. I am pleased to acknowledge support for this work from the CUNY Research Foundation (Grants no. 665305 and 668373) and from Battelle Columbus Division.

8. References

1. T. P. Das and E. L. Hahn, "Nuclear Quadrupole Resonance Spectroscopy Solid State Physics", Suppl. 1, (Academic Press, New York, 1958).
2. E. A. C Lucken, Nuclear Quadrupole Coupling Constants, Academic Press, New York (1969).
3. D. T. Edmonds, Physics Reports **29**, 233 (1977).
4. S. M. Klainer, T. B. Hirschfeld, and R. A. Marino, "Fourier Transform NQR", in Fourier, Hadamard and Hilbert Transforms in Chemistry. A. Marshal, ed. (Plenum Press NY, 1982).
5. D. G. Grabar, F. C. Rauch and A. J. Fanelli, J. Phys. Chem., **73**, 3514 (1969).
6. W. Connick, F. G. J. May, and B.W. Thorpe, Aust. J. Chem. **22**, 2685 (1969).
7. E. Artini, R. C. Accad. Lincei **24**, 274 (1915).
8. E. Hertel and G. Romer, Z. Phys. Chem. B, **2**, 77 (1930).
9. L. A. Burkardt and H. H. Bryden, Acta Cryst. **7**, 135 (1954).
10. W. R. Carper, L. P. Lavis and M. W. Extine, J. Phys. Chem. **86**, 459 (1982), and private communications (1982).
11. W. C. McCrone, Microchem. J. Symp. Ser. **2**, 243 (1962).
12. J. L. Soderberg, J. S. Back, C. L. Hakanson, U. S. Patent **3**, 620, 857 (1971).
13. D. K. Philp and B. W. Thorpe, J. Cryst. Growth **35** (2) 133 (1976).
14. M. A. Parry and B. W. Thorpe, Rep. -Aust. Mater. Res. Lab. **1978**, MRL-R-708 and **1979** MRL-R-748.
15. R. A. Marino and T. Oja, J. Chem. Phys. **56** 5453 (1972).
16. C. H. Townes and B. P. Dailey, J. Chem. Phys. **17**, 782 (1949).
17. E. Schempp and P. J. Bray, in Physical Chemistry: An Advanced Treatise Vol. 4, Academic Press, New York, 1970 p 521.
18. C. P. Cheng and T. L. Brown, J. Mag. Res. **28**, 391 (1977).
19. S. N. Subbarao and P. J. Bray, J. Chem. Phys. **67**, 3947 (1977).
20. C. S. Choi and J. E. Abel, Acta Cryst **B28**, 193 (1972).
21. J. H. Bryden, Acta Cryst. **B28**, 1395 (1972).

22. J. S. Ingman, G. J. Kearley, and S. F. A. Kettle, J. C. S., Faraday Trans. 1, **78**, 1817 (1982).
23. R. N. Brown and A. C. McLaren, Proc. Roy. Soc. (London), **A266**, 329, (1962).
24. C. S. Choi, H. J. Prask, and E. Prince, J. Appl. Cryst., **13**, 403, (1980).
25. C. S. Choi and J. E. Mapes, Acta Cryst., **B28**, 1357, (1972).
26. Z. Iqbal, Chem. Phys. Letters, **40**, #1, 41, (1976).
27. G. J. Kearly and S. F. Kettle, J. C. S., Faraday Trans. 1, **78**, 3691, (1982).
28. M. T. Rigglin, R. R. Knispel, and M. M. Pintar, J. Chem. Phys., **56**, 2911, (1972).
29. J. Herzfeld and A. E. Berger, J. Chem. Phys., **73**, 6021, (1980).
30. C. S. Choi and H. J. Prask, Acta Cryst. **B39**, 414 (1983).
31. C. S. Choi and H. J. Prask, Acta Cryst. **B38**, 2324 (1982).
32. B. W. Lucas, M. Ahtee, and A. W. Hewat, Acta Cryst. **B35**, 1038 (1979).
33. J. A. S. Smith, private communication (1988).
34. D. T. Edmonds, Physics Reports **C29**, 233 (1977).
35. N. Bloembergen, F. M. Purcell, R.V. Pound, Phys. Rev. **73**, 679 (1948).
36. Sook Lee and S. Z. Tang, Phys. Rev. **B31**, 1308 and **B32**, 2761 (1985)
37. Sook Lee and Anyl Shetty, Phys. Rev. **B35**, 1 (1987).
38. Sook Lee, private communication, (1987)
39. F. J. Owens, J. Macromol. Sci.-Phys., **B23**, 527 (1984).
40. E. Fukushima and S. B. W. Roeder, Experimental Pulse NMR, (Addison-Wesley, Reading, MA, 1981) 266 ff and references therein.
41. J. Hirshfeld and S. M. Klainer, J. Mol. Structure, **58** 63 (1980)
42. A. G. Landers, T. B. Brill and R. A. Marino, J. Phys. Chem **85**, 2618 (1981).
43. C. S. Choi, H. P. Boutin, Acta Cryst. **B26**, 1235 (1970).
44. A. G. Landers and T. B. Brill, J. Phys. Chem. **84**, 3573 (1980).
45. T. B. Brill, C. O. Reese, J. Phys. Chem. **84**, 1376 (1980).

PARTICIPANTS AT THE NATO ASI ON CHEMISTRY & PHYSICS OF ENERGETIC MATERIALS, SEP 3 TO 15, 1989. ALTAVILLA MILICIA, SICILY, ITALY.

Dr. Behain Amaee
Department of Chemistry
University of Manchester
Oxford Road
Manchester M13 9PL England

Dr. Theodore Axenrod
Department of Chemistry
The City College of the City
University of New York
138 Street & Convent Avenue
New York, New York 10031

Dr. Richard Behrens, Jr.
Combustion of Energetic Materials
Division, #8357
Sandia National Laboratory
Livermore, California 94550

Dr. Binay Bilgin
Istanbul Universitesi
Muhendislik Facultesi
Kimya Bolumu-Vezneciler
Istanbul, Turkey

Dr. Normand C. Blais
Chemistry & Laser Sciences Division
CLS-2, MS-G738
Los Alamos National Laboratory
Los Alamos, New Mexico 87545

Dr. J. Boileau
15 rue des Lions Saint Paul
75004 Paris, France

Professor Thomas B. Brill
Department of Chemistry & Biochemistry
University of Delaware
Newark, Delaware 19716

Dr. Surya N. Bulusu
Energetic Materials Division
U.S. Army ARDEC, Bldg. 3028
Picatinny Arsenal, New Jersey 07806-5000

Professor Giulio Ceccarelli
Istituto di Chimica Fisica
University of Pisa
Via Risorgimento 35
56100 PISA, Italy

Ms. Lydie Charon
Centre d'Etudes de Vaujours
Boite Postale No. 7
77181 Courtry, France

Mr. Donald Chiu
U.S. Army ARDEC
ATTN: SMCAR-AEE-BR
Bldg. 382
Picatinny Arsenal, New Jersey 07806-5000

Dr. John Connor
Superintendent, NP1 Division
Royal Armament Research & Development
Establishment
Fort Halstead
Seven Oaks Kent TN14 7BP UK

Mr. Seyfettin Dalgic
Trakya Universitesi Fen-Edebryat
Fakultesi Fisik Bolumu -
Edirne, Turkey

Dr. A. Davis
Royal Armament Research & Development
Establishment
Waltham Abbey, Essex
EN9 1AX England

Professor Sandor Fliszar
Department de Chimie
Universite de Montreal
C.P. 6128, Succ. A
Montreal (Quebec), Canada H3C 3J7

Professor Peter Gray
The Master's Lodge
Gonville and Caius College
Cambridge CB2 1TA England

Mr. Ronald Green
Chemistry Department
Howard University
525 College Street NW
Washington, DC 20059

Dr. N. Roy Greiner
Mail Stop G740
Los Alamos National Laboratory
Los Alamos, New Mexico 87545

Dr. Lee Harris
U.S. Army ARDEC
Bldg. 382 S
Picatinny Arsenal, New Jersey 07806-5000

Dr. Shmaryahu Hoz
Department of Chemistry
Bar-Ilan University
Ramat-Gan 52100 Israel

Dr. S. Iyer
U.S. Army ARDEC
Bldg. 3028
Picatinny Arsenal, New Jersey 07806-5000

Mr. Floyd R. Jackson
Chemistry Department
Howard University
525 College Street NW
Washington, DC 20059

Dr. Jerry P. Jasinski
Department of Chemistry
229 Main Street
Keen, New Hampshire 03431

Dr. Keerthi Jayasuriya
Geo-Centers Inc
U.S. Army ARDEC
Bldg. 3028
Picatinny Arsenal, New Jersey 07806-5000

Dr. Yvonne Lanzerotti
U.S. Army ARDEC
Bldg. 3022
Picatinny Arsenal, New Jersey 07806-5000

Mr. Yannis Lazarou
Department of Chemistry
University of Crete
P.O. Box 1470
71409 Heraklion, Crete, Greece

Mr. Michel Lefebvre
Lab Phys Chimie de la Combustion
1, place L. Pasteur
Louvain-La-Neuve, Belgium B-1348

Dr. Donald Liebenberg
Office of Naval Research
Department of Navy
800 North Quincy Street
Arlington, Virginia 22217-5000

Mr. Alan Macdonald
Chemical Systems Group
R.M.C.S.
Shrivenham
Swindon, SN6 8LA. UK

Professor A. Macpherson
Department of Mechanical Engineering &
Mechanics # 19
Lehigh University
Bethlehem, Pennsylvania 18015

Mr. Pascal Maffre
Laboratoire O.R.C.
Universite de Bourgogne
Faculte des Sciences
6 Bd. Gabriel, 21100 Dijon
France

Dr. Pietro Mangiaracina
4 Montclair Avenue
Monsey, New York 10952

Professor A.P. Marchand
Department of Chemistry
University of North Texas
NT Station, Box 5068
Denton, Texas 76203-5068

Professor Robert A. Marino
Department of Physics & Astronomy
Hunter College of the City University
of New York
695 Park Avenue
New York, New York 10021

Dr. Robert L. McKenney, Jr.
Eglin Air Force Base
ATTN: AFATL/MNE
Florida 32542-5434

Dr. Carl F. Melius
Energetic Materials Division
Combustion Research Facility
Sandia National Laboratory
Livermore, California 94550

Dr. Gerrit Minholts
DMKL/MBA-1/CVP
Rekenbureau
Alexander kazarm Gebouw 237
v.d. Burchlaan 31
2597 PC The Hague, Holland

Dr. Ian Murray
Royal Ordnance Place
Waltham Abbey, Essex
EN9 1AY England

Dr. Arnold T. Nielsen
Code 38503
Naval Weapons Center
China Lake, California 93555

Professor Simone Odier
Universite Pierre et Marie Curie
Dept de Recherche Physiques
Tour 22 1 er etage C 22-23
4 Place Jussieu
75252 Paris Cedex 05 France

Mrs. Elisabetta Palla
Via Dell 'Ozeretto, 15
56,100 PISA Italy

Mr. Paolo Palla
Via Dell 'Ozeretto, 15
56,100 PISA, Italy

Dr. Panos Papagiannakopoulos
Assistant Professor
Department of Chemistry
University of Crete
71409 Heraklion, Crete, Greece

Dr. G. Piermarini
Institute for Materials Science
National Bureau of Standards
Gaithersburg, Maryland 20899

Mr. James J. Pinto
RD #1, Box 255
Lafayette, New Jersey 07848

Professor Peter Politzer
Department of Chemistry
University of New Orleans
New Orleans, Louisiana 70148

Mr. Jaap Post
Systems Analyst
DMKL/MBA-1/CVP
v.d. Burchlaan 31
Postbus 90701
2509 LS 's-Gravenhage
The Netherlands

Mr. Thomas Russel
Department of Chemistry
University of Delaware
Newark, Delaware 19716

Dr. Rosario Sausa
U.S. Army Ballistics Research Laboratory
Interior Ballistic Division
ATTN: SLCRB-IB-I
Aberdeen Proving Ground
Maryland 21005

Mr. Stanley Semel
Geo-Centers Inc
762 Route 15 South
Lake Hopatcong, New Jersey 07849

Dr. Jorge Seminario
Department of Chemistry
University of New Orleans
New Orleans, Louisiana 70148

Dr. Scott A. Shackelford
Frank Seiler Research Laboratory
Air Force Academy
AFAL/DYCC
Colorado Springs, Colorado 80840

Dr. Jagadish Sharma
Materials Division, Room 34
Naval Surface Warfare Center
10901 New Hampshire Avenue
Silver Spring, Maryland 20903-5000

Dr. Robert W. Shaw
Army Research Office
P.O. Box 12211
Research Triangle Park
North Carolina 27709-221

Dr. A. Solomonovici
Department 24, Rafael, ADA
P.O. Box 2250
Haifa, 31021 Israel

Dr. Carlyle B. Storm
M-1, C920
Los Alamos National Laboratory
Los Alamos, New Mexico 87545

Dr. Samuel Trevino
Bldg. 235
National Institute of Standards &
Technology
Gaithersburg, Maryland 20899

Dr. Donald H. Tsai
Istar Inc
10400 Lloyd Road
Potomac, Maryland 20854

Mr. Yitshak Tzuk
Physics Department
Ben-Gurion University
Beer-Sheva 84105 Israel

Ms. Belkis Ustamehmetoglu
Department of Chemistry
Istanbul Technical University
Maslak Istanbul Turkey

Dr. B.J. van der Meer
TNO Prins Maurits Laboratory
P.O. Box 45
2280 AA Rijswijk, Holland

Ms. Valentina Vassilenko
Centro de Fisica Molecular
das Universidades de Lisboa
Complexo I.I.S.T.
Av Rovisco Pais
1000 Lisboa Portugal

Dr. Edouard Vauthier
D.R.P. Universite Pierre et
Marie Curie
4 Place Jussieu, Tour 22, EL
75252 Paris Cedex 05. France

Dr. Fred Volk
Fraunhofer-Institut fur Treib und
Explosivstoffe
Postfach 1240
D-7507 Pfinztal (Berghausen) FRG

Mr. Stuart Wright
Department of Chemistry
The University of Liverpool
P.O. Box 147, Liverpool L69 3BX
England

Dr. Jehuda Yinon
Isotope Department
The Weizmann Institute of Science
Rehovot 76100. Israel

Dr. Dimitris Zevgolis
Assistant Professor
Department of Physics
University of Crete
71409 Heraklion, Crete, Greece

Ms. Hanna Zuckermann
Department of Physical Chemistry
Hebrew University of Jerusalem
Jerusalem, 91904 Israel

SUBJECT INDEX

- Ab-initio methods,
 - based on HF equations **23**: 527
- Ab-initio molecular orbital calculations, by Gaussian 86 Code **23**: 533
- Ab-initio molecular orbital codes **23**: 526-528, 532
- Ab-initio (SCF) molecular orbital approach **9**: 176
- Ablation of explosive,
 - during laser pulse **29**: 657-659
- Aci-ion,
 - of nitromethane **23**: 533
 - in nitromethane decomposition **27**: 635
- Acoustic Levitation/FTIR
 - spectroscopy of droplets and bubbles **12**: 270-273
- Activation energies,
 - calculated, for C-N bond dissociation in nitromethane **23**: 536
- Activation energy change, ΔE **11**: 239
- Activation Volume change, ΔV **11**: 239
- Amine sensitization
 - of nitromethane **23**: 536,537
- Ammonia-nitromethane complex **23**: 537
- Ammonium nitrate (AN) **32**: 725
 - Hygroscopicity and dimensional instability **32**: 725
 - Phase transition **32**: 726,728
 - BB/MAS NMR studies **32**: 727
 - NMR spectrum of plastic phase **32**: 728,729
- Anisotropy of detonation in crystal **5**: 113
 - in pentrite **5**: 120
- Anomalous energy effects **9**: 178,179
 - isodesmic reaction procedure for **9**: 178
- Appearance energy measurements, with TOF velocity-spectra **14**: 338
- Arrhenius equation (relation) **11**: 240,242,244
- Arrhenius plots for β -HMX,
 - at different pressures **17**: 395
- Auger electron microscopy **25**: 571
- Auger electron spectroscopy **25**: 571
- Autocatalysis **2**: 13
 - Cubic **2**: 14,18
 - Quadratic **2**: 14
 - Reversible **2**: 18
- Autocatalytic decomposition **3**: 38
- Autocatalytic effects, on RDX decomposition **15**: 349
- Autoignition **1**: 1

- BAC-MP4 method, for thermochemical properties of nitramines **15**: 350
- BAC-MP4 procedure **3**: 23
 - Hierarchical diagram **3**: 24
- BKW equation of state **28**: 646
- Bond additivity corrections **3**: 25
- Bond breaking process in nitramines **9**: 190

- Bond dissociation energies **3**: 28; **7**: 149
 - calculated, for nitro, nitroso nitrite, nitrate and azido molecular species **3**: 30,32
 - for selected radicals **3**: 33
 - table of, for CH and CC bonds **7**: 154
- Bond fission of radicals **3**: 32
- Bond lengths and angles of nitromethane **23**: 532
- Bond polarities, theoretical correlation with sensitivities **5**: 82
- Broadband CARS **21**: 507
- Bubble model, of HMX decomposition **15**: 361,365
- Burn rate ratios
 - of HMX and HMX-d₈ **19**: 442
 - of RDX and RDX-d₆ **19**: 446
- C-N bond in nitroaromatics,
 - involvement in detonation **5**: 82
 - bond order and bond energy **5**: 83
- C-N bond scission,
 - HF study of **23**: 534
- C-NO₂ and N-NO₂ bonds,
 - importance for sensitivities **8**: 158
- Cage effect **11**: 235,238
- Cage molecules **28**: 647-650
 - calculated output of **28**: 650
- Cage structures **28**: 648
- Carbon clusters **21**: 502
- CAS-CI methods **23**: 527
- CH₂O formation in fast thermolysis of nitramines **13**: 288,289
- Chain structure in crystal lattice **5**: 94
 - in m-dinitrobenzene **5**: 95
 - in trinitrobenzene **5**: 96
 - in hexanitrobenzene **5**: 97
 - in nitrobenzene **5**: 99
 - in nitromethane **5**: 100
 - in pentrite **5**: 116-119
- Chapman-Jouget (CJ) conditions **21**: 478
- Charge neutralization energy (CNE) **7**: 150-152
- Chemical autocatalysis **2**: 14
- Chemical and physical inequivalence,
 - of NQR sites **32**: 720
 - of nitrogroups in nitrobenzenes **32**: 720,721
- Chemical ionization mass spectrometry **25**: 588
- Chemical kinetics model,
 - for propellant flames **4**: 56
 - chemical species used, in modeling RDX propellant flame **4**: 57
 - reaction rate coefficients table, for modeling RDX solid propellant flame **4**: 57-61
- Chemical oscillations and combustion instability **13**: 312
- Chemical reaction rate coefficients,
 - for modeling RDX flame **4**: 57
- Chemical sensitization of explosives **23**: 525

- Chemical shift anisotropy,
 - of nitrate ion of AN **32**: 727
- Chemical shift, in XPS **25**: 570,572
- Chemkin software package **4**: 52
 - gas phase subroutine **4**: 53
- CN, band sequence
 - in emission spectra of tetryl and mercury fulminate **29**: 679
- CN, Vibrational temperature of **29**: 678
- Collision cell,
 - in tandem mass spectrometry **30**: 685
- Collision induced dissociation (CID) **30**: 685; **31**: 695
- Compatibility problems,
 - study of, by XPS **25**: 583
- Coupled-cluster theory **23**: 527
- Critical energy criterion, **24**: 552,553
 - of Walker and Wasley, for detonation **24**: 555,558-560
- Critical energy values, for detonation **24**: 555
- Critical intensity, for initiation by laser pulse **29**: 658,659,664
- Critical temperature,
 - calculated, for different explosives **27**: 635
 - definition of **27**: 632
 - calculation of **27**: 632
 - plot against shock sensitivities of explosives **27**: 633,634
- Crystal densities **28**: 641
 - Stine's method **28**: 641
 - calculation of **28**: 642,643
- Combustion of nitramine propellant **4**: 53
- Combustion products,
 - at ambient pressure **22**: 512
 - in confinement **22**: 512
 - of black powder **22**: 515
 - of gun propellant **22**: 518
 - of gun propellant A5020 **22**: 516
- Compound Morse potential **10**: 199,200
- Computational studies of secondary nitramines **9**: 175
- Concerted decomposition **3**: 37
 - energetics of **3**: 37
- Continuum hydrodynamics **10**: 195
- Coupled cluster theory **23**: 527
- Critical self-heating,
 - expression for **1**: 3
- Crystal architecture **5**: 79

- DASAC software **4**: 56
- "d" spacings versus pressure,
 - for RDX solid phases **17**: 398
- Debye solid **10**: 203
- Decomposition energetics,
 - for NO₂ bond breaking **3**: 35
 - for HONO elimination **3**: 35

- Decomposition mechanisms
 - of energetic materials **23:** 531
- Decomposition of Energetic materials **3:** 21
- Degrees of freedom,
 - vibrational, rotational and translational **10:** 212,216
- Density function theory (DFT) **6:** 132
- Detonating material,
 - hydrodynamic history of **20:** 459
- Detonation Chemistry Studies **21:** 477
- Detonation of Condensed Explosives **20:** 457
- Detonation Products,
 - free expansion of **21:** 456
 - influence of initiation strength on **22:** 513,517
 - influence of pressurization on **22:** 513,520
 - of unconfined charges of TNT/NQ **22:** 521
 - of confined charges of TNT/NQ **22:** 522
- Detonation Properties **28:** 641
 - calculation of **28:** 642
 - of nitropolyhedranes and HMX **28:** 645
- Detonation regime,
 - non-shock **24:** 563
- Detonation thresholds,
 - in hazard assessments **24:** 551,552
- Detonation Wave
 - models for propagation **21:** 478
 - velocity of **21:** 486
 - progression through column of explosive **28:** 641
- Detonations in molecular crystals,
 - application of quantum chemistry to **5:** 79
 - application of molecular dynamics to **5:** 79
 - microscopic theory of **5:** 79
 - application of crystal structure analysis to **5:** 79
- Detonation Wave propagation,
 - cooperative mechanisms of **5:** 85,90
 - molecular dynamics models **5:** 102
 - 1-D model **5:** 102
 - 1-D results **5:** 104
 - 2-D model, dissipation energy **5:** 110,111
 - 2-D results **5:** 113
 - 2-D model, chemical energy **5:** 121
 - 3-D model, electronic excitation **5:** 129
- Diagnostics,
 - for in situ measurement of decomposition products **14:** 330
- Diamond anvil cell (DAC) **16:** 369; **17:** 392
 - NIST DAC **16:** 370
 - Basset DAC **16:** 372
 - Mao-Bell DAC **16:** 373
 - Holzaffel DAC **16:** 374
 - Merrill DAC **16:** 375
 - High pressure **17:** 392

- Diethylene triamine,
 - sensitization effect on crystalline explosives **23:** 538
 - sensitization effect on nitroalkanes **23:** 538
- Difluoramine,
 - electronic states **5:** 85,87
- Dislocation generation **10:** 222
- Dissociation of chemical bonds **7:** 143
- Dissociations,
 - endothermic and exothermic **10:** 212
- Dissociation energies for X-NO₂ bonds in
 - methylnitrate and methyl nitramine **23:** 537
- Di-*t*-butyl peroxide,
 - Spontaneous ignition of **1:** 1
- Dielectric field gradient tensor **32:** 715
 - asymmetry parameter of **32:** 715
- Drop-weight impact sensitivity **27:** 606
- Drop-weight impact sensitivities of,
 - nitroaromatics, Table **27:** 612
 - nitroaromatics with an alpha C-H linkage, Table **27:** 614
 - nitropyridine explosives, Table **27:** 615
 - nitroimidazole explosives, Table **27:** 615
 - nitropyrzazole explosives, Table **27:** 616
 - nitrofurazan and nitroosadiazole explosives, Table **27:** 616
 - nitro-1,2,4-triazoles, Table **27:** 617
 - nitro-1,2,3-triazole explosives, Table **27:** 618
 - nitro-pyrimidine explosives, Table **27:** 619
 - nitroaliphatic explosives, Table **27:** 619
 - nitroaliphatics with other functional groups, Table **27:** 620
 - nitramine explosives, Table **27:** 623
 - nitrate ester explosives, Table **27:** 627
 - nitroheterocyclic explosives, Table **27:** 627
- Effect of pressure on fast thermolysis of nitramines **13:** 303
- Electron impact (EI) fragmentation **31:** 695
- Electronic energy,
 - determination of **3:** 25
- Electronic Structure Calculations **3:** 23
- Electrostatic Potential, Computation **9:** 177
- Electrostatic potentials, of amines **9:** 179
 - of piperazine **9:** 180
 - of aza nitrogens **9:** 181
- Emission spectroscopy,
 - of laser irradiated explosives **29:** 653,654
- Endothermic dissociation **11:** 239,244
- Energy,
 - relaxation **11:** 239
 - transport **11:** 239
 - intra- and intermolecular exchange **11:** 239
- Energy of a hot spot **24:** 558
- Energy partitioning in chemical bonds **7:** 144

- Energy-per-unit area, E_c **24**: 552
 - critical value for detonation **24**: 552,553
- Energy relaxation processes **11**: 232
- Entropies **3**: 27
- Equilibrium conformation of
 - molecules in modelling decomposition **23**: 532
- Equilibrium constant, K_x **11**: 240
 - temperature dependence **11**: 244
- Ethylenediammonium dinitrate (EDD) **12**: 262-265
- Exothermic dissociation
 - energy distribution & exchange in **11**: 233
 - mechanism of **11**: 233
- Explosive output, calculated **28**: 646
- Explosiveness,
 - UK definition of **24**: 548
- Fast-heat-and-hold/FTIR spectroscopy **12**: 256
- Fast decomposition reactions **29**: 654,655
- Fast thermolysis/FTIR cell **12**: 257,258
- Fast thermolysis/FTIR spectroscopy **12**: 256
- Fast thermolysis products of,
 - aliphatic C-NO₂ compounds **13**: 294
 - alkylammonium nitrate salts **13**: 298-300
 - alkyne and nitroxide containing compounds **13**: 302
 - azidomethyl (-CH₂N₃) containing compounds **13**: 297
 - compounds containing -C(NO₂)₂X **13**: 302
 - furazan and furoxane containing compounds **13**: 301
 - mixtures of compounds **13**: 306
 - nitrate ester (O-NO₂) compounds **13**: 295
- Five-centered HONO elimination **3**: 34
- Force-field methods **23**: 529
- Force-field techniques **23**: 527,529
- Formation of HONO in fast thermolysis of nitramines **13**: 283-285
- Fourier transform infrared (FTIR) spectroscopy **12**: 255; **17**: 392
- Fragment attack,
 - response of propellants to **24**: 546
- Fragment impact,
 - vulnerability of explosives to **24**: 549
- Fragmentation map
 - of RDX **31**: 699
 - of HMX **31**: 700
 - of 1-nitroadamantane **31**: 704
 - of 1,3-dinitroadamantane **31**: 705
 - of 1,3,5,7-tetranitroadamantane **31**: 705
 - of polynitrobishomocubanes **31**: 707,708
- Fragmentation pathways **30**: 685,692
- Fragmentation pathways of ions **31**: 695
- Frank-Kamenetskii equation **27**: 632
- Free-energies **3**: 27
- Free energies of formation **3**: 36
- Fundamental vibrational frequencies **6**: 131

Furazan derivatives

of TATB **25**: 577; **26**: 588,595,599

from impacted TATB, XPS spectrum of **26**: 594

Furazan product from TATB **19**: 449

Furoxan derivatives of TATB **25**: 577; **26**: 588,595,600

from impacted TATB, XPS spectrum **26**: 594

Furoxan product from TATB **19**: 449

Gas formation rate **14**: 334,335

Gas formation rates,

of HMX **15**: 354-356

of HMX-d₈ **15**: 356,360

Gas phase RDX

ignition and flame chemistry **4**: 71

Gas product predictions for thermolysis of TDCD molecule

13: 293,294

Gas products of RDX under fast heating, % Composition vs time **12**: 260

pressure dependence **12**: 266

Geometry optimizations in computational work **9**: 176

Hartree-Fock equations,

solution of **23**: 527

Hartree-Fock method **3**: 23

calculations **3**: 24

Haratree-Fock theory **7**: 145

Heat of combustion **28**: 642

Heats of formation **28**: 641,642

calculation for TNT **28**: 644

Heats of formation, BAC-MP4 **3**: 27

comparison with experimental **3**: 28

Tables of **3**: 29,36

Hellmann-Feynman theorem **7**: 143,144

Herman-Skillman radial mesh **6**: 133

High energy CID in mass spectrometry **30**: 686

HMX,

isotopically labeled **14**: 341

pyrolysis products and ion signals **14**: 339-342

qualitative decomposition model **15**: 361

thermal decomposition products and rates of formation

14: 334,339,345

HMX, emission spectrum,

after laser irradiation **29**: 675

HMX, RDX,

thermal decomposition of **15**: 347

thermal decomposition products of **15**: 352

HN₃, decomposition of **6**: 140

HNCO detection in thermolysis of nitramines **13**: 290

HONO, from thermal decomposition of nitramines **12**: 261,262

Hotspots,

- critical size **24**: 561
- formation mechanisms **24**: 562,563
- mechanism of heating of **10**: 195,216
- XPS Study of **25**: 580; **26**: 587
- size of **26**: 589
- modes of generation **26**: 589
- concept of **26**: 588
- chemical nature, revealed by XPS **26**: 592
- as sensitization centers **26**: 599

Huckel approximations **5**: 82Huckel parameters for selected aromatic compounds **5**: 83,84Huzinaga's basis sets for C, N, Cl **6**: 136Hydrocarbons, CO and CO₂ upon fast thermolysis **13**: 290Hydrodynamic models **21**: 478Hydroxynitroaromatics, anomalous sensitizing effects **8**: 165Ignition and combustion of energetic materials **4**: 51Ignition and extinction **1**: 5Ignition of nitromethane **4**: 62

- temperature and major species profiles for **4**: 63

- decomposition mechanism for **4**: 64

Impact and shock sensitivities

- of common explosives **27**: 608

Impact, drop weight

- study of effects **26**: 590

Impact sensitivity,

- drop-weight **27**: 606

- tests **27**: 606

- based on oxygen balance **27**: 609

Impact/shock sensitivities,

- correlation with molecular properties **8**: 157

Induction periods,

- before ignition **1**: 2,8

Infrared microspectroscopic method **16**: 382Infrared multiphoton dissociation, (IRMPD) of RDX **15**: 349

Initiation criterion,

- by Lee, based on power density **24**: 558

Initiation/ignition mechanisms,

- by laser light **29**: 657

Initiation sensitivity,

- for laser light **29**: 655

Interactions

- harmonic **10**: 206

- non-linear **10**: 206

Interatomic potentials **10**: 196; **11**: 229

Intermolecular forces,

- many-body contribution to **23**: 527

Ion structure elucidation **30**: 686IR absorption spectra of gas products from RDX under fast heating **12**: 259

- IR spectra of RDX polymorphs,
at different pressures **17**: 400
- Isodesmic reaction energies,
tables of **9**: 183,184,186
- Isothermal decomposition studies of HMX **12**: 267-269
- Isothermal differential scanning calorimetry (IDSC) **18**: 417
 - of TNT **18**: 417
 - of TATB **18**: 423
 - of HMX **18**: 425; **19**: 436
- Isothermal Waves of Chemical Reaction **2**: 13
- Kamlet-Jacobs Simple Method (KJSM), **28**: 642
 - for calculation of detonation velocity and CJ pressure **28**: 642,644
- KDIE Studies **18**: 413; **19**: 433
 - TATB **18**: 422
 - TNT **18**: 417
 - HNBB **18**: 422
 - HMX **18**: 425; **19**: 435
 - RDX **18**: 428
 - of shock detonation of HMX **19**: 444
 - of shock detonation of RDX **19**: 447
- Kinetic Deuterium Isotope Effect (KDIE) **18**: 413; **19**: 433
 - application to combustion, explosion and detonation **19**: 434
 - comparison of thermal decomposition and explosion **19**: 439
 - in condensed phase **18**: 413
 - primary, secondary and inverse **18**: 416
- Kinetic Modelling techniques **23**: 526
- KIVA reactive hydrodynamics code **20**: 457,458
 - computer code **21**: 486
- Laser-induced fluorescence **21**: 507
- Laser irradiation,
of explosives **29**: 653,655
- Laser-schlieren movies **20**: 458
- LCGTO-X α (LSD) calculations **6**: 132-136
- Lead azide emission spectrum
after laser irradiation **29**: 666,672,673
- Lead styphnate emission spectrum
after laser irradiation **29**: 666-668,670,672,673
- Liquefaction at high heating rates **13**: 311
- Lone pair σ -conjugation, stabilization by **9**: 175,190
- Low energy CID,
in mass spectrometry **30**: 686
- Many-body interaction,
in closed shell systems **23**: 529
- Mass spectra of detonation products **21**: 495,497
- Mass spectrometry **31**: 695
 - conventional **14**: 330
 - limitations in decomposition studies **14**: 331

- Material properties,
 - effecting energetic materials behavior **14:** 327,328
- MCSCF methods **23:** 527
- Mechanical Coupling Coefficient,
 - during laser pulse **29:** 658
- Mercuric fulminate emission spectrum,
 - after laser irradiation **29:** 668,669,674
- Metalions,
 - effect of, on nitramine thermolysis **13:** 292
- Methyl nitramine,
 - reaction with H atoms **3:** 39
- MIKE-CID spectrometer **30:** 687
- Modeling of detonation **20:** 458; **21:** 486
- Molecular architectures of C-H-N-O atoms **28:** 641
- Molecular beam,
 - detection **21:** 480
 - mass spectroscopy **21:** 480
- Molecular dissociation
 - energy transport in **11:** 229
 - energy sharing in **11:** 229
- Molecular dynamics **10:** 195; **11:** 229
 - basis on force-field methods **23:** 529
 - model, one dimensional **10:** 197
 - three dimensional **10:** 198
 - two dimensional **10:** 217
- Molecular dynamics (MD) approach
 - to detonation studies **10:** 195
 - limitations of **10:** 196
- Molecular dynamics simulations
 - of chemical detonation **10:** 196
- Molecular geometry,
 - optimization **3:** 24
- Moller-plesset (MP) many-body perturbation theory **23:** 533
- Moller-plesset perturbation theory **3:** 25
- More powerful explosives **28:** 641
 - synthesis of **28:** 647
- Morse potentials, intermolecular **5:** 102
- Motion of dislocations **10:** 195
- MP2 and MP4 level calculations
 - with HF optimized geometry **23:** 535
- MS/MS
 - daughter ion experiment **30:** 691
 - parent ion experiment **30:** 691
 - neutral loss experiment **30:** 692
- MS/MS-CID **30:** 685

- MS/MS-CID spectra **31**: 695
 of trinitroaromatic compounds **31**: 695,698
 of RDX, HMX **31**: 699
 of nitroadamantanes **31**: 703
 of bishomocubanes **31**: 706
 of polynitrobiphenyl-2-amines **31**: 709-712
 of nitramines **31**: 701
 of TNX **31**: 697
- ¹⁴N NQR spectra of
 monoclinic TNT **32**: 717-719
 orthorhombic TNT **32**: 717-719
- ¹⁵N¹⁸O in study of mixing of products **21**: 507
 N₂O formation in nitramine decompositions **13**: 287,288
 N₂O/NO₂ branching ratios in nitramine decompositions **13**: 287,288
 N-NO₂ bond lengths in nitramines **9**: 187
 N-NO₂ bond strengths and shock sensitivities of nitramines **9**: 189
 Nitramines,
 computational studies of **9**: 175
 Nitramines HMX and RDX,
 thermal decomposition of **15**: 347
 Nitric oxide, solid
 detonation products of **21**: 504,505
 Nitroadamantanes **31**: 703
 Nitroaliphatics, shock sensitivities **8**: 166
 Nitroaromatics
 KDIE Studies **18**: 417-424
 Nitrocellulose,
 polymer chain dynamics of, by NMR/NQR **32**: 730
 glass-to-rubber transition **32**: 730,735
 N-15 NMR of **32**: 731-733
 Nitro cubanes **28**: 648
 Nitroethane,
 decomposition rate constants for **3**: 35
 Nitrogen 1s spectrum,
 of RDX **25**: 572
 of various explosives **25**: 571,572
 of HMX **25**: 573
 Nitrogroup conformation of α -TNT
 by NQR **32**: 721
 correlation with orbital occupation numbers **32**: 722
 Nitrogroup twist angle **32**: 722,724

Nitromethane,

- amine sensitization **27**: 635
- energetic electronic states **5**: 85,86
- excited state geometry optimization of **5**: 85,88
- methyl rotation barrier height **5**: 89
- intermolecular bond architecture in **5**: 123
- pressure dependence of melting point **17**: 403
- sensitization by amines **23**: 533
- thermal decomposition rate **17**: 404
- pressure effects on decomposition **17**: 405,409
- mechanism of decomposition **17**: 407
- NO formation in fast thermolysis of nitramines **13**: 285
- NO₂ density, ρ .N in molecular crystals,
 - definition of **5**: 90
 - table of, for nitrocompounds **5**: 91
 - versus detonation speed **5**: 93
 - versus (ⁿ50), impact sensitivity **5**: 93
- NO₂ formation in fast thermolysis of nitramines **13**: 281-283
- Nonvolatile residue (NVR),
 - catalytic activity of **15**: 364
 - ion signals from decomposition **15**: 361
 - of HMX, elemental analysis **15**: 353
- NQR/NMR Studies
 - of energetic materials **32**: 715
 - of ammonium nitrate **32**: 729,730
 - of nitrocellulose **32**: 730
- Nuclear quadrupole coupling **32**: 715
 - constant, e^2qQ **32**: 715
- Nuclear quadrupole resonance (NQR) **32**: 715
 - origin and detection **32**: 716
 - studies of RDX, HMX, and PETN **32**: 736
- OH radical,
 - from laser irradiation of RDX and HMX **29**: 655
- Optical polarizing microscopy **16**: 379; **17**: 392
- Orbital occupation numbers **32**: 720,722
- Ortho effect **31**: 696
- Oxygen balance **27**: 609
- Oxygen balance in C-H-N-O explosives **8**: 158
- PBX 9404,
 - threshold data for response to impact by steel rods **24**: 553,554
- Performance of explosives **27**: 605
- Phase diagram, equilibrium, for RDX **17**: 397
- Phase transitions,
 - of energetic materials **32**: 715
 - of ammonium nitrate **32**: 726
- Phonon scattering **10**: 201
- Photochemical initiation **29**: 655,658,660

- Photoelectron Spectroscopy,
 - ultraviolet (UPS) **25:** 575
 - synchrotron source **25:** 575
- Photoshock initiation **29:** 655,658,660
- Photothermal initiation **29:** 655,657,658
- Picric acid, emission spectrum,
 - after laser irradiation **29:** 671,672,677
- Picryltriazoles **8:** 167
- Politzer formula **7:** 145,146
- Politzer-Parr core valence separation **7:** 146
- Polymorphs,
 - of RDX **17:** 398
 - of HMX **17:** 393
- Polynitroadamantanes **28:** 652
- Polynitrobiphenyl-2-amines **31:** 709-712
- Polynitropolyhedranes **28:** 642
- Predissociative potentials,
 - intramolecular **5:** 127
- Pre-ignition of energetic materials,
 - molecular aspects **13:** 277
- Pressure dependence,
 - of rate constant of HMX **17:** 395
- Pressure effects,
 - on HMX and RDX decomposition rates **17:** 391,408
- Pressure measurement,
 - ruby fluorescence method **16:** 377,378
- Primary versus secondary nitramines upon fast thermolysis **13:** 291
- Projectile impact,
 - on cased explosives **24:** 550
 - protocol for **24:** 550
 - response of energetic materials to **24:** 545,546
- Propellant combustion **13:** 278
- Propellant vulnerability **24:** 546
- QM MO codes,
 - application to modelling energetic molecules **23:** 526
- Quantum chemical calculations **3:** 24
- Quantum mechanical methods **6:** 131
- Radical attack on energetic materials **3:** 38
- Rate Constant and equilibrium constant, for dissociation **11:** 240
- Rate-controlling Step **18:** 413,414; **19:** 433
- RDX,
 - shock initiated decomposition of **15:** 350
- RDX and HMX,
 - laser decomposition **29:** 670,671
- RDX, emission spectrum,
 - after laser irradiation **29:** 678
- RDX flame,
 - Sensitivity analysis **4:** 74,75
 - Chemical reactions governing lower rate **4:** 75

- RDX ignition modeling **4**: 65-70
 - temperature and major species concentration profiles **4**: 67,70
 - temperature-time profile for **4**: 67
 - gas phase chemistry **4**: 71-74
- Reaction front **10**: 216
 - thermally initiated **10**: 213
 - initiated by shock compression **10**: 213
- Reaction products
 - of propellants and explosives **22**: 511
 - of combustion and detonation **22**: 511
- Reaction zones, of TNT and RDX **21**: 483
- Regressions,
 - of impact measurements for various classes of explosives **27**: 610
- Relative bond strengths **23**: 533
 - in methyl nitrate
 - in nitromethane **23**: 532
- Ruedenberg approximation **7**: 145
- s-p Hybridization of orbitals,
 - determination by UPS and XPS **25**: 580
- Scanning electron microscope (SEM) **26**: 588
 - Micrographs of underwater shocked TATB **26**: 591
 - Micrographs of drop weight impacted TATB and TNT **26**: 592
- SCF Calculations **6**: 131; **23**: 528
 - limitations **6**: 132
- SCF-MO wave functions for polynitroaromatics **8**: 160
- Schlieren Photographs **21**: 477,489
- Secondary explosives,
 - emission spectra **29**: 670
- Second sound in a lattice **10**: 201
 - velocity of **10**: 205
 - longitudinal **10**: 207
- Semi-empirical methods,
 - MNDO, MNDO/3 and AMI **23**: 528
- Sensitiveness,
 - UK definition of **24**: 546
- Sensitivity,
 - UK definition of **24**: 548
- Sensitivity analysis, in modeling **4**: 74
- Sensitivity and electronic levels
 - of explosive molecules **25**: 582
- Sensitivity index,
 - definition of **27**: 610
 - plot against impact sensitivity of explosives **27**: 611,629-631,634
- Sensitivity, various kinds **8**: 158
- Sensitization Centers **26**: 587,588,599
- Shadowgraph images **21**: 490,493
- Shakeup spectra (XPS) of explosives **25**: 581

Shock detonation, KDIE Values
 of HMX **19**: 444
 of RDX **19**: 447
 of TNT **19**: 450
 Shock Detonation of Nitromethane **4**: 63
 temperature and major species profiles for **4**: 65
 Shock front **10**: 206,207,216
 velocity of **10**: 207
 Shock initiation of dissociation reactions **10**: 216
 Shock profile **10**: 208,211,212
 Shock sensitivity **27**: 606
 tests **27**: 605
 Shock sensitivity versus (n/M) R_{ave} **8**: 163
 table for nitramines **8**: 164
 table for nitroaliphatics **8**: 166
 Silver azide emission spectrum,
 after laser irradiation **29**: 664,665,672,673
 Single-determinent theory **23**: 528
 SMATCH/FTIR Spectroscopy **12**: 256, 268-270
 of nitrocellulose **12**: 271
 Solid state effects on thermal decomposition of energetic
 materials **13**: 306
 Soot formation,
 in combustion and detonation **21**: 502
 Sound Velocities, shear **10**: 203
 Spontaneous ignition **1**: 3
 Standard basis sets, categories **9**: 176
 STMBMS,
 quantification procedure **14**: 337
 STMBMS apparatus **14**: 327,332,333
 STMBMS technique,
 applied to HMX and RDX **15**: 348
 STO-3G method for
 energetic electronic states **5**: 83
 STO-3G minimal basis set **6**: 132
 Strain energies,
 theoretical and experimental **6**: 138
 Strain energies, calculated
 for cyclic systems **28**: 647
 Strand burner data,
 for nitrate salt propellants **13**: 315
 Stress Waves,
 longitudinal **10**: 203
 thermalization of **10**: 207
 Structural order,
 local **11**: 238
 Structural relaxation **10**: 195,208
 Structure and bonding of TNT **32**: 720
 Structure and first detected gases,
 correlations, general **13**: 280
 in nitramines **13**: 281-291

Structure/property/decomposition

- correlations **13**: 278
- studies under high heating rates **13**: 279
- Structure-sensitivity relationships **8**: 157
- Structure-thermolysis relationships **13**: 277
- Sub-ignition regime **25**: 573

Tandem BB mass spectrometer **31**: 695Tandem mass spectrometry **31**: 695Tandem mass spectrometry (MS/MS) **30**: 685B-B Configuration **30**: 687MIKE-CID **30**: 687Triple quadrupole **30**: 688Hybrid sector systems **30**: 689Four sector system **30**: 691daughter experiment **30**: 691parent experiment **30**: 691neutral loss experiment **30**: 692

TATB,

thermal decomposition **27**: 633TATB/TATB-d₆thermal decomposition products **18**: 424KDIE **18**: 422critical temperature **19**: 447Temperature profiling/FTIR spectroscopy **12**: 256, 262-264

Tetryl, emission spectrum

after laser irradiation **29**: 671,672

Thermal Coupling Coefficient,

of laser light **29**: 657,658Theoretical maximum density (TMD) **27**: 606

Thermal decomposition,

molecular aspects **13**: 277correlations with impact sensitivity **13**: 307

Thermal decomposition of HMX,

at 3.6 GPa and various temperatures **17**: 394rate equation for **17**: 394Thermal decomposition of energetic materials **12**: 255

Thermal decomposition of RDX

kinetics at different pressures **17**: 401IR spectra of products **17**: 403Thermal diffusion **10**: 201Thermal dissociation **11**: 235Thermal explosion theory **1**: 3Thermal explosions **1**: 1Thermal initiation of dissociation reactions **10**: 216Thermal relaxation mechanism **10**: 195,201,208Thermal runaway in closed systems **1**: 9

Thermal stability versus impact sensitivities in

nitroaromatics **8**: 169

Thermal wave,

in the condensed phase of burning propellants **13**: 313

- Thermochemical decomposition of TNT **18:** 417
 - mechanistic aspects **18:** 421
 - KDIE **18:** 418
 - condensed phase products **18:** 418; **19:** 450
- Thermochemical modeling **3:** 21; **4:** 51
- Thermochemical properties **3:** 21,22
 - BAC-MP4 method for **3:** 22
- Thermohydrodynamic calculations **28:** 645
- Three body energies **23:** 530,531
 - using Gaussian 86 code with 6-31 G basis set **23:** 530
- Three body interactions **11:** 247
- Threshold impact velocity,
 - plots against barrier thickness **24:** 555-557
- Tiger code calculations **28:** 645
- Time-of-flight, velocity analysis **21:** 482
 - measurements **21:** 490
- Time resolved mass spectral data,
 - relation to detonation process **20:** 457
- Time resolved molecular-beam
 - mass spectrometry **21:** 477, 480
- Time-to-exotherm studies,
 - of various compounds **13:** 308
- Time-to-explosion tests
 - of HMX and HMX-d₈ **19:** 440
- TNT
 - KDIE **18:** 418
 - Decomposition products of **18:** 418; **19:** 450
 - products from mechanical impact **19:** 451
- TOF velocity-spectra technique,
 - applied to decomposition of HMX and RDX **15:** 348
 - for molecular weights of pyrolysis products **15:** 334,336
- Townes-Dailey theory of NQR **32:** 720
- Transient infrared absorption (TRISP) **21:** 507
- Transit time of sound waves **11:** 235
- Transmission electron micrograph (TEM),
 - of HMX residue **15:** 353
- Transport software package, Chemkin **4:** 53
- Travelling isothermal waves **2:** 15
- Trigger linkage **27:** 632,633,635
- Trinitro-m-xylene **32:** 723
- UHF calculations **23:** 534
 - of activation energies
 - for unimolecular bond
 - scission to radicals **23:** 534
- Underwater shock,
 - study of effects **26:** 590
 - effects on TATB **26:** 591
- Unimolecular decomposition of HMX and RDX **3:** 43-46
- UPS, ultra violet photoelectron spectroscopy **25:** 575

- Vacancy clusters **10**: 216
- Valence region XPS spectra,
 - of explosives **25**: 580
- Vibrational energy relaxation **11**: 245
- V_{mid} , the electrostatic potentials at midpoint of C-NO₂ **8**: 159
- $V_{\text{mid,max}}$, **8**: 160
 - table for nitroaromatics **8**: 161
 - versus impact sensitivities **8**: 162
- Walker-Wasley criterion
 - of critical energy **24**: 552-554, 558-560
- Water-assisted reactions **3**: 39,41
 - of nitramide **3**: 41
 - of methylene nitramine **3**: 42
- Water formation,
 - in HMX decomposition **15**: 363
- Wavelength effect on laser induced decomposition **29**: 676
- "Weak interactions" between molecules **7**: 152
- $X\alpha$ local spin density approximation **6**: 131,132
 - atomization energies, table **6**: 137
- X-ray diffraction
 - energy dispersive **16**: 385; **17**: 392
 - of α and β RDX **17**: 399
- X-ray photoelectron spectroscopy (XPS) **25**: 569; **26**: 587,588
 - of impacted TNT **26**: 595,596
 - of shocked HMX **26**: 596
 - pyrolyzed HMX **26**: 597,598
 - core level spectra **25**: 570,572
 - valence region spectra **25**: 570,580
 - as a surface probe **25**: 571
 - of control and impacted AP **25**: 573,576
 - spectral resolution of **25**: 571
 - in forensic investigations **25**: 573
 - study of nitration of cellulose **25**: 575
- Zero-point energy (ZPE) **6**: 138
- Zero-point energy,
 - determination of **3**: 25
- Zero-point vibrational energy **18**: 414,415